

Srichand Hinduja  
Paulo Jorge da Silva Bartolo  
Lin Li  
Wen-Yuh Jywe *Editors*

---

# Proceedings of the 38th International MATADOR Conference

# Proceedings of the 38th International MATADOR Conference

Srichand Hinduja · Paulo Jorge da Silva Bartolo ·  
Lin Li · Wen-Yuh Jywe  
Editors

# Proceedings of the 38th International MATADOR Conference

 Springer

*Editors*

Srichand Hinduja  
School of Mechanical, Aerospace and Civil  
Engineering  
University of Manchester  
Manchester, UK

Paulo Jorge da Silva Bartolo  
School of Mechanical, Aerospace and Civil  
Engineering  
University of Manchester  
Manchester, UK

Lin Li  
School of Mechanical, Aerospace and Civil  
Engineering  
University of Manchester  
Manchester, UK

Wen-Yuh Jywe  
Department of Automation Engineering  
National Formosa University  
Huwei, Yunlin, Taiwan

ISBN 978-3-319-64942-9

ISBN 978-3-319-64943-6 (eBook)

<https://doi.org/10.1007/978-3-319-64943-6>

© Springer Nature Switzerland AG 2022

This work is subject to copyright. All rights are reserved by the Publisher, whether the whole or part of the material is concerned, specifically the rights of translation, reprinting, reuse of illustrations, recitation, broadcasting, reproduction on microfilms or in any other physical way, and transmission or information storage and retrieval, electronic adaptation, computer software, or by similar or dissimilar methodology now known or hereafter developed.

The use of general descriptive names, registered names, trademarks, service marks, etc. in this publication does not imply, even in the absence of a specific statement, that such names are exempt from the relevant protective laws and regulations and therefore free for general use.

The publisher, the authors and the editors are safe to assume that the advice and information in this book are believed to be true and accurate at the date of publication. Neither the publisher nor the authors or the editors give a warranty, expressed or implied, with respect to the material contained herein or for any errors or omissions that may have been made. The publisher remains neutral with regard to jurisdictional claims in published maps and institutional affiliations.

This Springer imprint is published by the registered company Springer Nature Switzerland AG  
The registered company address is: Gewerbestrasse 11, 6330 Cham, Switzerland

# Organisation

## Organising Committee

Professor Lin Li (*General Chair*)  
Professor Wen-Yuh Jywe (*Co-Chairman*)  
Professor Srichand Hinduja (*Co-Chairman*)  
Professor Paulo Jorge da Silva Bartolo  
Professor Chun-Jen Chen  
Professor Kuang-Chao Fan  
Professor Ming-Piao Tsai  
Professor Wen-Hsiang Hsieh  
Professor Chih-Hsiung Hu  
Professor Soek-Hee Lee  
Professor D. R. Hayhurst  
Professor P. Mativenga  
Professor Jing-Chung Shen  
Professor M. Smith  
Dr. C. Diver  
Dr. M. Domingos  
Dr. J. Francis  
Dr. R. Heinemann  
Dr. J. Methven  
Dr. A. Pinkerton  
Dr. M. Sheikh  
Dr. A Weightman

## International Scientific Committee

Professor J. C. Aurich, University of Kaiserslautern, Germany

Professor D. Biermann, Technical University of Dortmund, Germany  
Professor M. Brandt, RMIT University, Australia  
Professor K. Cheng, Brunel University, UK  
Professor B. Cheung, Hong Kong Polytechnic University, Hong Kong, China  
Professor Chee Kai Chua, Nanyang Technological University, Singapore  
Dr. K. Cooke, Teer Coatings Ltd, UK  
Professor B. Denkena, Leibniz University Hannover, Germany  
Professor J. R. Dufloy, Katholieke University Leuven, Belgium  
Professor F. Z. Fang, Tianjin University, China  
Professor Wei Gao, Tokyo University, Japan  
Professor D. K. Harrison, Glasgow Caledonian University, UK  
Professor X. Q. Jiang, University of Huddersfield, UK  
Dr. I. Kelbassa, Fraunhofer ILT, Germany  
Professor F. Klocke, RWTH Aachen, Germany  
Professor M. Kunieda, University of Tokyo, Japan  
Professor S. Kurokawa, Kyushu University, Japan  
Professor Z. Y. Jeng, Taiwan University of Science and Technology, Taiwan  
Professor B. Lauwers, Katholieke University Leuven, Belgium  
Professor J. Lawrence, University of Chester, UK  
Professor Y. S. Liao, National Taiwan University, Taiwan  
Professor Y. F. Lu, University of Nebraska, Lincoln, USA  
Professor J. Mazumder, University of Michigan, USA  
Professor J. A. McGeough, University of Edinburgh, UK  
Professor P. Maropoulos, University of Bath, UK  
Professor A. Y. C. Nee, National University of Singapore  
Professor M. K. Park, Pusan National University, South Korea  
Professor F. J. A. M. Van Houten, University of Twente, Netherlands  
Professor F. Vollertsen, BIAS GmbH, Germany  
Professor M. L. Zhong, Tsinghua University, China

# Preface

It gives us pleasure to introduce the Proceedings for the 38th International MATADOR conference. The proceedings include 77 refereed papers from several countries. A substantial number of papers are from China, Japan, India and Taiwan, which reflects the increasingly important role being played by the East Asian countries in manufacturing.

Since its inception in 1959, the MATADOR conferences have been held at various locations within the UK and overseas. The last conference was held at “home”, i.e. Manchester, and this conference is being held at The National Formosa University in Taiwan. It is the second time that this conference is being held in Taiwan.

The MATADOR conferences in the 1960s dealt with metal working fundamentals in cutting, grinding and forming and the design of machine tools. Since those early days, new areas of research in manufacturing have emerged which therefore have become part of the conference’s scope as well. A substantial part of this conference is devoted to laser material processing, additive manufacturing, micro-/nano-fabrication and manipulation. Other areas that are addressed in this conference include metrology and measurement. The conference has continued to attract good quality papers from traditional areas such as machining, design and systems engineering, and innovative manufacturing and design.

We would like to express our gratitude to all the members of the organising committee and to those members of the International Scientific Committee who kindly refereed the papers. Our special thanks to Prof. K. C. Fan whose efforts have made it possible for this conference to take place in Taiwan again. Our special thanks to Ms. Janet Adnams and her team for their assistance in organising this conference

from Manchester; Zhengyi Jiang for his assistance in formatting and preparing the Conference Proceedings; Profs. Wei Gao and So Ito for organizing JSPE Affiliation Sessions; Prof. J. C. Shen and his team for organising the conference at Formosa University.

We hope you find the papers interesting and stimulating.

Manchester, UK  
Manchester, UK  
Manchester, UK  
Huwei, Taiwan  
March 2015

Prof. Srichand Hinduja  
Prof. Lin Li  
Prof. Paulo Jorge da Silva Bartolo  
Prof. Wen-Yuh Jywe  
Co-Chairmen



# Contents

## Additive Manufacturing

**Stress Distribution and Crack Propagation Behavior of Solid  $Al_2O_3$ – $ZrO_2$  ( $Y_2O_3$ ) Eutectics Prepared by Laser Engineered Net Shaping** ..... 3  
D. J. Wu, L. F. Shi, G. Y. Ma, F. Y. Niu, Y. L. Zhang, and D. M. Guo

**Heat Dissipative Effects on Forming Quality of Filaments in FDM Process** ..... 23  
Yande Liang, Wen Cao, Fuben He, Kexin Wang, Hongzhe Zhang, Shaoxing Wang, and Baisen Yang

## Design and System Engineering

**Three-Dimensional Input System by Pinching Gestures for Vehicle Design** ..... 35  
K. Hoshino and K. Hamamatsu

## Innovative Manufacturing and Design

**Conformal Resist Coating Technique for TSV Manufacturing Process by Electrostatic Spray** ..... 49  
S. Kurokawa, T. Hotokebuchi, Y. Uchiyama, K. Miyachi, Y. Kobayashi, T. Hayashi, and K. Matsuo

**A Study on the Physical Mechanisms in Electro-discharge Machining Process** ..... 63  
Shitanshu S. Chakraborty, Gourav Mohata, Souradip Ghosh, and Ashish K. Nath

## Laser Processing

<b>Large Area Nano-gratings Fast Fabricated by Femtosecond Laser on Different Metal Surfaces</b> .....	83
Haiying Song and Shibing Liu	
<b>Experimental Investigation and FE Simulation of Heat Affected Zone in Water-Jet Assisted Underwater Laser Cutting Process of Mild Steel and Titanium</b> .....	91
Yuvraj K. Madhukar, Suvradip Mullick, Shitanshu S. Chakraborty, Som S. Thatoi, and Ashish K. Nath	
<b>Advanced Beam Shaping for Ultrafast Laser Micro-processing</b> .....	105
O. J. Allegre, J. Ouyang, W. Perrie, Y. Jin, S. P. Edwardson, and G. Dearden	
<b>Controlled Fracture of the Soda-Lime Glass with a Contact Ball-Lens in Nd-YAG Laser Thermal Cleavage</b> .....	115
Hung-Hsuan Yean and Jehnming Lin	
<b>High-Rate Laser Processing of Metals Using High-Average Power Ultrashort Pulse Lasers</b> .....	135
J. Schille, L. Schneider, L. Hartwig, and U. Loeschner	
<b>Laser Micro Machining Using Photonic Nanojets</b> .....	153
T. Uenohara, Y. Takaya, and M. Michihata	
<b>Deposition Characteristics and Microstructure of Ni60–Ni Composite Coating Produced by Supersonic Laser Deposition</b> .....	163
Jianhua Yao, Lijing Yang, Bo Li, Qunli Zhang, and Zhihong Li	
<b>2D and 3D Flexible Laser System for Precision Cutting, Welding and Drilling Applications</b> .....	175
M. Naeem and A. Montello	
<b>Study on the Effect of Focal Point Location and Incidence Angle of Laser on Cut Quality of Thick Stainless Steel Sheet by Yb-Fiber Laser</b> .....	191
S. Mullick, S. Shrawgi, A. Kangale, A. Agrawal, and A. K. Nath	
<b>Efficient Copper Micro Welding with Fiber Lasers Using Spatial Power Modulation</b> .....	211
A. Haeusler, B. Mehlmann, A. Olowinsky, A. Gillner, and R. Poprawe	
<b>Laser Micro Welding of Copper on Lithium-Ion Battery Cells for Electrical Connections in Energy Storage Devices</b> .....	225
Paul Heinen, Andre Haeusler, Benjamin Mehlmann, and Alexander Olowinsky	

**Cavity Pressure Dependence on Tensile-Shear Strength of Metal-Polymer Direct Joining** ..... 245  
 F. Kimura, S. Kadoya, and Y. Kajihara

**Machining**

**Using Taguchi Robust Design to Ultrasonic Vibration Assisted Turning AISI 1045** ..... 259  
 Wei-Tai Huang, Der-Ho Wu, and Yi-Siang Chen

**Simulation and Experimental Study on Material Removal Mechanism and Removal Characters of Ultrasonic Machining** ..... 269  
 Jingsi Wang, Keita Shimada, Masayoshi Mizutani, and Tsunemoto Kuriyagawa

**The Effect of Cutting Speed and Tool Material on Hole Quality When Reaming C355 Aluminium Alloy** ..... 281  
 R. Rattanakit, S. L. Soo, D. K. Aspinwall, P. Harden, B. Haffner, Z. Zhang, and D. Arnold

**Performance of Multi-margin Coated Tools in One-Shot Drilling of Metallic-Composite Stack Materials Under Varying Feed Rate and Pecking Conditions** ..... 295  
 C. L. Kuo, S. L. Soo, D. K. Aspinwall, W. Thomas, C. Carr, D. Pearson, R. M'Saoubi, and W. Leahy

**A Basic Investigation of Micro-grooving on Sapphire Wafer with Diamond Tools** ..... 313  
 H. Kasuga, A. Nemoto, N. Itoh, M. Mizutani, and H. Ohmori

**A Study of Surface Generation in Ultra-Precision Machining of Precision Rollers with Patterned Microstructures** ..... 325  
 C. F. Cheung, L. B. Kong, C. H. Mak, M. J. Ren, and S. J. Wang

**Reducing Delamination in Micro Drilling of Carbon Composite Materials** ..... 337  
 E. Pliusys and P. T. Mativenga

**Investigation of Different Cutting Conditions for CFRP Routing with Multi-tooth Tool** ..... 357  
 Kuang-Li Lee, Yao-Yang Tsai, and Kuan-Ming Li

**A New Technology to Achieve Precision Machining for CNC Machines Using Artificial Neural Network** ..... 369  
 Ganesh Kumar Nithyanandam, Matthew Franchetti, and Radhakrishnan Pezhinkattil

**Investigation on Position Dependency of Tool-Workpiece Compliance** ..... 389  
 D. Kono, P. Roh, and A. Matsubara

**Near-Dry and MQL Finish Machining of Mould Inserts** ..... 399  
 Y. L. Chan and X. Xu

**Finite Element Analysis of Machining Heat Treated Titanium Alloy Ti54M** ..... 415  
 Navneet Khanna and Vivek Bajpai

**Study on Frequency Correction in Ultrasonic Horn Design** ..... 429  
 Yande Liang, Jianyu Wei, Fuben He, Dong Chen, He Chen, Kexin Wang, Hongzhe Zhang, and Liming Shu

**Influencing the Process Stability for Tapping Through and Blind Holes by Taps with Radial Lubricant Supply** ..... 441  
 Andreas Steininger, Anton Siller, and Friedrich Bleicher

**On Deposition and Characterisation of TiN-WS<sub>2</sub> Composite Coating and Its Performance Evaluation in Dry Machining of AISI 1060 Steel** ..... 457  
 T. Banerjee and A. K. Chattopadhyay

**Digital Technologies for Splints Manufacturing** ..... 475  
 E. M. Meisel, P. A. Daw, X. Xu, and R. Patel

**Metrology and Measurement**

**A Novel Miniature Laser Diode Interferometer for Precision Displacement Measurements** ..... 491  
 L. M. Chen, K. C. Fan, and H. Zhou

**Design and Testing of a Contact-Type Micro Thermal Sensor for Defect Inspection on Nanometric Smooth Surfaces** ..... 501  
 Y. Shimizu, Y. Ohba, and W. Gao

**Diameter Measurement of Micro-sphere Based on Analysis of Two Wavelength Ranges of Whispering Gallery Modes** ..... 509  
 Masaki Michihata, Akifumi Kawasaki, Atsushi Adachi, and Yasuhiro Takaya

**Investigation of Surface Damages in Contact and Form Measurement with a Force Sensor-Integrated Fast Tool Servo** ..... 523  
 Y. D. Cai, Y. L. Chen, S. Ito, Y. Shimizu, and W. Gao

**Removing the Effects of Linear Axis Errors from Rotary Axis Ballbar Tests** ..... 533  
 J. M. Flynn, A. Shokrani, V. Dhokia, and S. T. Newman

**Tool Holder Sensor Design to Measure the Cutting Forces in CNC Turning for Optimization of the Process** ..... 551  
 Daniel Reyes Uquillas and Syh-Shiuh Yeh

**A Scanning Electrostatic Force Microscope for the Measurement of Material Distribution in Non-contact Condition** ..... 563  
 So Ito, Keiichiro Hosobuchi, Zhigang Jia, and Wei Gao

**Development of *Orthros*, A Thickness Evaluation System for Free Curved Plate-Basic Performance Based on the Measurement Principle** ..... 573  
 Y. Okugawa, N. Asakawa, and M. Okada

**Homodyne Interferometer Using Iodine Frequency Stabilized Laser Diode** ..... 587  
 Tung Thanh Vu, Y. Maeda, and M. Aketagawa

**Comparison of Accuracy Verification Method for X-Ray CT** ..... 601  
 K. Matsuzaki, O. Sato, H. Fujimoto, M. Abe, and T. Takatsuji

**Design of a Texture Monitoring System for PV Solar Cell Efficiency via 3-D Virtual Simulation** ..... 611  
 Richard Y. Chiou, Yongjin (James) Kwon, Tzu-Liang (Bill) Tseng, Michael Mauk, and Aurel Mathews

**Integration of Thermal and Dimensional Measurement—A Hybrid Computational and Physical Measurement Method** ..... 627  
 D. Ross-Pinnock, B. Yang, and P. G. Maropoulos

**Elimination of Gyro Rate Offset by Using a Rotating Mechanism for Large Scale Straightness Evaluation** ..... 641  
 T. Kume, M. Satoh, T. Suwada, K. Furukawa, and E. Okuyama

**Measurement and Compensation of Pivot Point Positional Error on Five-Axis Machine Tools** ..... 651  
 B. Yang, M. Chappell, J. E. Muelaner, G. Florussen, and P. G. Maropoulos

**A Novel Method of Rotational Error Analysis of Rotary Stages Based on Abbe Principle** ..... 661  
 Yi-Tsung Li and Kuang-Chao Fan

**Liquid Crystal Sensor for Label-Free Monitoring Hydrogen Peroxide Solution** ..... 671  
 Meng-Zhu Zhang, Li-Wei Jhang, and Shug-June Hwang

**An Investigation on Simulation and Identification of Diffracted Moiré Patterns Within Optical Encoders** ..... 679  
 Lei Zhao, Hui Ding, Kai Cheng, and Shi Jin Chen

**Micro/Nano Fabrication and Manipulation**

**Microfabrication of Three-Dimensional Structures Using Nanoparticle Deposition with a Nanopipette** ..... 693  
F. Iwata and J. Metoki

**Large Scale Periodic Structure Fabrication by Scratching Silica-Glass-Precursor Coating** ..... 703  
Sergey Bolotov, Masaharu Hashidume, Keita Shimada, Masayoshi Mizutani, and Tsunemoto Kuriyagawa

**Study of Chipping of Micro Channel in Glass Ultra-hard Material by Micro Machining Technologies** ..... 715  
Jack Y. C. Lin, Zheng-Han Hong, Tsung-Pin Hung, Tsai-Fa Chen, and Yu-Sen Wu

**Monitoring and Control of Machining Operations**

**Cutting Force Control for Multiple Repetitive Canned Cycles in Turning Operation** ..... 727  
Josuet Leoro and Syh-Shiuh Yeh

**Development of In-Situ Hybrid 3-D Measuring Methodology for Critical Dimension Inspection in Large-Scale Robot Machining of Composite Materials** ..... 737  
Liang-Chia Chen, Manh-Trung Le, and Chih-Jer Lin

**Welding**

**Laser Welding of Dissimilar Materials for Electric Vehicle Batteries** .... 751  
M. Naeem and A. Montello

**Dissimilar Metal Laser Beam Welding Between Aluminum and Copper** ..... 763  
Shikai Wu, Jianglin Zou, Rongshi Xiao, and Peng Dong

# **Additive Manufacturing**

# Stress Distribution and Crack Propagation Behavior of Solid $\text{Al}_2\text{O}_3\text{-ZrO}_2$ ( $\text{Y}_2\text{O}_3$ ) Eutectics Prepared by Laser Engineered Net Shaping



D. J. Wu, L. F. Shi, G. Y. Ma, F. Y. Niu, Y. L. Zhang, and D. M. Guo

**Abstract** For revealing the interaction between the crack formation and the stress distribution in the preparation of the solid  $\text{Al}_2\text{O}_3\text{-ZrO}_2$  ( $\text{Y}_2\text{O}_3$ ) eutectics by Laser Engineered Net Shaping (LENS), the stress distribution of  $\text{Al}_2\text{O}_3\text{-ZrO}_2$  ( $\text{Y}_2\text{O}_3$ ) eutectics in LENS process is calculated by the finite element method, and then the solid  $\text{Al}_2\text{O}_3\text{-ZrO}_2$  ( $\text{Y}_2\text{O}_3$ ) eutectics by LENS is prepared to analyze the crack formation mechanism and the interaction between the crack and stress. The results indicate, the numbers of the same layer re-melting during LENS process increased with the laser power increasing and the layer rising. As the re-melting numbers rising, the tensile stress of the cladding layer decreased and its fluctuation gradually weakened. Therefore keeping the more re-melting numbers in LENS process by increasing laser power could reduce the crack susceptibility of the eutectics by LENS. In addition, with the laser power increasing, the residual stress on the top layer of eutectics rise, and finally the residual stress on the cladding top and bottom were nearly the same. In the solid  $\text{Al}_2\text{O}_3\text{-ZrO}_2$  ( $\text{Y}_2\text{O}_3$ ) eutectics prepared by LENS, it was found, with the laser power increasing, the crack length and quantity decreased, and all crack were on the bottom. Considering the stress distribution by calculation, it was considered that the residual stress was not the important factor contributing to the crack formation, and the crack formation and propagation was concerned in the stress distribution in the LENS process. By the stress optimization, we obtained the structure of  $\text{Al}_2\text{O}_3\text{-ZrO}_2$  ( $\text{Y}_2\text{O}_3$ ) eutectics with near-free defects.

**Keywords** Additive manufacturing · Laser engineered net shaping ·  $\text{Al}_2\text{O}_3\text{-ZrO}_2$  ( $\text{Y}_2\text{O}_3$ ) eutectics

---

D. J. Wu (✉) · L. F. Shi · G. Y. Ma · F. Y. Niu · Y. L. Zhang · D. M. Guo  
Dalian University of Technology, Dalian, Liaoning 116024, People's Republic of China  
e-mail: [djwudut@dlut.edu.cn](mailto:djwudut@dlut.edu.cn)



## 1 Introduction

It is well known that the most effective approach to improve the thermal efficiency and the thrust-to-weight ratio of aero-engines is to increase the turbine inlet temperature. The inlet temperature that the aero-engines with a thrust-to-weight ratio over 10 require exceeds 1700 °C. However, the temperature capability of single crystal Ni-based super-alloys for the turbine blades is approximate 1180 °C, which is far from meeting the demands of the aero-engines with the high thrust-to-weight ratio [1, 2]. The directionally solidified  $\text{Al}_2\text{O}_3\text{-ZrO}_2$  ( $\text{Y}_2\text{O}_3$ ) eutectics have recently attracted considerable attention as promising candidate for the new generation structural materials for high-temperature applications, due to their outstanding mechanical properties and thermal and microstructural stability up to temperatures very close to the melting point [3–5].

Up to date, the oxide eutectic ceramics can be obtained through several different solidification methods such as Bridgman [6], Edge-defined film-fed growth (EFG) [7], Micro-pulling down (u-PD) [8, 9] and Laser heated zone re-melting (LHFZ) [10–12]. Among these methods, however, the Bridgman method is limited by the large interphase spacing (typically order of 20  $\mu\text{m}$ ), which deteriorates properties, and other methods are only able to prepare the samples with small size and simple shape. Laser Engineered Net Shaping (LENS) is a novel rapid additive manufacturing technique, which provides an ideal platform to rapidly produce large three-dimensional parts with any complex geometry directly from the powders of metals, alloys, or ceramics layer by layer without any preforming or post-processing, such as sintering or machining [13]. However, there will be large thermal stresses in the fabricated specimens due to the intensive heat input and high cooling rate in the LENS process and when the thermal stresses exceed the ultimate strength of materials, cracks will occur. To provide a fundamental insight into the interaction between the crack formation and the stress distribution in the preparation of the solid  $\text{Al}_2\text{O}_3\text{-ZrO}_2$  ( $\text{Y}_2\text{O}_3$ ) eutectics in LENS, it is essential to investigate the thermal behavior within the solid  $\text{Al}_2\text{O}_3\text{-ZrO}_2$  ( $\text{Y}_2\text{O}_3$ ) eutectics during the LENS. However, the LENS deposition is a rapid solidification process that occurs under the non-equilibrium conditions, and solidification is completed in a few milliseconds. Recording the temperature variation over such short times is a challenge with the experimental methods, given the limitations in response time as well as temperature resolution. Therefore, the numerical simulation such as with the finite element method (FEM) and the finite difference method (FDM), could be effectively implemented to understand the thermal history of the entire sample during deposition. A number of studies have simulated the thermal behavior during the LENS deposition. Ye et al. [14] developed a 3D finite element model to predict the temperature distribution during the process, especially near the molten pool. Their results showed well agreement with the experimental observations. Wang and Felicelli [15] predicted the temperature distribution during the deposition of SS316 as a function of time and process parameters by developing a 2D thermal model, but only for one layer of deposition. Later, they developed a 3D finite element model using the commercial software SYSWELD to study the

molten pool size by analyzing the temperature and phase evolution in stainless steel 410 (SS410) during the LENS deposition of a thin-walled structure [16]. Xiong et al. [17] studied the thermal behavior of WC–Co cermet during laser deposition involving complementary results from in-situ high-speed thermal imaging and 3D finite element modeling and provides a fundamental insight into the evolution of the microstructures. Long et al. [18] developed a 3D multi-track and multi-layer model for laser metal deposition shaping (LMDS) with ANSYS parametric design language (APDL), and detailed numerical simulations of temperature and thermal stress were conducted. The distribution of temperature, temperature gradient, von Mises stress, X-directional, Y-directional and Z-directional thermal stresses were studied. Kong et al. [19] developed a 3D multi-track and multi-layer finite element model during the laser metal deposition shaping (LMDS) process of Ti–6Al–4V (TC4) and the temperature field, temperature gradient, thermal stress field and distribution of residual stress were obtained. Although great progress has been made about the numerical simulation in the LENS, all the studies are mainly focused on the metals or their alloys. The literature shows the absence of a model for the prediction of the thermal behavior of oxide eutectic ceramics in the LENS process.

In this paper, we developed a 3D finite element model using the commercial software ANSYS to simulate the temperature and stress distribution of  $\text{Al}_2\text{O}_3\text{--ZrO}_2$  ( $\text{Y}_2\text{O}_3$ ) eutectics in LENS process. And the solid  $\text{Al}_2\text{O}_3\text{--ZrO}_2$  ( $\text{Y}_2\text{O}_3$ ) eutectics are also prepared to analyze the crack formation mechanism and the interaction between the crack and stress.

## 2 Numerical Simulation

In the simulation, the laser power adopted was 385 W, 454 W, 530 W and 582 W. The traverse velocity of the laser beam was set as 400 mm/min. The powder feed rate was set as 2.09 g/min and the diameter of the laser beam was 2 mm.

### 2.1 Assumption

To simplify the numerical simulation, the preceding assumptions are summarized below.

1. The effect of the inert gas, which is used to deliver the powders on the molten pool is neglected.
2. The  $\text{Al}_2\text{O}_3\text{--ZrO}_2$  ( $\text{Y}_2\text{O}_3$ ) deposit and the substrate are assumed to have isotropic properties.
3. The effect of latent heat due to the phase changes in the deposition process is neglected.

## 2.2 Thermo-mechanical Property of the $\text{Al}_2\text{O}_3\text{-ZrO}_2$ ( $\text{Y}_2\text{O}_3$ ) Eutectics

The thermo-mechanical property data of the  $\text{Al}_2\text{O}_3\text{-ZrO}_2$  ( $\text{Y}_2\text{O}_3$ ) eutectics used in the finite element analysis was obtained from [20–23]. The heat in the molten pool is not only conducted but also convected due to the fluid flow. In this paper, it was imitated by increasing the thermal conductivity of the material at temperatures over the melting point [24].

## 2.3 Modeling and Meshing

In the simulation, the  $\text{Al}_2\text{O}_3\text{-ZrO}_2$  ( $\text{Y}_2\text{O}_3$ ) was used for both the sample and the deposited substrate. The geometric model used in the simulation had the same outline as the prepared part. The modeled  $\text{Al}_2\text{O}_3\text{-ZrO}_2$  ( $\text{Y}_2\text{O}_3$ ) wall-shaped sample had the geometrical size of 20 mm (Length)  $\times$  3.46 mm (Width)  $\times$  6.75 mm (Height), corresponding to a 25-layer wall. The thin-wall sample was placed on the center of the substrate and the dimensions of the substrate was assumed to be 22 mm (Length)  $\times$  8 mm (Width)  $\times$  3 mm (Height). An eight-node solid70 element was chosen to discretize the geometric model. A dense mesh of finite elements was chosen for the sample/substrate contact interface and its surrounding area, where higher thermal gradients were expected. For comparison purposes, the finite element mesh and geometry of this  $\text{Al}_2\text{O}_3\text{-ZrO}_2$  ( $\text{Y}_2\text{O}_3$ ) sample and the prepared part are illustrated in the Fig. 1. As the laser beam moved along the positive X direction (shown in Fig. 2) for the first pass and along the opposite direction for the second pass in the next layer, there was a significant difference in the processing condition between the central and the edge of the sample. Therefore, the nodes shown in Fig. 2 were chosen as the characteristic points to demonstrate the variation of the temperature and thermal stress in the LENS process.

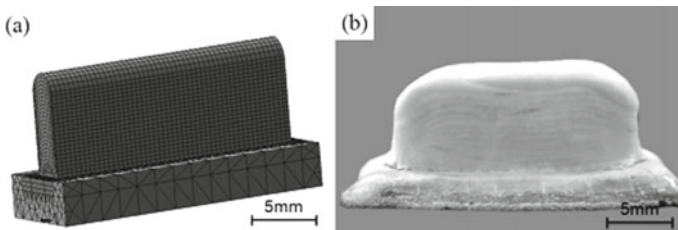


**Fig. 1** Images of **a** finite element model and **b** the prepared sample

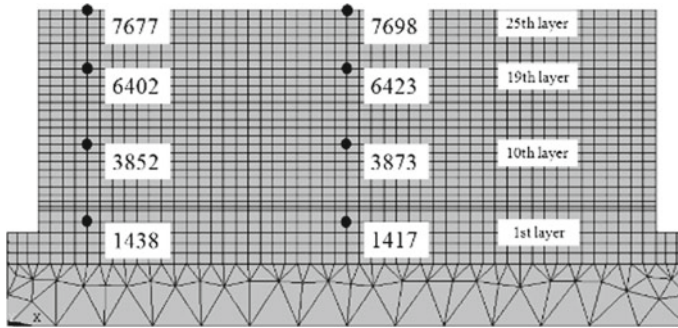


Fig. 2 Location of the characteristic points on the traverse section of the thin-wall sample

## 2.4 Initial and Boundary Conditions

For the properties of the  $\text{Al}_2\text{O}_3\text{-ZrO}_2$  ( $\text{Y}_2\text{O}_3$ ) were assumed to be isotropic, to calculate the temperature distribution, the finite element method was used to numerically solve the following heat conduction equation:

$$\rho(T)c(T)\frac{\partial T}{\partial t} - k(T)\left(\frac{\partial^2 T}{\partial x^2} + \frac{\partial^2 T}{\partial y^2} + \frac{\partial^2 T}{\partial z^2}\right) - Q = 0 \quad (1)$$

where  $T$  is temperature,  $t$  is time,  $k(T)$  is the thermal conductivity,  $\rho(T)$  is the density,  $c(T)$  is the specific heat and  $Q$  is the internal energy.

The initial condition in the computational domain is set to a uniform temperature field:

$$T(x, y, z, t = 0) = T_0 \quad (2)$$

An essential boundary condition is imposed on the bottom surface of the substrate, given by:

$$T(x, y, z = 0, t > 0) = T_0 \quad (3)$$

The initial temperature of the element to be formed was set at room temperature (298 K) and the initial thermal stress was zero. To reduce the computation time, a combined radiative and convective heat transfer coefficient was applied on the surface of the sample and the substrate, since the radiation term in the boundary condition made the analysis highly nonlinear [25]. The moving laser beam could be simulated automatically using an ANSYS parametric design language (APDL) program to provide a heat flux boundary condition (absorbed laser energy) at different positions and times. The laser heat was held for the birth time of that new element. The method applied here assumed a uniform energy distribution; part of the energy generated by

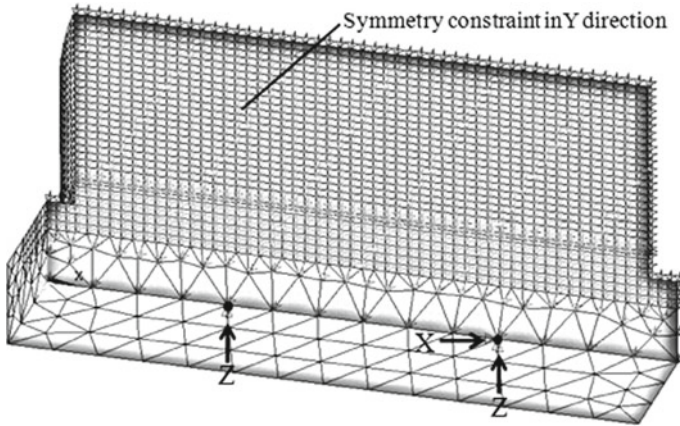


**Fig. 3** Constraints of degrees of freedom of the model

the laser beam was absorbed by the current deposited material and the rest by the front layer.

Before calculating the thermal stress in the LENS process, the degree of freedom of the sample should be restricted. The symmetry constraint was applied on the symmetry plane in the Y direction to restrict the displacement in the Y direction and the rotational degree of freedom in the X and Z direction. Considering the warping deformation of the  $\text{Al}_2\text{O}_3\text{-ZrO}_2$  ( $\text{Y}_2\text{O}_3$ ) substrate in the LENS process, it was not reasonable to apply the multiple constraints, therefore, the constraints applied on the substrate are shown in Fig. 3.

### 3 Verification Test

In this paper, the thermocouple was used to measure the temperature in the deposition process to verify the numerical simulations. The experimental parameters were as follows: the laser power was 385 W; the traverse velocity of the laser beam was set as 400 mm/min; the powder feed rate was 2.09 g/min and the diameter of the laser beam was 2 mm; the thermocouple bead was inserted into the deposition zone and the in-situ temperature data for the 25 deposition layers was obtained. It is observed from Fig. 4 that although there were some errors, the temperature curve predicted by the numerical simulation was consistent with the trend shown in the experiment data. It was acceptable to consider that the numerical simulation result was valid.

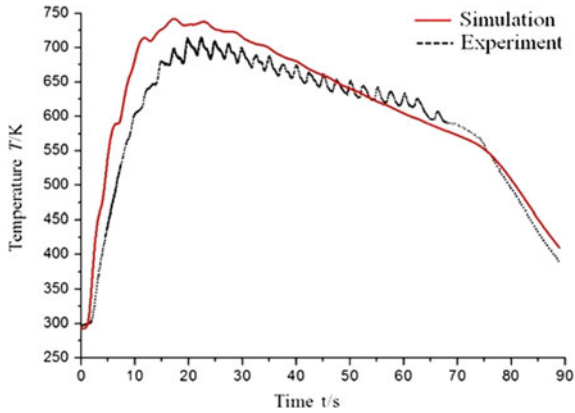


**Fig. 4** Comparison of the temperature curves between the numerical simulation and the experiment data

## 4 Result and Analysis of Temperature Distribution

### 4.1 Temperature Distribution

Figure 5 illustrates the temperature distribution of the thin-wall sample at the end of the LENS process (69 s), where the laser power is 385 W. The temperature distribution of other laser power was similar to that of 385 W. It could be observed from Fig. 5

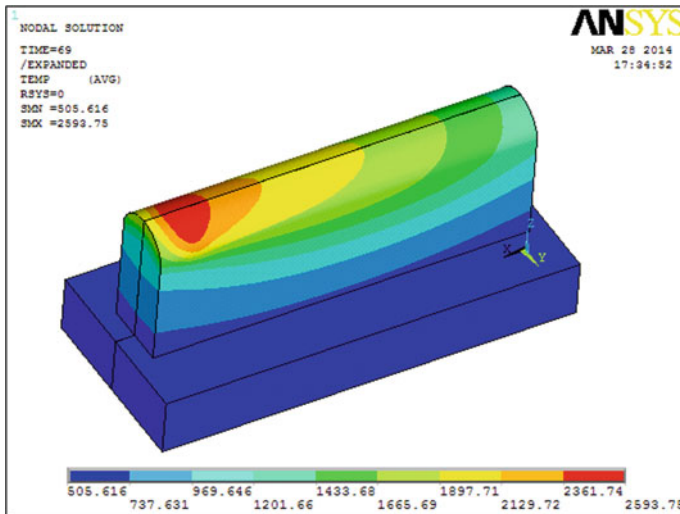


**Fig. 5** Temperature distribution of the thin-wall sample at the end of processing (P = 385 W)

that the heat mainly transferred from the top of the sample to the substrate, which meant the substrate beneath the wall was the sink of heat flux. It was also found that the molten pool was not spherical, but approximates an elliptical shape and the length of it was evidently larger than its width. The temperature gradient was relatively low at the end of the processing due to the integrated heat of the substrate and previous layers. As the thermal conductivity of the  $\text{Al}_2\text{O}_3\text{-ZrO}_2$  ( $\text{Y}_2\text{O}_3$ ) was low, the temperature of the  $\text{Al}_2\text{O}_3\text{-ZrO}_2$  ( $\text{Y}_2\text{O}_3$ ) substrate was high, indicating that there was a slow cooling process after the deposition.

## 4.2 Temperature Cycles of the Characteristic Points

Figure 6 displayed the thermal cycles of the different characteristic points shown in Fig. 2 for the laser power of 385 W. Each peak indicated that the laser beam passed over or near the pre-defined location, from initial layer to subsequent layer depositions. It could be observed that as the wall height increased, the nominal temperature of the characteristic points increased and the temperature at the edge of the thin wall was slightly lower than that at the center of the wall. Moreover, when the laser was shut off, the whole temperature of the sample dropped sharply and the temperature of the characteristic points in the upper layers decreased relatively quickly. But the changes were not significant after 20 s, which was an indication that the buck temperature of the sample had achieved a steady-state and temperature was now at a nominal value of about 500 K.

The temperature profiles of the mid-points of layers 1, 10, 19 and 25 for different laser power of 385 W, 454 W, 530 W, 582 W were presented in the Fig. 7.

It could be seen from Fig. 7a that the temperature of the characteristic point 1417 in the first layer reached a peak every time the laser gone over the mid-point of the sample, and then decreased to a minimum value before the laser started scanning a

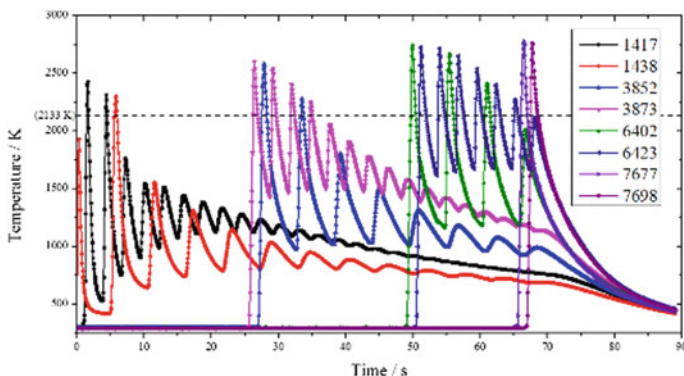


**Fig. 6** Temperature cycles of the characteristic points at different locations ( $P = 385$  W)

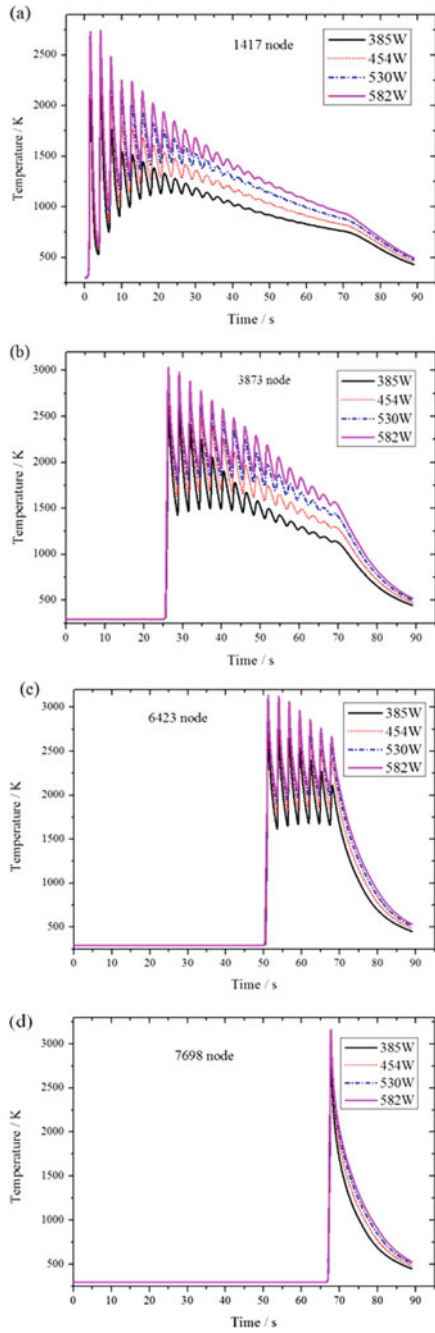


Fig. 7 Temperature profiles of the mid-points for different laser powers



new layer. Moreover, there was an acute fluctuation of the temperature in the initial period of the deposition and as more layers were deposited, the peak temperature for the first layer decreased. As the laser power increased, the average temperature became higher, due to the higher energy input.

It was observed from the Fig. 7b that the average temperature of the characteristic point 3873 in the 10th layer was obviously higher than that of the 1st and the fluctuation of the temperature was also alleviated, which was due to the integrated heat of the substrate and previous layers.

Compared to the characteristic points mentioned above, the average temperature of the characteristic point 6423 in the 19th layer was higher and the fluctuation of the temperature was also relatively alleviated, but the cooling rate after process was more rapid, as shown in the Fig. 7c. There was only once thermal cycle of the characteristic point 7698 in the 25th layer and its cooling rate after 69 s was the fastest, as shown in the Fig. 7d.

## 5 Result and Analysis of Thermal Stress

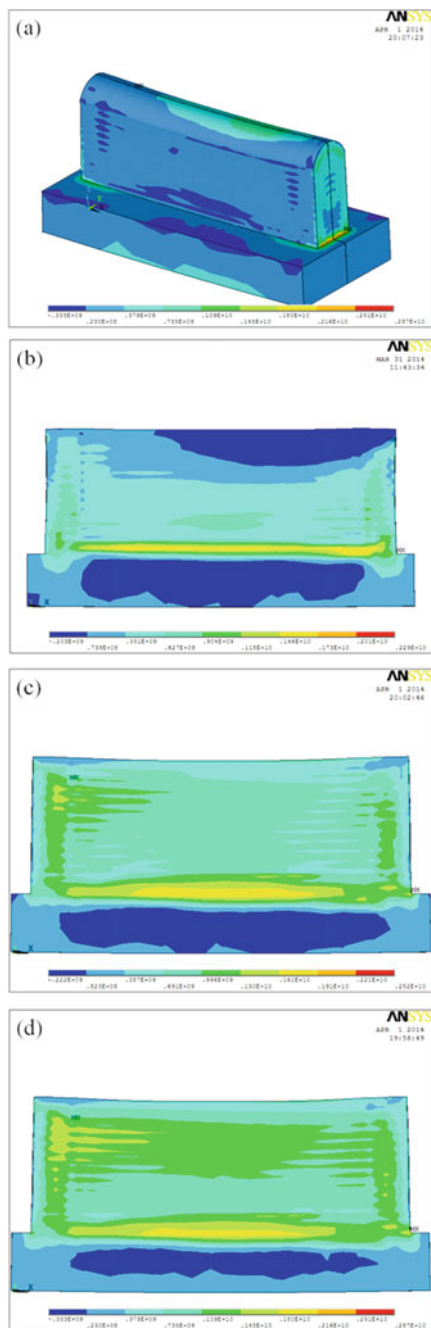
### 5.1 Thermal Stress Distribution

Figure 8 displayed the stress contours of the thin-wall sample for the laser power of 385 W at the different time from 69 to 89 s. Except the values, the stress distribution of other laser powers was similar to that of 385 W.

It can be seen from Fig. 8a that the tensile stress in the outer surface of the sample at 89 s was very low and the value of the stress in some regions was even negative, which meant the stress here was the compressive stress. The maximum tensile stress appeared in the contact area between the sample and the substrate, due to the restriction of the substrate. It was observed from Fig. 8b–d that the tensile stress inside the sample was relatively higher and it mainly concentrated on the boundary of the sample, which was caused by the different cooling rate between the inner and outer surface of the sample. The cooling rate of outer surface of the sample was relatively higher due to the high heat transfer coefficient, which would restrict the shrinkage distortion inner the sample. Therefore, there was a relatively higher tensile stress inside the sample while the stress of the outer surface was lower.

### 5.2 Thermal Stress Cycles of Characteristic Points

The thermal stress cycles of the mid-points of the layers 1, 10, 19 and 25 for different laser power of 385 W, 454 W, 530 W, 582 W were demonstrated. Considering that the fracture of the sample caused by the thermal stress was closely related to the temperature, the temperature cycles during the LENS process were also taken into



**Fig. 8** Stress contours of the thin-wall sample. **a** Outer surface at moment of 89 s, **b** Traverse section at moment of 69 s, **c** Traverse section at moment of 75 s, **d** Traverse section at moment of 89 s

consideration while analyzing the thermal stress variation. Besides, each layer would be reheated by the subsequent pass to above the melting point, and the stress generated before the last re-melting had no impact on the crack formation, therefore, the last re-melting that the characteristic point experienced was marked by the red line. Figure 9 presented the thermal stress cycles of the characteristic points mentioned above.

It could be observed from the Fig. 9a that there was an acute fluctuation of the thermal stress in the initial period of the deposition and as more layers were deposited, its fluctuation gradually weakened but the average stress increased. After 69 s, the stress of the characteristic point decreased firstly and then rose gently, but the rise is not evident. As the laser power increased, the average stress obviously decreased and the time needed to reach the solidification point was longer. Moreover, the fluctuation of the temperature and the thermal stress after the solidification point became more gently. 20 s later after the end of the process, the residual stress for different laser powers was all at a nominal value of about 1.8 GPa.

It can be seen from Fig. 9b that the average thermal stress of the characteristic point 3873 in the 10th layer was much lower than that of the 1st. And in the LENS process, as the laser power increased, the tensile stress of the cladding layer decreased while the re-melting numbers of it increased, which indicated that the intensity and the action time of the tensile stress all decreased with the laser power increasing. However, after the process, the tensile stress of characteristic point for higher laser power increased more rapidly. In 20 s, the residual stress of it was also much larger.

It can be observed from Fig. 9c that when the last cladding layer was deposited, the 19th layer was all reheated to above the melting point except that for the laser power of 385 W, indicating that the action time of the tensile stress which resulted in the crack formation and propagation of the sample was after the LENS process (after 69 s). In addition, as the laser power increased, the final residual stress of the cladding layer was also much higher, which was caused by the discordance of the shrinkage deformation of the sample.

The 25th layer was the last cladding layer and there was only once thermal stress cycle of the characteristic point 6423 in the 25th layer. Moreover, there was no evident variation law of the thermal stress and the final residual stress of this cladding layer was very low, as shown in the Fig. 9d.

The analysis mentioned above could be summarized as:

1. During the LENS process of the  $\text{Al}_2\text{O}_3\text{-ZrO}_2$  ( $\text{Y}_2\text{O}_3$ ) eutectics, the re-melting numbers of the same layer increased with the laser power increasing and the layer rising. As the re-melting numbers rising, the tensile stress of the cladding layer decreased and its fluctuation gradually weakened. Therefore keeping the more re-melting numbers in LENS process by increasing laser power could reduce crack susceptibility of the eutectics by LENS.
2. In the range of the laser power adopted in the experiments, with the laser power increasing, the residual stress on the top layers of eutectics rose, and finally the residual stress on the cladding top and bottom were nearly the same. Therefore crack susceptibility of the top and the bottom cladding layer was nearly the same.

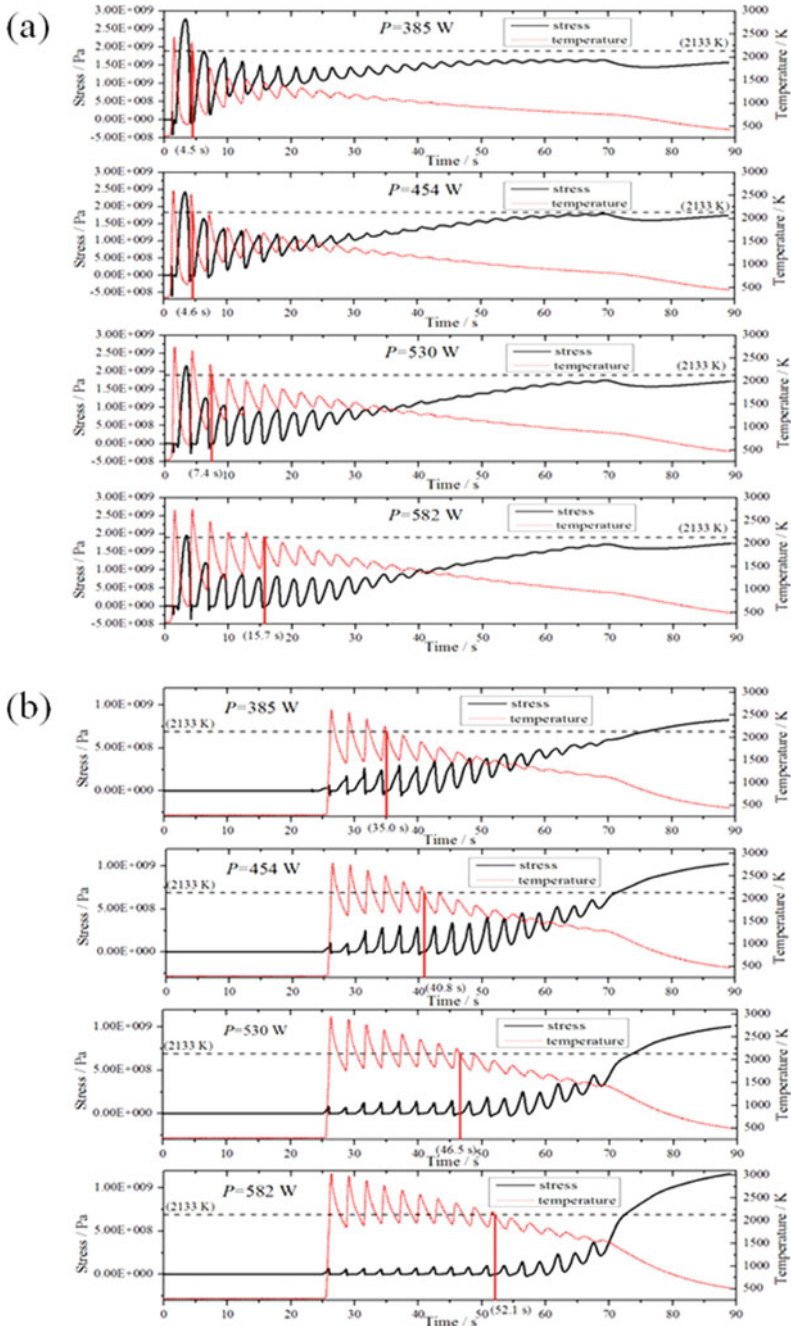


**Fig. 9** The stress curves of the characteristic points for different laser powers. **a** 1417, **b** 3873, **c** 6423, **d** 7698

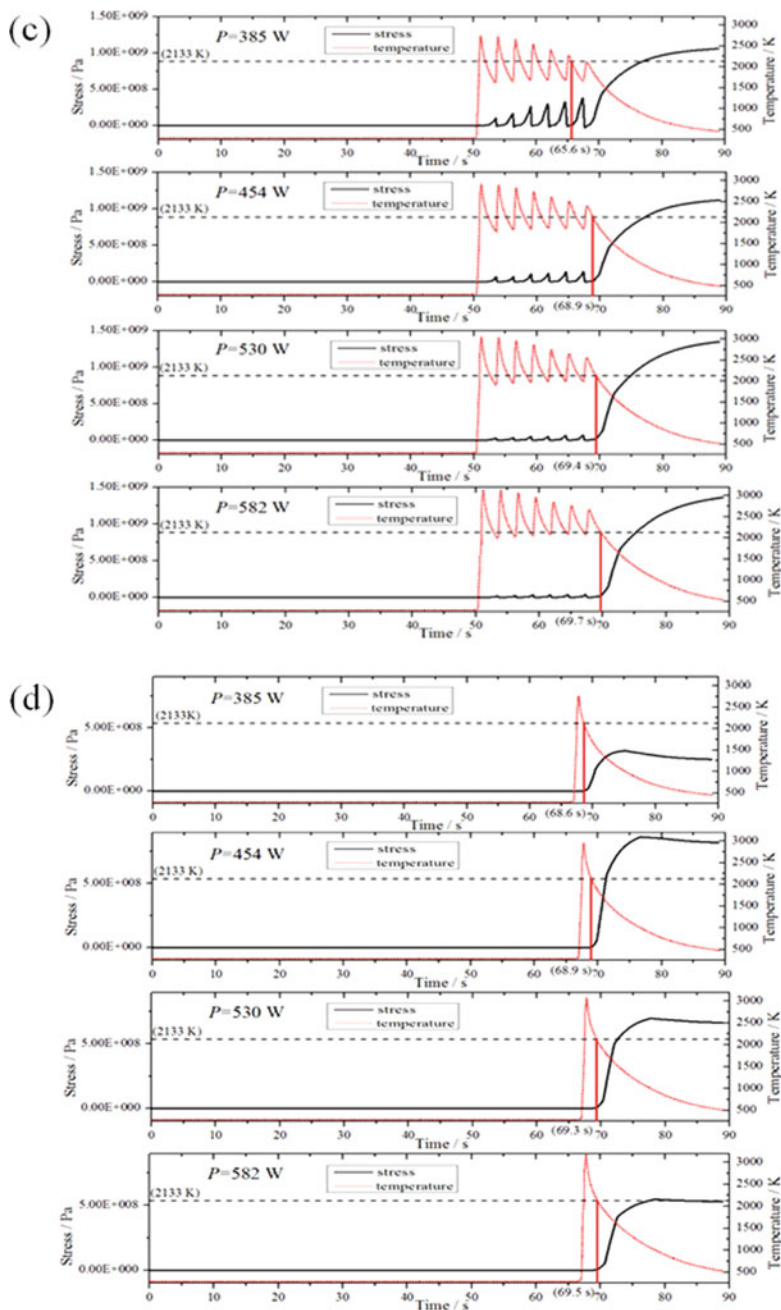


Fig. 9 (continued)

## 6 Mechanism of Crack Propagation in LENS of Solid $\text{Al}_2\text{O}_3\text{-ZrO}_2$ ( $\text{Y}_2\text{O}_3$ ) Eutectics

For a good understanding of the mechanism of crack propagation, based on the simulation results above, the LENS experiment was performed with the same parameters adopted in the simulation (laser power: 385 W, 454 W, 530 W and 582 W; traverse velocity: 400 mm/min.; powder feed rate: 2.09 g/min; diameter of the laser beam: 2 mm). The experimental equipment was RP-503F LENS system with a coaxial feeding nozzle. The continuous wave Nd:YAG laser with output power 1 kW was employed. All experiments were conducted with the high pure  $\text{Al}_2\text{O}_3$  (wt.% > 99.5%) and the  $\text{ZrO}_2$  (8 wt.%  $\text{Y}_2\text{O}_3$ ) ceramic powders of particle sizes in the range of 42–90  $\mu\text{m}$ . After drying at 100 °C for 4 h to eliminate moisture, the two kinds of ceramic powders were put in different containers of the powder feeder respectively and the flow rate of the powders was controlled independently. In this study, the preparation of  $\text{Al}_2\text{O}_3\text{-ZrO}_2$  parts was conducted by mixing ceramic powders with the eutectic ratio of 58.5 wt.%  $\text{Al}_2\text{O}_3$  and 41.5 wt.%  $\text{ZrO}_2$  [26]. To evaluate the cracks numbers of the samples for different laser power, the testing surface of samples was ground in the thickness direction and then repeatedly polished. Finally, the image of the traverse section was obtained by the optical microscope Olympus-MX40F and processed by the image processing software Image-Pro Plus, as shown in the Fig. 10.

Figure 10 shows the crack distribution of the solid  $\text{Al}_2\text{O}_3\text{-ZrO}_2$  ( $\text{Y}_2\text{O}_3$ ) eutectics prepared by LENS for different laser power. It could be observed from Fig. 10a–d that: in the range of the laser power adopted in the experiments, with the laser power increasing, the crack length and quantity decreased and all cracks were on the bottom of the solid  $\text{Al}_2\text{O}_3\text{-ZrO}_2$  ( $\text{Y}_2\text{O}_3$ ) eutectics.

In the range of the laser power adopted in the experiments, there were no evident cracks on the top of the solid  $\text{Al}_2\text{O}_3\text{-ZrO}_2$  ( $\text{Y}_2\text{O}_3$ ) eutectics and all cracks were on the bottom. But the analysis of the numerical simulation mentioned above illustrated that the final residual stress on the top and the bottom cladding layer was nearly the same and the crack susceptibility of the top and the bottom cladding layer was also nearly the same. From the comparison of the residual stress and cracks distribution, it was considered that the residual stress was not the main factor contributing to the crack formation, and the crack formation and propagation was concerned in the stress distribution in the LENS process. Moreover, the cracks distribution of the solid  $\text{Al}_2\text{O}_3\text{-ZrO}_2$  ( $\text{Y}_2\text{O}_3$ ) eutectics coincided with the numerical simulation results that as the cladding layer rose, the tensile stress of the cladding layer decreased and its fluctuation gradually weakened, therefore, the crack susceptibility of the eutectics was reduced.

In the range of the laser power adopted in the experiments, as the laser power increased, the crack length and quantity decreased. It agreed with the numerical simulation results that as the laser power increased, the tensile stress of the cladding layer decreased and its fluctuation gradually weakened, therefore, the crack susceptibility of the eutectics was reduced.

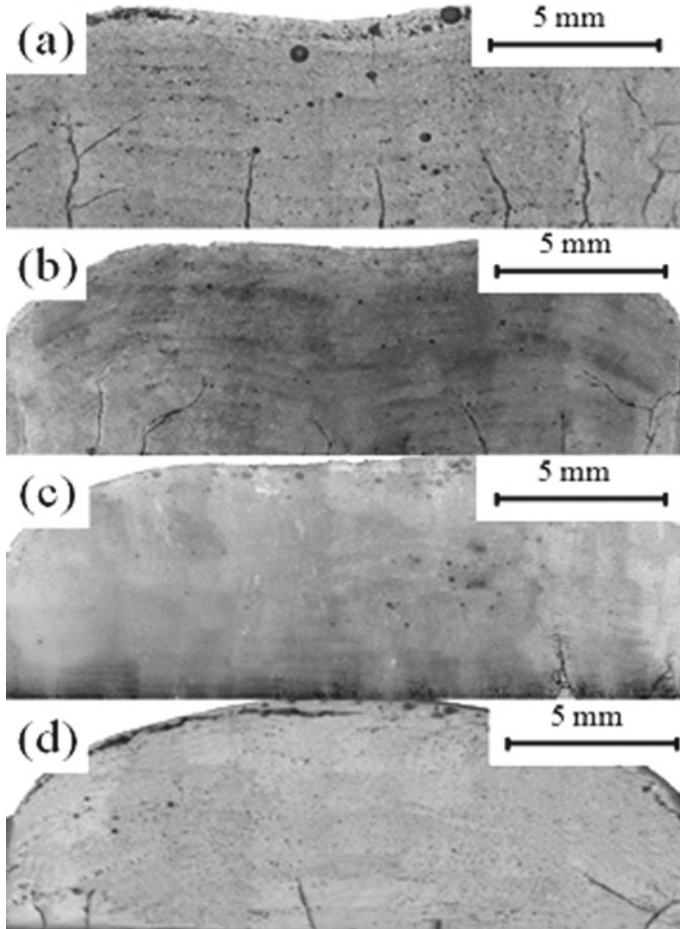


**Fig. 10** Distribution of cracks in transverse section of samples for different laser powers. **a** P = 385 W; **b** P = 454 W; **c** P = 530 W; **d** P = 582 W

## 7 Preparation of Solid $\text{Al}_2\text{O}_3\text{-ZrO}_2$ ( $\text{Y}_2\text{O}_3$ ) Eutectics with Near-Free Defects

According to the analysis of stress mentioned above, the structure of  $\text{Al}_2\text{O}_3\text{-ZrO}_2$  ( $\text{Y}_2\text{O}_3$ ) eutectics with near-free defects was obtained with the optimized process parameters (laser power: > 400 W; traverse velocity: 400 mm/min; powder feed rate: 2.09 g/min; diameter of the laser beam: 2 mm), as shown in Fig. 11.

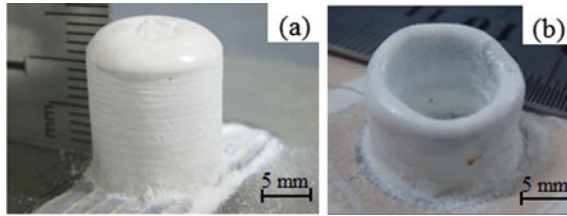


**Fig. 11** Structure of  $\text{Al}_2\text{O}_3\text{-ZrO}_2$  ( $\text{Y}_2\text{O}_3$ ) eutectic ceramic. **a** Cylinder, **b** Circular ring

## 8 Conclusions

To analyze the mechanism of the crack formation and the interaction between the crack and the stress, the stress distribution of  $\text{Al}_2\text{O}_3\text{-ZrO}_2$  ( $\text{Y}_2\text{O}_3$ ) eutectics in LENS process is calculated by the finite element method, and then crack distribution is obtained by the prepared solid  $\text{Al}_2\text{O}_3\text{-ZrO}_2$  ( $\text{Y}_2\text{O}_3$ ) eutectics. The conclusions are summarized below.

1. During the LENS process of the  $\text{Al}_2\text{O}_3\text{-ZrO}_2$  ( $\text{Y}_2\text{O}_3$ ) eutectics, the re-melting numbers of the same layer increased with the laser power increasing and the layer rising. As the re-melting numbers rising, the tensile stress of the cladding layer decreased and its fluctuation gradually weakened. Therefore, keeping more re-melting numbers in LENS process could reduce crack susceptibility of the eutectics by LENS.
2. In the range of the laser power adopted in the experiments, with the laser power increasing, the residual stress on the top layers of eutectics rose, and finally the residual stress on the cladding top and bottom were nearly the same. Therefore crack susceptibility of the top and the bottom cladding layer was nearly the same.
3. In the solid  $\text{Al}_2\text{O}_3\text{-ZrO}_2$  ( $\text{Y}_2\text{O}_3$ ) eutectics prepared by LENS, it was found, with the laser power increasing, the crack length and quantity decreased, and all crack were on the bottom.
4. Considering the stress distribution by calculation, it was considered that the residual stress was not the important factor contributing to the crack formation, and the crack formation and propagation was concerned in the stress distribution in the LENS process.
5. The structure of  $\text{Al}_2\text{O}_3\text{-ZrO}_2$  ( $\text{Y}_2\text{O}_3$ ) eutectics with near-free defects was obtained with the optimized process parameters.

**Acknowledgements** The authors would like to acknowledge the financial support from National Nature Science Foundation of China (No. 51175061, No. 51402037), Science Fund for Creative Research Groups (No. 51321004), Major State Basic Research Development Program of China (No. 2015CB057305) and China Postdoctoral Science Foundation Funded Project (No. 2014M551072).



## References

1. Waku Y, Nakagawa N, Wakamoto T, Ohtsubo H, Shimizu K, Kohtoku Y (1997) A ductile ceramic eutectic composite with high strength at 1,873 K. *Nature* 389:49–52
2. Williams JC, Starke EA Jr (2003) Progress in structural materials for aerospace systems. *Acta Mater* 51:5775–5799
3. Harlan NR, Merino RI, Pena JI, Larrea A, Orera VM, González C, Poza P, Lorca JL (2002) Phase distribution and residual stresses in melt-grown  $\text{Al}_2\text{O}_3\text{-ZrO}_2$  ( $\text{Y}_2\text{O}_3$ ) eutectics. *J Am Ceram Soc* 85:2025–2032
4. Sayir A, Farmer SC (2000) The effect of the microstructure on mechanical properties of directionally solidified  $\text{Al}_2\text{O}_3/\text{ZrO}_2$  ( $\text{Y}_2\text{O}_3$ ) eutectic. *Acta Mater* 48:4691–4697
5. Sayir A, Farmer SC (1995) Directionally solidified mullite fibers. *Mater Res Soc Symp Proc*
6. Schmid F, Viechnicki D (1970) Oriented eutectic microstructures in the system  $\text{Al}_2\text{O}_3/\text{ZrO}_2$ . *J Mater Sci* 5:470–473
7. Čička R, Trnovcová V, Starostin MY (2002) Electrical properties of alumina–zirconia eutectic composites. *Solid State Ionics* 148:425–429
8. Lee JH, Yoshikawa A, Fukuda T, Waku Y (2001) Growth and characterization of  $\text{Al}_2\text{O}_3/\text{Y}_3\text{Al}_5\text{O}_{12}/\text{ZrO}_2$  ternary eutectic fibers. *J Cryst Growth* 231:115–120
9. Lee JH, Yoshikawa A, Kaiden H, Lebbou K, Fukuda T, Yoon DH, Waku Y (2001) Microstructure of  $\text{Y}_2\text{O}_3$  doped  $\text{Al}_2\text{O}_3/\text{ZrO}_2$  eutectic fibers grown by the micro-pulling-down method. *J Cryst Growth* 231:179–185
10. Mesa MC, Oliete PB, Pastor JY, Martin A, Lorca JL (2014) Mechanical properties up to 1900K of  $\text{Al}_2\text{O}_3/\text{Er}_3\text{Al}_5\text{O}_{12}/\text{ZrO}_2$  eutectic ceramics grown by the laser floating zone method. *J Eur Ceram Soc* 34:2081–2087
11. Francisco I, Merino RI, Orera VM, Larrea A, Pena JI (2005) Growth of  $\text{Al}_2\text{O}_3/\text{ZrO}_2$  ( $\text{Y}_2\text{O}_3$ ) eutectic rods by the laser floating zone technique: effect of the rotation. *J Eur Ceram Soc* 25:1341–1350
12. Pardo JA, Merino RI, Orera VM, Pena JI, Gonzalez C, Pastor JY, Lorca JL (2000) Piezospectroscopic study of residual stresses in  $\text{Al}_2\text{O}_3\text{-ZrO}_2$  directionally solidified eutectics. *J Am Ceram Soc* 83:2745–2752
13. Yang J, Wang FD (2009) 3D finite element temperature field modeling for direct laser fabrication. *Int J Adv Manuf Technol* 43:1060–1068
14. Ye RQ, Smugeresky JE, Zheng BL, Zhou YZ, Lavernia EJ (2006) Numerical modeling of the thermal behavior during the LENS<sup>®</sup> process. *Mater Sci Eng, A* 428:47–53
15. Wang L, Felicelli S (2006) Analysis of thermal phenomena in LENS<sup>TM</sup> deposition. *Mater Sci Eng, A* 435:625–631
16. Wang L, Felicelli S, Gooroochurn Y, Wang PT, Horstemeyer MF (2008) Optimization of the LENS<sup>®</sup> process for steady molten pool size. *Mater Sci Eng, A* 474:148–156
17. Xiong YH, Hofmeister WH, Cheng Z, Smugeresky JE, Lavernia EJ, Schoenung JM (2009) In situ thermal imaging and three-dimensional finite element modeling of tungsten carbide-cobalt during laser deposition. *Acta Mater* 57:5419–5429
18. Long RS, Liu WJ, Xing F, Wang HB, Bian HY (2009) Effects of substrate preheating on thermal stress during laser metal deposition shaping. *Chin J Mech Eng* 45:241–247
19. Kong Y, Liu WJ, Wang YC, Bian HY, Zhao YH (2011) Numerical simulation of temperature field and stress field of direct laser metal deposition shaping process of titanium alloys. *Chin J Mech Eng* 47:74–82
20. Wang JF, Carson JK, North MF, Cleland DJ (2008) A new structural model of effective thermal conductivity for heterogeneous materials with co-continuous phases. *Int J Heat Mass Transf* 51:2389–2397
21. Sakaguchi S, Murayama N, Kodama Y, Wakai F (1991) The Piosson's ratio of engineering ceramics at elevated temperature. *J Mater Sci Lett* 10:282–284
22. Adams JW, Ruh R, Mazdiyasi KS (1997) Young's Modulus, flexural strength, and fracture of yttria-stabilized zirconia versus temperature. *J Am Ceram Soc* 80:903–908

23. Ye DL (2002) Handbook of practical mineral thermo-dynamics data. Metallurgical Industry Press, Beijing
24. Lindgren L (2001) Finite element modeling and simulation of welding. Part 2: Improved material modeling. *J Therm Stresses* 24:195–231
25. Zhao HH, Zhang GJ, Yin ZQ, Wu L (2011) A 3D dynamic analysis of thermal behavior during single-pass multi-layer weld-based rapid prototyping. *J Mater Process Technol* 211:488–495
26. Wilkes J, Hagedorn YC, Meiners W, Wissbach K (2013) Additive manufacturing of ZrO<sub>2</sub>-Al<sub>2</sub>O<sub>3</sub> ceramic components by selective laser melting. *Rapid Prototyping J* 19:51–55

# Heat Dissipative Effects on Forming Quality of Filaments in FDM Process



Yande Liang, Wen Cao, Fuben He, Kexin Wang, Hongzhe Zhang, Shaoxing Wang, and Baisen Yang

**Abstract** As known that heat dissipation plays a very important role in the Fused Deposition Modeling (FDM) process, it can obviously affect the forming quality of filaments and the strength of parts. However, there is not much research work on it. In this paper, based on theoretical analysis of FDM process, combining with the actual machining conditions, it investigates and presents three heat dissipative factors including the ventilation rate, the layered area and the envelope temperature. Some orthogonal experiments are implemented, in which the adhesive strength between the layers and the cross-sectional shrinkage rates are measured so as to evaluate the forming quality. The results indicate that lower ventilation rate, smaller layered area and higher envelope temperature will make the adhesive strength between layers of filaments stronger. Furthermore, the influence degree of the three factors is decreased sequentially and some methods to improve the heat dissipative conditions are also proposed.

**Keywords** Fused deposition modeling (FDM) · Heat dissipative conditions · Filaments · Adhesive strength

## 1 Introduction

Fused Deposition Modeling (FDM) is applied widely in the field of additive manufacturing. It makes the thermoplastic material extruded from a nozzle in a state of molten filament and deposited on the substrate or platform in the specified path layer by layer to build 3D entity. Among them, the bonding in adjacent filaments is relied on heat energy and surface potential [1].

At present, FDM commercial machine generally use ABS plastic which has three states which are viscous flow state, rubber and glass state from melting to solidifying

---

Y. Liang (✉) · K. Wang · H. Zhang  
School of Mechanical Engineering, Dalian University of Technology, Dalian 116024, China  
e-mail: [lydjx@dlut.edu.cn](mailto:lydjx@dlut.edu.cn)

Y. Liang · W. Cao · F. He · K. Wang · S. Wang · B. Yang  
Engineering Training Center, Dalian University of Technology, Dalian 116024, China

as an amorphous polymer [2–4]. The transition temperature between rubbery and glassy states is known as the glass transition temperature ( $T_g$ ). The macromolecular chain cannot cross the interface completely in a short-term thermal drive. Only part of backbone can interact with the macromolecular chain of the interface and the adjacent filaments, thus the cohesive force is generated [5]. The adhesive filaments are established on the basis of the inadequate diffusion of interfacial molecular, so the adhesive strength of 3D entity manufactured by FDM is lower than the intrinsic tensile strength of material. Meanwhile, the shrinkage and deformation in the process of filaments' phase transition can affect the size precision of 3D entity, and this effect is tightly correlated with the temperature variation of adhesion surface [6].

## 2 Strength Theory of Adhesive Filaments

Based on the theoretical model of diffusion welding, Yongnian et al. [7] presented the criterion (Eq. 1) for the adhesive strength of FDM filaments, and the relationship Eq. (2) between the adhesive strength of FDM filaments and the criterion by the tests.

$$\psi = \int_0^{\infty} \xi(T) \cdot e^{-k/T} dt$$

$$\xi(T) = \begin{cases} 1 & T \geq T_c \\ 0 & T < T_c \end{cases} \quad (1)$$

in which  $\psi$  is binding potential,  $T$  is the interface temperature,  $k$  is the constant of Binding potential,  $t$  is the diffusion time, and  $T_c$  is the critical temperature to achieve effective adhesive filaments. For ABS filaments,  $T_c = T_g$ .

$$\sigma = \alpha \cdot e^{-\beta/\psi} \quad (2)$$

in which  $\sigma$  represents the adhesive strength,  $\alpha$  and  $\beta$  are the constant parameters.

As formulas (1) and (2) shown above, the adhesive strength of filaments is related to the interface temperature and the diffusion time. The adhesive strength of interface increases with the temperature of the adhesive interface and the time of diffusion.

**Table 1** The characters of ABS-B501

Diameter	$T_g$	Density	Modulus of elasticity	Linear shrinkage rate	Melting temperature
1.75 mm	95 °C	1.05 g/cm <sup>3</sup>	2.2 GPa	0.4%	180–270 °C

**Table 2** Process parameters of test specimens

Layer thickness	Average speed of scanning	Scanning interval	Scanning mode
0.25 mm	30 mm/s	One filament width	Orthogonal by $-45^\circ/45^\circ$

**Table 3** The parameters of air duct

Internal diameter	Adjusting range of wind speed	Adjustment resolution	Resolution ratio
100 mm	0–6.0 m/s	0.1 m/s	$\pm 2.0\%$

### 3 Test and Analysis

#### 3.1 Equipment Preparation

The FDM test equipment is UP 3D printer produced by Beijing Tiertime Co. Ltd. The heating temperature of nozzle was set as 270°C and the diameter of nozzle was set as 0.3 mm. The material type of filaments was ABS-B501 [8, 9] with the characters as shown in Table 1. The technological parameters of specimens are shown in Table 2. The ventilation device was an adjustable air duct whose parameters as shown in Table 3. Figure 1 shows the internal structure of the forming chamber.

#### 3.2 Test Scheme

The adhesive strength among the layers of forming part is a macroscopic manifestation of the adhesive strength of filaments. In order to research the influences of ventilation rate  $u$ , the forming chamber temperature  $T_e$  and sedimentary area on adhesive strength, we designed a tensile test based on orthogonal method. Taking the tensile strength  $\sigma$  of whole layers and the minimum cross-sectional area  $A$  as the evaluation indexes, and using orthogonal Table L9 ( $3^4$ ), we arranged an orthogonal test with 3 factors and 3 levels [10, 11]. The test results are shown in Table 4. The factors between ventilation rate and forming chamber temperature were not independent. Since the orthogonal test only investigated the degree of influence on indexes, the first step was to apply a smaller influence factor as constant value, and the next step was to analyze a bigger influence factor. The ventilation of forming regional

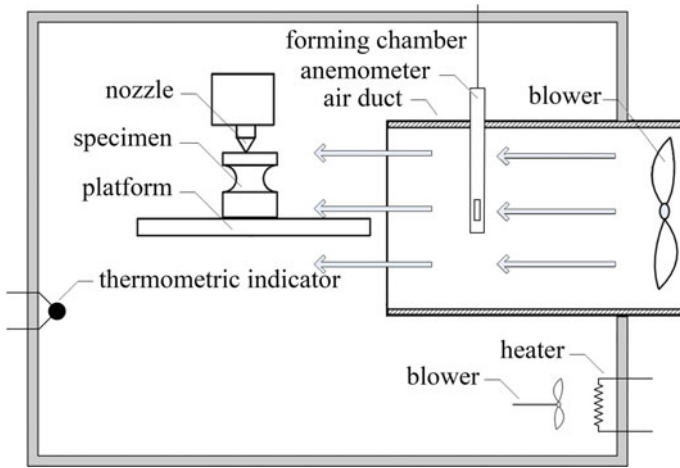


**Fig. 1** The diagram of test device

**Table 4** The orthogonal test results

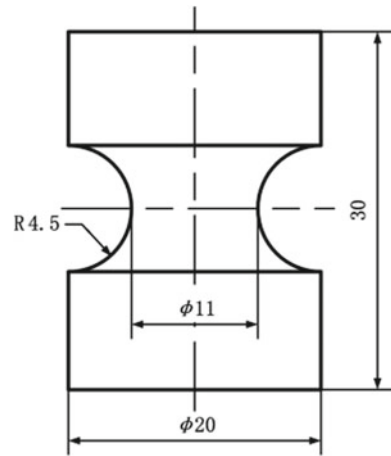
Group	$u$ (m s <sup>-1</sup> )	$T_e$ (°C)	$A$ (mm <sup>2</sup> )	$\sigma$ (MPa)	$\delta$ (%)
1	0	25	100	22.5	5.9
2	0	40	200	16.4	5.7
3	0	55	300	15.3	5.5
4	2	25	200	11.6	1.9
5	2	40	300	8.7	1.7
6	2	55	100	16.6	4.5
7	4	25	300	3.6	0.8
8	4	40	100	13.1	2.5
9	4	55	200	8.3	1.6

was provided by the adjustable air duct with a unilateral horizontal position. The distance between the air outlet and the center of forming area was set as 10 cm. The ventilation rate was defined by the wind speed which was measured at the position 10 cm ahead the air outlet without blocking.

The tensile specimen as illustrated in Fig. 2 was defined as the standard specimen ranged from different minimum cross-sectional areas. Each sampling group included 5 specimens with same cross-sectional area, and after placing for 24 h, the diameter of arc segment was measured by a caliper under the indoor conditions. After that, the average value of shrinkage of the minimum cross-sectional was calculated in each group. To set the loading speed as 0.2 mm/min, the tensile strength between the specimen layers could be measured by the tensile testing machine.

In order to study the qualities of adhesive filaments under different conditions, we observed microstructure of specimens in tensile fracture and arc segment area by

**Fig. 2** Interlaminar tensile test specimen model



the microscope. Furthermore, we also developed an additional test during forming process to detect the temperature changes in the center of minimum cross-sectional with a thermocouple for further studying the temperature variation of the adhesive interface between layers on different levels of each factor.

### 3.3 Results and Analysis

The orthogonal test results are shown in Table 4 and the trend charts of factors are shown in Fig. 3. The trends of two test indicators grow insignificantly with the increasing of temperature in the forming chamber, however, the trends decline

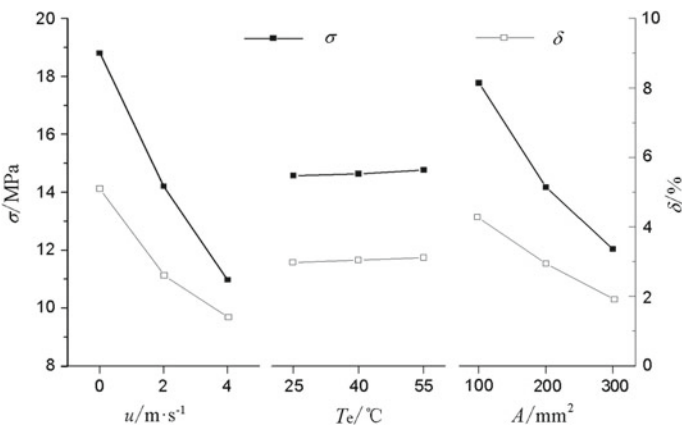
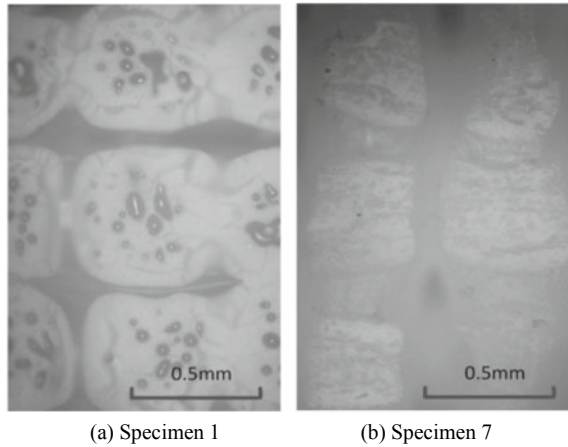


**Fig. 3** The trend charts of orthogonal tests

**Fig. 4** The section microscopic images of specimens (magnified  $\times 100$ )



significantly with the increasing of ventilation rate in forming region or stratified area. It indicates that the tensile strength of the whole layers and the precision of forming size appear the opposite trends to the change of each factor.

Figure 4 shows the section microscopic images of specimen 1 and specimen 7. The section of specimen 1 appeared stress-whitening phenomenon [12], which was the result of crazing or shear yield in polymeric materials under external force with the premise that the molecular chain (primary valences) had fractured [13]. The section of specimen 7 was smooth, so it could be inferred that filaments were bonded together primarily through Van der Waals' force. The analysis above indicated that in different heat dissipative conditions, the inner molecular chain's diffusions and the main mechanism of cohesion action were different. These factors influenced the tensile strength between the specimen layers.

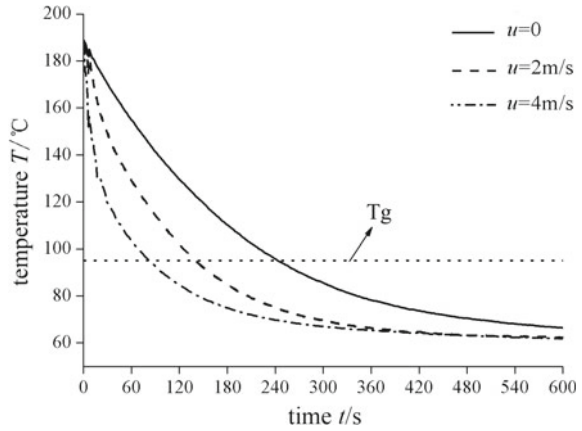
Considering little influence of forming chamber temperature effecting on indexes, the temperature was set as  $55\text{ }^{\circ}\text{C}$  and the other two factors were studied. Figure 5 shows the temperature variation curve of specimens processed in three different ventilation rates with the minimum cross-sectional area  $A = 100\text{ mm}^2$ . When the ventilation rate became higher, the temperature of measured point dropped faster and the temperature of filaments mainly stayed below  $T_g$ .

Figure 6 shows the temperature variation curve of specimens processed in three different cross-sectional areas with the ventilation rate  $2\text{ m/s}$ . When the sectional area was larger, the temperature of measured point sharply dropped in the first few seconds, and then appeared more obvious fluctuation by the influence of the upper temperature of filaments.

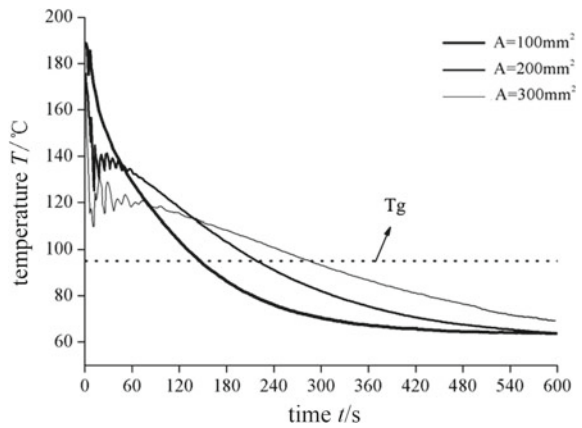
Figure 7a and b are the morphologies of longitudinal arc segments of the specimen 1 and 7 respectively. The vertical direction is the stratification machining direction. Filaments almost fill the entire region as shown in Fig. 7a. But there are some non-uniform gaps appearing in Fig. 7b, which represent the results of higher ventilation rate leading to a higher cooling velocity and the insufficient molecular diffusion of filaments. Figure 7c and d are longitudinal surface topography of two contrastive



**Fig. 5** Comparison of the temperature profiles of different ventilation rates



**Fig. 6** Comparison of the temperature profiles of different sectional areas



specimens processed in the same heat dissipative conditions of specimen 1 and 7 except for the scan distance interval of two filaments widths. In Fig. 7c, the floating part of the filaments is not solidified timely during the deposition process and thereby appearing to fall because of the gravity. In this case, the volume shrinkage and the extent of deformation of the filaments is changing faster than filaments linear shrinkage, which results in a larger extent contraction of the specimen, thus to affect the dimensional precision of the forming part in the horizontal direction. When the layer thickness is constant, the feed amount of the nozzle in the vertical direction is also constant, and the dimensional precision of the forming part in the vertical direction is not affected by the heat dissipative conditions.

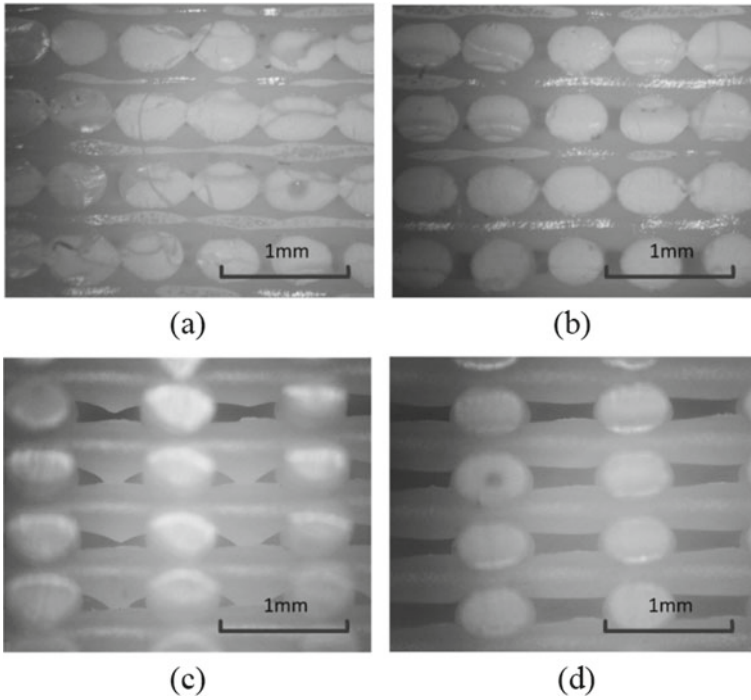
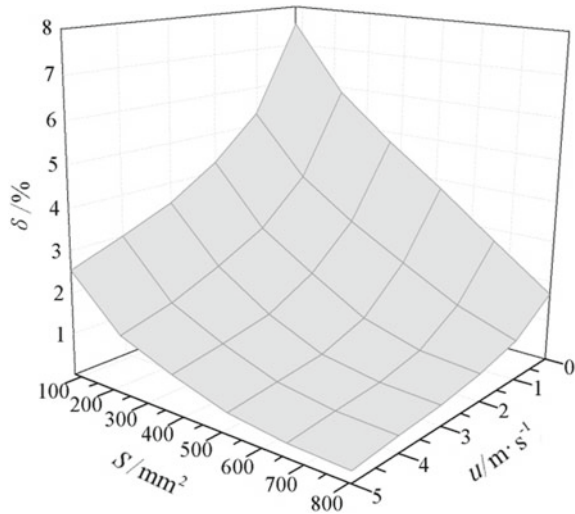


Fig. 7 The longitudinal sections for different specimens (magnified  $\times 50$ )

### 4 Quality Improvement

In order to improve the dimensional precision and adhesive strength of the forming part, the forming process should take shrinkage compensation or select an appropriate ventilation rate in certain thermal conditions. For example, forming part with a circular cross section, when the temperature of forming room achieves  $55\text{ }^{\circ}\text{C}$ , the relationship of the ventilation rates  $u$ , the area  $S$  and cross-sectional shrinkage  $\delta$  is drawn, as shown in Fig. 8, in which the graph data shows the average of the data of the height of 15 mm cylindrical specimens sectional shrinkage of specimen. In no ventilation of process conditions, when the cross-sectional area is larger than  $800\text{ mm}^2$ , the contraction rate is less than 2%. When the dimensional precision satisfies the requirements, it does not have to do the shrinkage compensation. When the cross-sectional area is smaller than  $800\text{ mm}^2$  and the contraction rate is more than 2%, it needs the temperature compensation or cross-sectional shrinkage in the appropriate ventilation rate to meet the requirements of dimensional precision.

**Fig. 8** 3D graphs of the relationship of  $u$ ,  $S$  and  $\delta$



## 5 Conclusion

From the test results and theoretical analysis in the paper, the following conclusions can be drawn.

- (1) The adhesive strength of filaments increases with the temperature of the adhesive interface and the time of diffusion. However, high interface temperature affects shrinkage volume of filaments and decreases the dimensional precision.
- (2) The adhesive strength of filaments increases with the temperature of forming chamber, and decreases with the ventilation rate of forming area and the layered area. Meanwhile, the dimensional precision decreases with the temperature of forming chamber, and increasing with the ventilation rate of forming area and the layered area. The temperature of forming chamber influences little on the adhesive strength and the dimensional precision, thus it can be set as 55 °C.
- (3) When to process the forming parts of minor size, for getting larger adhesive strength and higher dimensional precision, it is required to take shrinkage compensation or to select an appropriate ventilation rate in certain thermal conditions.

## References

1. Novakova Marcinova L, Novak Marcincin J (2012) Testing of materials for rapid prototyping fused deposition modeling technology. *World Acad Sci Eng Technol* 6(9):411–414
2. Rupinder S (2013) Some investigations for small-sized product fabrication with FDM for plastic components. *Rapid Prototyping J* 19(1):58–63

3. Guoliang X, Xiaomo W, Tianhua W (2011) Engineering heat transfer. China Electric Power Press (in Chinese)
4. Jose MA, Istina A, Rnando B (2012) Multi-criteria selection of structural adhesives to bond ABS parts obtained by rapid prototyping. *Int J Adhes Adhes* 33:67–74
5. Zheng F (2005) Strength and failure behavior of polymer material. Chemical Industry Press, pp 7–35 (in Chinese)
6. Tianming W, Juntong X, Ye J (2007) Prototype surface micro-precision in fused deposition modeling process. *Chin J Mech Eng* 20(1):100–105
7. Yongnian Y, Renji Z et al (2000) Research on the bonding of material paths in melted extrusion modeling. *Mater Des* 21(2):93–99
8. Gunay A, Fank S, et al (2013) Calculation of measurement uncertainty for plastic (ABS) material in flexural testing. *Int J Metrol Qual Eng* 1(4):29–33
9. Yongwu W, Weimin Y, Minqi X (2011) ABS resin and its application. Chemical Industry Press (in Chinese)
10. Babur O (2010) Influence of injection parameters and mold materials on mechanical properties of ABS in plastic injection molding. *Int Commun Heat Mass Transfer* 37(9):1359–1365
11. Yunyan L, Chuanbin H (2005) Experimental design and data processing. Chemical Industry Press (in Chinese)
12. Ting C, Guangcheng Z, Rui M (2009) Influence of stress whitening pretreatment on cell structure, foaming behavior, and mechanical properties of AN/MAA copolymer foam. *Polym-Plast Technol Eng* 37(9):897–904
13. Jie Y, Min H et al (2003) The quantitative analysis on fracture surface of polymeric materials. *Guizhou Sci* 2(1):5–8 (in Chinese)

# **Design and System Engineering**

# Three-Dimensional Input System by Pinching Gestures for Vehicle Design



K. Hoshino and K. Hamamatsu

**Abstract** Against the recent background of widespread of 3D technology in output devices, as seen in familiarization of 3D display techniques and commercial-availability of inexpensive 3D printers, the demand for intuitive 3D input interfaces has risen. Several studies of input interfaces capable of recognizing the gestures have been conducted but most of them use the user's fingers to enter the positions actually. These finger-based input interfaces are difficult to provide a so-called click & drag function (as in a mouse) and some of them request the user to take uncomfortable gestures. To address this problem, our study focused on pinching gestures. These pinching gestures provide superior benefits as the gestures, which may contribute to the input interfaces. These benefits include button-clicking-like input operation by means of contact between the fingers; user's comfortable gestures as in daily life; clicking action independent of input of positions and postures; and clear identification between ON and OFF. This study reports the method for detecting 3D finger positions and estimating 3D hand postures in pinching gestures based on information on depth images captured by a depth sensor.

**Keywords** Three-dimensional input system · Pinching gestures · Vehicle design

## 1 Introduction

Car body and body components should be together designed with design, function, and features so as to provide safety vehicle, comfortable driving, and high usability. But it always needs skilled hands with a lot of time, labour, and cost. Three-dimensional input system with highest usability is also needed for that.

To become skilled in the use of tools, typified by 3DCAD and 3DCG, for drawing the three-dimensional shapes of objects on a computer, a high-level of expertise and skill are often required. One of the reasons is less intuitive property of input interfaces as input devices, such as a mouse device, in processing three-dimensional objects.

---

K. Hoshino (✉) · K. Hamamatsu  
University of Tsukuba, 1-1-1 Tennodai, Tsukuba 305-8573, Japan  
e-mail: [hoshino@esys.tsukuba.ac.jp](mailto:hoshino@esys.tsukuba.ac.jp)

Against the recent background of widespread of 3D technology in output devices, as seen in familiarization of 3D display techniques and commercial-availability of inexpensive 3D printers, the demand for intuitive 3D input interfaces has risen. It is desirable that these interfaces enable any gestures that people take in the real world to be entered with no need for a special input device to ensure their intuitiveness. To satisfy this requirement, input interfaces need to recognize the gestures by people. Several studies of input interfaces capable of recognizing the gestures have been conducted but most of them use the user's fingers to enter the positions actually [1, 2]. These finger-based input interfaces are difficult to provide a so-called click & drag function (as in a mouse) and some of them request the user to make uncomfortable gestures [3, 4]. To address this problem, our study focused on pinching gestures.

When people pinch any object, basically their thumb and index finger come into contact with each other or separate them from each other. These pinching gestures provide superior benefits as the gestures, which may contribute to the input interfaces. These benefits include button-clicking-like input operation by means of contact between the fingers; user's comfortable gestures as in daily life; clicking action independent of input of positions and postures; and clear identification between ON and OFF.

Wilson et al. have proposed the method for recognizing pinching gestures using a RGB camera as one of GUI operation methods in the desktop environment [5]. This method makes an elliptical approximation for an internal region defined by the thumb and index finger and detects the position and posture based on the obtained information on the long and short axes of the ellipse. However, only data on relative variation for the posture parameter can be acquired; therefore, it is unsuitable for delicate input.

Moreover, Fukuchi et al. have incorporated the pinching gesture recognition function in gesture input for the table-top entertainment system [6]. In their technique, the gravity center of the internal region defined by the two fingers is assumed to be the coordinate for position input, a line connecting the gravity centers of the internal region and the arm region is used as posture input. Assuming that multiple users use the system simultaneously, this technique provides high-speed processing and allows for postures in the absolute direction; however, it detects the postures in only the direction close to the arm and does not capture the delicate movements of the fingers. In addition, both of the studies, which define the positions based on the gravity center of the internal region defined by the two fingers, are incapable of detecting the positions themselves.

This study reports the method for detecting 3D finger positions and estimating 3D hand postures in pinching gestures based on information on depth images captured by a depth sensor. Moreover, we propose a 3D input interface using the method proposed here.

## 2 System Configuration

The system configuration is as shown in Fig. 1. As can be seen from this figure, the image of a user's hand is captured by a depth sensor attached to the top of a monitor. The sensor DepthSense 325 (SoftKinetic) is used. This inexpensive TOF-type depth sensor is capable of capturing the images with a resolution of  $320 \times 240$  pixels at a maximum of 60 fps.

System input is depth map data, in which 3D coordinates are defined for each of the pixels acquired by the depth sensor. In the output, the finger positions, hand posture, and whether the fingers are in contact with each other or not are detected in pinching gestures as shown in Fig. 2.

Fig. 1 System configuration

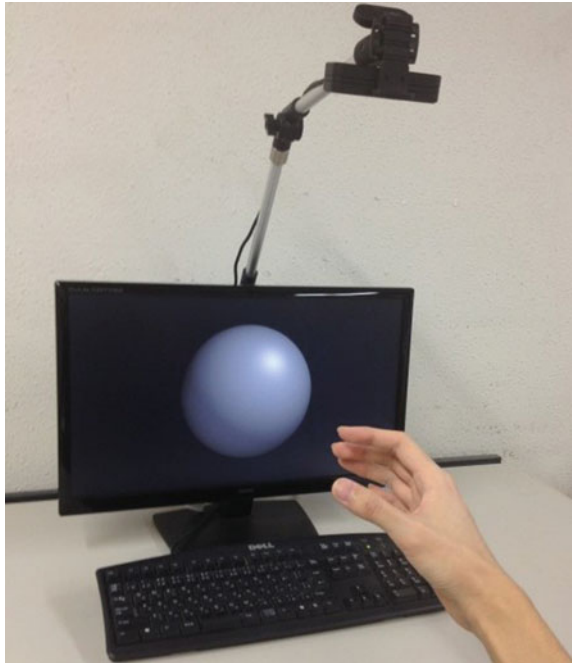
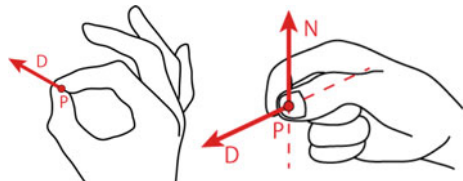
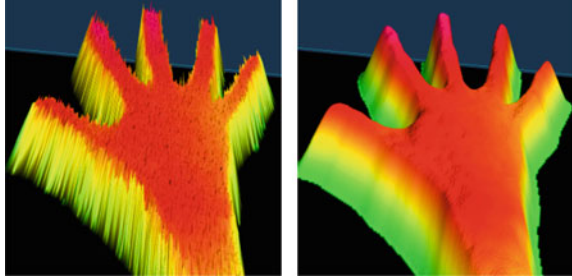


Fig. 2 System output





**Fig. 3** Noise cancellation using the filters



### 3 Pinching Gesture Recognition

#### 3.1 Filtering

The depth information acquired by the depth sensor has mixed noises and across the image is preprocessing for noise cancellation and smoothing using median and Gaussian filters (Fig. 3).

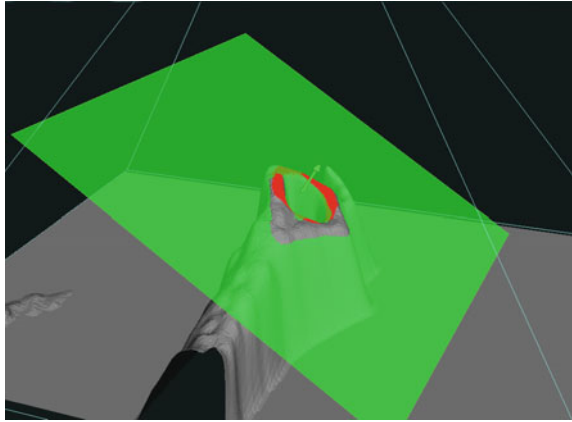
#### 3.2 Extraction of the Internal Contour Regions

To detect pinching gestures on the images, a focus is placed on the closed space defined by the fingers. To extract this close space as a region on the image, the depth gradient between the individual pixels on the depth image is used. The gradients in the x and y direction are calculated for the individual pixels on the noise-cancelled images using a  $3 \times 3$  Scharr filter and the norm of the obtained 2D gradient vector is assumed to be the gradient value for individual pixels. Then, binarization is performed based on the gradient values across the image, making it possible to extract the region corresponding to the hand contour (Fig. 4).

Next, whether any pinching gestures are made or not is detected. The contour regions are compared between the present and previous frames and the number of pixels of the region separated from the largest contour region is calculated. If the

**Fig. 4**  
Depth-gradient-based extraction of the contour region



**Fig. 5** Plane approximation

calculated value is larger than or equal to the threshold, it is determined that two fingers are in contact with each other, namely a pinching gesture is made. The detailed parameters for the pinching gesture are calculated based on the internal contour region in Fig. 4c, which is detected in this process. If the area of the separated contour region is smaller than the threshold, it is determined that no pinching gesture occurs.

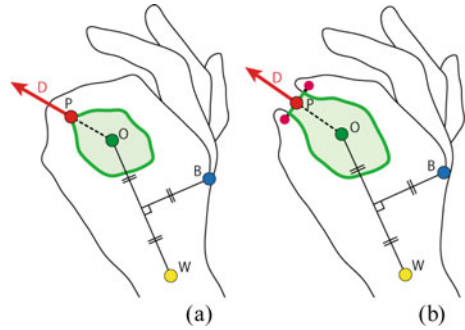
### 3.3 *Plane Approximation by Multi-regression Analysis*

To estimate the hand posture, the shape of the hand in the proximity of the fingers is approximated in a 3D plane based on 3D information on the hand and fingers around the internal contour as described in Sect. 3.2. The sampling points for the hand are extracted to use in approximation. First, the convex hull area the internal region is obtained. Then, the original convex hull area and the whole contour region found in Sect. 3.2 are subtracted from the region obtained from addition of image expansion gain to the area to extract the region as shown in Fig. 4d. The pixels within this region form a group of points, which have 3D coordinates, together, making it possible to approximate the group of points in the special plane by multi-regression analysis using the least-square method (Fig. 5).

### 3.4 *Extraction of Feature Points*

To determine the finger positions and hand postures, some feature points are defined in the plane obtained in Sect. 3.3. First, the center of gravity is calculated on the depth image based on the concave hull area obtained in Sect. 3.3 and the point in the 3D space obtained by projecting the found gravity point into the 3D approximation plane

**Fig. 6** Relationship between the internal contour region and the feature points



is assumed to be O. Second, a sphere, which may cover the finger region around this O point, is defined and the point close to the boundary of the sphere is extracted to obtain the region around the wrist. Third, the point obtained by projecting the center of gravity into the plane is defined as point W, which indicates the wrist position, in the same manner as that in obtaining the point O for this region. Fourth, out of the vertexes of a quadrangle having a line segment OW connecting the points O and W, as a diagonal, the point B on the back of the hand is defined to be B. Finally, among the pixels within the internal contour region obtained in Sect. 3.2, the point obtained by projecting the furthest point from the point B into the approximation plane is assumed to be point P. This point P is defined to be the position coordinate for the finger and used as system output. Moreover, assuming that the vector OP is a directional vector and the normal vector in the approximation plane be an upward vector, the 3D hand postures may be defined in the approximation plane (Fig. 6).

## 4 Pinching Gesture Detection by Finger Detection

When the fingers are not in contact with each other, the internal contour region as shown in the Sect. 3 cannot be extracted, leading to failure to define the finger position and hand postures. To address this problem, the finger positions are detected from the depth image and the contour region is cut off based on the finger position, making it possible to detect almost the same region as that obtained when the fingers are in contact with each other.

## 5 Pinching Gesture Recognition

When the fingers are not in contact with each other, the finger positions and hand postures cannot be defined because the internal contour region as shown in Sect. 3 may not be extracted. The finger positions are detected on the depth image and the

contour region is cut off based on the obtained finger positions, making it possible to detect almost the same region as that obtained when the fingers are in contact with each other.

### ***5.1 Finger Position Detection Using Image Isolation Levels***

The finger positions on the depth image correspond to the end point or extreme point when seen from the hand region. A large difference in depth may be observed between the pixels containing these points and the pixels in the proximity of them. To avoid this difference, the procedure described below is followed to evaluate the difference in depth between the individual pixels and those in the proximity of them and the finger region is extracted based on the values obtained from the evaluation.

First, 32 line segments radially extending from the target pixels on the depth image are defined. The lengths of these line segments are fixed in the 3D coordinate system and their size are preset to that about three times the actual finger size. Second, the individual pixels corresponding to the line segments and the target pixels are compared. If one or more pixels, of which difference in depth from the target pixels is larger than or equal to the thresholds, are detected among the pixels on the line segment extending toward one direction, it is assumed that the target pixels be isolated in the direction. In contrast, if the differences in depth between the pixels on the line segment and the target pixels are all within the threshold, they are assumed to have smooth continuity. This evaluation is performed on the line segments extending in 32 direction and the isolation levels of the target pixels from the pixels in the proximity of them are quantified using the grades of 32. These values are conveniently referred to as isolation levels and the isolation levels for the individual pixels are used for finger region extraction.

A schematic diagram explaining isolation evaluation is shown in Fig. 7. The center points shown in Fig. 7a and b represent the target pixels. In Fig. 7, the line segments in 16 directions are conveniently defined and the isolation levels for the target pixels are quantified; for example, out of 16 line segments, 15 isolated line segments in (a) and 10 in (b).

### ***5.2 Extraction of Finger Positions and the Internal Region***

To obtain the distribution of the end region as shown in Fig. 8a, the isolation evaluation is performed on all the pixels of the depth image. The region, which is rich in higher isolation level of pixels, corresponds to the finger region. The center of gravity of the pixel area (Fig. 8c), which belongs to both of a high isolation region and the contour region, is taken to the points most close to the tips of the fingers in the region, making it possible to detect the finger positions as shown in Fig. 8d. This method, independent of the hand silhouette shape, is capable of detecting robustly the finger

**Fig. 7** Isolation evaluation

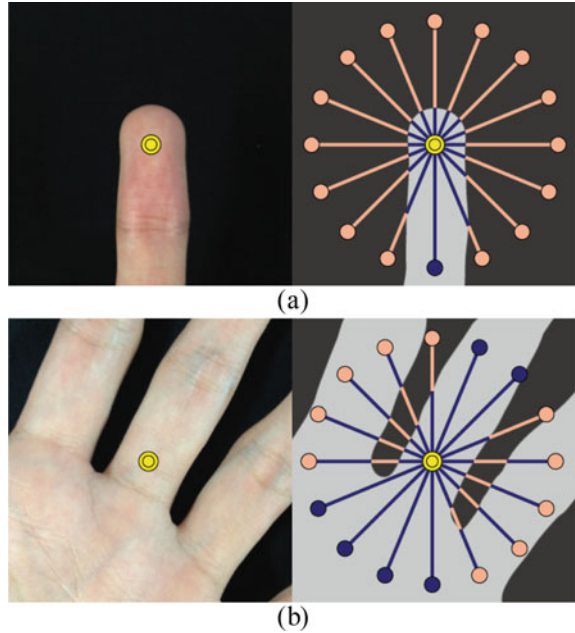


**Fig. 8** Finger position detection based on the isolation distribution



positions even from the area where any change in hand posture and finger position is difficult to detect. Finally, the pseudo internal region is extracted by separating the gradient region based on the line segment connecting the thumb position point and the point of the finger most close to the thumb point (Fig. 9). This region can be treated in the same manner as that of the internal contour region, making it possible to define the feature points. This enables the finger positions and hand posture to be estimated even when the fingers are not in contact with each other (Fig. 6b).

**Fig. 9** Pseudo internal contour region

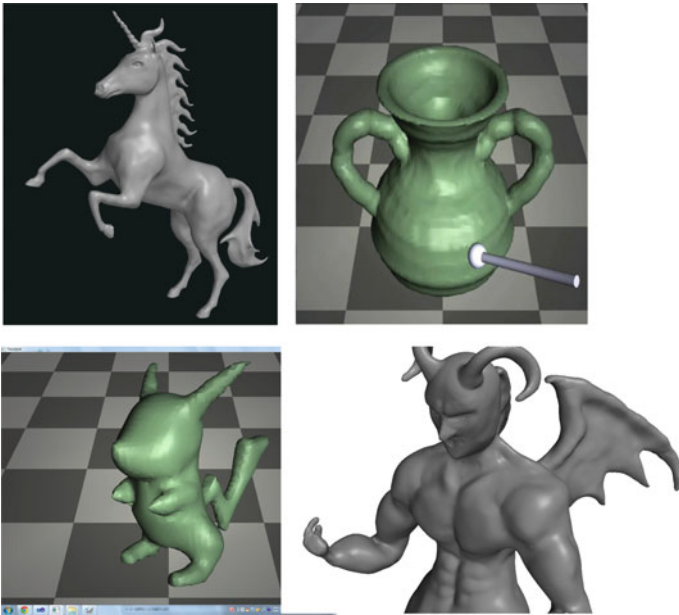


**Fig. 10** Examples of designed 3D shapes with gestures

## 6 Conclusion

To become skilled in the use of tools, typified by 3DCAD and 3DCG, for drawing the three-dimensional shapes of objects on a computer, high-level of expertise and skill are often required. One of the reasons is less intuitive property of input interfaces

as input devices, such as a mouse device, in processing three-dimensional objects. Against the recent background of widespread of 3D technology in output devices, as seen in familiarization of 3D display techniques and commercial-availability of inexpensive 3D printers, the demand for intuitive 3D input interfaces has risen. It is desirable that these interfaces enable any gestures that people take in the real world to be entered with no need for a special input device to ensure their intuitiveness. To satisfy this requirement, input interfaces need to recognize the gestures by people. Several studies of input interfaces capable of recognizing the gestures have been conducted but most of them use the user's fingers to enter the positions actually. These finger-based input interfaces are difficult to provide a so-called click & drag function (as in a mouse) and some of them request the user to take uncomfortable gestures. To address this problem, our study focused on pinching gestures. When people pinch any objects, basically their thumb and index finger come into contact with each other or separate them from each other. These pinching gestures provide superior benefits as the gestures, which may contribute to the input interfaces. These benefits include button-clicking-like input operation by means of contact between the fingers; user's comfortable gestures as in daily life; clicking action independent of input of positions and postures; and clear identification between ON & OFF. This study reports the method for detecting 3D finger positions and estimating 3D hand postures in pinching gestures based on information on depth images captured by a depth sensor. Moreover, we proposed a 3D input interface using the method proposed here. The proposed method, which allows the finger positions and hand posture to be recognized with no pinching gesture, may use the information on whether the fingers are in contact with each other or not as input independent of the finger positions and hand postures. In the future, we will evaluate the accuracy of the proposed method and system usability by conducting experiments on the subjects.

**Acknowledgements** A part of this research was conducted with the assistance of the Strategic Information and Communication R and D Promotion Programme (SCOPE) of the Ministry of Internal Affairs and Communication, KDDI Foundation, and the Adaptable and Seamless Technology Transfer Program through Target-driven R&D (A-STEP) of Japan Science and Technology Agency (JST). The authors would like to extend their sincere gratitude to these organizations.

## References

1. Fukumoto M, Suenaga Y, Mase K (1994) Finger-pointer: pointing interface by image processing. *Comput Graph* 18(5):633–642
2. Sato Y, Kobayashi Y, Koike H (2000) Fast tracking of hands and fingertips in infrared images for augmented desk interface. In: Fourth IEEE international conference on automatic face and gesture recognition, 2000. Proceedings. IEEE, pp 462–467
3. Von Hardenberg C, Bérard F (2001) Bare-hand human-computer interaction. In: Proceedings of the 2001 workshop on perceptive user interfaces. ACM, pp 1–8
4. Zhang Z (2003) Vision-based interaction with fingers and papers. In: Proceedings of the international symposium on the CREST digital archiving project, pp 83–106

5. Malik S, Laszlo J (2004) Visual touchpad: a two-handed gestural input device. In: Proceedings of the 6th international conference on Multimodal interfaces. ACM, pp 289–296
6. Wilson AD (2006) Robust computer vision-based detection of pinching for one and two-handed gesture input. In: Proceedings of UIST'06. ACM Press, pp 255–258



# **Innovative Manufacturing and Design**

# Conformal Resist Coating Technique for TSV Manufacturing Process by Electrostatic Spray



S. Kurokawa, T. Hotokebuchi, Y. Uchiyama, K. Miyachi, Y. Kobayashi, T. Hayashi, and K. Matsuo

**Abstract** Three dimensional IC packaging is a promising key technique for high performance electric and MEMS devices. Through-silicon-via (TSV) is one of the unique features to produce stacking IC devices and photolithography technique is normally used for manufacturing devices chips. Spin coating technique is well used in formation of photo-resist films on the flat wafers, but TSV is a kind of deep hole grooved in the wafer and it is quite difficult to form the conformal resist film thickness in via holes as well as the flat surface by using spin coating. The authors proposed a new technique to form the resist film not only on the wafer surface but in via holes by spray coating technique. Different types of spray including rotary atomizing and electrostatic spray were applied, and the performance of the electrostatic spray was superior to the other. Better electrostatic spraying conditions were investigated by using TSV-TEG wafer and MEMS-TEG wafer. Because the atomized particles get small and almost no accompanying air flow exists, it is found that the electrostatic spray is an effective method especially for TSV in a small diameter. This method is expected to be applied to the complicated three dimensional structures in MEMS field.

**Keywords** Spray coating · Photo-resist · Through-silicon via · MEMS · Electrostatic spray

---

S. Kurokawa (✉) · T. Hayashi  
Kyushu University, 744 Motoooka, Nishi-ku, Fukuoka 819-0395, Japan  
e-mail: [kurobe-@mech.kyushu-u.ac.jp](mailto:kurobe-@mech.kyushu-u.ac.jp)

T. Hotokebuchi · Y. Uchiyama  
Graduate School, 744 Motoooka, Nishi-ku, Fukuoka 819-0395, Japan

K. Miyachi · Y. Kobayashi  
New Component Division, Asahi Sunac Corp, 5050, Asahimae-cho, Owariasahi 488-8688, Japan

K. Matsuo  
Fukuoka Institute of Technology, 3-30-1 Wajiro-higashi, Higashi-ku, Fukuoka 811-0295, Japan

# 1 Introduction

Packaging density of semiconductor devices has been still going up and the thin-wiring technique are approaching the limit of miniaturization and device performance. Three dimensional IC packaging is a promising key technique for high performance electric and MEMS devices in the future. This technique utilizes TSV (Through Silicon Via) as an interlayer electrode for multiple layers of stacking chips or wafers vertically. TSV is formed by using the deep reactive etching technique, which is a part of the photo-lithography technique well used in semiconductor device manufacturing.

In TSV manufacturing, via holes are aligned first in the silicon substrate according to the required patterns and photo-resist is coated prior to the deep etching. The conventional coating method of the photo-resist is so-called spin coating, in which the silicon substrate rotates at high speed and the photo-resist is dropped onto the substrate surface. A thin film is formed by the centrifugal force and the thickness of the film is controlled by the rotational frequency of the substrate. The spin coating technique is generally used for thin film coating to flat-shaped substrates, however, it has a disadvantage of poor coating on the side-wall and the bottom face of via holes due to the resist flow along the direction of the centrifugal force. Another problem is that the material yield percentage of resist in the spin coating is very small.

The main objective of this research is to propose a new conformal resist coating method available for via holes to overcome the before-mentioned problems. The spray coating technique is one of the potential methods because atomized particles are possible to get into via holes and its material yield reaches more than 70%. There are several researches on spray coating for high topography surfaces [1–3] and for MEMS applications [4, 5], but main targets are convex structures and the size is in the range of millimeter to sub-millimeter order. The application for deep silicon cavities are tried [6], but there is no application for TSV, whose target is the hole shape and the size is in the range of several ten micrometer to micrometer order. For such small via holes, the first idea will be an ink-jet method [7], but it will be more suitable for the small area. In the case of a whole wafer surface, the more efficient method is preferable, so two methods are proposed here: one is utilizing a rotary atomizing spray and the other is with an electrostatic spray. The rotary atomizing spray can control the size of resist particles by changing the rotational frequency of the cup structure and the electrostatic spray can produce very tiny resist particles by Coulomb repulsion due to electrostatic charges. In both cases, smaller resist particles than via hole diameters could be available and it is expected for them to get into the holes. Experimental trials for conformal resist coating to via holes by the rotary atomizing spray are firstly reported here, and according to the discussions for the results, the improved trials by electrostatic spray are reported and discussed.

## 2 Resist Coating to Via Holes by Rotary Atomizing Spray

The most typical spray coating is so-called two-fluid method, which produces liquid particles by combining liquid flow and air flow inside the spray nozzle. The particles flow with air, and the particle size depends on the outlet pressure and the flow speed. In the case of via hole coating, the air flow is a fatal problem because the air pressure avoids the liquid particles getting into the holes. The different type of spray coating using one-fluid is also available, but in this case, the atomization is done by its high pressure outlet jet from the nozzle, which results in a quite high speed particle flow. Such a high speed particle flow must accompany with strong air flow, so the same problem as in the two-fluid method occurs.

The new atomizing spray proposed here is the rotary atomization method [8]. The simple structure is illustrated in Fig. 1.

The principle of rotary atomization is that the cup structural part rotates at high frequency and the supplied liquid resist is atomized by the centrifugal force. The resist particle size depends on the rotational frequency of the cup; the larger the rotational frequency is, the smaller the particle size is. The flow speed of the produced particles can be controlled independently to the particle size by the shaping air flow. This is a great advantage comparing to two-fluid or one-fluid method. Because the produced particles don't have to get high speed in order to be a small size, they could easily get into the via holes accompanying with the slow shaping air flow.

### 2.1 Experimental Setup

The prototype of the rotary atomizing spray coater used in this experiment is shown in Fig. 2. The nozzle can be scanned on a workpiece. The workpiece is a TSV-TEG (Test Element Group) wafer set on the hot plate installed in the coater with a vacuum

**Fig. 1** The schematic diagram of rotary atomizing spray coating

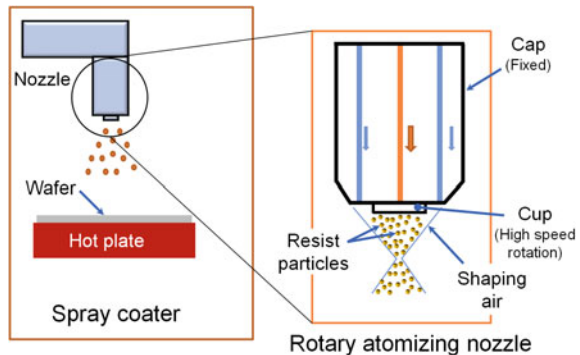


**Fig. 2** Rotary atomizing spray coater

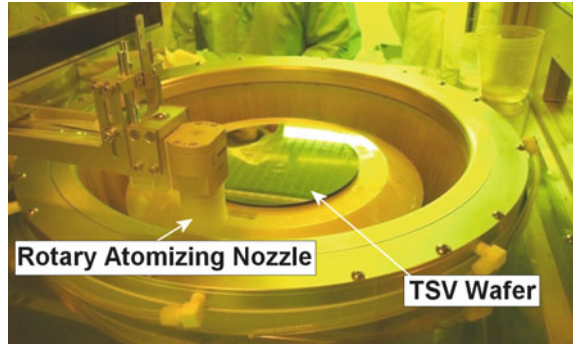
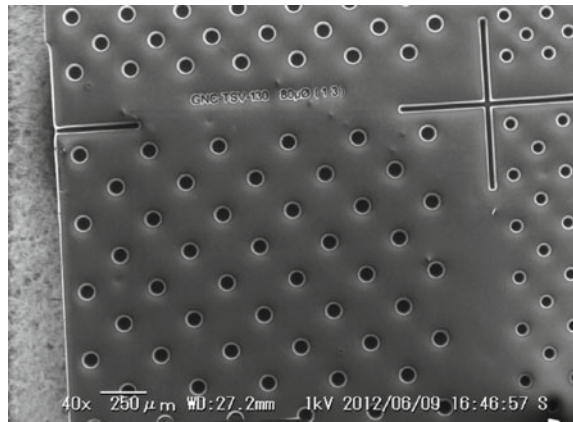


**Fig. 3** Example hole patterns on TSV-TEG wafer



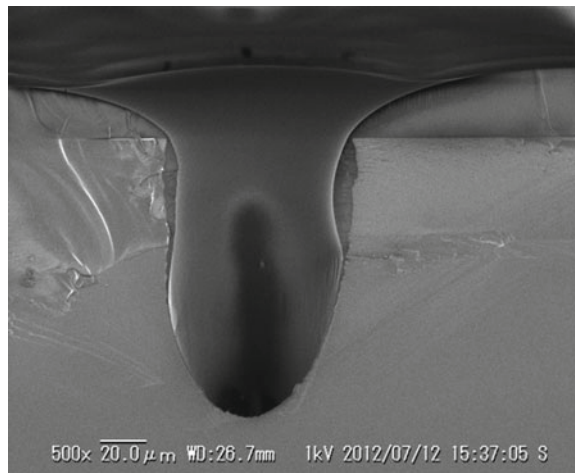
chuck. The TSV-TEG wafer has many via holes aligned on the silicon substrate as shown in Fig. 3. Via holes are prepared with different diameters from 20 to 80  $\mu\text{m}$ . The TEG wafer temperature can be kept at a specific condition during and after coating to control the dry and leveling conditions.

## 2.2 Results with Rotary Atomizing Spray

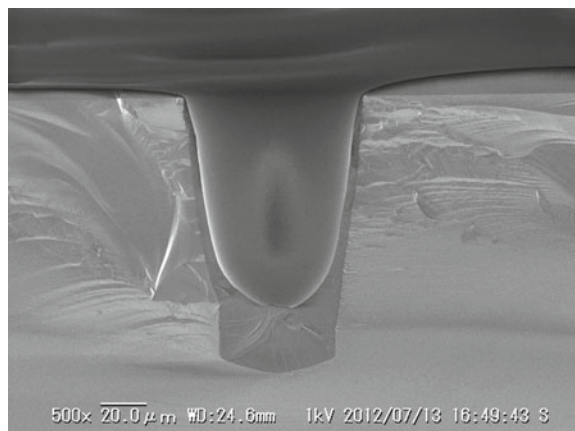
In order to get the smallest resist particles, the rotational frequency of the cup was set to the maximum of  $70000 \text{ min}^{-1}$ . The outlet rate of the resist was set to 6 g/min and spray distance to the wafer surface was 30 mm in the first condition. The scanning speed of the nozzle was changed from 3.3 to 10 m/min. The coated state was examined by observing the cross sectional image captured by SEM (Scanning Electron Microscope).

Figure 4 shows an example of a coated via hole of 60  $\mu\text{m}$  in diameter at a scanning speed of 3.3 m/min and at the hot plate temperature of 90  $^{\circ}\text{C}$ . The resist film was successfully formed inside the via hole, but the thickness of the film was quite large on the wafer top surface while the bottom film thickness in the hole was very small. The bottom thickness can be controlled by changing the hot plate temperature. Figure 5 shows the result coated at a hot plate temperature of 40  $^{\circ}\text{C}$ . The film thickness of the bottom in the hole got very large, but the thickness on the top surface got small comparing to Fig. 4. At lower temperature, drying phenomenon occurs slowly, so the duration of the resist flow gets long . This is good for the leveling of the film

**Fig. 4** Cross sectional SEM image of a coated via hole of 60  $\mu\text{m}$  in diameter (resist flow rate: 6 g/min, spray distance: 30 mm, nozzle scan speed: 3.3 m/min, hot plate temperature: 90  $^{\circ}\text{C}$ )



**Fig. 5** Cross sectional SEM image of a coated via hole of 60  $\mu\text{m}$  in diameter (resist flow rate: 6 g/min, spray distance: 30 mm, nozzle scan speed: 3.3 m/min, hot plate temperature: 40  $^{\circ}\text{C}$ )



thickness on the flat surface, but that results in the large amount of resist flow into the via hole. The conformal thickness might be controlled by keeping the optimized temperature in high accuracy, but it will be a quite sensitive process.

From the different point of view, one of the reasons for partly large thickness of the coated film is the large resist outlet rate. The thickness could be improved by reducing a resist outlet rate and a shaping air flow speed. The outlet rate of the resist was set to 1 g/min and long distances to the wafer were applied to avoid the particle agglomeration in the next condition.

Figure 6 shows the cross section of the coated via hole of 80  $\mu\text{m}$  in diameter at a spray distance of 200 mm. It is obvious that the amount of resist inside the hole was not enough and particle size seems quite large. The reason for this undesired state could be the early drying and partial agglomeration of the resist. It can be also recognized from the resist film roughness on the top surface of the wafer. The coated result at a shorter spray distance of 100 mm is shown in Fig. 7. The amount of resist and the particle size inside the hole were improved a little, but some dried-out small particles can be seen on the side wall of the hole. The early drying still seems to occur and the main reason is that the outlet rate of the resist was too small.

For more suitable conditions, the outlet rate of the resist was set to 3 g/min and the closer spray distance was selected from 50 to 100 mm with a scan speed of 3 m/min. Figure 8 shows the coated result of a via hole of 80  $\mu\text{m}$  in diameter.

The better condition was in the case of the spray distance of 75 mm. No agglomeration due to drying was observed and the film thickness conformality was improved, however, the bottom film thickness was still smaller than that on the wafer top surface. More precise coating may be achieved by controlling the wafer temperature in high

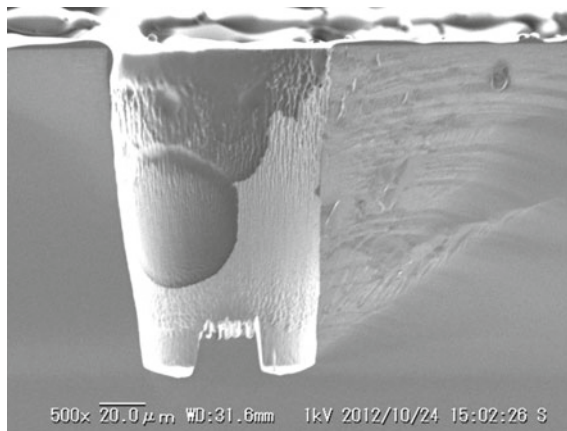


**Fig. 6** Coated via hole of 80  $\mu\text{m}$  in diameter with small outlet rate of the resist (resist flow rate: 1 g/min, spray distance: 200 mm, nozzle was fixed, hot plate temperature: 40  $^{\circ}\text{C}$ )

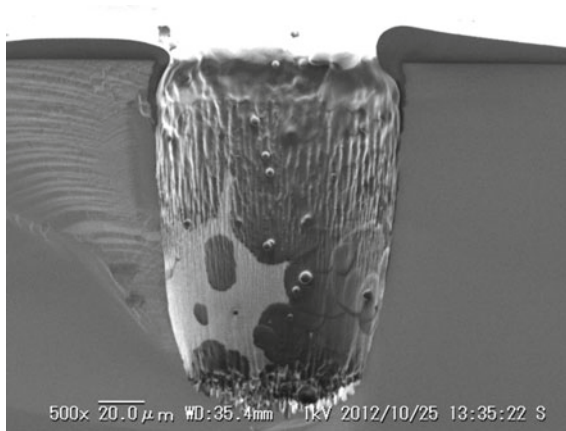


**Fig. 7** Coated via hole of 80  $\mu\text{m}$  in diameter with small outlet rate of the resist (resist flow rate: 1 g/min, spray distance: 100 mm, nozzle was fixed, hot plate temperature: 40  $^{\circ}\text{C}$ )

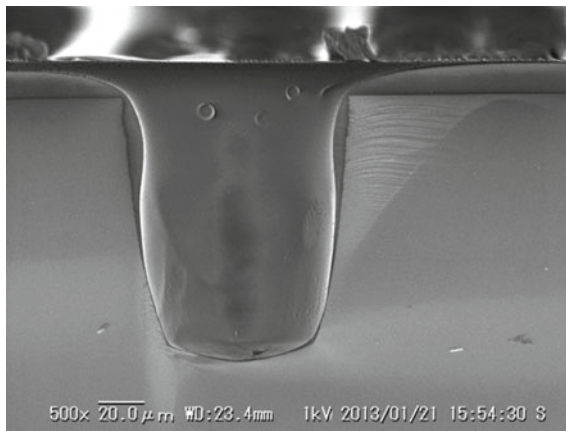


**Fig. 8** Coated via hole of 80  $\mu\text{m}$  in diameter with middle outlet rate of the resist (resist flow rate: 3 g/min, spray distance: 75 mm, nozzle scan speed: 3 m/min, hot plate temperature: 90  $^{\circ}\text{C}$ )

accuracy, but it will be necessary to carry out detailed trials. It is pity to say that there are still some difficulties in the case of a smaller via hole. For example, the result shown in Fig. 9 for a via hole of 20  $\mu\text{m}$  in diameter coated in the same conditions as in Fig. 8 shows that the amount of resist outlet is so large that the resist has covered the hole entrance completely. The rotary atomizing spray has a certain ability to achieve the conformal resist coating, but more essential improvement is necessary for smaller via holes.



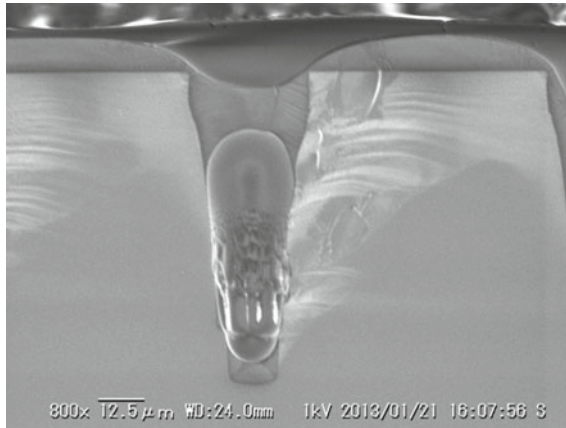


**Fig. 9** Coated via hole of 20  $\mu\text{m}$  in diameter with middle outlet rate of the resist (resist flow rate: 3 g/min, spray distance: 75 mm, nozzle scan speed: 3 m/min, hot plate temperature: 90  $^{\circ}\text{C}$ )

### 3 Resist Coating by Electrostatic Spray

From the results and discussions in the previous section, it has been clear that the amount of resist outlet should be small for small via holes and the rotary atomizing spray reaches the limitation for the via holes less than 30  $\mu\text{m}$  in diameter. In this section, a new promising technique for small via holes, so-called an electrostatic spray method is proposed and examined. The electrostatic spray was first developed for mass spectrometry [9], then applied for some deposition processes [10, 11]. This technique is still under development even in nozzle designs [12], but the produced particles by the electrostatic spray are essentially so small that it will be suitable for the coating inside the small via holes.

The basic construction of the proposed electrostatic spray nozzle is shown in Fig. 10.

Electrically-charged resist is discharged from the nozzle and the outlet resist is atomized by Coulomb repulsion due to an applied voltage between the nozzle and the ground electrode as shown in Fig. 11. The atomizing patterns are categorized into three mode; the first one is a single jet mode, in which the resist flows as a single stream of liquid thread; the second one is an atomization mode, in which the resist spreads into many tiny particles; the third one is a multi-jet mode, in which the resist flow are divided into several streams from the tip of the nozzle. In the case of large amount of outlet resist, the atomized voltage must be large comparing to the case of the small amount of resist outlet. The start voltage of atomization changes also according to the distance between two electrodes as well as the distance between the nozzle and the electrode.

**Fig. 10** Basic construction of electrostatic spray nozzle

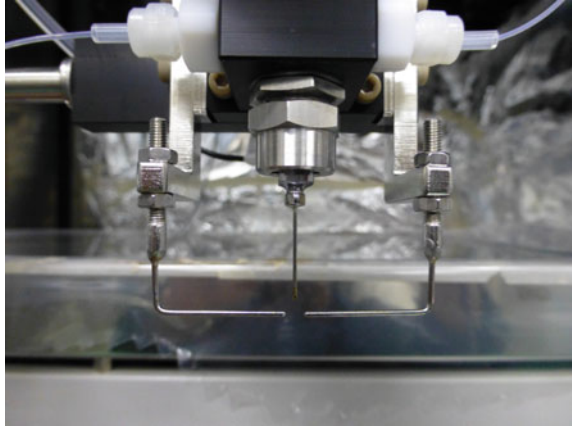
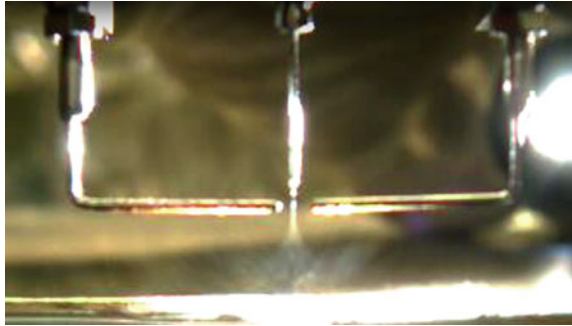


**Fig. 11** Atomization in electrostatic spray (captured by high speed camera)



The coating experiment was carried out on the same coater used in the previous section with the electrostatic spray nozzle in the atomization mode instead of the rotary atomizing one. The produced particles were so tiny that the spray distance to the TEG wafer was set close to the wafer surface of about 4–8 mm. The short spray distance has an advantage of efficient material use which results in high resist material yield.

### ***3.1 Coating to the TSV-TEG Wafer***

The same TSV-TEG wafer as in the previous section was used in this experiment. The spray conditions are as follows: the amount of resist outlet of 10  $\mu\text{L}/\text{min}$ , applied voltage of 2.8 kV, resist concentration of 15%, nozzle scan speed of 1.8 m/min, and hot plate temperature of 50  $^{\circ}\text{C}$ .

The coated result of the spray distance of 4 mm for a via hole of 80  $\mu\text{m}$  in diameter is shown in Fig. 12. The coated surface quality and the conformality were very good with the thickness of about 1  $\mu\text{m}$ . It is obvious that the particles got into the via hole enough and the advantage of electrostatic spray was shown clearly. Figure 13 shows the result of the spray distance of 8 mm. The side wall of the hole partly lacked resist films, but the film quality and the conformality is also good comparing to that of the rotary atomizing spray. The result for a via hole of 20  $\mu\text{m}$  in diameter was also shown in Fig. 14. The spray condition was changed to the double amount of resist

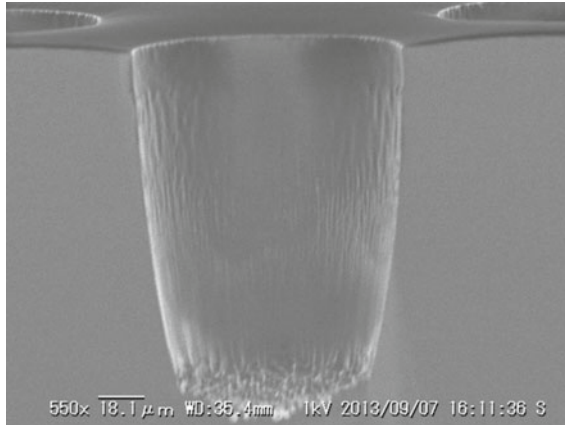


**Fig. 12** Coated via hole of 80  $\mu\text{m}$  in diameter by electrostatic spray (resist flow rate: 10  $\mu\text{L}/\text{min}$ , applied voltage: 2.8 kV, spray distance: 4 mm, nozzle scan speed: 1.8 m/min, hot plate temperature: 50  $^{\circ}\text{C}$ )

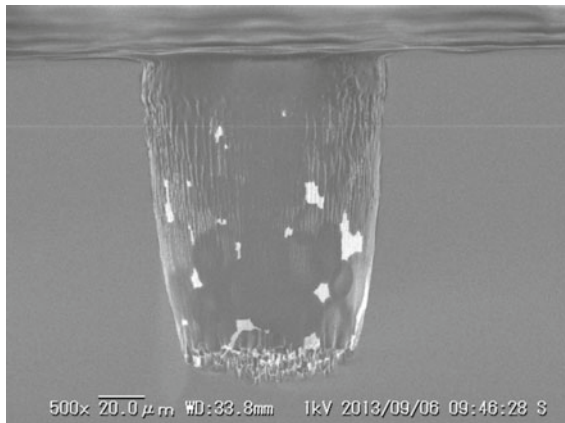


**Fig. 13** Coated via hole of 80  $\mu\text{m}$  in diameter by electrostatic spray (resist flow rate: 10  $\mu\text{L}/\text{min}$ , applied voltage: 2.8 kV, spray distance: 8 mm, nozzle scan speed: 1.8 m/min, hot plate temperature: 50  $^{\circ}\text{C}$ )

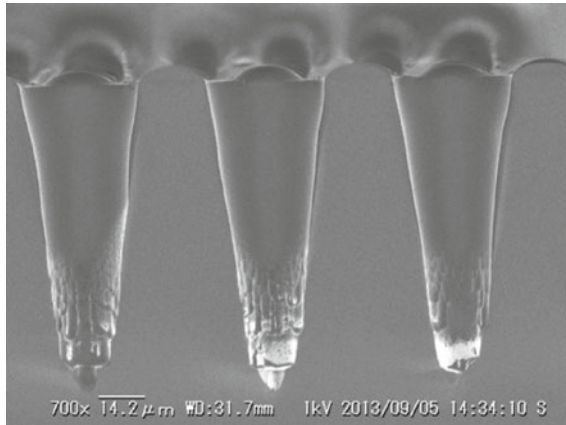


**Fig. 14** Coated via hole of 20  $\mu\text{m}$  in diameter by electrostatic spray (resist flow rate: 20  $\mu\text{L}/\text{min}$ , applied voltage: 2.8 kV, spray distance: 8 mm, nozzle scan speed: 1.8 m/min, hot plate temperature: 50  $^{\circ}\text{C}$ , the number of coatings: twice)

outlet (20  $\mu\text{L}/\text{min}$ ) and the recoating was carried out. The drastic improvement was obtained comparing to Fig. 9. The side wall film thickness was about 3  $\mu\text{m}$  and the high conformality was kept in via holes.

### 3.2 Coating to the MEMS-TEG Wafer

The electrostatic spray has a great potential to a wide range of TSV sizes and aspect ratios. Another example was tested here for exploring wider applications. The work-piece is a MEMS-TEG wafer which has many shallow rectangle pockets of a reverse pyramid shape on the silicon substrate as shown in Fig. 15. The length of a side of the upper surface square is about 160  $\mu\text{m}$  which is twice as large as the maximum TSV via hole diameter. It is useful for observing coating film thickness at the edge corner.

The spray conditions were almost the same as in Fig. 12. The resist outlet rate was selected as 10  $\mu\text{m}/\text{min}$  and recoating was carried out. The coated result is shown in Fig. 16. The film thickness on the upper corner is small while that on the bottom surface is large. This is because the leveling before drying occurred and the conformality got worse. To improve the conformality, the smaller outlet rate (5  $\mu\text{m}/\text{L}$ ) was selected and the coating was repeated 4 times (recoated). The coated result is shown in Fig. 17. It is clear that the conformality is improved as intended. The surface roughness got a little large because the leveling action was suppressed due to the small outlet rate of the resist. Anyway, the film thickness and the conformality can be easily and widely controlled by using electrostatic spray.

**Fig. 15** Example pocket patterns on MEMS-TEG wafer

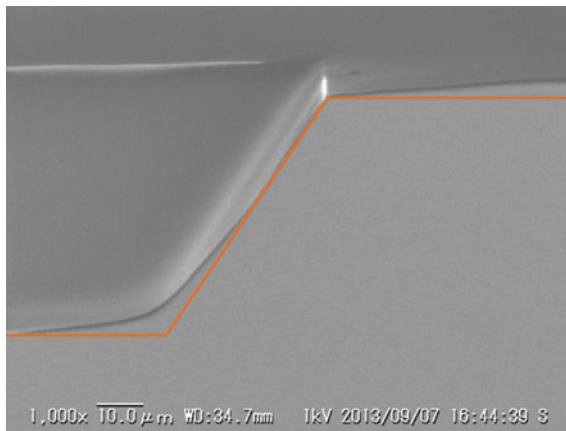
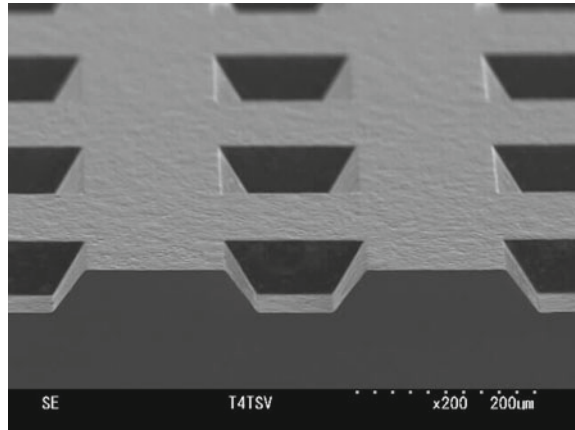


**Fig. 16** Coated MEMS pockets by electrostatic spray (resist flow rate: 10  $\mu$ L/min, applied voltage: 2.8 kV, spray distance: 4 mm, nozzle scan speed: 1.8 m/min, hot plate temperature: 50  $^{\circ}$ C, the number of coatings: twice)

## 4 Conclusions

Two different types of spray coating methods including rotary atomizing and electrostatic spray were applied for the TSV-TEG wafer coating. The performance of the electrostatic spray was superior to the rotary atomizing spray because the produced particles were very small. Better electrostatic spraying conditions were investigated by using TSV-TEG wafer and MEMS-TEG wafer. Because the atomized particles get small and almost no accompanying air flow exists, it is found that the electrostatic spray is an effective method especially for TSV in a small diameter. Recoating technique is also useful for a small diameter via hole and the better conformality control.

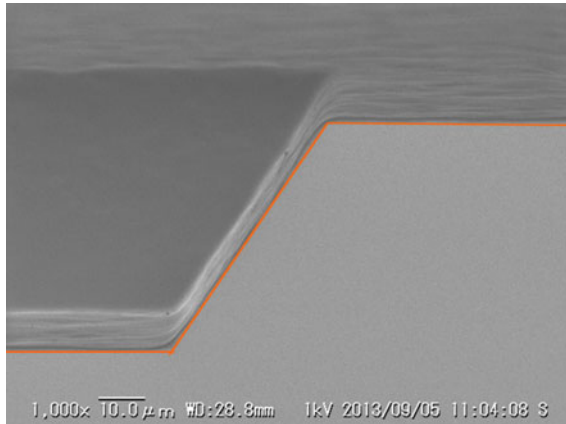


**Fig. 17** Coated MEMS pockets by electrostatic spray (resist flow rate: 5  $\mu\text{L}/\text{min}$ , applied voltage: 2.8 kV, spray distance: 4 mm, nozzle scan speed: 1.8 m/min, hot plate temperature: 50  $^{\circ}\text{C}$ , the number of coatings: 4 times)

This method may be expected to be applied to the complicated three dimensional structures in MEMS field.

## References

1. Nga PP (2002) Direct spray coating of photoresist—a new method for patterning 3-D structures. In: The 16th European conference on solid-state transducers, pp 182–185
2. Nga PP, Joachim NB, Pasqualina MS (2005) Spray coating of photoresist for pattern transfer on high topography surfaces. *J Micromech Microeng* 15:691–697
3. Nithi A, Karoon S, Jakrapong S, Wutthinan J, Oraphan T, Paweena D, Charndet H, Amporn P (2010) Improvement of photoresist film coverage on high topology surface with spray coating technique. *J Microscopy Soc Thailand* 24(1):42–46
4. Nga PP, Pasqualina MS, Joachim NB (2001) Spray coating of AZ4562 photoresist for MEMS applications. In: Proceedings of semiconductor advances for future electronics, pp 154–158
5. Shinya K (2013) Photoresist spray-coating for fabricating three-dimensional MEMS devices. *Toyota Res Rep* 66:81–82
6. Duk-Soo E (2007) Photoresist spray coating for resist film performance of deep silicon cavities. *J Korean Phys Soc* 50(6):1947–1951
7. Watanabe H (2008) Application of ink-jet technique for semiconductor manufacturing process (in Japanese). *SEMICON Japan Special* 1:107–111
8. Seike Y, Miyachi K, Shibata T, Kobayashi Y, Kurokawa S, Doi T (2010) Silicon wafer cleaning using new liquid aerosol with controlled droplet velocity and size by rotary Atomizer method. *Jpn J Appl Phys* 49:066701
9. Matthias SW, Matthias M (1994) Electro spray and Taylor-Cone theory, Dole's beam of macromolecules at last. *Int J Mass Spectrom Ion Processes* 136:167–180
10. Kunihiro A (2011) Electro spray deposition. *Mol Sci* 5:NP0013

11. Joon SK, Inyong P, Jae HJ, Sang SK (2013) Free-surface electro-spray technique using a multi-hole array. *J Aerosol Sci* 55:25–30
12. Cheng L, Marsha C, Weiwei Y, Aaron M, Weiwei D (2014) Ball point pen tips as robust cone-jet electro-spray emitters. *J Aerosol Sci* 77:10–15

# A Study on the Physical Mechanisms in Electro-discharge Machining Process



Shitanshu S. Chakraborty, Gourav Mohata, Souradip Ghosh,  
and Ashish K. Nath

**Abstract** Though electro-discharge machining (EDM) is in practical use for the last several decades, still several physical phenomena occurring during machining process are not well understood. For instance, it is well established that for higher material removal rate (MRR) in die sinking EDM of steel workpiece with copper tool the recommended polarity combination is positive tool and negative workpiece, usually called as normal polarity. However, in case of wire EDM for the same workpiece and tool materials combination, the opposite polarity combination is recommended for faster machining. Electro-discharge machining of steel and copper was done with both normal and reverse polarities for different pulse on-time. MRR was found to be lower in normal polarity than that in reverse polarity below certain pulse on-time, and beyond this MRR was higher in normal polarity. The crossover pulse on-time shifted towards higher values with increasing gap voltage. It was further observed that the crossover pulse on-time was higher for copper workpiece than that for steel at constant gap voltage. It was surprising to notice that the electrical discharge in both material combinations was equally regular for pulse on-time below crossover point in case of reverse polarity, but in case of normal polarity, while it was regular in copper, there was either no or infrequent discharge in steel. An attempt has been made to explain these observations analyzing various phenomena that could be involved in EDM, considering the behaviour of metal-debris (present in dielectric) interface, dynamics of space charge, and material properties, etc.

**Keywords** Electro-discharge machining · Polarity effect · Gap voltage · Pulse on-time

---

S. S. Chakraborty · G. Mohata · S. Ghosh · A. K. Nath (✉)  
Department of Mechanical Engineering, IIT Kharagpur, Kharagpur 721302, India  
e-mail: [aknath@mech.iitkgp.ernet.in](mailto:aknath@mech.iitkgp.ernet.in)

© Springer Nature Switzerland AG 2022  
S. Hinduja et al. (eds.), *Proceedings of the 38th International MATADOR Conference*,  
[https://doi.org/10.1007/978-3-319-64943-6\\_5](https://doi.org/10.1007/978-3-319-64943-6_5)



## 1 Introduction

Electrical discharge machining (EDM) is a non-traditional manufacturing process based on removing material from a workpiece by means of a series of repeated electrical sparks created between a tool, called the electrode and the workpiece. The tool and workpiece in die-sink EDM is usually placed in a dielectric fluid and electrical discharge is created by pulses at a high repetition rate in the range of 1–100 kHz [1, 2]. Electrical discharge in repetitive pulsed mode is used to prevent discharge converting into an uncontrolled arc, which could damage tool and workpiece. The pulse on-time ranges from a few  $\mu\text{s}$  to hundreds of  $\mu\text{s}$ , and sufficient time is provided in between two pulses to flush out debris created by discharge in the gap between tool and workpiece. This is a technique widely used in manufacturing industry for high-precision machining of all types of electrically conductive materials such as metals, metallic alloys, graphite, and even some ceramic materials, independent of their hardness.

As there is no direct physical contact between tool and workpiece in EDM, mechanical stresses, chatter and vibration problems are eliminated during machining. But, there are some limitations and drawbacks also. One of the major limitations is the slow material removal rate (MRR). The drawbacks include high rate of electrode wear, surface and subsurface damage and creation of thin and brittle heat affected zone. In order to alleviate these limitations and drawbacks, research is continuing abated to develop a better understanding of the process [1–4]; incorporate innovative techniques in EDM using ultrasonic vibration [5, 6], magnetic field [7, 8], different types of dielectric media including dry and near dry with different gases in machining environment [9], additive powders in dielectric fluids [10], and hybridizing with other machining processes such as electro-chemical machining [11].

In spite of its regular use in industry for about 75 years and, advancement and innovations through continued research, some of the phenomena occurring during EDM are not well understood [4]. When electrical voltage is applied between tool and workpiece with dielectric in between, an electrical spark is initiated by either ionization of some impurities or explosive evaporation of small particles locally bridging the gap [4, 12]. The initiation of an electrical spark is stochastic in nature and several phenomena take place in the gap during the process. They include ionization and plasma formation in the dielectric, interaction between electrons and ions, vaporization and melt ejection of tool and workpiece materials, and deposition of some of the liberated materials on tool and workpiece. It is rather difficult to describe all these phenomena in a common accepted theory and fully explain the mechanism of material removal in EDM [1].

It is well reported that, for higher MRR in die-sink EDM of steel workpiece with copper tool, the workpiece should be cathode (negative) and tool should be anode (positive). However, in case of wire electro-discharge machining (WEDM) the opposite polarities are preferred for the same workpiece and tool combination. It may be noted that the pulse on-time in case of WEDM is typically in the range of 10–25  $\mu\text{s}$ , while it is usually much longer in case of die-sink EDM. It has been

also reported that material removal by electrons at the anode is relatively more than by positive ions at cathode for shorter duration electrical discharge pulses ( $< 20 \mu\text{s}$ ) and vice versa for longer duration pulses ( $> 20 \mu\text{s}$ ) [2, 13]. Sufficient and detailed explanation of these observations are still lacking in literatures. The present study was motivated to investigate the effect of polarity for different pulse on-times on MRR and TWR (tool wear rate) in EDM of different workpiece and tool combinations under different gap voltages. An attempt has been made to provide physical explanations for various experimental observations.

## 2 Background Information

EDM is basically a thermo-mechanical process and the main material removal mechanism is vaporization and melt ejection [1–3]. The electrical spark produces a bubble containing high temperature plasma of ionized dielectric fluid and vapours of both tool and workpiece materials and, ejected debris in dielectric fluid between the tool and workpiece gap. When the spark ceases the temperature and pressure inside bubble decreases leading to the collapse of bubble. The dielectric fluid rushes on to the tool and workpiece surfaces and removes remaining molten materials from surfaces by cavitation effect. Details of EDM process and advancements made in this area can be found in several review articles [1–4, 14, 15].

Experiments have shown that MRR in a single pulse discharge is greater than the material removal per pulse in consecutive pulse discharges. For even identical input electrical energy conditions, MRR between discharges with higher peak currents at shorter discharge durations and those of lower peak currents at longer discharge durations is reported to be different [2].

Amorim et al. [16] reported that in electrical discharge machining of WC workpiece kept as anode with Cu, Cu–W and graphite tools as cathode, the tool wear rate was least in Cu–W tool followed by graphite and Cu. It is noteworthy that Cu has higher thermal conductivity and lower melting temperature than graphite which has lower thermal conductivity and higher melting temperature, while Cu–W possesses both the features. They showed that material removal rate and surface roughness increased with discharge current. However, there was an optimum pulse on-time for maximum MRR. Similar trend of variation in MRR was observed with the increase of duty cycle. Surface roughness continued its increasing trend with increased pulse on-time but showed no variation for increasing duty cycle.

Research and experimentation have shown that an appreciable amount of elements diffuse from the electrode to the workpiece and vice versa. These elements are transported in solid, liquid or gaseous state and alloyed with the contacting surface by undergoing a solid, molten or gaseous-phase reaction. The types of eroded electrode and work piece elements together with the disintegrated products of dielectric fluid significantly affect the material removal mechanism relating to the three phases of sparking, namely breakdown or ignition, steady state discharge and erosion. In addition, reversing the polarity of sparking alters the material removal phenomenon

with an appreciable amount of tool material depositing on the workpiece surface [1]. Other ways of explaining the material removal mechanism for short pulses are the effects of electrostatic forces and stress distribution acting on the cathode [1]. Thermal spalling has been also reported contributing to the material removal mechanism during the sparking of composite ceramics due to the physical and mechanical properties promoting abrupt temperature gradients from normal melting and evaporation [1]. The most commonly used technique for improving tool wear rate involves the electrode to make a planetary motion (trepanning) producing an effective flushing action, thus improving the part accuracy and process efficiency. The longitudinal tool wear can be compensated by applying an overlapping to-and-fro machining motion [1].

Xia et al. [13] reported that MRR in copper workpiece with copper tool was more when workpiece was anode for shorter discharge duration than when it was cathode; but, the trend reversed at higher discharge pulse durations. The difference of MRR between different polarities could not be explained by considering the energy distribution between tool and workpiece. It has been reported that nearly 40% and 25% discharge energy was coupled to anode and cathode respectively and this division was rarely affected by the discharge pulse duration [2]. Xia et al. [13] and Natsu et al. [17] investigated the effect of carbon adhesion to positive polarity workpiece on material removal under different machining conditions related to discharge duration, polarity, and dielectric flushing flow rate. Carbon is produced because of decomposition of hydrocarbon based dielectrics by electrical discharge. It was concluded that the difference in material removal amount between anode and cathode is mainly caused by the phenomenon of carbon adhesion onto the anode surface and not by energy distribution. However, this can't explain relatively higher MRR with reverse polarity at lower pulse on-time.

In the present work the effect of workpiece and tool polarity combination on MRR and TWR has been examined under different gap voltages for two different material combinations: copper (Cu) tool-mild steel (MS) workpiece (Cu-MS combination) and Cu tool-Cu workpiece (Cu-Cu combination) with varying pulse on-time. From here on the polarity combination of workpiece negative and tool positive would be referred as 'normal polarity' and the other polarity combination would be referred as 'reverse polarity', in line with the notation common for industrial EDM machines. A particular pulse on-time, as reported by Xia et al. [13] and Mishra [18], below and above which higher MRR is obtained for reverse and normal polarity respectively, would be termed as 'crossover pulse on-time'.

### 3 Experiment

The effect of electrode and workpiece polarity on material removal behavior was investigated in electrical discharge machining of two different workpiece materials, copper and mild steel with copper tool. Machining was carried out on a die-sinking EDM machine (model: Victor-1; manufacturer: Victory Electromake, Kolhapur,

India). Cylindrical rods of Cu of 6.25 mm diameter and 25 mm length were used as tool electrode. Mild steel specimens of 25 × 25 × 5 mm dimensions and copper discs of 20 mm diameter and 5 mm thickness cut out of ready stocks were used as workpiece. Pulse on-time was varied under both polarities and the resultant MRR and TWR were measured with the help of a weighing balance (model no.: AB265-S/FACT, Mettler Toledo make, resolution—10 μg). Machining was done for 3 min under each experimental condition and repeated 2–3 times to determine an average MRR and corresponding standard deviation. In order to observe the effect of tool polarity on MRR under different gap voltages machining was done at 30 V, 50 V and 70 V gap voltages. The peak current was maintained constant at 10 A throughout the experiment. The pulse on-time was gradually increased until one or two attainable values higher than that above which MRR for two different polarities crossed over. The pulse on- and off- times for different polarities and, tool and workpiece combinations are tabulated in Table 1. The discharge voltage and current were observed on a storage oscilloscope (model no.: 54625A, Agilent make). The highest pulse off-time attainable in the present machine corresponding to each pulse on-time was chosen to ensure the best possible flushing of debris produced in the gap between workpiece and tool during machining. The minimum pulse on-time and the corresponding maximum pulse off-time available with the machine were 5 and 18 μs respectively. While determining MRR the duty cycle was taken into account.

**Table 1** Parameter variations in experiments

<i>MS workpiece-Cu tool electrode, 30 V gap voltage, polarity: normal and reverse</i>							
Pulse on-time (μs)	5	7					
Pulse off-time (μs)	18	19					
<i>MS workpiece-Cu tool electrode, 50 V gap voltage, polarity: normal and reverse</i>							
Pulse on-time (μs)	5	7	9	11	15	19	23
Pulse off-time (μs)	18	19	20	21	23	25	27
<i>MS workpiece-Cu tool electrode, 70 V gap voltage, polarity: normal and reverse</i>							
Pulse on-time (μs)	5	7	9	11	15	19	23
Pulse off-time (μs)	18	19	20	21	23	25	27
<i>Cu workpiece-Cu tool electrode, 30 V gap voltage, polarity: normal and reverse</i>							
Pulse on-time (μs)	7	9	15	23	38	43	63
Pulse off-time (μs)	19	20	23	27	51	52	56
<i>Cu workpiece-Cu tool electrode, 50 V gap voltage, polarity: normal and reverse</i>							
Pulse on-time (μs)	7	9	15	23	38	63	96
Pulse off-time (μs)	19	20	23	27	51	56	110
<i>Cu workpiece-Cu tool electrode, 70 V gap voltage, polarity: normal and reverse</i>							
Pulse on-time (μs)	15	23	38	63	126		
Pulse off-time (μs)	23	27	51	56	114		

## 4 Results

Optical images of a few typical electrical discharge machined workpiece and tool surfaces, taken by ZEISS Stereo Zoom microscope (Discovery. V20), are presented in Figs. 1 and 2, along with the related experimental parameters. It is apparent that the surface morphology depends on whether electrons or +ve ions were bombarding the surface. Material deposition on tool can be also seen in Fig. 2d.

It was observed that there was a threshold pulse on-time ( $t_{on}$ ) for spark to occur readily and this minimum threshold was marginally higher for normal polarity than for reverse polarity in both tool–workpiece material combinations (Cu–Cu and Cu–MS). And, the threshold  $t_{on}$  increased with increasing gap voltage. The typical discharge voltage and current in Cu–Cu and Cu–MS combinations with normal (tool positive) and reverse (tool negative) polarity are shown in Fig. 3. The sparking parameters are 50 V gap voltage, 10 A peak current, 33  $\mu$ s pulse on-time and 50  $\mu$ s pulse off-time. It is seen that the peak discharge current that is attained in Cu–Cu combination is higher than that in Cu–MS combination, while the discharge sustaining voltage is lower. This indicates that the spark impedance in Cu–Cu combination is relatively less than that in Cu–MS combination. It is further observed that the current rise time

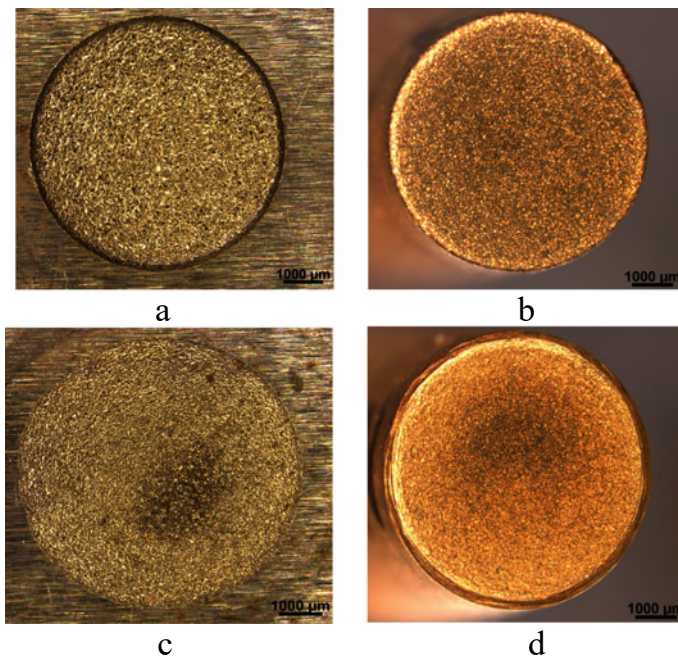


**Fig. 1** Optical images after EDM: **a** and **c** workpiece (MS), **b** and **d** tool (Cu) surfaces; polarity: **a** and **b** normal, **c** and **d** reverse; 50 V gap voltage, 9  $\mu$ s pulse on-time and 20  $\mu$ s pulse off-time (15  $\times$  magnification)

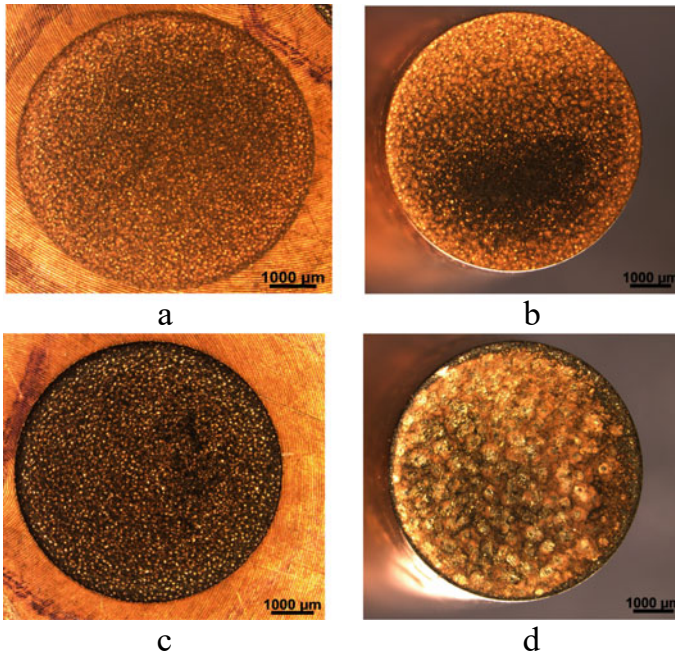


**Fig. 2** Optical images after EDM: **a** and **c** workpiece (Cu), **b** and **d** tool (Cu) surfaces; polarity: **a** and **b** normal, **c** and **d** reverse; 50 V gap voltage, 23  $\mu\text{s}$  pulse on-time and 27  $\mu\text{s}$  pulse off-time (15  $\times$  magnification)

in Cu–Cu combination is relatively longer than in Cu–MS combination. While in Cu–Cu combination the typical rise time of current is seen to be about 15  $\mu\text{s}$ , it is nearly 10  $\mu\text{s}$  in Cu–MS combination. This means that for pulse on-time shorter than the current rise time the discharge will not be able to reach the steady state at a set current. The spark discharge will be still in the build up stage. This is reflected in Fig. 4 for a typical case of 11  $\mu\text{s}$  pulse on-time and, gap voltage and peak current similar to that of Fig. 3. It is also seen that the current pulse is not as clean in reverse polarity as in normal polarity. This needs to be further investigated, however, it may be noted that the electric field distribution in the gap will not be symmetric because workpiece and tool, forming two electrodes of opposite polarities, have different surface areas.

The variation of MRR as a function of pulse on-time,  $t_{\text{on}}$  is presented in Fig. 5 for both material combinations and polarities at 30 V, 50 V and 70 v gap voltages. It was observed that spark did not occur at all in Cu–Ms combination at lower  $t_{\text{on}}$ , less than 7  $\mu\text{s}$  for 50 V gap voltage under normal polarity, while it occurred regularly with reverse polarity (Fig. 5d). The threshold value of  $t_{\text{on}}$  in case of Cu–MS combination under normal polarity increased more significantly with the increase of gap voltage than under reverse polarity (Fig. 5d, f). However, in case of Cu–Cu combination no significant difference in the frequency of occurrence of spark was observed with

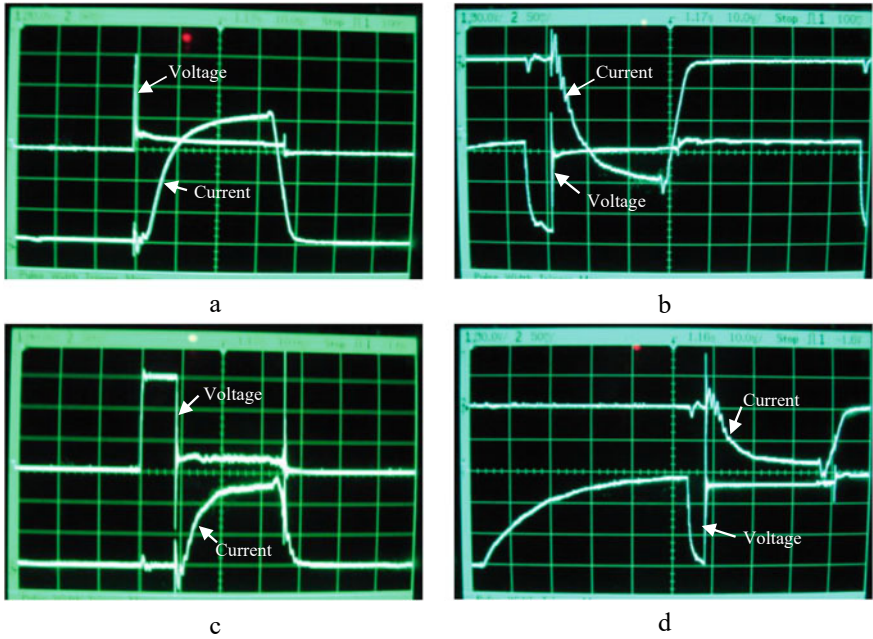


**Fig. 3** Voltage versus time and current versus time characteristics under 50 V gap voltage, 10 A peak current, 33  $\mu$ s pulse on-time and 50  $\mu$ s pulse off-time (Time scale, 1 division = 10  $\mu$ s) for **a** Cu-Cu, normal polarity; **b** Cu-Cu, reverse polarity; **c** Cu-MS, normal polarity and **d** Cu-MS, reverse polarity

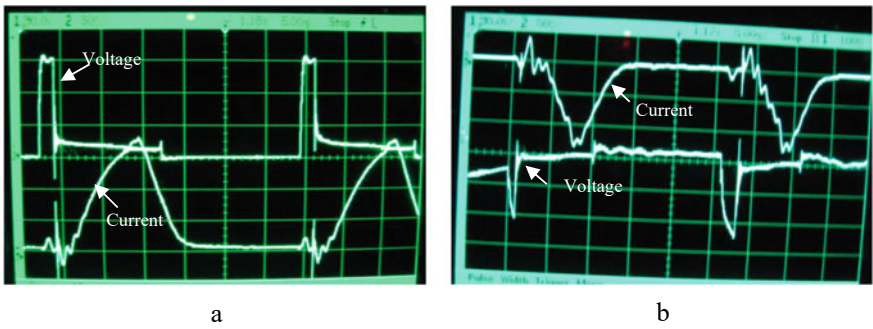


**Fig. 4** Voltage versus time and current versus time characteristics for EDM of Cu workpiece with 50 V gap voltage, 10 A peak current, 11  $\mu$ s pulse on-time and 21  $\mu$ s pulse off-time, (Time scale, 1 division = 5  $\mu$ s) under **a** normal and **b** reverse polarity

changing polarity, though MRR is different (Fig. 5a, c, e). The sparking being a stochastic phenomenon, the standard deviation of MRR in some of the experimental runs is relatively large compared to others. Nevertheless a general trend can be seen that MRR is more in reverse polarity in the lower range of pulse on-time; and as the pulse on-time is increased MRR increases for both polarities. However, beyond a certain higher pulse on-time MRR for normal polarity supersedes that for reverse polarity. Similar observation has been reported in Cu–Cu combination by Xia et al. [13]. Therefore, normal polarity is often recommended for machining in die-sink EDM.

The crossover pulse on-time is found to be lower for Cu–MS combination and tends to shift towards higher values with increasing gap voltage (Fig. 6). As apparent from the trend of variation of MRR with pulse on-time in Fig. 5b, the crossover pulse on-time in Cu-MS for 30 V could be below the machining range of pulse on-time.

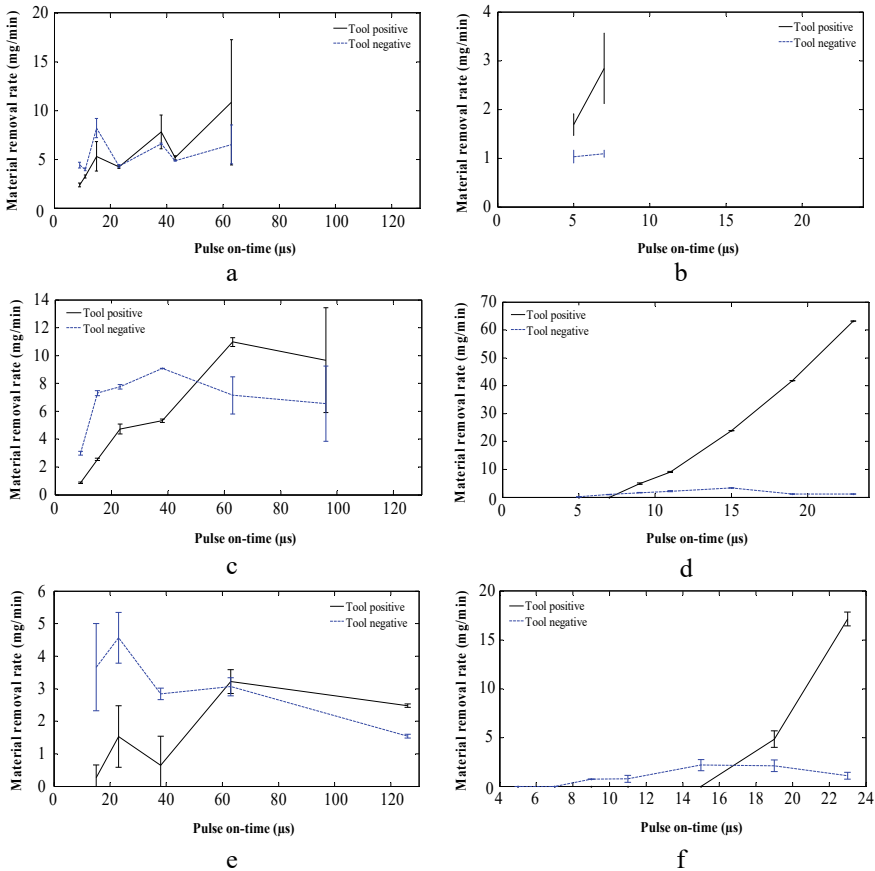


**Fig. 5** Variation of MRR with pulse on-time for EDM of Cu at gap voltages, **a** 30 V, **c** 50 V, **e** 70 V and MS at gap voltages, **b** 30 V, **d** 50 V, **f** 70 V



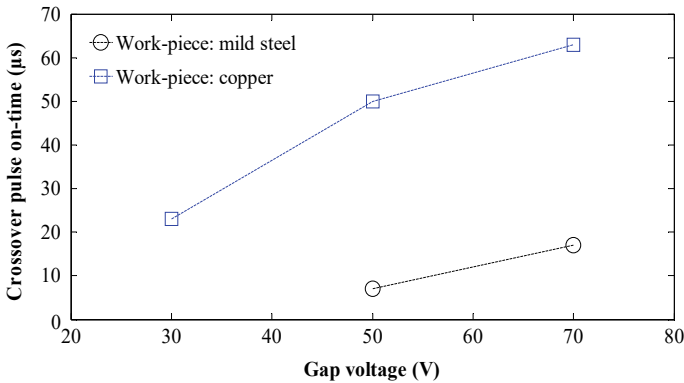


**Fig. 6** Variation of pulse on-time for crossover with gap voltage for different workpiece materials with copper tool

In case of Cu–Cu combination TWR followed the trend opposite to that of MRR, while for Cu–MS combination the trend of variation was similar to that of MRR.

## 5 Discussion

The following questions originating from the experimental results need to be answered:

- (i) Why is the behaviour of spark ignition so different with normal and reverse polarities in Cu–MS combination at short pulse on-time ( $\leq 7 \mu\text{s}$ ), but not in Cu–Cu combination?
- (ii) Why is MRR lower for normal polarity than for reverse polarity at lower range of pulse on-time, and why does the trend reverse after a crossover pulse on-time?
- (iii) Why does the crossover pulse on-time increase with gap voltage?
- (iv) Why is the crossover pulse on-time lower in mild steel than in Cu, when machined with Cu tool?
- (v) Why is the discharge sustaining voltage less and steady state current more in Cu–Cu than that in Cu–MS?

For explaining the experimental observations and answering the above questions, the mechanisms of discharge ignition between tool and workpiece in a dielectric, the plausible phenomena involved and their dependence of tool and workpiece material need to be examined. It is now well established that the electrical discharge is initiated by electrical conduction through debris present as impurities in dielectric, bridging the electrode gap [4, 12, 19, 20]. Schumacher [4, 12] and Luo [19], through their extensive studies on EDM process have demonstrated that debris play an important role in initiating the electrical spark and stabilizing the EDM process. Gatto et al.

**Table 2** Properties of workpiece materials obtained from [21–29]

Properties	Copper	Mild steel
Density (kg/m <sup>3</sup> )	8960	7854
Ultimate strength (MPa)	220	841
Specific heat (J/kg)	390	490
Melting temperature (K)	1358	1700
Boiling temperature (K)	2835	3143 (Fe)
Thermal conductivity (W/m K)	401	54
Electrical Conductivity (S/m)	$5.98 \times 10^7$	$7 \times 10^6$
Work function (eV)	4.53–50.1	4.67–4.81 (Fe)
Ionization potential (eV)	7.7264	7.9024 (Fe)
Electro–negativity	1.9	1.83 (Fe)
Fermi Energy level (eV)	7.0	11.1 (Fe)

[20] presented ample evidence of the presence of bridges of debris, which were observed and measured for the first time, in electrical discharge drilling in Al<sub>2</sub>O<sub>3</sub>–TiC composite. From these studies the dominant role of bridges of debris in igniting the electrical sparks is confirmed. However, the effect of tool and workpiece materials in igniting the spark as observed in the present study is not evident and therefore needs further discussions.

The various properties of Cu and MS, which may possibly affect the electrical discharge including its ignition and material removal, are listed in Table 2.

- (i) (i) The experimental observation of regular sparking in Cu–Cu combination with both polarities and in Cu–MS combination with reverse polarity, but not with normal polarity at shorter pulse on-time (< 7 μs at 50 V gap voltage) could be possibly explained considering the bridge of debris as a semiconductor material in contact with tool and workpiece made of different metals, and the contact behaviour. It has been reported that semiconductor–metal contact can either be Ohmic type which conducts the same for either polarity or, Schottky rectifier type which conducts more for one polarity, but not for the other [30]. The different behaviours of contacts depend on the type of metal and semiconductor materials and their surface conditions. From the above experimental observation it can be postulated that the tool and workpiece made of copper make Ohmic type contacts with debris, because of which spark ignition readily occurs for both polarities. And, in case of copper tool and workpiece made of steel, while the contact between the tool and debris is Ohmic type, it is like Schottky contact between the workpiece and debris. The modelled contacts are schematically shown in Fig. 7. In Ohmic contact (Fig. 7a) electrical conduction will take place irrespective of polarity. Schottky contact between MS workpiece and debris with normal polarity (MS workpiece negative and copper tool positive) will experience reverse bias if the bridge of debris acts like n–type

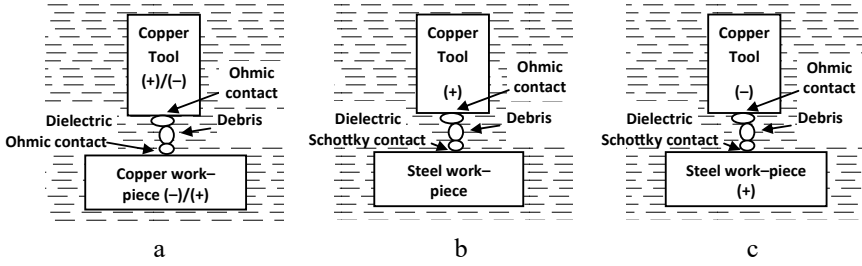


**Fig. 7** Schematic of tool and workpiece in dielectric with a debris bridge in the gap, **a** Cu-tool and Cu-workpiece at normal/ reverse polarity, **b** Cu-tool and steel workpiece at normal polarity; Reverse biased for n-type semiconductor, **c** Cu-tool and steel workpiece at reverse polarity; Forward biased for n-type semiconductor

semiconductor (electrons are the major carrier) and, this would deter electrical conduction. However, with reverse polarity (MS workpiece positive and copper tool negative) contact will be forward biased and electrical conduction could readily happen. The current density (current per unit cross-sectional area) through metal–semiconductor contact depends on temperature, besides material properties and can be given for forward and reverse biased conditions by the following equations [30]:

Under forward bias,

$$J = AT^2 \exp(-q\varphi_{BN}/kT) \exp(qV/kT) \quad (1)$$

Under reverse bias,

$$J = AT^2 \exp(-q\varphi_{BN}/kT) \quad (2)$$

where,  $J$  is the current density,  $A$  is the effective Richardson's constant,  $q$  is the electron charge,  $T$  is the absolute temperature,  $k$  is Boltzmann's constant, and  $V$  is the applied bias voltage.  $\varphi_{BN}$  is the Schottky barrier height =  $\varphi_M - \chi_S$ , where  $\varphi_M$  is the metal work function and  $\chi_S$  is the electron affinity of the semiconductor.

In reverse polarity the MS–debris bridge contact will be forward biased and the current will be mainly determined by the last exponent in Eq. 1. With the applied voltage the contact will conduct and initiate the spark ignition. In case of normal polarity the MS–debris bridge contact will be reverse biased and there will be only a very feeble current flowing across, and this may not be able to cause sufficient heating during the short pulse on-time for current build-up to ignite spark. With the increased pulse on-time heating could increase current even in reverse bias, (Eq. 2) leading to spark ignition. This could be a plausible explanation for the experimentally observed behaviour of spark ignition at low pulse on-time for different tool–workpiece material combinations with different polarities. This could be confirm by conducting single spark experiment at different currents in dielectric with and without debris.

Another way to explain the above experimental observation could be considering the large difference in electron drift velocity and mobility in copper and mild steel. They are approximately 3.7 and 5.85 times respectively higher in copper than in mild steel [28]. In electrical discharge between copper tool and MS workpiece electrons are to flow from MS in normal polarity and from copper in reverse polarity. Electron mobility being high in copper, in reverse polarity electrons may flow out of copper more readily than from MS in normal polarity due to relatively less electron mobility in the latter. With increasing pulse on-time as the contact temperature increases, the thermionic electron emission process could become dominant in releasing electrons and make the spark ignition independent of the above effect cast by the polarity of electrodes.

- (ii) Considering the above physical picture of discharge ignition, with the application of voltage between tool and workpiece discharge is initiated by the exploding debris-bridge due to current flow, which produces a large number of electrons and ions in the gap. Thus, the gap impedance reduces, which is indicated by a sharp fall of discharge voltage across the gap. Electrons accelerate in the applied electric field and cause further ionization through avalanche ionization process. It can be seen in Fig. 3, that the discharge current takes a certain amount of time to grow and reach its steady state value. For pulse on-time shorter than the current rise time (for example, Fig. 4a), discharge is still building up and yet not stabilised at the peak steady state value. Careful observation of Fig. 4a further reveals that the discharge voltage after the initial sharp fall is still reducing gradually as the current is building up. During this short discharge time the accelerated electrons bombard the workpiece held at positive potential (in reverse polarity) and remove a small amount of material through thermal process, viz. melting, vaporization and melt ejection by recoil pressure of vapour. In addition to their kinetic energy acquired in the electric field, electrons dissipate at anode an additional amount equal to the cathode work function which they had acquired at the cathode in order to get liberated.

The rise in surface temperature due to energy dissipation by electrons can be estimated by considering 1-D heat conduction in a semi-infinite solid. Neglecting heat loss due to radial heat conduction, the maximum temperature rise at the surface of a semi-infinite solid subjected to a uniform heat flux  $H$  for  $0 < t \leq t_{on}$  ( $t$  denotes time) can be estimated using Eq. 3 [31].

$$\Delta T = \frac{2H\sqrt{\kappa t_{on}}}{K\sqrt{\pi}} \quad (3)$$

where,  $\Delta T$  is the rise in temperature,  $K$  is the thermal conductivity,  $\kappa$  is the thermal diffusivity and  $t_{on}$  is the pulse on-time. Assuming same heat flux for both materials and putting the respective values of  $K$  and  $\kappa$  in Eq. (3) from Table 2, the time taken to reach to the melting point for Cu can be found to be almost 4 times higher as compared to that for MS. It may be noted that the MRR for Cu as workpiece was found to be similar order less than that for MS as workpiece (Fig. 5).

The positive ions which are accelerated in the same electric field would acquire the same amount of kinetic energy, but since they are heavy and large in size they undergo very frequent collisions with other particles produced in the gap and lose their kinetic energy in collisions. Therefore, they bombard cathode surface (workpiece in normal polarity) with relatively low kinetic energy causing correspondingly low material removal. This could be the reason of higher MRR in reverse polarity than in normal polarity for pulse on-time shorter than the discharge stabilising time.

It may be noted that in order to maintain the steady state current flow in discharge at higher pulse on-time, the cathode surface has to feed nearly same number of electrons into the discharge as are collected by the anode. This has to be provided by cathode mainly by positive ion bombardment and subsequently by thermionic emission. For shorter pulse on-time the root (end-point) of electrical spark on the cathode surface is still not sufficiently heated by positive ions to meet the steady state condition. As the pulse on-time is increased the number of positive ions reaching the spark root on the cathode increases. Due to the very high mobility of electrons than positive ions in the discharge they are repelled by cathode potential at a much faster speed than the positive ions will impinge on cathode. Therefore, there will be a very thin layer (a few mean free path of electrons,  $\sim \mu\text{m}$ ) near the cathode surface where electron density will be much less than positive ion density, and this leads to the formation of a positive charge space. The ion density increases with time and when it becomes large enough to produce space charge field comparable to the applied electric field, positive ions at the tip of this space charge will start bombarding the cathode surface with much higher kinetic energy. Under this condition, relatively free electrons in cathode get enough kinetic energy to overcome the work function and are ejected out. In steady state the electron emission from cathode by this process balances electrons which are bombarding the anode. With the increase of ion density during longer pulse on-time, the bombardment of ions at a very small area of the cathode surface (spark root) causes rise in temperature and this leads to thermionic emission of electrons. Under this condition a small amount of cathode surface material is melted and evaporated. The recoil pressure of vapour causes melt ejection also. Thus, all these processes will cause higher material removal from cathode surface due to positive ions bombardment in case of pulse on-time longer than the discharge stabilizing time.

It has been reported that as the electron density in a volume increases, the mutual repulsive force among them tends to enlarge the volume [32]. Thus, the area at which electrons are bombarding on the anode surface tends to broaden with the passage of time in long duration discharges. This will cause reduction in incident power density (power per unit area) at the anode. Due to this the temperature rise will be less and in turn material removal from anode surface will reduce. However, impinging ions at the cathode surface do not spread as much as electrons spread at anode, due to their large mass and inertia [33]. They imping on a relatively smaller area at cathode, causing high temperature rise which increases MRR.

From the above discussions it can be concluded that electrons will be more effective in material removal for reverse polarity (workpiece positive) for pulse on-time shorter than the discharge stabilizing time; and positive ions will be more effective

for relatively longer pulse on-time, by the time space charge field comparable to the applied field is formed near cathode.

- (iii) The growth of positive ions density in the discharge by electron avalanche ionization process and their arriving near the cathode surface to form the space charge would take certain amount of time. This will depend on the discharge sustaining voltage after ignition, types of positive ions produced in the discharge, and their drift velocity towards cathode, etc. With the increase of gap voltage, the physical separation between tool and workpiece where discharge ignition will occur is expected to increase. This will increase the drift time of positive ions to reach cathode and form space charge. This could be the reason for the shift of crossover pulse on-time towards higher value with increasing gap voltage.
- (iv) The experimental observation of lower crossover pulse on-time in Cu–MS than that in Cu–Cu (Fig. 5) could be due to the considerably smaller thermal diffusivity of MS ( $1.40 \times 10^{-5} \text{ m}^2/\text{s}$ ) than that of Cu ( $1.15 \times 10^{-4} \text{ m}^2/\text{s}$ ). As discussed earlier, the rise in temperature in MS will be faster for initiating thermionic emission of electrons from MS surface held at normal polarity, i.e. negative potential than in Cu.
- (v) The experimental observation of the marginally higher discharge sustaining voltage and relatively less steady state current in Cu–Ms than in Cu–Cu as seen in Fig. 3, could be explained as the following. At the initial stage of discharge current build-up the cathode point is not yet heated up to emit thermionic electrons. At this stage the cathode behaviour could be similar to glow discharge. It has been reported that the cathode voltage is higher for Fe as cathode than for Cu and the secondary Townsend ionization coefficient is smaller for Fe than for Cu [35]. The secondary Townsend coefficient is the measure of electron emission from cathode surface due to ion bombardment. The relative values of cathode voltage and Townsend coefficient in Ar discharge reported are 165 V and 130 V, and 0.038 and 0.08, respectively [34]. This would imply that the discharge sustaining voltage would be higher in case of Cu–MS than in Cu–Cu case in normal polarity and the steady state current would be less. However, it is also observed that the current rise time or discharge stabilizing time is relatively shorter in case of Cu–MS than in Cu–Cu in normal polarity (Fig. 3). This could be because of electron contribution by thermionic emission due to the gradual heating of cathode surface with passage of discharge time. The temperature rise would be relatively faster in case of MS cathode than in Cu due to its relatively lower thermal diffusivity than that of Cu, as discussed above.

## 6 Conclusions

Assuming the contact between copper and debris as Ohmic and that between mild steel and debris as Schottky; and considering the thermal and electrical properties

of different materials, the electrical discharge behaviour and material removal rate in electrical discharge machining of mild steel and copper with copper tool under different polarities could be explained qualitatively. Through this study an attempt has been made to provide a better insight of the complex phenomena involved in the EDM process.

## References

1. Ho KH, Newman ST (2003) State of the art electrical discharge machining (EDM). *Int. Machine Tools Manuf* 43:1287–1300
2. Kunieda M, Lauwers B, Rajurkar KP, Schumacher BM (2005) Advancing EDM through fundamental insight into the process. *CIRP Ann-Manuf Tech* 54:64–87
3. Abbas NM, Solomon DG, Bahari MdF (2007) A review on current research trends in electrical discharge machining (EDM). *Int J Mach Tools Manuf* 47:1214–1228
4. Schumacher BM (2004) After 60 years of EDM the discharge process remains still disputed. *J Mater Process Technol* 149:376–381
5. Iwai M, Ninomiya S, Suzuki K (2013) Improvement of EDM properties of PCD with electrode vibrated by ultrasonic transducer. *Procedia CIRP* 6:146–150
6. Srivastava V, Pandey PM (2012) Effect of process parameters on the performances of EDM process with ultrasonic assisted cryogenically cooled electrode. *J Manuf Process* 14:393–402
7. Teimouri R, Baseri H (2012) Effects of magnetic field and rotary tool on EDM performance. *J Manuf Process* 14:316–322
8. Teimouri R, Baseri H (2014) Optimization of magnetic field assisted EDM using the continuous ACO algorithm. *Appl Soft Comput* 14:381–389
9. Liqing L, Yingjie S (2013) Study of dry EDM with oxygen-mixed and cryogenic cooling approaches. *Procedia CIRP* 6:344–350
10. Ojha K, Garg RK, Singh KK (2011) Experimental investigation and modeling of PMEDM process with chromium powder suspended dielectric. *Int J Appl Sci Eng* 9:65–81
11. Qingfeng Y, Baorui W, Yongbin J, Fang L (2014) Research of lower tool electrode wear in simultaneous EDM and ECM. *J Mater Process Technol* 214:1759–1768
12. Schumacher BM (1990) About the role of debris in the gap during electric discharge machining. *Ann CIRP* 39(1):197–199
13. Xia H, Kunieda M, Nishiwaki N (1996) Removal amount difference between anode and cathode in EDM process. *Int J Electr Machining* 1:45–52
14. Schumacher BM, Krampitz R, Kruth JP (2013) Historical phases of EDM development driven by the dual influence of “Market Pull” and “Science Push.” *Procedia CIRP* 6:5–12
15. Muthuramalingam T, Mohan B (2014) A review on influence of electrical process parameters in EDM process. *Arch Civ Mech Eng*. <https://doi.org/10.1016/j.acme.2014.02.009>
16. Amorim FL, Weingaertner WL, Bassani IA (2010) Aspects on the optimization of die-sinking EDM of tungsten carbide-cobalt. *J Braz Soc Mech Sci XXXII* 5:496–502
17. Natsu W, Kunieda M, Nishiwaki N (2004) Removal Study on influence of inter-electrode atmosphere on carbon adhesion and removal amount. *Int J Electr Machining* 9:43–50
18. Mishra PK (1997) *Nonconventional machining*. Narosa Publishing, New Delhi, pp 102–105
19. Luo YF (1997) The dependence of interspace discharge transitivity upon the gap debris in precision electro discharge machining. *J Mater Process Technol* 68:121–131
20. Gatto A, Bassoli E, Denti L, Iuliano L (2013) Bridges of debris in the EDD process: going beyond the thermo-electrical model. *J Mater Process Technol* 213:349–360
21. [http://en.wikipedia.org/wiki/Ultimate\\_tensile\\_strength](http://en.wikipedia.org/wiki/Ultimate_tensile_strength). Retrieved on 19 Nov 2014
22. [http://www.engineeringtoolbox.com/specific-heat-metals-d\\_152.html](http://www.engineeringtoolbox.com/specific-heat-metals-d_152.html). Retrieved on 19 Nov 2014

23. <http://metals.about.com/od/properties/a/Electrical-Conductivity-In-Metals.htm>. Retrieved on 19 Nov 2014
24. [https://www.nde-ed.org/GeneralResources/MaterialProperties/ET/Conductivity\\_Iron.pdf](https://www.nde-ed.org/GeneralResources/MaterialProperties/ET/Conductivity_Iron.pdf). Retrieved on 19 Nov 2014
25. [http://en.wikipedia.org/wiki/Work\\_function](http://en.wikipedia.org/wiki/Work_function). Retrieved on 19 Nov 2014
26. [http://en.wikipedia.org/wiki/Ionization\\_energies\\_of\\_the\\_elements\\_\(data\\_page\)](http://en.wikipedia.org/wiki/Ionization_energies_of_the_elements_(data_page)). Retrieved on 19 Nov 2014
27. <http://hyperphysics.phy-astr.gsu.edu/hbase/tables/fermi.html#c1>. Retrieved on 19 Nov 2014
28. <http://uniweld.com/en/resources/product-info/alloys>. Retrieved on 19 Nov 2014
29. [http://www.engineeringtoolbox.com/boiling-temperature-metals-d\\_1267.html](http://www.engineeringtoolbox.com/boiling-temperature-metals-d_1267.html). Retrieved on 19 Nov 2014
30. [www.springer.com/cda/content/.../cda.../9780387755885-c1.pdf](http://www.springer.com/cda/content/.../cda.../9780387755885-c1.pdf). Retrieved on 19 Nov 2014
31. Ghosh A, Mallik AK (2005) Manufacturing science. EWP, New Delhi, p 387
32. DiBitonto DD, Eubank PT, Patel MR, Barrufet MA (1989) Theoretical models of the electrical discharge machining process I. A simple cathode erosion model. *J Appl Phys* 66(9):4095–4103
33. Patel MR, Barrufet MA, Eubank PT, DiBitonto DD, Theoretical models of the electrical discharge machining process II. The anode erosion model. *J Appl Phys* 66(9):4104–4111
34. Smirnov BM, Tereshonok DV (2014) Stability of the cathode layer of normal glow discharge in argon. *EPL* 107(55001):1–6. [www.epljournal.org](http://www.epljournal.org); <https://doi.org/10.1209/0295-5075/107/55001>



# **Laser Processing**

# Large Area Nano-gratings Fast Fabricated by Femtosecond Laser on Different Metal Surfaces



Haiying Song and Shibing Liu

**Abstract** A very prominent characteristic of the femtosecond laser induced nanostructures is the periodic shorter than laser wavelength. To improve its actual application value, in this work, we studied the characteristic of nano-texturing fabrication by fs laser scanning W (tungsten) metal surface, the regular uniform large area nano-gratings are fast fabricated on flat surface and cylindrical surface.

**Keywords** Large area nano-gratings · Femtosecond laser · Different metal surfaces

## 1 Introduction

Micro- and nano-structures produced on material surface can induced unexpected surface effects, such as microscale, mesoscopic, and quantum effects. These miracle physical effects are very important mechanical properties to realize peculiar micromechanical function surface. For example, the micro/nano structure on material surface similar to a lotus leaf surface, make the surface be of super-hydrophobicity and excellent self-cleaning properties. Such similar micro/nano structures on the wind turbine blades could enable them to withstand the harsh environment, such as rain, snow, etc. Thus, surface micro/nano-structuring processes have attracted increasing attention in recent years.

The traditional nano-texturing is achieved by photolithography with very complex steps and serious environmental impacts. One of the disadvantages about these nanoparticles or nano-structures achieved by photolithography is they are easy to fall off from the substrate or the surface. It is very important to achieve the nano-functional devices by a technology with large area, low cost and controllability on the original substrate. With advancements of femtosecond (fs) laser technology, the regular and periodic nanostructures produced directly with fs laser pulses on metal surfaces have attracted great interest [1–9]. Amongst the most prominent features of fs laser induced nanostructures are their highly regular periodicity and their size, which is shorter than

---

H. Song · S. Liu (✉)

Strong-Field and Ultrafast Photonics Lab, Institute of Laser Engineering, Beijing University of Technology, Beijing, China  
e-mail: [sbliu@bjut.edu.cn](mailto:sbliu@bjut.edu.cn)

© Springer Nature Switzerland AG 2022

S. Hinduja et al. (eds.), *Proceedings of the 38th International MATADOR Conference*,  
[https://doi.org/10.1007/978-3-319-64943-6\\_6](https://doi.org/10.1007/978-3-319-64943-6_6)

laser wavelength. To improve their viability in an industrial production environment, it is of great importance to demonstrate their production on actual devices surface. In this work, we studied the characteristic of nano-texturing fabrication by fs laser scanning tungsten (W) metal surface, and the regular large area nano-gratings are fast fabricated on flat surface, and then extended this technology to cylindrical tungsten metal surface.

## 2 Experiments and Results

The laser used in this experiment is an amplified Ti:sapphire fs laser system that generates 35 fs pulses about 3.5 mJ/pulse at a 1 kHz repetition rate with a central wavelength of 800 nm. The polished W metal samples were placed in three dimensional micro-positioning stages. The horizontally polarized 800 nm fs laser was focused on the samples through an  $f = 200$  mm lens in normal direction. The experiment set-up is shown in Fig. 1. The nano-gratings were obtained by scanning the samples using the micro-positioning stages, whilst the laser beam remained static. We performed the experiments in four steps.

First, the W sample surface was exposed by fs laser scanning with fluence of  $1.4 \text{ J/cm}^2$  at speeds of 0.94 mm/s, 1.25 mm/s, 1.56 mm/s, 1.88 mm/s respectively. Figure 2 shows the scanning electron microscope (SEM) pictures of the formed gratings. The average grating periodicities formed on the sample are measured to  $630 \pm 5 \text{ nm}$  respectively, they are almost the same. This demonstrates that the scanning

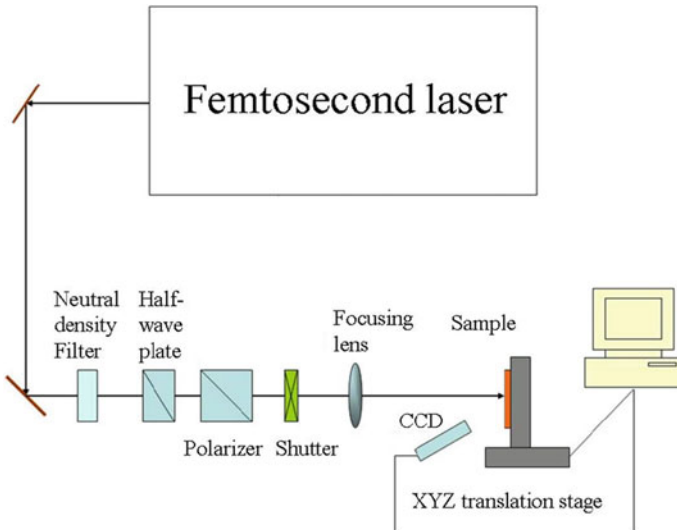
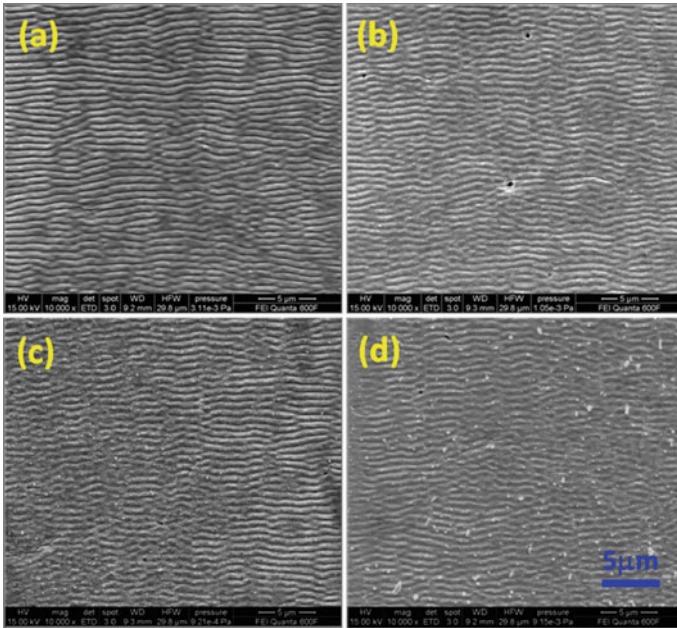


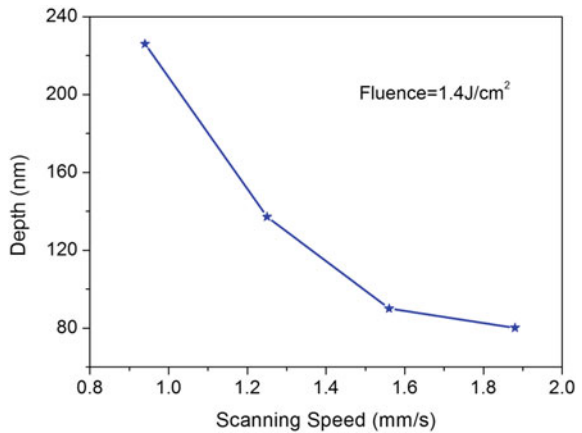
Fig. 1 Experiment set-up



**Fig. 2** SEM of nano-gratings formed by different scanning speeds under the fluence of  $1.4 \text{ J/cm}^2$ : **a** speed =  $0.94 \text{ mm/s}$ , **b** speed =  $1.25 \text{ mm/s}$ , **c** speed =  $1.56 \text{ mm/s}$ , **d** speed =  $1.88 \text{ mm/s}$

speeds on the W metal surface has no obvious effect to the grating periodicities. While, the main effects of the scanning speeds are the depth of the gratings, Fig. 3 shows the relation between the scanning speeds and the depths measured by atomic force microscope (AFM).

**Fig. 3** Relation between scanning speeds and depths measured by AFM



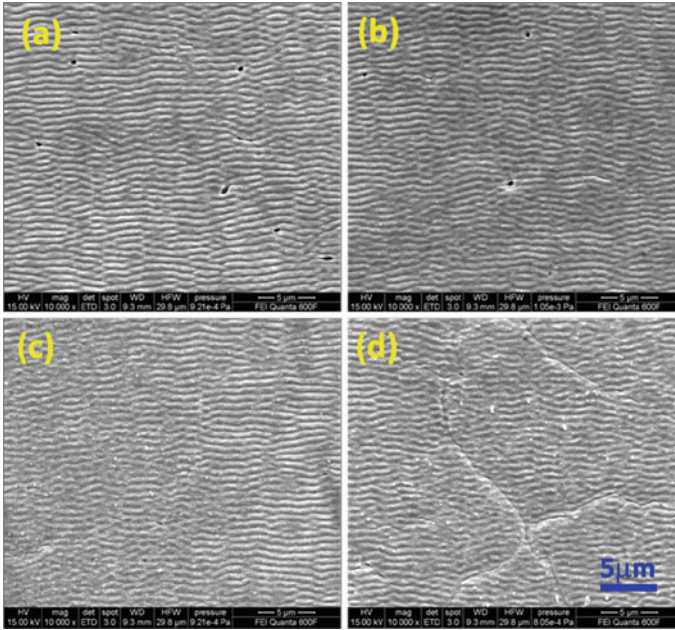


**Fig. 4** SEM of nano-gratings formed by different scanning fluence at the speed of 0.94 mm/s, the fluence are **a** 1.42 J/cm<sup>2</sup>, **b** 1.88 J/cm<sup>2</sup>, **c** 2.36 J/cm<sup>2</sup>, **d** 2.83 J/cm<sup>2</sup>

Second, the W sample surface was scanned by fs laser with the speeds of 0.94 mm/s under the fluence of 1.42 J/cm<sup>2</sup>, 1.88 J/cm<sup>2</sup>, 2.36 J/cm<sup>2</sup>, 2.83 J/cm<sup>2</sup> respectively. Figure 4 shows the scanning electron microscope (SEM) pictures of the formed gratings. The average grating periodicities formed are still measured to  $630 \pm 5$  nm respectively, they are almost the same. This demonstrates that the fluence on the W metal surface has no obvious effect to the grating periodicities. However, the main effects of the fluence are still the depth of the gratings, at the same time the surface morphology begin to take on cracks as the fluence rising according to Fig. 4d. Figure 5 shows relation between the scanning fluence and the depths measured by AFM.

The above two experiment groups show that the periodicities of the nano-gratings induced by the same wavelength fs laser pulse take on less difference, the main difference is the depth of the gratings, which is due to the laser pulse fluence accumulation at the same location, when the speed is faster the laser pulse residence time is shorter, and the fluence accumulation is lower, so the grating depth is inversely proportional to the scanning speed and proportional to the fluence.

Third, according to the above experimental results and conclusion the scanning speed and the fs laser exposure fluence all have no obvious effect on the induced nano-gratings periodicities. We adjusted an optimized parameter to induce regular nano-gratings, the scanning speed is 1.2 mm/s, the fluence is 1.5 J/cm<sup>2</sup>. We first performed a single scanning line on the sample surface along the horizontal direction as the SEM in Fig. 6, the width of the grating area is about 60 μm. Then by controlling the

**Fig. 5** Relation between scanning fluence and depths measured by AFM

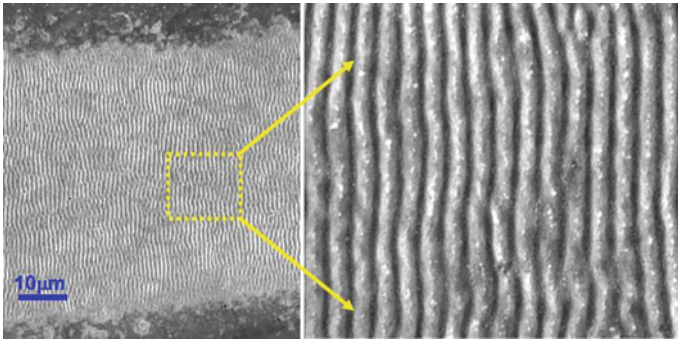
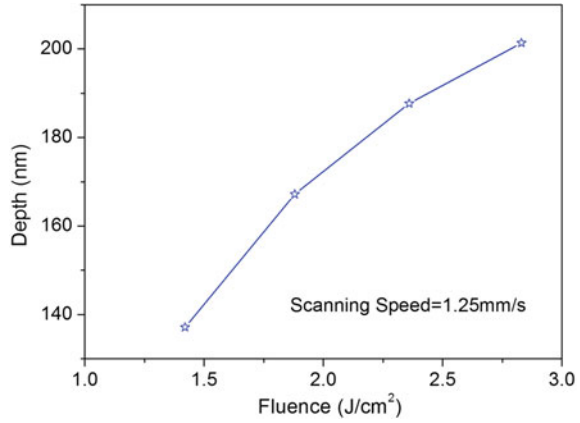


**Fig. 6** SEM of single scanning line about nano-gratings

micro-positioning stages, we adjusted the interval length from 0 to 30  $\mu m$  between two adjacent scanning lines in the vertical direction. The nano-gratings achieved are shown in Fig. 7. As the SEM shown in Fig. 7, the un-overlapped adjacent lines (Fig. 7a) leave a bit away from expectation, the overlapped too much adjacent lines takes on some melting appearance as in Fig. 7b, these two groups are not uniform gratings, while the interval length of 10  $\mu m$  is just the appropriate distance, the nano-structures surface takes on good joint as shown in Fig. 7c.

Under the above optimized exposure condition of the scanning speed 1.2 mm/s, the fluence 1.5  $J/cm^2$ , and the interval length 10  $\mu m$ , the nano-gratings of 630 nm periodicity with an area of 10 mm \* 1 mm can be quickly finished within 260 s in a very simple way of the above fs fabricated processing.

Fourth, to improve its actual application value, it is very important to fabricate the microstructures on the actual devices surface. So, the last experiment we tried to extend the plane scanning technology to cylindrical metal surface. A coarse polished cylindrical W metal was placed on a rotating stage, by redesigning the laser beam and the controlling system. The fs laser pulse with 1.5  $J/cm^2$  fluence is focused on

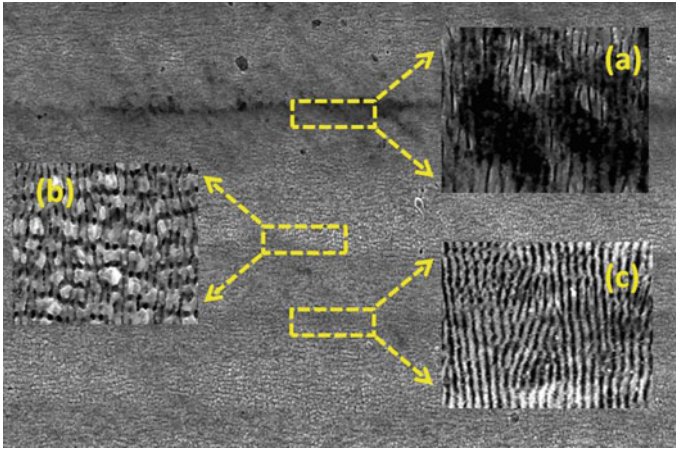


**Fig. 7** SEM of nano-gratings got by different joint distance: **a** the interval length is 0  $\mu\text{m}$ , **b** the interval length is 30  $\mu\text{m}$ , **c** the interval length is 10  $\mu\text{m}$

the sample surfaces by a  $f = 200$  mm lens, the rotational speed of the rotating stage is 0.24 rad/s. The W sample rotated together with the rotating stage by exposed in the fs laser pulse. The other process is similar to the third step, the interval of the overlapped two adjacent lines is also 10  $\mu\text{m}$ . A large area uniform gratings were achieved on the cylindrical W surface following the above process, as Fig. 8 shows the achieved gratings can reflect white light well. Further, if we want to get the same uniform nano-texturing on the non-plane surfaces, we can improve the laser fluence together with the rotating speed. The micro/nano-texturing on non-plane surface is a key step in many optical devices and electron devices machining, the above fs laser processing technology gives us a new way to achieve more surface function.

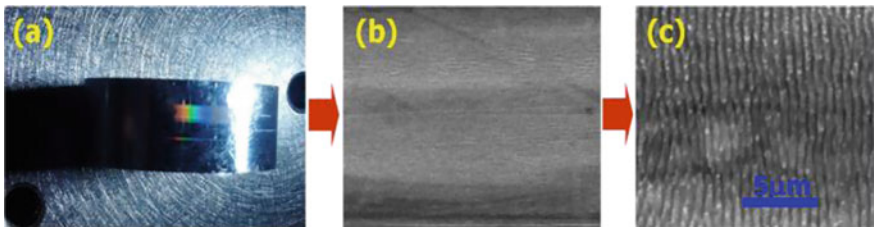


**Fig. 8** Large area nano-gratings achieved on the cylindrical surfaces: **a** picture of nano-grating reflecting white light, **b** and **c** SEM of nano-gratings

### 3 Conclusions

In this work, we studied the characteristic of the periodic nano-gratings fabricated by femtosecond (fs) laser scanning W (tungsten) metal surface, in two ways, one is comparing the effect of difference scanning speed to the nano-grating periodicities, another is comparing the effect of different scanning fluence. The results of the two ways show the exposure conditions under the same wavelength and the same repetition rate of fs laser make no obvious effect on the induced ripple periodicities. While the depth of the gratings is proportional to the scanning fluence and varies inversely with the scanning speed. Based on the optimized parameters, the regular large area nano-gratings on plane and cylindrical W metal surface are achieved in a rapid fs fabricating process.

**Acknowledgements** We gratefully acknowledge supports for this work from the National Natural Science Foundation of China (51275012) and the Beijing Commission of Education (KZ201110005001).

### References

1. Abbondanzieri EA, Greenleaf WJ, Shaevitz JW, Landick R, Block SM (2005) Direct observation of base-pair stepping by RNA polymerase. *Nature*, London 438:460–465
2. Fatima T, Howard MB, Matthew RP, Kim MJ, Yuan H (2011) Multi-scale surface texture to improve blue response of nanoporous black silicon solar cells. *Appl Phys Lett* 99:103501(1–3)
3. Kotsifaki DG, Kandyla M, Zergioti I, Makropoulou M, Chatzitheodoridis E, Serafetinides AA (2012) Optical tweezers with enhanced efficiency based on laser-structured substrates. *Appl Phys Lett* 101:011102(1–3)
4. Shimotsuma Y, Kazansky PG, Qiu J, Hirao K (2003) Self-organized nanogratings in glass irradiated by ultrashort light pulses. *Phys Rev Lett* 91:247405(1–4)
5. Vorobyev AY, Makin VS, Guo C (2009) Brighter light sources from black metal: significant increase in emission efficiency of incandescent light sources. *Phys Rev Lett* 102:234301(1–4)
6. Qi LT, Nishii K, Namba Y (2009) Regular subwavelength surface structures induced by femtosecond laser pulses on stainless steel. *Opt Lett* 34:1846–1848
7. Hwang TY, Guo CL (2011) Observation of femtosecond laser-induced nanostructure-covered large scale waves on metals. *J Appl Phys* 109:083521(1–4)
8. Rebolgar E, Vázquez de Aldana JR, Pérez-Hernández JA, Ezquerro TA, Moreno P, Castillejo M (2012) Ultraviolet and infrared femtosecond laser induced periodic surface structures on thin polymer films. *Appl Phys Lett* 100:041106(1–4)
9. Yang Y, Yang JJ, Xue L, Guo Y (2010) Surface patterning on periodicity of femtosecond laser-induced ripples. *Appl Phys Lett* 97:141101(1–3)



# Experimental Investigation and FE Simulation of Heat Affected Zone in Water-Jet Assisted Underwater Laser Cutting Process of Mild Steel and Titanium



Yuvraj K. Madhukar, Suvradip Mullick, Shitanshu S. Chakraborty, Som S. Thatoi, and Ashish K. Nath

**Abstract** In recent times, different approaches of water assisted laser cutting have been developed with assurances of many advantages over conventional gas assisted laser cutting. Since laser cutting is a thermo-mechanical process, thermal damage on substrate is expected that may be undesirable for many applications. Therefore, the generation of heat affected zone (HAZ) has been investigated for water-jet assist underwater laser cutting process in two different materials namely mild steel and commercial grade pure Ti having different thermal conductivity. A continuous wave (CW) Yb-fiber laser having low absorption in water was used. The effect of laser power, cutting speed and water pressure was investigated. HAZ was found to be less at top kerf than at bottom due to difference in convective heat loss. The difference in HAZ at top and bottom kerfs was larger in mild steel than Ti, specifically at bottom kerf. Finite element simulation was also carried out with different values of convection coefficients representing convection losses at the top and bottom surfaces, and the cut front. Experimental and simulation results were found to be in good agreement.

**Keywords** Fiber laser cutting · Water-jet assisted · Underwater · HAZ

## 1 Introduction

Laser cutting is a viable alternative of mechanical blanking utilised over four decades. It is a non-contact cutting process and now-a day's it is considered as an ideal tool for the production of sheet metal parts, achieving complex shapes, geometries etc. Laser cutting process has got many advantages over conventional machining such as; reduction in the requirement of fixturing, cutting almost all materials irrespective of their mechanical strength, high cutting speed, high precision, narrow kerf, minimum waste, low running cost etc. [1–3].

---

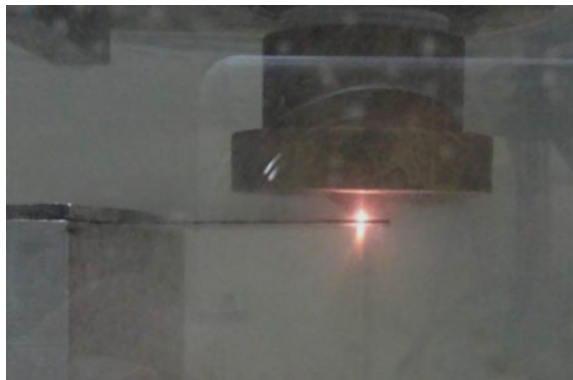
Y. K. Madhukar · S. Mullick · S. S. Chakraborty · S. S. Thatoi · A. K. Nath (✉)  
Department of Mechanical Engineering, IIT Kharagpur, Kharagpur 721302, India  
e-mail: [aknath@mech.iitkgp.ernet.in](mailto:aknath@mech.iitkgp.ernet.in)

In metals the cutting action is typically takes place by fusion process. The process include focussing of high power laser beam to a very small area causing intense heating and melting in narrow area, which is then expelled-out through bottom of cut by the action of a gas-jet [1, 4]. Since, the process requires heating and melting, the large amount of heat also gets dissipated into the base material within a short period [1]. This in turn, causes some defects such as increase in HAZ or brittleness at the edges. The dissipation of heat depends on both material's thermal properties and processing parameters such as sheet thickness, laser power, cutting speed, spot diameter etc. In general, the extension of HAZ reduces with the increase of cutting speed and laser power [4, 5]. However, it cannot be avoided, which is certainly undesirable in many applications. Since, it leads to change in material properties such as increase in brittleness, hardness, corrosion compliance, microcracks, poor weldability and formability [5–8].

In recent times, different approaches of water assisted laser cutting have been proposed by various researchers, such as underwater cutting [9], oxygen or gas assisted underwater cutting [10], water micro-jet guided cutting [11] etc. They had experienced that inclusion of water in laser cutting in any manner has many advantages over conventional gas assisted laser cutting. It includes more effective cooling of work-piece and ejected material, high plasma pressure due to confinement, quick removal of debris by water convection/evaporation, reduced atmospheric pollution, less burr and small focal spot size etc. [12].

In this paper the propagation behaviour of HAZ was investigated for recently introduced “water-jet assisted underwater laser cutting” process [13]. This process utilises a coaxial water-jet along with laser beam for ejecting molten material, while whole system, i.e. laser processing head and work-piece are kept in underwater. Figure 1 shows the typical image of ongoing process. The process has got many potential applications such as nuclear industry for cutting burnt fuel rods that needs to be cut underwater to avoid atmospheric contamination, and marine industry for repair works. In this type of repair works sub-segment cutting of damaged parts followed by subsequent welding is often required. HAZ is not desirable as it may lead to poor weldability and weld strength. As the heat propagation in metals depends

**Fig. 1** Photograph of on-going process of water-jet assisted underwater laser cutting



on their thermal conductivity and response with temperature, two materials, namely mild steel (MS) (SAE 1020) and titanium (Ti) (CpTi-G1) having different thermal conducting behaviour were chose for the purpose of evaluation. This grade of mild steel sheet is typically considered as a structural steel used in many industrial and household purposes. Whereas the titanium has always been of research interest due to its many potential applications in biomedical implants and aerospace industry. The aim of this investigation was also to find the effect of process parameters such as laser power, cutting speed, water-jet pressure etc. on the behaviour of HAZ.

## 2 Experimental Details

A continuous wave (CW) 2 kW Yb: fiber laser operating at  $1.07 \mu\text{m}$  wavelength has been used for conducting the cutting experiment. The laser beam delivery system is mounted on a 5-axis CNC work station capable to move at speeds up to 25 m/min. A hybrid processing head which allows water to flow coaxially with the laser beam has been designed and fabricated in-house to carry out the experiment. The experimental setup is schematically shown in Fig. 2. The complete details of laser system and experimental setup can be found elsewhere [14, 15].

Here, two lenses were used to focus the laser beam to a spot of  $\sim 220 \mu\text{m}$  diameter. As the absorption of fiber laser power in water is a function of laser intensity, water column height and water temperature, their effects were investigated and reported elsewhere [16]. In order to minimize the absorption loss in water, the dimensions of coaxial water-jet nozzle were so chosen that the laser beam has to travel a minimum distance before it is incident on the specimen. A water flow circuit was designed and

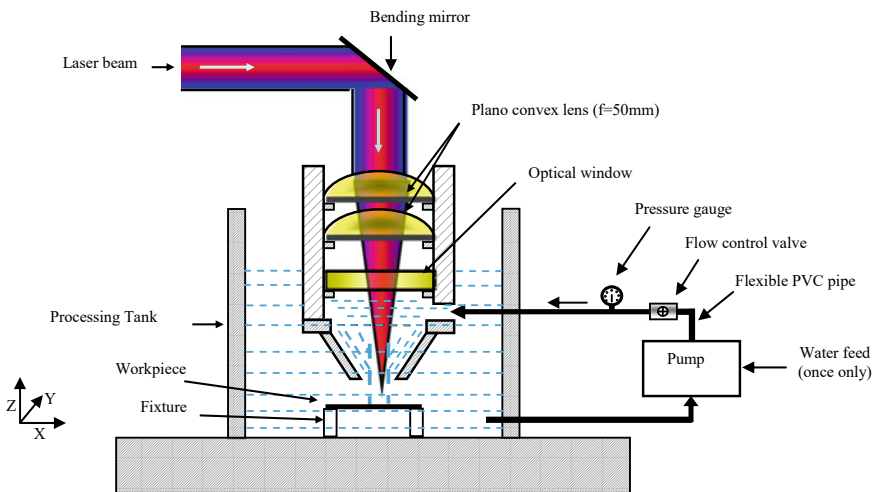


Fig. 2 Schematic of water-jet assisted laser cutting set-up

**Table 1** Water-jet velocity at different water pressures

Water stagnant pressure (bar)	Water-jet speed (m/s)
2	15
3	20
5	25
7	30
10	36
13	41
15	45

developed to maintain continuous flow and also to re-circulate the water in a close loop Fig. 2. The range of workable water-jet pressure that can be achieved with this system is in 1–16 bar range, maximum pressure limited by the damage threshold of utilised optical components. The water-jet velocity measured experimentally at different pressures is presented in Table 1. Thin sheets of mild steel sheet (SAE 1020) and titanium (CpTi-G1) having thickness of 0.4 mm and 0.15 mm respectively were used for the experiment.

The water-jet assisted underwater laser cutting experiment was conducted in CW mode of laser operation with varying laser power, cutting speed and water pressure in the range of 150–1350 W, 0.9–15 m/min and 2–13 bar respectively. The preliminary experiment was conducted to find the effect of focal position. The higher cutting speed and apparently minimum dross adhesion was realised when the laser beam was focused at the middle of the thickness and at the top surface in case of 0.4 mm thick Mild steel and 0.15 mm thick titanium respectively. Therefore, this was maintained throughout the experiment.

The formation of HAZ was analysed by measuring the length of change in grain structure. It was done by taking micro-picture for both top and bottom kerfs along the thickness direction. The standard polishing and etching procedure were followed before taking micro-pictures. The HAZ propagation and its behaviour were also tried to simulate using commercial finite element (FE) numerical simulation software ABAQUS 6.10. The simulation assumptions and methods were discussed in a subsequent section.

### 3 Results and Discussion

#### 3.1 Experimental Observations

The preliminarily experiment was conducted to find the maximum cutting speed for different laser powers while keeping the water-jet pressure constant. Laser powers were chosen in such a way that the maximum cutting speed would not exceed beyond 15 m/min. This limit of velocity was set to minimise lead-in and lead-out distances.

At higher speeds the lead-in and lead-out is more, which will make contour cutting difficult. In case of mild steel the maximum cutting speed for 900 W, 1100 W and 1350 W laser power were 5.3, 11 and 15 m/min respectively at a constant water-jet pressure of 7 bar. Whereas, in case of Ti the maximum cutting speed at 150 W, 300 W, 450 W and 600 W laser powers obtained were 3, 5, 12 and 15 m/min respectively at a constant water-jet pressure of 5 bar. At upper limits of cutting speed, in general some of the other common cutting defects such as formation of dross, taper and striation were observed to be significant. Similar defects were reported for gas assisted laser cutting also [3, 4]. In order to establish the process, one would like to have optimized zone of parameters where all defects are relatively small. Therefore, experimental runs were conducted for 90%, 70%, 50% and 30% of the maximum cutting speed for each laser power. Experiments were conducted for two replicates and HAZ was measured at top and bottom surfaces of both severed parts, and an average HAZ value of two replicates is considered. The coefficient of variation was under  $\pm 5\%$ .

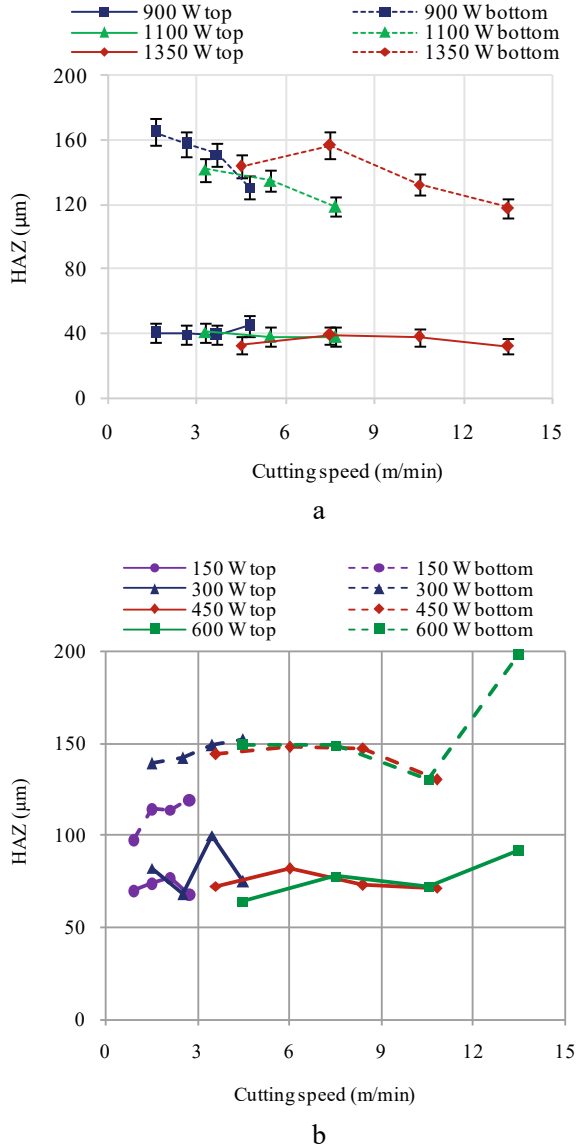
Figure 3 shows the variation of HAZ with different cutting speeds measured at both top and bottom surfaces for MS (Fig. 3a) and Ti (Fig. 3b). Since the thickness of MS and Ti specimens are very different (0.4 mm and 0.15 mm respectively), apart properties and corresponding laser power employed for cutting, therefore comparison of magnitudes of HAZs in these materials is not attempted, instead HAZs of top and bottom in same material have been compared. It can be seen that HAZ was always less at the top surface than that at the bottom surface. However, the difference tended to reduce with the increase of cutting speed in case of MS. HAZ at the bottom surface was marginally higher at the lowest laser power level, Fig. 3a. In case of Ti the difference in HAZ between top and bottom surfaces was almost constant irrespective of laser power and cutting speed Fig. 3b. However, HAZ was less at the lowest laser power level. The variations of HAZ with water-jet pressure in both materials are presented in Fig. 4a and b. Water-jet pressure was varied between 2 and 13 bars at constant laser power of 1350 W and 150 W for MS and Ti, respectively.

In MS, the HAZ on the top surface was almost constant at 3 bar and 7 bar water-jet pressure. However, at 13 bar pressure the HAZ tended to increase with the increase of cutting speed. It was observed that beyond 10.5 m/min, speed the repeatability in cutting result became poor. Therefore, HAZ for cutting speed beyond this has not been included in Fig. 4a. At the bottom surface HAZ tended to reduce with increasing cutting speed for all chosen water-jet pressure. It was found minimum for lower water-jet pressure of 3 bar.

In Ti, the HAZ was found varying with water-jet pressure for both surfaces, but remained almost constant with cutting speed. It was observed that HAZ at both top and bottom surfaces was significantly higher for 3 bar water-jet pressure than that for 5 and 7 bars, Fig. 4b. Reduction of water-jet pressure to 2 bar causes further increase in HAZ, therefore results of HAZ for water-jet pressure up to 3 bar only have been included in Fig. 4b. HAZ was minimum at 5 bar water-jet pressure and it increased again at 7 bar pressure.

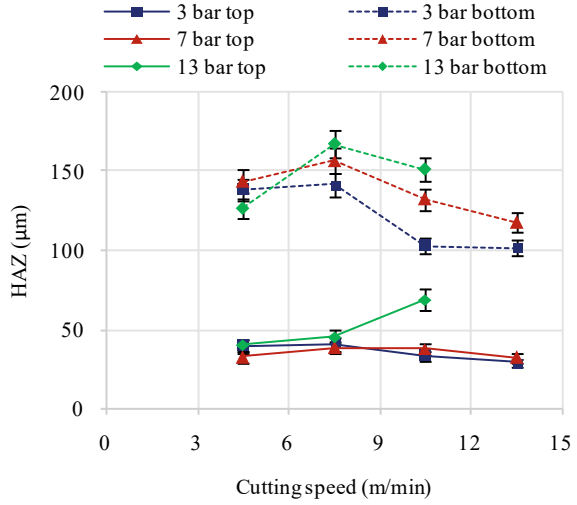
The water-jet assisted underwater laser cutting is a very complex process. The material removal depends on many factors such as laser power, cutting speed, viscosity of melt layer and shear pressure on it exerted by water-jet. The extent

**Fig. 3** Variation of HAZ with cutting speed for different laser powers, **a** MS at 7 bar of water-jet pressure, **b** Ti at 5 bar of water-jet pressure; coefficient of variation  $\leq \pm 5\%$

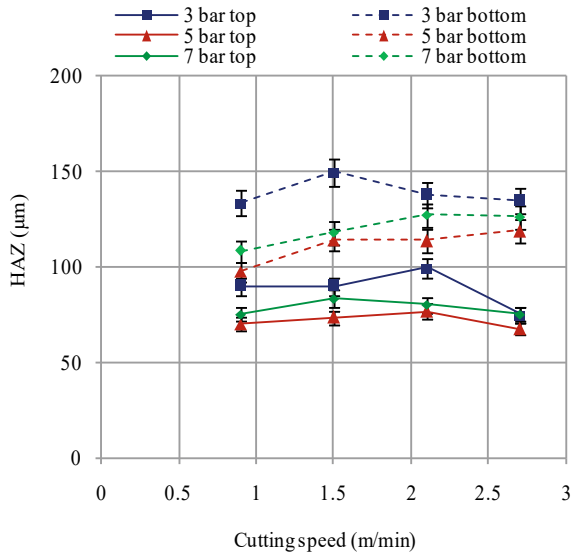


of HAZ will depend on the line energy, i.e. laser power divided by scan speed, thermo-physical property of material, mainly the thermal diffusivity and the cooling mechanism operative at the surfaces. This will also depend on the re-solidified melt layer at the cut surface and dross attached at the bottom kerf edge. During water-jet assisted underwater laser cutting process the top surface of work-piece faces continuous flow of water-jet, whereas the bottom surface remains in near stationary water.

**Fig. 4** Variation of HAZ for water-jet pressures, **a** MS, laser power = 1350 W, **b** Ti, laser power = 150 W



a



b

Thus, the top surface experiences forced heat convection and the bottom surface natural convection. In this type of cutting process forced convective heat transfer has been reported to be higher than conduction heat loss [13]. Therefore, depending upon the thermal conductivity, the HAZ may be mainly determined by convective cooling and have weak dependence on line energy, i.e. laser power and cutting speed,

especially at the top surface. Because of the convective heat transfer coefficient being larger than the natural convective heat transfer coefficient, HAZ is expected to be more at bottom surface compared to top surface. Further, the relative extent of HAZ at bottom surface compared to that at top surface is expected to be more in mild steel because of its higher thermal conductivity than that in Ti which has relatively lower thermal conductivity. The general trend of variation of HAZ at top and bottom surfaces in Figs. 3 and 4 conforms to the above. In mild steel the HAZ of bottom surface seems to be governed by mainly heat conduction and this could be the reason for the reduction in HAZ with increase of cutting speed and corresponding reduction in line energy, Figs. 3a and 4a. A marginally high HAZ at lower laser power in mild steel (Fig. 3a) could be due to the relatively low cutting speeds and thus, higher line energy compared to that at higher laser powers. In Fig. 3a, it is also seen that HAZ at top surface in mild steel abnormally increases at higher water jet pressure (13 bar) and cutting speed ( $> 7.5$  m/min). The increase of water jet pressure is expected to have higher cooling effect on the cut front along with increased shear force [17]. Moreover, at a too high pressure the water-jet could spread as it emerges out of the nozzle and also bounce at the surface. This may cause reduction in shear pressure and convective cooling [18]. As the cutting speed is increased to maximum at a constant laser power, the melt layer is expected to be more viscous at higher cutting speeds due to the reduction in line energy. All these effects may lead to re-solidification of some part of melt layer before it is ejected out and may cause abnormally high HAZ as shown in Fig. 4a. Such abnormal behaviour is not observed in case of Ti which could be because molten Ti is relatively less viscous than molten iron [19], therefore, could be reality ejected out at relatively low water-jet pressure, Fig. 4b. The optimum water jet pressure for minimum HAZ in Ti (Fig. 4b) could be due to the effects of higher water-jet pressure as discussed above.

### 3.2 FE Simulation

2D finite element simulation was carried-out to have a better insight of the process. Different values of convection coefficients were used to represent convection at the cut front, top and bottom surfaces. The cut-front and top surface will always bear forced convection due to continuous flow of water-jet; coefficient of forced convection can be calculated using equation [13, 17]

$$h_c = 0.797(K/d) * Re^{0.5} * Pr^{0.33}, \quad Pr > 3.0 \quad (1)$$

where,  $h_c$ —heat transfer coefficient,  $K$ —thermal conductivity of water,  $d$ —duct diameter (assuming the water flow through a circular duct of diameter equal to the average kerf-width),  $Re$ —Reynolds number  $(\rho v_w L/\mu)^{0.5}$ ,  $\rho$ —water density,  $v_w$ —water jet speed,  $L$ —characteristic length,  $\mu$ —dynamic viscosity, and  $Pr$ —Prandtl number.

The following assumptions are made in FE simulation modelling.



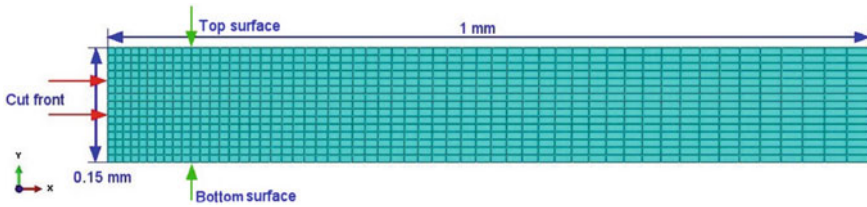


**Fig. 5** Finite element model utilised for simulation (Ti)

- The material is opaque.
- All material properties are isotropic but temperature dependant [20, 21].
- For successful cutting action, the cut-front temperature needs to be high enough to cause melting/softening of material that can be sheared-out by water-jet. This temperature was assumed to remain constant at melting temperature i.e. 1450 °C and 1670 °C for MS and Ti respectively, irrespective of laser power and cutting speed utilised. Also, this temperature was kept constant for any unit length through which the laser beam is passing.
- The material was assumed to get ejected through kerf as soon as the element temperature reached to melting temperature and the thermal conductivity was made zero there.
- The HAZ is represented by the region where temperature reaches the value in between re-crystallisation and melting at the end of heating cycle i.e. between 723–1450 °C and 880–1668 °C for MS and Ti respectively. In case of MS this 723 °C is typically considered as a lower critical temperature above which change in grain structure could occur [22]. Similarly, in Ti changes in grain structure starts from ‘ $\alpha$ ’, to ‘ $\beta$ ’ phase typically at 888 °C [23].

In order to minimise computational complication and time requirement the finer mesh was used at heating side and increasingly coarse mesh towards bulk material. Figure 5 shows the typical mesh distribution utilised in simulation. The FE model was discretized with standard linear heat transfer elements available in ABAQUS 6.10. Here, the cut front side of model represents the kerf wall tangential to which molten material is ejected-out. In order to achieve heat propagation from the cut front to base material, the cut front was exposed to constant temperature of melting, for the duration of laser interaction time. For unit length of the side kerf wall this interaction time would be  $d/v$ , where  $d$  is the laser spot diameter and  $v$  is the cutting speed. The surface film condition was defined in all four sides of model to represent convective losses or underwater condition. However, the employed film coefficient was different at different sides. Since, at cut front the convection coefficient would represent forced and its value would correspond to utilised water-jet speed, as the co-axial water-jet was used to eject the molten material. The top surface should also bear the force convection due to transverse flow of water in lateral direction. At top surface this convection coefficient would be lesser than that at cut front due to loss of water-jet speed after hitting the material surface. This convection coefficient

was calculated considering the water-jet speed after hitting the top surface to be 5% of its initial velocity. This assumed water-jet speed after hitting the top surface, gave good match between the HAZ predicted by simulation and that obtained in experiments as depicted in Fig. 6a–d for mild steel (a, b) and titanium (c, d). The other two surfaces will bear natural convection; the convection coefficient was kept constant at  $100 \text{ W/m}^2\text{C}$  [24].

In Figure 7a and b, it is observed that the trend of HAZ at top and bottom surfaces matches well with the experimental results for both materials.

Marginal deviations from experiment results could be because of the limitation of model to predict the actual dynamic behaviour of forced convective cooling. At the heated surface vaporisation of water film may occur which could change the interaction behaviour of water-jet; hence change in heat transfer coefficient. The model does not include pre-heating and post-heating due to conduction during laser

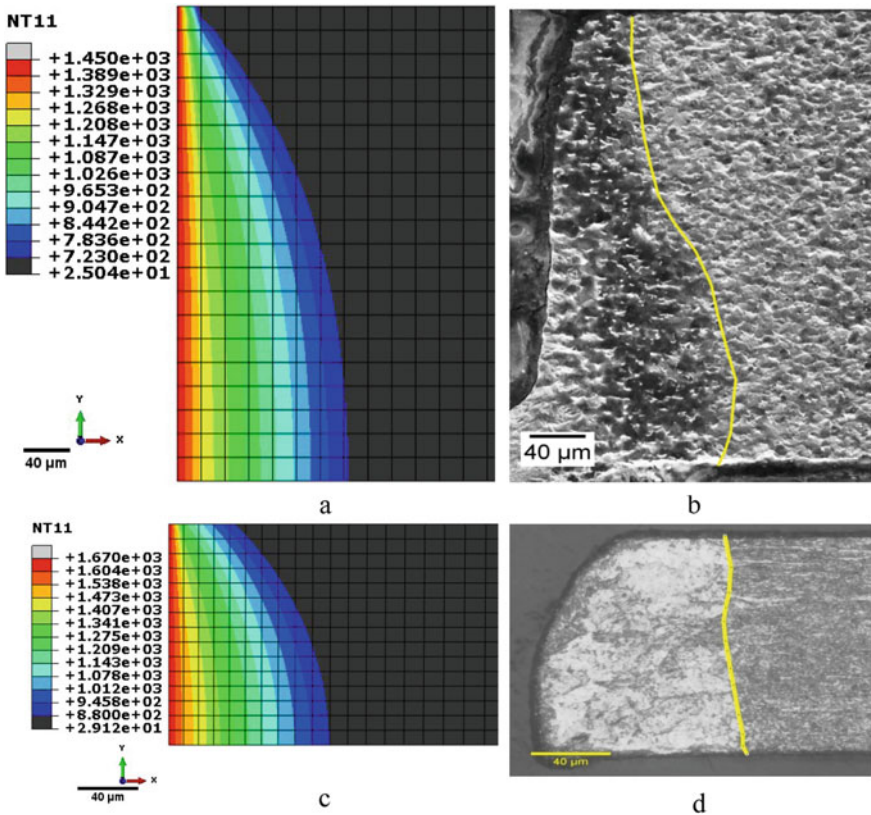
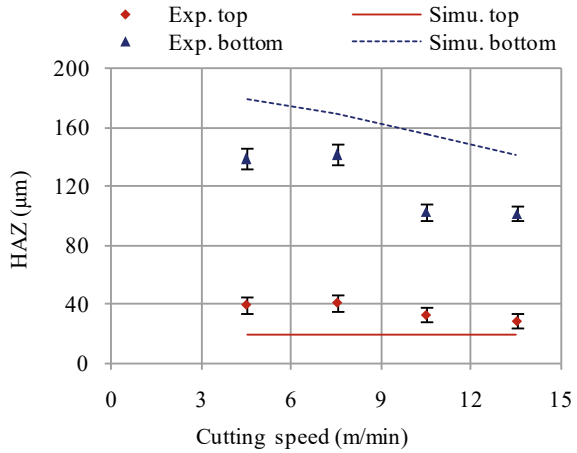
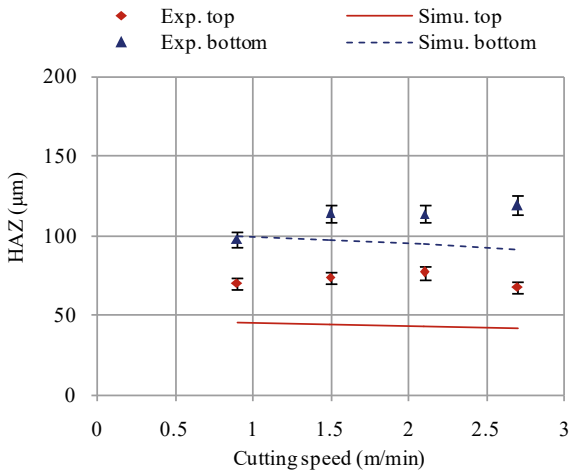


**Fig. 6** Typical temperature contours obtained through simulation at the end of heating cycle and SEM images of micro-structural of transverse cross section of laser severed sheets **a, b** for mild steel at 3 bar water-jet pressure, 1350 W laser power, and 13.5 m/min cutting speed; **c, d** for Ti at 5 bar water-jet pressure, 150 W laser power and 0.9 m/min cutting speed

**Fig. 7** Variation of HAZ obtained through simulation and experiment, **a** mild steel, 3 bar water-jet pressure, 1350 W laser power; **b** Ti, 5 bar water-jet pressure, 150 W laser power



a



b

scan. Therefore, in all cases the model predicted less HAZ than the experimental results; accept in case of mild steel specimen at the bottom surface. Relatively lower HAZ at the bottom surface in mild steel cutting could be because of a significant taper in kerf which will cause increase in water-jet velocity at the kerf exit; and this in turn could enhance the convective heat transfer. This has not been considered in the model. The experimental results will be compared with the conventional gas assisted laser cutting of these materials.

## 4 Conclusions

The following conclusions can be made based on the experimental and numerical studies of HAZ in water-jet assisted underwater laser cutting of thin sheets of mild steel (SAE 1020) and CP-Ti.

- HAZ at the top surface was mainly govern by the force convection of water-jet and therefore was less compared to that at the bottom surface which was getting cooled by natural convection in water.
- HAZ at the top surface was almost constant, irrespective of laser power and cutting speed.
- The difference in HAZs between top and bottom surfaces was relatively more in mild steel due to higher thermal conductivity, than in Ti.
- HAZ at bottom surface reduced with increase of cutting speed at constant laser power and water-jet speed. It depended mainly on line energy.
- Cutting process was more stable at lower range of water-jet pressure between 3 and 5 bar.
- A 2D model used in FE simulation predicted well the behaviour of HAZ.

**Acknowledgements** The authors would like to acknowledge Department of Science and Technology, New Delhi for their financial support for high power Yb-fiber laser and the Board of Research on Nuclear Science (BRNS), Mumbai for supporting various research activities. They will like to gratefully acknowledge the invaluable suggestions and help extended by the team members of Laser Material Processing Laboratory, Department of Mechanical Engineering, IIT Kharagpur in conducting the study. They are also thankful to Prof. S Paul and staffs of Machine tool and Machining laboratory, IIT Kharagpur for their help in preparation of samples.

## References

1. Steen WM, Mazumder J (2010) Laser material processing, 4th edn. Springer, New York
2. Sheng PS, Joshi VS (1995) Analysis of heat-affected zone formation for laser cutting of stainless steel. *J Mater Process Technol* 53:879–892
3. Sobih M, Crouse PL, Li L (2008) Striation-free fibre laser cutting of mild steel sheets. *Appl Phys A* 90:171–174
4. Rajaram N, Sheikh-Ahmad J, Cheraghi SH (2003) CO<sub>2</sub> laser cut quality of 4130 steel. *Int J Machine Tools Manuf* 43:351–358
5. Al-Mashikhi SO, Powell J, Kaplan A, Voisey KT (2011) Heat affected zones and oxidation marks in fiber laser–oxygen cutting of mild steel. *J Laser Appl* 23:042003
6. Shanjin L, Yang W (2006) An investigation of pulsed laser cutting of titanium alloy sheet. *Opt Laser Eng* 44:1067–1077
7. Ghany KA, Newishy M (2005) Cutting of 1.2 mm thick austenitic stainless steel sheet using pulsed and CW Nd:YAG laser. *J Mater Process Technol* 168:438–447
8. Rao BT, Kaul R, Tiwari P, Nath AK (2005) Inert gas cutting of titanium sheet with pulsed mode CO<sub>2</sub> laser. *Opt. Laser Eng.* 43:1330–1348
9. Sakka T, Iwanaga S, Ogata YH (2000) Laser ablation at solid–liquid interfaces: an approach from optical emission spectra. *J Chem Phys* 112(19):8645–8653

10. Komashko AM, Feit MD, Rubenchik AM, Perry MD, Banks PS (1999) Heat affected zones and oxidation marks in fiber laser–oxygen cutting of mild steel. *Appl Phys A* 69:S95–S98
11. Richerzhagen B (2001) Chip singulation process with a water jet-guided laser. *Solid State Technol* 44(4):S25-28
12. Kruusing A (2004) Underwater and water-assisted laser processing: Part 1—general features, steam cleaning and shock processing. *Opt Laser Eng* 41:307–327
13. Mullick S, Madhukar YK, Roy S, Kumar S, Shukla DK, Nath AK (2013) Development and parametric study of a water-jet assisted underwater laser cutting process. *Int J Machine Tools Manuf* 68:48–55
14. Madhukar YK, Mullick S, Shuklab DK, Kumar S, Nath AK (2013) Effect of laser operating mode in paint removal with a fiber laser. *Appl Surf Sci* 264:892–901
15. Madhukar YK, Mullick S, Nath AK (2013) Development of a water-jet assisted laser paint removal process. *Appl Surf Sci* 286:192–205
16. Mullick S, Madhukar YK, Kumar S, Shukla DK, Nath AK (2011) Temperature and intensity dependence of Yb-fiber laser light absorption in water. *Appl Opt* 50(34):6319–6326
17. Li CF, Johnson DB, Kovacevic R (2003) Modeling of waterjet guided laser grooving of silicon. *Int J Machine Tools Manuf* 43:925–936
18. Ravikumar SV, Jha JM, Mohapatra SS, Pal SK, Chakraborty S (2014) Experimental investigation of effect of different types of surfactants and jet height on cooling of a hot steel plate. *J Heat Transf* 136:072102–072110
19. Battezzati L, Greer AL (1989) The viscosity of liquid metals and alloys. *Acta Metall* 37:1791–1802
20. Tenga TL, Chang PH (1998) Three-dimensional thermomechanical analysis of circumferentially welded thin-walled pipes. *Int J Pres Ves Pip* 75:237–247
21. Ding H, Shin YC (2011) Dislocation density-based grain refinement modeling of orthogonal cutting of commercially pure titanium. In: Proceedings of the ASME international manufacturing science and engineering conference (MSEC2011), June 13–17, 2011, Corvallis, Oregon, USA
22. Ghosh A, Mallik AK. (2005) Manufacturing science. EWP, New Delhi
23. Badkar DS, Pandey KS, Buvanashakaran G (2010) Effects of laser phase transformation hardening parameters on heat input and hardened-bead profile quality of unalloyed titanium. *Trans Nonferrous Met Soc China* 20:1078–1091
24. [http://www.engineeringtoolbox.com/convective-heat-transfer-d\\_430.html](http://www.engineeringtoolbox.com/convective-heat-transfer-d_430.html). Cited at 20 Oct 2014

# Advanced Beam Shaping for Ultrafast Laser Micro-processing



O. J. Allegre, J. Ouyang, W. Perrie, Y. Jin, S. P. Edwardson, and G. Dearden

**Abstract** This paper details the use of novel beam shaping methods to improve the flexibility and speed of ultrafast laser micro-processes. The vector fields of a picosecond-pulse laser beam are shaped using a Spatial Light Modulator (SLM) and polarization optics, so that both the amplitude and direction of the electric field vectors are controlled with a high spatial resolution. This allows to shape the focal field landscapes obtained by focusing the beam with a low Numerical Aperture (NA) lens. A number of shaped vector beams are produced, including radially or azimuthally polarized vortex beams. All these beams are then used for surface ablation of titanium alloy substrates at low fluence to imprint Laser Induced Periodic Surface Structures (LIPSS). Thanks to their polarization dependent properties, LIPSS help to analyse the vector fields in the focal region. This analysis reveals for the first time how the orbital angular momentum associated with a vortex vector field induces complex focal field landscapes which fluctuate along the optical axis of the focusing lens. The produced shaped focal fields are also used for helical micro-drilling stainless steel and silicon substrates. The results are compared in terms of quality and efficiency, illustrating how the distinct machining properties associated with each beam make it best suited for specific processes or materials.

**Keywords** Beam shaping · Vector beam · Polarization · Ultrafast

---

O. J. Allegre (✉)

Department of Mechanical, Aerospace and Civil Engineering, The University of Manchester, Manchester M13 9PL, UK

e-mail: [olivier.allegre@manchester.ac.uk](mailto:olivier.allegre@manchester.ac.uk)

J. Ouyang · W. Perrie · Y. Jin · S. P. Edwardson · G. Dearden

Laser Group, School of Engineering, University of Liverpool, Liverpool L69 3GQ, UK

© Springer Nature Switzerland AG 2022

S. Hinduja et al. (eds.), *Proceedings of the 38th International MATADOR Conference*, [https://doi.org/10.1007/978-3-319-64943-6\\_8](https://doi.org/10.1007/978-3-319-64943-6_8)

## 1 Introduction

The last few years have seen increased research activity in the field of laser microprocessing with ultrashort pulses (pulse-length  $<10$  ps), where the laser energy interacts with the workpiece material with very little thermal damage and allows sub-micron resolution features to be manufactured [1]. A number of processes have benefited from this, including the drilling of fuel-injection nozzles [1], the dicing of silicon wafers, or the nanotexturing of biomedical functional surfaces [2]. Despite their potential, the low speed and lack of flexibility of early ultrashort-pulse laser microprocessing systems slowed down their industrial uptake. New methods to improve efficiency without decreasing quality would further expand the range of applications that benefit from these processes.

Laser beams with a space-variant electric field orientation and/or amplitude are often referred to as vector beams [3]. They include the beams with a radial or azimuthal polarization as well as those which carry an orbital angular momentum (i.e. beams with an optical vortex field). Recent studies have explored the use of vector beams in short-pulse laser microprocesses such as surface structuring, drilling and cutting [3, 4]. These early results highlighted the great potential of vector beams for improving ultrafast laser process efficiency and speed without compromising quality.

However, these early results were limited in scope and mainly compared beams with a pure radial and azimuthal polarization (i.e. without orbital angular momentum). Higher order vector beams with more complex fields which may be beneficial for specific ultrafast processes have not yet been investigated. Thus, in this paper we use an industrial picosecond-pulse laser processing system with a Spatial Light Modulator (SLM) and polarization optics to produce a number of vector beams, including radially and azimuthally polarized beams with and without an orbital angular momentum. The low Numerical Aperture (NA) focusing properties of each vector beam is analysed in detail. These beams are then used for helical drilling stainless steel and silicon substrates and the results are compared in terms of quality and efficiency.

## 2 Experimental Details

The experimental setup is shown in Fig. 1. The laser source is a High-Q picosecond-pulse laser system (10 ps pulse width, 1064 nm wavelength,  $M^2 < 1.3$ , 2W maximum average power, 50 kHz maximum repetition rate and a horizontal linear polarization output). The beam vector fields are structured using a SLM (Hamamatsu X10468-03) and a waveplate (S-waveplate, Altechna or quarter-waveplate, Newport), to convert the incident linearly polarized beam into a cylindrical vector beam or a circularly polarized beam respectively. A 4-f system (Lens 1 and 2 in Fig. 1) re-images the produced beam vector fields into the 10 mm input aperture of a scanning galvo (Nutfield). At the galvo output, the beam is focused with a flat field f-theta lens ( $f =$

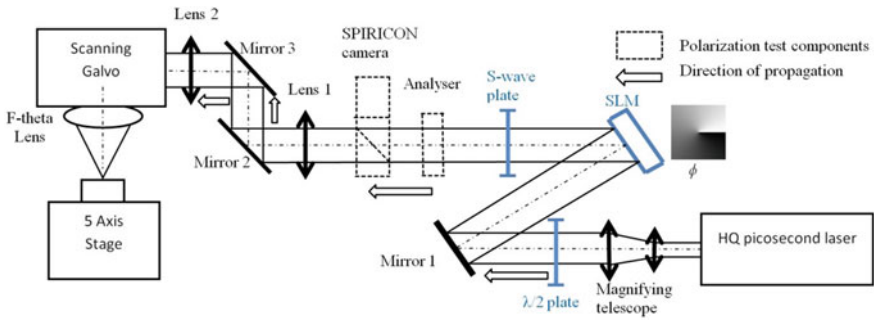


**Fig. 1** Experimental setup used to shape the vector field of a picoseconds-pulse laser microprocessing system

100 mm). For the surface ablation and drilling experiments, samples are mounted on a precision 5-axis motion control system (Aerotech) allowing accurate positioning in the focal plane. Prior to processing the samples, the beam is analyzed with a rotating polarizing filter and a SPIRICON beam profiler (see Fig. 1).

In the experiments, a number of beam vector field configurations are produced by tilting the S-waveplate optical axis to various angles. Henceforth, vector beams with a radial, an azimuthal, or an intermediate tilted polarization (see Fig. 2) are referred to as RP, AP and IP beams respectively. A circularly polarized beam is also used in some of the experiments, produced by replacing the S-waveplate with its fast axis tilted to 45°. This is referred to as CP beam

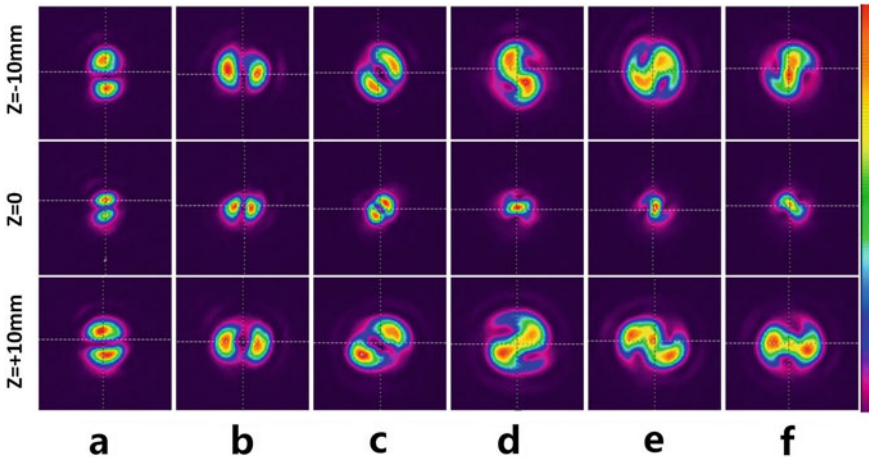


**Fig. 2** Intensity profiles of the focused beam, observed at various Z coordinates along the optical axis ( $Z = 0$  at focal plane, middle row). **a** RP beam. **b** AP beam. **c** IP beam. **d** RPOAM beam. **e** APOAM beam. **f** IPOAM beam. Intensity in arbitrary unit, transmission axis of polarizing filter oriented vertically



henceforth. For comparison purposes, an orbital angular momentum is then added to all these beams by using the SLM to induce an optical vortex phase wavefront with a topological charge value of  $l = 1$ , with the waveplate configured as before. Henceforth, the radially, azimuthally, intermediately and circularly polarized beams with an orbital angular momentum are referred to as RPOAM, APOAM, IPOAM and CPOAM respectively.

### 3 Results and Discussion

#### 3.1 Analysis of Focal Fields

A first method for analysing the focal fields consists in projecting the focused beam through the polarizing filter onto the SPIRICON profiler, located in a range of places along the optical axis of a focusing lens (Lens 1 in Fig. 1). The resulting intensity profiles shown in Fig. 2 reveal a clear distinction between the vector beams with and without orbital angular momentum. The RP, AP and IP beams with no angular momentum have a distinct double-lobe intensity profile (Fig. 2a–c), typical of annular vector beams [4], which is invariant as it propagates along the optical axis of the focusing lens (apart from the obvious scale factor, proportional to the distance away from the focal plane, see Fig. 2). On the other hand, all the beams with orbital angular momentum have a profile with non-zero intensity at the centre (Fig. 2d–f). It can be seen that the intensity profile varies significantly along the optical axis. At the focal plane, the profile is mostly Gaussian with peak intensity in the centre and has an approximate elliptical shape (see middle row in Fig. 2d–f). Note the long axis of the ellipse is dependent on the incident polarization (i.e. horizontal or vertical when the incident beam is radially or azimuthally polarized respectively, see Fig. 2d, e respectively).

#### 3.2 Surface Processing

To better understand the focal field properties, a second focal analysis method is used: each vector beam in turn is used to produce laser ablation spots (and thus imprint its intensity distribution) on the surface of titanium alloy samples (Ti6Al4V) placed in the focal region of the f-theta lens (Fig. 1). Using a laser fluence near the ablation threshold of the titanium alloy results in the growth of microscopic Laser Induced Periodic Surface Structures (LIPSS) within the ablation spots. The wavelength-sized LIPSS typically develop orthogonally to the local electric field vectors [5] and thus enable to analyse the vector field landscapes in the focal region [6], with a better accuracy than the optical analysis method above. The surface of the titanium samples is placed in a range of positions above or below the focal plane, producing patterns

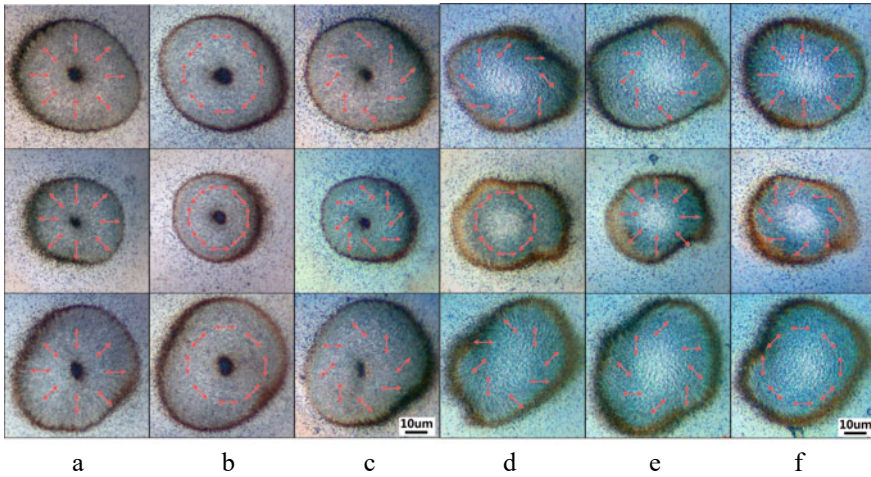


**Fig. 3** Optical micrographs showing the laser ablation spots produced along the optical axis with **a** RP beam, **b** AP beam, **c** IP beam, **d** RPOAM beam, **e** APOAM beam, **f** IPOAM beam. The ablation spots have been produced 500  $\mu\text{m}$  above the focal plane (top row), at the focal plane (middle row), and 500  $\mu\text{m}$  below the focal plane (bottom row). The red arrows indicate the polarization direction in each location

of LIPSS at each location. These locations are referred to as observation planes henceforth. For all the surface ablation experiments, the laser output is attenuated to produce an average fluence of  $\sim 0.4 \text{ J/cm}^2$  on the sample surface. The samples are exposed for a duration of 10 ms ( $\sim 50$  pulses at 5 kHz pulse repetition rate) whilst the beam remains static with regards to the sample. After laser exposure, the produced ablation spots are imaged with an optical microscope (see optical micrographs in Fig. 3).

The ablation spots produced when the incident beam is RP, AP or IP with no orbital angular momentum have a clear annular structure with zero intensity in its central region (Fig. 3a–c), which is consistent with that expected when focusing cylindrical vector beams with a low NA lens [4]. LIPSS are produced with a high uniformity within the ablation spots and indicate that the polarization state is maintained in all observation planes, with no variation along the optical axis of the focusing lens. Note the IP beam with an intermediate tilted polarization (Fig. 2c) produces LIPSS patterns with a spiral shape (see Fig. 3c).

The ablation spots produced when the incident beams had an orbital angular momentum of  $l = 1$  are shown in Fig. 3d–e. The geometry of the laser spots, with deeper ablation in the centre than around the edges, was consistent with a Gaussian-like intensity profile (albeit with some distortions due to steps in the vortex phase-maps induced with the SLM). From Fig. 3, it can be seen that LIPSS have been produced around the edges, but not in the centre of the focal spots. Further ablation experiments with various fluence values showed that it was extremely difficult to produce clear LIPSS in the centre of the laser focal spots. Furthermore, the incident

RPOAM beam produced a focal spot with LIPSS oriented in a radial pattern. As LIPSS are orthogonal to the local electric field [5], this suggests that the focal field was azimuthally polarized in these regions. These results show that incident radially and azimuthally polarized beams with an orbital angular momentum of  $l = 1$  typically produce a partial inversion of the polarization state at the focal plane. Looking at the fields away from the focal plane in Fig. 3, we can see that the patterns of LIPSS (and corresponding vector field landscape) clearly fluctuate along the optical axis of the focusing lens, in such a way that the states of polarization in the observation planes 500  $\mu\text{m}$  above and below the focal plane are orthogonal to each other (see top and bottom rows in Fig. 3d–f). For example the incident IPOAM beam produces a mostly radial polarization state at the observation plane 500  $\mu\text{m}$  above the focal plane (top micrograph in Fig. 3f). As the beam propagates to the observation plane 500  $\mu\text{m}$  below the focal plane, the polarization changes to a mostly azimuthal state (bottom micrograph in Fig. 3f). These important experimental results demonstrate the variability of the focal fields along the optical axis due to the orbital angular momentum and have significant implications for micromachining.

### 3.3 Microdrilling

Having demonstrated the ability to shape the focal fields into various complex landscapes, we now investigate the micromachining properties of some of these vector beams (i.e. RP, AP, RPOAM and APOAM beams). For comparison purposes, we also use linearly and circularly polarized Gaussian and annular beams (the latter are simply obtained by inducing an orbital angular momentum of  $l = 1$  to the linearly or circularly polarized Gaussian beams). We carry out helical drilling of stainless steel 302 sheets (370 and 500  $\mu\text{m}$  thick) and silicon wafers (500  $\mu\text{m}$  thick) which are typical processes used in industrial micromachining. All the drilling tests use a pulse energy of 80  $\mu\text{J}$  (i.e. an average fluence of 11.3  $\text{J}/\text{cm}^2$  at the focal plane) with a pulse repetition rate of 10 kHz, and the beam is scanned continuously along a circular path with a 100  $\mu\text{m}$  diameter and a 20 mm/s scan speed, using various laser exposure durations. These tests are repeated a number of times with each vector beam to average the results. After laser drilling, all the results are analysed with an optical microscope.

First, the results are assessed qualitatively by comparing the relative size, shape and edge quality of the drilled holes. Figures 4, 5 and 6, which show typical holes drilled in the silicon and steel substrates, highlight significant differences in the hole geometry produced with AP and APOAM beams (i.e. with an annular and Gaussian focal intensity profile respectively). This is especially visible with the exit holes, which are larger and smoother in the latter case (see for example Fig. 6a and b). In fact, the APOAM beam produces holes which are more similar to those made with the CP Gaussian beam (see exit holes, Fig. 6c). It is noted that the linearly polarised (LP) beam produces the worst drilling quality, (see for example Fig. 4d).

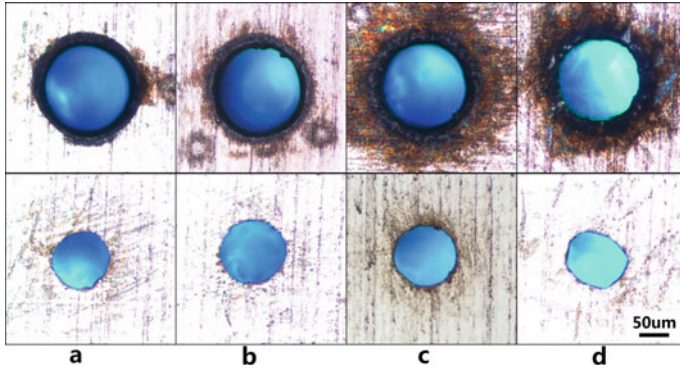


**Fig. 4** Optical micrographs showing drilling results on 370  $\mu\text{m}$  stainless steel sheet with: **a** AP, **b** APOAM, **c** CP and **d** LP beams at  $\sim 20$  s laser exposure duration. Top row showing the entrance and bottom row the exit

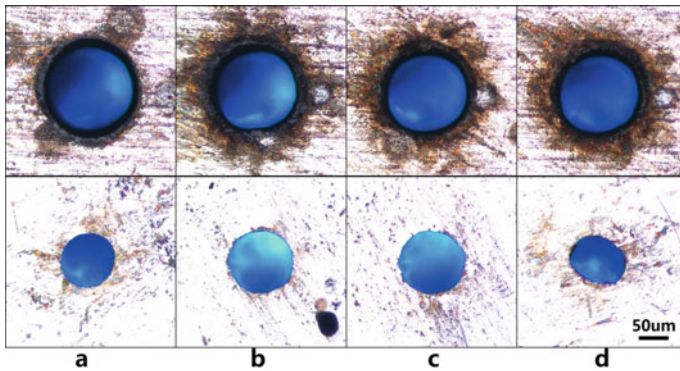


**Fig. 5** Optical micrographs showing drilling results on 500  $\mu\text{m}$  stainless steel sheet with: **a** AP, **b** APOAM, **c** CP and **d** LP beams at  $\sim 70$  s laser exposure duration. Top row showing the entrance and bottom row the exit

Next, we evaluate the drilling efficiency of the vector beams by measuring the diameter of the produced holes entrance and exit. The average diameter of holes drilled in the silicon and stainless steel plates are plotted in Fig. 7. Looking at the results obtained in the 500  $\mu\text{m}$  thick silicon and 500  $\mu\text{m}$  thick steel plates, the most noticeable feature is the similarity in the drilling characteristics of the RPOAM, APOAM and CP beams, since they all produce comparable hole geometries ( $\sim 125 \mu\text{m}$  diameter entrance and  $\sim 112 \mu\text{m}$  diameter exit for example in silicon i.e. a sidewall half-angle taper of  $\sim 1.5^\circ$ ). On the other hand, the RP and AP beams *without* angular momentum have broadly similar characteristics as the CPOAM beam (producing holes of  $\sim 142 \mu\text{m}$  diameter entrance and  $\sim 84 \mu\text{m}$  diameter exit in silicon i.e. a significantly larger half-angle taper of  $\sim 6.6^\circ$ ). These results can be understood since the former set of beams all produces Gaussian like focal intensity profiles,

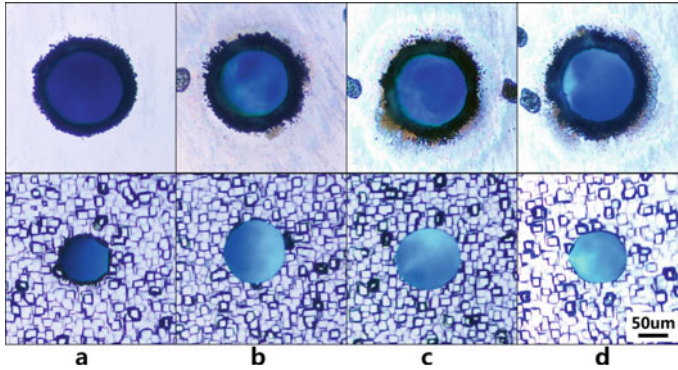


**Fig. 6** Optical micrographs showing drilling results on 500  $\mu\text{m}$  silicon wafer with: **a** AP, **b** APOAM, **c** CP and **d** LP beams at  $\sim 140$  s laser exposure duration. Top row showing the entrance and bottom row the exit

whereas the latter produces annular profiles with a lower peak intensity. In other words, the drilling properties in the 500  $\mu\text{m}$  thick silicon and steel plates are more influenced by the focal intensity distribution than the state of polarization

Looking at the drilling results in the 370  $\mu\text{m}$  thick stainless steel plate (Fig. 7), it can be seen that the distinction between the drilling properties of the annular beams (i.e. RP, AP and CPOAM) and those of the Gaussian beams (i.e. RPOAM, APOAM and CP) is less obvious than with the thicker plates. Within the set of annular beams, there is a clear influence of polarization on the diameter of the exit holes. The RP beam produces.

A  $\sim 10\%$  larger exit diameter than the AP beam ( $\sim 94$   $\mu\text{m}$  vs.  $\sim 86$   $\mu\text{m}$ ). This is the result of the better coupling efficiency of radial polarization, which mostly produces *p*-polarized internal reflections on the sidewalls during drilling [3, 4]. On the other hand, azimuthal polarization mostly produces *s*-polarized internal reflections, with a higher reflectivity that leads to increased losses through the hole exit aperture and thus a poorer coupling efficiency overall. The CPOAM beam produces an intermediate exit hole diameter ( $\sim 87$   $\mu\text{m}$ ). This results from the average of *p*- and *s*-polarized internal reflections during drilling typically seen with circular polarization [6], thus an intermediate coupling efficiency between that of radial and azimuthal polarization. Note that the RPOAM and APOAM beams induce a hybrid state of polarization at the focal plane as demonstrated in Sect. 3.2, and thus both produce exit holes with fairly similar diameters. In summary, these results illustrate how the beam vector fields can be tailored to specific applications requirements. By shaping the focal intensity profile and polarization distribution, the machining properties can be optimized for a given process or material. For example for an application requiring holes with reduced taper in 500  $\mu\text{m}$  thick silicon wafers (i.e. entrance and exit holes of similar diameter), a drilling process with a RPOAM or APOAM would be most appropriate, since it produces the lowest taper angle.

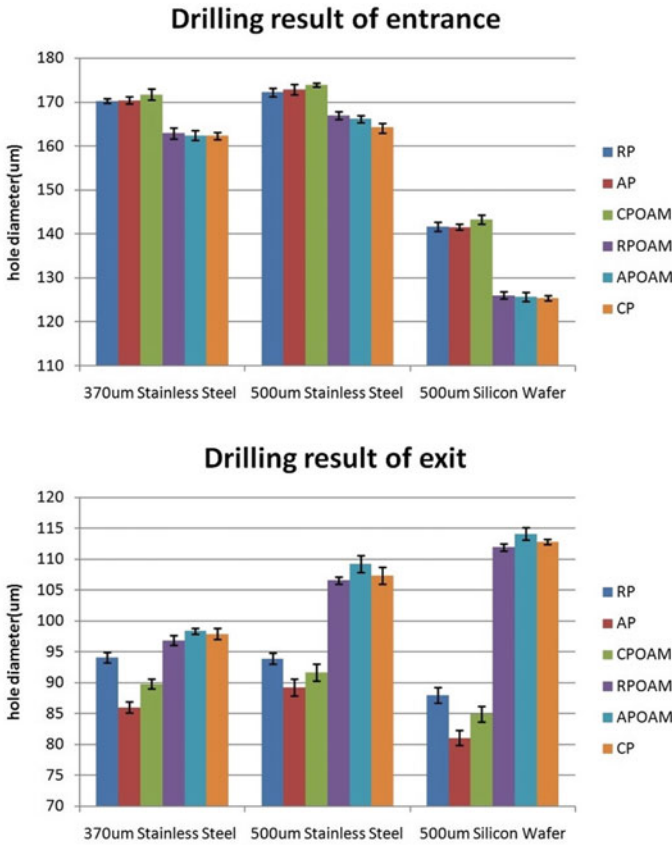


**Fig. 7** Average diameter of drilled hole entrance (top) and exit (bottom) in 370 μm thick stainless steel sheets (~ 20 s laser exposure duration), 500 μm thick stainless steel sheets (~ 70 s exposure duration), 500 μm thick silicon wafer (~ 140 s exposure duration) using shaped focal fields

## 4 Conclusions

In this paper, we have used novel beam shaping methods to accurately control the focal fields of ultrashort-pulse laser beams and influence their micromachining properties. A linearly polarized picosecond-pulse laser beam was structured using an SLM and waveplates, so as to produce radially and azimuthally polarized beams with or without orbital angular momentum. The vector fields obtained by focusing these beams with a low NA lens were analyzed by imprinting LIPSS on polished titanium alloy samples at near-threshold fluences. This revealed for the first time how the orbital angular momentum associated with a vortex wavefront induces structured field landscapes which fluctuate along the optical axis of the focusing lens. The produced vector beams were used for helical drilling, showing how the intensity profile and state of polarization in the focal plane influence the processing speed and

quality. These results illustrate how tailored vector beams can be used to optimize laser microprocesses. The great advantage of the method described here is its flexibility, with an almost infinite range of optical field combinations. Future work will further explore this potential, optimizing vector beams configurations for specific laser micromachining processes.

## References

1. Breiting D, Ruf A, Dausinger F (2004) Fundamental aspects in machining of metals with short and ultrashort laser pulses. *Proc SPIE* 5339:49–63
2. Stratakis E, Ranella A, Fotakis C (2011) Biomimetic micro/nanostructured functional surfaces for microfluidic and tissue engineering applications. *Biomicrofluidics* 5(1):013411
3. Allegre OJ, Perrie W, Edwardson SP, Dearden G, Watkins KG (2012) Laser microprocessing of steel with radially and azimuthally polarized femtosecond vortex pulses. *J Opt* 14(8):85601
4. Weber R, Michalowski A, Abdou-Ahmed M, Onuseit V, Kraus M, Graf T (2011) Effects of radial and tangential polarization in laser material processing. *Phys Procedia* 12:21–30
5. Guosheng Z, Fauchet PM, Siegman AE (1982) Growth of spontaneous periodic surface structures on solids during laser illumination. *Phys Rev B* 26(10):5366–5381
6. Allegre OJ, Perrie W, Bauchert K, Dearden G, Watkins KG (2012) Real-time control of polarisation in ultra-short-pulse laser micro-machining. *Appl Phys A* 107(2):445–454

# Controlled Fracture of the Soda-Lime Glass with a Contact Ball-Lens in Nd-YAG Laser Thermal Cleavage



Hung-Hsuan Yean and Jehnming Lin

**Abstract** The effects of the contact ball-lens on the soda lime glass in laser thermal cleavage with a cw Nd-YAG laser were investigated in this study. A contact ball-lens was adopted to generate a bending force on the crack formation of the soda-lime glass in the laser cutting process. The Nd-YAG laser beam (wavelength of 1064 nm) was focused through the ball-lens and transmitted to the soda-lime glass, which was coated with a carbon film on the surface with a bending force from a ball-lens to generate a tensile stress state on the surface cracking. The fracture was controlled by the contact ball-lens and a straight cutting was tested to demonstrate the feasibility. Experimental observations on the crack propagation from the leading edge, main section and trailing edge of the glass sheet were compared with various mechanical and thermal loadings. Further analyses on the stress under various laser powers and contact ball loadings were made to characterize the innovative technology. The results show that the distributions of the side crack at the leading and trailing edges are mainly dependent on the boundary condition, contact force, cutting speed and laser power. With the increase of the mechanical and thermal loadings, the region of the side cracks might be dramatically reduced with proper selection of the geometrical constraints. Therefore the application of the contact ball-lens is a possible way to control the fracture in laser cleavage with improved cutting qualities.

**Keywords** Laser cleavage · Controlled fracture · Contact ball lens

## 1 Introduction

Laser can be focused as a cutting tool to achieve a high energy density without the tool contact on the specimen. Since the laser machining has the flexibility for the rapid change of the product design and manufacturing, it is suitable for the process automation in the modern industry. In comparison with the conventional

---

H.-H. Yean · J. Lin (✉)

Department of Mechanical Engineering, National Cheng Kung University, Tainan, Taiwan  
e-mail: [linjem@mail.ncku.edu.tw](mailto:linjem@mail.ncku.edu.tw)



technologies, laser machining is one of the popular applications of the laser materials processing. According to the extraordinary cutting performance of the brittle materials by the laser beam in laser cleaving process, many studies have been carried out in literature. Normally the conventional cutting tool applied for the glass sheet was diamond tip, but the tool contact will cause a rapid wear and combine with rough cutting edges of the glass. Due to the heating with laser irradiation on the glass surface, the thermal stress state could be generated of the surface cracking on glass. Based on the moving path of the laser heating, the thermal cracking can be controlled in various ways, and the laser cleavage method can replace many conventional machining processes such as diamond cutting for the glass. Alternatively the laser cutting might generate a thermal stress on the glass sheet and cleave the glass surface with a following crack penetration under a mechanical loading, and it has successfully applied to cut the brittle materials such as ceramics and silicon wafers.

Many attempts have been made for the fracture control on brittle materials such as ceramics and glasses by laser cutting [1–5], Tsai et al. have studied the crack propagation of the ceramic substrate when cutting curves and asymmetrical straight lines. They found that the extension of the breaking frontier is larger than the movement of the laser spot, the actual fracture trajectory deviates from the desired trajectory [1]. Miyashita et al. [2] used a Nd-YAG laser to cut the soda lime glass with a continuous laser power of 500 W and cutting speed of 20 mm/s. The crack tip propagated after the turning point about 1.4 mm and formed a circular arc in another direction. They also use the finite element method to prove that the maximum tangential stress intensity factor  $K_{\theta_{\max}}$  is an important parameter to control the crack growth. In 2007 Tsai et al. [3] used a bending device on the glass sheet to break the glass sheet after the laser passing. A three-point bending device was clamped on the glass sheet so that the surface can be machined in a tensile stress state, then the crack propagation velocity was increased with a controlled deflection. More recently the control of the fracture of the straight line cutting with pulsed diode laser has been made by Nisar and Li et al. [4, 5]. In 2010 they have investigated the crack formation on the soda-lime glass cleaved by diode lasers [4]. The control of the deviation of the crack from the cutting path at the leading and tailing edges has been made by pulsed laser radiation to minimize the cut path deviation by reducing thermal stresses at optimum laser parameters, and the stress state has been simulated by FEM to verify this effect. Furthermore they found the thermal stresses generated during laser scanning are strongly dependent upon laser beam geometry [5], and their work also shows that the beam divergence inside the glass plays a significant role in the cutting path deviation at the edges of the glass.

The laser beam was applied to the glass cutting as a heat source. The heat was diffused into the glass from laser spot and dissipated into the surroundings. Thus the stress state was generated on the substrate surface to initiate the cracks, and the crack progressively followed with the laser beam [6].

The laser path might not consistent with the crack propagation in the laser cleavage of the brittle materials, therefore an innovative method was proposed to overcome the problem in the present study. A laser beam transmits through a contact ball-lens in a straight-line cutting to improve the crack control in the laser cleavage process.

The ball-lens with a contact force was used to bend the glass sheet in laser cleavage. Due to the bending moment, a stress state might enhance the crack tip generated by thermal stress on the surface heated by laser beam and the crack continuously propagates in the laser beam direction. Stress analyses were made to characterize the process for the further applications.

## 2 Experiment

The experimental arrangement is illustrated in the Fig. 1. A cw TEM<sub>00</sub> Nd-YAG laser with a wavelength of 1064 nm was focused through a convex silica lens and a BK7 ball-lens to irradiate on a soda-lime glass at a beam spot diameter of  $a_o$  on the bottom surface, where was coated with a carbon film of the thickness about 6 μm to increase thssse laser absorption up to 79%. The properties of the silica and BK7 les are listed in Tables 1 [7]. The soda-lime glass substrate with the dimensions of 76 mm × 25 mm × 1 mm was used in the experiment. Since the laser beam with a wavelength of 1064 nm through the soda-lime glass is considered as a high transmittance and

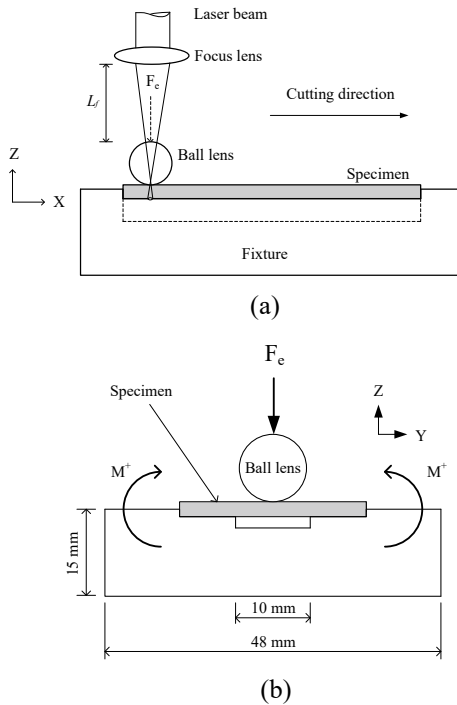


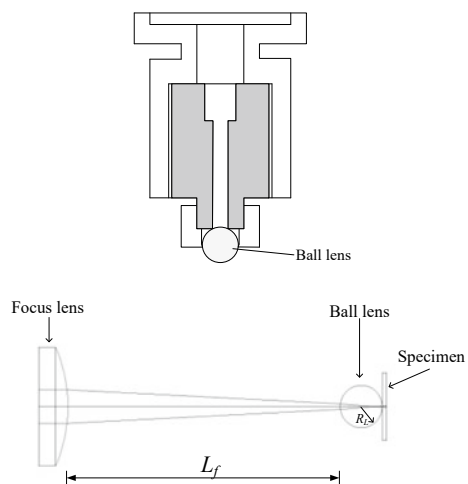
**Fig. 1** a Nd-YAG laser thermal cleavage with a contact ball-lens b Transverse cross-section view of the cutting front, where the laser cutting direction is along the x axis

**Table 1** Properties of the ball-lens [7]

Material	BK7
Density	2510 kg/m <sup>3</sup>
Thermal expansion coefficient	$8.6 \times 10^{-6}$ m/K
Thermal conductivity	1.12 W/m-°C
Specific heat	710 J/kg-K
Melting point	1400°C
Tensile strength	30 MPa
Rupture strength	690 MPa
Young's modulus	$8 \times 10^4$ MPa
Poisson's ratio	0.208

approximate 8% will be absorbed [8], therefore the heat affected zone is mainly on the bottom surface coated with the carbon film. As illustrated in Fig. 1b, two lateral edges of the glass specimen were clamped at a fixture with a groove of 10 mm in width and the ball-lens was pre-loaded by a contact force on the upper surface of the glass to create a bending moment on the glass substrate as illustrated in Fig. 1b, where the ball-lens was contacted to the upper surface of the glass specimen. According to the loading force  $F_e$  from the ball-lens on the glass substrate, it will generate a bending moment  $M^+$  towards the ball-lens and distribute a tensile stress state on the bottom surface of the substrate [9]. Therefore the tensile stress combined with the thermal stress on the heating zone due to the laser absorption by the carbon film on the bottom surface, the glass sheet will be cleaved with both mechanical and thermal loading in the crack propagation control.

The ball-lens system is illustrated in Fig. 2 and there are two sets of the ball-lens (lens radius  $R_L$  of 5 and 8 mm) adopted in the present study. The analysis of the beam

**Fig. 2** Lens system for the laser thermal cleavage with a contact ball-lens

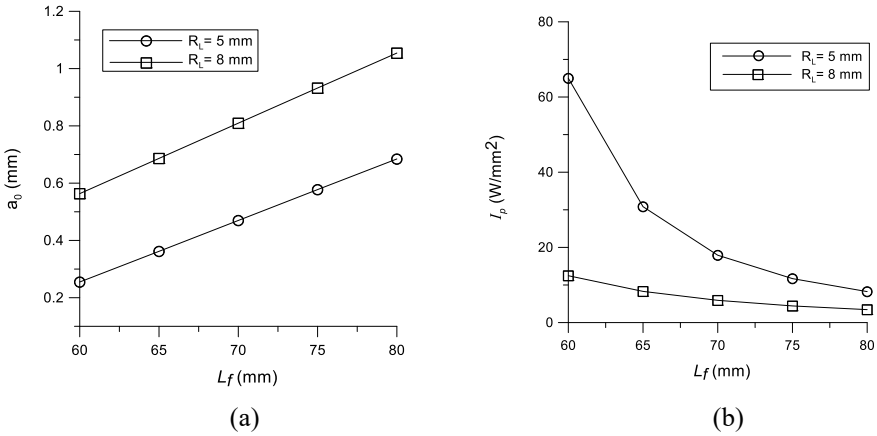


**Fig. 3** Relationships of the beam spot diameter (a), and laser intensity (b) with various stand-off distances and ball diameters

spot diameter was made by ZEMAX software. According to the stand-off distance  $L_s$  between the focusing lens and ball-lens as illustrated in Fig. 2b, the diameter of the beam spot  $a_o$  on the substrate surface coated with a carbon film was calculated. Without considering the reflection coefficient ( $R = 0$ ), it can be found that the increase of the stand-off distance will move the focus point out of the contact point and it will increase the beam spot diameter  $a_o$  on the glass surface as shown in Fig. 3a. As expressed in Eq. (1), the peak value of the density  $I_p$  at the laser beam center with the Gaussian mode was calculated and shown in Fig. 3b with various stand-off distances  $L_s$  and laser powers  $P$ . The beam spot diameter  $a_o$  was also measured with the by the glass and thermal paper and shown in Fig. 4.

$$I_p(x, y) = \frac{(1 - R) \times P}{\pi r_0^2} \times \exp\left[\frac{-2 \times (x^2 + y^2)}{r_0^2}\right] \tag{1}$$

where

$I_p$  is the laser intensity (W/m<sup>2</sup>).

$R$  is the reflectivity.

$P$  is the laser power (W).

$r_o$  is the radius of the laser beam spot (m).

The cutting process could be achieved under various loading of the contact ball-lens on an x–y table. The contact force of the ball-lens in the z-axis was measured by a load cell under the x–y table, and it was calibrated with various settings of in z axis. The process parameters for the present study are listed in Table 2.

**Fig. 4** Relationship between the beam spot diameter and stand-off distance

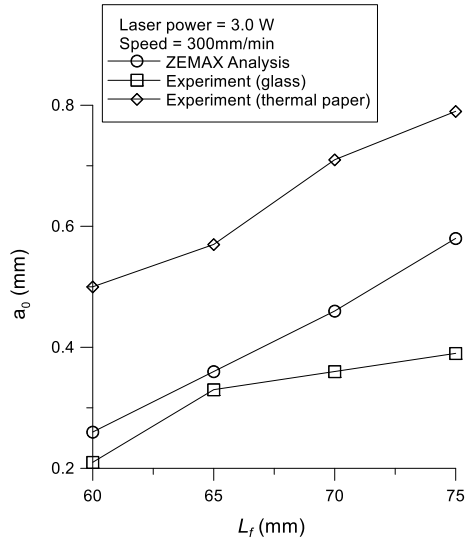


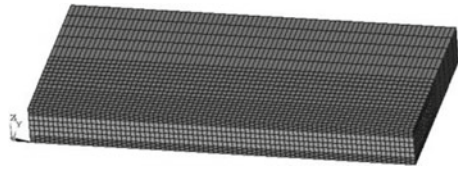
**Table 2** Process parameters of the laser cleaving

Specimen material	Soda-lime glass
Cutting speed	300 mm/min
Laser power	2 W, 2.25 W, 2.5 W, 2.75 W, 3 W
Pre-loads	0 N, 5 N, 10 N, 15 N
Focus lens focal length	70 mm
Ball-lens radius	5 mm
$L_f$	65 mm

### 3 Numerical Analysis

Since the laser cleaving process includes the temperature distribution, stress field and property variation, all of which are significantly inter-related. In order to simplify the analysis, the problem of the laser cleaving on glass sheets herein will be decoupled by two distinct analytical models: the thermal model and the mechanical model in the thermal-elastic numerical analysis. Using the software ANSYS, the element Solid 278 was adopted in the thermal analysis. According to the experimental setup, a half domain of the symmetrical plane with variable mesh grids is shown in Fig. 5, the dimensions of 10 mm × 5 mm × 1 mm are selected for the simplicity in computation. A fine meshing around the laser beam was applied to simulate the steep temperature gradients around the heating zone and the number of the meshed elements is 10,720. The domain meshes used for the thermal and stress analysis are the same, but the element type was replaced by Solid 185 to calculate the stress and displacement. The temperature dependent properties such as the thermal conductivity, specific heat,

**Fig. 5** Grid mesh applied to the stress analysis



Poisson’s ratio and Young’s modulus of soda-lime glass have been cited from the reference [10] and listed in Table 3.

Accordingly the following assumptions are selected in the numerical simulation.

- (1) The glass properties are homogenous, isotropic and temperature dependent.
- (2) The laser intensity distribution is Gaussian mode.
- (3) The thermal boundaries with free convection in the surrounding air are considered.
- (4) There is no phase change during laser heating.
- (5) The specimen is annealed before laser cleaving, and its initial condition is free of stress.
- (6) The stress–strain relationship of the glass substrate is perfectly elastic.
- (7) Body force has been ignored.

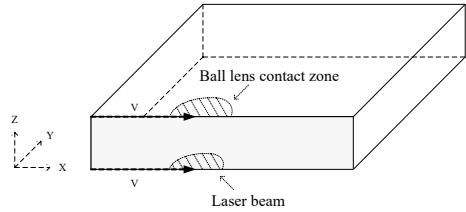
There are numerous factors affect the boundary conditions. The initial temperature of the specimen is assumed to be the ambient temperature of 25 °C. The heat convection has been considered from the surface of the glass substrate and the coefficient of the heat convection is quoted as 21 W/m<sup>2</sup> °C on the surfaces including the lower surface of the substrate. On the bottom surface as illustrated in Fig. 5, a circular Nd-YAG laser beam with the Gaussian mode intensity is selected and expressed in Eq. (1).

According to the results from ZEMAX for the stand-off distance  $L_f$  of 65 mm, the beam spot radius is 0.18 mm for the ball radius of 5 mm as shown in Fig. 3a. The substrate was clamped at the lateral sides, except for the leading and trailing edges, which were assumed to be free of stress in the analysis. On the upper surface as illustrated in Fig. 6, the stress loading from the contact ball is expressed in Eqs. (2) and (3), which is the Hertz equation of the stress distribution between two spheres

**Table 3** Physical properties of soda-lime glass [10]

Thermal conductivity, W/mK	1.03
Density, kg/m <sup>3</sup>	2520
Specific heat, J/kg	800
Thermal expansion coefficient, $\times 10^{-6} \text{ K}^{-1}$	8.7
Young’s modulus, MPa	7160
Poisson ratio	0.23
Softening temperature, °C	730
Average bending fracture strength, Mpa	49

**Fig. 6** Physical domain for the stress analysis with laser heating and contact force of the ball-lens



(or flat plane treated with an infinite large radius) under elastic deformation [11]. Since the cutting path is along the center line of the substrate, a symmetrical domain was selected in the computation and the center line is selected as the x axis and the displacements were assumed to be constrained at the lateral sides ( $U_x = U_z = 0$  at  $y = 5$  mm), and the leading and trailing edges are treated as free ends.

$$a = (3F_e A / 4k)^{1/3} \tag{2}$$

where

$a$  is the radius of the contact region.

$F_e$  is the loading force from the contact spheres.

$A = (1+\nu_1)/E_1 + (1+\nu_2)/E_2$ ;  $\nu$  and  $E$  are the Possion's ratio and Young's modulus of the corresponding sphere.

$k = 1/R_1 + 1/R_2$ ;  $R$  is the radius of the corresponding sphere.

$$P(x, y) = P_o \sqrt{1 - \left( \frac{x^2 + y^2}{a^2} \right)} \tag{3}$$

where

$P_o = 3F_e / 2\pi a^2$ ; the maximum contact stress.

$P(x,y)$  is the stress distribution in the contact region.

Based on Eq. (2), the corresponding radius of the contact region  $a$ , and the maximum contact stress  $P_o$  based on the equation of the Hertz stress are calculated and list in the Table 4 with various loading for the ball radius of 5 mm.

**Table 4** The contact area  $a$  and maximum contact stress  $P_o$  of the ball-lens with various loadings on the substrate

$F_e$ [N]	$a$ [mm]	$P_o$ [MPa]
5	0.0773	399.32
10	0.9741	503.12
15	0.1115	575.93

### 4 Numerical Results

With the above specified boundary condition, the numerical result for the cutting temperature from the edge of the specimen is shown in Fig. 7. Due to the cooling effects of the surrounding air on the edges, it can be found that the location of the peak temperature of the thermal cycles is close to the laser spot and the peak temperature at the leading edge is about 714°C, which is below the peak temperature of 793 °C at the center of the cutting path.

Based on the fracture modes in the glass cutting with laser, there are two components of the stress states dominating the cleavage process; the opening fracture mode and in-plane shear fracture mode [2]. According to the crack propagation, the normal stress  $\sigma_{yy}$  and shear stress  $\tau_{xy}$  in the straight cutting were calculated respectively in the present study. As shown in Fig. 8, the normal stress  $\sigma_{yy}$  is in tension and it occurs in front of the laser spot and rapidly changes to the compressive state in the laser center. Similar results for Gaussian beam mode in the glass laser cutting have been found in the reference [6] and the crack formation is mainly based on the opening modes in the cooling stage after the laser passing. According to various laser positions on the bottom surface, the temperature profiles along the cutting path under the laser power of 2.5 W, the average of the peak temperatures is around 750°C, and the corresponding stress state of the normal stress and shear stress are shown in Fig. 8 with various laser positions. The magnitude of the compressive stress is about 391 MPa at the laser position of 0.375 mm, and the stress at the leading edge is about 91.7 Mpa in tension during the cooling stage. Further results on the shear states are shown in Fig. 8b regarding the change of the stress  $\sigma_{xy}$  at various distances to the

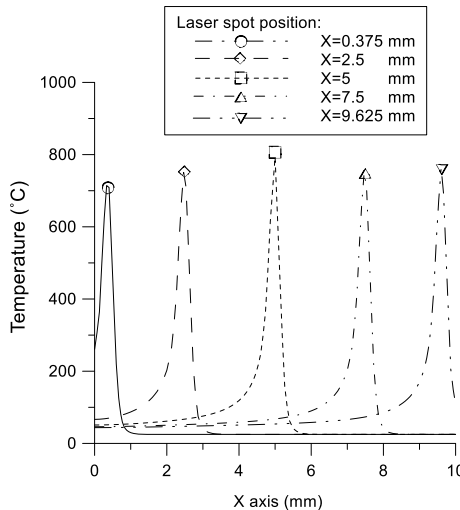


**Fig. 7** Temperature profiles of the substrate at various laser positions from the leading edge of the substrate under the laser power of 2.5 W



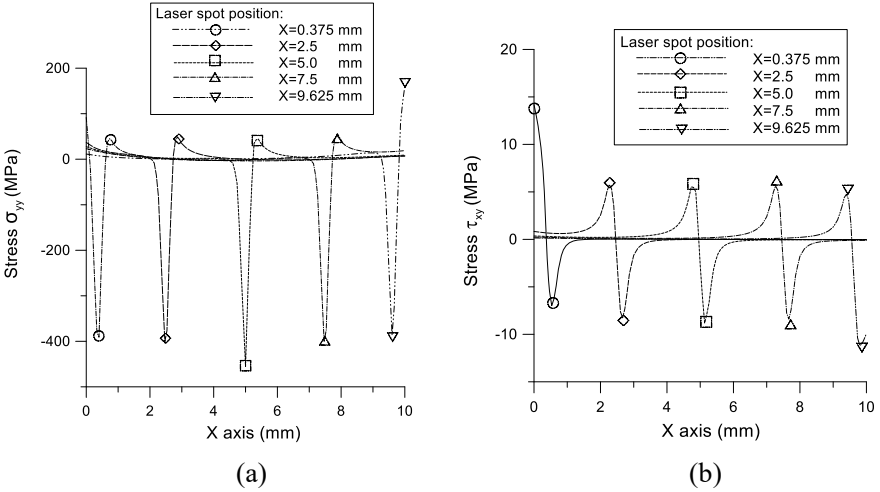


**Fig. 8** States of the normal stress  $\sigma_{yy}$  and shear stress  $\tau_{xy}$  along the x axis at various laser positions with the laser power of 2.5 W

leading edge of the substrate. As the laser beam passing through these locations, it can be found that the shear stress profiles are similar, except that near the leading edge of the substrate. It can be found that the peak value of the shear stress occurs at the leading edge and is much larger than that near the laser spot.

Figure 9 is the stress profile along the z axis as the laser beam at the 0.375 mm with various laser powers. It shows that the increase of the laser powers may rise up the magnitude of the compressive stress at the beam center stress. The deviation

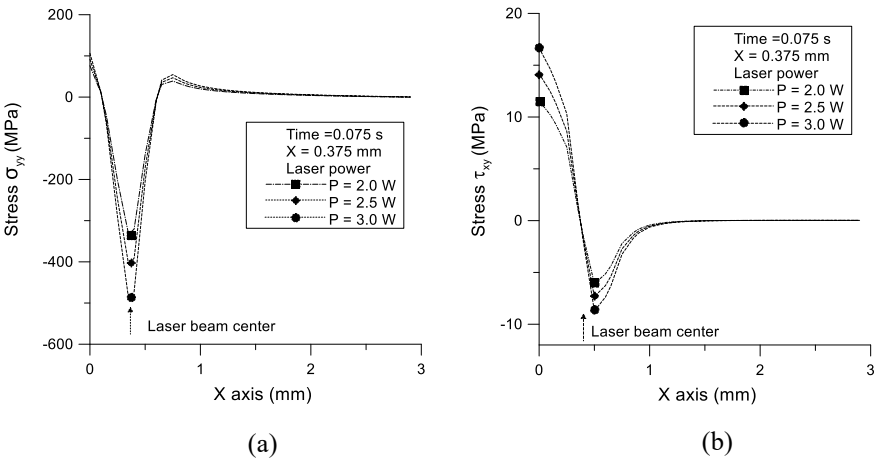


**Fig. 9** Distributions of the normal stress  $\sigma_{yy}$  and shear stress  $\tau_{xy}$  along x axis with various laser powers at the beam center of  $x = 0.375$  mm

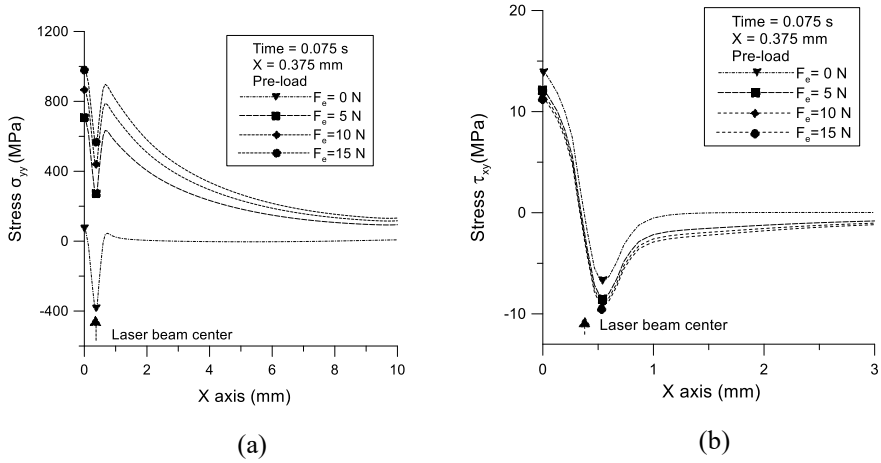


**Fig. 10** Distributions of the normal stress  $\sigma_{yy}$  and shear stress  $\tau_{xy}$  along x axis with laser power of 2.5 W and various loadings for the beam center at  $x = 0.375$  mm

of the crack propagation in the straight cutting is mainly affected near the edges of the substrate, and similar side cracks occurred at the leading and trailing edges of cutting path [4, 5].

With the various loading forces on the contact zone, the stress analysis has been made and the results are shown in Fig. 10. With the increase of the loading of the ball-lens, the magnitude of the normal and shear stresses are increased. There are tremendous changes of the normal stress distribution in the x axis. However, the effect on the shear stress with the contact loading is not significant.

The normal stress profiles along the z axis at the beam center and leading edge (behind the beam center at  $x = 0.375$  mm) with various laser power and contact forces are shown in Figs. 11 and 12 respectively. It can be found that the increase of the tensile stress on the bottom surface ( $z = 0$ ) with the contact force. Furthermore the maximum stress occurs at the leading edge after the laser passing at  $x = 0.375$  mm.

### 5 Straight-Line Cutting Results

The typical crack patterns in the straight-line cutting are shown in Fig. 13. It can be found that the side crack has always occurred at the leading and trailing edges, but it might randomly appear along the straight-line crack in the middle region (section B). The lengths  $L_A$ ,  $L_B$  and  $L_C$  are the regions corresponding to the crack distribution on the leading edge (section A), middle region (section B) and trailing edge (section C).

Figure 14 shows the effects of the laser power on the crack distribution, where the contact force of the ball-lens is set to zero. It can be found that the length  $L_A$  of the

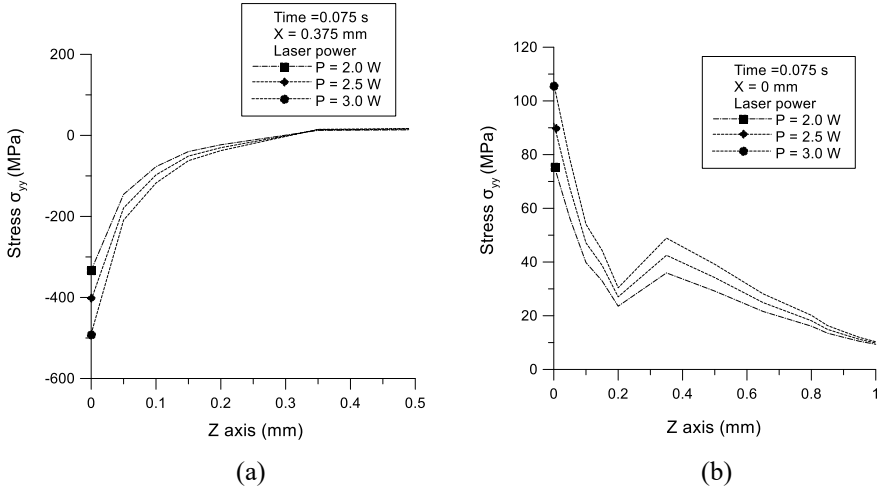


**Fig. 11** Distributions of the normal stress  $\sigma_{yy}$  along z axis at the beam center and behind the beam center at  $x = 0.375$  mm with variable laser powers

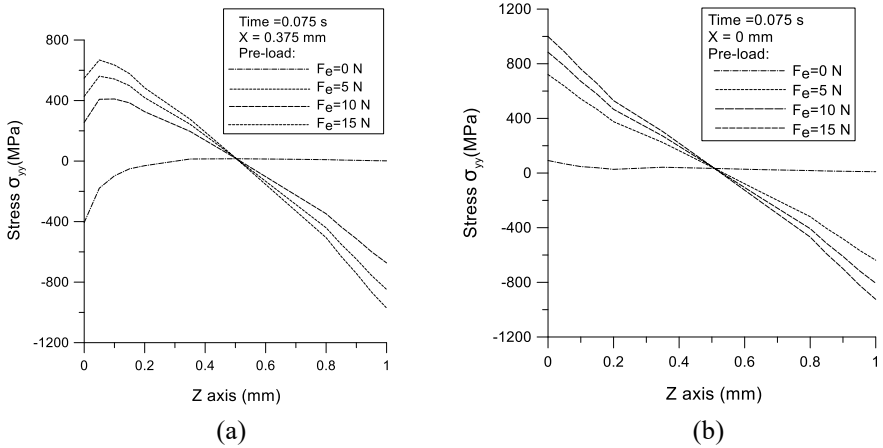


**Fig. 12** Distributions of the normal stress  $\tau_{yy}$  along z axis at the beam center (a) and behind the beam center at  $x = 0.375$  mm (b) with variable contact forces

side cracking in the leading edge increases with the laser power as shown in Fig. 14a, and the length  $L_B$  of the straight cut in the middle region increases with the laser power as shown in Fig. 14b. Furthermore there is no clear evidence of the change in the length  $L_C$  of the cracking region in the trailing edge with the laser power in the present study. It can be found that the length  $L_C$  is about 5 mm in average under various laser powers in the present study. Figure 14d shows the amount of the side

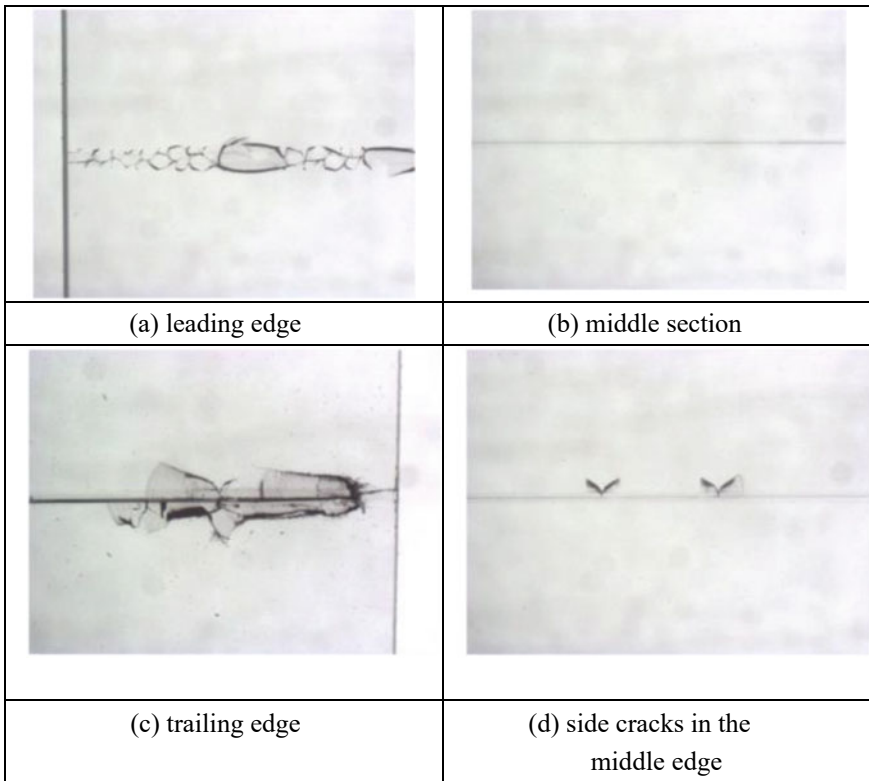
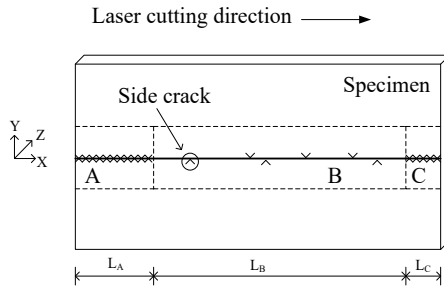


**Fig. 13** Typical crack patterns in the experiment

cracks  $D_s$  distributed in the middle region (the length  $L_B$ ) are similar with various laser powers.

As shown in Fig. 15, the length  $L_B$  of the crack distribution on the middle section at a constant laser power will be increase with various contact forces under 15 N. The increase of the ball-lens loading will reduce the length  $L_A$ , and it will improve the length  $L_B$  of the straight cut significant as shown in Fig. 15b. The length  $L_C$  of the

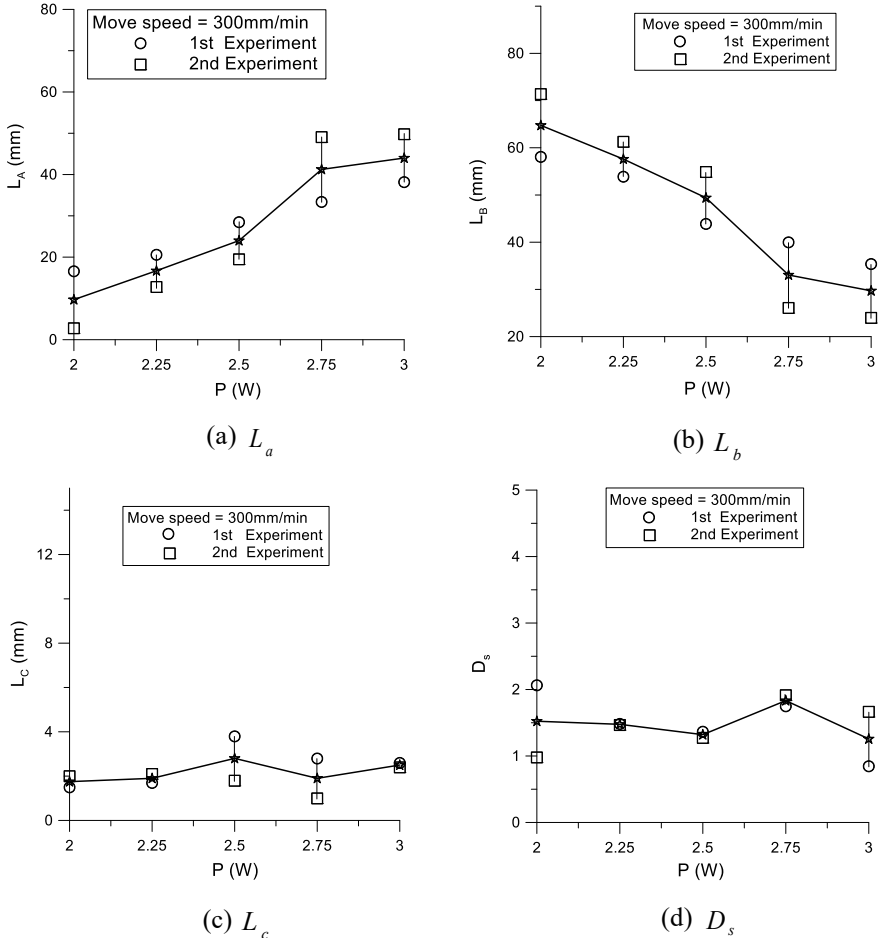


**Fig. 14** Relationships of the length of the cracking regions with various laser powers

crack distribution at the trailing edge is not much different under various loadings. However the amount of the side cracks  $D_s$  in the middle region will be affected with a large uncertainty as shown in Fig. 15d.

The side view of the crack at the trailing edge is shown in Fig. 16 with the cutting direction on the x axis. The crack width  $W_C$  defined in Fig. 16 was measured with various loadings of the ball lens.

According to the longitudinal cross-section view of the straight-line crack in the middle region, the depth of the crack  $h_d$  is denoted in Fig. 16 and measured with various loadings from the contact ball-lens.

The crack depth of the straight-line cutting in the middle region has been measured and shown in Fig. 17 with various laser powers. Furthermore Fig. 18 shows the results of the crack depth  $h_c$  in the straight cut with various loadings. According to these

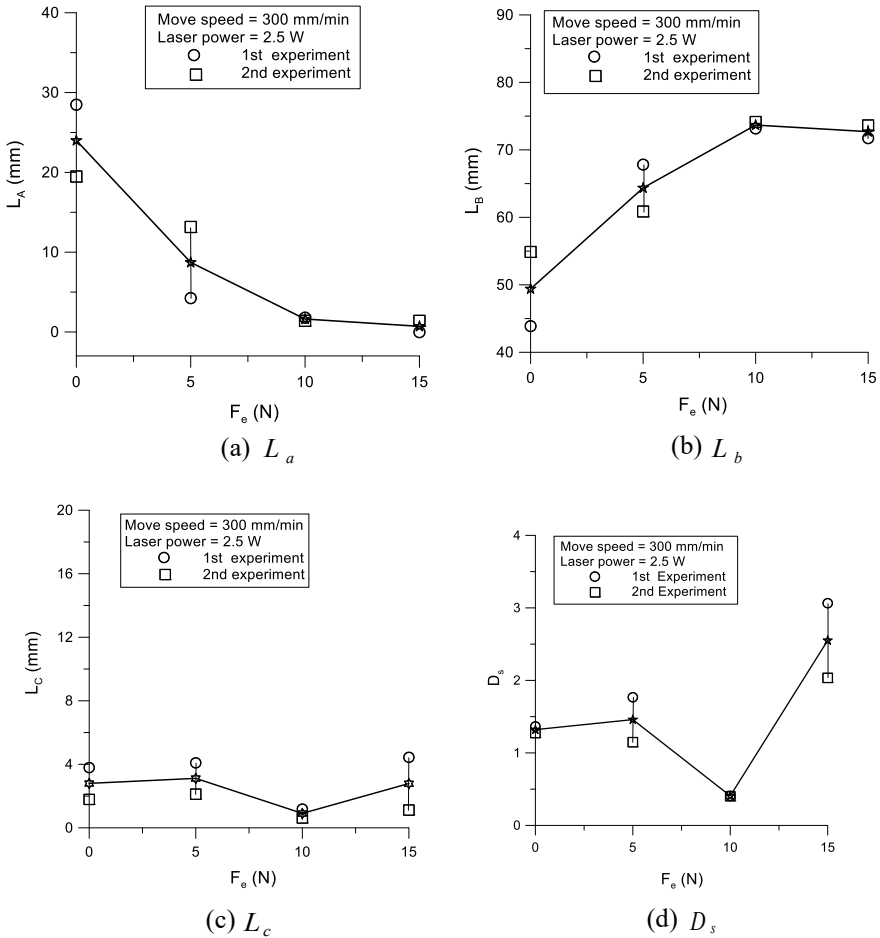


**Fig. 15** Relationship of the length of the cracking regions with various loadings

results, it can be found that the crack depth increases with the laser power below 3.0 W, and similarly with the loading force up to 15 N. The crack depth was measured in the middle region to obtain a uniform distribution. Due to the increase of the tensile stress on the cutting area with the increase of the laser power and ball loading on the bottom surface, the depth growth of the crack is controllable.

Since the loading force from the ball-lens will significantly rise up the stress state in tension on the bottom surface, it will enhance the crack depth in cutting. In order to characterize the cracking defects in the trailing edge under the laser power and contact loading, the width of the crack affected zone at the trailing edge was measured and shown in Figs. 19 and 20. It can be found that the loading force from the ball-lens is critical to cause the opening of the crack at the trailing edge as shown in Fig. 21. Apparently the width of the crack affected zone is increased with the loading force.

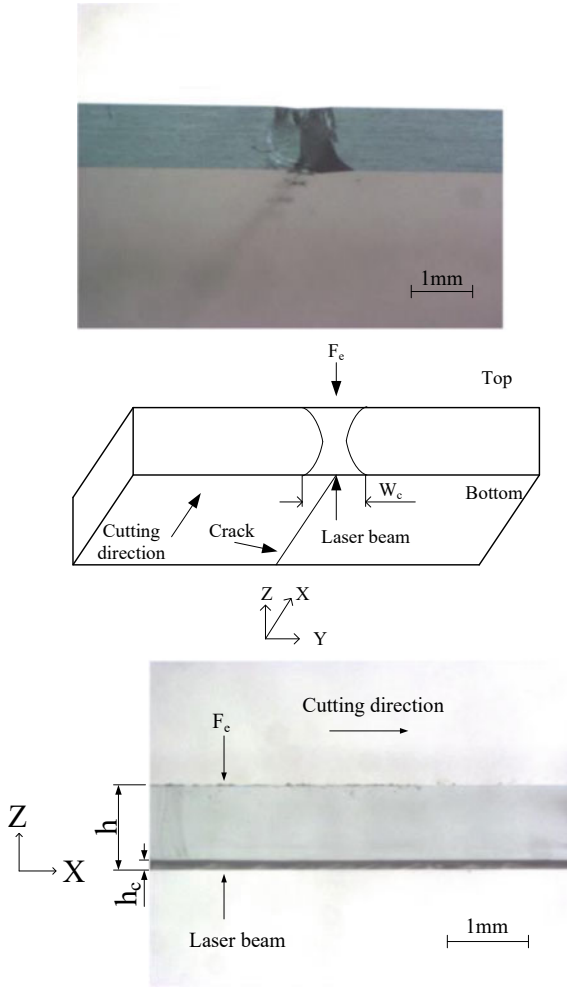


**Fig. 16** Definitions of the crack contours

As the loading up to 20 N, an unstable crack occurs frequently at the trailing edge. This type crack is mainly caused by even stress state at the end of the cutting path without the end support on the trailing edge.

## 6 Conclusions

In the straight-line cutting, the crack formation can be found in the opening mode and dominated by the normal stress, and the side crack would not affected by the

**Fig. 17** Relationship of the crack depth with various laser powers

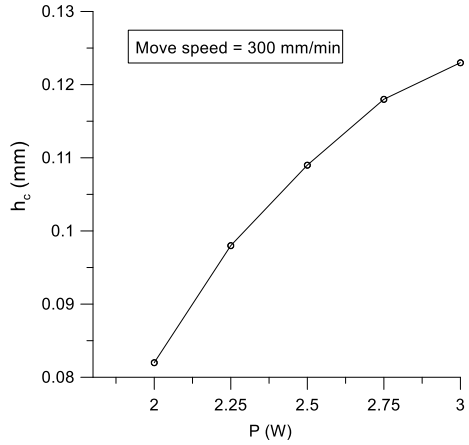
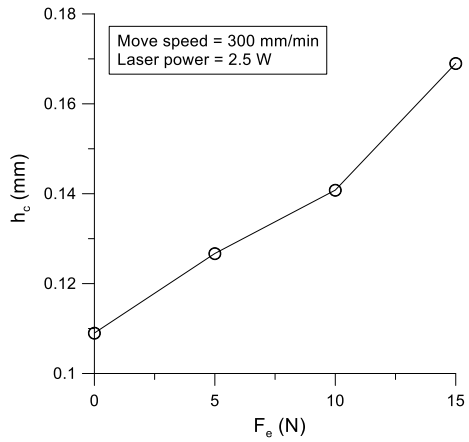


**Fig. 18** Relationship of the crack depth with various loadings of the ball-lens



shear stress with the laser power and contact force from the ball-lens. The cutting results show that the distributions of the side crack varies with the laser power and contact forces, especially in the leading edge. Therefore the micro-cracks could be successfully controlled by the ball-lens and affect the cutting quality mainly at the leading edge in the laser cleavage of glass. A comparison between the numerical and experimental results shows that the control of the crack formation mainly depends on the stress states. The tensile stress distribution due to the ball-lens would significantly reduce the amount of the side crack in the leading edge under a certain amount of the contact forces.



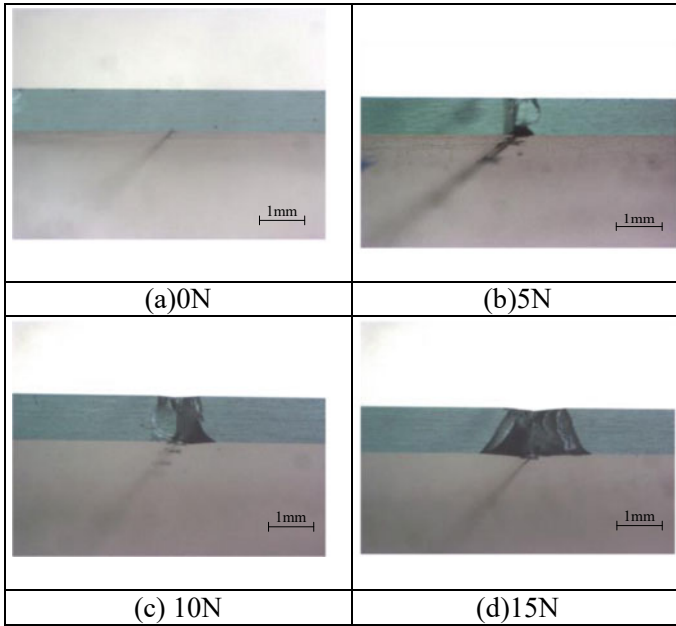


**Fig. 19** Photographs of the crack affected zone at the trailing edge

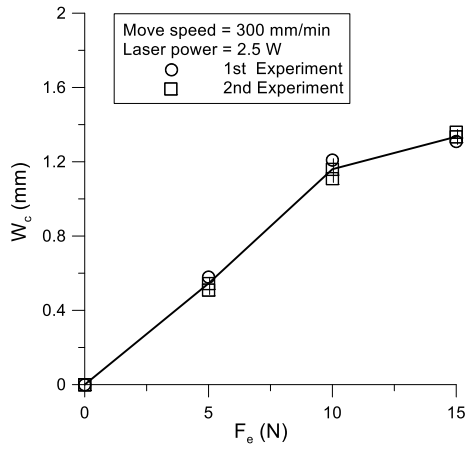
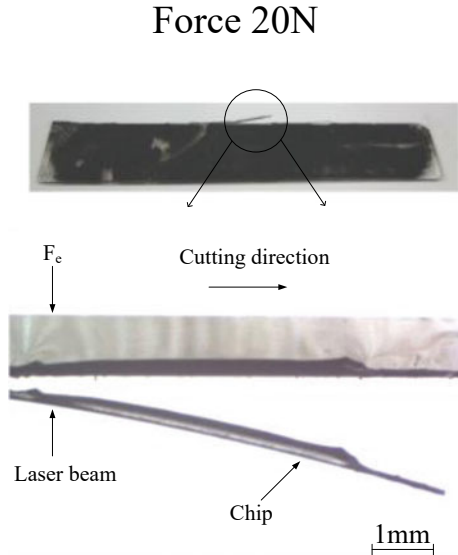


**Fig. 20** Relationship of the crack width with various loadings at the trailing edge

**Fig. 21** Typical end cracking with a loading up to 20 N



## References

1. Tsai CH, Chen CJ (2004) Application of iterative path revision technique for laser cutting with controlled fracture. *Opt Lasers Eng* 41:189–204
2. Miyashita Y, Mogi M, Hasegawa H, Sujatanod S, Mutoh Y (2008) Study on a controlling method for crack nucleation and propagation behavior in laser cutting of glass. *J Solid Mech Mat Eng* 2:12
3. Tasi CH, Lin BC (2007) Laser cutting with controlled fracture and pre-bending applied to LCD glass separation. *Int J Adv Manuf rechnol* 32:1155–1162
4. Nisar S, Li L, Sheikh MA, Pinkerton AJ (2010) The effect of continuous and pulsed beam modes on cut path deviation in diode laser cutting of glass. *Int J Adv Manuf Technol* 49(1–4):167–175
5. Nisar S, Li L, Sheikh MA, Pinkerton AJ, Safdar S (2010) The effect of laser beam geometry on cut path deviation in diode laser chip-free cutting of glass. *J Manuf Sci Eng Trans ASME* 132(1):0110021–0110029
6. Tsai CH, Liou CS (2003) Fracture mechanism of laser cutting with controlled fracture. *J Manuf Sci Eng Trans ASME* 125:519–528
7. Yuanyuan S, Zheng L, Limin S, Qiurui J, Shibo L (2013) Research on the thermal effect of long pulse laser irradiation BK7 glass. *Appl Mech Mater* 347–350:1123–1126
8. Cai N, Yang LJ, Wang Y, Tian ZG (2010) Experimental research of YAG laser cutting soda-lime glass sheets with controlled fracture. *Key Eng Mater* 431–432:507–510
9. Crandall SH, Dahl NC, Lardner TJ (1978) *An introduction to the mechanics of solids*. McGraw-Hill, New Delhi
10. Yamamoto K, Hasaka N, Morita H, Ohmura E (2008) Three-dimensional thermal stress analysis on laser scribing of glass. *Precis Eng* 32:301–308
11. Johnson KL (1985) *Contact mechanics*. Press Syndicate of the University of Cambridge, New York

# High-Rate Laser Processing of Metals Using High-Average Power Ultrashort Pulse Lasers



J. Schille, L. Schneider, L. Hartwig, and U. Loeschner

**Abstract** High-rate laser processing of technical grade stainless steel by using high-PRF ultrashort pulse lasers is studied in order to gain deeper insight into material removal for micro fabrication. For this, high-average power picosecond and femtosecond lasers are utilized, providing pulses of tens of MHz repetition rate and output powers of 76 W and 32 W, respectively. For (ultra)fast raster scanning of the laser beam, the laser systems are synchronized with a high-precision galvanometer scanner or rather an in-house developed polygon scan system. The influence of the processing parameters (laser power, pulse energy, pulse repetition rate, pulse duration, and fluence) on the ablation rate, removal efficiency, and throughput are studied. In picosecond laser irradiation of stainless steel, for example, the maximum material removal rate is 5.4 mm<sup>3</sup>/min, obtained with 76 W average laser power. This is lower than the removal rate of 6.8 mm<sup>3</sup>/min by using the femtosecond laser beam and 32 W average output power. The varying removal rate is the result of the different removal efficiency of picosecond and femtosecond laser pulses, which was determined in the experimental study of 0.071 mm<sup>3</sup>/W/min and 0.22 mm<sup>3</sup>/W/min, respectively, by using identical processing parameters except the pulse duration. Finally, the machining quality of laser processed micro cavities are evaluated by means of surface roughness measurements and SEM micrograph analysis. As a result, the mid-fluence range between 0.4 and 1.5 J/cm<sup>2</sup> is identified for ultrashort pulses as most suitable processing regime for micro fabrication with regard to removal efficiency, throughput, and machining quality.

**Keywords** High-rate · High throughput · Ultrashort pulse laser · Micro processing · Polygon

---

J. Schille (✉) · L. Schneider · L. Hartwig · U. Loeschner  
Laserinstitut Hochschule Mittweida, Technikumplatz 17, 09648 Mittweida, Germany  
e-mail: [schille@hs-mittweida.de](mailto:schille@hs-mittweida.de)

© Springer Nature Switzerland AG 2022  
S. Hinduja et al. (eds.), *Proceedings of the 38th International MATADOR Conference*,  
[https://doi.org/10.1007/978-3-319-64943-6\\_10](https://doi.org/10.1007/978-3-319-64943-6_10)

## 1 Introduction

Recent progress in developing high-average power ultrashort pulse lasers facilitates high-throughput machining with the potential to meet industrial needs in micro fabrication with regard to accuracy, precision efficiency and throughput. However, initial studies investigating high-PRF (pulse repetition frequency) ultrashort pulse laser processing identified heat accumulation and particle shielding as substantial ablation process influencing mechanisms [1–3]. Particle shielding effects are reported for pulses in the range of several hundred kilohertz that potentially will reduce material removal. In this time regime, the following irradiated laser pulses will be reflected, scattered and/or absorbed by ejecting particles and clusters which are produced by the preceding irradiated pulses. A further increase of the repetition rate to megahertz pulse repetitions, by contrast, enhances material removal which is mainly induced by heat accumulation. In this case, the time interval between successive pulses is too short for complete cooling of the irradiated area and thus heat accumulates in a narrow subsurface area. In particular for poor heat-conducting materials, the surface temperature rises gradually inducing enlarged heat affected zones but also material melting those detrimentally affects the processing quality.

Recently, a number of systematic studies investigated the influence of pulse duration, laser fluence and pulse repetition rate on material removal in high-PRF ultrashort pulse laser micro processing [4–9]. The analysis of the results obtained identified higher removal efficiency for femtosecond pulses than for pulses in the picosecond range. In addition it is demonstrated that by optimization of the processing parameters high-quality and melt-free micro-featured devices can be produced, even with high-PRF pulses. However, the presented removal rates ranging up to  $0.7 \text{ mm}^3/\text{min}$  does not fulfill industrial requirements in terms of throughput and productivity. This is mainly due to limited available maximum laser output power and can potentially be overcome by using high-average power high-PRF ultrashort pulse lasers. Thus, in a more recent approach, ten times higher material removal rates up to  $6.8 \text{ mm}^3/\text{min}$  were reported, obtained with femtosecond pulses of 20 MHz repetition rate and 30 W average output power [10].

In this work, high-rate laser processing of technical grade stainless steel is studied in order to gain deeper insight into complex high-PRF material removal. By using high-average power picosecond and femtosecond lasers, material removal is evaluated with respect to efficiency, throughput and quality. It is shown that high-average power high-PRF lasers in conjunction with (ultra) fast scan technologies seem to be a promising technology to scale the productivity in micro fabrication.

## 2 Optimisation of Material Removal in Ultrashort Pulse Laser Processing

In ultrashort pulse laser micro fabrication, the achievable ablation rate, removal efficiency, throughput, and machining quality are greatly influenced by the processing parameters. A number of studies investigating ultrashort pulse laser ablation confirmed that the ablation rate increases non-linearly with higher pulse energies or rather fluence, among others [11–14]. Furthermore, it is verified by G. Raciukaitis et al. [15] using picosecond laser radiation that most efficient material removal arises when the laser fluence is equal to

$$H_{opt} = e^2 \cdot H_{th} \approx 7.4 \cdot H_{th} \tag{1}$$

where  $H_{opt}$  is the optimum fluence and  $H_{th}$  is the threshold fluence. As a result, increasing the pulse energy in order to enhance material removal, the maximum achievable ablation rate will only be obtained by balancing the focus diameter to the optimum spot size. To emphasize this interrelation even for femtosecond laser pulses, a theoretical analysis of the influence of both laser spot diameter and pulse energy on the ablation rate is presented in Fig. 1. In this figure the theoretically achievable volume ablation rate  $V_{SP}$  is computed for stainless steel by using Eq. 1. The effective penetration depth  $\delta_{eff} = 15 \text{ nm}$ , focus radius  $w_0 = 11 \text{ }\mu\text{m}$  and ablation threshold  $H_{th} = 0.1 \text{ J/cm}^2$  were taken into calculation. These calculation input values were determined for stainless steel in our previous experimental studies [9].

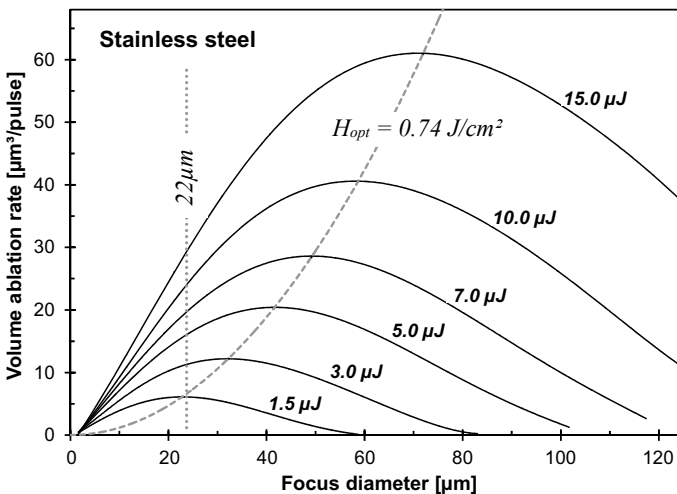


**Fig. 1** The volume ablation rate theoretically calculated as a function of the focus diameter, the pulse energy is varied in the range between 1.5  $\mu\text{J}$  and 15.0  $\mu\text{J}$ , the optimum fluence is indicated by a dashed line, the focus diameter of the experimentally studied femtosecond laser beam is pointed out by a dotted line

$$V_{SP} = \frac{\delta_{eff}}{4} \pi w_0^2 \ln^2 \left( \frac{H_0}{H_{th}} \right) \tag{2}$$

In Fig. 1 it can be seen, for example, that a pulse energy of 1.5  $\mu\text{J}$  will be the optimum for femtosecond laser pulses of 22  $\mu\text{m}$  focus spot diameter. By irradiating pulses of higher energy at same spot diameter, the volume ablation rate increases, but most efficient material removal only takes place when the fluence is at optimum level. For stainless steel, the optimum fluence is determined of 0.74  $\text{J}/\text{cm}^2$ , as indicated in the figures. This is about a factor of 7.4 above the ablation threshold which is in accordance with Eq. 1.

Figure 2 plots the calculated volume ablation rate as a function of the fluence; the focus diameter was varied in the range between 15 and 50  $\mu\text{m}$ . It can be seen for pulses of fixed diameter, on the one hand, that the volume ablation rate increases with higher fluence. On the other hand, for pulses at fixed fluence, the ablation rate increases with larger diameter. In both cases, whether increasing fluence or larger diameters, a higher amount of laser energy irradiates the substrate causing higher material removal. As another assessment criterion, the efficiency of material removal was evaluated in order to identify the optimum processing regime. For this, the calculated volume ablation rate values were divided by the pulse energy. The results obtained are presented in Fig. 2 by plotting the removal efficiency versus fluence.

The plot of the removal efficiency in Fig. 2 confirms that material removal is most efficient by irradiating pulses at 0.74  $\text{J}/\text{cm}^2$  fluence as already mentioned above in Fig. 1. Using this optimum fluence, the maximum achievable material removal per laser energy expenditure is about 4.1  $\mu\text{m}^3/\mu\text{J}$  for stainless steel. In addition, it is

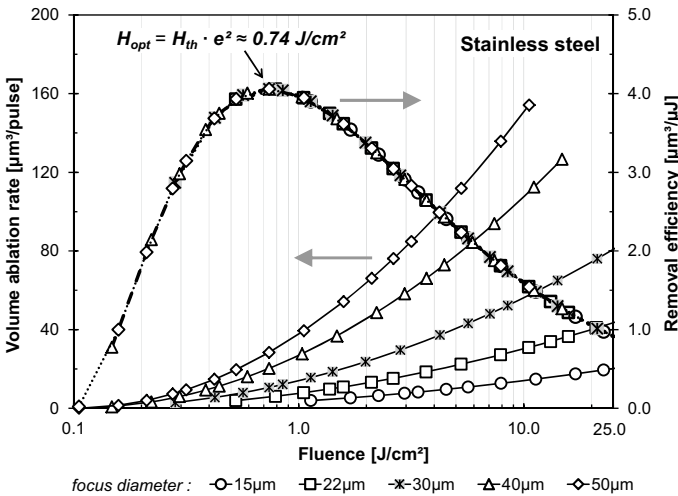


Fig. 2 The volume ablation rate and removal efficiency theoretically calculated as a function of fluence, the focus diameter is varied in the range between 15 and 50  $\mu\text{m}$

identified that maximum material removal can be achieved independently from the applied focus diameter or rather pulse energy, which varied depending on the focus spot size. From this finding it can be supposed that the maximum material removal rate can be achieved by different approaches. As long as the fluence is optimum, a high quantity of sharply focused low-energy laser pulses, as the first processing regime, or as second regime, a lower quantity of high-energy laser pulses of wider focus diameter will bring identical removal rates.

This functional relation is analysed more in detail in Fig. 3. Therein the removal rate  $MRR$  is calculated for varied processing conditions according to Eq. 3. In this equation  $V_{SP}$  is volume ablation rate and  $f_R$  is the repetition rate; the time interval is 1 min.

$$MRR = V_{SP} \cdot f_R \cdot 60s \tag{3}$$

By varying the focus diameter, the computed removal rates are shown in Fig. 3 as a function of the repetition rate and, for example, by taking into account a femtosecond laser system of 30 W average laser output power. It is shown that the maximum removal rate of 7.32 mm<sup>3</sup>/min can be obtained with different parameter sets. According to this, the most efficient processing points are addressed with their repetition rate, the corresponding pulse energy, and the focus diameter. However, in each case the maximum removal rate arises at the optimum fluence of 0.74 J/cm<sup>2</sup>.

According to Neuenschwander et al. [6, 16], for a given average laser power the maximum ablation rate can be obtained at an optimum repetition rate, or rather, the removal rate shows a maximum for optimum applied fluence. This functional

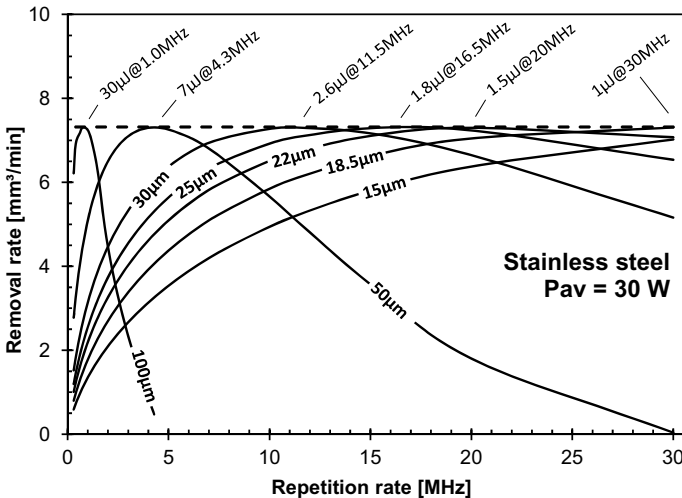


**Fig. 3** The removal rate theoretically calculated as a function of the repetition rate, the focus diameter is varied in the range between 15 and 100 µm, a femtosecond laser with 30 W average output powers is considered

interrelation is given in Eq. 4, where  $\dot{V}$  is the removable material volume per time interval,  $P_{av}$  is the average laser power,  $\delta$  is the effective penetration depth, and  $H_{th}$  is the ablation threshold.

$$\left. \frac{\dot{V}}{P_{av}} \right|_{\max} = \frac{2}{e^2} \cdot \frac{\delta}{H_{th}} \quad (4)$$

By taking into account the effective penetration depth of 15 nm, the removal efficiency of stainless steel calculates to 0.244 mm<sup>3</sup>/W/min. As a result, irradiating 30 W average laser powers to stainless steel, a material volume of 7.32 mm<sup>3</sup> can be theoretically removed per minute. This quantity has been already accounted in Fig. 3.

### 3 Experimental Details and Analysis Methods

Two different high average power high-PRF ultrashort pulse laser systems were investigated, a femtosecond laser supplying a maximum laser power of 31.7 W and maximum repetition rate of 19.3 MHz, and a picosecond laser with a maximum average power of 70.0 W and 20 MHz pulse repetition rate.

The picosecond laser was utilized with an in-house developed polygon mirror system, allowing two-dimensional raster scanning of the laser beam with maximum scan speeds of 880 m/s in polygon scan direction. With the adapted f-theta lens, the picosecond laser beam was focused onto the material surface to a spot size of 44 μm. Using this ultrafast polygon scan system, deflection of the picosecond laser beam was sufficiently high to reach the proposed optimum lateral pulse-to-pulse spacing of about half of focus radius [5, 17] even in case of megahertz repetitive pulses. According to Eq. 5 where  $v_S$  is the scan speed,  $d_P$  is the pulse-to-pulse spacing in scan direction, and  $f_R$  is the repetition rate, a scan speed of 200 m/s was required to get 10 μm pulse-to-pulse spacing at 20 MHz.

$$v_S = d_P \cdot f_R \quad (5)$$

The femtosecond laser beam was focused using a 255 mm f-theta lens in conjunction with a high-performance galvanometer scanner (*intelliSCANde*<sup>®</sup>, Scanlab AG) to a focus spot diameter of 22 μm. The maximum scan speed of the galvanometer scanner setup was 17 m/s. As a result, the optimum pulse-to-pulse spacing of about 5 μm was only achievable for pulses of 3.4 MHz repetition rate or lower.

By studying femtosecond pulses of higher repetition rate, the pulse-to-pulse spacing reduced, for example, to 3.5 μm or rather 0.9 μm for pulses of 4.83 MHz or 19.3 MHz, respectively. The laser parameters investigated in this study are summarized in Table 1.

For empirical estimation of the optimum processing parameters, cavities of standardized geometry were produced by raster scanning the focused laser beam. Laser



**Table 1** Summary of the parameters investigated in this study

	<i>sci-series</i> (Active Fiber Systems AG)	<i>PX series</i> (EdgeWave GmbH)
Wavelength $\lambda$ [nm]	1030	1064
Repetition rate $f_R$ [MHz]	19.3	20
av. laser power $P_{av}$ [W]	31.7	76
pulse energy $Q_{SP}$ [ $\mu$ J]	30.5	75
Pulse duration $\tau_H$ [ps] ( $\text{sech}^2$ )	0.35	10
Focus spot diameter $w_0$ [ $\mu$ m]	22.3	44
Fluence $H_0$ [ $\text{J}/\text{cm}^2$ ]	16.0	9.9
Scan speed $v_S$ [m/s]	17	200

raster scanning implies a network of overlapping parallel laser processed lines of constant hatch distance  $d_H$ , as shown in Fig. 4.

With increasing number of raster scan passes  $n_S$  processed on the sample surface, the cavity depth  $d_C$  increased. The cavity depths were measured using a confocal point sensor (*µscan CF*, nanoFocus AG) and, according to Eq. 6, from this value the experimentally achievable volume ablation rate  $V_{SP}$  was calculated.

$$V_{SP} = \frac{d_p \cdot d_H \cdot d_C}{n_S} \tag{6}$$

Finally, the machining quality was evaluated by means of the average surface roughness  $S_a$  of the laser processed cavity bottom surfaces. The roughness measurements were carried out using the confovis 3D measuring assembly *ConfoSurf CLV150*.

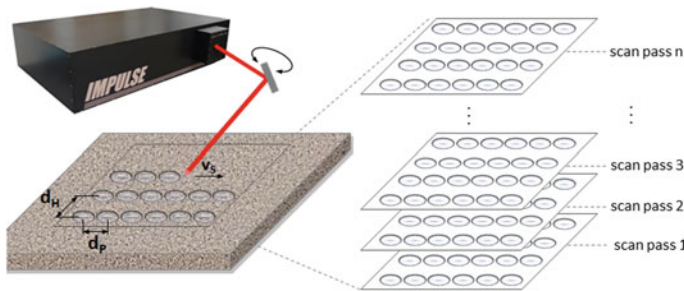


**Fig. 4** Sketch of the raster-scanning method, where  $d_p$  is lateral pulse-to-pulse spacing,  $d_H$  is hatch distance, and  $v_S$  is scan speed

## 4 Results and Discussion

### 4.1 Ablation Rate, Throughput and Efficiency

High-PRF ultrashort pulse laser ablation of technical grade stainless steel was investigated on the basis of cavity depths. Therefore, rectangular cavities with the dimension  $7.0 \times 0.5 \text{ mm}^2$  in length and width were produced using both the femtosecond and picosecond laser.

The volume ablation rates obtained with the femtosecond laser are plotted as a function of the fluence in Fig. 5. Furthermore, in order to evaluate the influence of the temporal pulse-to-pulse distance on material ablation, the repetition rate was varied in the range between 508 kHz and 4.38 MHz. The cavities were produced with 30 scan passes and constant lateral pulse-to-pulse spacing which was  $5 \text{ }\mu\text{m}$  in X- and Y-direction. As an exception, the pulse spacing reduced a little in scan direction to  $4.0$  and  $3.5 \text{ }\mu\text{m}$  at the higher repetition rates of  $3.86$  and  $4.83 \text{ MHz}$  which was due to the limited scan speed of the galvanomer scanner of  $17 \text{ m/s}$ .

Figure 5 points out that the volume ablation rate increased non-linearly with the fluence. The experimental data obtained in the fluence range between  $0.4$  and  $6.0 \text{ J/cm}^2$  are in good correlation to the modeled ablation curve, calculated according to Eq. 6. In addition, it can be seen in Fig. 5 that material removal is not or, in case of  $4.8 \text{ MHz}$  repetition rate, only marginally influenced by the repetition rate.

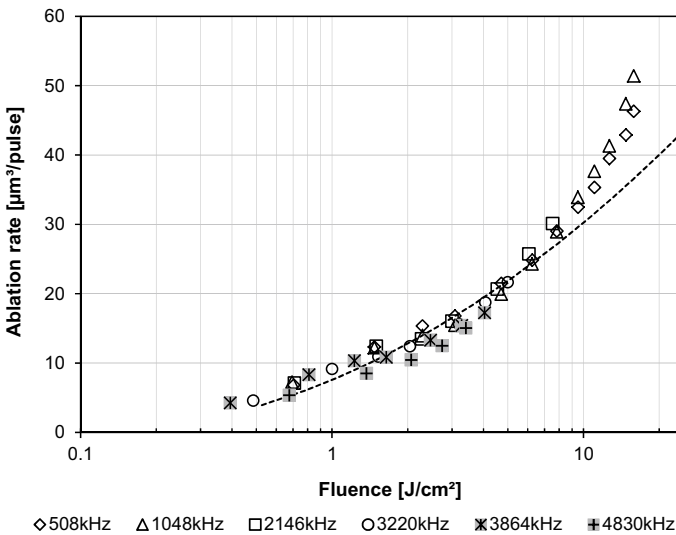


**Fig. 5** The experimentally determined volume ablation rate using the femtosecond laser with  $22 \text{ }\mu\text{m}$  focus diameter and  $31.7 \text{ W}$  maximum average output power, the repetition rate was varied in the range between  $508 \text{ kHz}$  and  $4.83 \text{ MHz}$

This finding agrees with the results presented by Neuenschwander et al. [18] who concluded for high-PRF picosecond laser radiation that ablation of stainless steel is not or only weakly affected by plasma/particle shielding and heat accumulation. This was in particular by irradiating pulses at optimum fluence and lateral pulse-to-pulse spacing of half of spot radius. However, our previous studies reveal that particle shielding losses (as detected in high-PRF femtosecond laser processing of stainless steel) will be overbalanced by heat accumulative effects [3, 5, 9]. We observed a significant increase of the ablation rate by irradiating pulses at 1 MHz repetition rate and wider lateral spacing, compared to the ablation results obtained with either lower repetition rates or smaller spacing or both [19]. From this it can be suggested that the role of the repetition rate or rather the temporal pulse-to-pulse distance in ultrashort pulse laser ablation is not fully clear and further research seems to be needed in this issue.

Figure 6 plots the material removal rate versus the fluence. The material removal rates are calculated in accordance with Eq. 2 by taking into account the experimentally volume ablation rates given in Fig. 5 and the pulse repetition rates. In addition, the material removal rates obtained in a previous work by using femtosecond pulses at 200 kHz repetition rate are included in the plot. In spite of the fact that the volume ablation rate was almost identical for pulses of similar fluence, see Fig. 5, in Fig. 6 the lowest investigated pulse repetition rate of 200 kHz yields the smallest material removal rate. This is the result of the lowest number of incident laser pulses per time interval, and the removal rate increases with higher pulse repetition rates. For a fixed

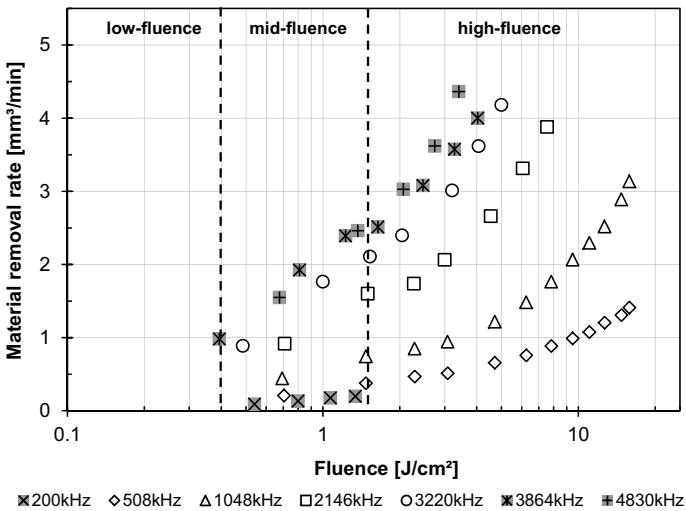


Fig. 6 The experimentally determined material removal rate using the femtosecond laser with 22 μm focus diameter and 31.7 W maximum average output power, the repetition rate was varied in the range between 200 kHz and 4.83 MHz

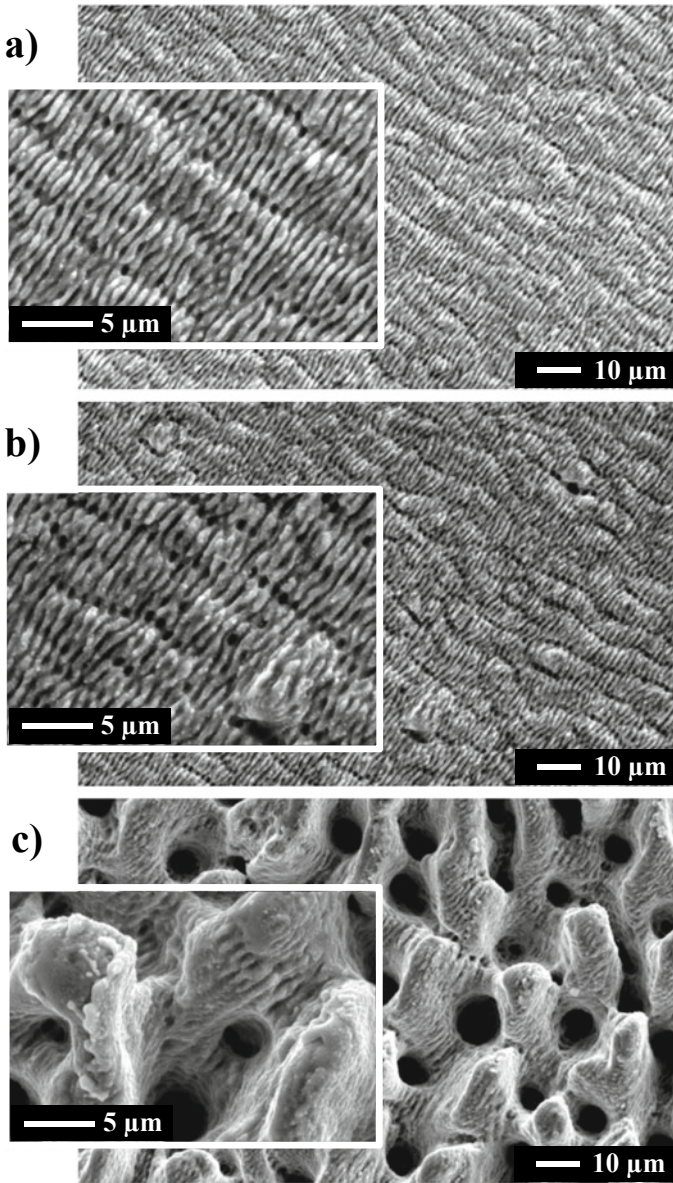
repetition rate, however, it can be seen that higher material removal was achieved with higher fluence.

In Fig. 6 the highest removal rate of  $4.36 \text{ mm}^3/\text{min}$  can be seen, obtained with pulses of  $3.4 \text{ J/cm}^2$  fluence and  $4.83 \text{ MHz}$  repetition rate. With regard to Sect. 2 it becomes obvious, on the one hand, that this fluence is not in the optimum range and thus the achieved removal rate is less than the theoretically estimated value of  $7.32 \text{ mm}^3/\text{min}$ . On the other hand, the poor quality of the cavity bottoms produced with these high-fluence pulses does not fulfill the requirements in micro fabrication for industrial applications. This can be observed, for example, in Fig. 7c showing a cone-like protrusion covered rough cavity bottom, produced with pulses of  $3.21 \text{ J/cm}^2$  fluence and  $3.22 \text{ MHz}$  repetition rate. In contrast, cavities with smooth and regularly ripple textured bottoms were machined by irradiating pulses of same repetition rate but lower fluence, such as shown in Fig. 7 a and b for pulses of  $0.49 \text{ J/cm}^2$  and  $1.0 \text{ J/cm}^2$  fluence, respectively.

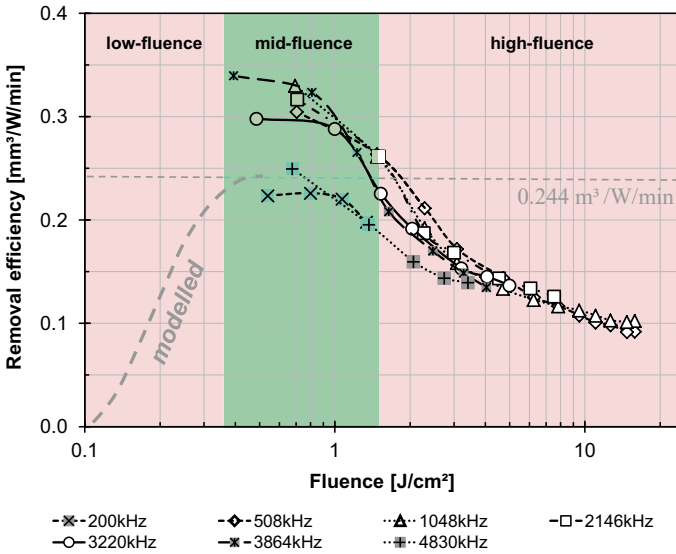
Based on these experimental findings, three different processing regimes are indicated in Fig. 6 with regard to their achievable processing speed and quality. In the low-fluence regime with fluence lower than  $0.4 \text{ J/cm}^2$ , high-quality machining outcomes can be produced but the processing speed is comparably low. In the mid-fluence regime as the second regime where the fluence is in the range between  $0.4$  and  $1.5 \text{ J/cm}^2$ , the laser process is highly efficient, providing maximum processing throughput and good machining qualities. Laser processing in the high-fluence regime with fluence higher than  $1.5 \text{ J/cm}^2$  will bring the highest removal rate per pulse. As major disadvantage of the third regime, there is an unsatisfactory level of machining quality, removal efficiency and throughput, as presented in Figs. 7 and 8.

Figure 8 evaluates the removal efficiency depending on the fluence, the repetition rate is varied. The removal rates were calculated by dividing the experimentally determined material removal from Fig. 6 by the irradiated average laser power. Nevertheless, high-fluence pulses yield the highest ablation rate and thus material removal rate but the highest removal efficiency can be observed for pulses in the mid-fluence range. For pulses of higher fluence, by contrast, the removal efficiency reduced. From this it can be supposed that only a certain amount of laser energy will be consumed for material removal which might be due to the fact that the laser ablated volume is influenced by energy penetration into the bulk. In addition, by keeping in mind that the ablation rate increases non-linearly with higher fluence, it can be suggested for high-fluence pulses that higher amounts of laser energy will most likely deposited as heat. This, in turn, lowers the process efficiency and will potentially have detrimental effects on the machining quality.

For low-fluence pulses it can be pointed out that steel ablation will take place as long as the fluence is above the ablation threshold. In Fig. 8 the low-fluence range is highlighted in red colour indicating that material ablation is inefficient. This is potential induced by the limited energy penetration into the depth which is mainly driven in the low-fluence regime by optical penetration instead of ballistic electron movement. As a result, the irradiated energy will be deposited in a narrow sub-surface volume which is considerably smaller than that volume which theoretically can be vaporized by considering the quantity of impinging laser energy.



**Fig. 7** SEM micrographs showing the bottom surface of laser processed cavities using the femtosecond laser at 3.22 MHz and fluence as follows: **a** 0.49 J/cm<sup>2</sup>, **b** 1.0 J/cm<sup>2</sup>, **c** 3.21 J/cm<sup>2</sup>



**Fig. 8** The experimentally determined removal efficiency of the studied femtosecond laser as a function of the fluence, the theoretically estimated removal efficiency is indicated by the dashed line

Most-efficient material removal arises in the mid-fluence range, as indicated in green in Fig. 8. The theoretically achievable removal efficiency of  $0.244 \text{ mm}^3/\text{W}/\text{min}$  is experimentally confirmed by pulses of the lower repetition rate of 200 kHz. By contrast, using pulses between 508 kHz and 3.86 MHz, the removal efficiency maximum was found to be  $0.33 \text{ mm}^3/\text{W}/\text{min}$ . This is considerably higher than the modelled removal efficiency. As a reason it can be supposed that heat accumulative effects, potentially occurring in high-PRF ultrashort pulse laser processing, enhances the efficiency of material removal. Furthermore, Fig. 9 identifies for pulses of 4.8 MHz repetition rate that their removal efficiency reduces to  $0.22 \text{ mm}^3/\text{W}/\text{min}$ , which is below the theoretical removal efficiency. This might be affected by plasma/particle shielding. Overall, the results obtained by studying the removal efficiency suggest that ultrashort pulse laser processing in the mid-fluence range seems to be the optimum for micro fabrication.

There is also a dependence of machining throughput on fluence and repetition rate, both associated by average laser power. In Fig. 9, the experimentally achieved volume ablation rate as well as the material removal rate is plotted as a function of the repetition rate. The plot illustrates that the ablation rate decreases significantly by using pulses of higher repetition rate. This is due to the fact that the pulse energy and thus the fluence decrease with increasing repetition rate as a result of the limited available maximum average laser output power.

Furthermore, as a general trend, a higher volume ablation rate was achieved with the femtosecond laser of 31.7 W average laser power although more than twice higher

laser power or rather laser energy at similar repetition rates were supplied by the picosecond laser. Explanations therefore can be found in a previous study, presenting higher material removal for femtosecond laser radiation than for picosecond laser beams [20]. It was reported that the effective energy penetration depth in steel has almost quadruplet by using femtosecond pulses compared to picosecond pulses of similar beam properties. As has been already argued above, energy penetration has a great effect on the volume ablation rate, see Eq. 6.

In addition, Figure shows a greater material removal rate for femtosecond laser pulses compared to picosecond pulses at similar repetition rate. For the investigated femtosecond laser, the highest material removal rate was 6.81 mm<sup>3</sup>/min, achieved with pulses of 19.3 MHz repetition rate, 0.85 J/cm<sup>2</sup> fluence and 31.7 W laser output power. In this case the fluence was in the optimum range, enabling most-efficient material removal. This becomes also obvious by dividing the experimentally removal rate by the applied laser power. As a result, the removal efficiency calculates to 0.21 mm<sup>3</sup>/W/min for pulses of 19.3 MHz, which is lower than the theoretical removal efficiency of 0.244 mm<sup>3</sup>/W/min or rather the data given in Fig. 8 where the maximum efficiency was 0.33 mm<sup>3</sup>/W/min. It should be mentioned here that the lateral pulse spacing was smaller than 1 μm at this high repetition rate, which was due to the limited scan speed of the galvanometer scanner (17 m/s). From this it can be supposed that particle shielding will diminish the removal efficiency by using high-PRF pulses in the range of 20 MHz. The next following laser pulses will strongly interact with the plume of plasma and/or ablated particles initiated by previous pulse irradiations.

The maximum removal rate of the high-PRF picosecond laser beam was 5.4 mm<sup>3</sup>/min, obtained with pulses of 0.5 J/cm<sup>2</sup> fluence, 20 MHz repetition rate

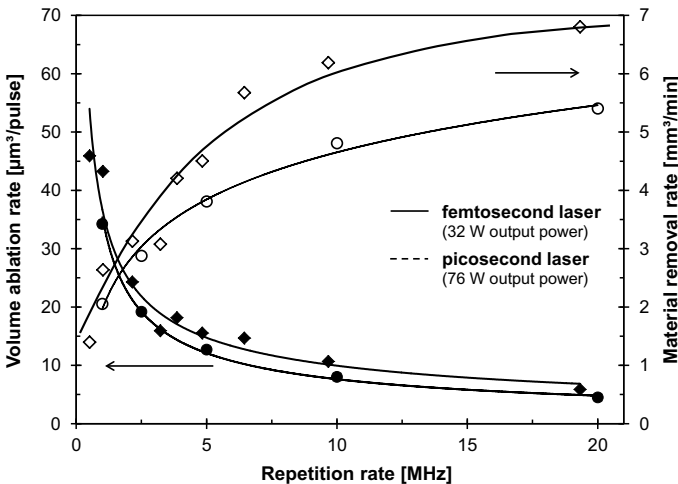


**Fig. 9** The experimentally determined volume ablation rate and the material removal rate as a function of the repetition rate, for each given data point the maximum available laser output power was applied, which was 31.7 W for the femto-second and 76 W for the picosecond laser

and maximum laser output power of 76 W. From this removal rate value the experimental removal efficiency was estimated of  $0.071 \text{ mm}^3/\text{W}/\text{min}$ . This is slightly less than the theoretical removal efficiency of  $0.081 \text{ mm}^3/\text{W}/\text{min}$ , calculated according to Eq. 2 by taking into account  $0.1 \text{ J}/\text{cm}^2$  threshold fluence and, in comparison to femtosecond pulses, a significant lower effective energy penetration depth of 5 nm.

Particle shielding, on the one hand, may cause the difference occurred between the experimental and theoretical removal efficiency although wider pulse spacing of  $10 \text{ }\mu\text{m}$  was used here. This spacing was achieved between high-PRF pulses of 20 MHz by using the polygon scanner and scan speed of 200 m/s. On the other hand, using picosecond pulses of 20 MHz, the fluence was not in the optimum range. This might be contributed to the fact that the removal efficiency reduced. A maximum fluence of  $0.5 \text{ J}/\text{cm}^2$  was available at 20 MHz even for 76 W average laser powers because of the focus diameter enlarged to be  $44 \text{ }\mu\text{m}$  by using the polygon scanner setup. However, the above results emphasize the previous statement that femtosecond laser pulses are more efficient for stainless steel removal than picosecond pulses in the same parameter range.

In Fig. 10, SEM micrographs of cavity bottoms produced using high average power picosecond and femtosecond lasers are placed opposite to each other. It is worth noting that pulse energy and fluence varied for the cavities those were made with almost identical repetition rates. This variance was due to different available maximum laser power and focus spot diameter of both laser systems to be compared. For each micrograph, the processing parameters as well as the average roughness  $S_a$  evaluated over the 3D surface are presented in Fig. 10.

In general, the cavities produced with higher pulse energy or rather fluence show strongly rugged coral-like micro featured bottoms. While picosecond laser ablation initiated more or less cone-like protruded surfaces, the femtosecond laser made cavities appeared fissured including a high number of micro holes. For the pulses of higher fluence, the surface roughness was measured to be  $S_a = 2.1 \dots 4.9 \text{ }\mu\text{m}$  for the femtosecond and  $S_a = 1.9 \dots 3.3 \text{ }\mu\text{m}$  for the picosecond laser beam, respectively. In case of lower fluence, considerably smoother surfaces were produced. The lowest roughness was achieved with pulses in the optimum fluence range, measured of  $S_a < 0.6 \text{ }\mu\text{m}$  for picosecond and  $S_a < 0.4 \text{ }\mu\text{m}$  for femtosecond pulses.

It is noteworthy that the smoothest cavity bottom was achieved with femtosecond pulses of 19.3 MHz although the pulse spacing was less than  $1 \text{ }\mu\text{m}$ . This is in contrast to our results obtained in previous studies, where rough cone-like protruded surfaces were observed for femtosecond pulses of  $1 \text{ J}/\text{cm}^2$  fluence, 1 MHz repetition rate, and  $1 \text{ }\mu\text{m}$  pulse spacing [3, 21]. High-quality smooth surfaces were obtained in this case by enlarging the pulse spacing in the range of half focus spot radius.

From the results obtained in this study it can be concluded that ultrashort pulse laser processing in the mid-fluence regime will facilitate the best machining outcomes with regard to their efficiency, throughput and quality. However, in high-rate laser processing using ultrashort pulse lasers with high average output power, (ultra)fast movement of the laser beam is essential to achieve the required lateral pulse-to-pulse spacing even for pulses of several MHz repetition rate. For this, polygon scan systems seem to be a promising technology, providing sufficiently high scan speeds in the



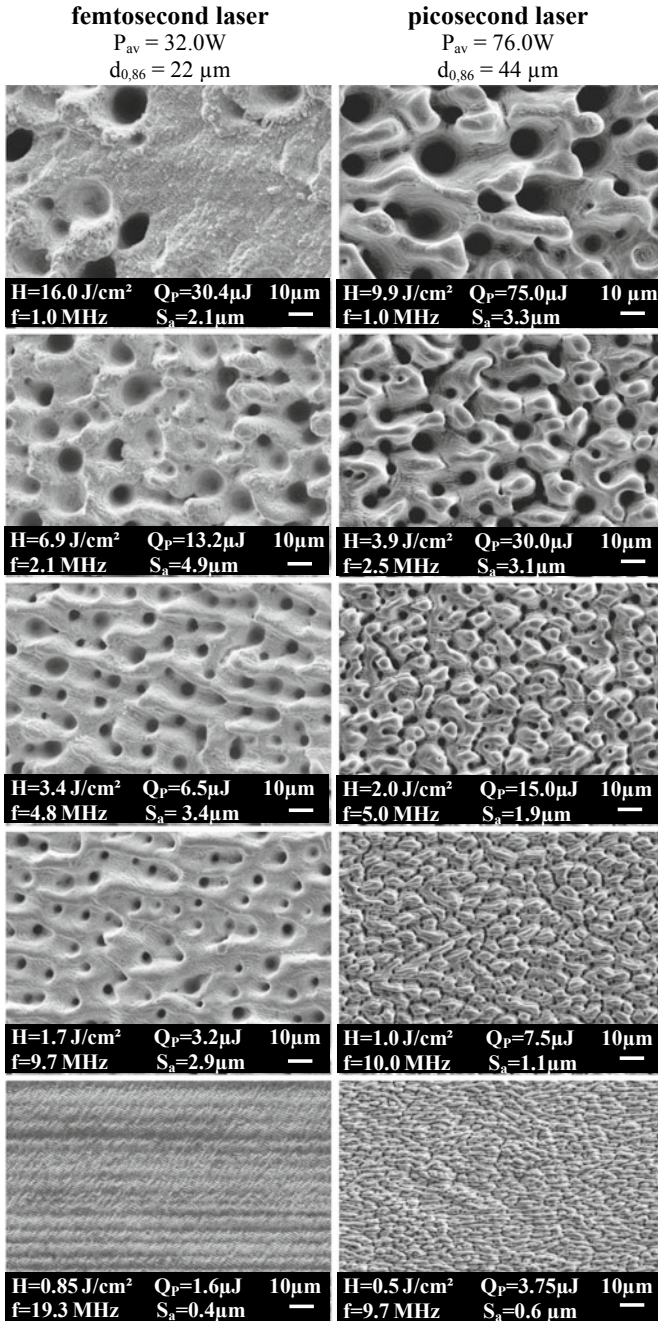


Fig. 10 SEM micrographs showing the surface bottom of laser produced cavities as obtained by using high average power femtosecond (left) and picosecond (right) laser beams, the maximum available average laser power was irradiated, the repetition rate was varied, the operating pulse energy and fluence as well as the average bottom roughness are presented

range of hundreds to thousands of meters per second. This was already successfully demonstrated in a previous work investigating an in-house developed two-axis polygon scanner [22].

## 5 Summary

High-rate laser processing of stainless steel using high-average power ultrashort pulse lasers in conjunction with (ultra)fast scan systems was studied. Initially, a theoretical analysis of material ablation identified the mid-fluence range as optimum process regime with regard to ablation rate and throughput. It was demonstrated for femtosecond laser pulses that most efficient material removal will take place when the fluence is 7.4 times above the ablation threshold. For this, the maximum removal efficiency was computed of  $0.244 \text{ mm}^3/\text{W}/\text{min}$  and therefore, by taking into account 30 W average laser powers, a maximum removal rate of  $7.32 \text{ mm}^3/\text{min}$  was calculated. It was shown that this maximum removal rate can be obtained with different parameter sets by balancing the focus diameter and the pulse energy to the optimum fluence of  $0.74 \text{ J}/\text{cm}^2$ .

In the experimental analysis, material removal was studied using high average power high-PRF ultrashort pulse lasers, a femtosecond laser with 31.7 W and a picosecond laser with 76 W average output power. It was found that both, volume removal per laser pulse (defined as volume ablation rate) and removable material volume per time increment (defined as material removal rate) increases with increasing fluence. Thereby no significant influencing effects of the repetition rate on the ablation rate were observed. However, it cannot be ruled out, therefore, that heat accumulation and particle shielding balancing each other in the studied range between 508 kHz and 4.83 MHz pulse repetitions. This hypothesis is supported by the analysis of the removal efficiency. While for high-PRF pulses in the range between 508 kHz and 3.8 MHz the removal efficiency enhanced to  $0.33 \text{ mm}^3/\text{W}/\text{min}$ , theoretically the removal efficiency was determined of  $0.244 \text{ mm}^3/\text{W}/\text{min}$ . By irradiating pulses of higher repetition rate the removal efficiency decreased to  $0.22 \text{ mm}^3/\text{W}/\text{min}$  and  $0.21 \text{ mm}^3/\text{W}/\text{min}$ , as obtained with pulses of 4.83 MHz and 9.3 MHz, respectively.

The maximum removal rate using the femtosecond laser and 31.7 W average powers was  $6.81 \text{ mm}^3/\text{min}$ . This was greater than  $5.4 \text{ mm}^3/\text{min}$  maximum removal rate as obtained with the picosecond laser by emitting more than twice higher laser power of 76 W. As main reason for this, the considerably lower removal efficiency of picosecond pulses was identified, which was estimated of  $0.071 \text{ mm}^3/\text{W}/\text{min}$  in the experimental study.

Finally, the processing quality was evaluated by SEM photographing and roughness measurements on the laser processed cavity bottoms. As a general trend it was found that the bottom roughness reduced with pulses of lower fluence. The smoothest cavity bottoms with average surface roughness of  $S_a < 0.6 \text{ }\mu\text{m}$  for the picosecond or  $S_a < 0.4 \text{ }\mu\text{m}$  for the femtosecond laser were produced with pulses in the mid-fluence range.

In conclusion, ultrashort pulse laser processing in the mid-fluence range will facilitate the best machining outcomes with regard to their efficiency, throughput and quality. Moreover, high-rate laser processing using high average power high-PRF ultrashort pulse lasers utilized in conjunction with (ultra)fast laser beam movement systems can be supposed as key enabling technology with the potential to substitute standard manufacturing technologies in modern micro fabrication.

**Acknowledgements** The presented results have been conducted in course of the project "Innoprofile Transfer—Rapid Micro/Hochrate—Laserbearbeitung" (03IPT506X), funded by the Federal Ministry of Education and Research. The authors gratefully acknowledge Felix Dreisow for his assistance in using the *sci-series* laser.

## References

1. Ancona A, Roeser F, Rademaker K, Limpert J, Nolte S, Tuennermann A (2008) High speed laser drilling of metals using a high repetition rate, high average power ultrafast fiber CPA system. *Opt Express* 16(12):8958–8968
2. Tan B, Panchatsharam S, Venkatakrishnan K, (2009), High repetition rate femtosecond laser forming sub-10 $\mu$ m diameter interconnection vias. *J Phys D Appl Phys* 42, 065102
3. Schille J, Ebert R, Loeschner U, Schneider L, Walther N, Regenfuss P, Scully P, Goddard N, Exner H (2009) An ultrafast femtosecond fibre laser as a new tool in rapid microtooling. In: *Proceedings of LAMP 2009—The 5th International Congress on Laser Advanced Materials Processing*: paper 151
4. Neuenschwander B, Bucher GF, Nussbaum C, Joss B, Muralt M, Hunziker UW, Schuetz P (2010) Processing of metals and dielectric materials with ps laser pulses: results, strategies, limitations and needs. In: *Proceedings of SPIE* 7584
5. Schille J, Schneider L, Loeschner U, Ebert R, Scully P, Goddard N, Steiger B, Exner H (2011) Micro processing of metals using a high repetition rate femto second laser: from laser process parameter study to machining examples. In: *Proceedings of 30th ICALEO 2011*: paper M102
6. Neuenschwander B, Jaeggi B, Schmid M (2013) From fs to sub-ns: Dependence of the material removal rate on the pulse duration for metals. *Phys Procedia* 41:794–801
7. Di Niso F, Gaudiuso C, Sibillano T, Mezzapesa FP, Ancona A, Lugarà PM (2013) Influence of the repetition rate and pulse duration on then incubation effect in multiple-shots ultrafast laser ablation of steel. *Phys Procedia* 41:698–707
8. Lopez J, Mincuzzi G, Devillard R, Zaouter Y, Hoenninger C, Mottay E, Kling R (2014) Ablation efficiency of high average power ultrafast laser. In: *Proceedings of ICALEO*: paper 401
9. Schille J (2013) Investigation of micromachining using a high repetition rate femtosecond fibre laser. Thesis, The University of Manchester, Manchester (UK)
10. Schille J, Schneider L, Mueller M, Loeschner U, Goddard N, Scully P, Exner H (2014) Laser micro processing using ultrashort laser pulses. *J Laser Micro/Nanoeng* 9:161–168
11. Nolte S, Momma C, Jacobs H, Tuennermann A, Chichkov BN, Wellegehausen B, Welling H (1997) Ablation of metals by ultrashort laser pulses. *J Opt Soc Am B* 14(10):2716–2722
12. Mannion P, Magee J, Coyne E, O'Connor GM, (2002) Ablation thresholds in ultrafast laser micro-machining of common metals in air. In: *Proceedings of SPIE* 4876, *Opto-Ireland 2002: optics and photonics technologies and applications*, vol 470, pp 470–478
13. Wynne AE, Stuart BC (2003) Rate dependence of short-pulse laser ablation of metals in air and vacuum. *Appl Phys A* 76:373–378
14. Nedialkov NN, Imamova SE, Atanasov PA (2004) Ablation of metals by ultrashort laser pulses. *J Phys D: Appl Phys* 37:638–643

15. Račiukaitis G, Brikas M, Gečys P, Voisiat B, Gedvilas M (2009) Use of high repetition rate and high power lasers in microfabrication: how to keep the efficiency high? *J Laser Micro/Nanoeng* 4(3):186–191
16. Neuenschwander B, Bucher GF, Hennig G, Nussbaum C, Joss B, Muralt M, Zehnder S, Hunziker UW, Schuetz P (2010) Processing of dielectric materials and metals with ps laser pulses. In: *Proceedings of 29th ICALEO 2010*: paper M101
17. Jaeggi B, Neuenschwander B, Hunziker U, Zuercher J, Meier T, Zimmermann M, Selbmann KH, Hennig G (2012) Ultra high precision surface structuring by synchronizing a galvo scanner with an ultra short pulsed laser system in MOPA arrangement. In: *Proceedings of SPIE 8243-20*
18. Neuenschwander B, Jaeggi B, Zimmermann M, Hennig G (2014) Influence of particle shielding and heat accumulation effects onto the removal rate for laser micromachining with ultra-short pulses at high repetition rates. In: *Proceedings of 33rd ICALEO 2014*: paper M1104
19. Schille J, Schneider L, Hartwig L, Loeschner U, Ebert R, Scully P, Goddard N., Exner H, (2012), Characterisation of interaction phenomena in high repetition rate femtosecond laser ablation of metals. In: *Proceedings of 31st ICALEO 2012*: paper M1003
20. Lickschat P, Schille J, Mueller M, Weissmantel S, Reisse G (2012) Comparative study on microstructuring of steel using pico- and femtosecond laser pulses. In: *Proceedings of 31st ICALEO 2012*: paper P145
21. Schille J, Ebert R, Loeschner U, Regenfuss P, Suess T, Exner H, (2008), Micro structuring with highly repetitive ultra short laser pulses. In: *Proceedings of LPM 2008—the 9th international symposium on laser precision microfabrication*
22. Loeschner U, Schille J, Streek A, Knebel T, Hartwig L, Hillmann R, Endisch C (2014) High-Rate laser micro processing using a polygon scanner system. In: *Proceedings of 33rd ICALEO 2014*: paper M1208

# Laser Micro Machining Using Photonic Nanojets



T. Uenohara, Y. Takaya, and M. Michihata

**Abstract** A photonic nanojet is a fine light beam with high energy density that is generated at the backside of a dielectric microsphere illuminated by the laser light. Not only the beam diameter of the photonic nanojet is smaller than the wavelength of the incident light, but also it propagates a long distance of several times the wavelength with maintaining high energy density. Moreover the energy density is higher than that of the incident beam. Using these specific properties of the photonic nanojets, we propose a novel laser micro machining method that enables a machining shape with a high aspect ratio. In this paper, the comparison between the machining property using just a focused laser beam and a photonic nanojet is investigated. The fluence threshold  $F_{th}$  of a Si was estimated  $100 \text{ mJ/cm}^2$  based on the test machining of a hole on a Si substrate surface using a focused laser beam. The photonic nanojet makes it possible to machine a fine hole with a diameter of 586 nm, a depth of 98 nm on the Si substrate surface by using laser illumination to microspheres arrayed on the Si substrate surface with a low fluence of  $2.5 \text{ mJ/cm}^2$ . In spite of the laser illumination to a microsphere with a lower fluence than  $F_{th}$ , machining of a submicron size hole could be realized. Since the photonic nanojet has a long propagation distance, the proposed method enables a machining shape with higher aspect ratio than 0.17 by scanning it in the propagation direction.

**Keywords** Laser machining · Photonic nanojet · High aspect ratio

## 1 Introduction

Recent years have seen tremendous developments in a number of micromachining technologies, such as lithography, mechanical or laser micro processing. In particular, laser micro machining enables high speed and flexible processing. However, most laser based processes have a limited precision, with a minimum feature size in the

---

T. Uenohara (✉) · Y. Takaya · M. Michihata  
Department of Mechanical Engineering, Osaka University, 2-1 Yamadaoka, Suita, Osaka, Japan  
e-mail: [uenohara@mech.eng.osaka-u.ac.jp](mailto:uenohara@mech.eng.osaka-u.ac.jp)

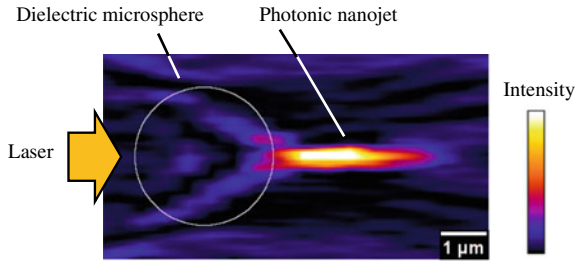


**Fig. 1** The measurement result of the intensity distribution of photonic nanojet generated by a diameter 3  $\mu\text{m}$  microsphere in size which is illuminated by the laser light with  $\lambda = 532 \text{ nm}$ . The intensity distribution is reconstructed by the stack of laser scanning confocal microscopy images [2]

micrometer range. Reducing the minimum feature size is desirable, as it would further expand the range of applications that benefit from laser micro machining.

In general, a focused laser beam is used in a laser machining. Especially the focal point of the focused laser beam has the smallest beam diameter and the highest energy density. But the beam diameter expands as increase of the defocus amount from the focal point. In order to get small beam diameter at the focal point the higher NA (numerical aperture) of an objective lens is needed, the shorter the focal length is. Considered these properties of a focused laser beam, it is difficult to machine a shape of higher aspect ratio than one with nanometer scale using a focused laser beam.

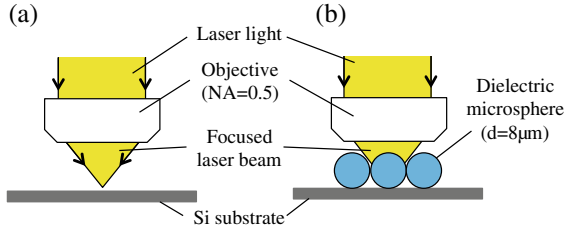
We propose a novel laser machining method using a photonic nanojet as a machining method to realize a shape of higher aspect ratio than one with nanometer scale. The photonic nanojet is a fine light beam with high energy density that is generated at the backside of a dielectric microsphere illuminated by the laser light [1]. Figure 1 shows the measurement result of the energy density distribution of photonic nanojet [2]. Not only the beam diameter of the photonic nanojet is smaller than the wavelength of the incident light, but also it propagates a long distance of several times the wavelength with maintaining high energy density. Moreover the energy density is higher than that of the incident laser beam. Considered these properties of a photonic nanojet, a photonic nanojet has a potential to realize a shape of higher aspect ratio than one with nanometer scale.

In this paper, a conventional laser micro machining process is compared with photonic nanojets machining to produce micro-holes. A suitable process fluence is identified in both cases.

## 2 Experimental Methods

Micro-holes are produced in a Si substrate, first using just a focused laser beam and then using photonic nanojets. The threshold fluence values are compared between both cases. The conventional laser drilling process uses a femtosecond laser with

**Fig. 2** Schematic diagram of the hole machining experimental **a** using a focused laser beam, **b** using a photonic nanojet. Microspheres are arrayed on a Si substrate



a pulse width of 100 fs (FWHM), wavelength of 800 nm, and repetition rate of 80 MHz. Figure 2 shows the schematic diagram of the experimental conditions using (a) a focused laser beam and (b) a photonic nanojet. First, the fluence threshold  $F_{th}$  is estimated by hole machining using just a focused laser beam in various fluences [ $\text{mJ}/\text{cm}^2$ ]. The incident laser light is focused by an objective lens with  $NA = 0.50$ , the beam spot diameter of the focal point is  $1.0 \mu\text{m}$ . The fluence is adjusted by changing the irradiation area on the Si substrate by defocusing while the incident laser power is constant. Second, the fluence threshold is estimated by hole machining using photonic nanojets in various fluences. A silica micro particle with refractive index  $n = 1.44$  and diameter of  $8.0 \mu\text{m}$  is used as a dielectric microsphere which is needed to generate a photonic nanojet. Silica micro particles are arrayed on a Si substrate surface to form a contact particle lens array (CPLA) [3, 4]. The focused laser beam illuminates the microsphere by corresponding each the center of an irradiation spot and a microsphere. In this experiment, it is so difficult to estimate the beam diameter of a photonic nanojet exactly that the fluence is evaluated by dividing the incident power and irradiation area.

After hole machining, the Si substrate is ultrasonic cleaned. The machined holes are measured by using an atomic force microscope (AFM), diameter and depth of the hole are evaluated by the cross sectional profile. Aspect ratio is calculated by dividing the hole depth in hole diameter.

### 3 Hole Machining Using Focused Laser Beam

The fluence threshold  $F_{th}$  is estimated based on hole machining using a focused laser beam. The initial fluence is adjusted to  $970 \text{ mJ}/\text{cm}^2$ . Hole machining is performed 25 points in each experimental condition. The irradiation pulse numbers is adjusted to 160,000 using a mechanical shutter. When the hole machining is possible in a certain fluence, hole machining is performed by setting the fluence lower than that of the former process. The same procedure is repeated until hole machining can't be performed.

The fluence threshold is estimated  $F_{th} = 100 \text{ mJ}/\text{cm}^2$  based on these measurements.

## 4 Hole Machining Using a Photonic Nanojet

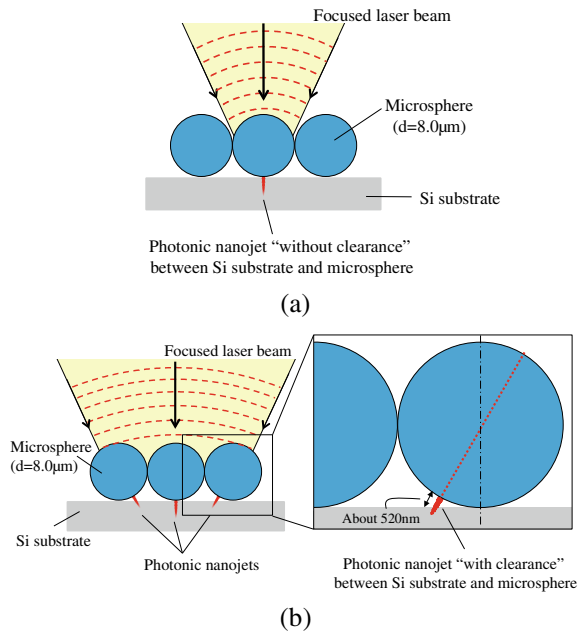
A photonic nanojet has an energy density distribution in propagation direction. In this paper, hole machining using two positions where the distance from a microsphere surface is different in photonic nanojet is investigated. The distance between a Si substrate surface and a microsphere surface is controlled by defocusing, which is specified in Sect. 4.1. According to the Ref. [2], the peak of the energy density of photonic nanojet appears at some distance away from the microsphere surface.

### 4.1 Machining Condition Associated with the Laser Irradiation Condition

The propagation direction of the photonic nanojet corresponds with the propagation direction of the incident laser light to microsphere. The converging angle of the focused laser beam is  $30^\circ$  for the  $NA = 0.5$  of the objective lens. In focused laser beam, the light of the center of the beam propagates perpendicularly to the Si substrate. On the other hand, the light away from the center of the beam propagates slantingly to the Si substrate.

Figure 3 shows the method to generate the photonic nanojets by way of laser irradiation to microspheres. When the irradiation laser beam spot diameter is smaller

**Fig. 3** Schematic diagram of the method to generate the photonic nanojets by way of laser irradiation to microspheres: **a** shows photonic nanojet without clearance between a Si substrate and a microsphere's bottom surface, and **b** shows photonic nanojet with clearance between a Si substrate and a microsphere's bottom surface





than microsphere diameter ( $d = 8.0 \mu\text{m}$ ), just one microsphere is illuminated, a photonic nanojet is generated from the microsphere and propagates perpendicularly to the Si substrate as shown in Fig. 3a. In this case, there is no clearance between the Si substrate and the microsphere's bottom surface, this photonic nanojet is referred to "photonic nanojet without clearance" in this paper. Hole machining using the photonic nanojet without clearance is specified in Sect. 4.2. On the other hand, when the irradiation laser beam spot diameter is larger than microsphere diameter ( $d = 8.0 \mu\text{m}$ ), surrounding microspheres are also illuminated by slanting laser beam, photonic nanojets generate from the surrounding microspheres and propagate slantingly to the Si substrate as shown Fig. 3b. In this case, there is a clearance between the Si substrate and the microsphere surface, this photonic nanojet is referred to "photonic nanojet with clearance" in this paper. The distance of the clearance between the Si substrate and the microsphere's bottom surface is about 520 nm considering the angle of the incident laser beam. In this experiment, the irradiation laser beam spot diameter is adjusted 16.0  $\mu\text{m}$ .

#### 4.2 Hole Machining Using the Photonic Nanojet Without Clearance

In this subsection, hole machining using the photonic nanojet without clearance is specified. The energy density of photonic nanojet is enhanced as compared to the energy density of the incident laser beam to microsphere. In this experiment, the initial fluence is adjusted 57  $\text{mJ}/\text{cm}^2$  which is lower than fluence threshold of  $F_{\text{th}} = 100 \text{ mJ}/\text{cm}^2$  estimated based on hole machining using a focused laser beam. The irradiation pulse number is adjusted 160,000, and holes are machined 10 points. When a hole is possible to be machined, hole machining is performed in lower fluence. This process is repeated until a hole couldn't be machined.

The photonic nanojet without clearance enables to machine a hole with the incident fluence to microsphere down to 10  $\text{mJ}/\text{cm}^2$ . Figure 4 shows AFM image of machined hole with  $F = 10 \text{ mJ}/\text{cm}^2$ . Diameter and depth are measured from a cross sectional profile of a machined hole, which are defined as shown in Fig. 4. The measurement results of hole size in diameter and depth are shown in Fig. 5. In the fluence lower than 20  $\text{mJ}/\text{cm}^2$ , both of the diameter and depth of the hole are increasing with

**Fig. 4** AFM image of machined hole using the photonic nanojet without clearance with 10  $\text{mJ}/\text{cm}^2$

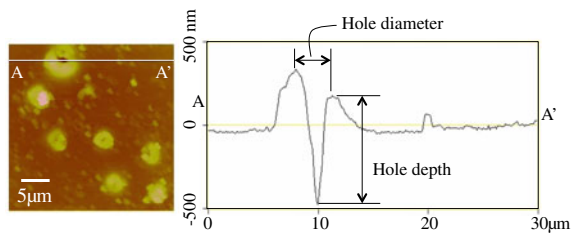
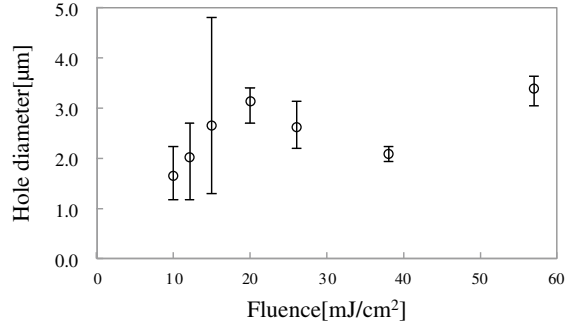
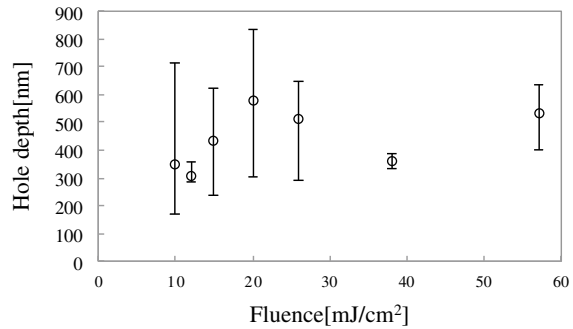


**Fig. 5** Measurement results of the machined hole using the photonic nanojet without clearance; **a** hole diameter, **b** hole depth. Error bars are represented by maximum and minimum



(a)



(b)

increasing the fluence. In the fluence higher than  $20 \text{ mJ/cm}^2$ , the diameter as well as the depth of the hole is not correlated with the fluence. Table 1 shows the aspect ratio calculated from the measured diameter and depth of the machined hole. The aspect ratio of machined holes is not very correlated with the fluence.

The fluence threshold  $F_{th}$  is  $100 \text{ mJ/cm}^2$ , but the incident fluence of  $10 \text{ mJ/cm}^2$  enables hole machining when using the photonic nanojet without clearance. This

**Table 1** Aspect ratio of machined hole using the photonic nanojet without clearance

Fluence [mJ/cm <sup>2</sup> ]	Average diameter of hole [μm]	Average depth of hole [nm]	Aspect ratio
57	3.40	531	0.16
38	2.11	363	0.17
26	2.63	516	0.20
20	3.12	583	0.19
15	2.66	435	0.16
12	2.03	309	0.15
10	1.68	351	0.21

concludes that the energy density of the photonic nanojet without clearance is enhanced to approximately 10 times the energy density of the incident laser beam. By looking at the cross sectional profile, it can be seen that the surroundings of the machined hole have a raised profile. This is thought to be because the microsphere arrayed on a Si substrate prevents ablated material from being removed, and the ablated material is accumulated around machined hole. In hole machining using the photonic nanojet without clearance, the low fluence enables hole machining, but the hole machining is not performed with high quality.

### 4.3 Hole Machining Using the Photonic Nanojet with Clearance

In this subsection, hole machining using the photonic nanojet with clearance is specified. Large laser irradiation spot diameter is needed to generate the photonic nanojet with clearance, so it is difficult to obtain higher fluence than  $5 \text{ mJ/cm}^2$ . Hole machining is performed with fluence 5 and  $2.5 \text{ mJ/cm}^2$ . The irradiation pulse number is adjusted 160,000, and holes are machined 12 points.

Hole machining using the photonic nanojet with clearance is possible down to  $2.5 \text{ mJ/cm}^2$  with the incident fluence to microsphere. Hole machining is possible all points out of 12 points with  $5 \text{ mJ/cm}^2$  and 1 point out of 12 points with  $2.5 \text{ mJ/cm}^2$ . Figure 6 shows AFM image of machined hole with  $F = 5 \text{ mJ/cm}^2$ . The measurement results are shown in Fig. 7. Hole diameter and depth are increasing with increasing the fluence in the same way as measurement results of Sect. 4.2. Submicron hole diameter is realized by using the photonic nanojet with clearance. Table 2 shows the aspect ratio calculated by hole diameter and depth of machined hole. The aspect ratio of the machined hole using the photonic nanojet with clearance is evaluated almost same as that of the machined hole using the photonic nanojet without clearance.

The fluence threshold  $F_{th}$  is  $100 \text{ mJ/cm}^2$ , but the incident fluence of  $2.5 \text{ mJ/cm}^2$  enables hole machining when the photonic nanojet with clearance is used. This shows the energy density of the photonic nanojet with clearance is enhanced to approximately 40 times the energy density of incident laser beam. Hole machining using the photonic nanojet with clearance is possible with lower fluence than by using the photonic nanojet without clearance. This shows that the energy density at the position away from microsphere surface is higher than at the position of microsphere

**Fig. 6** AFM image of machined hole using the photonic nanojet with clearance  $5 \text{ mJ/cm}^2$

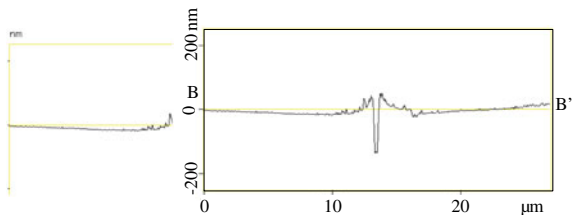
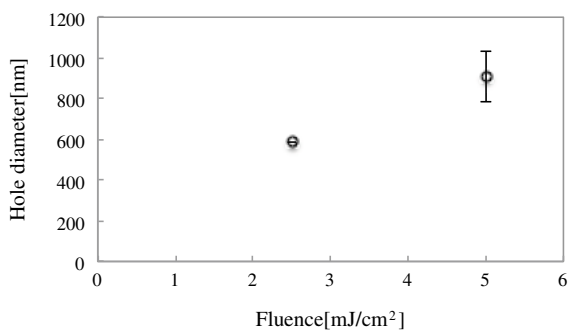
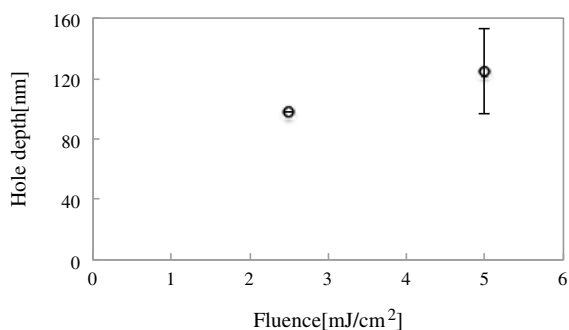


**Fig. 7** Measurement results of machined hole using the photonic nanojet with clearance; **a** hole diameter, **b** hole depth



(a)



(b)

**Table 2** Aspect ratio of machined hole using the photonic nanojet with clearance

Fluence [mJ/cm <sup>2</sup> ]	Average diameter of hole [nm]	Average depth of hole [nm]	Aspect ratio
5	907	125	0.14
2.5	586	98	0.17

surface. This special feature of photonic nanojet corresponds the fact referred in reference [2]. The swell around machined hole using the photonic nanojet with clearance is smaller as compared with using the photonic nanojet without clearance. The clearance between the Si substrate surface and the microsphere surface facilitates the ablated material removal.

## 5 Conclusion

A novel machining method using the photonic nanojet is proposed as the machining method of high aspect ratio shape with nanometer scale. The fluence threshold  $F_{th}$  of Si substrate is estimated  $100 \text{ mJ/cm}^2$  based on the basic experiment of hole machining using just a focused laser beam. Hole machining is possible with the fluence lower than  $F_{th}$  by using the photonic nanojet generated from the microsphere arrayed on Si substrate. The lowest incident fluence to microspheres is determined  $2.5 \text{ mJ/cm}^2$  by the hole machining using the photonic nanojet with clearance between the Si substrate and the microsphere surface. This shows that the energy density of the photonic nanojet is enhanced to approximately 40 times that of the incident laser beam. The aspect ratio of machined hole using the photonic nanojet is up to 0.21. In future work, we try to make it possible to increase the aspect ratio of the machined hole by scanning the photonic nanojet in propagation direction.

**Acknowledgements** This research was supported by JSPS KAKENHI Grant Number 24246028.

## References

1. Heifetz A, Kong S-C, Sahakian AV, Taflove A, Backman V (2009) Photonic Nanojets. *J Comput Theor Nanosci* 6:1979–1992
2. Ferrand P, Wenger J, Devilez A, Pianta M, Stout B, Bonod N, Popov E, Rigeneault H (2008) Direct imaging of photonic nanojets. *Opt Express* 16(10):6930–6940
3. Pena A, Wang Z, Whitehead D, Li L (2010) Direct writing of micro/nano-scale patterns by means of particle lens arrays scanned by a focused diode pumped Nd:YVO<sub>4</sub> laser. *Appl Phys A* 101:287–295
4. Hermansson K, Lindberg U, Hok B, Palmkog G (1991) Wetting properties of silicon surfaces. *IEEE*, pp 193–196

# Deposition Characteristics and Microstructure of Ni60–Ni Composite Coating Produced by Supersonic Laser Deposition



Jianhua Yao, Lijing Yang, Bo Li, Qunli Zhang, and Zhihong Li

**Abstract** Supersonic laser deposition (SLD) is a newly developed coating method which combines the supersonic powder stream produced by cold spray (CS) with synchronous laser heating of the deposition zone. This article presents a study of using the SLD technique to deposit Ni60–Ni composite coatings on 45# medium-carbon steel substrate (AISI 1045). The process was investigated to identify optimum parameters such as laser power. The microstructure of coating specimens and deposition characteristics was analyzed using scanning electron microscope (SEM) and energy dispersion spectrum (EDS), respectively. The results show that the SLD technique is able to achieve a dense crack-free coating with the optimal process parameter, because Ni particles are found to have deformed largely and be evenly distributed in the coatings, which benefit releasing residual stress developed in the composite coatings during the SLD process. The cross-section thickness of the Ni60–30 wt%Ni composite coatings increased with enhanced laser power. It is also found that a Ni-rich layer is generated at the interface between the coating and substrate. This softer Ni-rich layer serves as a transition layer to accommodate the adhesion between the coating and substrate.

**Keywords** Supersonic laser deposition · Laser irradiation · Ni60–Ni composite

## 1 Introduction

Ni60 is one of the most widely used self-fluxing Ni–Cr–B–Si–C alloy powders for conventional thermal spray. Adding Si, B, Cr elements in Ni-based alloy lowers its melting point down to 1050–1080 °C and increases alloy hardness up to 58–62 HRC [1]. The enhanced alloy shows excellent resistance to wear, corrosion, high

---

J. Yao (✉) · L. Yang · B. Li · Q. Zhang · Z. Li

Research Center of Laser Processing Technology and Engineering, Zhejiang University of Technology, Hangzhou 310014, China

e-mail: [laser@zjut.edu.cn](mailto:laser@zjut.edu.cn)

Zhejiang Provincial Collaborative Innovation Center of High-End Laser Manufacturing Equipment, Hangzhou 310014, Zhejiang, China

© Springer Nature Switzerland AG 2022

S. Hinduja et al. (eds.), *Proceedings of the 38th International MATADOR Conference*, [https://doi.org/10.1007/978-3-319-64943-6\\_12](https://doi.org/10.1007/978-3-319-64943-6_12)

temperature oxidation, and combined properties over a wide range of temperature [2]. Conventional Ni60 coatings are often prepared by high velocity oxygen fuel (HVOF), plasma spray and laser cladding (LC). In thermal spray process, plasma jets or process gasses are used to melt or partially melt the particles and to accelerate the powder to impact on a prepared substrate. Ni60 coatings deposited by plasma spray have some problems: high oxides, high porosity, non-uniform microstructure, weak coating adhesion strength, low deposition efficiency, owing to unmelting powder and high thermal stress [1, 3, 4]. Laser cladding (LC) technology uses high energy density of laser beam to melt feedstock material and the surface layer of substrate to form metallurgical bonding between coating and substrate [5, 6]. Ni60 coatings deposited by laser cladding showed that oxides such as FeB, Cr<sub>3</sub>C<sub>7</sub>, Ni<sub>3</sub>Si easily concentrated at the grain boundary, the structure stress and heat stress of the coating were generated by dendritic growth during rapid solidification, and high thermal gradients were induced during rapid cooling, all of which can lead to non-uniform intermetallic compounds and the initiation of cracks [7–9]. Although metallurgical combination between coating and substrate in laser cladding can improve coating adhesion strength, element component dilution of the coating can affect the performance of the coating and form a low hardness zone [10]. In order to solve these problems and improve the properties of the coatings, cold spray which is the newest spray techniques has attracted significant attention in recent years.

Cold spray is a process whereby metal powder particles remain in solid state under the condition of deposition but are deformed plastically to form a coating by a low temperature supersonic gas stream and ballistic impingement upon a suitable substrate [11, 12]. The particles' size of metal powder ranges from 5 to 50 μm and are accelerated by means of a high-velocity jet stream which is generated through the expansion of a pressurized, preheated nitrogen or air in a converging–diverging nozzle to exceed critical plastic deformation velocity [13, 14]. Cold spray is popular in depositing low hardness, heat sensitive and oxidation sensitive materials, such as Al, Cu, Ti, 316L stainless steel, Ni-based 25 alloy, amorphous material and so on [15–19], but it is difficult to deposit high hardness particles such as Stellite6, Ni60 and metal ceramic material or prohibitively expensive to process by cold spray [20].

In order to expand the application of cold spray technology, reduce the processing costs and improve coatings' performance and quality, the idea of combining cold spray with laser technology was proposed by O'Neill [21], known as supersonic laser deposition (SLD). This combination created a potential and advanced technology to produce high performance and high quality coatings. In SLD, laser is used to heat the deposition zone and soften both substrate and powder particles to allow the formation of a coating at a much reduced impact velocity, about half of that used in cold spray [21, 22]. Because SLD reduces particle deposition temperature and critical deposition velocity, Ni60 particles can be deposited more easily with this process. In this research, Ni60–30 wt%Ni composite was deposited on 45# medium carbon steel (AISI 1045) using SLD. Different laser powers were tested to optimize the deposition process. The microstructure and coating thickness were examined using scanning electron microscopy (SEM) and energy spectrum analysis (EDS).

## 2 Experimental Methods

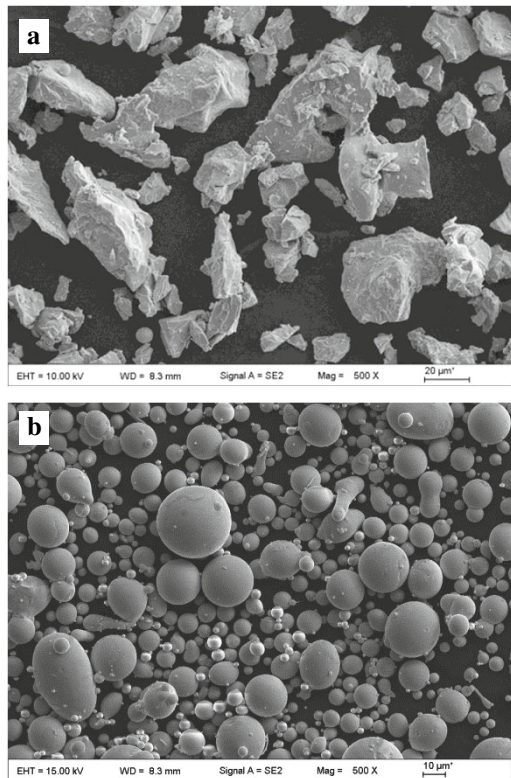
### 2.1 Composite Powder and Substrate Preparation

Commercially available pure Ni (99 wt%) powder and Ni60 alloy powder were sieved to obtain the powders having the size less than 50  $\mu\text{m}$ . Ni60 powder was prepared by gas atomization and its chemical composition is given in Table 1. The particle shape of pure Ni is irregular while that of Ni60 alloy powder is spherical, as shown in Fig. 1. The particle size distribution indicates that the powder's mean diameter is 35  $\mu\text{m}$  and 19  $\mu\text{m}$ , respectively. About 90% of Ni60 particles have a size below 26  $\mu\text{m}$ . The Ni60–30 wt%Ni composite powder was mechanically milled at a rate of 150 rpm for 2 h in alcohol environment. Stainless steel balls with 8 and 12 mm

**Table 1** Chemical composition of Ni60 alloy

Element	C	Cr	Si	B	Fe	Ni
wt. %	0.5	18	4.5	3.0	15.0	Bal

**Fig. 1** SEM morphology: **a** Ni powder (particles), **b** Ni60 powder (particles)



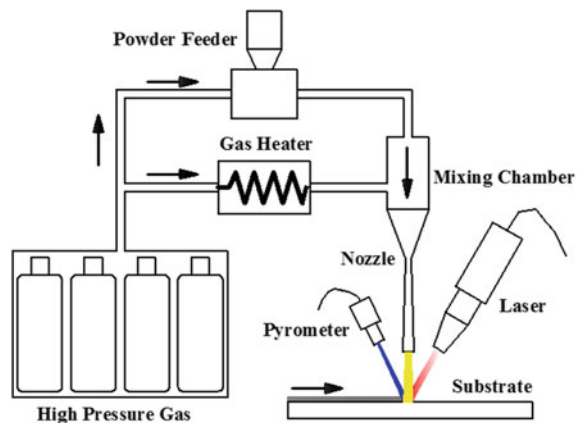


diameter were used as the grinding media, the ball-to-powder weight ratio was 35:1. The substrate is a  $100 \times 60 \times 10$  mm flat 45# medium carbon steel, whose surface was prepared by blasting using 24 Mesh  $\text{Al}_2\text{O}_3$ , then cleaning the surface of substrate by means of ultrasonic in alcohol medium.

## 2.2 Coating Preparation

The SLD system (Centre for Industrial Photonics, Institute for Manufacturing, University of Cambridge, UK, by Dr. W. O'Neill) used to prepare the Ni60-Ni composite coatings is shown schematically in Fig. 2. A high pressure (10–35 bar range) nitrogen gas supply was directly delivered to a converging nozzle. The feed-stock stream and carrier gas were mixed and passed through the nozzle where they were accelerated to supersonic speed. The high-velocity flying particles impacted a region of the substrate where a maximum power of 4 kW diode laser of 960–980 nm was synchronously irradiated. In the deposition process spraying zone and laser spot must match with each other. The temperature of deposited zone was monitored by a pyrometer whose temperature control precision was about  $\pm 2$ . Softened substrate and powder particles by means of laser allowed the formation of Ni60–30 wt%Ni composite coating at a much reduced impact velocity, which was about half of that used in cold spray. In this experiment, the nitrogen was used to accelerate the composite powder. The laser spot diameter was 5 mm, single track Ni60–30 wt%Ni composite coatings were deposited. The spraying distance was 30 mm; the traverse rate was 30 mm/s, the nitrogen temperature was 550 °C, the  $\text{N}_2$  pressure was 30 bar, the laser power varied from 2.5 to 2.8 kW with each increment of 100 W. The deposition temperatures of coatings which corresponded to the laser powers were measured by a pyrometer; the readings were 980 °C, 1000 °C, 1020 °C, 1040 °C, respectively.

**Fig. 2** Schematic showing of the SLD system



The coating specimens were sectioned and polished for microstructural analysis using SEM/EDS. The thickness of the coating layers was measured with the image analysis software of SEM. The effects of laser power on the characteristics of the coatings were studied.

### 3 Results and Discussion

The hardness of plain Ni60 coatings is about 60 HRC. It has been found that these coatings often contain cracks when produced by thermal spray or laser cladding. The SLD technology allows retaining powder particles' essential ingredients, and adding Ni particles to Ni60 can release thermal stresses to restrain cracking in the coatings. In addition, it was also observed that Ni particles were prone to concentrate at the coating/substrate interface, which improved the coating adhesion.

#### 3.1 Coating Thickness

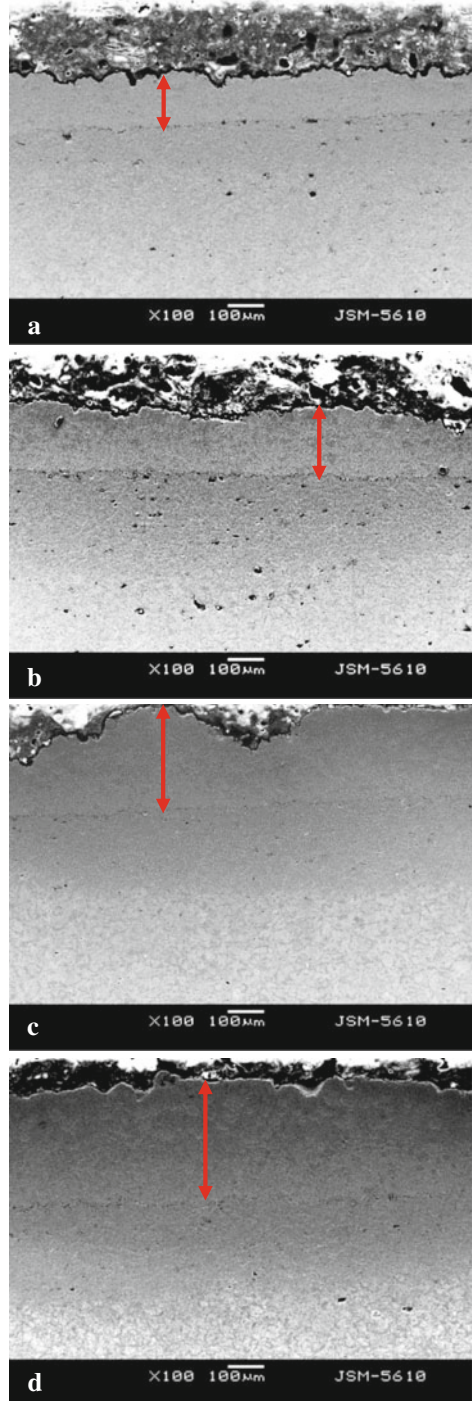
The coating thickness of the SLD-fabricated Ni60–30 wt%Ni composite coatings produced by various laser powers was evaluated with respect to peak thickness of the coatings, as shown in Fig. 3. It is observed that large tracks exist in the coatings produced with the powers of 2.5 kW and 2.8 kW, and the peak thickness of the coatings increases with enhancing laser power. Choosing three different position of single track to measure the peak thickness, the average peak values of the coatings produced with the four laser powers were  $130 \pm 6 \mu\text{m}$ ,  $192 \pm 8 \mu\text{m}$ ,  $285 \pm 11 \mu\text{m}$  and  $450 \pm 11 \mu\text{m}$ , respectively. This indicates that the deposition temperature of SLD can improve the thickness and density of the coatings effectively. With the laser power of 2.8 kW, the thickness of the coating is the most uniform.

#### 3.2 Microstructure and Cracking

##### 3.2.1 Microstructures of Ni60–30 wt%Ni Composite Coatings

The microstructures of the Ni60–30 wt%Ni composite coating specimens produced with the four laser powers were analyzed using SEM; the obtained images are presented in Fig. 4. It is observed that Ni particles are embedded uniformly in the Ni60 matrix for all the coating specimens, which implies that these particles have deformed significantly and enhanced the density of the coatings. In addition, it is found that the content and intensity of Ni particles are higher in the coating deposited at a laser powder of 2.8 kW than that of coating deposited by 2.5 kW.

**Fig. 3** SEM images of cross section of SLD Ni60–30 wt%Ni composite coatings showing peak coating thickness: **a** 2.5 kW, **b** 2.6 kW, **c** 2.7 kW, **d** 2.8 kW



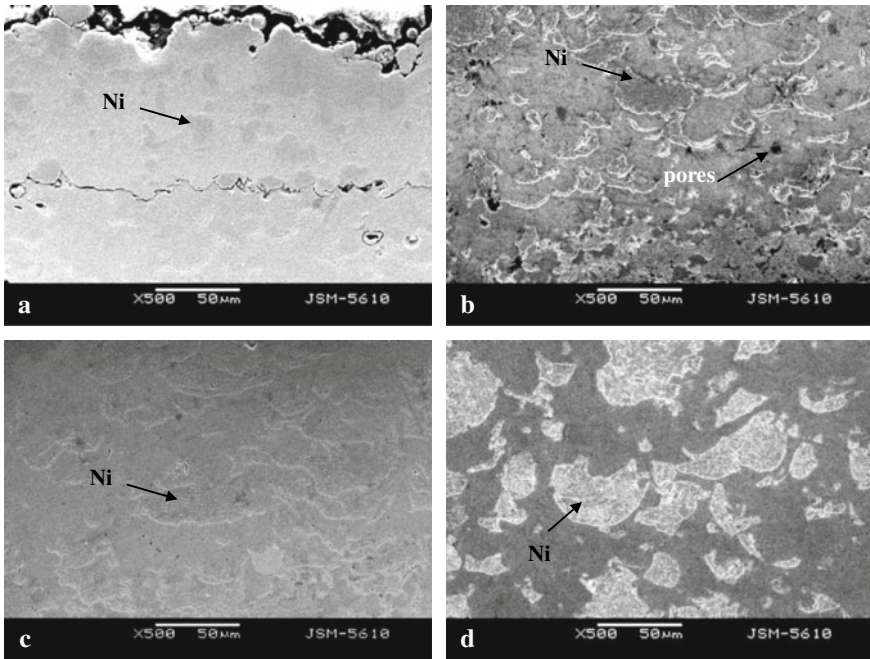
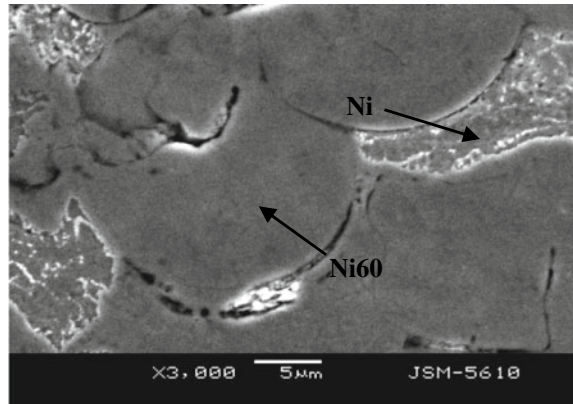


**Fig. 4** Microstructures of the Ni60–30 wt%Ni composite coatings: **a** 2.5 kW, **b** 2.6 kW, **c** 2.7 kW, **d** 2.8 kW

### 3.2.2 Cracking of Ni60–30 wt%Ni Composite Coatings

From Fig. 4 cracks are found in the coatings produced with the lower laser powers (lower deposition temperatures), but no obvious cracking is observed in the coatings deposited at the higher temperatures. This demonstrates that enhancing deposition temperature or laser power of SLD did not cause accumulation of stress, whereas it increased the coating thickness and intensity of the coating. However, Ni60 particles contained metallic compounds such as FeB,  $\text{Cr}_3\text{C}_7$ ,  $\text{Ni}_3\text{Si}$  which are easy to concentrate at grain boundaries. This usually causes cracking of coatings when produced with thermal spray or laser cladding. The higher the deposition temperature, the more the metallic compounds precipitated, thus the higher the thermal stress accumulated, leading to cracking of the coating. In the SLD process, the heat-affected zone can be reduced thus minimizing thermal stress and cracking. Moreover, pure Ni is relatively soft and Ni particles present in the coatings serve as tiny sponge particles which can release the stress of the coatings and effectively suppress cracks. As shown in Fig. 5, Ni particles deformed larger than Ni60 particles, and they are squeezed between Ni60 particles.

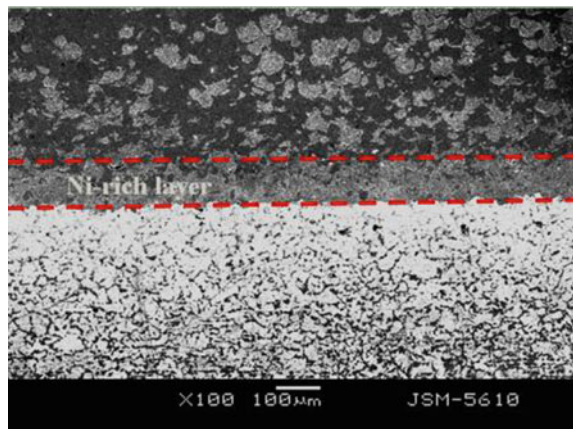
**Fig. 5** SEM image showing deformed Ni particles in the composite coating produced with 2.8 kW laser power



### 3.3 Ni-Rich Layer in the Ni60–30 wt%Ni Coatings

Observation of the fabricated Ni60–30 wt%Ni composite coating with 2.8 kW laser power discovered that Ni particles in the composite powders formed a Ni-rich layer at the coating/substrate interface. The presence of this layer in the coatings is like a sandwich, as shown in Fig. 6. The softer Ni-rich layer plays a role of transition layer for effective bonding between the hard coating and substrate. The element mapping EDS analysis confirmed the presence of the Ni-rich layer in the coatings, as shown in Fig. 7, higher Ni element concentration was found in the interfacial bond zone. Figure 7 shows the element distributions of Ni, Cr, Fe and Si in the Ni60–30 wt%Ni coating.

**Fig. 6** Ni-rich layer between coating and substrate in the Ni60–30 wt%Ni composite coating



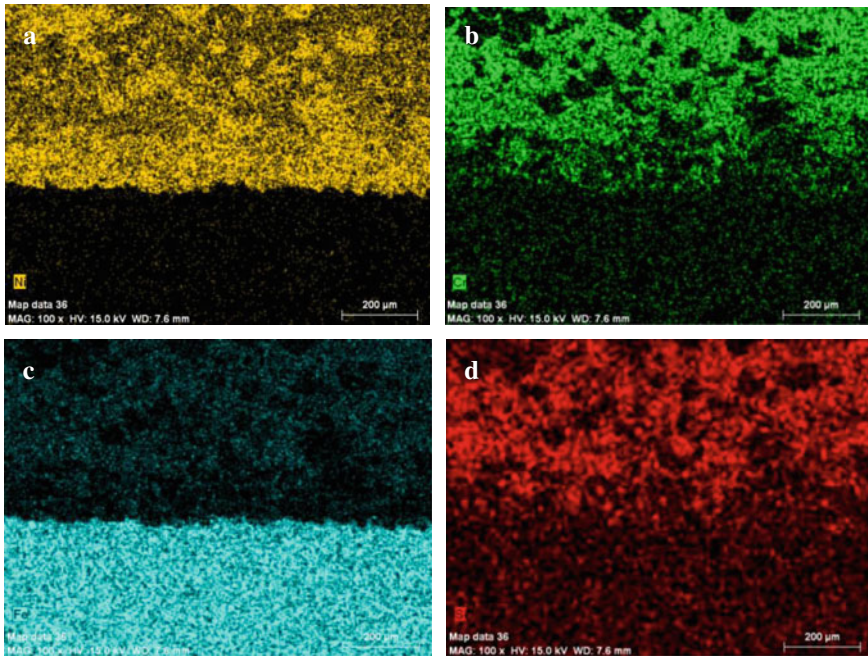


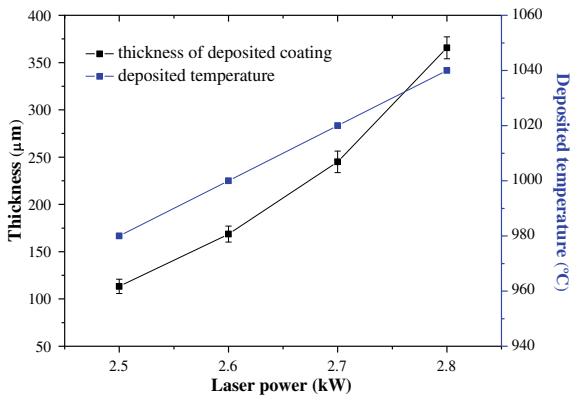
**Fig. 7** SEM/EDS mapping images of various elements in the Ni60–30 wt%Ni composite coating showing a Ni-rich layer interfacial zone: **a** Ni, **b** Cr, **c** Fe, **d** Si

### 3.4 Discussion

An analysis of the laser beam interaction with the Ni60–30 wt%Ni composite powder stream accelerated by post-heating high pressure  $N_2$  suggests that high-energy intensity of diode laser beam can quickly irradiate molecules of the gas and composite powder particles flying at a high speed. As a result, kinetic energies of the Ni60–30 wt%Ni powder particles and molecules of the gas were promoted via the convection process with the attendant effect of an increase in deposit temperature [23]. An increment in the kinetic energy of the atoms of the Ni60–30 wt%Ni particles via the conduction process translates loosening of their atomic bond energy, which then results in particle softening as their yield strengths are reduced [22]. Moreover, the laser irradiation also has a softening effect on the deposition zone and the surface of the substrate via the heat conduction process [21, 22]. All of these can enhance the deposition process of the powder particles with increased speed and deformation, which cannot be achieved by cold spray. Furthermore, appropriate deposition temperature for lower yield strength powder particles below their radiating temperature of laser beam can cause an increment in coating thickness as shown in Figs. 3 and 8.

Figure 8 presents the variations of deposition temperature and coating thickness of the composite coatings with laser power. It is known that Ni60 is of the type of self-fluxing alloy, adding Si, B, Cr elements in Ni-based alloy makes its melting

**Fig. 8** Variations of the coating thickness and deposition temperature of the Ni60–30 wt%Ni composite coating with applied laser power



point down to 1050–1080 °C [1]. Moreover, the melting point of pure Ni is higher than that of Ni60 alloy so that Ni60 particles were easier softened than Ni particles by the action of laser. The shapes of pure Ni and Ni60 alloy particles are irregular and spherical, respectively. According to the theory of gas dynamics, the gas drag coefficient of the non-spherical particles is greater than that of spherical particles. The gas force is proportional to the gas drag coefficient, as expressed by the equation below:

$$D = \frac{1}{2} \rho v_{rel}^2 A_p C_D \quad (1)$$

where  $D$  and  $\rho$  are the drag force and the density of accelerating gas, respectively;  $v_{rel}$  and  $A_p$  are the relative velocity of the gas to particle and the superficial area of particle, respectively. The studies by other researchers demonstrated that non-spherical particle could attain greater impacting velocity than spherical particle with the same process parameters, because non-spherical particle possesses larger shape form drag [24]. Therefore, it is found that Ni particles are distributed uniformly with large deformation in the Ni60 matrix, as seen in Fig. 4. These results indicated that Ni particles and Ni60 particles have different deposition cases, Ni particles uniformly distribute in composite coatings by completely deforming solid state, presented in Fig. 4.

Since the melting point of pure Ni is higher than that of Ni60 alloy, the Ni60 particles could be softened more severe than Ni particles by the laser heat. Owing to larger shape form drag of non-spherical Ni particles, the non-spherical Ni particles can attain greater impacting velocity than spherical Ni60 particles with the same process parameters. This made the Ni particles easier to deposit on the substrate than Ni60 particles. As well known, the process of spraying particles on the surface of substrate will cause plastic deformation of both materials due to particle impact and the interaction time is very short; so that almost no plastic deformation energy is lost. This provides the particles with adiabatic shear instability to deposit on the substrate. Li et al. suggested that the less the elastic limit of metallic particle, the

stronger the bonding between the coating and substrate is [25], as explained by the equation below:

$$\varepsilon_e = \frac{\varepsilon_s}{E} \quad (2)$$

where  $\varepsilon_e$ ,  $\sigma_s$  are elastic limit, yield strength and elasticity modulus, respectively. The elastic limit and hardness of pure Ni are less than those of Ni60 alloy. Therefore, Ni particles can be easier deposited on the substrate than Ni60 particles, which resulted in the Ni-rich layer at the interface of the coatings.

## 4 Conclusions

The dense, crack-free and well-bonded Ni60–30 wt%Ni composite coatings were deposited successfully on 45# medium carbon steel with a wide range of laser power or deposition temperature. The thickness of the Ni60–30 wt%Ni composite coatings increased with enhanced laser power. Microstructural examinations reveal that in the SLD process Ni particles with plastic deformation were uniformly embedded in the Ni60 matrix. The plastic deformation of Ni particles benefited releasing residual stress developed in the composite coatings during the SLD process, thus achieving crack-free and dense coatings. A Ni-rich layer formed at the interface between the coating and substrate. This softer Ni-rich layer plays a role of transition layer for the strong adhesion between the hard coating and substrate. The research results have shown that SLD is capable of depositing hard composite coating in good quality.

**Acknowledgements** The authors would like to appreciate financial supports from the National Natural Science Foundation of China (51475429), the Youth Foundation Projects of Natural Science Foundation of Zhejiang Province (LQ13E050012), and the Commonweal Technology Research Industrial Project of Zhejiang Province (2013C31012).

## References

1. Zhang XC, Xu BS, Tu ST, Xuan FZ, Wang HD, Wu YX (2008) Effect of spraying power on the microstructure and mechanical properties of supersonic plasma-sprayed Ni-based alloy coatings. *Appl Surf Sci* 254:6318–6326
2. Hong S, Wu YP, Li GY, Wang B, Gao WW, Ying GB (2013) Microstructural characteristics of high-velocity oxygen-fuel (HVOF) sprayed nickel-based alloy coating. *J Alloy Compd* 581:398–403
3. Gil L, Staia MH (2002) Influence of HVOF parameters on the corrosion resistance of NiWCrBSi coatings. *Thin Solid Films* 420:446–454
4. Kim HJ, Hwang SY, Lee CH, Juvanon P (2003) Assessment of wear performance of flame sprayed and fused Ni-based coatings. *Surf Coat Technol* 172:262–269
5. Sexton L, Lavin S, Byrne G, Kennedy A (2002) Laser cladding of aerospace materials. *J Mater Process Technol* 122:63–68



6. Vilar R (1999) Laser cladding. *J Laser Appl* 11:64–79
7. Boiciuc S, Levcovici DT (2009) Properties and application of laser cladding with Ni–Cr–B–Fe–Al ALLOY. *Metal Int* 14:49–53
8. Hemmati I, Ocelik V, De Hosson JTM (2013) Advances in laser surface engineering: tackling the cracking problem in laser-deposited Ni–Cr–B–Si–C Alloys. *Jom* 65:741–748
9. Hemmati I, Rao JC, Ocelik V, De Hosson JTM (2013) Electron Microscopy Characterization of Ni–Cr–B–Si–C Laser Deposited Coatings. *Microsc microanal* 19:120–131
10. Boiciuc S, Levcovici S, Levcovici DT, Gheorghies C (2008) Characterisation of hard coatings obtained by laser cladding process. *Metal Int.* 13:32–39
11. Alkhimov AP, Kosarev VF, Papyrin AN (1990) A method of cold gas-dynamic spraying. *Dokl Akad Nauk SSSR* 315:1062–1065
12. Kosarev VF, Klinkov SV, Alkhimov AP, Papyrin AN (2003) On some aspects of gas dynamics of the cold spray process. *J Therm Spray Technol* 12:265–281
13. Assadi H, Gartner F, Stoltenhoff T, Kreye H (2003) Bonding mechanism in cold gas spraying. *Acta Mater* 51:4379–4394
14. Stoltenhoff T, Kreye H, Richter HJ (2002) An analysis of the cold spray process and its coatings. *J Therm Spray Technol* 11:542–550
15. Ajdesztajn L, Jodoin B, Richer P, Sansoucy E, Lavernia EJ (2006) Cold gas dynamic spraying of iron-base amorphous alloy. *J Therm Spray Technol* 15:495–500
16. Li WY, Li CJ, Liao HL (2006) Effect of annealing treatment on the microstructure and properties of cold-sprayed Cu coating. *J Therm Spray Technol* 15:206–211
17. Li WY, Liao HL, Li CJ, Bang HS, Coddet C (2007) Numerical simulation of deformation behavior of Al particles impacting on Al substrate and effect of surface oxide films on interfacial bonding in cold spraying. *Appl Surf Sci* 253:5084–5091
18. Li WY, Zhang C, Guo XP, Xu JL, Li CJ, Liao HL et al (2007) Ti and Ti–6Al–4V coatings by cold spraying and microstructure modification by heat treatment. *Adv Eng Mater* 9:418–423
19. Ajdesztajn L, Jodoin B, Schoenung JM (2006) Synthesis and mechanical properties of nanocrystalline Ni coatings produced by cold gas dynamic spraying. *Surf Coat Technol* 201:1166–1172
20. Cinca N, Lopez E, Dosta S, Guilemany JM (2013) Study of stellite-6 deposition by cold gas spraying. *Surf Coat Technol* 232:891–898
21. Lupoi R, Sparkes M, Cockburn A, O'Neill W (2011) High speed titanium coatings by supersonic laser deposition. *Mater Lett* 65:3205–3207
22. Bray M, Cockburn A, O'Neill W (2009) The Laser-assisted Cold Spray process and deposit characterisation. *Surf Coat Technol* 203:2851–2857
23. Olakanmi EO, Tlotleng M, Meacock C, Pityana S, Doyoyo M (2013) Deposition mechanism and microstructure of laser-assisted cold-sprayed (LACS) Al–12 wt.%Si coatings: effects of laser power. *Jom* 65:776–783
24. Jodoin B, Ajdesztajn L, Sansoucy E, Zuniga A, Richer P, Lavernia EJ (2006) Effect of particle size, morphology, and hardness on cold gas dynamic sprayed aluminum alloy coatings. *Surf Coat Technol* 201:3422–3429
25. Li G (2007) Study and analysis on the effect of different incidence angles and materials property for intruding process in cold spraying. Dalian University of Technology

# 2D and 3D Flexible Laser System for Precision Cutting, Welding and Drilling Applications



M. Naeem and A. Montello

**Abstract** Laserdyne systems based in Champlin (Minneapolis, Minnesota, UAS) have been providing 2D and 3D systems over 25 years for laser material processing (cutting, drilling and welding) applications for a range of market sectors i.e. aerospace, medical, automotive etc. All Laserdyne systems are designed for precision laser processing small to large parts with different laser sources i.e. with CO<sub>2</sub>, Nd:YAG and fiber lasers. To date CO<sub>2</sub> (gas lasers) are being used mainly for cutting and welding applications whereas high peak power pulsed Nd:YAG lasers (solid state lasers) are used for drilling applications. The last decade has seen the rise of high power diode pumped fiber lasers. These new continuous wave (CW) and Quasi continuous wave (QCW) lasers have been demonstrated to be a serious alternative to Nd:YAG solid state lasers (SSL) and CO<sub>2</sub> gas lasers for different materials processing applications in a range of manufacturing industries. This paper describes cutting, welding and drilling results achieved in a range of materials used in aerospace applications. The processing trials were carried out with a Laserdyne System 430 fitted with a high power QCW fiber lasers.

**Keywords** Cutting · Drilling · Welding · QCW fiber laser · Laser system · Peak power · Average power · Wire feed

## 1 Introduction

Laser based manufacturing methods in the aerospace industry are extensively used to manufacture new parts or repair the parts which are already in service. Laser manufacturing techniques such as laser cutting and welding are relative new, whereas laser drilling is mature technique which has been used since early eighty. The three main laser processing techniques currently being used in the aerospace industry are highlighted in the following paragraphs.

---

M. Naeem (✉) · A. Montello  
Prima Power Laserdyne, 8600 109th Avenue North, Champlin, MN 55316, USA  
e-mail: [mohammed.naeem@primapower.com](mailto:mohammed.naeem@primapower.com)

Laser drilling holes are drilled into gas turbines; nozzle guide vanes and combustion rings primarily for cooling, (Fig. 1). In the modern jet engine the temperature of the gases can be as high as 2000 °C [1]. This temperature is higher than the melting point of the nickel alloy used in the combustion chamber and turbine blades. The way that the jet engines components are protected against these extreme temperatures is to use boundary layer cooling. The number of holes per component may vary from 25 to 40,000 (Table 1). As the cooling air passes over the surface it forms a cooling film, which protects the surface of the component from the high temperature combustion gases.

Cooling holes can be produced either by EDM (electrical discharge machining) or by laser. EDM or spark machining consists of an electrode, which is held above the workpiece to produce a small gap between the two surfaces. An increasing voltage is applied between the electrode and the workpiece until the electric field becomes so intense that there is an electrical breakdown at the tip of the electrode. A spark will discharge across the gap. Due to the very small cross sectional area very high current densities can result, around 1000 A mm<sup>-2</sup>. Typical temperatures in the region of the breakdown between electrode and workpiece, in the region of 5000–10,000 °C, are being achieved between electrode and workpiece. The EDM process uses discrete discharges to drill the hole. If a prolonged discharge is used then the ionisation channel will broaden resulting in reduced current density and damage to the tool and workpiece. This erosion can be intensified if a suitable liquid dielectric is used. It

**Fig. 1** Laser drilled component



**Table 1** Typical hole dimensions [1]

Component	Dia. (mm)	Wall thickness (mm)	Angle (°)	No. of holes
Blade	0.3–0.5	1.0–3.0	15	25–200
Vane	0.3–1.0	1.0–3.0	15	25–200
Afterburner	0.4	2.0–2.5	90	40k
Baseplate	0.5–0.7	1.0	30–90	10k
Seal ring	0.95–1.05	1.5	50	180
Cooling ring	0.78–0.84	4.0	79	4.2k
Cooling ring	5.0	4.0	90	280

can also act as a coolant and a flushing medium, helping to remove EDM debris. These fluids are based on paraffin, kerosene and other petroleum distillations. More recently however deionised water has been used. When used at high pressure the drilling technique is referred to as high speed EDM. The electrodes are made from a variety of materials. Graphite, copper, and copper tungsten are used, but brass is used extensively for hole drilling. For deep hole drilling tubular brass is used.

Although EDM is capable of producing good quality holes it is substantially slower than the laser and other disadvantages of this technique are:

- EDM is not suited to the production of holes at high or variable incidence angles where multi-wire heads cannot be used.
- EDM also requires really complex consumables tooling and electrolyte fluids, both of which contribute adversely to cost of hole production.
- To increase temperature capability of the engine blades and vanes, a thin coat of a heat-insulating zirconia ceramics is applied on the surface of the blades as a thermal barrier coating (Fig. 2). EDM is not suitable for drilling through ceramic or ceramic-coated materials.

When drilling TBC coated materials with EDM, the coating is normally ablated first with a Q-switched pulsed Nd:YAG laser (short pulses and high peak powers) followed by drilling with EDM. An example of this dual process is highlighted in Fig. 3 [2].

Laser cutting process offers a number of advantages including attractive processing speed, high productivity, low running cost, and ability to manufacture parts with complex shapes, excellent cut quality, non-contact operation, and ease of automation. This has led greater use of laser cutting in the aerospace industry. The laser cutting of 2D and 3D sheet metal is state-of-the-art and often outsourced to

**Fig. 2** Thermal barrier coated blade



**Fig. 3** Ablation + EDM drilling of coated material; 3 mm thick nickel based alloy with 0.65 mm thick coating; ablation cycle time 7 s; EDM cycle time 28 s; 45° from the surface

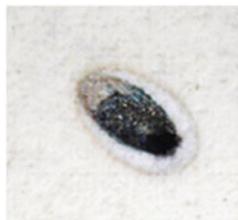


**Fig. 4** Laser cut shroud for the manufacture of compressor vane segments in Inconel 718 alloy



subcontractors. Laser cutting is fusion process and employs nitrogen assist gas for nickel based alloys i.e. Inconel 718 and argon assist gas for titanium based alloys i.e. Ti-6Al-4V. Laser cutting is a multiparameter process and with optimization of the parameters i.e. laser power, beam quality, spot size, gas pressure, focus position of the laser beam with respect to the workpiece, it is possible to produce crack and dross free cuts in a range of nickel and titanium based alloys. Figure 4 shows a laser cut shroud in IN718 material.

The role of **laser welding** in the aerospace industry has increased in importance over the past decade. Historically majority of the welding has been carried with either electron beam (EB) or tungsten inert gas (TIG); however this is slowly changing due to availability of high powered lasers. Laser welding can offer a number of advantages over both EB and TIG i.e.

- Laser welding involves few manufacturing stages, edge preparation, and joint fixturing being the most time-consuming auxiliary operations.
- The high beam power density creates a narrow, deeply penetrating weld pool, allowing through thickness welds to be made rapidly and accurately in a single pass without the presence of vacuum
- The low heat input creates a narrow heat affected zone (HAZ) with limited distortion and residual stresses, which reduces the need for reworking.
- The process is easily automated for high volume production.
- Filler materials especially with aluminum and its alloys can be used to achieve desired weld metallurgy and properties.
- Filler material is also used to compensate for the poor fit-up and mismatch for butt joint welding. Filler may also be used to improve the weld geometry.

Titanium, aluminum, and nickel alloys are routinely used for various applications in the aerospace industry. Titanium alloys, such as Ti6Al4V (6% Al, 4% V), Ti6242 (6% Al, 2% Sn, 4% Zr, 2% Mo) and TiCu2 (2%Cu) are widely used in aeronautic and aerospace structures e.g. blades and casings of compressor stages in turbojets. Nickel based super alloys (Inconel 718, Incoloy 909 and Single crystal 2000) are used in the jet engines where the temperatures are very high (1400 °C). Aluminium and its alloys (2000 series, 6000 series etc.) are most suited for structural members, especially fuselage and wing structures in airplanes. In airframe sections, attaching stringers that run along the length gives additional stiffness to the complete section.

## Laser sources

Several types of lasers are currently being used for materials processing (cutting, welding, and drilling) in the aerospace industry though the most common lasers are CO<sub>2</sub> (gas lasers) for cutting and welding applications and high peak power Nd:YAG lasers (solid state lasers) for drilling applications. The last decade has seen the rise of high power diode pumped fiber lasers. These new continuous wave (CW) and Quasi continuous wave (QCW) lasers have been demonstrated to be a serious alternative to Nd:YAG solid state lasers (SSL) and CO<sub>2</sub> gas lasers for different materials processing applications in the aerospace industry.

The fiber laser offers a number of key advantages over other laser sources which are currently being used in the aerospace industry i.e. high beam quality, stable pulsed and continuous power output, small foot print, etc. The high beam quality of the fiber laser enables the beam to be focused to a small spot with a correspondingly high energy density. This enables very fast and efficient processing, yielding welds and drilled holes with a high aspect ratio.

The fiber lasers also offer the potential to reduced total cost of ownership. With its 1 μm wavelength, the fiber laser has an absorption rate in metals at room temperature that is seven times higher than for the 10.6 μm wavelength of a CO<sub>2</sub> laser. It is well known that the use of laser processing requires relatively high capital investment costs. However, it is important to note that the operating costs of a laser system will also play an important role in determining the production costs.

The reduced cost of ownership of the fiber lasers is due to the high efficiency of the pump source and of extraction from the gain medium that leads to wall plug efficiency for the laser, typically around 25–30%, [3] compared to less than 12% for a CO<sub>2</sub> laser and a few percent for a flashlamp pumped Nd:YAG laser. This leads to reduced electrical supply requirements and lower electrical energy consumption which is the major cost factor in any laser high power laser system. The higher efficiency also contributes to a more compact laser head. Compared to other solid state lasers fewer mechanical components are needed in the laser construction. This leads to significantly lower cost base than equivalent power SSL. Indications are that as the pump laser diode prices continue to decrease with increasing manufacturing volumes fiber laser prices will continue to decrease.

The high power single or multi-mode fiber lasers are ideal for cutting and welding applications, however not suited for laser drilling which is the biggest application in the aerospace industry. The introduction of QCW fiber laser with its high peak power up to 20 kW and CW operation has changed all this. Now it is possible to use single laser source for drilling, cutting and welding. This paper highlights cutting, welding and drilling data achieved with IPG 20 kW QCW fiber fitted to Laserdyne 6axis laser machining system.

## 2 Experimental Details

The processing trials were carried out on Laserdyne 430 5–6 axis machining center, Fig. 5. The new laser system is designed for cutting, welding and drilling of 2D and 3D component parts requiring exact precision suitable for a range of industrial market sector including aerospace. The system 430 is fitted with third generation BeamDirector®, Fig. 6, capable of drilling at angles as low as  $10^\circ$  from the surface. Other features include Automatic Focus Control™ for capacitive part sensing, patented Optical Focus Control (OFC) for sensing of thermal barrier coated surfaces, ShapeSoft™ software for programming shaped holes, BreakThrough Detection™ for drilling clean, consistent holes with the minimum number of pulses, and mapping.

The system 430 was fitted with an IPG 20 kW QCW laser (Fig. 7). The beam from the laser was transmitted in a 100  $\mu\text{m}$  diameter fiber optic, which terminated in 140 mm collimated output housing.

Laser and processing parameters used for drilling, cutting and welding are highlighted in Table 2. Cutting, drilling and welding nozzles used during these trials are highlighted in Fig. 8.

**Fig. 5** Laserdyne 430 system, Turnkey flexible laser system for high precision cutting, welding and drilling applications

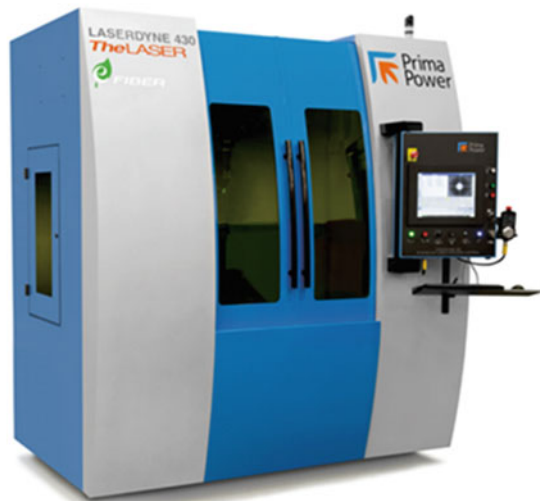


**Fig. 6** Third generation BeamDirector®—most compact on the market for drilling at angles as low as 10° from the surface



**Fig. 7** IPG 20 kW QCW fiber laser; 20 kW peak power; 2 kW average power; 200 J pulse energy

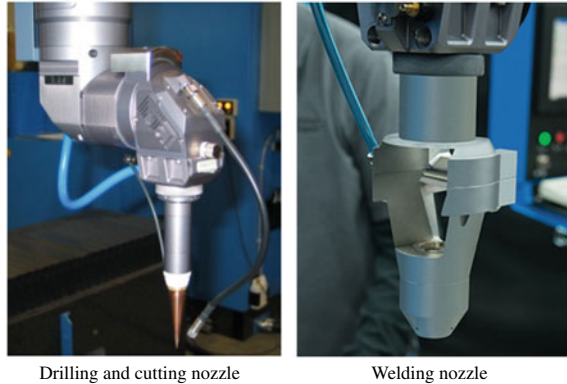


**Table 2** Parameters for drilling, cutting and welding

Parameters	Drilling	Cutting	Welding
Spot size (μm)	140	140	140–571
Processing gas	Oxygen	Nitrogen	Nitrogen and argon
Laser power	Pulsed	Pulsed	CW



**Fig. 8** Processing heads used for drilling, cutting and welding



### 3 Results and Discussion

#### 3.1 Drilling

Primary concern to the component designer is achieving adequate airflow through the holes so that the appropriate cooling is provided. Airflow is governed principally by the size and shape of the hole and hence the need for tight control of size, roundness and taper. There are other factors also to be considered; holes are often very closely positioned to one another on a component and any deviation in size may adversely encroach on other holes or even weaken the component locally. Excessive bell-mouthing or barreling is therefore undesirable in addition to recast layer and heat-affected zone.

The issue of the drilled hole quality is very important but is a subjective one. The qualities of a hole produced by laser drilling are judged on a number of different characteristics. The geometric factors are hole roundness, hole taper and variation in hole entrance diameter. The metallurgical factors are oxidation and recast layer. The recast layer, melted material that is not ejected from the hole by vapour pressure generated by the laser pulse, coats the wall of the hole leaving a thin layer of solidified metal. This layer can generate micro-cracks, which can propagate into the parent material. Drilling results show that it was possible to produce very good quality holes in a range of aerospace alloys. This high beam quality laser produced holes with minimum taper (<5%) and recast layer very similar to EDM drilled hole quality. The cross sections of some of the holes drilled at various angles to surface are highlighted in Fig. 9. The hole sizes were varied by adjusting the laser and processing parameters i.e. peak power, pulse energy, pulse width, trepan speed etc.

Combination of Laserdyne system with its very accurate motion control and high beam quality ( $M^2 < 10$ ), and top hat beam profile of the QCW fiber laser, it was possible to drill consistent holes in terms of roundness and metallurgy in a range of thicknesses down to 10 degrees to the surface. Table 3 shows typical average recast layer and taper of the holes drilled at different angles.

**Fig. 9** 2.54 thick nickel based super alloy, trepanned holes, 0.65 mm dia., Oxygen assist; peak power < 6 kW average recast layer < 50 μm

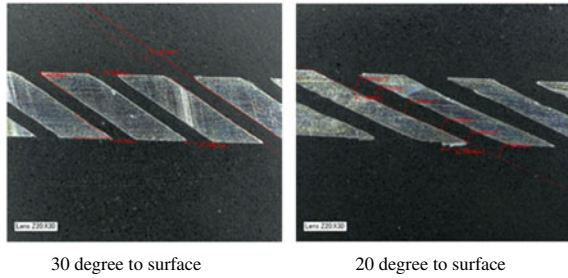


**Table 3** Average recast layer & taper (Trepanned holes; nickel based super alloy; Oxygen assist gas)

Material thickness (mm)	Drilling angle (°)	Hole dia (mm)	Average recast layer (μm)	Taper (%)
3.23	90	0.65	36	1.8
2.54	60	0.65	40	1.5
2.54	30	0.65	30	1.5
2.54	20	0.65	45	2

Drilling tests were also performed on Thermal barrier coatings (TBC) materials. These coatings are being widely applied in many types of engines and in aircraft’s gas turbines. To increase temperature capability of the engine blades and vanes, a thin coat of a heat-insulating zirconia ceramics is applied on the surface of the blades as a TBC. The cooling of the components causes a pronounced reduction of the metal temperature, which leads to a prolongation of the mechanical component’s lifetime. Alternatively, the use of TBC allows raising the process temperature, obtaining thus an increased efficiency. TBC usually consist of two layers (duplex structure). The first layer, a metallic one, is the so-called bond coat, whose function is, on the one side to protect the basic material against oxidation and corrosion and, on the other side, to provide with a good adhesion to the thermal insulating ceramic layer. Such a ceramic coating is mostly made of yttria partially stabilised zirconia (YSZ), since this material has turned out particularly suitable during the last decades. At present, there are two principle methods to apply thermal barrier coatings, one is plasma spraying and the other is electron beam physical vapour deposition (EB-PVD). These methods have been studied excessively to avoid mechanical and adherence problems between coatings and substrate [4–6].

Laser and processing parameters were developed to drill through the TBC and then drill through the metal. With correct set of parameters it was possible to drill holes without any laser drilling induced damage at the bond coat/substrate interface. No cracking or delamination of the TBC was detected, as shown in Fig. 10. Advanced Laserdyne special control system also allows to produce holes with minimum recast layer, as heighted in Fig. 11. With standard alone pulse laser parameters, the recast

**Fig. 10** TBC coated, 2.54 mm thick coated nickel based super alloy; trepanned holes, 0.56 mm dia., peak power < 5 kW, average recast layer 30  $\mu\text{m}$ , 0.50 mm thick coating; Oxygen assist;

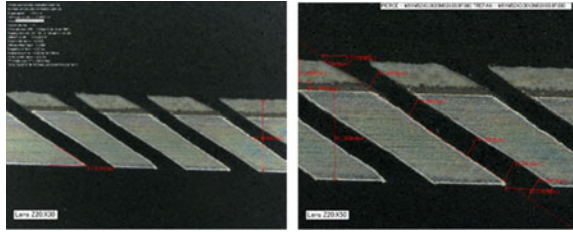
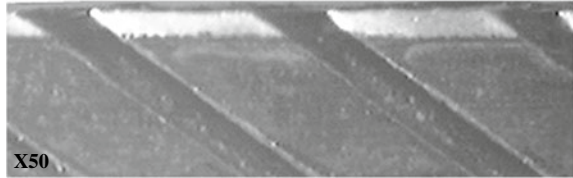
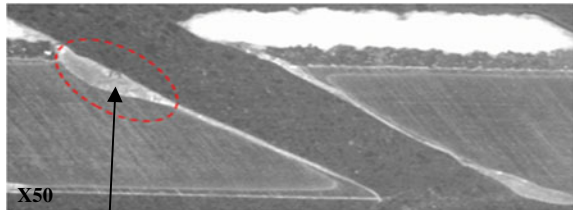


**Fig. 11** TBC turbine combustor liners drilled with advanced Laserdyne system control (a) and with conventional pulsed laser parameters (b), Oxygen assist; peak power < 5 kW



(a) Percussion drilled hole with Laserdyne system special control laser parameters to reduce recast layer in TBC materials



Recast layer varies from 100 $\mu\text{m}$  to 254 $\mu\text{m}$

(b) Percussion drilled with conventional pulse laser parameters

layer was excessively high (100–250  $\mu\text{m}$ ) and this increases with the hole depth and at acute drilling angles.

### 3.2 Laser Cutting

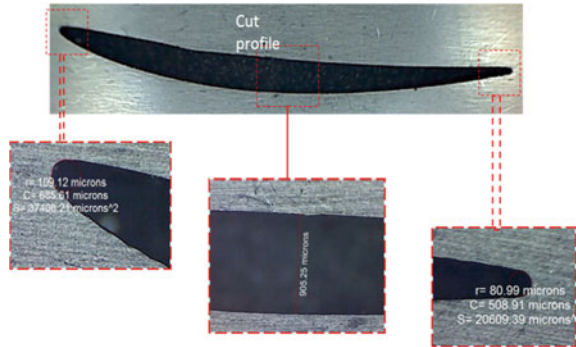
With the same set-up as for the drilling tests, cutting tests were performed on a range of nickel based alloys. The main requirement when cutting these alloys is to have oxide free cut edges without any dross or microcracking. With oxygen assist gas the cut is speed is fast compare to inert gas cutting but it leaves oxide layer at the surface so all the cutting tests were carried with oxygen free nitrogen assist gas.

Laser cutting is not all about having a very high beam quality/high average power laser, it is also very important to understand the detailed melt flow conditions in a narrow kerf width produced by small spot diameters in order to provide an opportunity to optimise the gas-jet/melt interaction of high brightness fiber laser. The laser cutting is entirely gas assisted (oxygen or inert), variables related to the assist gas have a

**Fig. 12** Aero-land based turbine engine component cutting (stator rings), no dross/spatter; nitrogen assist gas; 15 bar; peak power < 10 kW; cut speed < 1.5 m/min



Small clean pierce without any spatter



big influence on the cut quality. The material being cut generally determines the type of assist gas used during cutting. The assist gas pressures, nozzle design and standoff also play a vital role in governing the gas dynamics and, thereby, significantly influence the cut quality.

Regardless of material type and thickness, the laser cutting operation starts with a piercing process and this governs the overall the cut quality. Laser and processing parameters were developed both piercing and cutting.

Combination of Laserdyne system advanced software and cutting parameters (laser & processing), it was possible to produce very clean and spatter free pierce prior to cutting. Small clean piercing was produced without any excessive burning or blow out. The control piercing prolongs the cutting nozzle tip and focusing optics life. Figure 12 shows example of clean pierce and cut edge quality of 5 mm thick Inconel based alloy used for land turbine stator ring. The special feature of the Laserdyne systems allows cutting very narrow profile slot with very accurate control over dimensions of the slots.

### 3.3 Laser Welding

The main requirement when welding aero engine materials (nickel and titanium based alloys) are:

**Table 4** Laser and processing parameters to evaluate formation of porosity

Shield gas	Flow rate (l/min)	Spot size ( $\mu\text{m}$ )	Power density ( $\text{MW}/\text{cm}^2$ )	Pore size (mm)
Ar	30	142	12.63	0.5
Ar	30	571	0.781	0.35
N <sub>2</sub>	30	142	12.63	None
N <sub>2</sub>	30	571	0.781	None
Ar./He	30	142	12.63	0.25
Ar./He	30	571	0.781	0.30

Ar. Argon; N<sub>2</sub> Nitrogen; Ar./He (Argon 80% + 20% Helium mix)

- Clean top and bottom weld bead; i.e. no oxidization
- No porosity or cracking
- No undercut top and bottom weld bead
- Correct weld shape geometry.

Flexible laser system is capable of producing 2 and 3D autogenous welds and welds with filler material. The welding tests were carried out in two stages i.e.

1. A comprehensive investigation was performed into the influences of the shield gas and power density on the characteristics of the resulting welds, including the weld morphology, and the porosity formation. Table 4 shows laser and processing parameters which were used to investigate formation of porosity in Inconel 625 alloy. The samples were X-rayed to observe the porosity level.

There are two types of porosity that can occur during laser welding of aerospace alloys i.e. fine scale porosity (typically  $< 0.2$  mm diameter) and large scale porosity (typically  $> 0.5$  mm diameter).

Fine scale porosity is present in most fusion welds often close to fusion boundary. It is spherical in form and has no significant effect on the mechanical properties of the weld, unless present in a large numbers and clustered, when it may reduce the load bearing capacity of the weld. A likely cause of this type of porosity is the difference in solubility of gases in molten and solid (particularly applicable to porosity found close to the fusion line). In this case solidification would result in degassing at fusion boundary. Gas bubbles may form and become trapped at the solidification front. This type of porosity is therefore likely to be influenced by the shielding gas (i.e. type, flow rate etc.) used in the welding process.

Large scale porosity is defined as pores greater than 0.5 mm in diameter and is often found along the center line of the weld in the lower half of the weld bead. Due to its size it may have much more marked effects on the weld properties and may be more damaging. The mechanism of this type of porosity formation is probably explained in terms of instabilities in the welding keyhole, since the pores are generally irregular in shape and occur deep in the weld. The keyhole instabilities can occur either due to insufficient power density at the workpiece or formation of plasma

above the workpiece during laser welding. The latter is more likely to occur with high power CO<sub>2</sub> welding (10.6 μm wavelength).

2. Laser welding with the filler wire is a multiparameter process and there are a number of laser and filler wire parameters which determine the quality of the resultant weld. Some of the parameters which were investigated are listed below:

**Welding/filler wire speed:** The wire feed rate for a given air gap and plate thickness is an important parameter and is dependent on welding speed, the cross sectional area of the gap between the joint face and cross sectional area of the filler wire. The relationship is expressed as follows:

$$\begin{aligned} & \text{Wire feed rate (m/min)} \\ &= \frac{\text{Welding speed(m/min)} \times \text{Cross sectional area of gap (mm}^2\text{)}}{\text{Cross sectional area of the wire (mm}^2\text{)}} \end{aligned}$$

If the filler wire rate is too low the amount of heat generated from the laser beam will affect the wire and the material being welded may be able to melt a bigger section of the wire end. This may result in breaking a liquid metal bridge formed during the process, the formation of a drop at the end of the wire and momentary disturbance of the process stability.

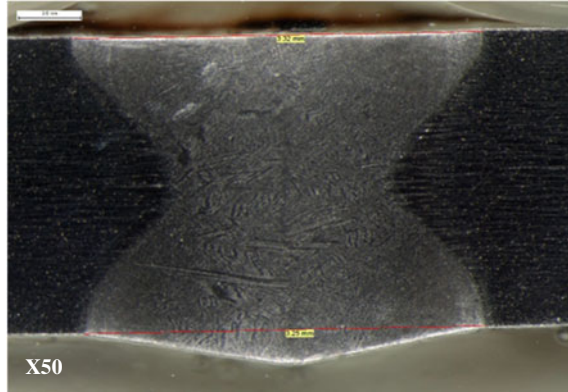
A high filler wire rate causes the energy supplied to the welding area to be insufficient for stable and permanent wire melting. The volume of liquid metal at the end of the wire and in the liquid metal bridge increases. A relatively large volume of the liquid metal flows to the weld pool, flooding the air gap. Additionally, non-melted wire enters the back area of the pool, pushing out the liquid metal, which, by solidifying, forms characteristic humps of the weld surface and porosity at the root of the weld. Excessive wire speed can also reduce the penetration depth, weld width and topbead height.

**Laser beam-filler wire interaction:** An exposed length of wire that is too short prevents the wire from being melted at the initial area of the bead, and the laser beam directly affected the material to be melted. In turn, an exposed length of wire that is too long causes the extended wire end to be pressed against the plate surface, and as a result, at the initial stage, the laser beam melts the wire through, dividing it into two parts. In consequence, the spot at which the process started was covered with a wire end welded onto the surface and difficult to remove. In an extreme case, the welded-on wire end could cause a collision with the gas shielding nozzle, disturbing or even eliminating the gas shielding.

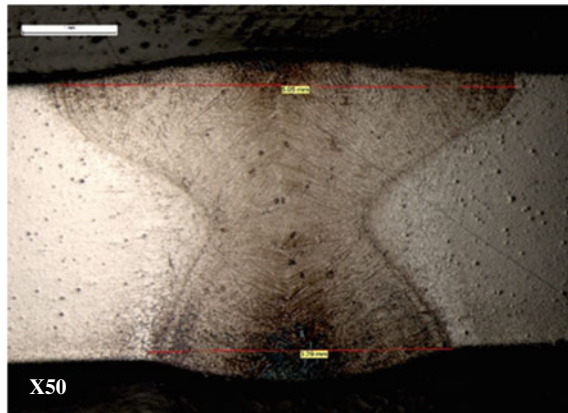
**Focused spot size:** The spot size should be close the filler wire diameter. With a small laser spot compare to the wire diameter, the welds will be full of porosity because the wire has not melted properly.

Majority of the aeroengine parts require laser welding with wire to compensate for the mismatch and poor fit of the parts, as well to produce correct weld geometry

**Fig. 13** Inconel 625 alloy, 3.2 mm thick, power density 0.78 MW/cm<sup>2</sup>; N<sub>2</sub> shielded gas 30 l/min; no porosity



Autogenous weld, slight undercut (1-3mm) at the topbead (not accetable); weld speed 0.8m/min



Weld made with filler material (no undercut at top or bottome bead); crown at the top and bottom is preferred; wire speed 1.2m/min; weld speed 0.8m/min

for good mechanical properties. Figure 13 highlights welds made with and without the filler material.

## 4 Summary

The processing tests (drilling, cutting and welding) carried out with the turnkey flexible laser system have shown that:

- Very little effort was required to change the set-up for the different process
- Good quality holes have been achieved with both coated and uncoated materials. The trepanned hole quality (roundness, recast layer, taper etc. is due to very

accurate motion control of 430 system. Combination of Laserdyne 430 system and QCW fiber laser makes it was possible to produce consistent holes in a range of nickel based superalloys at different angle of incidences.

- Small clean spatter free pierce and narrow profile slot with very accurate dimensions were produced in 5 mm thick land base turbine stator ring. Again it was combination of both 430 laser system (special machine software) and QCW fiber laser (pulsed laser parameters) which produced very good cutting results in a range of aerospace alloys.
- Laser and processing parameters were developed to weld a range of aeroengine materials. System is capable of welding 2 and 3D component with and without the filler material.

## References

1. Van Dijk MH, de Vilrger D, Brouwer JE (1989) Laser precision hole drilling in aero-engine components. In: Proceedings of the 6th conference on lasers in manufacturing, pp 237–247. ISBN 1-85423-047-6
2. Naeem M (2010) Laser percussion drilling of coated and uncoated aerospace materials with a high beam quality and high peak power lamp pumped pulsed Nd:YAG laser. In: Conference proceeding ICALEO 2010, Anaheim, California, USA, 26–30 Sept 2010
3. Norman S, Zervas MN, Appleyard A, Durkin MK, Horley R, Varnham MP, Nilsson J, Jeong Y (2004) Latest development of high-power fiber lasers in SPI. In: Proceedings of SPIE, vol. 5335: Fiber Lasers: Technology, Systems, and Applications, pp 229–237
4. Sivakumar R, Mordike, BL (1989) High temperature coatings for gas turbine blades, a review. *Surf Coat Technol* 37:139–160
5. Miller RA, Lowell CE (1982) Failure mechanisms of thermal barrier coatings exposed to elevated temperatures. *Thin Solid Films* 95, 265–273
6. Tsui YC, Clyne TW (1996) Adhesion of thermal barrier coating systems and incorporation of an oxidation barrier layer. In: Proceedings of thermal spray: practical solutions for engineering problems. In: Proceedings of the 9th natural thermal spray conference. ASM, Cincinnati, pp 275–284



# Study on the Effect of Focal Point Location and Incidence Angle of Laser on Cut Quality of Thick Stainless Steel Sheet by Yb-Fiber Laser



S. Mullick, S. Shrawgi, A. Kangale, A. Agrawal, and A. K. Nath

**Abstract** Fiber laser owing to its higher efficiency, beam quality, reliability and beam deliverability through optical fiber has a potential to outperform the more traditionally used CO<sub>2</sub> lasers in sheet metal cutting applications. However, it is found that the high focusability and shorter wavelength of this laser is advantageous for cutting thin metal sheets up to 2.0 mm only, while CO<sub>2</sub> laser still performs better in cutting thicker sheets. It has been reported that this has an unfavourable angle of incidence, resulting in poor absorption at metal surface. The narrow kerf produced by fiber laser may cause an earlier flow separation resulting in poor cut in thicker sheets. Therefore, the effect of focal point position and incidence angle, along with other process parameters, viz. laser power, cutting speed and O<sub>2</sub> gas pressure on cut quality of 4 mm thick steel sheet has been investigated. It has been found that cutting with the focal point located at the bottom surface with fixed stand-off distance makes the kerf-width wider, resulting in a better laminar gas flow through kerf for a longer distance, which reduces uncontrolled burning, producing a better quality cut. The change in laser incidence angle towards and away from the cut front, both improved the cut quality. Incidence angle influences the absorption of laser light, gas flow characteristics, laser intensity distribution and shear force at the surface. Results of the detailed parametric study are presented.

**Keywords** Fiber laser · Thick sheet · Laser cutting · Cut quality

## 1 Introduction

Laser cutting dominates the industrial laser applications and has become a reliable technique for industrial production. The most established laser beam source for laser cutting is CO<sub>2</sub> laser system that radiate at wavelength of 10.6 μm. This beam is preferred for its better absorptivity for a wide range of materials [1]. Whereas high-power solid-state disk and fiber lasers with a wavelength of about 1 μm seem to

---

S. Mullick · S. Shrawgi · A. Kangale · A. Agrawal · A. K. Nath (✉)  
Department of Mechanical Engineering, Indian Institute of Technology, Kharagpur, India  
e-mail: [aknath@mech.iitkgp.ernet.in](mailto:aknath@mech.iitkgp.ernet.in)

be an attractive and reliable alternative laser source, due to their high efficiency, beam guidance, beam quality and tight focusability [2–4]. However, due to relatively shorter wavelength and high focusability these lasers are preferred for machining thin sheets, whereas for thicker sheets the quality of cut has been reported to deteriorate [5–12]. The reasons behind the difference in performance between fiber laser and CO<sub>2</sub> laser are not yet fully understood. One of the reasons seems to be related to the dynamics of material removal, mainly the onset of recast ripples [7] and melt expulsion [8]. Another reason cited is the difference in wavelength, which affects the absorptivity behaviour at the cut front in thicker sections and on the cutting performances [11, 12].

It is reported that the angle of incidence for 1 μm wavelength of fiber laser in case of cutting thick sheets, remains in an unfavourable zone where the absorptivity on metal surface becomes lower than its maximum value [3, 11, 13]. It results in an inefficient laser coupling at the work-piece, deteriorating the cut quality. The calculated values of Brewster angle for molten steel are  $\Phi_{Br_{1.06\ \mu m}} = 82.6^\circ$  for fiber laser radiation and  $\Phi_{Br_{10.6\ \mu m}} = 88.7^\circ$  for CO<sub>2</sub> laser radiation [3]. As a result, for an incidence angle in the range  $\Phi_{in} > 85.9^\circ$ , CO<sub>2</sub> laser radiation is better absorbed by a molten ferrous surface than the radiation of fiber laser beam. It is reported that the expected angle of incidence in fiber laser cutting of medium and thick sheets are far away from optimum values at which absorptivity reaches its maximum, whereas absorptivity of CO<sub>2</sub> laser is high and nearly constant over a broad range of thickness [11].

The high focusability of fiber laser results in a very narrow kerf-width, due to which flow separation of assist gas inside kerf takes place at a lower depth [14]. This results in an unstable flow near bottom surface of the cut. This enhances the uncontrolled burning, non-uniform and inefficient removal of molten material from the bottom surface, resulting in a poor quality cut surface and wider bottom kerf-width.

Different reports suggest that the cut quality can be improved by focusing the laser beam below top surface [3, 15], as the beam waist position relative to top surface influences the kerf size and striation pattern. However, all the studies are carried out at variable stand-off distance (SOD), which also changes with the change in focal point position, thus changing the flow pattern inside the kerf.

In this study two different approaches have been investigated to improve the cut quality for 4 mm thick stainless steel sheet using Yb-fiber laser of 1.07 μm wavelength. The cutting has been carried out with oxygen gas assist. The first approach is to change the focal point position from top surface to middle and bottom surface at a constant SOD to study the effect of focal point position without changing the flow characteristics inside kerf. The change of focal point position from top to bottom surface is expected to enlarge the kerf-width, and this may improve flow pattern inside the kerf. This, in turn could result in a better and uniform removal of material, improving the cut quality. The second approach is to change the laser incidence angle by inclining the beam in both the directions, towards and away from the cut front, to study the effect of absorption phenomena of the laser beam along with gas flow characteristics on the cut quality.

## 2 Experimental Details

The experimental study of the effect of focal point position and incidence angle of laser beam at constant SOD on the cut quality of 4 mm thick stainless steel (SS 304) sheet was conducted using an Yb-Fiber laser of  $1.07 \mu\text{m}$  wavelength with coaxial oxygen gas assist. Two different sets of experiments were conducted.

The first set of experiments was carried out to study the effect of focal point position on cut quality, for which three different nozzles were designed and fabricated. The length of nozzle was adjusted such that the focal point position was 1, 3.5 and 5 mm away from the orifice of three different nozzles. With these nozzles the focal point position can be changed with respect to work-piece surface without changing the SOD. The experimental set-up and the schematic of nozzle are shown in Fig. 1. Parametric study and quality based optimization have been carried out for each nozzle. Experiments were conducted at constant SOD of 1 mm with different nozzles, so that the beam can be focused at the top and 2.5 mm and 4 mm below top surface, respectively. These nozzles are referred as nozzle 1, 2, and 3 respectively in rest of the paper. The spot diameter at focal point was measured to be  $\sim 250 \mu\text{m}$ . The fiber laser used has a non uniform beam profile instead of a Gaussian or flat top profile, as shown in Fig. 2 [16]. It has a central peak surrounded by two annular rings of smaller peaks. For this set of experiments, the process parameters chosen were laser power, cutting speed and assist gas pressure, whereas the output quality factors chosen were the ratio between bottom to top kerf-widths and the striation depth at

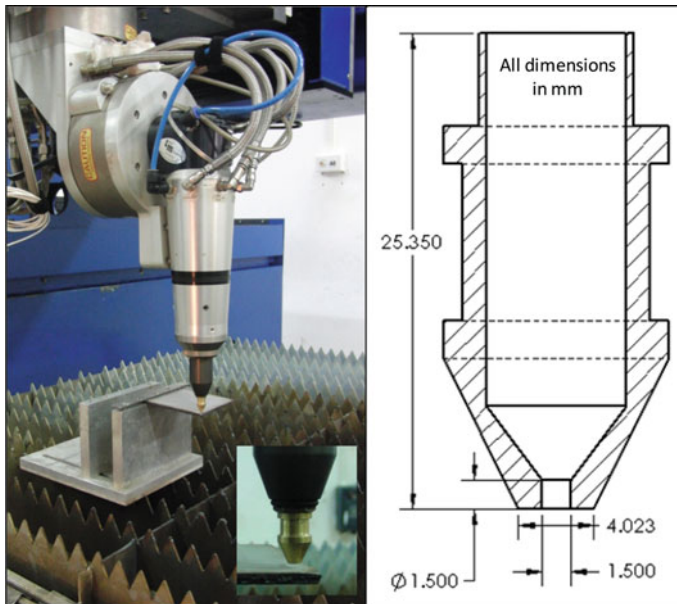
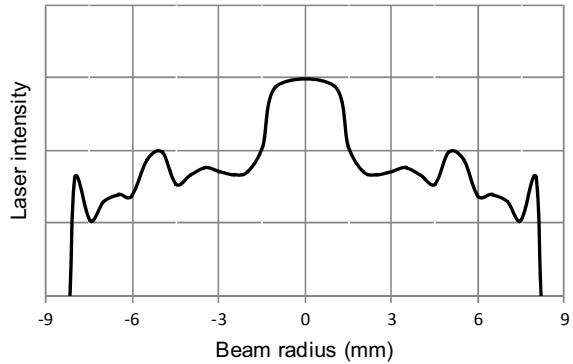


Fig. 1 Experimental set-up and schematic of the cutting nozzle

**Fig. 2** Beam intensity profile of the 2 kW Yb-Fiber laser [16]



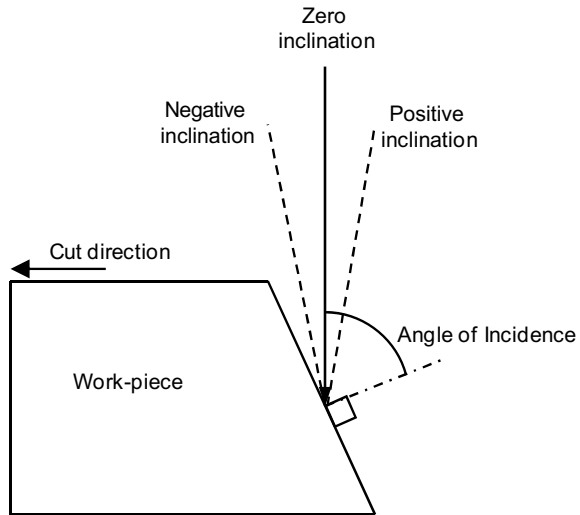
the cut surface. Striation depth is defined as the depth of cut after which uncontrolled material removal starts due to unstable flow of gas inside the kerf.

Response Surface Methodology (RSM) was applied for the above mentioned process parameters and output variables, using statistical software, Design-Expert V8. The experiments were designed based on three level Box-Behnken design. Box-Behnken method was chosen due to shorter range of process parameter instead of spherical central composite design (CCD). Another advantage of Box-Behnken design is that it does not contain combination of factors at which all the factors are simultaneously at their highest or lowest level, thus can avoid experiments under the extreme conditions [17]. This design can also be chosen instead of other variations of CCD, like face centred CCD, as this design is rotatable or nearly rotatable, and the rotatability is very important for a second order model to provide good predictions throughout the region of interest [18].

The experimental runs were conducted as per the design matrix given by the software. Second order polynomials were fitted to the experimental data, and step wise regression method was used to find out the significant model terms and the final regression equation. Afterwards the same software was used to generate different response plots and to carry out numerical optimization to find out the set of process parameters, at which the desired cut quality can be achieved. For the best quality cut the ratio of kerf width is expected to be near 1, whereas the value of striation depth is to be maximized to reduce the uncontrolled burning and removal of material at the bottom surface of work-piece.

The second set of experiments was carried out to study the effect of laser incidence angle on cut quality by changing the inclination of the beam. Zero inclination represents that the laser beam is normal to the work-piece surface, whereas positive and negative inclinations represent the bending of beam away and towards the inclined cut front, respectively, as shown in Fig. 3. Initial experiments were conducted for all the three nozzles, varying the inclination angle from  $0^\circ$  to  $5.4^\circ$  in both directions with an interval of  $1.8^\circ$ . Higher inclination was avoided as it tends to damage the tip of cutting nozzle. For all the experimental runs, the other three process parameters,

**Fig. 3** Laser incident to work-piece at different inclinations



i.e., laser power, cutting speed and gas pressure were kept constant at a set of values where it produces a good quality cut at zero inclination.

For both sets of experiments, 4 mm thick SS 304 specimens of 80 mm × 100 mm dimension were taken and 60 mm long straight slits were cut according to the specified set of parameters. The top and bottom kerf-widths were measured with the help of an optical microscope and an average of four measurements for both kerf-widths were recorded for each run. The striation depths were also measured from the photographs of cut surfaces taken by the optical microscope, and an average of twenty four measurements for each run was recorded.

### 3 Results and Discussion

#### 3.1 Study of focal Point Position

The study of cut quality for three different nozzles has been conducted using RSM, where the experiments were designed based on Box-Behnken design. Table 1 shows the process parameters and experimental design levels.

##### 3.1.1 Analysis of Variance (ANOVA) and Regression Model

Regression model for nozzle 1:

$$Kerf-ratio = -14.95811 + 0.013969 \times A$$

**Table 1** Process parameters and experimental design level for the study of cut quality

Process parameter	Unit	Code	Nozzle 1			Nozzle 2			Nozzle 3		
			Levels			Level			Level		
			-1	0	+1	-1	0	+1	-1	0	+1
Laser power	W	A	1075	1302	1530	1075	1302	1530	1075	1302	1530
Cutting speed	mm/min	B	1500	2000	2500	1500	1900	2300	1400	1800	2200
Gas pressure	bar	C	2.0	3.5	5.0	2.0	3.5	5.0	2.0	3.5	5.0

$$\begin{aligned}
&+ 0.011795 \times B - 1.72046 \times C \\
&- 8.83516E - 06 \times AB + 1.32601E - 03 \times AC \quad (1)
\end{aligned}$$

$$\begin{aligned}
\text{Striation-depth} &= 3.57706 - 3.82418E - 04 \times A \\
&- 1.23401E - 03 \times B - 0.12769 \times C \\
&- 2.10989E - 07 \times AB + 1.75824E - 04 \times AC \\
&+ 5.1E - 05 \times BC + 4.01769E - 07 \times B^2 \\
&- 0.022248 \times C^2 \quad (2)
\end{aligned}$$

Regression model for nozzle 2:

$$\begin{aligned}
\text{Kerf-ratio} &= -11.40088 + 9.54853E - 03 \times A \\
&+ 8.39114E - 03 \times B - 0.06926 \times C \\
&- 5.74176E - 06 \times AB + 6.00733E - 04 \times AC \\
&- 1.875E - 04 \times BC - 0.074683 \times C^2 \quad (3)
\end{aligned}$$

$$\begin{aligned}
\text{Striation-depth} &= 2.56424 - 1.49469E - 03 \times A \\
&+ 1.14229E - 03 \times B - 0.39136 \times C \\
&+ 2.98168E - 04 \times AC - 1.90833E - 04 \times BC \\
&+ 0.069976C^2 \quad (4)
\end{aligned}$$

Regression model for nozzle 3:

$$\begin{aligned}
\text{Kerf-ratio} &= 0.61285 + 6.48901E - 03 \times A \\
&- 4.52175E - 03 \times B + 0.88468 \times C \\
&- 2.91209E - 06 \times AB - 2.66667E - 04 \times BC \\
&+ 2.3137E - 06 \times B^2 - 0.081026 \times C^2 \quad (5)
\end{aligned}$$

$$\begin{aligned}
 \text{Striation-depth} = & -1.87331 - 4.40659E - 04 \times A \\
 & + 4.47584E - 03 \times B + 0.44561 \times C \\
 & - 1.09459E - 06 \times B^2 - 0.053171 \times C^2 \quad (6)
 \end{aligned}$$

Design Expert software, V8 was used to analyze the measured responses. Model significance test, significance test for each of the model term, and lack of fit test were carried out. A step wise regression method was selected to find out the significant model terms, and the resultant ANOVA tables for reduced quadratic model summarizing ANOVA for each response. The abstracted ANOVA tables for both the responses in all three nozzles are given in Table 2. Model sum of square (SS-model) represents the measure of variation or deviation from the mean value, and is used for describing how well a model represents its data. A non significant lack of fit signifies that the model can adequately describes the functional relationship between the experimental factors and response variables, whereas p-value if comes below the smallest level of significance, the data are considered to be significant. The Table also represents other adequacy measures  $R^2$ , Adjusted  $R^2$ , Predicted  $R^2$  and Adequate precision.  $R^2$  is known as the coefficient of determination, and indicates how close the data are to the fitted regression line. It is a measure of the amount of reduction in the variability of the response, predicted by the model, whereas adjusted and predicted  $R^2$  defines the predicting capability of the model. All the three  $R^2$  values should be high and in a close range to ensure better predictability and adequacy of the model. The values of adequate precision, a measure of signal to noise ratio, are much greater than 4 for all responses, which indicates that the model can be used to navigate the design space, or to optimize the responses efficiently [19]. The reduced regression equation including only the significant model terms, for both the responses in three different nozzles are given by Eqs. (1)–(6).

### 3.1.2 Discussion

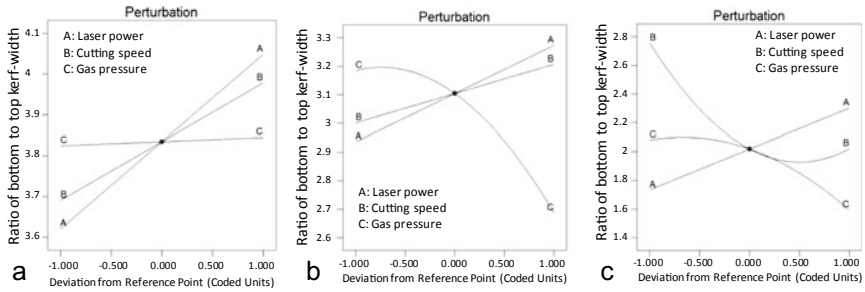
The variation in different quality variables with the change in process parameters are studied using RSM, and the perturbation curves showing main effects of process parameters on both quality factors for three different nozzles are presented here. Figure 4 shows the effect of process parameters on the ratio between bottom to top kerf-widths for different nozzles. In all cutting conditions the ratio remains higher than 1, because of the widening of kerf by uncontrolled material removal at the bottom surface. A smaller value of bottom to top kerf-widths' ratio is always preferable for a good quality cut.

Figure 5 shows a typical laser cut surface of a 4 mm thick SS 304 stainless steel sheet, where three distinct zone of material removal, zone 1–3 can be observed. The mechanisms of material removal in these three zones are different. The removal of material at zone 1 is dominated by partial vaporization of material and shearing force given by assist fluid. In zone 2 the removal is completely dominated by the shear

**Table 2** Abstracted ANOVA Table for all reduced quadratic models

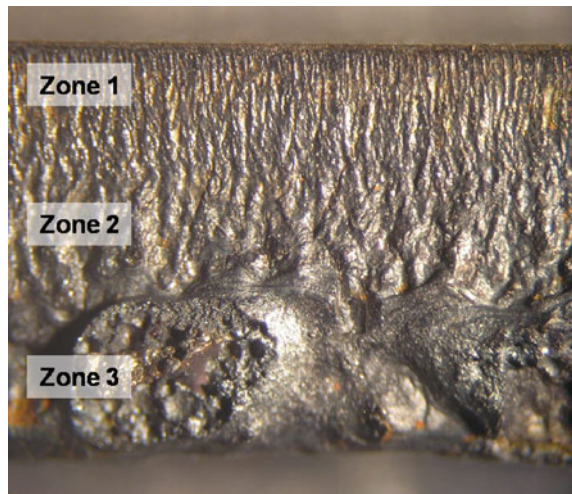
Nozzle	Response	SS-model	Degrees of freedom	Lack of fit	p-value	R <sup>2</sup>	Adj-R <sup>2</sup>	Pre-R <sup>2</sup>	Adq. precision
Nozzle 1	Ratio of kerf-width	5.39	5	Not significant	<0.0001 (significant)	0.9544	0.9241	0.8728	22.788
	Striation depth	0.28	8	Not significant	<0.0001 (significant)	0.9958	0.9901	0.9876	48.484
Nozzle 2	Ratio of kerf-width	2.22	7	Not significant	<0.0001 (significant)	0.9785	0.9571	0.8659	22.668
	Striation depth	0.84	6	Not significant	0.0003 (significant)	0.9339	0.8844	0.8608	12.802
Nozzle 3	Ratio of kerf-width	3.19	7	Not significant	<0.0001 (significant)	0.9877	0.9753	0.9485	35.849
	Striation depth	0.70	5	Not significant	<0.0001 (significant)	0.9551	0.9146	0.8289	17.821





**Fig. 4** Effect of process parameters (in coded units) on the ratio between bottom to top kerf-width for **a** nozzle 1, **b** nozzle 2 and **c** nozzle 3; actual values of process parameters corresponding to coded units are given in Table 1

**Fig. 5** Typical pattern of laser cut surface in thick steel sheet



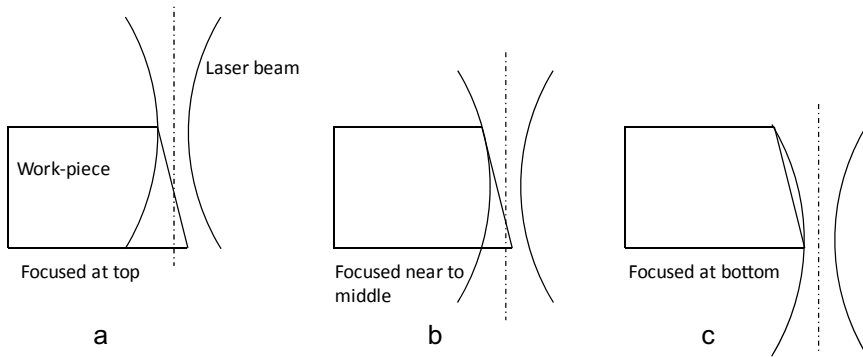
force produced by assist gas. However at the bottom surface the removal of material becomes more uncontrolled as the gas flow becomes unstable [14] and develops a large amount of radial velocity components as it approaches towards the bottom surface. This unsteady flow of oxygen gas also causes uncontrolled burning due to exothermic reaction. Thus, the molten material gets removed as lumps in this zone, instead of getting sheared off smoothly.

Figure 4 shows that the increase in laser power (factor A) results in an increase in kerf ratio for all nozzles. This indicates a higher rate of increase in bottom kerf compared to that of top kerf. With the increase in laser power, both the kerf-width is expected to increase due to higher heating. However, increase in laser power increases the melt layer thickness and its temperature producing low viscous melt layer. As the high temperature molten material flows toward bottom it can cause uncontrolled

burning of materials due to unsteady gas flow in this zone, resulting in a higher increase in the bottom kerf. This results in an increase in the ratio with laser power.

Figure 4 also represents the effect of cutting speed (factor B) on the kerf-width ratio for three different nozzles. It shows a continuous increase in the ratio with the increase in laser power for first two nozzles, and an opposite trend in the third nozzle which allows focussing of laser beam at the bottom. With the increase in cutting speed, the interaction time and line energy reduce, which could cause reduction of both kerf-widths, however, the rate of reduction may be different for top and bottom surfaces and also for different focusing conditions.

As the distance of the focal point from nozzle orifice is different for different nozzles, the laser spot diameter at the work-piece surface is different for a constant SOD of 1 mm. The calculated laser spot diameters at the surface were about 250, 350 and 630  $\mu\text{m}$ , for nozzle-1, 2 and 3 respectively. However, the measured values of average top kerf-width with three different nozzles are nearly 340, 530 and 680  $\mu\text{m}$ , respectively. It shows that in first two cases the values of top kerf-width are much larger compared to the theoretical one, whereas in the third case there is not much difference. This may be due to two reasons, first, the laser beam used in this study does not have a uniform beam intensity profile instead it has two annular rings surrounding the central high intensity lobe, as shown in Fig. 2 [16]. At higher energy these two side peaks may cause extra removal of material. The second reason is the exothermic reaction caused by oxygen, which tends to enlarge the kerf. For first two nozzles, where the power density at top surface remains reasonably high, the annular rings could be intense enough to effect material removal. However, in the third nozzle, where laser beam is focused at the bottom surface, the power density at top surface may not be sufficient for the annular rings to be effective for material removal. Also, the rate of exothermic reaction for first two conditions is expected to be more compared to the last one due to high power density. As the line energy reduces with the increase in cutting speed, the influence of annular rings may diminish. However, as the laser beam travels through kerf toward bottom it undergoes scattering and reflection from walls, which could direct the laser power towards centre. Thus, for first two cases the top kerf-width reduces at a faster rate compared to that of bottom kerf with the increase in cutting speed. Another reason could be the effect of exothermic reaction. Reduction in interaction time with the increase in cutting speed may cause a reduction in the effect of exothermic reaction at top surface. Whereas at bottom surface this may be sustained for a longer period of time due to the presence of molten layer. This may also cause a relatively higher rate of reduction in the top kerf-width with increasing cutting speed. In case of third nozzle, where laser beam is focused at the bottom surface, the power density at the top surface may not be sufficient for the annular rings to be effective for material removal. Therefore, in this case with the increase in cutting speed the rate of reduction in top kerf-width may not be so high, whereas the rate of reduction of bottom kerf may be higher due to two reasons. In this case laser beam is focused at the bottom surface as schematically shown in Fig. 6. With the increase of cutting speed the reduction in coupled laser power at the bottom surface is expected to be more in this case, compared to the focusing conditions of first two nozzles. Also, the increase in cutting speed causes an increase



**Fig. 6** Schematic of the focusing condition and beam interaction for **a** nozzle 1, **b** nozzle 2 and **c** nozzle 3

in the cut front inclination angle [20]. In this focusing condition, where the focal point lies at bottom edge, a small increase in the inclination angle may cause a slight defocusing of beam at the bottom edge, thus resulting in a reduction in coupled laser power at the bottom. These two reasons may be responsible for a higher rate of reduction in kerf-width at the bottom surface compared to that in top surface in this focusing condition. Therefore, the ratio of kerf-width follows a decreasing trend with the reduction in cutting speed; opposite to that of first two focusing conditions.

The effect of assist gas pressure (factor C) on the ratio between bottom to top kerf-widths is also shown in Fig. 4, for all three nozzles. In case of nozzle 1, the increase in gas pressure has no significant effect on the kerf-width ratio. The increase in oxygen gas pressure increases the shearing force and the rate of exothermic reaction at both kerfs. However, as the focal point lies at top surface with nozzle 1, the power density is highest there and the fluidity of molten material is also maximum. Thus, the increase in shear force should have a more prominent effect on the top kerf. At the same time, due to the smaller average top kerf-width in this case, the flow separation would take place at a lower depth [14]. It results in an unstable flow of assist gas at the bottom having large amount of radial velocity component in it. With the increase in gas pressure the instability becomes stronger, which causes an increase in the bottom kerf-width. Due to these two effects there is no significant change in the ratio of kerf-width. In case of second nozzle, laser beam is focused near the mid-thickness, therefore the average top kerf-width is larger compared to the previous case. This results in a stable flow of gas for a longer depth. Also, due to near uniform laser power density at both surfaces the effect of shear force remains almost the same. As can be seen in Fig. 6b, the centre line of laser beam and gas flow is near the bottom surface in this case, whereas in the previous case it was near mid-thickness. Since the maximum flow velocity will be along the central line, bottom edge may experience a higher cooling effect, and this could restrict the enlargement of bottom kerf. This could be a reason for a reduction in kerf ratio with the increase in gas pressure in case of second nozzle. In the third nozzle, there is also a reduction in the ratio with

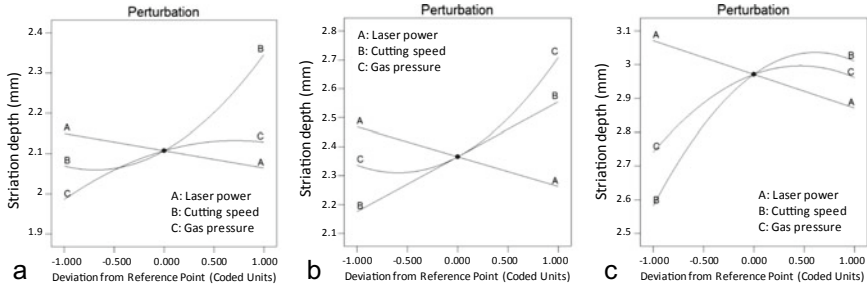


**Fig. 7** Effect of process parameters (in coded units) on striation depth for **a** nozzle 1, **b** nozzle 2 and **c** nozzle 3; actual values of process parameters corresponding to coded units are given in Table 1

the increase in gas pressure similar to second nozzle, though the reduction is much smaller. As can be seen in Fig. 6c both gas flow and laser power density are expected to be highest at the bottom edge due to which reduction in bottom kerf with the increase of gas pressure would be less compared with 2nd nozzle.

Figure 7 shows the effect of process parameters on striation depth. Striation depth is defined as the depth of cut after which uncontrolled burning and removal of material starts due to unsteady gas flow. Thus, a high value of striation depth represents a better cut quality. The graphs show that striation depth reduces with the increase of laser power. This could be due to higher melt temperature and increased fluidity at higher laser power (factor A), which could lead to uncontrolled burning along thickness, resulting in shortened striation depth.

Increase in cutting speed shows an opposite effect on the striation depth, increasing with the cutting speed, as can be seen in Fig. 7. This could be because of reduction in line energy with cutting speed, which would result in lower temperature rise of the melt front, producing relatively high viscous melt layer. This could reduce the chance of uncontrolled burning increasing the striation depth. However in case of nozzle 3, there is a slight reduction in the value of striation depth at a very high cutting speed. This may be due to higher cooling near the bottom surface as discussed earlier, resulting in insufficient melting, which can not be sheared off properly by the assist gas. This may results in non-uniform removal or attachment of molten material near the bottom surface, thereby reducing the striation depth.

Assist gas pressure has a positive effect on the striation depth in all cases, though rate of change is comparatively low in nozzle 1 and 3, and there is a slight reduction in the value at a very high pressure; whereas in nozzle 2, there is a steep increase in the striation depth with gas pressure. The average value of top kerf-width for nozzle 1 is much less than that of nozzle 2 and 3. The average value is nearly 350, 530 and 680  $\mu\text{m}$ , for the three nozzles, respectively. Increase in gas pressure results in a higher shear force, and also increases the rate of exothermic reaction, causing higher melting. In case of nozzle 1, due to very small top kerf-width the flow separation takes place at a relatively low depth and at low gas pressure [14]. Thus, a small increase in gas pressure improves the material removal, resulting in higher striation depth.

However, with further increase in oxygen pressure the flow becomes more unsteady after a small depth, resulting in more uncontrolled burning and removal of material at the bottom surface. This results in a shorter striation depth. In case of nozzle 2 the average top kerf width is much higher compared to that produced by nozzle 1. Due to wider kerf the flow remains steady up to a longer depth, even at a relatively higher gas pressure. Thus, even at a very high gas pressure there is no adverse effect of gas pressure on the striation depth. In nozzle 3, the kerf-width is even larger than that of nozzle 2. However, in this case the laser beam is focused at the bottom surface, causing the maximum intensity at the bottom surface. This results in higher melt layer thickness at the bottom surface of relatively higher fluidity. Thus, a very high gas pressure may cause uncontrolled removal of material at the bottom. Thus, with the increase in assist gas pressure, initially there is a sharp increase in the striation depth and there after a slight reduction in the depth for this focusing condition.

### 3.1.3 Cut Quality Optimization

Quality based optimization has been carried out for all three nozzles using the final regression model (Eqs. 1–6), and the optimization criteria for numerical optimization imposed for all sets is shown in Table 3. The optimum value for the first response, ratio between bottom to top kerf-width, is generally taken as 1 [21, 22]. But for the current experimental conditions the maximum value obtained for this response is much higher than the target value. Thus, this response has been minimized. The second response, striation depth has been maximized, as it is observed that it directly improves the surface quality of cut. Increase in striation depth indicates reduction in uncontrolled removal of material, thus, improvement in the cut quality. The solutions for the optimal cut condition, satisfying the imposed criteria, are presented in Table 4.

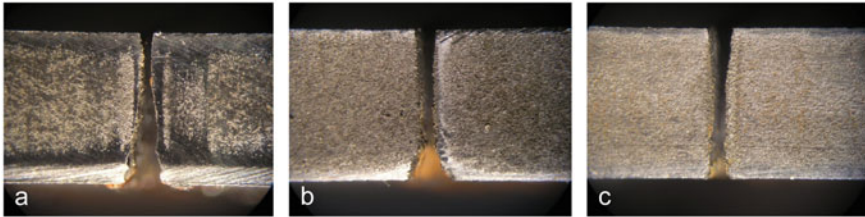
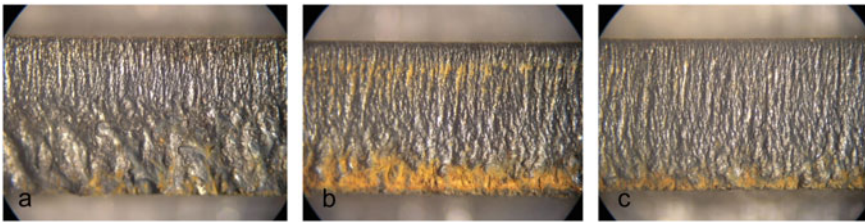
Table 4 presents the optimal set of process parameters and the corresponding response values for the three nozzles. The results show that a minimum laser power, moderate cutting speed and maximum gas pressure within the current range of process parameters can yield the best quality cut with a minimum value of kerf ratio and a reasonably high striation depth. Experimental runs were conducted at these set of process parameters and the photographs of laser cut samples for the three nozzles are shown in Figs. 8 and 9. There is a significant improvement in the cut quality from

**Table 3** Criteria for numerical optimization

Factors and response	Goal	Importance
Laser power	Is in range	3
Cutting speed	Is in range	3
Gas pressure	Is in range	3
Ratio between bottom to top kerf-width	Minimize	3
Striation depth	Maximize	5

**Table 4** Optimum solutions for all the three nozzles

Nozzle	Set	A (W)	B (mm/min)	C (bar)	Ratio of kerf-width	Striation depth ( $\mu\text{m}$ )	Desirability
Nozzle 1	1	1075	1500	3.5	2.46000	2.08775	0.814
Nozzle 2	1	1075	1500	5.0	1.80126	2.63488	0.845
Nozzle 3	1	1075	2000	5.0	1.26982	3.12505	0.860

**Fig. 8** Optimal quality of cut cross section of 4 mm thick SS 304 sheet, for **a** nozzle 1, **b** nozzle 2 and **c** nozzle 3**Fig. 9** Optimal quality of cut surface of 4 mm thick SS 304 sheet, for **a** nozzle 1, **b** nozzle 2 and **c** nozzle 3

nozzle 1 to 3, in terms of both kerf-width ratio and striation depth. The measured values of the kerf ratio for the optimal run conditions are 2.56, 2.10 and 1.15 for nozzle 1, 2 and 3, respectively, whereas the values of striation depth are 2.083, 2.720 and 3.192 mm for the three nozzles respectively. The measured values are within 95% prediction interval (PI) given by the software, and the percentage error is in the range of 0.2–14.2%, which is within the reasonable agreement.

### 3.2 Study of the Laser Incidence Angle

Effect of incidence angle on cut quality has been studied for the three nozzles, varying the inclination angle from 0 to  $5.4^\circ$  in both, positive and negative directions with  $1.8^\circ$

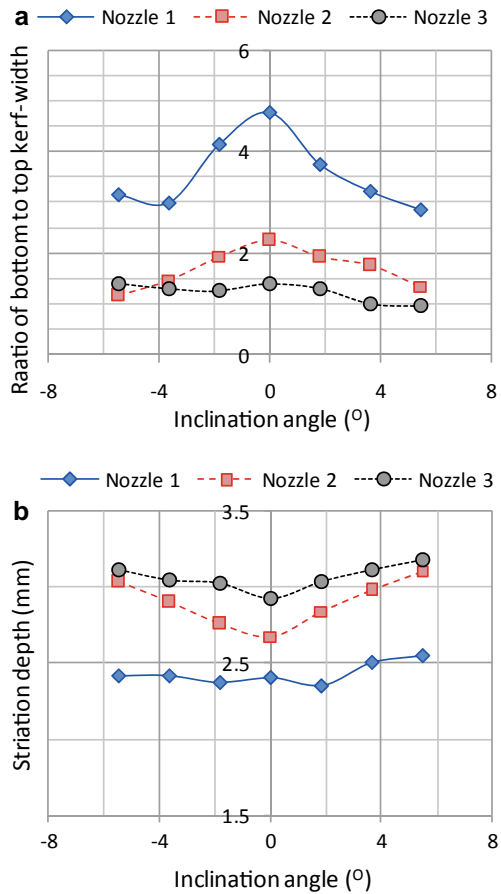
**Table 5** Process parameters for the study of incidence angle

Nozzle	Power (W)	Cut speed (mm/min)	Gas Pr. (bar)	SOD (mm)	Inclination angle (°)
Nozzle 1	1315	2500	4.0	1.0	(-)5.4 to (+)5.4
Nozzle 2	1210				
Nozzle 3	1150				

interval. For this set of experiments all other process parameters were kept constant as tabulated in Table 5.

The effect of inclination angle on cut quality, ratio between bottom to top kerf-widths and striation depth, are shown in Fig. 10. The results show that there is an improvement in quality for all the three nozzles, for both directions of inclination. However, nozzle 2 produces the maximum improvement in cut quality, but in terms of the absolute value of quality factors nozzle 3 performs the best. Further, at a very

**Fig. 10** Effect of inclination angle on **a** ratio of bottom to top kerf-width and **b** striation depth for all three focusing conditions



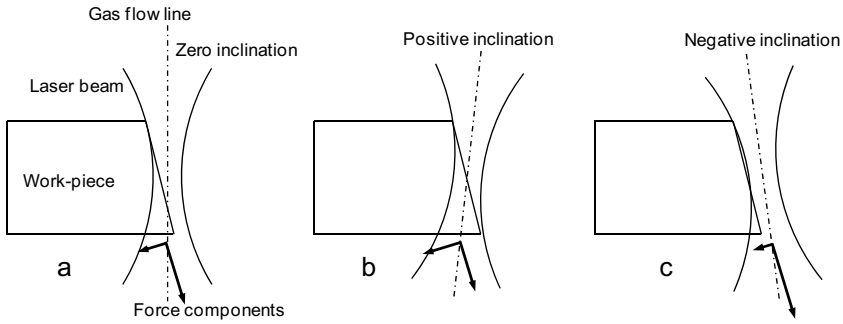


**Fig. 11** Laser beam interaction with work-piece and shear force component of assist gas at **a** zero, **b** positive and **c** negative inclination

high negative inclination, the cut quality starts deteriorating for two extreme focusing conditions, i.e. for nozzle 1 and 3 as shown in Fig. 10.

Inclination in both directions has certain effect on the absorption characteristics, laser power coupling to the work-piece and shear force applied by the assist gas. Previous reports [3, 11, 13] show that the average angle of incidence for cutting thick sheet using Yb-Fiber laser is much higher than its optimal value where absorptivity is maximum.

Thus, a reduction in incidence angle may improve the absorption characteristics of 1.07  $\mu\text{m}$  wavelength fiber laser beam. Angle of incidence is defined as the angle between the vertical to the inclined cut front and the center line of the laser beam (see Fig. 3). For a negative inclination the angle of incidence becomes more, whereas a positive inclination reduces the incidence angle. In this respect the positive inclination should be preferred for better absorption characteristics. At the same time the interaction between laser beam and inclined cut front changes with the change in inclination angle, as shown in Fig. 11. It is evident that a positive inclination offers a higher laser beam area interaction with the work-piece, whereas a negative inclination induces large amount of power loss due to direct transmission of laser beam through the cut kerf.

The change in the inclination angle of laser beam is also expected to change the gas flow characteristics and shear force applied by it on the molten pool. Figure 11b shows that, in positive inclination the flow interacts with the surface at a lower depth. This causes a large change in momentum, resulting in a more unsteady flow. In this inclination, the gas flow exerts a more impinging type of force on the molten pool, instead of shearing, where the force component in the direction of the removal of molten layer is less [Fig. 11b]. However, for a negative inclination the flow of assist gas is more parallel to the cut front surface, thus more stable flow is expected. Also the force applied by assist gas in this type of flow is more likely to promote shearing, as shown in Fig. 11c. This may result in a more efficient removal of material. Thus, material removal is expected to be more efficient and uniform in case of a negative inclination.



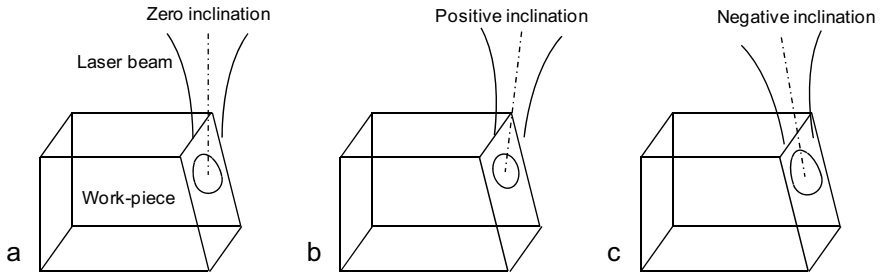


**Fig. 12** Projection of laser beam on inclined cut front at **a** zero, **b** positive and **c** negative inclination

Figure 12 shows the projected beam shape on the inclined cut surface of the work-piece, at different inclination angle of the laser beam, which also have effect on the intensity distribution within the beam spot area. Zero inclination results in a non uniform beam profile on the inclined cut surface [Fig. 12a]. This causes a non-uniform intensity distribution along depth. With the increase in depth, the width of laser beam profile increases due to divergence, resulting in a reduction in intensity from top to bottom of the beam spot area. Positive inclination produces a more circular spot on the surface, shown in Fig. 12b, with more uniform intensity distribution. However, a negative inclination results in a more non-uniform beam profile, having higher intensity difference from top to bottom of beam spot as shown in Fig. 12c. This is because the rear portion of beam has to pass a longer distance to strike the inclined cut surface. Thus, this inclination may have a negative effect on the cut quality, when the beam is focused at the top, as it makes the intensity distribution more non-uniform.

From the above discussions it may be concluded that, though a positive inclination improves the absorption characteristics and laser power coupling to the work-piece, it may cause an inefficient removal of material. Whereas, a negative inclination may produce a better shearing force on the molten metal pool, it causes a reduction in laser absorption and enhances the transmission loss, thus reducing the laser power coupling to the material. Thus, there is a relative improvement in cut quality for both the inclinations. However, the quality starts deteriorating beyond a particular inclination in the negative side. This may be because the transmission loss becomes very high beyond certain angle and the absorption may also reduce, thus reducing the laser coupling to work-piece drastically. However, this trend is more prominent at nozzle 1 and 3, where the beam is focused either at the top or bottom surface of work-piece. In case of focal point position at the middle, there is no such effect. Further experiments are underway considering all three process parameters, i.e., laser power, cutting speed, gas pressure for different inclination angles to study their combined effect, and to optimize the process parameters for the best quality cut.

## 4 Conclusions

Two different approaches have been investigated to improve the quality of oxygen assisted cutting in 4 mm thick stainless steel sheet using Yb-Fiber laser of 1.07  $\mu\text{m}$  wavelength.

The first approach was to shift the focal point position from top to bottom surface, without changing the stand-off distance to keep gas flow characteristics same inside the kerf for different focal point positions. It is observed that the cut quality improves as the focal point is shifted from top surface to bottom surface. As the focal point is shifted below, the top surface kerf becomes wider. This allows a more steady gas flow through kerf, which reduces the uncontrolled burning and ensures uniform melt removal by assist gas. This reduces the broadening of bottom kerf, producing a more uniform kerf throughout the thickness. This also improves the quality of cut surface, as the reduction in uncontrolled removal of melt layer results in a uniform striation pattern for a longer depth.

Second approach was to change the angle of incidence by changing the inclination of the beam, towards and away from the direction of cutting. Preliminary investigation shows that it tends to improve the quality of cut for both inclinations. The improvement is much prominent with laser beam focused at the mid-thickness; however, the overall best cut quality was achieved for positive inclination with laser beam focused at the bottom surface.

## References

1. Beltforte DA (2010) The worst is over. *Industrial Laser Solutions*, January/February 4–10
2. Ready JF (2001) LIA handbook of laser materials processing. Laser Institute of America, Magnolia Publishing Inc., Orlando, FL, USA, pp 425–470
3. Scintilla LD, Tricarico L (2013) Experimental investigation on fiber and CO<sub>2</sub> inert gas fusion cutting of AZ31 magnesium alloy sheets. *Opt Laser Technol* 46:42–52
4. Wandera C, Kujanpaa V, Salminen A (2011) Laser power requirement for cutting thick-section steel and effects of processing parameters on mild steel cut quality. *Proc Inst Mech Eng B J Eng Manuf* 225:651–661
5. Wandera C (2006) Laser cutting of austenitic stainless steel with a high quality laser beam. Masters Thesis, Lappeenranta University of Technology, Finland
6. Wandera C, Salminen A, Kujanpaa V (2009) Inert gas cutting of thick-section stainless steel and medium-section aluminum using a high power fiber laser. *J Laser Appl* 21:154–161
7. Scintilla LD, Tricarico L, Wetzig A, Beyer E (2013) Investigation on disk and CO<sub>2</sub> laser beam fusion cutting differences based on power balance equation. *Int J Mach Tools Manuf* 69:30–37
8. Poprawe R, Schulz W, Schmitt R (2010) Hydrodynamics of material removal by melt expulsion: perspectives of laser cutting and drilling. *Phys Procedia* 5:1–18
9. Wandera C, Kujanpaa V (2010) Characterization of the melt removal rate in laser cutting of thick-section stainless steel. *J Laser Appl* 22:62–70
10. Petring D, Schneider F, Wolf N, Nazery V (2008) The relevance of brightness for high power laser cutting and welding. In: *Proceedings of the 27th International Congress on Applications of Lasers & Electro-Optics*, Temecula, CA, USA, pp 95–103
11. Mahrle A, Beyer E (2009) Theoretical aspects of fiber laser cutting. *J Phys D Appl Phys* 42:507–515

12. Scintilla LD, Tricarico L, Mahrle A, Wetzig A, Beyer E (2011) Experimental investigation on the cut front geometry in the inert gas laser fusion cutting with disk and CO<sub>2</sub> lasers. In: Proceedings of the 30th international congress on applications of lasers & electro-optics (ICALEO), Orlando, FL, USA, pp 40–49
13. Powell J, Al-Mashikhi SO, Kaplan AFH, Voisey KT (2011) Fibre laser cutting of thin section mild steel: an explanation of the ‘striation free’ effect. *J Opt Lasers Eng* 49:1069–1075
14. Rao BT, Nath AK (2002) Melt flow characteristics in gas-assisted laser cutting. *Sadhana* 27:569–575
15. Karatas C, Keles O, Uslan I, Usta Y (2006) Laser cutting of steel sheets: Influence of workpiece thickness and beam waist position on kerf size and stria formation. *J Mater Process Technol* 172:22–29
16. Madhukar YK, Mullick S, Shukla DK, Kumar S, Nath AK (2013) Effect of laser operating mode in paint removal with a fiber laser. *Appl Surf Sci* 264:892–901
17. Ferreira SLC, Bruns RE, Ferreira HS, Matos GD, David JM, Brandao GC, da Silva EGP, Portugal LA, dos Reis PS, Souza AS, dos Santos WNL (2007) Box-Behnken design: An alternative for the optimization of analytical methods. *Anal Chim Acta* 597:179–186
18. Montgomery DC (2009) Design and analysis of experiments, 7th edn. Arizona State University, Willy India P. Ltd, pp 417–446
19. Design-Expert software (2000) V7, user’s guide, Technical manual. State-Ease Inc., Minnieapolis, MN
20. Scintilla LD, Tricarico L, Wetzig A, Mahrle A, Beyer E (2011) Primary losses in disk and CO<sub>2</sub> laser beam inert gas fusion cutting. *J Mater Process Technol* 211:2050–2061
21. Eltawahni HA, Olabi AG, Benyounis KY (2010) Effect of process parameters and optimization of CO<sub>2</sub> laser cutting of ultra high-performance polyethylene. *Mater Des* 31:4029–4038
22. Eltawahni HA, Hagino M, Benyounis KY, Inoue T, Olabi AG (2012) Effect of CO<sub>2</sub> laser cutting process parameters on edge quality and operating cost of AISI 316L. *Opt Laser Technol* 44:1068–1082

# Efficient Copper Micro Welding with Fiber Lasers Using Spatial Power Modulation



A. Haeusler, B. Mehlmann, A. Olowinsky, A. Gillner, and R. Poprawe

**Abstract** Joining of copper material in order to create a contact is an important task in electronics industry. Conventionally pulsed rod-based IR laser sources with low beam quality have a high energy input for welding copper due to large spot diameters. Fiber laser sources have high beam quality which allows small laser spots to be generated. Therefore, the threshold for deep penetration welding can be reached by using lower power. But when such small laser spots are used, the resulting connection area has to be enlarged. To achieve this, spatial power modulation has been introduced. The use of spatial power modulation—a linear feed with superposed circular motion—allows a significant expansion of process boundaries. The additional parameters of oscillation frequency and amplitude enable new strategies to control the laser welding process. This paper presents recent developments concerning process improvements and increase in efficiency by applying spatial power modulation. We discuss process regimes for spatial power modulation by analyzing the melt pool dynamic via high-speed videography. These regimes are an important aspect for process efficiency. Effects of heat conduction and spatial power modulation have been studied.

**Keywords** Laser micro welding · Spatial power modulation · Melt pool dynamics

## Notation

$A_s$	Oscillation amplitude [mm]
$f$	Focal length [mm]
$f_s$	Oscillation frequency [Hz]
$P$	Laser power [W]
$t$	Time [ms]

---

A. Haeusler (✉) · A. Gillner · R. Poprawe  
Chair for Laser Technology LLT, RWTH Aachen University, Steinbachstr. 15, 52074 Aachen, Germany  
e-mail: [andre.haeusler@ilt.fraunhofer.de](mailto:andre.haeusler@ilt.fraunhofer.de)

B. Mehlmann · A. Olowinsky · A. Gillner · R. Poprawe  
Fraunhofer Institute for Laser Technology ILT, Steinbachstr. 15, 52074 Aachen, Germany

© Springer Nature Switzerland AG 2022  
S. Hinduja et al. (eds.), *Proceedings of the 38th International MATADOR Conference*,  
[https://doi.org/10.1007/978-3-319-64943-6\\_15](https://doi.org/10.1007/978-3-319-64943-6_15)

U	Degree of overlap [-]
$v_f$	Feed rate [mm/s]
$\Phi$	Total oscillation angle [°]
$\varphi$	Periodical oscillation angle [°]

## 1 Introduction

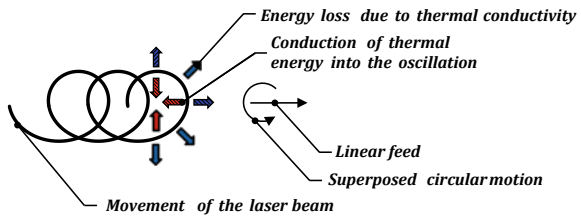
In laser beam welding for microtechnology applications, high brightness lasers – e. g. fiber lasers – are increasingly being used. When workable focusing conditions are applied, it is possible to obtain focal diameters of about several tens of micrometers. Those small focal diameters result, on the one hand, in advantageous smaller thermal energy input but, on the other hand, in lesser width of the weld seam. In an overlap joint welded by a high brightness laser beam, the connection area is small, which renders it less suitable for such applications. To increase the seam width and, thus, the strength of the connection, the line energy needs to be increased, resulting in a greater energy input per unit length.

To enlarge the cross section and to stabilize the welding process, spatial power modulation can be used. This means a linear feed with superposed circular oscillation, resulting in a stir movement. The circular oscillation is defined by an oscillation amplitude  $A_s$ , which is equivalent to the radius of a circle, and an oscillation frequency  $f_s$ . This technique was introduced by Martukanitz et al. [1] for laser macro welding with low feed rates ( $v_f \leq 33.3$  mm/s), low frequencies ( $f_s \leq 50$  Hz) and large amplitudes ( $A_s \leq 2$  mm). That technique already resulted in an enlarged fusion zone. The first usage of spatial power modulation with high brightness laser sources was published by Boglea et al. [2] for welding of plastic materials. The galvanometer scanners allowed for higher feed rates ( $v_f \leq 200$  mm/s), higher frequencies ( $f_s \leq 1$  kHz) and small amplitudes ( $A_s \leq 0.2$  mm), which are common for laser micro welding. This process was adapted for laser micro welding of metals and applied for a patent as SHADOW<sup>®</sup> welding using a Nd:YAG laser source [3] and for micro welding using a fiber laser [4, 5]. But due to the limitations of galvanometer scanners and necessary frequencies for higher feed rates, this technique is still limited to a few hundred mm/s [6].

In contrast to a conventional laser welding process, one using spatial power modulation can lead to a higher energy efficiency, which does not depend on the higher energy input, but on a better usage of the thermal energy inside the oscillation [6]. Figure 1 shows the movement of the laser beam by spatial power modulation including the effects of thermal conduction.

In this paper we observed the dynamic behaviour of the melt pool of CuSn6 by using high-speed videography. Additionally, we present the efficiency of the laser welding process with and without spatial power modulation.

**Fig. 1** Schematic sketch of the energy losses and conduction of thermal energy into the oscillation by spatial power modulation



## 2 Experimental Setup

The material used is CuSn6. The specimens were cut to the dimensions of 40 mm × 10 mm and had a thickness of 0.6 mm. The weld seam had a length of 15 mm. The relevant thermo-physical properties are summarized in Table 1.

The experiments were carried out using a SPI400C fiber laser with a central emission wavelength of 1070 nm and a maximum output power of 400 W. For each parameter set three welds were observed and compared. For beam positioning, focusing and creation of the circular motion, a galvanometric scanner (Newson A15) equipped with a f-theta lens (f = 163 mm) was used, which provides a theoretical focal diameter of 25 μm. The linear feed is provided by a linear axle. The high-speed camera is used, mounted non-coaxially at an angle of 12° normal to the sample. Figure 2 shows the experimental setup used.

So that the dynamics of the weld pool could be analyzed during a spatial power modulation of up to 2 kHz, all welds were observed at a frame rate of 30 kHz and a resolution of 768 × 320 px by a magnification up to 100×.

To analyze how the weld pool geometry is influenced by thermal conduction, a constant degree of overlap had to be maintained.

The degree of overlap U is defined [4] as

$$U = \frac{\sqrt{4A_s^2 - \left(\frac{v_f}{\pi \cdot f_s}\right)^2} - \frac{v_f}{2\pi \cdot f_s} \cdot \left(3\pi + 2 \cdot \arcsin\left(-\frac{v_f}{2\pi \cdot f_s \cdot A_s}\right)\right)}{\sqrt{4A_s^2 - \left(\frac{v_f}{\pi \cdot f_s}\right)^2} - \frac{v_f}{2\pi \cdot f_s} \cdot \left(\pi + 2 \cdot \arcsin\left(-\frac{v_f}{2\pi \cdot f_s \cdot A_s}\right)\right)} \quad (2.1)$$

where  $A_s$  is the oscillation amplitude,  $f_s$  the oscillation frequency and  $v_f$  the linear feed rate. At a constant degree of overlap, the oscillation amplitude is inversely proportional to the oscillation frequency.

**Table 1** Material properties of CuSn6 [7]

Material properties	CuSn6
Thermal conductivity [W/(m K)]	75
Solidus temperature [°C]	900
Liquidus temperature [°C]	1050

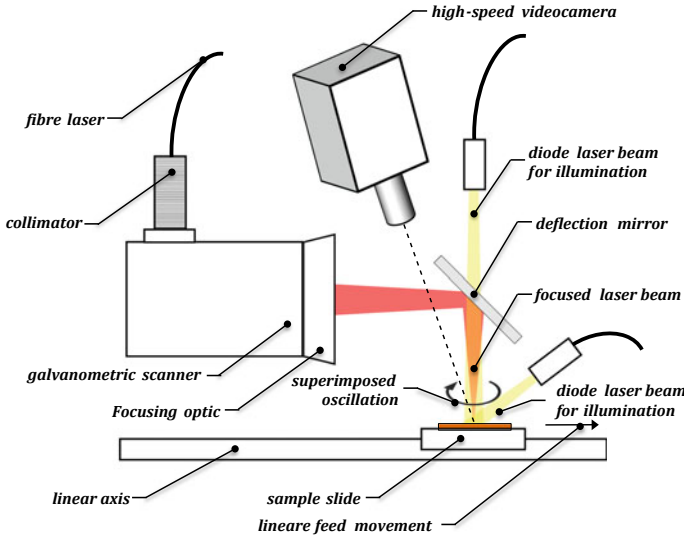
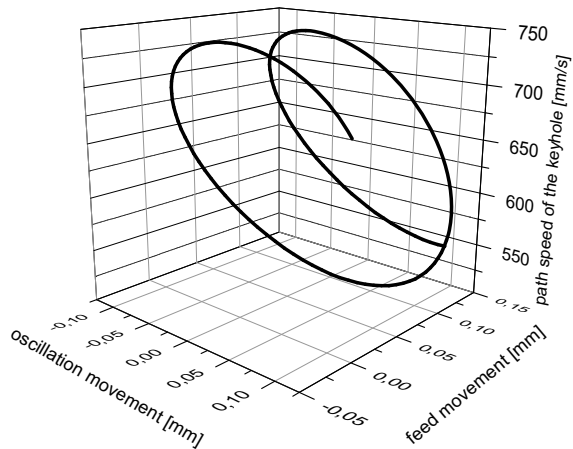


Fig. 2 Schematic sketch of the experimental setup

The actual spiral path of the keyhole is asymmetrical. This asymmetry leads to a higher speed of the keyhole (path speed) in the direction of the linear feed rate, which causes a lower energy input per unit length by the laser beam. Figure 3 shows the difference of the path speed of the keyhole at  $v_f = 75$  mm/s,  $A_s = 0.1$  mm and  $f_s = 1000$  Hz.

Even for small oscillation amplitudes ( $A_s \leq 0.1$  mm) at a feed rate of 75 mm/s, differences arise: about a 20% increase or decrease in the path speed of the keyhole. The constant power input results because of the different path speed of the keyhole

Fig. 3 Difference in the path speed of the keyhole by using spatial power modulation



in a various energy input per unit length, which can influence the behaviour, the geometry and the size of the melt pool decisively.

The parameters in the experiments, the oscillation amplitude and the oscillation frequency, were varied at a constant degree of overlap ( $\approx 0.5$ ). The experiments were evaluated by measuring of the molten pool area manually, in order to identify process regimes and to correlate these to the process efficiency. The efficiency was evaluated by preparing cross sections of the welds. In addition to the observations made using a high-speed video camera, recordings by a high-speed infrared camera with a maximum frame rate of 1 kHz ( $160 \text{ px} \times 128 \text{ px}$ ) were made.

### 3 Results Concerning the Observed Melt Pool Behaviour

When of the molten pool area is observed with high-speed videography during the laser welding process without spatial power modulation, a growth state can be seen at the beginning, followed by a balanced state (cf. Fig. 4).

At the beginning of the laser welding process, the molten pool area grows during a time of 2 ms up to about  $90,000 \mu\text{m}^2$ . After this time molten pool area remains constant. Figure 5 shows the molten pool area in relation to the oscillation angle of the spatial power modulation.

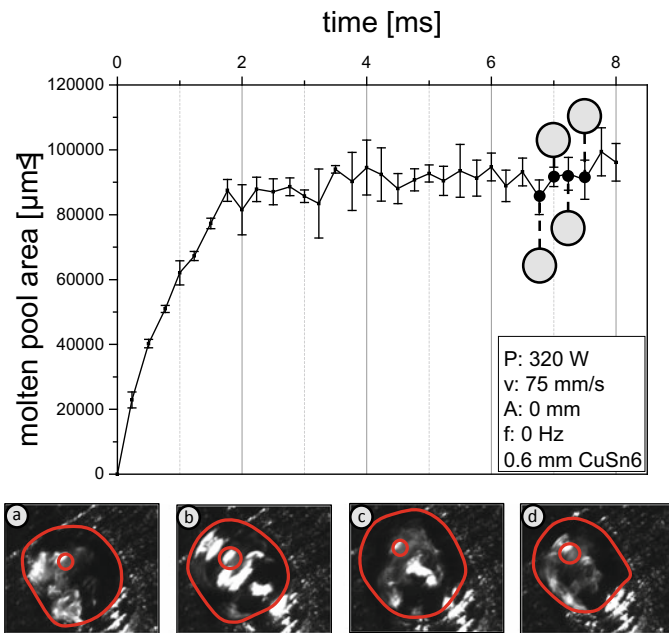
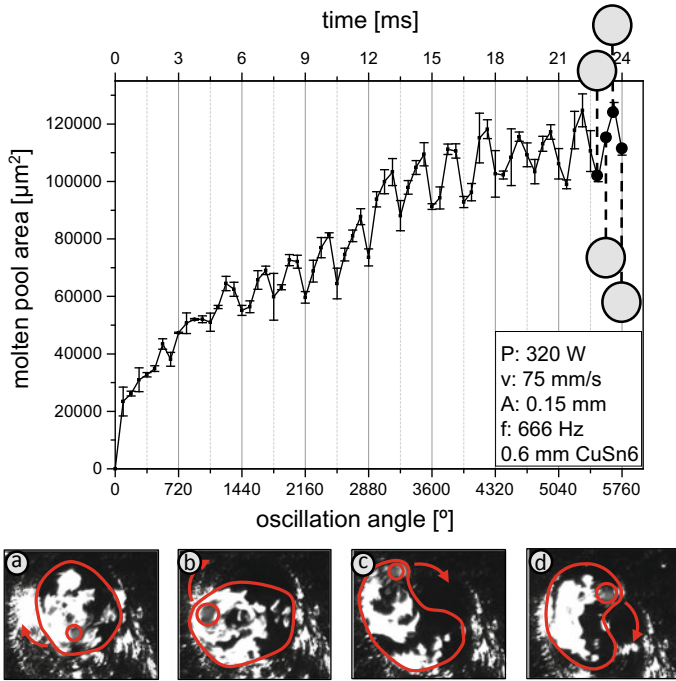


Fig. 4 Measured molten pool area over time for welds without spatial power modulation





**Fig. 5** Measured molten pool area over time for welds with spatial power modulation ( $A_s = 0.15$  mm;  $f_s = 666$  Hz)

In this case the growth state is much more pronounced than in welding without spatial power modulation. The molten pool area grows significantly up to an amount of about  $115,000 \mu\text{m}^2$  by an oscillation angle of  $4,320^\circ$  after which it oscillates around a mean value. Noticeable is the sinusoidal shape of the measured molten pool area over time, which passes through a local maximum and minimum during one oscillation. The molten pool area reaches a local maximum at  $90^\circ$  to  $180^\circ$  and falls to a minimum at  $270^\circ$ . The extrema are repeated every  $360^\circ$ .

Since the size and the circulation of the melt pool are so large, it is important to note the existence of a phase shift between melt pool area and keyhole path speed. The area and the circulation of the melt pool are shown in Fig. 6.

The observation shows the melt pool following the keyhole path speed continuously with a phase shift of about  $90^\circ$ .

The local maximum is created because of two boundary conditions. On the one hand, the path speed (cf. Fig. 6) reaches the maximum within an angle range of  $0^\circ$  to  $180^\circ$ . This leads to a larger expansion of the melt pool in the feed direction, which results in a larger melt pool area but also in a lower welding depth, based on the tilting of the keyhole [8]. On the other hand, because the path of the molten pool crosses an already melted and resolidified area, a more efficient use of the thermal

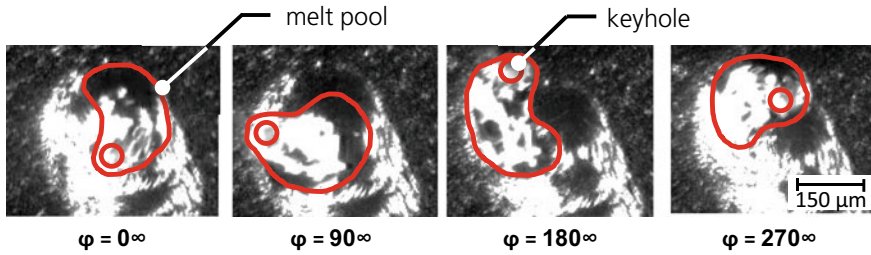


Fig. 6 Phase shift between melt pool and keyhole

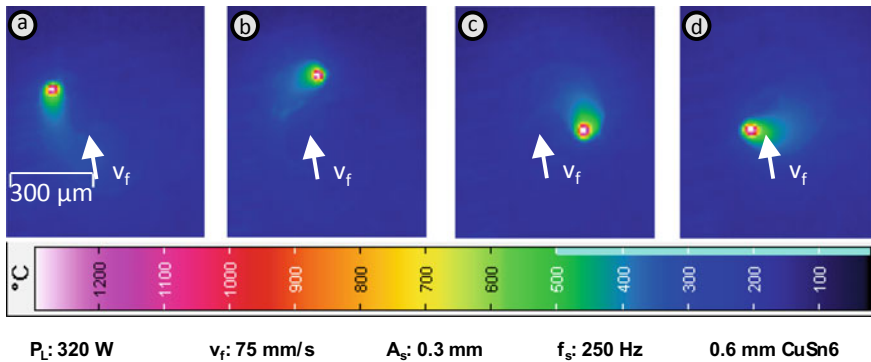
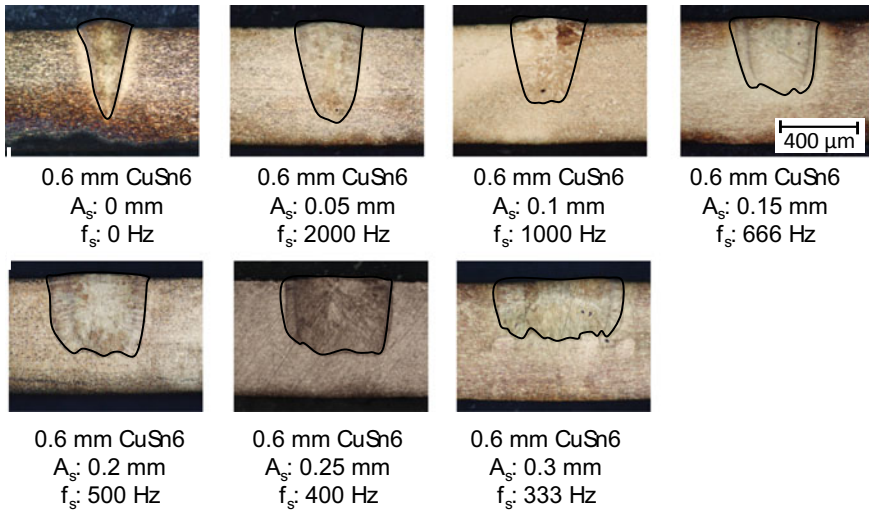


Fig. 7 Thermographic images of welding CuSn6 with the usage of spatial power modulation

energy takes place. This can be observed within an angle range of  $-45^\circ < \varphi < 45^\circ$ , while within an angle range of  $135^\circ < \varphi < 225^\circ$ , the melt pool on the surface shrinks.

Figure 7 shows high-speed thermographic images of welding CuSn6 with spatial power modulation. Because the different emission ratios are caused by the angle dependence of the emission and other physical conditions, the following results are only qualitative.

As the image (a) shows, a larger heating area is detected along the path of the keyhole. This is due to the higher speed along the path of the keyhole at this part of the oscillation. This results in a larger molten pool area at the surface of the weld seam. In image (b) a faster heat dissipation of the molten pool and the surrounded material, compared to image (a), is detected. These lower temperatures and the smaller size of the molten pool arise as a result of the material being molten for the first time. In image (c) the heating area gets larger because of the reduced speed during this part of the oscillation. In image (d) the melt pool becomes resolidified material, which has a higher temperature. For this reason the expansion of the area with a higher temperature is much bigger compared to the other images. The keyhole in the images (b) and (d) has the same speed along the path of the oscillation. The comparison between these two images show the much bigger heating area, which arises as it passes an area where material is already resolidified.



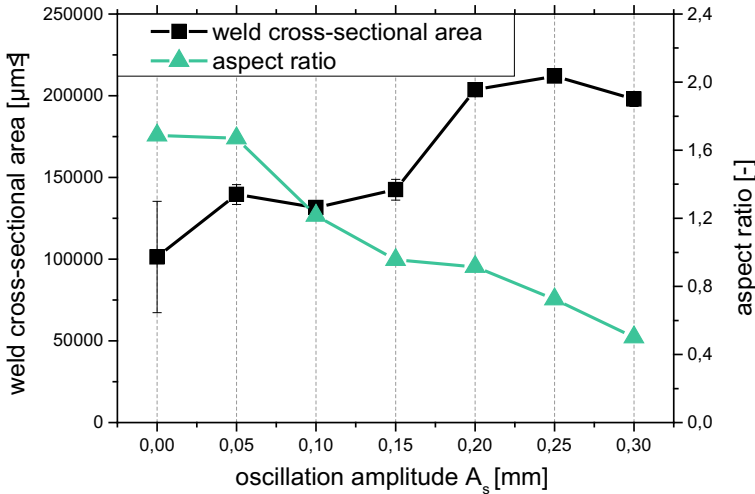
**Fig. 8** CuSn6 cross sections of welds by different spatial power modulation

Figure 8 shows the cross sections of the welds of CuSn6 made using different oscillation parameters. The weld made without using spatial power modulation is characterized by a high aspect ratio; this means the ratio of weld depth to weld width is high.

To keep the degree of overlap constant, the oscillation amplitude was increased and the oscillation frequency decreased, which, in turn, lowered the aspect ratio. On the one hand, the weld depth decreased, while on the other, the weld width increased because of the higher oscillation amplitude. Figure 9 presents the evaluation of the cross sections of CuSn6. The aspect ratio decreased linearly as expected with an increase of the oscillation amplitude. The weld cross-sectional area increased with a rising oscillation amplitude. At lower oscillation amplitudes ( $A_s \leq 0.15$  mm), a small increase in the cross-sectional area could be detected. When the oscillation amplitude was further increased, the cross-sectional area rose rapidly up to about  $210,000 \mu\text{m}^2$  at an amplitude of 0.25 mm. This maximum in the cross-sectional area indicates that the thermal energy input was used more efficiently at larger oscillation amplitudes for examined amplitudes up to 0.3 mm.

The analyses of the welding process with spatial power modulation via high-speed videography generally showed three different regimes of the molten pool. These different regimes are presented in Fig. 10.

For the stationary molten pool, the molten pool only moved with the linear feed, and the keyhole circulated continuously inside the molten pool. In this case, the diameter of the molten pool was the same as the width of the weld seam on the surface. A weaving molten (Fig. 10b) pool arises if the molten pool moves orthogonally to the feed movement. The diameter of the molten pool was smaller than the width of the weld seam. A circulating molten pool (Fig. 10c) can be observed if the molten



**Fig. 9** Evaluation of the cross sections of CuSn6 regarding the weld cross-sectional area and the aspect ratio

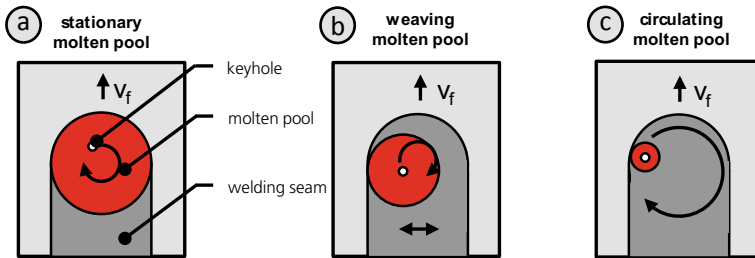


**Fig. 10** Regimes for the molten pool by laser welding of CuSn6 with spatial power modulation: **a** stationary molten pool, **b** weaving molten pool, **c** circulating molten pool

pool follows the keyhole along its path. Here the width of the molten pool was much smaller than the width of the weld seam.

These movement types depend very much on the characteristic variables of the welding process. It can be assumed that when the thermal conductivity, oscillation amplitude or the feed movement rise, a more circulating molten pool is generated. Also it can be assumed that a more stationary molten pool is caused by higher laser power or a higher oscillation frequency. Obviously, not only is a modification of the process parameters able to change the movement types of the molten pool, but the movement types also change during the whole laser welding process. At the beginning of this process, when spatial power modulation is used, right after the formation of the keyhole, a circulating molten pool could always be observed. The characteristic variables determine if the movement types of the molten pool will be maintained or changed into other types until a constant behavior can be detected.

When not only the melt pool is observed via high-speed videography but also the change of the parameters oscillation amplitude and frequency, a course of the movement types can be plotted. This is shown in Fig. 11.

The movement types stationary and circulating are separated by the movement type weaving. In the range of small oscillation frequencies, the movement type is determined by the molten pool area which would occur during laser welding without spatial power modulation. If the radius of the molten pool was smaller than the oscillation amplitude, a circulating molten pool was observed, otherwise a stationary one was. The boundary between stationary and circulating molten pool reached a minimum at an oscillation frequency of 750 Hz. Because path speed of the keyhole rose at higher oscillation frequencies, as it also did for large oscillation amplitudes, a stationary molten pool was observed.

The results show that, when spatial power modulation is used, laser welding produces large differences in the molten pool area during a single oscillation. As the cross sections demonstrate, this fact is reflected in the cross sectional area, too. Figure 12 shows the correlation between the maximum of the molten pool area and the cross sectional area of the welds.

As the figure shows, the graph of the maximum molten pool area and the maximum cross-sectional area are similar to each other. By using oscillation amplitudes  $< 0.2$  mm, the molten pool area fluctuated around a constant value without a significant rise, much like it did in the cross-sectional area. Oscillation amplitudes  $\geq 0.2$  mm caused a rise in the cross-sectional area and the molten pool area up to a maximum at  $A_s = 0.25$  mm.

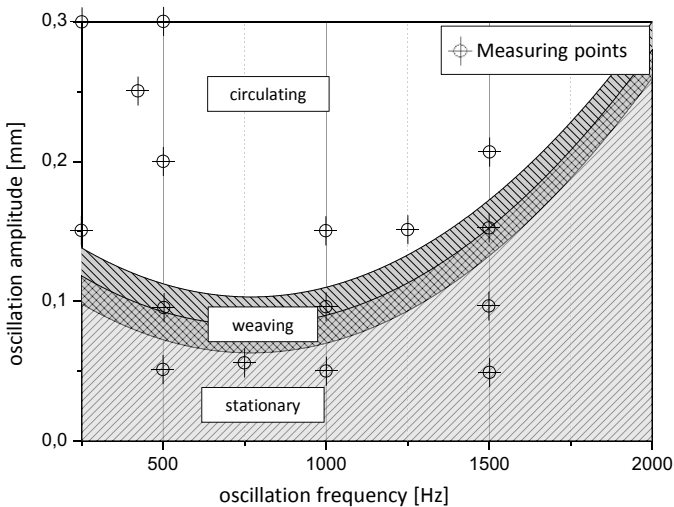


**Fig. 11** Assumed course of the movement types of the molten pool in relation to the oscillation frequency and the oscillation amplitude for this experimental setup

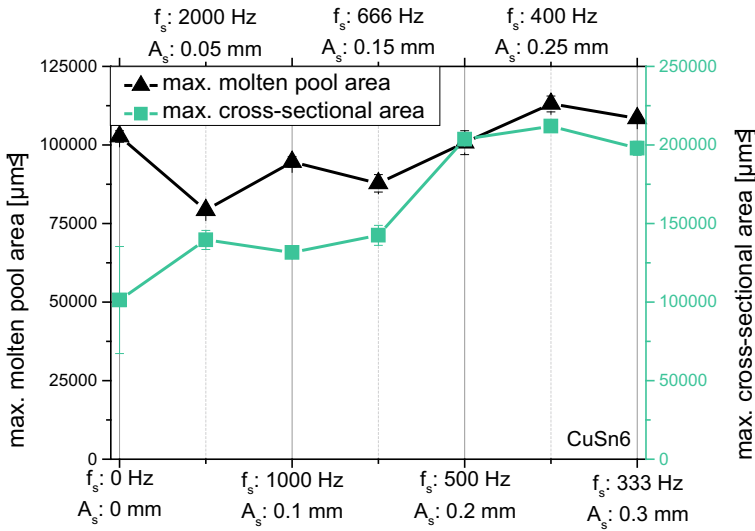


**Fig. 12** Correlation of the maximum molten pool area and the maximum cross-sectional area when welding CuSn6

The results show the largest melt pool area was detected within a keyhole position at an angle range of  $0^\circ$  to  $90^\circ$ . This angle range of the oscillation is responsible for the final size of the welded cross-section. In the area where the molten pool crosses over already molten and resolidified material, a larger thermal energy exists. This rise in the thermal energy is caused by a higher temperature, which leads to the maximum size of the molten pool area.

Figure 13 shows the longitudinal sections of CuSn6 by using different oscillation parameters.

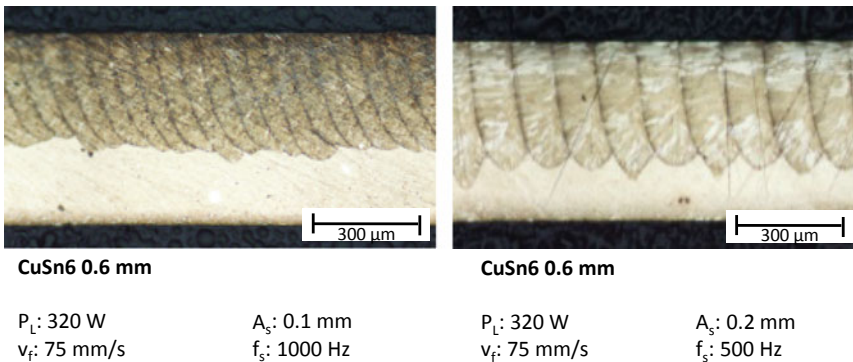


**Fig. 13** Longitudinal sections of CuSn6 by using different oscillation parameters

The longitudinal section of CuSn6 with an oscillation amplitude of 0.1 mm (Fig. 13 left) shows that the material melts entirely between the individual oscillations. Nevertheless, the figure of the longitudinal section shows a fluctuation of the weld depth due to process instabilities. By an increase of the oscillation amplitude to 0.2 mm, a higher fluctuation of the weld depth can be observed (Fig. 13 right). Because of the distance between the individual oscillation and the high heat conductivity, the area between the oscillations was not melted completely. This causes a higher fluctuation of the weld depth of about 20%.

## 4 Results Concerning the Process End

More information about melt pool behaviour can be gained by observing the solidification at the end of the weld seam. Figure 14 shows the setting behaviour of the melt pool during laser welding of CuSn6 with and without spatial power modulation for  $v_f = 75$  mm/s,  $P = 320$  W,  $A_s = 0,15$  mm and  $f_s = 666$  Hz. The laser power is switched off at the time  $t_0 = 0$  s.

Even though the highest temperature and the biggest molten volume are located at the front of the weld seam next to the keyhole, the center of the last molten volume moves opposite to the feed direction. Without spatial power modulation the distance between the position of the last molten volume and the last position of the keyhole was only about 100  $\mu\text{m}$ , whereas the distance with spatial power modulation increased up to about 200  $\mu\text{m}$ .

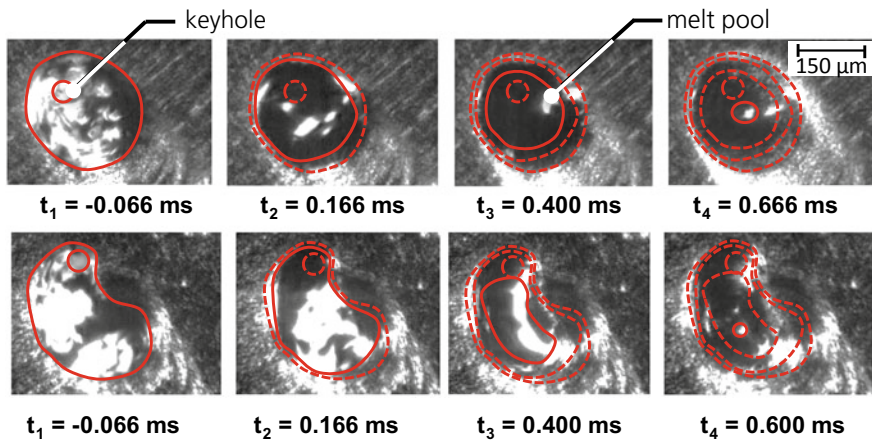


**Fig. 14** Solidification behaviour of CuSn6: Welding without spatial power modulation (top); welding with spatial power modulation (bottom). The dashed lines show the prior expansion of the molten pool

## 5 Conclusions

- 1 The usage of spatial power modulation during laser welding of CuSn6 caused a larger molten pool area with a sinusoidal shape during the individual oscillations by a degree of overlap of  $\approx 0.5$ .
- 2 The efficiency during laser welding was increased by using spatial power modulation, because the cross-sectional area increases by a factor of two at constant energy input per unit length.
- 3 The longitudinal sections of the weld seam of CuSn6 showed that the fluctuation of the weld depth rose when the oscillation amplitude was increased by using spatial power modulation.
- 4 The movement of the melt pool can be separated in the three different movement types: stationary, weaving and circulating. The parameters heat conductivity, laser power, oscillation amplitude, oscillation frequency and feed rate have an effect on the movement of the melt pool.
- 5 A better efficiency during laser welding with spatial power modulation depends on the movement of the melt pool. During the spatial power modulation with a stationary melt pool, no rise in efficiency could be observed. A circulating melt pool led to a sinusoidal shape and a rise of the molten pool area which was directly linked to the cross-sectional area of the weld.

**Acknowledgements** All presented investigations were conducted in the context of the Collaborative Research Centre SFB 1120 project A1 and were funded by Deutsche Forschungsgemeinschaft e. V. (German Research Foundation).

## References

1. Martukanitz R, Stol I, Tressler JF, Warren CJ (2005) Development of the laser stir welding process for aluminum laser beam welding. In: ICALEO 2005: Congress proceedings 2005, Miami, Florida, October 31–November 3. Laser Institute of America, Orlando, FL, pp 712–718 (LIA pub; #598, vol 98)
2. Boglea A, Bosse L, Olowinsky A, Bou S (2006) Fiber laser pick-and-join tool for welding of thermoplastics. In: ICALEO 2006: Congress proceedings 2006, Scottsdale, AZ, USA, October 30–November 2. Laser Institute of America, pp 383–388 (LIA pub; #599, vol 99)
3. Gedicke J, Olowinsky A, Artal J, Gillner A (2007) Influence of temporal and spatial laser power modulation on melt pool dynamics. In: 26th International congress on applications of lasers and electro-optics: ICALEO 2007, October 29 –November 1, 2007, Orlando, Florida, USA. Laser Institute of America, Orlando, FL, pp 816–822
4. Gedicke J, Olowinsky A, Mehlmann B (2010) Laser beam welding of DCB substrates. In: 11th international symposium on laser precision microfabrication (LPM), June 7–10, 2010 in Stuttgart, Germany
5. Schmitt F, Mehlmann B, Gedicke J, Olowinsky A, Gillner A, Poprawe R (2010) Laser beam micro welding with high brilliant fiber lasers. *J Laser Micro/Nanoeng* 5(3):197–203
6. Schmitt F (2012) Laserstrahl-Mikroschweißen mit Strahlquellen hoher Brillanz und örtlicher Leistungsmodulation [Dissertation]. Aachen



7. Deutsches Kupferinstitut (2005) DKI—Werkstoffkennblätter
8. Chang C (2000) Berechnung der Schmelzbadgeometrie beim Laserstrahlschweißen mit Mehrfokustechnik: Herbert Utz Verlag München

# Laser Micro Welding of Copper on Lithium-Ion Battery Cells for Electrical Connections in Energy Storage Devices



Paul Heinen, Andre Haeusler, Benjamin Mehlmann,  
and Alexander Olowinsky

**Abstract** Lithium-ion battery cells are increasingly being used as energy storage devices for electrically powered vehicles on account of their high energy density. Individual cells need to be connected electrically in order to make suitable battery packs. 18650-type cells—mainly used in notebooks and power tools—provide an ideal solution thanks to their low price and ready availability. Due to the comparably low capacity several cells must be connected in parallel to create larger cells. To guarantee long term stability overheating has to be avoided (degradation of the cells). Cooling below 0 °C lowers the energy output of cells. Hence Fraunhofer designed a battery concept for EV applications, in which cells are stored in a phase change material (PCM) which can buffer heat. The PCM has to be encapsulated in small leakage-free sub-units. A copper current collector is welded in overlap on the top of the battery can—the negative pole—made out of nickel-plated DC04 steel. The welding is done while the cell is charged and filled with the cathode and anode material, the separator and the liquid electrolyte. The copper collector is also used to encapsulate the PCM, therefore the weld must be liquid-tight. In this paper the laser micro welding process of copper material and 18650 cells is analyzed to describe the influence of process parameters (laser power, welding speed, spatial power modulation) on the resulting connection. The joint is characterized concerning reproducible tightness, electrical resistance, mechanical stability and possible damage to the cell.

---

P. Heinen (✉) · B. Mehlmann · A. Olowinsky  
Fraunhofer Institute for Laser Technology ILT, Steinbachstraße 15, 52074 Aachen, Germany  
e-mail: [paul.heinen@ilt.fraunhofer.de](mailto:paul.heinen@ilt.fraunhofer.de)

A. Haeusler  
Laser Technology LLT, RWTH Aachen University, Steinbachstraße 15, 52074 Aachen, Germany

**Keywords** Laser micro welding · Liquid-tight · 18650 Battery cells

## Nomenclature

$P$	Laser power [W]
$v_s$	Welding speed [mm/s]
$A_o$	Oscillation amplitude [mm]
$F$	Frequency [Hz]
$A$	Absorption coefficient [–]
$T_M$	Melting point [°C]
$T_V$	Evaporation temperature [K]
$w_F$	Focal radius [ $\mu\text{m}$ ]
$Pe$	Peclét number [–]
$\lambda_{th}$	Thermal conductivity [W/(m K)]
$\rho$	Density [ $\text{g}/\text{cm}^3$ ]
$c_p$	Specific heat capacity [J/(g K)]
$\kappa$	Thermal diffusivity [ $\text{mm}^2/\text{s}$ ]
$E_S$	Energy per section [J/mm]
WD	Weld depth [ $\mu\text{m}$ ]
CW	Connection width [ $\mu\text{m}$ ]
$c_{pk}$	Process capability index [–]

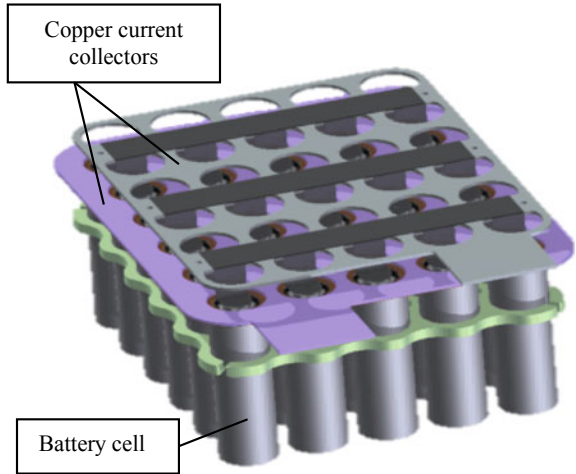
## 1 Introduction

Due to the high energy density of Lithium-ion battery cells of 18650-type (in this case 162 Wh/kg) the usage in energy storage devices increases. Furthermore these cells offer ready availability and low prices. To reach high and suitable energy capacity several of the cells have to be connected in parallel. The electrical connection is realised with overlap welding of a CuSn6 sheet on the nickel plated DC04 steel after production in charged and assembled state of the battery cells [1].

The major challenge in welding of batteries is melting both parts—here the CuSn6 sheet on top and the battery can on the bottom—without damaging the can and causing the electrolyte to leak or without damaging the seal.

For the use in electrically powered vehicles a light weight energy storage device has been designed by Fraunhofer in which 4800 Li-Ion cells of form-factor 18650 are connected. The capacity of the full pack is 36 kWh with a Voltage of about 300 V. To reach these values the battery cells have to be connected in parallel and serial configuration. Thirty cells are connected in parallel through a copper current collector (Fig. 1). This configuration is called a block. As a stable welding connection of a 1.5 mm thick copper sheet (Cu-OF) to a 0.3 mm thick metal part (DC04, battery

**Fig. 1** Block consisting of 30 parallel connected cells



can) is not possible, but necessary, to reach the desired conducting cross-section of  $A = 50 \text{ mm}^2$ , welding of a thin copper sheet (0.2 mm thickness, CuSn6) is used as the direct connection to the battery can. This sheet is welded to the thick copper connector. Eighty of these blocks are connected in series.

Inside a block and between the cells a PCM-slurry is being stored. For the design of the block to work, both terminals of the cells have to be connected from the top side. Therefore the welding of the negative terminal has to be conducted on a bent surface of the can. Due to the usage of PCM-slurry the connection has to be liquid tight.

The approach to these challenges for the weld joint of the negative pole and the results of experimental evaluations of the weld are presented in this paper.

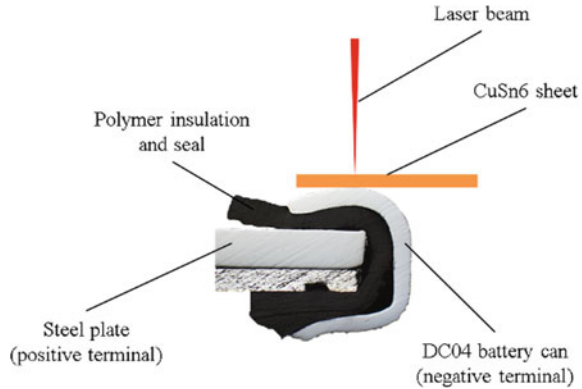
## 2 Workpiece Description, Layout of Needed Seam Parameters and Experimental Setup

In this chapter the description of the workpiece and welding task will be presented. Furthermore a theoretical consideration and pre-selection of welding parameters will be shown. The last part of this chapter is the description of the experimental setup and the analysis of specific used machine components.

### 2.1 Workpiece Description

The dissimilar material connection at the negative terminal was realized in overlap configuration with copper as the upper joining partner (Fig. 2). Below the DC04

**Fig. 2** Joining configuration



steel a polymer layer is used to insulate both terminals and seal the battery can. Furthermore the polymer layer holds the positive terminal in place.

### 2.2 Determination of Necessary Welding and Seam Parameters

Due to the high reflectivity ( $R = 97\%$ , [3]) of copper for laser beam radiation with a wavelength of 1070 nm high intensity is needed to create a stable keyhole welding process. That leads to the choice of a different copper alloy. For the calculation of the deep penetration power threshold formulas 2.1, 2.2 and 2.3 are used with the material data shown in Table 1. For a comparable calculation of the threshold of the deep penetration effect, measured values from [4] are used: CuSn6 ( $A = 7.9\%$ ), Cu ( $A = 6.3\%$ ) [5].

$$P_{DP, \min} = 2 \cdot \sqrt{\pi} \cdot \frac{T_V \cdot \lambda_{th} \cdot w_f}{A} \sqrt{\frac{Pe}{2} + 1.1} \tag{2.1}$$

$P_{DP, \min}$  minimal needed power to reach deep penetration threshold  
 $T_V$  evaporation temperature

**Table 1** Material properties used for calculating the power to reach deep penetration welding [4, 7, 8]

Material	Cu-OF	CuSn6
Absorptivity $A$ [%]	6.3	7.9
Thermal conductivity $\lambda_{th}$ [W/(m K)]	390	75
Density $\rho$ [kg/m <sup>3</sup> ]	8930	8820
Specific heat capacity $c_p$ [J/(kg K)]	390	377
Evaporation temperature $T_V$ [K]	2840	2843

- $\lambda_{th}$  thermal conductivity
- $w_f$  focal radius
- $A$  absorption coefficient
- $Pe$  Peclét number

$$Pe = \frac{w_f \cdot v_S}{\kappa} \tag{2.2}$$

- $Pe$  Peclét number [6]
- $w_f$  focal radius
- $v_S$  welding speed
- $\kappa$  thermal diffusivity

$$\kappa = \frac{\lambda_{th}}{\rho \cdot c_p} \tag{2.3}$$

- $\kappa$  thermal diffusivity
- $\lambda_{th}$  thermal conductivity
- $\rho$  density
- $c_p$  specific heat capacity.

With the given formulas the deep penetration power threshold is calculated as  $P_{DP,min,CuSn6} = 85 \text{ W}$  for CuSn6 and  $P_{DP,min,Cu} = 556 \text{ W}$  for Cu. With an increase in the welding speed the threshold increases slightly (Fig. 3). The difference in the deep penetration threshold between Cu and CuSn6 clarifies why CuSn6 has to be used for the connection of the cell and the copper connector.

**Fig. 3** Calculated deep penetration power threshold

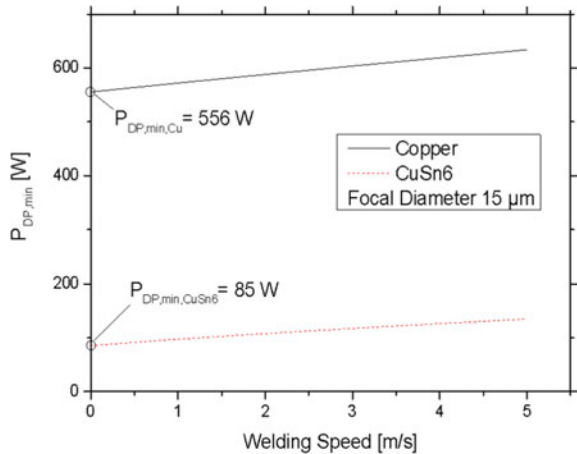


**Table 2** Electrical and mechanical properties of the used materials

Material	Cu-OF	Nickel	DC04 (1.0338)	CuSn6
Conductivity $\sigma$ [S*m/mm <sup>2</sup> ]	58	11.6	7.7	9
IACS** [%]	100	20	13	16
Increase factor $IF$ [–]	1	5	7.7	6.3
Tensile strength, yield, $R_{p0,2}$ [MPa]	33.3	59	210	193

A focusing optic with a focal length of 80 mm is used to reach a small focal diameter and reduce the needed power for the deep penetration threshold.

The absorption in the steel is much higher than in copper and the penetration depth is much higher as well. An appropriate strategy to reduce spiking effects<sup>1</sup> has to be chosen. Spiking means a spontaneous increase in the welding depth and results from melt pool dynamics [2]. A penetration depth of less than 200  $\mu\text{m}$  does not connect both parts and a penetration depth of more than 500  $\mu\text{m}$  leads to damage of the cell or the sealing.

The connection width can be estimated by the following approach: The conducting cross-section has to be  $A = 50 \text{ mm}^2$  for copper for the full energy pack. Therefore each conducting part in the serial connection has to reach the same conductivity. In the considered joining configuration  $n_{cells} = 30$  Li-Ion-battery-cells are connected in a parallel configuration. Thus each connection has to reach at least  $1.67 \text{ mm}^2$  of copper equivalent conducting area. With a diameter  $d_{seam} = 16.5 \text{ mm}$  for the weld seam, the seam width has to be at least  $b_{seam,elec} = 32 \mu\text{m}$  (Formula 2.4).

$$b_{seam,elec} = \frac{A}{n_{cells} * l_{seam}} = \frac{A}{n_{cells} * \pi * d_{seam}} \quad (2.4)$$

- $b_{seam,elec}$  needed seam width to reach electrical requirements  
 $A$  needed conducting cross section  
 $n_{cells}$  number of parallel cells  
 $l_{seam}$  seam length  
 $d_{seam}$  seam diameter.

The materials involved are Cu-OF, Nickel (as coating), DC04 and CuSn6. To reach the same conductivity for all connections as a first approximation an increase in the conducting cross-section by the reciprocal value of the IACS<sup>2</sup> is seen as sufficient (Table 2).

With the highest given increase factor  $IF, \max = 7.7$  at least a connection width of  $b_{seam,min,elec} = 246 \mu\text{m}$  is needed (Formula 2.5).

$$b_{seam,min,elec} = b_{seam,elec} \cdot IF_{\max} \quad (2.5)$$

<sup>1</sup> Spiking effects means a spontaneous increase in the welding depth and results from different incoupling behavior and melt pool dynamics (1).

<sup>2</sup> International annealed copper standard.

$b_{seam,min,elec}$	minimal needed seam width to reach electrical requirements
$b_{seam,elec}$	needed seam width to reach electrical requirements
$IF_{max}$	maximal increase factor.

Due to the cooling with the PCM-Slurry and the required tightness to avoid short-circuiting a sealed volume is generated. During charging and loading of the cells the PCM has a thermal expansion which results in a pressure increase of 0.4 bar. The area which has to bear the pressure is 13,200 mm<sup>2</sup>. This results in a force of  $F_{max} = 530$  N. Assuming that the force is divided equally on all 30 seams a force of  $F_{seam} = 18$  N will be applied to each seam. The needed minimal connection width to bear this force is calculated with the tensile strength of copper (33.3 MPa) and a seam diameter  $d_{seam} = 16.5$  mm as  $b_{seam,min,mech} = 10$  μm (Formula 2.6).

$$b_{seam,min,mech} = \frac{F_{seam}}{R_{p0,2} * \pi * d_{seam}} \tag{2.6}$$

$b_{seam,min,mech}$	minimum necessary seam width to reach mechanical requirements
$F_{seam}$	force applied to the seam
$R_{p0,2}$	Tensile Strength, Yield
$d_{seam}$	seam diameter.

As the necessary connection width to meet the electrical requirements ( $b_{seam,min,elec} = 246$  μm) is much higher than the necessary connection width for the mechanical requirements,  $b_{seam,min,elec}$  is the critical process limit.

Due to the natural deviation of the process the weld depth and connection width have to be increased or decreased by a proper safety margin. The necessary safety margin is determined experimentally.

### 2.3 Theoretical Approach for Welding Experiments

Due to the material combination CuSn6 on DC04 and the process requirements (seam width, weld depth) simple weld strategies are not sufficient to reach high process capability and stability.

The chosen approach in this application was spatial power modulation where the global beam feed is superposed with an oscillating movement (Fig. 4).

By the lateral movement of the laser beam the seam width is increased as well as the connection width. Furthermore the superposed oscillation leads to a decrease in the weld depth. In general a different deposition of the laser power can be seen by use of spatial power modulation compared to welding without oscillation (Fig. 5). Therefore the seam has more a “U”-shape than the typical “V”-shape. This is due to the movement of the keyhole through the material perpendicular to the global feed rate.

The use of spatial power modulation allows a more precise control of the welding depth [12, 13]. With high degrees of overlap the heat accumulation can be used to



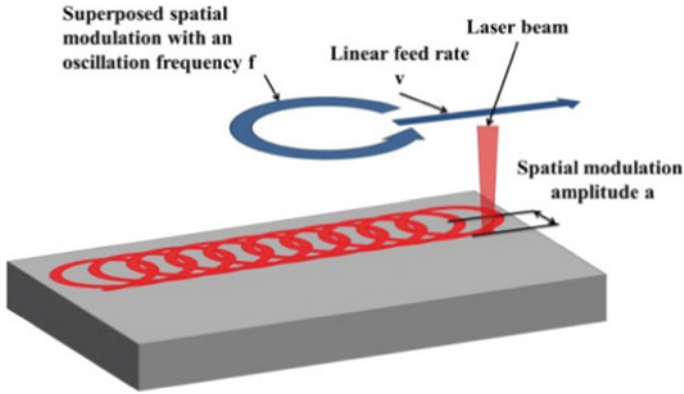
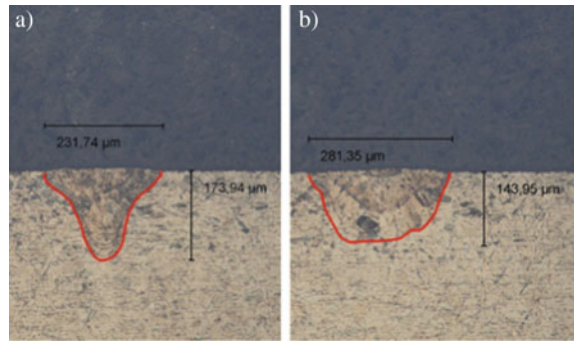


**Fig. 4** Diagram of spatial modulation incl. necessary parameters [11]

**Fig. 5** Influence from spatial power modulation on seam width and weld depth,  $P = 200$  W,  $v_S = 100$  mm/s, **a** no spatial power modulation, **b**  $A = 0,1$  mm,  $f = 1000$  Hz



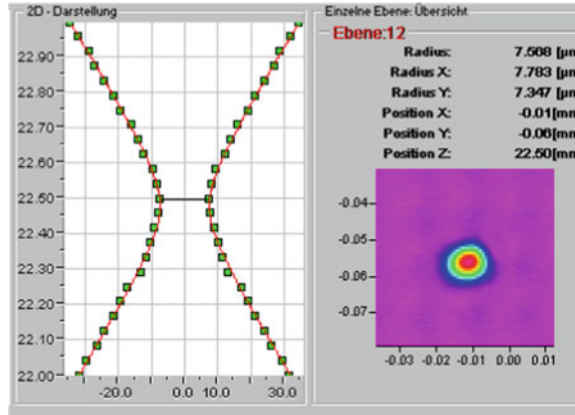
adapt the seam form and generate seams without interruptions in the surface [14]. Furthermore the gap bridging ability can be increased by melting more material, which is needed due to the bent surface of the DC04 battery can [14].

## 2.4 Experimental Setup

The experimental setup consisted of a 400 W single mode fiber laser and a 3D axis gantry to position the laser scanning head. Adapted to the scanning head was a camera for the manual positioning.

For the welding of each battery cell the scanner was positioned over the center of the battery cell and the contour was welded afterwards. Welding of multiple battery cells without repositioning of the scanner was not possible as the working area of the chosen lens (80 mm focal length) is too small ( $40 \times 40$  mm<sup>2</sup>). The measured

**Fig. 6** Results of caustic measurement of the chosen setup



focal diameter of the used experimental setup was  $d_F = 15 \mu\text{m}$  and the Rayleigh-length  $z_R = 0.12 \text{ mm}$  (Fig. 6). The intensity distribution was nearly Gaussian normal distribution with  $M^2 = 1.1$ .

An analysis of the scanning system was performed with a constant feed rate and low laser power in order to determine the system characteristics for the usage of spatial power modulation. The path was marked on a piece of metal. The distance of the marked loops was measured and therefore the reached frequency and amplitude were measured. The frequency analysis showed that the reached frequency was close to the setpoint frequency (Fig. 7).

With an increase in the oscillation frequency a decrease in the reached amplitude was observed (Fig. 8).

The decrease factor (DF) of the amplitude is calculated for an oscillation frequency of 1000 Hz and oscillation amplitudes from 50 to 200  $\mu\text{m}$ . DF for these values reaches

**Fig. 7** Results of frequency analysis

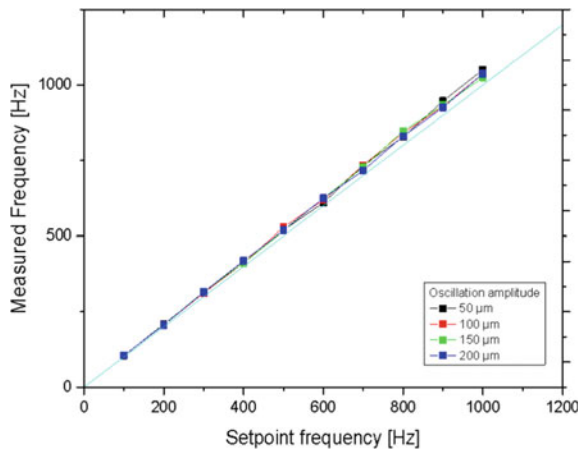


**Fig. 8** Results of amplitude analysis

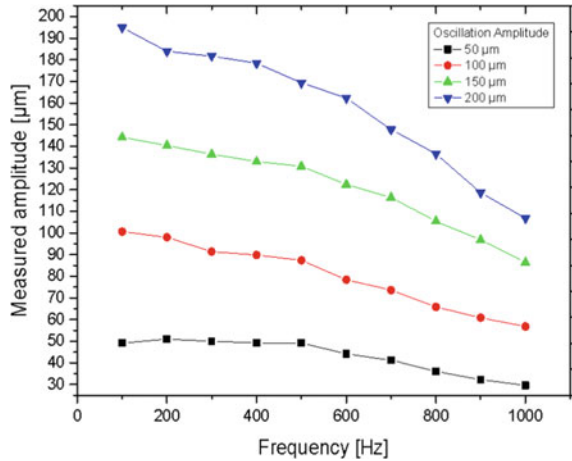


**Table 3** Decrease factor of the amplitude in dependency of the oscillation frequency

	Set-Amplitude [µm]			
	50	100	150	200
Frequency [Hz]	Measured amplitude [µm]			
100	49	101	144	195
1000	30	57	86	107
Decrease factor DF for 1000 Hz	59%	57%	58%	53%

from 53 to 59% whereas the mean decrease factor for oscillation amplitudes of 50, 100, 150 and 200 µm is 57% (Table 3).

This results in a necessary increase of the amplitude by the factor of 1.8 for frequencies around 1000 Hz. The necessary seam width is about  $b_{seam,min,elec} = 250 \mu\text{m}$  so the minimal value for the oscillation amplitude is calculated in first approximation with formula 2.7 as  $A_{calc,1000 \text{ Hz}} = 450 \mu\text{m}$  for 1000 Hz.

$$A_{calc} = \frac{1}{DF} \cdot b_{seam,min,elec} \tag{2.7}$$

- $A$  calculated oscillation amplitude
- $DF$  decrease factor
- $b_{seam,min,elec}$  minimal needed seam width to reach electrical requirements.

The exact needed value has to be adapted experimentally, as the thermal conduction and the molten pool diameter have to be considered further as well as a certain safety margin. As high degrees of overlap are needed to utilize the effect of heat accumulation a high oscillation frequency is used ( $f = 1000 \text{ Hz}$ ).

### 3 Experimental Details, Results and Discussion

First the parameters used in the experiments will be presented, then the analysis of the process results will be shown. The results will be discussed regarding the seam parameters, electrical resistance, tightness and process stability.

Earlier studies have shown the feasibility for the welding of CuSn6 and DC04 in the field of Li-Ion cell contacting. The experiments in this case have been conducted with an energy per section of 1.5–1.7 J/mm. The reached welding depth with a parameter set of  $P = 170$  W,  $v_S = 100$  mm/s,  $A = 0.15$  mm and  $f = 1$  kHz was 450  $\mu\text{m}$  and the connection width 190  $\mu\text{m}$  [1]. As the welding depth has been pretty high and the connection width has been under the critical process limit an increase in the energy per section (more molten material possible) and in the oscillation amplitude (higher seam width) is needed. As the necessary seam width has to be around twice as much as in the prior experiments from [1] considering the safety margin, the energy per section is increased by a factor of 2.

With the known process limits (welding depth and connection width) and parameter estimations (power, welding speed, amplitude and frequency) the number of experiments could be reduced to find a possible parameter area. After initial experiments the parameters shown in Table 4 were chosen for further analysis:

#### 3.1 Seam Appearance and Metallographic Analysis

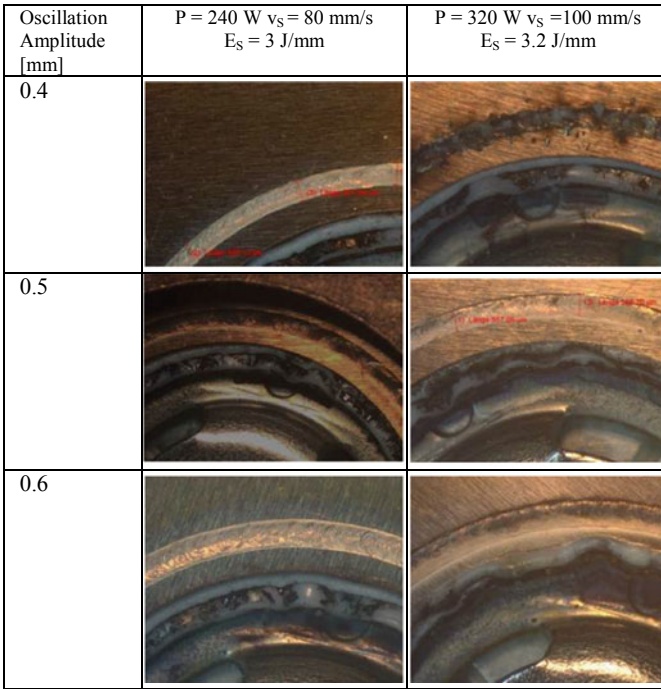
##### 3.1.1 Seam Appearance

The generated seams with energy per section of  $E_S = 3$  J/mm ( $P = 240$  W,  $v_S = 80$  mm/s) had in general a smooth surface with no seam defects. The welds with higher energy per section of 3.2 J/mm ( $P = 320$  W,  $v_S = 100$  mm/s) showed seam defects such as spatter, formation of pits, edge notches and undercut (Fig. 9, right).

The oscillation with high amplitudes (0.5–0.6 mm) could lead to the formation of edge notches and the formation of holes in the seam. This can be traced back to the sagging of the melt to the bent surface (Fig. 10).

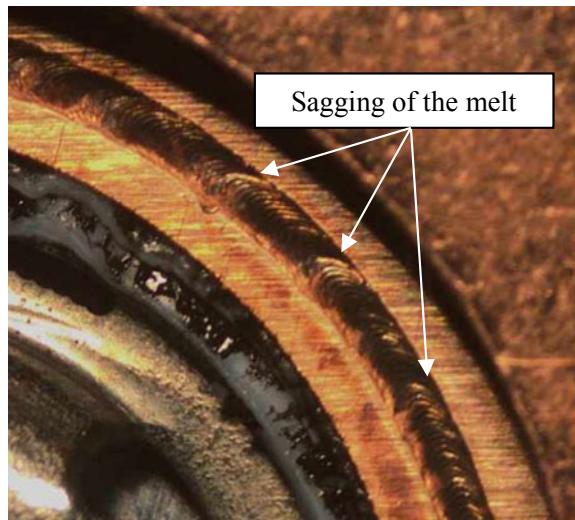
**Table 4** Parameter sets for further analysis

Power	240 W, 320 W
Welding speed	80 mm/s, 100 mm/s
Energy per section	3 J/mm, 3.2 J/mm
Oscillation frequency	700 Hz
Oscillation amplitude	0.4 mm, 0.5 mm, 0.6 mm



**Fig. 9** Dependency of seam appearance from oscillation amplitude and energy per section

**Fig. 10** Hole formation in welds with  $P = 240 \text{ W}$ ,  $v_S = 80 \text{ mm/s}$ ,  $A = 0.5 \text{ mm}$ ,  $f = 1000 \text{ Hz}$



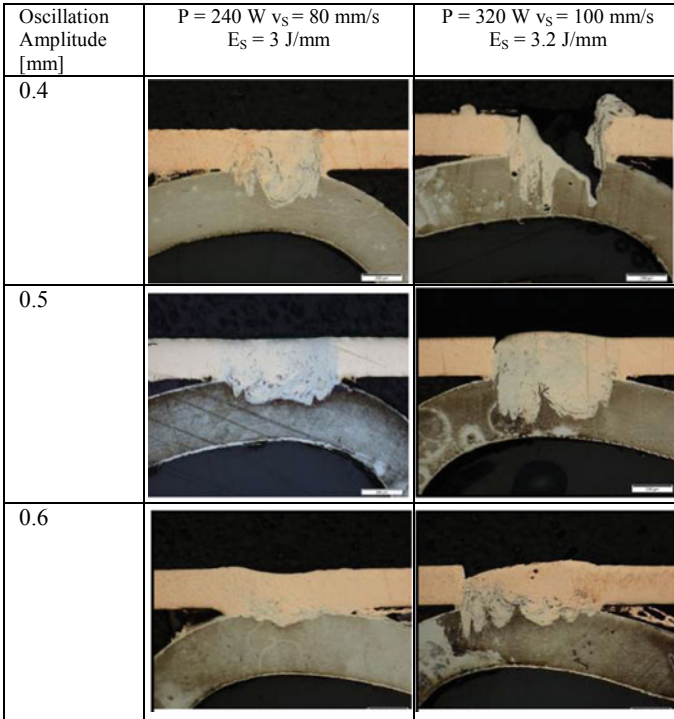


Fig. 11 Metallographic analysis of the examined samples

### 3.1.2 Analysis of Welding Depth and Connection Width

The visible seam defects for an energy per section of 3.2 J/mm were confirmed by metallographic analysis (Fig. 11, right). For the weld seams with an energy per section of 3 J/mm no seam defects could be detected (Fig. 11, left).

The reached connection width mainly depended on the set oscillation amplitude; no relation with the energy per section could be seen in the applied parameter area (Fig. 12). For welds with the described parameter sets the necessary connection width of more than 250 μm has been reached.

For all welds with an energy per section of 3.2 J/mm the weld depth was too high (Fig. 13) and therefore damage to the sealing could occur. The high welding depth and high deviation may result from spiking effects and the melt pool dynamics. The welds with lower energy per section of 3 J/mm showed weld depths between the limits for the weld depth. In general a reduction of the oscillation amplitude leads to an increase of the weld depth.

**Fig. 12** Dependency of connection width from oscillation amplitude

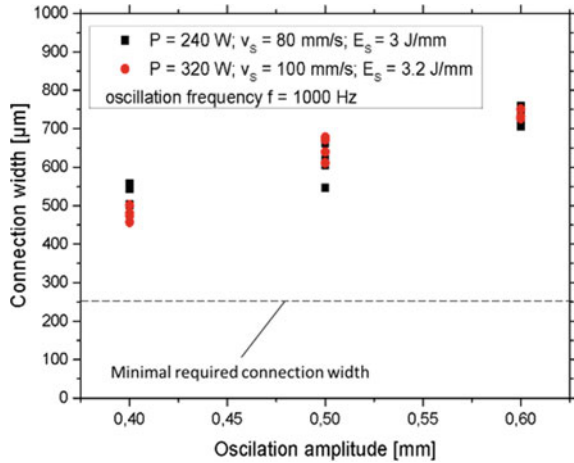
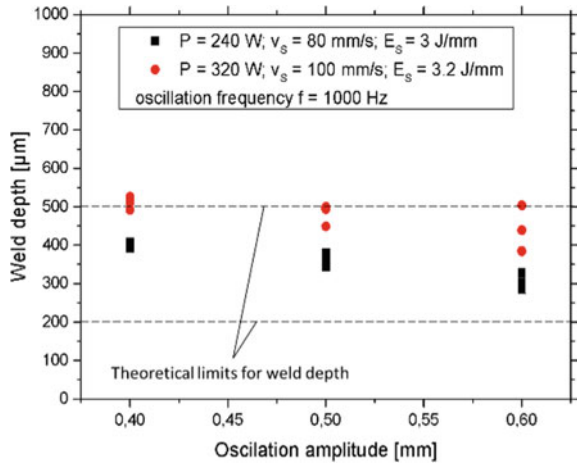


**Fig. 13** Dependency of welding depth from oscillation amplitude



### 3.2 Estimation of the Process Stability

The process stability was estimated with 4 measured values for each parameter set. The standard deviation was calculated and is shown in Figs. 14 and 15.

The standard deviation of the connection width had a maximum at 0.5 mm which was observed independently for both energies per section (Fig. 14). An increase of the standard deviation of the connection width could be seen as the energy per section was decreased.

The standard deviation of the weld depth increased with an increase of the oscillation amplitude as well as an increase in the energy per section (Fig. 15).

An opposing trend for the influence of an increase of the energy per section could be seen regarding the standard deviation of the weld depth and connection width.

**Fig. 14** Dependency of standard deviation of the connection width from oscillation amplitude

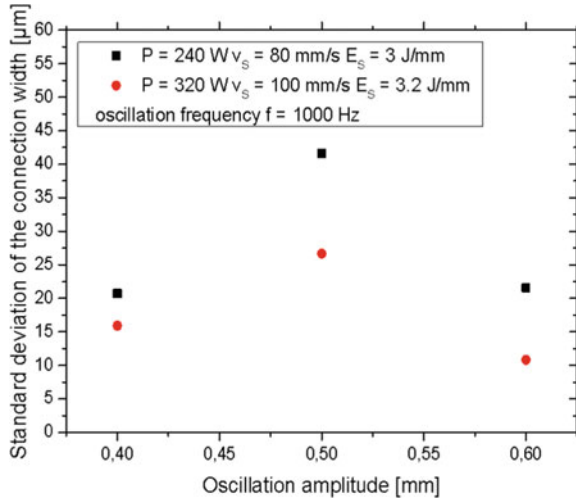
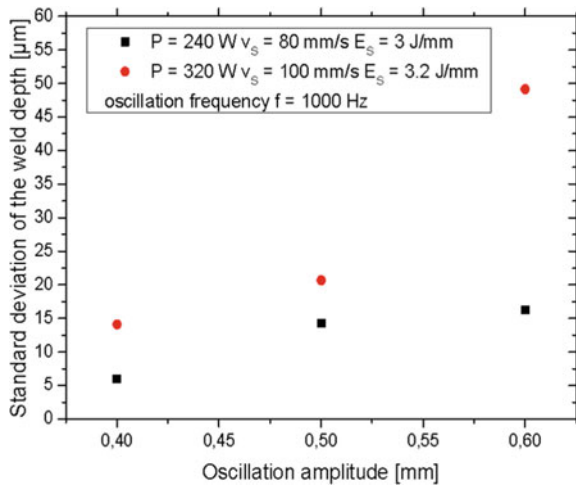


**Fig. 15** Dependency of standard deviation of the weld depth from oscillation amplitude



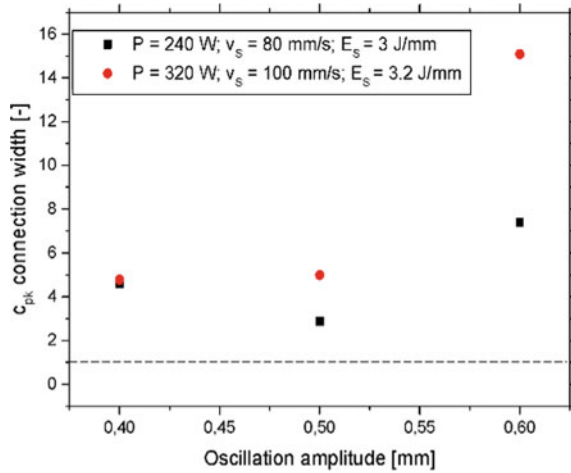
This can be lead back to the different melt pool dynamics due to different local keyhole movement speeds and keyhole formation.

A common approach to evaluate process stability numerically is the use of process capability indices [15] where the mean value and the deviation are set in relation with the tolerance limits (Formula 3.1).

$$c_{pk} = \min\left(\frac{UT - \mu}{3\sigma}; \frac{\mu - LT}{3\sigma}\right) \tag{3.1}$$



**Fig. 16** Dependency of process capability for connection width from oscillation amplitude and line energy



- $c_{pk}$  process capability index
- $UT$  upper tolerance border
- $LT$  lower tolerance border
- $\mu$  mean value
- $\sigma$  standard deviation.

Processes with process capability indices higher than 1 are commonly considered as stable processes, but the higher the process capability index is, the less process errors due to the natural process deviation occur. Considering the process capability for the connection width all sets of parameters reached stable processes (Fig. 16).

Considering the process capability for the weld depth all parameter sets with an energy per section of 3 J/mm showed stable processes but for a higher energy per section of 3.2 J/mm no stable process could be reached (Fig. 17).

The parameter set with  $P = 240 \text{ W}$ ,  $v_s = 80 \text{ mm/s}$ ,  $E_s = 3 \text{ J/mm}$  and an oscillation amplitude of 0.4 mm showed the highest process capability regarding the weld depth ( $c_{pk} = 5.6$ ).

### 3.3 Analysis of Electrical Resistance

The electrical resistance was measured with the four point resistivity method. A constant current of 7 A was connected to the battery housing and the copper connector. The voltage drop was measured with manual positioning of the measurement probes 4 times (Fig. 18) and then the resistance was calculated with Formula 3.2.

$$R = \frac{\Delta U}{I} \tag{3.2}$$

**Fig. 17** Dependency of process capability for weld depth from oscillation amplitude and line energy

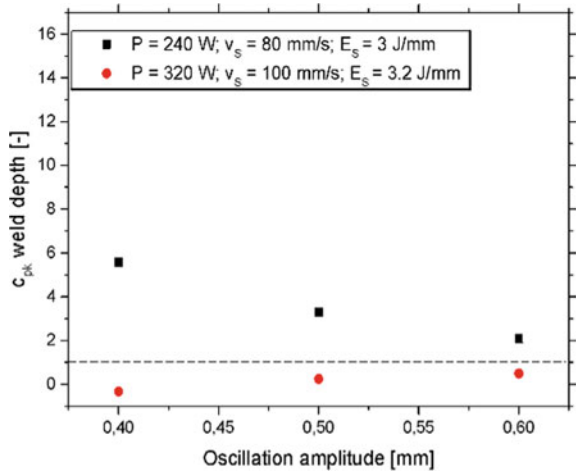


**Fig. 18** Measurement of the electrical resistance



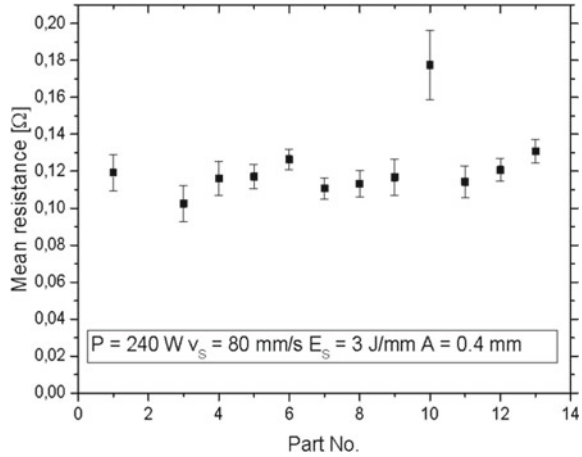
- $R$  resistance;
- $\Delta U$  voltage drop;
- $I$  current.

The measured resistance with the standard deviation for 4 measurements of 13 parts is shown in Fig. 19. The high resistance of the outlier (part no. 10) can be traced back to bad positioning and damage to the seam. Therefore part no. 10 was not used for the calculation of the mean resistance and the standard deviation for the mean value for these parts was 0.12 mΩ with a standard deviation of 0.02 mΩ.

With the measured resistance of 0.12 mΩ and the current of 5 A per cell a power loss of 3 mW per cell has to be expected (Formulas 3.3–3.5).

$$U = R \cdot I \tag{3.3}$$

**Fig. 19** Mean resistance for  $P = 240 \text{ W}$ ,  $v_S = 80 \text{ mm/s}$ ,  $E_S = 3 \text{ J/mm}$ ,  $A = 0.4 \text{ mm}$



$$P = U \cdot I \tag{3.4}$$

$$P = R \cdot I^2 \tag{3.5}$$

For the whole energy pack with 4,800 cells this results in a power loss of 14.4 W, which is acceptable.

### 3.4 Conclusion of Metallographic Analysis and Analysis of Process Stability

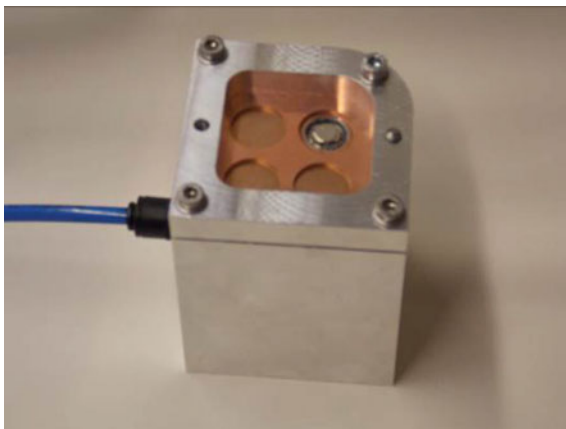
The analysis of the welding results showed stable processes for an energy per section of 3 J/mm. The parameter sets with an energy per section of 3.2 J/mm showed no process capability.

As the parameter set with an energy per section of  $E_S = 3 \text{ J/mm}$  and  $A = 0.6 \text{ mm}$  shows the lowest capability regarding the welding depth only the parameter set of  $A = 0.4 \text{ mm}$  and  $A = 0.5 \text{ mm}$  with  $E_S = 3 \text{ J/mm}$  were analyzed further.

### 3.5 Analysis of Seam Tightness

The seam tightness was analysed with a bubble test for which single battery cans were welded and clamped in an aluminium housing. The pressure (1 bar) was applied from inside with compressed air and then the whole test device (Fig. 20) was submerged under water.

**Fig. 20** Clamping device for analysis of seam tightness



Seams with  $A = 0.4$  mm and  $A = 0.5$  mm and  $E_S = 3$  J/mm showed tightness. As the welds show air tightness and the viscosity of the PCM is much higher than the viscosity of air, the welds can also be considered liquid-tight.

Nevertheless few welded samples showed leaking spots. The leakage in these cases can be traced back to inaccuracy in positioning of the seam. The inaccuracy leads to hole formation and sagging of the melt pool around the bent surface of the battery can, similar to welds with energy per section of 3.2 J/mm and 0.5–0.6 mm oscillation amplitude.

## 4 Summary and Outlook

The research task described in this paper was liquid-tight welding of 18650 Li-ion battery cells to form units with high capacity in an energy storage device. The necessary welding parameters and seam properties were investigated theoretically and then examined regarding connection width, weld depth, electrical resistance and tightness. The approach to reach proper weld depth and connection width as well as tightness was welding with spatial power modulation. The necessary connection width of more than 250  $\mu\text{m}$  could be reached as well as a weld depth between 200 and 500  $\mu\text{m}$  with demonstrated air tightness and therefore liquid-tightness. The power loss calculated for the measured resistance was 14.4 W which is acceptable compared to the total capacity of the pack. The process stability was examined considering the weld depth and connection width with the process capability indices. Process capability indices of 4.6 regarding the connection width and 5.6 regarding the welding depth have been reached for the parameter set with  $P = 240$  W,  $v_S = 80$  mm/s,  $E_S = 3$  J/mm and an oscillation amplitude of 0.4 mm which means, the process stability is given.

Future work should consider the evaluation of the reached mechanical strength. Furthermore an increase in the positioning accuracy is needed as this is the process factor with the highest influence on the tightness. For a more detailed analysis of the process stability the number of analyzed welds has to be increased to have better information value. Regarding the influencing parameters a more detailed analysis of the correlation between energy per section and connection width and weld depth is planned.

**Acknowledgements** This work was supported by the Fraunhofer Internal Programs under Grant No. 826 472 (“Fraunhofer System Research for Electromobility II” project). The authors would also like to thank the student assistants Sören Hollatz, Eric Limpert and Roman Kusnezow for the support.

## References

1. Mehlmann B, Olowinsky A, Thuilot M, Gillner A (2013) Spatially modulated laser beam micro welding of CuSn6 and nickel-plated DC04 steel for battery applications. In: Proceedings of LAMP2013—the 6th International Congress on Laser Advanced Materials Processing
2. Reiter MJ, Farson DF, Mehl M (2010) Control of penetration depth fluctuations in single-mode fiber laser welds. *J Laser Appl* 22(1):37
3. Hess A, Schuster R, Heider A, Weber R, Graf T (2011) Continuous wave laser welding of copper with combined beams at wavelengths of 1030 nm and of 515 nm. *Phys Procedia* 12:88–94
4. Engler S, Ramsayer R (2011) Poprawe R (2011) Process studies on laser welding of copper with brilliant green and infrared lasers. *Phys Procedia* 12:339–346
5. Beck M (1996) Modellierung des Lasertiefschweißens. Stuttgart: Teubner (Laser in der Materialbearbeitung)
6. Gedicke J (2011) Robuste Prozessführung beim Laserstrahl-Mikroschweißen mit hochbrillianten Strahlquellen. Shaker (Berichte aus der Lasertechnik), Aachen
7. DKI (2014) Werkstoffdatenblatt CuSn6, Cu; [cited 2014 Nov 17]. Available from: URL: <https://www.kupferinstitut.de/de/persoelicheberatung/shop-verlag-downloads/downloads/werkstoffe/werkstoff-datenblaetter.html>
8. Dausinger F (1995) Strahlwerkzeug laser: energiekopplung und prozesseffektivität [Univ., Habil.-Schr.--Stuttgart]. Stuttgart: Teubner (Laser in der Materialbearbeitung)
9. MATWEB. Material Data of Nickel [cited 2014 Nov 25]. Available from: URL: <http://www.matweb.com>
10. Robert Laminage SA. Material data sheet of DC04 [cited 2014 Nov 25]. Available from: URL: [www.robortlaminage.ch](http://www.robortlaminage.ch)
11. Mehlmann B, Gehlen E, Olowinsky A, Gillner A (2014) Laser micro welding for ribbon bonding. *Phys Procedia* 56:776–781
12. Poprawe R, Schmitt F, Gedicke J, Mehlmann B, Olowinsky A, Gillner A (2009) Systemtechnik zur örtlichen Leistungsmodulation beim Laserstrahl-Mikroschweißen. In: Vollertsen F (ed) Kolloquium Mikroproduktion: Beiträge der vier SFB der Mikrotechnik, Bremen, 28–29 Oct 2009. BIAS, Bremen
13. Schmitt F (2010) Laser beam micro welding with high brilliant fiber lasers. *JLMN* 5(3):197–203
14. Schmitt F (2012) Laserstrahl-Mikroschweißen mit Strahlquellen hoher Brillanz und örtlicher Leistungsmodulation. Techn. Hochsch, Aachen
15. Gevatter H (2006) Handbuch der Mess- und Automatisierungstechnik in der Produktion. 2. Aufl. s.l.: Springer. Available from: URL:[http://ebooks.ciando.com/book/index.cfm/bok\\_id/9304](http://ebooks.ciando.com/book/index.cfm/bok_id/9304)

# Cavity Pressure Dependence on Tensile-Shear Strength of Metal-Polymer Direct Joining



F. Kimura, S. Kadoya, and Y. Kajihara

**Abstract** This work experimentally investigates effects of molding conditions on tensile-shear strength of metal-polymer joining products, of which materials are joined by an IMDJ (Injection Molded Direct Joining) process. The IMDJ process is a particular insert molding using a special metal piece; on the surface of the piece, nano/micro scale structures (holes) are formed. This joining technology has been rarely applied to the real industries; nevertheless the technology has many merits for manufacturing processes. This is because the mechanism of the joining has not been revealed. One of approaches for revealing is to investigate a relationship between molding conditions and strength of the joining, which is the objective of this paper. In this particular work, we utilized aluminum pieces (A5052) and PBT (Polybutylene Terephthalate) materials for joining targets and focused on the pressure in the mold cavity as one of the molding conditions. Since the typical injection molding machine cannot measure and control the cavity pressure directly, a pressure sensor was embedded inside the mold. Time-course behavior of the pressure during molding cannot be represented by one parameter. To change the behavior, we manually controlled two parameters, injection volume and holding pressure, on the injection molding machine by feeding-back the measured value. Additionally, we carried out tensile tests to evaluate the strength of the IMDJ products, which were processed under various conditions. The test applied shear stress at the joining boundary surface to measure the tensile-shear strength of the joining. From the results of the tests, we discuss the effects of the pressure variations on the strength.

**Keywords** Metal-polymer joining · Insert molding · Mold condition measurement

---

F. Kimura (✉) · S. Kadoya · Y. Kajihara  
Institute of Industrial Science, The University of Tokyo, Tokyo, Japan  
e-mail: [fuminobu@iis.u-tokyo.ac.jp](mailto:fuminobu@iis.u-tokyo.ac.jp)

© Springer Nature Switzerland AG 2022  
S. Hinduja et al. (eds.), *Proceedings of the 38th International MATADOR Conference*,  
[https://doi.org/10.1007/978-3-319-64943-6\\_17](https://doi.org/10.1007/978-3-319-64943-6_17)

245

## 1 Introduction

Recently, polymer material is widely used in manufacturing fields such as automobile and portable computer industries since the polymer is light-weight and thus very useful from a viewpoint of energy and environmental affairs. However, we never substitute polymer for metal in all structures. We, therefore, need techniques of joining between the metal and the polymer structures.

In current state, typical/traditional metal-polymer joining methods are to use adhesion bonds or mechanical tools such as bolts/screws and rivets. However, a novel joining method has been proposed recently that is a metal-polymer direct joining. The direct joining has some substantial advantages in comparison with typical/traditional joining methods. One advantage is that the direct joining can reduce the weight of structures and can avoid troublesome parts managements since the technology does not require extra parts. Another advantage is that this technology can ease restrictions on designing or processing of the products caused by screwing. Thus, many research groups have studied the metal-polymer joining and have proposed various type of joining method; (i) using laser welding [1–5], (ii) using chemical bonding [6, 7], or (iii) micro/nano scale anchor effects [8–12].

The method (iii), which is a target of this paper, is based on a typical insert molding but utilizes a special insert metal piece; on a surface of the metal, micro/nano scale structures are formed. During injection molding process, a melted polymer material is forced into the surface structures. After the polymer cools and hardens in the mold cavity, the polymer and the inserted metal are joined. Typical insert molding uses macro scale anchor effect (interlocking), whereas this method uses micro/nano scale anchor effect to join metal and polymer parts. There is, therefore, no design restriction for interlocking in this method that is also one of the advantages. We call this method as an injection molded direct joining (IMDJ) process.

The IMDJ process has many advantages as described above. The process, however, has been rarely applied to the real industries since reliability of the joining is not high enough for industrial use. One of the reasons why the reliability is low is that a mechanism of the joining has not been revealed. For future applications of the IMDJ process, the mechanism must be revealed.

It is estimated that micro/nano scale anchor effect is a main joining mechanism. However, the other factors could affect the joining as well, for example, chemical bonding or intermolecular force (van der Waals' force) caused by enlargement of the real contact area between metal and polymer. Revealing the mechanism is a main motivation of our study. One of the approach to reveal the joining mechanism is to investigate effects of process conditions on characteristics of IMDJ products, such as joining strength and fatigue limit. It is considered that collecting the relationships between conditions and characteristics conduces to understanding of the mechanism. In this particular work, we focused on pressure in the mold cavity and tensile-shear

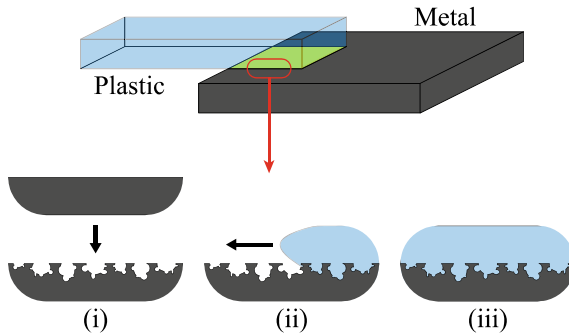


**Fig. 1** An overview of the IMDJ process and schematic enlarged cross-section illustrations of the metal polymer contact part. The process is divided into three steps; (i) forming micro/nano-structures, (ii) insert molding, and (iii) after-treatment

strength as the condition and the characteristic, respectively. To investigate the pressure effects, we processed the joined products by using pressure monitoring technique, and carried out tensile-shear tests. From the results of the tests, this paper shows that the cavity pressure and the strength have a positive correlation.

## 2 Injection Molded Direct Joining

### 2.1 Process Overview

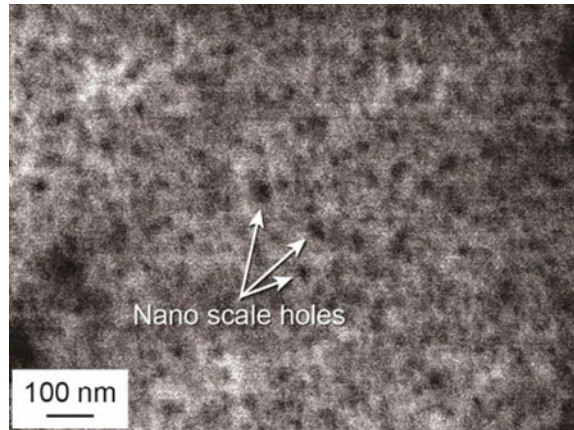
The IMDJ process can be divided into three steps as following; (i) forming micro/nano-structures, (ii) insert molding, and (iii) after-treatment. Figure 1 shows schematic cross-section views of enlarged boundary surface at each step of the process. At first step (i), the micro/nano-structures, which are holes in this particular work, are formed on surface of a metal piece. The injection molding is performed with inserting the surface-treated metal piece at step (ii). After molding, at step (iii), the joined product is annealed in order to relieve the internal stress of the polymer part. Additionally, an extra part of the product, which is a sprue or runner part, is removed at step (iii) as well. Then, the joined product is completed.

### 2.2 Materials and Equipment for Molding

The materials that were used in this work are aluminum alloy A5052 pieces and polybutylene terephthalate (PBT). To form micro/nano scale structures on the surface of the aluminum alloy piece, the piece was treated by Nano Molding Technology (NMT) process, which is a chemical treatment produced by Taiseiplas [10]. NMT



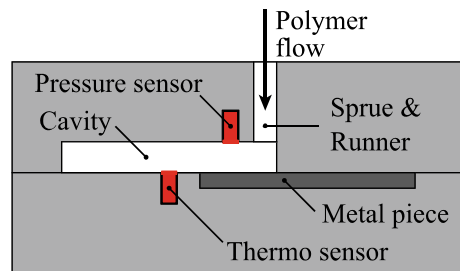
**Fig. 2** An SEM image of the surface of the metal piece. Nano scale holes are formed on the surface



process formed nano-scale holes (size: tens of nano meter) on the metal surface as shown in Fig. 2. The pelletized raw PBT materials (Toraycon(R) 1101G-X54, Toray) had been stored under an environment of 130 °C until starting molding (over four hours) in order to dry the materials.

For insert molding, we utilized a commercial injection molding machine (ROBOSHOT a-100iA Linear, FANUC) and an original mold. Figure 3 shows a schematic illustration of the mold. A pressure sensor (6158A, Kistler Japan) and a thermo sensor (EPSSZT-04.0 × 030, Futaba Corporation) were installed on the mold to measure pressure and temperature in the mold cavity, which typical injection molding machines cannot control or measure directly. The location of the pressure sensor is opposite side to the metal-polymer boundary surface (see Fig. 3) that was designed in order to estimate the pressure on the boundary surface. This is because the pressure on the boundary surface could be the most effective factor for polymer transferring to micro/nano holes and resultant joining strength. Figure 4 shows a time-course measurement example of cavity pressure. Monitoring the measurement results, we controlled the molding conditions, of which details are given later.

**Fig. 3** A schematic illustration of an original mold. A pressure sensor and a thermo sensor are installed on the mold, to measure cavity pressure and temperature



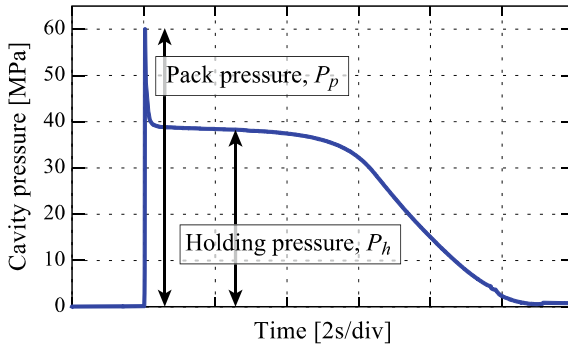


**Fig. 4** An example of a time-course measurement of the cavity pressure. The cavity pressure is represented by two parameters, pack pressure  $P_p$  and holding pressure  $P_h$

### 2.3 Molding Condition

Table 1 shows the molding (and after-treatment for the annealing) conditions used in the joining experiments. Since we focused on the cavity pressure as the condition affecting joining strength, other conditions are fixed. The fixed conditions were controlled by the injection molding machine setting. Although the machine can as well control force (or power) of an actuator for the injection, the force is not always proportional to the cavity pressure. This is because there is energy loss between the actuator force and the cavity pressure caused by viscosity of the melted polymer. Thus, dynamic pressure in the cavity cannot be directly controlled by the machine setting. On the other hand, (quasi-)static pressure can be controlled since it is not effected by viscosity.

A time-course behavior of the pressure, of which example is shown in Fig. 4, cannot be represented by one parameter since the state of injection process varies during molding. The process is divided into two states; one is an injection process, and the other is a pressure holding process. In this work, the peak pressure, which is obtained in the injection process, and amount of pressure in the holding process are called as a pack pressure,  $P_p$ , and a holding pressure,  $P_h$ , respectively. Since the holding pressure is static one, it can be controlled by the machine setting: target values are  $P_h = 20, 40,$  and  $60$  MPa. Whereas, the pack pressure is a kind of dynamic pressure and cannot be automatically controlled by the machine. Thus, we manually controlled the pack pressure by a trial-and-error adjustment. Based on the monitoring in each

**Table 1** Molding conditions

Injection speed	300 mm/s	Pressure holding time length	8 s
(Injection rate)	(94.2 cm <sup>3</sup> /s)	Mold temperature	140 °C
Annealing time length	4 h	Annealing temperature	130 °C
Cylinder temperature	270/275/265/245/10/75 °C (left: nozzle front   right: hopper)		

process, we adjusted the amount of injection volume so that the pack pressure is approximately equal to desired pressure values, which are  $P_p = 60, 90,$  and  $120$  MPa. The total number of condition combinations was nine ( $=3 \times 3$ ).

## 2.4 IMDJ Product

To complete the IMDJ process, we performed the annealing and removed the extra part as the after-treatments. Figure 5 shows a photo image of the completed IMDJ product. This figure also shows the image before removing the extra part. The metal piece and the polymer body are cuboids of  $18 \times 45 \times 1.5$  and  $10 \times 50 \times 3$  mm (width  $\times$  height  $\times$  thickness), respectively. The joining area is rectangle of  $5 \times 10$  mm. Under each condition, seven samples were processed (total: sixty three samples). We evaluated strength of the samples that is described in the next section.

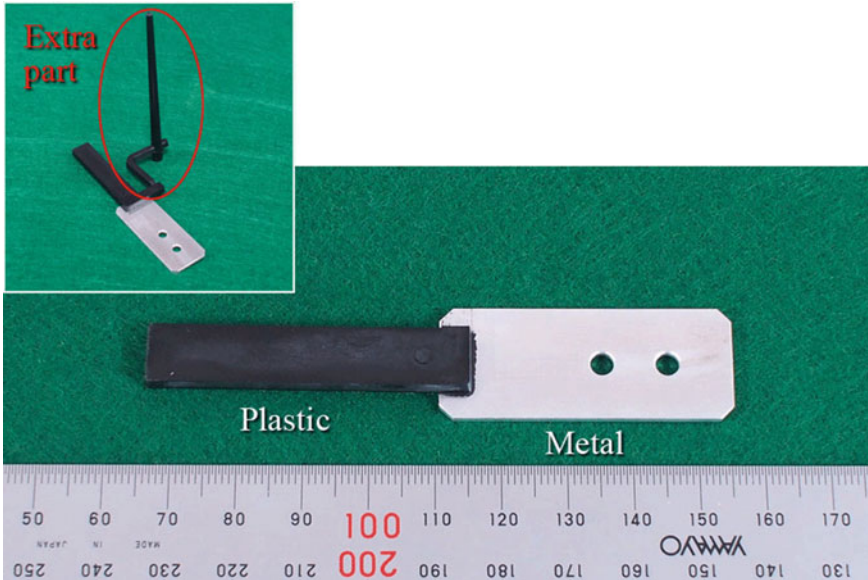


**Fig. 5** A photo image of the IMDJ product. The product is completed by removing an extra part

### 3 Tensile Shear Test

We carried out tensile shear tests in order to investigate the effects of the condition variations on the strength. This section describes a method of the test and measurement results. In addition, we analyze and discuss the results that shows relationships between the conditions and the strength.

#### 3.1 Method

For the tensile-shear measurements, we utilized a tensile test machine (AG-50kNG, SHIMADZU). Figure 6 shows a photo image and a schematic illustration of the experimental setup. To align the center of grippers and the joining boundary surface, the sample product was gripped with dummy pieces as shown in this figure. The test machine pulled the sample with pulling speed of 1 mm/min so as to apply shear stress at the boundary surface. During the test, the machine measured force applied to the grippers. We recorded maximum force before each sample was broken as the strength of the joining. Also note that all samples were stored in a desiccator for longer than twenty four hours under environment of approximately 24 °C and 40%RH before conducting the test.

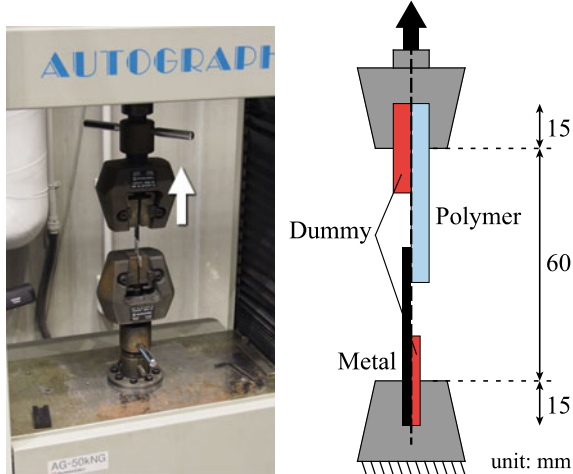


**Fig. 6** A photo image of a tensile test machine and a schematic illustration of grippers and an IMDJ sample. To align the center of the grippers and the joining boundary surface, dummy pieces were gripped as well

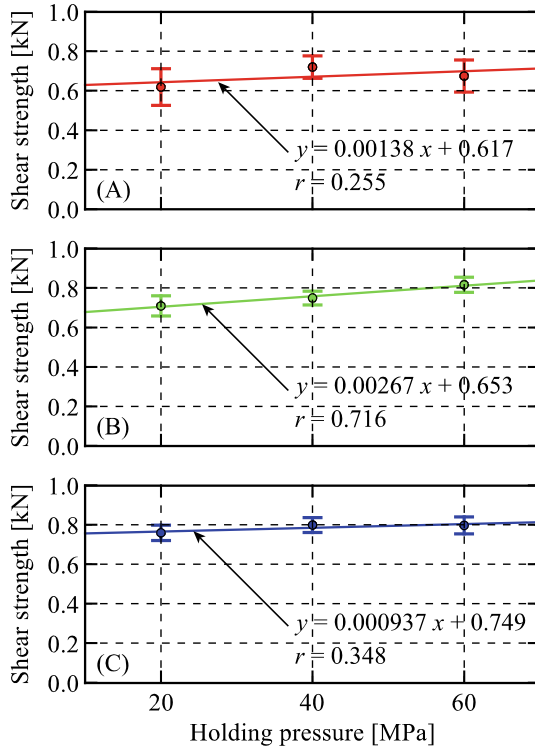


**Fig. 7** Measured strength against targeted holding pressure: **a**  $P_p = 60$ , **b**  $P_p = 90$ , and **c**  $P_p = 120$  MPa. Linear lines are fitting lines obtained by the method of least squares

### 3.2 Results, Analyses, and Discussions

Measurement results of the strength were plotted on Figs. 7 and 8. Figure 7 shows effects of the holding pressure under each pack pressure condition,  $P_p = 60$  (A), 90 (B), and 120 (C) MPa; the horizontal axes represent target values of the holding pressure. On the other hand, Fig. 8 shows effects of the pack pressure under each holding pressure,  $P_h = 20$  (A), 40 (B), and 60 (C) MPa; the horizontal axes represent measured values of the pack pressure. All vertical axes in both figures are the strength. Markers and error bars are mean values and standard deviations, respectively. Fitting lines, which are shown in each graph, were obtained by a following primary expression;

$$y = ax + b \tag{1}$$

where  $x$  and  $y$  are variable numbers of the horizontal and vertical axes of each plot, respectively. The coefficients  $a$  and  $b$  of each line were estimated by the method of least squares using the measured data. Additionally, we calculated coefficients of

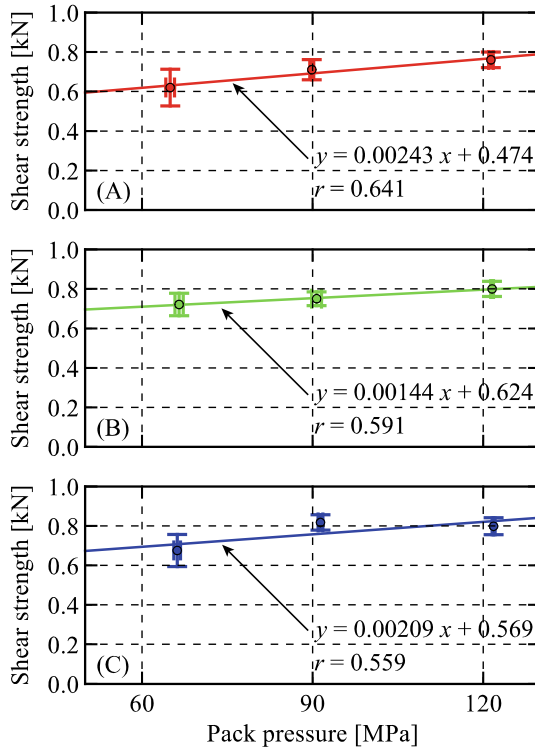


**Fig. 8** Measured strength against measured pack pressure: **a**  $P_h = 20$ , **b**  $P_h = 40$ , and **c**  $P_h = 60$  MPa. Linear lines are fitting lines obtained by the method of least squares

correlation,  $r$ , by using following equation.

$$r = \frac{\sum (x_i - \bar{x})(y_i - \bar{y})}{\sqrt{\sum (x_i - \bar{x})^2 \sum (y_i - \bar{y})^2}} \tag{2}$$

where  $x_i$  and  $y_i$  are each variable number of the horizontal and vertical axes of each plot, respectively, and  $\bar{x}$  and  $\bar{y}$  are average values of  $x_i$  and  $y_i$ . The calculated numbers are shown in Figs. 7 and 8. The coefficient of correlation is one of the indicator that represents the effects of  $x$  on  $y$ ; the larger  $r$  (max.  $r = 1$ ) means the stronger effect exists, and vice versa.

From the results, we can see that there are positive correlations between both pressure conditions, the holding pressure and the pack pressure, and the tensile-shear strength. Especially, the pack pressure tends to have strong effect compared to the holding pressure. Although the coefficient of correlation of holding pressure was maximum under  $P_p = 90$  MPa, we assumed this is an outlier in this work. Confirmation of this outlier is our future work.

The reason of the positive correlation is easily expected: the rate of polymer transferring to micro/nano structures would be increased under higher cavity pressure. Additionally, the pressure in former state of the molding, which is the injection state, is more effective than pressure holding state since the polymer cools and hardens as time goes by. However, this study has not confirmed this expectation. In future work, we will show the strict reasons.

## 4 Conclusion

This work experimentally investigates effects of molding conditions on tensile-shear strength of metal-polymer direct joining. The metal and polymer materials are joined by an injection molded direct joining (IMDJ) process. We processed the IMDJ products under various conditions of the cavity pressure, which was divided into a holding pressure and a pack pressure. To change the pressure, we utilized an original mold that can measure the cavity pressure.

To evaluate the IMDJ product samples, we carried out tensile-shear tests and measured the strength. From the measurement results, we confirmed the effects of the pressure variation on the strength: there are positive correlations between both pressure conditions and the tensile-shear strength. Especially, the effect of the pack pressure variation was stronger than that of the holding pressure variation.

**Acknowledgements** This work was supported by Futaba Electronics Memorial Foundation and The Foundation for the Promotion of Industrial Science. In addition, a part of the experiments was supported by Yokoi Laboratory, The University of Tokyo, Japan.

## References

1. Katayama S, Kawahito Y (2008) Laser direct joining of metal and plastic. *Scripta Mater* 59:1247–1250
2. Fortunato A, Cuccolini G, Ascari A, Orazi L, Campana G, Tani G (2010) Hybrid metal-plastic joining by means of laser. *Int J Mater Form* 3:1131–1134
3. Holtkamp J, Roesner A, Gillner A (2010) Advances in hybrid laser joining. *Int J Adv Manuf Technol* 47:923–930
4. Roesner A, Scheik S, Olowinsky A, Gillner A, Reisinger U, Schleser M, (2011) Laser assisted joining of plastic metal hybrids. *Physics Procedia Part B* 12:370–377
5. Bauernhuber A, Markovits T (2012) Laser assisted joining of metal pins and thin plastic sheets. *Phys Procedia* 39:108–116
6. Sasaki H, Kobayashi I, Sai S, Hirahara H, Oishi Y, Mori K (1999) Adhesion of ABS resin to metals treated with triazine trithiol monosodium aqueous solution. *J Adhes Sci Technol* 13:523–539
7. Kang ZX, Mori K, Oishi Y (2005) Surface modification of magnesium alloys using triazine dithiols. *Surf Coat Technol* 195:162–167

8. David M, Roman T, Diño WA, Nakanishi H, Kasai H, Ando N, Naritomi M (2007) A nanoscale understanding of the adhesion of polybutylene terephthalate on aluminum. *Surf Sci* 601:5241–5245
9. Uechi T, Agata H, Aoki K, Atarashi T, Tanae M, (2010) Semiconductor module. US Patent App. 12/656235
10. Nano Molding Technology. <https://taiseiplas.jp/nmt/>
11. D LAMP TM. <http://www.daicelpolymer.com/>
12. Laseridge TM. <http://www.polyplastics.com/>



# **Machining**

# Using Taguchi Robust Design to Ultrasonic Vibration Assisted Turning AISI 1045



Wei-Tai Huang, Der-Ho Wu, and Yi-Siang Chen

**Abstract** An ultrasonic vibration-assisted turning tool system is studied using the Taguchi robust design method. An experiment is conducted to measure surface accuracy for ultrasonic-vibration assisted turning of AISI 1045 steel, establishing the following optimal parameters: frequency of 20 kHz, voltage of 75 V, cutting speed of 150 m/min, and feed rate of 0.05 mm/rev. The differences between surface roughness with and without ultrasonic vibration-assisted turning are examined. It shown that surface roughness is lower with ultrasonic vibration-assisted machining than without.

**Keywords** Ultrasonic vibration-assisted turning tool system · Ultrasonic vibration-assisted machining · Taguchi robust design method

## 1 Introduction

Recent industrial developments have aimed at providing machining processes with increased cutting life, reducing surface roughness, and elevating the overall efficiency of cutting tools in various environments. Ultrasonic machining was first developed in 1950 [1]. Ultrasonic vibration-assisted turning is a technique combining ultrasonic vibration with a vibrating turning system. The technique of ultrasonic vibration has had wide application including weld processing of low melting point materials, cleaning processing and automatic feeders. Vibration-assisted machining is mainly used for machining super-hard materials (e.g., alumina, zirconia, sapphire, Si, quartz, tungsten, tool steel) [1, 2].

The character of ultrasonic vibration-assisted turning is intermittent cutting. It should satisfy the period of cutting which yields the chips. Vibration direction also affects machining. Machining direction can be categorized into one-dimensional and two-dimensional vibration [3, 4]. Amplitudes of ultrasonic vibration-assisted turning

---

W.-T. Huang (✉) · D.-H. Wu · Y.-S. Chen

National Pingtung University of Science and Technology, 1 Shuefu Road, Neipu, Pingtung 912, Taiwan

e-mail: [weитай@mail.npust.edu.tw](mailto:weитай@mail.npust.edu.tw)

© Springer Nature Switzerland AG 2022

S. Hinduja et al. (eds.), *Proceedings of the 38th International MATADOR Conference*, [https://doi.org/10.1007/978-3-319-64943-6\\_18](https://doi.org/10.1007/978-3-319-64943-6_18)

259

less than 20  $\mu\text{m}$ , can provide improved cutting efficiency, restrain cutting edge adhesion, and prolong cutting life [5, 6]. Ultrasonic vibration-assisted machining has been applied in Electrical Discharge Machining (EDM), Wire Electrical Discharge Machining (WEDM), turning, milling, drilling and boring [4–8]. It also can be applied in many traditional machining processes without a slurry, which is widely required in ultrasonic machining (USM). It is easy to adapt to traditional machining. The main goals of recent ultrasonic vibration-assisted turning systems are to reduce cutting forces, reduce abrasion of cutting tools and increase cutting life, improve surface quality, decrease tool temperature during cutting, and elevate overall machining efficiency or improve the selection of machining materials [2].

Many researchers have studied the effects of ultrasonic vibration-assisted turning systems. In 1987, Wang and Zhao used piezoelectric materials to induce vibrations in lathe tools in the cutting direction. At an amplitude of 18  $\mu\text{m}$ , vibrations can reduce the degree of surface roughness [2]. In 1994, Shamoto and Moriwaki adopted two-dimensional vibration in a cutting experiment, verifying that two-dimensional vibration-assisted machining can improve accuracy, efficiency and cutting tool life [9].

From 2004 to 2005, Mitrofanov's team studied the effects of amplitude and proved that cutting forces and surface roughness can be reduced at amplitudes of 10  $\mu\text{m}$  [10, 11]. In 2007, Nath's team used vibration assisted machining to turn aluminum alloys and measured cutting forces only half those in traditional machining [12].

In 2008, Heisel's team used an ultrasonic vibration-assisted turning system to turn ECu57 steels, to study surface accuracy and differences between traditional machining and ultrasonic vibration-assisted turning systems. They proved that ultrasonic vibration-assisted turning can reduce built-up edge (BUE) and produce better surface accuracy [13]. In 2008 Hsus's teams turned Inconel 718 at a fixed frequency of 20 kHz and used Taguchi analysis on various parameters. They found that a surface vibration-assisted turning system is better than traditional machining [14]. In 2009, Koshimizu used a lathe tool at a frequency of 19 kHz and an amplitude of 30  $\mu\text{m}$  in a vibration-assisted turning of titanium. His experiment found a decrease in temperature of the cutting tools, reduction in edge adhesion, and decrease the average cutting force by one-half to one-third [15]. In 2014, Silberschmidt's team showed after turning various materials and comparing surface roughness of various materials at a frequency of 20 kHz and an amplitude of 8  $\mu\text{m}$ , that harder materials perform better in ultrasonic vibration-assisted turning systems and they retain lower levels of residual machining stress [16].

## 2 Experimental Work

### 2.1 Purpose

The main purpose of this experiment is to develop an ultrasonic vibration-assisted turning system, with practical application to the turning of AISI 1045, and employ the Taguchi robust design method for static experiment planning and verifying its feasibility. The goal is to optimize workpiece surface roughness, studying the difference in surface roughness with and without ultrasonic vibration-assisted turning. The Taguchi robust design method uses an orthogonal table to establish factors for planning experiments. By studying the factors that influence surface roughness, analysis results are used to obtain an optimal combination of these factors.

### 2.2 Ultrasonic Vibration Assisted Turning System Set-up

This experiment use high-speed lathes in an ultrasonic vibration-assisted turning system for machining AISI 1045. Table 1 gives the chemical composition and properties of this materials AISI 1045. Table 1 records the parameters, which included surface roughness.

The power supply system is set up to use a function generator to generate power with a 20–40 kHz sine wave.

Power amplifiers are used in series to obtain the voltage and current required to drive the piezoelectric film and an oscilloscope is used to confirm the signal's frequency and waveform, in a frequency range of 20–40 kHz, Fig. 1 shows the overall configuration, Fig. 2 is the styles of tool with the actual erection tool are shown, Table 2 gives the specifications of the piezoelectric stacks.

**Table 1** Mechanical properties of AISI 1045 mold steel

Work material	AISI 1045
C	0.45
Si	0.25
Mn	0.65
Tensile strength (MPa)	600–720
Yield strength (MPa)	>360
Elongation (%)	>18
Hardness (HB)	205

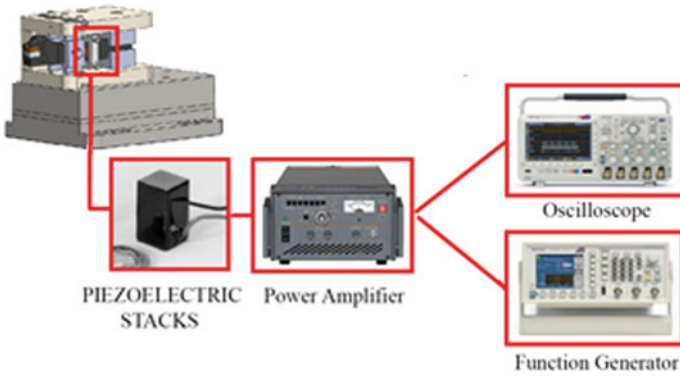


**Fig. 1** Ultrasonic vibration assisted turning system

**Fig. 2** Cutting tool system

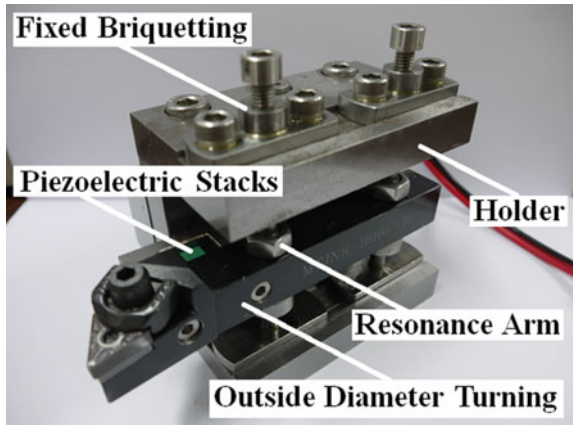


**Table 2** Specifications for piezoelectric stacks

<i>Mechanical</i>		
Dimensions (L × W × H)	mm	10 × 10v8
Compressive strength	N/m <sup>2</sup>	8.8 × 10 <sup>8</sup>
Youngs modulus	N/m <sup>2</sup>	4.9 × 10 <sup>6</sup>
Poisson ratio		0.34
Density	kg/m <sup>3</sup>	7900
<i>Electrical</i>		
Rated voltage	VDC	+100
Capacitance	nF	6500
<i>Performance (in 100VDC)</i>		
Free deflection	μm	+14.5
Blocked force	N	7000
Resonant frequency	Hz	69,000

### 2.3 Experimental Parameters

The cutting length of the AISI 1045 workpiece was 400 mm and the cutting depth 0.8 mm. A Taguchi robust design  $L_93^4$  orthogonal table of all cutting parameters for optimal surface roughness of the workpiece are shown in Table 3. Figure 3 is the surface roughness cause-effect diagram for the ultrasonic vibration-assisted turning tool system, to determine the optimal experimental surface roughness, and to establish whether ultrasonic vibration-assisted machining makes a difference.

**Table 3** Cutting parameters of Taguchi robust design method  $L_93^4$

Parameter	Level			Trial no	A (F)	B (V)	C ( $V_C$ )	D ( $S_0$ )
	1	2	3					
A Frequency (F)	0 kHz	20 kHz	40 kHz	1	1	1	1	1
				2	1	2	2	2
				3	1	3	3	3
B Voltage (V)	50 V	75 V	100 V	4	2	1	2	3
				5	2	2	3	1
C Cutting speed ( $V_C$ )	50 m/min	100 m/min	150 m/min	6	2	3	1	2
				7	3	1	3	2
D Feed rate ( $S_0$ )	0.05 mm/rev	0.13 mm/rev	0.24 mm/rev	8	3	2	1	3
				9	3	3	2	1

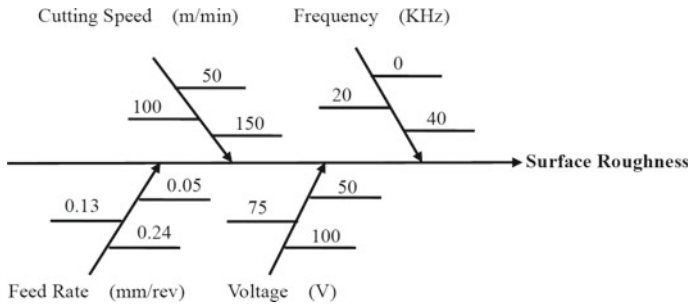


**Fig. 3** Surface roughness cause-effect diagram related to the ultrasonic assisted vibration turning tool system

### 3 Results and Discussion

#### 3.1 Experimental Results from Taguchi Robust Design Method

Table 4 presents a response table for all experimental signal-to-noise (S/N) ratios. Table 5 presents the measured results of the experiment and corresponding S/N ratios. Figure 4 shows the static Taguchi robust design method for all experimental S/N ratios. Figure 5 displays all experimental data for the Taguchi robust design method  $L_93^4$  table. The optimal parameters are (A2) frequency of 20 (KHz), (B2) voltage of 75 (V), (C3) cutting speed of 150 (m/min), and (D1) feed rate of 0.05 (mm/rev), with the fifth set of parameters in Table 3. The order of contributions in this experiment was cutting speed, frequency, feed rate, and voltage.

**Table 4** Response table S/N ratios

Factor	A	B	C	D
Level 1	-5.850	-5.161	-6.398	-2.654
Level 2	-2.835	-3.227	-4.176	-5.657
Level 3	-4.381	-4.678	-2.492	-4.755
Effect	3.015	1.935	3.906	3.004
Rank	2	4	1	3

**Table 5** Experimental results and corresponding S/N ratios

Trial	Experimental results ( $\mu\text{m}$ )			
	Sample 1	Sample 2	Sample 3	S/N ratio
1	2.239	2.241	2.236	-6.997
2	1.960	1.959	1.959	-5.843
3	1.722	1.721	1.715	-4.709
4	1.558	1.561	1.558	-2.691
5	0.804	0.807	0.809	1.858
6	2.113	2.114	2.114	-6.502
7	1.702	1.703	1.704	-4.625
8	1.926	1.927	1.925	-5.694
9	1.384	1.383	1.383	-2.822

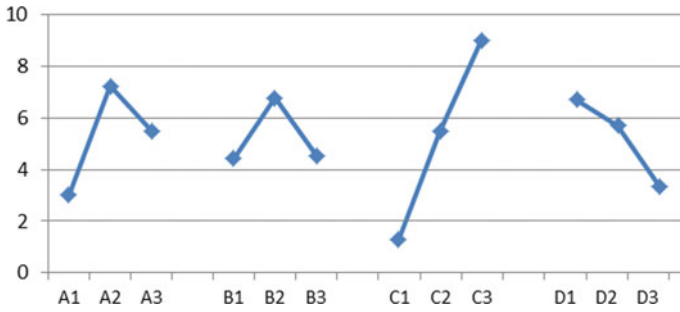


Fig. 4 Static Taguchi robust design method for all experimental S/N ratios

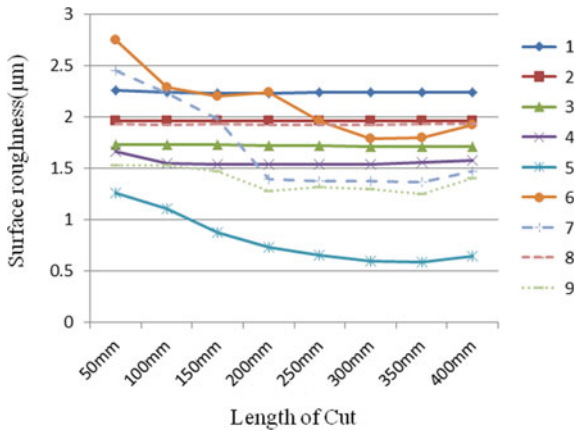


Fig. 5 Experimental data of Taguchi robust design method  $L_93^4$

### 3.2 Comparison of Results with and Without Ultrasonic Vibration-Assisted Turning

In determining whether ultrasonic vibration reduced workpiece surface roughness, it is found that the best parameter set for the Taguchi robust design method is A2B2C3D1, compared with no ultrasonic vibration-assisted turning system. The cutting length and depth are maintained at 400 mm and 0.8 mm to compare the surface roughness of the workpiece.

Figure 6 shows the surface roughness measurements, with and without ultrasonic vibration-assisted machining; with ultrasonic vibration-assisted turning the surface roughness stabilizes at a cutting length of 150 mm. This is obviously earlier than the results without ultrasonic vibration-assisted turning, which stabilized at a cutting length of 250 mm. Regardless of the cutting length, the surface roughness values with ultrasonic vibration-assisted machining are significantly better than without ultrasonic vibration-assisted machining.



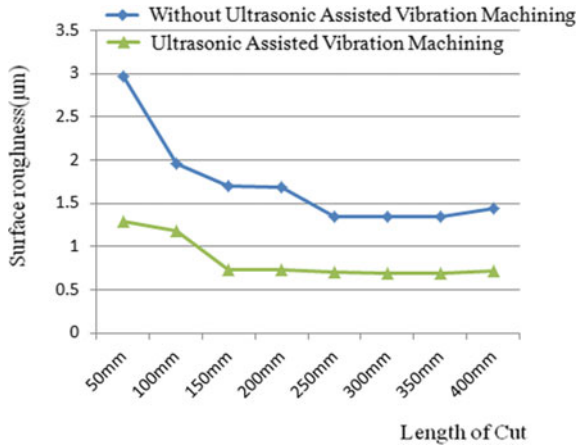


Fig. 6 Experimental results with and without ultrasonic vibration-assisted machining

## 4 Conclusions

This experiment, exploring the cutting parameters of an ultrasonic vibration-assisted turning system through a static Taguchi robust design method plan, has generated the following conclusions:

1. The use of ultrasonic vibration-assisted turning can provide improved surface roughness.
2. Taguchi results show that, in ultrasonic vibration-assisted turning, the greatest impact on surface roughness parameters is cutting speed.
3. Taguchi results show that the optimal cutting parameters are (A2) frequency of 20 kHz, (B2) voltage of 75 V, (C3) cutting speed of 150 m/min, and (D1) feed rate of 0.05 mm/rev, to achieve the best surface roughness values.

## References

1. Byrnel G, Dornfeld D, Denkena B (2003) Advancing cutting technology. *Ann CIRP* 52:483–507
2. Wang LJ, Zhao J (1987) Influence on surface roughness in turning with ultrasonic vibration tool. *Int J Mach Tool Manuf* 27(2):181–190
3. Tawakoli T, Azarhoushang B (2008) Influence of ultrasonic vibrations on dry grinding of soft steel. *Int J Mach Tools Manuf* 48:1585–1591
4. Rimkevičienė J (2009) Research and application of vibration assisted cutting. Kaunas University of Technology
5. Mitrofanov AV, Babitsky VI, Silberschmidt VV (2003) Finite element simulations of ultrasonically assisted turning. *Comput Mater Sci* 28:645
6. Babitsky VI, Mitrofanov AV, Silberschmidt VV (2004) Ultrasonically assisted turning of aviation materials: simulations and experimental study. *Ultrasonics* 42:81

7. Egashira K, Mizutani K (2002) Ultrasonic vibration drilling of microholes in glass. *Ann CIRP* 51(1):339
8. Breh DE, Dow TA (2008) Review of vibration-assisted machining. *Precis Eng* 32:153–172
9. Moriwaki T, Shamoto E (1995) Ultrasonic elliptical vibration cutting. *Ann CIRP* 44(1):31–34
10. Mitrofanov AV, Babitsky VI, Silberschmidt VV (2004) Finite element analysis of ultrasonically assisted turning of Inconel 718. *J Mater Process Technol* 153:233
11. Mitrofanov AV, Ahmed N, Babitsky VI, Silberschmidt VV (2005) Effect of lubrication and cutting parameters on ultrasonically assisted turning of Inconel 718. *J Mater Process Technol* 162–163:649
12. Nath C, Rahman M, Andrew SSK (2007) A study on ultrasonic vibration cutting of low alloy steel. *J Mater Process Technol* 192–193:159–165
13. Heisel U, Wallaschek J, Eisseler R, Potthast C (2008) Ultrasonic deep hole drilling in electrolytic copper ECu 57. *CIRP Ann Manuf Technol* 57:53–56
14. Hsu CY, Lin YY, Lee WS, Lo SP (2008) Machining characteristics of Inconel 718 using ultrasonic and high temperature-aided cutting. *J Mater Process Technol* 198:359–365
15. Koshimizu S (2009) Ultrasonic vibration-assisted cutting of titanium alloy. *Key Eng Mater* 389–390:277–282
16. Silberschmidt VV, Mahdy SMA, Gouda MA, Naseer A, Maurotto A, Roy A (2014) Surface-roughness improvement in ultrasonically assisted turning. *Procedia CIRP* 13:49–54

# Simulation and Experimental Study on Material Removal Mechanism and Removal Characters of Ultrasonic Machining



Jingsi Wang, Keita Shimada, Masayoshi Mizutani,  
and Tsunemoto Kuriyagawa

**Abstract** The UltraSonic Machining (USM) process is simulated by using Smoothed Particle Hydrodynamics (SPH) numerical simulation method. The influences of abrasive shape on material removal and abrasive wear are investigated. According to the simulation results, the abrasive shape has a strong influence on USM process. Using the abrasive with round shape is helpful to improve the machining efficiency. Experiments were also conducted to verify the SPH model. The experimental results agreed well with the simulation results.

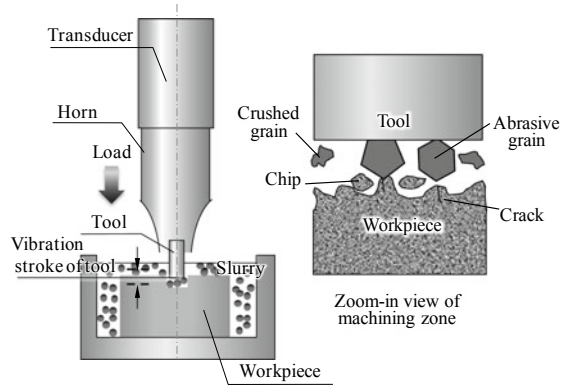
**Keywords** Ultrasonic machining · Abrasive shape · Smoothed particle hydrodynamics

## 1 Introduction

As a response to the increasing needs for manufacturing mechanical, electrical, optical, and biomedical micro-parts or micro-structures on hard and brittle materials, developing precision and efficient micro-machining techniques for hard and brittle materials becomes extremely significant. However, due to the superior properties such as high hardness and strength of these materials, it is still a great challenge to efficiently fabricate hard and brittle materials. Abrasive-based UltraSonic Machining (USM) has been widely proposed to meet the strict fabrication demands. In USM, an abrasive slurry generally comprising tough abrasive materials like silicon carbide, boron carbide, etc. flows through the working zone where a tool tip is vibrated. Loose abrasive particles under the vibrated tool tip are driven to penetrate the workpiece frequently, inducing countless tiny brittle fractures to remove material away. As the tool vibration frequency is in the ultrasonic domain over 20 kHz, high material removal rate can be obtained. Figure 1 shows a schematic of USM system. By reducing tool size, abrasive particle size, and vibration amplitude to the micro-scale,

---

J. Wang (✉) · K. Shimada · M. Mizutani · T. Kuriyagawa  
Department of Mechanical Systems and Design, Graduate School of Engineering, Tohoku University, 6-6-01 Aoba, Aramaki, Aoba-ku, Sendai 980-8579, Japan

**Fig. 1** Schematic of USM

USM is applied to micro-machining [1, 2]. The process only induces small mechanical force and rarely results in thermal damage or residual stress; therefore, it shows a higher flexibility for precise micro-machining of hard and brittle materials.

USM is determined by a large number of process parameters, such as tool vibration system, tool feed speed, slurry characteristics, and work materials. Also, because workpieces are set inside the abrasive slurry, the machining phenomena are not visible. All of these make it difficult for us to completely understand the USM process, and even harder to define an optimal combination of process conditions to meet a certain manufacturing requirement. In addition, because hard and brittle materials like glass and ceramics are always lack of ductility; cracks propagate easily on the machined surface. The brittle fracture leads to both material removal and the growth of surface cracks. Therefore, a thorough investigation and understanding of material removal mechanism and process characters of ultrasonic machining is extremely necessary in order to establish high precise and efficient micro-machining technique for hard and brittle materials. In this work, we use both simulation and experimental methods to discuss the material removal process in USM. The Smoothed Particle Hydrodynamics (SPH) numerical method is used in the simulations.

## 2 Material Removal Mechanism of USM

The detailed material removal mechanisms of USM have been summarized by previous researchers [3]: (1) mechanical abrasion by direct hammering of the larger abrasive particles against the workpiece surface; (2) micro-chipping by impact of the free-moving abrasive particles; (3) cavitation erosion from the abrasive slurry; and (4) chemical effects associated with the fluid employed. It is widely accepted that the first one: direct hammering dominates the main material removal in USM. And in one previous investigation by the present authors [4], it is found that almost no materials are removed when the distance between tool and workpiece is larger than

the abrasive particle size. The results also indicated that the direct hammering causes main material removal in USM.

### 3 Influence of Abrasive Shape on Material Removal and Abrasive Wear

Slurry characteristics have a large effect on USM process; the influences of abrasive size, abrasive material, and abrasive concentration on the USM can be learned from some previous studies [5–8]. However, arguments on the abrasive shape have rarely been referred. In this section, both the SPH simulations and experiments are conducted to investigate the influence of abrasive shape on material removal and abrasive wear.

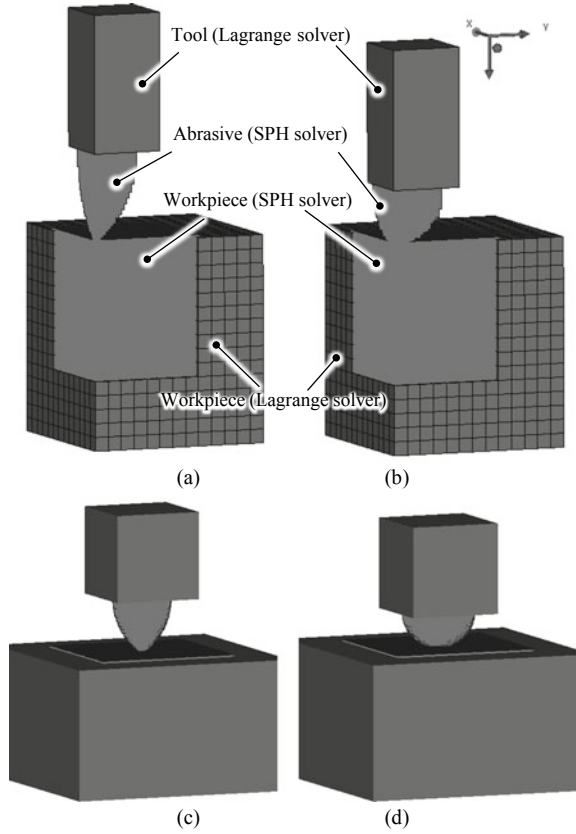
#### 3.1 SPH Simulation Methods

The simulation model was built using the SPH processor included in ANSYS AUTODYN, which is a well-known explicit software for solving nonlinear dynamics problems. Table 1 shows the simulation conditions, and Fig. 2 presents the simulation models. Ogive shape and semisphere shape of abrasives with the same volume were built to represent the abrasives with angular and round shape in real USM, respectively. Each model included: a vibrated tool built with Lagrange solver; one abrasive particle modeled with SPH solver; and a workpiece substrate constructed with both SPH and Lagrange solvers. In order to reduce the model size and calculation time, only a one-quarter symmetric, three-dimensional model was used. Figure 2c, d shows the mirror images along the symmetric planes. The parameters of each material and tool vibration conditions are detailed elsewhere [4, 9] and skipped here. One cycle of the hammering action is calculated with the simulation model.

**Table 1** Simulation conditions

Abrasive shape	Ogive, semisphere
Abrasive material	Al <sub>2</sub> O <sub>3</sub> , SiC
Abrasive volume	116 μm <sup>3</sup>
Workpiece material	Float glass
Tool material	SS304
Penetration depth	1 μm
Calculation time	5 μs

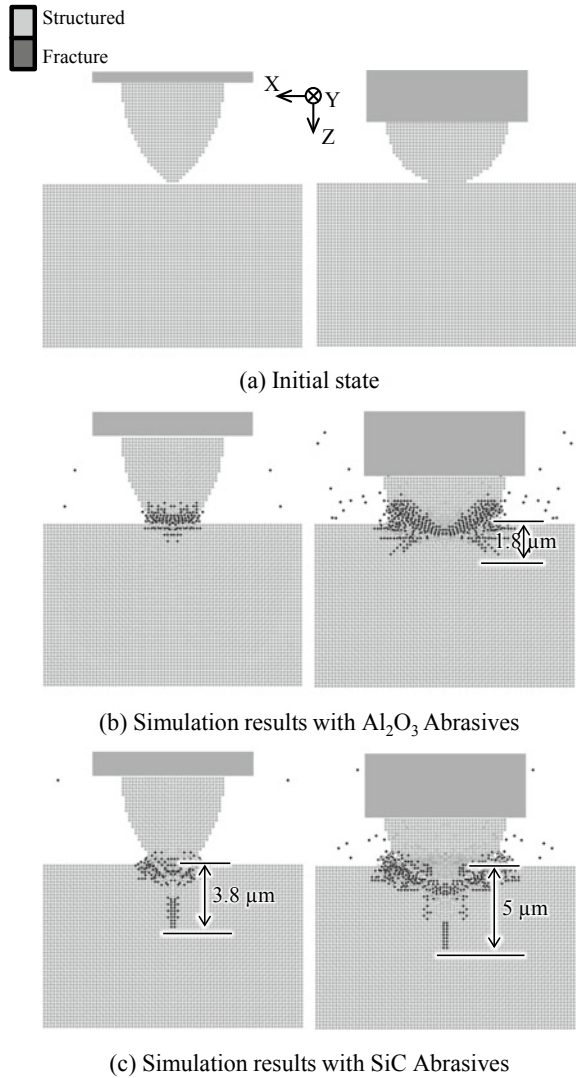
Fig. 2 Simulation models



### 3.2 SPH Simulation Results for Fracture Process of Involved Materials

Figure 3 presents cross sectional views at the Z-X plane of the simulation models. All structured parts are considered to be elastic at the initial state, and filled in gray color. The black elements appearing after the calculation indicate fractured parts. It is found that different degrees of fractures occurred in the work substrates by using different type of abrasives. A median crack propagates into the work material with a harder SiC abrasive, regardless of the abrasive shape. On the other hand, with Al<sub>2</sub>O<sub>3</sub> abrasive, the median crack does not appear; only shallow cracks initiate near the work surface. These results are well consistent with our previous investigations [9]. The abrasive shape also has a large influence on the crack propagation from the present calculation results. For both Al<sub>2</sub>O<sub>3</sub> and SiC abrasives, the work substrate fractures larger when using a semisphere shape abrasive. The depth of crack can be 5 μm when using a semisphere SiC abrasive, while only be 3.8 μm with an ogive SiC abrasive. It is considered to be the result of different degrees of pressure dispersion

**Fig. 3** Cross sectional views at the Z-X plane of the models



on the substrates. Figure 4 shows the fracture of the abrasives. The SiC abrasive resists crushing more easily; therefore smaller fractures occur in SiC abrasives. For all cases, the impact positions of the abrasives wear seriously.

Table 2 lists the fracture volume of substrates ( $V_s$ ) and wear volume of abrasives ( $V_a$ ) in all cases. The ratio of substrate fracture to abrasive wear ( $n = V_s/V_a$ ) for each case was calculated using the volume data and shown in the same table. Generally, the faster the substrate fractures and the slower the abrasive wears, the higher the machining efficiency is. Therefore, the value of  $n$  can be used to estimate the machining efficiency of USM.

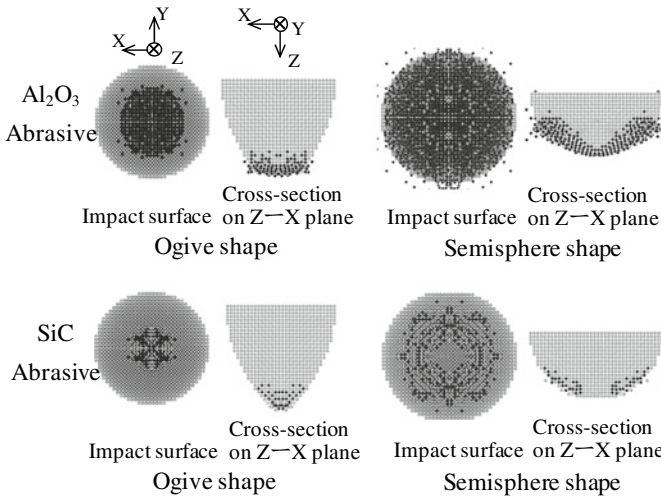


**Fig. 4** Fracture of abrasives

**Table 2** Fracture volume of substrates and abrasives

	Al <sub>2</sub> O <sub>3</sub> ogive	Al <sub>2</sub> O <sub>3</sub> semisphere	SiC ogive	SiC semisphere
$V_a$ ( $\mu\text{m}^3$ )	12.98	64.89	2.27	9.42
$V_s$ ( $\mu\text{m}^3$ )	1	10.11	13.73	63.58
$n = V_s/V_a$	0.08	0.16	6.05	6.75

The value of  $n$  is 0.08, 0.16, 6.05 and 6.75, from low to high of using Al<sub>2</sub>O<sub>3</sub> ogive abrasive, Al<sub>2</sub>O<sub>3</sub> semisphere abrasive, SiC ogive abrasive and SiC semisphere abrasive. For both Al<sub>2</sub>O<sub>3</sub> and SiC abrasives, the value of  $n$  is higher when using a semisphere shape than an ogive shape. The results imply that the abrasive shape is an important parameter for studying the USM process. Using abrasives with round shape is helpful to improve USM efficiency.

### 3.3 Experimental Validation for Simulation Results

A stationary ultrasonic drilling machine (Model: SD-100K; Taga Electric Co., Ltd., Japan) was used in our experiments. In order to confirm the influence of abrasive shape on USM process, water based slurries separately made of three different kinds of abrasives, i.e. green silicon carbide with angles (GC#2000), white alumina with angles (WA#2000), and alumina beads were employed. Figure 5 shows the SEM micrographs of the abrasives. A SS304 tool was applied to drill holes on soda-lime glass with the three kinds of slurries, respectively. In each case, only 0.5 mL of



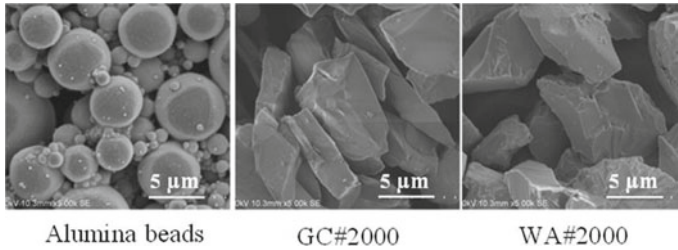


**Fig. 5** SEM micrographs of abrasives

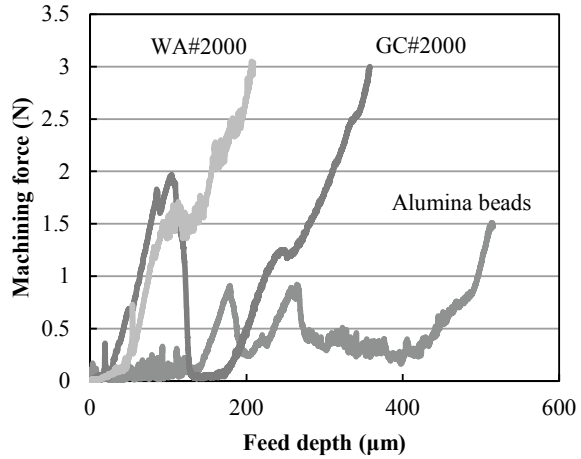
slurry was supplied at first, and no fresh abrasives were flowed into the cutting zone during machining. The detailed experimental conditions are listed in Table 3. A load cell is used during machining for monitoring the average force applied on the work substrate. The machining force is a very important parameter to evaluate the machining efficiency: when the material removal is not carried on smoothly, the force rapidly increases. It is because when the material removal rate is not higher than the feed speed, the clearance between the tool and the workpiece would decrease, inducing a decrease of the effective abrasives in the cutting zone. This leads to less and less material removal, finally resulting in cutting stagnation. Figure 6 presents the recorded data for machining force versus feed depth. According to our previous experimental experiences, when the machining force is higher than 3 N, the cutting process cannot continue effectively with the present ultrasonic drilling machine. It can be noticed that for both GC#2000 and WA#2000 abrasives, the machining force reaches 3 N, and the feed depth is larger for GC abrasives. In the case of alumina beads, the machining force is still lower than 3 N when the tool stops feeding. The feed depth is far larger than the other two cases. These experimental results imply that the material removal process is more effective and stable when using alumina beads abrasives. It supports the SPH simulation results that using abrasives with round shape is helpful to improve USM efficiency.

It also should be noticed that from the SPH simulation results, the value of  $n$  is much higher for SiC ogive abrasive than  $Al_2O_3$  semisphere abrasive, which hinted

**Table 3** Experimental conditions

Vibration frequency	61 kHz
Vibration amplitude	4 $\mu\text{m}_{p-p}$
Feed speed	1 $\mu\text{m/s}$
Workpiece	Soda-lime glass (1.2–1.5 mm thick)
Tool	SS304 ( $\phi$ 1 mm)
Abrasive type	GC#2000, WA#2000, Alumina beads
Concentration of abrasive slurry	20 wt% mixed with water
Amount of slurry	0.5 mL

**Fig. 6** Machining force



a higher machining efficiency for SiC ogive abrasive. However, the experimental results are different. The reason is considered to be the different forms of crack propagation in the substrate. For SiC ogive abrasive, the crack mainly propagates in the depth direction; however, for the semisphere abrasive, large cracks that propagate sideways toward the work surface are confirmed. In USM, large amount of microchips removal would be generated when the cracks initiated by adjacent abrasives intersect, and as a result yields large quantity of material removal. The intersection of cracks that was found by using a semisphere abrasive in SPH simulation is expected to make more material removal. Therefore, the feed depth is higher when using alumina beads than GC#2000 in the experiments.

Holes with a depth of 500 μm are then drilled with the three kinds of slurries respectively in order to check the abrasive fracture. Table 4 lists the detailed experimental conditions. When slurry made of WA#2000 was used, the feed speed was 0.5 μm/s. In the rest of the experiments, the feed speeds were 1 μm/s. The abrasive

**Table 4** Experimental conditions

Vibration frequency	61 kHz
Vibration amplitude	4 μm <sub>p-p</sub>
Machining depth	500 μm
Feed speed	0.5, 1 μm/s
Workpiece	Soda-lime glass (1.2–1.5 mm thick)
Tool	SS304 (φ 1 mm)
Abrasive type	GC#2000, WA#2000, Alumina beads
Concentration of abrasive slurry	20 wt% mixed with water
Flow rate of slurry	50 ml/min

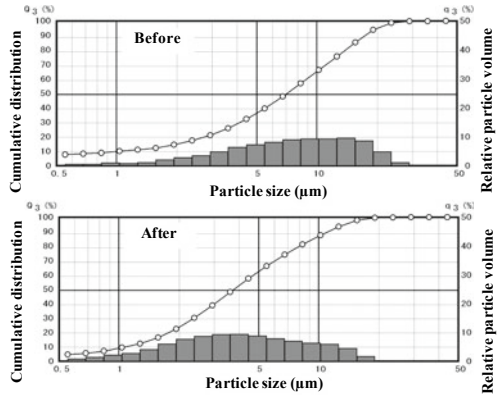
particle size distribution before and after machining was examined for each case and shown in Fig. 7. The volume for large abrasives decreases after machining for all kinds of slurries. And obvious transition can be identified for alumina beads, which indicates that the abrasive fracture is larger for this kind of abrasive. Table 5 lists the median diameter of abrasive particles before and after machining. The mean diameter decreases more seriously for the alumina beads. The results are good consistent with the simulation results.

## 4 Conclusions

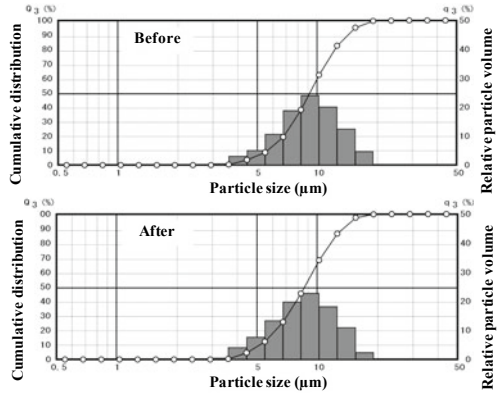
In this study, the influence of the abrasive shape on material removal of USM was investigated using both simulation and experimental methods. The propagation of the cracks in the substrate and the fracturing of the abrasive were demonstrated using the SPH model. The calculation results can well explain the experimental results. The major conclusions of this study can be summarized as follows:

1. The crack formation in substrate is strongly affected by the abrasive shape. When the abrasive shape is round without angles, large cracks that propagate sideways toward the work surface generate. This kind of crack is more helpful for material removing process.
2. The wear of abrasives that have different shapes is different, even though the abrasive material is the same. For the abrasive with an angular shape, only the material around sharp point fractures. While for the abrasives of round shape, the contact area between abrasive and substrate increases, inducing large fractures in both abrasive and substrate.
3. The SPH simulation results visually show the fracturing process in USM, and indicate that material removal efficiency is higher when using abrasive with round shape than angular shape.
4. The machining force is an extremely important parameter for studying the USM efficiency. When the material removal process does not go on smoothly, the machining force increases irreversibly. From the experimental results, the force keeps stable when machining a considerable depth of hole with alumina beads abrasives. It means that a higher machining efficiency can be obtained when using abrasives of round shape.
5. The good agreement between the simulation results and experimental results shows the validity of SPH model. In the future studies, the crack distribution on machined surfaces will be investigated with the help of SPH simulations. The crack problem has obstructed the applications of USM a lot. Therefore, we expect to provide a totally understanding of the crack formation using SPH method and make USM more effective to meet different manufacturing requirements.

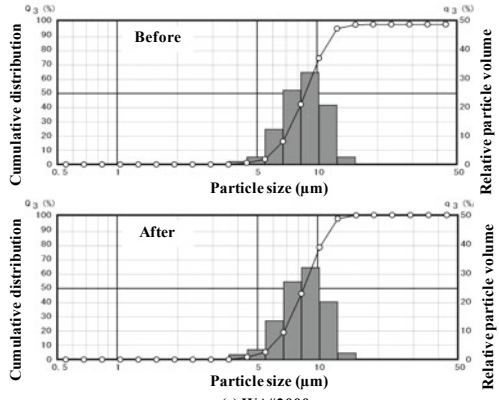
**Fig. 7** Particle size distribution before and after machining



(a) Alumina beads.



(b) GC#2000.



(c) WA#2000.

**Table 5** Median diameter before and after machining

	Alumina beads	GC#2000	WA#2000
Before ( $\mu\text{m}$ )	7.08	9.18	8.76
After ( $\mu\text{m}$ )	3.76	8.65	8.54

## References

1. Zhang C, Rentsch R, Brinksmeier E (2005) Advances in micro ultrasonic assisted lapping of microstructures in hard-brittle material: a brief review and outlook. *Int J Mach Tools Manuf* 45(7–8):881–890
2. Egashira K, Masuzawa T (1999) Microultrasonic machining by the application of workpiece vibration. *CIRP Ann Manuf Technol* 48(1):131–134
3. Thoe TB, Aspinwall DK, Wise MLH (1998) Review on ultrasonic machining. *Int J Mach Tools Manuf* 38(4):239–255
4. Wang J, Shimada K, Mizutani M, Kuriyagawa T (2013) Material removal in ultrasonic machining using smoothed particle hydrodynamics. *Int J Autom Technol* 7(6):614–620
5. Yu Z, Hu X, Rajurkar KP (2006) Influence of debris accumulation on material removal and surface roughness in micro ultrasonic machining of silicon. *Ann CIRP* 55(1)
6. Singh R, Khamba JS (2007) Taguchi technique for modeling material removal rate in ultrasonic machining of titanium. *Mater Sci Eng A* 460–461:365–369
7. Kumar V (2013) Optimization and modeling of process parameters involved in ultrasonic machining of glass using design of experiments and regression approach. *Am J Mater Eng Technol* 1(1):13–18
8. Bhosale SB, Pawade RS, Brahmkar PK (2014) Effect of process parameters on MRR, TWR and surface topography in ultrasonic machining of alumina-zirconia ceramic composite. *Ceram Int* 40:12831–12836
9. Wang J, Shimada K, Mizutani M, Kuriyagawa T (2014) Using smoothed particle hydrodynamics to examine influence of process parameters on ultrasonic machining. *Int J Autom Technol* 8(6):855–863

# The Effect of Cutting Speed and Tool Material on Hole Quality When Reaming C355 Aluminium Alloy



R. Rattanakit, S. L. Soo, D. K. Aspinwall, P. Harden, B. Haffner, Z. Zhang, and D. Arnold

**Abstract** A reaming operation is typically performed when the requirements for hole accuracy (form and size) and surface finish cannot be achieved solely by drilling. Experimental work was carried out to evaluate the influence of tool material/coating (uncoated carbide, CVD-diamond coated carbide and PCD) and cutting speed (32 and 96 m/min) on tool wear, cutting forces/torque and hole quality/integrity, when reaming pre-drilled (4.8 mm diameter) blind holes in cast, heat treated C355 aluminium alloy (~4.7% Si content). All of the reamers were 5.08 mm in diameter with trials undertaken at a constant feed rate of 0.12 mm/rev. Flank wear up to ~40  $\mu\text{m}$  was observed after ~1680 holes when employing the uncoated tungsten carbide (WC) reamers whereas no discernible signs of wear were seen on either the CVD-diamond coated or PCD tools at test cessation. Thrust forces were found to be ~50% higher when utilising the diamond coated reamers compared to the uncoated WC tools. Workpiece surface finish generally improved at the higher cutting speed with PCD tools producing roughness levels down to ~0.05  $\mu\text{m}$  Ra. Average hole out of roundness was below 5  $\mu\text{m}$  in all trials while corresponding cylindricity did not exceed 14  $\mu\text{m}$ . Material microhardness variation over the test duration was negligible and cross sectional micrographs showed no significant workpiece damage or deformation regardless of operating conditions.

**Keywords** Reaming · Diamond · Aluminium alloy

---

P. Harden—Formerly at Element Six Ltd.

---

R. Rattanakit · S. L. Soo (✉) · D. K. Aspinwall · P. Harden  
Machining Research Group, School of Mechanical Engineering, University of Birmingham,  
Edgbaston, Birmingham, UK  
e-mail: [s.l.soo@bham.ac.uk](mailto:s.l.soo@bham.ac.uk)

B. Haffner  
Doncasters Sterling, Colliery Lane, Exhall, Coventry, UK

Z. Zhang  
Doncasters Group Ltd., Millennium Court, First Avenue, Centrum 100, Burton-upon-Trent, UK

D. Arnold  
MAPAL Ltd., Old Leicester Road, Swift Park, Rugby, UK

## 1 Introduction

Aluminium alloys with silicon as the major alloying constituent typically form the basis for cast materials used in the automotive industry. The addition of silicon in aluminium aids castability, stimulates flow, enhances tensile strength, corrosion and wear resistance as well as minimising shrinkage during solidification and reducing thermal expansion of the cast component [1, 2]. The hard Si particles (~1000–1300 HK) however increases the abrasive characteristics of the workpiece material [3], which significantly reduces tool life, thereby making machining more expensive [4]. Roy et al. [5] carried out a comparative machinability study of cast pure aluminium against an aluminium alloy with 12% silicon (AlSi12) using uncoated and various coated carbide tools. An eightfold increase in flank wear from ~25  $\mu\text{m}$  for pure Al to 200  $\mu\text{m}$  for the eutectic alloy was recorded when turning the latter for 30 s at a cutting speed of 400 m/min and feed rate of 0.1 mm/rev, even when employing chemical vapour deposited (CVD) diamond coated inserts. Dwivedi et al. [6] investigated the influence of eutectic (12% Si) and hypereutectic (17% Si) cast Al-Si alloys on machinability and observed that higher silicon content increased bulk hardness of the workpiece material by ~5%, from 105 to 117 HV. This contributed to ~70% higher cutting forces and ~12% higher temperatures.

Uhlmann et al. [7] analysed the resulting tool wear mechanisms of nano-crystalline CVD diamond coated tools when machining aluminium alloys having 9% and 17% Si. The harder and more brittle hypereutectic AlSi17 alloy was highly abrasive, which led to fretting of the tool coating and displacement of the cutting edge. In contrast, the hypoeutectic AlSi9 material displayed a greater tendency to adhere to the tool surface causing built-up edge (BUE) formation and lower workpiece surface quality. Similarly, in studies concerning the high speed drilling of A383 Al-Si alloy, Farid et al. [8] found that adhered aluminium on the tools tended to plough the machined hole surface, producing irregular roughness profiles. Use of cutting fluid or minimum quantity lubrication (MQL) is recommended in order to reduce BUE when drilling aluminium alloys [9, 10]. In experiments performed using uncoated HSS drills with water spray ( $\text{H}_2\text{O}$ -MQL) on aluminium–silicon 319 alloys, Bhowmick and Alpas [11] showed that both BUE and adhered material on the tool decreased by 36% and 60% respectively when compared with dry cutting.

Reaming is classed as a secondary process that employs a multi-edge cutting tool to improve accuracy and reduce roughness of a hole surface by removing a small amount of material from the hole wall following a drilling operation. Compared with the drilling of aluminium alloy however, there is a limited amount of literature regarding tool performance and corresponding workpiece surface integrity when reaming aluminium alloys. Lugscheider et al. [12] evaluated the tool life of uncoated,  $\text{TiB}_2$ , TiBN and TiAlN coated WC tools when reaming AlSi12 alloy at a cutting speed of 150 m/min. Maximum tool flank wear after a cut length of 5 m did not exceed 25  $\mu\text{m}$ .

The present paper details experimental work to evaluate the influence of tool material and cutting speed on tool wear/life, cutting force, hole accuracy and surface

integrity following reaming of pre-drilled blind holes in cast C355 aluminium alloy, which is typically used in the manufacture of compressor impellers employed in automotive turbocharger systems.

## 2 Experimental Work

### 2.1 Workpiece Material, Tooling and Experimental Setup

The workpiece material employed was cast and heat treated (solution treated, quenched in hot water and air cooled followed by artificial ageing) C355 aluminium alloy having a nominal chemical composition of 93.5% Al, 4.7% Si, 1.2% Cu, 0.5% Mg and 0.1% Mn (weight percent). The cast material was face-milled and machined into rectangular blocks measuring  $340 \times 180 \times 30$  mm for principal tool wear experiments together with thinner strips of  $20 \times 180 \times 30$  mm utilised in cutting force and hole quality/dimensional accuracy evaluation, see Fig. 1. The mechanical properties of the alloy following heat treatment are detailed in Table 1.

The performance of uncoated and chemical vapour deposited (CVD) diamond coated solid tungsten carbide (K10, 10% Co binder) reamers were assessed against two different grades of brazed polycrystalline diamond (PCD) reamers, which were

**Fig. 1** Rectangular workpiece blocks and strips of C355 Al alloy

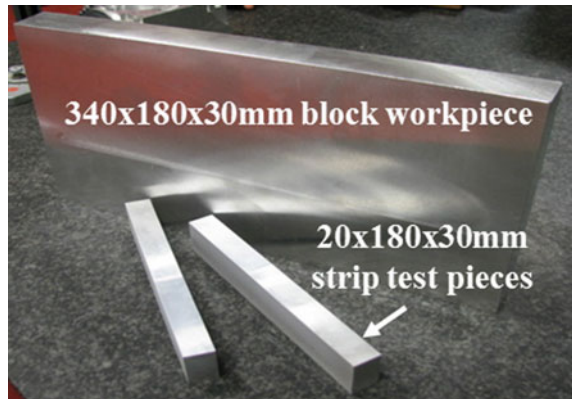


**Table 1** Mechanical properties of heat treated C355 Al alloy

Property	Value
Hardness (HK)	154
Ultimate tensile strength (MPa)	346.3
Proof stress (MPa, 0.2%)	271.7
Modulus of elasticity (GPa)	65.31
Elongation to failure (%)	6.5



**Fig. 2** **a** Uncoated WC and **b** brazed CTB002 PCD reamers

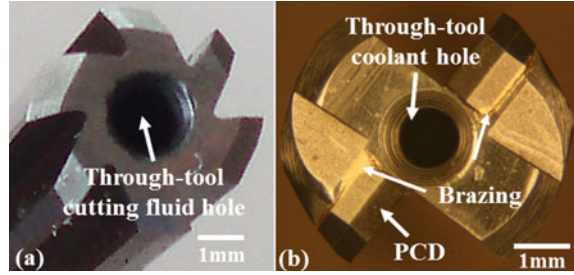
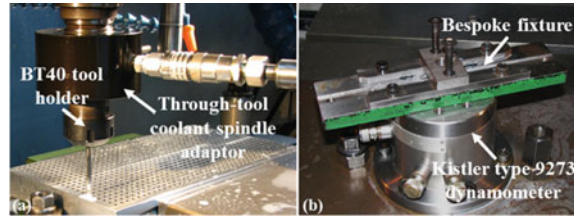


**Fig. 3** Experimental setup for **a** block and **b** strip workpieces



a unimodal fine grained (CTB002; 2  $\mu\text{m}$  grain size) and a multi-modal (CTM302; 2–30  $\mu\text{m}$  grain size) formulation. The room temperature hardness of the carbide substrate was 1550 HV, while the 3  $\mu\text{m}$  thick CVD-diamond coating was up to 10,000 HV. All of the reamers were straight ( $0^\circ$  helix), nominally 5.08 mm in diameter with a corner chamfer of  $0.5 \times 45^\circ$  and through-tool cutting fluid hole. The WC tools however were 6-fluted while the brazed PCD reamers had only 2 cutting edges, as shown in Fig. 2.

All tests were carried out on a Matsuura FX-5 high speed CNC vertical machining centre that was retrofitted with an internal through-tool coolant spindle adaptor (6000 rpm maximum rotational speed) incorporating a BT40 tool holder. A water-based emulsion containing 7–10% volume concentration of soluble mineral oil (Hocut 3380) was delivered at a flow rate of 12 l/min and pressure of 70 bar. The block workpieces were held in a large vice that was clamped onto the machine worktable, while the strip material was mounted in a bespoke fixture, attached to the dynamometer, see Fig. 3.

## 2.2 Test Parameters, Procedure and Experimental Array

A full factorial experiment was performed to assess the influence of tool material (4 levels) and cutting speed (2 levels) when reaming pre-drilled 4.8 mm diameter blind holes (28 mm depth) in C355 aluminium alloy. The reaming tests were performed on the same workpiece immediately following completion of the drilling operation, which was after 840 drilled holes (one rectangular block), without workpiece removal

**Table 2** Full factorial experimental array

Test No	Tool material	Cutting speed, m/min (rev/min)
1	Uncoated WC	32 (2000)
2	Uncoated WC	96 (6000)
3	CVD diamond coated WC	32 (2000)
4	CVD diamond coated WC	96 (6000)
5	PCD, CTB002	32 (2000)
6	PCD, CTB002	96 (6000)
7	PCD, CTM302	32 (2000)
8	PCD, CTM302	96 (6000)

from the vice in order to ensure reamer alignment. Results of the preceding drilling trials are detailed in a previous publication [13]. The end of test criterion was a total of 1680 holes (2 workpiece blocks) with measurement of tool wear (maximum flank wear,  $VB_{Bmax}$ ), cutting force/torque, hole geometrical accuracy and surface roughness performed on the first hole and at intervals of 280 holes thereafter. Table 2 details the experimental matrix, which show the combination of variable factor levels in each test. Feed rate was fixed at 0.12 mm/rev, tool overhang was 42 mm and runout did not exceed 10  $\mu\text{m}$ . No replications were carried out due to restrictions in terms of workpiece material and tooling availability.

Tool flank wear was measured using a WILD M3Z toolmakers microscope equipped with a X-Y digital micrometre platform (0.001 mm resolution), connected directly to a Canon 400D DSLR digital camera for image capture of new/worn reamers. A tilting table fitted with a bespoke fixture was employed to accommodate the through-tool cutting fluid spindle adapter arrangement (to avoid removing tool from collet) as well as to compensate for varying tool cutting edge angles in order to maintain optimum image focus. Thrust force and torque were measured using a Kistler 9273 drilling dynamometer, with recorded signals processed through a bank of Kistler type 5011 charge amplifiers connected to a computer running Dynoware software.

Reamed hole diameter was measured using a Diatest split ball probe (4.7–5.5 mm range) fitted with a Mitutoyo ID-C112MB digital indicator having a resolution of 0.001 mm. Geometrical parameters of the holes (roundness, cylindricity and parallelism) were assessed on a Taylor Hobson Talyrond 300 system equipped with a 3 mm ruby ball stylus. Five profiles were generated for each specimen with the measurements repeated three times. Following geometrical analysis of the holes, specimens were sectioned approximately 500  $\mu\text{m}$  from the hole centreline using wire electrical discharge machining (WEDM). The internal hole surface roughness ( $R_a$ ) was measured on a Taylor Hobson Form Talysurf 120L fitted with a 2  $\mu\text{m}$  radius diamond tipped stylus (0.8 mm cut-off and 4.0 mm evaluation length), see Fig. 4. Measurements were performed at 2 mm from hole entry and  $\sim$ 2 mm from the bottom of the hole.

**Fig. 4** Hole surface roughness evaluation. **a** Form Talysurf 120L unit and **b** measurement setup



Subsequently, the sectioned specimens were cold mounted in an epoxy resin mixture to avoid any metallurgical changes prior to the microhardness tests and microstructural analysis. The mounted samples were then ground and polished according to Buehler's four-step procedure for aluminium alloys using a Buehler Alpha twin-speed grinding/polishing unit. Microhardness depth profile measurements for the first and last holes (1 and 1680) were undertaken using a Mitutoyo HM 124 hardness tester with a Knoop diamond indenter (25 g load over 15 s duration). Optical investigation of subsurface damage and microstructural alterations of the cross-sectioned holes (following etching using Keller's reagent) was performed on a Leica microscope system fitted with a digital camera connected to a computer operating digital imaging software.

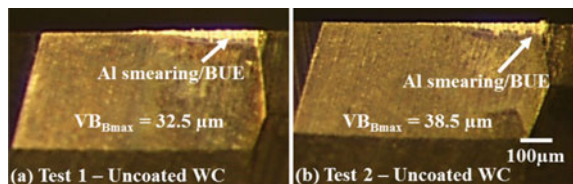
### 3 Results and Discussion

#### 3.1 Tool Wear and Forces

Evidence of aluminium workpiece smearing and BUE formation was observed on the tool flank face of the uncoated carbide reamers used in Tests 1 and 2 (32 and 96 m/min), with corresponding wear levels ( $VB_{Bmax}$ ) of up to 32.5 and 38.5  $\mu\text{m}$  respectively at test cessation, see optical micrographs in Fig. 5. These were comparable with results presented by Lugscheider et al. [14] when reaming AlSi12 alloy using PVD coated ( $\text{TiAlN}$  and  $\text{TiB}_2$ ) WC tools.

In contrast, no sign of workpiece material deposition/adhesion was visible on either the CVD diamond coated (Tests 3 and 4) or brazed PCD reamers (Tests 5 to 8) even after machining 1680 holes, see Fig. 6. Likewise, there were no discernible wear scars on any of the diamond-based reamers when viewed under the optical microscope.

**Fig. 5** Micrographs of worn uncoated reamers in **a** Test 1 and **b** Test 2 (after 1680 holes)



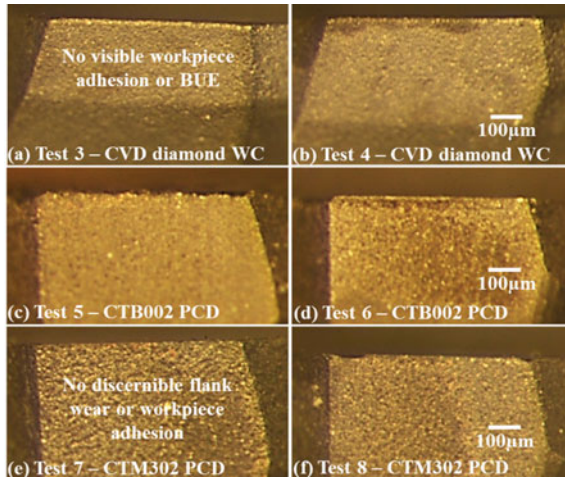


**Fig. 6** Micrographs of reamers at test cessation in **a** Test 3, **b** Test 4, **c** Test 5, **d** Test 6, **e** Test 7 and **f** Test 8

The progression of thrust force and torque during the reaming trials is detailed in Figs. 7 and 8 respectively. The CVD diamond coated reamers employed in Tests 3 and 4 were found to produce ~50% higher thrust force (ranging between 36 and 84 N) and 125% higher torque (ranging between 31 and 67 Ncm) compared to the standard uncoated carbide tools in Tests 1 and 2 at equivalent operating conditions. This was most likely due to the duller edge/larger cutting edge radius of the former as a result of the CVD diamond coating (3 µm thick) as illustrated in Fig. 9. Minimum thrust force (17–21 N) was achieved with both the fine (CTB002) and mixed (CTM302) grained PCD reamers when operating at the higher cutting speed of 96 m/min. Lower forces

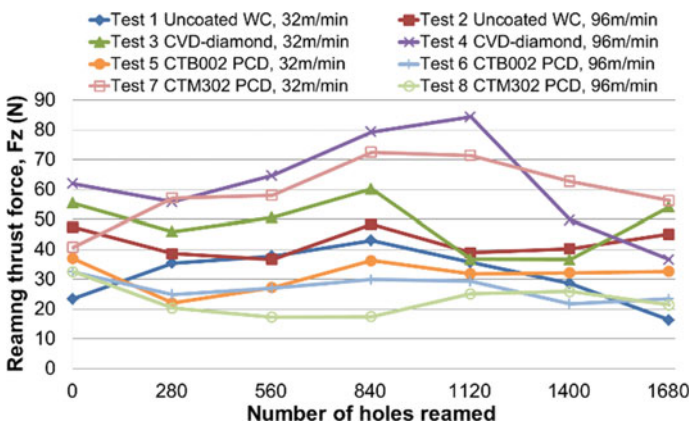


**Fig. 7** Variation in reaming thrust force over test duration

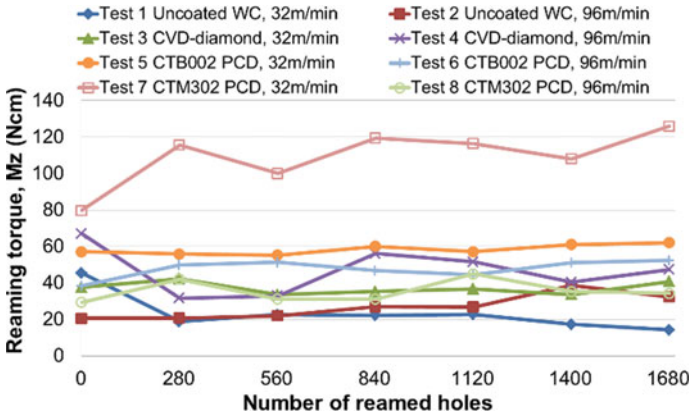
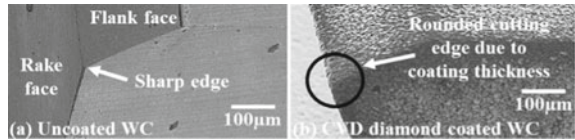


Fig. 8 Variation in reaming torque over test duration

Fig. 9 SEM images of new a uncoated WC and b CVD-diamond coated reamers



with increasing cutting speed were also reported by Wang et al. [15] when reaming ZL102 cast Al alloy using PCD tooling. The thrust force values in the current work did not exceed ~85 N in any of the trials.

With the exception of Tests 4 and 7, torque levels after hole 1 were generally stable throughout the test duration, a maximum value of 60 Ncm recorded when reaming with the CTB002 PCD at 32 m/min (Test 5). Conversely, the CVD diamond coated reamer operating at the higher cutting speed (Test 4) generated fluctuating torque (32–67 Ncm), while Test 7 involving the CTM302 grade produced the highest torque of 125 Ncm, although after hole 280 the rise was only ~26 Ncm to test cessation. The uncharacteristically high torque values measured in both Tests 4 and 7 were possibly due to the incidence of tool vibration during the trial. Figure 10 shows the typical unstable force signals observed when reaming using the CVD diamond coated WC and CTM302 PCD reamers.

### 3.2 Hole Geometric Quality

The variation in hole diameter following finish reaming over the test period is presented in Fig. 11. All of the holes machined with the uncoated and CVD diamond coated WC reamers were oversize by between 2 and 11 µm (compared with nominal size of the reamer). Conversely, both the PCD grades employed at the higher cutting

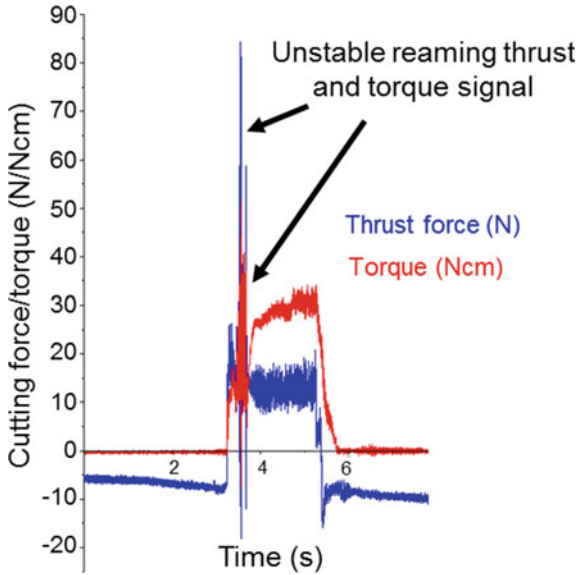


Fig. 10 Sample signal trace showing unstable thrust force and torque recorded in Tests 4 and 7

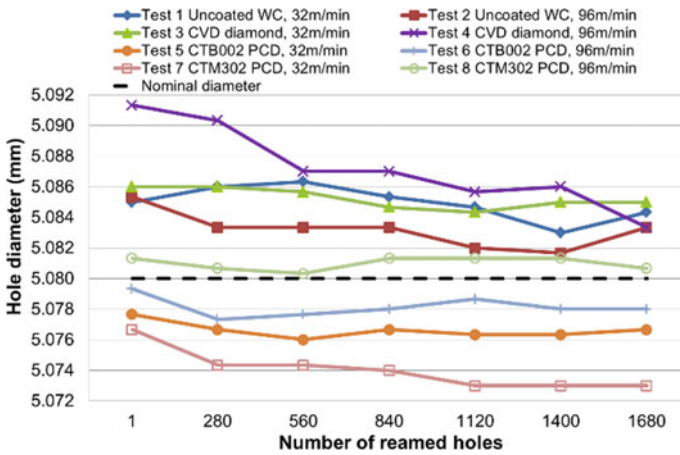
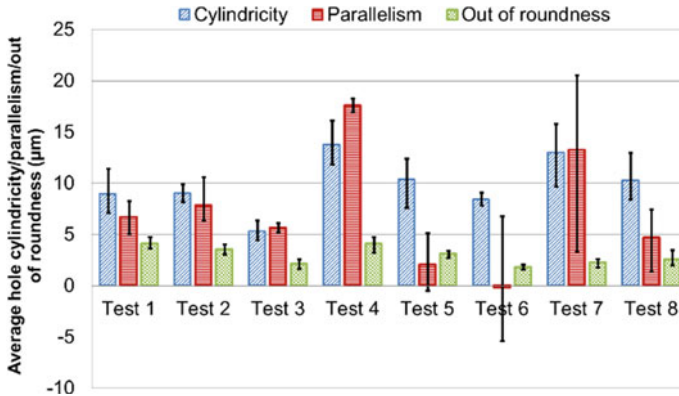


Fig. 11 Variation of reamed hole diameter over test duration

speed of 96 m/min in Test 6 (CTB002) and Test 8 (CTM302) resulted in holes with the lowest diametrical deviation, which were consistently within  $\pm 2 \mu\text{m}$  of the nominal reamer diameter (5.08 mm) over the entire duration of the experiment. The holes in Test 7 however showed a decreasing trend in size from 5.077 mm at the first hole to 5.073 mm at the last hole.



**Fig. 12** Average hole cylindricity, parallelism and out of roundness over test test duration

The hole geometric parameters for each test are shown in Fig. 12. The average out of roundness was typically less than  $\sim 4 \mu\text{m}$  in all of the experiments performed, with the best performance seen in Test 6 involving the CTB002 grade reamer ( $\sim 1.8 \mu\text{m}$ ). This represented a notable improvement compared to the results after drilling, where hole out of roundness generally varied between 5 and 7  $\mu\text{m}$  [13]. Hole cylindricity values did not exceed 14  $\mu\text{m}$  following reaming, the lowest value of 5.28  $\mu\text{m}$  corresponding to the CVD diamond coated tool utilised in Test 3 at 32 m/min. Similar hole accuracy was detailed by Yan et al. [16] following the reaming of AISi12 using PCD cutters. In terms of parallelism, positive values were measured in almost all of the tests undertaken, suggesting that the reamed holes tapered towards hole entry. In general, hole cylindricity and parallelism produced in Test 4 (CVD diamond) and Test 7 (PCD CTM302) were comparatively poor, possibly due to tool vibration/chatter. Additionally, the high thrust force (Fig. 7) and torque (Fig. 8) detailed previously further supports this observation.

### 3.3 Hole Surface Roughness and Integrity

Figures 13 and 14 show the progression of hole surface roughness ( $R_a$ ) measured at the entry and exit locations respectively. Aside from a number of uncharacteristic peaks/spikes in  $R_a$  recorded in Test 3 (hole 282) and Test 5 (hole 563), the workpiece surface quality was found to be generally better at the top (entry) of the reamed holes compared with that obtained towards the bottom. The unusual peaks were possibly due to flaws on the hole surfaces within the region of the evaluation length. The general trend also suggests that workpiece surface finish improved as cutting speed increased to 96 m/min. Previous published work relating to the machining of non-ferrous materials including aluminium alloys [17, 18] suggested that an increase in cutting speed raised the temperature within the machining zone, which led to

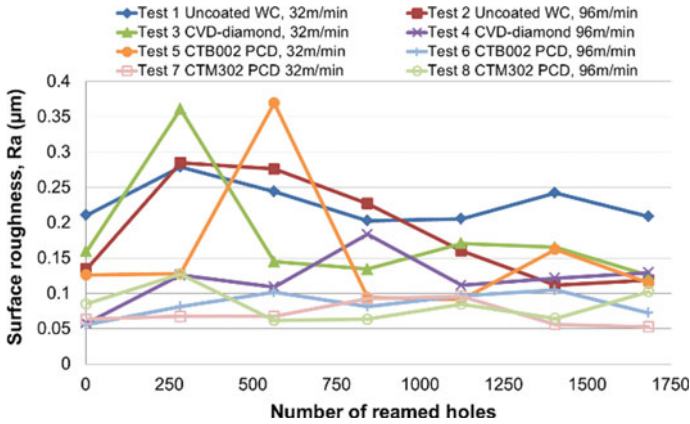


Fig. 13 Surface roughness near the hole entry

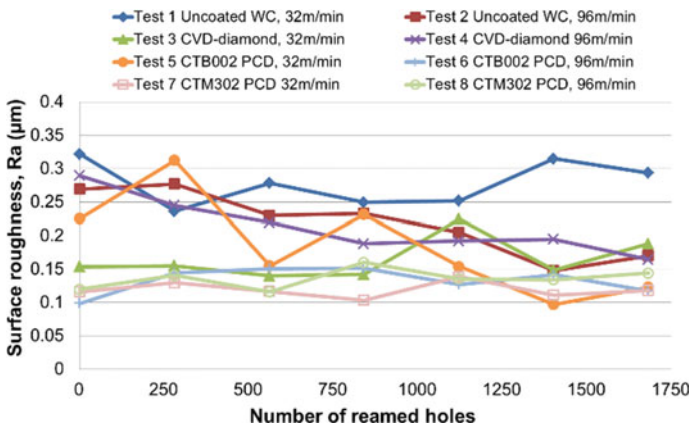


Fig. 14 Surface roughness near the bottom of the hole

thermal softening of the workpiece resulting in a considerable reduction in surface damage and roughness. Typically, the CTM302 grade PCD reamers produced the lowest and most consistent overall surface roughness (~0.05 μm Ra) regardless of the cutting speed, followed by the fine-grained CTB002. The PCD reamers also generated superior workpiece surface roughness compared to the CVD diamond coated and uncoated tools, due to their greater wear resistance and lower affinity to BUE formation/material adhesion.

Microhardness depth profiles measured perpendicular to the feed direction for tests at 32 and 96 m/min cutting speed are shown in Figs. 15 and 16 respectively. Minimal change in surface/subsurface microhardness level was observed in the majority of tests, although a hardened layer up to 24.6 HK<sub>0.025</sub> (~17%) above the bulk hardness to a depth of 75 μm was found in Test 4 involving the CVD diamond



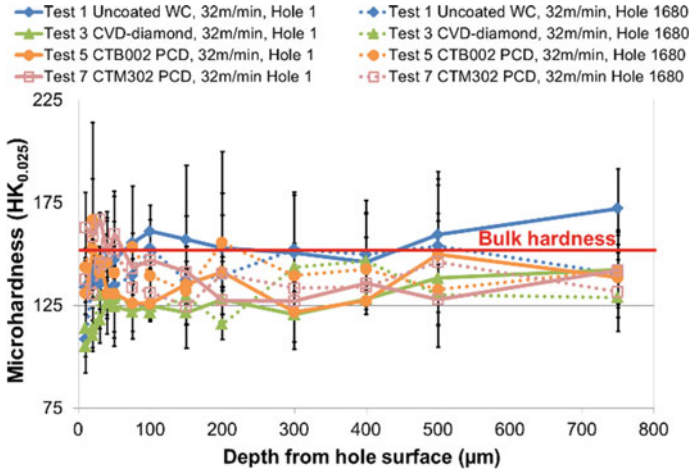


Fig. 15 Microhardness depth profile when machining at 32 m/min for the first and last holes reamed

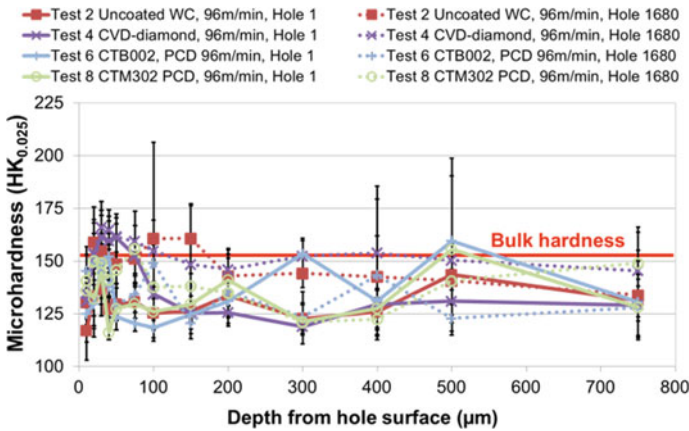


Fig. 16 Microhardness depth profile when machining at 96 m/min for the first and last holes reamed

tool at the start and end of tests. High silicon dispersion within the indentation area could have been the reason for the deviation in microhardness values.

Subsequent examination of the etched cross-sectioned samples from each trial revealed no major surface/subsurface microstructural damage or deformation even after reaming 1680 holes, regardless of the operating parameters, see Fig. 17. This was also in line with hole roughness observations in all tests, with surfaces being extremely consistent from the start to the end of the experiments. Furthermore, the pits found previously on the hole surfaces when drilling with uncoated WC tools [13], were successfully removed by the reaming operation.

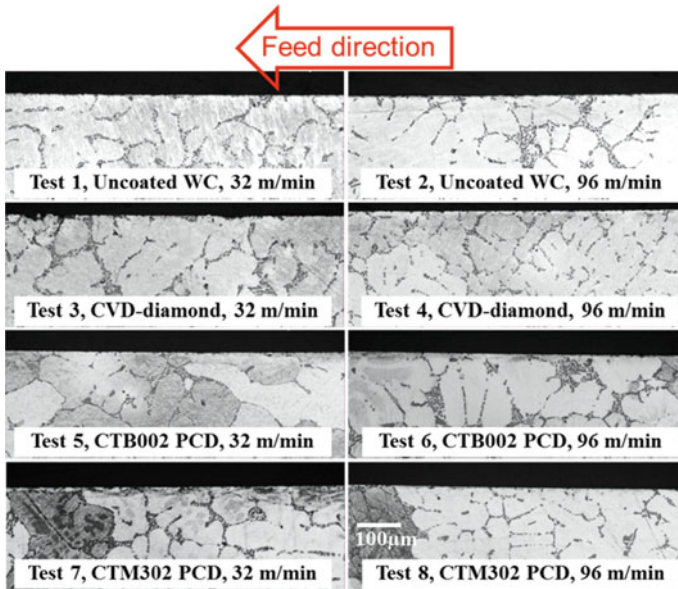


Fig. 17 Cross-sectional micrographs of hole subsurface microstructure at hole 1680 for all tests

#### 4 Conclusions

- Smearing of Al material and BUE was prevalent on the flank faces of the uncoated WC reamers when machining with both low (32 m/min) and high (96 m/min) cutting speeds. However, this was not apparent with the brazed PCD or the CVD diamond coated WC reamers, regardless of machining conditions.
- Tool flank wear scars were only visible on the uncoated WC tools, which were up to 32.5 and 38.5  $\mu\text{m}$  ( $\text{VB}_{\text{Bmax}}$ ) when reaming at 32 and 96 m/min respectively.
- Generally, the diameter of holes produced using the uncoated and CVD diamond WC coated reamers were oversized by up to 11  $\mu\text{m}$ . In contrast, hole diameter was within  $\pm 2 \mu\text{m}$  even after 1680 holes when employing the PCD tools (both CTB002 and CTM302 grades), at a cutting speed of 96 m/min.
- Reamed hole out of roundness values were  $< 5 \mu\text{m}$  for all the specimens assessed. The lowest surface roughness achieved was 0.05  $\mu\text{m}$  Ra when utilising the brazed PCD CTM302 reamers.
- There was minimal change in hole surface/subsurface microhardness following reaming, with the exception of Test 4 (CVD diamond coated WC tool), which showed a hardened layer  $\sim 25 \text{HK}_{0.025}$  above the bulk hardness to a depth of 75  $\mu\text{m}$ .
- Workpiece microstructure evaluation revealed no significant hole surface/subsurface damage in any of experiments, irrespective of tool material or cutting speed.

**Acknowledgements** The authors are grateful to the UK's Engineering and Physical Sciences Research Council (EPSRC) for funding an EngD studentship. We also wish to thank Doncasters Sterling, Mapal and Element Six for providing workpiece material, tooling and financial support for the research.

## References

1. Polmear I (2006) *Light alloys: from traditional alloys to nanocrystals*. Butterworth-Heinemann, UK
2. Sarkar AD, Clarke J (1980) Friction and wear of aluminium-silicon alloys. *Wear* 61(1):157–167
3. Ng EG, Szablewski D, Dumitrescu M, Elbestawi MA, Sokolowski JH (2004) High speed face milling of a aluminium silicon alloy casting. *CIRP Ann-Manuf Technol* 53(1):69–72
4. Bezerra AA, Machado AR, Souza AM, Ezugwu EO (2001) Effects of machining parameters when reaming aluminium–silicon (SAE 322) alloy. *J Mater Process Technol* 112(2–3):185–198
5. Roy P, Sarangi SK, Ghosh A, Chattopadhyay AK (2009) Machinability study of pure aluminium and Al-12% Si alloys against uncoated and coated carbide inserts. *Int J Refract Met Hard Mater* 27(3):535–544
6. Dwivedi DK, Sharma A, Rajan TV (2008) Machining of LM13 and LM28 cast aluminium alloys: part I. *J Mater Process Technol* 196(1–3):197–204
7. Uhlmann E, Reimers F, Byrne F, Klaus M (2010) Analysis of tool wear and residual stress of CVD diamond coated cemented carbide tools in the machining of aluminium silicon alloys. *Prod Eng Res Dev* 4(2–3):203–209
8. Farid AA, Sharif S, Idris MH (2011) Surface integrity study of high-speed drilling of Al-Si alloy using HSS drill. *Proc Inst Mech Eng Part B J Eng Manuf* 225(5):1–7
9. Haan DM, Batzer SA, Olson WW, Sutherland JW (1997) An experimental study of cutting fluid effects in drilling. *J Mater Process Technol* 71(2):305–313
10. Jayal AD, Balaji AK, Sesek R, Gaul A, Lillquist DR (2007) Machining performance and health effects of cutting fluid application in drilling of A390.0 cast aluminum alloy. *J Manuf Process* 9(2):137–146
11. Bhowmick S, Alpas AT (2008) Minimum quantity lubrication drilling of aluminium-silicon alloys in water using diamond-like carbon coated drills. *Int J Mach Tools Manuf* 48(12–13):1429–1443
12. Lugscheider E, Knotek O, Barimani C, Leyendecker T, Lemmer O, Wenke R (1999) PVD hard coated reamers in lubricant-free cutting. *Surf Coat Technol* 112(1–3):146–151
13. Rattanakit R, Soo SL, Aspinwall DK, Haffner B, Zhang Z, Arnold D, Harden P (2013) Evaluation of tool performance and hole quality when drilling C355 aluminium alloy using diamond coated and PCD drills. In: *Proceedings of the 37th international MATADOR conference*, 25–27 July 2012, Manchester, UK, pp 173–176
14. Lugscheider E, Knotek O, Barimani C, Leyendecker T, Lemmer O, Wenke R (1997) Investigations on hard coated reamers in different lubricant free cutting operations. *Surf Coat Technol* 90(1–2):172–177
15. Wang Y, Cui X, Xu H, Jiang K (2013) Cutting force analysis in reaming of ZL102 aluminium cast alloys by PCD reamer. *Int J Adv Manuf Technol* 67:1509–1516
16. Yan X, Li B, Li J, Yang L (2013) Analysis of the machining characteristics in reaming AlSi12 alloy with PCD reamer. *Int J Adv Manuf Technol* 69:2387–2399
17. Jeelani S, Musial M (1984) Effect of cutting speed and tool rake angle on the fatigue life of 2024–T351 aluminium alloy. *Int J Fatigue* 6(3):169–172
18. Moneim MEA (1981) Effect of drilling speed on the required torque and thrust force for non-ferrous materials. *Wear* 66(1):65–75

# Performance of Multi-margin Coated Tools in One-Shot Drilling of Metallic-Composite Stack Materials Under Varying Feed Rate and Pecking Conditions



C. L. Kuo, S. L. Soo, D. K. Aspinwall, W. Thomas, C. Carr, D. Pearson, R. M'Saoubi, and W. Leahy

**Abstract** The paper details an investigation into the influence of operating conditions and drill margin design on tool wear, hole accuracy and chip morphology when single-shot drilling Ti–6Al–4V/CFRP/Al7050 stack materials (6.35 mm diameter holes). A full factorial experiment involving 3 factors (feed rate, margin design and pecking strategy), each at 2 levels (total of 8 tests) was undertaken. Statistical analysis techniques incorporating analysis of variance (ANOVA) and main effects plots were employed to identify the significance of variable parameters on response measures. All holes were found to be undersized when utilising triple margin drills irrespective of feed rate or peck cycle, with average diameters typically  $\sim 20 \mu\text{m}$  smaller compared to those produced using the single margin design. The use of a pecking strategy together with triple margin drills however resulted in superior hole cylindricality, although none of the variables were statistically significant at the 5% level. In contrast, margin design had a substantial impact on minimising hole out of roundness, especially in the Ti and CFRP sections with corresponding percentage contribution ratios (PCR's) of  $\sim 96\%$  and  $70\%$  respectively. Lower wear rates were generally observed when drilling at the higher feed rate level regardless of pecking strategy or margin design. An analysis of the swarf revealed that packing and folding

---

C. L. Kuo · S. L. Soo (✉) · D. K. Aspinwall  
Machining Research Group, School of Mechanical Engineering, University of Birmingham,  
Edgbaston, Birmingham, UK  
e-mail: [s.l.soo@bham.ac.uk](mailto:s.l.soo@bham.ac.uk)

C. L. Kuo  
Department of Mechanical Engineering, National Taiwan University of Science and Technology,  
#43, Sec. 4, Keelung Road106, Taipei, Taiwan, ROC

W. Thomas · C. Carr  
Composites Research Centre, GKN Aerospace Services Ltd., Whippingham Road, East Cowes,  
Isle of Wight, Luton, UK

D. Pearson · R. M'Saoubi  
Seco Tools (UK) Ltd., Springfield Business Park, Alcester, UK

W. Leahy  
Element Six Ltd., Harwell, Didcot, UK

of the Ti and Al chips were prominent, particularly when operating with the triple margin drills due to a smaller curvature in the flutes, which impeded chip evacuation.

**Keywords** Drilling · Metallic-composite stacks · Hole accuracy

## 1 Introduction

The integrity and dimensional accuracy of fastener holes in metallic-composite stacks are critical considerations especially when they are subject to severe loading conditions in bolted/riveted joints within aircraft fuselage. The development of drilling process technology for producing such holes has therefore been a topic of intensive research over the past ~ 15 years. Early work by Ramulu et al. [1] focussed on assessing the effect of different tool materials (high speed steel, high speed steel-cobalt and tungsten carbide), cutting speed (6–55 m/min) and feed rate (0.03–0.25 mm/rev) on cutting force, tool wear and burr formation when wet drilling multi-directional graphite/bismaleimide (Gr/Bi) and titanium (Ti) stack workpieces. Elevated temperatures predominantly at the Ti layer corresponding to higher cutting speed operation dramatically increased tool wear and led to severe deterioration in hole quality. Not surprisingly, increased thrust force, torque and workpiece surface roughness were prevalent at higher feed rates, however a significant reduction in burr size and composite thermal damage was observed. The combination of low cutting speed and intermediate feed rate using carbide drills was recommended as preferred process conditions. In trials involving the drilling of Al/CFRP/Ti stacks, Brinksmeier and Janssen [2] concluded that the use of carbide step drills at low cutting speed (10 m/min) with minimum quantity lubrication (MQL) provided the best results in terms of hole quality and tool life. Hard titanium diboride ( $\text{TiB}_2$ ) and diamond coatings had limited impact. Furthermore, evacuation of Ti chips from the bottom of the stack was found to cause considerable damage at the CFRP/Ti junction together with erosion of the composite hole surface.

More recently, research on evaluating the influence of operating parameters, cutting environment and advanced diamond coatings on tool wear and hole accuracy/surface integrity when drilling 3 layer metallic-composite stacks has been reported [3, 4]. Shyha et al. [3] indicated that cutting environment had a dominant effect on overall hole quality when drilling Ti/CFRP/Al stacks with uncoated, chemical vapour deposited (CVD) diamond and hardmetal (AlTiN grains embedded within amorphous  $\text{Si}_3\text{N}_4$  matrix) coated carbide tools. Reduced surface roughness, burr height and delamination in the CFRP section together with minimal strain hardening in both the Ti and Al layers were evident when machining with high-pressure (70 bar) cutting fluid as opposed to spray mist. A comparative study on the performance of diamond like carbon (DLC) and CVD-diamond coated carbide drills when single-shot drilling Ti/CFRP/Al stacks showed that the former generally failed through progressive abrasion and workpiece material adhesion leading to fracture of the tool corner, while wear in the latter was principally characterised by flaking and

delamination of the coating [4]. The CVD-diamond coated drills however produced holes with superior cylindricity and diametrical accuracy together with lower burr formation, particularly at the exit locations.

Drill geometry design incorporating multiple cutting edges or margins has been developed to improve tool strength/rigidity. Ema et al. [5] showed that although hole accuracy improved when utilising a drill with 3 cutting edges, associated torque and thrust force levels were up to 50% and 100% higher respectively compared to a conventional two-fluted twist drill. Decreasing the web thickness at the chisel edge and tool inclination angle was found to reduce cutting forces and enhance hole surface quality. Similarly, Piquet et al. [6] demonstrated that use of a specially designed triple cutting edge tool with multiple facets was successful in minimising hole surface defects and geometrical errors (out of roundness, diameter etc.) when drilling thin (3 mm thick) carbon/epoxy composite plates.

The present paper details experimental work to evaluate the effect of drill margin design, feed rate and pecking cycle on tool wear and hole accuracy when single-shot drilling Ti/CFRP/Al stacks.

## 2 Experimental Work

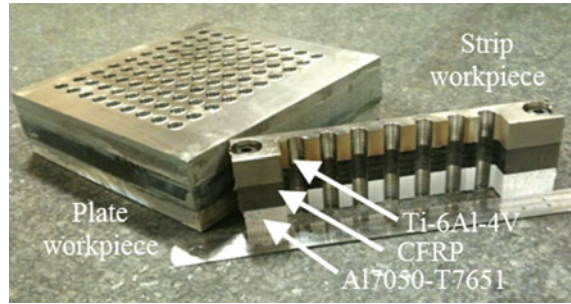
### 2.1 Workpiece Material, Tooling and Experimental Setup

The drilling trials were undertaken on 3-layer metallic/composite stacks comprising annealed Ti-6Al-4V titanium alloy, carbon fibre reinforced plastic (CFRP) composite (ACG MTM441/HTS-268-12K, fibre volume fraction = 56%) and age-strengthened A7050-T7651 aluminium alloy. Table 1 details the heat treatment conditions/lay-up configuration and mechanical/physical properties of the respective material sections in the stack. Each layer of the workpiece plates was 10 mm thick with square dimensions of 120 × 120 mm and was bonded together using a

**Table 1** Material specification/properties of the Ti, CFRP and Al workpiece specimens

Material specification	Ti-6Al-4V	CFRP	Al7050-T7651
Treatment/configuration	Annealed	[45°/0°/135°/90°/45°/0°] <sub>6s</sub>	Duplex aged, stabilised, stress-relieved
Density (g/cm <sup>3</sup> )	4.43	1.6	2.83
Hardness	350 HV	60–65 Barcol	171 HV
Thermal conductivity (W/mK)	7	1 ⊥ and 70 // to fibre direction	153
UTS (MPa)	950	2000	515
Modulus of elasticity (GPa)	115	150	72

**Fig. 1** Workpiece material stack plates for tool life testing and strips for force measurement and hole quality assessment



film adhesive (3M AF163) arranged in the order of Ti/CFRP/Al. Additional workpiece specimens in the form of thin strips measuring  $120 \times 17 \times 30$  mm were also prepared, which were mechanically joined using two M6 button head screws to enable easy disassembly for subsequent hole surface roughness, out of roundness and cylindricity analysis, see Fig. 1.

Tests were carried out on a Matsuura FX-5 vertical machining centre retrofitted with an internal through-tool coolant spindle adaptor system (6000 rpm maximum rotational speed) incorporating a BT40 tool holder. The cutting fluid employed was a water-based emulsion containing 6–8% volume concentration of soluble mineral oil (Hocut 3380), delivered at a flow rate of 30 L/min and pressure of 70 bar. Plate workpiece stacks used for tool life trials were mounted on a base plate with an array of predrilled (9 mm diameter) holes to provide support and clearance during drill exit from the material. In contrast, the strip specimens for hole accuracy assessment were held in a bespoke fixture, which was clamped onto the dynamometer, see Fig. 2. Results relating to cutting force and corresponding hole surface integrity are detailed in a previous publication [7].

Twin-fluted, solid carbide twist drills with equivalent geometry but having different margin designs (single and triple) were evaluated, see Fig. 3. The carbide material was a submicron grade (average grain size of  $0.6 \mu\text{m}$ ) with a 10% Co binder content providing a transverse rupture strength of  $\sim 3600$  MPa. All of the

**Fig. 2** Set-up of through-tool coolant spindle, workpiece fixturing and dynamometer

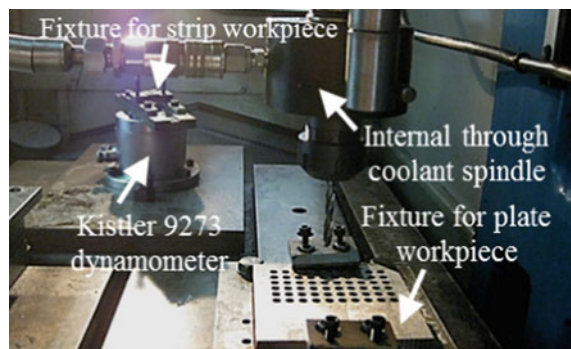


**Fig. 3** Point geometry of single and triple margin drills

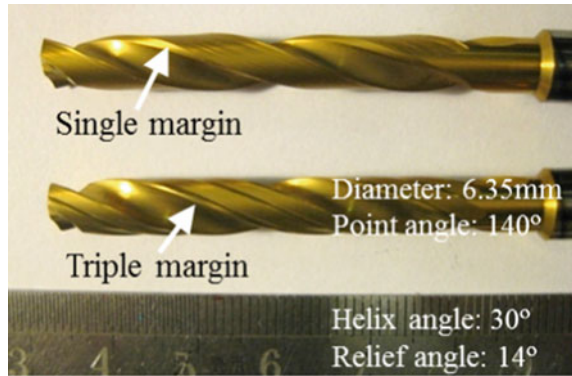


**Table 2** Properties of tungsten carbide substrate and TiAlN/TiN coating [8]

Property	WC-10Co	TiAlN/TiN
Density (g/cm <sup>3</sup> )	14.9	4.81
Microhardness	1580 HV <sub>30</sub>	30–35 GPa
Young's modulus (kN/mm <sup>2</sup> )	590	359–515
Coefficient of thermal expansion (10 <sup>-6</sup> /K)	5.5	6.5
Thermal conductivity (W/mK)	80	4.63

drills were 6.35 mm in diameter and coated with TiAlN/TiN. Table 2 details the key mechanical/physical properties of the tungsten carbide substrate (WC-10Co) and corresponding multilayer hardmetal coating [8].

## 2.2 Test Parameters, Procedure and Experimental Array

A full factorial experiment was performed to investigate the effect of margin design, feed rate and drilling strategy (each at 2 levels) when single-shot drilling the Ti/CFRP/Al stacks. Cutting speeds of 30/120/120 m/min were used for the Ti/CFRP/Al layers respectively. Table 3 details the variable factors together with their corresponding levels while the experimental array is shown in Table 4. Hole quality parameters were initially recorded at the first and tenth holes and thereafter

**Table 3** Variable factors and corresponding levels

Factor	Level 1	Level 2
Margin design	Single margin	Triple margin
Feed (mm/rev)	0.05	0.08
Drilling strategy	No pecking	Pecking with 2 mm retraction at each material layer interface



**Table 4** Full factorial experimental array

Test No	Margin design	Feed (mm/rev)	Drilling strategy
1	Triple margin	0.05	No pecking
2	Single margin	0.05	No pecking
3	Triple margin	0.08	No pecking
4	Single margin	0.08	No pecking
5	Triple margin	0.05	Pecking
6	Single margin	0.05	Pecking
7	Triple margin	0.08	Pecking
8	Single margin	0.08	Pecking

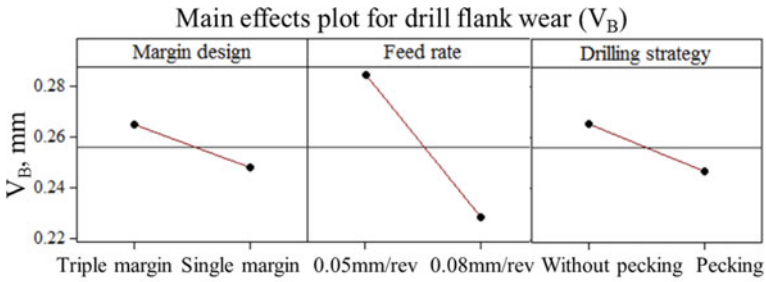
at intervals of 20 holes. Due to the limited availability of workpiece material, the end of test criteria was a flank wear ( $V_B$ ) of 300  $\mu\text{m}$  or maximum of 90 holes drilled.

Maximum flank wear on each cutting lip was measured (and the values averaged) using a toolmakers microscope equipped with a 2-axis platform employing digital micrometres having 1  $\mu\text{m}$  resolution. A digital camera (Canon EOS 400D) was also installed on the microscope via a special adaptor to capture micrographs of wear patterns on the drills, which were held in a modified rotary tilting table (0–45° angle). Hole quality parameters in terms of diameter, cylindricity and out of roundness were assessed using a Taylor Hobson Talyrond 300 by sampling three pitch points (entry, mid-point, exit) in each material layer (total of 9 axial positions). All measurements were replicated twice and the mean calculated. A special drilling methodology/sequence was also formulated to enable workpiece swarf produced near the hole entrance and exit in both the Ti and Al sections to be collected for chip morphology analysis using a Leica optical microscope together with a JEOL 6060 scanning electron microscope (SEM). This procedure was performed after every twenty holes drilled.

### 3 Results and Discussion

#### 3.1 Tool Wear

Figure 4 details the main effects plot for average maximum flank wear of the drills at test cessation together with the corresponding analysis of variance (ANOVA). The latter highlighted that feed rate had a significant effect on tool wear with a percentage contribution ratio (PCR) of 72.4%. This was supported by the drill flank wear data (after 90 holes) for each trial outlined in Fig. 5, which clearly showed lower wear rates when operating at the higher feed rate level of 0.08 mm/rev, regardless of margin design or pecking strategy. This was most likely due to the reduced contact duration between the drill and workpiece material at elevated feed rates.



ANOVA table		Drill flank wear				
Source of variance	D.F.	Seq. S.S.	M.S.	$F_{cal}$	P	PCR
Margin design	1	0.00058	0.00058	2.76	0.172	4.40%
Feed rate	1	0.00627	0.00627	29.90*	0.005	72.40%
Drilling strategy	1	0.00068	0.00068	3.24	0.145	5.67%
Residual	4	0.00084	0.00021			17.53%
Sums of squares		0.00837				

\* Significant at 5% level ( $F_{0.05} 1, 4=7.71$ )

Fig. 4 Main effects plot and ANOVA table of drill flank wear at test cessation

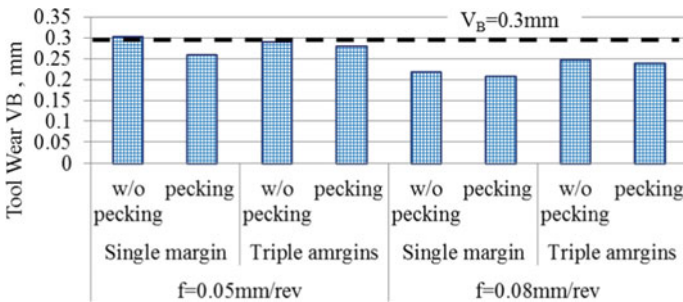
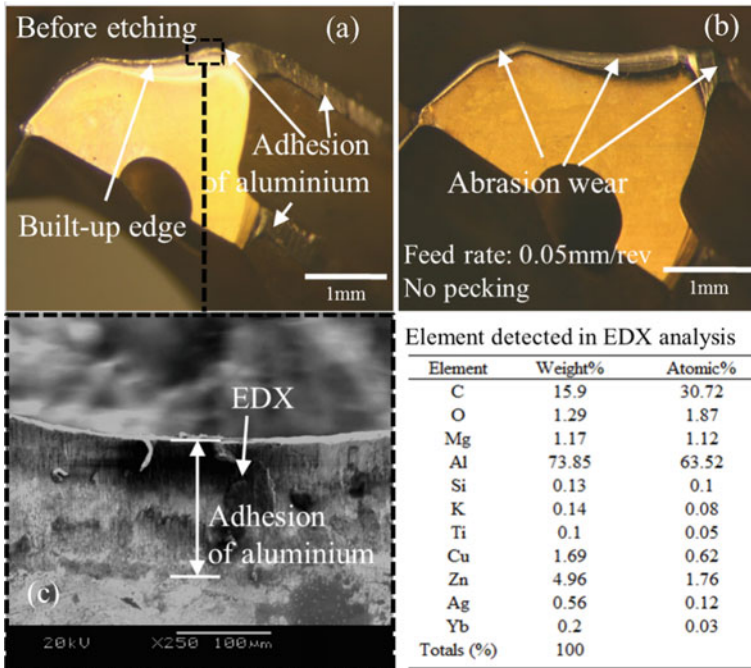


Fig. 5 Drill flank wear at test cessation (90 holes)

Figure 6 shows micrographs of wear modes observed on the triple margin drill at the end of Test 1, which was representative of results in the other trials. Built-up edge (BUE) of up to  $60 \mu\text{m}$  thickness was apparent along the entire cutting lip as well as the margin sections, see Fig. 6a. The adhesion of workpiece material at the chisel edge location was probably due to ploughing as a result of the low cutting speed, whilst the larger area of contact at the drill margins also promoted BUE formation. Subsequent removal of the adhered material/BUE by immersing drills in a 25% solution of sodium hydroxide (NaOH) revealed abrasion wear patterns; see Fig. 6b, which was particularly severe at the peripheral corner due to the location being that of maximum cutting speed. Examination of the drill flank area using energy dispersive



**Fig. 6** Micrographs of worn drill in Test 1 showing **a** BUE/workpiece adhesion, **b** abrasion wear pattern and **c** EDX analysis of flank face

spectroscopy (EDX) verified that the adhered material was primarily aluminium alloy as detailed in Fig. 6c.

Figure 7 shows cross-sectional micrographs of typical drill cutting edges in the new condition as well as at test cessation for both single and triple margin tools when machining at a feed rate of 0.05 mm/rev without pecking. The initial cutting edge radius of the drills as supplied was found to be ~ 33 μm and is illustrated in Fig. 7a. Deterioration of the edge geometry was evident mainly due to abrasion, with the edge

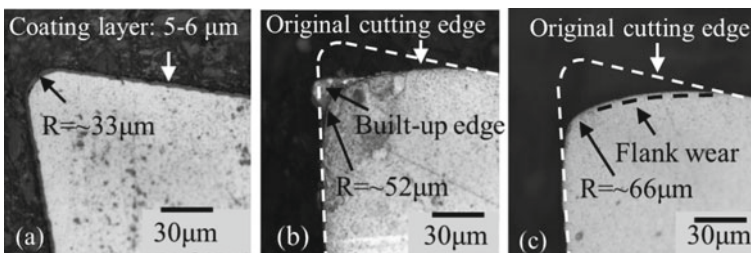


**Fig. 7** Micrographs of drill cutting edge when **a** new, **b** worn single margin and **c** worn triple margin when drilling at 0.05 mm/rev without pecking

radii of the single and triple margin drills increasing to ~ 52 and 66 μm respectively, after 90 holes. The greater edge rounding of triple margin drills was in line with tool flank wear results in Fig. 5, which was attributed to more intense rubbing with the machined hole surface.

### 3.2 Hole Diameter

According to Garrick [9], the typical overall diameter tolerance for holes in aerospace structures is 0.076 mm (± 0.038 mm). Figure 8 shows the evolution of average hole diameter (over all 3 material layers) with respect to the number of holes drilled in all tests. The results clearly highlighted two distinct data sets, where the single margin drills produced holes with superior diametrical accuracy (varying between 6.332 and 6.368 mm over the test duration), all of which were within the tolerance band, irrespective of operating conditions. In contrast, all of the holes produced using the triple margin geometry drills were undersized (< 6.35 mm), with the majority near or marginally below the lower tolerance limit of 6.312 mm, particularly after exceeding ~ 50 holes drilled. The variation in measured hole diameters however appeared to show no correlation with the tool wear results.

Table 5 details the associated ANOVA calculations with respect to hole diameter for each individual layer of the stack together with the overall average value. The results show that margin design is the principal significant factor affecting hole diameter in the Ti, CFRP and Al layers with corresponding PCRs of 80.26%, 88.09% and 89.33% respectively, whilst feed rate and drilling strategy had virtually no influence. The trends were similar when considering the overall average hole diameter with margin design showing an overwhelming PCR of ~ 93%. Further inspection of the triple margin drill geometry revealed a considerably larger corner radius of 220 μm as opposed to 85 μm in the single margin drills. The bigger radius essentially acts as

**Fig. 8** Variation of average diameter against number of holes drilled

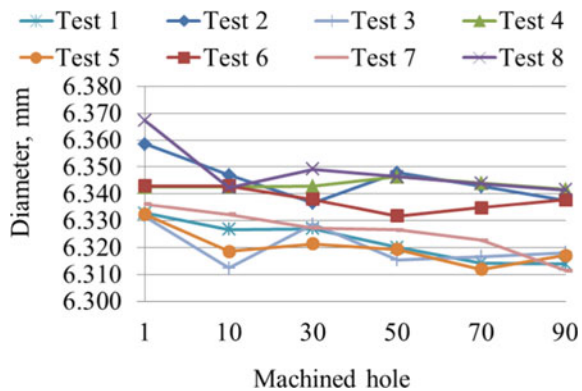


**Table 5** ANOVA table for hole diameter

Source of variance	D.F.	Seq S.S.	M.S	F <sub>cal</sub>	PCR (%)
<i>Overall average stack diameter</i>					
Margin design	1	0.00088	0.00088	93.82*	93.02
Feed rate	1	0.00001	0.00001	1.41	0.00
Drilling strategy	1	0.00000	0.00000	0.00	0.00
Residual	4	0.00004	0.00001		6.98
Sums of squares		0.00094			
<i>Diameter in Ti-6Al-4V section</i>					
Margin design	1	0.00047	0.00047	31.33*	80.26
Feed rate	1	0.00001	0.00001	0.66	0.00
Drilling strategy	1	0.00002	0.00002	1.33	1.16
Residual	4	0.00006	0.00002		18.58
Sums of squares		0.00056			
<i>Diameter in CFRP section</i>					
Margin design	1	0.00106	0.00106	65.88*	88.09
Feed rate	1	0.00006	0.00006	3.72	3.37
Drilling strategy	1	0.00000	0.00000	0.00	0.00
Residual	4	0.00006	0.00002		8.54
Sums of squares		0.00119			
<i>Diameter in A17050 section</i>					
Margin design	1	0.00123	0.00123	51.50*	89.33
Feed rate	1	0.00000	0.00000	0.00	0.00
Drilling strategy	1	0.00003	0.00003	1.50	0.74
Residual	4	0.00010	0.00002		9.94
Sums of squares		0.00135			

\*Significant at 5% level ( $F_{0.05, 1,4} = 7.71$ )

a chamfer at the peripheral corners, which tends to reduce the cutting/shearing efficiency and increase the incidence of ploughing/plastic deformation [10]. As a result, smaller hole diameters were produced when employing the triple margin drills.

Figure 9 outlines the measured mean diameter of the last hole drilled in each material section as well as the overall stack for all trials. No clear patterns were observed with respect to the variable factors, except that holes were generally larger in the Ti section compared to the CFRP and Al layers. This suggests possible tapering (larger at the top) or distortion of the hole shape/form due to process instability during drilling caused by tool run-out or wear.

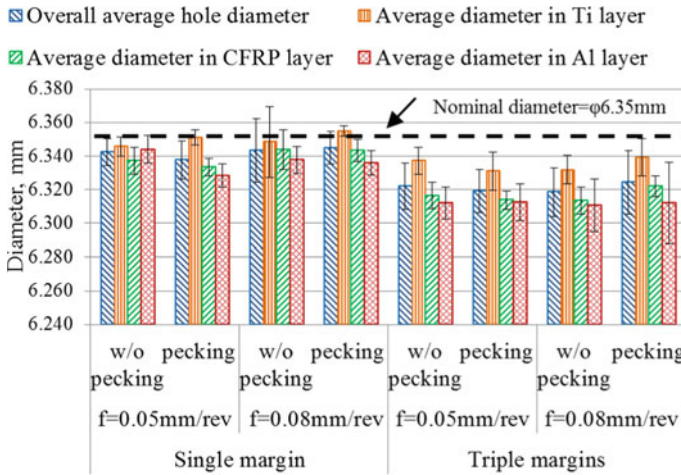


Fig. 9 Average hole diameters in each material layer and overall stack at test cessation

### 3.3 Hole Cylindricity and Out of Roundness

Figure 10 shows the overall average hole cylindricity for the stack together with out of roundness measurements in each material section over the test duration. The results indicate that the best overall hole cylindricity (55.6–61.2 μm) and lowest out of roundness values (< 30 μm) were obtained when operating with triple margin drills under a pecking strategy. In addition to the extended tool-workpiece contact

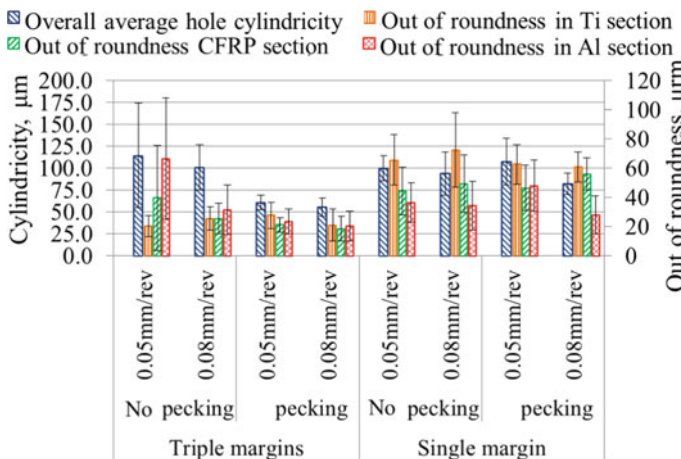


Fig. 10 Measurement of average hole cylindricity and out of roundness in each material layer and overall stack

time, the application of a peck cycle in combination with triple margin drills resulted in a ‘reaming’ action, which may have corrected/reduced any deviation in hole shape.

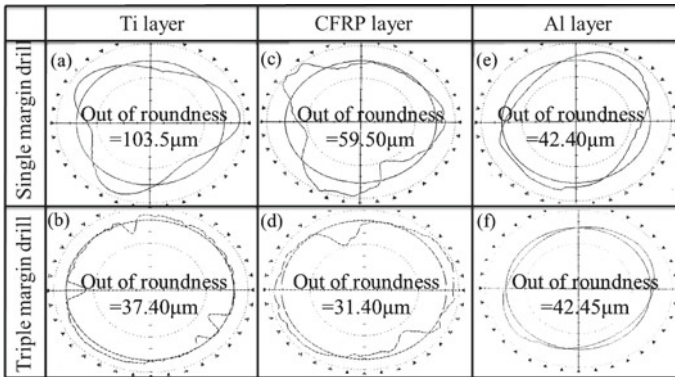
The corresponding ANOVA calculations detailed in Table 6 showed that while drilling strategy had a moderate influence on overall average hole cylindricity with a PCR of 31.28%, none of the variables were statistically significant at the 5% level. In contrast, margin design had a substantial effect on hole out of roundness in both the Ti and CFRP sections, with corresponding PCR’s of ~ 96% and 70% respectively. None of the variables however were statistically significant with regard to out of roundness in the Al layer, which was possibly due to increased stability provided by the hole walls in the preceding material sections of the stack.

Figure 11 shows hole roundness plots and corresponding out of roundness measurements in the Ti, CFRP and Al layers machined using single and triple margin

**Table 6** ANOVA table for cylindricity and out of roundness

Source of variance	D.F.	Seq S.S.	M.S.	F <sub>cal</sub>	PCR (%)
<i>Overall average stack cvlindricity</i>					
Margin design	1	334.5	334.5	1.07	0.67
Feed rate	1	324.5	324.5	1.04	0.36
Drilling strategy	1	1324.8	1324.8	4.23	31.28
Residual	4	1251.4	312.8		67.69
Sums of squares		3235.3			
<i>Out of roundness in Ti-6Al-4V section</i>					
Margin design	1	3486.0	3486.0	144.14*	96.13
Feed rate	1	1.7	1.7	0.07	0.00
Drilling strategy	1	16.7	16.7	0.69	0.00
Residual	4	96.7	24.2		3.87
Sums of squares		3601.2			
<i>Out of roundness in CFRP section</i>					
Margin design	1	1048.26	1048.26	13.79*	70.04
Feedrate	1	0.86	0.86	0.01	0.00
Drilling strategy	1	35.01	35.01	0.46	0.00
Residual	4	303.98	75.99		29.96
Sums of squares		1388.11			
<i>Out of roundness in Al7050 section</i>					
Margin design	1	2.5	2.5	0.01	0.00
Feed rate	1	455.3	455.3	2.27	16.32
Drilling strategy	1	298.5	298.5	1.49	6.26
Residual	4	803.2	200.8		77.42
Sums of squares		1559.5			

\*Significant at 5% level (F<sub>0.05</sub> 1,4 = 7.71)



**Fig. 11** Hole profiles and out of roundness values in each material section when using single and triple margin drills at a feed rate of 0.08 mm/rev without pecking

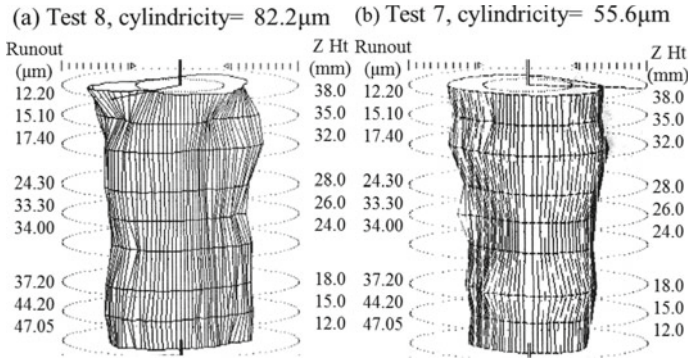
drills at a feed rate of 0.08 mm/rev under pecking conditions for the last holes drilled. The holes in the Ti and CFRP sections produced using single margin drills typically exhibited tri-lobed profiles with associated out of roundness levels exceeding 100  $\mu$ m, which was either due to tool run-out effects or chisel edge sliding (also known as ‘walking’) upon penetrating the workpiece surface. In contrast, the holes fabricated with triple margin drills showed significantly lower out of roundness, most likely due to the larger chamfer land (0.22 mm) at the peripheral corner of the tools. This was seen to reduce form deviations (i.e. tri-lobing) generated when employing the single margin drills, particularly in the Ti section, see Fig. 11a, b and the CFRP layer, see Fig. 11c, d. The triple margin drills possibly induced increased smearing of the matrix over the different directional plies as well as reducing the incidence of uncut fibres (tendency for greater bending or buckling of the fibres). While the difference in out of roundness values of the holes in the Al section was negligible, the hole profile accuracy was enhanced when employing the triple margin drills, as shown in Fig. 11e, f.

Figure 12 details the cylindricity and 3D form profiles of the last holes produced using triple and single margin drills in Tests 7 and 8 respectively (0.08 mm/rev feed rate with pecking). The poor cylindricity obtained when employing the single margin drill (82.2  $\mu$ m) is evident in Fig. 12a and contrasts sharply with the result for the triple-margin drill (Test 7) in Fig. 12b, albeit with some minor tapering.

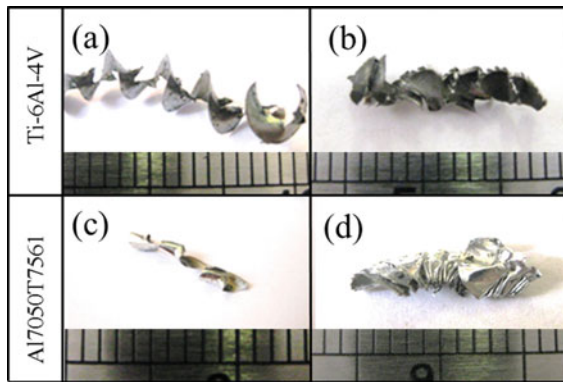
### 3.4 Chip Morphology

Figure 13 shows sample micrographs of representative Ti and Al chips generated when utilising triple margin drills (after 60 holes) under a feed rate of 0.05 mm/rev without pecking (Test 1). Continuous, conical shaped helical chips were generally formed as the tool initially entered the Ti layer; see Fig. 13a. This was due to the





**Fig. 12** Average cylindricity and 3D form profiles of the last hole machined using **a** single and **b** triple margin drills under a feed rate of 0.08 mm/rev with pecking



**Fig. 13** Chips from the Ti and Al layers when drilling with triple margin tool at feed rate of 0.05 mm/rev without pecking; **a** helical, **b** packed, **c** helical with long pitch, **d** folded

combination of up and side curling of the material caused by the varying cutting speed along the rake face and obstruction of the web section during rotation of the drill [11]. As the drill proceeded towards the bottom of the Ti plate, packing and fragmentation of the chips occurred, resulting in swarf having the form shown in Fig. 13b. This was attributed to the greater bending stresses induced by sustained contact with the hole wall, leading to periodic breakage of the chips.

When drilling the Al layer of the stack, chip shape at the entrance location remained largely helical, but with a longer pitch length as highlighted in Fig. 13c. This was most likely due to the higher ductility of Al, which was able to withstand greater deformation and therefore reduced curling of the chip [11]. Increased friction with the hole surface when moving deeper into the stack as well as the small flute curvature of the triple margin drills, retarded material flow and led to severely folded chips as shown in Fig. 13d. Additionally, the BUE/adhered material on the

drill cutting edge and margins shown previously in Fig. 6 most likely exacerbated the contact conditions at the tool-workpiece interface, which further hindered swarf evacuation from the hole.

Subsequent high magnification SEM analysis of the packed/folded chips is detailed in Fig. 14. The packed Ti swarf was characterised by fracture patterns at the outer section of the chip while the inner regions remained connected, see Fig. 14a. This was due to the differential angular velocity at the outer periphery and inner radius of the chip flow. In contrast, a continuous folded arrangement was observed in the Al chips with no obvious signs of fracture, which was attributed to its increased ductility compared to the Ti alloy. Such chips however are undesirable, as they are predisposed to clogging and can precipitate the risk of premature failure/fracture of the drill.

Figure 15a, b show cross sectional micrographs of typical titanium chips generated using triple and single margin drills respectively. While both exhibited serrated

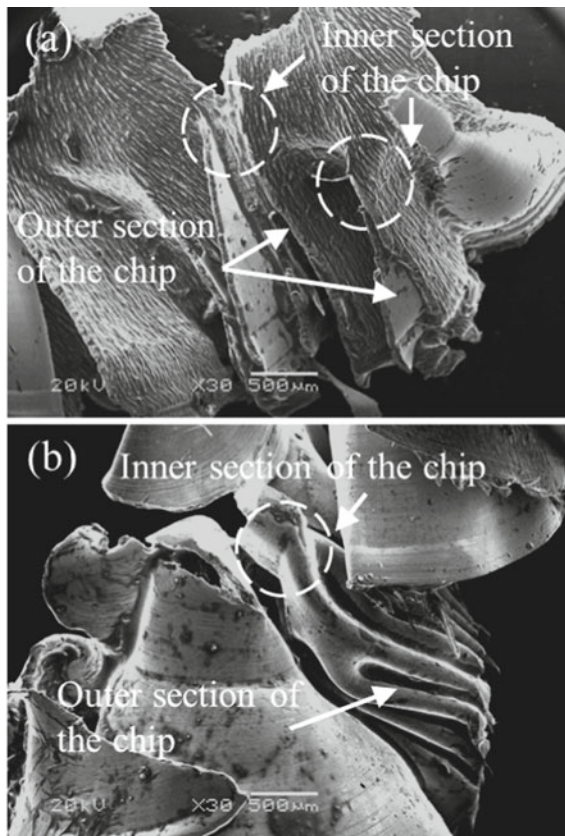


**Fig. 14** SEM examination of the **a** packed chips in the Ti layer, and **b** folded chips in the Al layer using a triple margin drill under a feed rate of 0.05 mm/rev without pecking

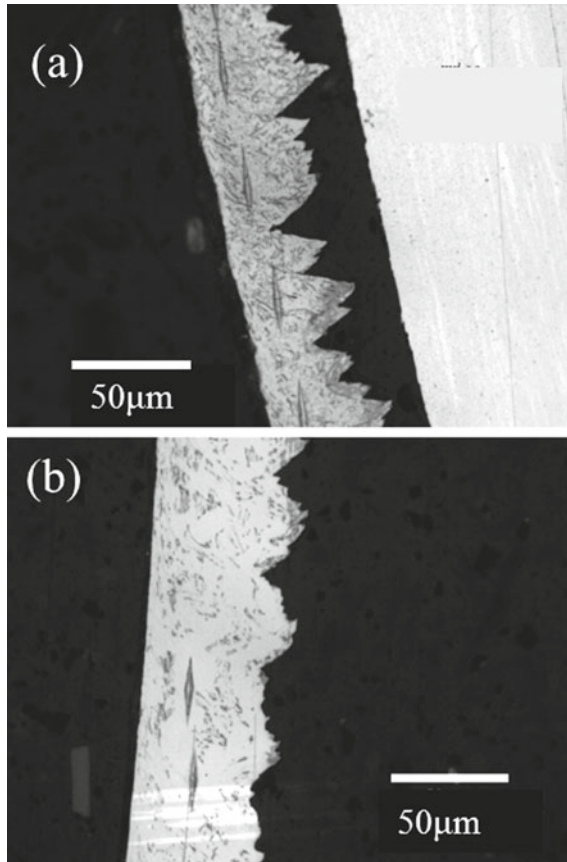


**Fig. 15** Cross section of Ti chips produced when drilling with **a** triple and **b** single margin drills under a feed rate 0.05 mm/rev without pecking

morphologies, more pronounced segmentation was evident in chips formed when machining with the triple margin drill. No evidence of adiabatic shear bands were found in any of the samples analysed, which suggests fracture from the free surface of the chip as the dominant formation mechanism of the saw tooth profile [12]. Furthermore, microhardness measurements showed no appreciable softening or hardening of the chip material (values ranged from 363 to 408  $HK_{0.025}$ ) regardless of the drill geometry.

## 4 Conclusions

- Feed rate was the sole statistically significant factor with respect to tool life (PCR of 72.4%), while the effects of margin design and drilling strategy were minimal. Reducing feed rate and drilling without pecking resulted in moderate increase in tool wear.
- Margin design had a significant influence on hole diameter, regardless of feed rate and drilling strategy. Triple-margin drills produced smaller holes due to the reduction in vibration resulting from increased contact with the machined surface.
- Although not statistically significant, drilling strategy had a moderate effect on overall average hole cylindricity with a PCR of ~ 31%, while the influence of margin design and feed rate were negligible.
- Hole roundness typically improved when employing triple margin drills, with margin design having a dominant influence on the out of roundness parameter in the Ti and CFRP layers.
- The titanium swarf varied from conical shaped helical chips at the entrance position to a packed morphology towards the bottom of the layer. Conversely, the higher ductility of the aluminium alloy resulted in longer pitched helical chips but which became heavily folded as the drill progressed further into the stack.

**Acknowledgements** The authors wish to express their gratitude to GKN Aerospace, Seco Tools and Element Six for the provision of workpiece material, tooling and financial support for the research.

## References

1. Ramulu M, Branson T, Kim D (2001) A study on the drilling of composite and titanium stacks. *Compos Struct* 54(1):67–77
2. Brinksmeier E, Janssen R (2002) Drilling of multi-layer composite materials consisting of carbon fiber reinforced plastics (CFRP), titanium and aluminum alloys. *CIRP Ann Manuf Technol* 51(1):87–90
3. Shyha I, Soo SL, Aspinwall D, Bradley S, Perry R, Harden P, Dawson S (2011) Hole quality assessment following drilling of metallic-composite stacks. *Int J Mach Tools Manuf* 51(7–8):569–578
4. Kuo CL, Soo SL, Aspinwall DK, Bradley S, Thomas W, M'Saoubi R, Pearson D, Leahy W (2014) Tool wear and hole quality when single shot drilling of metallic-composite stacks with diamond coated tools. *Proc IMechE Part B: J Eng Manuf* 228(10):1314–1322
5. Ema S, Fujii H, Marui E (1991) Cutting performance of drills with three cutting edges effects of chisel edge shapes on the cutting performance. *Int J Mach Tools Manuf* 31(3):361–369
6. Piquet R, Ferret B, Lachaud F, Swider P (2000) Experimental analysis of drilling damage in thin carbon/epoxy plate using special drills. *Compos Part A: Appl Sci Manuf* 31(10):1107–1115
7. Kuo CL, Soo SL, Aspinwall DK, Thomas W, Bradley S, Pearson D, M'Saoubi R, Leahy W (2013) The influence of tool geometry, feed rate and machining strategy on hole surface integrity following single-shot drilling of 3 layer metallic-composite stacks. In: *Proceedings of the 30th international manufacturing conference (IMC30)*, Dublin, Ireland, pp 104–113

8. Seco Tools (2008) Holemaking catalogue and technical guide
9. Garrick R (2007) Drilling advanced aircraft structures with PCD (Poly-Crystalline Diamond) Drills. SAE Technical Paper. 2007-01-3893
10. Ko SL, Chang JE, Kalpakjian S (2003) Development of drill geometry for burr minimization in drilling. *CIRP Ann Manuf Technol* 52(1):45–48
11. Nakayama K, Ogawa M (1978) Basic rules on the form of chip in metal cutting. *Ann CIRP* 27:17–21
12. Shaw MC, Vyas A (1993) Chip formation in the machining of hardened steel. *CIRP Ann Manuf Technol* 42(1):29–33

# A Basic Investigation of Micro-grooving on Sapphire Wafer with Diamond Tools



H. Kasuga, A. Nemoto, N. Itoh, M. Mizutani, and H. Ohmori

**Abstract** Micro-grooving on sapphire requires shallow depth of cut because of its hardness. An ultra-precise machining centre and diamond turning tools have improved this micro-grooving. The experimental results showed that the shapes of grooves were smooth, and the depth of grooves were less than 3.0 nm at the shallowest point. It indicated that the grooves were ductile regime, and nanometre-scale grooving was possible with this approach.

**Keywords** Micro machining · Sapphire · Cutting

## 1 Introduction

Micro-grooving is a common fabrication process and has many applications in industry and science such as bio-medical materials, heat exchangers and optical components [1–3]. Micro-grooves are fabricated by cutting, photolithography and atomic force microscope (AFM) scribing in a range of materials [4–6]. Sophistication, high functionality and miniaturization have needs for smaller features than ever before. Cutting by machining centre has some advantages in grooving on curved surfaces, sloped grooves and a wide range of materials including hard and brittle materials [7–9]. Micro-grooving for hard and brittle materials is related to critical

---

H. Kasuga (✉) · H. Ohmori

Materials Fabrication Laboratory, RIKEN, 2-1, Hirosawa, Wako, Saitama 351-0198, Japan  
e-mail: [h-kasuga@riken.jp](mailto:h-kasuga@riken.jp)

A. Nemoto

Faculty of Engineering, Yamagata University, 4-3-16, Jonan, Yonezawa City, Yamagata 992-8510, Japan

N. Itoh

College of Engineering, Ibaraki University, 4-12-1, Nakanarusawa, Hitachi 316-8511, Japan

M. Mizutani

School of Engineering, Tohoku University, 6-6, Aramaki Aza Aoba, Aoba-ku, Sendai 980-8579, Miyagi, Japan

depth of cut. There has been considerable works on the critical depth of cut for hard and brittle materials [10–12]. However, a few works on shallow grooves are seen.

Previous work on shallow grooves done by Otsuka demonstrated the fabrication of grooves with a depth of 80 nm on thin metal coated glass by cutting with a diamond tools [13]. There was very little variation in the groove depth and sharp edge in the groove condition. This extremely shallow groove was meaningfully related to thin metal coated substrate, and the groove depth was highly dependent on the coat thickness. It required sophisticated film-forming equipments and techniques.

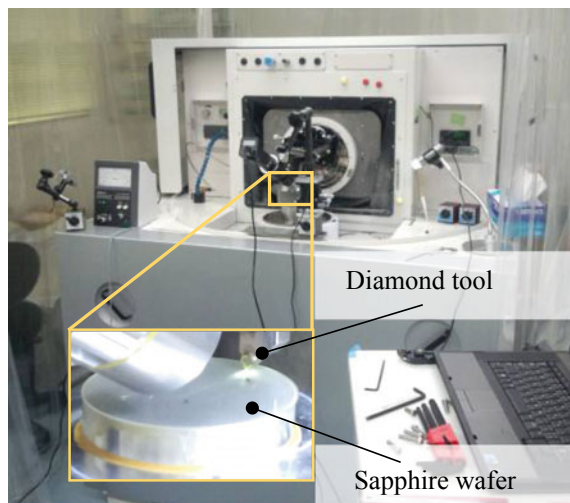
Much shallower grooves done by Versen et al. fabricated grooves having a depth of 3–4 nm on a GaAs surface by AFM scribing [14]. This extremely shallow groove was 30 nm in width and 10  $\mu\text{m}$  in length. AFM scribing is suitable for such extremely shallow and narrow grooving, whereas it is unsuitable for long grooving.

In order to accumulate the knowledge for extremely shallow and long grooves, some foundational experiments were conducted in a simplified experimental system. Some long sloped grooves were fabricated on a hard and brittle substrate by scribing with a diamond tool. Sapphire wafers were tested as a hard and brittle substrate. Sapphire is used in light emitting diode (LED) substrates, ultrahigh resolution optics and quantum electronics [15–17]. It could be expected to apply to these fields.

## 2 Experimental Setup

An ultra-precise machining centre (ROBONANO  $\alpha$ -0iB, FANUC) was used shown in Fig. 1. It has translational axes (X, Y and Z) and 2 rotational axes (B and C) with hydrostatic air bearings and 1 nm resolution each X, Y, Z axis and  $0.000001^\circ$  each B, C axis. Only X, Y and Z axes were used for the experiments.

**Fig. 1** External view of the ultra-precise machining centre

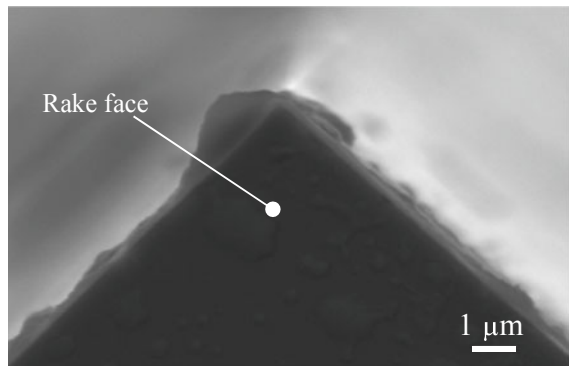


Polished sapphire wafers with a crystal orientation (0001) were tested as the specimens. The dimensions of the specimens were 50.8 mm (2 in.) in diameter and 0.43 mm in thickness. The arithmetic mean height ( $S_a$ ) of the surface was 0.17 nm. The grooves were created along the orientation flat of the wafer.

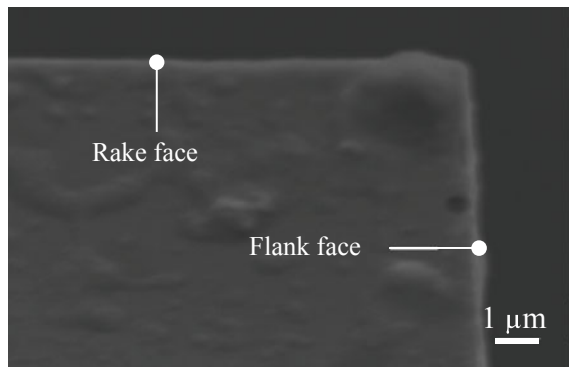
A single-crystal diamond with an opening angle of  $90^\circ$ , rake angle of  $0^\circ$  and flank angle of  $0^\circ$  was used for the tool. Figure 2a, b show scanning electron microscope (SEM) images of the tool coated with platinum before machining. Including the thickness of the coat, the tool nose radius was 70 nm by image measuring. In Fig. 2b, the rake face is shown in the upper side, the flank face is shown on the right side and the cutting edge is shown in the upper right. Including the thickness of the coat, the cutting edge radius was 20 nm by image measuring.

Figure 3 shows the cutting principle for micro-grooving. It was created by scribing a line. The tool increased the depth of cut and then decreased it for sloped grooves. The degree of the slope angle was 0.01, the maximum depth of cut was  $2\ \mu\text{m}$ , and feed rate was 2.5, 5.0, 10 and 20 mm/min. The lubrication conditions were dry cut. Table 1 summarizes the machining conditions.

**Fig. 2** **a** SEM image of the tool rake face side. **b** SEM image of the tool side face



**(a)** SEM image of the tool rake face side



**(b)** SEM image of the tool side face



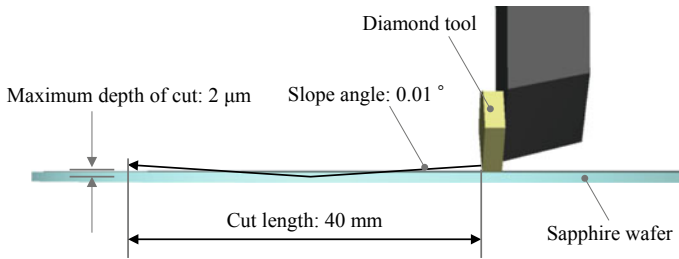


**Fig. 3** Schematic illustration of cutting principle for the micro-grooving

**Table 1** Experimental conditions

Slope angle	0.01°
Maximum depth of cut	2 μm
Feed rate	2.5, 5.0, 10, 20 mm/min
Cut length	40 mm
Cutting fluid	Dry

After the micro-grooving experiments, observations and measurements were conducted for the evaluations of the grooves. Cutting marks and cutting chips were observed by a digital microscopy (VW-6000, Keyence) and a confocal laser microscopy (VK-8500, Keyence). The width and depth of the grooves and the real surface texture were measured by an optical profiler (NewNiew 5302, zygo).

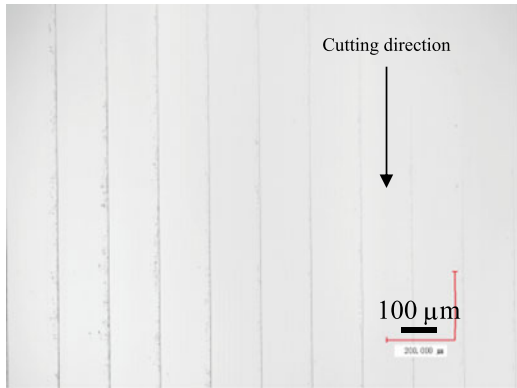
### 3 Results and Discussion

The micro-grooves are shown in Fig. 4a, a higher-magnification image is shown in Fig. 4b, and cutting chips are shown in Fig. 4c. The shapes of the grooves were shallow, the surfaces were smooth, and the shape of the cutting chips was curly and flow type. These results were consistent with characteristics of ductile regime. In addition, ductile-regime machined regions were seen in all the grooves, which were machined under the conditions that feed rates were from 2.5 to 20 mm/min.

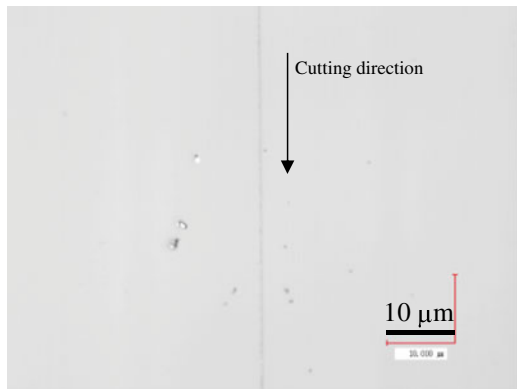
Figures 5a–d show surface properties of the grooves at each feed rate. The shapes of the grooves can be clearly seen. Although small chippings on the grooves were seen at the feed rate of 2.5 and 20 mm/min, the edges of the grooves were regular in shape. The relationship between chipping and feed rate could not be found in this experiment.

Figures 6a–d show cross-sectional profiles of the grooves. The depths of the grooves were less than 5.0 nm at each feed rate, while the widths of the grooves were 6–8 μm. The depths of the grooves were considerably shallow relative to the widths. The hardness of the specimen and the sharpness of the tool nose influenced the depths. Figure 7a–d show other cross-sectional profiles at shallower points. The

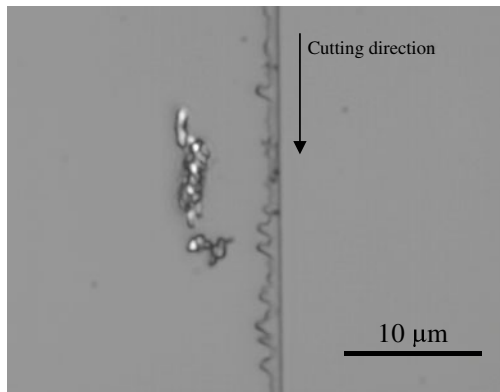
**Fig. 4** **a** Confocal laser microscopy images of the grooves: wide-field image of the grooves. Confocal laser microscopy images of the grooves: **b** high magnification image of the groove; **c** groove and cutting chips



**(a)**

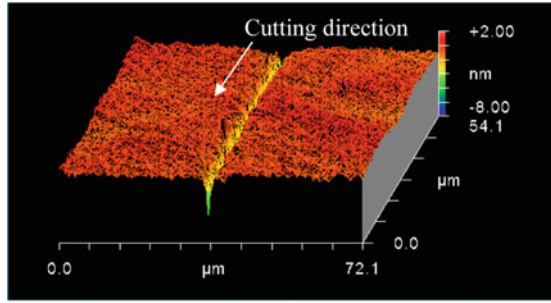


**(b)**

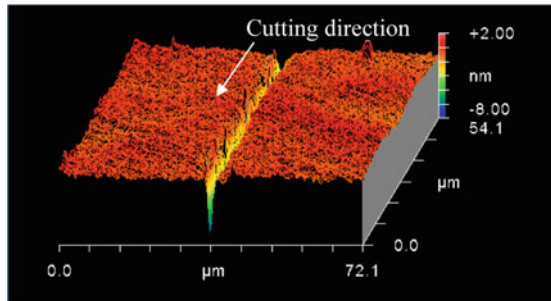


**(c)**

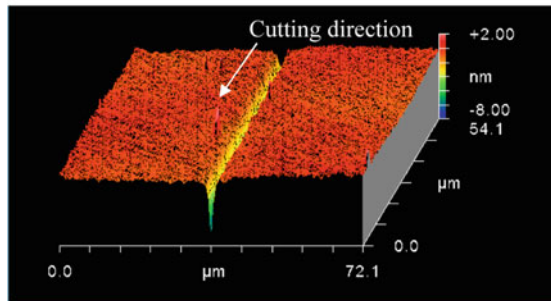
**Fig. 5** Surface properties of the grooves by the optical profiler **a** feed rate (*f*) 2.5 mm/min; **b** *f* 5.0 mm/min; **c** *f* 10 mm/min; **d** *f* 20 mm/min



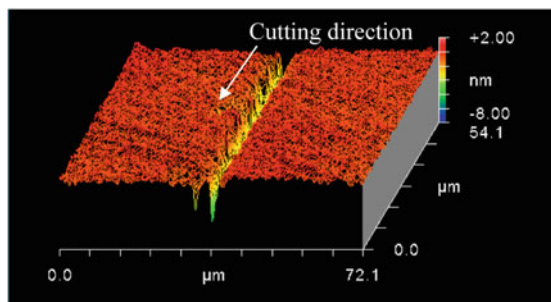
(a)



(b)

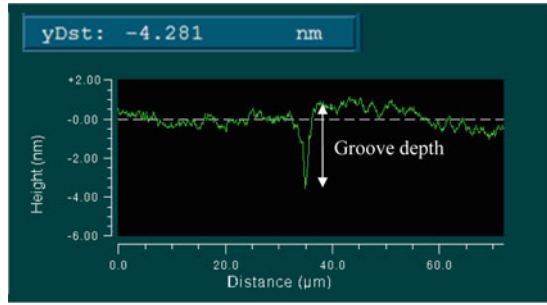


(c)

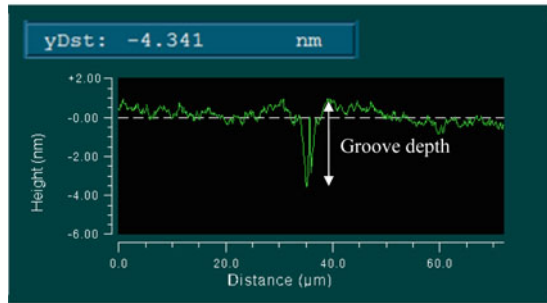


(d)

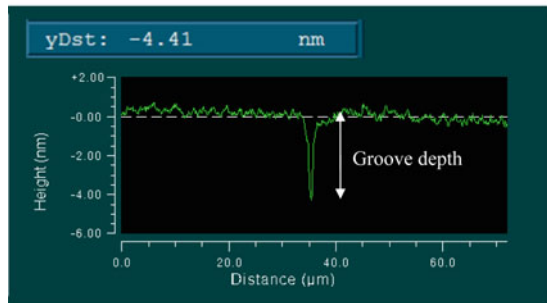
**Fig. 6** Cross-sectional profiles by the optical profiler **a** feed rate *f* 2.5 mm/min; **b** *f* 5.0 mm/min; **c** *f* 10 mm/min; **d** *f* 20 mm/min



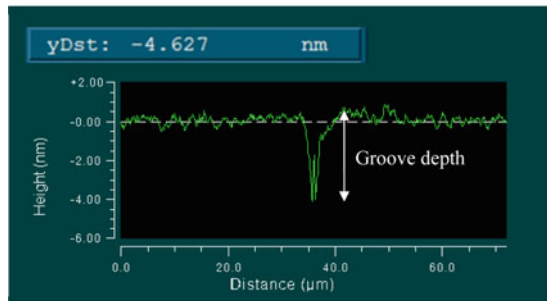
(a)



(b)

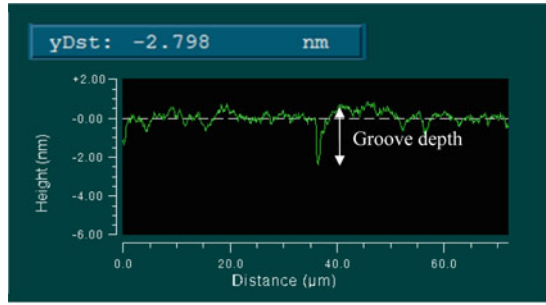


(c)

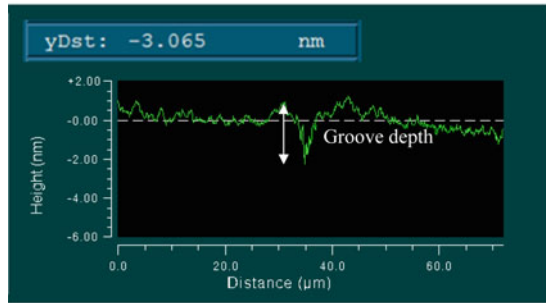


(d)

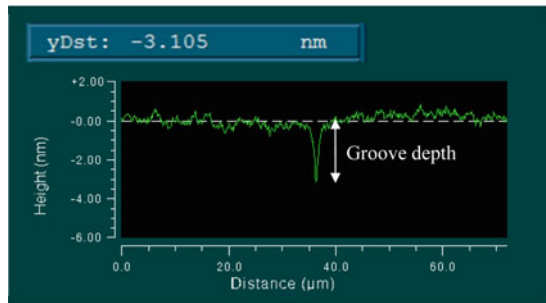
**Fig. 7** Another cross-sectional profiles **a** feed rate (*f*) 2.5 mm/min; **b** *f* 5.0 mm/min; **c** *f* 10 mm/min; **d** *f* 20 mm/min



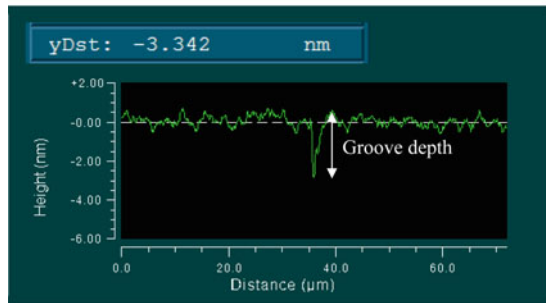
(a)



(b)

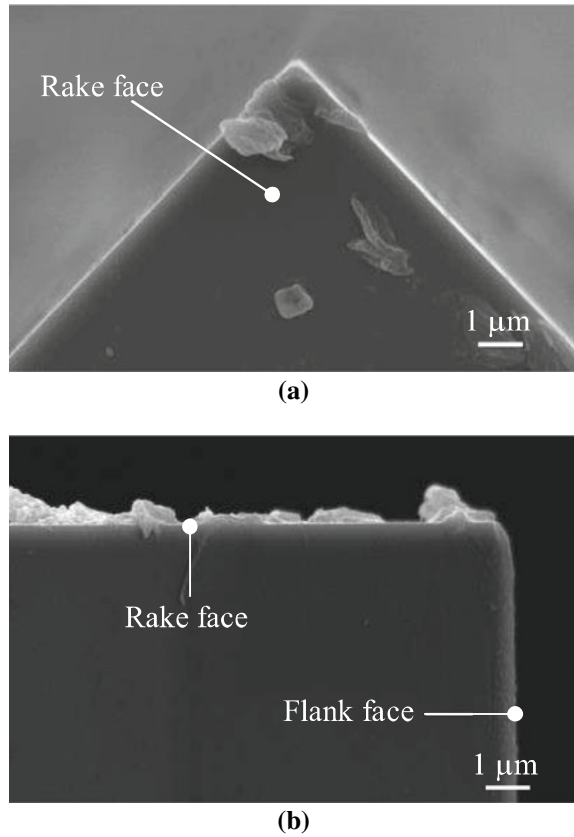


(c)



(d)

**Fig. 8** SEM images of the tool after experiments **a** rake face sided image; **b** side face sided image



depths of the grooves were less than 3.5 nm at each feed rate. It was less than 3.0 nm at the shallowest point. The specimen slightly swelled at a part of the edge in Fig. 7b. The height of the swell was less than 1 nm. It was caused by plastic side flow despite brittleness of the specimen.

Figure 8a, b show SEM images of the tool coated with platinum after machining. A part of flank face near the cutting edge was removed by wear. The tool nose radius and the cutting edge radius also increased. Including the thickness of the coat, the tool nose radius was 220 nm, and the cutting edge radius was 210 nm by image measuring. Although both edge radii increased, the tool had sufficient ability to machine.

## 4 Conclusion

These experimental results represent that grooves which were extremely shallow less than 3.5 nm and had sharp edges were created under the conditions that feed rates

were from 2.5 to 20 mm/min. It was less than 3.0 nm at the shallowest point. The shape of the cutting chips was curly and flow type. It was consistent with characteristics of ductile regime. The ductile-regime machined regions were seen in all the groves under the adopted feed rates including 20 mm/min. In addition, the tool had sufficient ability to machine, although the tool nose radius and the cutting edge radius increased after machining. It suggests a possibility for much higher speed micro-grooving of sapphire.

**Acknowledgements** This work was supported by JSPS KAKENHI (Grant-in-Aid for Encouragement) Grant Number 26917006.

## References

1. Flemming RG, Murphy CJ, Abrams GA, Goldman SL, Nealy PF (1999) Effects of synthetic micro- and nano-structured surfaces on cell behaviour. *Biomaterials* 20:573–585
2. Sommersa AD, Yub R, Okamoto NC, Upadhyayulac K (2012) Condensate drainage performance of a plain fin-and-tube heat exchanger constructed from anisotropic micro-grooved fins. *Int J Refrig* 35(6):1766–1778
3. Fang FZ, Wu H, Zhou W, Hu XT (2007) A study on mechanism of nano-cutting single crystal silicon. *J Mater Process Technol* 184:407–410
4. Yan J, Zhang Z, Kuriyagawa T, Gonda H (2010) Fabricating micro-structured surface by using single-crystalline diamond endmill. *Int J Adv Manuf Technol* 51(9–12):957–964
5. Dmitri I, Mossberg TW (2009) Fabricating radial groove gratings using projection photolithography. *NASA Tech Briefs*: 17
6. Jiang X, Wu G, Zhou J, Wang S, Tseng AA, Du Z (2011) Nanopatterning on silicon surface using atomic force microscopy with diamond-like carbon (DLC)-coated Si probe. *Nanoscale Res Lett* 6(1):518
7. Jackson MJ, Robinson GM, Whitfield MD, Ahmed W, Morrell JS (2014) Micro- and nanomachining. In: Ahmed W, Jackson MJ (eds) *Emerging Nanotechnologies for Manufacturing*, 2nd edn. William Andrew Publishing, New York
8. Dornfeld DA, Oliveira JFG, Lee D, Valente CMO (2003) Analysis of tool and workpiece interaction in diamond turning using graphical analysis of acoustic emission. *Annals CIRP* 52(1):479–482
9. Min S, Dornfeld DA, Inasaki I, Ohmori H, Lee D, Deichmueller M, Yasuda T, Niwa K (2006) Variation in machinability of single crystal materials in micromachining. *Annals CIRP* 55(1):103–106
10. Blackley WS, Scattergood RO (1991) Ductile-regime machining model for diamond turning of brittle materials. *Precis Eng* 13(2):95–103
11. Wang JJ, Liao YY (2007) Critical depth of cut and specific cutting energy of a microscribing process for hard and brittle materials. *J Eng Mater Technol* 130(1):011002.1–011002.6
12. Kasuga H, Mizutani M, Nemoto A, Ohmori H (2014) Mirror surface grinding of sapphire by coarse grain size diamond wheels. *Int J Nanomanuf* 10(3):309–318
13. Otsuka Y (2014) A novel diamond cutting method for producing fine grooves with 10-nm order depth. *J Japan Soc Prec Eng* 80(5):491–495
14. Versen M, Klehn B, Kunze U, Reuter D, Wieck AD (2000) Nanoscale devices fabricated by direct machining of GaAs with an atomic force microscope. *Ultramicroscopy* 82:159–163
15. Dobrovinskaya ER, Lytvynov LA, Pishchik V (2009) *Sapphire: material, manufacturing, applications*. Springer Publishing, New York

16. Budnikov AT, Vovk EA, Krivonogov SI, Danko AY, Lukiyenko OA (2010) Anisotropy of sapphire properties associated with chemical-mechanical polishing with silica. *Funct Mater* 17(4):488–493
17. Li ZC, Pei ZJ, Funkenbusch PD (2011) Machining processes for sapphire wafers: a literature reviews. *Proc Inst Mech Eng Part B: J Eng Manuf* 225(7):975–989



# A Study of Surface Generation in Ultra-Precision Machining of Precision Rollers with Patterned Microstructures



C. F. Cheung, L. B. Kong, C. H. Mak, M. J. Ren, and S. J. Wang

**Abstract** Precision rollers with patterned microstructures are increasingly adopted in the embossing process for manufacturing large dimensional optical plastic plates such as backlight guide used in LCD/LED displays. Due to the heavy load and high precision requirement at the same time, it is difficult to machine such precision rollers with patterned microstructures, and the machining process is thus also very expensive and time consuming. Research on the surface generation in ultra-precision machining of precision rollers is in demand so as to make the machining process more controllable and hence improve the machining accuracy. This paper presents a study on the analysis of surface generation in ultra-precision machining of precision rollers with patterned microstructures. Machining mechanism of the roller machining is explained, and then a kinematic error model is proposed, in which slide and spindle error motions are taken into account to predict the machining errors. Cutting experiments is conducted to machine V-groove microstructures on the precision roller. It is interesting to note that the model is able to predict and explain portion of the errors contributed to the overall errors in machining of the V-groove microstructure on the precision roller. The proposed research work is helpful for process optimization and control in ultra-precision machining of rollers with patterned microstructures, as well as the precision equipment development.

**Keywords** Precision roller · Micro-structured surfaces · Kinematic error model · Spindle error model · Surface generation · Ultra-precision machining

---

C. F. Cheung (✉) · L. B. Kong · S. J. Wang  
Guangdong Provincial Key Lab of Micro/Nano Machining Technology and Equipment,  
Guangdong University of Technology, Guangzhou, Guangdong, P.R. China  
e-mail: [Benny.Cheung@polyu.edu.hk](mailto:Benny.Cheung@polyu.edu.hk)

C. F. Cheung · L. B. Kong · C. H. Mak · M. J. Ren  
State Key Laboratory of Ultra-Precision Machining Technology, The Hong Kong Polytechnic  
University, Hung Hom, Kowloon, Hong Kong

## 1 Introduction

Microstructured surfaces, such as V-grooves and microlens arrays, are widely used in high value added optical products for enhancing the optical performance of the products, such as collimation, diffusion, focusing, re-direction, brightness enhancement and out-coupling [1]. Rolling imprint lithography is an enabling technology for the mass production of the micro-structured surfaces. For roll-to-roll technology, the quality of the manufactured surfaces relies heavily on the geometrical precision of the master roller drum which is normally required to be fabricated with sub-micrometre form accuracy and surface finishing in nanometers level [1].

Single-point diamond turning (SPDT) is an enabling machining technology for the fabrication of micro-structured surfaces [2]. In SPDT, the microstructures can either be machined by precision replication of the shape of the cutting tool on the workpiece, or cutting by Fast Tool Servo (FTS). However, the machining of the microstructures on cylindrical surfaces by SPDT is different from traditional face turning. This has imposed a lot of technical challenges in machining. This is particularly true for the large micro-structured rollers of which dimensions are up to 1 m long and 0.5 m in diameter. Although much research has been conducted on this subject in recent decades and some commercial roller machining equipments are available in the market [3], research work on the modelling and simulation of the roller machining process is still far from complete.

As a result, this paper presents a study on the analysis of surface generation in ultra-precision machining of precision rollers with patterned microstructures. Machining mechanism of the roller machining is firstly explained, and a kinematic error model is then proposed. Cutting experiments have been conducted for machining V-groove microstructures on a roller and the results are presented and discussed.

## 2 Machining Mechanism for V-groove Microstructures on a Roller Surface

Figure 1 shows the machining mechanism and motion axis configuration for machining V-groove microstructures on the cylindrical roller surface. The machine has two translational motion axes ( $X$ ,  $Z$ ) and one rotational axes ( $C$ ). The roller workpiece is mounted on the main spindle while the cutting tool is carried by the  $Z$ -slide. In the machining process, only  $Z$ -slide and  $C$ -slide (spindle) are involved in the cutting process.

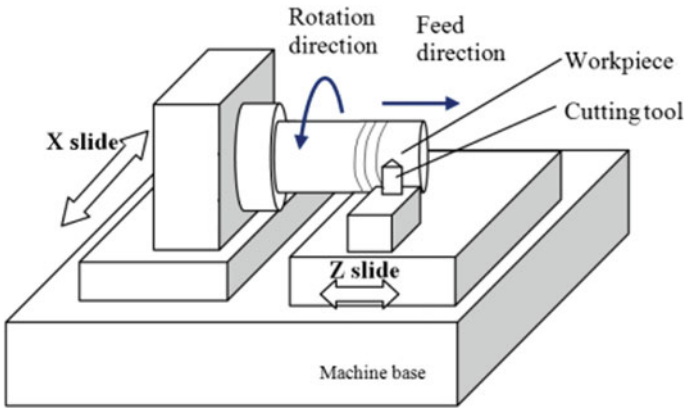
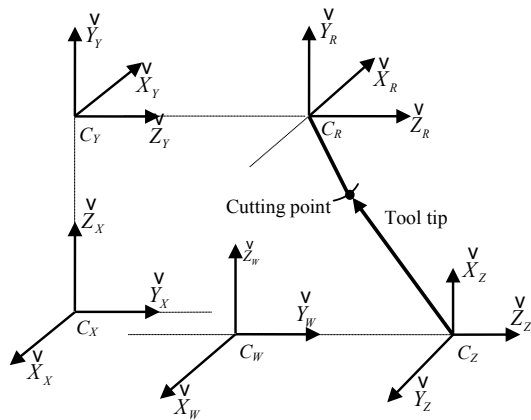


Fig. 1 Machining mechanism and the motion axis configuration

### 3 Error Model for Machining V-groove Microstructure

As shown in Fig. 2, a total of five coordinate frames are constructed to describe the kinematics structure of the machine tool.  $C_W = \begin{bmatrix} \vec{X}_W & \vec{Y}_W & \vec{Z}_W \end{bmatrix}$  is the world coordinate frame embedded in the machine bed;  $C_X = \begin{bmatrix} \vec{X}_X & \vec{Y}_X & \vec{Z}_X \end{bmatrix}$  is the moving coordinate frame embedded in the X stage;  $C_Z = \begin{bmatrix} \vec{X}_Z & \vec{Y}_Z & \vec{Z}_Z \end{bmatrix}$  is the moving coordinate frame embedded in the z stage;  $C_Y = \begin{bmatrix} \vec{X}_Y & \vec{Y}_Y & \vec{Z}_Y \end{bmatrix}$  is the moving coordinate frame embedded

Fig. 2 Coordinate frames of the machine tool



in the Y stage;  $C_R = \begin{bmatrix} \vec{X}_R & \vec{Y}_R & \vec{Z}_R \end{bmatrix}$  is the moving coordinate frame embedded in the rotation of the spindle.

In the present study, the homogeneous coordinate transformation matrix (HCTM) as given in Eq. (1) is used to describe the relative motion between different coordinate frames [4].

$$T = \begin{bmatrix} c(\beta)c(\gamma) & s(\alpha)s(\beta)c(\gamma) - c(\alpha)s(\gamma) & c(\alpha)s(\beta)c(\gamma) + s(\alpha)s(\gamma) & a \\ c(\beta)s(\gamma) & s(\alpha)s(\beta)s(\gamma) + c(\alpha)c(\gamma) & c(\alpha)s(\beta)s(\gamma) - s(\alpha)c(\gamma) & b \\ -s(\beta) & s(\alpha)c(\beta) & c(\alpha)c(\beta) & c \\ 0 & 0 & 0 & 1 \end{bmatrix} \quad (1)$$

where  $s()$  and  $c()$  are the abbreviation of sine and cosine function; a, b, and c are translational offsets in three axes;  $\alpha$ ,  $\beta$ , and  $\gamma$  are rotational angles along three axes. Hence, a kinematics model of the machine tool in the machining process can be established by the relative motion between the cutting tool and the workpiece which can be represented by Eq. (2):

$$T_{ZR} = (T_{WZ})^T T_{WX} T_{XY} T_{YR} \quad (2)$$

where  $T_{*,**}$  is the HCTM from  $C_{**}$  to  $C_*$ .

The error of a machine tool is the relative error motions between the cutting tool and the workpiece which can be described by the geometrical error of the moving components in the machine tool. For linear movement, i.e. the three translational moving stages, the geometrical error can be divided into six components, including displacement, two straightness error motions, roll, pitch, and yaw error motions, as shown in Fig. 3. By taking X stage as an example, with the consideration of geometrical error, the actual HCTM from  $C_X$  to  $C_W$  can be given by Eq. (3) as follows:

$$RT_{WX} = T_{WX} E T_X^W \quad (3)$$

where

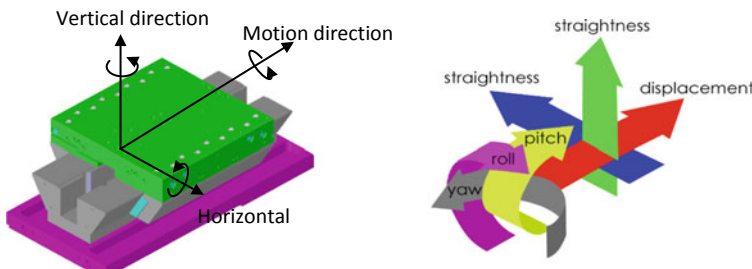


Fig. 3 Error components of a translational axis

$$ET_X^W = \begin{bmatrix} 1 & -\delta\gamma(x_X) & \delta\beta(x_X) & \delta x(x_X) \\ \delta\gamma(x_X) & 1 & -\delta\alpha(x_X) & \delta y(x_X) \\ -\delta\beta(x_X) & \delta\alpha(x_X) & 1 & \delta z(x_X) \\ 0 & 0 & 0 & 1 \end{bmatrix}$$

$\delta*(x_X)$  is a function which represents the relationship between the error components and the displacement of the X stage.

For rotational motion, i.e. the spindle, the geometrical error can also be described by 6 error components including two radial error motions, one axial error motions, the angular position error, and two tilt error motions. With the consideration of the geometrical error, the actual HCTM from  $C_X$  to  $C_W$  can be given by Eq. (4) as follows:

$$RT_{YR} = T_{YR} E T_R^Y \tag{4}$$

where

$$ET_R^Y = \begin{bmatrix} 1 & s(\tilde{\alpha})\delta\beta(\alpha) - c(\tilde{\alpha})\delta\gamma(\alpha) & c(\tilde{\alpha})\delta\beta(\alpha) + s(\tilde{\alpha})\delta\gamma(\alpha) & \delta x(\alpha) \\ \delta\gamma(\alpha) & c(\tilde{\alpha}) & -s(\tilde{\alpha}) & \delta y(\alpha) \\ -\delta\beta(\alpha) & s(\tilde{\alpha}) & c(\tilde{\alpha}) & \delta z(\alpha) \\ 0 & 0 & 0 & 1 \end{bmatrix}$$

$$\tilde{\alpha} = \alpha + \delta\alpha$$

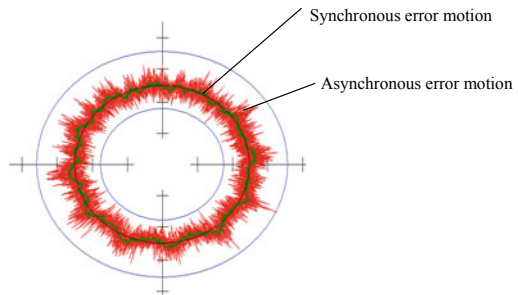
Hence, the geometrical error model of the Nanotech 350 machine tool can be established based on the kinematics model and the model equation can be given by Eq. (5) as follows:

$$Ek = |P_{ct} - (T_{ZW} E_{ZW})(T_{XW} E_{XW})^T (T_{YX} E_{YX})(T_{RY} E_{RY})^T P_{ct}| \tag{5}$$

where  $P_{ct}$  and  $P_{tt}$  are intended cutting point and the real location of the cutting tool tip.

Beside the kinematic errors, spindle error motion also affects the microstructured surface generation in the roller machining. As shown in Fig. 4, two import error

Fig. 4 Spindle motion error



motions are involved, which are synchronous error motion and asynchronous error motion. The former refers to the components of total error motion that occur at integer multiples of the rotation frequency, or average error motion; while the later is the portion of the total error motion that occurs at frequencies other than integer multiples of the rotation frequency. Asynchronous error motion comprises those components of error motion that are: (a) not periodic (b) periodic but occur at frequencies other than the spindle rotational frequency and its integer multiples, (c) periodic at frequencies that are subharmonics of the spindle rotational frequency. In the present study, only synchronous error motion is taken into account since it can be a systematic error factor, and can also be assumed as a harmonic vibration which is expressed as

$$E_v = A \cdot \cos(\omega \cdot t + \phi) \tag{6}$$

where,  $A$  is the amplitude,  $\omega$  is circular frequency,  $t$  is time, and  $\phi$  is initial phase.

As a result, the error model in the present study is expressed as:

$$Err = E_k + E_v \tag{7}$$

## 4 Experimental Studies

### 4.1 Experimental Design

A micro V-grooved roller made of Aluminum 6061 is machined by Nanotech 350 ultra-precision machine tool. The workpiece and specification of the V-grooves are shown in Fig. 5. Table 1 shows the machining parameters that are used in the experiment. The machine roller workpiece is measured by Talysurf PGI 1240, as shown in Fig. 6.

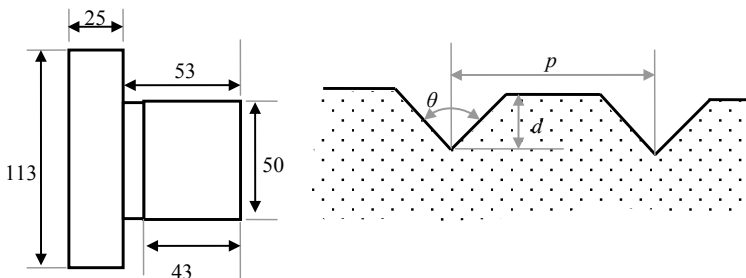
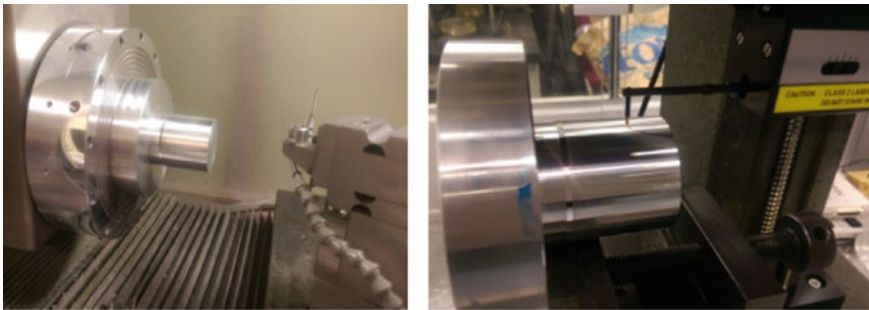


Fig. 5 Roller workpiece design

**Table 1** Machining parameters

Working distance (mm)	40
Spindle speed (rpm)	300
Depth of cut ( $\mu\text{m}$ )	5
Feed rate (mm/min)	6
No. of feed	1
Cutting tool	90° Sharp point tool
Workpiece material	Al
Machine tool	Moore Nanotech 350FG



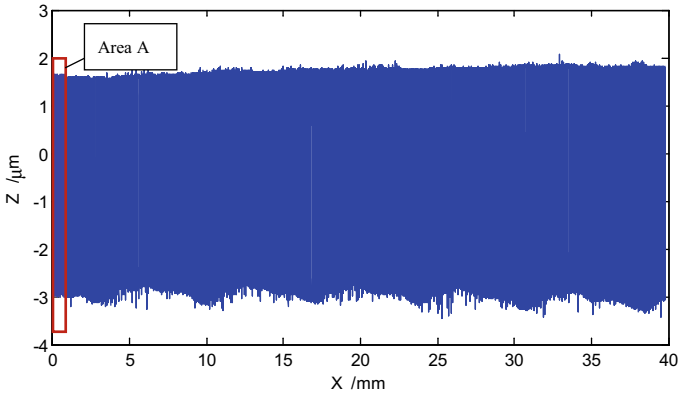
**Fig. 6** Machining and measurement of roller with V-groove microstructure

### 4.2 Results and Discussions

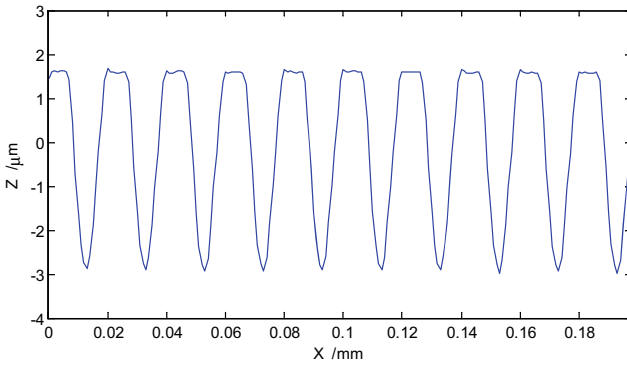
Figure 7 shows the measured results of the profile for the machined V-groove microstructures on the roller surface, Fig. 7a shows the whole data profile and Fig. 7b is the detailed profile for a small region to show more clearly for the V-groove profile. Figure 8 shows the analysis of the errors of the machined V-groove microstructures as compared with the designed specifications. Figure 8a shows the deviation of V-groove depth, and (b) shows the deviation of V-groove angle.

In the experimental study, only main spindle and Z-slide are involved in the motion during the machining. Figure 9 shows the error motion of the Z-slide and the segment used in the machining. Based on the error model proposed in the paper, kinematic errors caused by Z-slide motion are obtained and they are shown in Fig. 10. By comparing the predicted errors which are within  $0.02 \mu\text{m}$  with the results of the analyzed error within  $0.2 \mu\text{m}$  as shown in Fig. 8, it is interesting to note that the Z-axis slide motion is not the dominant source of error.

The spindle error motion is measured by a Spindle Error Analyzer (SEA) from Lion Precision. Figure 11 shows the setup for the measurement of the spindle error motion. The synchronous error motion of the spindle at spindle speed of 300 rpm is found to be about  $0.5 \mu\text{m}$ . Based on the model in the present study as shown in Eq. 6, the amplitude of the error motion ( $A$ ) can be obtained as  $= 0.25 \mu\text{m}$ . Frequency of



(a) Measured result for the surface profile of roller with V-shape microstructures



(b) Detailed profile for area A

**Fig. 7** Measured result of the machined roller with V-shape microstructures

the spindle vibration is found to be 6.7 Hz. Assume the initial phase is 0, then the spindle error motion is obtained as

$$Ev = 0.25 \cdot \cos(13.4\pi \cdot t) \tag{8}$$

Based on the machining parameters listed in Table 1, the spindle vibration along Z-slide is obtained, as shown in Fig. 12.

The errors of features for V-groove are also evaluated in parameters in terms of root-mean-square (RMS) and peak to valley height (PV). Table 2 shows a comparison of error parameters between the measured and the predicted results. From the results, it indicates that there is significant deviation between the predicted and the measured values, which shows that there is about half portion of errors in V-groove machining on the roller surface caused by kinematic errors and spindle error motion, and the other half portion of error might be due to the material swelling effects, as show in



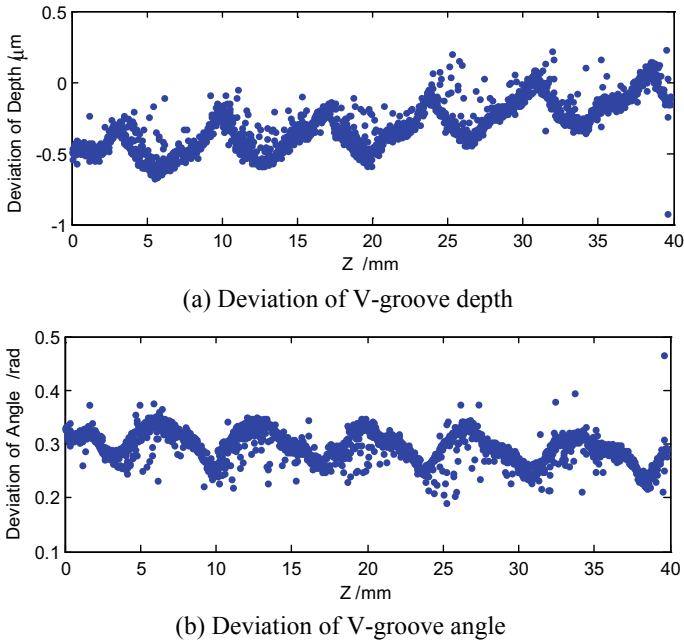


**Fig. 8** Analysis of errors of machined V-groove microstructures

Fig. 13. The material effect leads to the recovery of the bottom of V-groove, which consequently makes the depth of V-groove become smaller while the angle is bigger than the expected values. Machining burrs are also found in V-groove generation. These phenomena caused by material swelling have been preliminarily studied by the authors [5], and is further investigated in the future studies.

## 5 Conclusion

Precision rollers with patterned microstructures are increasingly adopted in the embossing process for manufacturing large dimensional optical plastic plates, and it is difficult to machine such precision rollers with patterned microstructures, and the machining process is thus also very expensive and time consuming. Research on the surface generation in ultra-precision machining of rollers is in demand so as to make the machining process more controllable and hence improve the machining accuracy. This paper presents a study on the analysis of surface generation in ultra-precision machining of precision rollers with patterned microstructures. An error model which takes into consideration of slide and spindle error motions has been built. A cutting experiment has been conducted to machine V-groove microstructures on the precision roller and the produced V-groove microstructures on the roller

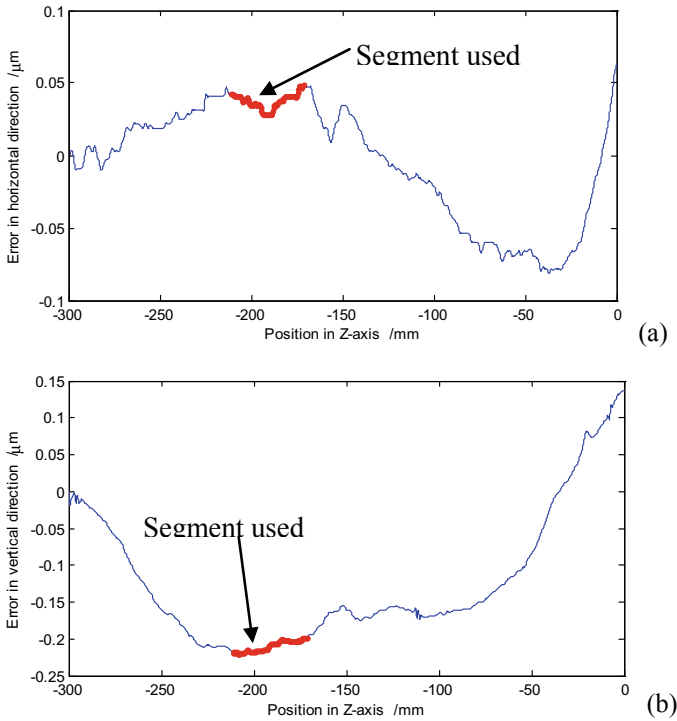


**Fig. 9** Z-slide motion errors and segment used in the machining: **a** in horizontal direction; **b** in vertical direction

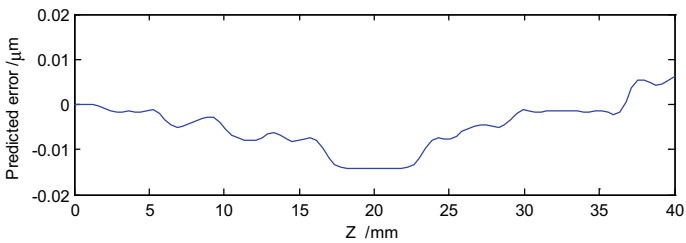


**Fig. 10** Effect of Z-slide motion error on V-groove microstructure (e.g. depth)

surface have been analyzed. A comparison between the predicted and measured results is made. It is interesting to find that there is about half portion of errors in V-groove machining on the roller surface is caused by kinematic errors and spindle error motion, while the other half portion of error might be due to the material swelling effects. The proposed research work is helpful for process optimization and control in ultra-precision machining of rollers with patterned microstructures.

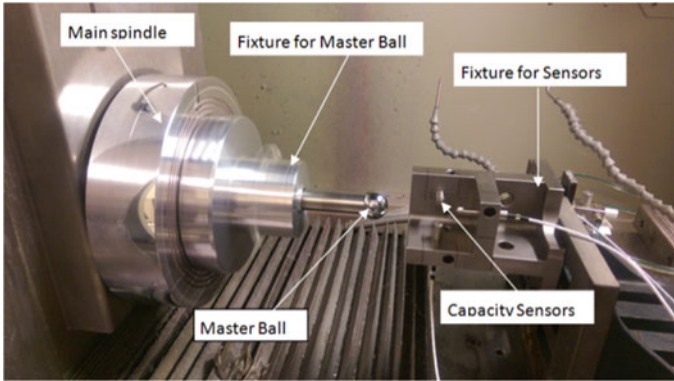


**Fig. 11** Setup for the measurement of spindle motion error

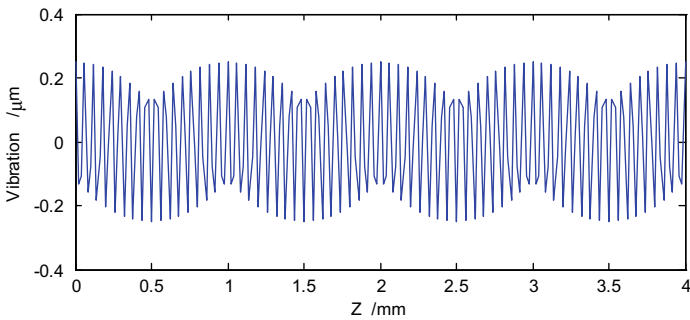


**Fig. 12** Spindle vibration along Z-slide

**Table 2** Comparison of error parameters between measured and predicted results

	Predicted	Measured	Deviation
	Error of depth ( $\mu\text{m}$ )		
RMS value	0.177	0.351	- 0.174
PV value	0.519	1.159	- 0.640
	Error of angle (rad)		
RMS value	0	0.2955	- 0.295
PV value	0	0.2748	- 0.2748

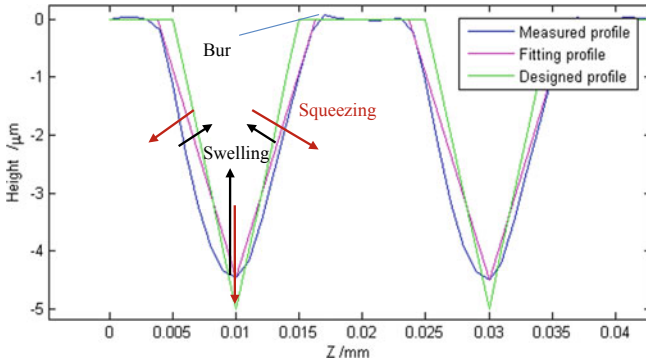


**Fig. 13** Material squeezing and swelling effects on V-groove generation

**Acknowledgements** The research work was supported by Guangdong Provincial Department of Science and Technology, Guangdong, P.R. China for The Introduction of Innovative R&D Team Program of Guangdong Province (Project no.:201001G0104781202). The authors would like to express their sincere thanks to the Innovation and Technology Commission of the Government of the Hong Kong Special Administrative Region (HKSAR) for the financial support of the research work under projects nos.: GHP/045/10SZ. The research work was also supported by a MPhil studentship (project account code: RTK7) from The Hong Kong Polytechnic University.

## References

1. Jiang X (2011) In situ real-time measurement for micro-structured surfaces. *Annals CIRP* 60:563–566
2. Lee W, To S, Cheung C (2005) Design and advanced manufacturing technology for freeform optics. The Hong Kong Polytechnic University, Hong Kong
3. Moriya T, Nakamoto K, Ishida T, Takeuchi Y (2010) Creation of V-shaped microgrooves with flat-ends by 6 axis control ultraprecision machining. *CIRP Ann Manuf Technol* 59:61–66
4. Johnson G, Cook W (1983) A constitutive model and data for metals subjected to large strains, high strain rates and high temperature. In: *Proceeding of the seventh international symposium on ballistics*, Hague, Netherlands, pp 541–547.
5. Kong L, Mak C, Cheung C, Lee W, To S, Ho W (2013) A study of effect of cutting strategy on surface generation in ultra-precision machining of micro-structured pattern rollers. *Key Eng Mater* 552:575–585

# Reducing Delamination in Micro Drilling of Carbon Composite Materials



E. Pliusys and P. T. Mativenga

**Abstract** Composite components are generally produced in near-final shape with the use of primary processes. However, an additional machining operation such as drilling is often needed. In mechanical drilling of composites delamination can be considered as the most critical damage. The aim of this work was to investigate ways of reducing delamination in drilling composite materials in micro drilling of thin carbon fibre reinforced laminates using a 0.5 mm twist drill. This is a challenging process considering the size of the drill and heterogeneous nature of the workpiece material. Taguchi orthogonal arrays were used to design experiments enabling the definition and ranking of significant machining input parameters. A mechanism for clamping and restraining the workpiece was developed and tested. The results proved to be very promising since a significant reduction in delamination damage was observed. Results show that the most significant parameters for entry and exit delamination are spindle speed and drill point angle. There is need to provide enough support to the component so that it can resist or be insensitive to thrust force as the drill approaches the end of the laminate. Conditions to minimise delamination, tool wear and to improve productivity are reported.

**Keywords** Micro drilling · Delamination · CFRP

## 1 Introduction

### 1.1 Composite Materials

Composite materials consist of two or more material phases which are combined at a macroscopic level but are not soluble in each other. They contain a strong reinforcing phase (usually fibres) and a more ductile matrix phase (usually polymeric). The aerospace industry was one of the first to adopt carbon fibre composites because of its weight savings that are achieved without compromising mechanical properties

---

E. Pliusys (✉) · P. T. Mativenga  
School of Mechanical, Aerospace and Civil Engineering, The University of Manchester,  
Manchester M13 9PL, UK

compared to metal alloys such as aluminium and titanium. The demand of composite materials is expected to grow rapidly due to continued use in construction of aircraft and increasing integration into other commercial sectors.

Carbon fibre has also been acknowledged in the motorsport industry, particularly in Formula 1, NASCAR, motorbike and powerboat production as they require strong and lightweight materials. Over the years, carbon fibre reinforced plastics (CFRP) became the main structural material in the sports industry. The commercial automotive industry perhaps holds the greatest potential for high performance composites, though it is constrained by high cost and slow production speeds. In the expanding wind energy market, demand for improved wind turbine capacity brings increase in average blade length that requires lighter and stiffer materials. The use of carbon composites provides the necessary stiffness without adding a tremendous amount of weight and results in more efficient electricity generation.

## ***1.2 Micro Machining***

The world is seeing a strong and rising demand for micro parts and miniaturised products and the use of microscale holes and features. For example, the use of semiconductors led to more compact electrical circuits which brings the need for components with micro dimensions to be manufactured. Therefore, mechanical micromachining is receiving great attention to manufacture miniaturised parts and products in the aerospace, automotive, biomedical, communications, electronics, environmental, optical and military industries. Applications, for instance are micro channels for lab-on-chip, shape memory alloys, medical devices, micro actuators, sensors, filters, fluidic graphite channels for fuel injection systems and many others.

One of the earliest attempts to describe micromachining was made by Masuzawa and Tonshoff and micromachining was defined as a branch of engineering that deals with production with dimensions of the features in order of microns (1–999  $\mu\text{m}$ ) [1]. In a later research, Masuzawa purposed the idea that the range of micromachining varies according to contemporary level of conventional technologies, person perspective, machining method, type of product and material [2]. Later on, Dornfeld classified it as material removal operation with geometrically defined cutting edges and tool engagement less than 1 mm [3]. While micromachining has been studied for other materials, there were hardly any reported studies investigating micro drilling of CFRP composites. The aim of this study was to address this knowledge gap.

## ***1.3 Challenges in Carbon Composite Drilling***

A number of problems can occur in composite drilling operations, namely, tearing of fibres, damage from heat, crack formation and delamination, which considerably decrease the composite resistance to either static loading or fatigue [4]. The most

significant damage can be considered to be delamination, as it results in reduction of the mechanical properties in the assembly of many components thus decreases reliability and performance of the final product. In delamination, adjacent plies separate within the laminate due to drill impacts occurring in the drilling process. This phenomena is very noticeable at the drill entrance as peel-up delamination and at the exit of the drill as push-out delamination.

When the drill enters the laminate it moves the first plies upward and the material spirals up before it is machined completely due to spindle movement and helical drill geometry. For the push-out delamination, the spindle speed at the tool centre is equal to zero, therefore the material located at the core of the drill bit experiences axial force and is pushed by deformation before being cut.

### 1.4 Delamination Characterisation

In order to fully comprehend delamination damage it needs to be appropriately monitored and analysed. Chen suggested the use of delamination factor,  $F_d$ , which is now most widely used to characterise delamination [5]. Delamination factor is found from the ratio of maximum diameter,  $D_{max}$  in the damaged area to the drilled hole diameter,  $D_0$ , Eq. (1) as illustrated in the Fig. 1:

$$F_d = \frac{D_{max}}{D_0} \tag{1}$$

However, carbon fibre polymers generally do not possess a uniform damage area when it delaminates due to their brittle nature. Hence, it often exhibits irregularly damaged zones with cracks and the above definition of delamination is not a robust representation of the damaged area. Considering this view, Davim proposed a new adjusted delamination factor,  $F_{da}$  which not only takes into account the conventional delamination factor,  $F_d$ (which represent the largest crack) but also includes the total damaged area given by Eq. 2 [7].

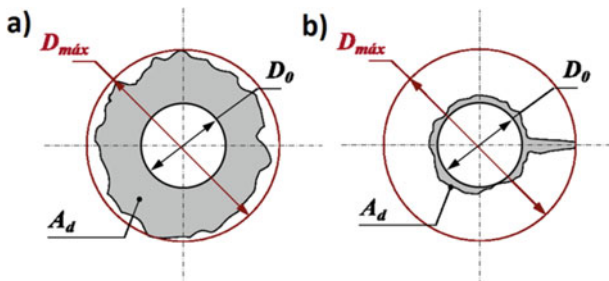


Fig. 1 Schematic delamination patterns for a uniform damage and b single crack [6]

$$F_{da} = F_d + \left( \frac{A_d}{A_{\max} - A_0} \right) (F_d^2 - F_d) \quad (2)$$

where  $A_d$  is the damage area,  $A_{\max}$ —the area corresponding to  $D_{\max}$  and  $A_0$  is the nominal area. The adjusted characterisation factor tends to the conventional delamination factor if the delamination area is minimal and is mainly due to the crack as seen in Fig. 1b. However, if the majority of delamination area is not only from the crack region and uniformly approaches  $D_{\max}$  as shown in Fig. 1a, the new adjusted factor presents a value equal to the square of the conventional delamination factor.

## 1.5 Tool Geometry

The drill geometry is an important factor as it has significant influence on the quality of the hole, particularly delamination occurrence. The drills for CFRP machining should exhibit high resistance to wear and abrasion resistance due to nature of the reinforcements which are highly abrasive. Lin and Chen and Wang confirmed the advantage of using carbide tools instead of high speed steel considering the tool wear at high speeds for fibre reinforced plastic drilling [8, 9]. However, carbide tool wear is greater than polycrystalline diamond (PCD) coated tools which produced better quality holes [10]. Despite that, the main drawback of using PCD tools in industry is high cost. In addition, Piquet used a twist drill with a specific tungsten carbide (micro grain) class drill which was tougher than ordinary carbides and cheaper than diamond drills [11]. Tungsten carbide drill was observed to produce better quality holes without a predrilled hole which was required to obtain satisfactory hole for twist drill.

Tsao and Hocheng compared the performance of different types of drills, namely, twist drill, saw drill, W-shape drill, core drill and step drill on the delamination [12, 13]. They found that special geometries can be operated at greater feeds without delamination compared to the twist drill. Controversially, Durão explored the impact of different types of drill geometries, specifically twist drill, straight flute drill, W-shape drill and step drill and recommended twist drill for minimal delamination [14].

Shyha investigated the performance of uncoated and titanium nitride (TiN)-coated step drill and twist drill and concluded that drill geometry and feed rate are the main factors contributing to the tool life and thrust force [15]. In terms of tool life, the uncoated tool step drill produced the highest number of satisfactory holes. Also, the stepped drill geometry and higher feed rates increased the tool life. When drilling CFRP, Murphy using TiN and diamond-like carbon (DLC) coated tungsten carbide drills reported no advantage of in reducing tool wear or workpiece damage [16].

Heisel and Pfeifroth investigated the influence on the machined component quality by varying the point angle of the cemented carbide twist drill between  $155^\circ$  and  $185^\circ$  [17]. The conclusion was drawn that increase in point angle results and increase in thrust force, improved hole quality at the entrance, especially concerning



delamination. However poorer holes were produced at the exit mainly due to the delamination.

Another important factor that needs to be considered is the size of the drill. Reducing the size of the tool leads to difficulty in controlling dimensional tolerances during drill manufacture. These irregularities in micro tools may downplay the advantages of precision process control, up-to-date machine and exceptional selection of process parameters [3].

## ***1.6 Tool Wear***

Tool wear plays a significant role in the hole quality since the wear changes the tool geometry when drilling large number of holes with the same tool. Lin and Chen studied two different types of tools, namely multifaceted drill and twist drill ( $d = 7$  mm) for the speed range between 9550 and 98,650 rpm. It was concluded that tool wear increases with the increase in cutting speed resulting in higher possibility for the delamination to occur [8]. In addition, Tsao and Hocheng analytically investigated the effect of tool wear [18]. The experimental observations demonstrated the increase in thrust force as the tool wear increases and higher rate of delamination. Also, higher feed rates were causing more delamination leading to a suggestion to reduce feed rates as the tool progressively wears.

Chen examined the effect of tool wear on the delamination factor and confirmed the relationship between the delamination factor and the flank wear with the number of holes drilled for the conventional twist drill [5]. It was observed that thrust force is increased as flank wear progresses resulting in more delamination due to the fact that drill is not capable of cutting the material at the same rate as it wears and starts pushing through. Furthermore, higher speed and low feed rate condition generates more heat that rises the temperature of the flank surface leading to more wear.

The hard and abrasive nature of fibres result in excessive tool wear and heat attributable to friction and a soft and sticky matrix clogs the cutting edge. Numerous researchers agreed on abrasive wear being the most dominant mechanism when machining carbon and glass composites [5, 10]. Furthermore, authors suggest that the abrasive wear mechanism due to the rubbing action of hard fibres is most noticeable on the flank face. Hence, flank wear is commonly used to analyse the wear progression of drills.

## ***1.7 Drilling Parameters***

The main aim of variation of drilling parameters is to improve the surface roughness of the hole and reduce thrust force when machining carbon composite material. A lot of researchers have studied the cutting speed and feed rate influence on thrust force, torque, tool life. Adaptation of the conventional drilling processes commonly

used in metalworking need to be carefully considered as inappropriate selection may lead to intolerable degradation of the material. Caprino and Tagliaferri, Tsao and Hocheng established feed rate to be most important factor when drilling GFRP triggering the hole damage [13, 19]. Using lower feed values prevents from significant damage. Enemuoh reported that combination of high speed and low feed value is recommended set up [20].

Sardiñas used multi-objective optimization method for cutting parameters selection for CFRP drilling and reported that higher removal rate results in more delamination [21].

### 1.7.1 High Speed Drilling

Many studies were conducted to assess the high speed drilling effects on composite materials. Gaitonde investigated the effects of spindle speeds of 4011, 7630, 38 197 rpm and feedrate of 0.03–1.5 mm/rev and drill point angle of 85°, 115°, 130° on delamination factor when machining carbon fibre reinforced composites [22]. From the study, it was observed that high speed drilling reduced damage at the entrance of the hole and least delamination was observed with lower feed and point angle for entrance and exit.

Karnik and Rubio performed further analysis on high speed drilling by examining spindle speed from 4000 to 40,000 rpm, feed rate of 0.025–2.25 mm/rev and point angle of 85°–130° [23, 24]. They recommended a combination of high spindle speed, particularly 40,000 rpm, and low feed rate and point angle to produce finest holes.

Krishnaraj examined the high speed drilling conditions on thin (2 mm) CFRP composite by varying input parameters, namely, spindle speed from 12,000, 16,000, 20,000 rpm and feed rate from 0.01, 0.05, 0.03 mm/rev using the twist drill with the point angle of 118° [25]. The conclusions agree with other researches findings that feed rate has high influence on thrust force and exit delamination. Optimal parameters recommended were a spindle speed of 12,000 rpm and federate of 0.137 mm/rev.

## 1.8 Back Up

In order to prevent composite plates from delamination of plies the thrust force needs to be counteracted. One of the ways to neutralise the negative impact of thrust force is to use support plates at both ends of the hole Fig. 2. This practice is commonly used in the industry. The results observed by Capello when comparing drilling with and without the support plate under the laminate using the twist drill showed high reduction in the push-out delamination for the prior method [26]. The author indicated that significant reduction in delamination can be achieved by limiting the workpiece deflection.

Tsao and Hocheng used 2 mm thick aluminium bottom support plate when drilling with saw and core drills [27]. They suggested that the support plate reduces the

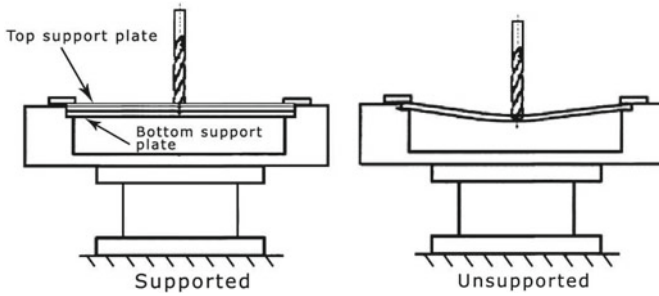


**Fig. 2** Supported and unsupported drilling [26]

possibility of the exit delamination as the critical thrust force limit is increased. Similarly to carbon fibre composites, printed circuit board (epoxy matrix composites reinforced with the glass fibre) is anisotropic and heterogeneous material. Hence, it also suffers from entrance and exit delamination when drilling micro holes. The use of thin aluminium sheet as a top support and wood based composite as a bottom backing plate to support the component is widely employed in Printed Circuit Board (PCB) micro drilling operations. Furthermore, the material selection for backing plates needs to be carefully considered as it could possibly exaggerate the tool wear.

## 1.9 Research Motivation

The motivations for this work was to improve the performance and quality of composite micro drilling processes by researching and reducing delamination damage.

## 2 Experiment

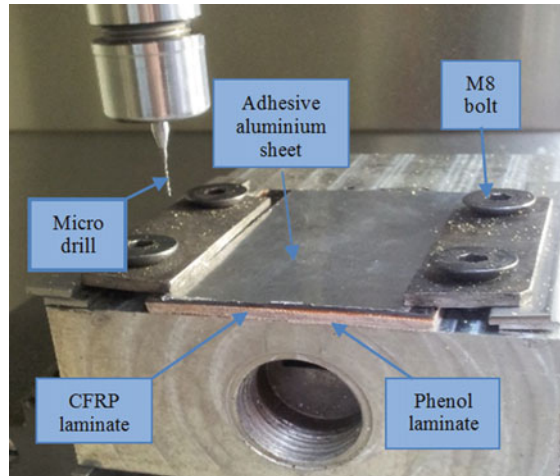
### 2.1 Experimental Setup and Analysis Procedures

#### 2.1.1 Machining Setup

Drilling experiments were conducted on a Mikron HSM400 CNC machine. The machine has a maximum spindle speed of 42,000 rpm, maximum feed rate of 40 m/min, maximum power of 13.5 kW and torque of 8.8 Nm.

In order to accommodate the CFRP sample, the jig seen in Fig. 3 was employed to secure the workpiece in a set position and allow support plates to be mounted. Four standard M8 bolts were fastened by applying a torque on each bolt of approximately 6 Nm to compress the CFRP specimen.

**Fig. 3** Jig used to secure CFRP sample in the Mikron HSM400 CNC machine



Pre-Preg carbon fibre composite samples of 1 mm thickness were used for the drilling tests. The pre-preg consisted of high modulus CF pre-impregnated with an epoxy resin matrix in controlled quantities before manufacturing the composite. Autoclave process was used for the production of final sheet. CFRP manufactured from pre-preg benefits from precisely controlled fibre-resin ratios, excellent quality, self-adhesion of layers and superb mechanical performance. Such a composite is often selected for high performance designs in wind energy, aerospace, motorsport and many other applications.

The specimens supplied by Easy Composites UK featured crossply stacking sequence of plies providing uniform mechanical properties of final component in all directions as plies are oriented perpendicular to each other. Furthermore, specimens tested had an immaculate surface finish on both, top and bottom sides, simplifying the inspection of damaged areas due to the machining operation.

Due to very limited availability of micro drill geometries designed for drilling composites, three twist drills shown in Fig. 4 were selected to investigate influence of different point angles on delamination factor. These drills were supplied by Rainford Precision UK.

All three chosen drills were manufactured from ultra-micro grain carbide and were of the same diameter (see Table 1).

Taguchi's experimental design, developed by Dr. Genichi Taguchi, was employed to determine the dominant contributing factors influencing the quality of micro holes and to optimising the levels for the input parameters. The parameters chosen for this study were, spindle speed, feed rate and drill point angle.

The Taguchi method reduces the variation in a process through a robust design of experiments. Taguchi established a technique for designing trials to examine how different parameters affect the mean and variance of a process performance characteristic. The main advantage of this analysis is that the latter method tests pairs of combinations of parameters instead of testing all possible combinations. Thus, the

**Fig. 4** Comparison of drills used with a toothpick



**Table 1** Specifications of tested tools

	Point angle (°)	Coating	Diameter (mm)
HAM	90	Uncoated	0.5
Kyocera	130	Uncoated	0.5
Union tool	150	UT coated	0.5

**Table 2** Parameters and levels used to construct L25 orthogonal array

Parameter	1	2	3	4	5
Drill point angle	90°	–	130°	–	150°
Feed rate (mm/min)	300	700	1100	1500	1900
Spindle speed (rpm)	8000	14,000	20,000	26,000	32,000

collection of the essential records identifies key factors most affecting product quality with the least possible amount of experimentation in a time and resource efficient way. In this case, a study with 3 parameters, each having 5 levels, would require 125 tests for full factorial investigation. Conversely, using Taguchi’s orthogonal arrays, only 25 experiments are needed. Finally, this particular scheme is simple and easy to apply to many engineering situations, making it a powerful yet simple technique.

Taguchi design involves using orthogonal arrays depending on the number of parameters and levels. Generally, the number of levels for all parameters in the experimental design is chosen to be the same to aid in the selection of the proper orthogonal array. For high speed drilling testing L25 orthogonal array was designed using the parameters and levels given in Table 2.

**2.1.2 Evaluation of Results**

For the post analysis of the quality of the holes produced KEYENCE VH-S30K free angle observation system was used to capture the images of machined holes. The

**Table 3** Classification of contribution

Contribution range	Degree of significance
Contribution > 50%	Highly significant
50% > Contribution > 10%	Significant
10% > Contribution	Not significant

affected area due to drilling operation was measured using Photoshop CS4 software in order to calculate conventional delamination factor,  $F_d$ , and adjusted delamination factor,  $F_{da}$ .

The Analysis of variance (ANOVA) was employed to study the characteristics of input parameters and their contribution and effect on machined hole quality. The ANOVA table gives degrees of freedom (DOF), sum of squares (SS), mean square (MS) and F ratio. DOF indicates the extent of information that can be uniquely determined from observed trial data while SS measures the deviation of the experimental data from the mean value. Also, mean square is the ratio of sum of squares to the degrees of freedom and F-ratio is the ratio of mean square of regression model to the mean square of residual error. Minitab statistical software was employed to perform investigation of Taguchi experimental data.

The contribution of the parameter is determined by Eq. (3) and is classified according to Table 3:

$$Contr(\%) = \frac{\text{sum\_of\_squared\_dev}}{\text{total\_sum\_of\_squared\_dev}} \times 100 \quad (3)$$

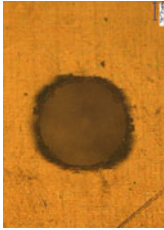
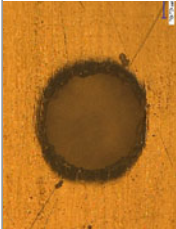
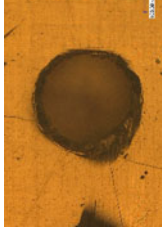
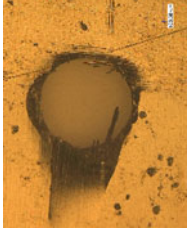
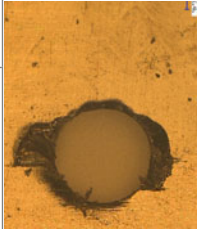
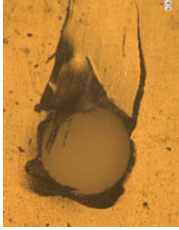
### 3 Results and Discussion

#### 3.1 Supported Versus Unsupported

Supported and unsupported drilling operations are compared in order to assess the importance of backing the workpiece. A 0.7 mm thick adhesive aluminium tape was used as a top support while Phenolic laminate was paced under the component and clamped to resist the thrust force as the drill approaches the bottom of the specimen. The spindle speed and feed rate were set to 10,000 rpm and 100 mm/min, respectively for 150° drill. 8 images were taken to determine conventional delamination factor,  $F_d$ , and adjusted delamination factor,  $F_{da}$ .

Table 4 presents typical samples of images taken for the evaluation of supported and unsupported processes. For the entrance, adhesive aluminium tape contributes to better circularity, however, the advantages are not very significant in this case. Observing the remarkable difference between the two set ups on the extent of damage

**Table 4** Quality of exit holes produced by 150° drill

	1st hole		210th hole		350th hole	
Supported by conventional backing plate		$F_d = 1.29$	$F_{da} = 1.59$		$F_d = 1.25$	$F_{da} = 1.49$
					$F_d = 1.40$	$F_{da} = 1.74$
Unsupported		$F_d = 1.58$	$F_{da} = 2.02$		$F_d = 1.89$	$F_{da} = 2.43$
					$F_d = 3.69$	$F_{da} = 5.12$

on exit holes, it is evident that supporting of last plies of the laminate provides significant reduction in damage due to the increased resistance to the thrust force. Furthermore, the analysis of calculated delamination factors for selected holes show excellent improvement in terms of damage minimisation for exactly the same input parameters. Considering the average values, the adjusted delamination factors are reduced by 6.6% for entrance and surprisingly by 123.8% for the exit of the component.

### 3.2 Taguchi L25—Drilling With Conventional Backing Plates

#### 3.2.1 Entrance

For the entrance, the variation of damage extent is obvious between experimental trials. The first 9 runs machined satisfactory holes due to the fact, that both, spindle speed and feed rate, were increased gradually. The complications start to arise when the combination of highest feedrate and lowest spindle speed was employed as the cutting tool is forced into the material too quickly.

Main effect graphs for means are plotted in Fig. 5. The horizontal line indicates the mean values. It is evident from the plots that spindle speed and feed rates are the crucial factors due to the large gradient of the graphs. It shows that delamination factor is lower when feed rate is reduced and spindle speed is increased. Controversially, all three different tool geometries tested are close to the mean values, 90° drill being the optimal choice. It agrees with the delamination theory gathered from literature

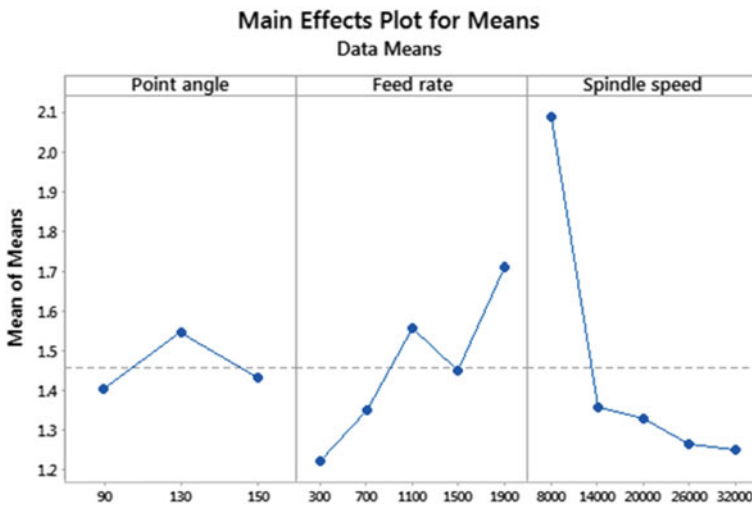


Fig. 5 Delamination factor for hole entrance after using conventional backing plates



**Table 5** ANOVA table for entrance

Source	DF	Seq SS	Adj SS	MS	F	Contribution (%)	Significance
Point angle	2	0.09366	0.05241	0.02621	0.21	1.8	Not significant
Feed rate	4	0.74938	0.69437	0.17359	1.36	14.7	Significant
Spindle speed	4	2.46512	2.46512	0.61628	4.84	48.4	Highly significant
Residual error	14	1.78374	1.78374	0.12741		35.0	
Total	24	5.09190				100	

review that delamination is minimum when low feed rate and high spindle speed is combined.

Analysis of variance table shown in Table 5 is employed to assess the impact of input parameters on the quality of the holes. Also, the contribution percentage is determined in the interest of deciding the significance of the factor. The ANOVA table indicates that spindle speed and feed rate contributes significantly by (48.4%) and (14.7%), respectively while point angle is least significant (1.8%) factor.

### 3.2.2 Exit

It was evident that the bottom surface quality of the drilled micro holes is unacceptable for all trials, except runs that are associated with lowest feed rate. This is due to the fact that material is pushed. Furthermore, 150° tool geometry tended to incompletely machine the hole resulting in formation of burrs. It was also noted that few of the micro holes were not even produced due to lack of exit backup allowing undesirable deflection of the sample.

Figure 6 represents the main effects plots. It is evident, that feed rate and point angle of the drill are most critical parameters. Observing the plots for drill geometry, it can be concluded that 130° point angle is an appropriate selection for this task.

According to the ANOVA table given in Table 6, the largest contribution can be accounted to point angle (29.7%) and feed rate (33.9%) whereas spindle speed is considered to be less important factor (6.2%) to push out delamination.

## 3.3 Using the Improved Clamping Method for Drilling

The new clamping mechanism for high speed drilling of CFRP is presented in Fig. 7 and compared with the old method for sandwiching the sample. The method used to perform Taguchi L25 experiments comprises of 2 purely horizontal fixing plates that were fastened and guided by four standard M8 bolts. However, it was obvious that this

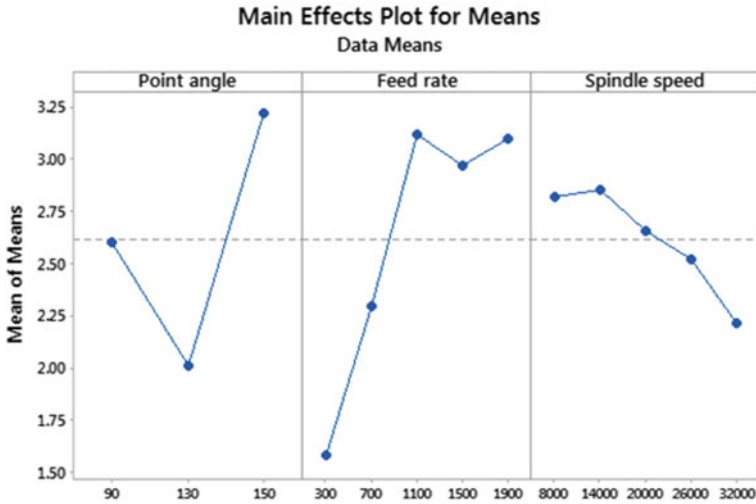


Fig. 6 Delamination factor for hole exit after using conventional backing plates

Table 6 ANOVA table for exit

Source	DF	Seq SS	Adj SS	Adj MS	F	Contribution (%)	Significance
Point angle	2	5.875	3.591	1.7954	4.20	29.7	Significant
Feed rate	4	6.717	6.699	1.6748	3.92	33.9	Significant
Spindle speed	4	1.227	1.227	0.3068	0.72	6.2	Not significant
Residual error	14	5.985	5.985	0.4275		30.2	
Total	24	19.804				100	

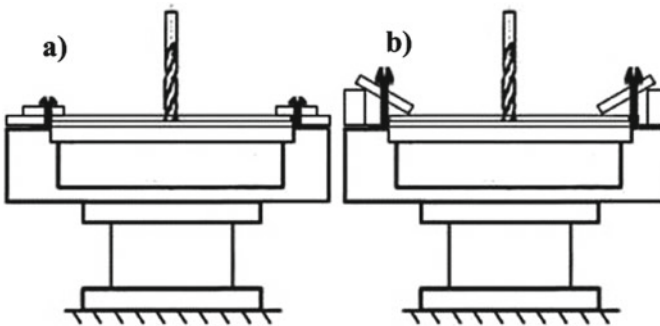


Fig. 7 (a) Conventional backing plate drilling and (b) new support squeezing the composite

fixing method is not sufficient to prevent from excessive damage when machining micro holes at high productivity rates. Therefore, the need for an improved clamping method arises that could squeeze the CFRP specimen in more effective way. For that reason, fixing plates were adjusted as shown in Fig. 7b to provide higher holding force in a vertical direction that is directly pressurising the workpiece against the bottom support plate. Also, the preliminary results yielded an undesired degree of damage on top surface using 0.07 mm thin aluminium sheet, hence a thicker sheet of 0.2 mm was placed to support top surface.

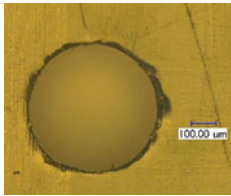
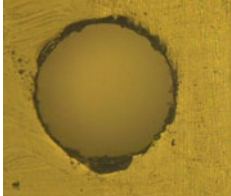
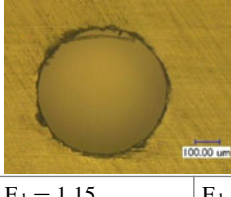
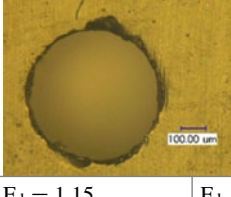
### 3.4 Taguchi L16

In order to investigate the new clamping method, Taguchi L16 orthogonal array was used. Appreciating the importance of high spindle speed, the range was extended to the maximum available spindle speed of 40,000 rpm. Furthermore, as more resistance to thrust force was expected from bottom support sheet, feed rate range was chosen to be between 1000 and 9000 mm/min. Yet again, fifty micro holes were machined for each trial and five images were captured for post analysis.

#### 3.4.1 Entrance

Table 7 presents images highlighting typical quality of micro holes at entrance produced by conducting Taguchi L16 experimental plan. Overall, the damage is considerably minimised due to the use of adhesive thicker aluminium sheet of 0.2 mm and lever support. It is evident that the micro holes possess adequate circularity,

**Table 7** Satisfactory holes drilled in trials 8 and 10

8			
	$F_d = 1.21$	$F_{da} = 1.29$	$F_d = 1.13$
10			
	$F_d = 1.15$	$F_{da} = 1.22$	$F_d = 1.15$

absence of thermal damage, separation of plies and fraying. Essentially, holes are completely drilled. This is due to the fact, that thicker aluminium sheet prevents run out of the drill, for instance, deflection of the drill tip to improve initial hole location accuracy and stops the first plies of component spiralling around the tool.

Figure 8 shows the response graphs plotted for calculated mean values. The graph illustrates that spindle speed is most important factor and values below 30,000 rpm may result in production of unsatisfactory holes. The recommendation is to use low drill point angle, low feed rate and high spindle speed to attain best quality of entrance surface possible.

Analysis of variance table shown in Table 8 is employed to judge the influence of input parameters on the entry delamination factor for improved clamping mechanism. Also, contribution percentage is determined in the interest of deciding the degree of significance for each factor. The ANOVA table indicates that spindle speed had the

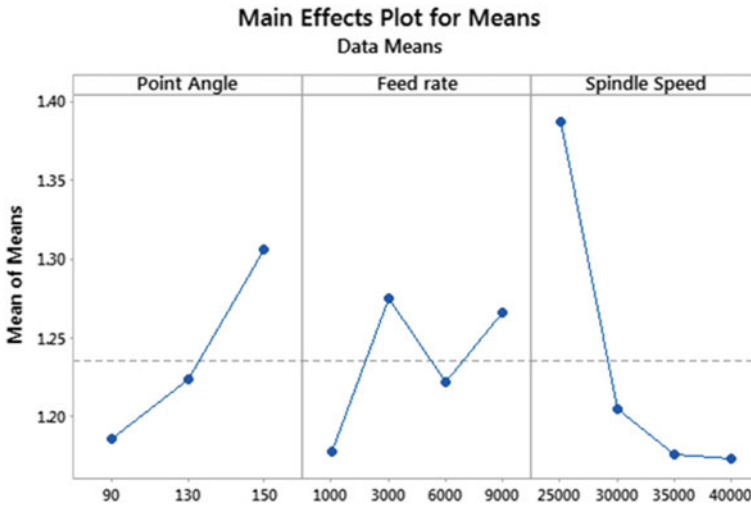


**Fig. 8** Main Effect Plots for Delamination factor for hole entrance after using new support squeezing the composite

**Table 8** ANOVA table for hole entrance delamination after new squeezing support system

Source	DF	Seq SS	Adj SS	MS	F	Contribution (%)	Significance
Point angle	2	0.03363	0.008818	0.004409	0.35	14.0	Not significant
Feed rate	3	0.02784	0.029299	0.009766	0.78	11.6	Significant
Spindle speed	3	0.09052	0.090519	0.030173	2.40	37.7	Significant
Residual error	7	0.08788	0.087881	0.012554		36.6	
Total	15	0.23986				100	

most significant effect with the highest contribution percentage of 37.7% followed by point geometry and feed rate at 14.2 and 11.6%.

### 3.4.2 Exit

Table 10 demonstrates the exit quality of typical micro holes produced using the upgraded clamping mechanism. It shows significant reduction in damaged areas compared with results observed in analysis of previous L25 orthogonal array. This reveals the importance of backup to elevate the critical thrust force that causes undesired delamination. In other words, the application of support plates can retard the onset of delamination growth and reduce delamination damage at the drill exit in the thin CFRP laminates, in particular at large feed rate.

The main effects plots for means are given in Fig. 9. The analysis recommends ideal cutting conditions to be at the lowest feed rate of 700 mm/min, maximum spindle speed of 40,000 rpm and 90° drill geometry. On the other hand, the delamination is lower revealing the suitability of proposed clamping mechanism for high speed drilling.

From the ANOVA table in Table 9 it can be inferred that push out delamination is primarily influenced by spindle speed. The contribution rate of spindle speed (71.8%) is greater than that of point angle (14.2%). Interestingly, the influence of main contributor to exit delamination, feed rate, for unsupported drilling setting, can be considered as least important parameter with only 5.6% contribution in this case (Table 10).

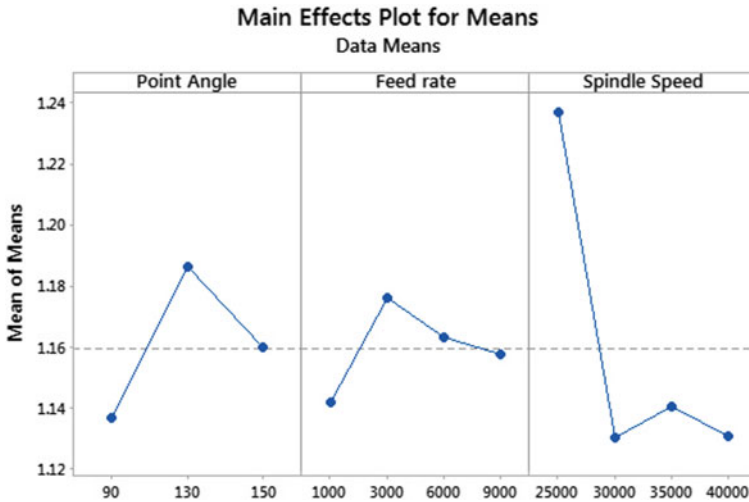
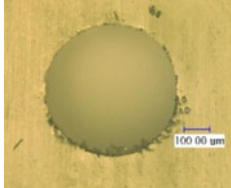
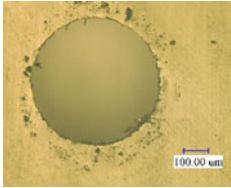
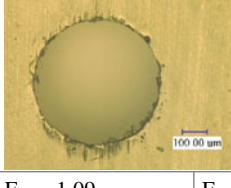
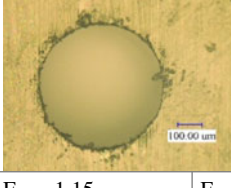


Fig. 9 Main Effect Plots for Delamination factor for hole exit after using new support squeezing the composite

**Table 9** ANOVA table for hole exit delimitation after new squeezing support system

Source	DF	Seq SS	Adj SS	MS	F	Contribution (%)	Significance
Point angle	2	0.006680	0.008379	0.004189	7.34	14.20	Significant
Feed rate	3	0.002615	0.002567	0.000856	1.50	5.55	Not significant
Spindle speed	3	0.033756	0.033756	0.011252	19.71	71.75	Highly significant
Residual error	7	0.003997	0.003997	0.000571		8.50	
Total	15	0.047048				100	

**Table 10** Satisfactory holes machined in trials 8 and 10

8			
	$F_d = 1.09$	$F_{da} = 1.11$	$F_d = 1.10$
10			
	$F_d = 1.09$	$F_{da} = 1.11$	$F_d = 1.15$

### 4 Conclusions

The study in this paper focused on characterisation of delamination damage when micro drilling carbon fibre reinforced composite materials. The vision is to develop strategies to minimise the extent of this type of defect.

The research built on a literature review where the challenges in drilling of composite materials and possible solutions were recognised. However, no studies tackling machining of carbon laminates at micro scale were found. Therefore, the fundamental theories of the macro domain were used to broaden the knowledge regarding the influence of cutting parameters, drill type and geometry on produced feature quality. Also, based on the promising studies found in the literature, the use of support plates was examined drawing a lesson from PCB drilling operations. Adjusted delamination factor is a better characterisation factor of damage induced by drilling operation than conventional delamination factor as it takes the extent of damaged regions in to account.

The following conclusions can be made:

- When micro drilling CFRP, it is recommended to use wood based phenolic laminate for the bottom side to minimise push out delamination and thin adhesive aluminium sheet for the top side to resist peel up delamination.
- When high speed drilling, mainly with higher spindle speed and higher feed values, the push-out delamination at exit is the principal cause of delamination. The peel-up delamination at entrance, generally, is less significant compared with push-out.
- Applying an active angle bracket support or resolved force on the top face of the component hence upgrading the clamping device effectiveness, the resistance to thrust force is increased, providing the ability to cut at much higher feed rate with no significant delamination.
- ANOVA statistics indicated spindle speed and drill geometry to be the most significant parameters considering the improved fixing system.
- It is recommended that for reducing delamination in micro drilling of CFRP, a high speed, ideally 40,000 rpm and tool point angle of 90° are the optimal combination for high speed drilling.
- Future work is looking at design of adjustable clamping which allows regulation of the force used to press the specimen against the support plates. The influence of clamping force analysis could be employed to further develop a clamping mechanism knowing its correlation to damage.

## References

1. Masuzawa T (1997) Keynote papers. *CIRP Ann Manuf Technol* 46(2):621–628
2. Masuzawa T (2000) State of the art of micromachining. *Technol CIRP Ann Manuf* 49(2):473–488
3. Dornfeld D, Min S, Takeuchi Y (2006) Recent advances in mechanical micromachining. *CIRP Ann Manuf Technol* 55(2):745–768
4. König W, Grass P (1989) Quality definition and assessment in drilling of fibre reinforced thermosets. *CIRP Ann Manuf Technol* 38(1):119–124
5. Chen W (1997) Pergamon. *Int J Mach Tools Manuf* 37(8):1097–1108
6. Shyha I et al (2010) Effect of laminate configuration and feed rate on cutting performance when drilling holes in carbon fibre reinforced plastic composites. *J Mater Process Technol* 210(8):1023–1034
7. Davim J, Rubio J, Abrao A (2007) A novel approach based on digital image analysis to evaluate the delamination factor after drilling composite laminates. *Compos Sci Technol* 67(9):1939–1945
8. Lin SC, Chen IK (1996) Drilling carbon fiber-reinforced composite material at high speed. *Wear* 194(1–2):156–162
9. Wang X, Wang L, Tao J (2004) Investigation on thrust in vibration drilling of fiber-reinforced plastics. *J Mater Process Technol* 148(2):239–244
10. Iliescu D et al (2010) Modeling and tool wear in drilling of CFRP. *Int J Mach Tools Manuf* 50(2):204–213
11. Piquet R et al (2000) Experimental analysis of drilling damage in thin carbon/epoxy plate using special drills. *Compos A Appl Sci Manuf* 31(10):1107–1115

12. Hocheng H, Tsao CC (2006) Effects of special drill bits on drilling-induced delamination of composite materials. *Int J Mach Tools Manuf* 46(12–13):1403–1416
13. Tsao C, Hocheng H (2004) Taguchi analysis of delamination associated with various drill bits in drilling of composite material. *Int J Mach Tools Manuf* 44(10):1085–1090
14. Durão LMP et al (2010) Drilling tool geometry evaluation for reinforced composite laminates. *Compos Struct* 92(7):1545–1550
15. Shyha IS et al (2009) Drill geometry and operating effects when cutting small diameter holes in CFRP. *Int J Mach Tools Manuf* 49(12–13):1008–1014
16. Murphy C, Byrne G, Gilchrist MD (2002) The performance of coated tungsten carbide drills when machining carbon ® re-reinforced epoxy composite materials. In: *Proceedings of the institution of mechanical engineers*, 216 Part B (Mar 2001), pp 143–152
17. Heisel U, Pfeifroth T (2012) Influence of point angle on drill hole quality and machining forces when drilling CFRP. 1:471–476
18. Tsao CC, Hocheng H (2007) Effect of tool wear on delamination in drilling composite materials. *Int J Mech Sci* 49(8):983–988
19. Caprino GTV (1995) Pergamon. *Int J Mach Tools Manuf* 35(6):817–829
20. Enemouh EU, El-Gizawy AS, Okafor AC (2001) *Int J Mach Tools Manuf* 41:1795–1814
21. Quiza Sardñias R, Rivas Santana M, Alfonso Brindis E (2006) Genetic algorithm-based multi-objective optimization of cutting parameters in turning processes. *Eng Appl Artif Intell* 19(2):127–133
22. Gaitonde VN et al (2008) Analysis of parametric influence on delamination in high-speed drilling of carbon fiber reinforced plastic composites. *J Mater Process Technol* 203(1–3):431–438
23. Karnik SR et al (2008) Delamination analysis in high speed drilling of carbon fiber reinforced plastics (CFRP) using artificial neural network model. *Mater Des* 29(9):1768–1776
24. Campos Rubio J et al (2008) Effects of high speed in the drilling of glass fibre reinforced plastic: evaluation of the delamination factor. *Int J Mach Tools Manuf* 48(6):715–720
25. Krishnaraj V et al (2012) Optimization of machining parameters at high speed drilling of carbon fiber reinforced plastic (CFRP) laminates. *Compos B Eng* 43(4):1791–1799
26. Capello E (2004) Workpiece damping and its effect on delamination damage in drilling thin composite laminates. *J Mater Process Technol* 148(2):186–195
27. Tsao CC, Hocheng H (2005) Effects of exit back-up on delamination in drilling composite materials using a saw drill and a core drill. *Int J Mach Tools Manuf* 45(11):1261–1270



# Investigation of Different Cutting Conditions for CFRP Routing with Multi-tooth Tool



Kuang-Li Lee, Yao-Yang Tsai, and Kuan-Ming Li

**Abstract** The main focus of this paper is in the use of the Taguchi method to compare the tool wear under different cutting condition. In this investigation, we define the area of tool wear to be the tool-life index. The reason is that the main wear type in milling CFRP is abrasive wear, and the wear area has a positive relationship to the milling length. Based on this, an L18 orthogonal tests were conducted to get a relationship between cutting conditions and tool wear. The conditions include spindle speed, feed rate, and different type of coating.

**Keywords** GFRP composites · Taguchi · Trimming · Routering · Multitooth tool · End milling

## 1 Introduction

Composites are one of the most widely used materials because of their adaptability to different situations and the relative ease of combination with other materials to serve specific purposes and exhibit desirable properties. A glass fibre reinforced plastics (GFRP) composite is considered to be an economic alternative to various heavy exotic materials. Glass-fibre-reinforced plastic (GFRP), an advanced polymeric matrix composite material, the use of GFRP composites in engineering applications such as automotive, aircraft and manufacture of space ships and sea vehicles industries have increased considerably in recent years due to their light weight, high modulus, specific strength, superior corrosion resistance, high fracture toughness and resistance to chemical and micro-biological attacks [1].

Generally GFRP composite are manufactured to near shape components. Achieving an acceptable surface quality with conventional methods of machining has been found to be extremely difficult due to the isotropic and heterogeneous nature of these materials. In order to extend the applications of GFRP, milling becomes

---

K.-L. Lee (✉) · Y.-Y. Tsai · K.-M. Li  
National Taiwan University, No. 1, Sec. 4, Roosevelt Rd., Da'an, Taipei 106, Taiwan (R.O.C.)  
e-mail: [R02522740@ntu.edu.tw](mailto:R02522740@ntu.edu.tw)

essential for removal of excess material to produce a well defined and high quality surface [2].

López de Lacalle and Lamikiz [3] investigated the milling of carbon fibre reinforced plastic using multiflute tools with different crystal structures and coatings for end mills.

Caprino et al. [4] showed that the increase in flank wear caused the vertical force to increase in plain cutting. In this research, it revealed that tool wears always related positively to the cutting length, while cutting length increasing will rise the increasing rate of vertical force and rise the friction. Therefore, that the reason why after meters of cutting the spindle appeared warning about low torque sometimes.

All the above works contributes to the practice of using multitooth tools, while the use of the multitooth milling tool and the relationship between tool-wear and processing parameters were rarely discussed in design experiments. This paper presents a trend of tool-wear with different spindle rave, feed rate and coateds that are nACRo and PCD for end milling.

## 2 Experimental Procedure

### 2.1 Materials, Tools and Experimental Setup

The composite materials used in the tests is made of epoxy matrix reinforced with fiber glass fabric using hardener was produced by hand-lay up procedure with 3.8 mm thickness (20 lay-ups) having a fiber orientation of 0/90°.

Experiments have been carried out with IMCO multitooth composite router in solid carbide. The three different coated carbide tools which are PCD and nACRo shown in Fig. 1, have a diameter of 6 mm with multiple flutes.

A vertical machining centre with 22 kW IDD spindle power and a maximum spindle speed of 8000 rpm was used to perform the tests. The holder of the composite material was made as shown in Figs. 2 and 3, to make sure that vibration and displacements are eliminated.

**Fig. 1** From top to bottom:  
first one is PCD coated,  
second is nACRo coated, and  
third is uncoated one



**Fig. 2** The aluminum holder of the laminate composite plate

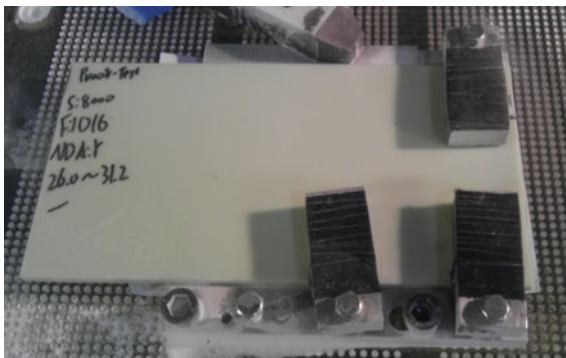


**Fig. 3** The laminate composite plate size of 300 × 130 × 3.8 mm height



**Fig. 4** The optical microscope



## 2.2 Measurements

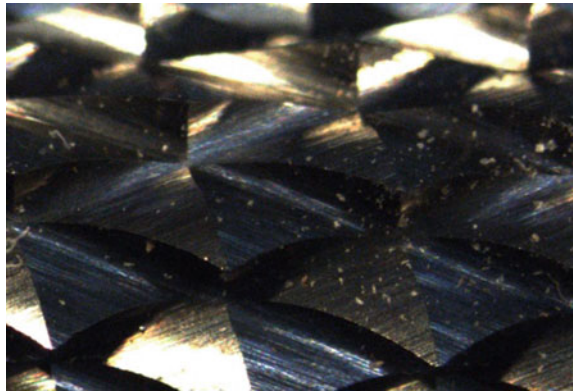
An optical microscope equipped with a CCD camera as shown in Fig. 4 was used to measured flank wear and obtain pictures of tools flutes. The optical enlargement ratio of it is 20 times the original object.

Figure 5 shows the brand new tool edge of the multi-tooth tool, and Fig. 6 shows the tool flank wear after meters of milling.

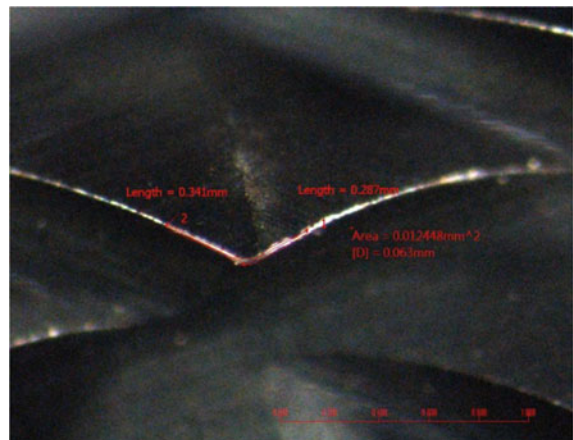
Because the microscope can only get a limited part of the edge, we took a part of entire wear and got average width of flank wear, finally, used this number timed total length of cutting edge to get entire tool flank wear.

For getting tool wear objectively, first, we made a standard test for ten metres and checked that the flank wear of every tooth was quite similar to each other as shown in Figs. 7 and 8. As the result, we can note that the middle of whole worn tooth in the cutting section has the most average tooth wear of all. Based on this result, we

**Fig. 5** The brand new tool edge



**Fig. 6** Tool edge that has been worn



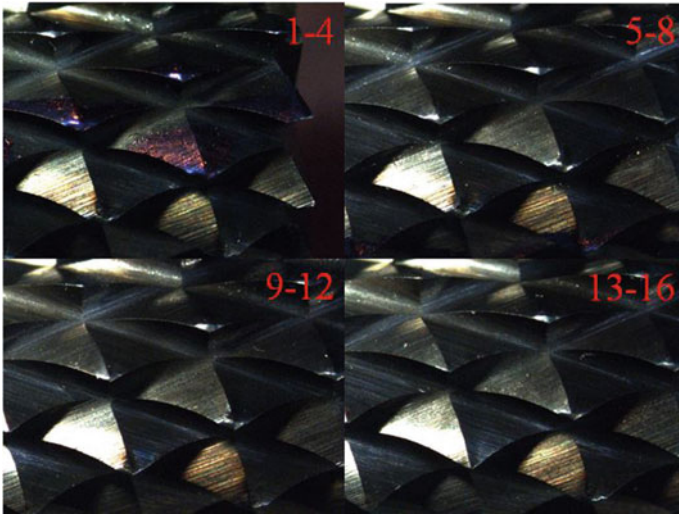


Fig. 7 First sixteen tool edge of entire cutting tool

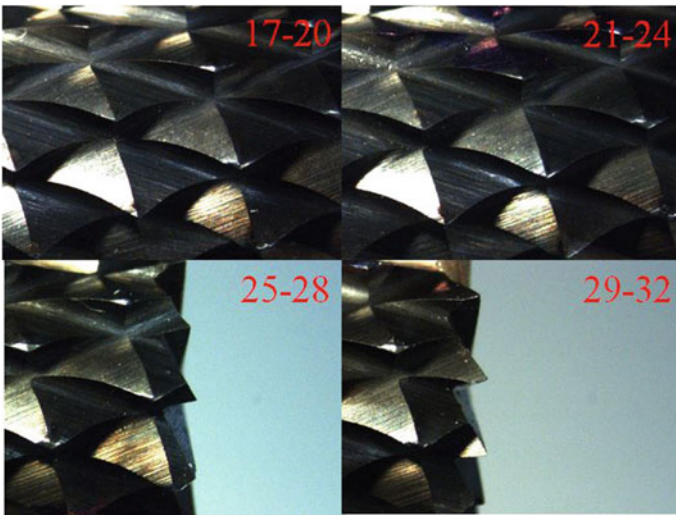
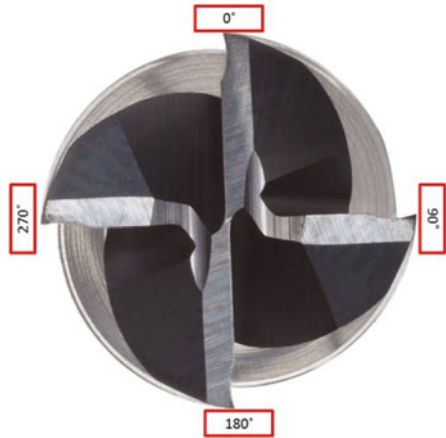


Fig. 8 Last sixteen tool edge of entire cutting tool

choose this place to measure tool wear and picked four points in a period of 5 m cutting length. Figure 9 shows the four points; after 5 m of machining we used these points (marked: 0, 90, 180, 270) to determine the average tool wear.

**Fig. 9** The standard of pick up measure points



### 2.3 Taguchi Method

Taguchi’s method has been used widely in engineering analysis. These techniques consist of a plan of experiments with the objective of acquiring data in a controlled way, executing these experiments, in order to obtain information about the behavior of a given process.

For the elaboration of experimental plan we used the method of Taguchi for three factors with three levels. The array chosen was the L18 which has eighteen rows corresponding to the number of tests. Table 1 indicates the factors to be studied and the assignment of the corresponding levels. Table 2 shows the three cutting parameters and the three values used for each parameter in the Taguchi L18 orthogonal experimental tests.

## 3 Experimental Procedure

The results of the milling tests allowed the evaluation of the GFRP composite material manufacture by hand-lay up, using two different coated carbide routers. The tool life was evaluated by flank wear area of tools and increasing rate of tool flank wear.

**Table 1** Factors to be studied and the assignment of the levels to the factors

Factors	Level		
	1	2	3
A: Spindle speed (rpm)	600	7000	8000
B: Feed rate (mm/min)	1016	1270	1524
C: Coated	None	nACRo	PCD

**Table 2** L18 orthogonal array list

Experimental number	A	B	C
	Spindle speed	Feed rate	Coated
No. 1	6000	1016	None
No. 2	6000	1270	nACRo
No. 3	6000	1524	PCD
No. 4	7000	1016	None
No. 5	7000	1270	nACRo
No. 6	7000	1524	PCD
No. 7	8000	1016	nACRo
No. 8	8000	1270	PCD
No. 9	8000	1524	None
No. 10	6000	1016	PCD
No. 11	6000	1270	None
No. 12	6000	1524	nACRo
No. 13	7000	1016	nACRo
No. 14	7000	1270	PCD
No. 15	7000	1524	None
No. 16	8000	1016	PCD
No. 17	8000	1270	None
No. 18	8000	1524	nACRo

### 3.1 Influence of the Cutting Parameters on the Flank Wear Area

Figures 10 and 11 compare the flank wear area between different spindle speeds and different coated materials on solid carbide tool. Figure 10 compares same solid carbide tools at 6000 and 8000 rpm, and it is clearly shown that the higher spindle speed caused larger average wear width “W” which was determined from the flank wear area divided by the wear length.

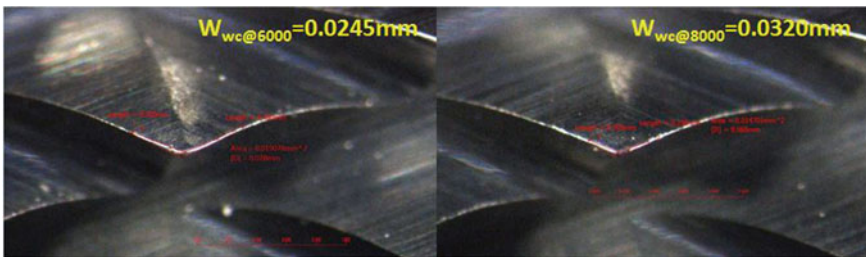


**Fig. 10** Flank wear of same solid carbide tools under different spindle speed

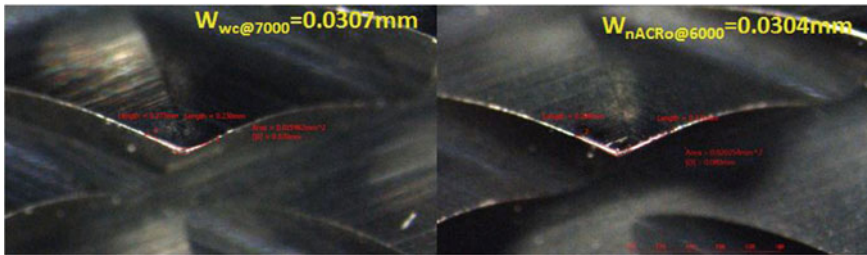


Fig. 11 Flank wear of same solid carbide tools with and without nACRo coating

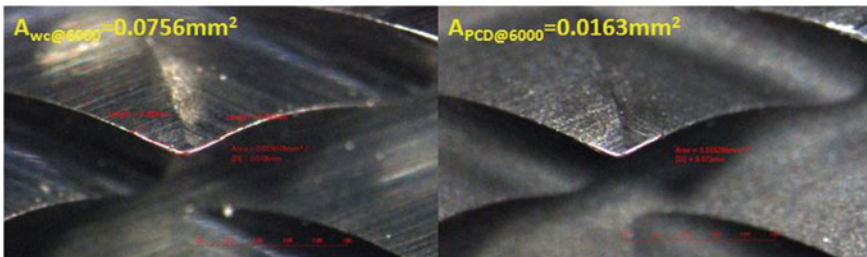


Fig. 12 Flank wear of solid carbide tools with and without PCD coating

Figure 11 compares the same carbide tool with and without nACRo coated, it reveals that this kind of coated does not have a great resistibility to flank wear. The average width of wear is almost the same.

Figure 12 shows the flank wear area of an uncoated solid carbide tool and a PCD coated tool. Because all the flank wear in the PCD coated tool is concentrated at the top of the cutting edge, in this comparison we chose the wear area instead of wear width to compare tool wear more objectively. The total wear area for the carbide tool was determined by the average wear width times the full wear length of cutting edge i.e. 3.084 mm.

### 3.2 Influence of the Cutting Parameters on the Flank Wear Area

Table 3 shows the final wear area and the increasing rate of wear area after 10 m milling test in L18 Taguchi experiments design. The increasing rate of wear area was determined by wear area values that were measured every 2.5 m. The least square method was used to get the slope of the increasing rate (Tables 4).

From Fig. 13, for spindle speed and feed rate, the lower value will get the better result which means if we choose 6000 rpm and 1016 mm/min we can have the most



**Table 3** Results of entire L18 list experiments

Experimental number	A	B	C	The final wear area	Increasing rate of wear area
	Spindle speed	Feed rate	Coated		
No. 1	6000	1016	None	0.0838	0.0102
No. 2	6000	1270	nACRo	0.0811	0.0095
No. 3	6000	1524	PCD	0.0180	0.0022
No. 4	7000	1016	None	0.0971	0.0113
No. 5	7000	1270	nACRo	0.0921	0.0107
No. 6	7000	1524	PCD	0.0306	0.0032
No. 7	8000	1016	nACRo	0.0740	0.0085
No. 8	8000	1270	PCD	0.0435	0.0042
No. 9	8000	1524	None	0.0847	0.0103
No. 10	6000	1016	PCD	0.0208	0.0022
No. 11	6000	1270	None	0.0848	0.0093
No. 12	6000	1524	nACRo	0.0870	0.0101
No. 13	7000	1016	nACRo	0.1051	0.0116
No. 14	7000	1270	PCD	0.0184	0.0020
No. 15	7000	1524	None	0.0985	0.0122
No. 16	8000	1016	PCD	0.0159	0.0018
No. 17	8000	1270	None	0.0986	0.0120
No. 18	8000	1524	nACRo	0.1003	0.0119

**Table 4** Response of signal to noise ratios for the increasing rate of flank wear

Level	Factor		
	S (rpm)	F (mm/min)	Coated
1	44.4852	44.4444	39.2888
2	43.1816	43.2904	39.7108
3	43.2759	43.2081	51.9432

**Table 5** Response of signal to noise ratios for the final wear area

Level	Factor		
	S (rpm)	F (mm/min)	Coated
1	25.7593	25.5928	20.8200
2	24.2730	24.3340	20.9844
3	20.9807	24.6600	32.7824

gradual slope of wear increasing. While among different types of coating, PCD has a dramatic improvement on resist abrasive wear at tool flank.

Figure 14 also shows the same trend as Fig. 13, the lower speed and feed rate can result in a better tool life. PCD coating is best one to resist tool wear.

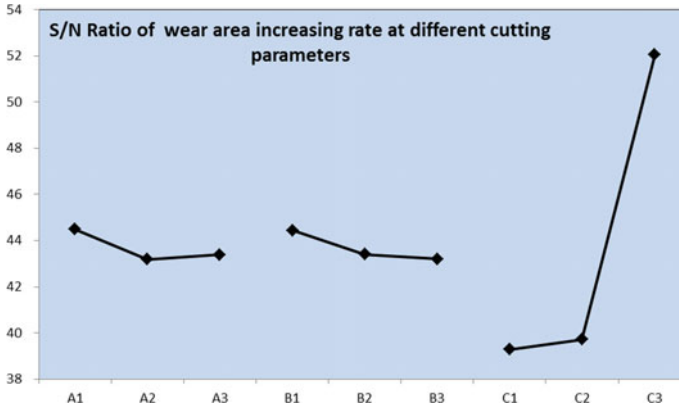


Fig. 13 First sixteen tool edge of entire cutting tool

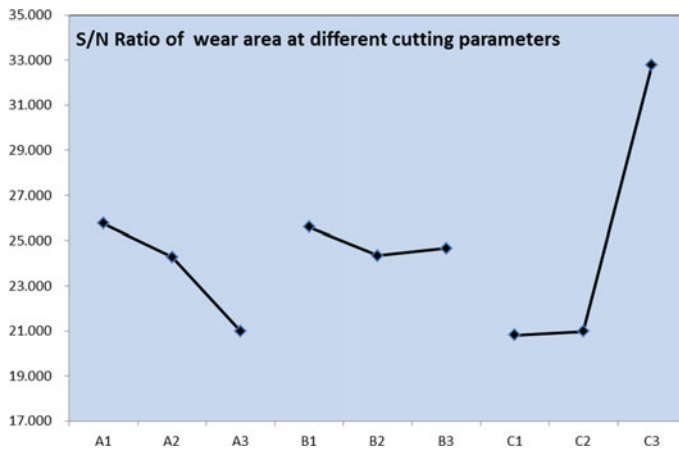


Fig. 14 First sixteen tool edge of entire cutting tool

### 4 Conclusion

This study describes an experimental approach to investigate the trend of tool wear; it tries to estimate the cutting parameter which can achieve maximum tool life by using design of experiments. The results are summarized below.

- Regarding spindle speed, a higher speed causes a larger wear area in multitooth carbide tools. So, to minimise wear and achieve the longest tool life, one should choose the lowest spindle speed taking into account torque surface roughness required.

- A lower feed rate can result in a longer tool life, but for manufacturing efficiency, increasing the feed rate by 1.5 times increased the tool wear by only 10 percent. So, if a higher efficiency is required, increasing the feed rate is a great way.
- A PCD coating can improve tool life dramatically but its cost is also higher. Before choose this kind of coating, one should consider whether its performance is worth the additional cost.

## References

1. Hull D, Clyne TW (1996) An introduction to composite materials, 2nd edn. Cambridge University Press
2. Edwards KL (1998) An overview of the technology of fiber-reinforced plastics for design purposes. *J Mater Des* 49:1–10
3. López de Lacalle N, Lamikiz A, Campa FJ, Valdivielso AFDZ, Etxeberria I (2009) Design and test of a multitooth tool for CFRP milling. *J Compos Mater* 43(26):3275–3290
4. Caprino G, De Iorio I, Nele L, Santo L (1996) Effect of tool wear on cutting forces in the orthogonal cutting of unidirectional glass fibre-reinforced plastics. *Comp Part A: Appl Sci Manuf* 27(5):409–415

# A New Technology to Achieve Precision Machining for CNC Machines Using Artificial Neural Network



Ganesh Kumar Nithyanandam, Matthew Franchetti,  
and Radhakrishnan Pezhinkattil

**Abstract** Precision machining is a process where material is removed from a component to very tight tolerances. A final product could be made of several components. A cumulative error in process variations is measured based on process variations existence in each component. This could lead to product rejection for crucial sensitive components. The current CNC machines are unable to achieve this very tight tolerance throughout the machining cycle and on a consistent basis. The customers also demand such tightly tolerance products not only at a given point of measurement but throughout the product. Therefore, manufacturers are constantly seeking for new technology, method or process to achieve such very tight tolerances in machining. This paper addresses development of a new technology to increase the precision of machining in CNC machines. In this, an indigenously designed portable fixture with and without laser detection system is developed, which is mounted on an existing CNC machine. This portable fixture has the intelligence developed using artificial neural network to monitor the machining operations and takes appropriate actions (controls) when process variations go outside the targeted value in real-time. A case study in aircraft component is presented as an example. This paper represents experiments using a Makino high speed CNC milling machine, conducted using Design of experiments. The results are promising results and recommendations based on findings are discussed in this paper.

**Keywords** Precision machining · Artificial neural network · Cumulative error · CNC machines

---

G. K. Nithyanandam (✉)

Department of Mechanical Engineering, PSG College of Technology, Coimbatore, India

M. Franchetti

Department of MIME, The University of Toledo, Toledo, USA

R. Pezhinkattil

PSG Institute of Advanced Studies, Coimbatore, India

© Springer Nature Switzerland AG 2022

S. Hinduja et al. (eds.), *Proceedings of the 38th International MATADOR Conference*,  
[https://doi.org/10.1007/978-3-319-64943-6\\_26](https://doi.org/10.1007/978-3-319-64943-6_26)

369

# 1 Introduction

A high precision component is defined as a part being machined with a very low tolerance variation. Figure 1 shows the tolerance variation in a component. In this figure, black dots represent the occurrence of tolerance variation during normal machining, whereas the blue dots represent the occurrence of precision machining. There are several parameters affect the precision machining. In this study, optimum cutting parameters such as cutting speed, feed rate and depth of cut are considered, which would influence the precision machining.

A finished assembled product consists of several sub-components. Evidences [1, 2] show that there are tolerance variations exist in each component. Figure 1 shows those tolerance variations ( $d_0, d_1, d_2, \text{etc.}$ ) in the machined component. When such parts are assembled together, cumulative tolerance variation occurs in the final product. Therefore, it is imperative to machine each component to tighter tolerance, to be specific, closer to the targeted mean (blue dots in Fig. 1), not only at a particular point of the component, but throughout the machined surface, as shown in Fig. 2.

In this paper, an attempt is made to achieve this precision machining for milling. For this, several modules are carried out, which are covered in the following sections.

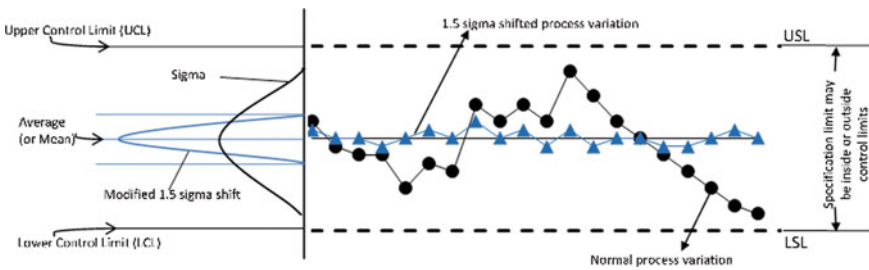
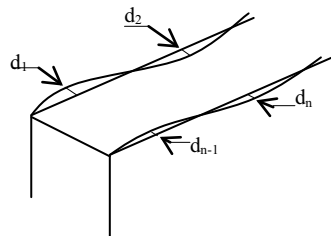


Fig. 1 Process tolerance variations

Fig. 2 Tolerance variations in a component



## 2 Literature Survey

Machining components to tighter tolerance is always a challenge. Dhole et al. [3] argue that with the current technology, it is not possible to produce such a perfect smooth surface, whatever may be the manufacturing processes. Therefore, researchers seek for new method or technology to achieve them. Saikumar et al. [4] demonstrated machining components using adaptive control system. In their approach, optimum cutting parameter value is entered via open source controller which then sends the signals to the CNC system. With this approach, the limitation exists based on the open source control being used. Therefore, in this study, a new thinking is applied to eliminate this limitation.

Design of experiments (DOE) is a systematic approach to conduct experiments in most efficient and cost effective method with appropriate selection of factor combinations and their levels. The DOE is also defined as formal mathematical method for systematic planning and conducting scientific studies that change experimental variables together in order to determine their effects of a given response [5, 6]. In other words, DOE identifies how factors (Xs) alone, and combined affect a process and its output (Ys) [7]. Analysis of variance (ANOVA) is a statistical technique to determine which factor has more influence on the response (output). ANOVA was used for analyzing and interpreting the experimental results. Surasit [8] and Sanjit [9] used ANOVA to study the effect of cutting speed, feed rate and depth of cut on roughness in end milling of aluminum work piece. In this study, DOE with two-way ANOVA is used to derive the mathematical model connecting workpiece tolerance variations influenced by cutting speed and feed rate.

Though the first engineering application is introduced in 1969, the metal cutting operations related ANN applications were seriously taken up only in the past few years. There are several types of artificial neural networks such as feed forward back propagation neural network, RBF network, Kohonen self-organizing network, recurrent Neural network, modular neural network, etc. are available. Haghddadi et al. [10] used back propagation algorithms to predict the hot deformation behaviour of aluminium alloys. Mortaza Aghbashlo et al [11] used feed forward artificial neural network to predict exothermic performance of spray drying process. Ardestani et al. [12] used feed forward artificial neural network in medical field to predict the parameters corresponding to two different knee rehabilitations based on pre-rehabilitation gait patterns. MatLab [13] suggested feed forward back propagation is the best suited technique for using in any predictive methodology. Ozel and Nagir [14] used back-propagation neural network to predict tool wear on chamfered and honed CBN cutting tools on hardened H-13 steel work piece with wide range of cutting parameters. Similarly, Sanjay et al. [15] used ANN to predict tool wear with different cutting parameters in drilling of mild steel work pieces using HSS twist drills. Benardos and Vosnaikos [16] suggested three modeling techniques to predict surface roughness, which were classified as experimental models, analytical models and artificial intelligence (AI)-based models. They suggested that the experimental models are used to predict surface roughness with higher accuracy but it takes longer duration and are

costly. The analytical models are also used to estimate surface roughness but they do not consider parameters such as tool vibrations, etc. Zain et al. [17] used artificial neural network (ANN) to predict surface roughness in milling operation.

From the above literature survey, it is clear that feed forward back propagation algorithm is widely used for manufacturing applications. The feed-forward back propagation is a non-recurrent network which contains inputs, outputs, and hidden layers; the signals can only travel in one direction.

### 3 Methodology

The methodology defines the procedure how the research need to be designed and executed. It helps to connect the dots of other researchers how they used their methods and technique to analyze the data. Figure 3 shows the methodology adopted to develop the new technology to achieve the precision machining for CNC milling machine. This methodology helps to identify the problem statement and implement them in accordance with the literature review that are collected.

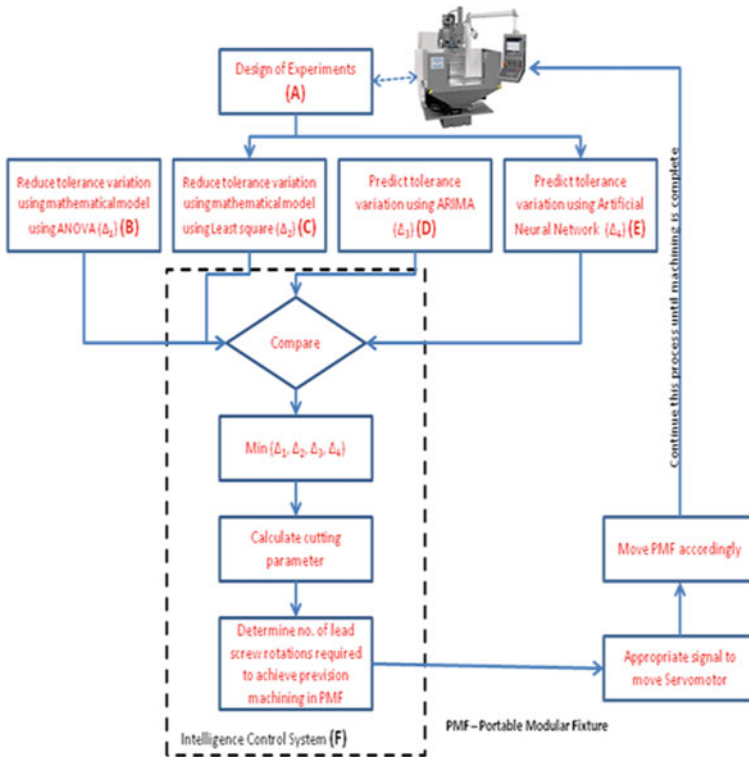
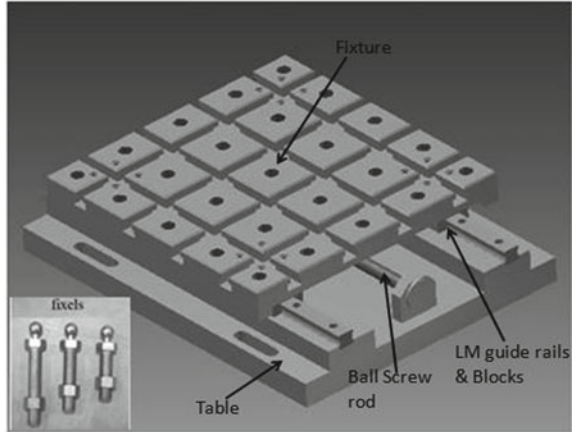


Fig. 3 Methodology of this research

**Fig. 4** Portable modular fixture mechanism



The design of experiments (A) is conducted to optimize the factors affecting the precision machining operation. The data collected during this experiment is used as the test data for other modules. Three mathematical models (B) are developed to minimize the process tolerance variation based on cutting parameters. The first mathematical model is derived using ANOVA (B); the second model is determined using least square method (C); and the last model is forecast using ARIMA (D). For this, design of experiment data is used. This data is collected at the beginning of this experiment. In addition, artificial neural network (E) module is also used to predict the optimum cutting parameters to minimize tolerance variations, but in real-time.

The intelligence control system (F) compares the resultant of each module (B, C, D and E) in real-time and takes the minimum value affecting the tolerance variations. This data is then sent or transmitted to the servomotor of the portable modular fixture (see Fig. 4) via intelligence control system. The intelligence control system is developed using C#.

The above process continues until the machining cycle is complete. Thus, a new technology is devised without interfering the CNC machine architecture. Several experiments are carried out to prove that this technology helps to achieve the precision machining for milling.

## 4 Experimental Setup

The workpiece material used in this study is Aluminum alloy 6061, which is widely used in aerospace and automobile industry. Table 1 shows the composition of Aluminum alloy 6061 and its HRC is rated under 32. The workpiece sample selected is a rectangular piece representing an aircraft rib component, with 100 mm length  $\times$  80 mm width  $\times$  25 mm depth.



**Table 1** Chemical composition of aluminum alloy 6061

Material	Specification
Al	Bal
Mg	0.8–1.2
Si	0.4–0.8
Fe	Max 0.7
Cu	0.15–0.4
Zn	Max 0.25
Ti	Max 0.15
Mn	Max 0.15
Cr	0.04–0.35
Other	0.05

Milling is a cutting process that uses a milling cutter to remove materials from the surface of the workpiece. The workpiece is machined to 2 mm thickness, as shown in Fig. 5.

In this study, three sets of experiments are carried out:

1. Conduct normal milling operation in the CNC Milling machine (see Fig. 6).
2. Mount the portable modular fixture system (Fig. 4) on the CNC machine and repeat the above experiments. In this, no real-time machining data is collected. The intelligence control system is developed using artificial neural network (E). It helps to predict the optimum cutting parameter based on DOE data (A) throughout the study. This system sends appropriate signal to the servomotor of the portable modular fixture to achieve precision machining. Figure 7 shows the portable modular fixture with intelligence control system mounted on the CNC machine.

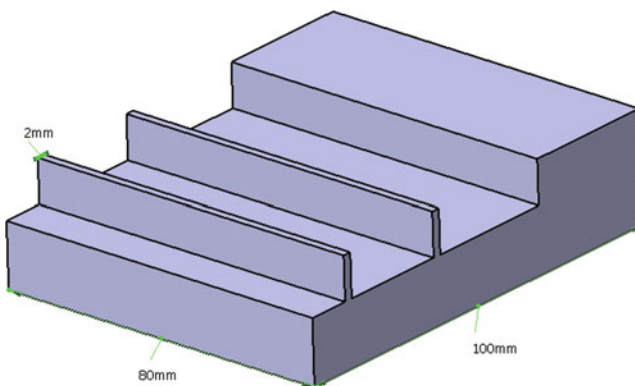


**Fig. 5** Sample workpiece

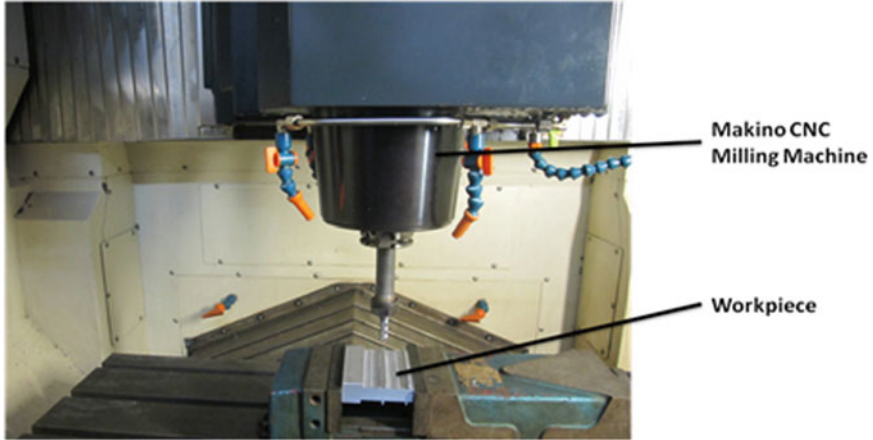


Fig. 6 Normal milling operation in CNC machine

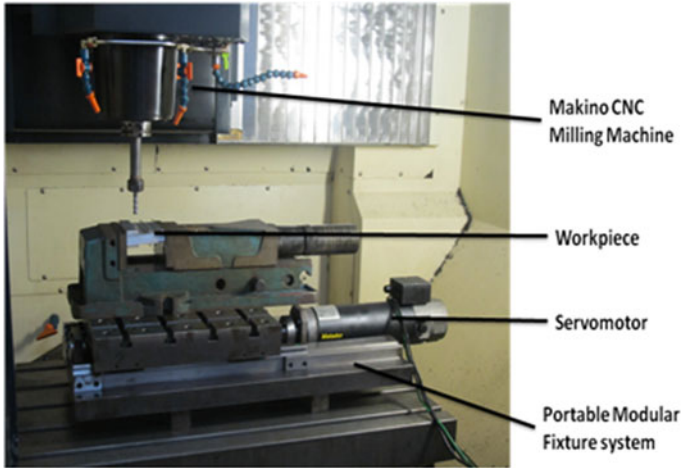
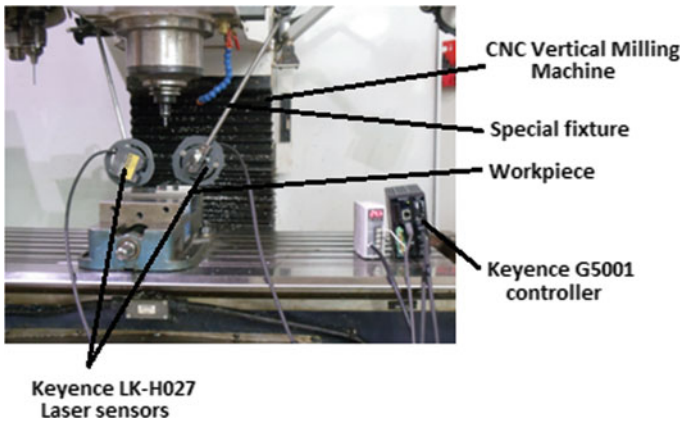


Fig. 7 Intelligence control system without laser detection system

3. Mount the portable modular fixture system on the CNC machine and repeat the same experiments defined experiment #1. In this, workpiece machining thickness is measured in real-time using two non-contact Keyence LK-H027 laser sensors. The two sensors are mounted facing to each other on a special fixture, which is fixed on the CNC milling machine. The data acquisition layer is configured to collect 100 data points per second at the point where the laser sensor is shooting. The data is collected via USB port to a dedicated computer using Keyence G5001 controller. An external program is developed using C# to transfer the data from the controller to Microsoft SQL server database in

real-time. The same intelligent control system in experiment #2 is used in this setup also. Here, DOE data (A) and real-time data collection are used for decision making process. This system monitors and sends appropriate signal to the servomotor of the portable modular fixture via Netduno controller in real-time to achieve precision machining. Figure 8 shows the intelligence control system with laser detection system mounted on the CNC machine for real-time data collection.

The depth of cut is set at same for all the experiments. Therefore, it is ignored. Twenty five different combinations of experiments with three replications are carried out. Thus, a total of 75 experimental data are collected. Table 2 shows the levels used in the design of experiments conducted at the University of Toledo and its workpiece thickness value for the first replication.



**Fig. 8** Intelligence control system with laser detection system

**Table 2** Experimental results using design of experiments-machining 2 mm thickness

Spindle speed (A)—RPM	Feed rate (B)—mm/s				
	8	12	16	20	24
2000	2.0155	2.0225	2.0263	2.0314	2.0276
3000	2.0136	2.0403	2.0361	2.0460	2.0403
4000	2.0117	2.0136	2.0136	2.0444	2.0352
5000	2.0288	2.0288	2.0422	2.0206	2.0314
6000	2.0206	2.0187	2.0244	2.0187	2.0180

### 4.1 Mathematical Model Using ANOVA

From the preliminary study [18], it was observed that both spindle speed and feed rate are significant factors affecting the tolerance variation in the component. In addition, feed rate has more significant effect over the tolerance variations when compared to spindle speed.

From the experimental data, a mathematical model to obtain the precision machining is derived as:

$$y = 2.02 - 0.00141A + 0.00323B \tag{1}$$

where A—spindle speed (RPM); B—feed rate (mm/s).

It is interesting to observe that similar mathematical model is also derived from the experiments conducted at PSG College of Technology.

### 4.2 Mathematical Model Using Least Square

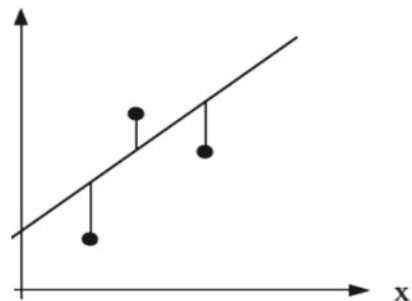
The tolerance variation exists in the workpiece is expressed in linear form (see Fig. 9), which is generalized from a straight line.

In this study, two least square models are considered. The first model is mean least square (MLS) approximation. It is a procedure to determine the “best fit” line to the data [19]. It deals with the measured data contaminated with random error [20]. The error of the dependent variable is considered and the local approximation is carried out in the vertical direction [21], as shown in Fig. 10.

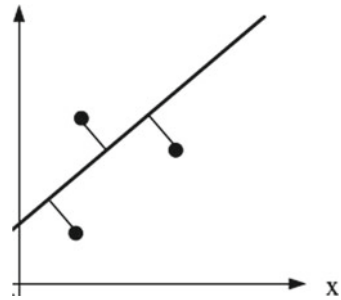


Fig. 9 Tolerance variations represented in linear form

Fig. 10 Local approximants of MLS



**Fig. 11** Local approximants of AMTLS



**Table 3** Experimental results of MLS and AMTLS

	Mean, $\delta$	a	b	CEIV	Var
MLS	0.516	1394	0.001	0.19	0.076
AMTLS	0.873	1282	0.001	0.27	0.025

The second model is adaptive moving total least square (AMTLS) approximation. This model considers the errors of all the variable, which is considered as errors-in-variables (EIV) and weight function. In this, a parameter  $\lambda$  is introduced to associate with the direction of local approximation. The error of the dependent variable is considered and the local approximation is carried out in the orthogonal direction [21], as shown in Fig. 11.

With the above data (Table 2), MLS and AMTLS models are executed to determine the “best fit” model. From Table 3, it is clear that AMTLS model would help to achieve precision machining. Therefore, it is selected for the study.

### 4.3 Forecasting Model Using ARIMA

Auto-regression Integrated Moving Average (ARIMA) model is a Box-Jenkins approach of a time series analysis. It helps to predict future points in the series based on the autocorrelations in the data. This model can be viewed as a “filter” that tries to separate the signals from the noise (tolerance variations). Then this signal is extrapolated into the future to obtain forecasting. For this study, ARIMA (p, d, q) is used to predict the tolerance variation based on two independent variables (spindle speed and feed rate). Here, p donates autoregressive order, d denotes differencing order and q denotes moving average order.

In this model, autocorrelation (ACF) and partial autocorrelation (PACF) graphs are used to determine the orders of AR and MA. ACF graph helps to find the order of moving average, whereas PACF graph helps to find the order of autoregressive. If the PACF of the differenced series displays a sharp cutoff and/or the lag-1 autocorrelation is positive; then the lag at which the PACF cutoff is the indicated number of AR terms.

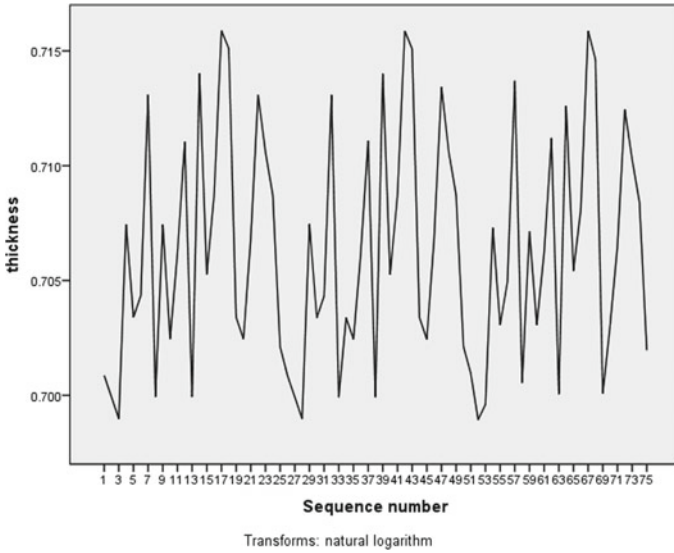


Fig. 12 Time series analysis for tolerance variations

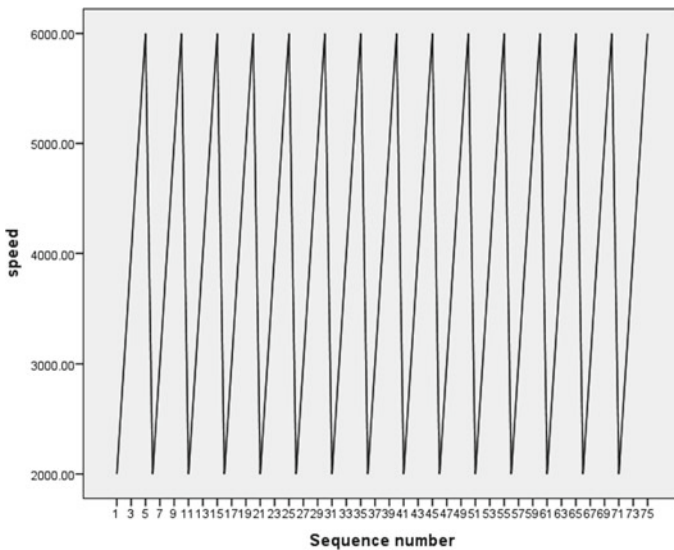
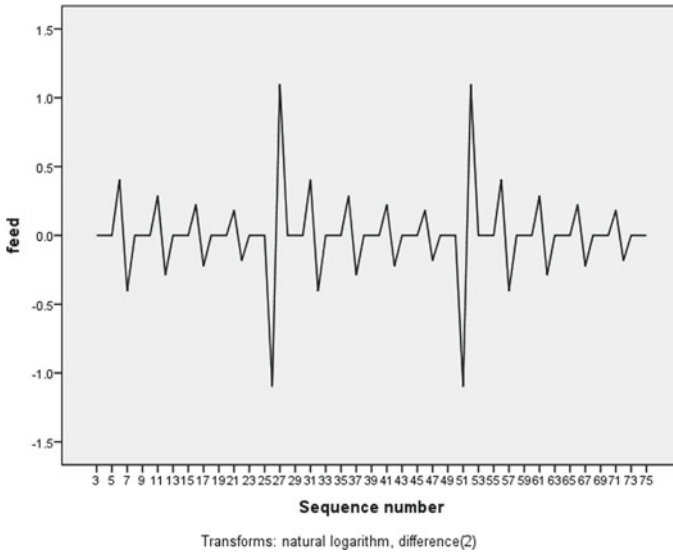


Fig. 13 Time series analysis for spindle speed

Similarly, if the ACF of the differenced series display a sharp cutoff and/or the lag-1 autocorrelation is negative, then the lag at which the ACF cutoff is the indicated number of MA terms.



**Fig. 14** Time series analysis for feed rate

ARIMA models are created based on Table 2. Figures 12, 13 and 14 show time series graph for tolerance variations, spindle speed and feed rate respectively.

Based on this, ARIMA parameters ( $p$ ,  $d$ ,  $q$ ) need to be determined. For this, ACF and PACF graphs are drawn. From this, ARIMA models are determined as  $(101)(000)(101)$  and  $(101)(000)(020)$  for the given study (see Figs. 15 and 16).

For each ARIMA model, forecasting of tolerance variation is determined. Tables 4 and 5 depicts the forecasted values with upper and lower control limits for  $(101)(000)(101)$  and  $(101)(000)(020)$  respectively. In this, last five forecasting values are shown in the Tables. Figures 17 and 18 shows the forecasting of tolerance variations based on  $(101)(000)(101)$  and  $(101)(000)(020)$  respectively.

From these two models, “best fit” model needs to be determined. For this, forecasted values and actual values of tolerance variations need to be plotted (see Fig. 19). From the Figure, it is noted that  $(101)(000)(020)$  model is better than  $(101)(000)(101)$  model. This model is used as final model to predict the optimum cutting parameters to achieve precision machining, which is used as input to intelligence control system (F).

#### **4.4 Predicting Optimum Cutting Parameter Using ANN**

Artificial Neural Network (ANN) is a mathematical model mimicking the real life behavior of neurons in a human brain. Usually, all ANN models are to learn, adapt to changes and mimic the human thought process with little or no human interaction.

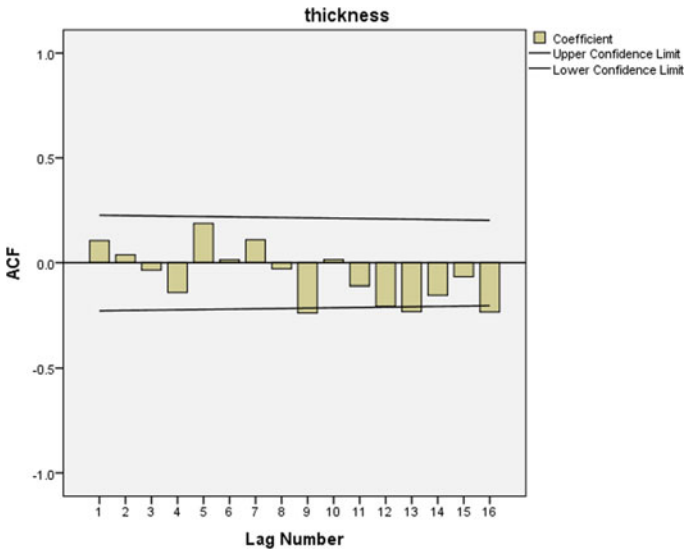


Fig. 15 ACF graph representing tolerance variations

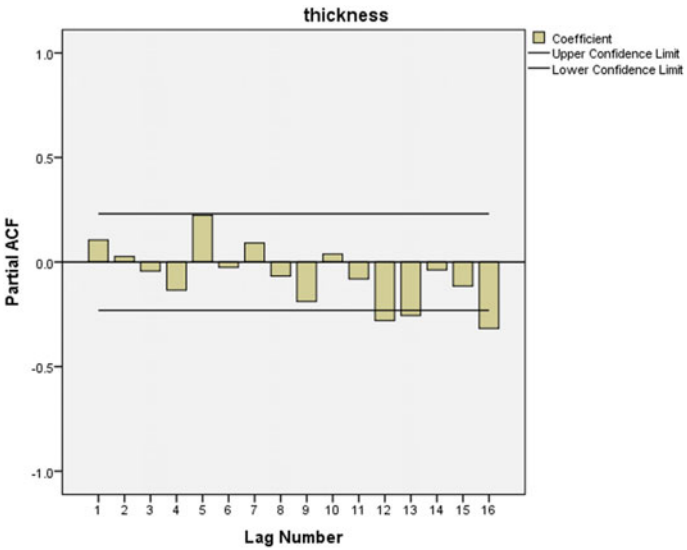


Fig. 16 PACF graph representing tolerance variations



**Table 4** Forecasting for (101)(000)(101) model

	71	72	73	74	75
Forecast	2.034	2.039	2.035	2.029	2.026
UCL	2.049	2.055	2.052	2.046	2.043
LCL	2.019	2.022	2.019	2.012	2.009

**Table 5** Forecasting for (101)(000)(020) model

	71	72	73	74	75
Forecast	2.032	2.031	2.027	2.024	2.024
UCL	2.050	2.049	2.046	2.042	2.042
LCL	2.014	2.013	2.009	2.006	2.006

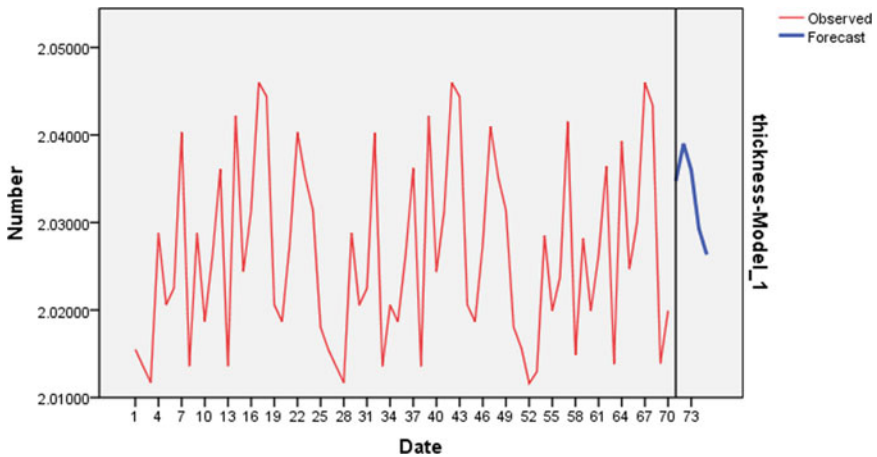


**Fig. 17** Forecasting tolerance variation based on (101)(000)(101) model

In this study, ANN is used to predict the optimum cutting parameters in real-time. For this, identification of the optimum ANN parameters is important.

In ANN network, feed forward back propagation algorithm is used. This model is executed using Table 5. The training set and test set defined for ANN network is 98:2 ratio. From the preliminary study, it is determined as: (a) three hidden layers with 21–17–6 combination of neurons produces the lowest average error as  $\pm 0.0512 \mu\text{m}$ ; (b) two hidden layers with 7–7 neurons produces the lowest average error as  $\pm 0.059 \mu\text{m}$ ; and (c) one hidden layer with 29 neurons produces the lowest average error of  $\pm 0.000903 \mu\text{m}$ . Therefore, for this study, one hidden layer with 29 neurons is considered. For this condition, following transfer functions are used: sigmoid at input layer, tanh at hidden layer and logistic at output layer.

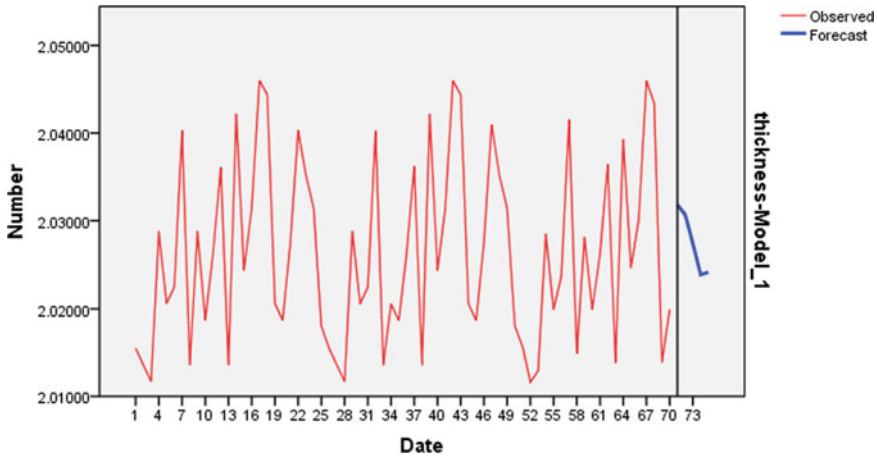
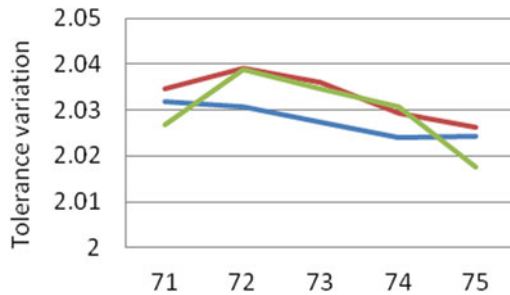


Fig. 18 Forecasting tolerance variation based on (101)(000)(020) model

Fig. 19 Forecasting versus actual values graph



The ANN network is trained and tested using the design of experiments data (Table 2). Figure 20 shows the ANN architecture to reduce the workpiece tolerance variations.

### 4.5 Intelligent Control System

The intelligent control system consists of hardware and software. The hardware requirements are portable modular fixture with servomotor capability, laser detection system, which is explained in the Sect. 4 and Netduino controller. The software requirements are feed forward back propagation algorithm and business intelligent unit. Both these modules are written in C#.

The business intelligent unit collects the data from different modules (A to E) and real-time data collection using laser detection system. Whenever there is a deviation exists between the measured value and the targeted value of the workpiece thickness,

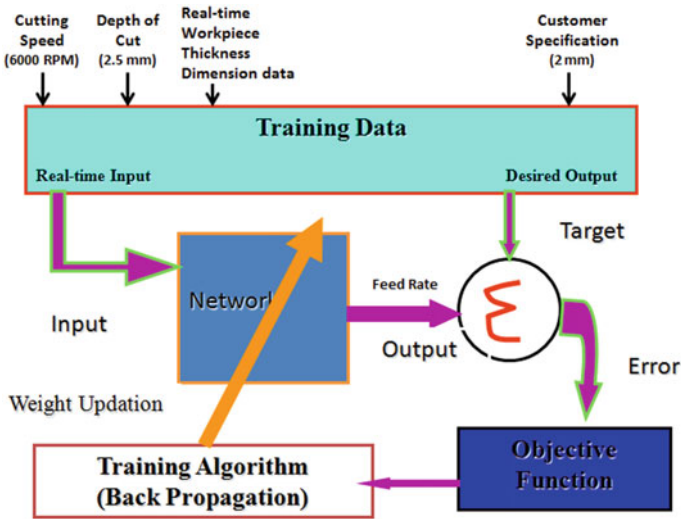


Fig. 20 ANN architecture for feedback mechanism

then the business intelligent unit analyses the data to determine the optimum cutting parameters to achieve precision machining. Then this data is transmitted to servomotor of the portable modular fixture via Netduino controller. In other words, the signal from the business unit determine fraction of turn needed in the lead screw of the portable modular fixture to minimize the tolerance process variations from previous data point. Figure 21 illustrates the schematic diagram of the intelligence control system with portable modular fixture. The process continues until the machining operation is complete.

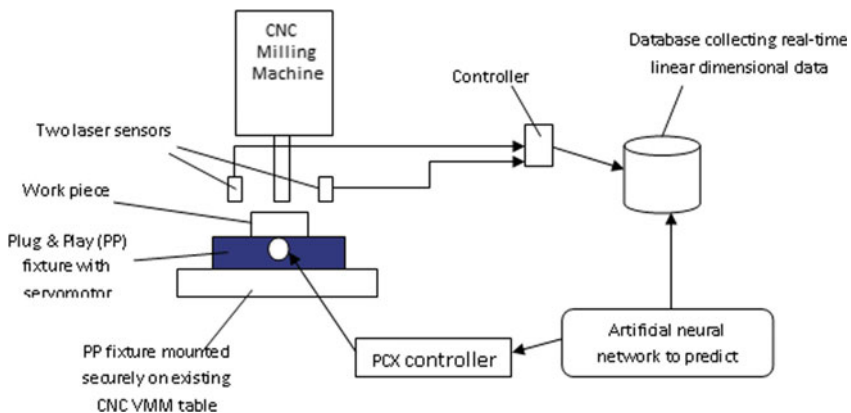


Fig. 21 Schematic diagram of an adaptive control system

### 5 Results and Discussion

From the design of experiments, the optimum spindle speed and optimum feed rate are determined as 6000 RPM and 6.8 mm/s respectively. From Eq. 1, the optimum feed rate is generated as:

$$Feed\ rate(B) = \frac{(y - 2.02 + 0.00141A)}{0.00323} \tag{2}$$

where, y—minimum tolerance variation, A—spindle speed (RPM).

Similar, the mathematical model to determine optimum feed rate is generated using Adaptive Moving Total Lease Square (AMTLS). Both these mathematical models are written using C#. Again, the optimum feed rate is also determined using ARIMA (101)(000)(020) model. Here, ARIMA model is generated using IMB SPSS software. The data used in the above mathematical models are static (design of experiments data only).

The artificial neural network feed forward back propagation is also used to predict the optimum feed rate based on spindle speed and real-time measured thickness value. Here, the data used are design of experiments (static data) and real-time data. To ensure this system robust, the complete business unit is developed using C#.

From the above, the optimum cutting parameters are determined. These values are entered in the CNC machine. A sample workpiece is machined to verify whether 2 mm thickness with ± 0.011 mm tolerance is achievable throughout the machining cycle. Once the machining is completed, the workpiece dimensions are measured using digital Vernier caliper. In a workpiece, 20 data points are measured at specific distance.

Two groups of experiments were carried out. The first group of experiments is conducted at PSG College of Technology. In this, experiments #1 and #2 are carried out using High Speed Makino CNC vertical milling machine. Doering [22] describe true distribution for precision machining is continuous uniform or rectangular distribution. He suggested using X-bar chart for precision machining applications. Figure 22 shows the control chart of experimental result of normal milling vs.

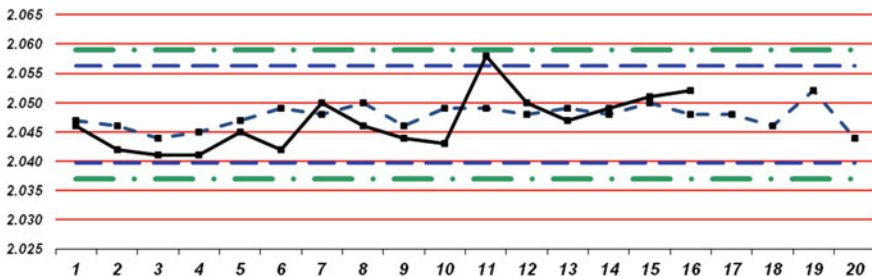
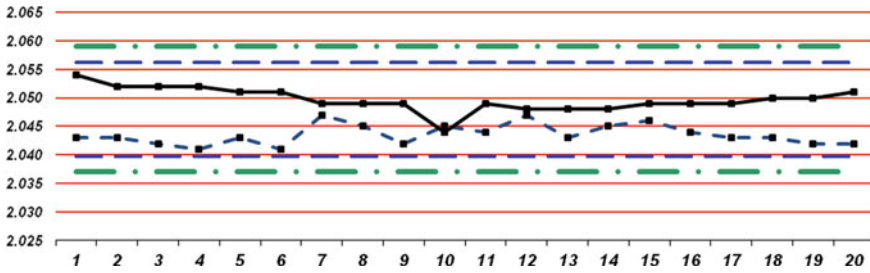


Fig. 22 Control chart comparing normal operation versus intelligence control system using Makino CNC milling machine



**Fig. 23** Control chart comparing normal operation versus LDS and Intelligence control system using Willis CNC milling machine

portable intelligence system. In the figure, the blue dotted line represents the normal milling; whereas, the black straight line represents the portable intelligence system. It is important to note that the portable intelligence system shows more dimensional variation when compared to normal milling. In addition, there is a huge spike in reading at 10th data point. Then, there is a gradual increase in dimensional variation at data points 14, 15 and 16. Since there are three continuous increases in dimensional variation, measured data after data point 16 are off no-use.

The second group of experiments was conducted at The University of Toledo. In this, experiments #1 and #3 were carried out using Willis RMS 40 CNC vertical milling machine. Figure 23 shows the control chart of experimental result of normal milling versus portable intelligence system with laser detection system. In the figure, the blue dotted line represents the normal milling; whereas, the black straight line represents the portable intelligence system with laser detection system. It is important to note that the portable intelligence system shows less dimensional variation when compared to normal milling. In addition, the data points are gradually moving closer to the target mean.

## 6 Conclusions

With the current technology, a component could be machined within a tolerance specification. However, the customers demand to machine the critical components to be machined to a tighter tolerance on a consistent basis, which is a huge challenge. This paper demonstrates a new approach to achieve the precision machining for CNC milling operation without interfering the existing CNC architecture. This technology is successful only when laser detection system is implemented along with portable modular fixture mechanism and intelligence control system. A similar attempt was made without laser detection system but not successfully. In that case, normal milling operation provides better results.

The ANOVA, the least square and the ARIMA models are used to determine the optimum cutting parameters using static design of experiments data; whereas ANN

feed forward back propagation is used not only static design of experiments data but also real-time workpiece dimensional thickness variations.

## 7 Future Work

With the current technology, the components are machined within tolerance specification. However, when these tolerance specifications lie closer to the upper limit or lower limit, it could create cumulative variation error. This may lead to product rejections. Therefore, it is important to machine the components to tighter tolerance. Even though this paper demonstrated a new technology to achieve this precision machining, there are several areas need to addressed. The following activities need to be carried out in future study:

- Install laser detection system and conduct similar experiments to verify the machine dependent ability issues.
- Currently, ANN parameters are determined based on DOE data. The program need to be modified to determine the ANN parameters based on real-time data.
- Currently, feed forward back propagation algorithm is used to predict the optimum cutting parameters. The business intelligent unit needs to test other artificial intelligence tools.
- The experiments carried out using Aluminum 6061 alloy. It should be tested with other materials.
- In addition, the performance of the portable modular fixture could be improved by: (a) fine machining the lead screw of the modular fixture; (b) selection of servo-motor; (c) design of the coupling between servomotor and lead screw mechanism; and (d) correct selection of ANN parameters.

## References

1. Ganesh Kumar N, Franchetti M, Radhakrishnan P (2013) Near minimum material zone: a new concept to reduce the weight of the aircraft components in machining using lean six sigma methodology. In: ASME 2013 international mechanical engineering congress and exposition 2B: advanced manufacturing
2. Ganesh Kumar N, Akesh Kumar G, Radhakrishnan P (2012) Development of an on-line probing system for dimensional accuracy in CNC turning. In: 28th National convention of mechanical engineers and national seminar on emerging technologies in product development for safe and sustainability mobility
3. Dhole NS, Naik GR, Prabhawalkar MS (2012) Optimization of milling parameters of En33 using Taguchi parameter design approach. *J Eng Res Stud* 3:70–74
4. Saikumar S, Shumugam MS (2012) Investigations into high-speed rough and finish end-milling of hardened EN24 steel for implementation of control strategies. *Int J Adv Manuf Technol* 63:391–406
5. Juran in: *Six Sigma Green Belt certification book* (2013)

6. Information on Wikipedia <http://www.wikipedia.org/>
7. Information on ASQ <http://asq.org/>
8. Surasit R, Jaknarin C, Romadorn B, Worapong B (2012) An investigation of optimum cutting conditions in face milling semi-solid AA 7075 using carbide tool. *Int J Innov Manag Technol* 3
9. Sanjit M, Saurav D, Asish B, Pradit KP (2010) Parametric optimization of CNC end milling using entropy measurement technique combined with grey-Taguchi method. *Int J Eng Sci Technol* 2:1–12
10. Haghdadadi N, Zarei-Hanzaki A, Khalesian AR, Abedi HR (2013) Artificial neural network modeling to predict the hot deformation behavior of an A356 aluminum alloy. *J Mater Des* 49:386–391
11. Mortaza A, Hossien M, Shahin R, Ashkan M (2012) The use of artificial neural network to predict exergetic performance of spraydrying process: a preliminary study. *J Comput Electron Agric* 88:32–43
12. Ardestani MM, Chen Z, Wang L, Lian Q, Liu Y, He J, DichenLia JZ (2014) Feed forward artificial neural network to predict contact force at medial knee joint: application to gait modification. *J Neurocomput* 139:114–129
13. Information on MatLab (2013)
14. Ozel T, Nadgir A (2002) Prediction of flank wear by using back propagation neural network modeling when cutting hardened H-13 steel with chamfered and honed CBN tools. *Int J Mach Tools Manuf* 42:287–297
15. Sanjay C, Neema ML, Chin CW (2005) Modeling of tool wear in drilling by statistical analysis and artificial neural network. *J Mater Process Technol* 170:494–500
16. Bernardos PG, Vosniakos GC (2003) Predicting surface roughness in machining: a review. *Int J Mach Tools Manuf* 43:833–844
17. Zain AM, Haron H, Sharif S (2010) Prediction of surface roughness in the end milling machining using artificial neural network. *Expert Syst Appl* 37:1755–1768
18. Ganesh Kumar N, Selvamaan S, Selvaraj P, Radhakrishnan P (2014) Optimization of cutting parameters of CNC milling for aircraft components using design of experiments. *Appl Mech Mater* 598:164–168
19. Miller SJ The method of least square. Williams College notes. <https://web.williams.edu>
20. Lei Z, Tianqi G, Ji Z, Shijun JM, Ming H, Xiangbo L (2013) An improved moving least squares method for curve and surface fitting. *Math Prob Eng* (article ID 159694)
21. Lei Z, Tianqi G, Ji Z, Shijun J, Qingzhou S, Ming H (2014) An adaptive moving total least squares method for curve fitting. *Measurement* 49:107–112
22. Doering B (2010) Correct SPC: the correct use of SPC in precision machining. <http://elsmar.com/forums>

# Investigation on Position Dependency of Tool-Workpiece Compliance



D. Kono, P. Roh, and A. Matsubara

**Abstract** This paper proposes a method to investigate the direction and position dependencies of the tool-workpiece compliance of machine tools. In the proposed method, a compliance map is used for comprehensive investigation of the compliance. The definition of the tool-workpiece compliance and the basic idea of the compliance map are described. Then, an experiment was conducted to obtain the compliance map of a three axis prototype of a machine tool. The direction of the excitation force and the workpiece position were suggested to suppress the vibration.

**Keywords** Tool-workpiece compliance · Position dependency · Direction dependency · Machine tool · Vibration

## 1 Introduction

The compliance of the tool-workpiece loop of a machine tool (tool-workpiece compliance), which determines the dynamic relative displacement between the tool and the workpiece due to process forces, greatly influences the machining performance such as the machining accuracy and the productivity. The tool-workpiece compliance can change depending on the excitation direction and position in the workspace. Therefore, the machining performance is limited if the tool-workpiece compliance is small in a specific condition.

Two countermeasures can be used to solve this problem. One is to decrease the direction and position dependencies of the tool-workpiece compliance by modifying the machine tool. Law et al. proposed to use the topology optimization for machine tool design to decrease these dependencies of the chatter stability [1]. The other is

---

D. Kono (✉)

Kyoto University, c1S09, C3, Kyotodaigaku Katsura, Nisikyo-ku, Kyoto 615-8540, Japan  
e-mail: [kono@prec.kyoto-u.ac.jp](mailto:kono@prec.kyoto-u.ac.jp)

P. Roh

IWF, ETH Zurich, ETH Zentrum, LEE, Leonhardstrasse 21, C8092 Zurich, Switzerland

A. Matsubara

Kyoto University, c1S09, C3, Kyotodaigaku Katsura, Nisikyo-ku, Kyoto 615-8540, Japan

© Springer Nature Switzerland AG 2022

S. Hinduja et al. (eds.), *Proceedings of the 38th International MATADOR Conference*,  
[https://doi.org/10.1007/978-3-319-64943-6\\_27](https://doi.org/10.1007/978-3-319-64943-6_27)

389



to avoid the specific condition with small tool-workpiece compliance by modifying the workpiece fixation and the tool path [2–5]. For both the countermeasures, it is required to comprehensively investigate the direction and position dependencies of the tool-workpiece compliance in three dimensions.

Tounsi et al. has measured the tool-workpiece compliance in three dimensions [6]. However, the position dependency of the compliance is not discussed in their study. Although abovementioned Law et al. used a 2D contour plot to show the direction and position dependencies of the chatter stability [1], the frequency dependency of the compliance was not shown in the plot.

The final goal of this research is to propose a comprehensive investigation method of the tool-workpiece compliance. In this paper, a compliance map is proposed to investigate the direction and position dependencies of the compliance. The definition of the tool-workpiece compliance and the basic idea of the compliance map are described at first. Then, an experiment is conducted to obtain the compliance map of a prototype of a three axis machine tool for demonstration.

## 2 Compliance Map of Machine Tool

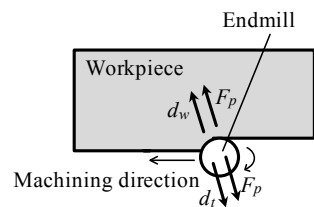
### 2.1 Tool-Workpiece Compliance

Figure 1 illustrates a schematic of an end milling process. In Fig. 1,  $F_p$  represents the process force that excites the tool and the workpiece,  $d_t$  and  $d_w$  represent the tool and workpiece displacements caused by the process force, respectively. The reactive displacement  $d_{rel}$  between the tool and workpiece is obtained using

$$d_{rel} = d_t - d_w \quad (1)$$

The amplitude variations of  $d_{rel}$  depending on the machining position in the workspace and the direction of  $F_p$  are investigated using the tool-workpiece compliance. In this paper, the tool-workpiece compliance is defined as the frequency response of  $d_{rel}$  to  $F_p$ . For both  $F_p$  and  $d_{rel}$ , the positive direction is the direction that the tool and the workpiece separate.

**Fig. 1** Schematic of end milling process



The tool-workpiece compliance against a force in a certain direction has three components; a compliance about the displacement in the excitation direction (main compliance); and two compliances about the displacement in the perpendicular direction to the excitation direction (cross compliance). Therefore, when the tool-workpiece compliance is strictly evaluated in three dimensions, nine components are required at least.

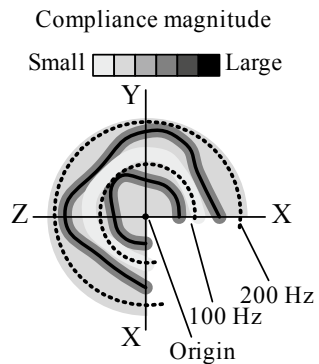
### 2.2 Basic Idea of Compliance Map

For comprehensive investigation of the direction and position dependencies of the tool-workpiece compliance, the compliance must be compared for several directions and positions. However, it is difficult, using general plots such as the Bode plot and the Nyquist plot, to compare those compliances because many data must be plotted at the same time.

The compliance map is proposed for comprehensive investigation of the direction and position dependencies of the tool-workpiece compliance. The compliance map consists of several radial plots. The example of the radial plot of the compliance magnitude is shown in Fig. 2. Figure 2 represents the direction dependency of the compliance magnitude at a certain position. The magnitude is represented in gray scale. The excitation direction and the frequency are represented by the argument and the radius, respectively. To show the excitation direction in three dimensions, the directions in the XY, the YZ and the ZX planes are shown in the first, the second and the third quadrants, respectively. By comparing several radial plots at different positions, the position dependency of the compliance is investigated.

Any data can be plotted in the radial plot depending on what is focused on. For example, when the overall vibration characteristic is evaluated, the magnitudes of the main compliance and the cross compliance are plotted. The compliance magnitude about the displacement in a specific direction is plotted when the vibration in that direction is the problem to be solved.

Fig. 2 Example of radial plot for compliance map



### 3 Experiment

#### 3.1 Machine Tool Used in Experiment

An experiment is conducted to investigate the dependencies of the tool-workpiece compliance on the position and the excitation direction. A prototype of a machine tool is used in the experiment. Figure 3 shows the appearance of the machine. The machine has three linear axes driven with ball screw drives. Granite is used for materials of the bed and the X axis. The material of other bodies is steel.

Each drive is controlled by a commercial CNC (Mitsubishi Electric). The controller uses a PI control for the motor current loop, a PI control for the velocity loop and a P control for the position loop. Other major specifications of the machine are listed in Table 1.

The machine is usually used to fabricate a flat surface by planer cutting with a non-rotational tool such as diamond bites. The tool is attached to the tool post. The workpiece is fixed on the table with a small vice.

**Fig. 3** Appearance of prototype used in experiment

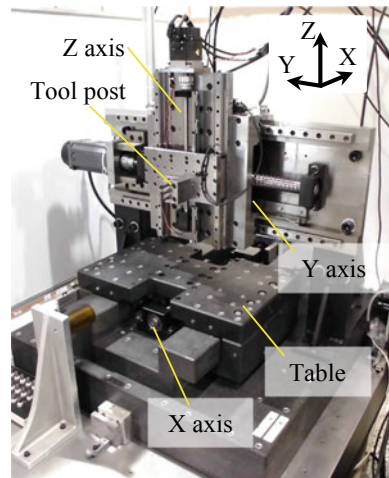


**Table 1** Specifications of prototype

Axis	X	Y	Z
Travel (mm)	100	240	200
Maximum feed rate	10 m/min		
Ballscrew lead (mm)	8	10	5
Guideway	Aero static	Rolling (ball)	
Driven mass (kg)	35	47	4
Control type	Full closed		Semi closed
Encoder resolution (nm)	1	20	

### 3.2 Experimental Method

The tool-workpiece compliance is measured at several workpiece positions in the entire workspace to investigate its position dependency. Furthermore, at each position, the machine is excited in several directions to investigate the direction dependency of the compliance.

The experimental setup for the Y direction excitation is shown in Fig. 4. A dummy tool and a dummy workpiece are attached to the machine. The tool and the workpiece are excited using a piezo electric actuator inserted between them. The excitation force is measured with a three dimensional force sensor (Kistler) installed on the tool. The relative displacement between the tool and the workpiece is obtained using three dimensional accelerometers (PCB Piezotronics). The accelerometer sensitivity is  $50 \text{ mV/m/s}^2$ . The force sensor sensitivity is  $7.8 \text{ pC/N}$  in the X and Y directions and  $3.8 \text{ pC/N}$  in the Z direction.

For excitation, the preload of 50 N is given to the piezo electric actuator. Then, the swept sine signal with the frequencies of 1–300 Hz is input to the actuator for 60 s. The sampling frequency is set to 3 kHz. The tool-workpiece compliance is obtained from measured force and relative displacement using the Fourier transform.

The excitation is conducted in five directions including the Z direction and four other directions in the XY plane. Figure 5 shows the setup in each excitation direction in the XY plane. In Fig. 5, symbols T and W represent the tool and the workpiece, respectively. Hexagon bars are used for the tool and the workpiece. The workpiece position is fixed and the tool is located at different positions to change the excitation direction. For Y and  $30^\circ$  excitations, the tool and the workpiece are rotated  $90^\circ$  about the Z axis from their orientation for X and  $60^\circ$  excitations.

Fig. 4 Experimental setup

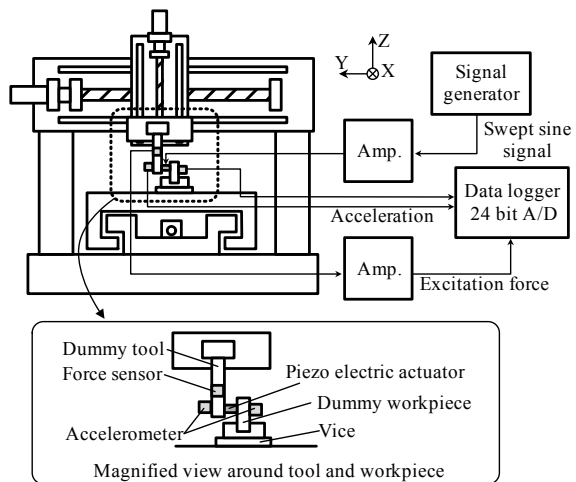
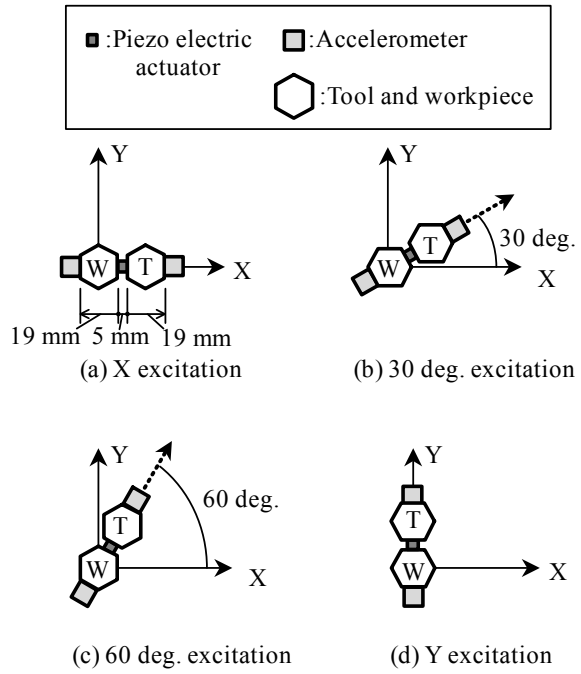
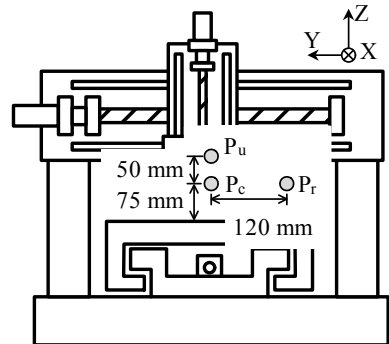


**Fig. 5** Setup for four excitation directions in XY plane



The tool-workpiece compliance is measured at three workpiece positions  $P_c$ ,  $P_r$  and  $P_u$  shown in Fig. 6. Position  $P_c$  is located at almost the center of the workspace. Positions  $P_r$  and  $P_u$  are shifted from  $P_c$  in the Y and Z directions, respectively.

**Fig. 6** Workpiece positions in measurement



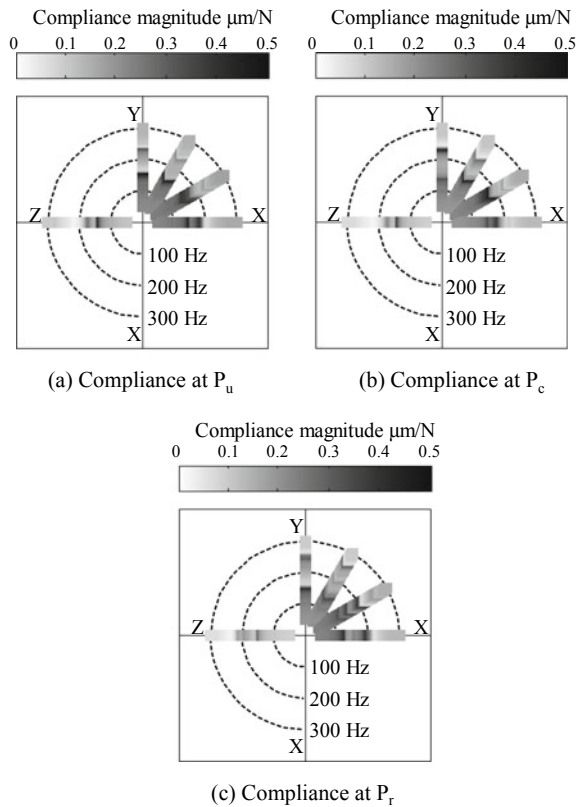
### 3.3 Experimental Result

#### 3.3.1 Investigation of Overall Vibration Characteristic

The compliance map is used to approximately determine the better position and excitation direction to suppress the vibration for general use. Figure 7 shows the obtained map of the main compliance magnitude. The compliance for frequencies lower than 50 Hz is omitted in Fig. 7 because of its low coherence. By comparing compliances at three positions, the position dependency of the compliance is small because the results in Fig. 7a–c look similar overall.

Then, the direction dependency of the compliance is investigated. In Fig. 7a–c, the compliance in the Z direction is smaller than others. Therefore, the cutting force should be aligned in the Z direction. The compliances in the XY plane look similar overall. However, if the cutting process has a periodic cutting force fluctuation with a specific frequency, a better force direction can be suggested because each compliance has resonance peaks and anti resonance valleys at different frequencies.

Fig. 7 Map of main compliance magnitude

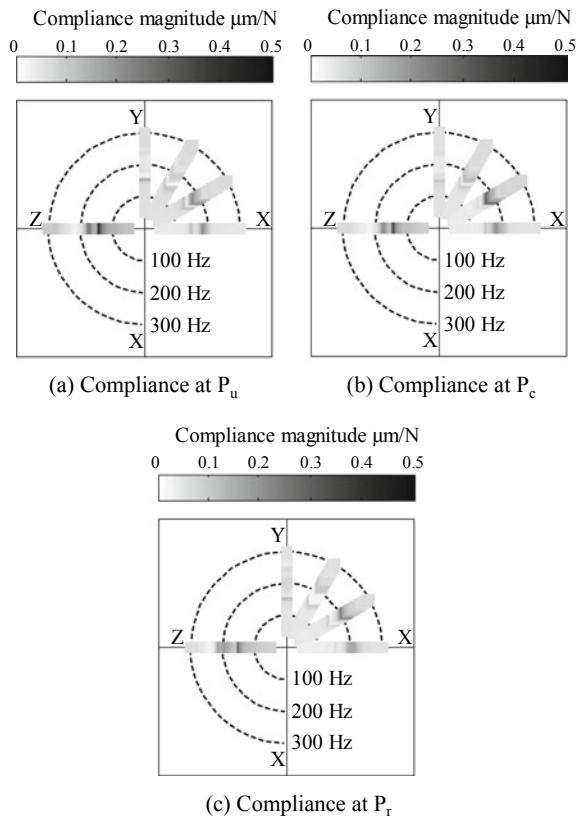


### 3.3.2 Investigation of Vibration in a Specific Direction

Because the machine is usually used for planer cutting parallel to the XY plane, the vibration in the Z direction influences the machining accuracy. In this machining, the cutting force acts mainly in the Z direction and the cutting direction in the XY plane. Therefore, in this section, the vibration in the Z direction is focused on to determine the better cutting direction.

Figure 8 shows the map of the compliance magnitude about the Z displacement. In Fig. 8a–c, the magnitude with the 60° excitation looks smallest in the XY plane. In addition, the magnitude with the 60° excitation in Fig. 8c is smaller than those in Fig. 8a, b. This result shows that the cutting should be conducted in the 60° direction at the position  $P_r$ .

**Fig. 8** Map of compliance magnitude about Z displacement



## 4 Conclusions

A method was proposed to evaluate the tool-workpiece compliance. In this method, the position and the direction dependencies of the compliance are investigated using the compliance map. The compliance of a machine tool prototype was experimentally investigated using the proposed method. By comparing the magnitude of the main compliance, it is concluded that the process force should be aligned in the Z direction to suppress the vibration for general cases. In addition, the position dependency of the compliance was small. The magnitude of the Z displacement was also compared to reduce the machining error in planer cutting with a non-rotational cutting tool. In this case, the cutting should be conducted in the direction rotated by  $60^\circ$  in counter clockwise from the X direction. It was also found that the end of the Y travel is better position for the workpiece.

**Acknowledgements** This work was supported by KAKENHI (26820021). The authors also like to thank Dr. Johannes Heidenhain GmbH.

## References

1. Mohit L, Yusuf A, Srikantha P (2013) Rapid evaluation and optimization of machine tools with position-dependent stability. *Int J Mach Tools Manuf* 68:81–90
2. Yusuke K, Atsushi M, Shinji N, Kazuhiro I, Iwao Y (2012) Cutting path design to minimize workpiece displacement at cutting point: milling of thin-walled parts. *Int J Autom Technol* 6:638–647
3. Yusuke K, Atsushi M, Iwao Y (2013) Optimization of cutting path for minimizing workpiece displacement at the cutting point: changing the material removal process, feed direction, and tool orientation. *Procedia CIRP* 5:31–36
4. Lee CM, Kim SW, Choi KH, Lee DW (2003) Evaluation of cutter orientations in high-speed ball end milling of cantilever-shaped thin plate. *J Mater Process Technol* 140:231–236
5. Lee CM, Kim SW, Lee YH, Lee DW (2004) The optimal cutter orientation in ball end milling of cantilever-shaped thin plate. *J Mater Process Technol* 153–154:900–906
6. Najeh T, Alain O (2000) Identification of machine–tool–workpiece system dynamics. *Int J Mach Tools Manuf* 40:1367–1384



# Near-Dry and MQL Finish Machining of Mould Inserts



Y. L. Chan and X. Xu

**Abstract** Traditionally, metal cutting fluid or lubricant is used in finishing operations of die and mould manufacture to reduce the rate of tool wear, which in turn improves surface quality. However, metal cutting fluid has negative effects on the environment, and also increases the total production cost. The minimum quantity lubrication (MQL) technique is considered to provide the same level of performance as the flood coolant method, and offers financial benefits by saving coolant direct and associated costs. It has therefore grown to be an increasingly popular alternative lubrication method in certain HSM applications. In this study, the effects of Near-Dry and MQL machining on surface roughness, tool wear, dimensional accuracy and machining time were compared using the Design of Experiments (DOE) technique. In terms of surface roughness and tool wear, there were no significant differences. Nevertheless, MQL machining produced more accurate results than Near-Dry machining in dimensional deviation. The regression models show that feed-rate has a larger effect on surface roughness and machining time than step-over, while depth of cut has no significant effect on surface roughness. Based on the test piece shape, an optimal machining time of 3.55 h and a good surface finish of 0.28  $\mu\text{m}$  can be achieved by using a small feed-rate (0.03 mm/tooth), a large step-over (0.1 mm) and a large depth of cut (0.2 mm). When combining the MQL technique with the right cutting conditions in modern die and mould manufacturing, machining time and polishing time can be reduced, which leads to an overall saving in production cost. Using the Near-Dry and MQL techniques for different finish machining situations can therefore be a good economical solution.

**Keywords** Minimum quantity lubrication · High-speed machining · Die and mould manufacturing

---

Y. L. Chan (✉) · X. Xu

Department of Mechanical Engineering, The University of Auckland, Auckland, New Zealand  
e-mail: [simon.chan@camex.co.nz](mailto:simon.chan@camex.co.nz)

© Springer Nature Switzerland AG 2022

S. Hinduja et al. (eds.), *Proceedings of the 38th International MATADOR Conference*,  
[https://doi.org/10.1007/978-3-319-64943-6\\_28](https://doi.org/10.1007/978-3-319-64943-6_28)

399

## 1 Introduction

In modern daily life, main commodities are either partially or fully produced in dies and moulds, be it an automobile or an aeroplane component, a kitchen plastic container or a drink bottle, a component of a washing machine or a refrigerator, a mobile phone or a computer. With the surging demand for these products globally, the die and mould manufacturing industry around the world is facing the tough challenge of having to produce more complex moulds in shorter lead times but with more competitive prices.

However, modern die and mould manufacturing is a demanding and difficult engineering task due to the complex sculptured surfaces of intricate moulding geometry and relatively high material hardness [1]. More than 60% of the total production time of die and mould is spent in manufacturing the functional components which often include complex sculptured surfaces. A significant portion of which is spent on machining and polishing operations, accounting for approximately two thirds of the manufacturing costs [2]. The introduction of high-speed machining (HSM) technology during the mid-1990s revolutionised die and mould manufacturing practice by reducing the effort for finishing and polishing operations, thereby cutting down the production time. However, the main disadvantage of HSM is tool-life reduction, especially in machining difficult-to-machine materials such as nickel-based alloys, titanium alloys, and hardened steels [3, 4]. With an increase in cutting speed, the temperature of the cutting zone increases, promoting accelerated wear of the cutting tool. A traditional way to overcome this problem is the use of water-based cutting fluids, also called coolants. The basic functions of cutting fluids are to provide cooling, lubrication and to remove chips from the cutting zone.

Unfortunately cutting fluid has its own flaws. Firstly it is expensive. Research studies on machining processes [5–7] show that while the cost of cutting tools is only 2–8% of the total production expenses, the costs related to the use of cutting fluids range from 7 to 17%. Secondly, cutting fluids have a negative impact on the health and wellbeing of workers. Astakhov [7] reviewed that exposure through skin contact could result in conditions such as dermatitis or folliculitis. Repeated inhalation of coolant mist could also cause decreased lung functions and respiratory diseases, e.g. asthma, bronchitis and hypersensitivity pneumonitis. Exposure to some cutting fluids and/or their additives might even cause cancer. In order to reduce the costs of production and to comply with increasingly strict environmental and occupational safety regulations, research and development since the mid-1990s has focused on the total elimination (dry) or huge reduction (near-dry) of cutting fluids. This new manufacturing philosophy was a great advancement in the metal cutting industry [6].

By using advanced cutting tool materials and cutter geometry, dry cutting has been shown to be very successful in certain types of machining processes [5, 6]. However, in finishing operations of die and mould manufacturing with hardened steels, dry machining fails to produce high dimensional accuracy and good surface finishes. Consequently, minimum quantity lubrication (MQL) machining is being considered an alternative. Machado and Wallbank [8] proved by mathematical calculation that

only a small portion of the total amount of cooling lubricant used should be needed to effectively lubricate the tool-chip interface.

### ***1.1 HSM of Hardened Steels in Die and Mould Manufacturing***

In modern die and mould manufacturing, the most common machine tool configurations are 3-axis horizontal and vertical milling centres. However, the new trend is to utilise simultaneous 5-axis milling centres so that complex components can be machined in only one setup, a process which cannot be achieved by a 3-axis machine. The three main advantages of 5-axis milling are: the ability to work on all sides of the component in one setup; the avoidance of tool tip cutting; and the use of shorter cutting tools. Studies by Baptista et al. [9] and Dimitrov and Saxter [10] showed that, in comparing with 3-axis milling, better surface finish, 77% reduction in the total lead-time and an 87% reduction in the overall cost were achieved with simultaneous 5-axis machining.

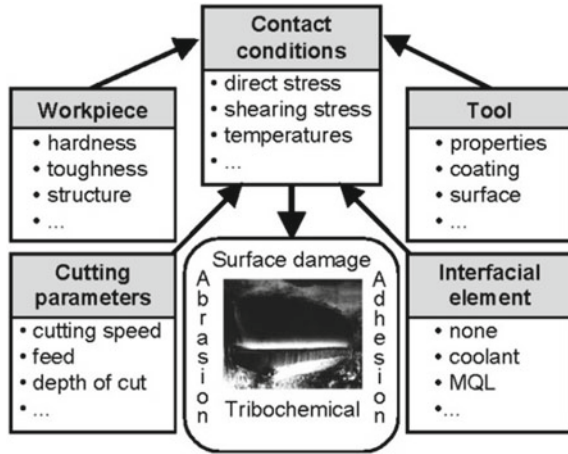
As mentioned in previous section, a major drawback of using HSM is tool life reduction. Finzer [4] and Schulz [11] suggested four different approaches, i.e. right cutting tool material, right cutting tool, optimization of machining parameters, and proper machining strategy to tackle this problem. The key to applying HSM technology in modern die and mould manufacturing practice to reduce production time while maintaining the required surface finish is indeed implementation of these four approaches simultaneously.

### ***1.2 Minimum Quantity Lubrication in HSM***

MQL techniques use only a very small amount, ranging from 4 to 50 mL/h, of oil lubricant during the machining process. Compared to the conventional flood coolant method, in which about 20 L/min are consumed, the difference is 24,000–300,000 fold. The basic mechanism of MQL is mixing air and oil lubricant into an aerosol by an atomisation (Venturi) process, with droplets the size of 1–5  $\mu\text{m}$ . The aerosol mixture can be supplied to the cutting zone via either an external or internal supply system. Each of these systems has proven to be suitable for individual areas of application [6]. The present health regulation (OSHA) for the concentration of aerosols in air is 5  $\text{mg}/\text{m}^3$  which may be reduced to 0.5  $\text{mg}/\text{m}^3$  [12].

In order to implement MQL techniques successfully into the ever demanding metal cutting industry, it is essential to have a better understanding of the friction and wear mechanism of cutting tools. Weinert et al. [6] suggested that the cutting process can be considered as a tribological system, with the cutting tool as the basic body and the workpiece as the counterpart (Fig. 1). All elements of the tribological system have to

**Fig. 1** Cutting process as a tribological system (excerpted from [6])



be adapted to the specific requirements of MQL machining, in particular, the cutting tool material and the tool coating (basic body), the workpiece material (counterpart) and the MQL medium (interfacial element).

MQL techniques have been widely adopted into the aerospace and automotive industries for the machining of gray cast iron, aluminium alloy and titanium. However, scant research work has been done on MQL applications in the die and mould manufacturing industry. Therefore, the purpose of this study is to investigate the potential benefit of integrating the widely established HSM technology with MQL techniques in modern die and mould manufacturing.

### 1.3 Surface Roughness

The most commonly used surface roughness parameters in the metal cutting industry is  $Ra$ , the arithmetic mean of the absolute values of the evaluation profile deviations from the mean line. In machining of sculptured surfaces with a ball-nose milling cutter, the theoretical average surface roughness is traditionally predicted by the spherical-tool approximation model [13] which is expressed as:

$$Ra_{(SphericalTool)} = \frac{f_z^2 + a_e^2}{8D} \tag{1}$$

where  $D$  is the cutter diameter,  $f_z$  is the feed-rate per tooth, and  $a_e$  is the step-over.

From Eq. 1, the theoretical surface roughness can be minimized by decreasing the feed-rate and/or the step-over, or by increasing the ball nose end mill cutter diameter. In finishing operations of die and mould components with sculptured surfaces, quite often the maximum cutter diameter used is limited by the part geometry. Therefore, in this application the theoretical surface roughness is affected only by feed-rate and

step-over. The results of a numbers of experimental studies on high-speed milling of hardened steel [14–18] have shown that both feed rate and step-over are influential machining parameters on surface roughness.

## 2 Experimental Setup

This research study was industry-orientated; experiments were carried out in the production workshop of a selected die and mould manufacturing company with its standard machining equipment. Experiments designed for this study were based on the four approaches in HSM [4, 11] and the four tribological elements in MQL [6]. The test piece was designed specifically for this study (Fig. 2); it resembled a core insert of an injection mould, with several sculptured free-form surfaces and an inclined planar surface where surface roughness and dimensional accuracy measurements were recorded.

All cutting tests were performed on a Spinner U5-620 5-axis high-speed machining centre. The machining centre has a built-in pneumatic unit supplying lubricated compressed air for dry machining. The air is mixed with low viscosity (10 cSt) hydraulic oil (Castrol Hyspin AWS 10) at 600 kPa by Venturi effect through the top of the in-line oil reservoir. In view of the presence of hydraulic oil as lubricant, this cutting environment could be considered as a form of MQL, and thus named as “Near-Dry” throughout this study. In the MQL setup, Accu-Lube dual nozzles

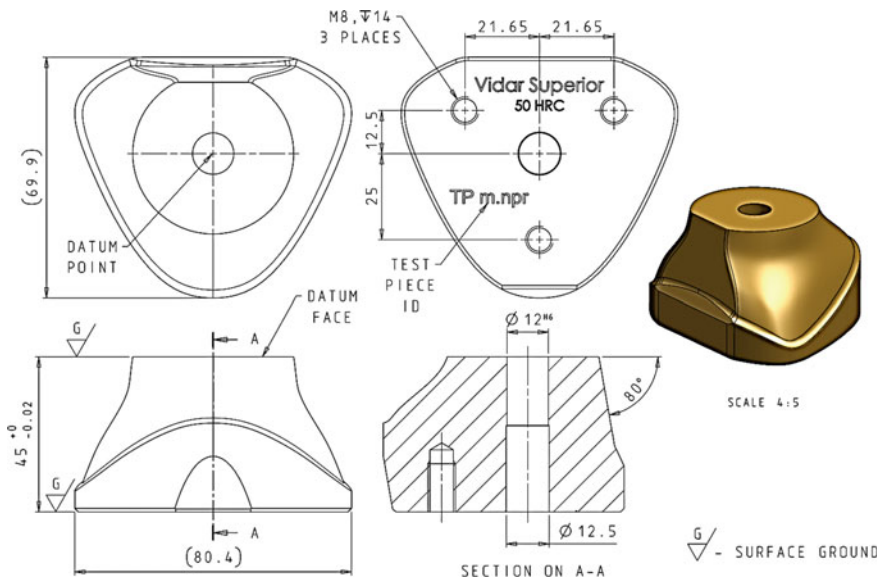


Fig. 2 Detail drawing of the test piece

external MQL supply system was used. Based on the study by Yan et al. [19], the MQL nozzles were set at the proven most effective position of  $60^\circ$  elevated angle and  $120^\circ$  with reference to feed direction (Fig. 3). The MQL lubricant (Accu-Lube LB-1000) used was a bio-degradable vegetable-based oil with added extreme-pressure (EP) additives. It has a specific gravity of 0.93 and viscosity of 39 cSt at  $40^\circ\text{C}$ . Based on recommendations by the manufacturer, the MQL lubricant flow rate was set at 4.5 mL/h/nozzle under delivery air pressure of 600 kPa.

The material chosen was “Vidar Superior” (modified AISI H11), a newer grade of chromium-molybdenum-vanadium alloyed hot work tool steels produced by Uddeholm Sweden. Table 1 shows the chemical composition of the material.

Since the main focus of this study is on the HSM finishing process, all test pieces were prepared for the main cutting tests (finishing) through roughing, heat treatment (hardened to 50 HRC), and semi-finishing processes, as commonly used in the die and mould manufacturing industry. As the physical size of the test piece was relatively small, 0.4 mm of material stock was left on each test piece from the semi-finishing

**Fig. 3** Mounted test piece with MQL nozzles

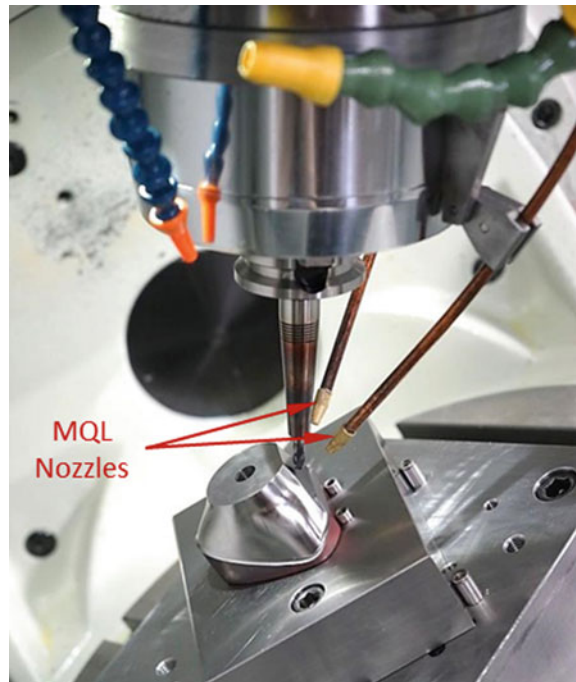


**Table 1** Chemical composition of Vidar superior

Chemical composition (%)					
C	Si	Mn	Cr	Mo	V
0.36	0.3	0.3	5.0	1.3	0.5

process, to ensure that the cutting tools could cover sufficient surface area in the main cutting tests (finishing) for any noticeable tool wear to happen. This allowed four complete passes of tool paths to create the final shape. ISCAR 6 mm 4-flutes TiAlN PVD coated solid carbide ball-nose end mills were selected for this study, and were held in shrink-fit tool holders to ensure minimum run-out and maximum rigidity. The total run-out was measured to be 0.006 mm. The type of machining strategy used was “5-axis Variable Zig Streamline” with Relative Vector of  $-30^\circ$  from Siemens NX8 CAM software. Based on a previous study by Toh [20], climb (down) milling with upward feed and horizontal step-over tool path orientations were chosen for the experiments.

A Mitutoyo SURFTEST SJ-210 surface roughness tester was used to evaluate the surface finish of the inclined planar surface of the test pieces (Fig. 4). The instrument was set to evaluate Ra, the arithmetic mean roughness, according to ISO4287:1997 roughness standard, with cut off length and sampling length set at 0.8 mm, and number of sampling lengths were set at 5. The tool paths created by the CAM software for this area were not rectilinear, therefore the surface roughness along the feed and the step-over directions were both examined. Six positions on the surface arranged in a uniform pattern were chosen for examination. Three measurements were taken at each positions, the average of the total thirty-six measurements was used for analysis.

A Blum TC50 touch probe installed in the U5-620 machining centre was used to measure the dimensional accuracy of the test pieces (Fig. 5). The dimension of three predetermined positions on the inclined planar surface was measured. The measured values were compared against the theoretical CAD values, and their differences ( $\delta y$ ) were used for analysis.

**Fig. 4** Surface roughness measurement

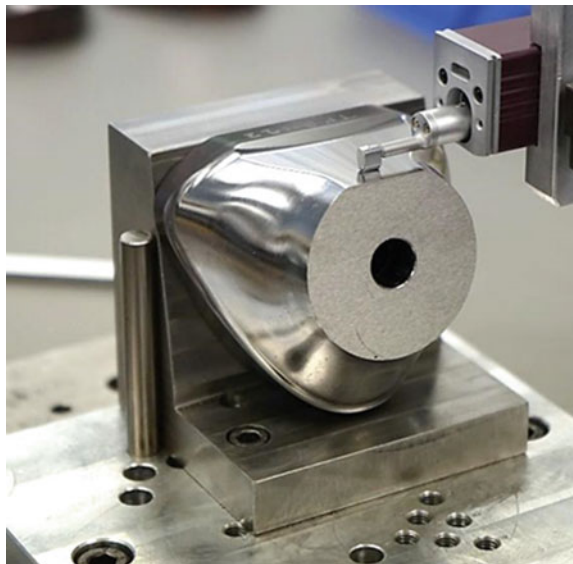


**Fig. 5** Dimensional accuracy measurement



A Leica MZ16 optical microscope, connected to a personal computer, was used to observe the flank wear of the cutting tools. Images of the cutting edge, under  $100\times$  magnifications were recorded by Irfan View 3.98 image capture software for flank wear measurement. The image of the Olympus 0.01 mm reference specimen was also recorded for measurement calibration. The flank wear was measured by means of the Fiji image processing software. Figure 6 shows a brand new unworn cutting edge.

## 2.1 Design of Experiments

A three-factors two-levels One-Half ( $2^{3-1}$ ) Fractional Factorial DOE design [21, 22] was chosen to investigate the effect of feed-rate ( $f_z$ ), step-over ( $a_e$ ) and depth of cut ( $a_p$ ) on surface roughness and machining time under Near-Dry and MQL machining. In the One-Half ( $2^{3-1}$ ) DOE design, the results of the experiment could be expressed in terms of a mathematical regression model, written as

$$\hat{y} = \beta_0 + \beta_1x_1 + \beta_2x_2 + \beta_3x_3 \quad (2)$$

where  $\hat{y}$  is the estimate of the response,  $x_1$ ,  $x_2$ , and  $x_3$  are the coded variables of feed-rate, step-over, and depth of cut respectively, and  $\beta$  s are regression coefficients.



**Fig. 6** Unworn cutting edge

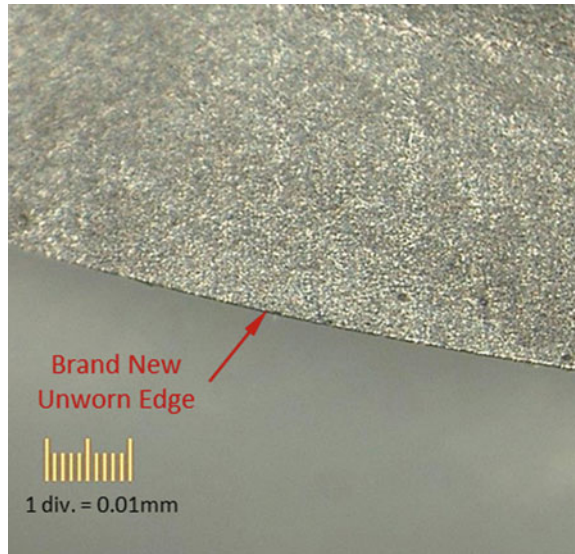


**Table 2** Level of factors of the experiment design

Factor	Factor level	
	Low (-)	High (+)
Feed-rate (mm/tooth)	0.03	0.06
Step-over (mm)	0.05	0.1
Depth of cut (mm)	0.1	0.2

The level of factors and their combinations are shown in Tables 2 and 3, respectively. The high and low values of the three factors were selected based on common practice in the die and mould manufacturing industry.

**Table 3** Factor values corresponding to machining parameter set

Machining parameter Set	Feed-rate	Step-over	Depth of cut
	$f_z$ (mm/tooth)	$a_e$ (mm)	$a_p$ (mm)
1	0.03	0.1	0.1
2	0.03	0.05	0.2
3	0.06	0.05	0.1
4	0.06	0.1	0.2

### 3 Results and Discussion

The complete results data are listed in Table 4. One-way ANOVA test was performed with the significance level set at 5% ( $\alpha = 0.05$ ) to establish the significance of the differences in surface roughness, dimensional accuracy and tool wear between the Near-Dry and MQL cutting environments. Table 5 shows the ANOVA results for Surface Roughness, Dimensional Accuracy and Tool Wear, respectively. The results showed that in all three cases, the values of “ $F$ ” (0.616, 3.397, 0.472) were less than “ $F_{crit}$ ” (4.6), and all the “ $P$ -value” (0.446, 0.087, 0.503) were greater than “ $\alpha$ ” (0.05). This indicated that statistically there was no significant difference in surface roughness, dimensional accuracy and tool wear between Near-Dry and MQL machining.

**Table 4** Complete results data of experiments

	Machining parameter set	Surface roughness	Dimensional deviation	Tool wear	Machining time
		$Ra$ ( $\mu\text{m}$ )	$\delta y$ (mm)	$VB$ (mm)	(h)
Near-dry	1	0.285	- 0.007	0.010	7.3
		0.255	0.007	0.013	7.3
	2	0.237	0.066	0.017	6.8
		0.216	0.043	0.012	6.8
	3	0.297	0.081	0.014	9.5
		0.332	0.033	0.012	9.5
	4	0.377	0.006	0.009	2.5
		0.419	0.038	0.014	2.5
MQL	1	0.289	0.017	0.012	7.3
		0.290	0.025	0.012	7.3
	2	0.249	0.025	0.008	6.8
		0.250	- 0.012	0.014	6.8
	3	0.385	0.012	0.013	9.5
		0.324	- 0.001	0.012	9.5
	4	0.438	0.012	0.013	2.5
		0.419	0.019	0.011	2.5

**Table 5** ANOVA results

ANOVA			
	$F$	$P$ -value	$F_{crit}$
Surface roughness	0.616	0.446	4.600
Dimensional accuracy	3.397	0.087	4.600
Tool wear	0.472	0.503	4.600

### 3.1 Surface Roughness

Surface roughness values between Near-Dry and MQL machining were very similar under each of the different machining parameter combinations (Table 4). Overall, Near-Dry machining produced slightly lower surface roughness than MQL (within the magnitude of 1/100th of  $\mu\text{m}$ ) but the differences were statistically insignificant. A recent study by Yan et al. [19] suggested that improvement in surface finish could be achieved by utilizing higher MQL oil flow rate. However, the results from this study showed otherwise; better surface finish was associated with lower oil flow rate, 0.4 mL/h in Near-Dry and 9 mL/h in MQL. A possible explanation of this phenomenon is that the viscosity of the oil lubricant has a more dominant effect on surface finish than its flow rate. A study of MQL lubricant properties by Tai et al. [23] indicated that low fluid viscosity was correlated with good machinability.

From the factorial experiment, regression models for surface roughness were established, for Near Dry (Eq. 3) and for MQL (Eq. 4).

$$Ra_{(Near-Dry)} = 0.044 + 3.6f_z + 1.28a_e \quad (3)$$

$$Ra_{(MQL)} = 0.061 + 4.07f_z + 1.16a_e \quad (4)$$

Both equations can be used to predict surface roughness in relation to feed-rate and step-over. For example, if feed-rate = 0.03 mm/tooth and step-over = 0.1 mm, the resulting surface roughness will be 0.28  $\mu\text{m}$  under Near Dry and 0.30  $\mu\text{m}$  under MQL. Compared with 0.23  $\mu\text{m}$  calculated by the spherical-tool approximation model (Eq. 1), the prediction from the regression models were 22–30% higher. This showed that the traditional approximation model can only be used as a rough estimation.

It can be seen from these two equations that feed-rate has a more dominant effect on the resulting surface finish than step-over, as it has a larger regression coefficient than that of step-over. This means that, in order to achieve a better surface finish (low surface roughness), a lower feed-rate is preferable. When comparing the two equations, the “MQL” model has a slightly larger feed-rate coefficient than that in the “Near-Dry” model. This implies that when using the “MQL” model for prediction, feed-rate has greater influence on surface roughness than in the “Near-Dry” model.

### 3.2 Tool Wear

The tool (flank) wear on all sixteen milling cutters was measured and was found to be very small, ranging from 0.009 to 0.017 mm (Table 4). These differences proved to be insignificant irrespective of the differences in machining parameters and lubrication methods. They were all well below the tool-life criterion of 0.1 mm, which is typical for finishing operations in die and mould manufacturing practice [24]. One of the contributing factors for the small flank wear was the high-performance

coating of the milling cutters. The milling cutters used in this study were made of fine grade solid carbide, PVD coated with submicron substrate of TiAlN. This high-performance coating is known to excel at machining difficult-to-machine materials such as hardened steels and nickel-based alloys; its superior oxidation resistance provides excellent performance in high-temperature machining [21].

When comparing the wear pattern on the cutting edges after machining under the two different lubrication methods, worn edges resulting from Near-Dry and MQL machining were even (Figs. 7 and 8). This was the result of abrasive wear. A possible explanation of the constant small flank wear phenomenon is that after the initial wearing or run-in of approximately 0.01 mm as shown in the results, further wear

**Fig. 7** Flank wear from near-dry machining

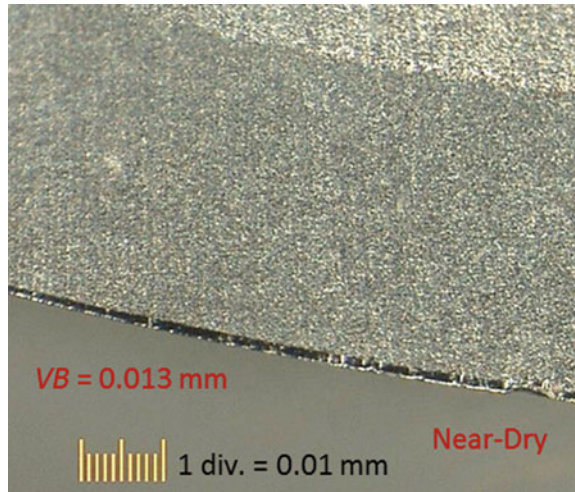
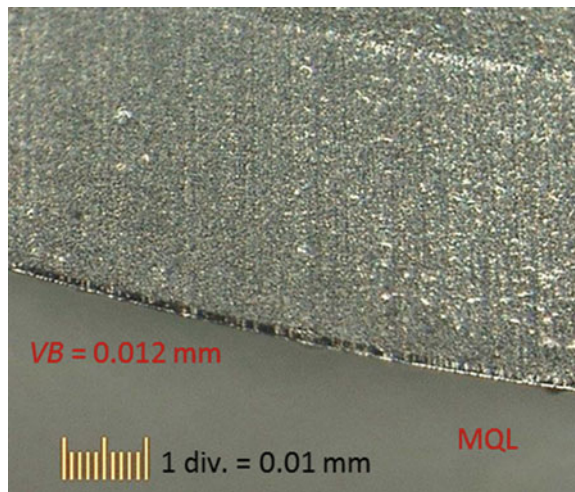


**Fig. 8** Flank wear from MQL machining



occurred at such a slow rate that even after more than 9 h of machining (using machining parameter set “3”) the additional amount of wear was insignificant.

### 3.3 Dimensional Accuracy

In HSM finishing operation of die and mould components, the accuracy of the machined workpiece is affected by the rigidity (e.g. tool overhang and vibration) and the accuracy (e.g. geometry and flank wear) of the cutting tool [4]. The milling cutter and holder used in this study were carefully chosen to eliminate possible errors caused by the above mentioned factors. The maximum variation in cutting diameter was measured to be 0.005 mm and the total run-out of the milling cutter was 0.006 mm.

Experiments performed on Near-Dry and MQL machining showed that the average dimensional deviation was 0.035 mm and 0.015 mm respectively. Although these differences were statistically insignificant, the dimensional deviation amount will determine the types of dies and moulds these two lubrication methods are capable of producing. For example, the accuracy produced by MQL machining fell within the tolerance requirement for injection moulds and forging dies [25], while that produced by Near-Dry machining fell within the tolerance requirement for die casting dies [25].

As discussed in the previous section, the tool wear was all similarly small in the experiments. This suggested that tool wear was not the contributing factor to the cause and the variation of dimensional error of the machining. A possible cause for the dimensional errors could be cutter deflection. As the tool wear was very small in this study, most of the frictional energy created during the cutting process, which normally would have caused tool wear [21], could be transformed into a reactional force perpendicular to the machined surface, thus causing cutter to deflect. A possible explanation for the dimensional variations could be that different frictional forces were generated by the cutting actions in the two lubrication methods, thereby causing the cutters to deflect in different amounts. As far as the properties of these two lubricants are concerned, the MQL lubricant (LB-1000) contains an EP additive that withstands higher load [23]. Moreover, compared with the machine-built-in Near-Dry setup, the MQL setup provided a higher mist concentration as the nozzles were a lot closer to the cutting zone. EP additives and high mist concentration have been found to be best correlated with good cutting performance [23], thus explaining the higher accuracy performance of MQL.

### 3.4 Machining Time

From the results of the factorial experiment, a regression model for machining time was established (Eq. 5), allowing the prediction of required machining time based on feed-rate, step-over and depth of cut.

$$MT = 18.6 - 35f_z - 65a_e - 37.5a_p \quad (5)$$

All three regression coefficients in this model are of a negative value, which means that using the upper level of the three parameters, e.g. 0.06 mm/tooth, 0.1 mm and 0.2 mm respectively, will result in the shortest machining time required, i.e. 2.5 h. Using this model in conjunction with the surface roughness model (Eqs. 3 or 4), the shortest possible machining time required to produce the best surface finish can be predicted.

As previously discussed, surface roughness is not affected by the depth of cut while lower feed-rate (0.03 mm/tooth) will produce lower surface roughness. Hence the best combination of machining parameters is  $f_z = 0.03$  mm/tooth,  $a_e = 0.1$  mm and  $a_p = 0.2$  mm. This will produce a surface roughness of 0.28  $\mu\text{m}$  (using Eq. 3) in 3.55 h of machining time. By reducing the step-over value, e.g. to 0.05 mm, the surface roughness will be lowered by a small amount to 0.22  $\mu\text{m}$ , but the machining time will be increased to 6.8 h. This means that it will take 3.25 h longer to achieve an insignificant gain in surface finish.

## 4 Conclusion

Experimental methodologies have been developed for investigating the potential benefits of applying the MQL technique in the die and mould manufacturing industry. Cutting performance in terms of surface roughness, tool wear, dimensional accuracy and machining time were examined. Experiments carried out on Near-Dry and MQL machining revealed that their performances were comparable. While they produced workpieces of the same surface roughness, workpieces from MQL machining had a higher dimensional accuracy. Based on these results, MQL may be more suited for the manufacturing of injection moulds and forging dies, while Near-Dry will be preferred for the manufacturing of die cast dies. Mathematical models for predicting surface roughness and machining time were established, which confirms that feed-rate had a larger effect on surface roughness than step-over, while the depth of cut had no significant effect. An optimal machining time of 3.55 h and good surface finish of 0.28  $\mu\text{m}$  can be achieved by using a small feed-rate (0.03 mm/tooth), a large step-over (0.1 mm) and a large depth of cut (0.2 mm).

When combining the MQL technique with the right cutting conditions in modern die and mould manufacturing, machining time and polishing time can be saved, thus contributing to an overall saving in production cost. In conclusion, the use of Near-Dry and MQL techniques in different finish machining situations can be a good economical solution for the die and mould manufacturing industry. However, as there are still limitations in applying this technique, in particular to the finishing operation, the implementation in real life application has still to be thoroughly planned on a job by job basis.

**Acknowledgements** We are grateful to CAMEX Limited for providing the machinery and equipment. Special Steels and Metals Limited for the test piece materials, and ISCAR Pacific Limited for some of the cutting tools required in this study. We would especially like to thank Mr. Terry Poole for his help in programming the cutting tool paths and his assistance in operating the 5-axis machining centre. Without his expertise, the experiments would not have proceeded so smoothly.

## References

1. Altan T, Lilly BW, Kruth JP, König W, Tönshoff HK, van Luttervelt CA et al (1993) Advanced techniques for die and mold manufacturing. *CIRP Ann Manuf Technol* 42(2):707–716
2. Fallbhömer P, Altan T, Tönshoff HK, Nakagawa T (1996) Survey of the die and mold manufacturing industry—practices in Germany, Japan, and the United States. *J Mater Process Technol* 59(1–2):158–168
3. Schulz H, Moriwaki T (1992) High-speed machining. *CIRP Ann Manuf Technol* 41(2):637–643
4. Finzer T (1999) High speed machining (HSC) of sculptured surfaces in die and mold manufacturing. In: Olling GJ (ed) *Machining impossible shapes*. US, Springer, pp 333–341
5. Klocke F, Eisenblatter G (1997) Dry cutting. *CIRP Ann Manuf Technol* 46(2):519–526
6. Weinert K, Inasaki I, Sutherland JW, Wakabayashi T (2004) Dry machining and minimum quantity lubrication. *CIRP Ann Manuf Technol* 53(2):511–537
7. Astakhov VP (2008) Ecological machining: near-dry machining. In: Davim JP (ed) *Machining: fundamentals and recent advances*, pp 195–223
8. Machado AR, Wallbank J (1997) The effect of extremely low lubricant volumes in machining. *Wear* 210(1–2):76–82
9. Baptista R, Simões JFA (2000) Three and five axes milling of sculptured surfaces. *J Mater Process Technol* 103(3):398–403
10. Dimitrov D, Saxer M (2012) Productivity improvement in tooling manufacture through high speed 5 axis machining. *Procedia CIRP* 1(1):277–282
11. Schulz H (2003) High-speed machining. In: Dashchenko SAI (ed) *Manufacturing technologies for machines of the future 21st century technologies*. US, Springer, pp 197–214
12. Dixit US, Sarma DK, Davim JP (2012) Dry machining. In: *Environmentally Friendly Machining*. Springer US, Boston, MA, pp 19–28
13. Jung T-S, Yang M-Y, Lee K-J (2004) A new approach to analysing machined surfaces by ball-end milling, part I. *Int J Adv Manuf Technol* 25(9–10):833–840
14. Krajnik P, Kopač J (2004) Modern machining of die and mold tools. *J Mater Process Technol* 157–158(SPEC.ISS.):543–552
15. Vivancos J, Luis CJ, Costa L, Ortiz JA (2004) Optimal machining parameters selection in high speed milling of hardened steels for injection moulds. *J Mater Process Technol* 155–156(1–3):1505–1512
16. Gopalsamy BM, Mondal B, Ghosh S, Arntz K, Klocke F (2009) Investigations on hard machining of Impax Hi Hard tool steel. *Int J Mater Form* 2(3):145–165
17. Cui X, Zhao J, Jia C, Zhou Y (2012) Surface roughness and chip formation in high-speed face milling AISI H13 steel. *Int J Adv Manuf Technol* 61(1–4):1–13
18. Yue CX, Liu XL, Sun DW, Wu MY (2012) Research on machined surface quality of high speed hard machining for harden steel. *Adv Mater Res* 500:82–88
19. Yan L, Yuan S, Liu Q (2012) Influence of minimum quantity lubrication parameters on tool wear and surface roughness in milling of forged steel. *Chinese J Mech Eng* 25(3):419–429
20. Toh CK (2006) Cutter path orientations when high-speed finish milling inclined hardened steel. *Int J Adv Manuf Technol* 27(5–6):473–480
21. Astakhov VP (2006) *Tribology of metal cutting*, 1st edn. Elsevier, Briscoe BJ
22. Montgomery DC (2008) *Design and analysis of experiments*, 7th edn. Wiley Inc.

23. Tai BL, Dasch JM, Shih AJ (2011) Evaluation and comparison of lubricant properties in minimum quantity lubrication machining. *Mach Sci Technol* 15(4):376–391
24. Elbestawi MA, Chen L, Becze CE, El-Wardany TI (1997) High-speed milling of dies and molds in their hardened state. *CIRP Ann Manuf Technol* 46(1):57–62
25. Fallböhmer P, Rodríguez C, Özel T, Altan T (2000) High-speed machining of cast iron and alloy steels for die and mold manufacturing. *J Mater Process Technol* 98(1):104–115



# Finite Element Analysis of Machining Heat Treated Titanium Alloy Ti54M



Navneet Khanna and Vivek Bajpai

**Abstract** Cutting forces and cutting tool temperature after machining processes on titanium alloys is of great interest to industry in controlling tool life and surface integrity of the manufactured critical structural components. Nowadays, finite element method (FEM) for machining processes is constantly attracting researchers and scientists to continuously understand the chip formation mechanisms, heat generation, tool-chip friction, cutting forces and quality of the machined surfaces. The current research is an attempt to model machining performance of newly developed titanium alloy Ti54M using FEM. Cutting and feed forces and cutting tool temperature predicted by numerical simulations are compared with experimental results.

**Keywords** Finite element method · Titanium alloy · Forces · Temperature

## 1 Introduction

Currently, metal cutting is one of the most common manufacturing processes and the finite element method has become the main instrument to simulate machining operations [1]. It constitutes a complex process involving a variety of physical phenomena, such as plastic deformation, frictional contact, thermo-mechanical coupling and chip and burr formation mechanisms [2]. Experimental approaches to study the machining processes are important but they can be replaced by FEM analysis, especially when a wide range of parameters is involved such as machining conditions, material of the workpiece, and tool types are involved. Process features such as tool geometry and cutting parameters directly influence cutting forces, chip morphology, tool life, and final product quality [3, 4].

---

N. Khanna (✉)

Mechanical Engineering Department, IITRAM (Government of Gujarat Initiative), Ahmedabad 380026, India

e-mail: [navneetkhanna@iitram.ac.in](mailto:navneetkhanna@iitram.ac.in)

V. Bajpai

School of Engineering and Technology, Mahindra Ecole Centrale, Hyderabad, India

© Springer Nature Switzerland AG 2022

S. Hinduja et al. (eds.), *Proceedings of the 38th International MATADOR Conference*, [https://doi.org/10.1007/978-3-319-64943-6\\_29](https://doi.org/10.1007/978-3-319-64943-6_29)

415

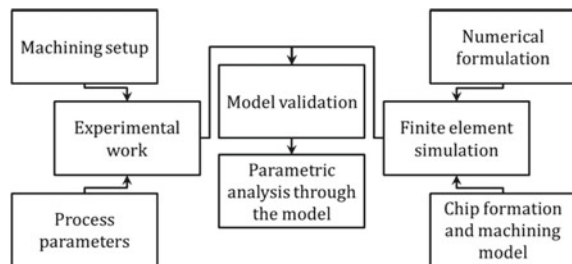
Temperature prediction is of critical importance because it governs thermally activated wear mechanisms. Komanduri and Hou [5] gave a comprehensive review of the state-of-the art in empirical methods. The prediction of cutting temperature fields and heat partition still presents a major challenge. Since the measurement of temperatures in machining operations is difficult, validation of any model is a challenge. A true predictive model should predict the temperature fields taking into account the empirical uncertainty [6, 7].

The Titanium alloys are one of the most difficult materials to machine because of their low thermal conductivity and low elastic modulus, which lead to high cutting temperatures and tool vibrations respectively. The machining of titanium alloys is one of the principal challenges for their application [8, 9]. However, in order to increase the machinability, new titanium alloys are being developed. One of those new alloys is TIMETAL<sup>®</sup> 54 M (Ti54M), developed by TIMET (Largest sponge producer in the United States), an  $\alpha + \beta$  alloy that provides cost benefits with superior machinability. The strength is comparable to similarly processed Ti6Al4V alloy [10–13].

Kosaka [8] observed significant impact of the alloy chemistry on machinability and claimed Ti54M alloy exhibiting superior machinability compared to Ti6Al4V alloy. During the development work of Ti54M alloy, it was realized that the machinability also depends on the heat treatment conditions, i.e. with strength and microstructure, as well as chemistry [9]. Materials with coarse microstructures are more difficult-to-cut than the ones with finer microstructures. [10] also found better machinability of Ti54M over Ti6Al4V at high cutting speeds. [11] analyzed the effect of heat treatment on the machinability of Ti54M (forged condition) and Ti6Al4V (mill annealed condition) alloys. For both the alloys, decrease in specific forces were reported with increasing cutting speed up to around 80 m/min and then increase with the cutting speed as shown in Fig. 1. This effect was more pronounced in case of feed force. However, [12] concluded during drilling operation that Ti6Al4V exhibits superior machinability than Ti54M in term of tool life performance. It is noticed that in most of the research findings, Ti54M has finer microstructure than Ti6Al4V. Therefore, the rationale behind the better machinability of Ti54M alloy over Ti6Al4V alloy can be the finer microstructure of Ti54M alloy. The microstructure of an alloy can be changed by heat treatment without affecting other variables.

Prediction of industry-relevant parameters requires prediction of fundamental process variables as a prerequisite [7]. Hence, in this paper the model of orthogonal

**Fig. 1** Overview of the simulation process



machining for cutting forces and cutting tool temperature is mainly proposed to predict and analyze the cutting process based on finite element method for Ti54M alloy in different heat treated conditions—annealed,  $\beta$  annealed and solution treated plus aged (STA). To the best of authors’ knowledge, this is the first ever attempt to model the machining performance for this newly developed titanium alloy using finite element methods.

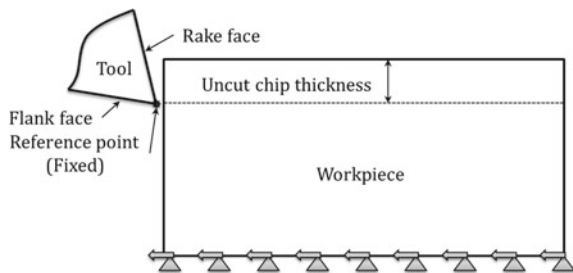
## 2 Finite Element Modelling

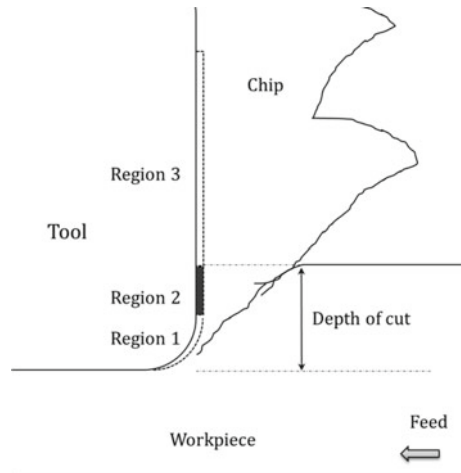
Finite element package Abaqus® explicit 6.12 has been used in the modeling of the machining process at dry machining condition on the three heat treated samples. Figure 1 shows a flow chart of the process. The experimental works were performed to validate the current model. The FEM module is supported by two inputs namely: the numerical formulation and the chip formation mechanism. Geometrical modeling, interactions between matching surfaces and nodes, the loading/boundary conditions, initial conditions and the mechanical/thermal properties of the workpiece come under the numerical formulation. The chip formation mechanism consist explanation of the machining model and the criteria of the chip formation. In this case element deletion has been considered after the degradation of the original stiffness of the material under various loading conditions in machining.

### 2.1 Numerical Formulation

Figure 2 shows the schematic of the simulation process. The turning operation is converted in the 2D orthogonal machining to get fast and simplification of the complicated process. The work piece is a moving body by giving velocity to the bottom nodes and the tool has been fixed to cut the material. The tool elements are coupled with the reference point to provide the boundary conditions. The cutting forces can be measured at the reference point. At this situation stress on the tool elements will remain zero. The initial temperature of the tool and workpiece is kept

Fig. 2 Schematic of the process



**Fig. 3** Chip tool interaction

at 300°K (room temperature). Four-node plane strain thermally coupled quadrilateral, bilinear displacement and temperature, reduced integration, hourglass control (CPE4RT) elements are used for the workpiece and the tool.

Based on the explanation of Sima and Ozel [14], the tool faces are broken in to three regions. The interaction between tool rake and flank face to the tool nodes has been defined at three levels. Figure 3 shows the tool chip interaction. Three regions of the interaction were visible in the figure. The interaction started from the sticky zone (region 1). It is defined on the tool nose curve. The second zone (region 2) has constant shear friction value and defined at the end of the tool nose and ends at the level of the unmachined surface. The third zone (region 3) of interaction is defined between the tool nodes and the remaining portion of the rake face. The coefficient of friction was set at 1, 0.8 and 0.5 for the region 1, region 2 and region 3, respectively.

## 2.2 Material Model

The chip formation has been modeled through the removal of the elements after failure. Element deletion is considered to remove the element from the analysis, which, reflects in the chip formation. The element deletion is based on the degradation of the original stiffness of the material. Deformation under machining is defined through the Johnson–Cook (JC) constitutive material model [15]. Since machining is a high strain rate process and the JC model can handle large strains and strain rates, therefore, JC model is suitable for most of the machining processes. Additionally, the JC model can define temperature-dependent material properties. The following formula is used to express the equivalent stress in the JC model:

**Table 1** Material properties (Ti54M)

Material property	STA/annealed/ $\beta$ annealed
Density (kg/m <sup>3</sup> )	4400
Tensile modulus (GPa)	124/110/117
Inelastic heat fraction, $\beta$	0.9
Poisson's ratio, $\nu$	0.32
Temperature (°K)	Specific heat capacity $C_m$ (J/kg K)
77	540
752	624
1472	724
Temperature (°K)	Conductivity (W/mK)
77	7
752	11
1472	16

**Table 2** Material constants for Ti5Al4V [16]

Constant	A (Mpa)	B (Mpa)	n	C	m
Value	1098	1092	0.9	0.01	1
Constant	D <sub>1</sub>	D <sub>2</sub>	D <sub>3</sub>	D <sub>4</sub>	D <sub>5</sub>
Value	- 0.09	0.25	- 0.5	0.01	4

$$\bar{\sigma}_{eq} = [A + B(\bar{\epsilon}^p)^n] \times \left[ 1 + C \ln \frac{\dot{\bar{\epsilon}}^p}{\dot{\bar{\epsilon}}_0^p} \right] \times \left[ 1 - \left( \frac{\theta_{work} - \theta_{room}}{\theta_{melting} - \theta_{room}} \right)^m \right] \quad (1)$$

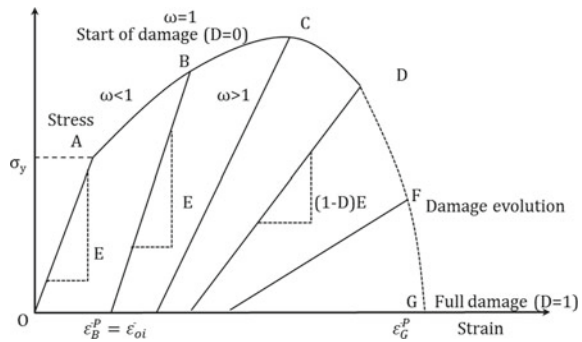
The terms A, B, n, C, and m are denoting material constants,  $\bar{\epsilon}^p$  is the strain and  $\dot{\bar{\epsilon}}^p$  is the strain rate. Temperature dependent material properties and JC constants for Ti6Al4V are given in Tables 1 and 2.

Figure 4 shows material characteristics in the elastic and the plastic regions and the material response before complete failure. The curve section OA represent elastic region followed by plastic-yielding and strain hardening in the AB section of the curve. Damage to the stiffness of the material starts at point B (D = 0) and goes up along the curve. Element deletion is set at F where D = 0.7.

### 2.3 Simulation and Chip Formation

Simulations have been performed with the machining parameter depth of cut 0.15 mm and two cutting speeds 40 m/min and 80 m/min. Machining simulation and chip formation is shown in Fig. 5. Segmented chips with the shear bands have been formed

**Fig. 4** Mechanical characteristics of the material [16]



during the machining. The chip shape is common as in the most of the titanium alloys machining. Figure 5a–c show the stress distribution, shear bands via principal strain and the temperature distribution.

### 3 Model Validation

#### 3.1 Experimental Work

Orthogonal dry machining of 5 s duration was conducted on a Lagun vertical CNC milling machine (Fig. 6). The infrared camera system is adapted into the Vertical CNC Milling Center, as seen in Fig. 6a, b. The workpiece was carefully integrated into the tool holder on the spindle. Workpiece is rotated and fed into the stationary tool attached to the dynamometer. During the temperature measurements in the CNC machine, in order to isolate the camera and the objective from the chips and any flying particles that are present in the environment of CNC machine, protection is provided. The tubular workpiece, the dynamometer, and the cutting insert are placed in order to perform orthogonal cutting tests. The experiments are carried out with thin-tubes of 2 mm wall thickness with three variants of Ti54M titanium alloy. The cutting inserts were Sandvik tungsten carbide inserts (Model: TNMG 160408–23 H13A), without any coating or chip breakers. To ensure edge sharpness, a new tool insert was used for each test. All the applied inserts were examined by a sensofar optical profiler in order to verify the cutting edge radius is within  $34 \pm 2 \mu\text{m}$ . Each test was carried out three times to check uncertainty in the result. All the details regarding inserts, cutting conditions and machine toll is presented in Table 3.

In the experiments, the most interesting area to be captured was the rake face. Therefore, the IR camera is focused on this region; starting from the tool tip. Each video is captured and saved as an image sequence, containing each frame of the video. Some of these frames are obstructed with chips, therefore, only the images, where the rake face is clearly seen, are taken into consideration. The force measurement

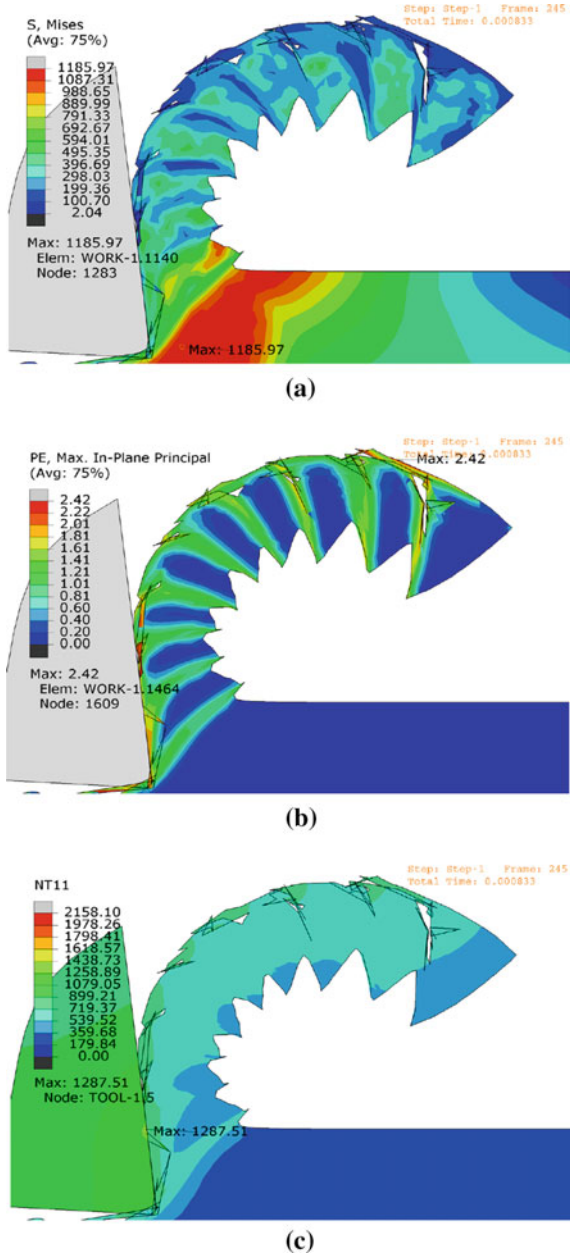
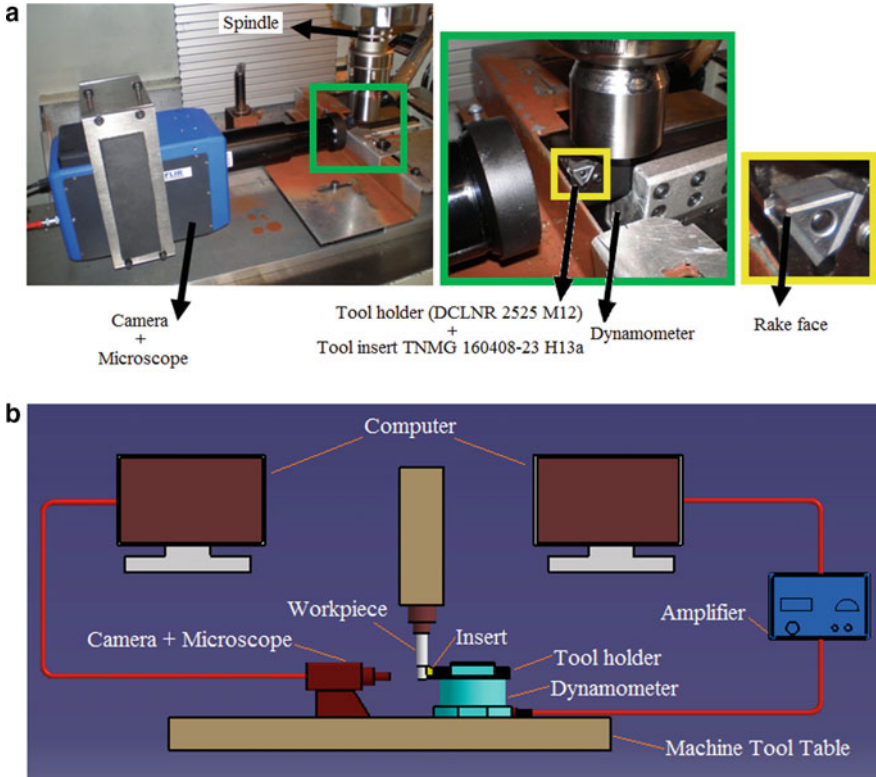


Fig. 5 Chip formation **a** stress distribution, **b** shear bands, **c** temperature distribution



**Fig. 6** a Experimental setup and b Schematic of experimental setup

**Table 3** Tooling details

Cutting conditions	<b>Cutting Speed:</b> 40 and 80 m min <sup>-1</sup>
	<b>Undeformed Chip Thickness (<math>t_f</math>)</b> = 0.1–0.15–0.25 mm
	<b>Depth of Cut (<math>p</math>)</b> = 2 mm
<b>Cutting tools</b> • Tool holder (DCLNR 2525 M12) • Tool insert TNMG 160408–23 H13A	<b>Rake Angle (<math>\gamma_0</math>)</b> = 7°
	<b>Cutting Edge Inclination Angle (<math>\gamma_s</math>)</b> = 0°
	<b>Cutting Edge Angle (<math>\gamma_R</math>)</b> = 0°
	<b>Corner Radius (<math>r_{\gamma_0}</math>)</b> = 0
	<b>Cutting Edge Roundness (<math>r_{\gamma_0}</math>)</b> = 34 ± 2 μm
	<b>Chip Breaker</b> = - 15
	<b>Grade</b> = (H13A) K15 micrograin
<b>Coolant</b>	<b>Dry Machining (No Coolant)</b>
<b>Workpiece Dimensions</b>	<b>Outer Diameter:</b> 48 mm
	<b>Inner Diameter:</b> 44 mm
<b>Machine Tool</b>	<b>Lagun CNC Vertical Machining Centre</b> (RPM: 18,000, Power: 15 kW, Torque: 80Nm)



system included a three-component Kistler dynamometer, a Kistler charge amplifier, with data acquisition carried out by MEDATEK software.

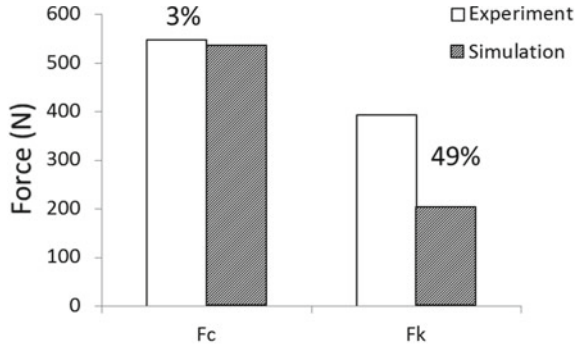
### 3.2 Results and Discussion

A comparison between experimental and simulated cutting and feed forces at 40 m/min is shown in Fig. 7a–c. A comparison between experimental and simulated cutting and feed forces at 80 m/min is shown in Fig. 8a–c. For all numerical tests, feed forces are underestimated but the cutting forces are estimated with high accuracy for all the heat treated conditions of Ti54M titanium alloy. It can be seen that cutting forces are matched between simulation and experiment, and the finite element method is feasible and effective in replacing the traditional experimental method with finite element simulation. But there are some errors between simulation experiments; in particular the feed forces result from some factors are neglected in simulation process. Firstly, the model of cutting tool is simplified and regarded as rigid in ideal condition, which will have effect on the forces. In addition, since the limitation of computer performance and parameters of workpiece material, it will lead to the errors of forces between simulation and experiment. As shown in Figs. 7 and 8, the experimental feed force is around one half the cutting force. The same tendency should be obtained for numerically simulated forces. The main reason which would explain the mismatch between experimental and simulated forces might be related to the choice of the JC parameters. Many material constants can be found in literature for the Ti6Al4V alloy [17, 18] but none has been mentioned in any literature for Ti54M alloy. Considering the feed forces, the greater mismatch is 49% in STA condition. Moreover, the stronger the alloy the higher the feed forces.

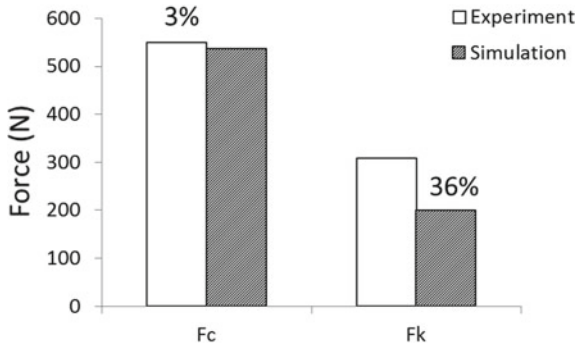
The comparative analysis of the experimental mean rake face temperature and the rake face temperature simulation is carried out for three variants of Ti54M alloy. The first Fig. 9a is for cutting velocity of 40 m/min and a feed rate of 0.15 mm/rev. The validation of the experimental mean rake face temperature and the rake face temperature simulation is illustrated in this figure. The second Fig. 9b is for cutting velocity of 80 m/min and a feed rate of 0.15 mm/rev. The validation of the experimental mean rake face temperature and the rake face temperature simulation is given in this figure. For the analysis of the tool rake temperature distribution, a distance of 0.3 mm, starting from the tool tip, is taken in to consideration due to the fact that this is the area that can be viewed most clearly in the IR images.

For both of these cases, it can be easily seen that the results of the experiments conducted for different cutting velocities and heat treated conditions of titanium alloy show good agreement with the simulations.

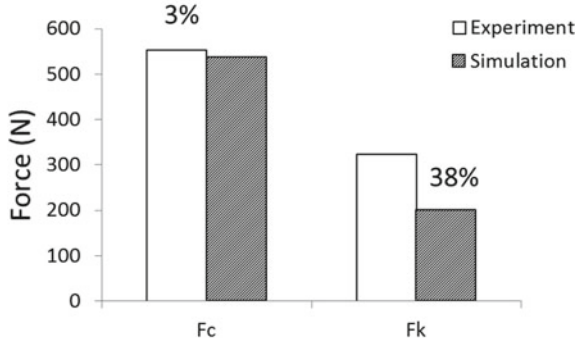
From above results, it can be observed that (a) as cutting speed increases, the forces decrease and the cutting temperature increases; (b) as feed rate increases, the cutting force and the cutting temperature increases and the feed force decreases; and (c) as the hardness of the workpiece increases due to heat treatment, both the forces and the cutting temperature increases.



(a)



(b)



(c)

**Fig. 7** Model validation through the experimental results at a cutting speed 40 m/min and feed 0.15 mm/rev, the heat treatment condition is **a** STA, **b** annealed, **c**  $\beta$  annealed

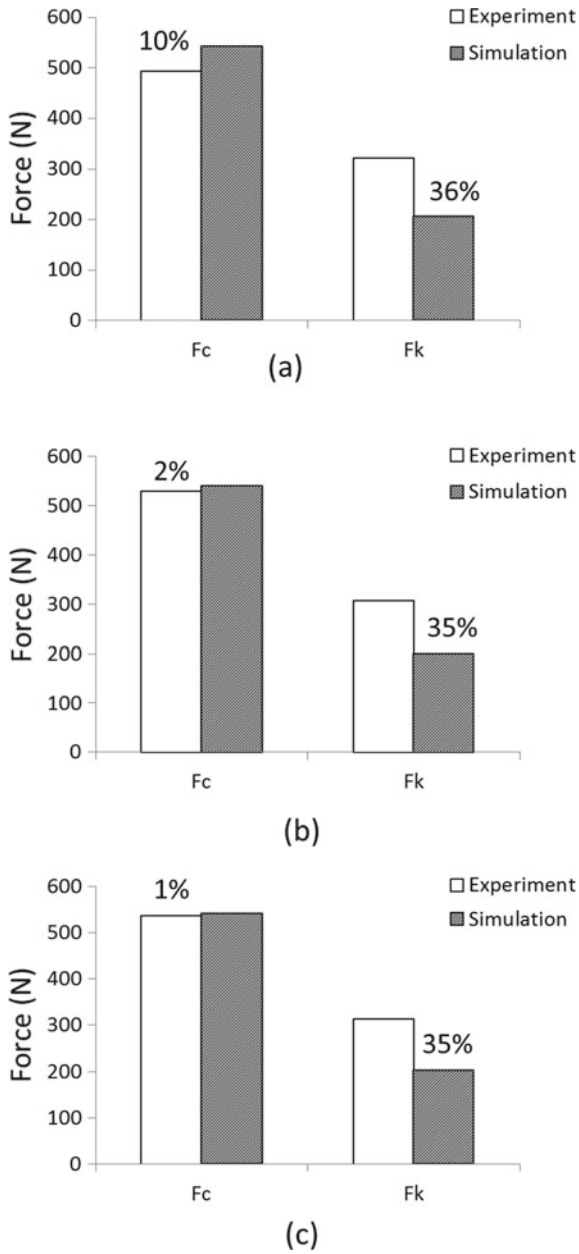


**Fig. 8** Model validation through the experimental results at a cutting speed 80 m/min and depth of cut (feed) 0.15, the condition is **a** STA, **b** annealed, **c**  $\beta$  annealed

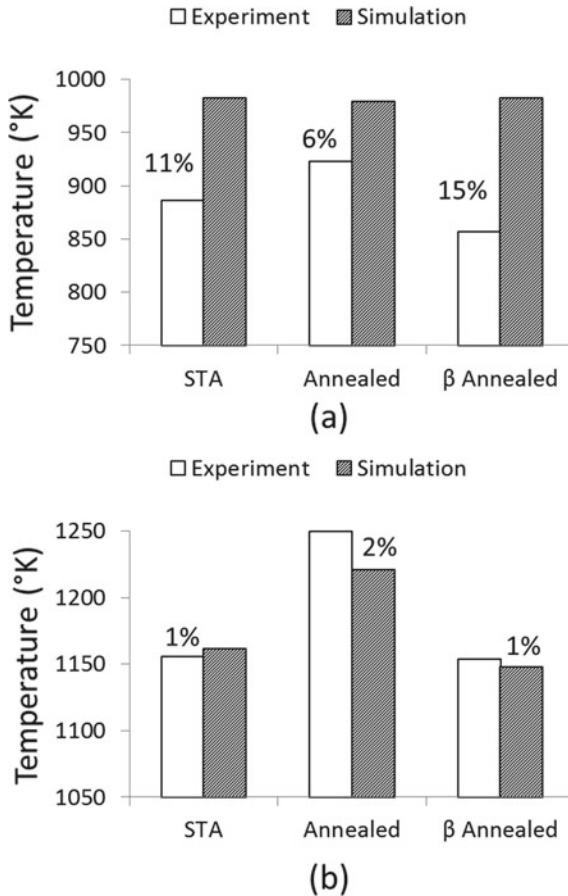


**Fig. 9** Model validation via machining temperature obtained from the experiments at a depth of cut (feed) 0.15 and cutting speed **a** 40 m/min, **b** 80 m/min

## 4 Conclusions

This paper presents a model developed by using finite element modeling (FEM) for predicting forces with cutting tool temperature at different cutting speeds for three variants of newly developed titanium alloy under dry cutting conditions. It was found that there is good agreement between the trend of cutting force and cutting tool temperature at different cutting speeds. Therefore, finite element modeling is useful to predict the value of forces and cutting tool temperature rather than conducting experiments. FEM can lead to reduced machining time and manufacturing cost as well. This is because the cutting force and cutting tool temperature have been predicted with reasonable accuracy. It is also found that the feed force does not match well between simulation and experimental work. The main reason which would explain

the mismatch between experimental and simulated forces might be related to the choice of the JC parameters. Many material constants can be found in literature for the Ti6Al4V alloy but none has been mentioned in any literature for Ti54M alloy.

**Acknowledgements** A crucial part of this research was conducted within the collaboration of BITS Pilani (India) and MGEP (Spain) to facilitate Dr. Navneet Khanna to undergo training within the High Performance Cutting Research Group of University of Mondragon—Faculty of Engineering (MGEP) and he is thankful to them. He is extremely grateful to the associated faculty and staff members at MGEP for their support.

## References

1. Bil H, Kilic S, Tekkaya A (2004) *Int J Mach Tools Manuf* 44:933
2. Trent, Wright (2000) *Metal cutting*. Butterworth-Heinemann
3. Marusich, Ortiz M (1995) *Int J Num Meth Eng* 38:3675
4. Maranhao C, Davim JP (2012) the role of flow stress and friction coefficient in fem analysis of machining: a review. *Rev Adv Mater Sci* 30:184–188
5. Komanduri R, Hou ZB (2001) Thermal modeling of the metal cutting process. Part 1: temperature rise distribution due to shear plane heat source. *Int J Mech Sci* 42:1715–1752
6. Davies MA, Ueda T, M'Saoubi R, Mullany B, Cooke AL (2007) On the measurement of temperature in material removal processes. *CIRP Ann Manuf Technol* 56(2):581–604
7. Arrazola PJ, Özel T, Umbrello D, Davies M, Jawahir IS (2013) Recent advances in modelling of metal machining processes. *CIRP Ann Manuf Technol* 62(2):695–718
8. Kosaka Y, Fanning JC, Fox SP (2004) Development of low cost high strength alpha/beta alloy with superior machinability. In: *Proceedings of the 10th world conference on titanium*, pp 3028–3034
9. Kosaka Y, Fox SP (2004) Influences of alloy chemistry and microstructure on the machinability of titanium alloys. In: *Cost affordable titanium*, TMS conference, pp 169–176
10. Venkatesh V, Kosaka Y, Fanning J, Nyakana S (2007) Processing and properties of Timetal 54M. In: *11th world conference on titanium*, Kyoto, Japan, pp 713–716
11. Armendia M, Garay A, Iriarte LM, Arrazola PJ (2010) Comparison of the machinabilities of Ti6Al4V and TIMETAL® 54M using uncoated WC-Co tools. *J Mater Process Technol* 210:197–203
12. Rahim EA, Sharif S (2006) Investigation on tool life and surface integrity when drilling Ti-6Al-4V and Ti-5Al-4V-Mo/Fe. *JSM E Int J* 49:340–345
13. Khanna N, Davim JP (2014) Design-of-experiments application in machining titanium alloys for aerospace structural components. *Measurement*
14. Ozel T, Sima M, Srivastava AK (2010) Finite element simulation of high speed machining Ti-6Al-4V alloy using modified material models. *Trans NAMRI/SME* 38:49–56
15. Johnson GR, Cook WH (1983) A constitutive model and data for metals subjected to large strains, high strain rates and high temperature. In: *7th international symposium on ballistics*, Netherlands, pp 541–547
16. Bajpai V, Lee I, Park HW (2014) Finite element modeling of three-dimensional milling process of Ti-6Al-4V. *Mater Manuf Process* 29(5):564–571
17. Li L, He N (2006) A FEA study on mechanisms of saw-tooth chip deformation in high speed cutting of Ti-6Al-4V alloy. In: *Fifth international conference on high speed machining (HSM)*, Metz, France, pp 759–767
18. Calamaz M, Coupard D, Girod F (2008) A new material model for 2D numerical simulation of serrated chip formation when machining titanium alloy Ti-6Al-4V. *Int J Mach Tools Manuf* 48(3):275–288

# Study on Frequency Correction in Ultrasonic Horn Design



Yande Liang, Jianyu Wei, Fuben He, Dong Chen, He Chen, Kexin Wang, Hongzhe Zhang, and Liming Shu

**Abstract** When the acoustic horn vibrates longitudinally, due to the influence of Poisson effect of elastic deformation, the longitudinal vibration along axis will arouse the transverse vibration along the radial direction. In the traditional design progress of acoustic horn, the transverse vibration is ignored usually, and it results that the actual resonant frequency is lower than the theoretical resonant frequency. To make the theoretical resonant frequency corresponding with the actual resonant frequency, the transverse vibration is taken into account, then the correctional frequency formulas are deduced in the common radius ratios range. Simulation experiment is made by finite element method, the result shows that the frequency correction coefficient can improve the accuracy and efficiency for ultrasonic horn design.

**Keywords** Acoustic horn · Transverse vibration · Resonant frequency · Correction coefficient

## 1 Introduction

The ultrasonic horn is an important part applied to the acoustic levitation system [1], whose main functions are to magnify the displacement of particle in mechanical vibration and to reduce the energy loss. The ladder-type of ultrasonic horn has a big amplification coefficient and simple geometrical shape, which can be manufactured easily, so it is applied widely in ultrasonic application field, such as ultrasonic machine, ultrasonic welding, etc. [2].

In traditional methods, the design and calculation of ultrasonic horn are based on wave dynamics equation of slender horns with one-dimensional variable cross-section vibrating longitudinally and ignoring the transverse vibration. In this case, the actual resonant frequency is lower than the theoretical resonant frequency. To

---

Y. Liang (✉) · J. Wei · F. He · D. Chen · H. Chen · K. Wang · H. Zhang · L. Shu  
School of Mechanical Engineering, Dalian University of Technology, Dalian 116024, China  
e-mail: [lydjx@dlut.edu.cn](mailto:lydjx@dlut.edu.cn)

Y. Liang · K. Wang  
Engineering Training Center, Dalian University of Technology, Dalian 116024, China

improve the ultrasonic horn's vibration performances and to make the actual resonant frequency approaching the design frequency, there has been many people studying on the design of ultrasonic horn. Yanzhi et al. [3] exploited the resonance equations to study the design method of horn owning a single shape with or without loads. Liquan [4] used simulation software to research the affection of external shape on the vibration performance. Shuyu et al. [5] corrected the frequency formulas of the conical horn and the exponential horn respectively. However the section of ladder-type ultrasonic horn is not continuous, so the stress distribution is a little complex at the interface. At present, most of correctional frequency formulas are mainly obtained from experiments. Minhui et al. [6] presented the relationship curves between the correctional frequency coefficients and the radius ratios of ladder-type ultrasonic horns after many experiments. Although the influences of resonant frequency affected by the external shape of horns are obtained through simulations and experiments, which can be used to correct the calculation frequency of horns, the results are not universal because of the experimental materials. In order to make the design of horns be more widely adaptive, this paper focuses on the simply ladder-type horn so as to correct their frequencies respectively by the theoretical analysis and the finite element simulation.

## 2 Vibration Theory of Horn Design

Based on the classical theory of one-dimensional variable cross-section horn, assuming that the horn is made up of the material which is isotropy with uniform density, disregarding the mechanical damping, regarding the stress distributing evenly on the cross-section and the plane wave spreading along the axis, the plane wave propagation equation [7] can be expressed by

$$\frac{\partial^2 \xi}{\partial x^2} + \frac{1}{s} \frac{\partial s}{\partial x} \frac{\partial \xi}{\partial x} + k^2 \xi = 0 \quad (1)$$

in which,  $\xi$  is the displacement of longitudinal vibration,  $s = s(x)$  represents the area function,  $k = \omega/c$  represents the number of waves,  $\omega$  is the circumferential angular frequency,  $c = \sqrt{E/\rho}$  represents the propagation velocity of horn,  $E$  is Young's modulus of material and  $\rho$  is the density of material.

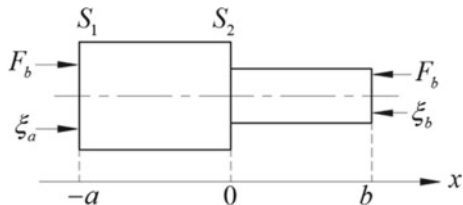
Figure 1 shows a ladder-type ultrasonic horn, the section areas of two parts are  $S_1$  and  $S_2$  respectively, the length of thick part is  $a$  and the length of thin part is  $b$ .

If the cross-sections of two parts are the same,  $\partial s/\partial x = 0$ , the Eq. (1) can be rewritten as

$$\frac{\partial^2 \xi}{\partial x^2} + k^2 \xi = 0 \quad (2)$$

The solution is

**Fig. 1** Schematic of a ladder-type ultrasonic horn



$$\begin{cases} \xi_a = (A_1 \cos kx + B_1 \sin kx), & (-a < x < 0) \\ \xi_b = (A_2 \cos kx + B_2 \sin kx), & (0 < x < b) \end{cases} \quad (3)$$

here  $A_1, B_1, A_2, B_2$  are undetermined coefficients, which are determined by boundary condition.

When the two ends of horn are free, the frequency equation of ladder-type horn is

$$S_1 \sin ka \cdot \cos kb + S_2 \cos ka \cdot \sin kb = 0 \quad (4)$$

If the horn vibrates without external loads, the enlargement factor  $M_p$  can be defined by

$$M_p = \frac{S_1 \sin ka}{S_2 \sin kb} = N^2 \frac{\sin ka}{\sin kb} \quad (5)$$

Equations (4) and (5) indicate that, when  $a = b = \lambda/4$  and the displacement node  $x_0 = 0$ , that is, the length of two parts of the ladder-type ultrasonic horn are the same, so the value of enlargement factor  $M_p$  is the maximum.

### 3 Frequency Correction on Longitudinal Vibration

Assuming that the displacement along the  $x$  axis direction is  $\xi_x$ , so that the strain of longitudinal vibration can be defined by  $\varepsilon_x = \partial \xi / \partial x$ , the velocity is defined by  $v_x = d\xi_x / dt$ . Based on the Rayleigh Approximation Theory [8], the transverse strain is  $\varepsilon_r = -\mu \partial \xi_x / \partial x$  (in which  $\mu$  is Poisson ratio), the transverse displacement is  $\xi_r = r \varepsilon_r = -r \mu \partial \xi_x / \partial x$  (in which  $r$  is the radius), and the transverse vibration velocity is  $v_r = d\xi_r / dt = -r \mu \partial v_x / \partial x$ . The quality of the differential unit of the horn is  $dm = 2\pi \rho r dr dx$ , so that the longitudinal vibration kinetic energy  $E_x$  and the transverse kinetic energy  $E_r$  can be expressed by the Eqs. (6) and (7) respectively as below

$$E_x = \iint \frac{1}{2} v_x^2 dm \frac{\pi \rho}{2} \int_0^l v_x^2 R(x)^2 dx \quad (6)$$



$$E_r = \iint \frac{1}{2} v_r^2 dm = \frac{\pi \rho \mu^2}{4} \int_0^l \left( \frac{\partial v_x}{\partial x} \right)^2 R(x)^4 dx \tag{7}$$

If ignoring the transverse vibration, the total kinetic energy of system and the equivalent mass  $m_{eq}$  will decrease. Because of existing  $f = 1/2\pi \cdot \sqrt{K/m}$  (in which  $K$  is the elastic coefficient), the calculative resonant frequency seems to be bigger than the actual resonant frequency. The ratio of the longitudinal resonant frequency  $f'$  with the transverse vibration and  $f$  without the transverse vibration can be defined by

$$\beta = \frac{f'}{f} = \sqrt{\frac{m}{m_{eq}}} = \sqrt{\frac{E_x}{E_x + E_r}} \tag{8}$$

here  $\beta$  represents the frequency correction coefficient.

In order to make the horn's actual frequency to approach the design frequency, it is required to correct the length  $l$ . Thus the correctional length  $l'$  is

$$l' = \beta l \tag{9}$$

For the horn with the consistent cross-section, when the two ends are free,  $\xi = A \cos(\pi x/l)$ ,

So that

$$\int_0^l \left( \frac{\partial v_x}{\partial x} \right) dx = \frac{\pi^2}{l^2} \int_0^l v_x dx \tag{10}$$

$$\frac{E'_x}{E'_x + E'_r} = 1 + \frac{\mu^2 \pi^2 R^2}{2l^2} \tag{11}$$

combining with equations from (8) to (11), the correctional frequency formula can be expressed

$$\beta^l = \left( 1 + \frac{\mu^2 \pi^2 R^2}{2l^2} \right)^{-\frac{1}{2}} \tag{12}$$

For the common ladder-type horn, defining that the radius of thick part is  $R$ , the thinner radius is  $r$ , the longitudinal velocities are represented by  $v_{xa}$  and  $v_{xb}$  respectively. If  $R = r$ , according to the previous boundary conditions, so  $A_1 = A_2 = 0$ ,  $B_1 S_1 = B_2 S_2$ , so  $\xi_b/\xi_a = B_2/B_1 = S_1/S_2 = N^2$ ,  $v_{xb}/v_{xa} = \xi_b/\xi_a = N^2$ . In order to calculate the longitudinal vibration kinetic energy  $E_x^L$  and the transverse kinetic energy  $E_r^L$ , the length  $l$  and the radius  $R$  are referred, only when to obtain the calculation of  $E_r^L$ , the affection of ladder surface should be also considered. Therefore  $E_x^L$  and  $E_r^L$  can be expressed by

$$E_x^L = \frac{\pi\rho}{2} R^2 \int_0^l v_{xa}^2 dx = \pi\rho R^2 \int_0^{\frac{l}{2}} v_{xa}^2 dx \tag{13}$$

$$\begin{aligned} E_r^L &= \frac{\pi\rho\mu^2}{4} \left( R^4 \int_{-\frac{l}{2}}^0 \left( \frac{\partial v_{xa}}{\partial x} \right)^2 dx + R^4 \int_0^{\frac{l}{2}} \left( \frac{\partial v_{xb}}{\partial x} \right)^2 dx \right) \\ &= \frac{\pi^3 \rho \mu^2}{4l^2} (1 + N^4) R^4 \int_0^{\frac{l}{2}} v_{xa}^2 dx \end{aligned} \tag{14}$$

Therefore the correctional frequency formula of ladder-type horn is expressed finally

$$\beta^L = \left( 1 + \frac{(1 + N^4)}{2} \cdot \frac{R^2 \mu^2 \pi^2}{2l^2} \right)^{-\frac{1}{2}} \tag{15}$$

### 4 Simulation Experiment

The finite element method has high-precision in modal analysis, its calculating progress is simple, and the results are given using the form of numerical solutions which can be translated to figures through post-process module. In this paper, the simulation experiment primarily applied Ansys 12.1 software to implement finite element analysis to investigate the relationship between the correctional frequency coefficients and the radius ratio of ladder-type ultrasonic horns. After defining  $R = 19$  mm and a series of  $r$ , the radius ratios  $N$  are showed in Table 1.

The experimental material was Duralumin, whose density  $\rho$  was 2790 kg/m<sup>3</sup>, Young modulus  $E$  was 71.5GPa, Poisson radio  $\mu$  was 0.34, and the initial design frequency  $f_0$  was 20 kHz, the length of each part was calculated as  $a = b = 63.3$  mm based on the traditional design theory. In the simulation, the type of Solid 187 (inhere definition of software) was selected as the basic 3D solid meshing element. The dimensions of the mesh were set as 3 mm, the meshed model using tetrahedral free allocation law as illustrated in Fig. 2.

**Table 1** The horn dimenstins of each group

NO	1	2	3	4	5	6	7	8	9	10
$r/mm$	18	17	16	15	14	13	12	11	10	9.5
Radius ratio $N$	1.056	1.118	1.188	1.267	1.357	1.462	1.583	1.727	1.900	2.000
NO	11	12	13	14	15	16	17	18	19	
$r/mm$	9	8	7	6	5	4	3	2	1	
Radius ratio $N$	2.111	2.375	2.714	3.167	3.800	4.750	6.333	9.500	19.00	

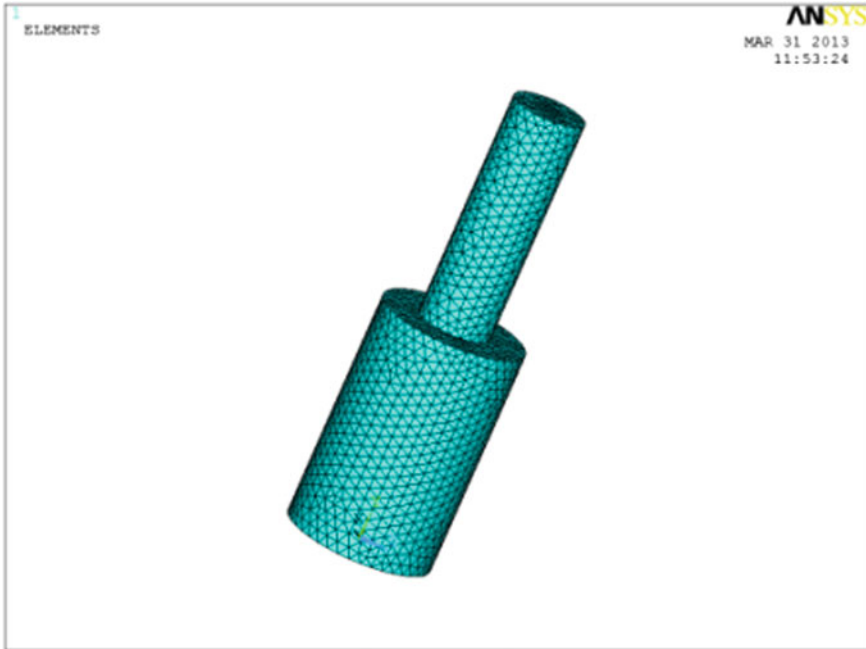


**Fig. 2** The meshed model of ladder-type ultrasonic horn using Solid 187

To promote the modal analysis by Block Lanczos method, searching the range from 18 to 22 kHz, meanwhile, to set the modal expanding step as 50. After the analysis, the result of each step was read through the post-process modules, and the contour map of corresponding displacement of the longitudinal vibration was shown in Fig. 3.

The longitudinal frequency  $f'$ , the correctional coefficient  $\beta'$ , the theoretical correctional coefficient  $\beta^L$ , and the deviation ratio  $\delta$  between  $\beta^L$  and  $\beta'$  of each group in the simulation were all indicated in Table 2.

From Tables 1 and 2, when  $N \geq 3.2$ , the difference between the theoretical correctional coefficient and simulation was bigger,  $\delta$  was over 10%, when  $N < 3.2$  the Eq. (15) which adopted as the correctional frequency formula became available. If  $N < 2.4$ , the theoretical value was closed to the simulation and the precision was higher. The relationship curve between  $\beta'$  and  $\ln N^2$  was illustrated in Fig. 4.

When  $N = 3.2$  or  $\ln N^2 = 2.3$ , the correctional frequency coefficient reached the minimum value. When  $\ln N^2 > 2.3$  or  $N^2 > 10$ , the condition of local resonance vibration was satisfied [9]. The frequency can be calculated as the frequency formula of the thin horn, one of whose end was fixed at the ladder surface and the other end was free. According to the correctional frequency formula (2), the smaller the radius was, the greater the correctional coefficient became. If  $\ln N^2 > 2.3$ , the correctional coefficient became greater as the  $\ln N^2$  increased. This agreed with the results achieved by

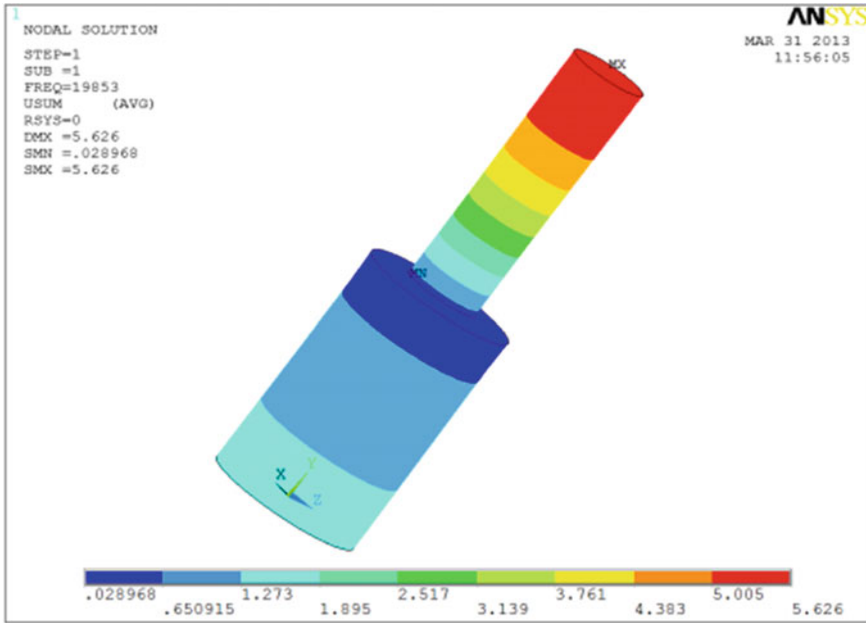


Fig. 3 The contour map of corresponding displacement of the longitudinal vibration

Huimin [6] after processing the actual experiment for many times (the correctional frequency coefficient  $\beta^L$  reached a minimum value when  $\ln N^2 \approx 2.4$ ).

### 5 Design Evaluation

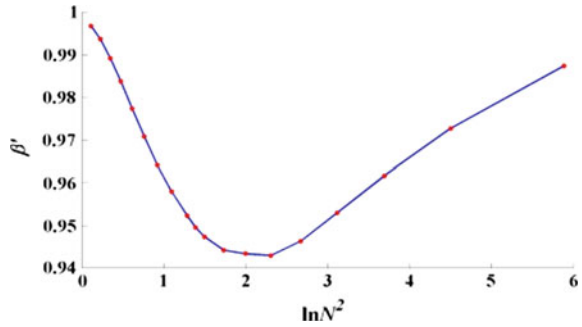
A ladder-type horn was also designed to evaluate the horn design, grouped with a bending vibration disc, to construct a compound vibrator of ultrasonic levitation. Through the measurements of levitation experiments, the applicability and availability of frequency correction method were verified.

The experimental ultrasonic transducer’s frequency was set as 20.000 kHz, the output diameter was  $D = 38$  mm (the two end diameters of horn were 38 mm and 20 mm respectively). The material of horn was applied with 45 carbon steel, the density  $\rho = 7850$  kg/m<sup>3</sup>, the Young modulus was  $E = 211$ GPa, Poisson ratio was  $\mu = 0.3$ . Based on the traditional design theory, the length of horn was calculated as  $l = \lambda/2 = 129.6$  mm. In the simulation experiment, the actual longitudinal resonant frequency was 18.936 kHz, the deviation with 20 kHz was 5.18%. After correcting the horn by the correctional formula (15), the correctional length was  $l^L = \beta^L l = 125.5$  mm, the longitudinal resonant frequency in simulation was corrected as 19.711 kHz, the deviation with 20 kHz decreased to 1.45%.

**Table 2** Comparison of simulated correctional coefficients and theoretical correctional coefficients

NO	1	2	3	4	5	6	7	8	9	10
$F'/\text{kHz}$	19.934	19.873	19.783	19.674	19.546	19.416	19.282	19.160	19.047	18.992
$\beta'$	0.9967	0.9937	0.9892	0.9837	0.9773	0.9708	0.9641	0.9580	0.9524	0.9496
$\beta^L$	0.9929	0.9919	0.9905	0.9887	0.9862	0.9826	0.9774	0.9696	0.9578	0.9495
$\delta$ (%)	0.38	0.18	0.14	0.51	0.91	1.22	1.38	1.21	0.57	0.1
NO	11	12	13	14	15	16	17	18	19	
$f'/\text{kHz}$	18.948	18.885	18.869	18.859	18.927	19.060	19.233	19.453	19.747	
$\beta'$	0.9474	0.9443	0.9435	0.9430	0.9464	0.9530	0.9617	0.9727	0.9873	
$\beta^L$	0.9390	0.9088	0.8590	0.7779	0.6529	0.4835	0.2969	0.1369	0.0345	
$\delta$ (%)	0.88	3.76	8.95	17.5	31.01	49.26	69.12	85.92	96.5	

**Fig. 4** The curve of  $\beta'$  versus  $\ln N^2$



A contrast experiment of acoustic levitation was implemented on the initial and correctional horns. The result showed that the horn after correcting was able to levitate a disc stably, but the one without correction was not. The experimental phenomenon were illustrated in Fig. 5.

## 6 Conclusion

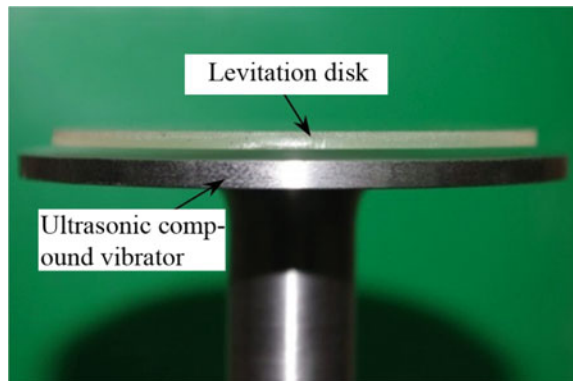
From the experimental results and theoretical analysis in the paper, the following conclusions can be drawn.

- (1) The factors causing the actual resonant frequency higher than the design frequency were analyzed. The main reason was that the horn transverse vibration was ignored while it vibrates longitudinally, which made the equivalent mass become smaller and the design resonant frequency increase.
- (2) The correctional frequency coefficient was also introduced and the formulas of ladder-type horn were deduced. The significance of frequency correcting was to make the design frequency satisfy with the actual frequency, uniformed the design frequency and actual frequency, improve the effectiveness of horn's working and decrease the energy loss in the transfers.

**Fig. 5** The phenomenon of levitation experiment



(a) The ultrasonic compound vibrator



(b) The levitating phenomenon

## References

1. Xiping H, Jie G (2006) A review of ultrasonic solid horn design. *Tech Acoust* 25(01):82–86 (in Chinese)
2. Zhao S, Wallaschek J (2011) A standing wave acoustic levitation system for large planar objects. *Arch Appl Mech* 123–139
3. Yanzhi S, Xiaojun C, Xiangchen L et al. (2011) The analysis and design of single ultrasonic transformer. *New Technol New Process* 26–28. (in Chinese)
4. Liqun W (2010) The influence of horn shape size change on the performance of ultrasonic longitudinal vibration. *Mach Des Manuf* 212–213. (in Chinese)
5. Shuyu L, Fucheng Z, Xiaowu G et al (1990) The frequency correction to the large cross section horns due to the lateral effect. *J Shanxi Normal Univ (Nat Sci Ed)* 1–34. (in Chinese)
6. Minhui W, Shanhui B, Changqing J (2004) Effect of cross-section area ratio between two ends of a step-bar ultrasonic transformer on the resonance frequency. *Tech Acoust* 242–245. (in Chinese)

7. Zhongmao L (1987) The principle and design of ultrasonic horn. Science Press, Beijing, pp 95–100. (in Chinese)
8. John WS, Baron R (1877) The theory of sound. The Cambridge University Press, London, pp 194–197
9. Guoliang F, Chongfu Y, Zhongmao L (1982) A new tool system for processing small deep hole by ultrasonic. Tech Acoust 2–7. (in Chinese)



# Influencing the Process Stability for Tapping Through and Blind Holes by Taps with Radial Lubricant Supply



Andreas Steininger, Anton Siller, and Friedrich Bleicher

**Abstract** The large number of drills and taps in automotive power train components make these processes to a considerable machining step. Due to the fact that hypoeutectic Al-Si alloys tend to adhere on the tool surface, the machinability of these alloys is challenging. In times of modern light-weight design, every gram counts. Therefore material, which is not necessarily needed, is removed from these components, designwise. One result of such steps is an increased number of clearance holes at the power train components. The requirements of short cycle times due to cost reasons induce the manufactures to machine blind holes and clearance holes with one tapping tool to reduce the non-productive time of tool changes. These tools normally have a centred internal coolant supply providing sufficient chip evacuation. Especially the adhesion of Al has a negative influence on the chip transportation and leads to an increase of stochastic inclinations of clogging the chip flute. In course of the present work, it is shown that this tendency increases when the chips are not properly flushed out of the flutes. Obviously this process instability increases when machining clearance holes by tools with a centred internal coolant supply. Sandvik also detected this problem and patented a tapping tool with a central bore and radial coolant channels for every flute in the area of the tool chamfer. According to this idea a tool was designed by finite element method for mechanical structure. Also fluid dynamic studies have been created to determine the lubricant flow. With prototypes of such a tapping tool, cutting tests were performed in Al-Si alloys compared to conventional tapping tools.

**Keywords** Tapping · Chip removal · Coolant supply

## 1 Introduction

The high number of required connecting components along the automotive power train components make internal thread tapping to one of the most demanding

---

A. Steininger (✉) · A. Siller · F. Bleicher  
Technical University of Vienna, Getreidemarkt 9/311, 1060 Wien, Austria  
e-mail: [steininger@ift.at](mailto:steininger@ift.at)

machining operations. If process instabilities occur, the result is usually a tool failure and the consequence is tap breakage. Due to the fact that the workpiece material encloses the tool, a fracture results in a clogged borehole with the broken tool consisting of hard material. From an economic point of view such an incident is a disaster as thread tapping operations are nearly amid the final machining processes. So there are two costly decisions to make: re-working or rejecting the work piece. Nevertheless many other issues are also associated with the process stability like the dimensional accuracy, thread form errors and surface roughness of thread forms. These failures are usually detected by the quality check after the machining or during the assembling.

The influence of the machine tools is in addition also to be considered. Here the synchronous interaction between the rotation of the spindle and the axial motion of the feed axis is fundamental [1]. Especially when the revolution speed and the feed rate decelerate, subsequently stop, and after that accelerate in the reverse direction. During this section of the process, the rotational speed and the feed rate have to be tuned accurately.

The importance of the knowledge about the tapping process fundamentals, which are related to the chip formation, the chip transportation and the tribological behaviour of the work-piece/tool system are rather complex. The chip formation itself is dependent on the number of cutting lands, the chamfer length/angle, the pitch, the rake angle and optionally the angle of helical flute. All these parameters entail that every chamfered cutting edge has a different nominal width of cut and also the radial diameter at the gate part is changing constantly with the pitch [1].

Moreover, the aspect of the machined material is also evident. The objective of this study is to determine the indicators for the process stability of the thread tapping process in hypoeutectic Al-Si alloys. Particularly Aluminium with its tendency of adhering at the cutting edge and the rake face is influencing the chip formation in a negative way, as due to an occurring build up edge (BUE) the cutting edge is not geometrically defined anymore [1]. Besides Aluminium is also responsible for so-called build up layers (BUL) in the rake face [4]. Here are also the tribological interactions between work piece material, tool material/coating and the metal fluid aspects responsible [5]. This fact is also influencing the chip transportation and evacuation in a stochastic manner, because chips can adhere to such BUL.

## 2 Tool Failures in Thread Tapping Processes

One major issue for designated tool failures is the chip evacuation. Previous studies have also indicated that clogged flutes are very common [6]. The chips are pressed in the flutes to a conglomerate and act like a barrier, which clamps the tool in the borehole. In the worst-case scenario, the tapping tool cannot resist and a tool breakage is the result.

This phenomenon leads in both major process steps, during the forward chip formation process (FCFP) as well as in the backward tool removing process (BTRP),

to tool breakages. During the FCFP the risk of clogging chip flutes increases with the borehole depth because the removed material is rising with the depth and if there is the tendency of clogged flutes, additional chips cause pressure against the affected lands until the critical load is exceeded. Throughout the BTRP the problem occurs directly after the change of the rotary motion of the spindle. The chip conglomerate runs the risk of being pinched between the lateral surface of the bore and the relief of the tool. In Fig. 1 such an incident is depicted (Fig. 2).

Apart from adhesion wear, another factor typically influencing process stability is the tribological wear. This phenomenon typical occurs at the flank and depends on the frictional conditions, hence on pressure as well as on the temperature between the tool and the workpiece. In previous studies, this effect was primarily related to thread forming [5], but it is also crucial in thread tapping because of the enclosed

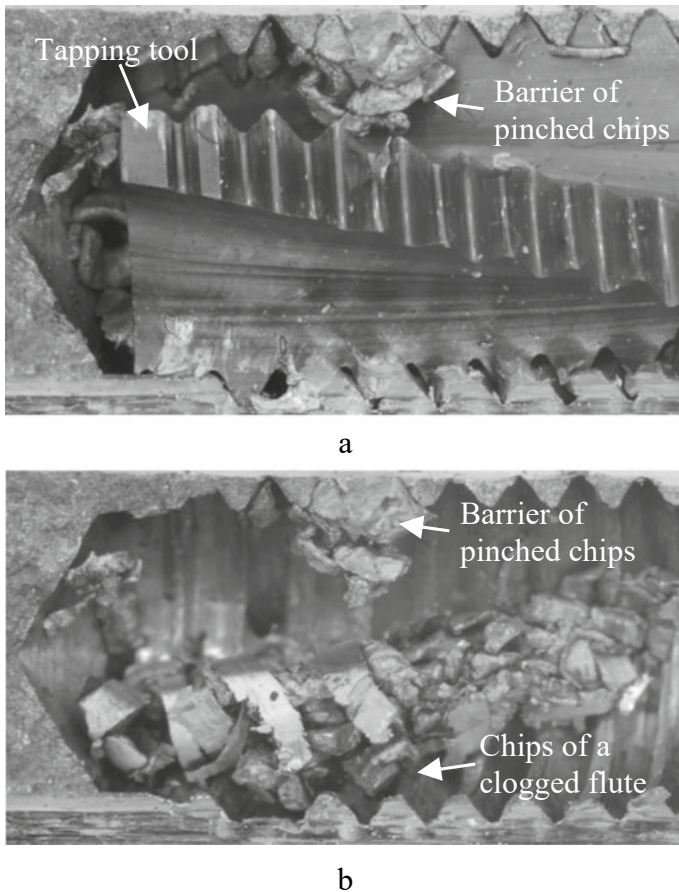
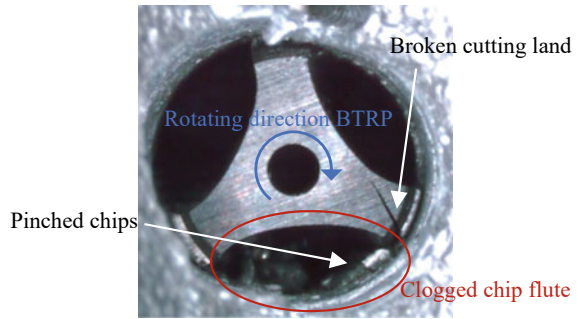


**Fig. 1** Sliced workpiece with tool failure, with **a** tapping tool and **b** removed tool

**Fig. 2** Broken tapping tool in a through hole



frictional interaction between the tool flank and the workpiece. Thus this process is in general sensitive towards the interaction of the tribological pairing [5].

Apart from application errors like inaccurate tool clamping, wrong borehole diameters/depths or machine codes, the clogged flutes are the reasons for tool failures.

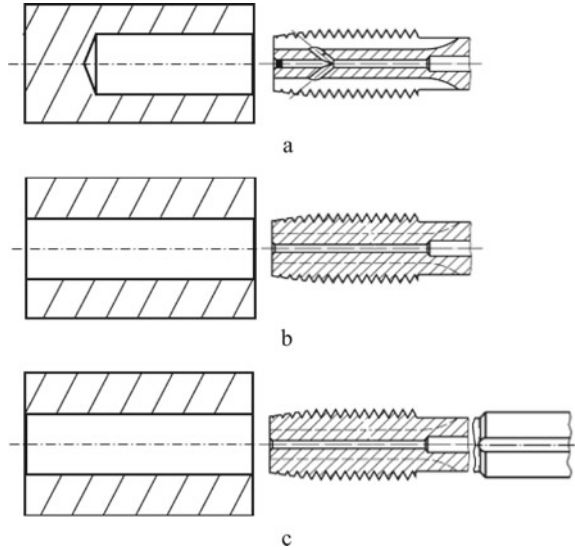
### ***2.1 Improved Tribological Interaction and the Chip Transportation in Tapping Through and Blind Holes***

There are several approaches to improve the interaction between the contact partners, namely the workpiece, the tool, the coating and the metalworking fluid (MWF). In previous works the interactions between MWF and tapping tools have been evaluated [5, 7]. Also several different coatings on HSS or tungsten carbide tools have been tested [1] and [2].

For through holes and blind holes there are different approaches to design tool geometry for tapping tools. On the one hand, for the through holes, spiral point taps with straight flutes are recommended. Here external nozzles provide the MWF supply. In addition, axial grooves along the tool shank or internal supply with radial outlets to flush the chips through the holes are common. On the other hand for blind holes the chips have to be evacuate in the opposite tool feed direction. Therefore, spiral flutes are applied and the MWF supply is realised by axial internal coolant holes.

All these cooling strategies show weaknesses when machining through holes and blind holes with one tool. Using spiral point taps is not satisfying as the removed chips are tempted into the blind hole (see Fig. 3a). Subsequently the chips will act as a barrier and as a consequence as a mechanical punch if the tap clearance is not long enough. By machining through holes with internal coolant supply there is no sufficient support of the fluid (see Fig. 3b) and with rising machining depths also the risk of tool failure increases. Therefore, it is very common to make a compromise and apply an internal coolant supply (axial) and additional grooves along the tool shank (see Fig. 3c). However, when machining through holes, this is also not very suitable because the MWF is not transported to the effective working area.

**Fig. 3** MWF supply **a** internal radial, **b** internal axial, **c** internal axial and grooves along the tool shank [8]



## 2.2 Improved Metalworking Fluid Supply for Tapping Through and Blind Holes

Supplying the effective working area with MWF is the aim in thread tapping to improve the process stability and the tool life. Sandvik also sees this as a fundamental aspect and thus they patented (Fig. 4) a tapping tool where the coolant flows out of the axially running cooling channel and is diverted radially outwards at a diversion element [9]. This provides an appropriate MWF supply for machining blind holes as well as for through holes.

Based on this patent and on the DIN 4000–80, tapping tools were designed to improve the coolant supply (Fig. 5). FEM and CFD simulations based on measurements of equivalent machining tests have evaluated the tools.

**Fig. 4** Patent form Sandvik with diversion element [9]

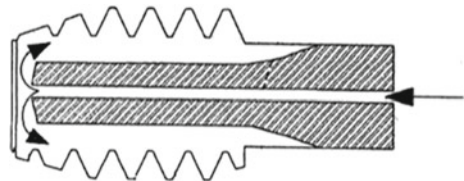
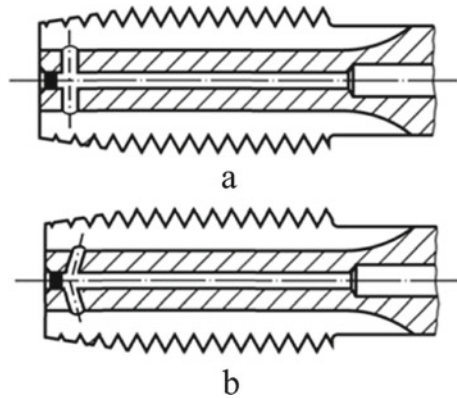


**Fig. 5** Tool with rectangular radial outlets (a), tool with inclined radial outlets (b)



### 3 Experimental setup

#### 3.1 Pre-experiments of Thread Tapping in Hypoeutectic Al-Si Alloy with a M6 Tungsten Carbide Tapping Tool

All experiments were performed on a horizontal milling machine (DMG-Mori NHX 9000) with a constant feed rate of 1 mm/rev and a cutting speed of 49 m/min. A rigid clamping chuck was used in order to avoid the damping of the effect of the feed force. This feed force ( $F_z$ ) and the forward/backward torque  $M_z$  were measured by a piezoelectric dynamometer with four 3-component force sensors (Type: Kistler 9129AA: X, Y, Z  $\pm$  10 kN). In Fig. 6 the so-called measurement workpiece can be seen.

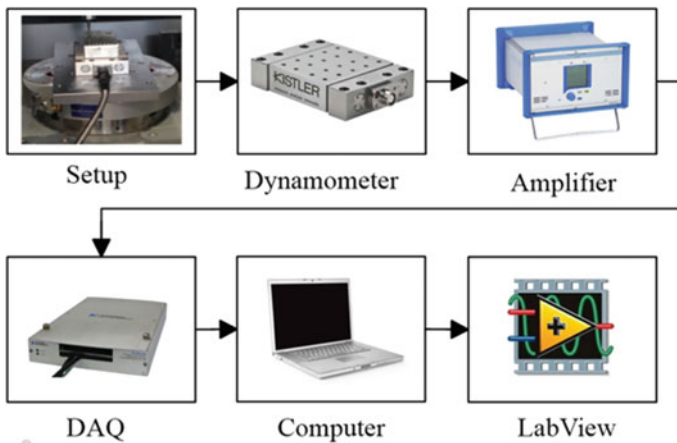
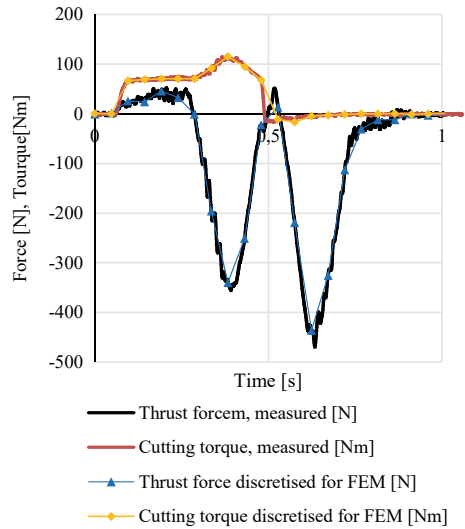


**Fig. 6** Measurement chain

**Fig. 7** Measurement of thrust force and cutting torque



In Fig. 7 a typical signal of the process forces is shown. The average cutting torque during the FCFP ranges between 0.7 and 1.2 Nm and the absolute values of the thrust force is between 400 and 500 N. These measured values are representative for a new tool. According to these measurement signals, a discretisation was performed to get the loading cases of the thrust force and the cutting torque for the following FEM simulation.

The tapping operations were conducted with internal MWF supply. Additionally, a measurement of the flow rate has also been performed, as can be seen in Fig. 8. Therefore, a tapping tool with an internal supply diameter of 1 mm was clamped in a chuck and the internal fluid supply was turned on with an adjusted capacity of the pump up to 30 bar. The mean value of the measured flow signal was around 1.66 L/min, as can be seen in Fig. 9.

In addition to the flow rate measurement, machining tests were made with different pumping capacities. Therefore the conventional tapping tool with internal coolant supply was used with the same parameters as in the pre-experiments. The main focus

**Fig. 8** Measurement of the flow rate



Flow sensor

Tool with 1 mm  $\phi$  of internal supply

**Fig. 9** Signal of flow sensor at 30 bar pumping capacity with

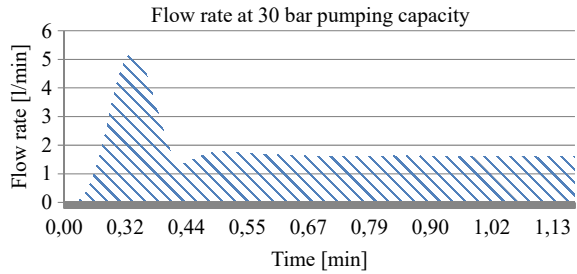


**Fig. 10** Chips dimensions with no MWF supply



here was also on the chip formation process and if the chip dimension relates to the flow rate. Thus the chips have been collected during the machining process and were analysed with a microscope. During the first setup no MWF supply was purchased. The following pumping capacities were designated at 20, 40 and 80 bar. According to the measurements the adjusted pumping capacities resulted in 1.19, 1.91, and 2.65 L/min of average flow rate (Fig. 10).

As it can be seen in Figs. 11, 12 and 13, no significant difference can be seen concerning the dimensions. The type of chips most often observed in the different experiments were the discontinuous chips. Additionally, also spiral-helical chips occurred when no MWF supply was provided.

### 3.2 FEM Simulation of Tapping Tools with Improved MWF Supply

For the FEM simulation the signals of the cutting force measurement have been discretised. Based on this evaluation two load cases have been defined. The first one is based on the measurements and is equivalent to the process forces using a new tool. The other load case represents a worn tool, therefore the discretised values have



**Fig. 11** Chips dimensions  
with MWF supply of  
1.19 L/min (20 bar)



**Fig. 12** Chips dimensions  
with MWF supply of  
1.91 L/min (40 bar)

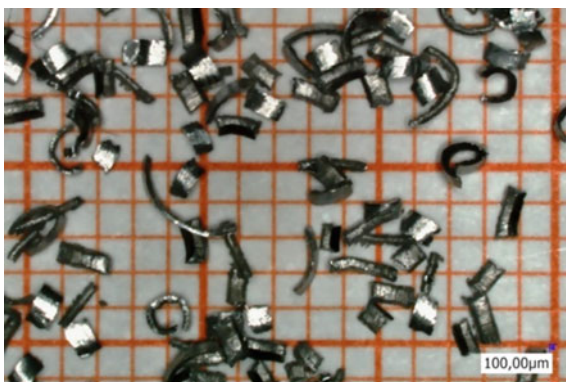


**Fig. 13** Chips dimensions  
with MWF supply of  
2.65 L/min (80 bar)



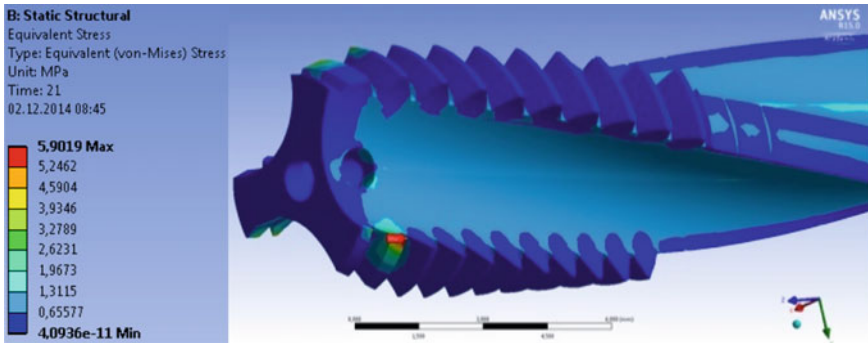


**Fig. 14** FEM simulation

been multiplied by the factor 1.3 according to the empirical analytical approach for the cutting force calculation from Victor and Kienzle [10]. The aim of the FEM simulation is predicting the behaviour of the adopted tool regarding realistic load cases, e.g. to determine the influence of the sectional weakening of the core diameter. Hence, several simulations with a variety of different positions of the radial outlets were calculated. The positions were displaced along the z-axis. In addition the angle of the chip flow in the rake face, depending on the rake angle  $\gamma_p$ , the angle of helical flute  $\gamma_f$  and the chamfer angle  $\kappa_r$  was considered that the outlets are not positioned directly where the chips are passing by.

To get realistic results of the FEM simulation, the contact width of the thrust force and the cutting torque were set equal to the depth of cut (Fig. 14).

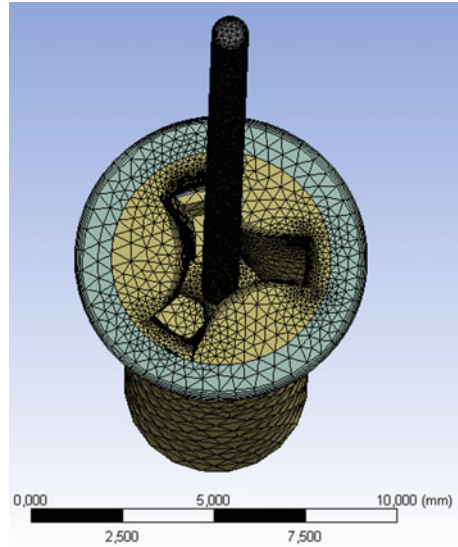
### ***3.3 CFD Simulation of Tapping Tools with Improved MWF Supply***

The diameter of the radial outlets were determined to provide the same flow rate of the MWF as the conventional M6 tapping tool and the applied axial coolant supply. In according to the FEM simulation the diameter of the coolant outlets were determined to guarantee the tool stability and the flow rate of 1.66 L/min (Figs. 15 and 16).

### ***3.4 Experiments of Thread Tapping of Through Holes and Blind Holes with M6 Tungsten Carbide Tapping Tools***

After the simulation and evaluation of the results two different types of the adopted coolant supply tools were manufactured. The radial outlets have been eroded with a

**Fig. 15** Control volume of CFD simulation with inflated mesh



electric discharge machining (EDM) drilling machine and the internal axial coolant was clogged at the tool tip, as the coolant flows out of the radial outlets. All experiments have been performed with the same process parameters as the pre-experiments mentioned in Sect. 2.1. For evaluating the process stability, the experiments were performed with conventional tapping tools and the tools with improved MWF supply. Each tool has to perform 1.100 threaded holes and the performances of the tools were compared.

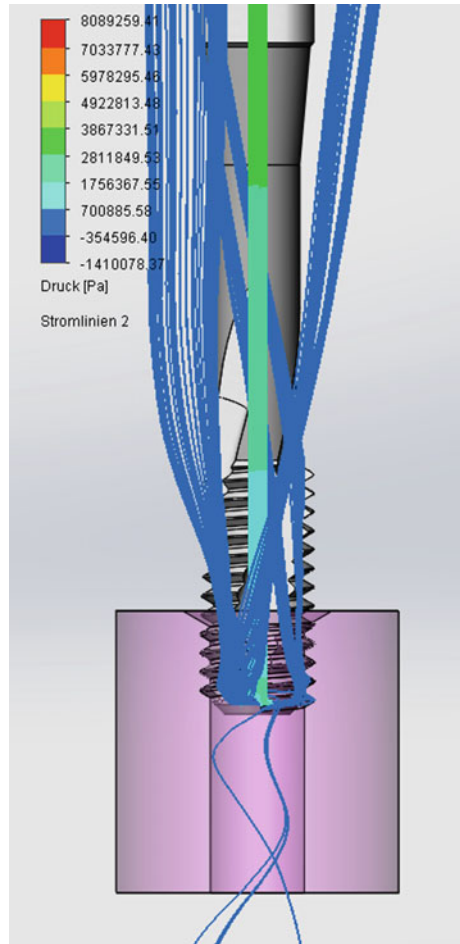
The rectangular workpiece was the same hypoeutectic Al-Si alloy as in the pre-experiments, with dimensions of  $370 \times 420 \times 30$  mm and two times 1.100 holes were arranged. In the first experiment setup tapping drill holes were arranged alternatingly, namely through holes were followed by blind holes. Thus, there were 50% blind holes and 50% through holes in one experimental setup.

The focus of the second experiment setup was shifted slightly to through holes. More specifically, three through holes were followed by one blind hole. Hence, there were 75% through holes and 25% blind holes in the second experimental setup.

## 4 Results and Discussion

In the first experimental setup, the distribution of through holes and blind holes was equal and so a tool had to perform 1.100 threads. The process was performed for all tools in the same conditions. In this first experimental stage both types of tapping tools performed without any conspicuousness. Thus all tools managed the quantity

Fig. 16 CFD simulation



of 1.100 taps with appealing quality. The machined threads were checked with a thread gauge (Fig. 17).

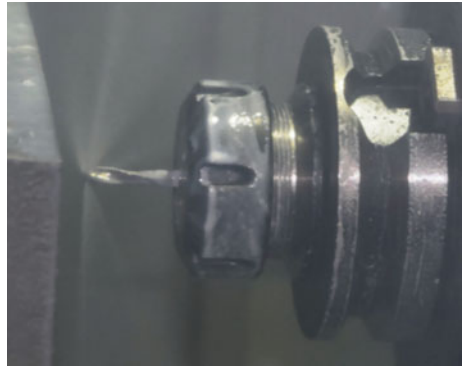
After the first experimental stage, the tools had to perform again 1.100 thread holes. The distribution of the thread holes and the blind holes was about 75–25%.

The conventional M6 tungsten carbide tapping tool with the axial coolant supply showed here process instabilities. The first conventional tool was able to perform 106 thread holes, thereupon a tool failure occurred. This incident encountered while machining a through hole. The experiment was re-performed with a new conventional tool. Here again a tool failure was observed after 506 thread holes. In addition, this failure also occurred during machining a through hole. The workpiece with the broken tools was analysed in the same way as in Fig. 2. Here also the reason for the tool failure was insufficient chip evacuation. The chips acted as a barrier the tool could not overcome and a broken tool was the result.

**Fig. 17** MWF supply is insufficient for through holes

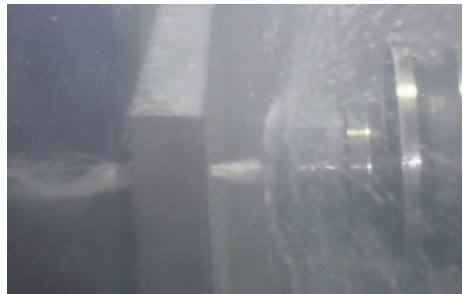


**Fig. 18** MWF supply with radial outlets



Subsequently, the machining test were performed with the tools with adopted MWF supply. Opposed to the conventional tapping tools both types of the adopted tools had no problems to perform the required quantity of 1100 thread holes. With respect to this performance, the argument for the adoption of the coolant supply is significant (Fig. 19).

**Fig. 19** MWF supply during machining with adopted tool



## 5 Conclusion

The influence of the process stability in thread tapping of through holes and blind holes has been investigated.

The following conclusions can be drawn from this study:

1. One major issue for tool failures is the chip evacuation. Clogged flutes are very common [6] and the chips are pressed in the flutes to a conglomerate and act as a barrier, which clamps the tool in the borehole. In the worst-case scenario, the tapping tool cannot resist and a tool breakage is the result.
2. If no MWF supply is purchased, spiral-helical chips occur in addition to the discontinuous chips. Apart from that, different flow rates or pumping capacities do not show a significant impact on the chip formation.
3. Machining through holes and blind holes is very challenging because the metal-cutting fluid supply needs to be sufficient for chip evacuation. Therefore a tool with adopted coolant supply is needed.
4. A tool with adopted coolant supply was designed. The demands for the tool stability and the coolant flow rate were simulated via FEM and CFD using empiric values, obtained by previous measurements.
5. The tool with adopted coolant supply showed outstanding performances in machining through holes and blind holes. Here the performance was, 50% higher than with conventional tools.

## References

1. Ahn JH, Lee DJ, Kim SH, Kim HY, Cho KK (2003) Effects of synchronizing errors on cutting performance in the ultra-high-speed tapping. *CIRP Ann Manuf Technol* 52:53–56. [https://doi.org/10.1016/S0007-8506\(07\)60529-0](https://doi.org/10.1016/S0007-8506(07)60529-0)
2. Steininger A, Siller A, Bleicher F (2015) Investigations regarding process stability aspects in thread tapping Al-Si alloys. In: 25th DAAAM International Symposium on Intelligent Manufacturing & Automation, Elsevier, ISSN: 1877-7058, S. 1124–1132
3. Bhowmick S, Lukitsch MJ, Alpas AT (2010) Tapping of Al-Si alloys with diamond-like carbon coated tools and minimum quantity lubrication. *J Mater Process Technol* 210:2142–2153. <https://doi.org/10.1016/j.jmatprotec.2010.07.032>
4. List G, Nouari M, Géhin D, Gomez S, Manaud JP, Le Petitcorps Y et al (2005) Wear behaviour of cemented carbide tools in dry machining of aluminium alloy. In: 15th international conference on wear materials, vol 259, pp 1177–1189. <https://doi.org/10.1016/j.wear.2005.02.056>
5. Fromentin G, Bierla A, Minfray C, Poulachon G (2010) An experimental study on the effects of lubrication in form tapping. *Tribol Int* 43:1726–1734. <https://doi.org/10.1016/j.triboint.2010.04.005>
6. Elgallad EM, Samuel FH, Samuel AM, Doty HW (2010) Machinability aspects of new Al-Cu alloys intended for automotive castings. *J Mater Process Technol* 210:1754–1766. <https://doi.org/10.1016/j.jmatprotec.2010.06.006>
7. Srivastava AK, Finn ME, Kinney MA (2004) Tool/work material/cutting fluid interaction while tapping into AA-319 and AA-A356 T6 lost foam aluminum castings, vol 32, pp 263–270

8. Emuge-Werk Richard Glimpel (Lauf P. Handbuch der Gewindetechnik und Frästechnik: Anwendungen, Tipps, Tabellen (2004) Publicis Corporate Publ., Erlangen
9. Giessler Josef. Patent DE10246871A1—Gewindewerkzeug mit Kühlmittelzufuhr Thread tool with coolant supply—Google Patente 2004. <http://www.google.com/patents/DE10246871A1?cl=en&hl=de>. Accessed 14 Nov 2014
10. Tschätsch H, Dietrich J (2008) Praxis der Zerspantechnik: Verfahren, Werkzeuge, Berechnung; mit 148 Tabellen. Vieweg + Teubner, Wiesbaden

# On Deposition and Characterisation of TiN-WS<sub>2</sub> Composite Coating and Its Performance Evaluation in Dry Machining of AISI 1060 Steel



T. Banerjee and A. K. Chattopadhyay

**Abstract** Hard-lubricious composite coating consisting of hard TiN phase and soft lubricious WS<sub>2</sub> phase were deposited with a hard TiN under layer on steel discs, high speed steel blocks and ISO K10 grade tungsten carbide inserts. For comparison, pure TiN coatings were also deposited on the same substrates. Pulsed DC Closed Field Unbalanced Magnetron Sputtering was employed for the deposition of the coatings. The coatings were characterised with energy dispersive X-ray microanalysis, grazing incidence X-ray diffraction, field emission scanning electron microscopy, scratch adhesion test, nanoindentation test and pin-on-disc tribological test. The multilayered coating consisting of TiN-WS<sub>2</sub> top layer with TiN under layer showed greater adhesion with the substrate and less friction coefficient as compared to pure TiN coating. The machining test conducted on AISI 1060 steel revealed that the tool coated with TiN-WS<sub>2</sub> composite coating with TiN under layer exhibited the least cutting forces (axial, radial and tangential components) not only in comparison to the uncoated carbide tool but also in comparison to the TiN coated tool in the experimental cutting speed domain of 30–230 m/min because of the lubricious action of the WS<sub>2</sub> phase present in the top TiN-WS<sub>2</sub> layer. Tool life tests conducted at the highest cutting velocity of 230 m/min with feed of 0.2 mm/rev and depth of cut of 2 mm also revealed the superior performance of the (TiN-WS<sub>2</sub>) on TiN coated tool as the multilayer coating could effectively slow down the growth of crater and flank wear respectively by facilitating easier sliding of chip over the tool rake surface and generation of lesser tangential cutting force.

**Keywords** TiN-WS<sub>2</sub> composite coating · Tribological test · Dry machining

---

T. Banerjee (✉) · A. K. Chattopadhyay  
Department of Mechanical Engineering, Indian Institute of Technology Kharagpur, Kharagpur,  
West Bengal 721302, India

T. Banerjee  
Department of Production & Industrial Engineering, National Institute of Technology  
Jamshedpur, Jamshedpur, Jharkhand 831014, India



## 1 Introduction

Currently a great deal of research is being conducted worldwide towards achieving dry machining in order to gradually do away with the use of coolants and lubricants which contain environmentally hazardous materials. Survey carried out at the German Automotive Industry suggest that the cost associated with procurement, set-up establishment, maintenance, monitoring, post-treatment and disposal of liquid lubricants range in between 7 and 17% of the total manufacturing cost which largely overshadows the tooling cost estimated to be around 2–4% [1]. However, the coolants and lubricants play vital roles of removing the heat generated during machining thereby reducing cutting zone temperature and also facilitate lubrication at the chip-tool interface. The cooling and the lubricating action improve the tool life and also allow increasing the cutting velocity and thereby material removal rate which directly affects the productivity. Therefore, any attempt to minimize or remove the use of coolants and lubricants should address alternative means of performing the functions meant for them. One such means is the use of coated cutting tools with in-built solid lubricating provision.

MoS<sub>2</sub> or WS<sub>2</sub> are widely acknowledged for their solid lubricating behavior. However, their susceptibility to atmospheric moisture and oxidation coupled with their poor mechanical properties like low hardness and poor adhesion to the substrate restrict their application in severe mechanical application domains like dry machining. Though, improvements in structural and mechanical properties of such coatings have been achieved through addition of different metals like Ti, Cr, Au, Ag, Zr etc. [2, 3], yet the application of such composite coatings has been mainly limited to drilling and milling which utilize low cutting velocities and therefore encounter low cutting temperatures [4]. Some researchers also explored the machining performance of such composite coatings like MoS<sub>2</sub>-Zr, WS<sub>2</sub>-Zr in dry turning and encouraging results were reported [5]. Recent trend has been to prepare composite films by co-deposition of soft lubricious MoS<sub>2</sub> or WS<sub>2</sub> into hard ceramic matrices like TiN, TiB<sub>2</sub>, CrN etc. [6]. The hard matrix will provide abrasive wear resistance while the soft inclusions will provide lubricious effect. Significant improvement in mechanical and tribological properties of such hard-lubricious films as compared to pure ceramic films has been reported by researchers and therefore they stand as promising candidates as coatings for dry turning. Addition of hard ceramic under layers like TiN, DLC can further augment the performance of the top composite hard-lubricious layer by increasing its load bearing capacity [6]. The present work reports on the deposition, characterisation and machining performance of TiN-WS<sub>2</sub> composite coating with a hard TiN under layer and the comparison of its machining performance with uncoated and pure TiN coated tools.

## 2 Experimental Methods and Conditions

Two different coating architectures S1 and S2 as represented in Table 1 were deposited on AISI 1040 steel discs (25 mm diameter and 8 mm thickness), M2 grade HSS blocks (10 mm × 10 mm × 25 mm) and ISO K10 grade tungsten carbide inserts with nominal geometry of SNMA 120408. Before deposition, the steel discs and HSS blocks were polished to obtain a surface finish of Ra = 50 nm or better. The steel discs were used for tribological tests and the HSS blocks were used for other physical and mechanical characterisations. Before loading into the deposition chamber, the substrates were thoroughly cleaned with 1 N NaOH solution, rinsed with deionised water, dehumidified with isopropyl alcohol and finally dried with hot air blast. A closed field unbalanced magnetron sputtering system with twin cathode configuration was used for the deposition of the coatings. The system consisted of one Ti target and one WS<sub>2</sub> target. The targets had dimensions of 254 mm × 127 mm × 12 mm and had a purity of 99.9%. The system was initially pumped down to a base pressure of approximately 1 × 10<sup>-3</sup> Pa with the help of a diffusion pump backed by a roots pump and a rotary pump. The targets as well as the substrate were powered with the help of three pulsed DC power supply units (Advanced Energy Pinnacle Plus) having maximum power capacity of 5 kW each. The targets were operated in the ‘current regulation’ mode and the substrate was operated in the ‘voltage regulation’ mode. Argon and Nitrogen were respectively used as the sputtering and reactive gases and were flown in at 15 sccm and 11.5 sccm respectively for both S1 and S2 coating architectures. The process started with the sputter cleaning of the targets with the shutters in the closed condition. This was followed by Ti-ion etching of the substrates with pulsed (200 kHz, 80% ON) bias of – 500 V and Ti cathode current of 1 A (200 kHz, 80% ON) for removing the oxide impurities. Then a Ti interlayer of about 250 nm thickness was deposited to improve film-substrate adhesion and minimization of residual stresses. The Ti cathode current was set to 5 A (200 kHz, 60% ON) during deposition of TiN for both S1 and S2 while the WS<sub>2</sub> cathode current was set to 0.1 A (100 kHz, 60% ON) for deposition of the top layer of TiN-WS<sub>2</sub> in coating architecture S2. A substrate bias of – 50 V (200 kHz, 60% ON) was maintained during the entire deposition duration. All the depositions were carried out at a process pressure of 0.3 Pa and process temperature of 200 °C.

**Table 1** Different coating architectures

Specimen code	Coating architectures
S1	TiN
	Ti adhesion layer
	Substrate
S2	TiN-WS <sub>2</sub>
	TiN
	Ti adhesion layer
	Substrate

The surface morphology and the cross sectional structure of the coatings were observed with a Field Emission Gun Scanning Electron Microscope (Carl Zeiss, Supra 40) equipped with Energy Dispersive X-Ray Analyzer (20 keV) which was used for the analysis of the chemical composition of the coatings. The crystalline structure of the coatings were studied with X-ray diffraction in grazing incidence mode (Philips, PANalytical PW 3040/60 X'Pert PRO instrument) with Cu K $\alpha$  (45 kV, 40 mA) radiation of 0.15418 nm wavelength at an incident angle of 2°. The GIXRD profiles were later analysed with X-pert Hi-Score software and peaks were identified by comparing with Joint Committee on Powder Diffraction Standards data files.

The adhesion of the coatings deposited on polished M2 grade HSS blocks were evaluated with the help of a Scratch Adhesion Testing Machine (TR-101 M5, DUCOM) equipped with a Rockwell C diamond stylus of 0.2 mm tip radius. During scratch testing, the normal load was continuously increased from 10 to 80 N with a loading rate of 5 N/mm. The software WINDUCOM 2004 coupled with the instrument enabled the visualization of the variation of the friction force with scratch length and normal load. The sudden increase in the friction force represented the failure of the coating and the corresponding normal load was considered the critical load (Lc<sub>3</sub>). However, for verifying the exact location as well as the nature of failure, the scratch tracks were later observed with optical microscope (ZEISS AxioCam ERc5s Inverted Metallurgical Microscope).

The hardness of the coatings deposited on polished M2 grade HSS substrates were measured with a nanoindenter (TI950 Tribonanoindenter, Hysitron Inc., Minnesota, MN, USA) fitted with a Berkovich probe of 50 nm approximate tip radius. A peak load of 8 mN and loading–unloading time of 10 s each were set during the measurements. The hardness of the coatings was later calculated from Oliver-Pharr method.

The tribological properties of the coatings were evaluated through pin-on-disc test in a tribometer (CSM instruments) at 25–30 °C and 50 ± 5 relative humidity. A bearing steel ball (AISI 52100) of 6 mm diameter was used as the counter body. The tests were done using a normal load of 10 N, sliding velocity of 10 cm/s and for a fixed sliding distance of 700 m.

The performance of the different coated and uncoated turning inserts was evaluated during turning of AISI 1060 steel. All the turning tests were carried out in a heavy duty lathe (Make: Hindustan Machine Tools (HMT) Ltd., Bangalore, India; Model: NH22) fitted with variable spindle drive. The experimental conditions for turning test are summarized in Table 2.

During the turning tests, the cutting velocity was varied through four steps viz. 30, 77, 130 and 230 m/min, with a constant feed of 0.2 mm/rev and depth of cut of 2 mm in order to find out the effect of cutting velocity on cutting forces for the uncoated and coated tools. Each machining run was conducted for 10 s during which three components of the cutting force namely axial force (P<sub>x</sub>), radial force (P<sub>y</sub>) and tangential force (P<sub>z</sub>) were measured with a three component piezo-electric type dynamometer (Make: Kistler Instruments AG, Switzerland; Type: 9257B), charge amplifiers (Model: 5015A 1000) and digital oscilloscope. After 10 s of machining, the condition of rake and principal flank surfaces of the inserts were examined using optical microscopy (SZ 1145TR PT Zoom Stereo microscope, Olympus). The built up

**Table 2** Details of work material, cutting tools and machining conditions

Workpiece material	AISI 1060 steel C-0.58, Mn-0.65, S-0.036, P-0.026 with rest Fe
Inserts used	(i) Uncoated tungsten carbide insert of ISO K10 grade, WC + 6% Co (insert T0) (ii) TiN coated T0 (insert T1) (corresponding to coating architecture S1) (iii) (TiN-WS <sub>2</sub> ) on TiN coated T0 (insert T2) (corresponding to coating architecture S2)
Insert designation	SNMA 120408
Tool geometry (ORS)	– 6°, – 6°, 6°, 6°, 15°, 75°, 0.8 mm
Cutting velocity (m/min)	30, 77, 130, 230
Feed (mm/rev)	0.2
Depth of cut (mm)	2
Environment	Dry

material on the rake surface of the tool was then chemically dissolved using a solution of conc. H<sub>2</sub>SO<sub>4</sub> and deionised water (ratio of 1:10 by volume respectively) followed by rinsing with deionised water and dehumidification with isopropyl alcohol. The rake and flank surface of the inserts were again examined using optical microscopy in order to have a clear view of the degree of wear on the different coated and uncoated tools. Further, tool life tests for the uncoated tool T0 and the coated tools T1 and T2 were conducted at the highest cutting velocity of 230 m/min, feed of 0.2 mm/rev and depth of cut of 2 mm.

### 3 Results and Discussion

#### 3.1 Chemical Composition

The chemical composition of the coatings as obtained from EDAX analysis is presented in Table 3. It can be seen that pure TiN coating corresponding to coating architecture S1 was almost stoichiometric. However, it has been observed that co-deposition of TiN and WS<sub>2</sub> in the top layer of the coating architecture S2 resulted in severe depletion of sulphur thereby yielding a S/W at.% ratio of only 0.4. Such

**Table 3** EDAX analysis of coating architectures S1 and S2

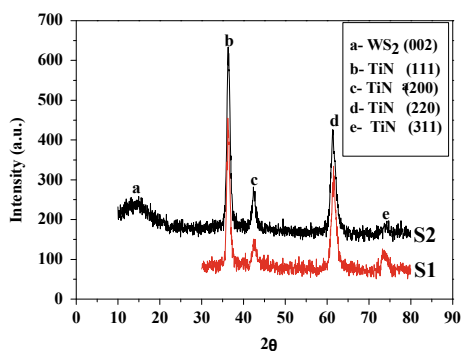
Specimen code	Atomic percentage				
	Ti	N	W	S	S/W
S1	49.7	50.3	–	–	–
S2	48.2	48.6	2.3	0.9	0.4

depletion of sulphur from the film has been observed by many researchers and has been attributed to a number of factors like different sputtering rates of tungsten and sulphur when sputtered from a compound target, different degree of scattering in the gas phase, different sticking co-efficient during film growth, presence of reactive gases like  $N_2$ ,  $CH_4$  which hinders the total combination of W and S and finally preferential re-sputtering of sulphur from the growing film due to energetic particle bombardment [7, 8]. Literature also suggest that pulsed DC sputtered  $MoS_2$  or  $WS_2$  coatings exhibit lower S/Mo or S/W ratio as compared to those produced through RF or DC sputtering [7]. The reason may be attributed to the enhanced ionization of the plasma during pulsed DC operation resulting in bombardment of high energetic  $Ar^+$  ions on the growing film and subsequent re-sputtering of sulphur. The application of pulsed substrate biasing which aims to draw more ion current toward the substrate for obtaining denser coating growth also augments such re-sputtering of sulphur which is the case in the present work. However, it has been reported that despite a very low S/Mo or S/W ratio, the pulsed DC sputtered  $MoS_2$  or  $WS_2$  films exhibited prominent orientation of the (002) basal plane which is beneficial for obtaining good tribological performance [3, 9].

### 3.2 Structure

Figure 1 shows the GIXRD spectra of the monolayer TiN coating (S1) and the multilayer ( $TiN-WS_2$ ) on TiN coating (S2). Both the coating architectures showed crystalline planes of TiN namely (111), (200), (220) and (311) and (111) was the preferred orientation in both the cases. For the multilayer coating (S2), the presence of the (002) basal plane of  $WS_2$  phase along with the crystalline peaks of TiN suggest co-existence of both  $WS_2$  and TiN as separate entity in the composite matrix. For composite coating like  $TiN-MoS_2$  some authors have suggested the segregation of Mo and S in the composite matrix and no separate  $MoS_2$  phase could be detected [10, 11]. The presence of  $WS_2$  as a separate phase in the basal orientation may be more important for achieving good tribological properties.

**Fig. 1** GIXRD spectra of coatings architectures S1 and S2



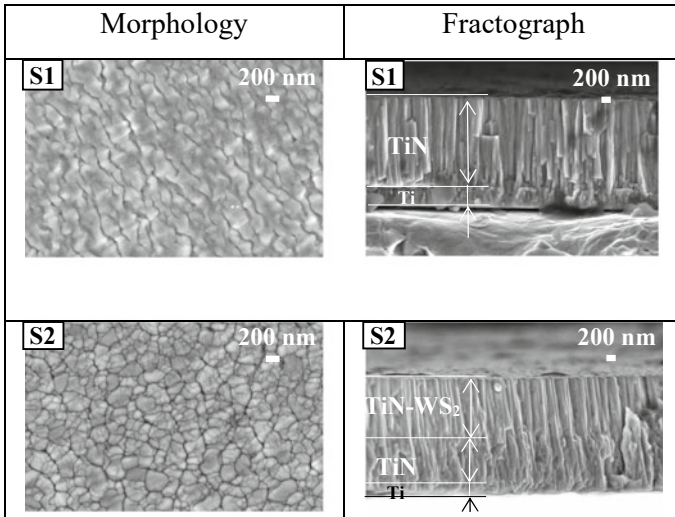


Fig. 2 Surface morphology and cross sectional structure of coating architectures S1 and S2

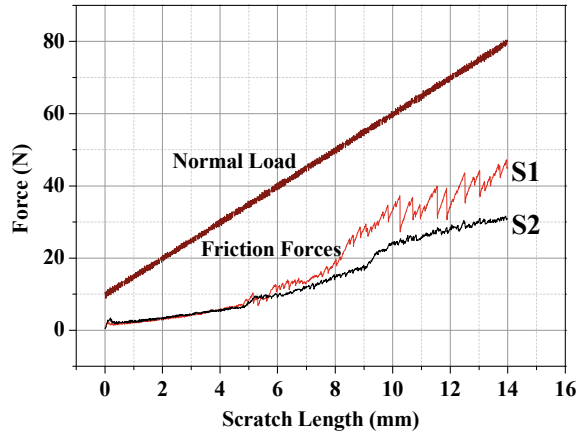
### 3.3 Study of Morphology and Cross-Section of the Coatings

Surface Morphology and cross-sectional structure (fractograph) of the two different coating architectures are presented in Fig. 2. Coating S1 i.e. pure TiN coating showed elongated agglomerated grains. The TiN coating fractograph showed closely packed dense columnar structure. Coating S2 represents a bi-layer coating, which can be clearly observed from the cross sectional structure of architecture S2. The bottom layer is a pure TiN coating which acts as a hard supporting layer for the top composite layer consisting of TiN and WS<sub>2</sub> phases. Co-deposition of WS<sub>2</sub> with TiN refined the grain size as compared to pure TiN which is clearly revealed from the morphologies of S1 and S2. Such reduction in grain size due to co-deposition has also been reported in the literature for composite coatings like TiN-MoS<sub>2</sub>, CrB<sub>2</sub>-MoS<sub>x</sub> composite coatings and has been attributed to the competitive growth of hard (TiN, CrB<sub>2</sub>) and soft (MoS<sub>2</sub>) phases in the composite matrix [12, 13].

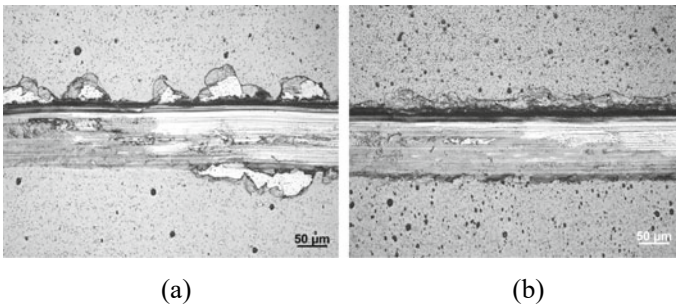
### 3.4 Scratch Adhesion Test

Figure 3 shows the representative plots for variation of friction forces along with increase in normal force for the two different coating architectures. The sudden rise of the friction indicates failure of the coating from the middle of the scratch track and the corresponding normal load is known as the critical load (L<sub>C3</sub>). Monolayer TiN coating (S1) showed an average critical load (L<sub>C3</sub>) of 47 N while the multilayer coating (TiN-WS<sub>2</sub>) on TiN coating showed an average critical load (L<sub>C3</sub>) of 55 N.

**Fig. 3** Representative plots for variation of friction forces with normal load during scratch testing of coating architectures S1 and S2

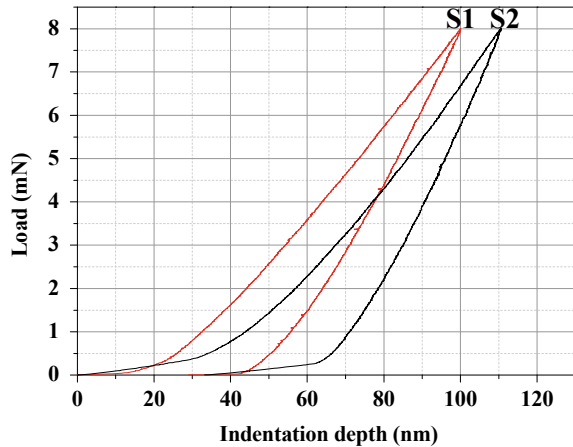


Increase in adhesion strength of such duplex coating system compared to single layer hard coating was also observed by other researchers and was attributed to the development of low tensile stress and low shear stress at coating surface and coating-substrate interface respectively [14]. Figure 4 shows the optical images of the failure zones of the scratch tracks for the two coating architectures. It may be observed that severe coating delamination occurred around the edges of the scratch track near the failure zone for coating S1 indicating high brittleness of the ceramic TiN film. However, such delaminations were significantly reduced for the multilayer coating S2 possibly because the soft  $WS_2$  phase present in the top TiN- $WS_2$  layer could restrict the propagation of cracks.



**Fig. 4** Optical images of failure zones of scratch tracks for **a** coating S1 and **b** coating S2

**Fig. 5** Representative loading–unloading plots obtained from nanoindentation measurements for coating architectures S1 and S2



### 3.5 Nanoindentation Test

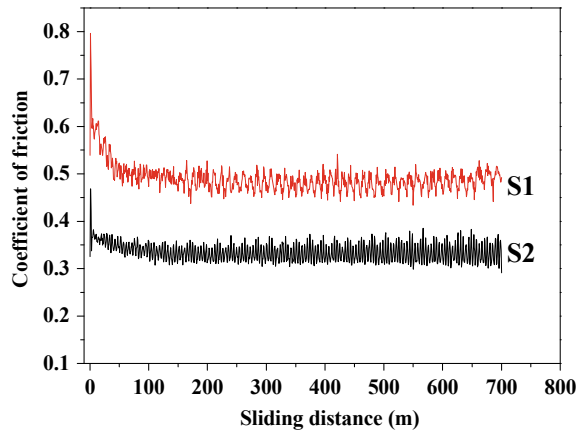
The representative loading–unloading curves obtained from nanohardness measurements of the coatings S1 and S2 are presented in Fig. 5. Fifteen indentations were taken for each sample and in each case, the depth of indentation was less than 1/10th of the total coating thickness in order to minimize the effect of substrate hardness. The nanohardness of TiN coating (S1) was found to be 29 GPa which conforms well to the mostly reported values in literature. Addition of soft WS<sub>2</sub> phase to hard TiN phase decreased the nanohardness of the multilayer coating to 25 GPa due to the formation of a composite matrix of hard and soft phases [12].

### 3.6 Pin-on-Disc Tribological Test

The variation of coefficient of friction with sliding distance for the two coating architectures are presented in Fig. 6. The friction coefficient profiles of both the coatings showed an initial running in period up to an approximate sliding distance of 50 m after which a steady state value was reached which continued up to the end of the tribological test. The running in period can be attributed to gradual smoothing of the asperities present both in the coatings and the counter-body. Once the asperities get leveled out, the friction drops and attain a steady state value. Monolayer TiN coating (S1) showed a steady state friction coefficient of 0.5. High fluctuations in friction coefficient were noticed in this case. However, the multilayer coating (TiN-WS<sub>2</sub>) on TiN (S2) showed a lesser steady state friction coefficient of 0.35 because of the presence of soft lubricious WS<sub>2</sub> in the top layer. The fluctuations in friction coefficient were also reduced in this case. Both the coatings did not undergo any failure up to the maximum test limit of 700 m.



**Fig. 6** Variation of friction coefficient with sliding distance for coating architectures S1 and S2



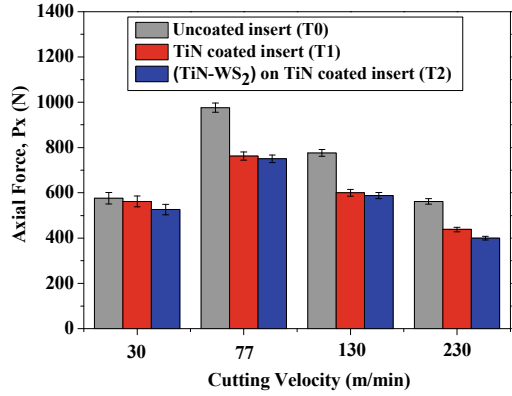
### 3.7 Machining Performance Test

Figure 7 shows the nature of variation of different components of cutting force with increase in cutting velocity ( $V_c$ ). Increase in cutting velocity causes an increase of rate of shear strain of the work material as well as an increase in the shear zone temperature. These two have opposing effects on the shear strength of the work material. The increase in the shear strain rate increases the shear strength of the work material while the increase in shear zone temperature tends to soften the work material thereby reducing its shear strength. When the cutting velocity was increased from 30 to 77 m/min, the increment in shear strain rate possibly had a dominating effect over the shear zone temperature increment which resulted in an increase in all the components of the cutting forces. With further increase in cutting velocity from 77 up to 230 m/min, the softening of the work material due to temperature rise had a dominating effect over the shear strain rate effect which resulted in subsequent drop in all the cutting forces. The change in cutting velocity from 30 to 77 m/min also changed the nature of chip formation from discontinuous chips to continuous chips which in turn changed the nature of contact at the chip-tool (insert) interface from intermittent short length contact to continuous bulk contact (Fig. 8a and b). Such long and bulk contact promoted high friction at the chip-tool contact zone which also participated in increasing the cutting forces.

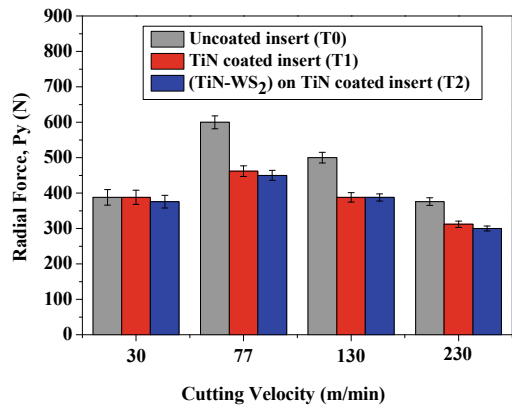
TiN coating, known for its wear-resistance and anti-welding property against steel played its role in reducing the cutting forces at all cutting velocities. Addition of  $WS_2$  to TiN further reduced the cutting forces because of its lubricious property as evident from Fig. 7.

Figure 9 shows the images of the rake surfaces of the cutting tools after 10 s of dry machining at different cutting velocities and Fig. 10 shows the corresponding images after removal of built up material by acid solution. It can be seen from Fig. 9 that at lowest cutting velocity i.e. 30 m/min, material built up occurred on the rake surface of the uncoated tool T0. The amount of built up material was much lesser when

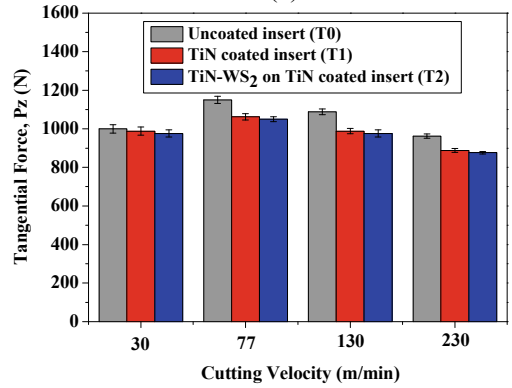
**Fig. 7** Variation of **a** axial force ( $P_x$ ), **b** radial force ( $P_y$ ) and **c** tangential force ( $P_z$ ) with cutting velocity ( $V_c$ )



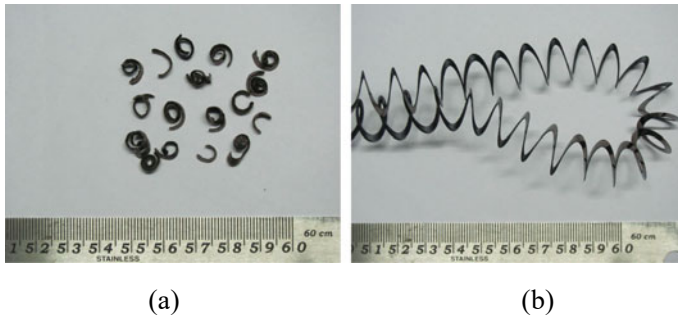
(a)



(b)



(c)

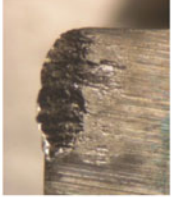
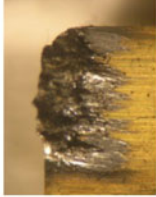
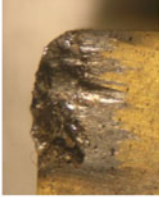








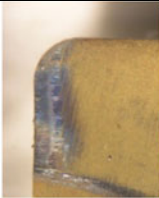


**Fig. 8** Nature of chips produced by the uncoated insert at cutting velocity of **a** 30 m/min and **b** 77 m/min

machining was conducted at higher cutting velocities viz. 77, 130 and 230 m/min. However, the increase in cutting velocity led to formation of crater on the rake surface of uncoated tool T0 which progressively increased with the cutting velocity. The growth of crater wear with increase in cutting velocities can be attributed to the increase in chip-tool interface temperature which promotes diffusion of carbon from the tool to the chip.

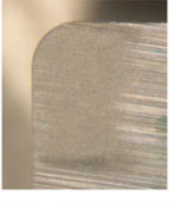
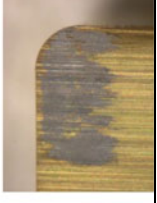


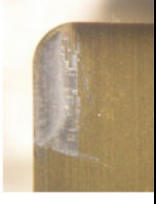


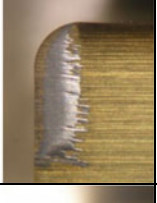
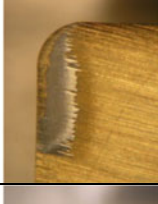



It can be also noticed from the cleaned rake surfaces of uncoated tool T0 in Fig. 10, as the cutting velocity increased, the length of the sliding mark of the chip on the tool decreased which indicates a reduction in chip-tool contact length. It may be attributed to the chip curling effect which occurs because of large difference in temperature between the bottom and the top surfaces of the sliding chip. Though TiN coating is well known for its anti-welding property against steel, yet in the present case, it could not prevent the built up of material on the rake surfaces of the tool T1 when machining was conducted at lowest cutting velocity of 30 m/min. After removal of built-up material, it was revealed that the coating was partially removed from the chip-tool contact zone (Fig. 10). At the lowest cutting velocity of 30 m/min, fluctuation of force occurred because of formation of short discontinuous chips which led to the fracture of the coating at the rake surface. Work material therefore deposited on those regions where coating got removed. The same phenomenon prevailed also for the multilayered tool T2. However, the wear resistance of the coated tools (T1 and T2) as compared to the uncoated tool (T0) was revealed as the cutting velocity was progressively increased. For both the coated tools (T1 and T2), the crater wear at higher cutting velocities was much lesser as compared to the uncoated tool T0 as evident from Figs. 9 and 10. The multilayered tool T2 also outperformed the TiN coated tool T1 in terms of resistance against crater wear formation when machining was done at 130 and 230 m/min.

In order to estimate the relative wear resistance of the tools T0, T1 and T2, the machining tests were prolonged at the highest cutting velocity i.e. 230 m/min. Optical images in Figs. 11 and 12 show the crater and flank wears respectively for the different tools with machining duration. Crater and flank wear started growing on the uncoated carbide tool T0 at a very rapid rate and after 30 s of machining, large size worn area

Cutting Velocity (m/min)	Condition of rake surface		
	Uncoated (T0)	TiN coated (T1)	(TiN-WS <sub>2</sub> ) on TiN coated (T2)
30			
77			
130			
230			





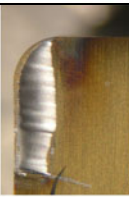


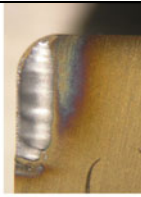
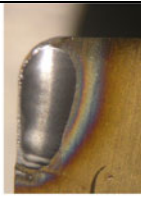
**Fig. 9** Optical images of the rake surface of uncoated and different coated turning inserts after machining for 10 s with different cutting velocities

appeared on the rake surface. The uncoated tool was withdrawn from machining test at the end of 30 s as the average flank wear reached approximately 300 μm (Fig. 12). Both the coated tools T1 and T2 performed much better than the uncoated tool T0 in terms of resisting the growth of both crater and flank wear. However, the tool T2 performed better than the tool T1 as evident from the corresponding micrographs in Figs. 11 and 12. The TiN coated tool T1 failed at the end of 90 s due to wear of the rake and flank and plastic deformation of the principal cutting edge. The (TiN-WS<sub>2</sub>)

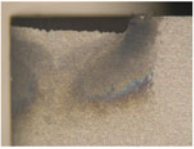
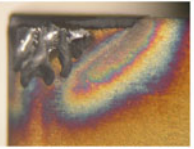
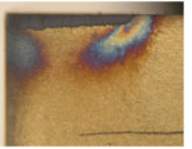
Cutting Velocity (m/min)	Condition of rake surface		
	Uncoated (T0)	TiN coated (T1)	(TiN-WS <sub>2</sub> ) on TiN coated (T2)
30			
77			
130			
230			

**Fig. 10** Optical images of the rake surface of uncoated and different coated turning inserts after machining followed by removal of built up material

on TiN coated tool T2 outperformed the tool T1 as machining could be continued further up to 130 s until the flank wear reached approximately 300 μm. There is scope of further improving the performance of both the coatings by incorporating micro-blasting to the carbide substrates before deposition. Optimization of the target pulsing frequency and duty cycle during sputtering is also important because they play major roles in deciding the stress near the cutting edge, critical for edge retention of the coating and preventing any undesirable flaking.

Machining Duration (s)	Condition of rake surface		
	Uncoated (T0)	TiN coated (T1)	(TiN-WS <sub>2</sub> ) on TiN coated (T2)
10			
30	 Tool life over		
90		 Tool life over	
130			 Tool life over

**Fig. 11** Optical images of the rake surfaces of uncoated and different coated turning inserts after different durations of machining at cutting velocity of 230 m/min

Condition of principal flank surface		
Uncoated (T0)	TiN coated (T1)	(TiN-WS <sub>2</sub> ) on TiN coated (T2)
		
Tool life over after 30 s	Tool life over after 90 s	Tool life over after 130 s

**Fig. 12** Optical images of the flank surfaces of uncoated and different coated turning inserts after different durations of machining at cutting velocity of 230 m/min

## 4 Conclusion

The major conclusions that can be drawn from the current work are as follows:

- GIXRD analysis of the (TiN-WS<sub>2</sub>) composite coating with TiN underlayer showed separate existence of TiN and WS<sub>2</sub> phases in the composite matrix.
- Addition of WS<sub>2</sub> to the TiN matrix refined the microstructure because of competitive growth of the TiN and WS<sub>2</sub> phases.
- The multilayer coating i.e. (TiN-WS<sub>2</sub>) on TiN showed greater adhesion and less friction coefficient as compared to pure TiN coating.
- The multilayer coated insert outperformed the uncoated and the TiN coated inserts during tool life tests conducted at cutting velocity of 230 m/min.

## References

1. Klocke F, Eisenblätter G (1997) Dry cutting. *CIRP Ann Manuf Technol* 46(2):519–526
2. Renevier NM, Fox VC, Teer DG, Hampshire J (2000) Coating characteristics and tribological properties of sputter-deposited MoS<sub>2</sub>/metal composite coatings deposited by closed field unbalanced magnetron sputter ion plating. *Surf Coat Technol* 127:24–37
3. Banerjee T, Chattopadhyay AK (2014) Structural, mechanical and tribological properties of WS<sub>2</sub>-Ti composite coating with and without hard under layer of TiN. *Surf Coat Technol* 258:849–860
4. Renevier NM, Lobiondo N, Fox VC, Teer DG, Hampshire J (2000) Performance of MoS<sub>2</sub>/metal composite coatings used for dry machining and other industrial applications. *Surf Coat Technol* 123:84–91
5. Jianxin D, Wenlong S, Hui Z, Jinlong Z (2008) Performance of PVD MoS<sub>2</sub>/Zr-coated carbide in cutting processes. *Int J Mach Tools Manuf* 48:1546–1552

6. Gangopadhyay S, Acharya R, Chattopadhyay AK, Paul S (2009) Pulsed DC magnetron sputtered MoS<sub>x</sub>-TiN composite coating for improved mechanical properties and tribological performance. *Surf Coat Technol* 203:3297–3305
7. Särhammar E, Strandberg E, Sundberg J, Nyberg H, Kubart T, Jacobson S, Jansson U, Nyberg T (2014) Mechanisms for compositional variations of coatings sputtered from a WS<sub>2</sub> target. *Surf Coat Technol* 252:186–190
8. Nossa A, Cavaleiro A (2001) The influence of the addition of C and N on the wear behaviour of W-S-C/N coatings. *Surf Coat Technol* 142–144:984–991
9. Efeoglu I, Bulbul F (2005) Effect of crystallographic orientation on the friction and wear properties of Mo<sub>x</sub>S<sub>y</sub>-Ti coatings by pulsed-dc in nitrogen and humid air. *Wear* 258:852–860
10. Goller R, Torri P, Baker MA, Gilmore R, Gissler W (1999) The deposition of low-friction TiN-MoS<sub>x</sub> hard coatings by a combined arc evaporation and magnetron sputter process. *Surf Coat Technol* 120–121:453–457
11. Haider J, Rahman M, Corcoran B, Hashmi MSJ (2005) Deposition and characterization of hard-solid lubricant coating by closed-field magnetron sputtering. *Surf Coat Technol* 200:1080–1083
12. Gangopadhyay S, Acharya R, Chattopadhyay AK, Paul S (2009) Composition and structure–property relationship of low friction, wear resistant TiN–MoS<sub>x</sub> composite coating deposited by pulsed closed-field unbalanced magnetron sputtering. *Surf Coat Technol* 203:1565–1572
13. Audronis M, Leyland A, Kelly PJ, Matthews A (2008) Composition and structure-property relationships of chromium-diboride/molybdenum-disulphide PVD nanocomposite hard coatings deposited by pulsed magnetron sputtering. *Appl Phys A* 91:77–86
14. Li S, Deng J, Yana G, Zhang K, Zhang G (2014) Microstructure, mechanical properties and tribological performance of TiSiN-WS<sub>2</sub> hard-lubricant coatings. *Appl Surf Sci* 309:209–217



# Digital Technologies for Splints Manufacturing



E. M. Meisel, P. A. Daw, X. Xu, and R. Patel

**Abstract** This paper will detail a proposed methodology for utilising digital technology for orthotic production, specifically for Ankle Foot Orthotics (AFOs) used to treat children with prolonged plantar flexion. Splints created by traditional methods from thermoplastic materials involve long, labour-intensive and messy production which is highly dependent on the skill of the clinician. An orthotic produced by digital means can be made lighter, with more ventilation and greater aesthetic appeal than existing splints. The stages of production to which digital technology can be applied include surface capture, data processing, design and production. A novel production methodology has been established and a functioning prototype has been created as a proof of concept. The methodology proposed is unique when compared to existing studies for the digital production of orthotics as it focuses on practical implementation and ease of use so that it may be applied to the Mass Customisation of orthotics.

**Keywords** Orthotics · Mass customisation · Additive manufacture · Digital production · Reverse engineering

## 1 Introduction

A side effect of chemotherapy is damage to the nervous system, in particular, the peripheral nerves. As a result of this some patients are faced with the inability to control the flexure position of their foot and experience prolonged plantar flexion, or, foot drop. A splint can be used to maintain the foot in a neutral position, or at least the best possible position which the patient can tolerate long term. A splint or orthotic can be defined as a device used to support, align or correct deformities or to improve the function of movable parts of the body. The particular focus of this paper is an Ankle Foot Orthosis (AFO) for children.

---

E. M. Meisel · P. A. Daw · X. Xu (✉) · R. Patel  
Department of Mechanical Engineering, The University of Auckland, 20 Symonds Street,  
Auckland, New Zealand  
e-mail: [xun.xu@auckland.ac.nz](mailto:xun.xu@auckland.ac.nz)

The traditional splint fabrication process involves, a plaster-of-paris cast of the patient's leg profile being taken and then an AFO fabricated by draping a Low Temperature ThermoPlastic (LTTP) over it. This process is labour intensive, inefficient and can lack consistency depending on the clinical orthotist. The traditional splint fabrication process also lacks consideration for requirements of children. With high growth rates and a manufacturing time of several weeks, the effective time period patients are treated by the splint is reduced. Additionally, the splints currently being produced are struggling to achieve a desirable level of patient comfort and ventilation, resulting in compliance issues.

It is proposed that many of the highlighted issues could be overcome through using Additive Manufacturing (AM) and digital technologies. Digital technologies include 3-Dimensional (3D) scanners which allow for physical objects to be captured in 3D space and Computer-Aided Design (CAD) software. By combining AM and digital technologies, there is the potential to develop a more sophisticated and efficient fabrication method for orthotics.

## 2 Background Research

Existing resting splints which are designed for children with prolonged plantar flexion are low cost and very basic. They are available in standard sizes with no customisation, meaning that often they are either too narrow or wide for the calf of the patient. These splints are often bulky, heavily padded and poorly ventilated. These are all contributing factors to patient discomfort. Figure 1 depicts a typical night splint.

Some of the fundamental issues with current orthotic products are that they are:

- Bulky;
- Poorly ventilated;
- Aesthetically unappealing.

**Fig. 1** A standard night splint for preventing plantar flexion



## **2.1 Application of Digital Technology**

The application of digital technology to splints manufacturing can vastly improve on the issues identified. Some studies have already investigated the use of digital technology in orthotic production, however, the majority of these are focused on highly complex, highly accurate data and orthotic products rather than considering a widely applicable methodology for the Mass Customisation (MC) of splints.

### **2.1.1 Surface Capture**

Telfer and Woodburn [14] conducted a meta-analysis of thirty-eight studies on appropriate skin surface capture methods, including using scanners to capture foot dimensions. The study found that accurate and repeatable scans of foot shape could be created and that potential exists for 3D data to replace the traditional and more basic system of flat image anthropometric databases [14]. It has been found that a lack of standardisation exists in scanning protocol however. Li et al. [5] proposed that close range digital photogrammetry using commercial Single Lens Reflex (SLR) cameras is an effective, lower resolution alternative to laser scanning in the fields of prosthetics and orthotics. The method involves capturing multiple 2 Dimensional (2D) photos around the subject which can later be mathematically intercepted to create 3D points and form a model. The object must have easily distinguishable feature points or texture for photogrammetry methods to work effectively, however the method is only tested with a very basic shape in the case study [5, 14].

### **2.1.2 Application of CAD**

A paper by Telfer et al. [13] aimed to establish the effect which operator technique has on the reproducibility of custom foot orthosis design using CAD software. The study found that consistent use and experience with using CAD software may improve the reproducibility of designs by a CAD operator [13]. Seepersad [12] investigated modern challenges in AM such as, representing and optimising intricate geometries. The paper recognises that current CAD design software lacks usability for designing products such as a prosthesis socket with a patient-specific inner produced by AM [12]. Implementation of digital technology in a medical field will require a focus on usability for individuals who have a low-level of CAD expertise [3, 13].

### **2.1.3 Prostheses**

One major medical area in which digital technology can be applied is the production of prostheses. Vukašinović et al. [15] investigated the possibility of computer-aided surface reconstruction for prosthesis manufacture in order to improve the aesthetics,

improve the quality and reduce the manufacturing time. In the paper a highly accurate, water-tight human finger model is created using dense cloud-point data which is converted to a triangular mesh surface [15]. The idea that a virtual database of human shapes could be created for prosthesis production has been proposed [14, 15]. A major advantage of digital technology in prosthesis design is that it allows mirror image parts to be easily created and save weeks of work by a technician or artist.

Digital technologies have been used for the design and manufacture of prostheses such as orbital prostheses for artificial eyes after reconstructive craniofacial surgery. A white light scanner was used in a paper by Bibb et al. [2] to capture surface data and the study method compared favourably to current impression methods. It was found that the accuracy of data was more than adequate for the purpose and that cost was the only real drawback to a digital method [2].

### 2.1.4 Orthotics

The area with which this study is most concerned is the production of orthotics, or splints, aided by digital technology. The application of surface capture and design software in this area is similar to that in prosthetic design. Many of the requirements, such as feasibility and clinical outcomes transfer directly. A pilot study by Palousek et al. [7] has effectively demonstrated that digital technologies can be applied to print wrist orthoses through Reverse Engineering (RE), CAD modelling and AM [7]. The manufactured item in the case study compared well with a standard orthosis and was deemed appropriate by experts. One main benefit of this process is contactless data capture. The paper recommends that macro functions or merging of a scan onto an orthosis template are potential methods for speeding up the digital process [3, 7].

The use of contactless data capture has been further backed up by Paterson et al. [8]. This paper reviewed data capture methods which were used in MC of wrist splints through AM, or the 'MC-AM' relationship [8]. Digitised anatomical surface data which can be manipulated and translated into a compatible file format for 3D printing is key for designing both wrist and lower limb splints. The paper concludes that, from several options studied, the best solution is to conduct indirect 3D laser scanning with the use of an intermediate positive plaster cast form. Point cloud data can be converted to a polygonal mesh within 3D CAD based software and so this offers a reduced processing time when compared with other methods. Plaster is an effective material for scanning due to its matte appearance and the creation of a plaster cast prevents scanning errors due to motion [8].

A paper by Pilley et al. [10] follows the production of a burns therapy pressure splint using structured light scanning, CAD and AM. It is recommended that an intermediate plaster model be used [8, 10]. An intermediate 3DP-Zcorp printed model of the patients face was formed and duplicated in plaster-of-paris. The plaster model was adjusted in order to localise pressure on the scars. After this the standard method of vacuum forming of plastic over the plaster model was followed to produce a mask which is held in place by Velcro straps. The method was found to be patient friendly,

fast, cost-effective and accurate. Main advantages included patient comfort and the non-contact data capture method [10]. This removes the need for risky anaesthetic procedures during the plaster-of-paris bandage forming process for children.

A variety of literature sources demonstrate a requirement for digital technology for the production of splints, for example for contactless surface capture and customised manufacture. All of the studies reviewed described digital production methods which are overly complex and costly as they focused on achieving highly accurate results for single case orthotic production. It is proposed that further focus needs to be placed on establishing a practical, implementable methodology which could be applied for MC of splints. This was one major area that was addressed in this study. More focus also needed to be placed on processing surface data in a fast and straightforward manner to account for clinicians with little or no CAD experience. It has been identified that expensive scanning techniques offer a higher level of accuracy than is required and so cheaper and simpler scanning techniques should also be trialled.

### 2.2 Biomechanics of the Ankle

An understanding of the biomechanics of an ankle is useful in understanding how forces would act on a splint during walking. These forces will result in stress, strain and torsion in a splint. If we focus on the simple case of a night splint (which is not worn while walking), the majority of force,  $F$ , will act downward and is simply due to the mass of the limb. It can be defined as mass,  $m$  multiplied by gravitational acceleration,  $g$ :

$$mg = F \tag{1}$$

There are two major Degrees Of Freedom (DOF) at the ankle with which we are concerned in relation to splints. These have been depicted in neutral position in Fig. 2, where  $\theta$  represents the angle through which motion can occur.

**Fig. 2** Degrees of freedom at the ankle joint (Anon 2014)

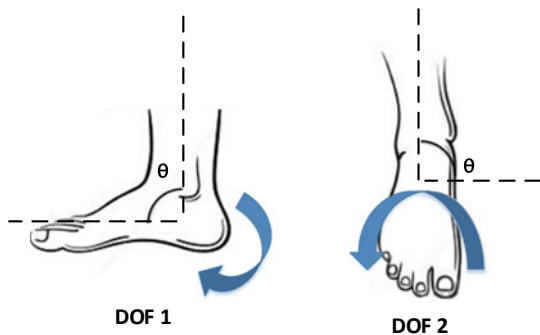


**Fig. 3** Dorsiflexion and plantarflexion of the foot [6]

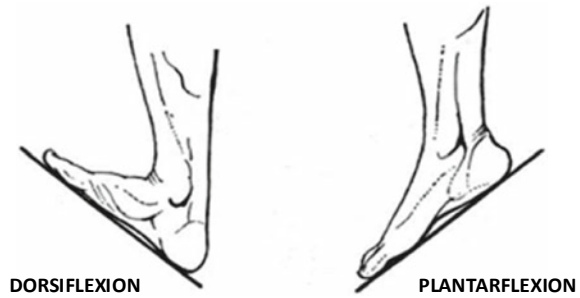


**Fig. 4** Pronation and supination of the foot [6]



The medical terms for movement in DOF 1 are plantarflexion and dorsiflexion depending on the direction of rotation. This can be seen in Fig. 3. The motion depicted will occur during normal walking, with the foot undergoing around 10–30° of rotation in dorsiflexion and 20–50° of rotation in plantarflexion.

When describing motion in DOF 2 the terms used are pronation and supination. This can occur between + 30° and – 30° from neutral and has been depicted in Fig. 4. Motion in this direction should be minimal during normal walking. One major function of a splint is to restrict walking movement to rotation in DOF 1 only. Orthotists may also use foam supports under the foot in order to ensure that this is properly controlled.

To summarise, lower limb orthotics can be classed in one of the two main categories mentioned; these are day splints and night splints. For a splint used during the day the primary function is to control walking within a normal range of motion. For night, or resting splints, the purpose is to keep the ankle rigidly in a neutral alignment where  $\theta = 90^\circ$  referring to Fig. 2.

Due to the obvious differences in weight bearing areas there are different padding and structural requirements for night splints compared to day splints. Padding is most important in the heel region of a night splint but is usually placed under-foot and around the calf in a day splint. In terms of ventilation gaps, these should be placed to avoid any known pressure points. Radial support describes material which wraps around the limb, for example around the ankle over the malleoli. A day splint may require differing levels of ankle stiffness and therefore radial support at the ankle, depending on the patient condition. A night splint remains rigid at the ankle joint.

### 3 Methodology

An effective methodology by which a splint can be produced through digital means has been established. This methodology is the result of a refined design process which has been developed throughout the study, resulting in a robust and repeatable method. The design of each splint will differ slightly according to the preferences and medical condition of the patient but the majority of the features will be consistent if the proposed methodology is utilised. Ultimately this solution could be implemented in hospitals and used by clinicians with little or no technical experience.

Figure 5 shows the scientific ICAM DEFinition for Function Modeling (IDEF0) diagram for the methodology proposed to produce a functional splint. Inputs are shown on the left of each process box with outputs on the right. Controlling measures such as requirements and standards are shown entering from above while the mechanisms, which are the tools used to make the process possible, enter the box from below. The digital technology, equipment and software used has been specified in

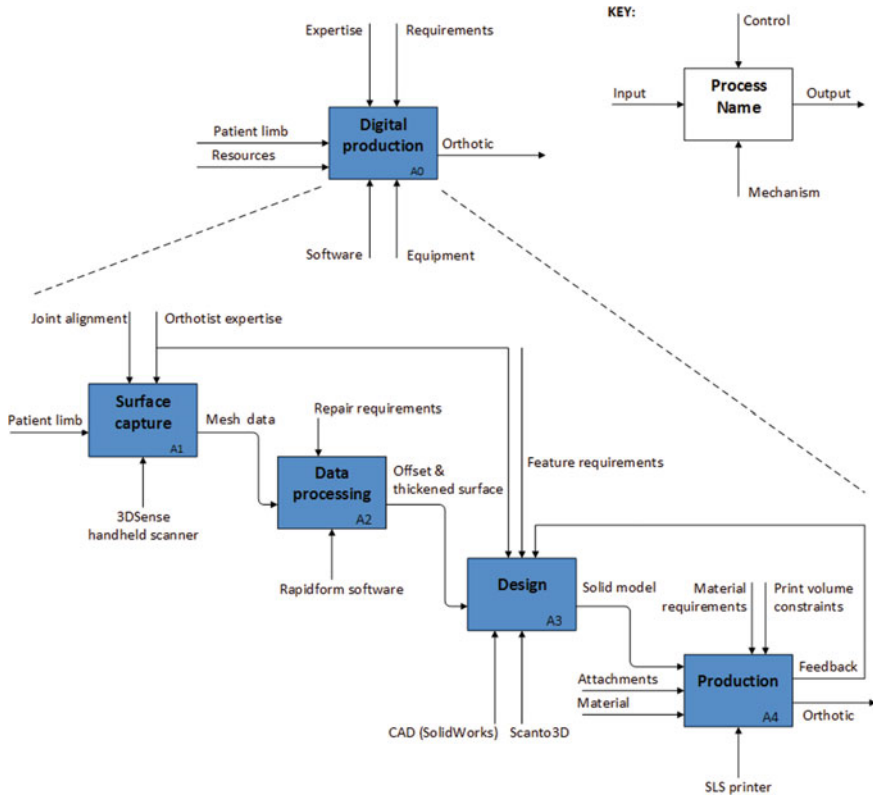


Fig. 5 IDEF0 diagram methodology established for the production of splints

the diagram for each of the stages; surface capture, data processing, design and production.

## 4 Surface Capture

The purpose of surface capture is to obtain information about an object, namely its shape, and develop a virtual 3D model. Literature suggests there are number of methods by which a patient's leg profile could be captured. These are Computed Tomography (CT), Magnetic Resonance Imaging (MRI), 3D scanning or anthropometric measurement [9]. In terms of safety, accuracy, unobtrusiveness and cost, 3D laser scanning was the considered the best option for splints manufacturing.

3D scanning utilises a number of different methods to capture a surface, some being laser, photogrammetry or structured white light. The methodology developed utilises the 3DSense handheld scanner by 3D Systems for capturing surface data. This scanner uses photogrammetry technology to capture the skin topography in one large piece which can then be cropped and saved as a surface or solid. This makes it a far simpler option which effectively cuts out a major data processing step. A handheld scanner is not reliant on the skill of the user and so can capture surfaces with adequate accuracy and completeness when used by a clinician. Surface detail accuracy is lower with a 3DSense than a 3D laser scanner, however, a more user friendly methodology was a priority over high levels of resolution in this study.

## 5 Data Processing

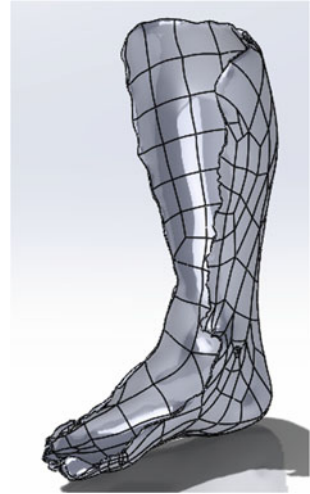
Data processing is used to collectively describe the conversion of basic surface data into a modifiable solid, feature design and exportation in a printable format. Typically, in existing digital fabrication methods the most challenging aspect of data processing is to convert the mesh surface into a modifiable solid. For example, it has been proposed by Bhongale [1] that Rhino 3D software may be used to create a surface model of the limb after which a draping function is used to create another model around the original one [1]. However, this method is tedious and time consuming. The option of taking model slices to then create a solid sweep model was considered as well as the possibility of using a modifiable standard base part.

Various data conversion packages are available online but many are complex and still require large amounts of time for processing. The most simple and effective method found was to convert the surface to a modifiable CAD model using a SolidWorks package. The RE function provided in SolidWorks by the ScanTo3D add-in allowed the surface to be directly edited in the CAD environment [11].

The handheld scanner has the advantage of producing a complete surface scan in the form of mesh data. No further repair or multi-scan alignment is required. Rapidform software can be used to offset, thicken and re-orientate the surface before



**Fig. 6** Thickened scan model taken from the patient lower limb



importing the model into SolidWorks [4]. Offsetting the scanned surface itself greatly simplifies the process of obtaining a solid as a watertight model is not required such as with previously proposed methods [8, 7, 15]. The advantage of using a SolidWorks RE add in is that the model is imported directly into a CAD environment. The thickened scan model can be seen in Fig. 6. Modifications within the CAD environment give functionality to the splint.

Features which were applied to the lower limb orthotic were:

- A moulded hard exterior shell at the back of the calf and under the foot;
- Gaps for ventilation and aesthetic appeal;
- Attachment points for straps.

Design features for the concept were incorporated by applying a variety of CAD functions to the model, such as sketching, extruding and filleting operations. The scanned surface of the toes was removed so that a flat under-toe support in the shape of the patient's foot could be created as seen in Fig. 7. The shape of the splint has radial support around the ankle, reaching mid-way across the medial-malleolus and lateral-malleolus and is designed to give the joint increased stiffness.

Ventilation gaps were added under the toe area with some in the calf support area also. The cut-out pattern has been made more symmetrical for aesthetic appeal. Smoothed edges have been incorporated in the model to prevent the splint catching on objects or irritating the skin. Once manipulated to incorporate the required features the solid part can be saved and exported as an STereoLithography (STL) file for 3D printing as seen in Fig. 8.

**Fig. 7** Extrusion of the orthotic undertoe section

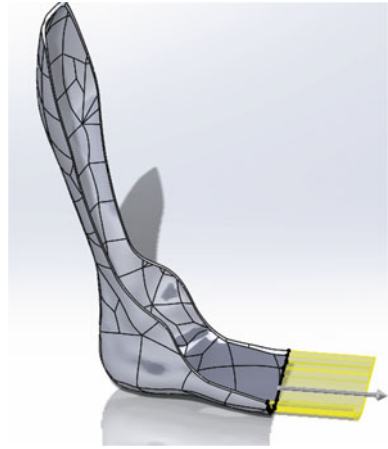
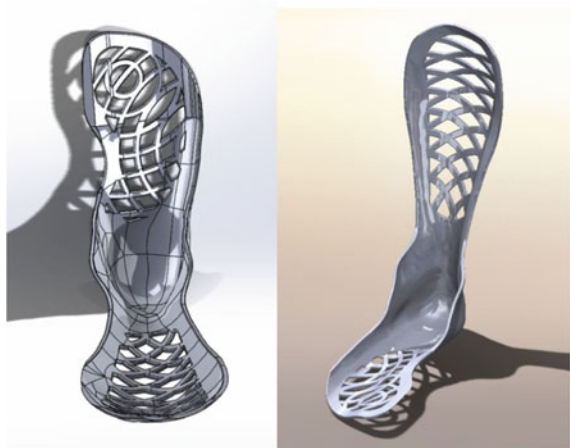


**Fig. 8** Iteration 3 CAD model in SolidWorks



## 6 Production by Additive Manufacture

The traditional method of splint manufacture is labour intensive, lacks consistency and gives the patient little in terms of customisation. It was proposed that by applying AM to the fabrication process, these issues could be improved or eliminated. One flow on benefit was also a reduced time to manufacture, allowing patients, in particular children, to have their splint application time extended before requiring a clinical visit.

Using AM allows for intricate geometries to be fabricated, leading to aesthetically appealing designs that also provide structural support. By combining AM and structural optimisation, there is also the potential to reduce the weight of the splint. Each splint can be structurally tested and optimised with specific ventilation gap designs

**Fig. 9** Printed prototype AFO with straps attached



so that each patient receives a splint that is low cost, light weight and customised to their foot and aesthetic appeal.

With continued growth, there have been a number of different types of AM developed. It was found that Selective Laser Sintering (SLS) would best meet the fabrication requirements when comparing this method to others, such as Fused Deposition Modelling (FDM). This is because SLS printing with powder offers large build volumes, low waste, high levels of detail and quality. The material chosen for printing was nylon for its biocompatible properties and appropriateness for long-term contact with skin.

Once printed, traditional attachments were applied to the final splint product to make it functional. A 'D ring' was fixed to the upper calf support of the orthotic with a rivet. This allows for rotation of the calf strap and also makes the splint easier to put on. A figure-of-8 arrangement of the straps was used for maximum support around the ankle. Velcro holds the straps in place and allows for easy adjustment. Blue foam padding was added to the inside of the heel region. These attachments can be seen in Figs. 9 and 10. The total cost of producing the orthotic including attachments was approximately \$80 USD and it took around 24 h to print. The intention was for the concept to form a fully functional orthotic designed specifically for night use.

## 7 Discussion

In addition to improving on traditional splint production, a procedure has been established with distinct advantages over existing digital methods as described in the literature review. The scanning method proposed is simple and cost effective as it does

**Fig. 10** Printed AFO as worn by a patient when resting



not produce data with unnecessarily high resolution. A practical, repeatable methodology has been established which is relatively easy to use compared to other research conducted so far. No watertight limb model is required, making this a unique and effective methodology for practical implementation. Fundamentally, a methodology has been established which is not only relevant to one case study but which can be applied repeatedly to produce multiple customised splints.

Although simple steps were aimed for, the methodology which was established does rely on the CAD operator having a medium level of skill and experience. It was also found that it is particularly difficult to deal with natural shapes in a CAD environment which typically deals with well-defined geometries. For example the addition of strap loops to our concept was challenging due to the asymmetrical, organic shape of the limb surface. In many cases the features in CAD were applied by best fit determined by the operator rather than as the result of specified dimensions.

## 8 Splint Technologies

A side project by Bhongale [1] has investigated the possibility of making splints 'smart'. This refers to attaching sensors to the splint to measure temperature, heart-rate and humidity for example. This can indicate whether or not the patient is wearing their orthotic and if they are comfortable in terms of temperature and ventilation. The signal received by the sensor can be sent to an android phone application. A preliminary circuit board and android application has been created but further work will focus on developing the software, reducing the size of the circuit board and integrating sensors into the splint.

## 9 Conclusions

Several conclusions can be derived from the research and development achieved by this project:

- It is proposed that applying digital technology to the production of splints can greatly improve the current manufacturing process and the resulting orthotic product;
- The manufacture of a splint can be achieved more quickly, with less labour required and more affordably through the use of digital technology. This enables a non-contact surface capture and removes the need for creating multiple plaster casts;
- The resulting orthotic can be customised easily and produced with a superior level of aesthetic appeal. It can be made light-weight and well ventilated through the application of cut-outs;
- A practical, scientific methodology has been proposed for the digital scanning, data-processing and production of a splint which can be utilised repeatedly, rather than in isolation, for the purposes of MC;
- The scanning solution proposed is the 3DSense handheld scanner which is portable, affordable, relatively easy to use and produces data in an adequate resolution;
- The speed and ease of data processing for splint design is achieved with Rapidform software to repair and edit the scan mesh and SolidWorks CAD software to conduct reverse engineering and feature design on the orthotic;
- The methodology proposed has been used to successfully produce a fully functioning night splint by SLS which can be used by a patient with foot-drop condition;
- Future work will need to focus on developing a fixture for stabilising the limb during surface capture, clinical trials and further simplifying the CAD design stage of the production process;
- The methodology can be developed further to consider the production of day splints. For this stage further focus should be placed on biomechanical models of the ankle during walking, structural optimisation of the splint and also print material properties.

## References

1. Bhongale S (2013) Digital technologies for splints manufacturing. MECHENG 787, The University of Auckland, Auckland
2. Bibb R, Freeman P, Brown R, Sugar A, Evans P, Bocca A (2000) An investigation of three-dimensional scanning of human body surfaces and its use in the design and manufacture of prostheses. *Proc Inst Mech Eng [H]* 214(6):589
3. Colombo G, Filippi S, Rizzi C, Rotini F (2010) A new design paradigm for the development of custom—fit soft sockets for lower limb prostheses. *Comput Ind* 61(6):513–523

4. Geomagic, Manufacturing the future, viewed 23rd April 2014. <http://www.rapidform.com/home/>
5. Li G-k, Gao F, Wang Z-g (2011) A photogrammetry-based system for 3D surface reconstruction of prosthetics and orthotics. In: Proceedings of the annual international conference of the IEEE engineering in medicine and biology society (EMBS), vol 33, pp 8459–8462
6. O’rahilly M, Carpenter S (2014) Basic human anatomy. Dartmouth Medical School, viewed 2 Sept 2014. [http://www.dartmouth.edu/~humananatomy/figures/chapter\\_17/17-6.HTM](http://www.dartmouth.edu/~humananatomy/figures/chapter_17/17-6.HTM)
7. Palousek D, Rosicky F, Koutny D, Stoklasek P, Navart T (2014) Pilot study of the wrist orthosis design process. *Rapid Prototyp J* 20(1):27–32
8. Paterson AMJ, Bibb RJ, Campbell RI (2010) A review of existing anatomical data capture methods to support the mass customisation of wrist splints. *Virtual Phys Prototyp* 5(4):201–207
9. Paterson AM, Bibb RJ, Campbell RI (2012) Evaluation of a digitised splinting approach with multiple-material functionality using Additive Manufacturing technologies. Loughborough Design School, Loughborough University, Leicestershire, LE11 3TU. <http://utwired.engr.utexas.edu/lff/symposium/proceedingsArchive/pubs/Manuscripts/2012/2012-50-Paterson.pdf>
10. Pilley MJ, Hitchens C, Rose G, Alexander S, Wimpenny DI (2011) The use of non-contact structured light scanning in burns pressure splint construction. *Burns* 37(7):1168–1173
11. ScanTo3D, viewed 2nd June 2014. <http://www.solidworks.com/sw/products/3d-cad/ScanTo3D.htm>
12. Seepersad CC (2014) Challenges and opportunities in design for additive manufacturing. *3D Print Addit Manuf* 1(1):10–13
13. Telfer S, Gibson KS, Hennessy K, Steultjens MP, Woodburn J (2012) Computer-aided design of customized foot orthoses: reproducibility and effect of method used to obtain foot shape. *Arch Phys Med Rehabil* 93(5):863–870
14. Telfer S, Woodburn J (2010) The use of 3D surface scanning for the measurement and assessment of the human foot. *J Foot Ankle Res* 3(1):19
15. Vukašinović N, Kolšek T, Duhovnik J (2007) Case study—surface reconstruction from point clouds for prosthesis production. *J Eng Des* 18(5):475–488

# **Metrology and Measurement**

# A Novel Miniature Laser Diode Interferometer for Precision Displacement Measurements



L. M. Chen, K. C. Fan, and H. Zhou

**Abstract** Laser displacement interferometers are widely used in industry for the accuracy calibration of machine's positioning errors. Its main requirement is to provide a very accurate and stable wavelength as the basic length unit. To meet this point, conventional laser interferometers adopt various frequency stabilized techniques in order to stabilize the wavelength. The cost is high and the size is bulky. This paper presents a novel laser diode displacement interferometer with small size, low cost and centimeter range. Instead of stabilizing the frequency, a new technique of measuring real-time wavelength of the laser is proposed. The wavelength is detected by the principle of spectrometer. The temperature influence on the grating pitch and laser beam drift can also be compensated in real-time. Calibrated in a temperature controlled chamber by a commercial laser interferometer, the wavelength accuracy reaches the order of  $10^{-6}$  displacement up to 50 mm with accuracy less than 20 nm. It is possible to be a new feedback sensor for all high precision and small range linear stages.

**Keywords** Laser diode interferometer · Wavelength detection · Displacement measurement

## 1 Introduction

Due to the advent of micro/nano technology, many high precision and short range linear stages require ultraprecision feedback position sensors. Conventional linear encoders have only accuracy to micrometers. Although the laser interferometer is a powerful tool widely used as the calibrator in industries with long working distance and high resolution [1, 2], it is high cost and bulky in size. Some high precision equipment, such as IC steppers and nanopositioning machines, adopt laser interferometer

---

L. M. Chen · K. C. Fan (✉)  
National Taiwan University, Taipei 10617, Taiwan  
e-mail: [fan@ntu.edu.tw](mailto:fan@ntu.edu.tw)

K. C. Fan · H. Zhou  
Hefei University of Technology, Hefei 230009, China



as feedback sensor [3, 4], but they are all very expensive. He–Ne lasers are commonly used as the light source of commercial laser interferometers [5, 6]. They are, however, too big to be equipped in the small-sized nanopositioning stages. The recent maturity of the semiconductor manufacturing has made laser diodes smaller and cheaper. There are many applications of laser diodes, for instance, the optical surface profilers, optical communication and distance measurements. Frequency modulation is mostly needed when driving laser diodes [7, 8]. There are modulation techniques proposed in many papers [9, 10]. Nevertheless, the methods are too complicated and the modulators are of high cost and massive, which are obstacles to reduce the size of laser interferometer. For Michelson laser interferometer, laser wavelength is a decisive parameter. Conventional laser interferometers adopt various frequency stabilized techniques in order to stabilize the wavelength. The cost is high and the size is bulky. The aim of this paper is to develop a miniature and low cost laser diode interferometer without modulating laser frequency. It adopts the principle of diffraction with the use of a transparent grating and autocollimators to calculate real time wavelength so as to maintain high precision in long distance measurements.

## 2 System Design

### 2.1 Phase Encoding Module

When the laser beam is emitted from a laser diode, it will be divided into P and S beams by PBS1 in the interferometry module, as shown in Fig. 1. The P-beam propagates along the path of Q2-MM-Q2, where MM represents the moving mirror in Fig. 1, and turns into an S-beam; meanwhile, the S-beam propagates along the path of Q1-BS1-RF-BS1-Q1, where RF represents the reference mirror in Fig. 1, and turns into a P-beam. The two beams combine at Q3. Due to the perpendicularity in polarization, they cannot interfere. With the use of a phase encoding module composed by BS2, PBS2 and PBS3 to produce phase shifts, the four interference fringe signals with  $90^\circ$  phase shift can be detected by PD1 to PD4 [11–13].

### 2.2 Principle of Autocollimator

The optical path of autocollimator is shown in Fig. 2. A flat mirror is placed perpendicularly to the optical axis of the collimating lens. The light beam is transmitted from the source and reflected back along its path by the flat mirror. If the mirror tilts with an angle of  $\theta$ , the reflected beam will be changed by an angle of  $2\theta$  through the collimating lens and focused on a QPD (Quadrant Photodetector) installed at the focal plane.

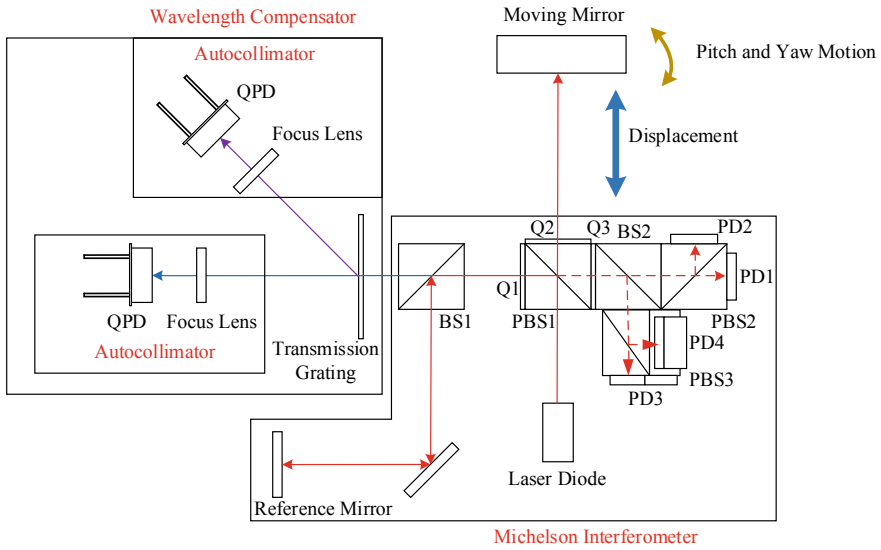


Fig. 1 Configuration laser diode interferometer

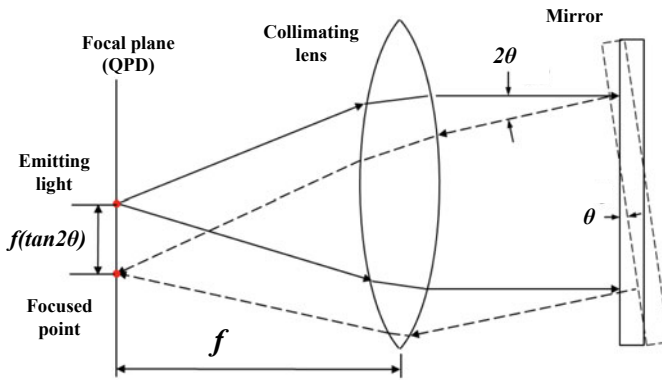
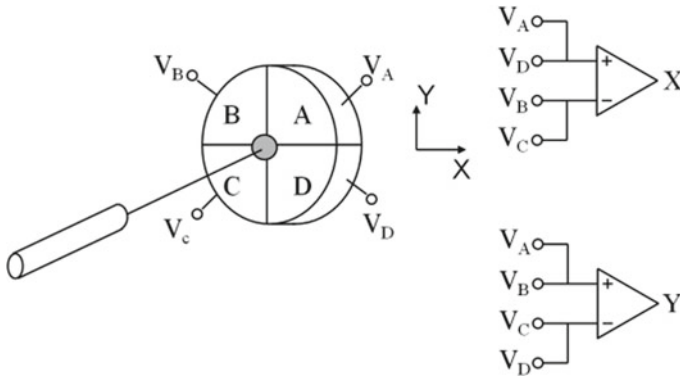


Fig. 2 The optical path of autocollimator

According to the principle of optical autocollimator, the tilted angle  $\theta$  will result in the focused spot being shifted laterally by  $2f \tan \theta$ , where  $f$  is the focal length of collimating lens. The QPD works as a position sensor by detecting voltage differences of the four photodetectors, as shown in Fig. 3. By analyzing the positions of the beam projected onto the QPD, pitch ( $\theta_x$ ) and yaw ( $\theta_y$ ) angles can be expressed as the following equations:

$$\theta_x = k_x \frac{(V_A + V_D) - (V_B + V_C)}{V_A + V_B + V_C + V_D} \tag{1}$$



**Fig. 3** Signals analysis of QPD

$$\theta_y = k_y \frac{(V_A + V_B) - (V_C + V_D)}{V_A + V_B + V_C + V_D} \tag{2}$$

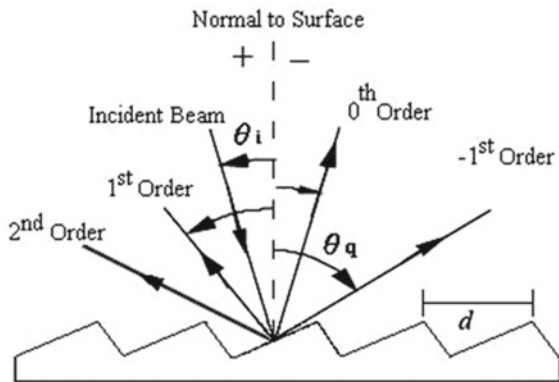
where  $k_x$  and  $k_y$  are the calibrated parameters in pitch and yaw motions. The signal normalization is necessary because the laser intensity may vary.

### 2.3 Wavelength Compensator

As shown in Fig. 1, part of the laser beam will be split at BS1. When the light impinges a grating, diffraction beams, as shown in Fig. 4, observe the law of grating equation as following:

$$d(\sin \theta_i + \sin \theta_q) = m\lambda, \quad m = 0, \pm 1, \pm 2... \tag{3}$$

**Fig. 4** The principle of diffraction



where  $d$  is the pitch of grating,  $\theta_i$  is incident angle,  $\theta_q$  is diffraction angle and  $m$  is the order of diffraction. Laser wavelength is sensitive to the surrounding environment. It can be detected by measuring the variation of the diffraction angle if other parameters remain constant. In this study, the laser beam is transmitted from Q1 to BS1 as Fig. 1 shows, and impinges to the transparent grating. By measuring the variation of +1st order diffraction angle, detected by an autocollimator, the real-time laser wavelength can be predicted.

It has to be noted that the laser beam could drift with time, which affects the incident angle on the grating. Hence, another autocollimator is installed to detect the angle drift of 0th order beam, in which no diffraction happens. In addition, thermal expansion of grating pitch must be considered as well. The thermal expansion coefficient provided by the vendor (Edmund Optics) is  $1.7 \times 10^{-5}$  and the pitch is 1000 nm at 25 °C. Combining those mentioned above, the grating equation can be modified to

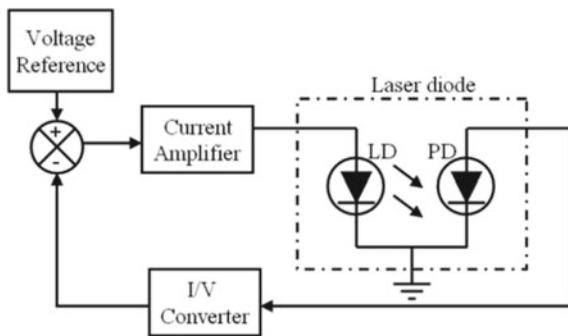
$$\lambda = d_0(1 + \alpha(T - 25))(\sin(\theta_i + \theta_{drift}) + \sin(\theta_q + \Delta\theta_q)) \tag{4}$$

where  $d_0$  is the grating pitch at 25 °C,  $\alpha$  is its thermal expansion coefficient,  $T$  is room temperature,  $\theta_i$  is the initial incident angle,  $\theta_q$  is the nominal +1<sup>st</sup> diffraction angle,  $\theta_{drift}$  is angle of beam drift and  $\Delta\theta_q$  is the angle variation of the first order diffraction beam.

### 2.4 Automatic Power Control of Laser Diode

It is known that laser diode’s intensity is sensitive to temperature. For lacking of modulating frequency in this paper, it is necessary to stabilize the intensity of laser diode. An automatic power control (APC) circuit is thus used as a driver to reach a long term stabilization of laser intensity. As shown in Fig. 5, laser diode’s power is detected by a photodetector. Comparing to the reference voltage, the electrical

Fig. 5 The schematic plot of automatic power control



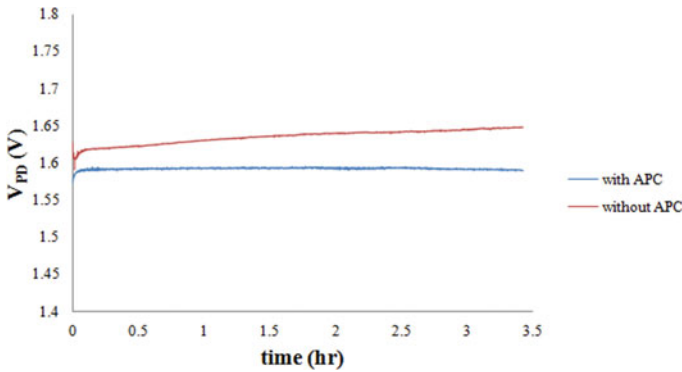


Fig. 6 Comparison between with and without APC

current to laser diode would be feedbacked when the intensity varies. Figure 6 shows the experimental results in which the laser power could be stably controlled with APC.

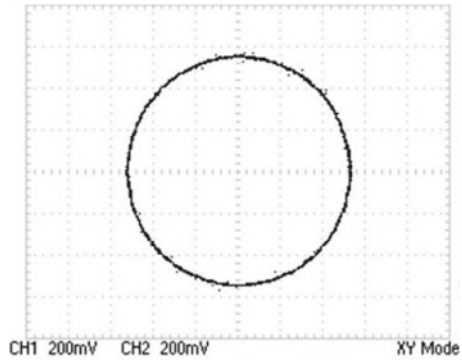
### 3 Experimental Results

The wavelength compensator has to be calibrated to ensure its performance. The calibrator in this research is MI-5000 laser interferometer made by SIOS Co. of Germany, as shown in Fig. 7, which is a retroreflector type stabilized He-Ne laser interferometer. It has 1 nm resolution. The laser diode interferometer was installed in coaxial with MI-5000. The moving mirror and retroreflector were actuated back and forth to correct the wavelength at different circumstances. Figure 8 shows a good Lissajous circle of the developed diode laser interferometer. The equation of Michelson interferometer in measuring distance is:

Fig. 7 MI-5000 laser interferometer [14]



**Fig. 8** The Lissajous signal figure of interference



$$\Delta d = \frac{\lambda}{2} \times \phi \tag{5}$$

where  $\Delta d$  is displacement,  $\lambda$  is wavelength, and  $\phi$  is phase change. It is evident that positioning error would be in linear relationship if the wavelength is incorrect. Therefore, from the calibrated curve of positioning error, the wavelength of laser diode can be compensated by multiplying the slope. In other words, the module can be calibrated once wavelengths and other parameters in (4) are recorded. The coaxiality of laser diode interferometer and the stage was less than  $1 \mu\text{m}$ . Based on the principle of cosine error; the coaxial error was within  $0.025 \text{ nm}$  in a travel of  $50 \text{ mm}$ , which can be neglected. Experimental results of wavelength prediction are listed in Table 1 and Fig. 9. Apparently, an order of  $10^{-6}$  accuracy, which is listed as wavelength prediction error ratio in Table 1, was reached in wavelength compensation. Figure 10 shows the experimental results of a comparison with MI-5000. Up to the range of  $50 \text{ mm}$ , the position errors of laser diode interferometer are less than  $\pm 20 \text{ nm}$ .

**Table 1** Comparison results of wavelength compensation

Times	1	2	3	4	5
Calibrated wavelength (mm)	637.6549	637.6538	638.0461	638.0621	638.062
Temperature ( $^{\circ}\text{C}$ )	26.6	26.6	27.7	27.9	28
Predicted wavelength (mm)	637.6520	637.6482	638.0388	638.0641	638.067
Error (mm)	-0.0029	-0.0056	-0.0074	0.0020	0.0050
Wavelength prediction error ratio	-4.548E-06	-8.782E-06	-1.144E-05	3.134E-06	7.836E-06

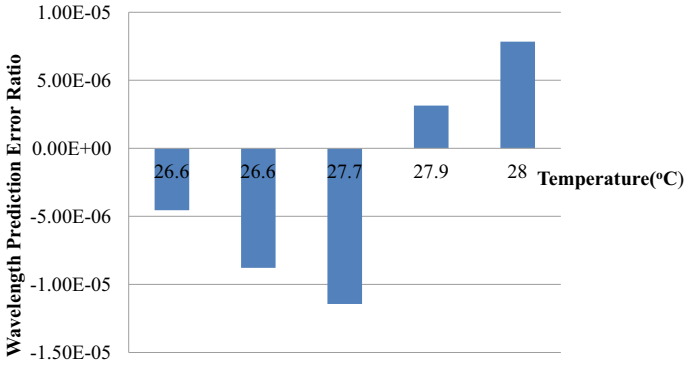


Fig. 9 Wavelength error at different room temperatures

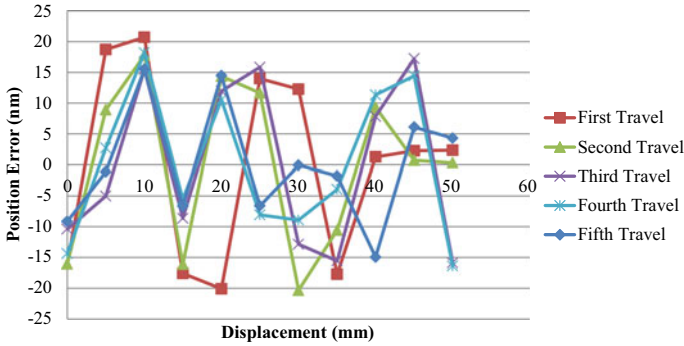


Fig. 10 Position error of laser diode interferometer

### 4 Conclusion

A low cost novel miniature laser diode interferometer with wavelength compensation has been developed. It is a Michelson type interferometer and the four interference current signals, phase shifted by a phase encoding module, are detected by four photodetectors. The wavelength compensation method is based on the principle of diffraction, which is used in most spectrometers. It is equipped with two optical autocollimators to detect the angular drift of laser beam and the real-time wavelength. Its wavelength prediction can reach to  $10^{-6}$  accuracy. The laser diode interferometer can be used as any linear feedback sensor in high precision stages.

## References

1. Bobroff N (1993) Recent advances in displacement measuring interferometry. *Meas Sci Technol* 4(9):907–926
2. Schwenke H et al (2008) Geometric error measurement and compensation of machines—an update. *CIRP Ann Manuf Technol* 57(2):660–675
3. Schattenburg ML, Smith HI (2002) The critical role of metrology in nanotechnology. *Proc SPIE* 4068:116–124
4. Jäger G et al (2010) Nanomeasuring and nanopositioning engineering. *Measurement* 43(9):1099–1105
5. Qiangxian H, Xiaowei L, Lala S (2009) Homodyne laser interferometric displacement measuring system with nanometer accuracy. In: 9th international conference on electronic measurement & instruments, 2009. *ICEMI '09*, p 1-908-912
6. Topcu S et al (2005) Improving the accuracy of homodyne Michelson interferometers using polarisation state measurement techniques. *Opt Commun* 247(1–3):133–139
7. Hartmann L, Meiners-Hagen K, Abou-Zeid A (2008) An absolute distance interferometer with two external cavity diode lasers. *Meas Sci Technol* 19(4):045307
8. Dobosz M, Zamiela G (2012) Interference fringe detection system for distance measuring interferometer. *Opt Laser Technol* 44(5):1620–1628
9. Lee J-Y, Tsai S-K (2011) Measurement of refractive index variation of liquids by surface plasmon resonance and wavelength-modulated heterodyne interferometry. *Opt Commun* 284(4):925–929
10. Pollinger F et al (2009) Diode-laser-based high-precision absolute distance interferometer of 20 m range. *Appl Opt* 48(32):6188–6194
11. Birch KP (1990) Optical fringe subdivision with nanometric accuracy. *Precis Eng* 12(4):195–198
12. Požar T, Gregorčič P, Možina J (2011) Optimization of displacement-measuring quadrature interferometers considering the real properties of optical components. *Appl Opt* 50(9):1210–1219
13. Heydemann PLM (1981) Determination and correction of quadrature fringe measurement errors in interferometers. *Appl Opt* 20(19):3382–3384
14. <http://sios.de>



# Design and Testing of a Contact-Type Micro Thermal Sensor for Defect Inspection on Nanometric Smooth Surfaces



Y. Shimizu, Y. Ohba, and W. Gao

**Abstract** This paper presents a design study on a contact-type micro thermal sensor for detection of defects on smoothly-finished surfaces such as magnetic disks, sapphire substrates for LED fabrication and so on. Due to miniaturization of structures to be fabricated on such smooth surfaces, inspection of small defects is becoming a critical issue to be addressed for the assurance of the product quality. To achieve further better resolution for defect detection, a new concept employing a contact-type micro thermal sensor has been proposed. In the proposed concept, a defect on a surface is detected by capturing a frictional heat generated at contacts between the thermal sensor and a defect. A thermally-sensitive area of the thermal sensor is therefore required to be on the top of the sensor surface profile. In this paper, fabrication process of the sensor is modified in such a way that a dummy layer is inserted just beneath a sensing element layer. As a result, the thermally-sensitive area can be lifted up compared with the previous design of the thermal contact sensor. To verify the feasibility of the modified thermal sensor, some contact detection tests have been carried out.

**Keywords** Defect inspection · Contact sensor · Measurement

## 1 Introduction

Strong demands on precision products, which require smooth surface finished with surface roughness of on the order of sub-nanometer, can be found in various fields such as magnetic storage industry [1], optics industry, semiconductor industry and so on [2]. Since required tolerances for such smooth surfaces are becoming tighter, smooth surface finishing with a smaller number of defects are also desired. For verification of the surface quality, it is important to carry out surface inspection with a measurement resolution high enough to qualify required surface precision.

---

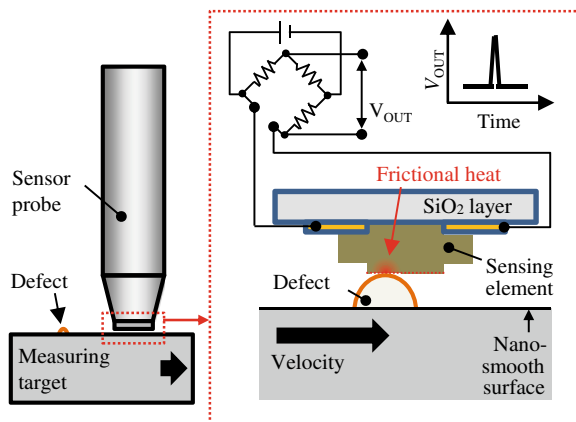
Y. Shimizu (✉) · Y. Ohba · W. Gao  
Tohoku University, 6-6-01, Aramaki Aza-Aoba, Aoba-ku, Sendai 980-8579, Japan  
e-mail: [yuki.shimizu@nano.mech.tohoku.ac.jp](mailto:yuki.shimizu@nano.mech.tohoku.ac.jp)

© Springer Nature Switzerland AG 2022  
S. Hinduja et al. (eds.), *Proceedings of the 38th International MATADOR Conference*,  
[https://doi.org/10.1007/978-3-319-64943-6\\_35](https://doi.org/10.1007/978-3-319-64943-6_35)

For inspections of nanometric smooth surfaces, optical methods based on laser scattering, which detects defects on a target surface by capturing scattered lights generated when defects are illuminated by incident laser beams, have been used so far [3, 4]. With the employment of highly-sensitive photodetectors and the enhancement of image processing technologies, resolution of the defect detection has been improved. As a result, in current, existences of defects with a size of on the order of several-ten nm can be detected [5]. Since scattered light intensity is in accordance with the Rayleigh scattering limitation [5], sizes of the detected defects can precisely be verified. On the other hand, however, too small defects cannot be detected when the scattered light intensity becomes below detectable minimum intensity of the photodetector. It is said that defects with a diameter of smaller than 10 nm are difficult to detect even if a high-sensitive photodetector is employed in measurement systems. Therefore, a new inspection method, which enables to find out further smaller defects on nanometric smooth surfaces, is required [6].

The motivation of this research is to establish a new method for detection of a small defect, whose diameter is smaller than 10 nm, on a nanometric smooth surface. A new concept of a defect inspection method, in which surface defects are to be detected by sweeping a smooth surface with a micro thermal sensor, has been proposed by the authors [7]. A schematic of the proposed method is shown in Fig. 1. To realize the methods, there are many issues need to be addressed; at first, a highly-sensitive micro thermal sensor, which can detect the tiny quantity of frictional heat on the order of microwatts [7] generated at a contact with a defect on a measuring surface, needs to be developed. A precise control of a constant gap between the measuring surface and the tip of the sensor probe, on which tip the micro thermal sensor is mounted, is also required. As the first step, the authors have developed a first prototype micro thermal sensor with a simple structure consisting of electrodes and a thin-film resistance, which is referred to as a sensing element [8] by using photolithography process. In addition, feasibility of the fabricated micro thermal sensor as a contact detection sensor was tried to be verified. Throughout some experiments, it was verified that

**Fig. 1** Defect inspection on nanometric smooth surfaces by using a contact-type micro thermal sensor



the developed micro thermal sensor could distinguish an applied rate of heat supply of down to  $10 \mu\text{W}$ , and could be used as a contact detection sensor [8]. In addition, it was also confirmed that the micro thermal sensor can detect slight contact with a sphere whose diameter was approximately  $50 \mu\text{m}$  [9]. Meanwhile, it has not been sure whether the micro thermal sensor can detect a contact with a defect whose diameter is on the order of several-ten nm, which is close to the target value of the proposed method.

In this paper, experiments are carried out to verify the feasibility of the micro thermal sensor on detection of defects whose diameters are on the order of several-ten nm. In the experiments, by employing an AFM probe whose tip diameter is  $40 \text{ nm}$  and making it contact with the micro thermal sensor, a contact between the micro thermal sensor and a small defect is simulated.

## 2 Fabrication of the Contact-Type Micro Thermal Sensor

A schematic of a micro thermal sensor used in this research is shown in Fig. 2 [9]. In terms of the proposed defect detection method, an area of the thermal element sensitive against frictional heat is preferred to be on the top of the micro thermal sensor. In the sensor structure, an additional layer, which is referred to as a dummy layer in this paper, was therefore inserted just beneath the sensing element so that a part of the sensing element could be on the top surface of the micro thermal sensor. In the fabrication of the first prototype sensor, wet etching process was employed for patterning of both electrodes and the sensing element. However, it was difficult to assure the pattern widths due to high etching rates of a chromium (Cr) layer on a silicon substrate. In the second prototype sensor fabrication, a dry etching process was therefore employed. Figure 3 shows a flowchart of the fabrication process [9]. The thermal element, which is positioned in-between a pair of electrodes, is sputtered on the substrate through an aperture of the resist layer. The shape of the aperture is easy to control by the mask pattern used for the lithography. After that, resist layer and

**Fig. 2** A schematic of the second prototype micro thermal sensor [9]

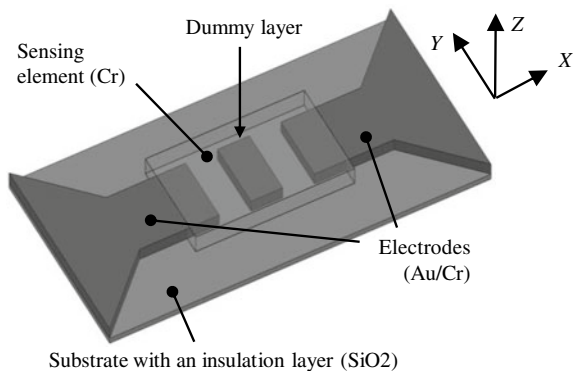


**Fig. 3** A flowchart of the sensor fabrication [9]

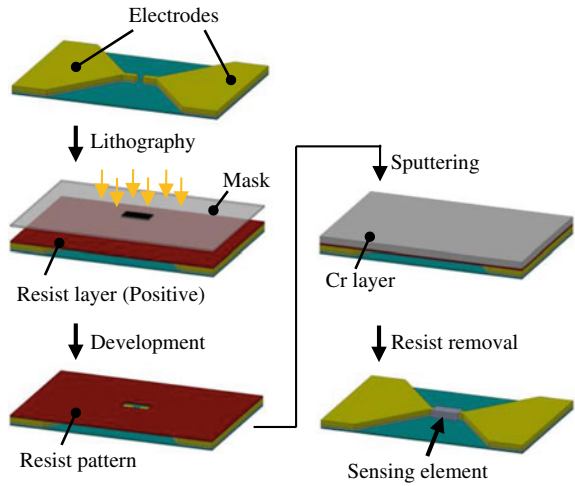
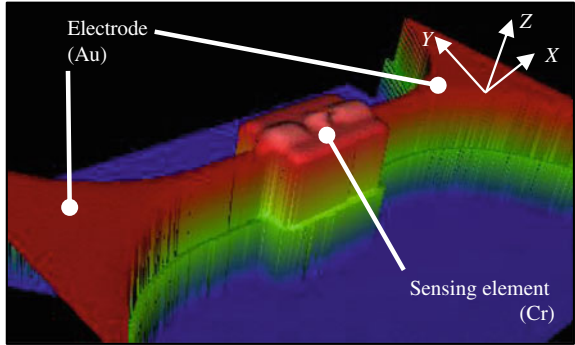


**Fig. 4** Fabrication of the micro thermal sensor



Cr layer are removed away from the substrate, which is referred to as rift-off process [10]. This removal process does not affect the sensing element, and is suitable for the sensor fabrication since it is more robust than the wet etching process. Figure 4 shows a three-dimensional microscopic image of the fabricated second prototype thermal element.

### 3 Verification of the Feasibility of Fabricated Micro Thermal Sensor for Defect Detection

Experiments were carried out to confirm the feasibility of the fabricated micro thermal sensor on detection of defects with a diameter of on the order of several-ten nm. An AFM probe with a tip diameter of 40 nm was employed to simulate a contact between

the thermal element and a defect to be detected; in the experiment, the tip of the AFM probe was utilized instead of defects on a smoothly-finished surface.

Figure 5 shows a schematic of the experimental simulation with the AFM probe. One of the advantages of employing the AFM probe in this experiment was that the contact detection sensitivity of the developed thermal sensor could be compared directly with the highly-sensitive AFM probe. In addition, the contact point could be determined precisely since the AFM probe could measure sensor profile. Furthermore, load at contact could also be controlled by adjusting the Z-directional position of the AFM probe with respect to the thermal sensor.

To build up the experimental setup in a simple apparatus, a self-detective AFM probe, in which a piezoelectric (PZT) resistance sensor was mounted on its cantilever, was employed. Figure 6 shows a block diagram of the system developed for the experiment. A constant DC bias voltage was applied to the thermal sensor through a

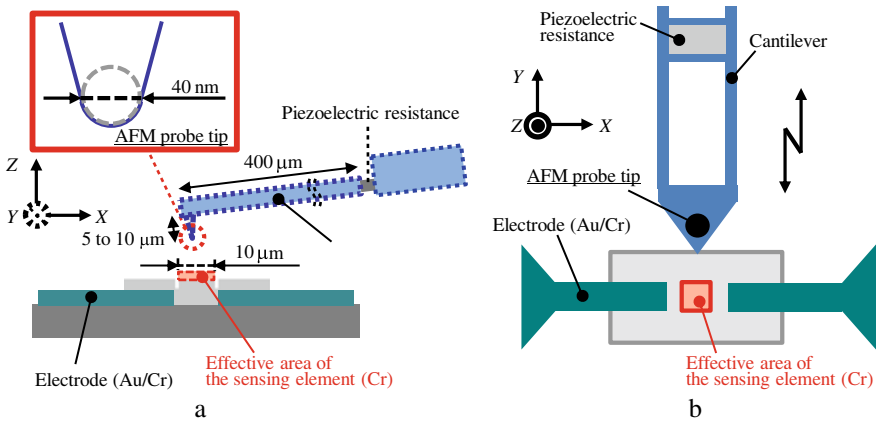
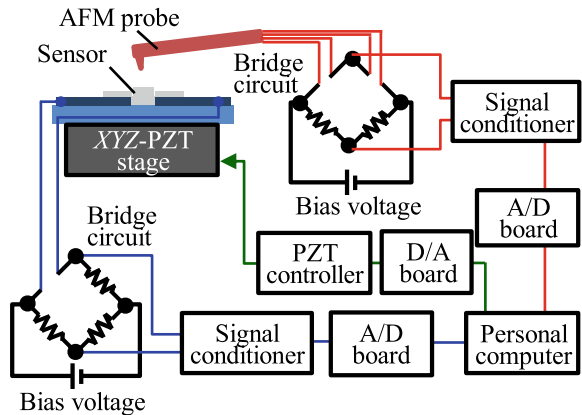
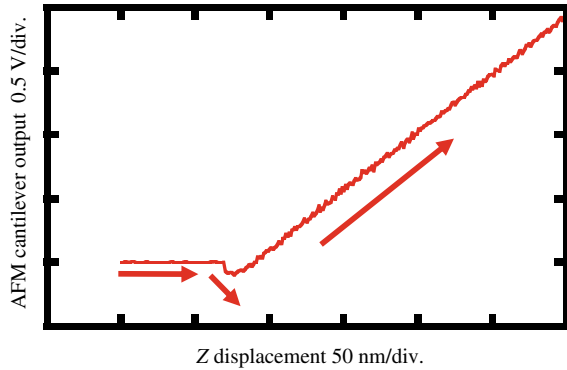


Fig. 5 Schematic of the developed system. a Side view; b top view

Fig. 6 Block diagram of the developed system



**Fig. 7** Force curve of the AFM probes

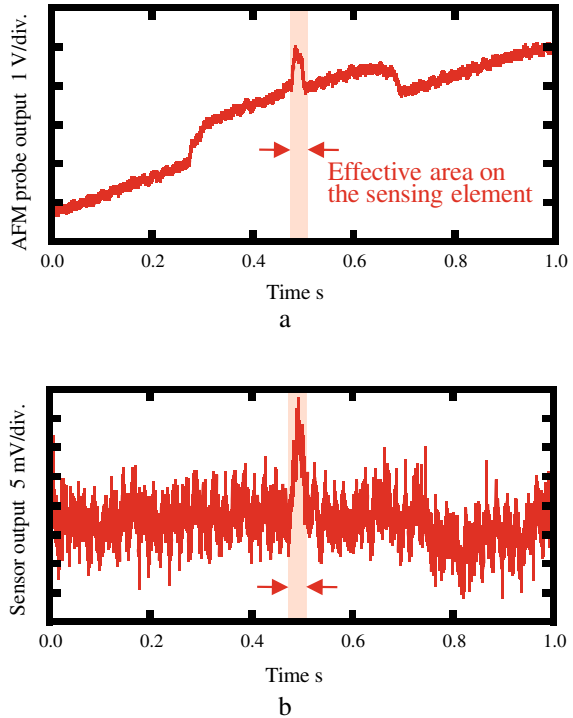


bridge circuit. The deviation of the electric resistance of the thermal element due to the deviation of the sensor temperature was then processed by using a commercial signal conditioner (CDV-700A, Kyowa Electronic Instrument), and the processed signal was captured by a personal computer via an A/D board. In the same manner, signal of the PZT sensor on the AFM probe was processed as shown in Fig. 6. The substrate of the thermal sensor was mounted on a 3-axis PZT stage so that the effective area of the sensing element in the thermal sensor could be positioned precisely with respect to the AFM probe.

At first, the thermal sensor was made to approach the AFM probe by using the PZT stage, while the voltage output of the PZT sensor on the AFM probe was monitored. Figure 7 shows the deviation of the PZT sensor output with respect to the Z-displacement of the thermal element. At the beginning of the contact between the AFM tip and the thermal sensor, a slight decrease of the PZT sensor output, which is referred to as a “snap in” [11], was clearly observed. After that, the voltage output of the PZT sensor increased in proportional to the Z-displacement of the thermal sensor. From the approach curve in Fig. 7, the sensitivity of the AFM tip was found to be 9.13 mV/nm.

After the AFM tip was made to contact with the thermal sensor surface, relative translational motion in the Y-direction was applied between the AFM probe and the thermal sensor. The X-directional position of the AFM probe on the thermal element was adjusted so that the AFM probe would trace the effective area of the sensing element on the thermal sensor. Figure 8 shows the voltage outputs of the PZT sensor on the AFM probe and the thermal sensor. Both the voltage outputs were captured via the A/D board simultaneously. In the experiment, the relative velocity between the thermal sensor and the AFM probe was set to be 50  $\mu\text{m/s}$ . It was clearly observed that the voltage output of the thermal sensor was increased when the AFM probe was in contact with the effective area on the sensing element in the thermal sensor. From these results, it was verified that the fabricated micro thermal sensor can detect defects whose diameters are on the order of several-ten nm. It should be noted that the experiments in this paper were carried out in the condition that the Z-directional position of the AFM probe was not controlled in a closed-loop control, and therefore

**Fig. 8** Outputs of **a** the AFM probe; **b** the micro thermal sensor



the load applied to the AFM probe was not controlled precisely as well. Further detailed experiments with the controlled load and faster PZT probe scanning will be carried out as future work.

## 4 Summary

To verify the feasibility of the developed thermal sensor on the detection of a small defect, whose diameter is on the order of several-ten nm, second prototype thermal sensor was fabricated, and experimental simulation was carried out by using a self-detective AFM probe equipped with a piezoelectric resistance sensor. It was verified in experiment that the developed thermal sensor can detect a contact with a measuring target whose diameter is approximately 40 nm. Further detailed experiments will be carried out with a closed-loop control of the AFM probe in Future work. Furthermore, tasks required for the development of the proposed method such as an integration of the thermal element into the sensor probe, as well as the development of the control method for the gap between the thermal element surface and the measuring surface would also be carried out as future work.

**Acknowledgements** This project was supported by Japan Society for the Promotion and Science (JSPS).

## References

1. Marchon B, Olson T (2009) Magnetic spacing trends: from LMR to PMR and beyond. *IEEE Trans Magn* 45:3608–3611
2. Brinksmeier E, Mutlugünes Y, Klocke F, Aurich JC, Shore P, Ohmori H (2010) Ultra-precision grinding. *Ann CIRP* 59:652–671
3. Lonardo PM (1991) Surface characterization and defect detection by analysis of images obtained with coherent light. *Ann CIRP* 40:541–544
4. Takami K (1997) Defect inspection of wafers by laser scattering. *Mater Sci Eng: B* 44:181–187
5. Brun R, Moulin C, Schwarzenbach W (2012) Defect inspection challenges and solutions for ultra-thin SOI. In: *Proceedings of 23rd annual SEMI (New York, USA)*, pp 67–71
6. [www.itrs.net](http://www.itrs.net). Accessed Nov 2014
7. Lu W, Shimizu Y, Ito S, Gao W (2012) Design and experiment of thermal contact sensor detecting defects on si wafer surface. *Key Eng Mater* 523–524:826–831
8. Shimizu Y, Lu Y, Ohba Y, Gao W (2014) Feasibility study on the concept of thermal contact sensor for nanometre-level defect inspections on smooth surfaces. *Meas Sci Technol* 25:094002 (11pp)
9. Shimizu Y, Ohba Y, Gao W (2014) Design of fabrication process of a thermal contact sensor for surface defect inspection. *J Adv Mech Des Syst Manuf* 8:14-00099 (14pp)
10. Feuer MD, Prober DE (1981) Projection photolithography-liftoff techniques for production of 0.2- $\mu\text{m}$  metal patterns. *IEEE Trans Electron Devices* ED-28:1375–1378
11. Hutter JL, John Bechhoefer J (1993) Calibration of atomic-force microscope tips. *Rev Sci Instr* 64:1868–1873



# Diameter Measurement of Micro-sphere Based on Analysis of Two Wavelength Ranges of Whispering Gallery Modes



Masaki Michihata, Akifumi Kawasaki, Atsushi Adachi,  
and Yasuhiro Takaya

**Abstract** Probe calibration is now key technique to improve the measurement uncertainty of micro-coordinate measuring machines (micro-CMMs). This study proposes a new method of measuring a micro-sphere diameter for micro-CMM probing system based on whispering gallery modes (WGMs). Depending on the incident wavelength, different WGMs will be excited in the micro-sphere, resulting in WGM wavelengths, which is a quantity to be measured in experiment. Then, it is crucial to determine the mode numbers corresponding to WGM wavelengths in order to estimate the micro-sphere diameter. The mode numbers are determined with a least-squares method comparing theoretical and measured spectra of WGMs wavelengths. This method tends to cause an error of mode numbers due to the measurement noises in the WGM wavelengths. In this paper, this method was newly developed with two separate WGM wavelength ranges to determine the mode number accurately.

**Keywords** Micro-sphere · Diameter measurement · Whispering gallery mode

## 1 Introduction

A coordinate measuring machine (CMM) is a standard measuring instrument to evaluate dimensions and geometric shapes of products. Recently, dimensional measurement for micro-scale products such as micro-nozzule, micro-lens are highly demanded, for that, high accurate small CMMs (micro-CMMs) have developed in many institutes and companies [1]. One of the most challenging problems on micro-CMMs is the probing system [2]. Many types of the micro-probing system have proposed so far, and a size of the spherical tip is of the order of several tens micrometers [3–6]. The tips are so small that the probe calibration has become a key issue to be addressed these days. A typical diameter of the spherical tips is 50  $\mu\text{m}$  or less and materials used are mainly glass or tungsten carbide [7]. In order to assure the sphericity of these tips, several methods have been proposed [8–11]. Most of them

---

M. Michihata (✉) · A. Kawasaki · A. Adachi · Y. Takaya  
Department of Mechanical Engineering, Osaka University, 2-1 Yamadaoka, Suita, Osaka, Japan  
e-mail: [michihata@mech.eng.osaka-u.ac.jp](mailto:michihata@mech.eng.osaka-u.ac.jp)

are not suitable for the tips smaller than  $100\ \mu\text{m}$  and not precise enough. Considering the total measurement uncertainty of micro-CMMs, the uncertainty in the probe calibration should be less than  $10\ \text{nm}$ . Therefore we are dedicated to developing the new precise diameter measurement technique for micro-CMMs probe tips.

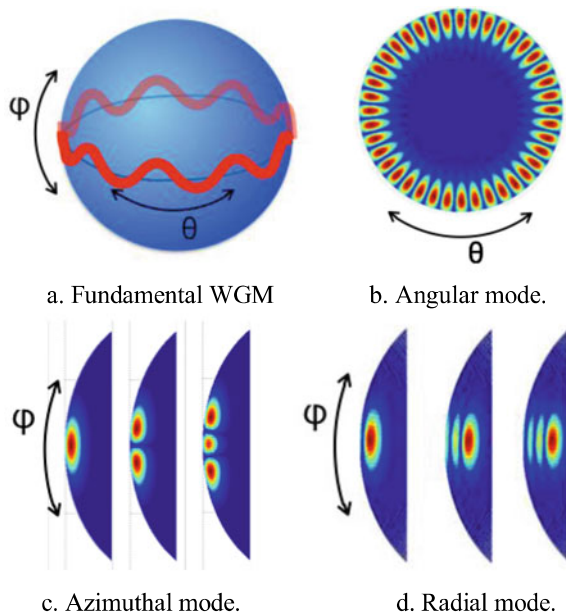
## 2 Measurement Principle

### 2.1 Whispering Gallery Mode

We have proposed the new method to measure a diameter of the spherical tips for micro-CMMs on a basis of whispering gallery mode (WGM) resonance [12]. WGM is the mode that a light resonates inner layer of the sphere at specific conditions such as shown in Fig. 1a. This is also known as morphological resonance. The conditions to excite WGMs are mainly related to the wavelength of the light, the refractive index and the diameter of the sphere, so the diameter can be estimated based on the analysis of the wavelengths to excite WGM (WGM wavelengths).

It should be noted that there are three types of WGM; angular mode Fig. 1b, azimuthal mode Fig. 1c and radial mode Fig. 1d. Depending on these mode numbers, the WGM wavelengths are different. For azimuthal and radial mode, the spatial distributions of the electromagnetic field is also dependant with the mode numbers. Particular the mode numbers, where the electromagnetic distributions are the most

**Fig. 1** Whispering gallery mode resonance with three different modes



narrow shown at the left image in Fig. 1c and d, are named fundamental WGM (F-WGM). For the azimuthal mode, F-WGM is the highest mode number, for the radial mode, F-WGM is the lowest.

## 2.2 Diameter Measurement

In experiments, it is possible to detect only the F-WGM by optimizing the WGM excitation method [12], which means that azimuthal and radial mode numbers are able to be identified, requiring the angular mode numbers in order to estimate the diameter of the spherical tip. Relation between the diameter, the WGM wavelength, and the angular mode number is shown in the following equation [13].

$$D = \frac{\lambda_{qlm}}{\pi n_s} \left( \ell + \frac{1}{2} + \alpha_q \sqrt[3]{\frac{2\ell + 1}{4}} - \Delta \right) \quad (1)$$

where,  $D$  is the diameter of the sphere,  $\lambda_{qlm}$  is the WGM wavelength,  $n_s$  is the refractive index of the sphere,  $\ell$  is the angular mode number,  $q$  is the radial mode number,  $\alpha_q$  is the absolute value of the  $q$  th zero of the Airy function.  $\Delta$  is the shift of the WGM wavelength by the polarization given by

$$\Delta = \begin{cases} \gamma \sqrt{\gamma^2 - 1} & \text{for TE mode} \\ \gamma^{-1} \sqrt{\gamma^2 - 1} & \text{for TM mode} \end{cases} \quad (2)$$

where,  $\gamma$  is  $n_s/n_0$  and  $n_0$  is the refractive index of surrounding medium. The dispersion for the refractive index of the sphere was considered using Sellmeier's equation. Equation (1) shows that the diameter can be calculated using the measured WGM wavelengths and the estimated angular mode number. Only the WGM wavelengths can be measured experimentally. It is hard to estimate the angular mode number from single WGM wavelength. Therefore, based on the several WGM wavelengths, the diameter and the angular mode numbers is going to be estimated. The procedures are explained such as follows.

**Step 1** Obtain several F-WGM wavelengths,  $\lambda_m$  experimentally like shown in Table 1.  $\lambda_m$  means the measured WGM wavelengths.

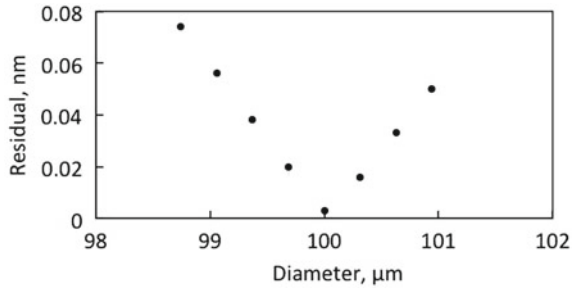
**Step 2** Calculate theoretical F-WGM wavelengths,  $\lambda_c$  using Eq. (1) for the fixed angular mode numbers and the various diameters. Substitute the experimental wavelengths from the theoretical ones, then average the these differences to calculate the residual,  $\delta_D$ , for each diameter, that is

$$\delta_D = \frac{1}{N} \sum_i^N |\lambda_m^i - \lambda_c^i| \quad (3)$$

**Table 1** Procedure to estimate the angular mode number and the diameter of a microsphere

Obtained wavelengths, $\lambda_m$ , nm	Theoretical values																
	Angular mode number, $l$ , and theoretical wavelengths, $\lambda_c$ , nm																
1509.70	322	1509.82	323	1509.79	324	1509.76	325	1509.73	326	1509.70	327	1509.67	328	1509.64	329	1509.61	
1505.00	323	1505.06	324	1505.05	325	1505.03	326	1505.02	327	1505.00	328	1504.99	329	1504.98	330	1504.96	
1500.34	324	1500.33	325	1500.34	326	1500.34	327	1500.34	328	1500.34	329	1500.34	330	1500.34	331	1500.34	
1495.70	325	1495.64	326	1495.65	327	1495.67	328	1495.68	329	1495.70	330	1495.71	331	1495.73	332	1495.74	
1491.09	326	1490.97	327	1491.00	328	1491.03	329	1491.06	330	1491.09	331	1491.12	332	1491.14	333	1491.17	
Candidate diameter, $\mu\text{m}$	98.744		99.058		99.372		99.686		100.000		100.314		100.628		100.942		
Residuals, nm	0.074		0.056		0.038		0.020		0.003		0.016		0.033		0.050		

**Fig. 2** Residuals against diameter of experimental and theoretical wavelengths



where,  $N$  is the number of the WGM wavelengths within the considered wavelength range. Found the diameter where the residuals  $\delta_D$  is minimum as the candidate diameter.

**Step 3** Shift the angular mode numbers by one and repeat same calculations as step 2. Such theoretical values are shown in Table 1.

**Step 4** Among the all sets of calculated (candidate) diameters and residuals, the set including the minimum residuals are selected, obtaining the estimated diameter and the angular mode number such as shown in Fig. 2. In this case, the minimum residual is 0.003 nm, which value is derived from the rounding error during the calculations.

### 3 Simulation of Diameter Measurement

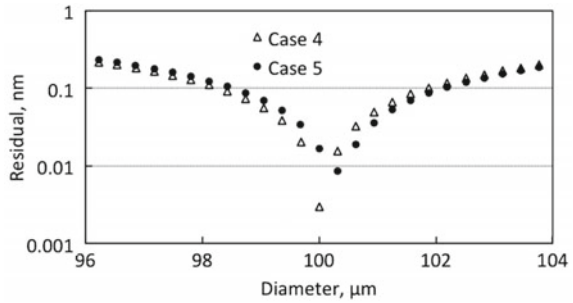
#### 3.1 One WGM Range

The diameter of a micro-sphere is determined based on the analysis of several WGM wavelengths. In that determining process, the angular mode numbers are firstly estimated from the WGM wavelengths. However, the values of WGM wavelengths are very similar to the neighbouring ones with different angular mode numbers, so if there is measurement noises in the WGM wavelengths, the diameter is not accurately measured. Therefore firstly, it is simulated the performances and robustness of the algorithm estimating the diameter.

Here, it is supposed to measure the sphere with 100.000  $\mu\text{m}$  in a diameter. A material of the sphere is BK-7 glass. The WGM wavelength range is around 1500 nm, and the five WGM wavelengths are considered. Polarization of WGM was assumed as TE mode. Under these conditions, theoretical WGM wavelengths and angular mode numbers are calculated using Eq. (1) and shown in left column of Table 2. To simulate the proposed algorithm, noises are added to the theoretical WGM wavelengths, that is, the simulated WGM wavelengths are sum of the theoretical WGM wavelengths and the random noises. The random noise are generated with an amplitude 0.03 nm. In previous experiment, repeatability of measuring WGM wavelengths was  $\pm 0.02$  nm [14], so the simulated noise was reasonable.



**Fig. 3** Residuals of estimation process in 1500 nm wavelength ranges for case 4 and 5 in Table 2



Simulated data was generated for 5 cases shown in center column of Table 2. The estimated diameters of a sphere and the angular mode numbers were estimated based on the simulated WGM wavelengths using the proposed algorithm. The results were also listed in right column of Table 2.

The estimated diameters are well agreed at around 100.000  $\mu\text{m}$ . However, only Case 5 has an error of 314 nm, because the different angular mode numbers was detected. See the detail residuals during the calculated processes for cases 4 and 5 shown in Fig. 3. Minimum residuals are smaller than 0.01 nm. This proved that even very small noises in measurement of the WGM wavelengths cause the errors in the most fitted diameter, which leads the detection of the different angular mode numbers, resulting in the errors of 0.3  $\mu\text{m}$  in diameter. In other words, this measurement method is quite precise if the angular mode numbers were estimated accurately. Here it must be aware of that the residual is not only the parameter to determine the angular mode numbers. The values of the candidate diameter should be taken into account. Therefore we propose the analysis of two WGM wavelength ranges using these parameters (candidate diameter, angular mode number) to determine the accurate angular mode numbers.

### 3.2 Two WGM Range

It is hard to detect the angular mode numbers determinably if one range of WGM wavelengths is considered. Therefore two ranges are used to enhance the accuracy to detect the angular mode number. Here the effect of this algorithm is confirmed via simulation.

Beside the previous 1500 nm wavelength range, 1400 nm is also considered. The simulation conditions are same as the previous simulation except the wavelength range. Theoretical WGM wavelengths are calculated, shown in Table 3. Simulated WGM wavelengths are also generated with same manner as the previous simulation. Table 3 shows the estimated angular mode numbers and diameters with using one WGM wavelength range. In this case, cases 1, 2 and 4 are agreed well and there are errors of  $\pm 0.293 \mu\text{m}$  in case 3 and 5. Same as 1500 nm wavelength range, the error is

**Table 3** Simulation data in estimating the diameter using 1400 nm wavelength range

Theoretical value		Theoretical wavelengths + random noises, nm					Estimated angular mode number				
Angular mode number	Wavelengths, nm	Case 1	Case 2	Case 3	Case 4	Case 5	Case 1	Case 2	Case 3	Case 4	Case 5
349	1408.56	1408.55	1408.57	1408.55	1408.54	1408.58	349	349	350	349	348
350	1404.46	1404.47	1404.46	1404.44	1404.46	1404.48	350	350	351	350	349
351	1400.39	1400.41	1400.40	1400.42	1400.41	1400.37	351	351	352	351	350
352	1396.35	1396.32	1396.35	1396.33	1396.32	1396.33	352	352	353	352	351
353	1392.33	1392.31	1392.32	1392.35	1392.34	1392.32	353	353	354	353	352
Diameter, $\mu\text{m}$		Estimator diameter, $\mu\text{m}$									
100.000		100.000	100.000	100.293	100.000	100.293	100.000	100.000	100.293	100.000	99.707



**Fig. 4** Residuals in estimating process of 1500 and 1400 nm wavelength range for case 5 in Tables 2 and 3

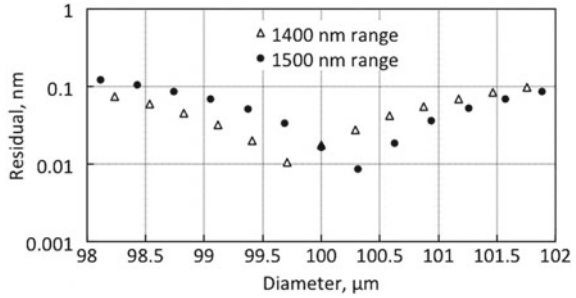


**Table 4** Detail values of the estimated diameter and residuals in around 1000  $\mu\text{m}$  in Fig. 4

1400 nm-range		1500 nm-range		Difference in diameter, nm
Candidate diameter, $\mu\text{m}$	Residual, nm	Candidate diameter, $\mu\text{m}$	Residual, nm	
99.413	0.020	99.371	0.051	42
99.707	0.011	99.685	0.034	22
100.000	0.018	99.999	0.017	1
100.291	0.028	100.314	0.009	-23
100.584	0.042	100.627	0.019	-43
100.877	0.056	100.941	0.036	-64

derived from the detection of the different angular mode numbers. Here we consider the case 5 for both WGM wavelength ranges, which is the case that the angular mode numbers were not accurately measured because the only minimum residuals are focused on. In Fig. 4, the residuals versus the candidate diameters are shown. As shown, the minimum residuals are not at 100.000  $\mu\text{m}$  for both cases, which is because of the measurement noises. The detail values of them around 100  $\mu\text{m}$  are listed in Table 4. In an aspect of the candidate diameter, 100.000  $\mu\text{m}$  are very well agreed, the difference is 1 nm only, but because of the added noise, residuals are not minimum. Therefore, not only the residuals but also the candidate diameters should be taken into account, which results in the accurate detection of the angular mode numbers and diameter. Performance of this algorithm, which is the analysis of the two range of WGM wavelengths, is going to be confirmed via experiment.

## 4 Experimental Setup

To excite and measure the WGM, a light is introduced into the sphere through a tapered optical fiber. A portion of this tapered fiber is stretched such that its diameter is reduced to a few microns. In the tapered section, the optical fiber core is also stretched, allowing light to propagate in the clad. Through total internal reflection

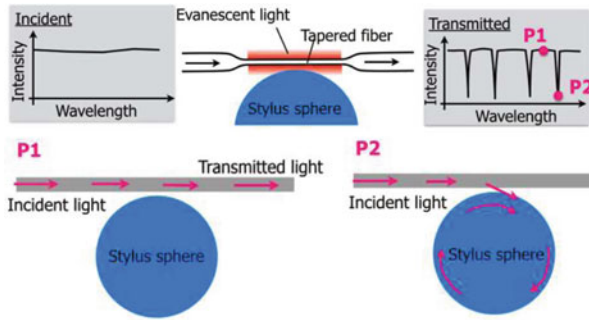
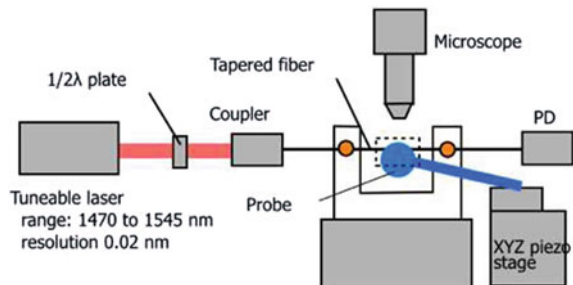


**Fig. 5** Schematics of excitation and measurement of WGM

at the interface with the air, the evanescent light is thus localized along the tapered portion of the fiber. When the stylus sphere is exposed to the evanescent light (see Fig. 5), the light is coupled into the sphere at wavelengths that correspond to the WGMs. To determine these WGM wavelengths, the amount of light transmitted past the tapered portion of the optical fiber is observed as a function of the wavelength. A drop in the measured transmitted light should correspond to light coupling into the sphere and thus the identification of a WGM wavelength.

The experimental setup is shown in Fig. 6. The light source is a tunable external cavity laser diode with an average output power of 15 mW. The laser wavelength can be tuned in 0.02 nm increments (1470–1545 nm). The laser line width is 300 kHz. The laser input was coupled to the tapered fiber (minimum diameter of the tapered portion is 1  $\mu\text{m}$ ) via the polarization controller. The fiber's other end was connected to a photodiode to measure the transmitted light intensity. The tapered fiber was fixed to a holder attached to the micrometer stage. The stylus sphere to be measured was fixed to a holder attached to the XYZ piezostage (5 nm resolution). The tapered fiber and stylus sphere were observed using a microscope. The glass stylus sphere was made by heating a thinned glass pipette with a tungsten wire. The glass sphere diameter was 80  $\mu\text{m}$ , which was roughly estimated by optical microscopy. The material of the sphere was BK-7 glass. For measurements, the separated distance between the micro-sphere and the sphere must be maintained to excite F-WGM. For that, the

**Fig. 6** Experimental setup



transmitted power via the tapered fiber was monitored. When the sphere is close enough to the tapered fiber within the area of the evanescent light, the transmitted power is decreased. Thus the separation distance is adjusted, where the transmitted light is decreased 10%.

### 5 Measurement Result

In our measurement system, the tunable wavelength range is 1470–1545 nm, so the following two wavelength ranges are used; 1470–1490 nm as shorter wavelength range, 1525–1545 nm as the longer wavelength range. The measurement results of the WGM wavelengths for both wavelength ranges are shown in Fig. 7. These transmitted intensities are normalized with the intensities without the sphere. Although the adjustment of the separation distance were not enough to reduce the WGM wavelengths without F-WGM, the F-WGM was still clear enough to be identified. Four F-WGM wavelengths were obtained in both wavelength ranges and the black arrows in Fig. 7 indicate the F-WGM wavelengths. The obtained F-WGM wavelengths were summarised in Table 5. The residuals and the candidate diameters of the sphere was estimated using the proposed algorithm with the measured four WGM wavelengths when assuming the TE mode of WGMs. The results were shown in Fig. 8 and Table 6. For shorter wavelengths, the minimum residual is 0.012 nm at the diameter of 75.867  $\mu\text{m}$ , but 0.013 nm at the diameter of 76.176  $\mu\text{m}$  is comparably small. For the longer wavelength range, the residuals of 0.010 nm are minimum at the diameter of

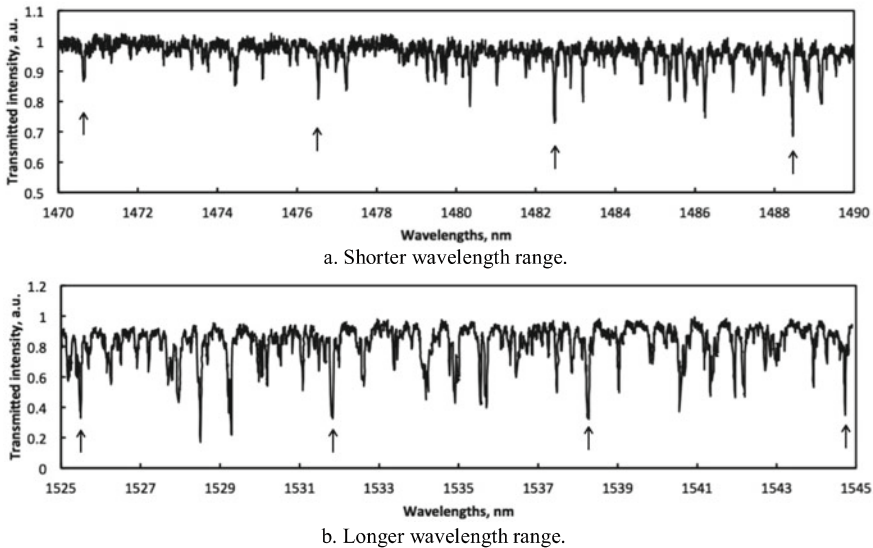
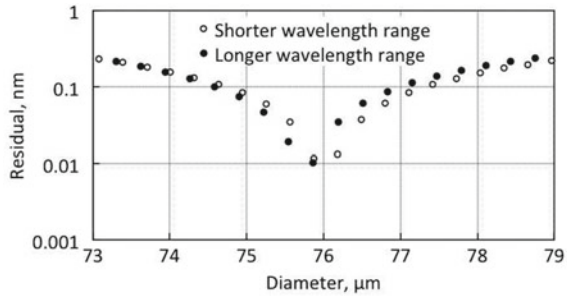


Fig. 7 Transmitted light

**Table 5** Experimentally obtained F-WGM wavelengths

Measured WGM wavelengths, nm	
Shorter range	Longer range
1470.65	1525.49
1476.53	1531.84
1482.48	1538.24
1488.46	1544.73

**Fig. 8** Residuals in longer and shorter wavelength ranges



**Table 6** Candidate diameters in longer and shorter wavelength range near 76 μm in Fig. 8

Shorter wavelength range		Longer wavelength range		Difference in diameter, nm
Candidate diameter, μm	Residual, nm	Candidate diameter, μm	Residual, nm	
75.249	0.059	75.224	0.019	25
75.558	0.035	75.546	0.010	12
75.867	0.012	75.866	0.034	1
76.176	0.013	76.187	0.061	-11
76.485	0.037	76.508	0.087	-23

75.866 μm. As a result, the estimated diameters with considering the minimum residuals are agreed with the difference of 1 nm at 75.866 μm. However it was almost likely to be obtain the different diameter for shorter wavelength if such case, the error would be 291 nm. If considering the candidate diameters also, both cases are again well agreed at 75.866 μm. The other diameter has difference more than 10 nm. Therefore based on the residuals and the candidate diameters, clearly the 75.866 μm is the most likely to be the accurate diameter. Thus analysis of the residuals and the candidate diameter for the angular mode numbers and the diameter can be estimated accuracy and precisely of the order of 1 nm although the absolute accuracy of diameter measurement results must be validated as the future work.

## 6 Conclusion

In this study, we proposed the diameter measurement method for the probing system of micro-CMMs on a basis of analysis of WGM wavelengths. There three kinds of modes in WGM; azimuthal, radial and angular mode. The diameter of a spherical tip can be calculated by determining the three mode numbers. It is possible to identify the mode numbers for azimuthal and radial modes by detecting the fundamental WGM. Therefore, the angular mode number is remained to be considered. However, there are noises in measurements of the WGM wavelengths, inducing detection errors in the angular mode numbers. The error of just one causes error of a few hundreds nm in the resultant estimated diameter. Therefore new algorithm to analyze the WGM wavelengths in two wavelength ranges was proposed. In that process, the residuals and the candidate diameters are focused on. Through the simulations and experiments, it was confirmed that this algorithm enhances performance of the diameter measurement as precise as a few nm. As future works, absolute accuracy of the measurement results is confirmed.

**Acknowledgements** This work was financially supported by the Mitutoyo Association for Science and Technology (MAST) and JSPS Grant-in-Aid for Challenging Exploratory Research (No. 24656102).

## References

1. Claverley JD, Leach RK (2014) A review of the existing performance verification infrastructure for micro-CMMs. *Precis Eng* (in press)
2. Takamasu K (2011) Present problems in coordinate metrology for nano and micro scale measurements. *Mapan* 26(1):3–14
3. Ito S, Kodama I, Gao W (2014) Development of a probing system for a micro-coordinate measuring machine by utilizing shear-force detection. *Meas Sci Technol* 25:064011
4. Hidaka K, Schellekens PHJ (2006) Study of a small-sized ultrasonic probe. *CIRP Ann* 55(1):567–570
5. Claverley JD, Leach RK (2013) Development of a three-dimensional vibrating tactile probe for miniature CMMs. *Precis Eng* 37(2):491–499
6. Michihata M, Takaya Y, Hayashi T (2008) Development of the nano-probe system based on the laser-trapping technique. *CIRP Ann* 57(1):493–496
7. Sheu DY, Cheng CC (2012) Assembling ball-ended styli for CMM's tactile probing heads on micro EDM. *Int J Adv Manuf Technol* 65(1):485–492
8. Fan KC, Wang N, Wang, ZW, Zhang H (2014) Development of a roundness measuring system for microspheres. *Meas Sci Technol* 25:064009
9. Chen L-C (2007) Automatic 3D surface reconstruction and sphericity measurement of micro spherical balls of miniaturized coordinate measuring probes. *Meas Sci Technol* 18:1748
10. Spaan HAM, Widdershoven I, Morel MAA (2006) Novel calibration techniques and applications for touch probes with nanometre accuracy. In: *Proceedings of the 6th EUSPEN international conference*, p 386
11. Küng A, Meli F, Thalmann R (2007) Ultraprecision micro-CMM using a low force 3D touch probe. *Meas Sci Technol* 18:319–327

12. Michihata M, Adachi A, Hayashi T, Takaya Y (2014) Measurement of probe-stylus sphere diameter for micro-CMM based on spectral fingerprint of whispering gallery modes. *CIRP Ann* 63(1):469–472
13. Vassiliev VV, Velichansky VL, Ilchenko VS, Gorodetsky ML, Hollberg L, Yarovitsky AV (1998) Narrow-line-width diode laser with a high-Q microsphere resonator. *Opt Commun* 158:305–312
14. Michihata M, Gake R, Hayashi T, Takaya Y (2013) Fundamental verification of diameter measurement of a micro-CMM probe by using whispering gallery mode resonance. In: *Proceedings of the international symposium on measurement technology and intelligent instruments*

# Investigation of Surface Damages in Contact and Form Measurement with a Force Sensor-Integrated Fast Tool Servo



Y. D. Cai, Y. L. Chen, S. Ito, Y. Shimizu, and W. Gao

**Abstract** This paper presents the investigation of surface damages of the workpiece during the process of tool positioning by using a force sensor-integrated fast servo (FS-FST) on a three-axis ultra-precision lathe. The cutting tool itself on the FS-FTS is employed as a force-controlled stylus probe to make contact with the workpiece surface and measure the forms of the fabricated micro-structures by servo controlling the tool displacement to keep a constant contact force. Experiments were carried out to demonstrate the surface damage degrees by varying the set contact force between the tool tip and the workpiece surface.

**Keywords** Surface damage · Form measurement · Force sensor · Fast tool servo · Diamond tool · Tool positioning

## 1 Introduction

The technique of fast tool servo (FTS) is widely used for ultra-precision diamond cutting of micro-structured surfaces such as Fresnel lens [1], diffractive optical components [2, 3] and free form micro-optics [4, 5]. The authors have developed a force sensor integrated FTS referred as FS-FTS. Apart from precision fabrication of micro-structured surfaces the FS-FTS can be also used for tool positioning, in which the tool is employed as a force-controlled stylus profiler to scan across the fabricated micro-structures based on contact force feedback control. The developed FS-FTS have been used for a couple of applications such as fabrication of micro-structured surfaces [6, 7], tool positioning for stitching fabrication [8] and measurement of tool edge contour [9], respectively.

---

Y. D. Cai (✉) · Y. L. Chen · S. Ito · Y. Shimizu · W. Gao  
Department of Nanomechanics, Tohoku University, Sendai 980-8579, Japan  
e-mail: [caiyd@dlut.edu.cn](mailto:caiyd@dlut.edu.cn)

Y. L. Chen  
State Key Laboratory of Fluid Power Transmission and Control, Zhejiang University, Hangzhou 310027, China

One of the good applications of the FS-FTS is the fabrication of large area micro-structured surfaces [10–12]. The micro-structured surfaces require the individual micro-structure cells to have accurate three-dimensional (3D) geometries with well controlled spacing over a large area. However, since tool wear is an unavoidable phenomenon in the time-consuming cutting process with an extremely long length of cutting path, the machining accuracy decreases with the increase of the cutting path, which is one of the major problems in fabrication of a large area micro-structured surface. Therefore, it is necessary to replace the worn tool with a new one for stitching fabrication of micro-structures over the remained uncut area. In order to set the new tool accurately in a tool holder of the FS-FTS, which is essentially required for the stitching fabrication, it is desired to develop a precision tool positioning method for setting the new tool in the required position with micro-meter accuracy.

The conventional tool positioning methods include probing the cutting edge with a contact probe, measuring a workpiece that has been machined to a prescribed geometry, and determining the location of the cutting edge using an optical system [13]. However, all the conventional methods can be only employed for setting the tool to the start point of the programmed tool path at the beginning of the fabrication process. In addition, the mentioned methods require additional measurement instruments which will cause a complicated configuration on the machine.

In order to deal with the shortcoming of the conventional methods, the authors have proposed a new tool positioning method based on the FS-FTS [14]. By applying this method, the location of the new tool can be accurately identified without using any additional measuring instrument. In this method, the new cutting tool on the FS-FTS is firstly brought to make contact with the fabricated surface by monitoring the output of the force sensor of the FS-FTS. After contact is established, the diamond tool is employed to scan the surface forms of the fabricated micro-structures by servo controlling the contact force. Since both contact detection and surface form measurement by the diamond tool are both based on contact force, the contact force between the micro-tool cutting edge and the workpiece will make damages on the micro-structure surface. In order to maintain the smooth finish of the micro-structured surface, it is important to investigate and reduce the damages during the scanning.

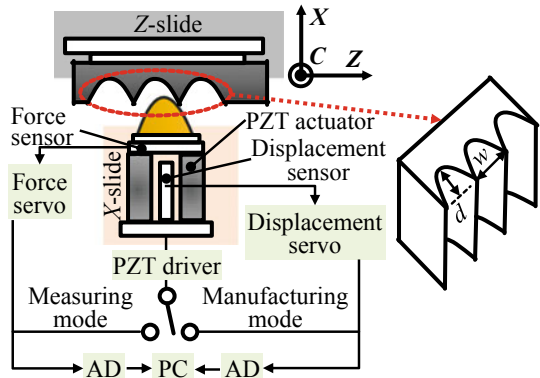
In this paper, the principle of the FS-FTS and the surface measurement by the diamond tool on the FS-FTS are introduced. Experiments of establishment of tool-workpiece contact, scanning across a flat surface and scanning across a micro-structure are carried out respectively to investigate the surface damage caused by the contact force between the diamond tool tip and the workpiece surface.

## 2 Principle of Tool Positioning

Figure 1 shows the schematic of the FS-FTS on a three-axis ultra-precision lathe. This system can be operated based on two modes, which is measuring mode and manufacturing mode, respectively. The changing of the operation mode between the manufacturing mode and the measuring mode is only controlled by a switch



**Fig. 1** Schematic of a force-controlled fast tool on a precision lathe

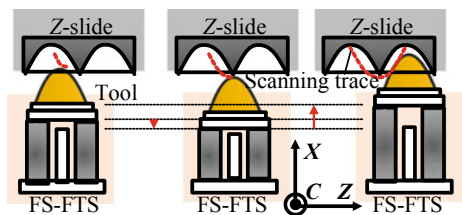


that connects to the PZT driver. It makes FS-FTS convenient for multi-time form measurement of the fabricated surface in the midst of ultra-precision fabrication [15].

A workpiece is mounted onto the spindle of the three-axis precision lathe. The FS-FTS with the single point diamond cutting tool is mounted on the X-slide, and the spindle house is installed on the Z-slide of the precision lathe. The cutting depth of the micro-structures can be controlled by the Z-side of the precision lathe or the PZT actuator of the FS-FTS. The contact force between the tool tip and the workpiece surface can be monitored by the force sensor of the FS-FTS. The displacement sensor equipped on the FS-FTS is used for the measurement of the motion displacement of the diamond tool along the X-direction.

When tool replacement is required in the process of diamond cutting, the steps for setting the new tool to the fabrication interrupted point consists of two steps. Firstly, the new tool is approached to the workpiece surface along the X-direction until the output of the force sensor reaches a set threshold value. By monitored the force sensor output in real time, the contact moment can be established. The movement distance of new tool along the X-direction is detected by the displacement sensor of the FS-FTS or the linear encoder of the X-slid of the precision lathe. Secondly, the workpiece is moved along the Z-direction for the cutting edge of new tool to scan a small region on the surface, as shown in Fig. 2. During the scanning, the contact force between the tool tip and the workpiece surface is kept constant by servo controlling the tool displacement along the X-direction, so that the surface form of the fabricated

**Fig. 2** Schematic of the scanning process along Z-direction



workpiece can be traced by the diamond tool tip. The scanning displacements along the  $X$ - and  $Z$ -directions are obtained by the displacement sensor of the FS-FTS and the linear encoder of the  $Z$ -slide, respectively. Since during the tool positioning process, the interaction between the diamond tool and the workpiece surface is maintained by the contact force, it is unavoidable that it would cause damage to the measured area on the workpiece surface. As the first step of reducing the surface damage caused by tool scanning, it is necessary to investigate the relationship between the damage degree and the set contact force. The next section is to experimentally investigate the damage of workpiece surface during the contact and form measurement by the diamond cutting tool.

### 3 Experiment and Results

#### 3.1 Contact-Damage in Workpiece-Tool Contact

To make the tool-workpiece contact, the tool was moved by the  $X$ -slide of the precision lathe to directly approach the workpiece along the  $X$ -direction while monitoring the output of the force sensor of the FS-FTS. In order to increase the detection sensitivity of the contact force, an AC force modulation method was employed. The diamond tool was oscillated at an amplitude of 1 nm with a constant frequency 220 Hz in the  $X$ -direction by the PZT actuator of the FS-FTS. The output signal of the force sensor was connected to a lock-in amplifier, the reference frequency of which was also set to be 220 Hz. By this way, the signal of the contact force can be amplified without the influence of noise at other frequency. During the process of tool-workpiece contact, contact damages were generated on the workpiece surface by the contact force between the tool and the workpiece. To demonstrate the contact damage clearly, the cutting tool was brought to make contact with the workpiece surface by several of contact times. The contact force of each time was set to be 0.15 mN. Figure 3 shows the three-dimensional (3D) surface profile of the contacted workpiece with different times of contact measured by using a commercial scanning white light interferometer (ZYGO NewView 7300). For clarity, Fig. 4 shows the  $C$ -directional sectional profile of damaged surface on the conditions of one time contact (Fig. 4a), two-time contacts (Fig. 4b) and seven-time contacts (Fig. 4c), respectively.

**Fig. 3** Characterization of the contact-damage caused by workpiece-tool contact

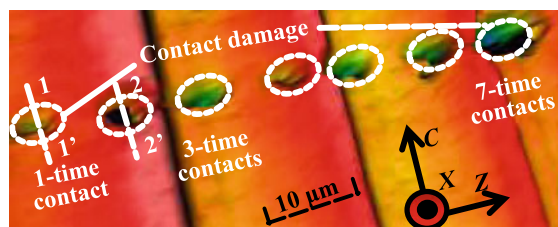
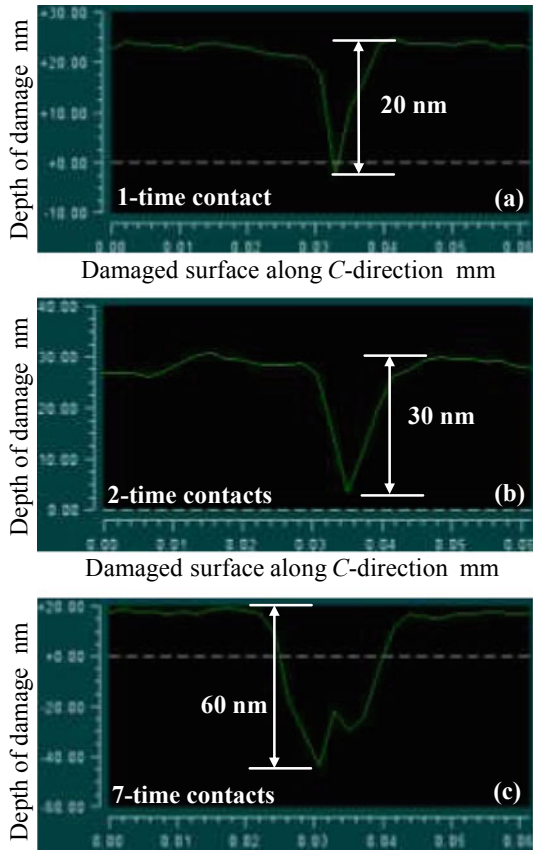


**Fig. 4** Damages in different times contact



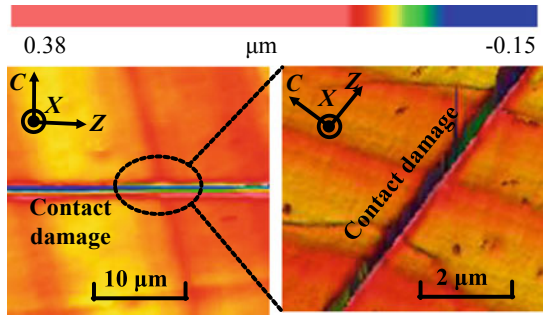
As shown in Fig. 4, the damage depth at one-time contact was 20 nm, and that of two-time contacts and 7-time contacts were 30 nm and 60 nm, respectively. It can be seen that the depth of damage was enlarged when the contact times increased. It is considered to be due to the repeated damage when multi-time contacts were applied.

It can be seen that setting the tool to make a tool-workpiece contact for the beginning of fabrication process or the form measurement will cause the damage of workpiece surface.

### 3.2 Contact-Damage in Scanning a Planar Workpiece

The second step of the tool positioning method is controlling the tool cutting edge to scan across the fabricated micro-structured surface along the Z-direction. For simplicity, the cutting tool was firstly brought to scan a flat surface with diamond turned mirror-finish. The scanning experiment was carried out at an aluminum flat

**Fig. 5** Contact-damage in scanning a planar workpiece



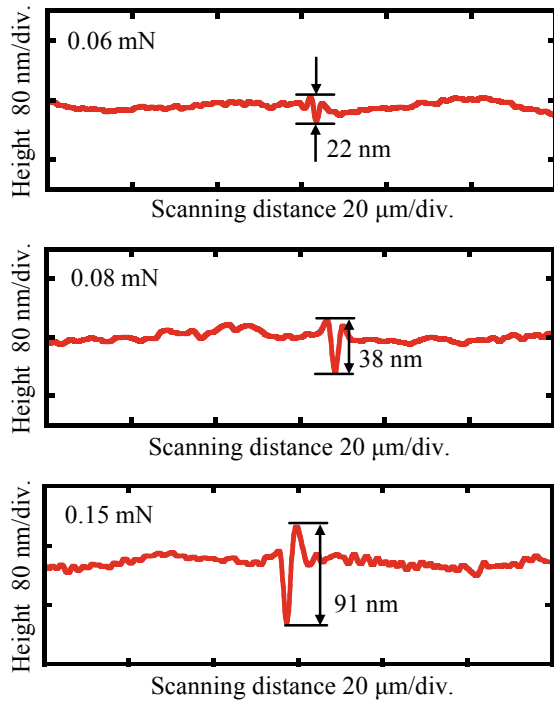
workpiece based on the measuring mode of the FS-FTS. During the scanning, the contact force between the cutting edge of diamond tool and the flat surface is kept constant by servo control of the tool displacement. Because of the used soft material (aluminum), although the contact force was controlled to be a relatively low level, there would be unavoidable surface damage contact damages.

The scanning speed and the contact force were set to be  $10 \mu\text{m}/\text{min}$ . and  $0.15 \text{ mN}$ , respectively. The scanned flat workpiece was measured by the commercial scanning white light interferometer. Figure 5 shows a measured 3D profile image around the scanned area of the flat workpiece. It can be seen that damage occurred over the whole process of the scanning. To investigate the relationship between the degree of the damage and the value of the contact force, different contact forces, which were  $0.06 \text{ mN}$ ,  $0.08 \text{ mN}$  and  $0.15 \text{ mN}$ , respectively, were set in the experiment. The *C*-directional sectional profile of scanned flat workpiece is shown in Fig. 6. The damage depths at contact forces of  $0.15 \text{ mN}$ ,  $0.08 \text{ mN}$  and  $0.06 \text{ mN}$  were evaluated to be approximately  $22 \text{ nm}$ ,  $38 \text{ nm}$  and  $91 \text{ nm}$ , respectively. It can be seen that the depth of damage increased with the increase of the contact force. In addition, the increase of the damage depth is nonlinear relation with the value of the contact force. An intensive analysis of the nonlinear relationship will be carried out as a future work.

### 3.3 Contact-Damage in Scanning a Microstructure Array

Experiment was then extended to the case when the diamond tool scanned across a micro groove array along the *Z*-direction. The micro groove array was fabricated by using the FS-FTS. When the cutting pitch is smaller than the width of a single groove, two neighbouring grooves will have an overlapping boundary in the middle between each other, which forms a sharp line structures. The depth and pitch of the micro groove array were set to be  $2.0 \mu\text{m}$  and  $45 \mu\text{m}$ , respectively. After the micro groove array was fabricated by the FS-FTS, the operation mode of the FS-FTS was changed from the manufacturing mode to the measurement mode. Based on a force feedback control loop of the FS-FTS, the FS-FTS with the diamond tool regarded as a force-controlled stylus probe was brought to scan across the sharp line structures along the

**Fig. 6** Evaluation of contact-damage in scanning a planar workpiece



Z-direction. The scan displacement along the X- and Z-directions is monitored by displacement sensor of the FS-FTS and the linear encoder of the Z-slide, respectively. By combining the two scanning displacements, the tool scan trace can be obtained.

During the scanning, similar to the case using tool to scan the flat workpiece, the contact force between the tool cutting edge and the workpiece surface will generate damages on the micro groove array. Figure 7 shows the 3D surface profile of scanned micro groove array measured by the commercial scanning white light interferometer. The scan speed was set to be 200 nm/s. It can be clearly seen that the surface finish of the micro-structures form is decreased after the scanning. It was considered to be due to the damages generated by the tool cutting edge during the scanning.

**Fig. 7** Profile of the sharp line structure. **a** 3D surface profile. **b** Contact-damage in scanning the sharp line structure

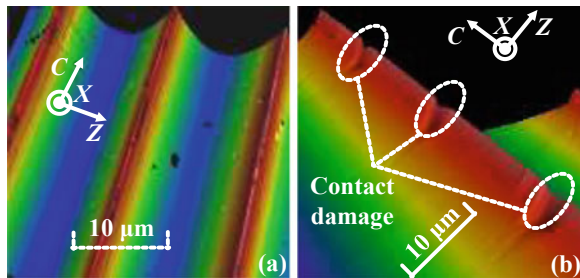
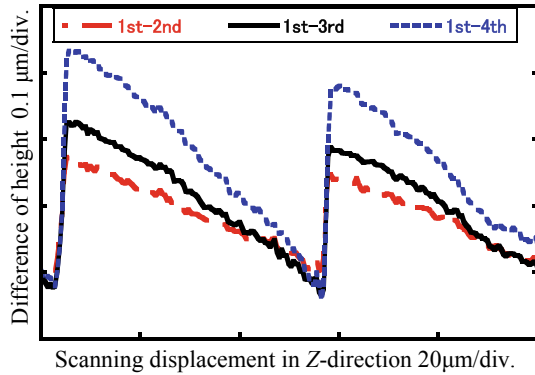


**Fig. 8** Repeated scan image of the sharp line structure



The repeated scanning experiment was carried out to further confirm the damages on the micro groove array. The scan distance and scan speed were set to be  $140\ \mu\text{m}$  and  $200\ \text{nm/s}$ , respectively. The measured results were plotted in Fig. 8. The difference of surface height between the first scan and the consequent of three scans were evaluated to be  $173\ \text{nm}$ ,  $226\ \text{nm}$  and the  $333\ \text{nm}$ , respectively. It can be seen that the difference of surface height increased when the scanning repeated.

Based on the above analysis, it can be seen that the degree of workpiece surface damages was not only influenced by the value of contact force, but also by the contact times and the stability of the force feedback control loop. In the future work, in order to reduce the damages on the machined surface, the intensive analysis of interaction between the workpiece and the diamond tool will be carried out.

## 4 Conclusion

A method of using the FS-FTS for tool-workpiece contact detection and surface form measurement has been introduced. Precision contact between the diamond tool and the workpiece surface can be established by monitoring the force sensor output of the FS-FTS in real time. The surface form of the fabricated workpiece can be scanned by using the diamond tool as a force-controlled stylus probe. During the scanning, the contact force between the cutting tool tip and the surface is kept to be constant by servo controlling the tool displacement, so that the surface form can be traced by the diamond tip. In the contact detection and the surface form measurement, it is unavoidable that the contact force will cause damage to the workpiece surface.

Experiments of investigating the contact damage and the damages when the diamond tool was brought to scan across a flat surface and a micro groove array were carried out, respectively. The damage depth was evaluated to be a few tens of nanometers when the contact force was controlled to be below  $0.1\ \text{mN}$ . In the future, a mathematical model will be established to analyze the surface damage phenomenon caused by the contact force during the scanning process. Molecular simulation (MD)

of the tool contact and scanning process, improvement of the force feedback control system to reduce the surface damage will also be carried out as future works.

## References

1. Ludwick SJ, Chargin DA, Calzaretta JA, Trumper DL (1999) Design of a rotary fasttool servo for ophthalmic lens fabrication. *Precis Eng* 23(4):253–259
2. Gao W, Araki T, Kiyono S, Okazaki Y, Yamanaka M (2003) Precision nano-fabrication and evaluation of a large area sinusoidal grid surface for a surface encoder. *Precis Eng* 27(3):289–298
3. Gao W, Aoki J, Ju BF, Kiyono S (2007) Surface profile measurement of a sinusoidal grid using an atomic force microscope on a diamond turning machine. *Precis Eng* 31:304–309
4. Zhou J, Li L, Naples N, Sun T, Yi A-Y (2013) Fabrication of continuous diffractive optical elements using a fast tool servo diamond turning process. *J Micromech Micro Eng* 23(7):075010
5. Dumond JJ, Low HY (2012) Recent developments and design challenges in continuous roller micro- and nanoimprinting. *J Vac Sci Technol B* 30(1):695–714
6. Bruzzone AAG, Costa HL, Lonardo PM, Lucca DA (2008) Advances in engineered surfaces for functional performance. *CIRP Ann Manuf Technol* 57(2):750–769
7. Evans CJ, Bryan JB (1999) ‘Structured’, ‘‘textured’’ or ‘engineered’ surfaces. *CIRP Ann Manuf Technol* 48(2):541–556
8. Hanif K, Andreas G, (2013) Interdisciplinary design: new lessons from architecture and engineering
9. Chen YL, Gao W, Ju BF, Shimizu Y, Ito S (2014) A measurement method of cutting tool position for relay fabrication of microstructured surface. *Meas Sci Technol* 25:064018 (10pp)
10. Patterson SR, Magrab EB (1985) Design and testing of a fast tool servo for diamond turning. *Precis Eng* 7(3):123–128
11. Woronko A, Huang J, Altintas Y (2003) Piezoelectric tool actuator for precision machining on conventional CNC turning centers. *Precis Eng* 27(4):335–345
12. Miguel A, Justino F, Alain G, Fernando V (2009) Effect of tool setting error on the topography of surfaces machined by peripheral milling. *Int J Mach Tools Manuf* 49(1):36–52
13. Gao W, Chen YL, Lee KW, Noh YJ, Shimizu Y, Ito S (2013) Precision tool setting for fabrication of a microstructure array. *CIRP Ann Manuf Technol* 62:523–526
14. Gao W, Tano M, Araki T, Kiyono S, Park ChH (2007) Measurement and compensation of error motions of a diamond turning machine. *Precis Eng* 31:310–316
15. Chen YL, Wang S, Shimizua Y, Ito S, Gao W, Ju BF (2015) An in-process measurement method for repair of defective microstructures by using a fast tool servo with a force sensor. *Precis Eng* 39:134–142

# Removing the Effects of Linear Axis Errors from Rotary Axis Ballbar Tests



J. M. Flynn, A. Shokrani, V. Dhokia, and S. T. Newman

**Abstract** As the complexity of machined parts increases and geometric tolerances become more challenging, the need be able to verify geometric errors within five-axis machine tools has never been greater. A body of research has been undertaken to demonstrate that the telescoping magnetic ballbar may be used in five-axis machine tool accuracy testing, leading to its recent inclusion in international standards. This paper highlights the fact that geometric errors within linear axes can lead to the falsification of rotary axis error diagnosis. In response, this research identifies a method through which to compensate the effects of linear axis errors from the measurements taken during rotary axis testing. Through experimentation, it is shown that linear error effects may be almost entirely removed from tests that identify radial offset errors, and significantly reduced in tests to identify rotary axis tilt errors. It is proposed that this research has significant potential in machining high-value and complex components, where frequent checking of machine tool geometric errors is required.

**Keywords** Ballbar · Accuracy testing · Five-axis · CNC

## 1 Introduction

Five-axis machine tools (5A-MTs) can change the relative position and orientation of a cutting tool with respect to a workpiece using five degrees of freedom. 5A-MTs are therefore capable of producing complex three-dimensional parts with a reduced number of set-ups and more generic tooling compared with three-axis alternatives. A popular 5A-MT structure is shown in Fig. 1 and its configuration may be denoted as Z-Y-X-A-C, from tool-tip to workpiece. As shown, the rotary axes revolve about the Cartesian X and Z-directions, and are housed within a tilting-rotary table. This kinematic configuration shall form the focus of this paper.

---

J. M. Flynn (✉) · A. Shokrani · V. Dhokia · S. T. Newman  
Department of Mechanical Engineering, University of Bath, Bath, UK  
e-mail: [J.M.Flynn@bath.ac.uk](mailto:J.M.Flynn@bath.ac.uk)



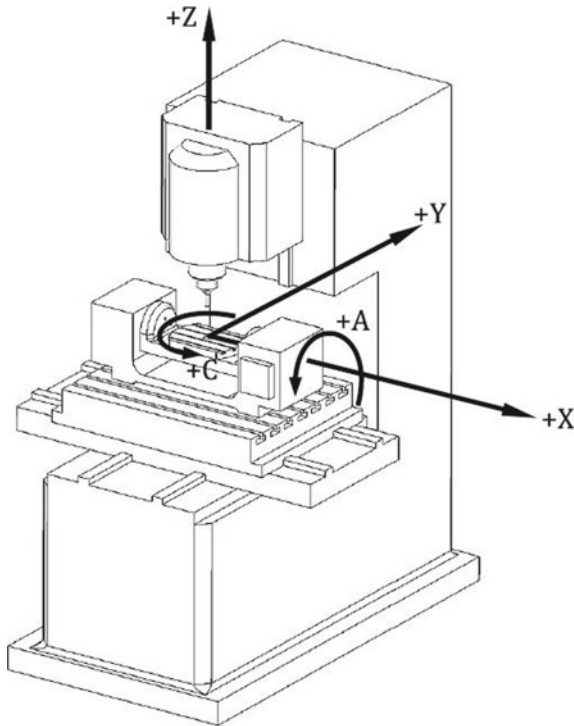


**Fig. 1** An example five-axis machine tool configuration, with rotary axes A and C housed within a tilting-rotary table. From tooltip to workpiece, the axis kinematic chain is Z-Y-X-A-C

As the expectation for part complexity and longevity increases, and automated assembly becomes more prevalent, geometric tolerances are becoming increasingly challenging for machined parts [1]. Consequently, there has never been a more pressing need to verify a 5A-MT's geometric, dynamic, controller-based, thermo-mechanical and static loading errors [2]. Amongst the most fundamental of these errors are those present in the geometry of the machine tool axes, the most basic of which remain constant regardless of axis position, namely location errors [3].

Conceived by Bryan in 1982 [4], the Telescoping Magnetic Ballbar (ballbar) utilizes a precision linear transducer to detect radial deviations as the tool-tip moves about a fixed centre-pivot in a circular toolpath (Fig. 3). The ballbar has become an established tool in the identification of geometric, dynamic and controller-related errors in three-axis machine tools due to its low measurement uncertainty, ease of operation and comparatively low cost [5, 6]. Following the emergent research of Sakamoto et al. in the late 1990s [7], the repertoire of the ballbar has expanded to include five-axis machine tool accuracy testing.

Industry has expressed a desire to be able to rapidly verify the geometric accuracy of five-axis machine tools [8]. In response to this, research has begun to focus on the development of error testing methods that can be used to identify error sources

in both linear and rotary axes, with minimal set-up requirements and low testing durations e.g. [9, 10]. In support of this, error diagnosis techniques and algorithms have also become more complex in an attempt to extract a greater number of error sources from fewer measurements. Following this trend, this research aims to employ the ballbar to measure and separate both linear and rotary axis geometric errors.

## 2 Five-Axis Machine Tool Ballbar Testing

There are a broad range of technologies and methods used in five-axis machine tool accuracy testing, including direct and indirect measurement of machine tool geometric errors. The authors refer the reader to three comprehensive literature reviews [2, 6, 11] and related international standards [3, 12, 13] for further information on a cross-section of this area of machine tool metrology.

The ballbar may be used to verify the position and orientation of a rotary axis average line by strategically aligning the ballbar's sensitive direction throughout a circular tool-path about the rotary axis. In most cases, this alignment is best described using a cylindrical coordinate system, where the ballbar may be aligned radially, axially and tangentially with respect to the average line [3, 13, 14].

The radial ballbar alignment is often used to identify the centre of rotation (i.e. radial offset errors in the average line) by fitting a least squares circle to the ballbar length data. Similarly, it is common to use an axial ballbar alignment to identify the orientation of the plane of rotation (Fig. 5, Toolpath 1). This method has been the driving force behind the widely regarded research of Tsutsumi et al., who identified that eccentricities in ballbar plots could be related to rotary axis errors [14, 15].

Alternative strategies exist to identify the location of the average line and the orientation of the plane of rotation. Radial tests undertaken at two axially separated locations may be used to construct a vector describing the rotary axis average line's position and orientation e.g. [16, 17]. Alternatively, an oblique axial alignment may be used when there is limited axis travel, or movement of the linear axes during the test is undesirable [18]. Finally, testing toolpaths exist that require a synchronized motion between four or five axes [19]. These synchronized motions are often used to simulate machining of a cone-frustum [20]. Although useful in their own right, these methods are not considered further due to current lack of detailed error source information that may be gleaned from the results.

Each of the methods described, so far, are generally sufficient to extract the location errors of a rotary axis; not position-dependent component errors. If a more comprehensive error model is required, alternative measurement strategies have been devised to measure the component errors of a rotary axis. In this case, the ballbar is aligned to a Cartesian reference direction, rather than a cylindrical coordinate reference. For example, aligning the ballbar to the nominal X-direction measures the error motion of the centre-pivot in X. This process may be repeated for the Y and Z directions, which are later combined to infer the position of the centre-pivot throughout the rotary axis motion [7, 21]. It is the experience of the authors that these

methods require detailed characterization and compensation of linear axis errors, and are easily corrupted by synchronization errors between axes and set-up errors. Consequently, these methods have been mentioned for completeness, but are not covered further in this paper.

## ***2.1 Current Limitations and Opportunities in Five-Axis Ballbar Testing***

If the tip of the tool-cup can be positioned on the average line of a rotary axis (e.g. Fig. 5, Toolpaths 3 and 4), a radial ballbar alignment is maintained simply by actuating the rotary axis; limiting interference from linear axis errors. However, if this is not possible, axial and radial ballbar alignments may only be maintained by tracing the motion of the rotary axis using at least two linear axes (Fig. 5, Toolpaths 1 and 2). Linear axis errors are now able to adversely affect the results of rotary axis verification. To date, this issue has been circumvented by employing the following caveat:

*Before rotary axes are verified, all linear axes must first be tested and suitably compensated, such that their geometric errors are sufficiently small to be considered negligible* (This caveat has been constructed by the authors based on the approaches found in existing literature e.g. [14, 15], and any works using the same toolpaths).

Although desirable, this caveat is not always practical, as it is time-consuming to pre-compensate the linear axes. Therefore, the aim of this research is to develop a set of ballbar tests that will enable users to first verify the linear axes of a five-axis machine tool, and then latterly remove the effects of linear axis errors from subsequent rotary axis ballbar tests. The authors are not aware of any existing publication that addresses this issue with ballbar testing. As such, the motivations behind this research are twofold:

1. Significant time-savings will be made in 5-axis machine tool verification, as the need to pre-calibrate the linear axes before testing the rotary axes will be removed. This has particular application in the manufacture of high-value parts, where machine tool verification may be required at least once per part.
2. The corruption of rotary axis verification results due to linear axis errors will be greatly reduced compared with tests that do not consider the effects of linear axis errors.

## **3 Theory and Simulation**

As described in the previous section, axial and radial rotary axis tests require the use of at least two linear axes if the tool-tip cannot be placed on the rotary axis average line. In order to prevent geometric errors from the linear axes falsifying the results of

Squareness XY [E <sub>C0Y</sub> ]	Squareness YZ [E <sub>A0Z</sub> ]	Squareness ZX [E <sub>B0Z</sub> ]
Datum = X-axis	Datum = Y-axis	Datum = X-axis

**Fig. 2** Diagrammatic explanation of the three squareness errors between the linear axes of a machine tool

the rotary axis tests, it is necessary to first characterise the linear axis errors. These effects may then be retrospectively compensated from the rotary axis test results.

### 3.1 Linear Axis Location Errors and Measurement

This research is concerned with the squareness errors between each linear axis pair, namely: E<sub>C0Y</sub>, E<sub>A0Z</sub> and E<sub>B0Z</sub> (detailed in Fig. 2). The three squareness errors are identified using planar tests in the XY, YZ and ZX planes, respectively, as prescribed by ISO 230-4 [22] and the Renishaw QC20 ballbar software [5]. These toolpaths are depicted in Fig. 3.

### 3.2 Rotary Axis Location Errors and Measurement

The location errors for an axis of rotation are defined for the rotary axis average line. These include two offset errors (one in each nominally perpendicular direction to the axis of rotation) and two tilt errors (one about each nominally perpendicular direction to the axis of rotation). An example of these errors is shown in Fig. 4 for the A-axis rotating about the X-direction.

To isolate the effects of the linear axis errors on the rotary axis testing results, a further four toolpaths are used (Fig. 5). Toolpath 1 aligns the ballbar axially with respect to the A-axis average line. The centre pivot is placed at the same height as the A-axis average line, but offset in the negative Y-direction by 85 mm to maximize the radius of the circular motion. The X-position of the centre-pivot is arbitrarily set to zero and shall remain the same for all four tests. The A-axis is exercised through the full 360° of arc, and the tool-tip traces this motion using a synchronised YZ-plane motion. It should be noted at this stage that all tests run in a clockwise and counter-clockwise direction.

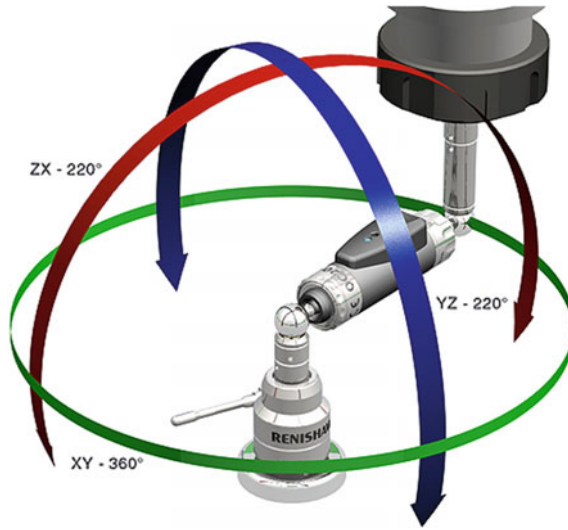
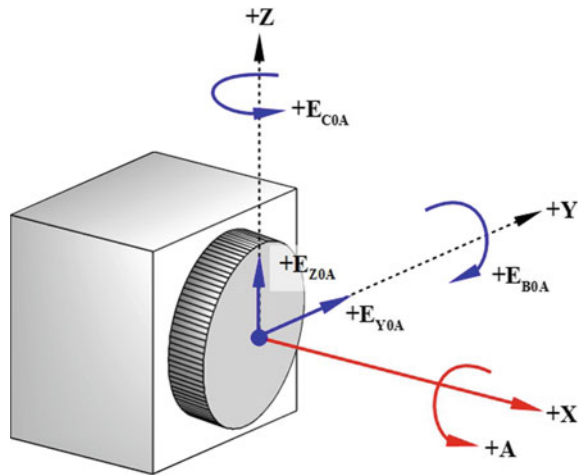


**Fig. 3** Diagrams showing the ballbar connected between a tool-cup held in the spindle, and centre-pivot mounted to the machine tool’s table. Arrows represent the three planar test toolpaths to identify squareness errors between linear axis pairs [5]

**Fig. 4** Location errors of an A-axis as outlined in ISO 230:1-2012 [3]



Toolpath 2 aligns the ballbar radially with respect to the A-axis average line. Keeping the centre-pivot in the same position as Toolpath 1, the radial alignment is maintained by the tool-tip tracing a larger circular motion via synchronized YZ interpolation. Due to the risk of collision, the A-axis could only rotate through 220° of arc; however, this is still deemed sufficient for circle-fitting purposes. Toolpaths 1 and 2 are used to identify tilt and offset errors of the A-axis average line, whilst being influenced by linear axis errors.

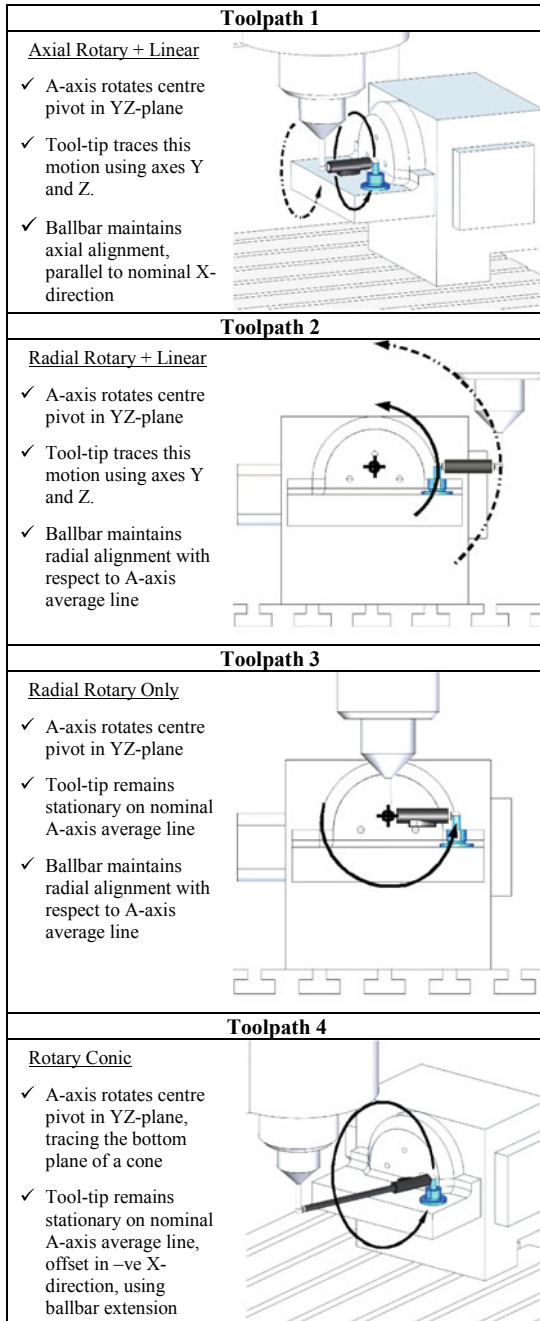


**Fig. 5** Four toolpaths used to identify the effects of linear axis errors on rotary axis testing

Toolpaths 3 and 4 are used to identify tilt and offset errors in the rotary axis average line, without the need for synchronized interpolation of the linear axes, hence, the tool-tip remains stationary during these tests. Toolpath 3 places the tool-tip on the A-axis centre-line at the arbitrarily established X0 coordinate. The centre-pivot is offset in the negative Y-direction by 100 mm, which is the calibrated ballbar length. The A-axis is then driven in isolation to describe a circular path of radius 100 mm. Once again, due to risks of collision, a full circle of arc is not possible during this test. Instead, a partial arc of 150° is used. With a smaller partial arc, circle-fitting is still feasible; however, the uncertainty associated with the fitted circle parameters can increase significantly compared with a complete circle. Further uncertainty analysis is required to quantify this effect.

Toolpath 4 is derived from the work of [18] and uses a ballbar extension to increase the calibrated ballbar length to 300 mm. The centre-pivot remains in the same location as described in Toolpath 3. The A-axis is driven through the full 360° of arc, such that the centre-pivot motion describes the base of a cone and the stationary tool-tip represents the apex. The use of a considerably longer ballbar means that the alignment of the ballbar approximates an axial alignment, and will be predominantly sensitive to tilt errors in the plane of rotation.

### 3.3 Identifying Tilt Errors in Rotary Axes

By aligning the ballbar's sensitive direction axially with respect to the rotary axis average line, its length becomes a close approximation of the distance to the plane of rotation with small tilt angles (Fig. 6). Hence, approximations of the 3D Cartesian coordinates of the centre-pivot rotating about the A-axis are given as follows:

$$x_{CP} = x_T + (L_0 + \delta L) \quad (1)$$

$$y_{CP} = O_Y \cos(\theta_A) \quad (2)$$

$$z_{CP} = O_Y \sin(\theta_A) \quad (3)$$

where  $x_T$ ,  $y_T$  and  $z_T$  are the commanded tool-tip coordinates,  $O_Y$  represents the perpendicular offset of the centre-pivot from the nominal A-axis average line in the Y-direction,  $L_0$  is the calibrated ballbar length,  $\delta L$  is the measured ballbar extension, and  $\theta_A$  is the commanded A-axis position.

The plane of best fit is defined as passing through the centroid of the three-dimensional coordinate data of the centre-pivot locations. For 'm' measured centre-pivot locations, the centroid is identified as the mean  $x$ ,  $y$  and  $z$  positions of these points, namely:  $\bar{x}$ ,  $\bar{y}$  and  $\bar{z}$ . The centre-pivot locations are then centred about this centroid, and stored in a  $m \times 3$  matrix  $\mathbf{A}$ .

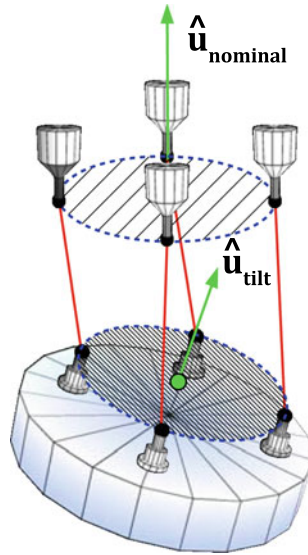


**Fig. 6** Example of axial ballbar alignment being used to measure the distance from the tool-tip to the plane of rotation

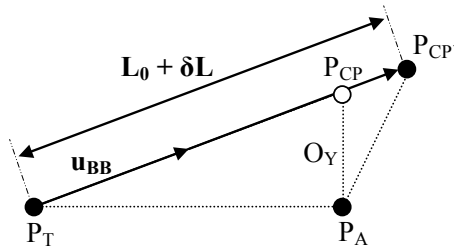


**Fig. 7** An example of how the ballbar’s length is used to infer the centre-pivot’s location during a conic test, as in Toolpath 4

$$\mathbf{A} = \begin{bmatrix} x_1 - \bar{x} & y_1 - \bar{y} & z_1 - \bar{z} \\ \vdots & \vdots & \vdots \\ x_m - \bar{x} & y_m - \bar{y} & z_m - \bar{z} \end{bmatrix} \tag{4}$$

The Singular Value Decomposition (SVD) of the matrix  $\mathbf{A}$  is defined as:

$$\mathbf{A} = \mathbf{U}\mathbf{S}\mathbf{V}^T \tag{5}$$

where  $\mathbf{U}$  and  $\mathbf{V}$  are orthogonal matrices, and  $\mathbf{S}$  is a diagonal matrix containing the singular values. The columns of  $\mathbf{V}$  are the orthonormal basis of the data contained



in  $\mathbf{A}$ , and may be thought of as the semi-axes of an ellipsoid enclosing the data. The column of  $\mathbf{V}$  that corresponds to the column of the smallest singular value in  $\mathbf{S}$  yields the unit vector of the least squares plane of best fit. This is equivalent to the smallest principle component of the data, thereby representing a minimization of the orthogonal distance of the points to the plane. This unit vector and the centroid of the data are sufficient to characterize a plane that is parallel to the plane of rotation.

### 3.4 Identifying the Plane of Rotation Using Conic Ballbar Test

The use of a conic ballbar test to identify rotary axis tilt errors has been proposed in [18]. An adapted version of this method is employed here to assist in the identification of rotary axis tilt errors, without the use of linear axis actuation.

Using the set-up and motion profile described for Toolpath 4, the centre-pivot traces the perimeter of a cone's circular base. The ballbar connects the points on this base to the apex of the cone using a calibrated ballbar length of 300 mm. In the case that there are no tilt errors in the A-axis average line, the vector describing the ballbar's length and orientation is denoted  $\mathbf{v}_{BB}$ , and is calculated using Eq. 6. This is then converted into a unit vector,  $\mathbf{u}_{BB}$ , describing only the ballbar's orientation (Eq. 7).

$$\mathbf{v}_{BB} = \mathbf{p}_{CP} - \mathbf{p}_T \quad (6)$$

$$\mathbf{u}_{BB} = \frac{\mathbf{v}_{BB}}{|\mathbf{v}_{BB}|} \quad (7)$$

In Eq. 6,  $\mathbf{p}_T$  is the commanded tool-tip position, which remains constant, and  $\mathbf{p}_{CP}$  is the position of the centre-pivot for a given rotary axis position. The Y and Z-coordinates are calculated using Eqs. 2 and 3, and the X-coordinate is zero. Having established the direction vector of the ballbar, this may be used to approximate the distance from the point  $\mathbf{p}_T$  to the points  $\mathbf{p}_{CP}$  as the A-axis rotates. This is achieved by multiplying the unit vector,  $\mathbf{u}_{BB}$ , by the associated ballbar length measurement for the given rotary axis position, as shown in Fig. 7. Although this is an approximation of the true interaction between the centre-pivot and the tool-tip, its accuracy has been verified for small tilt and offset errors using a kinematic model. It was found that the effects of the approximation on the identification of the tilt errors were negligibly small. This is largely due to the fact that the 300 mm ballbar length renders the ballbar significantly more sensitive to the tilt errors of the rotary axis than the radial offset errors, as its orientation approaches axial alignment.

### 3.5 Identifying the Centre of Rotation Using Radial Ballbar Tests

When using the radial ballbar alignment, the length of the ballbar is used to measure radial deviations of the centre-pivot from its nominal circular path. As the centre-pivot is fixed to the table, radial deviations are assumed to be caused by offsets in the location of the rotary axis average line.

Using the commanded rotary axis angle and the measured ballbar length, the position of the centre-pivot throughout the motion is calculated. As the ballbar remains perpendicular to the X-direction, error components acting in this direction are assumed to have negligible effect on the extension of the device. Consequently, the identification of the centre of rotation reduces to 2D problem by fitting a least squares circle to the calculated centre-pivot positions in the YZ plane. The Y and Z coordinates of the centre-pivot are calculated as follows:

$$y_{CP} = (O_Y \pm \delta L) \cos(\theta_A) \quad (8)$$

$$z_{CP} = (O_Y \pm \delta L) \sin(\theta_A) \quad (9)$$

The use of  $\pm$  denotes whether the extension of the ballbar increases (Toolpath 3) or reduces (Toolpath 2) the radial separation of the centre-pivot and the rotary axis average line. Once the coordinates are identified, a least squares circle is fitted using the ‘Hyper-Fit’ algebraic least squares fitting algorithm defined by Al-Sharadqah et al. [23].

## 4 Experimental Methodology and Results

The effects of linear axis squareness errors on rotary axis test results were investigated via experimentation. Using a DUGARD Eagle 850 machine tool, with a retro-fitted Tanshing A-axis, measurements were taken using the Renishaw QC20 ballbar. This machine tool was chosen as it was known to have sizeable geometric errors in both the linear and rotary axes. Figure 1 shows that the C-axis is more accessible to the tool-tip than the primary A-axis, and has unrestricted rotational motion. For this reason, all experiments were undertaken on the A-axis, whose axis average line was sufficiently exposed to allow tool-tip access. The theory and findings of this investigation may be generalised to the C-axis without complication.

Mapping and removing the effects of linear axis errors from rotary axis tests is a six stage process:

1. Conduct linear axis volumetric ballbar tests in the XY, YZ and ZX planes to identify linear axis squareness errors, the YZ-plane orientation, and the ovality of circular motions in this plane.

2. Undertake radial ballbar test, without linear axis actuation, using Toolpath 3. This provides benchmark values for the radial offset errors.
3. Utilise Toolpath 2 to identify the radial offset errors, inclusive of linear axis error effects.
4. Identify benchmark values for the tilt errors in the A-axis average line using the conic test shown in Toolpath 4.
5. Toolpath 1 is used to identify tilt errors in the A-axis average line, inclusive of linear error effects.
6. Using the information gathered in step 1, remove the perceived linear axis error effects from the results gathered in stages 3 and 5. Finally, compare these values with the benchmark values from stages 2 and 4.

### 4.1 Step 1: Linear Axis Squareness Errors

The squareness errors between the linear axis pairs were identified and the results are detailed in Table 1. The centre-pivot was placed on the A-axis centre-line, offset by 120 mm in the negative X-direction to avoid collision with the rotary axis. It was assumed that the measurements taken at this location would be representative of the motion undertaken during the rotary axis tests; however, this requires further validation in future work. Taking the X-axis as the datum axis, the following linear axis direction unit vectors were constructed:

$$\mathbf{u}_Y = [0.0001393 \ 0.9999999 \ 0]^T$$

$$\mathbf{u}_Z = [0.0001577 \ 0.0000407 \ 0.9999999]^T$$

Taking the cross product of these two vectors yields a unit vector that is normal to the 'true' YZ-plane:

$$\mathbf{u}_{YZ} = [0.9999999 \ -0.0001393 \ -0.0001577]^T$$

**Table 1** Identified squareness errors between the linear axes of the machine tool

Squareness XY, $E_{C0Y}$ [ $\mu\text{m}/\text{m}$ ]	Squareness YZ, $E_{A0Z}$ [ $\mu\text{m}/\text{m}$ ]	Squareness ZX, $E_{B0Z}$ [ $\mu\text{m}/\text{m}$ ]
-139.3	-40.7	-157.7

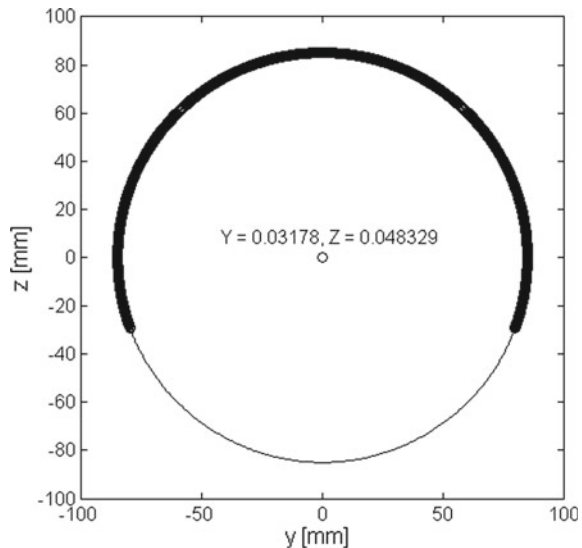
### 4.2 Steps 2 and 3: Radial Offset Errors in the A-Axis

Toolpaths 2 and 3 were used to identify the radial offset errors in the A-axis. In each case, the least squares circle of best fit was generated for the approximated centre-pivot locations and its centre was used to identify the radial offset errors. These errors are listed in Table 2 and an example of a least squares circle being applied to the results from Toolpath 2 are shown in Fig. 8. It can be seen from Table 2 that the identified value for radial offset error,  $E_{Y0A}$ , does not seem to be particularly sensitive to the effects of linear axis squareness errors. However, the offset error  $E_{Z0A}$  has changed by approximately  $7 \mu\text{m}$ .

**Table 2** Identified radial offset errors for the A-axis using toolpaths 2, 3 and also the compensated results from toolpath 2

<b>Without linear axis errors</b>	
$E_{Y0A}$ [mm]	$E_{Z0A}$ [mm]
0.0312	0.0416
<b>With linear axis errors—uncompensated</b>	
$E_{Y0A}$ [mm]	$E_{Z0A}$ [mm]
0.0318	0.0483
<b>With linear axis errors—compensated</b>	
$E_{Y0A}$ [mm]	$E_{Z0A}$ [mm]
0.0318	0.0408

**Fig. 8** Least squares circle fit to the results from toolpath 2



In an attempt to compensate the adverse effects of ovality in the linear axis motion, the ‘true’ motion of the tool-tip may be characterized by employing Eq. 10.

$$\begin{bmatrix} x_s & y_s & z_s \end{bmatrix}^T = x \cdot \mathbf{v}_x + y \cdot \mathbf{v}_y + z \cdot \mathbf{v}_z \quad (10)$$

where  $x_s$ ,  $y_s$  and  $z_s$  represent the ‘true’ tool-tip coordinates as a result of the linear axis squareness errors,  $\mathbf{v}_x$ ,  $\mathbf{v}_y$ , and  $\mathbf{v}_z$  are the direction unit vectors of the linear axes, and  $x$ ,  $y$  and  $z$  are the commanded tool-tip coordinates. Using this model, the same testing process is simulated. Throughout the motion path of the test, the radial separation of the ideal tool-tip path and the tool-tip path under the influence of linear axis errors is identified. This separation is then subtracted from the relevant ballbar measurements taken during Toolpath 2, and the centre-pivot locations are recalculated using Eqs. 8 and 9. Using the same circle fitting algorithm, the radial offset errors are recalculated and the results are shown in Table 2. It can be seen that the effects of the linear axis ovality are almost entirely removed. The residual discrepancies are  $0.6 \mu\text{m}$  and  $0.8 \mu\text{m}$  for errors  $E_{Y0A}$  and  $E_{Z0A}$ , respectively, which represent 2.6% and 2% of the magnitude of the benchmarked values.

### 4.3 Steps 4 and 5: Tilt Errors in the A-Axis

To identify the tilt errors of the rotary axis, inclusive of linear axis error effects, Toolpath 1 is used. Conversely, to identify the tilt errors without linear axis error effects, Toolpaths 4 is used. In each case, the toolpaths help approximate the centre-pivot’s location as it moves under the actuation of the rotary axis. The coordinates of these locations are then used to generate least squares planes of best-fit that are parallel to the ‘true’ plane of rotation. This plane is represented using the centroid of the centre-pivot location data and a unit vector that is normal to the plane; defining its orientation. An example of the least squares plane being fitted to the data from Toolpath 1 is shown in Fig. 9.

Comparing the orientation of the identified unit vector with the nominal X-direction, the tilt errors of the axis are readily identified. Table 3 contains the tilt errors identified both with and without linear axis motion and it can be seen that there is a significant difference between the two. In the case of error  $E_{C0A}$  there is a difference of approximately  $199 \mu\text{rad}$ , which is 54% of the total error magnitude identified without linear axis motion. In error  $E_{B0A}$  there is a difference of approximately  $220 \mu\text{rad}$ , which is 48% of the magnitude of the error identified without linear axis motion. It can therefore be concluded that the squareness errors between the linear axes significantly affect the outcome of rotary axes tests where linear axis motion is used.

In an attempt to compensate the adverse effects of linear axis errors from the results gained in Toolpaths 1 and 2, the previously identified linear axis errors are

**Fig. 9** Axial plane fit, inclusive of linear axis error effects

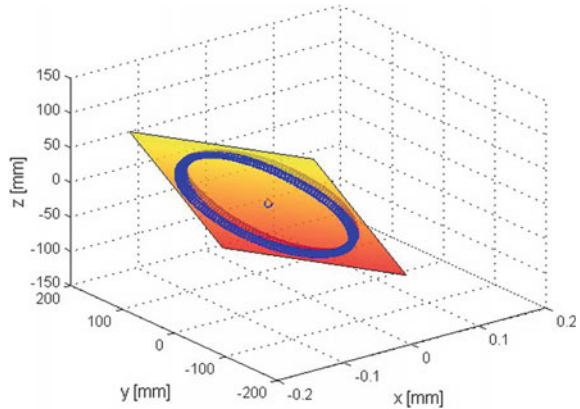


**Table 3** Identified tilt errors for the A-axis using toolpaths 1 and 4, and also the compensated results from toolpath 1

<b>Without linear axis errors</b>	
<b><math>E_{C0A}</math> [rad]</b>	<b><math>E_{B0A}</math> [rad]</b>
0.00036736	-0.00045442
<b>With linear axis errors—uncompensated</b>	
<b><math>E_{C0A}</math> [rad]</b>	<b><math>E_{B0A}</math> [rad]</b>
0.00056671	-0.00067439
<b>With linear axis errors—compensated</b>	
<b><math>E_{C0A}</math> [rad]</b>	<b><math>E_{B0A}</math> [rad]</b>
0.00042748	-0.00051674

employed. The ‘true’ motion of the tool-tip may be characterized by employing Eq. 10, as described for the radial test compensation.

As the ballbar has an axial alignment in Toolpath 1, any error component from the linear axes that acts in the X-direction will change the extension of the ballbar. Therefore, by comparing the ‘true’ tool-tip coordinates with the commanded tool-tip coordinates, the effect of the linear axes on the ballbar extension may be predicted and subsequently removed from the recorded ballbar length measurements. These altered extension values may then be used to recalculate the centre-pivot locations using Eqs. 1–3. The same plane fitting algorithm is then used to identify a new plane of best fit for the A-axis motion. The newly identified tilt errors are presented in Table 3. The results show that the new discrepancies are 60  $\mu$ rad and 62  $\mu$ rad for EC0A and EB0A, respectively. These values represent 16% and 14% of the benchmark values from the tests without linear axis interference.

## 5 Conclusions and Future Perspectives

The research presented in this paper identified that the presence of squareness errors within the linear axes of a five-axis machine tool significantly affects the results of accuracy tests on the rotary axis where linear axes are used. The axial tests, used to identify tilt errors, were the most susceptible to the linear axis error effects. In the worst case, the discrepancy between one of the benchmark tilt error values and the value identified in the presence of linear axis errors was equal to 54% of the original benchmark magnitude.

Rather than laboriously pre-calibrating the linear axis errors before testing the rotary axes, this research presents a method to remove the effects of linear axis errors in the analysis of the rotary axis test data. This resulted in the linear axis effects being almost completely removed from radial testing data. The compensation of axial test data to identify tilt errors was less successful; however, the discrepancy between the benchmark and identified values reduced from circa 50% to approximately 15% for both tilt errors, showing a marked improvement.

This investigation shows strong potential for the use of compensated rotary axis testing methods, to remove the need for linear axis calibration before rotary testing. Further tests are required to quantify the uncertainty associated with these compensated measurements. There is also a requirement to repeat these tests on another machine tool to further validate its efficacy.

**Acknowledgements** The authors are pleased to thank the Engineering and Physical Science Research Council (EPSRC No. EP/K504245/1) and our industrial partner for their support during this research.

## References

1. Mckeown P (1987) The role of precision engineering in manufacturing. *CIRP Ann Manuf Technol* 36(2)
2. Sakwenke H, Knapp W, Haitjema H, Weckenmann A, Schmitt R, Delbressine F (2008) Geometric error measurement and compensation of machines—an update. *CIRP Ann Manuf Technol* 57(2):660–675
3. ISO 230-1:2012: Test code for machine tools—Part 1: Geometric accuracy of machines operating under no-load or quasi-static conditions. International Organization for Standardization, Geneva, Switzerland
4. Bryan JB (1982) A simple method for testing measuring machines and machine tools. *Precis Eng* 4(2):61–69
5. Renishaw (2013) QC20-W ballbar system [Online]. Available at: <http://www.renishaw.com/en/qc20-w-ballbar-system--11075>. Accessed 6 Aug 2013
6. Kwasny W, Turek P, Jedrzejewski J (2011) Survey of machine tool error measuring methods. *J Mach Eng* 11(4)
7. Sakamoto S, Inasaki I, Tsukamoto H, Ichikizaki T (1997) Identification of alignment errors in five-axis machining centers using telescoping ballbar. *Trans Jpn Soc Mech Eng* 63(605):262–267

8. Currier D (2013) SAMULET—manufacturing R&D programmes. <http://www.aerospace.co.uk/> [Online]. Available at: <http://www.aerospace.co.uk/media/94014/IoM-Presentation-to-NWAA-Version-2.pdf>. Accessed 22 Jul 2013
9. Bringmann B, Knapp W (2006) Model-based ‘chase-the-ball’ calibration of a 5-axes machining center. *CIRP Ann Manuf Technol* 55(1):531–534
10. Zargarbashi SHH, Mayer JRR (2009) Single setup estimation of a five-axis machine tool eight link errors by programmed end point constraint and on the fly measurement with Capball sensor. *Int J Mach Tools Manuf* 49(10):759–766
11. Ibaraki S, Knapp W (2012) Indirect measurement of volumetric accuracy for three-axis and five-axis machine tools: a review. *Int J Autom Technol* 6(2):110–124
12. ISO 230-7:2006: Test code for machine tools—Part 7: Geometric accuracy of axes of rotation. International Organization for Standardization, Geneva, Switzerland
13. ISO 10791-6:2014: Test conditions for machining centres—Part 6: Accuracy of speeds and interpolations. International Organization for Standardization, Geneva, Switzerland
14. Tsutsumi M, Saito A (2003) Identification and compensation of systematic deviations particular to 5-axis machining centers. *Int J Mach Tools Manuf* 43(8):771–780
15. Tsutsumi M, Tone S, Kato N, Sato R (2013) Enhancement of geometric accuracy of five-axis machining centers based on identification and compensation of geometric deviations. *Int J Mach Tools Manuf* 68:11–20
16. Zargarbashi SHH, Mayer JRR (2006) Assessment of machine tool trunnion axis motion error, using magnetic double ball bar. *Int J Mach Tools Manuf* 46(14):1823–1834
17. Ibaraki S, Kakino Y, Akai T, Takayama N, Yamaji I, Ogawa K (2010) Identification of motion error sources on five-axis machine tools by ball-bar measurements (1st report)—classification of motion error components and development of the modified ball bar device (DBB5). *J Jpn Soc Precis Eng* 76(3):333–337
18. Jiang X, Cripps RJ (2015) A method of testing position independent geometric errors in rotary axes of a five-axis machine tool using a double ball bar. *Int J Mach Tools Manuf* 89:151–158
19. Tsutsumi M, Saito A (2004) Identification of angular and positional deviations inherent to 5-axis machining centers with a tilting-rotary table by simultaneous four-axis control movements. *Int J Mach Tools Manuf* 44(12–13):1333–1342
20. Uddin MS, Ibaraki S, Matsubara A, Matsushita T (2009) Prediction and compensation of machining geometric errors of five-axis machining centers with kinematic errors. *Precis Eng* 33(2):194–201
21. Lee K, Lee D, Yang S (2012) Parametric modeling and estimation of geometric errors for a rotary axis using double ball-bar. *Int J Adv Manuf Technol* 62:741–750
22. ISO 230-4:2005: Test code for machine tools—Part 4: Circular tests for numerically controlled machine tools. International Organization for Standardization, Geneva, Switzerland
23. Al-Sharadqah A, Chernov N (2009) Error analysis for circle fitting algorithms. *Electron J Stat* 3:886–911



# Tool Holder Sensor Design to Measure the Cutting Forces in CNC Turning for Optimization of the Process



Daniel Reyes Uquillas and Syh-Shiuh Yeh

**Abstract** Cutting forces in machining operation are of great importance. There is a need to measure these forces by a simple and low cost solution. The present work covers the design and construction of a sensor to measure cutting forces generated in turning with a CNC Lathe by attaching strain gauges directly inside of the tool holder, one on each side of the rectangular shank, to measure strain and estimate these forces. The first section is an introduction of the process and a review of related and similar works. The second section covers the hardware design of the sensor. In the third section the signal conditioning procedure and implementation is detailed. The fourth section has the calibration procedure and real cutting tests results. The last section has the conclusions and applications.

**Keywords** Cutting force · Strain gauges · Tool holder

## 1 Introduction

Forces generated during metal cutting are directly related with the cutting conditions and have an influence on the generation of heat, tool wear, quality of machined surface and accuracy of the workpiece [1]. The purpose of measuring forces that appear in metal cutting is to understand the cutting mechanism such as the effects of cutting variables on the cutting force, the machinability of the work piece, the process of chip formation, chatter and tool wear [2]. The values obtained by engineering calculations have some errors compared to the experimental measurements.

In the past decade, several researchers have designed and developed cutting force measuring systems using direct and indirect approach methods. Most of the developed measuring systems are designed as three force components dynamometers with

---

D. R. Uquillas

Graduate Institute of Mechatronic Engineering, National Taipei University of Technology, No. 1, Sec. 3, Chung-Hsiao E. Road, Taipei 10608, Taiwan

S.-S. Yeh (✉)

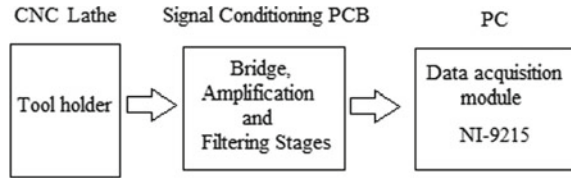
Department of Mechanical Engineering, National Taipei University of Technology, No. 1, Sec. 3, Chung-Hsiao E. Rd, Taipei 10608, Taiwan  
e-mail: [ssyeh@ntut.edu.tw](mailto:ssyeh@ntut.edu.tw)

© Springer Nature Switzerland AG 2022

S. Hinduja et al. (eds.), *Proceedings of the 38th International MATADOR Conference*,  
[https://doi.org/10.1007/978-3-319-64943-6\\_39](https://doi.org/10.1007/978-3-319-64943-6_39)

551

**Fig. 1** Schematic of the process



complex data acquisition systems. Yaldiz and Unsacar [3] designed a three component dynamometer using strain gauges in an octagonal-ring arrangement. Shi and Gindy [4] developed an online monitoring system for the cutting forces in turning.

Some work in turning process was done by Li in [5], where inexpensive current sensors and the cutting force model were used to estimate the components of the cutting force. Apichatbanlue and Suksawat described an approach that implements a direct measurement method using a miniature load cell that was inserted in the toolholder as the sensing device in [6]. This approach gives good performance and results but does not work or estimate the components values of the cutting force and does not check the cross sensitivity.

In this paper the principle of measuring the cutting forces by using strain gauges placed inside of the tool holder is evaluated and tested. To accomplish this task a sensor is designed, its signal needs to be conditioned and then calibrated.

In order to measure the bending strain generated by the cutting forces, the configuration for the signal conditioning is a  $\frac{1}{2}$  Wheatstone bridge. After which an amplification stage is necessary. This was implemented using an instrumentation amplifier and an analogic active filter in a PCB. The signal was acquired using a cDAQ connected with the 9215 analog input module. Labview was used as the software to acquire and store the data from the sensor.

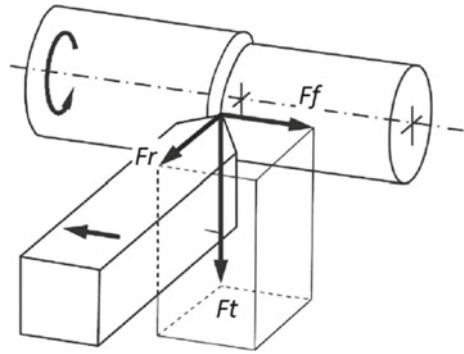
The calibration procedure was performed by applying known weights to the tool holder and then estimating the value of the forces. The sensor was implemented and tested to evaluate its performance in different cutting conditions (Fig. 1).

## 2 Sensor Design and Fabrication

During the turning process a cutting force is generated, which is the resultant of three component forces tangential force ( $F_t$ ), which is usually the largest force component, and acts in the direction of the cutting speed., Feed force ( $F_f$ ) which is the force component acting on the tool in the direction parallel with the direction of feed (axial force), and radial force ( $F_r$ ) which is the third component pushing the cutting tool away from the work in radial direction [7] (Fig. 2).

The design of the sensor consists of four chambers one on each side of the tool holder shank to place the strain gauges. It also has a hole across the shank to pass the cables of the strain gauges. The four strain gauges are placed on each face of the tool holder in order to measure the strain generated by the tangential force and the

**Fig. 2** Cutting forces in turning operation

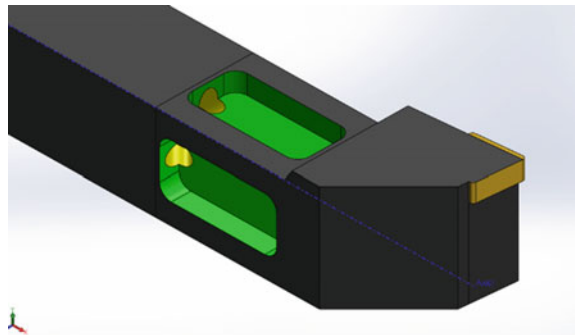


feed force during cutting. Measuring only the tangential force and the feed force we can estimate the resultant value with a good approximation, given the percentages relation.

The chosen configuration for the strain gauges is  $\frac{1}{2}$  Wheatstone bridge. Hence, there are two pairs of strain gauges, the first one (top and bottom) is for the tangential force, the second pair (right and left) is for the feed force. In this way we can estimate the components of the cutting force and also we can check cross-sensitivity (Figs. 3 and 4).

An analysis of the strain in the design was done to ensure the best location to attach the strain gauges. This was done in the software Solidworks and we can see in Fig. 5 that the location selected in the design has a considerable strain given the applied forces.

**Fig. 3** CAD of the tool holder design



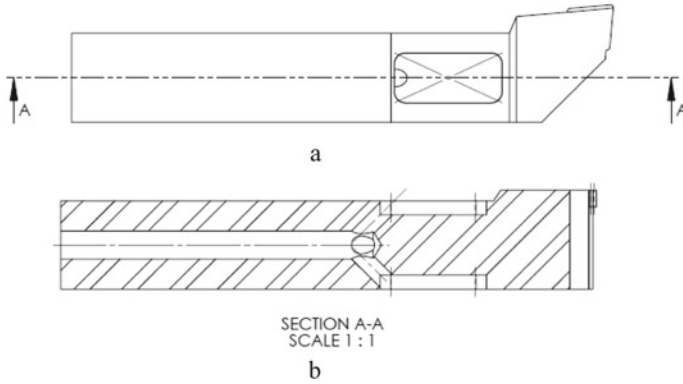


Fig. 4 Diagram of the tool holder. a Top view; b front section view

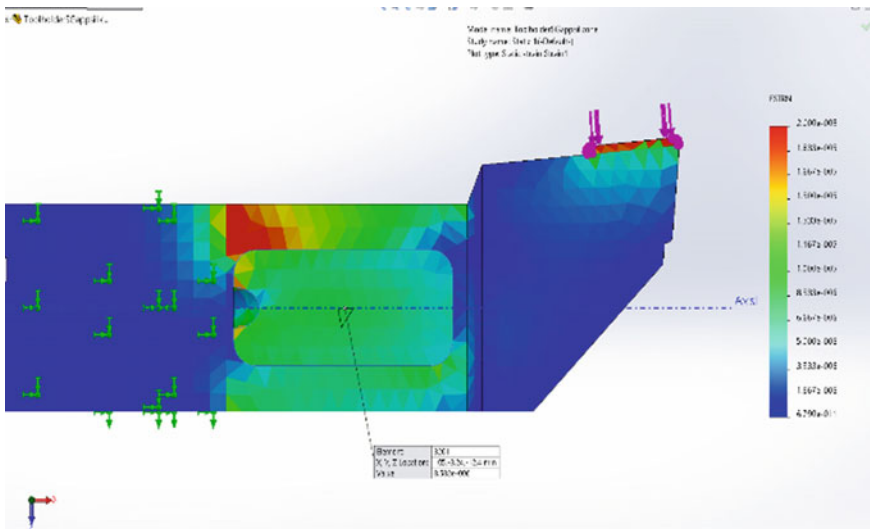


Fig. 5 Strain analysis of the tool holder design

### 3 Signal Conditioning

The strain gauge approach to measure the cutting forces consists in attaching 4 strain gauges on the faces of the tool holder. These strain gauges need a signal conditioning circuit.

The circuit consists of some stages that can be described into three major ones (Fig. 6).

In order to test the designed amplifier with the strain gauge approach, reduce the noise as much as possible, and have a simpler connection interface with the system,

**Fig. 6** Stages of signal conditioning



**Fig. 7** PCB boards



a PCB was the best solution. The PCB was designed and implemented after several tests of the different stages.

The final layout consists of two amplifier channels in the same board. With the optional feature to choose between  $\frac{1}{4}$  bridge configuration and  $\frac{1}{2}$  bridge. With one of these boards we can connect the four strain gauges in  $\frac{1}{2}$  bridge configuration or two individual strain gauges in  $\frac{1}{4}$  bridge configuration (Fig. 7).

## 4 Calibration

For the calibration of the sensor the method used was to apply known weights to the tool holder in the tangential and feed direction and then obtain the signal response from the sensor. The configuration used was  $\frac{1}{2}$  Wheatstone bridge to read the change of signal in both direction of the forces, this helps us to check the influence that cross sensitivity has in the measuring.

### 4.1 Data Analysis

Five measurements were taken for each weight and then averaged to obtain the points for the relation between the sensor signal and the force applied.

With the data obtained the noise and offset was also calculated and evaluated. The tests are similar to Fig. 8, so we analyze the average value for each section to obtain the change, the offset and the noise.

The calibration curve is plotted after reading the signal change for different weights up to 250 N in variable steps. For the tangential direction we need to translate the force that is applied when hanging the weight on the head of the tool holder to obtain the value as if the force was on the tip of the tool holder (Fig. 9).

Interpolation was used to obtain the corresponding values of the force that is being applied on the tip of the tool holder. The relation between signal voltage change and force applied on each direction is defined for the feed and the tangential direction.

**Fig. 8** Signal measurement for calibration

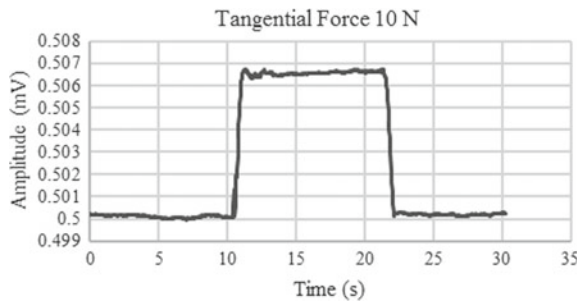
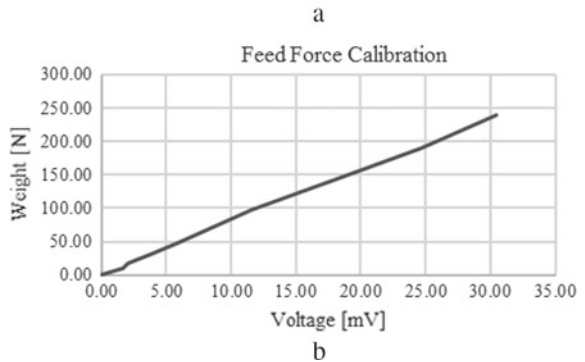
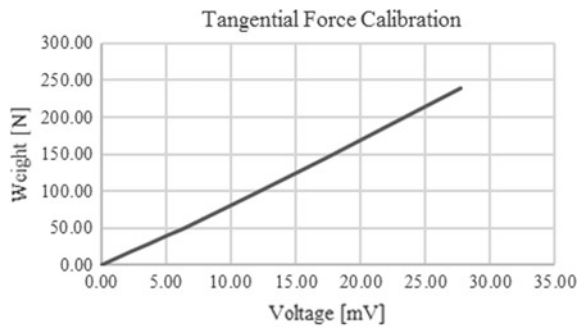


**Fig. 9** Calibration curves. **a** Tangential force; **b** feed force



## 5 Cutting Tests

Once the calibration was completed cutting tests were conducted to evaluate the performance of the sensor. The sensor application for this contribution is the optimization during canned cycles. Therefore, the tests were done using the G71 code to reduce the diameter of the workpiece.

For these tests different conditions were used. The main variable that was changed was the depth of cut, because it is the one that has a big influence on the cutting force when changed. The machine used is TB-20YBC from Tongtai, the work piece material used was Aluminum 6061 cutting without coolant.

For all the tests the terminology used is as follows (Table 1; Figs. 10, 11, 12 and 13):

- $d$  = depth of cut
- $S$  = spindle speed
- $f$  = feedrate

The values of every test are summarized in Table 2, these were compared with the values obtained calculating with the formulas for turning as the reference of the cutting forces. We can see in the figures some disturbance in the measurement, this appeared because the chipbreak from cutting came in contact with the sensor.

The formulas used for this were:

$$Fc = Ks * d * f^u \tag{1}$$

$$Ks = \frac{1 - 1.01\gamma_o}{h^{mc}} * K_{c1.1} \tag{2}$$

$$h = f * \sin(Kr) \tag{3}$$

where

- $F_c$  = Cutting Force
- $K_s$  = Specific Cutting force
- $d$  = depth of cut
- $f$  = feed
- $h$  = chip thickness (mm)

**Table 1** Cutting tests parameters

Parameter	Test 1	Test 2	Test 3	Test 4
$d$ [mm]	1	2	3	4
$S$ [rpm]	2000	2000	2000	2000
$f$ [mm/min]	0.15	0.15	0.15	0.2

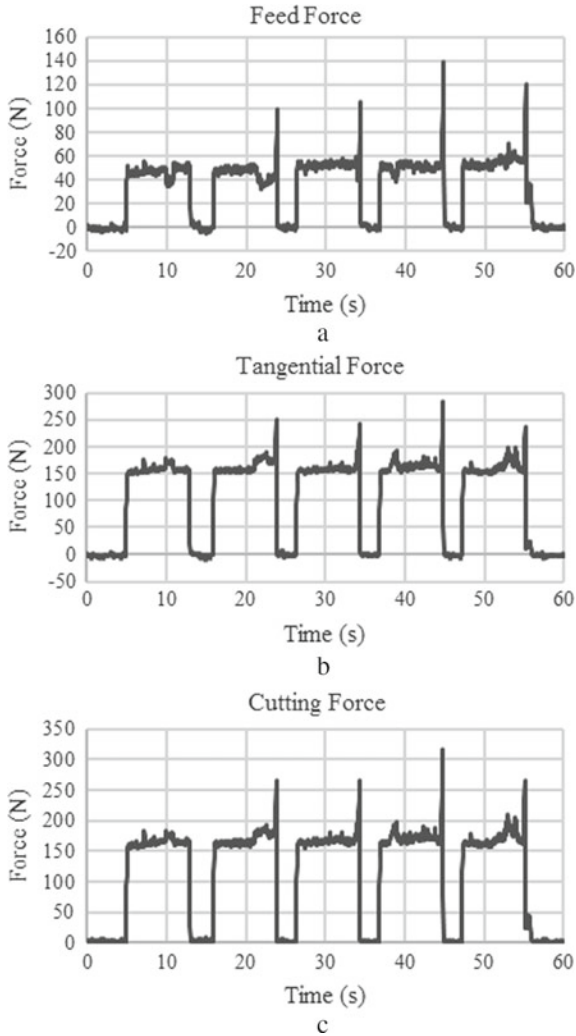


**Fig. 10** Cutting test 1 mm depth of cut. **a** Tangential force; **b** feed force; **c** cutting force

- $\gamma_o = \text{Cutting rake angle } (^{\circ})$
- $Kc_{1,1} = \text{Specific cutting force for } h = 1 \text{ mm } b = 1 \text{ mm}$
- $Kr = \text{Cutting edge angle } (^{\circ})$

For aluminum and the cutting tool used:

- $\gamma_o = -6^{\circ}$
- $Kc_{1,1} = 700$
- $mc = 0.25$
- $Kr = 95^{\circ}$



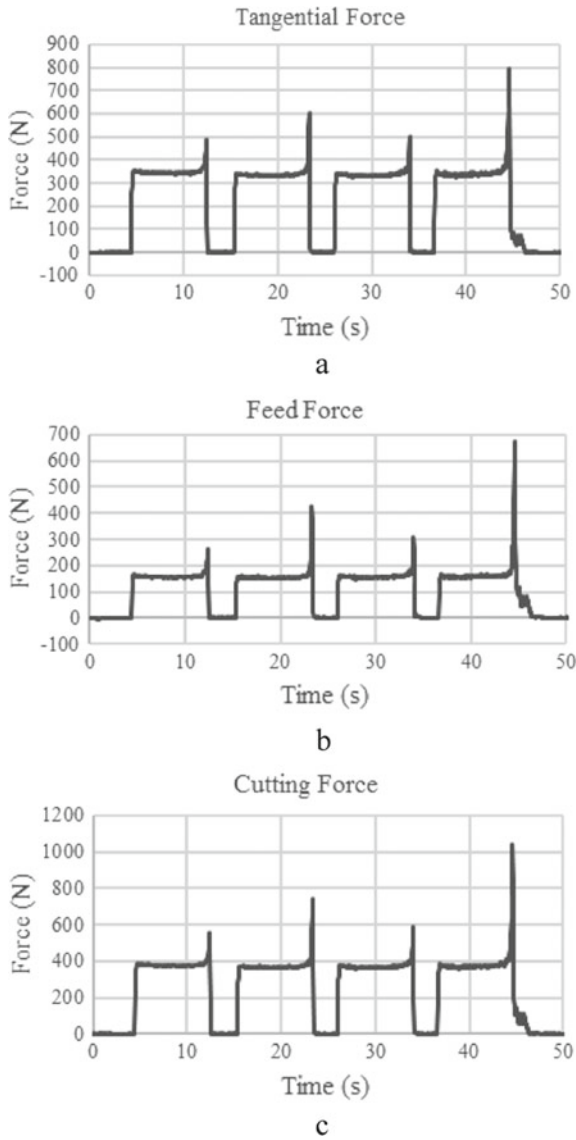
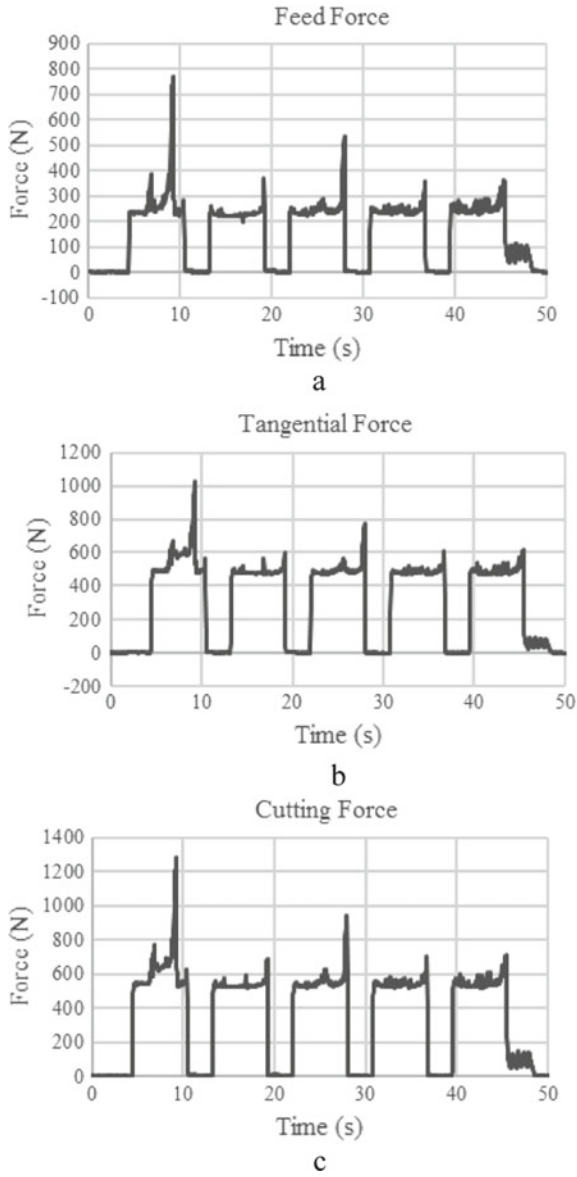


Fig. 11 Cutting test 2 mm depth of cut. a Tangential force; b feed force; c cutting force

## 6 Conclusions

The proposed approach of using strain gauges attached inside of the tool holder as the sensor to measure the cutting force was successfully implemented. The force



**Fig. 12** Cutting test 3 mm depth of cut. **a** Tangential force; **b** feed force; **c** cutting force

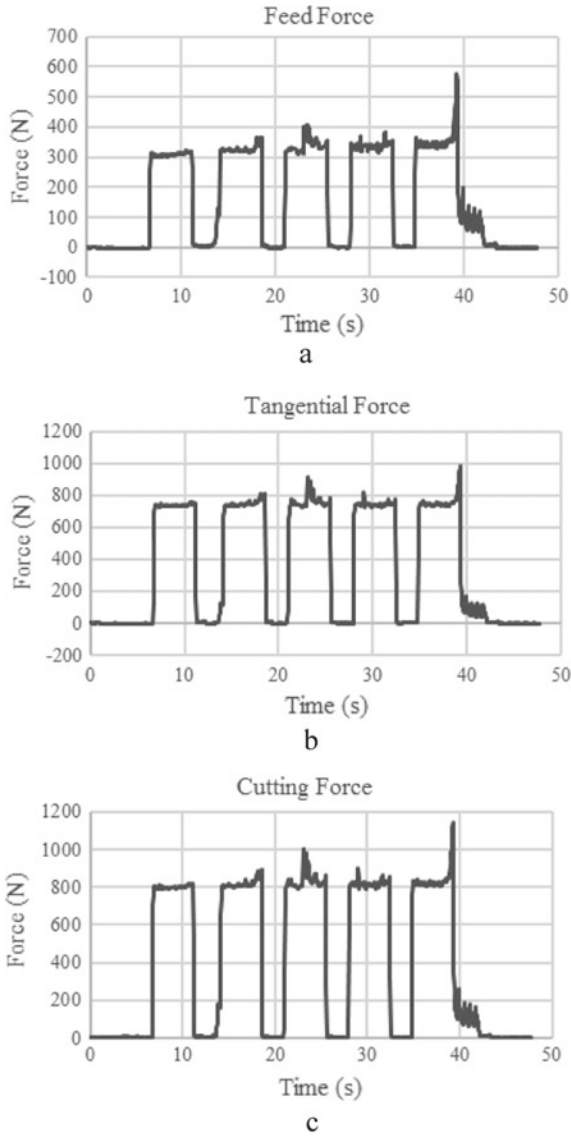


**Fig. 13** Cutting test 4 mm depth of cut. **a** Tangential force; **b** feed force; **c** cutting force

components, tangential and feed, were estimated with the calibration and the sensor was tested in real cutting conditions showing a good performance.

Evaluating the forces obtained from the cutting tests and comparing them with the calculated values from equations we can see that the sensor measurement has a good approximation. Analyzing the cutting tests an influence of temperature in the

**Table 2** Reference and experimental cutting force comparison

Depth of cut [mm]	Calculated reference [N]	Experimental tests [N]	Error %
1	186	170	8.6
2	373	380	1.8
3	560	550	1.78
4	920	800	13

measurement which caused a small drift was detected, after some tests using coolant we can see that the problem was solved.

The solution implemented is a simple low cost alternative to measure the cutting forces with good reliability.

## References

1. Tlustý J, Andrews GC (1983) A critical review of sensors for unmanned machining. *Ann CIRP* 32-2:611-622
2. Yaldiz S, Unsacar F, Saglam H, Isik H (2007) Design, development and testing of a four-component milling dynamometer for the measurement of cutting force and torque. *Mech Syst Signal Process* 21:1499-1511
3. Yaldiz S, Unsacar F (2006) Design, development and testing of a turning dynamometer for cutting force measurement. *Measurement* 39(1):80-89
4. Shi D, Gindy NN (2007) Development of an online machining process monitoring system: application in hard turning. *Sens Actuators, A Ser* 135:405-414
5. Li X (2005) Development of current sensor for cutting force measurement in turning. *IEEE Trans Instrum Meas* 54(1)
6. Apichatbanlue U, Suksawat B (2011) Data acquisition system for main cutting force measurement in turning operation. In: 11th international conference on control, automation and systems, 26-29 Oct 2011, Gyeonggi-do, Korea
7. Radovanović M, Dašić P, Janković P (2006) Experimental determination of cutting force by longitudinal turning of C60E steel. *Romanian Technical Sciences Academy. MOCM*; 12-2

# A Scanning Electrostatic Force Microscope for the Measurement of Material Distribution in Non-contact Condition



So Ito, Keiichiro Hosobuchi, Zhigang Jia, and Wei Gao

**Abstract** A scanning electrostatic force microscope (SEFM) has been developed for the measurement of the surface profile in non-contact condition. The SEFM probe can detect the electrostatic force between the probe tip and the sample surface by utilizing the configuration of frequency modulation atomic force microscope, therefore, the SEFM allows the scanning of the surface profile in no-contact condition. The absolute tip-to-sample distance can be calculated without the influence of the surface charge of the sample surface by utilizing a dual-height method. On the other hand, since the difference of the surface charge is caused by the difference of the contact potential difference (CPD) between the probe material and the sample material, it will be possible to recognize the difference of the material on the sample surface in non-contact condition by detecting the difference of the CPD on the surface. The value of the CPD can also be calculated based on the dual-height method. Therefore, both the surface profile and the material distribution will be able to be measured simultaneously. In this paper, the feasibility of the CPD measurement based on the SEFM has been investigated. Relationship between the electrostatic force and the CPD has been evaluated, and then the detection sensitivity of the CPD has been confirmed by simulation. The difference between the profile measurement and the CPD measurement in the case of the scanning of the same sample has been compared experimentally.

**Keywords** Material distribution · Scanning electrostatic force microscope · Contact potential difference

## 1 Introduction

Scanning probe microscopes (SPMs) have been applied for the surface profile measurement because they can realize three-dimensional profile measurement with nanometer-scale resolutions. In particular, non-contact SPMs involving a non-contact

---

S. Ito (✉) · K. Hosobuchi · Z. Jia · W. Gao  
Department of Nanomechanics, Tohoku University, 6-6-01, Aramaki Aza Aoba, Aoba-ku, Sendai 980-8579, Miyagi, Japan  
e-mail: [so.ito@pu-toyama.ac.jp](mailto:so.ito@pu-toyama.ac.jp)

© Springer Nature Switzerland AG 2022  
S. Hinduja et al. (eds.), *Proceedings of the 38th International MATADOR Conference*,  
[https://doi.org/10.1007/978-3-319-64943-6\\_40](https://doi.org/10.1007/978-3-319-64943-6_40)

563

atomic force microscopes (NC-AFM) and scanning tunneling microscope (STM) are useful tools for the surface profile measurement because they can achieve the surface scanning in non-contact condition [1]. As for the novel non-contact SPM, a scanning electrostatic force microscope (SEFM) has been developed [2]. The SEFM employs the electricstatic force gradient which is acted between the probe tip and the sample surface, so that the tip-to-sample distance can be extended over 200 nm. This tip-to-sample distance is significantly larger than the distance of the conventional non-contact SPMs of several nanometer, this long operating distance contributes to the avoidance of the probe collision and the improvement of the scanning speed. In the SEFM, the influence of the electric field distribution on the sample surface can be eliminated by the dual-height method. On the other hand, the distribution of the material will be able to be detected by the probe of the SEFM because the electrostatic force distribution is generated by the contact potential distribution (CPD) of the material surface [3]. The conventional SPMs are also utilized for the measurement of the various kinds of the physical properties such as the surface potential [4], friction force [5] and magnetic force [6], because the probe tip can detect the local interactions based on the contact-type SPMs. On the other hand, since the SEFM can realize the noncontact scanning above the sample surface, the material distribution can be measured by the CPD measurement in noncontact condition. Consequently, the surface profile and material distribution can be measured by the same probe simultaneously.

In this paper, the feasibility of the CPD measurement is investigated by using the SEFM probe. By changing the kinds of the sample material, the relationship between the electrostatic force and the CPD was investigated. The sensitivity of the CPD detection was evaluated by the simulation. The simultaneous measurement of the CPD and surface profile was carried out by using the same probe, and then those measurement results were compared experimentally.

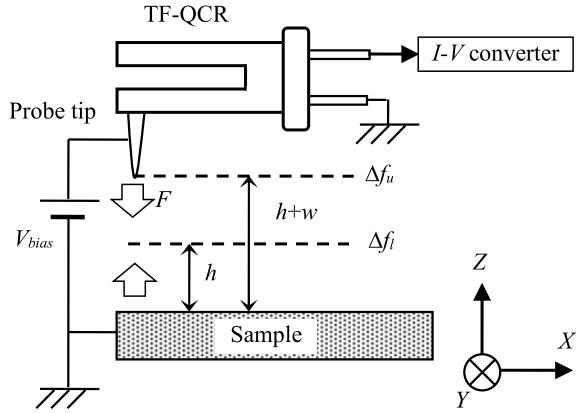
## 2 Experimental principle

Figure 1 shows the basic schematic of the SEFM with the dual-height method [2]. In order to obtain the CPD value, it is necessary to measure the electrostatic force and the tip-to-sample distance. The bias voltage  $V_{bias}$  is applied between the tungsten probe and the sample to generate the electrostatic force  $F$ . The electrostatic force which effects the probe tip can be expressed as follows.

$$F = \frac{1}{2} \pi \varepsilon_0 \varepsilon_r (V_{bias} + V_{CPD})^2 \frac{R}{h} \quad (1)$$

where,  $R$  is the tip radius,  $h$  is the tip-to-sample distance,  $\varepsilon_0$  and  $\varepsilon_r$  are the dielectric charges at the vacuum and air, respectively.  $V_{CPD}$  is the contact potential difference (CPD) between the probe material and the sample material. The probe is attached

**Fig. 1** Schematic diagram of SEFM



at the one-beam of the tuning fork quartz crystal resonator (TF-QCR) to detect the electrostatic force. The probe is oscillated by the TF-QCR on its resonance frequency. When the bias voltage is applied between the probe tip and the sample, the frequency of the probe oscillation is shifted. During the lower trace, the shift amount  $\Delta f_l$  of the probe oscillation frequency can be expressed as follows.

$$\Delta f_l = \frac{1}{2} \frac{f_0}{k} \pi \epsilon_0 \epsilon_r (V_{bias} + V_{CPD})^2 \frac{R}{h^2} \quad (2)$$

In Eq. 2,  $f_0$  is the resonance frequency of the probe, and  $k$  is a Young's modulus of the TF-QCR beam. When the trace gap  $w$  is applied to the tip-to-sample distance, which means scanning in the upper trace, the frequency shift  $\Delta f_u$  can be indicated as below.

$$\Delta f_u = \frac{1}{2} \frac{f_0}{k} \pi \epsilon_0 \epsilon_r (V_{bias} + V_{CPD})^2 \frac{R}{(h+w)^2} \quad (3)$$

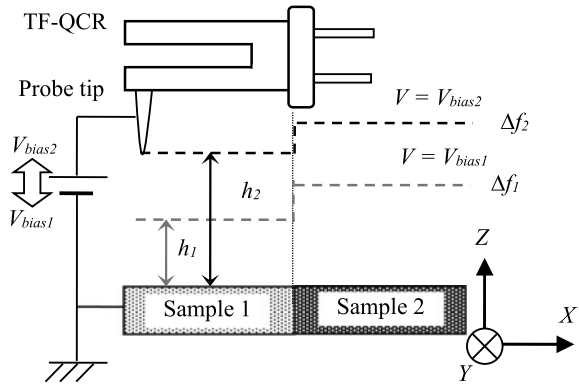
In the dual-height method, the absolute tip-to-sample distance  $h$  can be calculated by utilizing Eqs. 2 and 3, and shown as follows.

$$h = w \frac{\sqrt{\Delta f_u / \Delta f_l}}{1 - \sqrt{\Delta f_u / \Delta f_l}} \quad (4)$$

Consequently, since the absolute tip-to-sample distance can be calculated by Eq. 4, the surface profile of the measuring object can be obtained as the difference between the trajectory of the lower trace and the tip-to-sample distance.

On the other hand, the measurement principle of the CPD is shown in Fig. 2. With regard to the CPD measurement, the tip-to-sample distance is calculated twice by changing the bias voltage between the probe tip and the sample surface. Firstly,

**Fig. 2** Measurement principle of CPD



the tip-to-sample distance  $h_1$  is calculated with applying the bias voltage of  $V_{bias1}$  by utilizing Eq. (4). Then, the bias voltage is set to be  $V_{bias2}$  and the tip-to-sample distance  $h_2$  is calculated. The frequency shifts which are corresponding to the bias voltage  $V_{bias1}$  and  $V_{bias2}$  can be expressed as follows.

$$\Delta f_1 = \frac{1}{2} \frac{f_0}{k} \pi \epsilon_0 \epsilon_r (V_{bias1} + V_{CPD})^2 \frac{R}{h_1^2} \tag{5}$$

$$\Delta f_2 = \frac{1}{2} \frac{f_0}{k} \pi \epsilon_0 \epsilon_r (V_{bias2} + V_{CPD})^2 \frac{R}{h_2^2} \tag{6}$$

By utilizing Eqs. (5) and (6), the  $V_{CPD}$  can be calculated as follows.

$$V_{CPD} = \frac{h_1 V_{bias2} \sqrt{\Delta f_1} - h_2 V_{bias1} \sqrt{\Delta f_2}}{h_2 \sqrt{\Delta f_2} - h_1 \sqrt{\Delta f_1}} \tag{7}$$

When the tip-to-probe distance is constant as the distance  $h$ ,  $h_1$  and  $h_2$  can be cancelled. Consequently,  $V_{CPD}$  can be rewritten as the following equation.

$$V_{CPD} = \frac{V_{bias2} \sqrt{\Delta f_1} - V_{bias1} \sqrt{\Delta f_2}}{\sqrt{\Delta f_2} - \sqrt{\Delta f_1}} \tag{8}$$

As shown in Eq. 8, when the tip-to-sample distance is maintained constant,  $V_{CPD}$  can be calculated by changing the bias voltage applied between the probe tip and the sample surface. In the case of the SEFM, the probe tip can scan the sample surface in noncontact condition by utilizing the closed-loop control based on the electrostatic force detection. During the second scanning, the probe tip can trace the trajectory of the first probe scanning path without the closed-loop control of the tip-to-sample separation. Therefore, since it is possible to scan the same probe trace by changing the bias voltage, the CPD value can be calculated by utilizing Eq. 8. However, in the actual measurement, the tip-to-sample distance is significantly influenced by the



thermal drift. As a result, the CPD value in this experiment is carried out based on Eq. 7. The tip-to-sample distance is calculated based on the probe scanning path under the closed-loop control, thus, the CPD value is obtained by both of frequency shift amounts and the tip-to-sample distances.

### 3 Experiment and Discussions

#### 3.1 Experimental Configuration of SEFM

Figure 3 shows the schematic diagram of the scanning electrostatic force microscope in this study. As described in Sect. 2, a tungsten probe, which is sharpened by the electrochemical etching process, is attached on one-beam of the TF-QCR by the conductive epoxy. The probe is oscillated by the TF-QCR on its resonance frequency. The oscillation signal of the probe tip can be detected by using the piezoelectric effect of the quartz crystal, and amplified by a current-to-voltage ( $I-V$ ) converter. Since the probe is attached on the beam of the TF-QCR by the conductive epoxy, it is possible to apply the bias voltage between the probe and the sample through the electrode of the TF-QCR. The frequency of the probe can be maintained constant by the self-oscillation circuit. When the bias voltage is applied, the frequency of the probe oscillation is shifted according to the intensity of the electrostatic force. The shift amount of the probe oscillation is detected by the phase-locked loop (PLL) circuit, and fed into an analogue-to-digital (A/D) converter of the personal computer (PC). The TF-QCR is mounted on the Z-directional scanner driven by the piezoelectric actuator (PZT). The displacement of the Z-scanner is detected by using a linear encoder. The resolution and nonlinearity are 0.5 and 10 nm over a stroke of 50  $\mu\text{m}$ ,

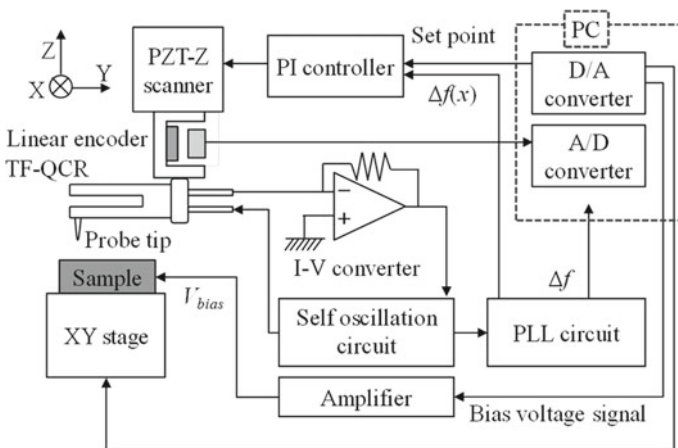


Fig. 3 Experimental configuration of CPD measurement system based on the SEFM

respectively [Ref.]. Since the electrostatic force is changed by the distance between the probe and the sample surface, the amount of the frequency shift is a function of the tip-to-sample distance. The frequency shift amount can be maintained constant by using the method of a frequency modulation AFM. The frequency shift signal which is detected by the PLL circuit is fed into a SPM controller to maintain the frequency shift amount constant.

The bias voltage, which is applied between the probe tip and the sample surface to generate the electrostatic force, is controlled by the digital-to-analogue (D/A) converter of the PC. The bias voltage signal comes from the D/A converter and amplified 15 times by an amplifier. The electrode of the probe tip is connected to the  $I$ - $V$  converter, which is used for the detection of the probe oscillation, and the electric potential of the probe tip can be kept zero owing to the vertical short of the operational amplifier. As a result, the potential difference between the probe tip and the sample surface will coincide with the output of the bias voltage amplifier.

### 3.2 Measurement of CPD

The relationship between the frequency shift of the probe oscillation and the tip-to-sample distance was evaluated on different materials. Au grating fabricated on the Cr coated-glass substrate was used as the sample in this experiment. The designed pitch and amplitude of the Au/Cr grating were  $20\ \mu\text{m}$  and  $100\ \text{nm}$ , respectively. The probe tip was approached toward the sample surface in  $1\ \text{nm/step}$ . During the approaching, the probe displacement in  $Z$ -direction and the frequency shift amount were recorded simultaneously by the A/D converter of the PC, and the sampling frequency was set to  $5\ \text{kHz}$ . The average value of 50 data points sampled per step was employed as the measurement value. Figure 4 shows the relationship between the frequency shift amount and the tip-to-sample distance when the bias voltage was set to  $-50\ \text{V}$ . The tip-to-sample distance shown in the horizontal axis is calculated by Eq. 4. The

**Fig. 4** Relationship between the tip-to-sample distance and the frequency shift of the probe oscillation

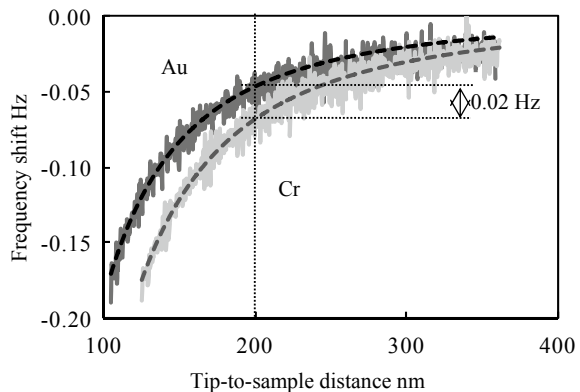
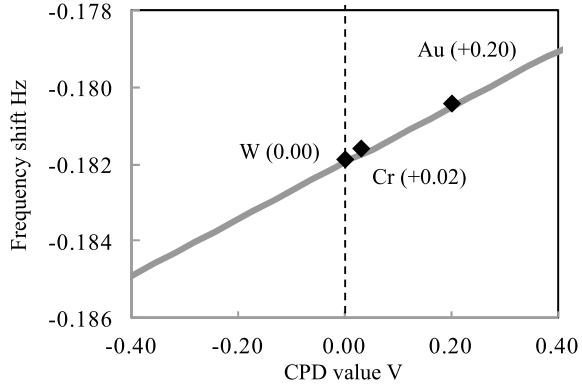


**Fig. 5** Calculated CPD value with respect to tungsten



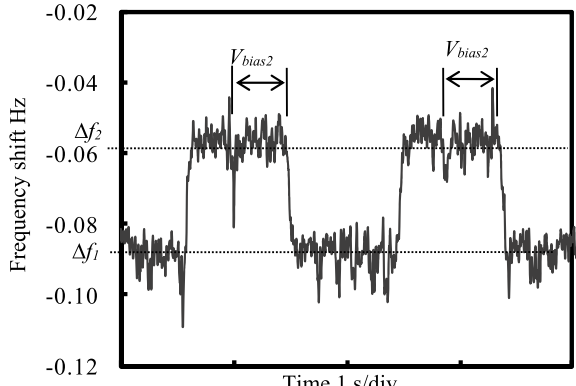
dotted line shown in Fig. 4 indicates the fitting curve of the frequency shift. It can be seen that the frequency shift amount is proportional to the square inverse of the tip-to-sample distance. The difference of the frequency shift amount between two materials was 0.02 Hz at 200 nm of the tip-to-sample distance. The shift amount of the probe frequency was also calculated by Eq. 5. Figure 5 shows calculation result of the CPD value with respect to the tungsten probe. The tendency of the difference between the CPDs of Au and Cr was similar to Fig. 4.

The CPD value is calculated by utilizing Eq. 7. Table 1 indicates the set values of frequency shift amount and the bias voltage. Figure 6a shows the frequency shift with respect to the bias voltage variation. Figure 6b indicates the probe displacement during the measurement of Fig. 6a. The CPD value is calculated according to Fig. 6. The averaged values of the calculated CPDs were  $-16.47$  V (W-Cr) and  $-15.62$  V (W-Au), respectively. The calculated values are much different in comparison with the previous researches (W-Cr:  $+18.4$  mV, W-Au:  $+202.3$  mV). This difference would be induced by the operation in the air atmosphere. In the air, the water layer with nanometric thickness exists on the material surface [7]. Therefore, due to the thickness of the thin layer, the CPD value would be varied significantly [8]. Consequently, the CPD value measurement based on the SEFM can distinguish the difference of the material on the surface.

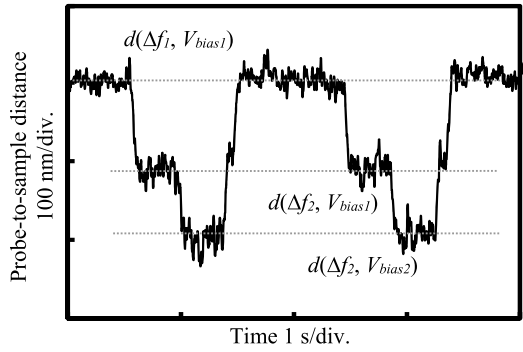
**Table 1** Parameter set in the CPD measurement

Set point of frequency shift (Hz)	Bias voltage (V)	Probe position
$\Delta f_1 = -0.087$ Hz	$V_{bias1} = 45$ V	$d(\Delta f_1, V_{bias1})$
$\Delta f_2 = -0.057$ Hz	$V_{bias1} = 45$ V	$d(\Delta f_2, V_{bias1})$
$\Delta f_1 = -0.057$ Hz	$V_{bias2} = 55$ V	$d(\Delta f_2, V_{bias2})$

**Fig. 6** Experimental result of CPD value measurement



(a) Frequency shift and bias voltage



(b) Tip-to-sample displacement

### 4 Conclusion

A measurement method of the CPD value has been proposed by utilizing the SEFM. By measuring the frequency shift amount of the probe oscillation and Z-directional displacement of the probe tip, the CPD value of the sample surface can be detected in noncontact condition. Since the difference of the materials can be distinguished in noncontact condition, this method will be applicable for the materials distribution measurement of the micro- and nanometric devices.

### References

1. Giessibl FJ (1997) Forces and frequency shifts in atomic-resolution dynamic-force microscopy. Phys Rev B 56(24):16010–16015
2. Gao W, Goto S, Hosobuchi K, Ito S, Shimizu Y (2012) A noncontact scanning electrostatic force

- microscope for surface profile measurement. *CIRP Ann Manuf Technol* 61:471–474
3. Herbert BM (1977) The work function of the elements and its periodicity. *J Appl Phys* 48:4729
  4. Takahashi T (2011) Photoassisted Kelvin probe force microscopy on multicrystalline Si solar cell materials. *Jpn J Appl Phys* 50:08LA05
  5. Meyer G, Amer NM (1990) Reprinted with permission from simultaneous measurement of lateral and normal forces with an optical-beam-deflection atomic force microscope. *Appl Phys Lett* 57(20):2089
  6. Hosaka S, Kikukawa A (1992) Study of magnetic stray field measurement on surface using new force microscope. *Jpn J Appl Phys Parts 2*(31):908–911
  7. Matsuoka H, Fukui S, Takahisa K (2003) Influence of the meniscus force for contact recording head dynamics over a randomly undulating disk surface. *IEEE Trans Magn* 39:864–869
  8. Kim HK, Kang SJ (2011) Effective work function control of indium-tin-oxide electrodes. *J Korean Phys Soc* 59(4):L2655–L2657

# Development of *Orthros*, A Thickness Evaluation System for Free Curved Plate-Basic Performance Based on the Measurement Principle



Y. Okugawa, N. Asakawa, and M. Okada

**Abstract** At present, for thickness inspection of sheet metal processed product having free curved surface in a manufacturing process, some typical points are selected experientially by operator. The selected points are generally measured with a point micrometer for accuracy and practicality. In this case, it is difficult to measure the thickness of whole range with non-destructive method. The study deals with an automatic measurement and evaluation system for free curved plate thickness using an industrial robot and two laser displacement sensors, called *Orthros*. The robot is used as a workpiece positioning device and the static dual-head thickness measuring unit composed of faced two displacement sensors measures the thickness of the workpiece with non-destructive method. The measuring procedure comprises three steps. First, the workpiece shape is measured by the system to acquire the shape data as a point cloud. Then, a thickness measuring path including the surface normal vectors and the measurement forwarding vectors is generated from the acquired shape data. Finally, the thickness is measured when the robot moves to match the calculated normal direction and the laser irradiation direction at each measuring point. The thickness data is displayed in relation to the shape data according to the needs of operator as a color map, etc. In this paper, the measurement principle and the basic performance of *Orthros* is described. In addition, the result of the actual thickness measurement is presented and discussed.

**Keywords** Thickness measurement · Path planning · Industrial robot

## 1 Introduction

In general, thickness of a sheet metal processed product, such as a car body, has been measured by using a point micrometer which is based on the contact principle from the upper and lower side of the workpiece. Although the principle is simple and reliable, still there is a problem that the acquisition of large amount of data is caused

---

Y. Okugawa · N. Asakawa (✉) · M. Okada  
Graduate School of Natural Science and Technology, Kanazawa University, Kakuma-machi,  
Kanazawa 9201192, Japan  
e-mail: [nasakawa@se.kanazawa-u.ac.jp](mailto:nasakawa@se.kanazawa-u.ac.jp)

© Springer Nature Switzerland AG 2022  
S. Hinduja et al. (eds.), *Proceedings of the 38th International MATADOR Conference*,  
[https://doi.org/10.1007/978-3-319-64943-6\\_41](https://doi.org/10.1007/978-3-319-64943-6_41)

573

by the long measurement time. In addition, the geometric restriction of a micrometer makes it difficult to conduct non-destructive measurement [1]. In many actual cases, several particular points selected by the operator are measured and evaluated. In other words, since the measurement areas are selected depending on the subjectivity of the operator, the evaluation result of the workpiece is due to the skill of the operator. On the other hand, the commercial simulation software of press forming [2] show a thickness distribution map as a color contour chart. If there is not high-density measurement data, it is difficult to evaluate the simulation results. In this study, we propose a thickness measurement system composed of laser displacement sensors and an industrial robot, called *Orthros*. In this paper, the measurement principle of the system and the basic performance are reported. Moreover, validity of the system is evaluated by the experimental result.

## 2 Configuration of *Orthros*

Figure 1 shows the configuration of *Orthros* and the coordinate system of the robot. A dual-head thickness measuring unit composed of two point-type laser displacement sensors (LK-G150, Keyence Co., reference distance of 150 mm, measuring range of  $\pm 40$  mm, positioning accuracy of  $\pm 0.04$  mm) measures the thickness of the workpiece. The sensors are placed to share the same optical axis and to have the distance of 300 mm by considering its reference distance. The system uses a 6-axis vertical articulated industrial robot (HP-6, Yasukawa Electric Co., payload of 6 kg, positioning repeatability of  $\pm 0.08$  mm) as a workpiece positioning device.

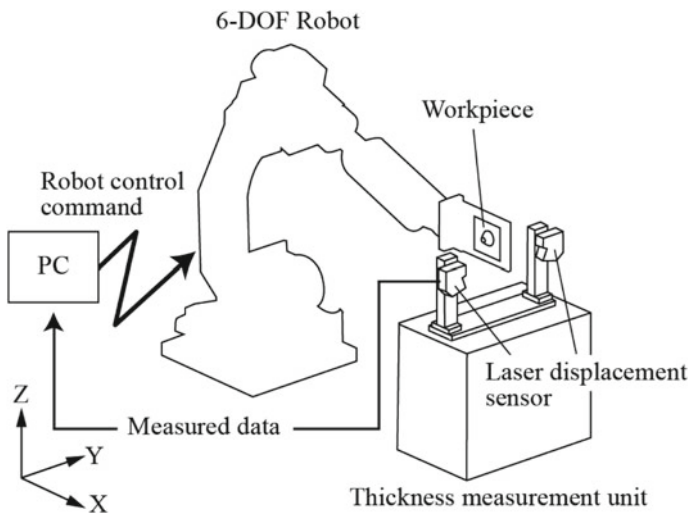


**Fig. 1** Configuration of *Orthros*

Since the system measures the workpiece shape in process, a thickness measurement path is automatically generated without CAD data or other extra information of the workpiece.

### 3 Principle of Thickness Measurement

In the system, the thickness is measured on the basis of the simple principle “Make subtract between the measuring positions of both side” as shown in Fig. 2. The distance  $D_C$ , between the two sensors, is 300 mm, and each sensor measures  $D_A$  and  $D_B$ . Therefore, the thickness  $t$  is calculated by Eq. (1).

$$t = D_C - (D_A + D_B) \quad (1)$$

The thickness measurement through this method is a popular technique for flat plates [3, 4]. To accurately calculate thickness of a free curved plate according to the aforementioned method, the laser irradiation normal to the measuring surface is required. The system realizes this condition according to the following procedure.

- (1) Thickness measuring point  $\mathbf{P}_{W_i}$  ( $i = 1 \sim n$ ), normal vector  $N_i$  and forwarding vector  $F_{W_i}$  are defined as shown in Fig. 3.  $\mathbf{P}_{W_i}$  is generated based on the shape scan shown in Sect. 4.2.  $N_i$  and  $F_{W_i}$  are calculated from  $\mathbf{P}_{W_i}$ . Here,  $n$  is the number of the measuring points.
- (2) Measuring center point  $\mathbf{P}_T$  expressing the center point of the unit, measuring vector  $T$  and measuring direction vector  $D$  are defined in the thickness measuring unit as shown Fig. 4.
- (3) The robot realizes the position and posture of the workpiece to match ( $\mathbf{P}_{W_i}$ ,  $N_i$ ,  $F_{W_i}$ ) and ( $\mathbf{P}_T$ ,  $T$ ,  $D$ ).

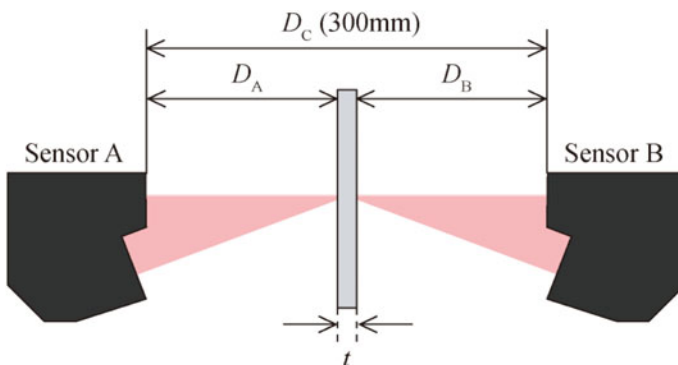


Fig. 2 Principle of the thickness measurement



Fig. 3 Workpiece model

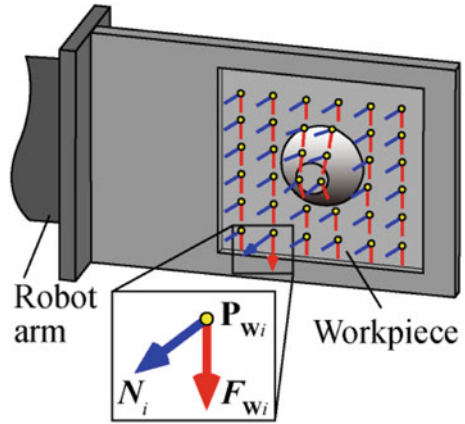
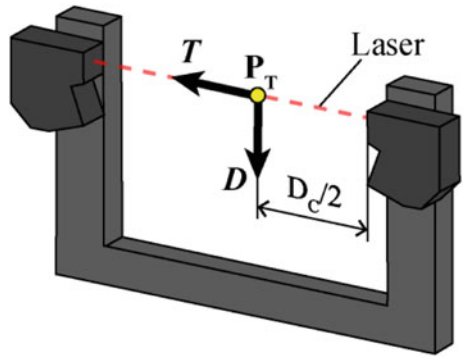


Fig. 4 Measuring unit model



## 4 Measurement Procedure

### 4.1 Overview

For the thickness measurement on the basis of the above-mentioned principle, the system has to measure the workpiece shape in advance. The thickness measurement path is generated on the basis of the acquired shape data. Therefore, the measurement procedure can be followed in two steps: (1) shape measurement and (2) thickness measurement. Flow chart of the measurement procedure is shown in Fig. 5.

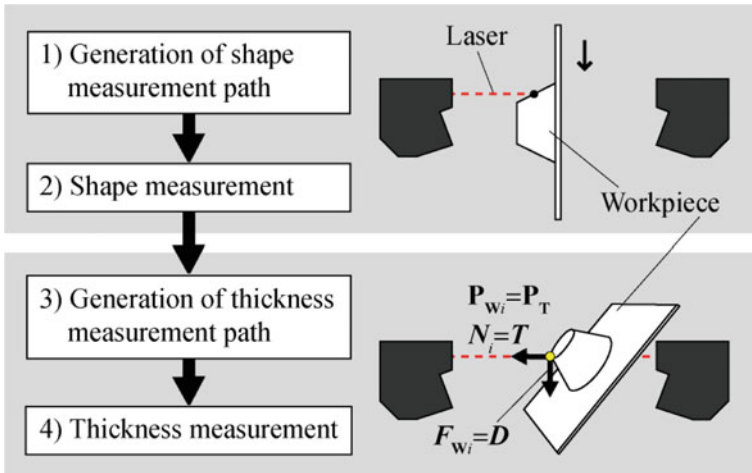
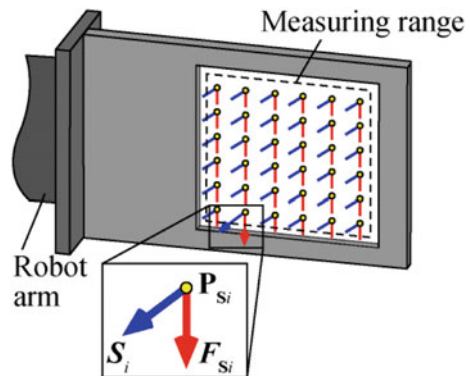


Fig. 5 Measurement procedure

### 4.2 Shape Measurement

The workpiece shape is scanned using one laser sensor. The shape measurement postures are constant in the whole ordered measuring range. The length of scan interval for surface direction is decided on the basis of the required pitch in the thickness measurement. Shape measuring point  $P_{Si}$  which is arranged in lattice pattern on a flat surface, shape measuring vector  $S_i$  and forwarding vector  $F_{Si}$  are defined as shown in Fig. 6. A sequence of  $(P_{Si}, S_i, F_{Si})$  is defined as a shape measurement path. A shape measurement path is converted to a robot control command, that  $(P_{Si}, S_i, F_{Si})$  matches  $(P_T, T, D)$ , and transferred to the robot. Then, a three dimensional shape data is acquired from the measuring positions and the outputs of the sensor

Fig. 6 Shape measurement path



representing the height of the workpiece. These points are defined as the thickness measuring points  $\mathbf{P}_{W_i}(i = 1 \sim n)$ .

### 4.3 Thickness Measurement

The system calculates subtractions of the positions of the adjacent points and the cross products on each measuring point to generate  $(\mathbf{P}_{W_i}, \mathbf{N}_i, \mathbf{F}_{W_i})$ . While these values are strictly different on the upper and lower side of the workpiece, we assume they are the same because of the thinness of the target workpiece. A sequence of  $(\mathbf{P}_{W_i}, \mathbf{N}_i, \mathbf{F}_{W_i})$  is defined as a thickness measurement path. In the same manner as the shape measurement, a thickness measurement path is converted to a robot control command, that  $(\mathbf{P}_{W_i}, \mathbf{N}_i, \mathbf{F}_{W_i})$  matches  $(\mathbf{P}_T, \mathbf{T}, \mathbf{D})$ , and transferred to the robot.

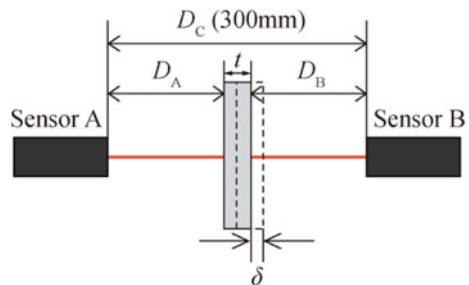
## 5 Effect of the Robot Errors on the Thickness Measurement

The positioning repeatability and the posture error of the robot are concerned with accuracy of the thickness measurement based on the generated thickness measurement path. In this section, the effects of these errors on the thickness measurement are investigated.

### 5.1 Positioning Repeatability

The positioning repeatability of the robot used in the system,  $\delta$ , is  $\pm 0.08$  mm. The effect of  $\delta$  should be discussed separately in the thickness direction and the surface direction of the workpiece. The thickness is calculated by use of the output of each laser sensor as shown in Eq. (1). Hence, if there is  $\delta$  in the thickness direction as shown in Fig. 7, the thickness  $t$  is calculated by Eq. (2).

**Fig. 7** Positioning repeatability in thickness direction



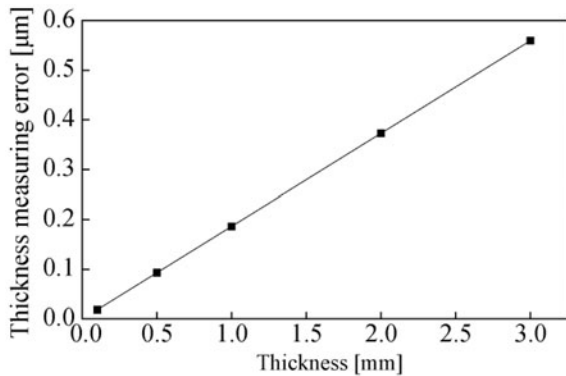
$$\begin{aligned}
 t &= D_C - \{(D_A + \delta) + (D_B - \delta)\} \\
 &= D_C - (D_A + D_B)
 \end{aligned}
 \tag{2}$$

In other words,  $\delta$  would be removed automatically since we measure the distance from both sides (Sensor A and B). Therefore, there is no effect of  $\delta$  on thickness calculation within the measuring range of the laser sensor. The thickness measuring accuracy in the thickness direction depends on the accuracy of the sensor. On the other hand, the positioning accuracy more than  $\delta$  cannot be guaranteed for the surface direction. Therefore, the thickness measured value by the system is defined as the representative value within the positioning repeatability, circle with radius of 0.08 mm, in the surface direction.

### 5.2 Posture Error

The posture error indicates the angle difference between the command value and the actual measured value when the posture of the end of the robot arm varies around each axis of the robot coordinate system. The verification of the posture error was conducted through the experimental study. The posture error  $\theta$  is measured when the end of the robot arm varies around X and Z axis at the intervals of  $5^\circ$  within the measuring range  $45^\circ$  to  $45^\circ$  in the workspace of the robot. From the experimental results, the maximum  $\theta_x$  is  $0.84^\circ$  and  $\theta_z$  is  $0.72^\circ$ . Figure 8 shows the thickness measuring error of the workpiece having thickness 0.1–3 mm in accordance with the maximum posture error. The measuring error in accordance with the posture error is sufficiently small.

**Fig. 8** Thickness measuring error in accordance with the maximum posture error



## 6 Experiment

The experimental measurement was performed to verify validity of the developed system. Table 1 shows the experimental conditions. Figure 9 shows the workpiece and measured area. The workpiece shape makes it difficult to measure the thickness by a standard size micrometer. Figure 10 shows the generated shape measurement path. From this figure, all  $S_i$  and  $P_{S_i}$  found to be same-direction vectors and equally-spaced points, respectively. Figure 11a shows the shape measurement by the system, and Fig. 12 shows the acquired shape data. Also, the thickness measurement path, which is generated from the shape scan data, is shown in Fig. 13. As shown in Fig. 11b, the robot moves to match the laser beam axis and normal vector. The thickness distribution maps, which are generated from the measurement result by the system and the point micrometer, are shown in Figs. 14 and 15. Here, we define the measured value by the point micrometer as true thickness of the workpiece. Table 2 shows the measurement time of each method and the measuring error of the system on the basis of the measurement by the point micrometer. The maximum error was 37  $\mu\text{m}$ . In addition, the measurement time of the system was about 10% of that of a point micrometer. It was considerably shorter. To facilitate the inspection, the system is capable to draw the measurement result in three dimensions as shown in Figs. 16 and 17. Figure 17 shows the thickness distribution of whole range and on the profile.

**Table 1** Experimental conditions

Workpiece	Material	Aluminium (A1050)
	Size	125 × 135 mm
	Thickness	0.5 mm
	Shape	Partial sphere
Measuring range		60 × 60 mm
Measuring interval		3 mm

**Fig. 9** Workpiece and measured area

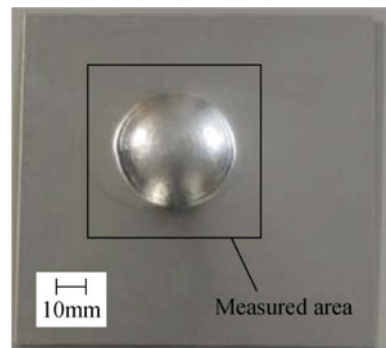
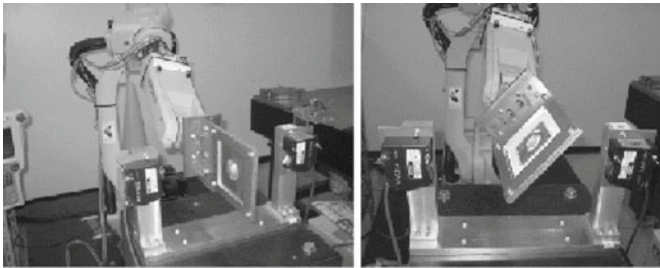
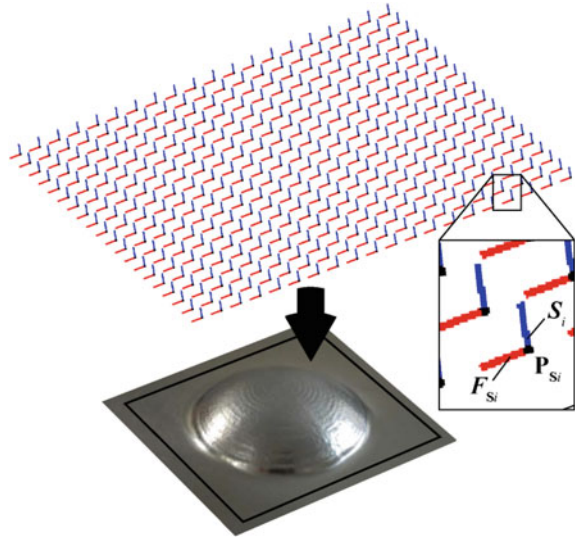


**Fig. 10** Shape measurement path



(a) Shape measurement

(b) Thickness measurement

**Fig. 11** Robot under measurement

## 7 Conclusion

An automatic thickness measurement and evaluation system using an industrial robot and laser sensors was developed. The experimental results are summarized as follows:

- (1) Thickness of a free curved plate was measured according to the automatically generated measurement path.
- (2) The measurement time was considerably shorter in comparison with the conventional method (point micrometer).
- (3) The thickness distribution maps, which are associated with the shape data, were generated.

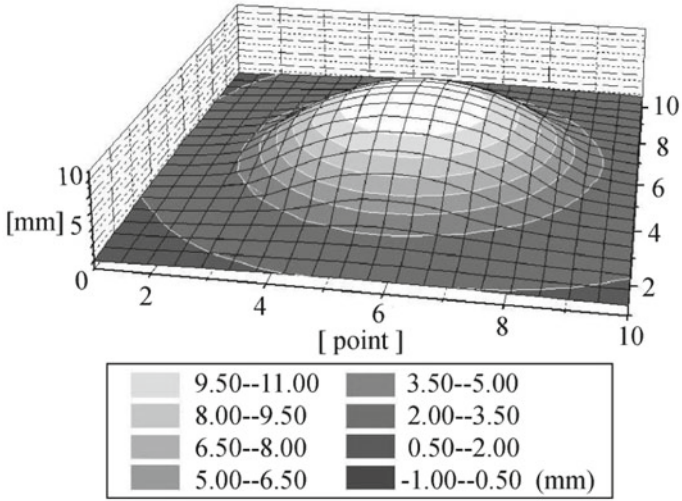


Fig. 12 Shape measurement result

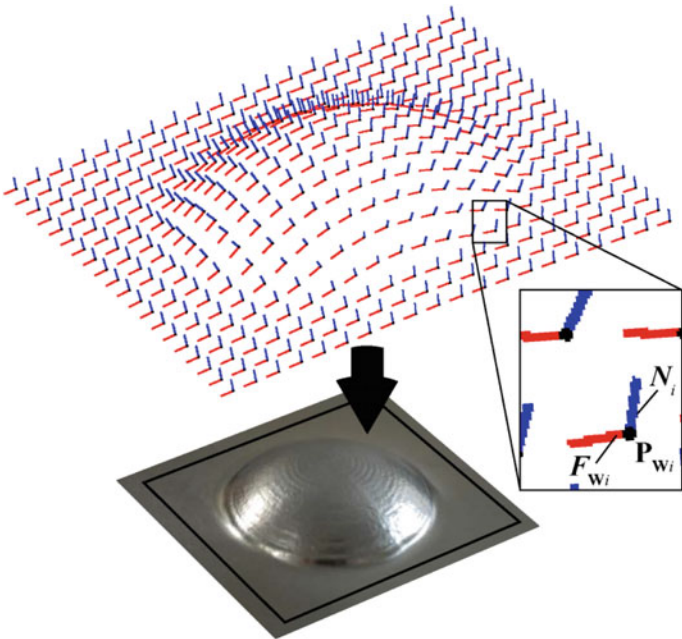
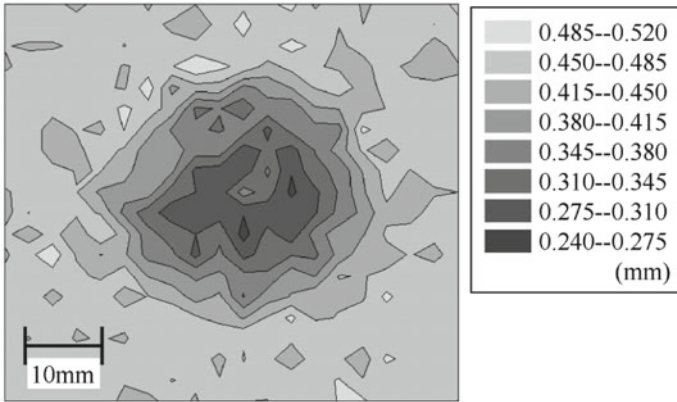
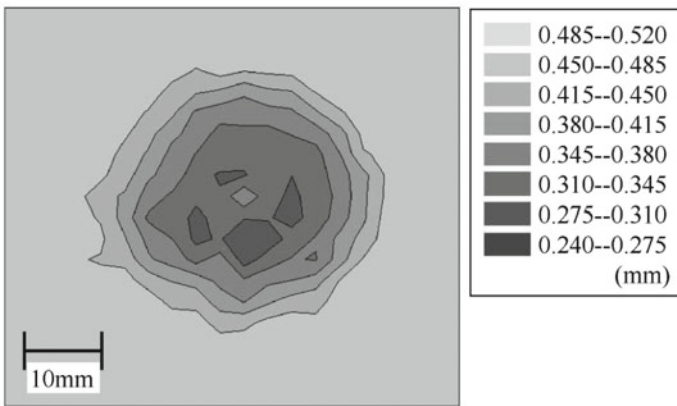


Fig. 13 Thickness measurement path



**Fig. 14** Thickness measurement result by the system



**Fig. 15** Thickness measurement result by a point micrometer

**Table 2** Comparison on time and error

	Time (h)	Maximum error (mm)
Point micrometer	4.8	-
Developed system	0.5	0.037



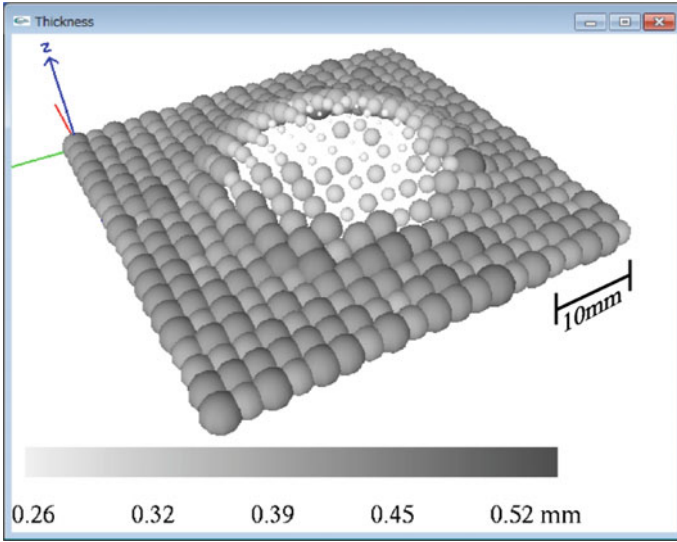


**Fig. 16** Three dimensional thickness distribution map drawn by sphere

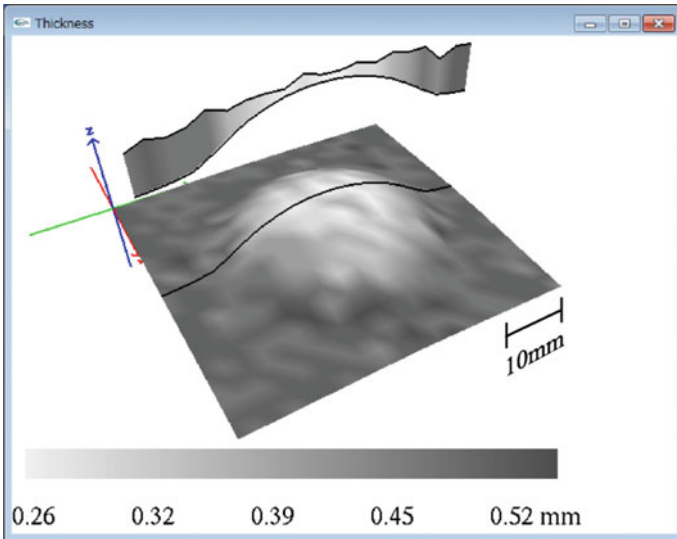


**Fig. 17** Three dimensional thickness distribution maps of whole range and part of the profile drawn by contour

## References

1. The Japan Society for Technology of Plasticity (2000) Plain press forming. The Nikkan Kogyo Shimbun (in Japanese)
2. JSTAMP. <http://www.jstamp.jp/en/index.html>
3. Ogasawara A, Naito S, Kominami H, Yamamoto T (1995) Plate thickness measuring instrument. Japanese patent disclosure H7-280526
4. Welch D (2010) Thickness measurements using laser triangulation. *Sensors* 27(4)

# Homodyne Interferometer Using Iodine Frequency Stabilized Laser Diode



Tung Thanh Vu, Y. Maeda, and M. Aketagawa

**Abstract** In this paper, we propose the use of sinusoidal frequency modulation on a laser diode (LD) to achieve both the frequency stabilization of the LD and a displacement measurement by the homodyne interferometer. The central frequency of the LD is locked to a Doppler broadened transition of iodine molecule ( $I_2$ ) near the wavelength of 634 nm. The frequency of the LD is modulated across the Doppler-broadened transitions of iodine molecule and the lock-in technique is utilized to detect absorption signal. This homodyne interferometer can be constructed without high cost and complexity, and can obtain an accuracy of nanometer order in displacement measurement.

**Keywords** Frequency stabilization · Laser diode · Iodine · Absorption · Homodyne interferometer

## 1 Introduction

A displacement measurement with an uncertainty of less than nanometer is crucial to many fields of the modern technology such as the nanotechnology, the precision engineering, the optical metrology, the semiconductor manufacturing, etc. Laser interferometer is widely utilized for the displacement measurement at nanoscale, because of its inherent accuracy. Moreover, this method can keep the traceability to the definition of the meter, if the wavelength is calibrated. Recently, an LD is selected as a light source because of its high efficiency, compact size and longer lifetime by comparing with gas lasers. Moreover, the LD offers direct frequency modulation through an injection current modulation [1] and large frequency tuning that are widely utilized in laser spectroscopy. However, the long term drift of the laser frequency,

---

T. T. Vu (✉) · Y. Maeda · M. Aketagawa  
Department of Mechanical Engineering, Nagaoka University of Technology, Kamitomioka  
1603-1, Nagaoka 940-2188, Niigata, Japan  
e-mail: [tung.vuthanh@hust.edu.vn](mailto:tung.vuthanh@hust.edu.vn)

T. T. Vu  
School of Mechanical Engineering, Hanoi University of Science and Technology, Hanoi 100000,  
Vietnam

typically at a rate of several megahertz per minute, must be improved before it can be applied for high accurate displacement measurements [2]. Frequency stability can be obtained by locking the LD frequency to atomic or molecule transitions [2–6].  $I_2$  molecule offers some absorption lines that can be used as frequency references. To detect the absorption signal buried in the noise, the frequency of the laser is modulated across the absorption lines.

The relative frequency stability of the commercial laser sources, Zygo, Agilent or Renishaw, around  $10^{-8}$  per hour with thermal stabilization [7–9]. However, these He–Ne laser sources are voluminous, low power. Otherwise, frequency stability of LD can obtain  $10^{-9}$  order for Doppler broadened transition locking [3] and  $10^{-12}$  for hyperfine transition locking [5].

A sinusoidal frequency (phase) modulation technique [10–12] is effective for the displacement measurement by an interferometer. Recently, Madden et al. have reported the availability of the sinusoidal frequency modulation on an LD to a Michelson interferometer [13]. They used the Lissajous diagram [14] to obtain the optical path movement (equivalence to displacement) using 2nd and 3rd harmonic modulated signals. To draw the exact Lissajous diagram with the sinusoidal frequency modulation, it is needed to know the value of the modulation index. In the sinusoidal frequency modulation for the Michelson interferometer, the value of the modulation index varies with the frequency modulation amplitude and the optical path difference between the two arms.

Therefore, Madden et al. almost fixed both the frequency modulation amplitude and the optical path difference, and determined the modulation index. To increase a measurable range of the Michelson interferometer with the sinusoidal frequency modulation on the LD, and to use the Lissajous diagram simultaneously, it is required to know the dynamic change of the modulation index due to the optical path change. Some papers [15–17] have proposed the dynamic modulation index measurements using spectrum intensity of the interference signal. Then the displacement measurement of an interferometer can be calculated using the value of the modulation index. However, since these methods have not used the Lissajous diagram, the accuracy of the displacement measurement is not enough.

In this paper, first, we propose the combination method to stabilize the LD frequency to  $I_2$  absorption lines, and to measure the displacement for a Michelson interferometer using the sinusoidal frequency modulation on the LD. Secondly, we propose the enhancement of the measurable displacement range while keeping the measurement accuracy by combining the estimation of the dynamic modulation index change and the Lissajous diagram, respectively. Lastly, we report preliminary experiments and discussion.

## 2 Principle

### 2.1 Detection of the Linear Absorption Lines of $I_2$

The principle of the homodyne interferometer using the  $I_2$  frequency stabilized LD is illustrated in Fig. 1. This system is divided into two parts, the frequency stabilized LD source and the homodyne interferometer.

In order to detect the Doppler broadened absorption lines of  $I_2$ , the frequency of the LD is scanned by changing injection current or temperature of the laser. A beam splitter 1 (BS1) is employed to divide the output laser into two beams, one beam passes through the  $I_2$  cell and the other enters to a Michelson interferometer. These linear absorption signals are detected as a decreasing in the intensity when the frequency of the LD across the transition lines of  $I_2$ . A balanced photodetector (BPD) is utilized to detect absorption signals and reduces the effect of intensity fluctuation of the laser. The linewidth of these transition lines are broadened mostly due to Doppler broadening effect. However, the frequency stabilization is expected to be  $10^{-9}$  order [3].

We use frequency modulation technique [10–12] to lock frequency of the LD to the center of the  $I_2$  absorption line at the wavelength of near 634 nm (numerical order of 153 in the iodine absorption spectra [18]). The frequency of laser source is modulated by sinusoidal current signal and the first harmonic signal is detected using a lock-in amplifier (LIA). To lock the laser frequency, the output signal from the LIA is fed back to current driver via the PID controller. Then, the LD that its frequency is lock to the absorption transition of  $I_2$  is used for the homodyne interferometer.

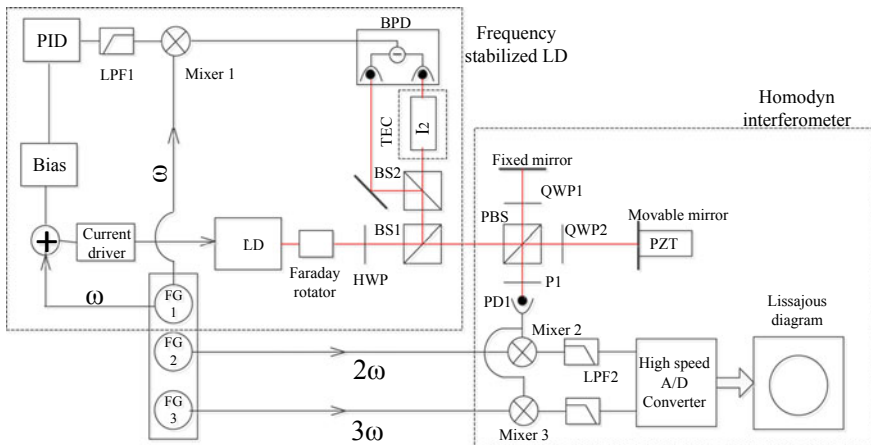


**Fig. 1** Schematic diagram of the homodyne interferometer. LD: laser diode; HWP: half wave plate; QWP: quarter wave plate; BS: beam splitter; PBS: polarized beam splitter; BPD: balanced photodetector; PD: photodetector; FG: function generator; LPF: low pass filter; TEC: thermoelectric cooler. PZT: piezo electric actuator

## 2.2 Homodyne Displacement Measuring Interferometer

A sinusoidal frequency modulation technique is effective for the displacement measurement by an interferometer. The output beam from BS1 is directed to the Michelson interferometer. The moving mirror was driven by a piezo electric actuator (PZT). To increase a measurable displacement of the Michelson interferometer with the sinusoidal frequency modulation on the LD, and to use the Lissajous diagram simultaneously, it is required to know the dynamic change of the modulation index due to the optical path change. The dynamic modulation index can be calculated from the power spectrum of the interferometer intensity [15–17].

In general, the frequency modulation using sinusoidal signal of output laser is given as

$$f(t) = f_0 + \Delta f \sin 2\pi f_m t \quad (1)$$

where  $\Delta f$  is frequency modulation amplitude,  $f_m$  is modulation frequency,  $f_0$  is carrier frequency. The phase component can be derived by equation below

$$\phi(t) = \int_0^t 2\pi f(t) dt = 2\pi f_0 t - \frac{\Delta f}{f_m} \cos 2\pi f_m t + \phi_0 \quad (2)$$

where  $\phi_0$  is the initial phase of laser source. For homodyne interferometer, the phases of the reference and measurement arms can be written as

$$\phi_r = 2\pi f_0 t - \frac{\Delta f}{f_m} \cos 2\pi f_m t + \phi_0 \quad (3)$$

$$\phi_m = 2\pi f_0(t - \tau) - \frac{\Delta f}{f_m} \cos 2\pi f_m(t - \tau) + \phi_0 \quad (4)$$

where  $\phi_r$ ,  $\phi_m$  are the phases of the reference and measurement arms, respectively,  $\tau$  is a delay time between them. The different phase between the reference and the measurement arms is given by

$$\phi_m - \phi_r = -2\pi f_0 \tau - \frac{2\Delta f}{f_m} \sin \left[ 2\pi f_m \left( t - \frac{\tau}{2} \right) \right] \times \sin \left[ 2\pi f_m \left( \frac{\tau}{2} \right) \right] \quad (5)$$

Because the delay time  $\tau$  is negligibly small so that Eq. (5) can be simplified by using trigonometric approximations [19]

$$\sin \left( 2\pi f_m \cdot \frac{\tau}{2} \right) \approx 2\pi f_m \cdot \frac{\tau}{2}$$

and

$$\sin\left[2\pi f_m\left(t - \frac{\tau}{2}\right)\right] \approx \sin 2\pi f_m t$$

Equation (5) can be rewritten as the following equation

$$\phi_m - \phi_r = -2\pi f_0 \tau - 2\pi \Delta f \tau \sin 2\pi f_m t \quad (6)$$

The intensity of resulting beam can be derived as the equation below

$$\begin{aligned} I &= E_{0r}^2 + E_{0m}^2 + 2E_{0r}E_{0m} \cos(\phi_m - \phi_r) \\ &= E_{0r}^2 + E_{0m}^2 + 2E_{0r}E_{0m} \cos(2\pi f_0 \tau + 2\pi \Delta f \tau \sin 2\pi f_m t) \\ &= E_{0r}^2 + E_{0m}^2 + 2E_{0r}E_{0m} \cos(m \sin 2\pi f_m t + \phi) \end{aligned} \quad (7)$$

where

$$m = 2\pi \Delta f \tau = \frac{4\pi \Delta f n L}{c} \quad (8)$$

$$\phi = 2\pi f_0 \tau = 4\pi \frac{nL}{\lambda_0} \equiv 4\pi \frac{n\Delta l}{\lambda_0} \quad (9)$$

where  $m$  is a modulation index,  $n$  is the refractive index,  $L$  is a different length between the two arms including an initially unbalanced length and a displacement;  $\Delta l$  is the displacement,  $\lambda_0$  is the wavelength of laser source. Since the optical phase  $\phi$  shown in Eq. (9) has ambiguity of integer times  $360^\circ$ , the range of  $\Delta l$  shown in Eq. (9) must be  $0 < \Delta l < \lambda_0/2$ . However, the accumulation measurement of  $\Delta l$  can induce the length measurement.

Using Bessel function, Eq. (7) is expanded as

$$\begin{aligned} I &= E_{0r}^2 + E_{0m}^2 \\ &+ 2E_{0r}E_{0m} \left[ \cos \phi \left\{ J_0(m) + 2 \sum_{k=1}^{\infty} J_{2k}(m) \cos(2k)2\pi f_m t \right\} \right. \\ &\left. - \sin \phi \left\{ 2 \sum_{k=1}^{\infty} J_{2k-1}(m) \sin(2k-1)2\pi f_m t \right\} \right] \end{aligned} \quad (10)$$

Because of the effect of amplitude modulation, the characteristic of direct frequency modulation via injection current, we do not use the first harmonic. Using the lock-in amplifier we can extract the intensity of two orthogonal signals, 2nd and 3rd harmonic terms, from Eq. (10) as the equations below [13]

$$I_2 = 2E_{0r}E_{0m}J_2(m) \cos(\phi) \quad (11)$$

$$I_3 = -2E_{0r}E_{0m}J_3(m) \sin(\phi) \quad (12)$$

From Eqs. (11) and (12) we can obtain the Lissajous diagram. Then the Lissajous diagram can be utilized for tracking phase shift. The phase shift can be calculated as

$$\phi = \arctan\left(-\frac{J_2(m)I_3}{J_3(m)I_2}\right) \quad (13)$$

The relationship between phase shift and the displacement  $\Delta l$  is given as the following equation

$$\Delta l = \frac{\lambda_0}{4\pi n} \phi \quad (14)$$

From the Eqs. (13) and (14), we can determine the displacement using  $I_2$ ,  $I_3$ ,  $J_2(m)$ , and  $J_3(m)$ . To draw the exact Lissajous diagram, we must know the value of the modulation index  $m$ . From the power spectrum of the interferometer intensity shown in Eq. (10), we can estimate the modulation index  $m$ .

### 3 Preliminary Experiment and Discussion

#### 3.1 $I_2$ Linear Absorption Detection

In order to detect  $I_2$  linear absorption signal, a normal laser diode (HL63163DG Oclaro, Inc.) that emitted 30 mW at near 634 nm was utilized. The output laser was directed through an 80 mm long  $I_2$  cell (Ophos Instruments, Inc.). The temperature of  $I_2$  cell was stabilized at 20 °C using a thermal electric cooler (TEC 3-6 Thorlabs, Inc.). Slow frequency scanning of 1 Hz and triangular scanning amplitude of about 12 GHz were supplied to LD to probe the absorption lines. Some absorption lines are shown in Fig. 2. The wavelength of LD was concurrently measured using the high resolution wavelength meter (WS6/600 High finesse Laser and Electronics Systems GmbH, Inc.). The frequency of the LD was locked to the center of an isolated linear absorption line at the wavelength near 634.6 nm using first harmonic lock-in technique. The locking signal was produced by sinusoidal modulating the injection current and then the first derivative signal was detected by lock-in amplifier (model 830 Stanford Research Systems). A frequency modulation of 10 kHz and an amplitude modulation of about 6 GHz were used. The locking signal is shown in Fig. 3. The locking signal is distorted slightly due to additional amplitude modulation. This locking signal was fed to a PID controller and then feedback to the laser current supply to close the loop. The frequency change of the LD was roughly measured in 3600 s using the wavelength meter. The comparison of the wavelength change in both the free run and the stabilized operations of the LD is shown in Fig. 4. Figure 5 shows the wavelength fluctuation (peak to peak) of about 0.25 pm (187 MHz) for 3600 s for the stabilized operation. It shows a relative frequency stability (ratio between



**Fig. 2** I<sub>2</sub> linear absorption detection

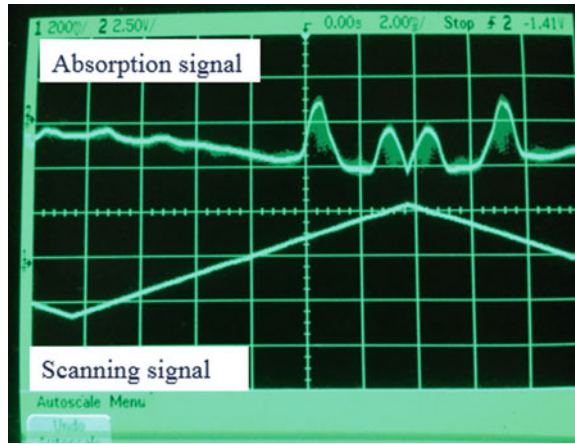
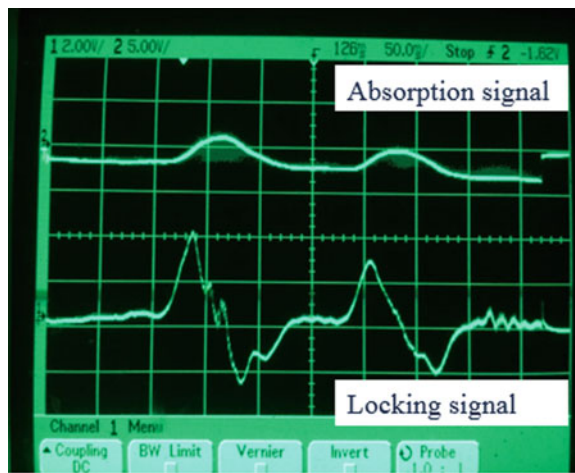


**Fig. 3** Locking signal



the frequency change and the carrier frequency) is approximately  $4 \cdot 10^{-7}$  order. The accuracy of the wavelength fluctuation measurement was limited due to the accuracy of the wavelength meter.

### 3.2 Homodyne Interferometer

To confirm our measurement method for homodyne interferometer, we built an experimental system shown in Fig. 6. The moving mirror was driven by a PZT. We applied a triangular signal with an amplitude of  $1 \mu\text{m}$  and a frequency of 1 Hz to the PZT

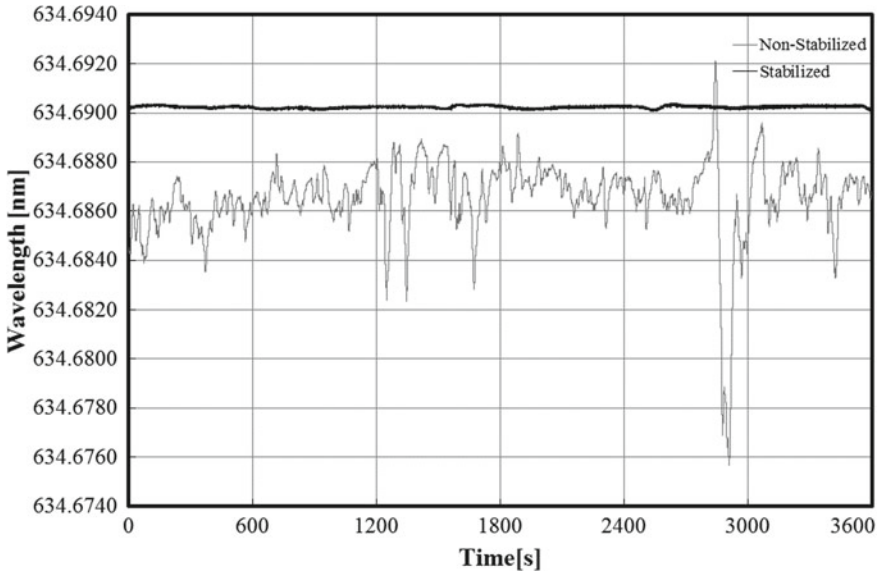


Fig. 4 Comparison between the free running and the stabilized operations of the LD for 3600 s

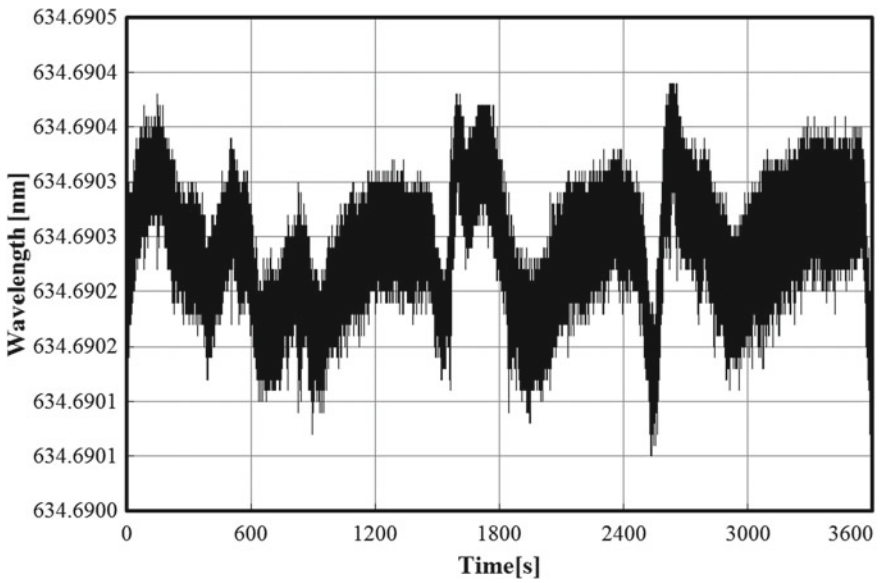
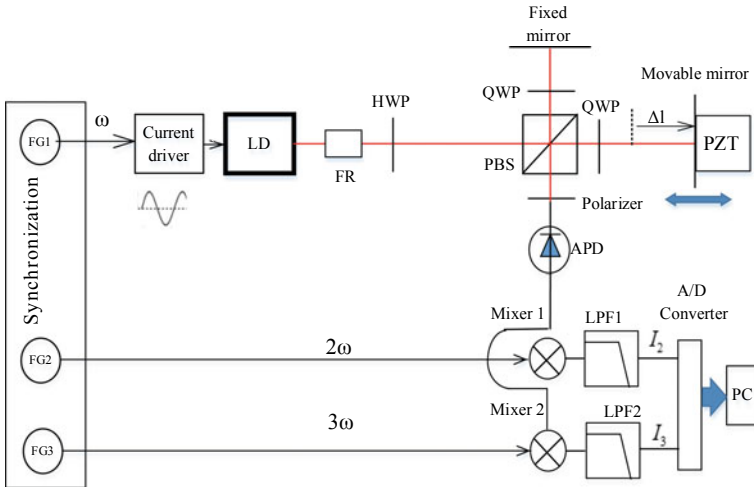


Fig. 5 Wavelength change of the stabilized LD for 3600 s



**Fig. 6** Experimental setup of homodyne interferometer

(Physik Instrumente L.P.) The measurement conditions in our experiment are shown in Table 1.

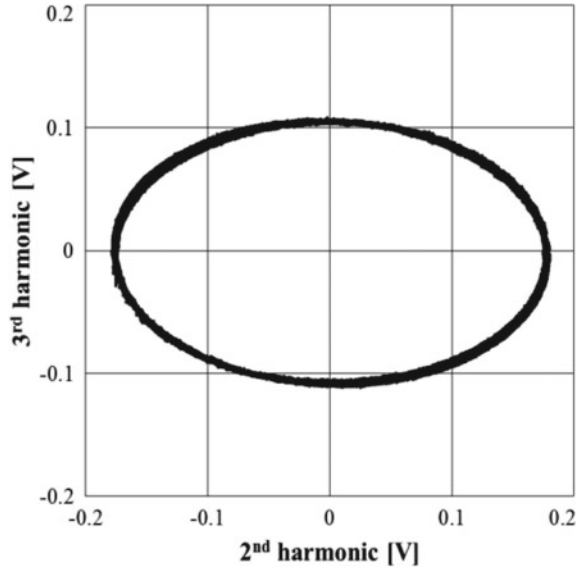
In Fig. 7, The Lissajous diagram is deformed due to the variation of the intensity of the laser source, the misalignment of the optics and the unequal amplitude between 2nd and 3rd harmonics. From Fig. 7, we can estimate the power spectrum of the interferometer intensity, also estimate the modulation index (lateral amplitude/vertical amplitude is proportional to  $J_2(m)/J_3(m)$ ). In Table 1, we also show the estimated modulation frequency amplitude. Therefore, we can obtain the normalized Lissajous diagram by using the following equations [13]

$$I'_2 = \frac{I_2 J_3(m)}{\sqrt{[I_2 J_3(m)]^2 + [I_3 J_2(m)]^2}} = \cos(\phi) \tag{15}$$

**Table 1** The measurement conditions application for homodyne interferometer

Laser diode source	HL63163DG
LD wavelength $\lambda_0$	634 nm
Modulation index $m$	4.01 rad
Frequency modulation amplitude $\Delta f$	960 MHz
Unbalanced length $L$	0.1 m
Frequency modulation for LD	30 kHz
Operating frequency of PZT	1 Hz
Amplitude of PZT stage	1 $\mu$ m
Sampling time	5 s
Cut off frequency of low pass filter	300 Hz

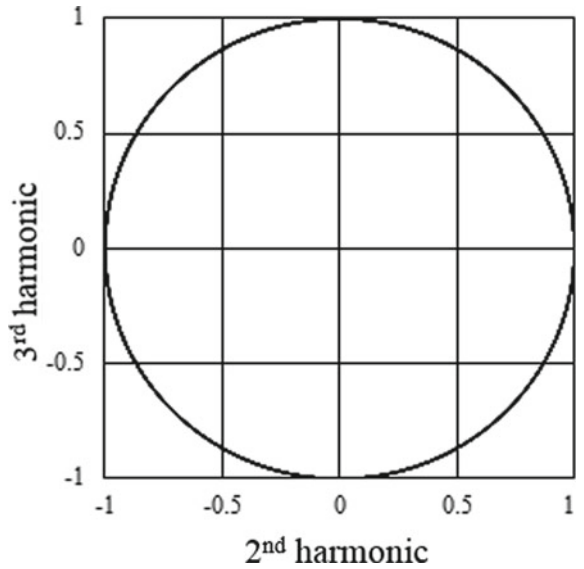
**Fig. 7** Lissajous diagram of second and third harmonics



$$I'_3 = \frac{I_3 J_2(m)}{\sqrt{[I_2 J_3(m)]^2 + [I_3 J_2(m)]^2}} = \sin(\phi) \tag{16}$$

The normalized Lissajous diagram is shown in Fig. 8.

**Fig. 8** Normalized Lissajous diagram of second and third harmonics



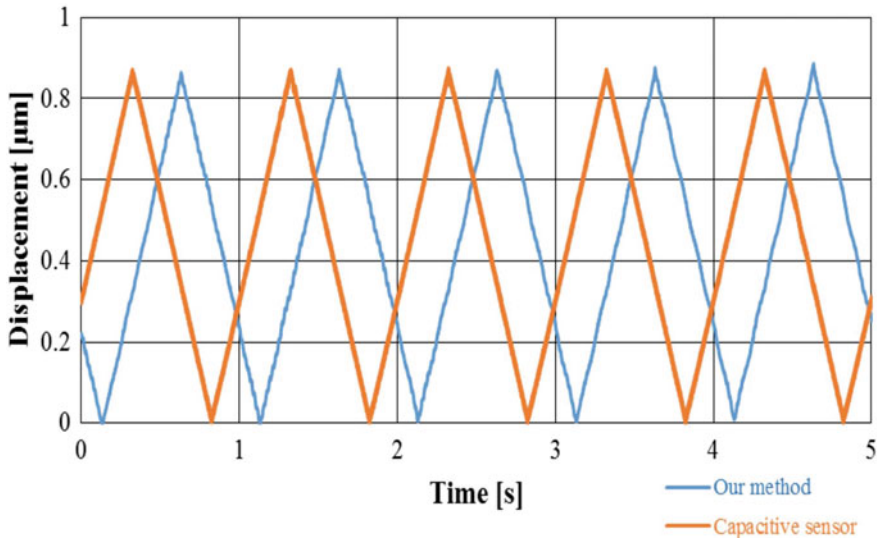


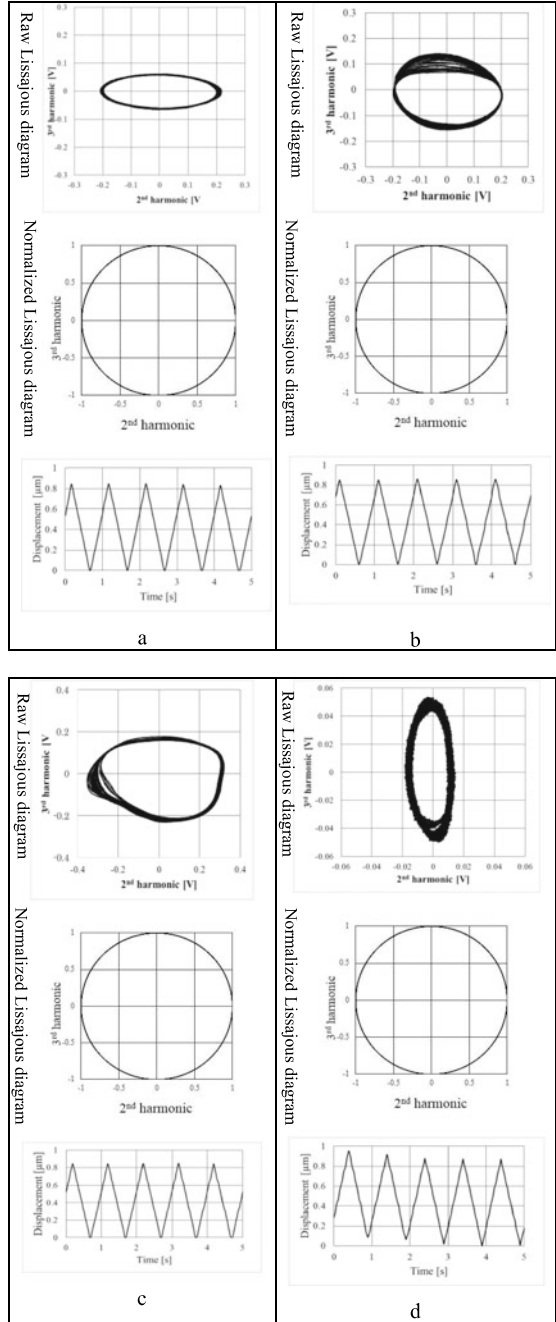
**Fig. 9** The displacement measurement result

The radius and center of the normalized Lissajous diagram are 1 and the origin. The displacement result is shown in Fig. 9. This result was confirmed with the measured result using capacitive sensor (Series 4830, Probe model 2806L, MicroSense LLC) with the same operating condition of PZT. The  $\pm 10 \mu\text{m}$  operating range, bandwidth of 100 Hz and the measurement resolution of 0.7 nm were used in this experiment. This experiment confirms that we can get the Lissajous diagram from 2nd and 3rd harmonics of the interference signal.

From Eq. (8), the modulation index depends on both the unbalanced length  $L$  between two arms of the interferometer and the frequency modulation amplitude  $\Delta f$ . Figure 10 shows some Lissajous diagrams with different values of modulation index causing by changing the unbalanced length.

The measurement resolution was also confirmed using electro-optic modulator (EOM 4002 Newport Corporation). A virtual displacement with frequency of 10 kHz and amplitude of 16 nm was produced using the EOM. The experimental setup and the result are shown in Figs. 11 and 12, respectively. In Fig. 12, a displacement noise is less than nanometer. This result show that our method can obtain high measurement resolution.

**Fig. 10** Measurement results with some values of modulation index, frequency modulation of 30 kHz, frequency modulation amplitude of 960 MHz, causing by changing unbalanced length; **a**  $L = 0.3$  m,  $m = 12.03$  rad; **b**  $L = 0.5$  m,  $m = 20.05$  rad; **c**  $L = 0.7$  m,  $m = 28.07$  rad; **d**  $L = 0.9$  m,  $m = 36.09$  rad



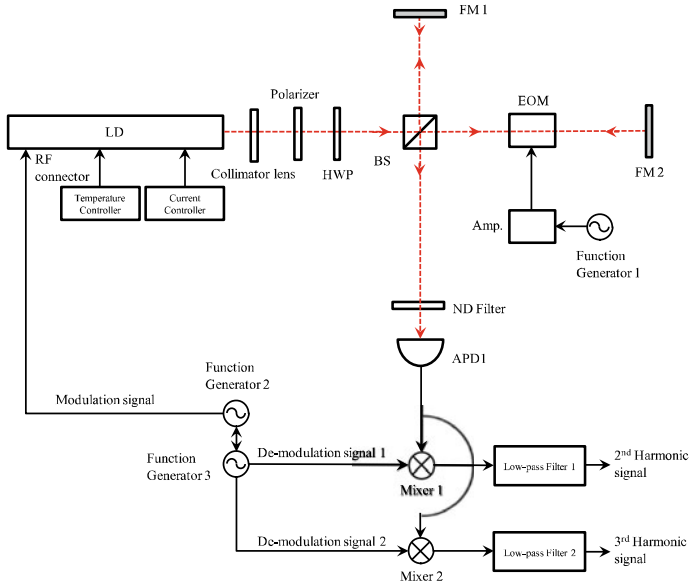


Fig. 11 Experimental setup of virtual displacement measurement

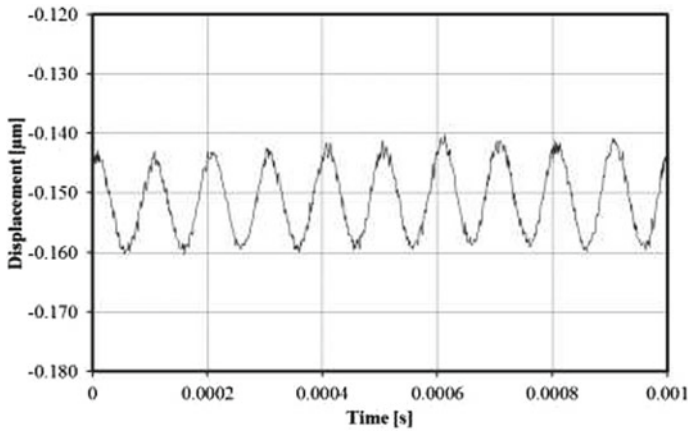


Fig. 12 Virtual displacement measurement

## 4 Conclusion

In conclusion, the experiments show that our method can obtain the displacement measurement resolution of nanometer order. For the future, we will improve the frequency stability of the LD to get higher resolution of homodyne interferometer.

## References

1. Tatsuno K, Tsunoda Y (1987) Diode laser direct modulation heterodyne interferometer. *Appl Opt* 26(1):37–40
2. Arie A, Schiller S, Gustafson EK, Byer RL (1992) Absolute frequency stabilization of diode-laser-pumped Nd:YAG laser to hyperfine transition in molecular iodine. *Opt Lett* 17(17):1204–1206
3. Ludvigsen H, Holmlund C (1998) Frequency stabilization of a GaAlAs semiconductor laser to an absorption line of iodine vapour. *Rev Sci Instrum* 63(4):2135–2137
4. Arie A, Byer RL (1993) Frequency stabilization of 1064-nm Nd:YAG lasers to Doppler-broadened lines iodine. *Appl Opt* 32(36):7382–7386
5. Talvitie H, Merimaa M, Ikone E (1998) Frequency stabilization of a diode laser to Doppler-free spectrum of molecular iodine at 633nm. *Opt Commun* 152:182–188
6. Ye J, Swartz S, Jungner P, Hall JL (1996) Hyperfine structure and absolute frequency of the  $^{87}\text{Rb}$   $5P_{3/2}$  state. *Opt Lett* 21(16):1280–1282
7. Zygo, Laser head, ZMI series
8. Agilent, Laser head, Agilent 5517 series
9. Renishaw, HS20 laser head
10. Sasaki O, Okazaki H (1986) Sinusoidal phase modulating interferometry for surface profile measurement. *Appl Opt* 25(18):3137–3140
11. Suzuki T, Sasaki O, Higuchi K, Maruyama T (1989) Real time displacement measurement in sinusoidal phase modulating interferometry. *Appl Opt* 28(24):5270–5274
12. Sasaki O, Yoshida T, Suzuki T (1991) Double sinusoidal phase-modulating laser diode interferometer for distance measurement. *Appl Opt* 30(25):3617–3621
13. Madden M, Aketagawa M, Kumagai T, Maeda Y, Okuyama E (2014) Concurrent measurement method of spindle radial, axial and angular motions using concentric circle grating and phase modulation interferometers. *Meas Sci Technol* 25:094005
14. Kinnstaetter K, Lohmann AW, Schwider J, Streibl N (1988) Accuracy of phase shifting Interferometry. *Appl Opt* 27(24):5082–5089
15. Sudarshanam VS, Srinivasan K (1989) Linear readout of dynamic phase change in a fiber optic homodyne interferometer. *Opt Lett* 14(2):140–142
16. Jin W, Zhang LM, Uttamchandany D, Culshaw B (1991) Modified  $J_1 \dots J_4$  method for linear readout of dynamic phase changes in a fiber-optic homodyne interferometer. *Appl Opt* 30(31):4496–4499
17. Marc, al LAP, Higuti RT, Kitano C (2012) A simplified and higher dynamic range version of the  $J_1 \dots J_4$  method for optical phase measurement. *Microwave Opt Technol Lett* 54(2):387–392
18. Gerstenkorn P, Luc S (1977) Atlas du spectre d'absorption de la molécule d'iode, 15734–15756  $\text{cm}^{-1}$ . Laboratoire Aimé Cotton, CNRS II, Orsay (France)
19. Zheng J (2004) Analysis of optical frequency-modulated continuous-wave interference. *Appl Opt* 43(21):4189–4198



# Comparison of Accuracy Verification Method for X-Ray CT



K. Matsuzaki, O. Sato, H. Fujimoto, M. Abe, and T. Takatsuji

**Abstract** X-ray computed tomography (X-ray CT) has been occupying indispensable position in geometrical and dimensional measurements in industry, which is capable of measuring both external and internal dimensions of industrial products. Since there have been no international standard for evaluating measuring performance of industrial X-ray CT, it is hard to compare the measurement accuracy of X-ray CT supplied by different manufacturers. Although evaluation procedures for conventional coordinate measuring machines (CMMs) have been proposed and standardized, they cannot be applied for X-ray CT as they are. A hole plate and a step cylinder are examined to see which is a more suitable material standard for evaluating the measurement performance of X-ray CT. Experimental result shows that the step cylinder reveals the effect of penetration length more apparently.

**Keywords** X-ray CT · Dimensional measurement · Performance evaluation · Standardization

## 1 Introduction

X-ray computed tomography (X-ray CT) which was initially invented for medical application has been utilized to non-destructive testing (NDT) in industry. Recently, usage of X-ray CT for geometrical and dimensional measurements in industry is increasing. The X-ray CT whose metrological performance is guaranteed is named dimensional X-ray CT.

Dimensional X-ray CT has some advantages over conventional CMMs. The biggest advantage is that it is only-one technology for measuring both external and internal dimensional features with non-destructive manner [1]. It is also advantageous that they are able to capture measurement data in a short period of time with high spatial density compared with conventional CMMs, so that the parts having complex or small geometry can be measured efficiently.

---

K. Matsuzaki (✉) · O. Sato · H. Fujimoto · M. Abe · T. Takatsuji  
National Metrology Institute of Japan, AIST Tsukuba Central 3, Umezono 1-1-1, Tsukuba  
305-8563, Ibaraki, Japan  
e-mail: [kazya.36.matsuzaki@aist.go.jp](mailto:kazya.36.matsuzaki@aist.go.jp)

The performance evaluation procedure for CMMs has been published as ISO 10360 series. Manufacturers or users of CMMs are able to compare the performance of CMMs. There is, however, no international standard published for evaluating measurement performance of dimensional X-ray CT. Manufacturers claim the accuracy of their X-ray CT by their own procedures. To overcome current undesirable situation, a performance evaluation procedure for X-ray CT is under discussion to be a new extension of ISO 10360 series in ISO/TC 213/WG 10.

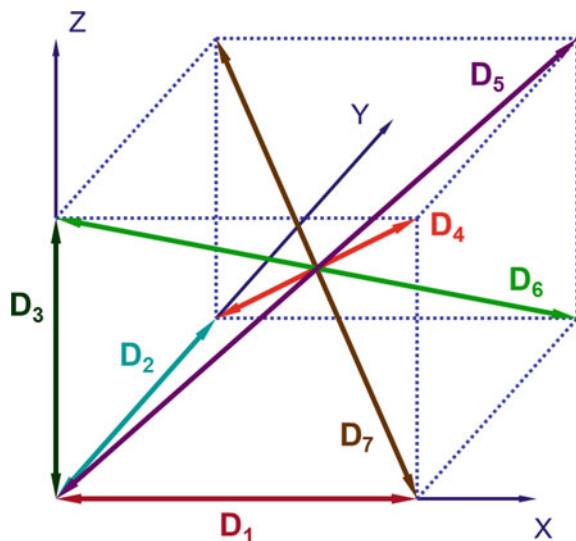
This paper introduces the performance evaluation procedure using a step cylinder with intention to propose it to standardization of performance evaluation of dimensional X-ray CT.

## 2 Existing Evaluation Procedure for CMMs

One of the evaluation procedures published in ISO 10360 is designed to demonstrate the length measuring performance of CMMs by executing a set of length measurement (Fig. 1) [2]. The measurements are performed along seven different directions in the measurement volume. Five lengths are allocated in each direction. Each length is measured three times repeated. The total of 105 length measurement result is collected for evaluating length measurement performance of CMM. Result of this procedure reveals influence of geometric error sources, e.g. scale error, straightness, squareness, and so on.

Measurement performance of dimensional X-ray CT is not only affected by the above geometric error sources, but also affected by many other error sources specific to principle of X-ray CT, such as material influence when X-ray penetrates workpiece

**Fig. 1** Direction on measurement method for CMM



to be measured. A measurement procedure suitable for performance evaluation of X-ray CT is demanded.

### 3 Proposed Measurement Procedure

Measurement along seven directions of the hole plate was proposed as the measurement procedure for X-ray CT with in WG10 [3]. Seven directions and five lengths described in the draft documents are schematically shown in Fig. 2. The hole plate is so fixed with inclined position against the rotation axis of the rotary table of X-ray CT as to cover dominant portion of the measurement volume.

Since penetration length of X-ray when hole plate is measured is not significantly varied, the measurement result of hole plate may not always reveal influence of error sources which is dependent of penetration length of X-ray.

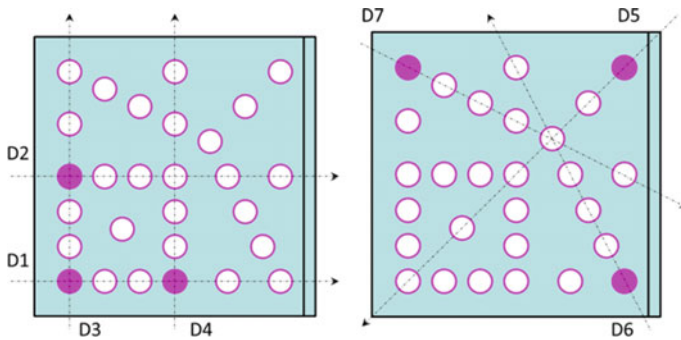


Fig. 2 Directions using hole plate

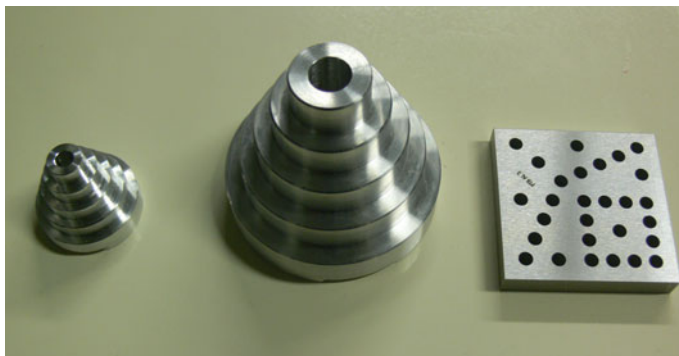
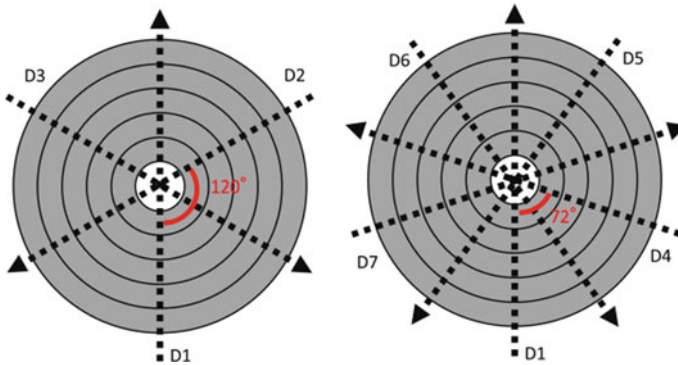


Fig. 3 Photograph of material standard



**Fig. 4** Measurement lines allocated on step cylinder

We propose a measurement procedure using a step cylinder (Fig. 3), which keeps convention composed of seven directions and five lengths.

The step cylinder is a stack of discs each having a different external diameter and the same internal diameter. By default, the step cylinder is placed so as its symmetrical axis coincides with the rotation axis of the X-ray CT. When X-ray is illuminated from the perpendicular direction with respect to the symmetrical axis, the penetration lengths of the rays which pass through the respective discs vary.

Proposed seven directions allocated on the step cylinder are shown in Fig. 4. Five lengths are realized by five different external diameters of the step cylinder. Size measurement performed on the step cylinder may reveal measurement error of X-ray CT due to material penetration more seriously than that done on the hole plate.

## 4 Experiment

### 4.1 Instrument

The X-ray CT system used in this research is SMX-225CTS manufactured by Shimadzu Corporation as shown in Fig. 5.

Table 1 depicts summary of the specifications.

### 4.2 Material Standard of Size

The hole plate and the step cylinder both made of aluminum which have been calibrated by CMM with tactile probing system in NMIJ are measured. Measurement error is defined as deviation of measurement result from the calibrated value.

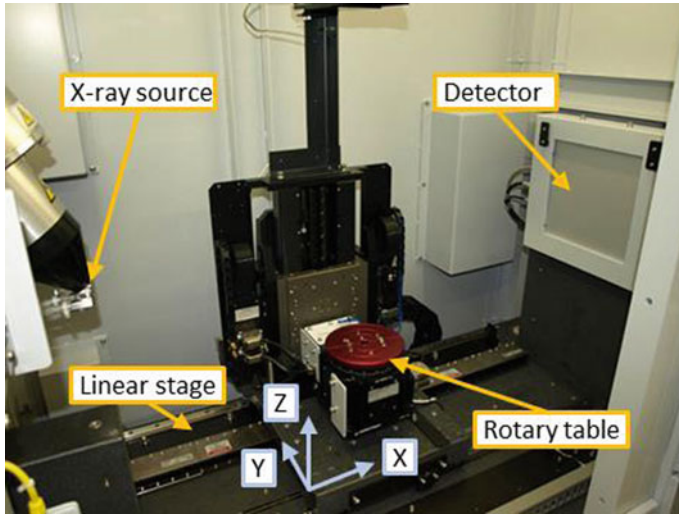


Fig. 5 Photograph of X-ray CT

Table 1 Specifications of X-ray CT

Source type	Microfocus
Maximum tube voltage	225 kV
Image detector	Flat panel
Size of detector	200 mm × 200 mm
Temperature control	20 °C ± 0.5
Spindle error of rotary table	<1 μm

### 4.3 Measurement Procedure

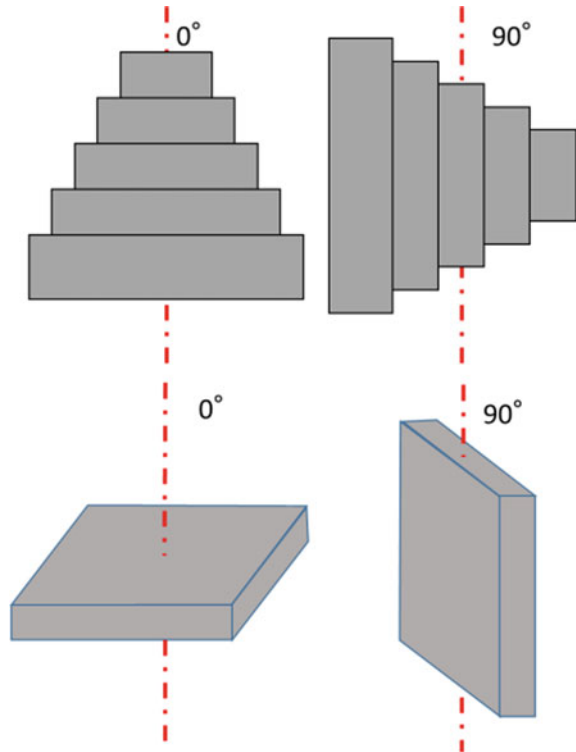
Measurement positions of the step cylinder and that of the hole plate are shown in Fig. 6.

Measurement is performed in accordance with Bi-directional measurement specified in ISO 10360 on both the hole plate and the step cylinder as shown in Fig. 7. Bi-directional measurement is realized by distance measurement composed of two points. Each of two points has diametrically opposite in respective normal directions of the surface to be measured.

### 4.4 Experimental Result

The 3D reconstructed images are shown in Fig. 8.

**Fig. 6** Inclination angle of material standard in respect of rotation angle of X-ray CT



Figures 9, 10 and 11 show the measurement error of the hole plate, the diameter of external cylinder of the step cylinder and the diameter of internal cylinder of the step cylinder, respectively. In these figures, the horizontal axis indicates the measured length, the vertical axis the measurement error. The red line draws maximum errors estimated from measurement data as a rough indication.

The results of the hole plate scatter a lot, however no obvious length dependent tendency can be observed. There is a systematic bias in the measurement error. We suppose the bias can be caused by form deviation each hole appeared in the reconstructed image due to the beam hardening effect. This result indicates the scale factor of the X-ray CT has been correctly adjusted.

The external measurement result of the step cylinder in 90° orientation represents the similar tendency in measurement error with that of the hole plate. Information of the diameter of external cylinder is derived from a single transmission image taken when the symmetric axis is in parallel with the X-ray axis.

The external measurement result of the step cylinder in 0° orientation represents measurement length dependent tendency in the measurement error. It is likely caused by significantly varied penetration length.

We had expected measurement length dependent tendency in internal diameter measurement. Unfortunately the scattering of the experimental results is too large in

**Fig. 7** Bi-directional measurement on **a** hole plate and **b** step cylinder

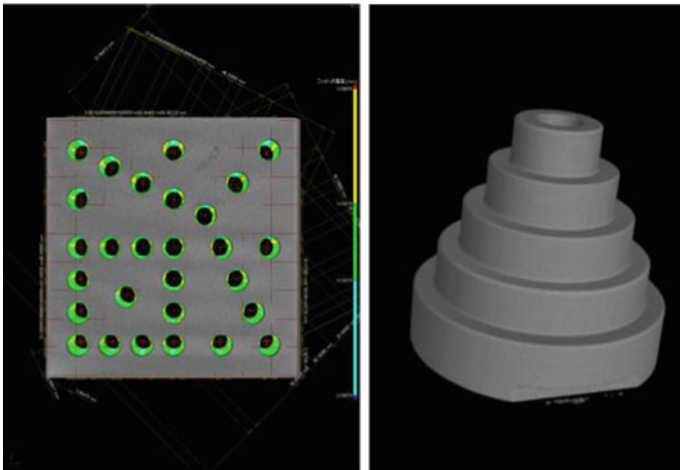
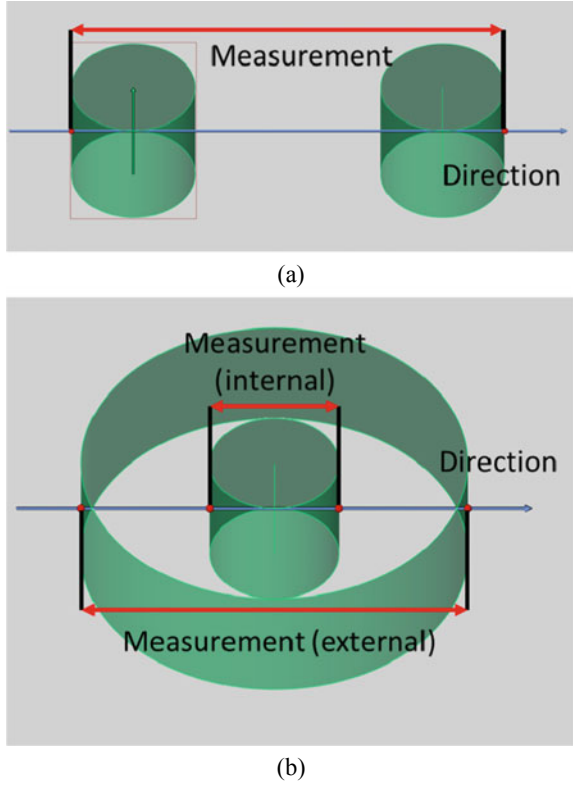


**Fig. 8** The result of measurement on X-ray CT

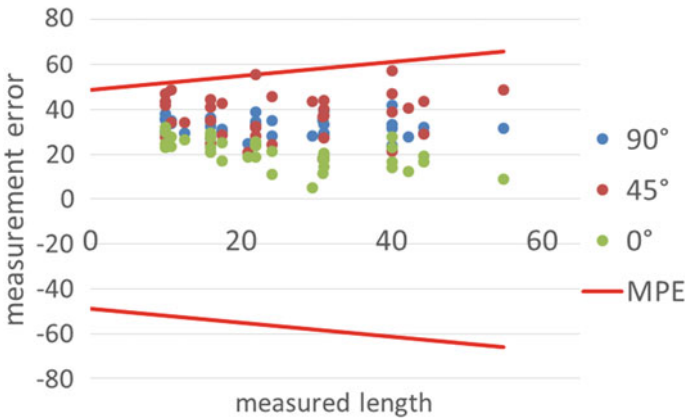


Fig. 9 The measurement error using hole plate

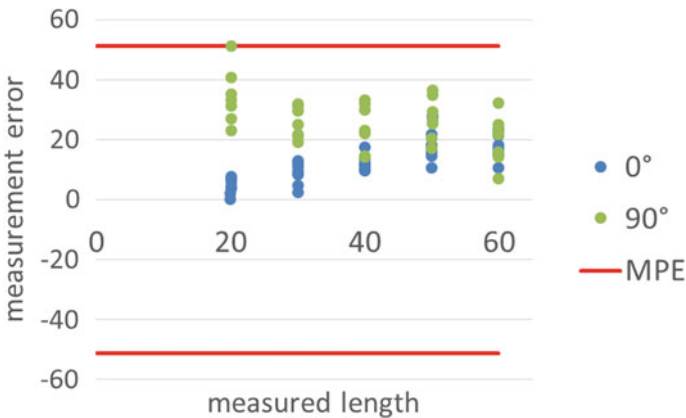


Fig. 10 The measurement error of external of stepcylinder

which the measurement length tendency is completely buried. This scattering may come from surface finish of internal cylinder.

Bi-directional measurement error is influenced by local form deviation observed on 3D reconstructed data obtained on X-ray CT. A set of measurements is performed around direction 1 with intentional directional variation in range between  $-5^\circ$  and  $+5^\circ$  with  $0.5^\circ$  increment. P-V value of measurement results in these direction are shown in Fig. 12. It is noted that measurement error on internal cylinder is more dispersive than that on external cylinder.

It is recognized that fluctuation observed in data depicted in Fig. 12 influences that in Figs. 9, 10 and 11. Further analysis will be needed to clarify influence of material penetration independent of fluctuation caused by local form deviation observed on 3D volume data. A potential approach is to utilize representative point which allows



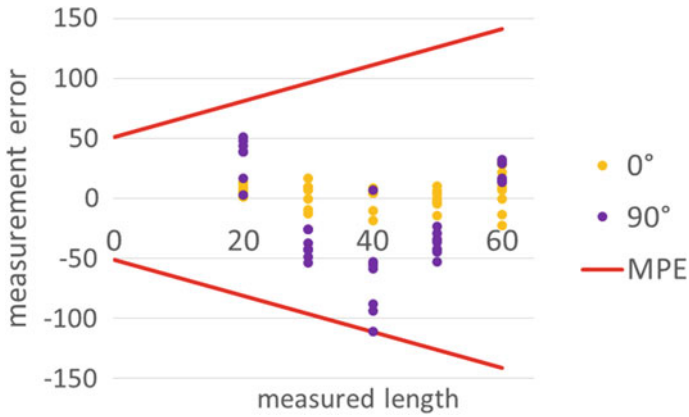


Fig. 11 The measurement error of internal of stepcylinder

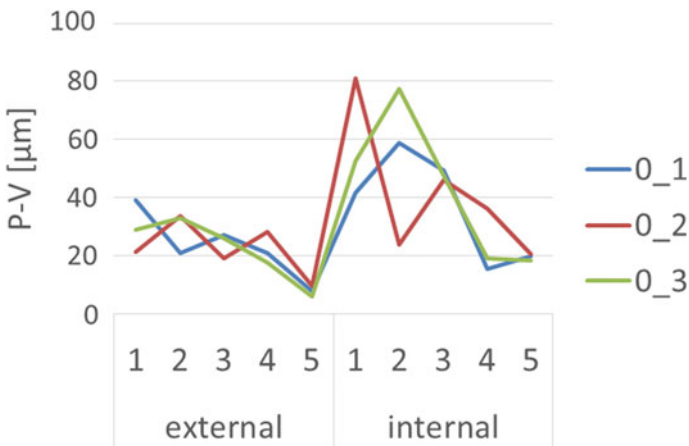


Fig. 12 P-V value of the result data

certain averaging benefit with in specified condition as standardized in ISO 10360-8 [4].

The evaluation procedure using a step cylinder may reveal some errors which is not represented by using hole plate. These errors can be related to penetration length. Measurement on step cylinder may give significant impact on performance evaluation of X-ray CT.

## 5 Summary

Measurement error observed on the step cylinder for performance evaluation of X-ray CT is discussed. As a result of experiment with the proposed procedure, measurement error which may not be obvious when the hole plate is measured can be revealed more significantly. Characteristic and mechanism of measurement error on step cylinder will have to be studied further.

## References

1. Kruth JP, Bartscher M, Carmignato S, Schmitt R, De Chiffre L, Weckenmann A (2011) Computed tomography for dimensional metrology. *CIRP Ann Manuf Technol* 60:821–842
2. ISO 10360-2:2009. Geometrical product specifications (GPS)—acceptance and reverification test for coordinate measuring machines (CMM)—part 2: CMMs used for measuring linear dimensions
3. Bartscher M, Sato O, Hartig F, Neuschaefer-Rube U (2014) Current state of standardization in the field of dimensional computed tomography. *Meas Sci Technol* 25:064013
4. ISO 10360-8:2013. Geometrical product specifications (GPS)—acceptance and reverification tests for coordinate measuring systems (CMS)—part 8: CMMs with optical distance sensors

# Design of a Texture Monitoring System for PV Solar Cell Efficiency via 3-D Virtual Simulation



Richard Y. Chiou, Yongjin (James) Kwon, Tzu-Liang (Bill) Tseng, Michael Mauk, and Aurel Mathews

**Abstract** An automated system in conjunction with a novel optical laser metrology technique has been designed via 3-D virtual simulation to study textured silicon wafers used for solar cell manufacturing. Texture has long been known as one of the critical surface parameters affecting solar cell efficiency. The paper presents the integration and implementation of automated processes, based on the sequence control specifications and requirement of the PLC (programmable logic controller) using 3-D simulation to create a virtual test environment. This visual interface is integrated into the virtual environment, which is designed to model the logical and kinematic functions of the automated system. The programming is akin to the traditional text based programming conducted with actual robots, as it is responsible for controlling I/O, time delays, and motions along with basics. The process is tested virtually using 3-D software simulation before they are used in a full-scale physical plant. The paper provides effective solution by combining an I/O and 3D graphic simulator to validate PLC code for implementation into a physical system with examined kinematics in energy manufacturing. In addition to virtual simulation, an experimental study of surface roughness effect on laser light scattering from textured surfaces is described. The results and the system proposed are useful in implementing laser light scattering instruments for on-line monitoring of solar cell manufacturing processes which produce surface roughness patterns.

**Keywords** Solar cell · Virtual simulation · Energy efficiency

---

R. Y. Chiou (✉) · M. Mauk · A. Mathews  
Department of Engineering Technology, Drexel University, 3001 Market Street, Philadelphia, PA 19104, USA  
e-mail: [ryc23@drexel.edu](mailto:ryc23@drexel.edu)

Y. Kwon  
Division of Industrial & Information Systems Engineering, Ajou University, Suwon 443–749, South Korea

T.-L. Tseng  
Department of Industrial, Manufacturing and Systems Engineering, The University of Texas at El Paso, El Paso, TX 79968, USA

## 1 Introduction

This paper explores the use of virtual simulation of industrial robotic workcell for optimal design and automation of a texture monitoring system for solar cell energy efficiency. Robotic workcell simulation is gradually adopted by the manufacturing industry. With the rise of automation technology, new generations of software are emerging which are known as virtual commissioning. Virtual commissioning includes the physical layout of the industrial robots, the kinematic motions, as well as the optimization algorithms. It simulates the robot controllers, sensors, and human machine interfaces. Signals to and from these devices are transmitted to and from emulated or physical models. This virtual shop platform provides a safe environment to validate robotic codes for any kinematic motion and sensor reaction of the factory floor components, before it is downloaded into the physical controller. In addition to the safety features, virtual commissioning also saves cost from redundant components, programming error, and debugging time, before the shop is actually built [1–6].

Solar energy is one of the most promising renewable energies. Cell efficiency depends on the silicon dopant, light intensity and wavelength, optical thickness and surface texture. The efficiency of current solar cells is around 20% but some specialized surface texturing processes can help boost efficiency up to 25%. As with any new technological paradigm, new challenges have emerged which are unique to the renewable energy manufacturing. The manufacturing difficulty of such processes implies a higher cost, making them prohibitive. One of these challenges in particular is the development of effective monitoring technologies to compensate for the decentralized nature of remote solar cell surface quality monitoring and control [7–12].

In the paper, the simulation is based on state-based object models and their interconnection to a graphical 3D model. Components built in the virtual platform are a close approximation of the robotic workcell. In addition to the 3D virtual environment, the robotic models need to be developed properly to complete the simulation. This project demonstrates the result of simulation to evaluate the functionality of the virtual robotic workcell integrated with a solar cell roughness quality monitoring system.

## 2 Virtual System

PLCStudio is a simulation tool used to create and test a virtual model of a physical automation system. The virtual design of an automation system in PLCStudio is divided into three main sub-processes: creating the 3D component models, creating the I/O model, and creating the 3D cell model. These three stages are necessary to run the simulation and evaluate the PLC code.

## 2.1 Creation of 3D Component Model

The first step is to create all the 3D component models to be used in the process simulation. The 3D component models used in this simulation include the YK250, YK220, F1010-700, conveyer belt, photoelectric switch, breadboard, the two mounting blocks for the SCARA robots, and a circular disk. Some of the more complex components used in this simulation, such as the SCARA robots, had 3D component models already created and available for download from the internet. The simpler components such as the photoelectric sensor and the disk were created from scratch in SolidWorks. These simple parts were then saved as a generic .stl file so that they could be imported into PLCStudio.

The complex components that required moving parts (such as the SCARA robots) were modeled around their joints necessary for their movements. This means that the moving parts of a component were modeled independently of the whole component so that they could have their own axis and be able to move in a prismatic and revolutive method.

## 2.2 Creation of 3D Cell Model

The next step is to create the 3D cell model consisting of all the 3D components. The 3D cell model is the general layout for the process simulation and allows for placement of the 3D component models in specific orientations and locations. The final 3D cell can be seen in Fig. 1.

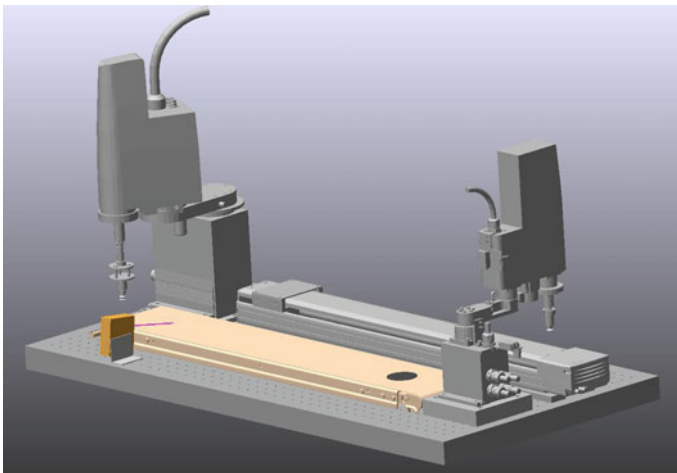


**Fig. 1** 3D cell model

**Table 1** PLC model symbol table

Num	Name	HW addr	DB addr	Data type	Used in device
1	D20	10.1		BOOL	Photosensor
2	D23	10.4		BOOL	F1010-700, YK220
3	D24	10.3		BOOL	YK220
4	D25	10.2		BOOL	F1010-700, YK250
5	DO22	Q0.0		BOOL	Conveyor
6	MOVA1	Q0.3		BOOL	F1010-700
7	MOVA2	Q0.4		BOOL	F1010-700
8	MOVE1	Q0.1		BOOL	YK250
9	MOVE2	Q0.2		BOOL	YK250
10	MOVE3	Q0.5		BOOL	YK220
11	MOVE4	Q0.6		BOOL	YK220
12	Start	10.0		BOOL	Start

### 2.3 Creation of I/O Model

The I/O model contains all the inputs and outputs of the components in the cell in addition to the state diagrams that are used to define the motion of the components. The inputs and outputs used in the simulation are listed in the symbol table, seen in Table 1. The names of the inputs and outputs used in the virtual system are kept the same as in the physical system for consistency.

Next, state diagrams are created for each component in the simulation in order to define their motions. These state diagrams, shown in Fig. 2, reflect the components' transitions to different states based on PLC outputs in addition to providing the PLC with inputs. The state diagrams for the YK250, YK220, and F1010-700 are based on each of their slave programs stored in the teach pendants.

### 2.4 Creation of PLC Ladder Logic

PLCStudio does not possess the capabilities for PLC programming and simulation and therefore relies upon external 3rd party PLC programming software. This external programming software is called SIMATIC STEP 7 and is used to create the PLC ladder logic. It was validated and implemented into the physical system. The virtual PLC ports were linked through the interface between PLCStudio and STEP 7 as seen in Fig. 3. Identical names and HW addresses in both of the PLCStudio and STEP 7 symbol tables are necessary for compatibility between the two programs.

The ladder logic, shown in Fig. 4, is the PLC code developed in order to be implemented into the physical system following its validation on PLCStudio. This PLC code is written in order to perform a simple automation process that operates

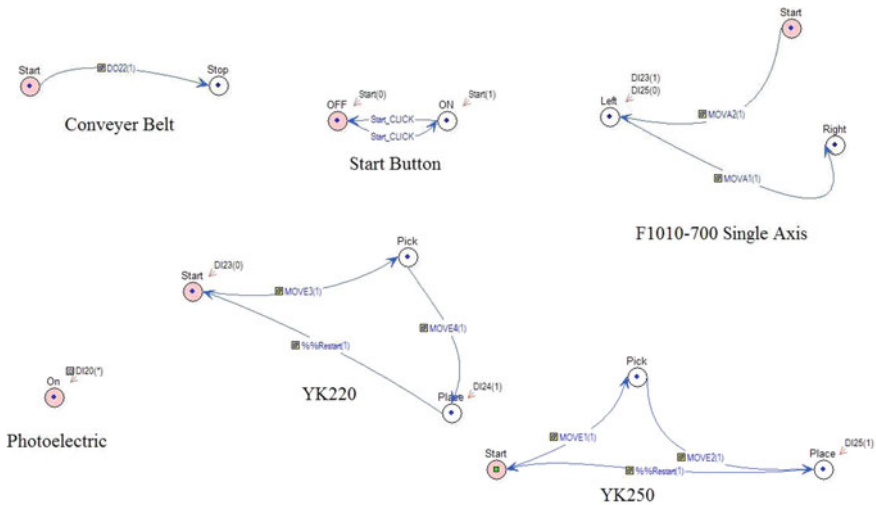


Fig. 2 State diagrams

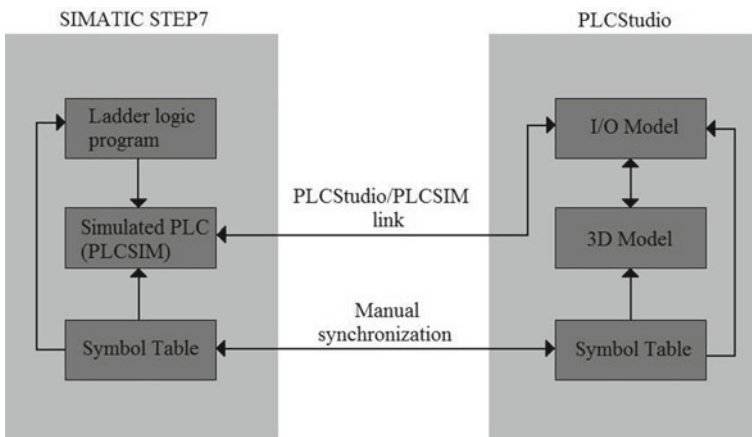
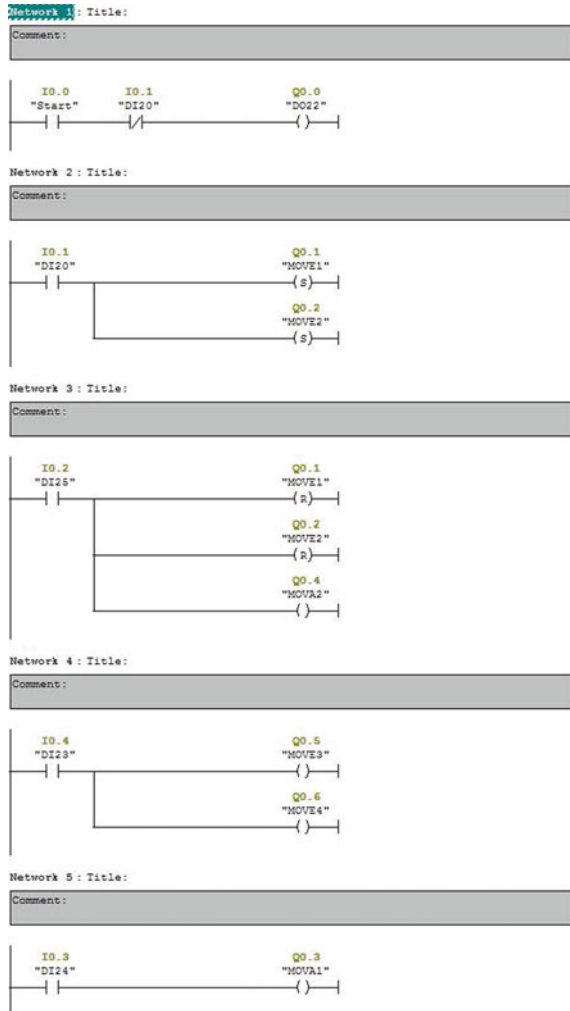


Fig. 3 Connection between PLCStudio and STEP 7

continuously. This automation process began by placing the disk on the conveyer belt and using a 'start' button to start the process. The conveyer transports the disk towards a photoelectric switch. The photoelectric switch detects the disk and turns off the conveyer belt. Once the conveyer is turned off, the YK250 SCARA robot picks up the disk and places it on the F1010-700 single axis. The F1010-700 transports the disk back across the cell where the YK220 SCARA robot picks it up and places it back on the conveyer belt where it originally started. The disk is once again transported towards the photoelectric switch and the process starts over, operating in a continuous loop.

**Fig. 4** Siemens PLC ladder logic created using SIMATIC S7



### 2.5 Testing of the Virtual System

Testing the virtual system and validating the ladder logic in PLCStudio required the use of PLCSIM. After the ladder logic was written in STEP7, it is downloaded into PLCSIM. PLCSIM is a PLC simulator that allows the ladder logic to run virtually and be linked to the ports specified by the symbol table in PLCStudio. The SIMATIC S7 ladder logic is downloaded into PLCSIM and then initiated. At the same time, the simulation is started in PLCStudio. The simulation is turned on and off using a toggle button accessed in the Control Panel in PLCStudio as shown in Fig. 5.



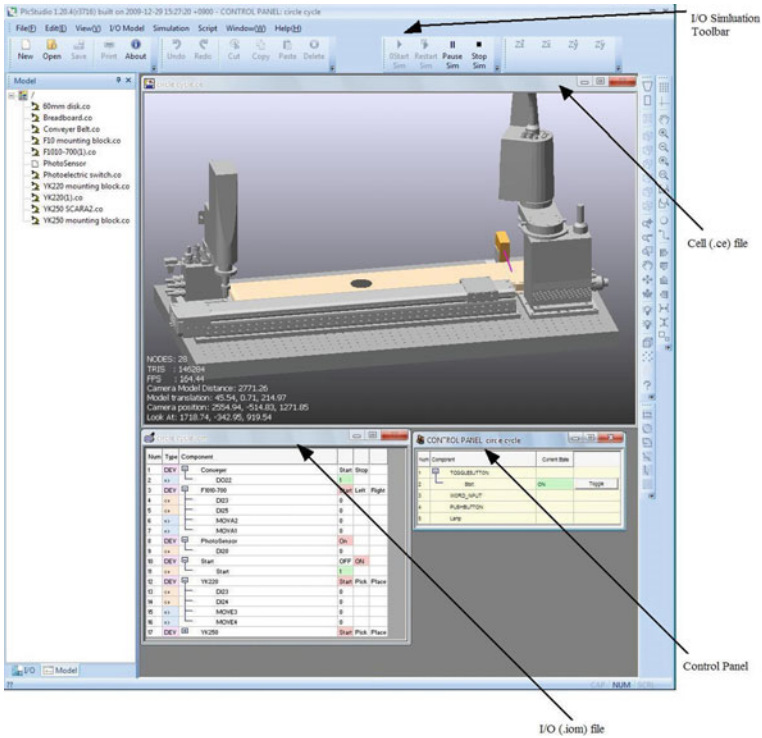


Fig. 5 PLC model program window and the virtual system

### 3 Testing of the Physical System

Following the validation of the PLC code in PLCStudio, it is implemented into the physical system. However, the PLC code can not be directly downloaded into the physical PLC due to the different programming software used in the simulation. The physical system operated using the Allen Bradley RSLogix 5000 PLC format while the virtual system in PLCStudio used the Siemens SIMATIC S7. Due to the incompatibility between the two PLC formats, the SIMATIC S7 ladder logic developed for the PLCStudio simulation has to be manually transferred into the RSLogix format.

The virtual system created in PLCStudio is identical to the physical system in many ways. The placement and orientation of the 3D component models in the cell in PLCStudio are the same as in the physical cell. Each device used in the simulation had the same dimensions and movements as the physical device it is modeled after. A side by side comparison of the virtual system and physical system can be seen in Fig. 6.

Additionally, the physical system behaved the same as the virtual system after implementing the validated ladder logic. Both systems took approximately the same amount of time to transport the opaque disk around the cell and return it to its starting

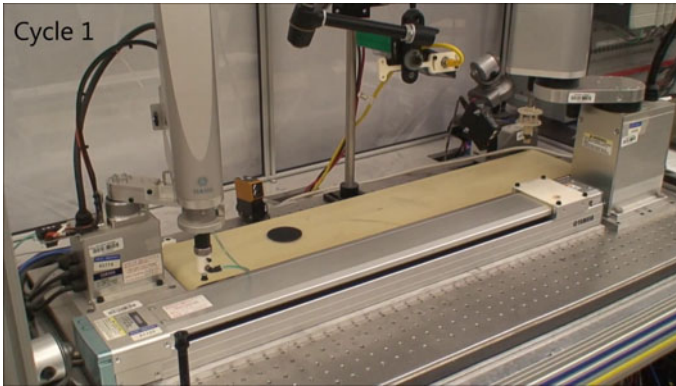


**Fig. 6** The physical system of robotic workcell

position. The physical system had a cycle time of 16 s while the virtual system had a cycle time of 15.4 s. The small difference in the cycle times was expected due to the different speeds at which the virtual and physical robots operate.

Due to the many versions of programming software available, standard ladder logic programming software is nonexistent. Different PLC manufacturers use different ladder logic programming software. The physical system operated using the Allen Bradley RSLogix 5000 PLC format while the virtual system in PLCStudio used the Siemens SIMATIC S7. Instruction sets, symbols, memory addressing, hardware configuration and user interface are some of the differences between Siemens and Allen Bradley software. Although the two ladder logic appear different they function in the same manner and perform the same automation process.

### ***3.1 Laser Light Scatter Imaging Processing***

To investigate surface characterization and to correlate surface roughness to other factors that might influence the efficiency of the solar cell, a laser light scatter testing device was designed. One of the methods incorporated was the LaserCheck<sup>®</sup> surface roughness testing. The Model 6212 Lasercheck<sup>®</sup> Surface Roughness Gage is used in the research as shown in Fig. 7. LaserCheck uses a Laser Light Scatter measurement technique to make precise and repeatable non-contact surface roughness measurement in the 0.01 to 10 micron range. The laser light scatter device has a user friendly LCD interface to scan, store and send data.

Measurements are taken by triggering the laser, which is aimed at the surface, and the reflected and scattered light distribution is detected by the photodiode array. This distribution data is then sent to the control unit where the  $R_a$  value is calculated for the area measured by the laser. It is key to note that the  $R_a$  measurement is not a measurement of the roughness at a single point, but a calculated average roughness



Fig. 7 Lasercheck<sup>®</sup> sensor and controller

value of the area covered by the laser beam. The formula for calculating the  $R_a$  value is  $R_a = \frac{1}{n} \sum_{i=1}^n |y_i|$ , where  $y_i$  is the surface height (microns) measured from the mean line. To communicate and collect data from the Laser Check device an RS232 serial cable is connected between the control unit and either a PC or a serial server.

### 3.2 Remote Robotic Workcell

Utilizing robots in the process of performing surface roughness scanning allows for both full automation as well as precise and repeatable measurements. The two robots used in this cell are the Yamaha YK250X SCARA four-axis robot and the Yamaha F1010-700 one-axis robot. The measurement head of the Laser Check system is mounted to the tool arm of the SCARA robot. The piece to be scanned is mounted to the one-axis robot. The scan is performed by incrementing the one-axis robot in what shall be designated as the  $y$ -axis  $i$  number of times. Once completed, the one-axis robot moves back to its initial position and the SCARA robot increments in what shall be designated as the  $x$ -axis, and the one-axis robot begins its incrementing cycle again. This process repeats  $j + 1$  times,  $j$  being the number of increments the SCARA robot makes. This produces a 2D array or matrix of data:  $M_{i+1,j+1}$ , which can later be used to plot a 3D graph. The robotic workcell can be seen in Fig. 8.

To make the system fully automated there must be a way for the robots to send and receive signals from each other, as well as to and from LabVIEW and the Laser Check control unit as shown in Fig. 5. To accomplish these connections a PLC is used. The type of PLC used for this automation system is an Allen Bradley Control Logix unit. A simple PLC ladder logic diagram is employed to coordinate certain inputs to in turn trigger specific outputs. The ladder logic is used in this system. This ladder logic basically functions as a form of virtual wiring between components. The first rung connects an output from the one-axis robot to the laser trigger of the Laser Check control unit. Whenever the robot's program sends that output, it turns on the laser. The second and third rungs connect an output and input from one robot to the input and output of the other. This allows the robot's to signal when, for instance,

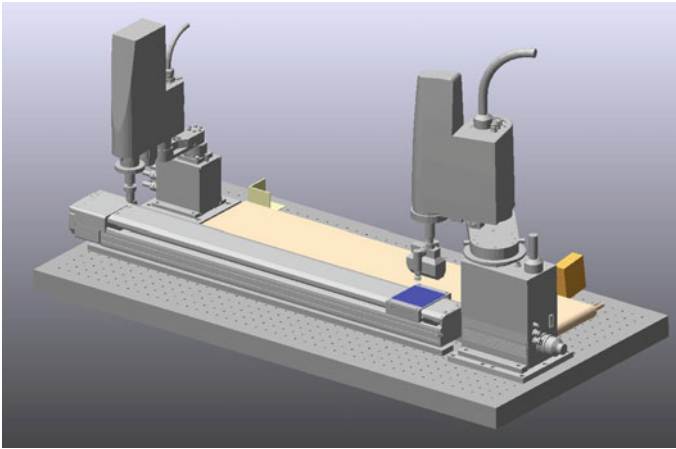


**Fig. 8** Robotic workcell for solar cell surface roughness monitoring

they are both in the initial position and ready to start a scan. The ladder logic is not the only way that the PLC is used in the automation system. The LabVIEW program can access and flip bits in the PLC via an Ethernet connection. These connections are used to initiate the robots' programs remotely as well as control the timing of data flow into the LabVIEW program.

To initiate the connection between either the serial port or serial server a configuration block, specific to the type of connection, is used. Once the connection is established, TCP/IP or Serial Read/Write blocks are used to issue a call for data to the Laser Check system and then read the data that comes in. To control the flow of data in, such that data is not erroneously read twice or skipped over, a case structure is employed, which is triggered by the falling edge of the laser trigger in the PLC. This essentially allows the program to read the data only right after the laser turns off. The data that flows in comes in the form of an ASCII string. To convert this into a floating point value, the string is parsed and header and footer values are removed. The remaining value is then converted to a float value using a type cast function. This data is then sent along and placed into a 2D array that is a set of 1D arrays that represent each scan along the face of the material. This array is then sent to the 3D graph and table on the front panel, as well as to an external spreadsheet file.

As mentioned earlier, there are two instances of this program that connect to the Laser Check system differently. One connects to the Laser Check system using the serial connection on the PC being used. The second involves hooking the serial connection to a serial server, which the program then accesses via an internet connection. The main difference between the two is that the first program requires a local connection, whereas the second can be performed remotely. The front panel's controls for both programs are shown in Fig. 9.

There are minor differences between both front panels, which can be seen on the left side of each. These differences are due to differences in connecting and reading

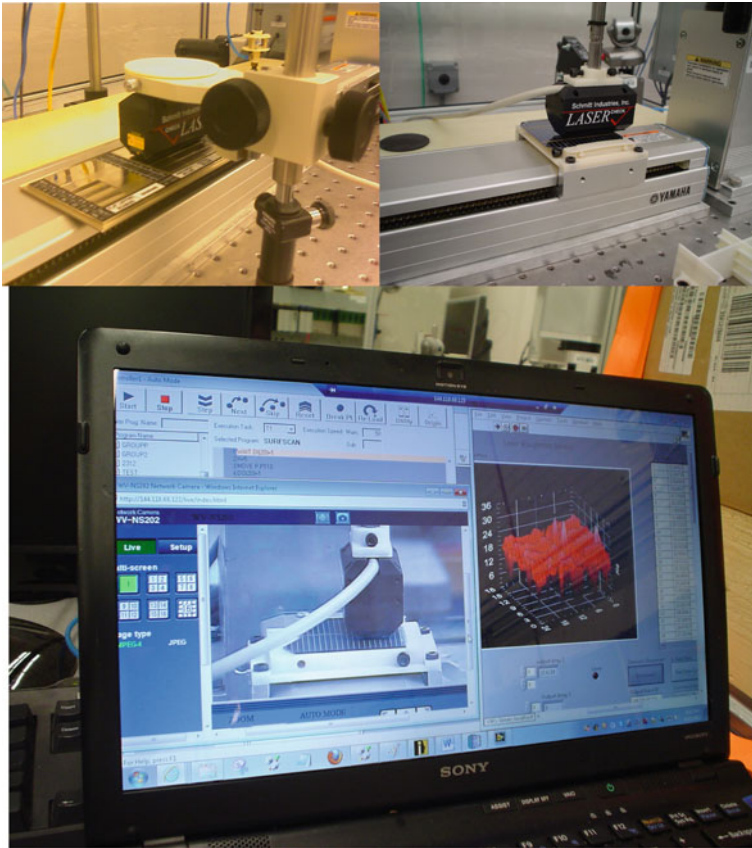


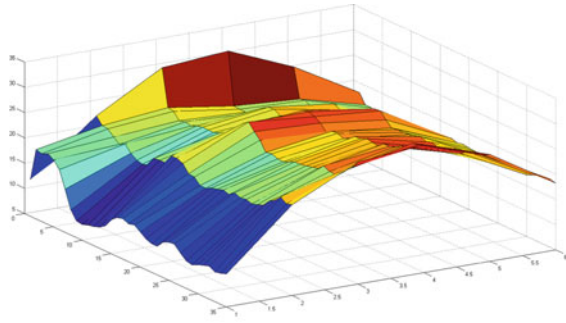
Fig. 9 LabVIEW serial and Ethernet front panels respectively

from the serial connection either locally or via Ethernet. The two buttons on the right are responsible for connecting to the robots and subsequently running their programs. The graph in the middle of the screen plots the 3D data that comes, and the table next to that displays all of the data as it comes in.

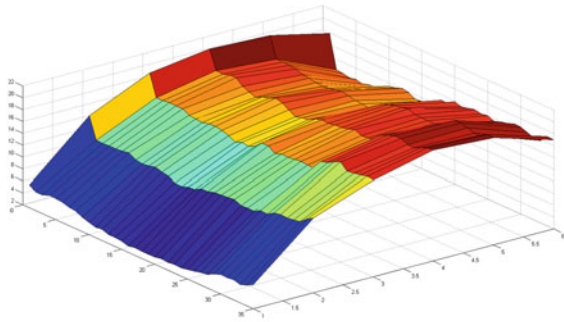
#### 4 Data Analysis/Discussion

To ensure that these values accurately represent the quantitative roughness of the pieces several calibration and comparison steps were taken. The Laser Check system was first calibrated using the calibration block specifically designed for this type of milled piece in Fig. 10. Once completed, the Laser Check machine was again tested with calibrated pieces with a known roughness value to verify that the readings were within the tolerances. Then as an extra step, visual and physical inspection of the

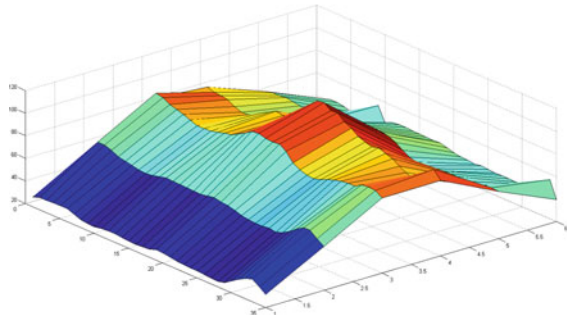
**Fig. 10** Milled aluminum samples with varying roughness values



(a) FD15/SP10,000 ( $R_a = 20.07 \mu m$ )



(b) FD15/SP1,000 ( $R_a = 13.7 \mu m$ )



(c) FD10/SP5,000 ( $R_a = 60.78 \mu m$ )

surfaces of each of the pieces was performed. The pieces were analyzed under a microscope in comparison with calibrated blocks. Also physical testing was done on the rougher piece and a calibrated piece using the fingernail test. Based on the sum of these steps, the system provides accurate surface roughness data.

The data were collected from both the traditional milled aluminum surface roughness testing as well as the solar cell surface roughness testing. Starting with the milled aluminum allowed for verification of the system. This is because we were able to both calibrate the system specifically for the type of milled piece, as well as compare the collected data with a calibrated value to determine the accuracy. Cutting was performed with 7075-T6 aluminum on a vertical milling machine by an end mill with a diameter of 12.5 mm. The three sample aluminum pieces were all 19 mm × 50 mm × 5.3 mm, with 0.1 mm milled off the top of each. The three samples had differing roughness values that were a result of the speed and method of milling. The FD value is the feed rate in inches per minute, and the SP value is the spindle speed in rpm. Thusly, FD15/SP5000 means a feed rate of 15 in/min and a spindle speed of 5,000 rpm.

The usefulness of the automated surface roughness measurement system described up to this point, depends upon the quality of data that can be collected. Figure 11 shows example plots of the data, plotted with MATLAB, collected from the described system. The x and y axes correspond to the rows and columns of data collected, in this case 11 by 50. The z axis displays the measured  $R_a$  values. The data come from 3 separate scans of the monocrystalline and polycrystalline solar cells are shown in Fig. 11.

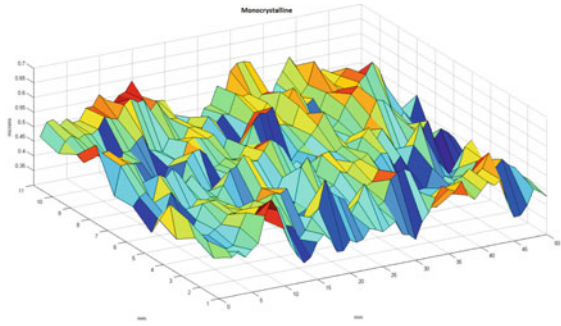
Three different samples were measured in this study. All three pieces are of different roughness values. The three samples consist of two polycrystalline solar cells and one monocrystalline solar cell. The reason for using different roughness values is obvious as the relationship between surface roughness measurements for both systems needs to be determined over a range of values to accurately determine any functional relationship that might be present.

The choice in using both monocrystalline and polycrystalline solar cells is also a conscious one. The reason being, as measured data confirms, that using the laser system to measure both kinds of solar cells yields certain characteristics unique to each type.

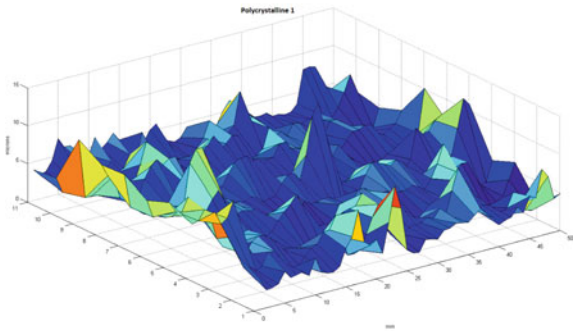
## 5 Conclusion

The utilization of various technologies and industrial components allows for the creation of a fully automated surface roughness measurement system. The implementation of such a system into the field of solar cell testing and development would allow for non-contact testing versus a traditional contact profilometer. Preliminary testing shows a good degree of repeatability that can be improved upon as this project moves forward.

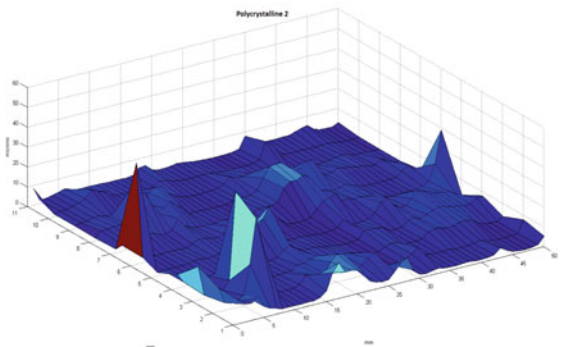
**Fig. 11** Monocrystalline and polycrystalline surface roughness graphs



(a) Monocrystalline solar cell ( $R_a = 1.57\mu m$ )



(b) Polycrystalline solar cell ( $R_a = 5.08\mu m$ )



(c) Polycrystalline solar cell ( $R_a = 2.40\mu m$ )



## References

1. Park HT, Kwak JG, Wang GN, Park SC (2010) Plant model generation for PLC simulation. *Int J Prod Res* 48(5):1517–1529
2. Lee JS, Hsu PL (2005) A systematic approach for the sequence controller design in manufacturing systems. *Int J Adv Manuf Technol* 25(7–8 / April):754–760
3. Klingstam P, Gullander P (1999) Overview of simulation tools for computer-aided production engineering. *Comput Ind* 38(2):173–186
4. Al-Ahmari AMA, Ridgway K (1999) An integrated modeling method to support manufacturing system analysis and design. *Comput Ind* 38:225–238
5. Anglani A, Grieco A, Pacella M, Tolio T (2002) Object-oriented modeling and simulation of flexible manufacturing system: a rule based procedure. *Sim Mod Prac Theory* 10:209–234
6. Manesis S, Akantziotis K (2005) Automated synthesis of ladder automation circuits based on state-diagrams. *Adv Eng Softw* 36:225–233
7. Trein J, Schwarzbacher, Th A, Hoppe B (2008) FPGA implementation of a single pass real-time blob analysis using run length encoding. In: MPC-workshop
8. Zaydoon T, Mohammad N (2014) Efficiency response of a silicon solar cell to the photo-chemical etching process. *Int J Appl Innov Eng Manag* 3(4):74–84
9. Chandra M, Rakesh A, Pujahari M (2014) Comparison of 2D and 3D screen printed metallization on multicrystalline silicon solar cells. *J Energy Power Sources* 1(3):141–146
10. Velidandla V, Xu J, Hou Z, Wijekoon K, Tanner D (2011) Texture process monitoring in solar cell manufacturing using optical metrology. In: 37th IEEE photovoltaic specialists conference, Seattle, June 2011
11. Kranz C, Wyczanowski S, Dorn S, Weise K, Klein C, Bothe K, Dullweber T, Brendel R (2012) Impact of the rear surface roughness on industrial type PERC solar cells. In: 27th European photovoltaic solar energy conference, Frankfurt, Germany, 24–28 Sept 2012
12. Al-Kindi G, Shirinzadeh B, Zhong Y (2008) A vision-based approach for surface roughness assessment at micro and nano scales. In: ICARCV, pp 1903–1908

# Integration of Thermal and Dimensional Measurement—A Hybrid Computational and Physical Measurement Method



D. Ross-Pinnock, B. Yang, and P. G. Maropoulos

**Abstract** In dimensional metrology, often the largest source of uncertainty of measurement is thermal variation. Dimensional measurements are currently scaled linearly, using ambient temperature measurements and coefficients of thermal expansion, to ideal metrology conditions at 20 °C. This scaling is particularly difficult to implement with confidence in large volumes as the temperature is unlikely to be uniform, resulting in thermal gradients. A number of well-established computational methods are used in the design phase of product development for the prediction of thermal and gravitational effects, which could be used to a greater extent in metrology. This paper outlines the theory of how physical measurements of dimension and temperature can be combined more comprehensively throughout the product lifecycle, from design through to the manufacturing phase. The Hybrid Metrology concept is also introduced: an approach to metrology, which promises to improve product and equipment integrity in future manufacturing environments. The Hybrid Metrology System combines various state of the art physical dimensional and temperature measurement techniques with established computational methods to better predict thermal and gravitational effects.

**Keywords** Thermal variation modelling · Metrology · Light controlled factory

## 1 Introduction

Factories of the future have been the subject of much discussion and research in recent years. One such approach is the Light Controlled Factory [1], where optical metrology is traceably woven into the manufacturing process for increased product and equipment integrity.

Dimensional metrology is subject to thermal effects on measurement uncertainty in two main ways. The first is as the measurand will undergo thermal expansion, contraction and distortion. Secondly, measurements carried out using

---

D. Ross-Pinnock (✉) · B. Yang · P. G. Maropoulos  
Laboratory for Integrated Metrology Applications (LIMA), Department of Mechanical Engineering, University of Bath, Claverton Down, Bath BA2 7AY, UK  
e-mail: [d.ross-pinnock@bath.ac.uk](mailto:d.ross-pinnock@bath.ac.uk)

© Springer Nature Switzerland AG 2022  
S. Hinduja et al. (eds.), *Proceedings of the 38th International MATADOR Conference*,  
[https://doi.org/10.1007/978-3-319-64943-6\\_45](https://doi.org/10.1007/978-3-319-64943-6_45)

627

optical measurement-based technologies will be subject to refractive index variations associated with ambient temperature [2].

Even constant, uniform temperatures that are not 20 °C can be problematic, and it follows that transient ambient temperature modelling is even more challenging still [3, 4].

Two major points are made in the Guide to Uncertainty of Measurement (GUM) [5] that highlight the importance of working towards the integration of thermal and dimensional measurement:

- “7.1.3 Numerous measurements are made every day in industry and commerce without any explicit report of uncertainty.”
- “3.3.2 In practice, there are many possible sources of uncertainty in a measurement, including: ... d) inadequate knowledge of the effects of environmental conditions on the measurement or imperfect measurement of environmental conditions”.

The first point illustrates how uncertainty evaluation is often neglected, meaning that a number of measurements are recorded that do not give an indication of how close that measurement is likely to be to the True Value. Following this, it is stipulated that the instrument uncertainty can be inferred from the traceability of the calibration. The second point is particularly pertinent to this paper, as part of that uncertainty evaluation must include some characterisation of the environment in which the measurement is taken. In terms of uncertainty evaluation, this shows that relying on the calibrated instrument alone does not give a complete indication of the uncertainty of all measurements taken outside of the standard environment.

The same year as the last International Temperature Scale of 1990 was published, the literature on thermal effects was reviewed since 1967 and illustrated the extent of the challenges faced at that time [6]. Progress has been made in a number of areas, however much the same problems exist today.

Taking a hybrid computational and physical measurement-based approach offers the benefit of being able to quantitatively predict thermal and gravitational effects on products and equipment in non-standard metrology environments. This is of particular benefit to manufacturing in measurement assisted assembly (MAA) [7], which is increasingly applied in the aerospace industry [8].

## 2 Ambient Temperature Variation

Thermal gradients are often present at large volumes, with some indoor environments experiencing gradients of 3–5 °C. Over the course of the day, the temperature is likely to change by several degrees depending on the location. Temperature is considered to be one of the critical parameters in assembly processes, for example [9].

Significant effort and expense is involved in designing and characterising the performance of high specification metrology buildings, as was the case at Finland’s

Centre for Metrology and Accreditation (MIKES) [10]. Large volume enclosures have been created that exhibit ultra-high thermal stability of less than 1 mK [11].

For many companies, the business case for investment in closely controlling temperature is difficult to make, even for those involved in the manufacture of high value products. Rather than engaging thermal variation directly, it would be constructive for metrologists to instead accept measure temperature fluctuations and non-uniformities as they occur, using these measurements to make informed predictions about their effects. Even the most thermally stable environments will have some error, meaning that the same principle can be applied to go beyond what is currently possible.

### 3 Temperature Measurement

Initial research on the Light Controlled Factory identified key industrial temperature measurement technologies [12]. The scope of the review was to identify those technologies that were mature, commercially available and could operate over an extended range around room temperature (0–50 °C). A number of these sensor types could operate at much wider temperature ranges, which allows for the monitoring of various hot and cold processes that may be found in the assembly environment. These technologies will provide physical temperature measurement data to update thermal variation models, which can subsequently be used in thermal compensation.

Thermal expansion of different materials has been considered in relation to the uncertainty required for dimensional and temperature measurement. If the linear coefficient of thermal expansion is:

$$\alpha_L \Delta T = \frac{\Delta L}{L} \quad (1)$$

Which can be used to provide the change in temperature  $\Delta T$  representing the temperature measurement accuracy required:

$$\Delta T = \frac{\Delta L}{\alpha_L L} \quad (2)$$

where  $\alpha$  is the coefficient of thermal expansion ( $\mu\text{m m}^{-1} \text{ }^\circ\text{C}^{-1}$ ),  $\Delta T$  is the change in temperature ( $^\circ\text{C}$ ),  $\Delta L$  is the change in length ( $\mu\text{m}$ ) and  $L$  is the original length (m).

Values have been estimated for four commonly used materials:

- Aluminium 6061 [13]
- Titanium Alloy Ti6Al-4V [14]
- Structural Steel A36 [15]
- Invar [16].

These estimated values of  $\Delta T$  have been assigned colours to indicate the accuracy of temperature measurement required with red indicating particularly challenging measurements and green being the least challenging as shown in Fig. 1.

As can be seen in Tables 1, 2, 3 and 4, the temperature measurement capability requirement becomes far more important for materials that are more susceptible to thermal expansion as would be expected. This generalized estimation is useful in the selection of temperature measurement technologies to be used in thermal variation modelling. It must be noted that these values are merely for estimation and in reality there will be some uncertainty in the coefficient of thermal expansion.

For more challenging measurement scenarios over long distances where low dimensional uncertainty is required, more invasive sensor types will need to be used.

**Fig. 1** Colour coding of different levels of temperature measurement accuracy required

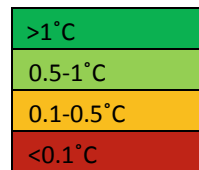


**Table 1** Table of required temperature measurement for dimensional measurement scenarios of Aluminium 6061

CTE ( $\mu\text{m.m}^{-1}.\text{°C}^{-1}$ )	L (m)	$\Delta L$ ( $\mu\text{m}$ )	$\Delta T$ (°C)
23.6	5	50	0.424
23.6	5	40	0.339
23.6	5	30	0.254
23.6	5	20	0.169
23.6	5	10	0.085
23.6	10	50	0.212
23.6	10	40	0.169
23.6	10	30	0.127
23.6	10	20	0.085
23.6	10	10	0.042
23.6	20	50	0.106
23.6	20	40	0.085
23.6	20	30	0.064
23.6	20	20	0.042
23.6	20	10	0.021

**Table 2** Table of required temperature measurement for dimensional measurement scenarios of structural steel A36

CTE ( $\mu\text{m}\cdot\text{m}^{-1}\cdot\text{C}^{-1}$ )	L (m)	$\Delta\text{L}$ ( $\mu\text{m}$ )	$\Delta\text{T}$ ( $^{\circ}\text{C}$ )
8.3	5	50	1.205
8.3	5	40	0.964
8.3	5	30	0.723
8.3	5	20	0.482
8.3	5	10	0.241
8.3	10	50	0.602
8.3	10	40	0.482
8.3	10	30	0.361
8.3	10	20	0.241
8.3	10	10	0.120
8.3	20	50	0.301
8.3	20	40	0.241
8.3	20	30	0.181
8.3	20	20	0.120
8.3	20	10	0.060

In most cases however, taking temperature measurements of the measurand and its environment will be preferable to solely monitoring temperature at the instrument.

#### 4 Thermal Modelling and Computational Methods

A range of computational methods are available for metrology and modelling are used in industry. Simulation of thermal expansion, contraction and distortion is currently carried out at the product design stage, whereas this approach casts it in a more operational role.

The empirical modelling techniques can be employed if the thermal errors can be considered as a function of some critical discrete temperature points on the machine structure, and these temperature points need to represent the thermal field of the entire machine structure. For example, for machine tool thermal error modelling, a set of thermal sensors and a set of displacement sensors need to be placed at the appropriate locations of the structure in order to measure the temperatures and displacements. The coordinates and the temperature of the selected locations are initially measured as the

**Table 3** Table of required temperature measurement for dimensional measurement scenarios of Titanium Alloy Ti6Al-4V

CTE ( $\mu\text{m}\cdot\text{m}^{-1}\cdot\text{C}^{-1}$ )	L (m)	$\Delta\text{L}$ ( $\mu\text{m}$ )	$\Delta\text{T}$ ( $^{\circ}\text{C}$ )
12.1	5	50	0.826
12.1	5	40	0.661
12.1	5	30	0.496
12.1	5	20	0.331
12.1	5	10	0.165
12.1	10	50	0.413
12.1	10	40	0.331
12.1	10	30	0.248
12.1	10	20	0.165
12.1	10	10	0.083
12.1	20	50	0.207
12.1	20	40	0.165
12.1	20	30	0.124
12.1	20	20	0.083
12.1	20	10	0.041

reference. The data then records in a series of time periods during the warm-up and machine operations. A relationship between the thermal error and the temperature can be established based on these data using suitable algorithms, such as Multiple Regression Analysis (MRA), Genetic Algorithms (GA) or Artificial Neural Network (ANN) [17].

The effect of temperature upon the tolerance stack-up of assemblies is of great interest here. Various software packages can perform tolerance analysis on assemblies and methods for tolerance analysis have recently been the subject of a comparative review [18]. One 2013 study of assemblies in the automotive industry recommended that assembly variation simulations should be combined with thermal expansion simulation, rather than considered separately [19].

Composite materials are being used with increasing frequency in a number of industries, with the automotive and aerospace sectors being the most notable. Modelling composite materials can be difficult due to their relative non-uniformity and variation so this is an area that is being continually developed. The dimensional variation of composites has been simulated using FEA and studied for different types of simple structural assembly [20].

**Table 4** Table of required temperature measurement for dimensional measurement scenarios of Invar 36

CTE ( $\mu\text{m}\cdot\text{m}^{-1}\cdot\text{C}^{-1}$ )	L (m)	$\Delta\text{L}$ ( $\mu\text{m}$ )	$\Delta\text{T}$ ( $^{\circ}\text{C}$ )
1.3	5	50	7.692
1.3	5	40	6.154
1.3	5	30	4.615
1.3	5	20	3.077
1.3	5	10	1.538
1.3	10	50	3.846
1.3	10	40	3.077
1.3	10	30	2.308
1.3	10	20	1.538
1.3	10	10	0.769
1.3	20	50	1.923
1.3	20	40	1.538
1.3	20	30	1.154
1.3	20	20	0.769
1.3	20	10	0.385

The prediction of the environmental change is required in large volume metrology in order to compensate measurement uncertainty and thermal-structural errors. Numerical Weather Prediction (NWP) [21] has the potential for use in ambient conditions prediction in large volume metrology applications. Overall, there are several similarities: similar environmental conditions (such as temperature, humidity and pressure); both time dependent; both aim to predict the environmental change using the initial measurements. However, from a practical point of view, the challenge would be gathering large sets of real measurement and sufficient history data of ambient conditions of the real site to train the programme to achieve accurate predictions.

Modelling indoor ambient temperature has been studied for a number of applications, perhaps none more so than in Heating, Ventilation and Air Conditioning (HVAC). In addition to temperature, air flow has also been modelled within buildings [22]. As well as personal comfort (analogous here also to product and equipment integrity), the modelling of ambient temperature in HVAC applications is also important for the improvement of energy efficiency, with one building seeing 20% improvements [23]. This modelling has often been achieved through the use of thermal network analysis [24]. While HVAC may seem disconnected from manufacturing,



the characterisation and prediction [25, 26] of room temperatures could be useful for daily dynamic thermal variation modelling.

## 5 Hybrid Physical and Computational Metrology Concept

Hybrid Metrology System is defined here as a system that utilises the measurement of more than one physical quantity to inform virtual computational models of the measurand within the context of its environment.

The Hybrid Metrology System is designed to be a modular system so that measurement and computational capabilities can be added or removed. In this case, dimensional and temperature measurement will be measured, although other measurements could also be taken as appropriate.

The overall anatomy of the Hybrid Metrology System consists of the physical and digital domains. The measurand and instruments occupy the physical domain within the inspection environment. Via the data acquisition and inspection software, measurement data can then be used within the digital domain to simulate thermal effects and predict their resulting impact upon dimensions and tolerance stack-up in assemblies. One example of a possible configuration of the Hybrid Metrology System can be seen in Fig. 2.

In order to validate the model, deterministic simulation data must be compared against measurement data. Any discrepancies in the model predictions can be accounted for could be performed iteratively. Statistical analysis and machine learning methods offer efficient model development. Whilst running complex simulations is computationally expensive, cloud computing services may offer an advantage to the Light Controlled Factory. One possibility is cloud computing combined with part simplification algorithms to create dynamic virtual assembly process models. Processing in this manner could also be used to network several different sites in larger companies so that modelling improvements can be realised with Big Data techniques globally throughout organisations, rather than at individual sites. Figure 3 illustrates levels of increasing developmental complexity for a Hybrid Metrology System.

Uncertainty evaluation as discussed earlier is fundamental to the creation of a traceable metrology system of any kind. Uncertainty models are currently under development for a range of instruments that give uncertainty estimations for specific measurements taken. Due to the modular design of the hybrid metrology system, this can be incorporated as new uncertainty models are developed for each instrument. The uncertainty of the simulations themselves will also need to be evaluated.

Srinivasan created an integration framework for product lifecycle management (PLM) which supports information-sharing between the realms of engineering and wider business. This framework allows for the connection of separate software modules [27]. Monitoring the condition of equipment has been considered in the context of product lifecycle management (PLM). It could be possible to include temperature measurement data and the hybrid metrology system as part of this framework [28].

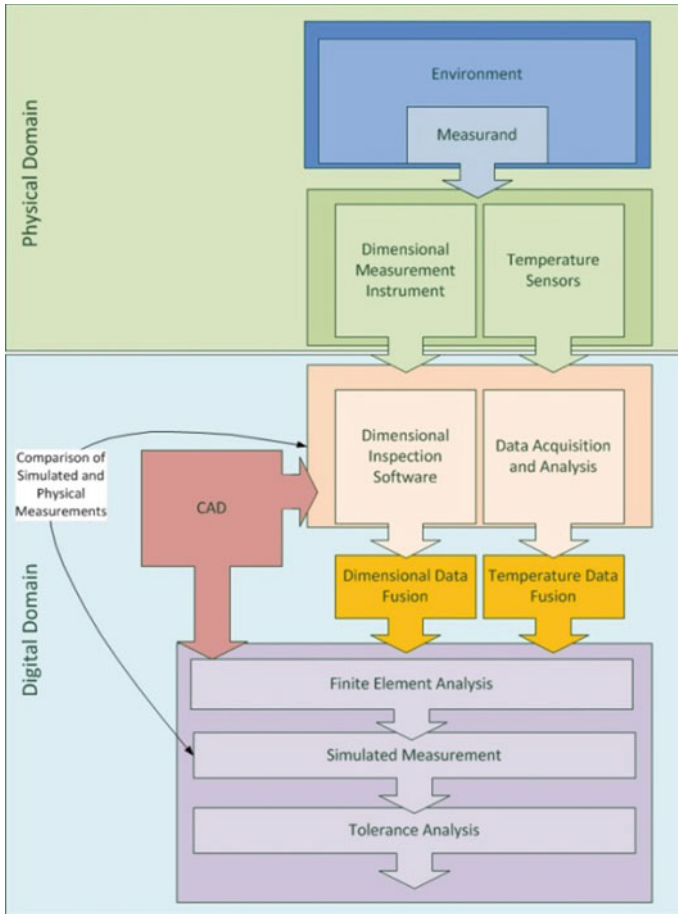


Fig. 2 One example of a hybrid metrology system configuration

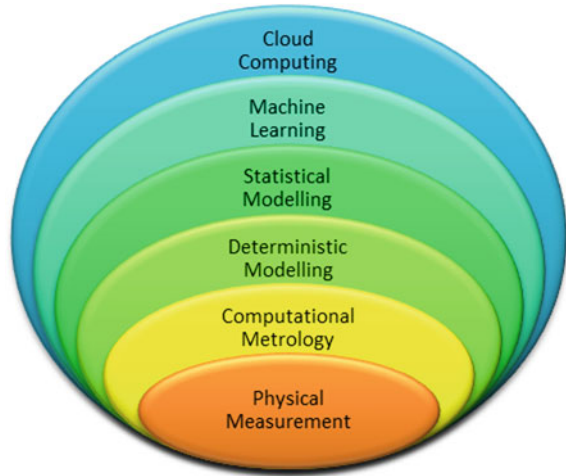
## 6 Thermal Compensation

Using the predictions from the hybrid metrology systems paves the way for improvement in manufacturing as thermal effects can be largely offset using thermal compensation.

Measurement and subsequent compensation of thermal effects has been the focus of various studies. This is particularly true for machining processes where the temperatures present are often beyond room temperature and the specifications of machined components are demanding—ultra precision machining for example requires sub-micron tolerances.

Machine tool errors attributable to thermal effects can be corrected in real time on machine tools [29].

**Fig. 3** Diagram showing levels of developmental complexity in hybrid metrology systems



In large scale assembly, the products are often high value and specifications are becoming increasingly challenging. This area has in recent years received a great deal of attention in order to improve assembly through increased measurement capability. As tooling is relied upon to hold assemblies, active thermal compensation has been identified as one potential solution to compensating for thermal expansion effects in large scale tooling for aerospace applications [30]. Often the parts of an assembly are compliant, where gravitational effects can also occur. The theoretical basis for a biomimetic system for dimensional error compensation in compliant assemblies has been outlined which could inform the Hybrid Metrology System approach applied in such cases [31].

FEA has also been employed for machine tool error prediction in last decade. FEA was used to simulate the effects of the major internal heat sources such as bearings, motors and belt drives of a small vertical milling machine (VMC) and the effects of ambient temperature pockets that build up during the machine operation [32]. The agreement with the experiment results range varies from 65 to 90%. The offline simulation can also reduce the machine downtime.

## 7 Conclusion

The challenges faced in industrial dimensional metrology for manufacturing due to thermal and gravitation effects have been introduced and discussed. Whilst this is an area that has been researched for a number of years, thermal effects continue to contribute a great deal to measurement uncertainty and product quality.

A generalised developmental theory of hybrid computational and physical measurement has been outlined, with reference to some applicable lessons learned from earlier works in the field of thermal variation modelling in the literature.

Research has been done in a number of specific areas and this particular approach seeks to create a wider framework to exploit these learnings in an industrial context, as part of the Light Controlled Factory. Suggestions have been made as to where hybrid metrology can fit within existing and novel product lifecycle management (PLM) frameworks.

The hybrid metrology system concept has been discussed with some illustration of how a number of physical and computational metrological techniques can be used as part of a hybrid metrology system. The hybrid metrology system has been defined as a system that employs a number of physical quantities to inform computational models of the measurand within its local environment. An example hybrid metrology system has been given to illustrate how the system could potentially be structured but the particular configuration will depend upon the final application. Thermal compensation techniques offer the ability to address thermal effects based upon predictions made by the hybrid metrology system. Ultimately, the hybrid metrology system is intended to have a practical, modular design that is traceable through uncertainty-consciousness.

## 8 Future Work

Following on from this theoretical basis and outline of the Hybrid Metrology System concept, future work is needed to look at the technologies that go to form the Hybrid Metrology Toolkit. Such a toolkit will provide a practical methodology and framework, which can serve as the basis for preliminary experimental studies in thermal variation modelling. Case studies need to be carried out in both laboratory-based and industrial environments in order to validate the methodology. Uncertainty evaluation of the modelling also needs to be carried out, which will require the modelling of uncertainty in physical dimensional and thermal metrology as well as evaluating the uncertainty of the computational models.

**Acknowledgements** The authors would like to gratefully acknowledge the financial support of the EPSRC, grant EP/K018124/1, “The Light Controlled Factory”. We would also like to thank the industrial collaborators for their contribution and the Department of Mechanical Engineering at the University of Bath.

## References

1. Muelaner JE, Maropoulos PG (2014) Large volume metrology technologies for the light controlled factory. In: *Procedia CIRP special edition for 8th international conference on digital enterprise technology—DET 2014—disruptive innovation in manufacturing engineering towards the 4th industrial revolution*, 25 March 2014–28 March 2014. Elsevier. <https://doi.org/10.1016/j.procir.2014.10026>

2. Estler WT, Edmundson KL, Peggs GN, Parker DH (2002) Large-scale metrology—an update. *CIRP Ann Manuf Technol* 51(2):587–609
3. Wilhelm RG, Hocken R, Schwenke H (2001) Task specific uncertainty in coordinate measurement. *CIRP Ann Manuf Technol* 50(2):553–563
4. Swyt DA (1994) Uncertainties in dimensional measurements made at nonstandard temperatures. *J Res Natl Inst Stand Technol* 99(1):31–44
5. BIPM (2008) Evaluation of measurement data—guide to the expression of uncertainty in measurement
6. Bryan J (1990) International status of thermal error research. *CIRP Ann Manuf Technol* 39(2):645–656
7. Maropoulos PG, Muelaner JE, Summers MD, Martin OC (2014) A new paradigm in large-scale assembly—research priorities in measurement assisted assembly. *Int J Adv Manuf Technol* 70(1–4):621–633
8. Mei Z, Maropoulos PG (2014) Review of the application of flexible, measurement-assisted assembly technology in aircraft manufacturing. *Proc Inst Mech Eng, Part B: J Eng Manuf* 228(10):1185–1197
9. Armillotta A, Semeraro Q (2013) Critical operating conditions for assemblies with parameter-dependent dimensions. *Proc Inst Mech Eng, Part B: J Eng Manuf* 227(B5):735–744
10. Lassila A, Kari M, Koivula H, Koivula U, Kortström J, Leinonen E, et al (2011) Design and performance of an advanced metrology building for MIKES. *Meas J Int Meas Confederation* 44(2):399–425
11. Zhao Y, Trumper DL, Heilmann RK, Schattenburg ML (2010) Optimization and temperature mapping of an ultra-high thermal stability environmental enclosure. *Precis Eng-J Int Soc Precis Eng Nanotechnol* 34(1):164–170
12. Ross-Pinnock D, Maropoulos PG () Identification of key temperature measurement technologies for the enhancement of product and equipment integrity in the light controlled factory. In: *Procedia CIRP special edition for 8th international conference on digital enterprise technology—DET 2014—disruptive innovation in manufacturing engineering towards the 4th industrial revolution, 25 March 2014–28 March 2014*. Elsevier. <https://doi.org/10.1016/j.proci.201410019>
13. Boresi AP, Schmidt RJ, *Advanced mechanics of materials*, 6th edn. Wiley
14. ASME (2004) *ASME Boiler and Pressure Vessel Code, Section II—Materials (Includes Addenda for 2005 and 2006)*. American Society of Mechanical Engineers, 2006
15. Yang B, *Stress, strain, and structural dynamics—an interactive handbook of formulas, solutions, and MATLAB toolboxes*. Elsevier
16. Flitney R, *Seals and sealing handbook*, 6th edn. Elsevier
17. Chen JS (1996) Neural network-based modelling and error compensation of thermally-induced spindle errors. *Int J Adv Manuf Technol* 12(4):303–308
18. Chen H, Jin S, Li Z, Lai X (2014) A comprehensive study of three dimensional tolerance analysis methods, pp 1–13
19. Lorin S, Lindkvist L, Söderberg R, Sandboge R (2013) Combining variation simulation with thermal expansion simulation for geometry assurance. *J Comput Inf Sci Eng* 13(3):031007
20. Chensong D, Chuck Z, Zhiyong L, Ben W (2004) Assembly dimensional variation modelling and optimization for the resin transfer moulding process. *Model Simul Mater Sci Eng* 12(3):S221
21. Gustafsson N, Huang XY, Yang XH, Mogensen K, Lindskog M, Vignes O et al (2012) Four-dimensional variational data assimilation for a limited area model. *Tellus Ser A Dyn Meteorol Oceanol* 64
22. Tuomaala P, Rahola J (1995) Combined air flow and thermal simulation of buildings. *Build Environ* 30(2):255–265
23. Qi Luo QL, Ariyur KB (2010) Building thermal network model and application to temperature regulation. In: *IEEE international conference on control applications*, pp 2190–2195
24. Chen H, Wang X (2013) A modified zone model for estimating equivalent room thermal capacity. *Front Energy* 7(3):351–357

25. Ellis C, Hazas M, Scott J (2013) Matchstick: a room-to-room thermal model for predicting indoor temperature from wireless sensor data. In: 2013 ACM/IEEE international conference on information processing in sensor networks (IPSN), 8–11 April 2013
26. Afram A, Janabi-Sharifi F (2014) Theory and applications of HVAC control systems—a review of model predictive control (MPC). *Build Environ* 72:343–355
27. Srinivasan V (2011) An integration framework for product lifecycle management. *Comput Aided Des* 43(5):464–478
28. Fathi M, Holland A, Abramovici M, Neubach M (2007) Advanced condition monitoring services in product lifecycle management. In: IEEE international conference on information reuse and integration, pp 245–250
29. Ford DG, Postlethwaite SR, Allen JP, Blake MD (2000) Compensation algorithms for the real-time correction of time and spatial errors in a vertical machining centre. *Proc Inst Mech Eng Part B J Eng Manuf* 214(3):221–234
30. Muelaner J, Martin OC, Maropoulos PG (2011) Metrology enhanced tooling for aerospace (META): strategies for improved accuracy of jig built structures. SAE Aerotech 2011: SAE International
31. Wells LJ, Camelio JA (2013) A bio-inspired approach for self-correcting compliant assembly systems. *J Manuf Syst* 32(3):464–472
32. Mian NS, Fletcher S, Longstaff AP, Myers A (2011) Efficient thermal error prediction in a machine tool using finite element analysis. *Measur Sci Technol* 22(8):085107

# Elimination of Gyro Rate Offset by Using a Rotating Mechanism for Large Scale Straightness Evaluation



T. Kume, M. Satoh, T. Suwada, K. Furukawa, and E. Okuyama

**Abstract** Straightness evaluations by detecting tangential angles of the straightness are considered to be advantageous for evaluating large objects. Among them, a method using a gyro can be applied in a horizontal plane and has no limitation for its evaluation distance. However, even the most stable gyro has considerable fluctuation called a gyro rate offset in its angular signal and it becomes a dominant error source. We had demonstrated that the gyro rate offset can be eliminated by periodical reversal measurement by using a conventional fiber optic gyro (FOG) unit. Here, we adopted a rotating mechanism with a rotating rate up to several revolutions per second for performing faster reversal measurement in order to eliminate faster fluctuations in the gyro rate offset. Analysis and experiment show that the gyro rate offset can be derived and eliminated together with an alignment error of the gyro direction. Finally, we derive an angular signal to be detected for our straightness evaluation with a reasonable signal waveform.

**Keywords** Straightness evaluation · Gyro · Rate offset · Reversal measurement · Fiber optic gyro (FOG) · Large object

## 1 Introduction

We study large scale straightness evaluation method by detecting tangential angles of the straightness [1–3]. It is considered to be advantageous for evaluating large objects because it is not affected by scanning locus of the straightness detector. The

---

T. Kume (✉)

Mechanical Engineering Centre, High Energy Accelerator Research Organization (KEK), 1-1, Oho, Tsukuba, Ibaraki 305-0801, Japan  
e-mail: [tatsuya.kume@kek.jp](mailto:tatsuya.kume@kek.jp)

M. Satoh · T. Suwada · K. Furukawa

Accelerator Laboratory, High Energy Accelerator Research Organization (KEK), 1-1, Oho, Tsukuba, Ibaraki 305-0801, Japan

E. Okuyama

Faculty of Engineering and Resource, Akita University, 1-1, Tegata gakuen-machi, Akita 010-8502, Japan

© Springer Nature Switzerland AG 2022

S. Hinduja et al. (eds.), *Proceedings of the 38th International MATADOR Conference*, [https://doi.org/10.1007/978-3-319-64943-6\\_46](https://doi.org/10.1007/978-3-319-64943-6_46)

locus is predominantly used as a reference in other conventional methods; however, it is difficult to be defined accurately enough as the object becomes large. We had performed straightness evaluation for a 71-m-long part of our linear particle accelerator with a standard deviation of less than  $49\ \mu\text{m}$  by using a precise inclinometer [1]. We also evaluated the straightness for a distance up to 206 m by using the method and demonstrated that the straightness evaluation by detecting tangential angles is valid for large objects [2]. However, the method using an inclinometer cannot be applied for evaluating a straightness in a horizontal plane, and the straightness is affected by earth roundness because an inclinometer uses a direction of gravity as a reference.

Gyros are detectors, which are sensitive to angular velocities (rates) and are widely used for navigation systems, posture detections, image stabilizations, etc. They have no limitation for their evaluation distance, while those for autocollimators are limited to be 100 m at longest. Moreover, sensitive gyros can resolve  $\mu\text{rad}$  of angles without affected by gravity, which is the same level as highly precise inclinometers. Therefore, precise gyros are seems to be promising for evaluating large scale straightness; however, even the most stable gyro has a rate offset of several hundred  $\mu\text{rad}$  per hour. A rate offset is fluctuation of the angular signal and is considered to be dominant error source for precise gyros. A rate offset of several hundred  $\mu\text{rad}$  per hour is not acceptable for evaluating tangential angles with an accuracy of several  $\mu\text{rad}$ , which we aim to detect. It follows that we should eliminate the rate offset for adopting the gyro into the straightness evaluation. We had demonstrated that the rate offset can be eliminated together with effect of the earth rotation by periodical reversal measurement with a period of 60 s by using a conventional fiber optic gyro (FOG) unit [3].

Here, we adopt a rotating mechanism with a rotating rate up to several revolutions per second (rps) in order to realize continuous reversal measurements with a shorter interval for eliminating influences caused by faster changes of the rate offset. An analysis shows that the rate offset can be derived by differences between two gyro angular signals with one rotation period apart. On the other hand, experiments show that alignment error of the gyro setting direction affects its angular signal; however, the error can be eliminated together with the rate offset by measurements for multiple rotating rates. Finally, we derive an angular signal to be detected for straightness evaluation.

## 2 Principle

Figure 1 shows straightness evaluation using a rotating gyro, where  $x$  axis is defined as a running direction of the straightness,  $S$ , while  $y$  and  $z$  axes are perpendicular to the  $x$  axis. The gyro rotates around a rotating axis,  $r$  with a constant angular velocity,  $\omega_g$ .  $r$  is perpendicular to the gyro sensitive axis,  $g$ , around which the gyro has an angular sensitivity. The projections,  $\theta_y$  and  $\theta_p$  on the  $x$ - $y$  and  $x$ - $z$  planes of the angular deflection of  $r$  against  $x$  can be detected by the gyro. They correspond to the first-order differences of the straightness for the section divided by points, a and b. The



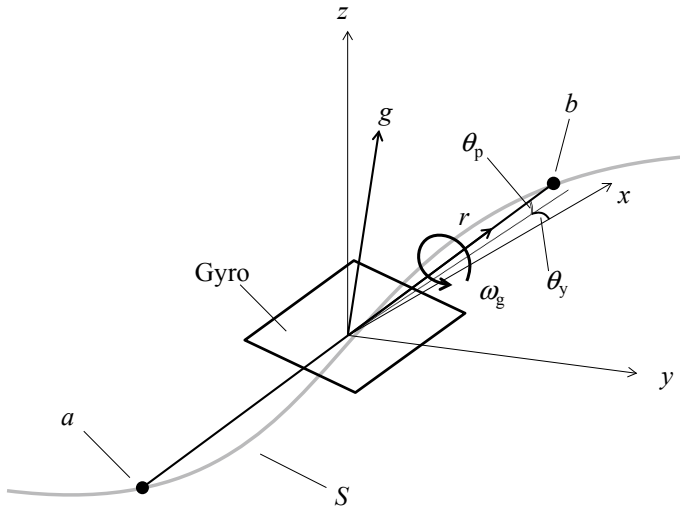


Fig. 1 Straightness evaluation using a rotating gyro

straightness can be derived by integrating the detected angles with transferring the rotating gyro toward  $x$  direction.

Figure 2 shows an analysis model for a continuously rotating gyro. Here, we consider a reference plane,  $P$  and a line on it. The line is defined to be a rotating axis,  $r$ . The gyro is set on the plane with its sensitive axis,  $g$  perpendicular to  $r$ . It follows that the gyro rotates to the direction to which the gyro has no angular sensitivity. On the other hand, Fig. 3 shows an earth rotation model, where  $\omega$  stands for an angular velocity of the earth rotation ( $\approx 73 \mu\text{rad/s}$ ), and  $\alpha$  and  $\beta$  stands for a latitude of the gyro position and a deflection angle of the rotating axis from a meridian.

An angular signal detected by the gyro,  $\theta(t)$  for time,  $t$  is expressed as

$$\theta(t) = \theta_0 + \sin^{-1} \{ \cos(\omega_g \cdot t) \cdot \sin(\theta_y) + \sin(\omega_g \cdot t) \cdot \sin(\theta_p) \}$$

Fig. 2 Analysis model for continuously rotating gyro

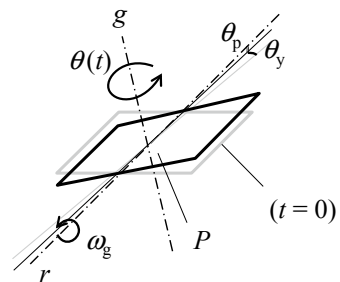
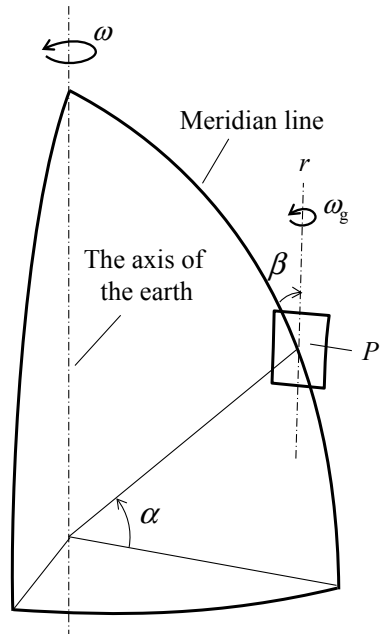


Fig. 3 Earth rotation model



$$\begin{aligned}
 &+ \frac{\omega}{\omega_g} \sin(\alpha) \cdot \sin(\omega_g \cdot t) \\
 &+ \frac{\omega}{\omega_g} \cos(\alpha) \cdot \sin(\beta) \cdot \{1 - \cos(\omega_g \cdot t)\} + r_0 \cdot t, \tag{1}
 \end{aligned}$$

where  $\theta_0$  and  $r_0$  stands for an angular offset and a rate offset of the gyro,  $\theta_y$  and  $\theta_p$  stands for a horizontal and a vertical component of the deflection angle of the rotating axis against its initial direction. Here we assume that the initial direction of the reference plane,  $P$  is horizontal at  $t = 0$ .

In Eq. (1), angles,  $\theta_y$  and  $\theta_p$  to be detected are expressed by the second term, being modulated by an angular velocity of the gyro rotation, while the other terms are errors to be compensated, where the third and the fourth term can be obtained by knowing  $\alpha$  and  $\beta$ ; however, the first and the fifth term cannot be obtained.

We eliminate the first term based on reversal measurement. A difference between angular signals of the gyro for half rotation period apart is expressed as

$$\begin{aligned}
 \theta\left(t + \frac{\pi}{\omega_g}\right) - \theta(t) &= -2 \sin^{-1} \{ \cos(\omega_g \cdot t) \cdot \sin(\theta_y) + \sin(\omega_g \cdot t) \cdot \sin(\theta_p) \} \\
 &- \frac{2\omega}{\omega_g} \sin(\alpha) \cdot \sin(\omega_g \cdot t) \\
 &+ \frac{2\omega}{\omega_g} \cos(\alpha) \cdot \sin(\beta) \cdot \cos(\omega_g \cdot t) + \frac{\pi r_0}{\omega_g}. \tag{2}
 \end{aligned}$$

A rate offset,  $r_0$  still remains in Eq. (2), while a difference between angular signals for one rotation period apart is expressed as

$$\theta\left(t + \frac{2\pi}{\omega_g}\right) - \theta(t) = \frac{2\pi r_0}{\omega_g}. \tag{3}$$

It shows that the gyro rate offset can be derived from a difference between angular signals of the gyro for one rotation period apart by knowing an angular velocity of the gyro rotation.

### 3 Experiment

We validate the relation expressed by Eq. (3) by using a conventional FOG unit and a custom-made rotating mechanism. Figure 4 shows a photograph of the mechanism with an FOG unit. The FOG unit is TA4265N1510 by Tamagawa Co., Ltd, which is small (Size, 65 mm × 130 mm × 85 mm), light (Weight, 1.5 kg), wide range (Range, ±180°), fast (Operation cycle, 100 Hz) and accurate (Drift, 3°/h-rms). The rotating mechanism is driven by an AC servomotor with an adjustable rotating rate from 0 to 4 rps.

Figure 5a, b show angular signals obtained from the rotating gyro and their differences between one rotation period apart, respectively. They are for rotating rates of 0.05, 0.1, 0.2, 0.5, 1, and 2 rps. The mechanism is placed at the latitude,  $\alpha$  of 36° and the gyro rotation axis is headed to north ( $\beta \doteq 0^\circ$ ) in the horizontal plane. Considering the relation expressed by Eq. (2), for the conditions of  $\theta_y, \theta_p \doteq 0$  and  $\omega_g \gg \omega, r_0$ , an angular outputs should be almost constant for the scale expressed in Fig. 5a; however, there can be remarkably seen proportional components to time,  $t$ . It is considered to be caused by an alignment error,  $\psi$  of the gyro direction against perpendicular

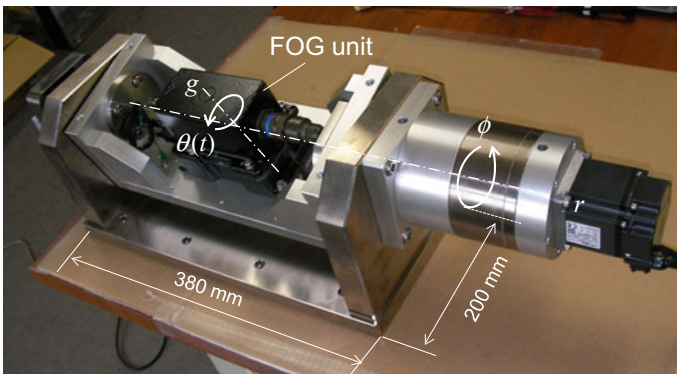
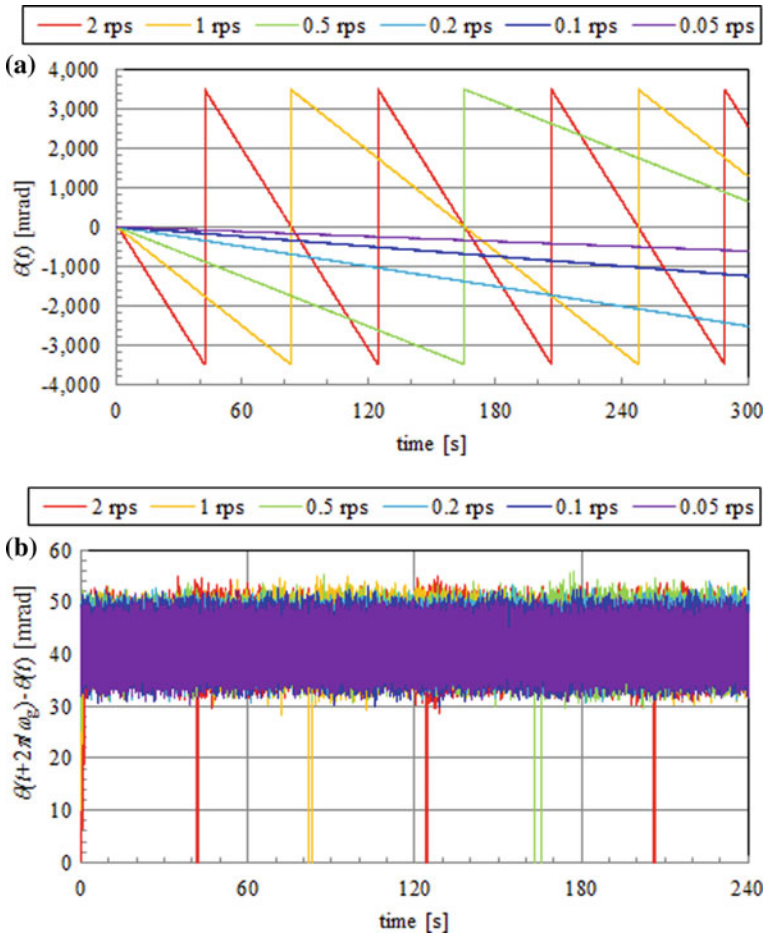


Fig. 4 Gyro rotating mechanism and an FOG unit



**Fig. 5** **a** Angular signals of the rotating gyro; **b** angular signal differences between one rotation period apart

direction to the rotating axis as shown in Fig. 6. It follows that the angular velocity of the gyro rotation,  $\omega_g$  has a component for the gyro sensitive direction as  $\omega_g \cdot \sin(\psi)$ . Then the relation expressed by Eq. (3) becomes

$$\theta\left(t + \frac{2\pi}{\omega_g}\right) - \theta(t) = \frac{2\pi}{\omega_g} \cdot \{r_0 + \omega_g \cdot \sin(\psi)\}. \tag{4}$$

Equation (4) is rewritten to be

$$\theta\left(t + \frac{2\pi}{\omega_g}\right) - \theta(t) = r_0 \cdot T + 2\pi \cdot \sin(\psi), \tag{5}$$

**Fig. 6** Rotating gyro with an alignment error,  $\psi$  of the gyro direction,  $g$

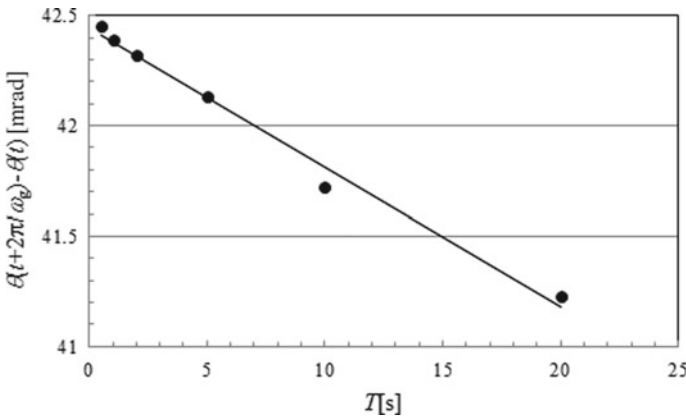
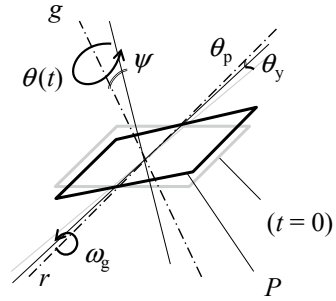


**Fig. 7** Angular signal differences,  $\theta(t + 2\pi/\omega_g) - \theta(t)$  between one rotation period apart as a function of the gyro rotating period,  $T$

where  $T = 2\pi/\omega_g$  stands for a rotation period of the gyro.

Figure 7 shows differences,  $\theta(t + 2\pi/\omega_g) - \theta(t)$  between the angular signals for one rotation period apart as a function of gyro rotation period,  $T$ . The relation is obtained from the measurements expressed by Fig. 5a, b. From the relation expressed by Eq. (5), the slope of the graph stands for the gyro rate offset,  $r_0$ , while the alignment error of the gyro direction,  $\psi$  can be derived by the intercept of the graph,  $2\pi \cdot \sin(\psi)$ . In this case,  $r_0 = -63.1 \mu\text{rad/s}$  and  $\psi = 6.8 \text{ mrad}$ , respectively.

### 4 Discussion

The value of the derived gyro rate offset,  $r_0 = -63.1 \mu\text{rad/s}$  is close to that derived in the former measurement of  $r_0 = 61 \mu\text{rad/s}$ , where periodical reversal measurement with an interval of 60 s was performed [3]. The difference in the plus/minus sign between them is caused by difference between the definitions of their coordinates.

While the alignment error,  $\psi = 6.8$  mrad of the gyro direction seems to be reasonable considering structure of the rotating mechanism and their assembly process, where their alignment accuracies depend on their machining accuracies. Therefore, both of the derived values are considered to be fairly reliable.

Then, we derive angular deflections,  $\theta_y$  and  $\theta_p$  of the gyro rotating axis, considering an alignment error,  $\psi$  of the gyro direction.

Equation (1) becomes

$$\begin{aligned} \theta(t) = & \theta_0 + \sin^{-1}\{\cos(\omega_g \cdot t) \cdot \sin(\theta_y) + \sin(\omega_g \cdot t) \cdot \sin(\theta_p)\} \\ & + \frac{\omega}{\omega_g} \sin(\alpha) \cdot \sin(\omega_g \cdot t) \\ & + \frac{\omega}{\omega_g} \cos(\alpha) \cdot \sin(\beta) \cdot \{1 - \cos(\omega_g \cdot t)\} \\ & + \{r_0 + \omega_g \cdot \sin(\psi)\} \cdot t, \end{aligned} \quad (6)$$

while Eq. (2) becomes

$$\begin{aligned} \theta\left(t + \frac{\pi}{\omega_g}\right) - \theta(t) = & -2 \sin^{-1}\{\cos(\omega_g \cdot t) \cdot \sin(\theta_y) + \sin(\omega_g \cdot t) \cdot \sin(\theta_p)\} \\ & - \frac{2\omega}{\omega_g} \sin(\alpha) \cdot \sin(\omega_g \cdot t) \\ & + \frac{2\omega}{\omega_g} \cos(\alpha) \cdot \sin(\beta) \cdot \cos(\omega_g \cdot t) \\ & + \frac{\pi}{\omega_g} \{r_0 + \omega_g \cdot \sin(\psi)\}. \end{aligned} \quad (7)$$

The relations expressed by Eqs. (4) and (7) leads a relation,

$$\begin{aligned} & \sin^{-1}\{\cos(\omega_g \cdot t) \cdot \sin(\theta_y) + \sin(\omega_g \cdot t) \cdot \sin(\theta_p)\} \\ & = \frac{1}{4} \left\{ \theta\left(t + \frac{2\pi}{\omega_g}\right) - 2\theta\left(t + \frac{\pi}{\omega_g}\right) + \theta(t) \right\} \\ & + \frac{\omega}{\omega_g} \{-\sin(\alpha) \cdot \sin(\omega_g \cdot t) + \cos(\alpha) \cdot \sin(\beta) \cdot \cos(\omega_g \cdot t)\}. \end{aligned} \quad (8)$$

Equation (8) expresses that angular deflections,  $\theta_y$  and  $\theta_p$  of the gyro rotating axis modulated by the gyro rotation,  $\omega_g$ , expressed by  $\sin^{-1}\{\cos(\omega_g \cdot t) \cdot \sin(\theta_y) + \sin(\omega_g \cdot t) \cdot \sin(\theta_p)\}$ , can be derived by a second-order difference of angular signals of the gyro for half and one rotation period apart expressed on the first term of the right hand side and the values obtained from  $\alpha$ ,  $\beta$ ,  $\omega$ , and  $\omega_g$  as a function of  $t$  expressed by the second term.

Figure 8 shows the modulated angular deflection,  $\sin^{-1}\{\cos(\omega_g \cdot t) \cdot \sin(\theta_y) + \sin(\omega_g \cdot t) \cdot \sin(\theta_p)\}$  as a function of  $t$  for the case  $\alpha = 36^\circ$ ,  $\beta = 0^\circ$ ,  $\omega = 73 \mu\text{rad/s}$ , and  $\omega_g = 2\pi \text{ rad/s}$ , which is for a gyro rotating rate of 1 rps.

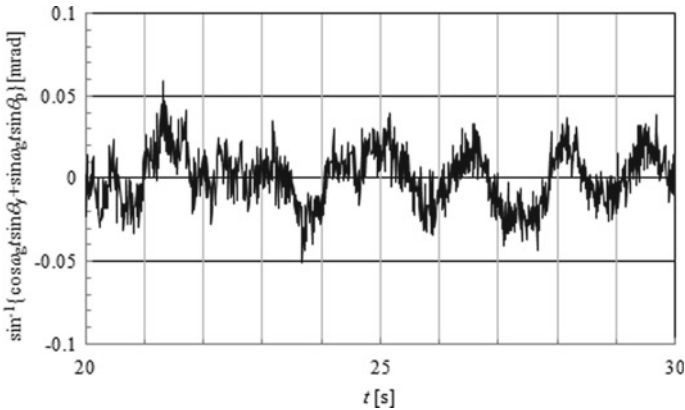


**Fig. 8** Angular signal modulated by the gyro rotation obtained from the measurement of the gyro angular signal based on the relation expressed by Eq. (8)

There can be seen an angular signal modulated by a gyro rotating period of  $T = 1$  s. Here, the signal is filtered by using running averaging for reducing high-frequency noise components shown in an angular signal of the gyro. At present, validity of the obtained signal can't be evaluated accurately; however, a signal waveform that its amplitudes and periods of the signal are considered to be reasonable.

## 5 Conclusion

Straightness evaluations by detecting tangential angles of the straightness are considered to be advantageous for evaluating large objects. We study a large scale straightness evaluation by using a gyro for detecting tangential angles of the straightness.

A rate offset which is fluctuation of an angular signal of gyro is considered to be a dominant error source for a precise gyro. Here, we adopted a rotating mechanism with a rotating rate up to several rps in order to realize continuous reversal measurements with a shorter interval for eliminating influences caused by faster changes of the rate offset.

An analysis shows that the rate offset can be derived by differences between two angular signals with one rotation period apart.

Experiments show that alignment error of the gyro direction affects angular signals of the gyro; however, the error can be derived and eliminated together with the rate offset from measurements for multiple rotating rates.

Angular deflections of a gyro rotating axis, which we aim to detect, modulated by the gyro rotation are derived by second-order difference of angular signals of the gyro for half and one rotation period apart and values obtained from  $\alpha$ ,  $\beta$ ,  $\omega$ ,  $\omega_g$ , and

*t.* At present the obtained angles can't be evaluated accurately; however, amplitudes and periods of the signal are considered to be reasonable.

**Acknowledgements** The authors thank Prof. M. Yamanaka and members in Mechanical Engineering Center at KEK for encouraging and supporting our studies. This work was supported by Collaborative Development Research Program of KEK (2014-ARL-2) and JSPS KAKENHI Grant Number 25420077.

## References

1. Kume T, Okuyama E, Satoh M, Suwada T, Furukawa K (2013) Large-scale accelerator alignment using an inclinometer. *Precis Eng* 37:825–830
2. Kume T, Satoh M, Suwada T, Furukawa K, Okuyama E (2015) Straightness evaluation using inclinometers with a pair of offset bars. *Precis Eng* 39:173–178
3. Kume T, Satoh M, Suwada T, Furukawa K, Okuyama E (2014) Large scale straightness evaluation using a gyro-reversal measurement for eliminating gyro drift. In: The 15th international conference on precision engineering, B27, Kanazawa, Ishikawa, Japan, July 22–25, pp 239–242



# Measurement and Compensation of Pivot Point Positional Error on Five-Axis Machine Tools



B. Yang, M. Chappell, J. E. Muelaner, G. Florussen, and P. G. Maropoulos

**Abstract** Measuring and compensating the pivot points of five-axis machine tools is always challenging and very time consuming. This paper presents a newly developed approach for automatic measurement and compensation of pivot point positional errors on five-axis machine tools. Machine rotary axis errors are measured using a circular test. This method has been tested on five-axis machine tools with swivel table configuration. Results show that up to 99% of the positional errors of the rotary axis can be compensated by using this approach.

**Keywords** Machine tool pivot point · Measurement · Error compensation

## 1 Introduction

With increasing demand for high precision manufacturing, five-axis machine tools became more and more important to allow parts with complex features to be machined. Compared to three-axis machines, five-axis machine tools have more complicated kinematic configurations. In order to machine high value parts with the required precision, one of the main challenges is to accurately measure and compensate the rotary axis pivot points [1].

Flaws in components and joints are the dominant error sources in five-axis machine tools, which lead to inaccurate alignment in rotary axes. These error sources can be classified as geometric errors, thermally induced errors and dynamics errors [2]. Geometric errors are the most significant factor affecting a machine's accuracy [3].

Several methods of testing the geometric accuracy of rotary axes have been introduced by ISO 230-1:2012 [4]. One of the conventional methods to measure rotary

---

B. Yang (✉) · M. Chappell · J. E. Muelaner · P. G. Maropoulos  
Department of Mechanical Engineering, University of Bath, Claverton Down, Bath, North East  
Somerset BA2 7AY, UK  
e-mail: [b.r.yang@bath.ac.uk](mailto:b.r.yang@bath.ac.uk)

G. Florussen  
IBS Precision Engineering, Esp 201, 5633 AD Eindhoven, The Netherlands

axis error is to use a touch trigger probe to measure the location of a spherical artefact [5]. The master ball is mounted on the rotary table which is then positioned at discrete angles. The touch probe determines the 3D position of the master ball by measuring five points to establish the actual location of the axis of the rotary table. Ball bar test are also widely used to test the rotary axes, recent research has been focused on development of double ball bar testing [6]. The development of R-test [7] allows three-dimensional errors of rotary axes to be measured. This method uses three proximity sensors to measure a sphere located on a rotary axis while the axis is rotated in synchronised motion with circular interpolation by two linear axes. The synchronised motion means that if no errors are present there will be no motion of the spindle relative to the sphere. Displacements of the ball relative to the spindle mounted sensors therefore provide measurement of the machine errors.

It has always been an engineering effort to reduce measurement time and facilitate automated or semi-automatic testing approaches to allow a rapid machine tool verification before major machining operations. This research is a continuous study of rapid machine tool verification [8] research by the University of Bath. This paper aims to develop a novel rapid automatic compensation approach for five-axis machine rotary axis pivot point positional errors by using novel circular test method performed by R-test [7]. An algorithm is developed and its implementation is experimentally investigated.

## 2 Machine Tool Configurations

Three machine tool kinematics configurations are investigated. As shown in Fig. 1, the first type is machine configured with a swivel head, the second type is machine configured with a swivel table and finally a machine configuration combining a swivel head and a swivel table. Measurement and compensation of machine configured with a swivel table is presented in this paper.

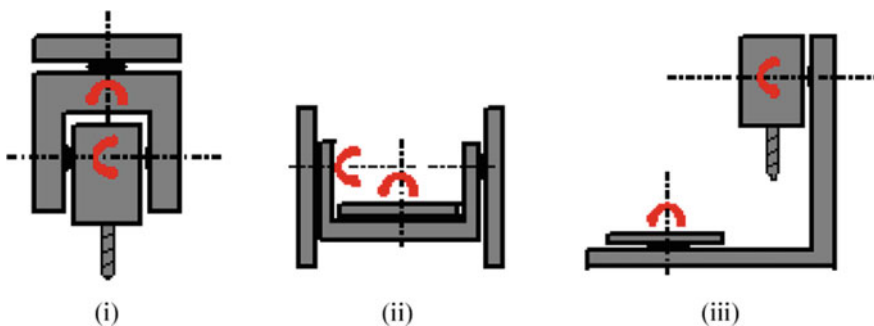


**Fig. 1** Three different machine tool kinematics configurations: (i) swivel head; (ii) swivel table and (iii) swivel head + swivel table

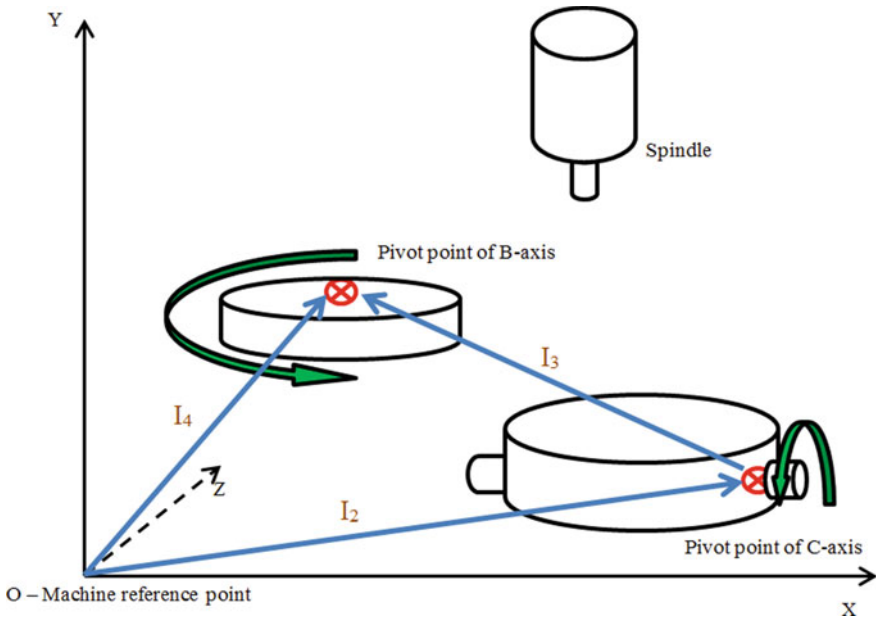


Fig. 2 Kinematic chain of machine tool with swivel table

The kinematic chain of machine tool configured with a swivel table is illustrated in Fig. 2. The 1st rotary axis of the transformation is the B-axis and the 2nd rotary axis is the C-axis. The kinematics transformation can be described as follows:

$$\vec{I}_4 = -(\vec{I}_2 + \vec{I}_3) \tag{1}$$

where;  $\vec{I}_2$  is the distance from the machine reference point to the pivot point of the 1st rotary axis,  $\vec{I}_3$  is the distance from the pivot point of the 1st rotary axis to the pivot point of the 2nd rotary axis and  $\vec{I}_4$  is the closure of the  $\vec{I}_4 = -(\vec{I}_2 + \vec{I}_3)$  vector chain.

Similarly, the kinematic transformation of machine with swivel head can be described as follows:

$$\vec{I}_1 = -(\vec{I}_2 + \vec{I}_3) \tag{2}$$

where;  $\vec{I}_2$  is the distance for the tool adapter to the pivot point of the 2nd rotary axis,  $\vec{I}_3$  is the distance from the pivot point of the 2nd rotary axis to the pivot point of the 1st rotary axis and  $\vec{I}_1$  is the closure of the  $\vec{I}_1 = -(\vec{I}_2 + \vec{I}_3)$  vector chain.

The kinematic chain of machine tool configured with a swivel head and a swivel table can be described as follows:

$$(\vec{I}_3 + \vec{I}_4) = -(\vec{I}_2 + \vec{I}_1) \quad (3)$$

where;  $\vec{I}_3$  is the distance from the machine reference point to the 2nd rotary axis,  $\vec{I}_4$  is the closure of the  $\vec{I}_4 = -\vec{I}_3$  vector chain,  $\vec{I}_2$  is the distance from the tool adapter to the pivot point of the 1st rotary axis,  $\vec{I}_1$  is the closure of the  $\vec{I}_1 = -\vec{I}_2$  vector chain.

The sign of the offset vectors are established according to the ISO 841 [9] standard using the right hand rule, which is also consistent with the ISO 230 [10] standards.

### 3 Development of Automatic Compensation Approach

The framework of the automatic compensation approach is presented in Fig. 3. The compensation approach uses measurement of the pivot point position of machine rotary axis to update the kinematics chain of machine tool configurations. By re-balancing the kinematics chain, corrected machine vectors are calculated to update the relevant parameters in the machine's controller. The approach was then implemented in Matlab to develop automatic pivot point compensation software.

First, a machine tool archive file must be generated from the machine controller. The program starts with reading machine information from an archive file to detect the kinematics configuration and also obtain relevant machine parameters such as pre-defined pivot point positions and the rotational vector of rotary axis. Once the machine type is confirmed, a physical measurement of the machine rotary axis pivot point is required. Based on the measurement results, the compensation parameters are calculated and the machine kinematics chain can be rebalanced. A machine readable update file is generated after each measurement, the program is finished when all axes are checked and all compensated results are within requirements.

The developed framework is applicable to all three machine configurations described above.

## 4 Measurement and Compensation

### 4.1 Measurement Strategy

Measurement and compensation of two five-axis machine tools with swivel table configuration are presented here. Figure 4a shows a machine configured with B + C rotary axis and figure b. shows a machine with A + C axis configuration.

A static measurement approach was used to measure both machines. The sphere artefact was positioned off the centreline to the measured axis (A, B or C). For the first machine, the B axis operation ranges from  $-15^\circ$  to  $+100^\circ$ , the machine was programmed to carry out a static measurement sequence with step angle of  $15^\circ$  from

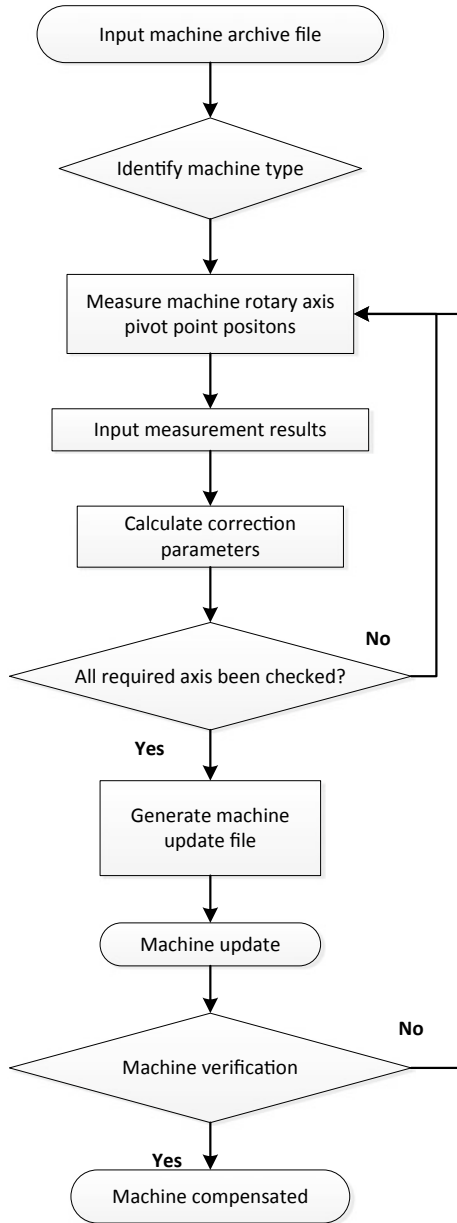
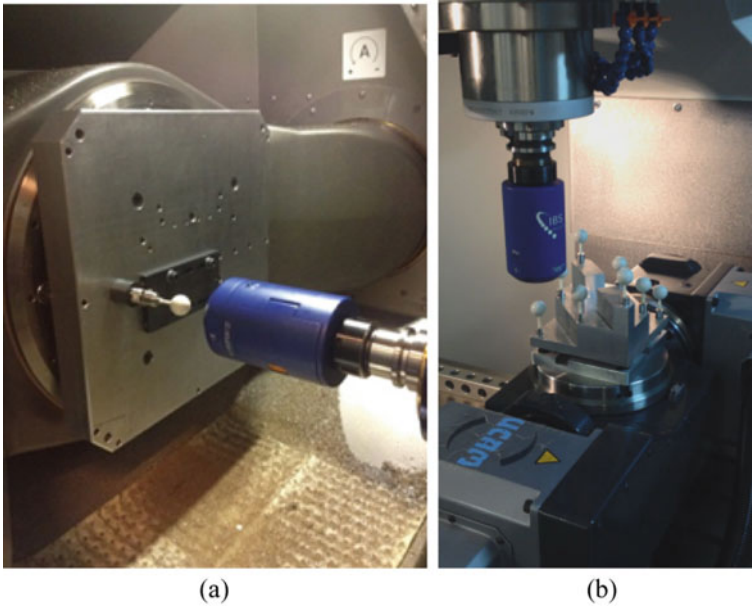


Fig. 3 Compensation flowchart for pivot point



**Fig. 4** Two machine tools with swivel table configuration were tested. **a** Machine with vertical spindle with B axis + C axis configuration, **b** machine with horizontal spindle with A axis + C axis configuration

$-10^{\circ}$  to  $+95^{\circ}$  using bidirectional setting. For the C axis, the measurement point was taken at stand still point with  $30^{\circ}$  step angle with one revolution clockwise (CW) and one revolution counter clockwise (CCW) set up.

For the second machine, the A axis operation ranges from  $-80^{\circ}$  to  $+80^{\circ}$ , the machine was programmed to carry out a static measurement sequence with step angle of  $15^{\circ}$ . The C axis measurement set up remains the same as the first machine.

Notation of machine rotary axis pivot point errors are listed in Table 1 according to the ISO 230 standards [10]. When measuring and compensating pivot points of machine configured with swivel table, the first rotary axis (A or B-axis) should be

**Table 1** Notation of machine rotary axis pivot point errors according to ISO 230 standard [10]

Pivot point location errors of machine rotary axis	
$E_{xob}$	Position error of B in X-axis direction
$E_{zob}$	Position error of B in Z-axis direction
$E_{xoc}$	Position error of C in X-axis direction
$E_{yoc}$	Position error of C in Y-axis direction
$E_{yoa}$	Position error of A in Y-axis direction
$E_{zoa}$	Position error of A in Z-axis direction

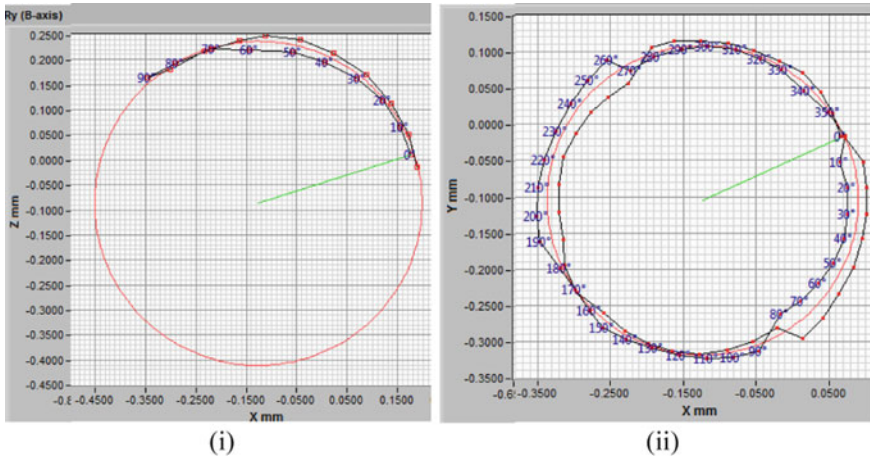


**Fig. 5** Measurement results of machine tool with B + C axis configuration. (i) B-axis before compensation. (ii) C-axis before compensation

also compensated first since the positional accuracy of second rotary axis (C-axis) is dependent to first rotary axis.

### 4.2 Compensation Results

The measurement results of the machine pivot point location before compensations are shown in Fig. 5. Significant pivot point location errors for both B and C axis were observed for the first machine. For B axis, the measured value of  $E_{xob}$  is  $-126 \mu\text{m}$  and  $E_{zob}$  is  $-87.2 \mu\text{m}$ . For C axis, both  $E_{xoc}$ ,  $E_{yoc}$  errors are over  $100 \mu\text{m}$ . For the second machine with A + C axis configuration, the measured errors  $E_{yoa}$  and  $E_{zoa}$  of A axis is  $-6.4 \mu\text{m}$  and  $-36.4 \mu\text{m}$  respectively. For C axis, about  $30 \mu\text{m}$  error was observed for both  $E_{xoc}$ ,  $E_{yoc}$ . The results show that the errors observed from both machines significantly affect the accuracy of the rotary axis, therefore, compensations are required.

Figure 6 shows the verified measurement results. Detailed data are presented in Tables 2 and 3 respectively for two measured machine types. For the first machine,  $E_{xob}$  error is largely reduced from  $-126 \mu\text{m}$  to  $0.6 \mu\text{m}$ , also more than 99% of errors in  $E_{zob}$  are compensated. For C axis, more than 95% of errors of the pivot point location are compensated. For the second machine, excellent compensation results are also achieved.

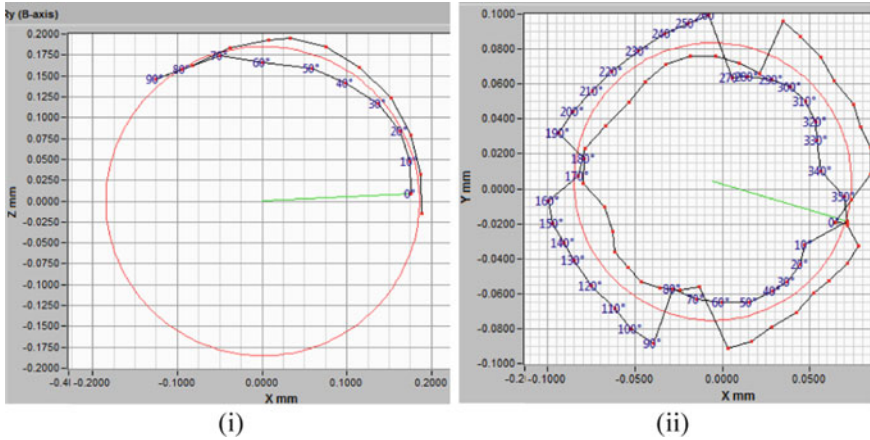


**Fig. 6** Measurement results of machine tool with B + C axis configuration. (i) B-axis after compensation. (ii) C-axis after compensation

**Table 2** Compensated pivot point location of machine with B + C axis configuration

	$E_{xob}$ ( $\mu\text{m}$ )	$E_{zob}$ ( $\mu\text{m}$ )	$E_{xoc}$ ( $\mu\text{m}$ )	$E_{yoc}$ ( $\mu\text{m}$ )
Uncompensated	-126	-87.2	-123	-105.2
Compensated	0.6	0.1	-5.5	4.2
Improvement (%)	99.5	99.9	95.5	96

**Table 3** Compensated pivot point location of machine with A + C axis configuration

	$E_{yoa}$ ( $\mu\text{m}$ )	$E_{zoa}$ ( $\mu\text{m}$ )	$E_{xoc}$ ( $\mu\text{m}$ )	$E_{yoc}$ ( $\mu\text{m}$ )
Uncompensated	-6.4	-36.4	-33.1	-28.9
Compensated	-0.3	-0.5	0.5	-0.3
Improvement (%)	95.3	98.6	98.5	99

## 5 Conclusions

A novel automatic compensation approach for five-axis machine tool rotary axis pivot point is presented in this paper. Three different machine tool kinematic configurations, swivel head, swivel table, swivel head + swivel table, can be compensated by this approach. The software automatically detects the machine type and calculates the compensated parameter for machine update. Measurements of two Trunnion machine tools, one with A + C rotary axis configuration, and one with B + C rotary axis are demonstrated, results show that up to 99% of pivot point positional errors are corrected. The pivot point verification and compensation approach is rapid, once the tool has been set up and the process takes around 10 min.



**Acknowledgements** The authors would like to gratefully acknowledge the financial support of the EPSRC, grant EP/K018124/1, “The Light Controlled Factory”, the EPSRC Case Award with NPL and the European Regional Development Fund grant reference 071\_000000203337. Thanks also go to the industrial collaborators for their contribution as well as the Department of Mechanical Engineering at the University of Bath.

## References

1. Jiang L, Ding G, Li Z, Zhu S, Qin S (2012) Geometric error model and measuring method based on work table for five axis machine tools. *Proc IMechE Part B J Eng Manuf* 227(1):32–44
2. Lei W, Paung IM, Yu C (2009) Total ballbar dynamic tests for five-axis CNC machine tools. *Int J Mach Tools Manuf* 49(6):488–499
3. Ibaraki S, Knapp W (2012) Indirect measurement of volumetric accuracy for three-axis and five-axis machine tools: a review. *Int J Autom Technol* 6(2):110–124
4. ISO230-1 (2012) Test code for machine tools—part 1: geometric accuracy of machines operating under no-load or quasi-static conditions. ISO.
5. Schwenke H, Knapp W, Haitjema H, Weckenmann A (2008) Geometric error measurement and compensation of machines—an update. *CIRP Ann Manuf Technol* 57:660–675
6. Jinag X, Cripps RJ (2014) A method of testing position independent geometric errors in rotary axes of a five-axis machine tool using a double ball bar. *Int J Mach Tools Manuf* 89:151–158
7. Muelaner JE, Yang B, Davy C, Verma MR, Maropoulos PG (2014) Rapid machine tool verification. In: *The 8th international conference on digital enterprise technology*, Stuttgart, Germany
8. Weikert S, Knapp W (2004) R-test, a new device for accuracy measurements on 5-axis machine tools. *CIRP Ann Manuf Technol* 53(1):429–432
9. International Organization for Standardization (2001) International Standard ISO 841: industrial automation systems and integration—numerical control of machines—coordinate system and motion nomenclature, 2nd edn. International Organization for Standardization, Geneva
10. International Organization for Standardization (2006) International Standard Committee Draft ISO/CD 230/1.4: test code for machine tools—part 1: geometric accuracy of machines operating under no-load or quasi-static conditions. International Organization for Standardization, Geneva

# A Novel Method of Rotational Error Analysis of Rotary Stages Based on Abbe Principle



Yi-Tsung Li and Kuang-Chao Fan

**Abstract** Abbe error is the inherent systematic error in linear displacement measurement due to the measuring axis is not in line with the moving axis. Similar to the Abbe principle, in the rotary stage the plane of rotary encoder cannot be on the same plane as the rotating table. The gap in between can also be regarded as Abbe offset. Due to the inherent tilt error and eccentric error of the working table in the rotary stage, such an offset would result in the lateral displacement of the encoder's sensing point. The actual measured angle is, therefore, different from the commanded angle, causing the rotational angle of the rotary stage. In this paper, a novel method of analyzing rotational error based on Abbe principle is proposed. Experimental results verified the correctness of the proposed method.

**Keywords** Rotary stage · Abbe error · Rotational error

## 1 Introduction

Rotary indexing devices are widely used in industry, such as in robotic arms, machine tools and coordinate measuring machines (CMM). In multi-axis real-time movement control, the cutting tool can be operated in the normal direction to cut the free form curved surface. Indexing table is also applied to CMM for measuring components which are of complicated shape. In a multi-axis machine, the rotational accuracy of the rotary axis is as important as those of the linear axes. Consequently, how to measure the accuracy of rotary devices is essential. The basic terminology used in the rotary measurement is based on the ASME B89.3.4 "Axes of Rotation and ISO 230-7 Geometric Accuracy of Axes of Rotation" standards [1, 2] specifying the radial error motion, axial error motion and tilt error motion. In recent studies, optical measurements for angle and displacement have widespread application in spindle tilt and eccentric measurement. Anandan et al. [3] proposed a ultrahigh speed miniature spindles error measurement system utilizing two laser Doppler vibrometer (LDV)

---

Y.-T. Li · K.-C. Fan (✉)

Department of Mechanical Engineering, National Taiwan University, 106 Taipei, Taiwan  
e-mail: [fan@ntu.edu.tw](mailto:fan@ntu.edu.tw)

© Springer Nature Switzerland AG 2022

S. Hinduja et al. (eds.), *Proceedings of the 38th International MATADOR Conference*,  
[https://doi.org/10.1007/978-3-319-64943-6\\_49](https://doi.org/10.1007/978-3-319-64943-6_49)

661

systems. It is shown that the average radial motion, synchronous radial error motion value and the standard deviation of the asynchronous radial error motion vary significantly with the spindle speed due to dynamic effects. They also applied three LDVs and rotary axis with a custom-fabricated sphere-on-stem precision artifact to simultaneously measure three-dimensional displacements [4]. The measured motion data are post-processed to obtain the synchronous and asynchronous components of the axial and radial error motions in both fixed-sensitive and rotating-sensitive directions, as well as the synchronous error motion values and the standard deviation of asynchronous error motions. Aketagawa et al. [5] introduces a measurement system for spindle radial, axial and angular motions using concentric circle grating and phase modulation interferometers. However, the experimental set-up is too complex and part of this error may be caused from the assembly error. Wang et al. [6] proposed a method with laser tracker on the basis of multi-station and time-sharing measurement principle. Based on the GPS principle, the actual coordinates of each measuring point during the turntable rotation can be determined by the measured data at different base stations. Then the motion error of turntable at different rotational angle can be determined by comparing the actual coordinates of each measuring point with its theoretical coordinates. Murakami et al. [7] proposed an optical measurement system for the simultaneous measurement of the five-degrees-of-freedom error motions of high-speed micro spindles utilizing two laser diodes, two PDs, two QPDs and some optical components. Measurement errors can be separated into three-dimensional (X, Y, Z) errors and two angular ( $\theta_X$ ,  $\theta_Y$ ) errors by theoretical analysis.

Abbe error is the inherent systematic error in precision positioning stages, machine tools, and measuring instruments [8]. It defines that the measuring apparatus is to be arranged in such a way that the distance to be measured is a straight-line extension of the graduation used as a gauge. Similar to the Abbe principle, in the rotary stage the plane of rotary encoder cannot be on the same plane as the rotating table. The gap in between can also be regarded as Abbe offset. Due to the inherent tilt error and eccentric error of the working table in the rotary stage, such an offset would result in the lateral displacement of the encoder's sensing point. The actual measured angle is, therefore, different from the commanded angle, causing the rotational angle of the rotary stage. In this paper, a more physical point of view is proposed to analyze the cause of rotational error from Abbe principle. The correctness is verified by experimental results.

## 2 Geometric Errors of Rotary Table

Rotary table has a rotational axis. It is known that there are six geometric errors, including three linear errors and three angular errors. Linear errors can be separated into axial errors and eccentric errors; angular errors can be separated into tilt error and rotation error. As shown in Fig. 1,  $\delta_X$ , and  $\delta_Y$  are radial errors,  $\delta_Z$  is axial error;  $\varepsilon_X$  and  $\varepsilon_Y$  are tilt errors,  $\varepsilon_Z$  is rotation error.

An ordinary rotation mechanism (including Encoder) is as shown in Fig. 2.

**Fig. 1** Geometry errors in rotary axis

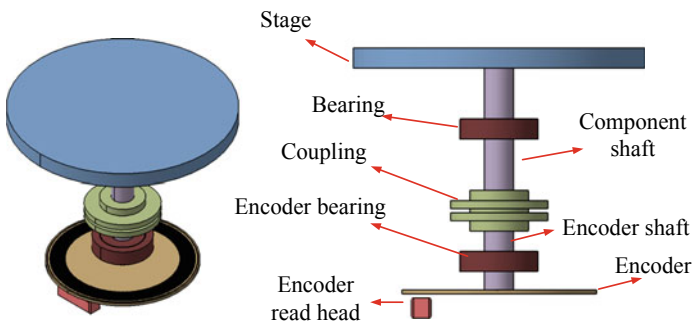
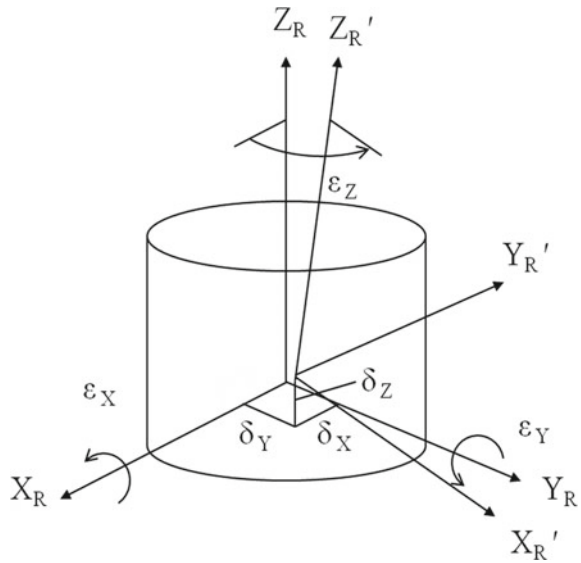


**Fig. 2** The structure of rotation mechanism

Figure 3 shows the coordinates of rotation mechanism. The rotation mechanism includes stage coordinates and encoder coordinates. The influencing factors of Abbe offset of the rotation mechanism are as follows: the distance from encoder center to encoder read head ( $L_0$ ), the radius of encoder ( $r_E$ ), the height from stage to encoder ( $Z_S$ ).

As shown in Fig. 4, owing to the tilt angle ( $\beta_S$ ) of the stage, a center offset ( $\delta$ ) would occur. When rotating ( $\theta$ ), the tilt angle may cause eccentric error  $\delta_X(\theta)$  and  $\delta_Y(\theta)$ .

Due to the eccentric of encoder, the positioning error of encoder read head would occur, as given in Fig. 5 and Eq. (1).

$$\delta_X(\theta) = \delta(\theta) \times \cos\varnothing$$

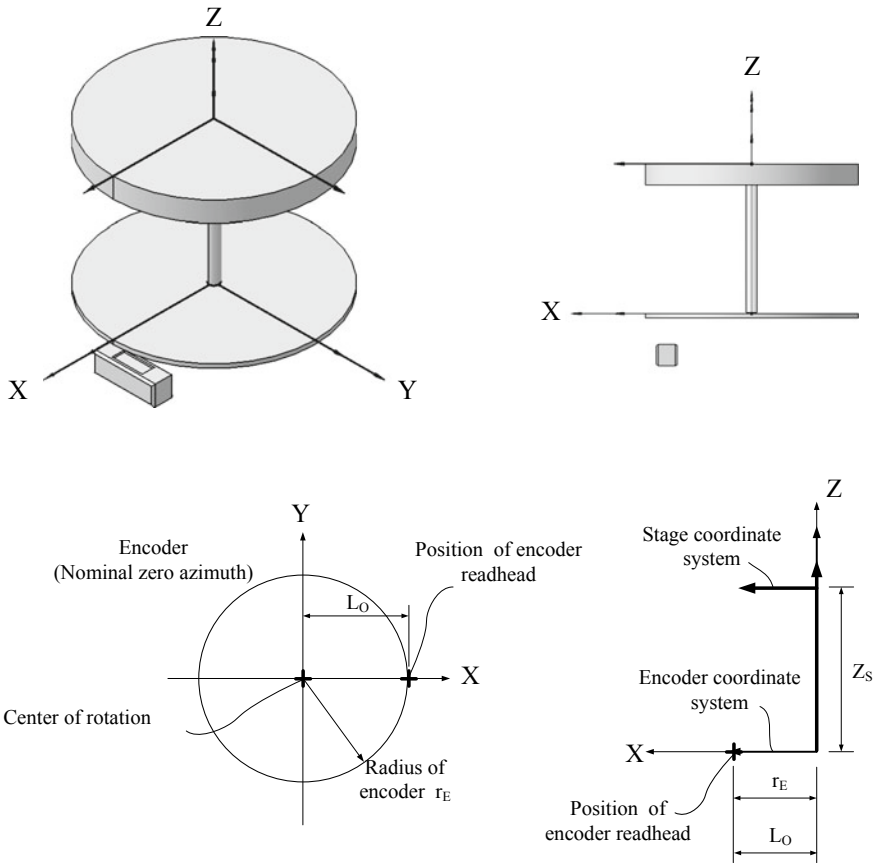
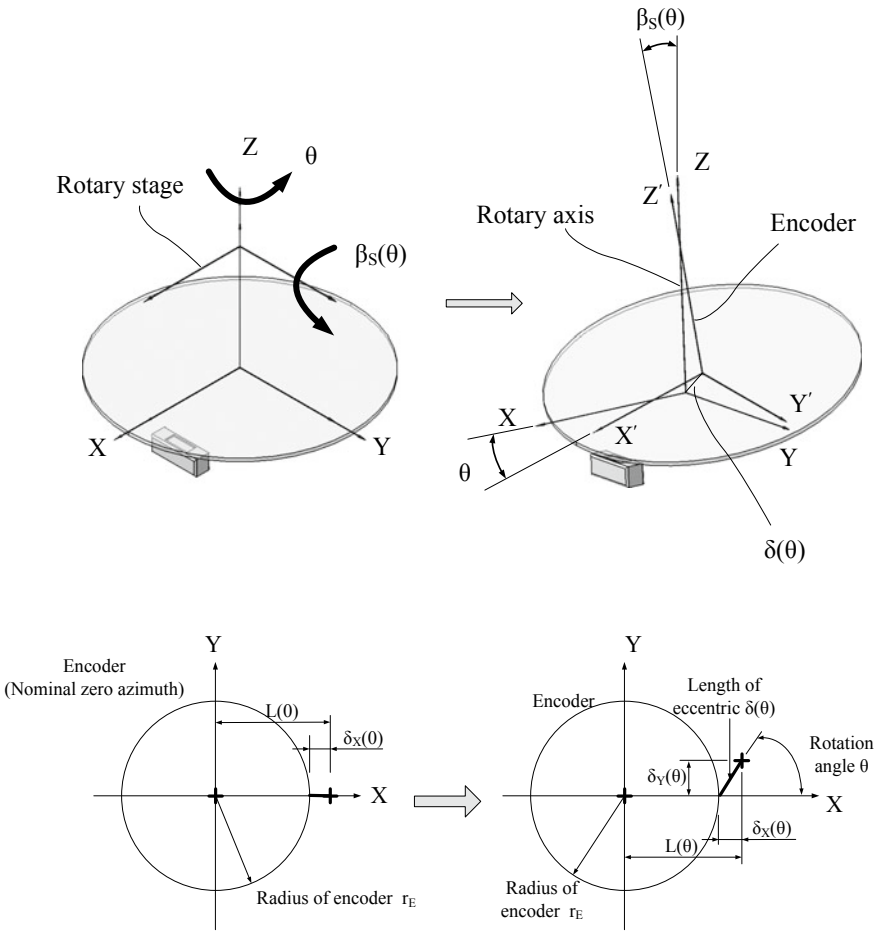


Fig. 3 The coordinates of rotation mechanism

$$\begin{aligned}
 \delta_Y(\theta) &= \delta(\theta) \times \sin\varnothing \\
 \varepsilon_Z(\theta) &= -\tan^{-1}\left(\frac{\delta_Y(\theta)}{r_E}\right)
 \end{aligned}
 \tag{1}$$

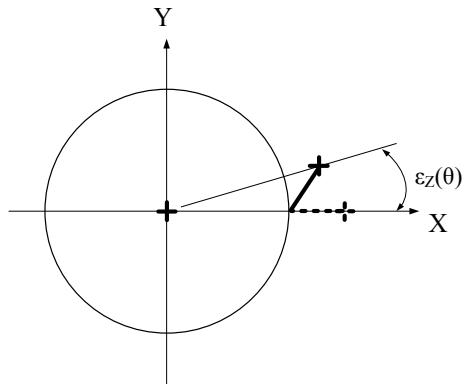
### 3 System Setup of the Measuring Device

As shown in Fig. 6, the rotary stage is driven by a step motor. The rotary stage is connected to an encoder to measure the stepper rotational errors. An optical measurement system is installed on the rotary stage to measure the stepper rotational errors simultaneously. The measurement system is composed of an autocollimator and a polygon. The autocollimator contains a laser diode, goniometer stage, optical



**Fig. 4** The abbe offset of rotation mechanism

**Fig. 5** The positioning error of encoder read head



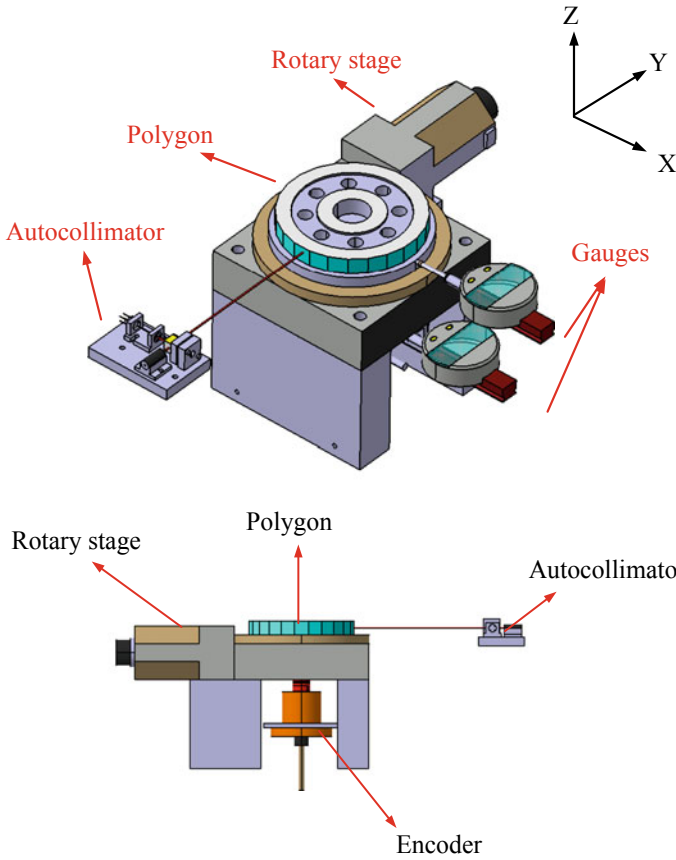


Fig. 6 Experimental setup

elements and a QPD. The autocollimator was calibrated by the HP5529A angular interferometer and the residual error is less than 1 arc-sec in the measuring range of  $\pm 150$  arc-sec. Tilt errors and eccentric errors are measured by traditional method, which uses two dial gauges to detect the radial shift of the spindle in different axial positions. When the rotary table rotates, the tilt errors and eccentric errors can be determined by two dial gauges installed at heights of working plane and encoder separately.

### 4 Experimental Verification

From Eq. (1), rotating errors are due to tilt and eccentric errors. The corresponding Abbe offset during rotational motion can be measured from the structure. Figure 7

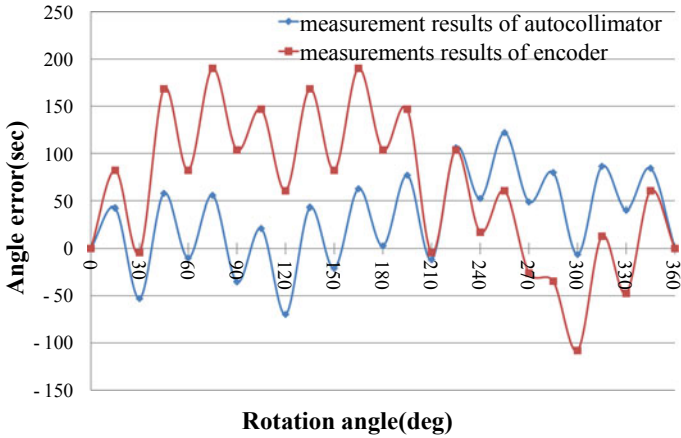


Fig. 7 Measured rotational errors

shows the results of rotational errors measured by the optical system and the encoder. The differences between those are shown in Fig. 8. The tilt errors and eccentric errors are measured and determined by two dial gauges, as shown in Fig. 9. Based on Eq. (1), calculating the rotational error from the tilt error and Abbe offset, the results are very close to the measured error, as shown in Fig. 10. This can prove that the Abbe error could affect the positioning of the rotary stage.

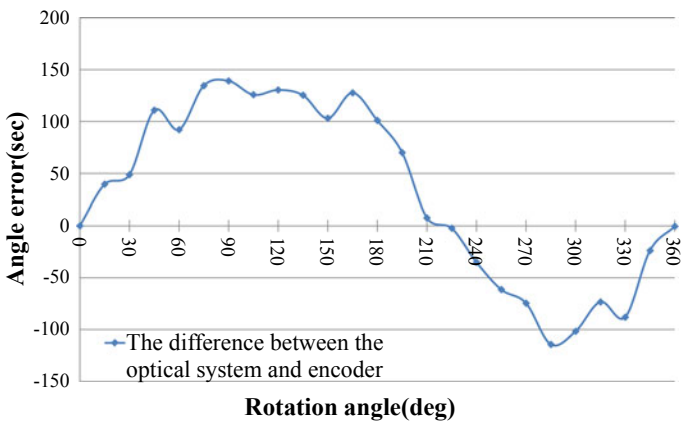


Fig. 8 Difference between the optical system and encoder



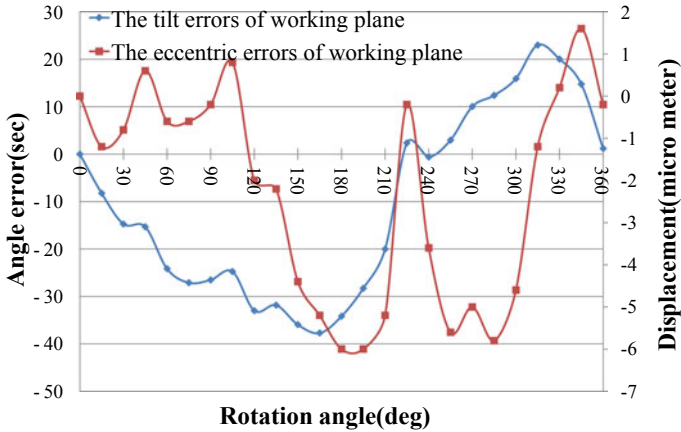


Fig. 9 The tilt errors and eccentric errors

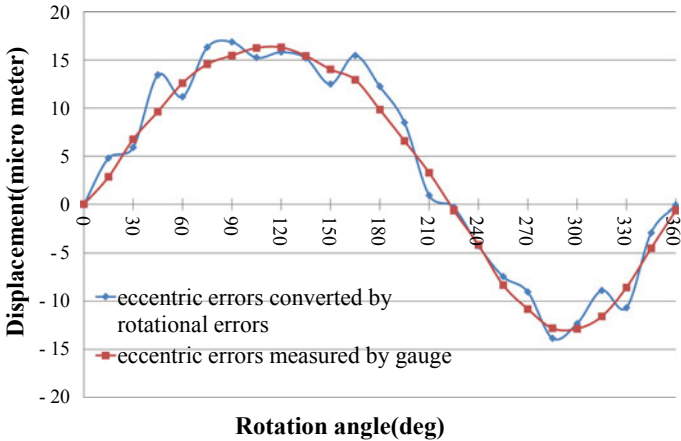


Fig. 10 Comparison of measured and calculated rotational errors

### 5 Conclusions

In this paper, a novel method of rotational error analysis of rotary stages caused by tilt errors and eccentric errors are proposed. The traditional method of analyzing rotational errors is on the working plane. From another viewpoint, the proposed method is to analyze the rotational errors from the tilt error and eccentric error, which will be enlarged by the height difference between the working plane and encoder. It is based on the well known Abbe principle and is more physically sensible. Experiments on rotary stage have been conducted and the correctness of the proposed method has been verified by the error analysis.

## References

1. ASME (2010) ASME B89.3.4-2010 axes of rotation: methods for specifying and testing
2. 230-7, I (2006) Test code for machine tools. Part 7: geometric accuracy of axes of rotation
3. Anandan KP, Tulsian AS, Donmez A, Ozdoganlar OB (2012) A technique for measuring radial error motions of ultra-high-speed miniature spindles used for micromachining. *Precis Eng* 36(1):104–120
4. Anandan KP, Ozdoganlar OB (2013) An LDV-based methodology for measuring axial and radial error motions when using miniature ultra-high-speed (UHS) micromachining spindles. *Precis Eng* 37(1):172–186
5. Aketagawa M, Madden M, Uesugi S, Kumagai T, Maeda Y et al (2012) Spindle error motion measurement using concentric circle grating and phase modulation interferometers
6. Wang J, Guo J, Zhou B, Xiao J (2012) The detection of rotary axis of NC machine tool based on multi-station and time-sharing measurement. *Measurement* 45(7):1713–1722
7. Murakami H, Katsuki A, Sajima T (2014) Simple and simultaneous measurement of five-degrees-of-freedom error motions of high-speed microspindle: error analysis. *Precis Eng* 38(2):249–256
8. Abbé E (1890) Meßapparate für Physiker. *Zeitschrift für Instrumentenkunde* 10:446–448

# Liquid Crystal Sensor for Label-Free Monitoring Hydrogen Peroxide Solution



Meng-Zhu Zhang, Li-Wei Jhang, and Shug-June Hwang

**Abstract** The liquid crystal (LC)-based sensor has received growing interest in recent years, due to the real-time detection of chemical reaction based on the stimuli-induced reorientation of LC molecules. In this work, a LC-based sensor for label-free identification of hydrogen peroxide ( $\text{H}_2\text{O}_2$ ) solution is demonstrated. The biosensor is achieved mainly by using amine-reactive layer and LC film. As the reaction layer is reacted with the hydrogen peroxide, the alignment of LC molecules will be disturbed, and then the color and brightness of this LC-sensing device will be changed. By analyzing the change in brightness caused by the reaction between the reaction layer and  $\text{H}_2\text{O}_2$  solution, the relationship between analytes concentration and reaction time can be established. As a result, the reaction time of hydrogen peroxide can be easily obtained and then the analytes concentration can be probed. The proposed LC biosensor has the advantages of low-cost, real time, label free and fast response.

**Keywords** Liquid crystal · Biosensor · Hydrogen peroxide

## 1 Introduction

In the food industry, the hydrogen peroxide ( $\text{H}_2\text{O}_2$ ) is often employed in the applications of the fungicides, preservatives, and bleaching agents. However hydrogen peroxide is an unstable substance, which easily react with oxygen and water to release out heat energy. Although it's nonflammable, but it is a strong oxidant with high toxicity. If uncaredful ingestion or inhalation of this substance happens, the hydrogen peroxide irritates the gastrointestinal tract and even severely increases the risk of ulcers and bleeding. Therefore excessive exposure to hydrogen peroxide will seriously endanger human health.

A sensor device for detecting hydrogen peroxide with fast response time, simple fabrication, and label free has received growing interests in recent years. There are

---

M.-Z. Zhang · L.-W. Jhang · S.-J. Hwang (✉)  
Department of Electro-Optical Engineering, National United University, Miaoli, Taiwan  
e-mail: [june@nuu.edu.tw](mailto:june@nuu.edu.tw)

several technologies proposed, such as electrochemical method [1, 2], chromatography [3], spectrometry [4], chemiluminescence [5] and so on. But most of these technologies are more complicated and costly. The LC-based sensor have been demonstrated to be excellent candidates for real-time, label-free, highly selective chemical and biological sensors. Since liquid crystals have the unique property of birefringence and a specific orientation, a LC-based biosensor has been reported to improve the shortcomings of the traditional sensors [6, 7], such as high cost, complex, long detection time and huge instrument. In this work, we combine the LC material to detect the oxidation reaction between the antioxidant and the amine-sensing layer. Based on the response time required by the orientational transition of LC molecules, hydrogen peroxide solution with different concentration can be monitored. Besides, a sensing layer made by different concentrations of N-(2-aminoethyl)-3-(trimethoxysilyl)propylamine (AEAPS) solution, 200 mM, 300 mM, 150 mM, were applied to study the impacts of the receptor concentration of sensing layer on the detection limit of the oxidant solution.

## 2 Experiment

### 2.1 Sensing Principle

The principle of the LC-based detection system is demonstrated as shown in Fig. 1. First of all, N-(2-aminoethyl)-3-(trimethoxysilyl)propylamine (AEAPS) as molecular receptors are immobilized on the homeotropic alignment layer (Fig. 1a), suggesting that LC molecules with a homeotropic orientation (perpendicular to the substrate surface). And then, a thin layer of LC is confined onto the substrate. When the LC-based sensor is exposed to target analytes solutions (hydrogen peroxide solution), which can penetration through LCs and binds to the molecular receptors on the substrate surface. If the binding of the analytes to the molecular receptors is stronger than the binding of the LCs, hydrogen peroxide could competitively adsorb at the AEAPS-coated interface, leading to the anchoring transition of LC from homeotropic

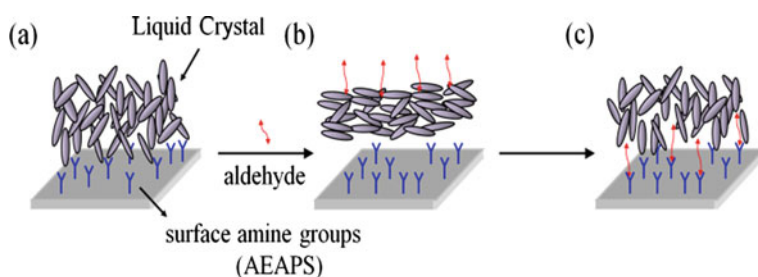


**Fig. 1** Target analytes affect the alignment direction of liquid crystal

to planar/tilted orientation (Fig. 1b). After the reaction of the amine-group molecular receptors and hydrogen peroxide analytes is completely done, the anchoring force of the homeotropic alignment layer will make LCs realigned vertically (Fig. 1c). As the reorientation of LCs happens, the transmitted light intensity under the cross-polarized microscope is changed.

## 2.2 Fabrication of LC-Based Sensor

In this work, surface coupling agent, octadecyldimethyl(3-trimethoxysilylpropyl) ammonium chloride (DMOAP), is applied to make LC molecules homeotropically aligned. The clean glass substrate was first immersed into an aqueous solution containing 2% (w/v) of DMOAP solution for 1 h, then rinsed with copious amounts of deionized water and dried in a 100 °C vacuum oven. Next, the DMOAP-coated glass substrate were immersed in AEAPS aqueous solution to make a amine-group sensing layer. Finally, a 100-mesh copper grid (width ~ 250 μm; depth ~ 20 μm) was placed onto an optimal amine-terminated glass substrate. Approximately ~0.5 μL of nematic liquid crystal (NLC, GLL 90148) was dispensed onto the copper grid, and excess NLC was carefully removed with a capillary tube. Finally, different concentrations of H<sub>2</sub>O<sub>2</sub> solution were injected into the LC biosensor and the transient response of analytes solution to receptors was monitored, respectively.

## 3 Experimental Results and Discussion

Herein, H<sub>2</sub>O<sub>2</sub> solution with different concentration was sensed. The analytes solution as an oxidant significantly reacts with the sensing layer on the glass surface and then disrupts the alignment of LC molecular, so bright optical images of a LC sample are observed during the monitoring period. As the reaction is finished, the anchoring force of vertical alignment layer makes LCs return to the initial homeotropic orientation, so dark state is found.

### 3.1 The Sensing Property of AEAPS Layer Made by 200 mM

Figure 2 shows the observed images under the exposure of the H<sub>2</sub>O<sub>2</sub> solution with different concentration exposed to the LC sample. As the analytes solution is injected into the LC sensor, bright optical images of LCs are observed because the LC-aqueous interface leads to a planar orientation of the LC molecules near the interface caused by the flow force of the injected solution. After some time, the images changes gradually from the bright to dark state, indicating that the initial orientation of LCs is changed from planar/tilted to homeotropic orientation. According to the experimental results,

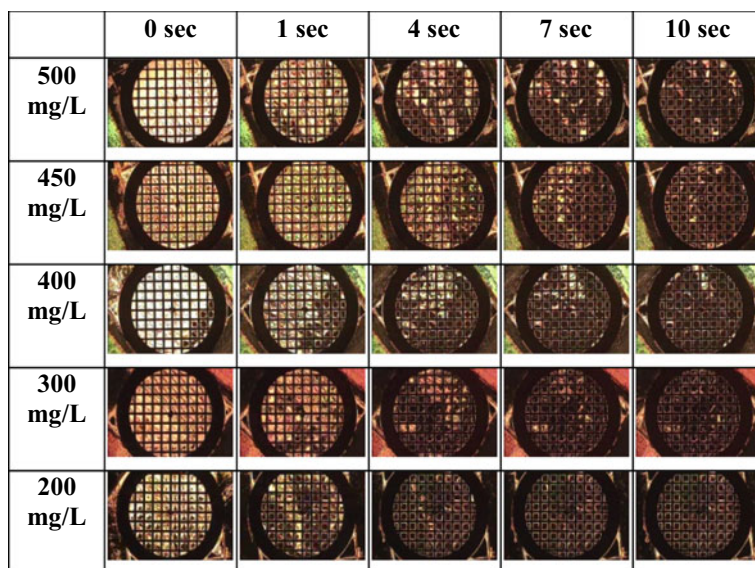


**Fig. 2** Cross-polarized optical images of LCs after analytes aqueous solution exposed to LCs for different  $\text{H}_2\text{O}_2$  solution concentrations

the response time required to recover the initial alignment of LC molecule increases with the concentration of hydrogen peroxide aqueous solution. In order to obtain a quantitative analysis from the observed images, the gray scale analysis was carried out by using the NI Vision Assistant image processing software.

Figure 3 demonstrates the transient gray scale intensity for different solution concentration. Based on the experimental results of Fig. 3, longer response time was

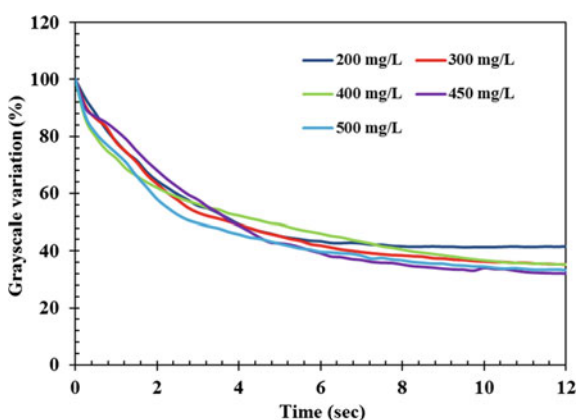


**Fig. 3** A transient grayscale variation of LC sensor for different concentration of hydrogen peroxide solution for 200 mM-AEAPS sensing layer

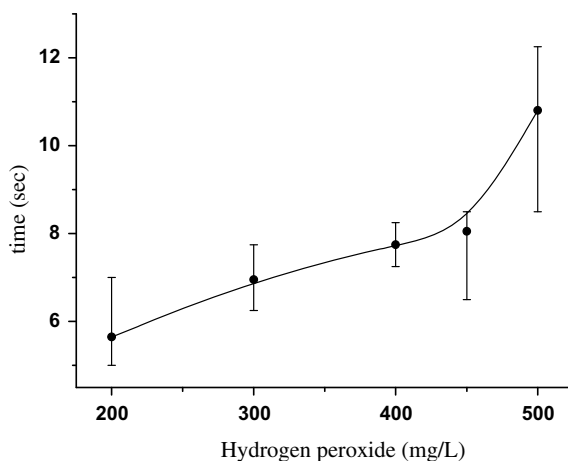


**Fig. 4** The dependence of the hydrogen peroxide solution concentration on the response time for 200 mM-AEAPS sensing layer

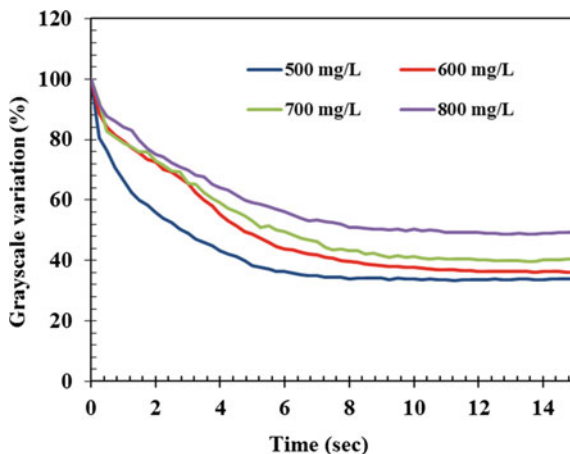
required for a higher concentration of hydrogen peroxide solution. To precisely obtain the response time of a LC sensor, we define the complete reaction time occurred at that nearly all values of the grayscale variation lie within three standard deviations of the mean in a normal distribution. As shown in Fig. 4, the influence of  $\text{H}_2\text{O}_2$  concentration on the response time has been achieved. The response time lengthens with increasing the  $\text{H}_2\text{O}_2$  concentration. Furthermore, we found the detection limit of  $\text{H}_2\text{O}_2$  aqueous solution is at 200–500 mg/L. As the analyte concentration is below the detection limit, the response time is too fast to accurately catch the images. On the contrary, the solution with higher concentration beyond the limit requires much longer response time.

To extend the detection limit of analytes aqueous solution, the sensing layer was made by the concentrations of AEAPS solution with 150 mM and 300 mM, respectively.

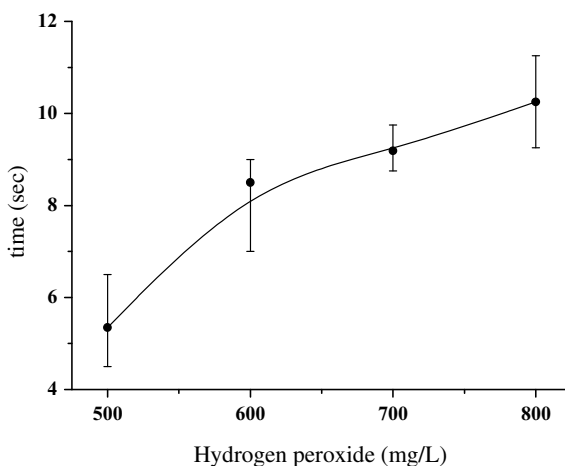
### 3.2 Sensing Layer Prepared by 300 mM-AEAPS Solution

Figure 5 demonstrates the transient grayscale variation for different  $\text{H}_2\text{O}_2$  solution concentration. We found the sensing characteristics agrees with the results of Fig. 3 well. The  $\text{H}_2\text{O}_2$  solution with higher concentration requires longer response time. As also shown in Fig. 6, the influence of  $\text{H}_2\text{O}_2$  concentration on the response time is achieved. The response time lengthens with increasing the  $\text{H}_2\text{O}_2$  concentration. In addition, we found the detection limit range of  $\text{H}_2\text{O}_2$  concentration is increased to be 500–800 mg/L. As a result, we can increase the AEAPS concentration to effectively raise the detection range of aqueous  $\text{H}_2\text{O}_2$  solution.

**Fig. 5** A transient grayscale variation of LC sensor for different concentration of hydrogen peroxide solution for 300 mM-AEAPS sensing layer



**Fig. 6** The dependence of the hydrogen peroxide solution concentration on the response time for 300 mM-AEAPS sensing layer



### 3.3 Sensing Layer Prepared by 150 mM-AEAPS

In this experiment, different concentrations of the analyte aqueous solution at 25, 50, 100, 200, 300, 400, 500 mg/L are monitored, respectively. We found the response time is too fast to accurately obtain for all solutions. The measured response time is almost the same for the  $H_2O_2$  concentrations at 25–500 mg/L. These phenomena are caused by the density of amine-group sensing layer is too low to provide the reaction with oxidant. Maybe decreasing the concentration of the analyte aqueous solution below 25 mg/L, the sensing properties of the proposed LC sensor can be precisely detected. The study of monitoring lower concentration of analyte solution will be done in the future.



## 4 Conclusion

We have demonstrated a LC-based oxidant sensor for real-time and label-free to monitoring  $\text{H}_2\text{O}_2$  solution. The orientational transition of LCs is easily observed by optical measurement during detecting  $\text{H}_2\text{O}_2$  aqueous solution. The detection principle is based on the orientational transition of LCs with a surface reaction between  $\text{H}_2\text{O}_2$  and surface amine groups. The orientational response of LCs to analyte solution is the result of competitive interactions between  $\text{H}_2\text{O}_2$  molecular and surface amine group such that a random planar to a homeotropic orientation. The variation of optical signals induced by surface reaction can therefore be probed in a real-time manner, and the optical appearance of LC-biosensor can be observed by the naked eye without requiring the complex instrumentation. This LC-based sensor system shows a wide detection limit of  $\text{H}_2\text{O}_2$  concentration dependent on the amine-group surface density. This work demonstrates the development of a simple and cost-effective LC-based hydrogen peroxide sensor.

**Acknowledgements** The authors would like to thank the National Science Council of Taiwan for financially supporting this research under contracts No. 103-2221-E-239-003.

## References

1. Garguilo MG, Proctor A, Michael AC (1993) Amperometric sensors for peroxide, choline, and acetylcholine based on electron transfer between horseradish peroxidase and a redox polymer. *Anal Chem* 65:523–528
2. Vreeke M, Maidan R, Heller A (1992) Hydrogen peroxide and beta-nicotinamide adenine dinucleotide sensing amperometric electrodes based on electrical connection of horseradish peroxidase redox centers to electrodes through a three-dimensional electron relaying polymer network. *Anal Chem* 64:3084–3090
3. Nakashima K, Wada M, Kuroda N, Akiyama S, Imai K (1994) High-performance liquid chromatographic determination of hydrogen peroxide with peroxyoxalate chemiluminescence detection. *J Liq Chromatogr* 17:2111–2126
4. Matsubara C, Kawamoto N, Takamura K (1992) Oxo [5, 10, 15, 20-tetra (4-pyridyl) porphyrinato] titanium (IV): an ultra-high sensitivity spectrophotometric reagent for hydrogen peroxide. *Analyst* 117:1781–1784
5. Chen W, Li B, Xu C, Wang L (2009) Chemiluminescence flow biosensor for hydrogen peroxide using DNAzyme immobilized on eggshell membrane as a thermally stable biocatalyst. *Biosens Bioelectron* 24:2534–2540
6. Bi X, Yang KL (2008) Real-time liquid crystal-based glutaraldehyde sensor. *Sens Actuators B* 134:432–437
7. Yang K-L, Cadwell K, Abbott NL (2005) Use of self-assembled monolayers, metal ions and smectic liquid crystals to detect organophosphonates. *Sens Actuators B* 104:50–56

# An Investigation on Simulation and Identification of Diffracted Moiré Patterns Within Optical Encoders



Lei Zhao, Hui Ding, Kai Cheng, and Shi Jin Chen

**Abstract** Depending on characteristics of high accuracy and resolution combined with a relatively low price, optical encoders as high-precision positioning sensors are broadly utilized in every application field where position and speed measurements are required for position or motion control, such as machine tools, CMM. As for machine tools, optical encoders are the metrology gauge of the measurement system, which quantify the motion displacement of machine tools on the basis of interference fringes named moiré patterns. However, due to numerous error factors such as geometric errors, thermal deformation having impact on the spatial distribution of moiré patterns, the displacement signals from encoders to CNC system almost contain deviations so that it results in motion error of axes of machine tools. To address this issues, this paper investigates the formation of moiré patterns by grating equation and diffractive theory and identifies them through a proposed refining criterion. Theoretical analysis and simulation result show that the research can provide a potential opportunity to assess the influence of error factors of machine tools on the readout of linear encoders.

**Keywords** Diffracted moiré patterns · Optical encoder · Refining criterion · Fourier transform

## 1 Introduction

As the functional requirements of components and products become more sophisticated and their dimensional tolerances become tighter, the accuracy enhancement of machine tools is increasingly essential for the machine tool users and manufacturers [1]. In order to enhance the accuracy of machine tools particularly in process, it

---

L. Zhao · H. Ding · K. Cheng (✉) · S. J. Chen  
School of Mechatronics Engineering, Harbin Institute of Technology, Harbin 150001, China  
e-mail: [kai.cheng@brunel.ac.uk](mailto:kai.cheng@brunel.ac.uk)

K. Cheng  
Department of Mechanical and Aerospace Engineering, Brunel University London, Uxbridge UB 3PH, UK

is necessary to carry out quantitative analysis on errors sources such as geometric error on the measurement system of machine tools. Due to high resolution per cost ratio, strong stability to environmental factors such as temperature, humidity and liquid splash, linear optical encoders as high-precision positioning sensors have been frequently and widely adopted to construct the measurement system of machine tools, particularly ultra-machine tools [2]. Based on the interference fringes called moiré patterns produced by the relative displacement between double gratings, linear optical encoders can achieve 10 nm resolution, 1  $\mu\text{m}$  accuracy or even higher. However, comparing with high-precision of optical encoders, machine tools own lower accuracy. One main reason for this phenomenon is that numerous error factors of machine tools such as geometric errors, thermal deformation and errors induced by cutting vibrations and forces have some impact on the volumetric distribution of moiré patterns, which directly determines the displacement signals accepted by the control system.

So far, the literature devoted to this aspect of linear encoder's behavior is unfortunately not abundant, comparing with the considerable amount of work on analyzing errors of machine tools [3]. Alejandre and Artes [2–7] as engineers of Fagor Company make a big contribution to this area. In their opinions, the encoder itself is considered as an error source and analyzed on the value of different kinds of errors inside it: strain and displacement errors, thermal errors and errors caused by vibrations. Additionally, the experimental result shows that the measurement error of linear encoders can be three times its precision, and wide areas of large measuring uncertainty are present in the frequency span. Song [8] explores that the unwanted additional tilt angle change of the index grating relative to the scale grating causes comparatively large displacement errors in linear encoders and develops a hardware compensation method.

As mentioned above, moiré patterns are the basis of measuring relative displacement for optical encoders, so it is essential and necessary to investigate the direct influence of external error factors on them. To address this issues, this paper takes a reflective-type linear encoder for example to illustrate the simulation and identification of moiré patterns.

## 2 Optical Simulation of Reflective-Type Linear Encoders

### 2.1 Introduction to Reflective-Type Linear Encoders

A reflective-type optical encoder in Fig. 1 composes of a reflective phase grating named the scale grating, a transparent phase grating called the index grating, a LED light source, a condenser lens, and a set of photocells. The scale grating is installed on a scale and the index grating is located in the scanning head. From the view of Fig. 1, the propagation process of light wave can be explained as follows: (1) After a beam of spherical light wave emitted by the LED passes through the condenser lens, it is

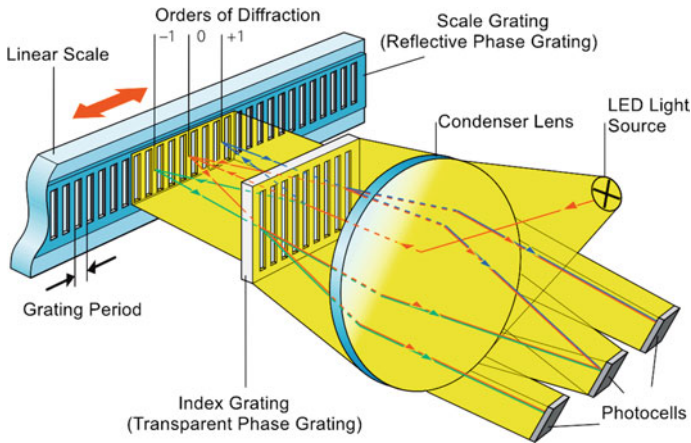


**Fig. 1** Mechanical sketch of the arrangement of components of a reflective optical encoder [9]

transformed into a beam of plane light wave; (2) When the plane wave is via the scale grating, it is diffracted into three beams of light wave with equal luminous intensity; (3) With regard to each beam of light, the diffraction and reflection occur in the scale grating and most of luminous intensity is averagely split into the reflected diffraction orders + 1 and - 1; (4) Once again, these diffracted waves cause diffraction when they meet at the scale grating; (5) Lastly, these beams of light interfere and then produce periodic moiré patterns with alternating light intensity on the photocells which convert moiré patterns into electrical signals. Subsequently, CNC system of machine tools based on the signals generates NC code to achieve position control. According to description above, the optical system of an encoder in Fig. 1 can be simplified as illustrated in Fig. 2. As a relative motion between gratings happens along X direction, electrical signals undergo changes in phase which determine axis movements of a machine tool, accompany with the translation shift of moiré patterns. To analyze the moiré patterns, two ways based on grating equation and diffractive theory are proposed.

## 2.2 Optical Simulation Based on Zemax

For a phase grating, it is considered that it is made up of a set of slits with equal space  $d$ , which must be wider than the wavelength of interest to generate diffraction. Assuming a beam of plane wave of monochromatic light with wavelength  $\lambda$  incidents with the polar angle  $\theta$  and orientation angle  $\phi$ , the spatial direction of  $m$  order diffracted wave is determined by grating equation expressed as:

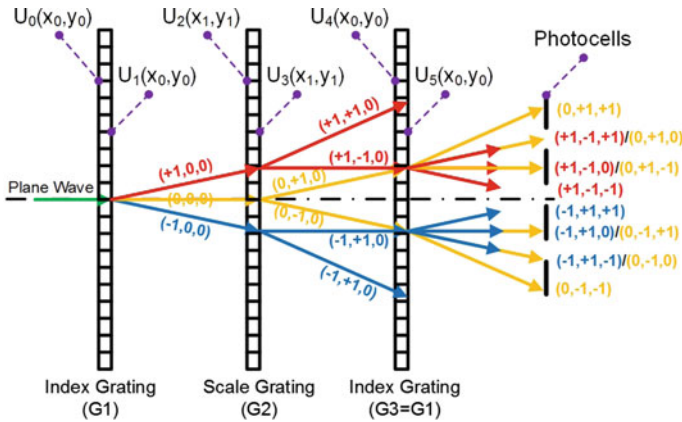


**Fig. 2** Schematic diagram of the wavefront change of a plane wave travelling through the optical system of an encoder

$$\begin{cases} n_l \sin \theta_m \cos \phi_m = \sin \theta \cos \phi + m \frac{\lambda}{d} \\ n_l \sin \theta_m \sin \phi_m = \sin \theta \sin \phi \end{cases} \quad (1)$$

where  $\theta_m$  and  $\phi_m$  represent the polar angle and orientation angle of  $m$  order diffracted wave,  $n_l$  the refractive index of the phase grating. Combing grating equation with ray tracing, it provides an opportunity to calculate the spatial distribution of moiré patterns of the optical system in Fig. 2 and then is verified through a commercial optical software Zemax. The simulation model given in Fig. 3a is built. Figure 3b shows the simulation result when the energy efficiency parameters of the index grating and the scale grating in  $-1, 0, +1$  order are set as (0.33, 0.33, 0.33) and (0.5, 0, 0.5), respectively.

### 2.3 Optical Simulation Based on VirutalLab

Due to lack of a parameter to stand for the phase shift caused by phase grating in Eq. 1, diffractive theory is used to analyze the optical system as well, from the view of wavefront function. In Fig. 2, the travelling journey of wavefront function of a plane wave can be described as:

$$U_0(x_0, y_0) \rightarrow U_1(x_0, y_0) \rightarrow U_2(x_1, y_1) \rightarrow U_3(x_1, y_1) \rightarrow U_4(x_0, y_0) \rightarrow U_5(x_0, y_0)$$

Based on Fourier Transform, the journey can be modeled as Eq. 2:

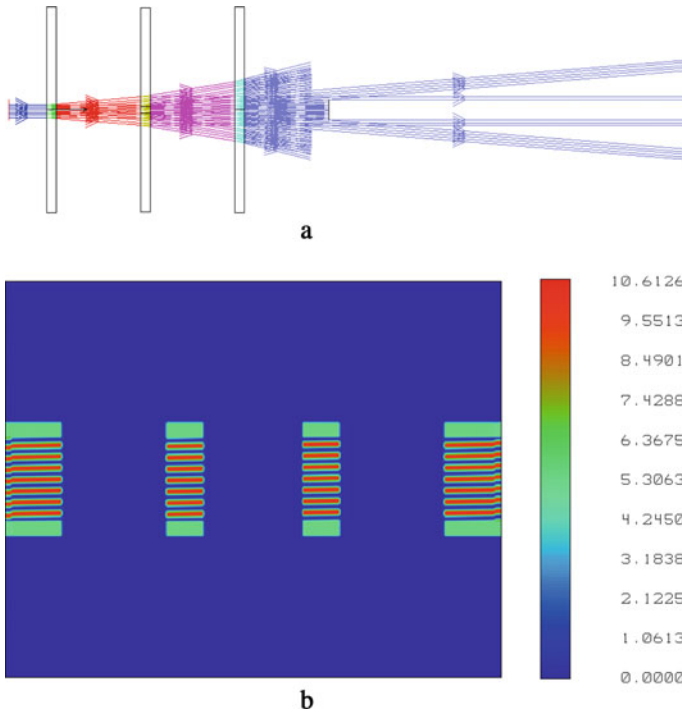


**Fig. 3** The model (a) and result (b) of the optical system according to Fig. 2 based on Zemax

$$\begin{cases}
 \mathbb{F}\{U_1(x_0, y_0)\} = \mathbb{F}\{U_0(x_0, y_0)\} \otimes \mathbb{F}\{t_1(x_0, y_0)\} \\
 \mathbb{F}\{U_2(x_1, y_1)\} = \mathbb{F}\{U_1(x_0, y_0)\} \cdot \mathbb{F}\{h(x_1, y_1)\} \\
 \mathbb{F}\{U_3(x_1, y_1)\} = \mathbb{F}\{U_2(x_1, y_1)\} \otimes \mathbb{F}\{t_2(x_1, y_1)\} \\
 \mathbb{F}\{U_4(x_0, y_0)\} = \mathbb{F}\{U_3(x_1, y_1)\} \cdot \mathbb{F}\{h(x_0, y_0)\} \\
 \mathbb{F}\{U_5(x_0, y_0)\} = \mathbb{F}\{U_4(x_0, y_0)\} \otimes \mathbb{F}\{t_1(x_0, y_0)\} \\
 U_5(x_0, y_0) = \mathbb{F}^{-1}\{\mathbb{F}\{U_5(x_0, y_0)\}\}
 \end{cases} \tag{2}$$

where  $t(x, y)$  is a function based on the comb function and rectangular function to define the physical structure of a phase grating, as described in Eq. 3:

$$t(x, y) = (e^{j\phi_2} - e^{j\phi_1}) \left[ \text{rect}\left(\frac{x}{a}\right) \otimes \frac{1}{d} \text{comb}\left(\frac{x}{d}\right) \right] + e^{j\phi_1} \tag{3}$$

$h(x, y)$  represents the propagation of light wave in the free space, defined as Eq. 4.

$$h(x, y; x_0, y_0) = \frac{\exp\left[ jk\sqrt{z^2 + (x - x_0)^2 + (y - y_0)^2} \right]}{j\lambda\sqrt{z^2 + (x - x_0)^2 + (y - y_0)^2}} \tag{4}$$

In this paper, a software named LightTrans VirtualLab is applied to handle the propagation described by Eq. 2. With VirtualLab, the simulation model is constructed as displayed in Fig. 4a and the result is shown in Fig. 4b when the phase parameter  $\varphi_2$  of the index and scale grating is separately equal to 2.008 and 3.142, which is evaluated in accordance with Fourier transform of Eq. 3 and energy distribution in all diffractive directions.

Comparing Fig. 3b with 4b, there are two main conclusions to be drawn. On one hand, the simulations both produce four clusters of moiré patterns individually with the same numbers of fringes. On the other hand, with respect to the same phase between every cluster of moiré patterns in Fig. 3b, there is an obvious phase difference in Fig. 4b and the major reason is that the phase grating makes an effect on the phase of the plane wave during travel.

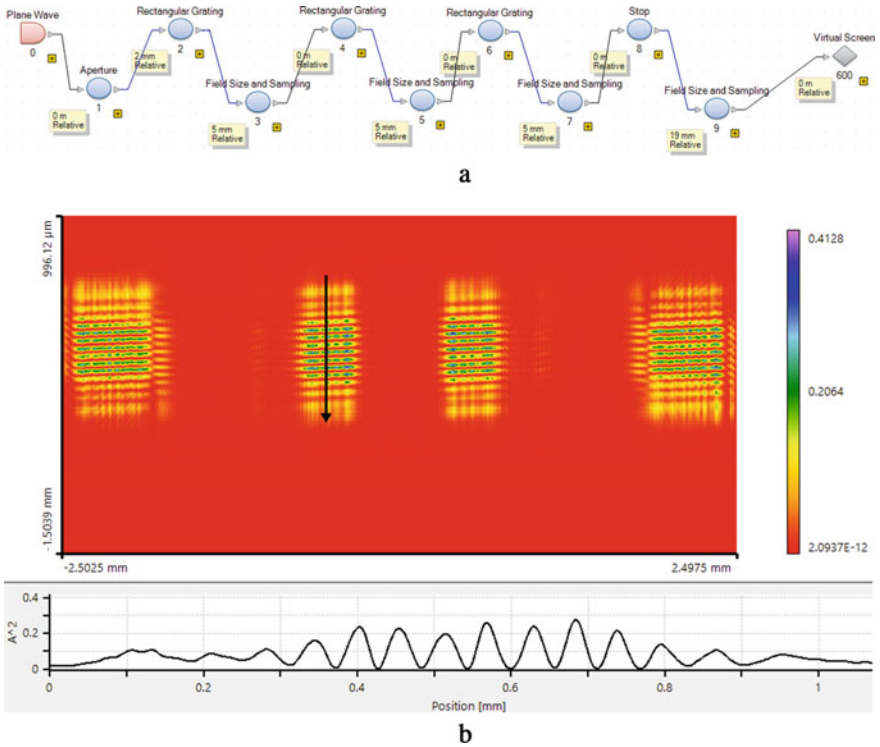


Fig. 4 The model (a) and result (b) of the optical system according to Fig. 2 based on VirtualLab

### 3 Identification of Period and Phase of Moiré Patterns by the Proposed Criterion

Generally, a mathematical description of moiré patterns can be given by Eq. 5 [2]:

$$S(x) = B + A \sin\left(2\pi \frac{x}{p} + \varphi\right) \tag{5}$$

where  $A$  is the amplitude,  $B$  the signal’s mean value,  $\varphi$  the signal’s phase,  $x$  the measured position and  $p$  the period of moiré patterns. To identify and estimate the period  $p$  and phase  $\varphi$ , a novel approach is developed. In this paper, the left-most cluster of moiré patterns in Fig. 3b is chosen to explain this approach in detail.

According to the symmetry of the optical system in Fig. 2, it can be concluded that  $\varphi$  is equal to  $\pi/2$  and  $B$  is a constant value. From Fig. 5, it can be seen that the data from the left-most cluster of moiré patterns appears significant periodicity, which represents the actual signal  $S'(x)$  with respect to  $S(x)$ . The influence of some noise signals such as harmonic signals and Gaussian noises results in the difference between  $S(x)$  and  $S'(x)$  and thus  $S'(x)$  can be deduced as Eq. 6:

$$S'(x) = S(x) + \sum_{k=2}^n A_k \sin\left(2\pi k \frac{x}{p} + \varphi_k\right) + A_G \frac{1}{\sqrt{2\pi}\sigma} \exp\left[-\frac{(x-a)^2}{2\sigma^2}\right] \tag{6}$$

On account of  $S(x)$  occupying major proportion of  $S'(x)$ , Spectrum amplitude of  $S'(x)$  in the frequency domain obtain the maximum peak value at the point  $f_1 = 1/p$ . However, due to discreteness of  $S'(x)$ , its FFT results, marked as  $F\{S'(x)\}$ , possess a set of discrete value  $\{f'_n\}$  ( $n = 0, 1, \dots$ ) with same interval in the frequency coordinate system. Therefore, it is inevitable to cause the fence effect which leads to the phenomenon that the frequency  $f'_1$  where  $F\{S'(x)\}$  obtains the maximum peak value is not consistent with  $f_1$ . So, in order to solve this problem, a novel approach

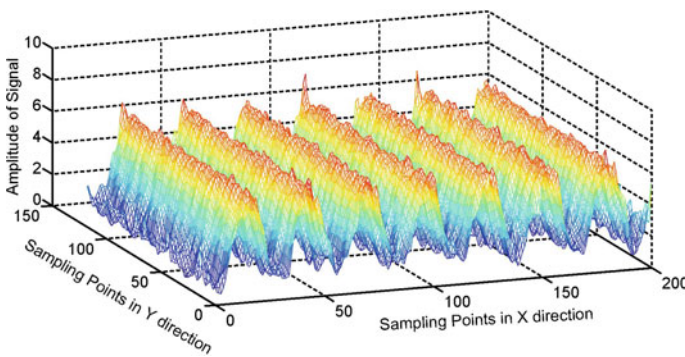
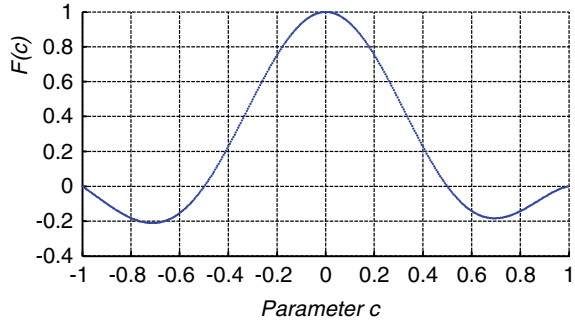


Fig. 5 The data from the left-most cluster of moiré patterns in Fig. 3b, handled by MATLAB



**Fig. 6** The value of function  $F(c)$  in Eq. 8 when  $c$  varies in the range  $(-1, 1)$



is proposed to refine the gap between  $f_1$  and  $f'_1$ . Firstly, it is supposed that an initial value of  $f_1$  is  $f'_1$ . Secondly, according to the influence of effect fence, it can be judged that  $f_1$  should be located in the range of from  $f'_1 - \Delta f'$  to  $f'_1 + \Delta f'$ . Thirdly, to determine the position of  $f_1$ , the range is equally divided into  $N$  parts to create a set of discrete points and then any one  $f_x$  of these points value can be described as:

$$f_x = f'_1 + c' \cdot 2\Delta f' / N = f_1 + c \cdot 2\Delta f' / N \tag{7}$$

where  $\Delta f'$  is the interval between any two points of  $\{f'_n\}$ . Lastly, a mathematic criterion is developed as Eq. 8 to settle the parameter  $c$ :

$$F(c) = \frac{\int_{-T}^T S'(x) \cdot \cos(2\pi f_x x) dx}{(\sqrt{1/f_x})^3} \tag{8}$$

On the basis of orthogonality of trigonometric function and without consideration of Gaussian noises, the numerical solution of Eq. 8 is displayed in Fig. 6. Clearly, when parameter  $c$  is equal to zero where  $f'_1 = f_1$ , the function obtains the maximum value. Hence, the period of moiré patterns can be calculated by Eqs. 7 and 8.

Furthermore, the phase can be figured out by Eq. 9:

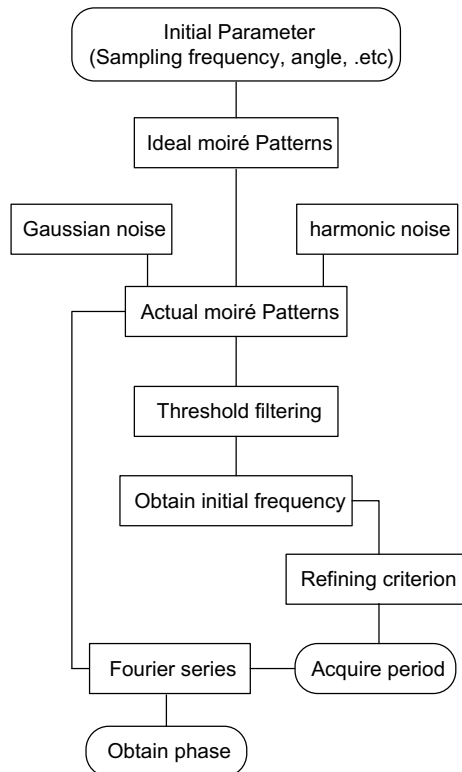
$$\begin{cases} a_k = \frac{2}{T} \int_{-T/2}^{T/2} S'(x) \cos(2\pi k f_1) dx \\ b_k = \frac{2}{T} \int_{-T/2}^{T/2} S'(x) \sin(2\pi k f_1) dx \\ \varphi_k = \arctg\left(\frac{a_k}{b_k}\right) \end{cases} \tag{9}$$

### 4 Simulation Verification of Identification of Moiré Patterns

To prove this novel approach in theory, a simulation system is constructed with MATLAB. In this system, the moiré patterns are randomly created by random functions. Simultaneously, Gaussian noises and harmonic noises are brought in to represent the noise signals during the process of analysing moiré patterns. The schematic diagram of the simulation system is illustrated as Fig. 7 and the ideal and actual signal of moiré patterns generated is given in Fig. 8.

Figure 9a shows the result of period  $p$  with the condition that phase  $\varphi = 0$  and tilt angle of moiré patterns  $\alpha = 1^\circ$  as the simulation system runs 40 times, which can obtain 40 sampling points. The blue squares named ‘Ideal Period’ are the actual period from the ‘Initial Parameter’ module and the red stars named ‘Identified Period’ figure the predicted period estimated by the refining criterion. Similarly, Fig. 9b displays the result of phase  $\varphi$  with the assumption that period  $d = 0.85$  and  $\alpha = 1^\circ$ . It is clear that the approach proposed in this paper is available in the identification of moiré patterns.

Fig. 7 Schematic diagram for the simulation system



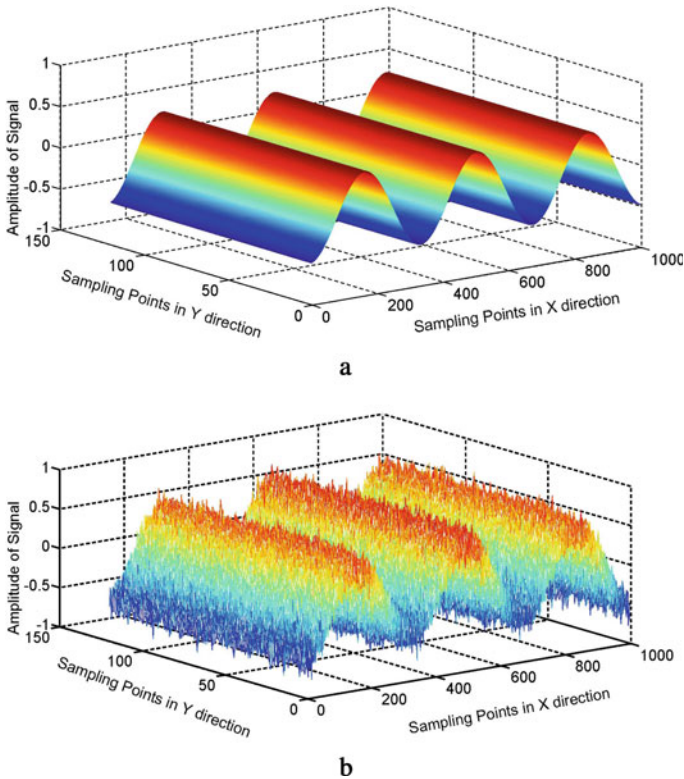
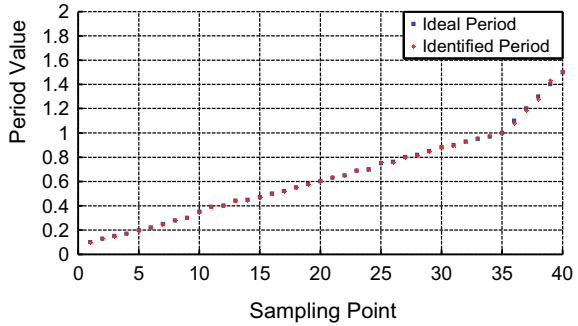


**Fig. 8** The ideal (a) and actual (b) signals of moiré patterns generated by the simulation system

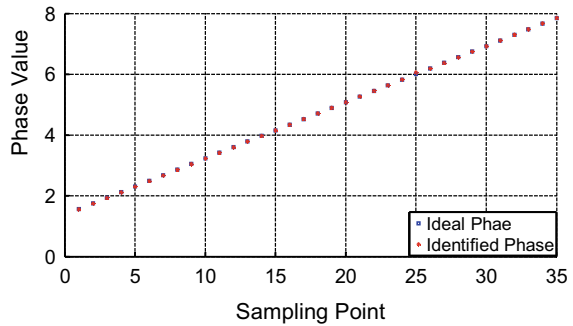
## 5 Conclusions

In this paper, two ways based on Zemax and VirtualLab are proposed to simulate moiré patterns of a reflective double optical encoder and two conclusions are drawn: (1) Both of the simulation results are consistent without considering the influence of the grating's phase on travelling wave; (2) The simulation by VirtualLab shows there is an obvious phase difference between every cluster of moiré patterns, with respect to that by Zemax. To estimate the period and phase of moiré patterns, a novel approach is theoretically derived and tested by a simulation system with MATLAB. The simulation result verifies the fact that the approach has an access to identify the period and phase of moiré patterns. In summary, the research presents a possibility to assess the impact of the dynamic real errors of machine tools on the readout of optical encoders determined by moiré patterns, although it needs to be further evaluated and validated experimentally.

**Fig. 9** Simulation result of period (a) and phase (b) identified by the simulation system



a



b

## References

- Schwenke H et al (2008) Geometric error measurement and compensation of machines—An update. *CIRP Ann Manuf Technol* 57(2):660–675
- Lopez J, Artes M (2012) A new methodology for vibration error compensation of optical encoders. *Sensors (Basel)* 12(4):4918–4933
- Artes M, Alejandre I (2004) Machine tool errors caused by optical linear encoders. *Proc Inst Mech Eng Part B J Eng Manuf* 218(1):113–122
- Alejandre I, Artes M (2006) Thermal non-linear behaviour in optical linear encoders. *Int J Mach Tools Manuf* 46(12–13):1319–1325
- Alejandre I, Artés M (2007) Method for the evaluation of optical encoders performance under vibration. *Precis Eng* 31(2):114–121
- López J, Artés M, Alejandre I (2011) Analysis of optical linear encoders’ errors under vibration at different mounting conditions. *Measurement* 44(8):1367–1380
- López J, Artés M, Alejandre I (2012) Analysis under vibrations of optical linear encoders based on different scanning methods using an improved experimental approach. *Exp Tech* 36(6):35–47
- Song J-H, Kim K-C, Kim SH (2000) Reducing tilt errors in moiré linear encoders using phase-modulated grating. *Rev Sci Instrum* 71(6):2296–2300
- [www.heidenhain.com](http://www.heidenhain.com)

# **Micro/Nano Fabrication and Manipulation**

# Microfabrication of Three-Dimensional Structures Using Nanoparticle Deposition with a Nanopipette



F. Iwata and J. Metoki

**Abstract** In this paper, we developed a novel and simple technique of three-dimension structure fabrication using a nanopipette. The nanopipette is a tapered glass capillary with an aperture size of sub-micrometer in diameter. The nanopipette was filled with a colloidal solution including metal nanoparticles. As for fabrication of the pillar, the pipette edge is contacted on the substrate, and then it was moved upward with keeping deposition of the metal colloidal solution. The diameter of the pillar is dependent on the aperture size of the pipette. By this technique, it is possible to deposit at any position in atmosphere. To improve the reproducibility of the formation, the amount of deposition of the Au colloidal solution was controlled by feedback loop that maintains the pre-defined constant current under electrophoresis deposition. In addition, we have evaluated machine characteristic of the microstructures using the manipulator within Scanning Electron Microscope (SEM). This technique would be expected as a fabrication method for micro and nanometer-scale devices.

**Keywords** Nanofabrication · Nanodeposition · Nanoparticles · Electrophoresis · Manipulaor

## 1 Introduction

Fabrication techniques for three-dimensional (3D) nano and microstructures have been developed to construct various micro and nanometer-scale devices, such as micro-electro-mechanical systems (MEMS). Focused-ion beam (FIB) and stereolithography have been used to fabricate 3D structures [1–4]. However, these fabrication techniques require restricted environments such as vacuum and solutions. Moreover, the equipment involved is very expensive. Therefore, alternative, lower cost fabrication techniques are needed. We developed a novel technique of 2D nano and micro scale deposition of nano materials using a nanopipette in atmosphere [5–7].

---

F. Iwata (✉) · J. Metoki

Department of Mechanical Engineering, Graduate School of Engineering, Shizuoka University, 3-5-1, Johoku, Hamamatsu 432-8561, Japan  
e-mail: iwata.futoshi@shizuoka.ac.jp

© Springer Nature Switzerland AG 2022

S. Hinduja et al. (eds.), *Proceedings of the 38th International MATADOR Conference*,  
[https://doi.org/10.1007/978-3-319-64943-6\\_52](https://doi.org/10.1007/978-3-319-64943-6_52)

693

In this paper, we describe a fabrication technique of 3D structures by depositing nano particles using the nanopipette. By moving the substrate downward while depositing, pillars were fabricated. To fabricate smooth structure, a novel deposition technique using constant current feedback was proposed. In addition, we evaluated mechanical properties of the fabricated pillars using a micro cantilever of an atomic force microscope (AFM).

## 2 Experimental Set-Up

### 2.1 Method for Local Electrophoresis Deposition

Figure 1 shows the deposition method of nanoparticles using the nanopipette. The nanopipette is a tapered glass capillary with an aperture of sub-micrometer in diameter. In this study, the nanopipette was filled with Au colloidal solution (particle size: 3 nm in diameter). To deposit the nanoparticles on the substrate, the pipette edge was brought into contact with the substrate surface. In aqueous solution in the pipette, the colloidal nanoparticles are negatively charged in the solution due to its Zeta potential, thus, by applying the voltage between the electrode inserted into the pipette and the conductive substrate, electrophoresis deposition can be achieved. To fabricate the pillar structure, the substrate is moved downward while depositing the nanoparticles. Here, to stabilize the deposition, the current following the aperture of the nano pipette while depositing was maintained by feedback control.

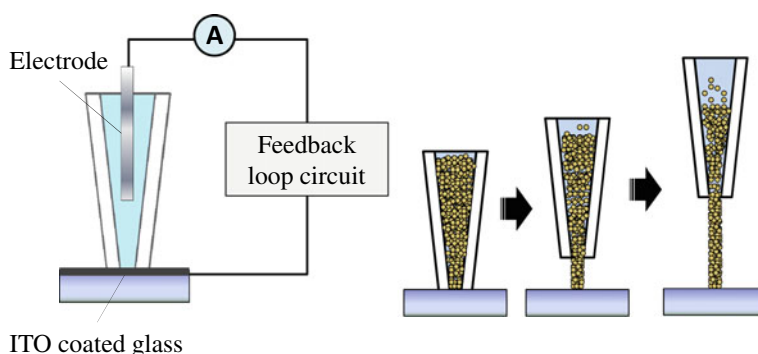
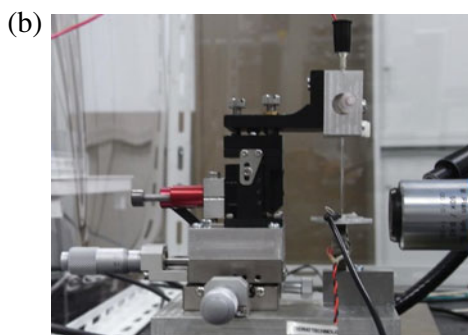
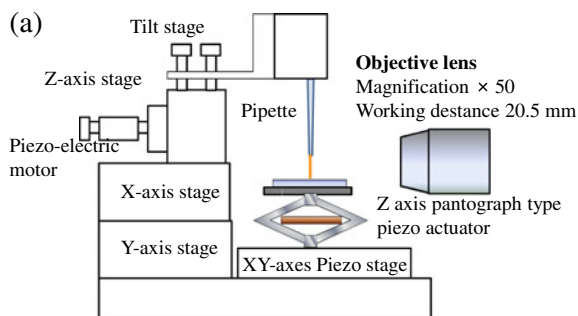


**Fig. 1** Current feedback electrophoresis deposition method of nanoparticles using a nano pipette

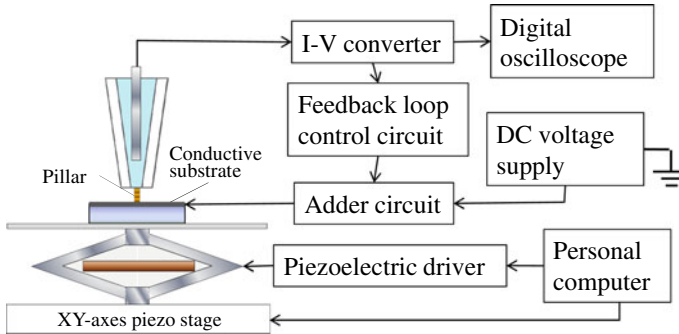
## 2.2 Experimental Setup for 3D Structures

Figure 2a and b show a schematic of the experimental setup and its photograph. The nanopipette was prepared by thermal pulling of the capillary glass tube using a commercial pipette puller. The diameter of the aperture was  $1.5\ \mu\text{m}$ . As a conductive substrate, a slide glass coated with indium tin oxide was employed to apply voltage between the substrate and electrode wire inside the nanopipette for electrophoresis deposition. In order to form a meniscus between the pipette edge and the substrate, the hydrophilicity of the substrate was increased by ultrasonic cleaning and ultraviolet irradiation. For precise positioning of the nanopipette on the substrate surface, X, Y and Z axis positioning stages driven by piezoelectric motors were used. For fabrication of 3D structures, a pantograph-type piezoelectric actuator ( $150\ \mu\text{m}/150\ \text{V}$ ) was used to ensure that the substrate would move down smoothly while depositing nanoparticles continuously. The pantograph-type piezoelectric actuator was driven by a piezoelectric driver. The approach of the nanopipette to the substrate and sequential deposition was observed using an optical microscope with a long-working distance objective lens (WD 20.5 mm, 50x). In this study, to stabilize the amount of colloidal solution deposition, current flowing through the nanopipette was controlled under electrophoresis deposition. Figure 3 is a schematic diagram of the experimental setup for measurement and control of the current under electrophoresis deposition. The current flowing through the nanopipette was detected using an I-V converter.

**Fig. 2** Set up for fabrication of micro three-dimensional structures using the nanopipette **a** Experimental set up of the nanopipette deposition **b** Photograph of the setup







**Fig. 3** Schematic diagram of the deposition system configuration for measurement and control of the current under electrophoresis deposition

The output signal from the I-V converter was entered into the feedback controller that maintained the current at a pre-defined level under electrophoresis deposition by controlling the applied potential between the conductive substrate and the electrode inside the nanopipette.

### 3 Experimental Results and Discussion

#### 3.1 Electrophoresis Deposition

In order to define the appropriate set point of the current for feedback control of electrophoresis deposition, the current during fabrication of pillars was measured without feedback control of applied voltage. Figure 4a shows the behavior of the current through the nanopipette under electrophoresis deposition for fabrication of

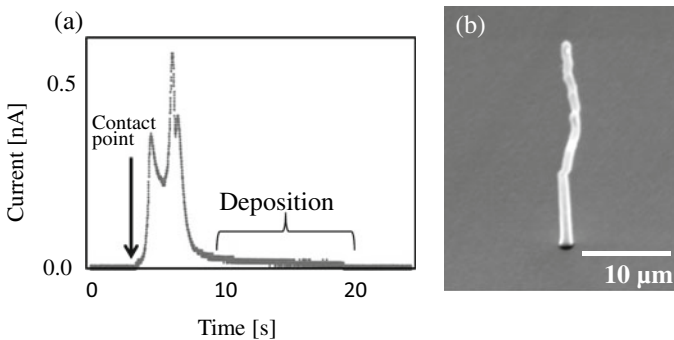


**Fig. 4** Pillar deposition by applying a constant voltage. **a** Current behavior of the deposition. **b** SEM image of the fabricated pillar

the pillar. A current of approximately 0.7 nA was detected when the pipette contacted the substrate, and then gradually decreased. The decrease in current would be due to the increase in the resistance of the pillar being fabricated in the deposition process.

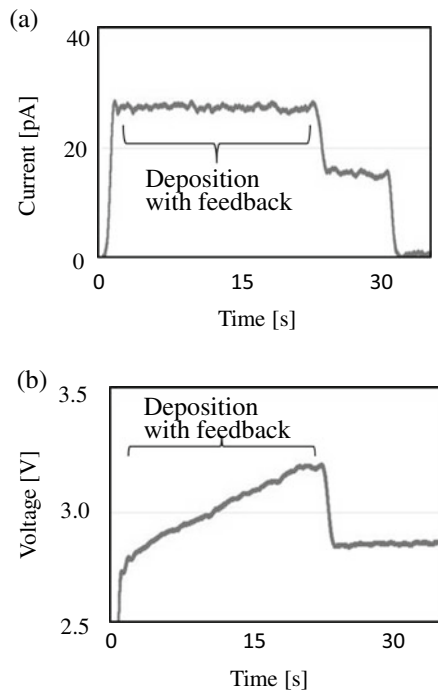
Figure 4b shows an SEM image of a pillar fabricated without feedback control of the current. There are many constrictions on the surface of the pillar. It was difficult to deposit the nanoparticles continuously at the same deposition rate because the density of the particles around the pipette edge decreased due to consumption of particles by pillar creation. As a result, constrictions appeared on the surface of the pillar. The current behavior reflects the amount of the deposition and the shape of the fabricated pillar. Thus, we theorized it might be possible to fabricate a uniform pillar by maintaining a pre-defined current using the feedback control.

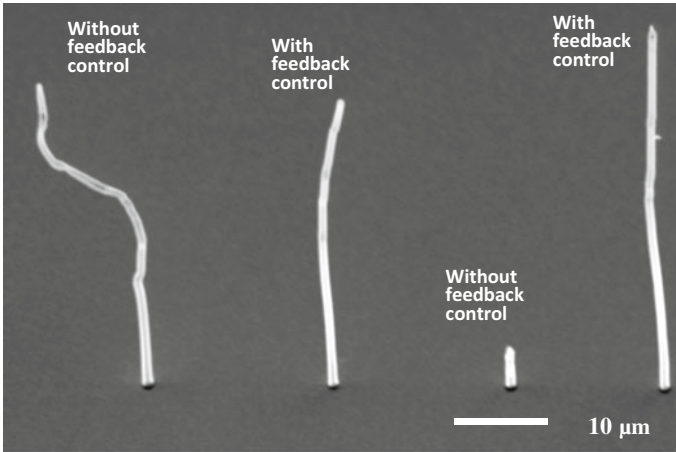
Figures 5a and b show the current and the voltage, respectively, applied to the substrate under feedback control deposition. As may be seen in the figures, the applied voltage increased to maintain a constant current of 30 pA.

Figure 6 shows an SEM image of pillars fabricated with and without feedback control. With feedback control, the surface of the pillar is smooth, and the constrictions and necking decreases compared to those without feedback control. In our experiments, with current feedback control it was possible to fabricate several pillars with high reproducibility.

Figure 7 shows the average length of the pillars fabricated at different velocity of the z axis Piezo stage moved downward while depositing. The pillars were fabricated

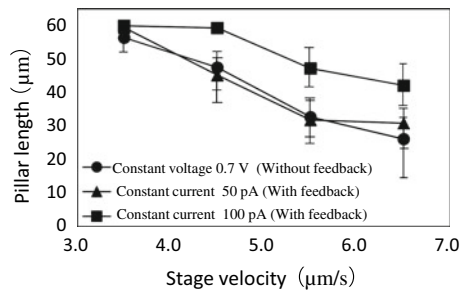
**Fig. 5** Pillar deposition by current feedback control. **a** Current behavior of the deposition. **b** Voltage behavior of the deposition





**Fig. 6** SEM image of fabricated pillars. The pillars were alternately fabricated without feedback and with feedback

**Fig. 7** Average pillar length as a function of stage velocity moving downward while depositing for pillar fabrication



with three different conditions. One is fabrication by applying constant voltage of 0.7 V without current feedback. The others are fabrications with current feedback of 50 and 100 pA. The pillars were fabricated with 60 μm displacement of the z-axis Piezo stage. The velocity was changed from 3.5 μm/s to 6.5 μm/s in increments of 1.0 μm/s. The average length was calculated from 30 pillars fabricated at each velocity. As shown in the figure, in all three conditions, the lengths of the pillars decreased with increasing the stage velocity. When the velocity of the stage increases, it might be difficult to maintain deposition with constant amount of nanoparticles because of saturation of supplying speed of the nanoparticles under electrophoresis migration. As a result, constrictions appeared on the surface of the pillar and finally breaking of the pillar occurred on the way to creation the pillar.

By comparing with the pillar fabrications with current feedback of 100 and 50 pA, the lengths of the pillar fabricated with 100 pA current feedback were significantly longer than that of pillars fabricated with 50 pA current feedback. By setting the higher current value for the current feedback, the migration force of the nanoparticles

increased, as a result, the electrophoresis deposition would be carried out under better condition.

### 3.2 Evaluation of Mechanical Properties of Pillars

Figure 8 is a schematic diagram of the manipulator used to measure the mechanical properties of the pillars inside the vacuum chamber of the SEM. The manipulator moves an AFM cantilever in the three orthogonal directions ( $X$ ,  $Y$  and  $Z$  axes). In order to measure the deflection of the pillars, it was necessary to observe them from the side; thus, the substrate was placed vertically with respect to the objective lens using the sample holder, which could be rotated around the  $Y$  axis with the piezoelectric motor.

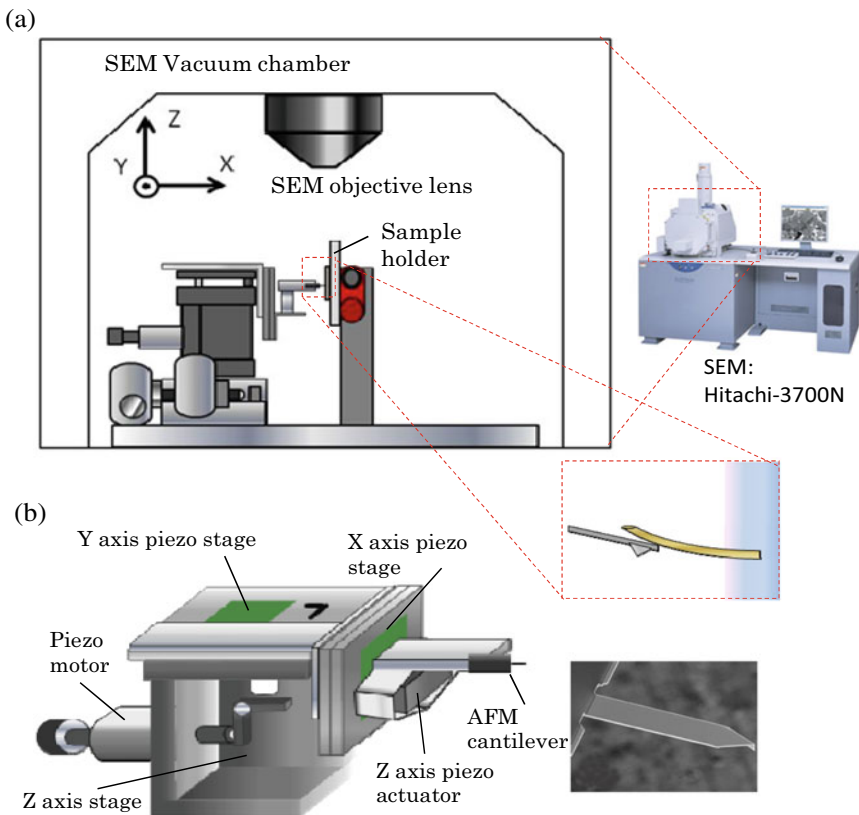


**Fig. 8** Evaluation of the mechanical properties of the fabricated pillars. **a** Set up for evaluation of mechanical properties of the pillar inside the chamber of the SEM. **b** A manipulator to measure the deflection of the pillar. AFM cantilever is mounted on the manipulator arm

For the operation, it was necessary to avoid contact between the manipulator and the objective lens. Thus, in this system, an infrared camera was placed inside the SEM chamber to monitor the clearance between the manipulator and the objective lens from the side.

Young's modulus of the pillar was evaluated by measuring the deflection of the fabricated pillars. The pillar was pushed and bent with the AFM cantilever mounted on the manipulator. Both deflections of the pillar and the cantilever were observed using the SEM. The loading force applying to the pillar can be calculated from the parameters of deflection and the spring constant of the cantilever. Young's modulus is

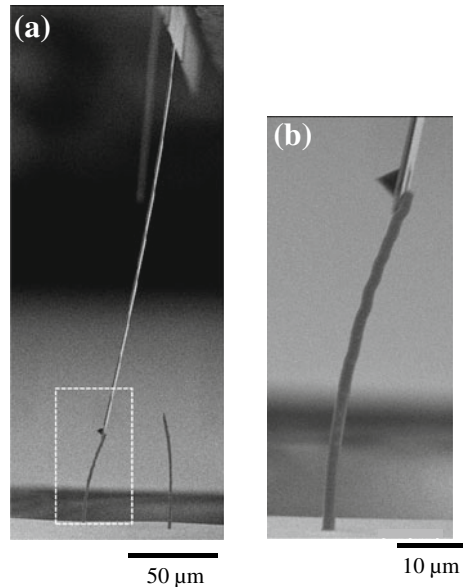
$$E = \frac{pl^3}{3xI} \quad (1)$$

where  $p$  is the load,  $l$  is the length of the pillar,  $x$  is the deflection of the pillar and  $I$  is second moment of area. Figure 9 shows SEM images of the bending pillar. The deflections of the pillar and the cantilever are shown in Fig. 9a and b, respectively.

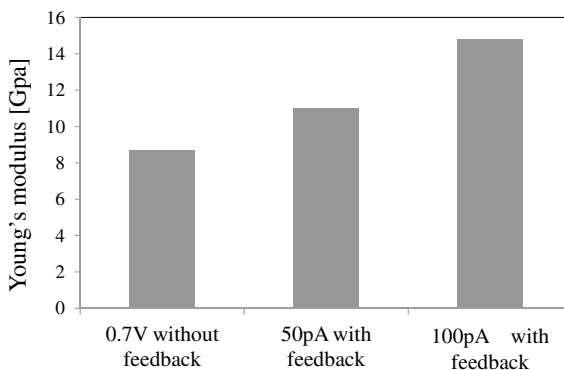
Young's modulus of the pillar could then be obtained by measuring the parameters of the deflection of the cantilever, the length, diameter and deflection of the pillar in the SEM images.

Figure 10 shows Young's modulus of the pillars fabricated with the three different conditions: without feedback and with feedback of 50 and 100 pA. The fabrications were carried out at stage velocity of 3.5  $\mu\text{m/s}$ . As shown in the figure, the values of Young's modulus of the pillars fabricated with current feedback are higher than that

**Fig. 9** Bending of the pillars. **a** Measurement of deflection of the cantilever. **b** Measurement of deflection of the pillar



**Fig. 10** Young's modulus of the pillars fabricated with different conditions



of the pillar fabricated without current feedback. Additionally, Young's modulus of pillar fabricated with current feedback of 100 pA is higher than that of pillar fabricated with current feedback of 50 pA. As described the average lengths of the pillars in Fig. 7, by setting a higher current value for the current feedback, the force of electrophoresis migration increased, as a result, the deposition with high density nanoparticles were carried out for fabrication of the stiffer pillar.

However, this value (15 GPa) was smaller than that of Au bulk (78 GPa). With regard to the colloidal solution used in the study, mercaptosuccinic acid used as a protective agent was adsorbed on the Au particles. Thus, the protective agents would have reduced the stiffness of the pillars. Future research will investigate post-processes such as annealing and baking in order to improve stiffness.

## 4 Conclusion

We developed a novel technique for fabricating micrometer scale 3D structures by electrophoresis deposition of colloidal nanoparticles using a nanopipette. The amount of deposition of the Au colloidal solution was dependent on the current flowing through the nanopipette under electrophoresis deposition. By controlling the current under the electrophoresis deposition, the pillars were successfully fabricated with high reproducibility. The stiffness of the fabricated pillars was evaluated using an AFM cantilever equipped with a manipulator inside the SEM vacuum chamber. Young's modulus of the pillar fabricated with current feedback was higher than that of pillar fabricated without current feedback.

**Acknowledgements** This work was supported by Grant-in-Aid for Scientific Research from the Ministry of Education, Culture, Sports, Science and Technology of Japan (MEXT) and CREST of the Japan Science and Technology Agency (JST).

## References

1. Matsui S, Kaito T, Fujita J, Komuro M, Kanda K, Haruyama Y (2000) Three-dimensional nanostructure fabrication by focused-ion-beam chemical vapor deposition. *J Vac Sci Technol B* 18:3181–3184
2. Ishida M, Fujita J, Ichihashi T, Ochiai Y, Kaito T, Matsui S (2003) Focused ion beam-induced fabrication of tungsten structures. *J Vac Sci Technol B* 21:2728–2731
3. Maruo S, Nakamura O, Kawata S (1997) Three-dimensional microfabrication with two photon absorbed photopolymerization. *Opt Lett* 22:132–134
4. Miwa M, Juodkazis S, Kawakami T, Matsuo S, Misawa H (2001) Femtosecond two-photon stereo-lithography. *Appl Phys Lett* 73:561–566
5. Iwata F, Sumiya Y, Sasaki A (2004) Nanometer-scale metal plating using a scanning shear-force microscope with an electrolyte-filled micropipette probe. *Jpn J Appl Phys* 43:4482–4485
6. Iwata F, Sumiya Y, Nagami S, Sasaki A (2004) Submicrometre-scale fabrication of polycarbonate surface using a scanning micropipette probe microscope. *Nanotechnology* 15:422–426
7. Iwata F, Nagami S, Sumiya Y, Sasaki A (2007) Nanometre-scale deposition of colloidal Au particles using electrophoresis in a nanopipette probe. *Nanotechnology* 18:105301(5pp)

# Large Scale Periodic Structure Fabrication by Scratching Silica-Glass-Precursor Coating



Sergey Bolotov, Masaharu Hashidume, Keita Shimada, Masayoshi Mizutani, and Tsunemoto Kuriyagawa

**Abstract** Anti-reflection, light diffusion, diffraction, the major optical functions used in cameras, led displays and other devices. Highly-ordered micro-structures on surfaces are commonly used to obtain those functions, and development of fabrication method of those in large scale, high efficiency, high precision became an important issue due to increase of optical devices demand. In this paper a new method to fabricate highly-ordered micro patterns on glass was performed by scratching the half-reacted silica-glass-precursor coating, and fabrication mechanism was discussed. As silica-glass-precursor perhydropolysilazane (PHPS) solution was spin-coated on glass substrate to obtain coating with thickness around  $0.6\ \mu\text{m}$ , and heat-cured at  $80\text{--}250\ ^\circ\text{C}$  to consolidate surface of coating with variety of reaction distribution in coating. In the scratch test a stylus was oscillated at  $45\ \text{Hz}$  and drawn at  $5\text{--}25\ \mu\text{m/s}$  as load increased. Highly-ordered-periodic-structures with pitch around  $1\ \text{mm}$  were obtained by scratching, with a  $50\ \text{mm}$ -apex-radius stylus, the coating which was cured at  $100\ ^\circ\text{C}$  for  $12\ \text{h}$ . By degreasing scratch draw speed pattern pitch was decreased under  $1\ \mu\text{m}$ . Simulation has been conducted in order to estimate reaction rate distribution in the coating. From the simulation results it was found that there are two layers in the coating, reacted layer beneath coating surface and unreacted layer near PHPS-substrate boundary. It was considered that reacted layer on surface reduces friction so that film does not break off while scratching while unreacted layer enable deformation of coating.

**Keywords** Perhydropolysilazane · Reaction–diffusion simulation · Scratch test

## 1 Introduction

The solar photovoltaic power generation is expected to become one of the future energy supplies, and improvement of its light conversion efficiency is required. By applying antireflection structure on solar cells surface, conversion efficiency can be

---

S. Bolotov (✉) · M. Hashidume · K. Shimada · M. Mizutani · T. Kuriyagawa  
School of Engineering, Department of Mechanical Systems and Design, Tohoku University, 1-5-3  
Nishinenishi, Tsuchiura, Ibaraki, Sendai, Japan  
e-mail: [sergey.bolotov@dexerials.com](mailto:sergey.bolotov@dexerials.com)

© Springer Nature Switzerland AG 2022

S. Hinduja et al. (eds.), *Proceedings of the 38th International MATADOR Conference*,  
[https://doi.org/10.1007/978-3-319-64943-6\\_53](https://doi.org/10.1007/978-3-319-64943-6_53)

703



increased due to decrease of reflectance [1]. Such technology to obtain optical functionality with submicron periodic structure can be used to increase devices performance.

Fabrication of micro structure has been fabricated with laser texturing, nanoimprint lithography and reactive ion etching [2–4]. Heitz et al. reports the laser-induced processing for fabrication the nano-ripple structures surfaces which can be used for self-organization of gold coatings and interaction with biological cells [2]. Inomata et al. reports a large area fabrication method, of antireflective surfaces for solar cells, by reactive ion etching [3]. Hauser et al. developed a roller nanoimprint lithography process to fabricate honeycomb texturing [4].

However, those processes are high cost and application for large surfaces is difficult. In this research new method was developed to fabricate periodic structures by scratching surface. Firstly silica-glass precursor is coated on substrate, next the coating is heat cured and finally the coating is scratched with stylus oscillation. In this method, it enhance plastic deformation while scratching by making heat-cured coating half-reacted with highly reacted layer beneath surface and less reacted surface inside. Therefore, just by scratching a functional surface, such as surface with ripple structure, can be easily fabricated. Moreover, this method is applicable for large surfaces and does not require expensive equipment.

In this paper, fabrication of sub-micron pitch structures was demonstrated and mechanism of formation was discussed. Firstly, effect of scratch speed and scratching load to structure pattern was considered. Also, the effect of heat curing time to formation condition was examined. Next, a reaction diffusion simulation conducted in order to observe the reaction rate in the coating. Finally, the mechanism of formation was discussed.

## 2 Experimental Methodology

In this section it is explained the preparation of coating, and the scratch test conditions.

The proposed method consists of four steps: application of a silica-glass precursor on silica glass, heat curing to not completely convert a silica-glass precursor coating in to glass, scratching to form a submicron pitch structure. A silica-glass precursor i.e. Perhydropolysilazane (PHPS) diluted with dibutylethel by 20% solution (Toresmile ANN-120, Sanwa Kagaku Corp.) was used. The solution is spin-coated on a glass substrate at rotation speed of 1000 rpm and rotation time 30 s. After that coated samples were cured in 100 °C for 12–37 h. Coating thicknesses of prepared samples were measured with a white-light interferometer (Talysurf CCI, Taylor Hobson Ltd.) soon after application and after heat curing is shown in Table 1. The average of three points was taken in the measurement.

The scratch test was conducted with the micro-scratch tester (CSR-2000 RHESCA Corp.) shown in Fig. 1. The motion during scratching is illustrated in Fig. 2. The stylus pressing a sample surface oscillates on surface plane vertically to a sample drawing direction. Depends on experiment purpose, the pressing load was kept constant or

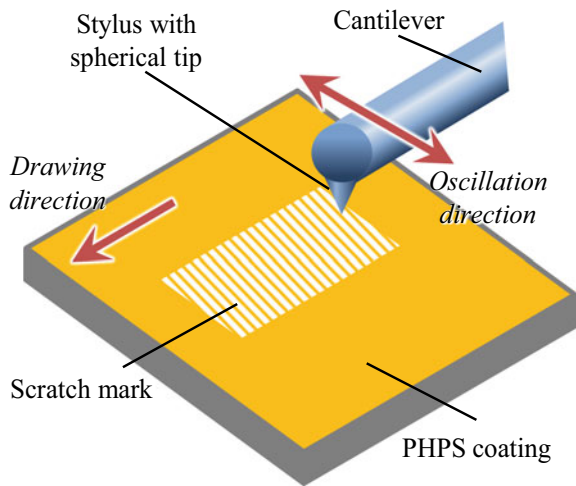
**Table 1** Thickness of PHPS coating

Sample number	Curing time (h)	Coating thickness ( $\mu\text{m}$ )	
		Before curing	After curing
1	37	0.679	0.520
2	18	0.695	0.616
3	13	0.551	0.437

**Fig. 1** The micro-scratch tester (CSR-2000 RHESCA Corp.)



**Fig. 2** Motion of the stylus during scratch



increased as sample drew. Also, the scratch speed and the load increase rate were changed. The oscillation frequency and amplitude were fixed to 45 Hz and 100  $\mu\text{m}$ , respectively. A diamond stylus with 50  $\mu\text{m}$  radius tip was used in this paper. The scanning electron microscope (SEM) (Hitachi Corp.) and the white-light interferometer were used to observe scratch marks.

### 3 Experiment Results

#### 3.1 Scratch Test Results

To observe an effect of scratch load, samples were scratched with load increasing as sample drawing. Figure 3 shows SEM photographs of scratched coating which was heat cured for 37 h. In Fig. 3a–d represents the surface scratched at different load. From the picture it can be confirmed, when the load is low then ripple structure is formed, in the other side, when the load is increased wrinkle structure is formed.

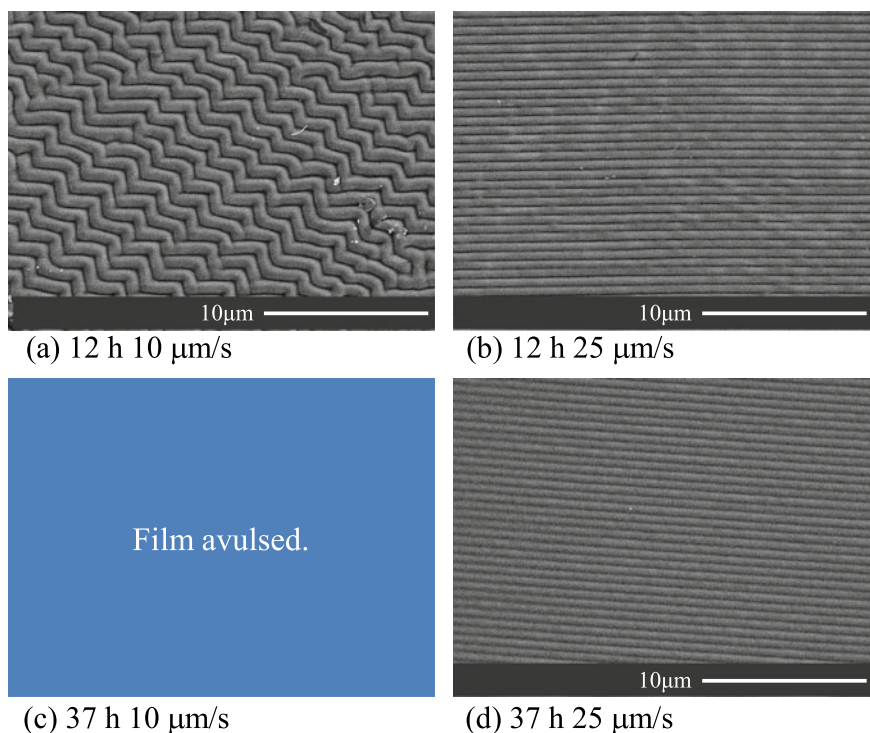


**Fig. 3** Structures formed at different load. The sample was cured in 100  $^{\circ}\text{C}$  for 37 h, scratch speed being 25  $\mu\text{m}/\text{s}$

Further load been increased the wrinkle structure disappears. The transition point from ripple structure to wrinkle structure was at load been around 100 mN.

To consider an effect of scratch speed to the structure formation, scratch load fixing to 100 mN, several scratches with different scratch speed was conducted. Figure 4a–d shows the SEM photograph of scratched surfaces with different heat curing time and scratch speed. It can be seen that the wrinkle structure was formed with scratching speed of  $10\ \mu\text{m/s}$  on a sample heat cured for 12 h. However, on a sample heat treated for 37 h coating avulsed. On the other side, both samples heat cured for 12 and 37 h scratched with scratching speed of  $25\ \mu\text{m/s}$  have ripple structure. In light of previous results (Fig. 3), the scratch load might be too low to form wrinkle structure.

A surface topography, cross-section profile and FFT spectrum for the wrinkle structure and ripple structure are represented in Figs. 5 and 6, respectively. Both structures are form scratch mark of sample heat cured for 37 h and scratched at  $25\ \mu\text{m/s}$ . The scratch condition except scratch load are the same, however a pitch and structure height of wrinkle structure is wider and higher compare to a ripple structure one.

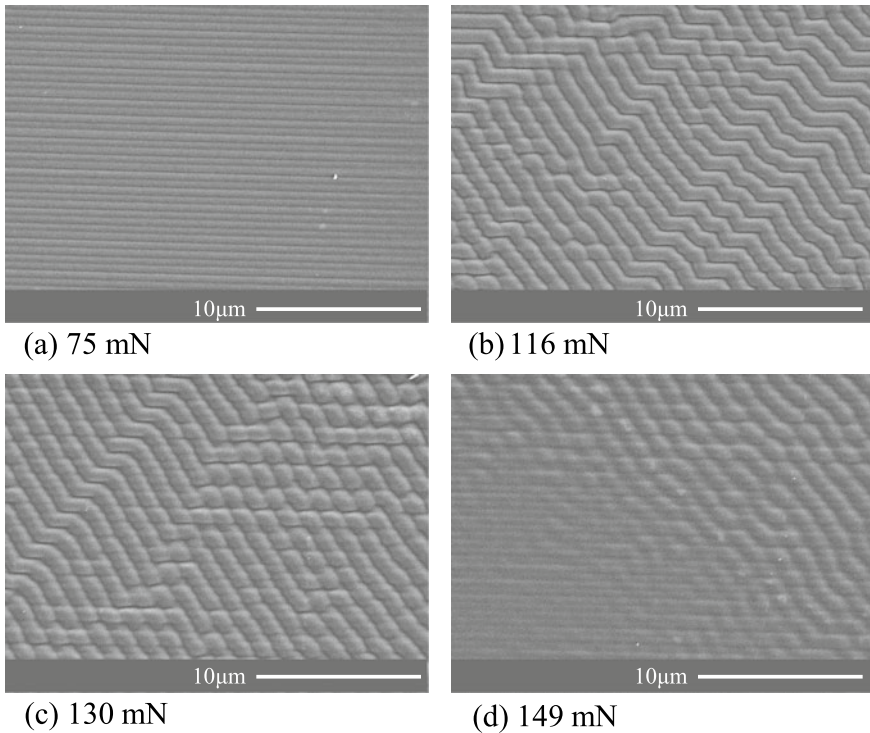
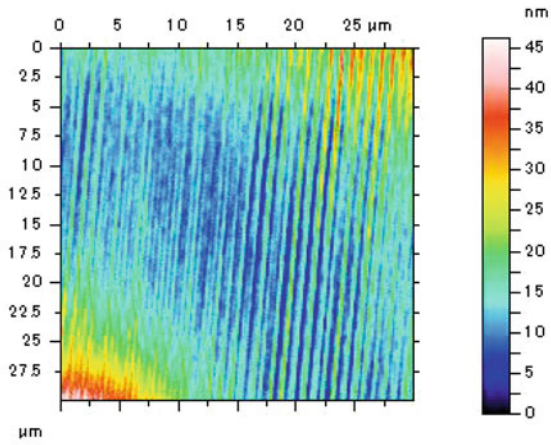
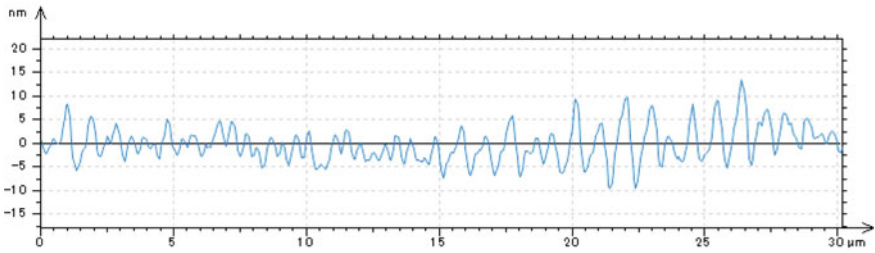


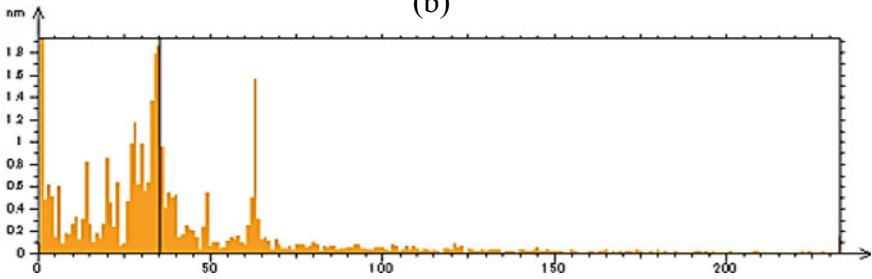
**Fig. 4** Structures formed at different scratch speeds for samples with different curing time, as load controlled to be constant



(a)



(b)



Pitch: 0.864  $\mu\text{m}$ , Amplitude: 1.865 nm

(c)

**Fig. 5** **a** Surface topography, **b** cross-section profile and **c** FFT graph of cross-section profile of the structure

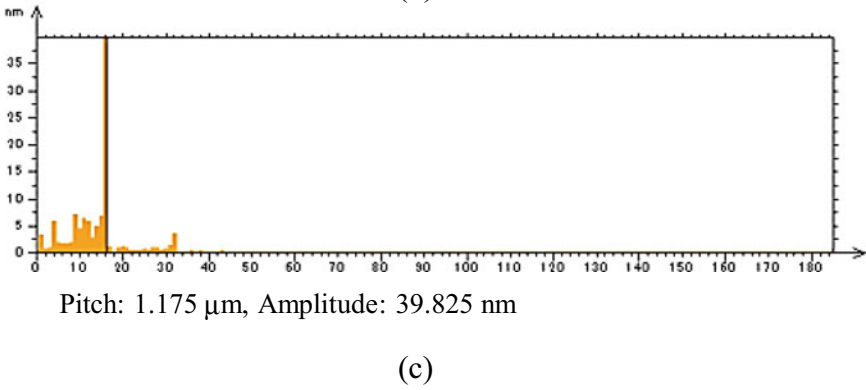
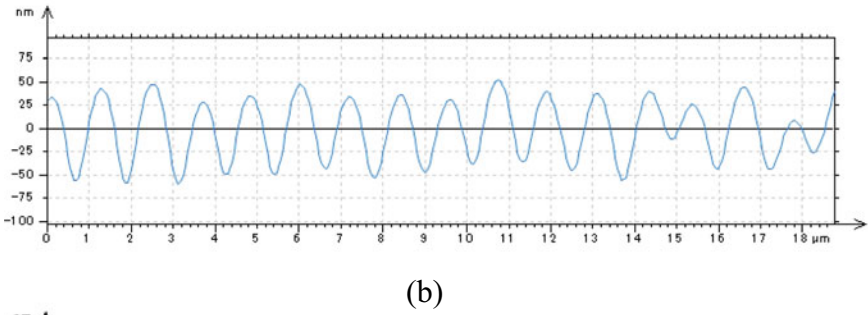
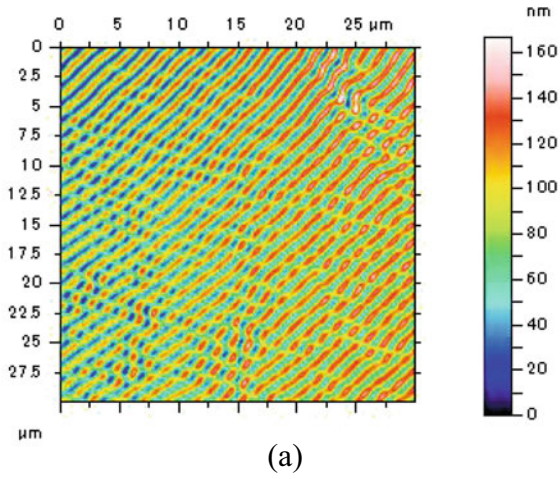
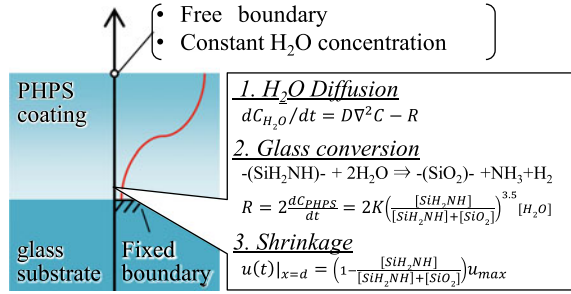


**Fig. 6** **a** Surface topography, **b** cross-section profile and **c** FFT graph of cross-section profile of the structure

**Fig. 7** 1D diffusion–reaction simulation model



*Output: Distribution of glass conversion rate*

### 3.2 Diffusion–Reaction Simulation Results

Using one-directional simulation, the glass conversion rate distribution was evaluated. An explanatory diagram of 1D diffusion–reaction simulation model and equations used in the model are shown in Fig. 7. The simulation model takes it X-axis in coating thickness direction. In versatile multi-physics simulation software COMSOL Multiphysics, transportation of diluted-species mode was used to analyze the diffusion of water species and reaction of PHPS in the coating, and also a moving mesh mode was used to simulate shrinkage of PHPS coating due to glass conversion. To simulate the shrinkage, displacement towards the substrate of the node on top surface is calculated based on reaction rate inside the coating, and nodes inside are distributed at regular intervals at every step of calculation. Table 2 represents values of parameters used in the simulation. The reaction orders and the reaction rate coefficient in the reaction rate equation determined based on Bauer et al. and Morlier et al. research [5, 6]. The diffusion coefficient is calculated from the water transmission rate and the Hildebrand solubility parameter which was taken from rubbers one [7]. The coating thickness was set to a value near experiments one and the maximum shrinkage displacement was, considering Günthner et al. report it being around 50%, set to 0.2 μm [8]. The water concentration at the surface was set to 0.75 mol/m<sup>3</sup> which is absolute humidity of the room experiment conducted. The analysis time was 10<sup>5</sup> s i.e. around 27 h.

The simulated distribution of glass conversion rate at every 1000 s is shown in Fig. 8. From Fig. 8 the glass concentration increases from surface gradually, and all coating almost converts into glass at 10,000 s. In the process of reaction, there

**Table 2** Parameters in the simulation model

Reaction coefficient	K	1.6789 × 10 <sup>4</sup> mol/(m <sup>3</sup> s)
Diffusion coefficient	D	1.8271 × 10 <sup>-14</sup> m <sup>2</sup> /s
Maximum shrinkage displacement	u <sub>max</sub>	0.2 μm
Coating thickness	D	0.5 μm

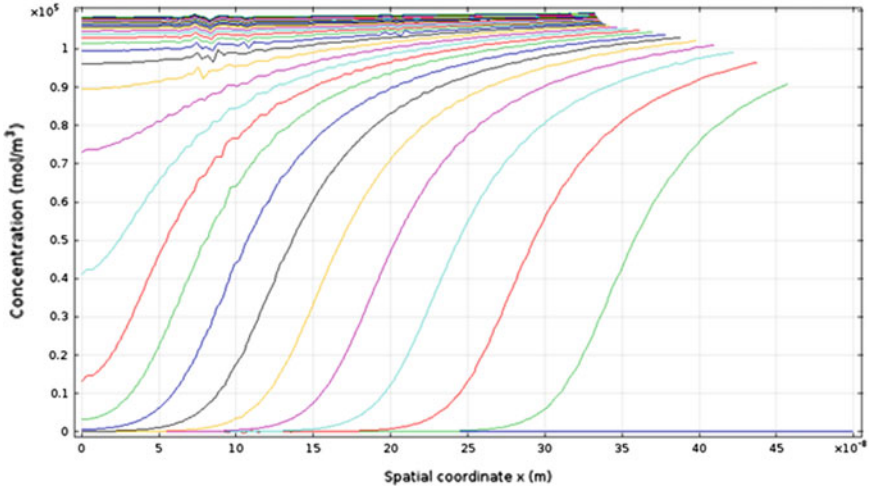


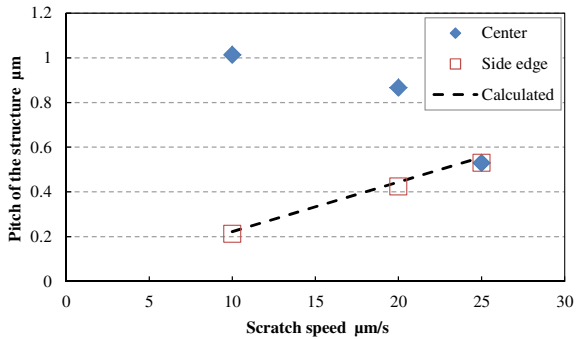
Fig. 8 Glass conversion rate distribution in coating depth direction

are two layers the highly reacted and lower reacted ones. The coating condition is thought to have those two layers.

### 4 Discussion

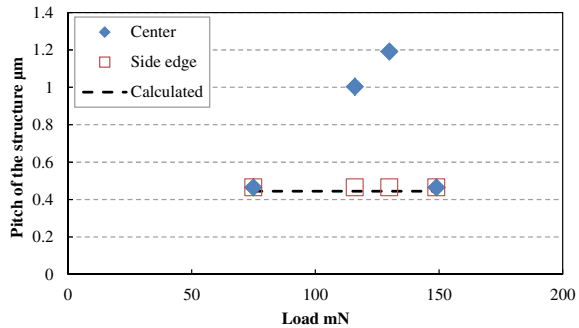
The formation mechanism of micro-structures is discussed in this section. Relationship of the pitch size of structure with load and scratch speed is shown in Figs. 9 and 10. In graph filled squares corresponds to the pitch of structure in the center, and unfilled squares corresponds to the pitch of small scratch marks at the edge of the scratch mark. The dash line in the graph represents pitch size calculated from the stylus vibration frequency and the scratch speed. Comparing with the SEM picture

Fig. 9 Relationship of pitch of the structure and scratch speed





**Fig. 10** Relationship of pitch of the structure and scratch load



in Fig. 4, the pitch of the ripple structure is the same with the calculated pitch, on the other hand it of the wrinkle one is 2–5 times bigger than that. It can be considered that ripple structure is formed directly by stylus motion, and wrinkle structure had some influence of stresses around stylus during its formation.

The finite element simulations about stresses around stylus during scratching have been reported by Hayakawa et al. and Kawabata et al. [9, 10]. According to Hayakawa's research, an interfacial normal tensile stress occurs in front of a stylus moving direction, and both an interfacial shear stress and an interfacial normal tensile stress occurs at both stylus sides [9]. In Kawabata's research, those stresses, at sides and at front of stylus, provokes embossment of coating [10]. The ripple structure is that embossment that remained after scratching. The wrinkle structure considered to be a combined ripple structure which has been distorted by stresses behind stylus.

The structure of coating is also considered to further the formation of those structures, due to its hard layer beneath the coating surface and soft layer between hard substrate and upper layer. Bull S. J. reports the influence of the hardness relationship between coating and substrate [11–13]. When coating harness is harder than substrate one, then an embossment occurs in front of stylus, and when it breaks coating began to remove. In case of soft coating on hard substrate, coating began to remove due to tensile stress in the back of the stylus moving direction. The PHPS coating on a hard glass substrate, used in proposed method, obtain a hard surface layer and a soft inner layer. When scratching load is low, scratching mechanism can be considered the same as that of a hard coating on a soft substrate, so that, an embossment can be easily formed. When scratching load is increased, embossment is considered to growth and combine previous embossments formed during scratch. Further, scratching load increasing, the influence of the substrate increase and an embossment disappears.

The wrinkle structure is highly ordered, however, patterns are partly different. If the formation phenomenon is as mentioned above, glass conversion distribution and coating thickness variability in a plane may affect to patterns. Also, as reported in researches of scratch test, friction coefficient of coating, scratch speed, surface roughness and design of machine may have some influence to structure formation conditions [14–16]. Those parameters have to be considered in future work.

## 5 Conclusion

In this paper, the new method to fabricate submicron structures is proposed and demonstrated. By scratching an incompletely reacted coating submicron structure can be formed. The conclusion of the paper is as follows;

- The ripple structure and the wrinkle structure are fabricated when scratching load was below 100 mN and around 100–140 mN, respectively, on the PHPS coating which was heat cured in 100 °C for 37 h.
- The ripple structure pitch depends on the scratching speed and stylus oscillation frequently. However the wrinkle structure have pitch 2–5 times bigger than that calculated from scratching speed and stylus oscillation frequency.
- The diffusion–reaction simulation is conducted to find that there are two layers, an harder and an softer ones, in the heat cured PHPS coating.
- It is considered that the embossment around stylus is forming those structures. The wrinkle structure is considered to be a combined and distorted ripple structure. Two layers in the PHPS coating is considered to further the formation of those structures.

## References

1. Hava S, Auslender M (2000) Design and analysis of low-reflection grating microstructures for a solar energy absorber. *Sol Energy Mater Sol Cells* 61(2):143–151
2. Heitz J, Reisinger B, Fahrner M, Romanin C, Siegel J, Svorcik V, (2012) Laser-induced periodic surface structures(LIPSS) on polymer surfaces. In: Paper presented at: 14th international conference on transparent optical networks, 2–5 July. Coventry, England
3. Inomata Y, Fukui K, Shirasawa K (1997) Surface texturing of large area multicrystalline silicon solar cells using reactive ion etching method. *Sol Energy Mater Sol Cells* 48:237–242
4. Hauser H, Michl B, Schwarzkopf S, Kübler V, Müller C, Hermle M, Bläsi B (2012) Honeycomb texturing of silicon via nanoimprint lithography for solar cell applications. *IEEE J Photovoltaics* 2(2):114–122
5. Bauer F, Decker U, Dierdorf A, Ernst H, Hiller R, Liebe H, Mehnert R (2005) Preparation of moisture curable polysilazane coatings part I: elucidation of low temperature curing kinetics by FT-IR spectroscopy. *Prog Inorganic Coatings* 53:183–190
6. Morlier A, Cros S, Garandet JP, Alberola N (2012) Thin gas-barrier silica layers from perhydropolisilazane obtained through low temperature curings: a comparative study. *Thin Solid Films* 524:62–66
7. Yasuda T (2000) Testing methodology and evaluated results of plastics dynamic characteristics part 4. *Plastics* 51(5):74–84
8. Günthner M, Wang K, Bordia RK, Motz G (2011) Conversion behavior and resulting mechanical properties of polysilazane-based coatings. *J Eur Ceram Soc* 32:1883–1892
9. Hayakawa K, Mori H, Mitsui M, Nakamura T, Tanaka S (2010) Finite element analysis on interfacial stress of scratch test. *J JSTP* 52(610):1181–1186
10. Kawabata S (2007) Prediction of coating damage mechanisms by stress analysis of hard coating. *Denso Tech Rev* 12(2):47–53
11. Bull SJ, Rickerby DS, Matthews A, Leyland A, Pace AR, Valli J (1988) The use of scratch adhesion testing for the determination of interfacial adhesion: the importance of frictional drag. *Surf Coat Technol* 36:503–517

12. Bull SJ (1997) Failure mode maps in the thin film scratch adhesion test. *Tribol Int* 30(7):491–498
13. Bull SJ, Berasetegui EG (2005) An overview of the potential of quantitative coating adhesion measurement by scratch testing. *Tribol Int* 39:99–114
14. Bless MH, Winkelman GB, Blkenende AR, den Toonder JMJ (1999) The effect of friction on scratch adhesion testing: application to a sol-gel coating on polypropylene. *Thin Solid Films* 359:1–13
15. Malzbender J, de With G (2001) Analysis of scratch testing of organic-inorganic coatings on glass. *Thin Solid Films* 386:68–78
16. Nemeth S (2008) Modelling of the scratch resistance of particle filled sol-gel coatings on aluminium. *Thin Solid Films* 516:5355–5359

# Study of Chipping of Micro Channel in Glass Ultra-hard Material by Micro Machining Technologies



Jack Y. C. Lin, Zheng-Han Hong, Tsung-Pin Hung, Tsai-Fa Chen,  
and Yu-Sen Wu

**Abstract** Glass material is widely used as a structural and functional material in micro channel biochips. Micro channels have been created using micro manufacturing technologies such as micro electro mechanical systems or micromechanical manufacturing technologies. Deep holes and micro channels with a high slenderness ratio (width/depth) can be obtained by using micro ultrasonic machining technology. The results indicate that chipping increases with increasing feed rate. However, as the rotational speed was increased, the average chipping is about the same. Hence, for best surface quality, the feed rate should be low.

**Keywords** Microfluidic channel · High slenderness ratio · Micro-ultrasonic machining system · Ultra-precision machining system

## 1 Introduction

To create a micro-channel device, the selection of materials and machining method is critical. Materials commonly used for micro channel include single-crystal silicon chips, glass, metals, and polymers. Single-crystal silicon has good thermal stability and chemical inertness, allowing high-precision three-dimensional (3D) structures to be produced. PMMA and poly-dimethylsiloxane (PDMS) are easily processed and low cost, making them very suitable for mass production. However, these materials have low melting points and poor material strength. Glass materials are commonly used as biochips for biological applications due to their biocompatibility and ease of reuse. Therefore, glass-based chips are commonly used in research and development units. However, the brittleness of glass make it difficult to process and control

---

J. Y. C. Lin (✉) · Z.-H. Hong (✉) · T.-P. Hung · T.-F. Chen · Y.-S. Wu  
Mold & Precision Machining Technology Section, Micro/Meso Mechanical Manufacturing R&D  
Department, Metal Industries Research & Development Centre (MIRDC), Kaohsiung, Taiwan  
e-mail: [yclin@mail.mirc.org.tw](mailto:yclin@mail.mirc.org.tw)

Z.-H. Hong  
e-mail: [zheng@mail.mirc.org.tw](mailto:zheng@mail.mirc.org.tw)

with precision. Therefore, the development of high-quality and high-precision micro-manufacturing methods for glass-based materials is necessary [1–3]. Various techniques have been applied to control micro channels, including mechanical machining methods such as micro-milling [4], micro ultrasonic machining, and micro electrical discharge machining (EDM), lithographic and electrolytic etching [5, 6], as well as energy beam technology such as ultra-short-pulse laser machining [7].

Due to its good reliability, high impact strength, and transparent properties, tempered glass is widely used in the touch panel of smart phone. However, with the increasing of hardness of glass surface, the tempered glass is hardly to machining. For the rapid and mass manufacturing, the yield rate must be controlled. Previous literature has shown that the ultrasonic assisted machining is easily to drill for brittle and hard materials [8]. Among the current machining techniques, rotary ultrasonic machining (RUM) is an efficient and economical technique available for hard-brittle materials, particularly in producing complex contours. Extensive experimental investigations revealed that material removal rate (MMR) obtained from the RUM process was nearly 6–10 times higher than that from conventional grinding (CG) process under the similar machining conditions. Other advantages of the RUM process included the considerable reduction in the cutting force without disproportionately deteriorating the surface/subsurface quality. Although RUM process, acted as a productive technique, has been widely applied to manufacture brittle material components, the improvement mechanisms of the ultrasonic vibration on the cutting force are still not very clear, leaving many uncertainties in optimizing the process parameters to further reduce the cutting force. Considering that the diamond tool was ultrasonically vibrated in the direction perpendicular to the specimen surface, Spur and Holl [8] assumed that the abrasives located on the tool end face were intermittently contacted with the material. Moreover, the repeated contact disruptions together with the impulse-like alternating loads would promote the abrasive splintering, whereas distinctly suppress its flattening as demonstrated. Therefore, the cutting edges of the abrasives were presumably increased, thus reducing the average cutting force of the diamond tool in the RUM process. These explanations mentioned above were mostly ground on the assumption that the abrasives were intermittently contacted with the specimen surface. Previous literature shows that the ultrasonic vibration assisted machining has tiny cutting force and stress. Therefore, this paper presents the development of rotational ultrasonic vibration assisted machining chuck and base on the proposed chuck to drill in chemical tempered glass.

## 2 Chosen Material and Micro-manufacturing Methods

Material properties are the first consideration for 3D micro channel. The chosen material must have good chemical properties, such as biocompatibility and chemical stability. In addition, the quality and precision of micro-manufacturing methods depend on the material. Glass was selected as the substrate material in the present

study due its low coefficient of thermal expansion, good wear resistance and biocompatibility, and high light penetration resistance. The brittleness of glass makes it difficult to process and precisely control, making it a good test material. Micro ultrasonic machining and ultra-precision machining were used to fabricate 3D microfluidic structures.

### 3 Five-Axis Machine for Using Ultrasonic Vibration Assisted Milling and Drilling

A five-axis machine combined with an ultrasonic-vibration-assisted machining chuck effectively manufactures structures in high-brittleness materials such as glass by using ultrasonic-vibration-assisted milling and drilling, as shown in Fig. 1a.

The rotational ultrasonic-vibration-assisted machining chuck was designed by the Metal Industries Research & Development Centre (MIRDC), as shown in Fig. 1b. The chuck total length and maximum diameter are 225 and 128 mm, respectively. The transducer has a maximum amplitude in the axial direction at a resonance frequency of 21.9 kHz. In addition, simple harmonic motion is induced at a frequency of 19.8 kHz. The generator scans the frequency automatically before machining in the range of 18–22 kHz. Detailed specifications of the ultrasonic chuck and generator are shown in Table 1. The specifications of the five-axis milling machine are listed in Table 2. The five-axis dynamic milling and drilling, high speed, high efficiency, and low residual stress allow free-form surfaces to be created with good machining quality.

For high brittle material machining of 3D microfluidic structure, the deep hole is manufactured by using five-axis ultrasonic assisted machining. It can use the five-axis dynamic milling and drilling, high speed, high efficiency machining, low machining residual stress to obtain the free-form surface and good machining quality.

Before machining, a special fixture was needed to be designed, shown in Fig. 2. The material of fixture is acrylic and designs the passageway for air flow. Then, connected to vacuum pump to suck the tempered glass. The tempered glass dimension is  $150 \times 85 \times 0.7$  mm, and fixed on the vacuum fixture.

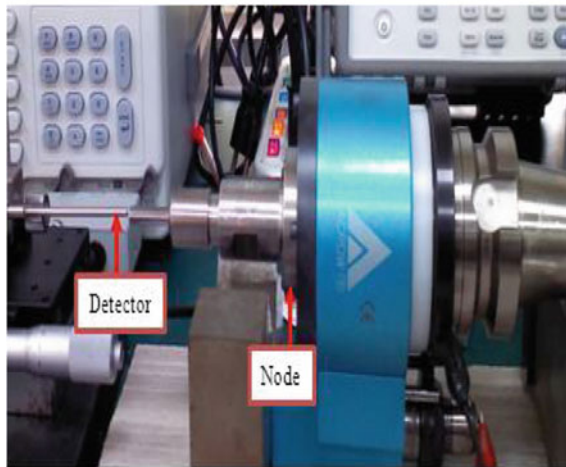
### 4 Experimental Results

The experiment results were measured by microscope and captured the picture to calculate the chipping area. The measure values include hole diameter  $r$ , maximum chipping diameter  $R$ . Then the average chipping length  $L$  can be calculated, and it could be expressed as follow:

$$L = R - r = ((A - a)/\pi)^{1/2} \quad (1)$$



(a)



(b)

**Fig. 1** a Five-axis milling machine, b ultrasonic-vibration-assisted machining chuck

where  $A$  is the maximum chipping area,  $a$  is hole area,  $R$  means the maximum chipping radius, and  $r$  stand for hole radius.

Deep holes were machined into the glass plate in the drilling process. The 2-mm-thick plate of glass was machined with ball end mills made of diamond. A series of drilling tests were performed to investigate the chipping area of hole inlet with various amplitude and feed rate.

**Table 1** The specification of ultrasonic chuck

Item	Technical specification
Length	225 mm
Maximum diameter	128 mm
Frequency	$20 \pm 2$ kHz
Amplitude	3–10 $\mu\text{m}$
Maximum speed	8000 rpm
Runout	< 5 $\mu\text{m}$
Working voltage	100–220 V

**Table 2** Specification of five-axis milling machine

Item	Technical specification
Maximum machining size	750 × 600 × 500 mm
Minimum size of micro-holes	$\Phi$ 0.05 mm (aspect ratio $\geq 10$ )
Dimensional accuracy	$\leq \pm 0.5$ $\mu\text{m}$
Surface roughness (Ra)	$\leq 20$ nm

**Fig. 2** Vacuum fixture

The machining parameters were: a rotational speed of 6000, 7000, and 8000 rpm, a feed rate of 10, 20, and 30 mm/min, and a temperature of  $25 \pm 1$  °C. Each parameter drill 12 holes. The experiment result showed rotational ultrasonic vibration assisted drilling is helpful to decrease the glass chipping and increase yield rate in drilling chemical tempered glass, shown in Fig. 3a. While the rotational speed is at 6000 rpm without ultrasonic vibration assisted, the tempered glass break, shown in Fig. 3. With ultrasonic vibration assisted drilling, the hole inlet and outlet chipping length are small than 0.03 mm, shown in Fig. 3a and b.

The average abrasive grain size of the diamond tool was 15–37  $\mu\text{m}$ . The chipping decreased when the rotational speed was increased to 8000 rpm, as shown in Fig. 4a



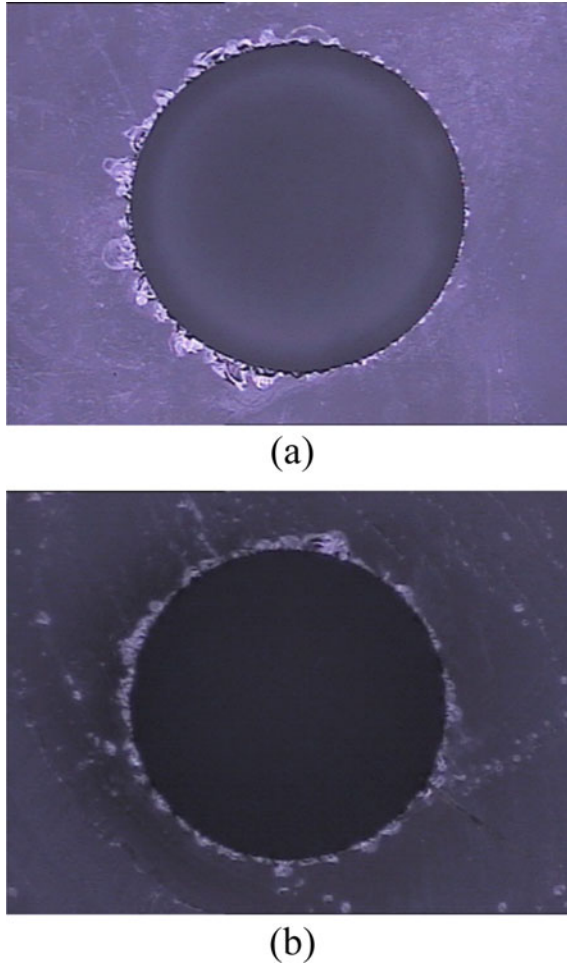


**Fig. 3** Chemical tempered glass (Corning Gorilla Class 3) ultrasonic vibration assisted drilling with rotational speed of 6000 rpm, feed rate of 8 mm/min, and 15  $\mu\text{m}$  abrasive grains: **a** top side **b** back side

and b. When the feed rate was increased from 10 to 30 mm/min, the chipping increased by around 30%. Hence, for best surface quality, the feed rate and rotational speed should be low and the abrasive grain size of the diamond tool should be small. Table 3 shows the machining parameters of ultrasonic drilling.

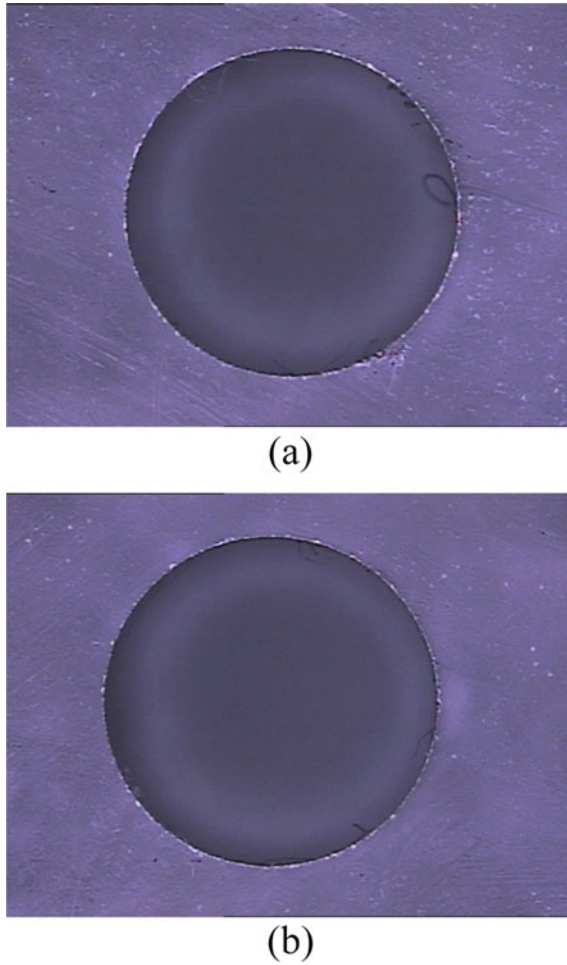


**Fig. 4** Chemical tempered glass (Corning Gorilla Class 3) ultrasonic vibration assisted drilling with rotational speed of 8000 rpm, feed rate of 8 mm/min, and 15  $\mu\text{m}$  abrasive grains: **a** top side **b** back side

## 5 Conclusions

This paper investigated the microfluidic channel fabrication process by micro ultrasonic machining for glass. Deep holes and micro Channel with a high slenderness ratio (width/depth) can be obtained by using micro ultrasonic machining technology. In the proposed approach, the natural frequency has good agreement with experiment results. The tolerance is 9.59% approximately. Using the proposed ultrasonic chuck to tempered glass drilling, the main conclusions of the present study can be summarized as follows:

**Table 3** Machining parameters and glass chipping value

Speed (rpm)	Feed rate (mm/min)	Amplitude ( $\mu\text{m}$ )	Avg. chipping L (mm)
6000	10	3	0.025
6000	20	5	0.027
6000	30	7	0.031
7000	10	5	0.025
7000	20	7	0.030
7000	30	3	0.031
8000	10	7	0.025
8000	20	3	0.029
8000	30	5	0.032

1. In this study ultrasonic vibration assisted chucks was designed and used to the tempered glass drilling process.
2. The experiment results showed that the feed rate would influence the chipping length. While the feed rate increases to 30 mm/min, the chipping value increases 30% approximately.
3. Based on the experiment results, one hole arise crack in drilling 120 holes. The yield rate is 99.17%.
4. The chipping increases with increasing feed rate. For best surface quality, the feed rate should be low.
5. As the rotational speed was increased, the average chipping is about the same.

## References

1. Zheng B, Tice JD, Ismagilov RF (2004) Formation of droplets of in microfluidic channels alternating composition and applications to indexing of concentrations in droplet-based. *Anal Chem* 76:4977–4982
2. Yang Z, Matsumoto S, Goto H, Matsumoto M, Maeda R (2001) Ultrasonic micromixer for microfluidic systems. *Sensor Actuat A-Phys* 93:266–272
3. Zhang H, Tumarkin E, Peerani R, Nie Z, Sullan RM, Walker GC, Kumacheva E (2006) Microfluidic production of biopolymer microcapsules with controlled morphology. *J Am Chem Soc* 128:12205–12210
4. Nakano M, Korenaga A, Korenaga A, Miyake K, Murakami T, Ando Y, Usami H, Sasaki S (2007) Applying micro-texture to cast iron surfaces to reduce the friction coefficient under lubricated conditions. *Tribol Lett* 28:131–137
5. Menezes PL, Kishore KSV, Lovell MR (2010) Response of materials during sliding on various surface textures. *J Mater Eng Perform* 20:1438–1449
6. Borghi A, Gualtieri E, Marchetto D, Moretti L, Valeri S (2008) Tribological effects of surface texturing on nitriding steel for high-performance engine applications. *Wear* 265:1046–1051
7. Gattass RR, Mazur E (2008) Femtosecond laser micromachining in transparent materials. *Nat Photon* 2:219–225

8. Kuo KL, Tsao CC (2012) Rotary ultrasonic-assisted milling of brittle materials. *Trans Nonferrous Met Soc China* 22:793–800

# **Monitoring and Control of Machining Operations**

# Cutting Force Control for Multiple Repetitive Canned Cycles in Turning Operation



Josuet Leoro and Syh-Shiuh Yeh

**Abstract** The objective of the present research is to control the cutting force during the machining process by using a fuzzy-logic controller to adjust the feed rate. The selection of the fuzzy controller is due to the fact that the cutting process is nonlinear and hard to determine. For the approach presented in this contribution, a maximum cutting force needs to be input, as it is going to be the reference for the fuzzy controller. The initial parameters for the cutting process are selected by using the information from the tool provider or the knowledge of the part programmer. Most researches choose the initial feed rate to be zero, which as shown in our approach would produce unnecessary overshoots. During the machining process the feed rate is adjusted in order to maintain the cutting force in the input value. However, an additional consideration is done. Since during a rough turning operation multiple repetitive canned cycles are used, the cutting force will drop down to zero when the tool returns to start the next cycle. For this stage, the controller should not act because the machine will return with a fast movement. During each cycle the feed rate obtained from the tuned cutting operation will be saved and used in the next cycle. Because the depth of cut and spindle speed are fixed, a similar cutting force as for the last cycle is expected. The cutting force control and machining time improvement results obtained in real cutting tests are presented.

**Keywords** Fuzzy controller · Rough turning operation · Machining time improvement

---

J. Leoro (✉)

Graduate Institute of Mechatronic Engineering, National Taipei University of Technology, No. 1, Sec. 3, Chung-Hsiao E. Rd, Taipei 10608, Taiwan

S.-S. Yeh

Department of Mechanical Engineering, National Taipei University of Technology, Taipei, Taiwan

© Springer Nature Switzerland AG 2022

S. Hinduja et al. (eds.), *Proceedings of the 38th International MATADOR Conference*,  
[https://doi.org/10.1007/978-3-319-64943-6\\_55](https://doi.org/10.1007/978-3-319-64943-6_55)

727

## 1 Introduction

Conventional computer numerical control (CNC) machining systems suffer from the drawback that their operating parameters, such as feed rates, cutting speeds, and depth of cut, are programmed off-line with no provisions for on-line adjustments. The selection of these parameters is based on data from machining handbooks and on the experience and knowledge of the part programmer [1].

Cutting conditions are usually complicated, difficult to predict and changeable, and so it is inevitable that conservative parameters are selected for protection against the tool failures or machine vibrations. The material removal rate is directly related with these parameters, therefore the productivity is not optimal.

Using a closed loop control to update these parameters during the machining process is a solution. In order to close the loop, a variable to be controlled must be selected. Since direct measurement of the conditions experienced by the tool in the cutting zone is impractical, an indirect assessment has to be made [2]. Cutting force is an alternative variable that can be measured and controlled and has a direct relationship with the process itself. The cutting force as the variable to be controlled has a wide use for research purposes in turning and milling operations by different control approaches [2–5]. The method and constraints used for controlling the cutting force can determine the improvement of the machining time, the cutting force control accuracy and the cutting tool protection.

## 2 Control Variable

The cutting force in a turning operation is directly related with the workpiece material, the cutting tool and the cutting parameters. In [6] an approach for the estimation of the cutting force is made following Eq. 1.

$$F_c = K_s \times d \times f^u \quad (1)$$

where  $K_s$  is the specific cutting energy,  $d$  is the depth of cut,  $f$  is the feed and  $u$  is a constant that depends on the machining conditions where  $0.6 < u < 1$ . The specific cutting energy is related with the cutting tool and the workpiece material, therefore it cannot be controlled during the cutting process. The depth of cut is defined by the part programmer in each operation. This variable could change during the cutting process. However, it hardly can be used to control the cutting force. The feed is the only variable that can be used to control the cutting force during the machining process. The relation between the feed rate  $vf$  (mm/min) and the feed  $f$  (mm/rev) is given by Eq. 2.

$$f = vf/N \quad (2)$$

where  $N$  (rpm) is the spindle speed. In a real application, for some machines the feed rate and the spindle speed can be changed by using the machine feed rate override and spindle override respectively. In this research the feed rate is selected as the variable to be controlled while the spindle speed is kept constant.

In previous approaches of force control for turning operations, a fast change of feed rate is applied [3, 5, 7]. Using a fast change of feed rate prevents the cutting tool from standing high forces for a considerable time when a fast change of force occurs i.e. a change of depth. However, a fast change of feed rate could also damage the cutting tool and corrupt the surface roughness of the machined part. Therefore, it is necessary to consider a smooth change of feed rate to protect the tool.

### 3 Controller Design

Since the cutting process is nonlinear and hard to determine, a fuzzy-logic controller can be used to control the cutting force. The objective of the controller is to maintain the cutting force in an allowable value input by the user. The initial parameters for the cutting process are selected by using the information from the tool provider or the knowledge of the part programmer. The inputs to the adaptive controller are inferred from the desired force  $F_d$  and the cutting force  $F_c$ . The output of the controller is the feed rate adjustment. The block diagram of the adaptive control system is shown in Fig. 1.

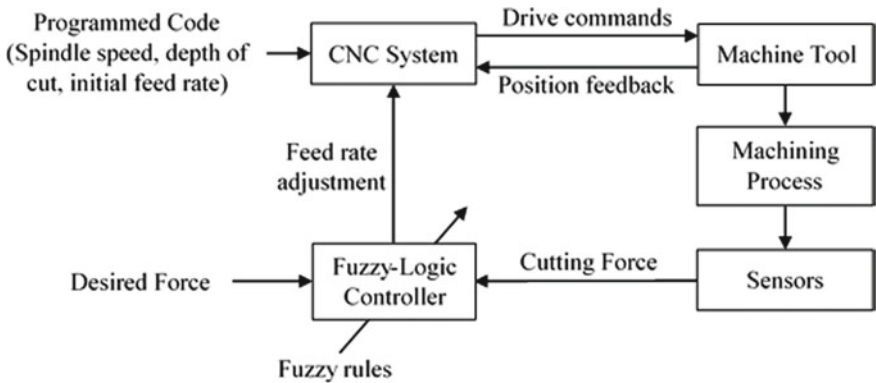


Fig. 1 Block diagram of the adaptive control system



### 3.1 Controller Inputs and Output

The proposed fuzzy-logic controller is based on the fuzzy logic controller proposed by [8]. By using as reference the desired cutting force, and the measurement of the actual cutting force, the error and change of error are calculated. The error and change of error are normalized by using the desired force. By doing so, the same input membership functions can be used for different input desired force. Then the normalized values are the inputs of the fuzzy controller. The calculation of the controller inputs are shown in Eqs. 3 and 4.

$$E' = (F_d - F_c)/N \quad (3)$$

$$dE' = E' - E'_0 \quad (4)$$

where  $E'$  is the normalized actual error,  $E'_0$  is the normalized last error and  $dE'$  is the normalized change of error. The controller output is obtained from the fuzzy inference engine and then it is multiplied by a proportional coefficient  $K_p$ . The feed rate adjustment is then calculated by using Eq. 5.

$$vf_n = vf_0 + K_p \times CO \quad (5)$$

where  $vf_n$  is the next feed rate,  $vf_0$  is the actual feed rate and  $CO$  is the controller output. The selection of the variable  $K_p$  adjusts the speed of change of the feed rate. As mentioned before, a smooth change of feed rate is proposed. Therefore  $K_p$  must be selected taking into account this consideration.

### 3.2 Membership Functions

The membership functions for the designed controller have seven sets for each variable. The inputs membership functions are shown in Fig. 2a. The error and change of error use the same membership functions. The output has the membership functions shown in Fig. 2b. The inputs variables and the output variable use the same linguistic variables, NB: Negative Big, NM: Negative Medium, NS: Negative Small, Z: Zero, PS: Positive Small, PM: Positive Medium and PB: Positive Big.

### 3.3 Fuzzy Rule Base

The objective of the controller is to converge the cutting force to a reference value fast enough to protect the tool. Additionally, an acceptable accuracy is intended to be reached. It is important to remark that for a rough turning operation a high noise

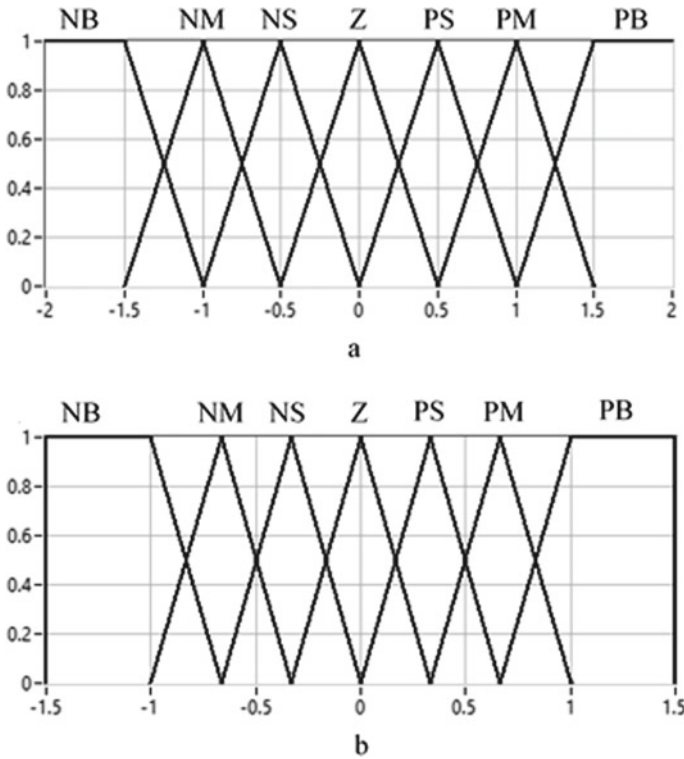


**Fig. 2** Membership functions; **a** error and change of error membership functions; **b** control output membership functions

is expected when measuring the cutting force. Therefore, a small error could be pure noise depending on the selection of the desired force, since the error is normalized. By taking into account these requirements, the fuzzy rule base is selected as shown in Table 1.

**Table 1** Fuzzy rule base of the fuzzy controller for a rough turning operation

$E'/dE'$	NB	NM	NS	Z	PS	PM	PB
NB	NB	NB	NB	NM	NM	NS	Z
NM	NB	NB	NM	NM	NS	Z	PS
NS	NB	NM	NM	NS	Z	PS	PS
Z	NM	NM	NS	Z	PS	PM	PM
PS	NS	NS	Z	PS	PM	PM	PB
PM	NS	Z	PS	PM	PM	PB	PB
PB	Z	PS	PM	PM	PB	PB	PB

## **4 Considerations for Rough Turning Operations**

The controller shown in previous section adjusts the feed rate in order to reach the desired input force. Nevertheless, it is also important to consider when a feed rate adjustment should be applied. In this research, it is considered that this adjustment must be done only in rough cutting operations, because other operations may need a constant feed rate. Therefore the controller is applied in multiple repetitive canned cycles managed by G-codes G70, G71 and G72. These cycles are performed with the same depth of cut, spindle speed and feed rate except for the final pass. Then the feed rate override can be used to perform the force control.

### ***4.1 Situations Present in Multiple Repetitive Canned Cycles***

There are two situations to consider for the multiple repetitive canned cycles. The first situation is when the cutting tool is not in contact with the workpiece. This happens for every cycle, when the tool is approaching to the workpiece and when the tool is returning for the next cycle. The second situation is when the cutting tool is in contact with the workpiece. This happens during the turning process itself. For the first situation, the controller must not act because it is not in the contact with the workpiece and therefore the cutting force is zero. For the second situation, the controller must act to control the cutting force.

### ***4.2 Managing Controller Activation and Deactivation***

In order to manage the activation and deactivation of the force controller, the knowledge about the cutting process is used. One can expect that the cutting force when there is no contact with the workpiece has a value of zero, with possible little oscillations due to noise in the sensor signal, which can happen for different reasons including vibration of the machine. The force value is evaluated and if it is less than a small value, one can infer that the cutting tool is not in contact with the workpiece. The controller is deactivated while the force value maintains below this threshold. A value of 10 N was found to be a good threshold value considering the noise.

### ***4.3 Advantages of the Controller Activation and Deactivation***

In the first cycle, before the tool engages the workpiece, the feed rate will be the one recommended by the tool provider. The controller will not act, therefore a constant feed rate is used. In many researches [3, 7, 9], the action of the controller and initial

feed rate is not considered; instead the controller is always active and a zero feed rate is used at the beginning. This creates unnecessary overshoots, because the cutting force is zero and the controller response increases the feed rate to reach the desired cutting force. However, the force is zero for this situation and the feed rate will increase until a maximum limit is reached. Once the workpiece is engaged a high feed rate creates the force overshoot. This is avoided by using the technique explained before.

After the force converges to the desired value, the feed rate is expected to have a low oscillation value. This value can be saved and used for the next cycle. By using the controller deactivation at the end of each cycle, when the tool returns for the next cycle, the feed rate will not change until the next contact with the workpiece. Since for each cycle the machining conditions are similar, the cutting force is expected to be similar. Therefore using the last feed rate for the next cycle will improve the machining process, because only small changes of feed rate are necessary. Additionally, the cutting tool life is extended because of small changes of feed rate during the cutting process.

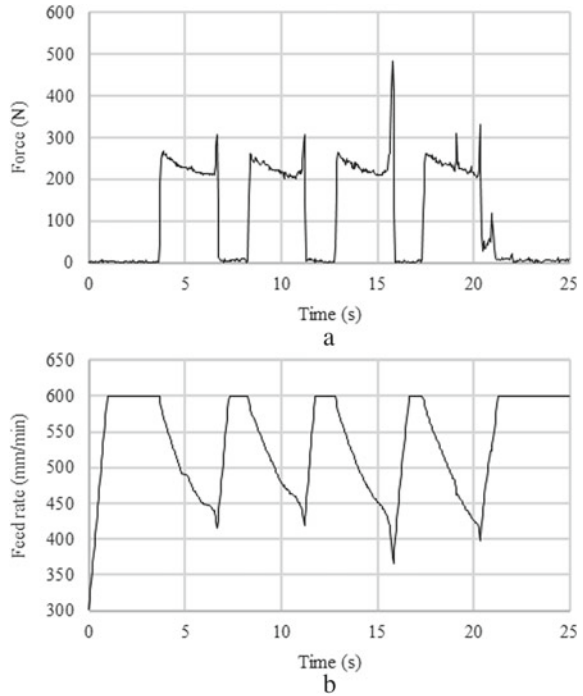
## 5 Experimental Results

The present controller approach was applied in a Tong Tai TB-20YBC machine. The workpiece material is Aluminum 6061. A spindle speed  $S = 2000$  (rpm) and initial feed rate  $vf_0 = 300$  (mm/min) were used for all the experiments. A reduction of diameter of a cylindrical workpiece was used as cutting test. Therefore the length of cut for every cycle is the same. A value of  $K_p = 20$  was selected. It is important to remark that at the end of each cycle the cutting tool is not returning with  $45^\circ$ . This is because at the time when the experiments were done, the machine parameters were configured to do a  $90^\circ$  return. For this reason, at the end of each cycle an overshoot happens.

Two experiments were performed to validate the present approach. The first experiment without managing the fuzzy controller activation, and the second experiment managing the fuzzy controller activation. For the second experiment, firstly the force response with constant feed rate  $vf = 300$  (mm/min) is shown, then a desired force 20% higher is selected based on the maximum force obtained. Finally, the present approach is applied. It is important to remark that at the end of each cycle the cutting tool is not returning with  $45^\circ$ . This is because at the time when the experiments were done, the machine parameters were configured to do a  $90^\circ$  return. For this reason, at the end of each cycle an overshoot happens.

For experiment 1, a length of cut  $L = 20$  (mm), a depth of cut  $d = 1$  (mm) and a desired force  $F_d$  (N) were used. The force response of experiment 1 is shown in Fig. 3a. The problem of the overshoot at the beginning of each cycle is noticeable. The desired force is not reached during the cutting time because the length of cut is not enough and the overshoot does not allow enough time for controlling the force.

**Fig. 3** Cutting results of experiment 1; **a** Force response; **b** Feed rate response



In Fig. 3b, the feed rate saturation to the maximum value when there is no contact with the workpiece can be noticed.

For experiment 2, a length of cut  $L = 40$  (mm) and a depth of cut  $d = 1$  (mm) were used. The force response of experiment 2 without controller is shown in Fig. 4. From this experiment an average maximum force of 170 N can be noticed. The calculated desired force is 200 N. The force response applying the present approach is shown in Fig. 5a. The desired cutting force is reached in a small lapse of time. The initial overshoot in each cycle is avoided. The feed rate adjustment is shown in In Fig. 5b.

**Fig. 4** Cutting results of experiment 2 without using the fuzzy controller

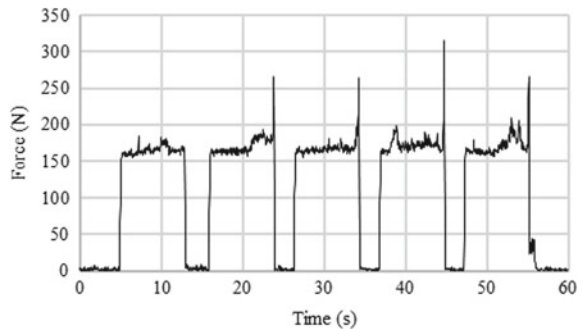
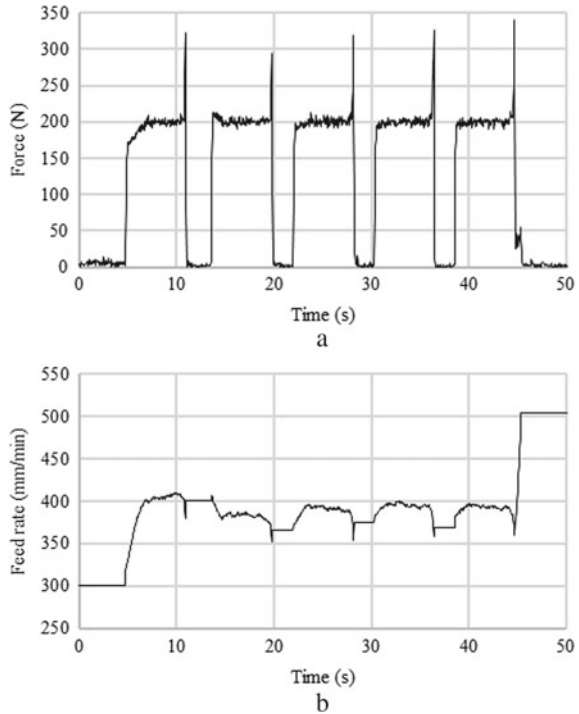


**Fig. 5** Cutting results of experiment 2 managing fuzzy controller activation; **a** Force response; **b** Feed rate response



The feed rate is adjusted smoothly and not much change of feed rate is necessary between cycles.

By comparing the force response when applying the constant feedrate and the force response when applying the present approach, the time improvement can be calculated in experiment 2. The beginning time is taken the first contact with the workpiece, and the end time is taken when the last cycle finishes. When using constant feed rate the machining time is  $t_1 = 51.5(s)$  and when applying the present approach is  $t_1 = 41.3(s)$ . The time improvement is of approximately 20%. This is expected since for higher feed rate, higher cutting speed is obtained.

## 6 Conclusions

In the present paper, a fuzzy-logic controller is designed to control the cutting force for rough turning operations. When designing the controller, a smooth change of feed rate is considered to prevent tool damage. Additional considerations were done to improve the force control for rough turning operations. The situations that happen in multiple repetitive canned cycles when there is and there is not contact between the cutting tool and the workpiece were taken into account. Controller activation and

deactivation for this situations is proposed to improve the force control. This avoid unnecessary overshoots at the beginning of each cycle and save the feed rate from the last cycle for the next cycle. By experiments, the force control of the present approached is verified. The results show that using the present approach can improve the machining time around 20% when using a 20% higher desired force, for the specific shown case.

## References

1. Rangwala SS, Dornfeld DA (1989) Learning and optimization of machining operations using computing abilities of neural networks. In: IEEE transactions on systems, man, and cybernetics, vol 19, no 2, pp 299–314 (Mar/Apr)
2. Allen R, Huang K (1994) Self-tuning control of cutting force for rough turning operations. Proc-Inst Mech Eng Part B J Eng Manuf 208(3):157–165
3. Toutant R, Balakrishnan S, Onyshko S, Popplewell N (1993) Feedrate compensation for constant cutting force turning. IEEE Control Syst 13:44–47
4. Rober SJ, Shin YC (1996) Control of cutting force for end milling processes using extended model reference adaptive control scheme. ASME J Manuf Sci Eng 339–347 (Aug)
5. Pitstra WC, Pieper JK (2000) Controller designs for constant cutting force turning machine control. ISA Trans 39:191–203
6. Koren Y (1983) Computer control of manufacturing systems, 1st edn. McGraw-Hill, New York
7. Wang N, Liang J, Yang G (2003) Neuro-fuzzy control for turning processes. In: IEEE proceedings of the American control conference (June)
8. Li H-X, Gatland HB (1995) A new methodology for designing a fuzzy logic controller. In: IEEE transactions on Systems, man, and cybernetics, vol 25, no 3, pp 505–512 (Mar)
9. Lian R-J, Lin B-F, Huang J-H (2005) A grey prediction fuzzy controller for constant cutting force in turning. Int J Mach Tools Manuf 45:1047–1056

# Development of In-Situ Hybrid 3-D Measuring Methodology for Critical Dimension Inspection in Large-Scale Robot Machining of Composite Materials



Liang-Chia Chen, Manh-Trung Le, and Chih-Jer Lin

**Abstract** The article presents a hybrid 3-D measuring methodology to address a critical common problem in a large scale space of robot machining of composite materials, especially assembly holes or geometric features to be accurately machined on a free-form shell of composite materials. The referred machining volume can be ranged  $1 \text{ m}^3$  up to  $10 \times 10 \times 10 \text{ m}^3$  or larger, which is commonly needed in aerospace space industries. The developed hybrid 3-D measuring methodology integrates a highly accurate touch-triggered probe and an optical 3-D surface profilometer as its sensor fusion configuration. The accuracy of the robot machining space is pre-calibrated and compensated by the accuracy traceability transferred from a pre-calibrated coordinate measurement machine (CMM) by measuring the mold fixture attached to the machined part. More importantly, the key development in this research is the measurement integration of touch-triggered (for holes or other inaccessible features by the optical) and optical sensing (for freeform surfaces) by linking the geometric features with some pre-defined unique or invariant machined geometry, such as specific geometric centers or positions. The accurate extraction of the theses important positioning targets from both the measured data plays non-trivial key in achieving accurate measurement especially in a large-scale working volume. From our preliminary experimental test and verification, using the developed methodology, the maximum positioning error of the composite material shells machined by an industrial robot can be improved from several hundred micrometers down to less than  $100 \mu\text{m}$  when a machining volume is up to  $2 \times 2 \times 2 \text{ m}^3$ . Three to five fold improvement of the machined accuracy is achievable.

**Keywords** 3-D measurement · Absolute measurement · Structured light pattern · Critical dimension inspection

---

L.-C. Chen

Department of Mechanical Engineering, National Taiwan University, No.1, Sec. 4 Roosevelt Rd., Taipei 106, Taiwan

L.-C. Chen · M.-T. Le (✉) · C.-J. Lin

Graduate Institute of Automation Technology, National Taipei University of Technology, No. 1, Sec. 3, ZhongHsiao East Rd., Taipei 106, Taiwan

© Springer Nature Switzerland AG 2022

S. Hinduja et al. (eds.), *Proceedings of the 38th International MATADOR Conference*,  
[https://doi.org/10.1007/978-3-319-64943-6\\_56](https://doi.org/10.1007/978-3-319-64943-6_56)

737



## 1 Introduction

A hybrid measurement system is introduced that has been used successfully to perform high accuracy measurements in in-situ machining environments. The articulated arm robots have been widely used and plays a critical role in aerospace industries for aero-structure production for many years. Industrial robots have been strongly developed, that offer airframe manufacturers significant benefits in cost, flexibility and reliability. Robotic drilling cells can reduce assembly line footprint and increase drilling accessibility in large scale space. In spite of confronting with high demands in aerospace assembly, robot systems now have not been able to meet customer requirements, especially in machining or assembly accuracy. To accomplish high quality manufacturing specification in airplane production, a positioning error of machined features shall be strictly controlled with a maximally allowable error to be commonly less than a few tens of micro meters in a large scale size. Moreover, the modern robots usually possess an inevitable weakness in its less structure rigidity when compared with its usual counterpart, multiple machining centers, especially for its positioning accuracy control with respect to the defined machine coordinate system. In addition, accurate measurement and machining of the freeform shapes of composite materials also introduces an unavoidable difficulty when the machined geometric information has to be synthesized with the machine coordinate system seamlessly.

To resolve the key problem as described above, Lei [1] employed the fundamental theory of a wavelet transform and edge detection method to develop an automated vision inspection system for the critical size measurement of workpieces. Ji [2] introduced a constraint-based non-linear least-squares framework for simultaneously estimating camera parameters and reconstructing 3-D circular machine features from single image. Mitul [3] developed an intelligent and confident system for automatic surface defect quantification in 3-D space. To realize automated 3-D inspection on robot, Ning [4] developed a robot integrated 3-D area-sensing system to automatically inspect 3-D shape of an automotive sheet metal. Meanwhile, the real time 3-D shape inspection using gray code line shifting (GCLS) principle with better accuracy in detection than other patterns was introduced by Tsai [5] and Shi [6]. In addition, the power of point cloud was used for developing a 3-D efficient edge detection, feature extraction, object segmentation and registration algorithm which is providing the efficient performance in processing of 3-D shape inspection [7–15].

Although some work has been done to date, more investigation and development need to be conducted in depth to ensure the performance of in-situ 3-D inspection and machining accuracy in aerospace industry. Apparently, the previous work has touched little on achieving a more comprehensive solution in enhancing positioning accuracy by bringing in sensor fusion for extracting critical geometric machining features.

Therefore, the research developed a hybrid 3-D measuring methodology to address a critical common problem in a large scale space of robot machining of composite materials, especially assembly holes or geometric features to be accurately machined

on a free-form shell of composite materials. The referred machining volume can be ranged  $1 \text{ m}^3$  up to  $10 \times 10 \times 10 \text{ m}^3$  or larger, which is commonly needed in aerospace space industries.

## 2 Methodology

In the approach, the developed hybrid 3-D measuring methodology integrates a highly accurate touch-triggered probe and an optical 3-D surface profilometer which was designed and fabricated at NTU as its sensor fusion configuration, as shown in Fig. 1.

The accuracy of the robot machining space is pre-calibrated and compensated by the accuracy traceability transferred from a pre-calibrated coordinate measurement machine (CMM) by measuring the mold fixture attached to the machined part, as shown in Fig. 2. The compensated robot's spatial error in large space can be denoted by

$$\begin{aligned} X_c &= 2 * X_{cmm} - X_r \\ Y_c &= 2 * Y_{cmm} - Y_r \\ Z_c &= 2 * Z_{cmm} - Z_r \end{aligned} \quad (1)$$

$$\begin{aligned} n_{x2} &= 2 * n_x - n_{x1} \\ n_{y2} &= 2 * n_y - n_{y1} \\ n_{z2} &= 2 * n_z - n_{z1} \end{aligned} \quad (2)$$

where  $(X_c, Y_c, Z_c, n_{x2}, n_{y2}, n_{z2})$ ,  $(X_{cmm}, Y_{cmm}, Z_{cmm}, n_x, n_y, n_z)$ ,  $(X_r, Y_r, Z_r, n_{x1}, n_{y1}, n_{z1})$  represent the compensated robot coordinate with orientation vectors, the CMM measured coordinate with orientation vector (on the mold fixture) and the robot measured coordinate on drill holes of workpiece with orientation vector, respectively.

More importantly, the key development in this research is the measured data synthesis of touch-triggered (for holes or other inaccessible features by the optical) and optical sensing (for freeform surfaces) by critically extracting and seamlessly integrating the geometric features on some pre-defined unique or invariant machined geometry, such as specific geometric centers or positions. The accurate extraction of the theses important positioning targets from both the measured data plays non-trivial key in achieving accurate measurement especially in a large-scale working volume.

To calibrate the robotic 3-D optical sensing measurement system, many existing solutions only deal with the traditional calibration between the robot and machined-part. Three system calibration should be developed and performed, that includes the robot calibration for verification of robot kinematics, machined-part calibration for obtaining the workpiece coordinate that is the transformation matrix from the machined-part coordinate to the robot coordinate and the robot sensor calibration for identifying the transformation matrix from the 3-D optical sensing coordinate to the robot end-effector. In the developed method, to achieve robot sensor calibration, an

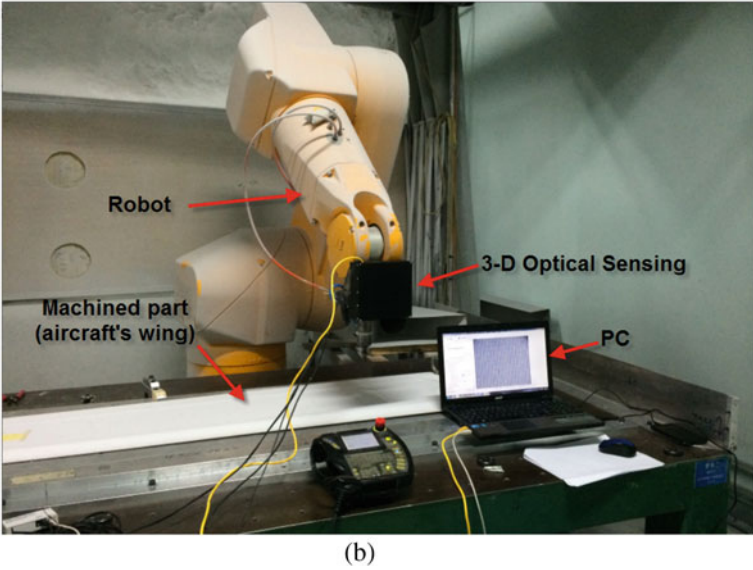
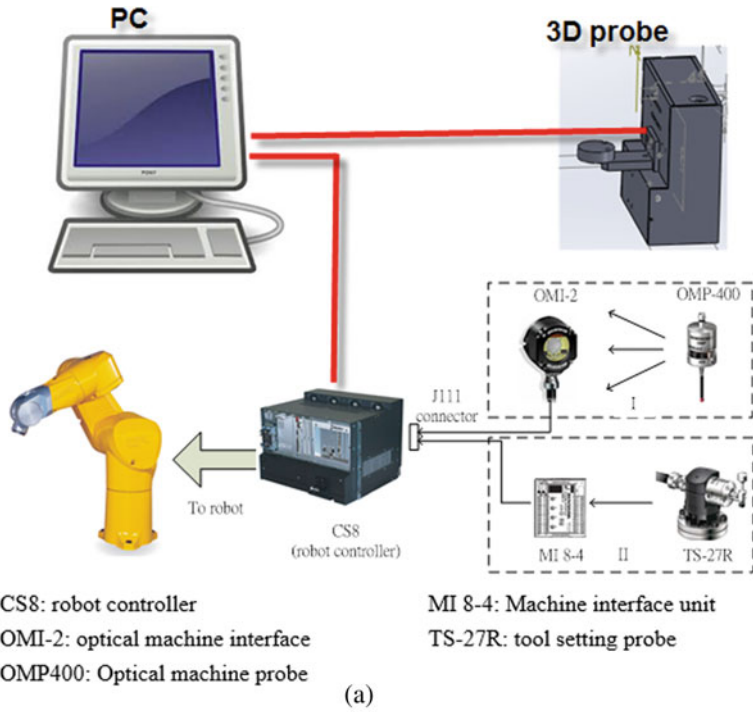


**Fig. 1** The developed hybrid 3-D measuring methodology: **a** the diagram of highly accurate touch-triggered probe OMP400 and **b** the Optical 3-D surface profilometer being integrated with the robot end effect

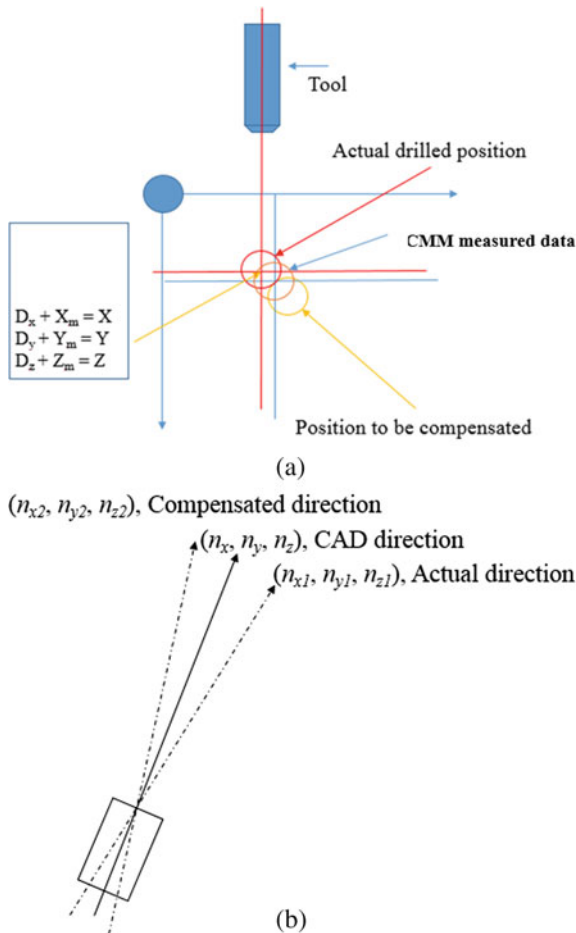


**Fig. 2** The pre-calibrated and compensated method of the robot machining space (spatial errors for estimation of): **a** feature position; **b** normal vector of geometric feature

iterative closest point (ICP)-based algorithm was developed. The strategy employed here is that the mold fixture for shell machining can generally provide a known pre-calibrated geometric shape that match its CAD models with high accuracy is measured by touch-triggered probe for purpose of calibration in identifying the robot space error, especially the positioning error with respect to the machined features. Meanwhile, this also offers a unique advantage to apply an ICP-based method to accurately determine the transformation matrix from the robot end-effector to 3-D optical probe being mounted onto it.

To inspect the critical dimension of holes in large-scale robot machining of freeform surface composite materials, the normal vector of machined geometric features plays a crucial role because the normal vector on a freeform surface has

a significant correlation with the measured and machined accuracy. Moreover, with accurate normal vector of the geometric feature, the critical geometric can be matched with the part model without ambiguity.

The maximum-area-direction of a flat-patch is the defined direction when the detecting patch is orthographically projected along this direction, in which the projected image of the patch has a maximum area [16].

The average normal of a patch can be defined as follows

$$\vec{n}_{average} = \frac{\sum_{i=1}^p a_i \vec{n}_i}{\sum_{i=1}^p a_i} \Big/ \left\| \frac{\sum_{i=1}^p a_i \vec{n}_i}{\sum_{i=1}^p a_i} \right\| \quad (3)$$

where  $a_i$ ,  $\vec{n}_i$  are the area and normal vector of triangle (a surface is a collection of all the connected triangles corresponding to a parametric surface and a patch is a collection of  $n$  ( $n \geq 1$ ) connected surfaces), respectively.

The image area of a patch in orthographical projection without scaling factor can be computed as:

$$A = \sum_{i=1}^p a_i |\vec{n}_i \cdot \vec{v}| \quad (4)$$

where  $\vec{v}$  is the vector of orthographical projection. To calculate  $\vec{v}$  as  $A$  reaches to its maximum, the following relation can stand:

$$\frac{dA}{d\vec{v}} = 0 \quad (5)$$

$\vec{v}$  can be further determined as:

$$\vec{v} = \frac{\sum_{i=1}^p a_i \vec{n}_i}{\sum_{i=1}^p a_i} \Big/ \left\| \frac{\sum_{i=1}^p a_i \vec{n}_i}{\sum_{i=1}^p a_i} \right\| \quad (6)$$

From Eqs. (3) and (6), it is concluded that the maximum-area-direction can be considered as the same direction as the average normal vector.

In our method, due to unavoidable signal delay between the touch-triggered probe and the robot controller and again its excessive measuring time, the sensor cannot be employed for a direct general feature inspection. Fortunately, in the hybrid sensing strategy developed here, 3-D optical sensing is employed and developed for critical dimension inspection. Our method is comprehensively outlined in Fig. 3, which begins by capturing point clouds in range images for 3-D optical probe. A reference plane is then detected by applying the RANSAC method to extract the uniform region as the plane fitting for machined-parts dimensional inspection. Following this, the edge of geometric features in the machined workpiece are extracted by using the developed 3-D edge detection method that extracts the critical geometric features, such as accurate depth, surface normal vectors or surface curvatures. Meanwhile, the method also employs the detected optical color image to identify critical

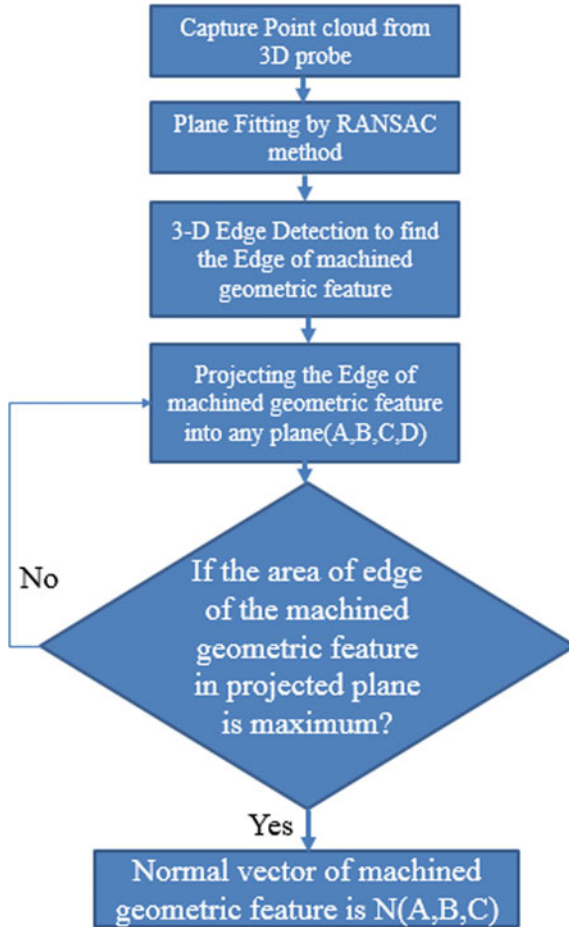


Fig. 3 Flow chart for calculating the normal vector of machined geometric feature

contour edges for data synthesis between 2-D and 3-D geometric information. With the method, critical dimension and normal vector of the geometric features of the machined part can be accurately extracted when least squares approximation methods are employed for the best fitting between the measured data and part model. Therefore, the critical dimension of the geometric features can be extracted and determined accurately.

### 3 Experiments and Analyses

The feasibility of the proposed method has been tested by implementing a hybrid sensing system using a touch-triggered probe (Renishaw OMP400) and a high-speed 3-D optical surface profilometer which are attached to the end-effect of an industrial robot arm (Staubli RX170b).

The developed 3-D optical surface profilometer is shown in Fig. 4. It mainly includes a LED light fringe generator with 850 nm of wavelength capable of generating and projecting invisible fringe patterns and a high resolution CCD with a high speed acquisition rate of up to 60 frames per second. A five-step phase-shifting fringe principle based on triangulation principle is employed to measure surface profiles with a depth measuring precision of 5  $\mu\text{m}$  in a range of 30 mm.

Figure 5 illustrates the experiment results that obtained by the developed method. Figure 5a shows the range image of 3-D optical sensing with a field of view of  $24 \times 32 \text{ mm}^2$ ; Fig. 5b and d illustrate the 3-D edge geometry being extracted while the normal vector, circular features, position and dimension of machined hole are all detected and shown in Fig. 5c and e. The measured error is defined as the deviation from the CMM measured data ( $X_{\text{cmm}}, Y_{\text{cmm}}, Z_{\text{cmm}}, D_{\text{cmm}}$ ) and the actual measured data ( $X_m, Y_m, Z_m, D_m$ ). From the analysis on the measured errors shown in Table 1 (it was verified that the maximum positioning error of the in-situ machined error was within 85  $\mu\text{m}$ ). It indicates that the maximum positioning error of composite material shells machined by an industrial robot, can be reduced from its original deviation with a range of 400  $\mu\text{m}$  to less than 100  $\mu\text{m}$ . Four folds of the machined accuracy can be achieved while the critical geometric features can also be measured and verified automatically.

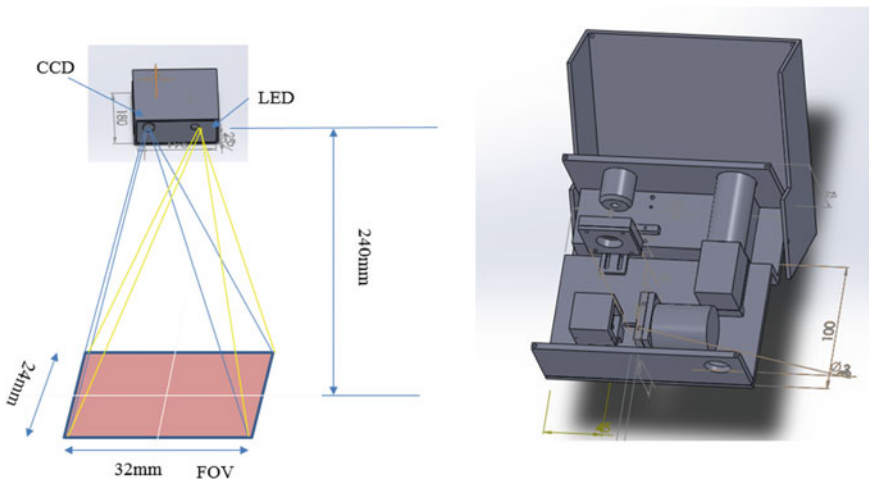
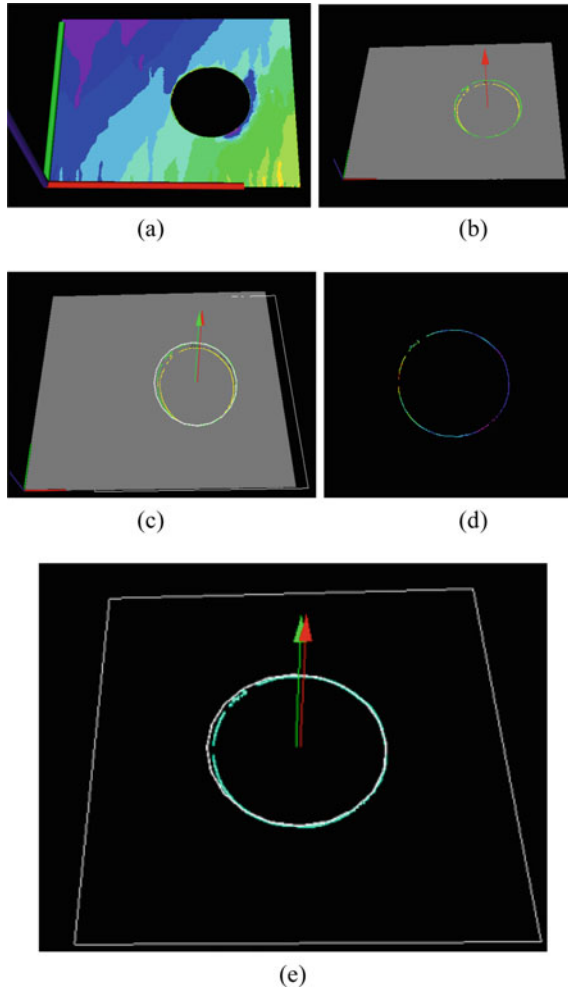


Fig. 4 3-D vision system employed in the experiment



**Fig. 5** 3-D measuring methodology for critical dimension inspection: **a** The detected 3-D range image; **b** and **d** show the results of 3-D edge detection; **c** and **e** are the results of critical dimension inspection with the normal vector and circular features of a machined hole

**Table 1** Positioning errors of composite material shells machined by an industrial robot (Staubli RX170b)

$X_{cmm}$	$Y_{cmm}$	$Z_{cmm}$	$D_{cmm}$	$X_{cad}$	$Y_{cad}$	$Z_{cad}$	$D_{cad}$	$E_x$	$E_y$	$E_z$	$E_d$	Error
32.976	- 0.012	0.0	6.383	33.060	0.0	0.0	6.35	- 0.084	- 0.012	0.0	0.033	0.085
- 0.011	0.007	0.0	6.369	0.0	0.0	0.0	6.35	- 0.011	0.007	0.0	0.019	0.013
0.049	100.064	0.0	6.380	0.0	100	0.0	6.35	0.049	0.064	0.0	0.030	0.081
33.120	99.999	0.0	6.383	33.060	100	0.0	6.35	0.060	0.001	0.0	0.033	0.060



## 4 Conclusions

In the article, an in-situ hybrid 3-D measuring methodology for critical dimension inspection in large-scale robot machining of composite materials was successfully developed for enhancement of the machining accuracy in using large-scale robot machining for composite materials. Meanwhile, the robot sensor calibration problem can be solved to obtain accurate transformation matrix by using an ICP-based algorithm. From our preliminary experimental test and verification, the maximum positioning error of the composite material shells machined by an industrial robot can be improved from several hundred micrometers down to less than 100  $\mu\text{m}$  when a machining volume is up to around  $2 \times 2 \times 2 \text{ m}^3$ . Four folds of machined accuracy is achievable and the critical dimension of the machined geometric features, such as Euclidean distances, coplanarity, parallelism and orthogonality in in-situ aircraft structure production can be inspected with high accuracy.

**Acknowledgements** The authors would convey their great appreciation to Aerospace Industrial Development Corporation (AIDC), Taichung, Taiwan for the fund support to the research and development of the work. We would like to acknowledge all the support we received from the staff in AIDC's Technique Development Group and 3-D Vision group of NTU's AOI Lab for their contributions to the work.

## References

1. Lei LC, Zhou XJ, Pan MQ (2005) Automated vision inspection system for the size measurement of work piece, IMTC 2005
2. Ji Q, Haralick RM (1998) 3-D reconstruction of circular machine features from a single image for inspection
3. Tailor M, Petzing J, Jackson M (2014) An intelligent and confident system for automatic surface defect quantification in 3-D, ICMT 2014
4. Xi N, Shi Q, Zhang C (2010) Developing a robot-aided area sensing system for 3-D shape inspection. *J Manuf Sci Eng*
5. Tsai M, Hung C (2005) Development of a high-precision surface metrology system using structured light projection. *Measurement* 38(3):236–247
6. Shi Q, Xi N, Chen H, Chen Y (2005) integrated process for measurement of free-form automotive part surface using a digital area sensor. In: *Proceeding of the international conference on robotics and automation*, pp 578–583
7. Choi C, Trevor A, and Christensen HI (2013) RGB-D edge detection and edge-based registration. In: *IROS 2013, IEEE/RSJ*
8. Aldoma A, Vincze M, Blodow N, Gossow D, Gedikli S, Rusu R, Bradski G (2011) CAD-model recognition and 6DOF pose estimation using 3D cues. *ICCV Workshops 2011*:585–592
9. Chen LC, Le MT, Nguyen XL (2012) Automatic 3-D optical detection on orientation of randomly oriented industrial parts for rapid robotic manipulation. In: *AUSMT vol 2, no 4*
10. Lu F, Milios E (1997) Robot pose estimation in unknown environments by matching 2D range scans. *J Intell Rob Syst* 18(3):249–275
11. Pauly M, Keiser R, Gross M (2003) Multi-scale feature extraction on point-sampled surfaces. *Comput Graph Forum* 22(2003):281–289

12. Shi Q, Xi N, Chen Y, Sheng W (2006) Registration of point clouds for 3D shape inspection. In: IEEE international conference on intelligent robots and systems, pp 235–240
13. Zhang S (2010) Recent progresses on real-time 3D shape measurement using digital fringe projection techniques. *Opt Lasers Eng* 48:149–158
14. Shi Q, Xi N, Chen H, Chen Y (2005) Calibration of robotic area sensing system for dimensional measurement of automotive part surfaces. In: IROS 2005, IEEE/RSJ
15. Sheng W, Xi N, Song M, Chen Y (2003) CAD-Guided sensor planning for dimensional inspection in automotive manufacturing. *IEEE/ASME Trans Mechatron* vol 8, no 3
16. Sheng W, Xi N, Song M, Chen, Y, Rankin III J (2000) Automated CAD-Guided automobile part dimensional inspection. In: Proceeding of the international conference on robotics and automation

# **Welding**

# Laser Welding of Dissimilar Materials for Electric Vehicle Batteries



M. Naeem and A. Montello

**Abstract** Today's requirements on vehicles with internal combustion engine are characterized by more sophisticated emission regulations, rising fuel prices and higher driver's demand on driving dynamic, comfort in line with increased environmental awareness. For that reason, more and more car manufacturers throughout the world are focusing on electric vehicles. The battery technology currently in use is lithium ion batteries because these are smaller and lighter than current automotive power batteries (generally, Nickel Metal Hydride). This technology can provide power equivalent to current technology at a smaller size and lighter weight, or more power at an equivalent size and weight. The batteries used in the electric vehicle batteries (EVB) are constructed from a combination of different materials and these materials pose particular challenges to be joined together. The battery has to operate safely and reliably for the whole of the life cycle stipulated by the vehicle manufacturer, and that is at least ten years. In this work, we will provide welding data for aluminium 3000 series, pure copper and joints between copper and aluminium alloy materials with fiber lasers.

**Keywords** Aluminium alloy · Pure copper · Dissimilar material joints · Intermetallic compound · Laser power · Laser focus position · Mechanical properties

## 1 Introduction

The batteries used in electric vehicles (EVB) are constructed from a combination of different materials and these materials pose particular challenges to be joined together. In battery and pack manufacture, there are a number of similar and dissimilar materials that need to be joined i.e.

---

M. Naeem (✉) · A. Montello  
Prima Power Laserdyne, 8600 109th Avenue North, Champlin, MN 55316, USA  
e-mail: [mohammed.naeem@primapower.com](mailto:mohammed.naeem@primapower.com)

© Springer Nature Switzerland AG 2022  
S. Hinduja et al. (eds.), *Proceedings of the 38th International MATADOR Conference*,  
[https://doi.org/10.1007/978-3-319-64943-6\\_57](https://doi.org/10.1007/978-3-319-64943-6_57)

- Aluminium alloys
- Pure copper
- Aluminium–copper
- Copper—stainless steel
- Copper to pure nickel
- Aluminium to pure nickel
- Nickel coated steels

The electric current carrying components inside a lithium-ion battery are made of copper or aluminum alloys and are the external buss bars that need to be joined to the outside terminals to connect a series of cells. Aluminium alloys (3000 series) and pure copper which are the main materials need to be laser welded either in similar or dissimilar configurations to produce electrical contact to the positive and negative outside terminals. The main welded joints are overlap, butt and fillet. The final welding step in the cell assembly is the seam sealing of the aluminium cans to create a barrier for the internal electrolyte and welding of tab material to negative and positive terminals to create the electrical contacts for the pack.

The weldability of dissimilar metals depends on many different factors. The physical properties have a high influence on the amount of energy coupled in and the heat transfer [1]. Illustrated in Table 1 is the weldability of metal pairs. In the welding of dissimilar metals, good solid solubility is essential for sound weld properties. This is achieved only with metals having compatible melting temperature ranges. If the melting temperature of one material is near the vaporisation temperature of the other, poor weldability is obtained and often involves the formation of brittle intermetallics.

When joining dissimilar materials, there may be certain advantages in using laser welding even though brittle intermetallics may tend to form. Since the weld itself is narrow, the volume of intermetallics may also be reduced to acceptable limits. Again, it may be possible to offset the beam in one direction or the other, thus allowing some control over composition of the resulting alloy. Although it may be possible to produce a sound joint by these methods on a laboratory scale, it is more difficult to achieve similar control under production conditions. Mixing the molten metal in a

**Table 1** Weldability of metal pairs

	Al	Ag	Au	Cu	Pt	Ni	Fe	Ti	W
Al	–	C	X	C	X	X	X	X	X
Ag	C	–	S	C	S	C	D	C	D
Au	X	S	–	S	S	S	C	X	N
Cu	C	C	S	–	S	S	C	X	D
Pt	X	S	S	S	–	S	S	X	X
Ni	X	C	S	S	S	–	C	X	X
Fe	X	D	C	C	S	C	–	X	X
Ti	X	C	X	X	X	X	X	–	X
W	X	D	N	D	X	X	X	X	–

laser weld seldom produces a chemically homogeneous fused zone between the two dissimilar materials. Although the average chemical composition of the weld may be acceptable, local heterogeneity can be responsible for the presence of brittle zones. It will also be apparent that minor variations in the beam position can significantly influence the relative proportions of the two main constituents in the weld zone.

In Table 1, Metals (Al: aluminum; Ag: silver; Au: gold; Cu: copper; Pt: platinum; Ni: nickel; Fe: iron; Ti: titanium; W: tungsten) joined using LBW and their results (C: Complex structures may exist X: Intermetallic compounds formed; undesirable combination S: Solid solubility exists in all alloy combination D: Insufficient data for proper evaluation N: No data available) are shown in [2].

Majority of joining of dissimilar metals in the past has been carried out with pulsed lamp Nd:YAG lasers [3, 4]. Lamp-pumped lasers are capable of producing long, multi-ms, pulses with peak powers many times the rated average power of the laser, provided that the duty cycle is sufficiently low. This ability stems from the flash-lamp itself which is often more constrained by the maximum average thermal load than the peak power output. High peak powers pulsed lamp pumped Nd:YAG lasers coupled with pulse shaping makes these laser ideal for welding dissimilar materials. The shaping of pulses is of great importance since the temperature has to be controlled in the region where the two molten phases are mixed. Weld depth that is too deep—which can lead to defective joints—and also insufficient weld depths can be avoided by adjusting the high starting power and the correct decreasing power to the joint geometry and the material properties of the pulse shape.

Compared to conventional lamp pumped Nd:YAG laser, fiber laser offers a number of advantages when welding dissimilar materials. The big advantage of these new laser sources is the beam quality or focusability. Focusability is understood as the ability to achieve a small focus diameter with a given optical element. It is defined by the inverse beam parameter product (BPP) [5]:

$$\text{Focusability} = 1/\text{BPP} = 4/\Theta L.dL \quad (1)$$

The small focus diameter of the fiber lasers offers a number of advantages during laser welding i.e.

- High power density at the workpiece
- Reduced heat input and heat affected zone
- The volume of intermetallics may also be reduced to acceptable limits.

Fiber laser welding can be either carried with a single mode fiber laser with average power exceeding 2 kW or with multi- mode fiber lasers with laser powers excess of 17 kW. Multi- mode fiber lasers normally consist of several single mode fiber lasers coupled into one fiber with a reduced beam quality. However the beam quality is still good enough to use small core diameter fibers (thus enabling very high power density at the workpiece. From an applications perspective, both single and multi-mode fiber lasers have their advantages and disadvantages when welding dissimilar materials.

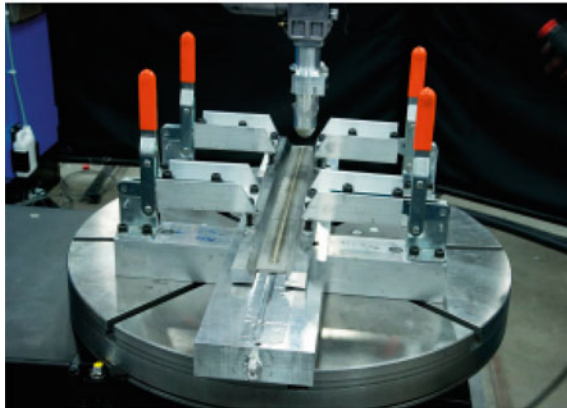
This paper highlights welding results achieved with a 2 kW multi-mode fiber laser with pure copper, aluminium alloy and dissimilar joint between copper and aluminium.

## 2 Experimental Details

The welding tests were conducted on Laserdyne 430 system with IPG 2 kW continuous wave multimode fiber laser with the beam quality of  $\leq 4$  mm mrad. Figure 1 shows



(a)



(b)

**Fig. 1** Experimentatl set-up; **a** 430 6-axis machining centre fitted with 2 kW fiber laser; **b** clamping fixture which produces constant pressure along the length of weld

**Table 2** Thermophysical properties of Cu and Al

Metals	CTE X10 <sup>-6</sup> K <sup>-1</sup>	LHF Jg <sup>-1</sup>	SH JK <sup>-1</sup> kg <sup>-1</sup>	TC Wm <sup>-1</sup> K <sup>-1</sup>	MP deg C
Al	23.5@ 0-100C	388	900@ 25C	237@ 0-100C	660
Cu	17.0@ 0-100C	205	388@ 25C	401@ 0-100C	1083
Fe	12.1@ 0-100C	272	444@ 25C	81@ 0-100C	1535

*CTE* Coefficient of thermal expansion; *LHF* Latent heat of fusion; *SH* Specific heat; *TC* Thermal conductivity; *MP* Melting point

a Laserdyne 430 system together with the clamping fixture used during the welding tests. The beam from the laser was transmitted in a 100  $\mu\text{m}$  diameter fiber, which terminated in Laserdyne welding head nozzle fitted with focusing optics and the calculated spot size at the workpiece was 143  $\mu\text{m}$ . Laser welding experiments were performed on various EVB materials, however only copper and aluminium welding data is reported in this paper.

The most important thermophysical properties of the corresponding metals are shown in Table 2. Although these values refer to pure metals and some properties are temperature dependent, the data provided a basic reference for assessing the weldability and deriving the welding strategy.

Parameters and welding speeds were adjusted to produce welds with consistent topbead and underbead with minimal spatter and undercut. Gas shielding for the weld topbead was supplied coaxially through the welding nozzle. This welding nozzle (patent pending) has a number of unique features which improves the weld quality during laser welding of difficult materials.

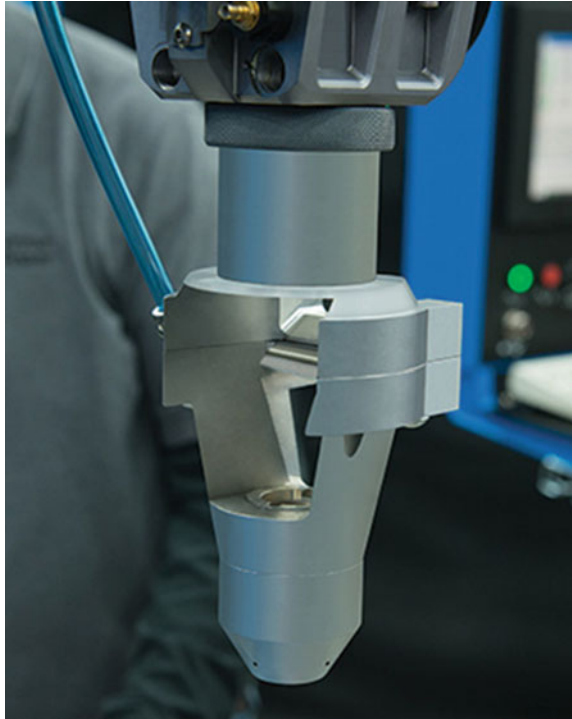
The nozzle (Fig. 2) is intergated with high pressure air cross jet. The cross-jet provides a high velocity gas barrier that prevents molten metal spatter and fumes from the weld zone and from contaminating the protective lens cover slide. Critical to this design is that the cross-jet does not contaminate or otherwise interfere with the welding shield gas. The cross-jet nozzle can be used with the entire range of shield gas delivery devices including welding shoe and coaxial gas nozzle tip. The shielding gas shoe provides a controlled atmosphere for the weld zone while it is molten and while it is cooling at a temperature which won't be compromised by the ambient atmosphere. This is particularly important when trying to minimize porosity in the weld. An important benefit of the design of the focusing lens/shield gas assemblies for laser welding is that they can be changed quickly in order to vary the focused spot size.

### 3 Results and Discussions

Laser and processing parameters have been developed to weld a range of EVB materials including 3000 series (Al–Mn) aluminium alloys, pure copper and combination



**Fig. 2** Laserdyne welding nozzle (patent pending)



of copper and 3000 series aluminium alloys. Aluminium alloys and pure copper which are the main materials need to be welded either in similar or dissimilar configurations to produce electrical contact to the positive and negative outside terminals. The main welded joints are overlap because these joints are less demanding to part fit up and tolerances. Under optimum laser and processing it was possible to crack and porosity free welds in pure copper and 3000 aluminium alloy. Typical cross sections of the copper and aluminium alloy welds are highlighted in Figs. 3 and 4 respectively.

Welding tests carried out with aluminium to copper have highlighted that no single parameter controls weld quality whereas it is a combination of both laser and processing parameters which has a significant effect on the weld quality of these joints.

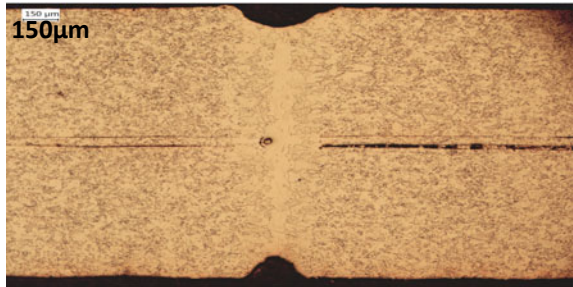
Laser output modulated output from high power continuous wave lasers (Fig. 5) can also help with cracking and porosity. Modulation produces welds with controlled heating and cooling. This reduces the freezing range of the weld metal minimizing tendencies for solidification cracking in aluminium alloys while reducing formation of brittle intermetallics during the dissimilar material welding process.

Power density, an optical power per unit area, is important parameter when welding highly reflected materials. The high initial reflectivity of reflective materials can be overcome provided the intensity of the laser focused beam is sufficiently high. The absorption rate increases remarkably as the temperature of the material

**Fig. 3** C101 pure copper;  
1.6 kW CW power, N<sub>2</sub> shield  
gas



2x1.0 mm thick overlap joint



0.75+50 μm foil+0.75 mm overlap joint

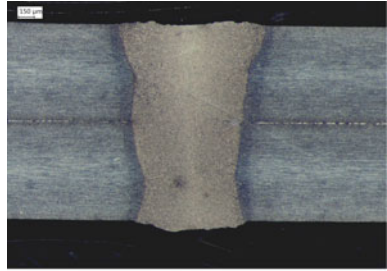
rises. Both aluminium and copper require higher power intensity compare to steels for laser weld initiation. Whereas welding with reduced power density can lead to problems with the back reflection.

Laser spot position respect to the workpice, it may be possible to offset the beam in one direction or the other, thus allowing some control over composition of the resulting alloy.

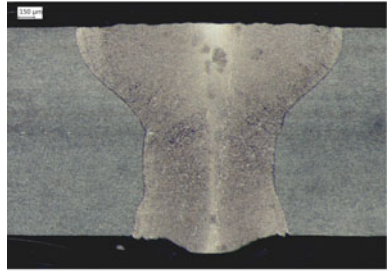
Welding tests carried out with copper to aluminium alloy showed it was possible to weld these together in both overlap and butt joint configuration respectively (Fig. 6). However, under close examination of the overlap joint, it appears there are some micro cracks at the lower part of the weld (Fig. 7). The Cu–Al phase diagram (Fig. 8) [6] shows a wide range of Cu–Al phases that may be formed during welding. In addition, during non- equilibrium cooling conditions are known to promote the formation of CuAl<sub>2</sub> [2], Fig. 9 shows EDX spectra near the bottom of the weld. These cracks are brittle in character, which drastically reduces the tensile strength (Table 3).

Further work is in progress to produce welds with reduced intermetallics which hopefully will improve the mechanical properties.

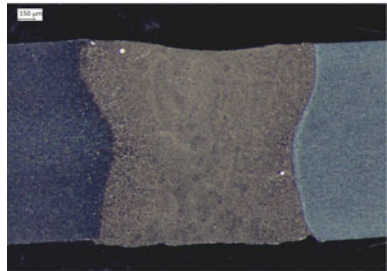
**Fig. 4** 3003 Al alloy,  
1.6 kW CW average power,  
N<sub>2</sub> shield gas



2x1.0mm overlap joint

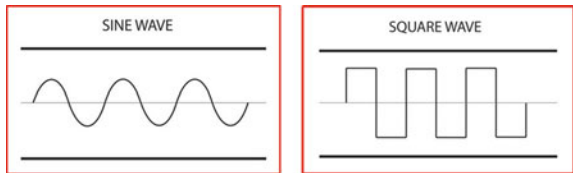


2x1.5mm overlap joint



1.0+1.0mm butt joint

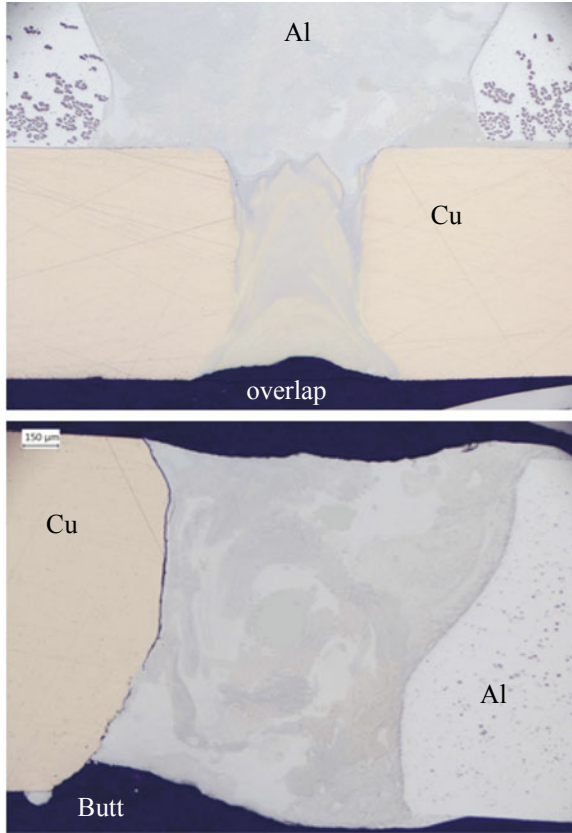
**Fig. 5** Example of laser  
outputs from CW fiber laser



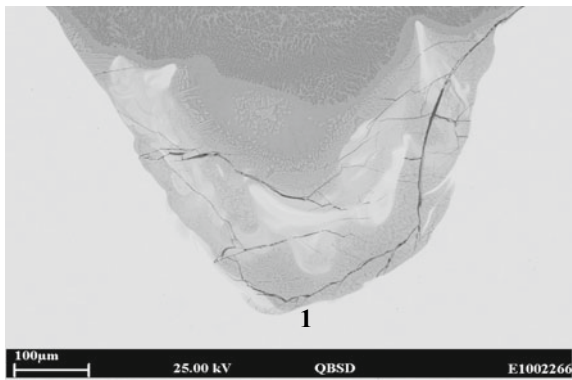
## 4 Summary

Extensive testing programs have been conducted by Prima Power Laserdyne on laser welding electric vehicle battery materials. These tests, which are ongoing, covered

**Fig. 6** Dissimilar material joint, 1.6 kW power, N<sub>2</sub> shield, unetched micrograph



**Fig. 7** SEM micrograph of the root of the weld between Al alloy and Cu with a nominal magnification scale



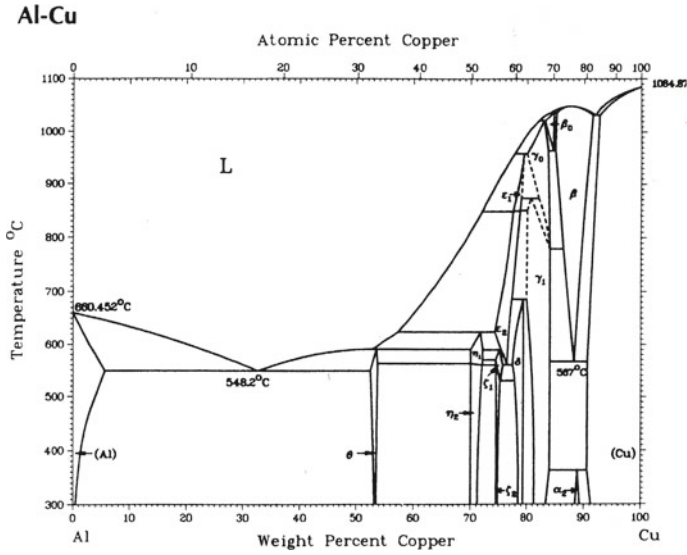


Fig. 8 Al-Cu phase diagram [6]

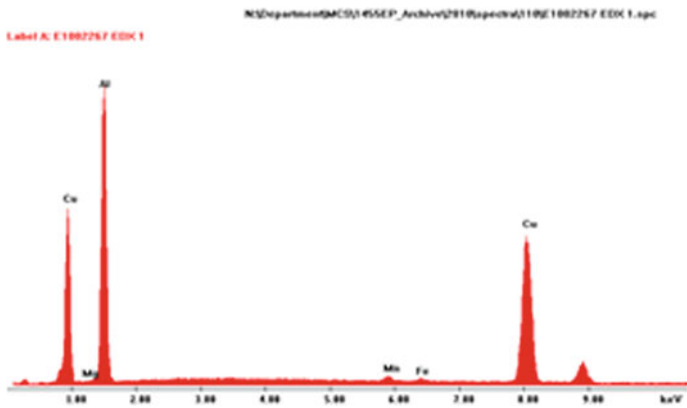


Fig. 9 EDX spectra near the bottom of the weld (location 1 in Fig. 7)

Table 3 Tensile strength data

Material	Joint type	Tensile strength (MPa)
3003 Al	Overlap	150
3003 Al	Butt	170
C101 Cu	Overlap	220
C101 Cu	Butt	210
Al + Cu	Overlap	60
Al + Cu	Butt	65

a broad range of processing and laser parameters to explore and examine crack sensitivity and porosity. The results have highlighted that:

- Sound welds in both aluminium alloy and pure copper were produced with the fiber laser.
- The bio-metallic joints of aluminium and copper had intermetallic phase which reduced the tensile strength of the weld joints.

## References

1. Klages K, Ruettimann C, Olowinsky, AM (2003) Laser beam micro welding of dissimilar metals. In: Proceeding of ICALEO 2003. Laser Institute of America, Jacksonville
2. Naeem M, Jessett R, Withers K (2010) Welding of dissimilar materials with 1 kW fiber laser. In: Proceeding of ICALEO 2010. Laser institute of America, Anaheim, California
3. Naeem M (2006) Microjoining of dissimilar metals with pulsed Nd:YAG laser. In: Pacific International Conference on Applications of Lasers and Optics, PICALEO 2006, Melbourne, Australia (March)
4. Naeem M (2008) Microwelding performance comparison between a low power (125 W) pulsed Nd:YAG laser and a low power (100–200 W) single mode fiber laser. In: Pacific International Conference on Applications of Lasers and Optics PICALEO 2008, Beijing, China (April)
5. Dausinger F (2002) Benefit of enhanced focusability of new YAG-lasers. In: Proceedings of the EALA, Bad Nauheim/Frankfurt, Germany
6. Metals handbook, metallography structures and phase diagrams, vol 8. American Society for Metals, p 259

# Dissimilar Metal Laser Beam Welding Between Aluminum and Copper



Shikai Wu, Jianglin Zou, Rongshi Xiao, and Peng Dong

**Abstract** In this study, AA1060 aluminum alloy and T2 copper with a thickness of 3 mm were joined by Yb:YAG Disc laser welding. Three joint types, namely laser fusion welding (LF joints), laser deep penetration braze-fusion welding (LPB-F joints) and laser deep penetration braze welding (LPB joints) were obtained depending on the amount of melted copper in the Al/Cu interface. Furthermore, the micro-hardness and mechanical properties of these joints were investigated in detail. The experimental results show that the tensile strengths of LF joint, LPB-F joint and LPB joint are 79 MPa, 94.5 MPa and 52 MPa, respectively. A maximum tensile strength is obtained in LPB-F joint, which is close to that of the 1060 aluminium alloy. The primary reason is that  $Al_2Cu_3$  and  $Al_2Cu$  intermetallic compounds with a comparatively greater hardness exist in the transition layer.

**Keywords** Laser deep penetration-braze welding · Aluminum · Copper · Mechanical properties

## 1 Introduction

The rapid development of modern industrial technology that uses new materials, technologies, and low-cost designs has resulted in many innovative breakthroughs in equipment manufacturing. The advantageous properties of different materials (such as strength, plasticity, toughness, abrasive resistance, corrosion resistance, electrical conductivity, thermal conductivity, etc.) can be used by adopting dissimilar alloy structures in mechanical design and component manufacturing processes [1]. This reduces the manufacturing costs of structures while still producing high-quality performances. Aluminum-copper dissimilar metal joints exhibit extensive potential applications in fields such as electric engineering, chemical engineering and refrigeration industry due to their excellent mechanical properties and high electrical and

---

S. Wu (✉) · J. Zou · R. Xiao · P. Dong  
Institute of Laser Engineering, Beijing University of Technology, Beijing 100124, China  
e-mail: [wushikai@bjut.edu.cn](mailto:wushikai@bjut.edu.cn)

thermal conductivity. For example, using Al–Cu composite structures in power electronic and refrigerator radiators reduces consumption costs and creates a light-weight structure. With the development of new dissimilar alloy welding techniques, the use of Al–Cu connections is receiving increasing attention worldwide.

Currently, aluminum and copper are generally joined by means of fusion welding, braze welding and pressure welding. However, when performing fusion welding the incomplete fusion and impurities can easily be caused due to the large differences between Cu and Al melting points and brittle intermetallic compounds with large electrical resistances may formed at the interface between aluminum and copper. Moreover, the linear expansion coefficient of Cu is 1.5 times larger than that of Al, and cracks are likely to be generated during the solidification process, adding to the difficulties associated with fusion welding of Al/Cu joints. In braze welding, several brittle phases, such as  $\text{CuAl}_2$ ,  $\text{Cu}_2\text{Al}$  and  $\text{Cu}_3\text{Al}_2$  phases, are easily produced in the interface of the two metals. These phases reduce the strength and plasticity of the brazing seams. Additionally, in order to removal the dense aluminum oxide film, some corrosive brazing fluxes must be used. The absorption of water by the brazing fluxes causes severe corrosion in the brazing seams, as well as producing harmful environmental pollution. In addition, specialized welding equipment and complex technology in pressure welding of Al/Cu joints limited its applications.

Laser welding has several advantages over traditional welding methods, such as low heat inputs, precision-controlled energy inputs and action sites. As a result, the effects induced by the differing physical properties of the metals and the intermetallic components can be reduced or even eliminated by using laser welding, which make laser welding become a feasible means for Al/Cu joining [1–4]. In general, the regulation of the contents of intermetallic components is key factor in laser welding of Al–Cu joints. Mai et al. [5] concluded that the energy input could be reduced by using a pulse laser and that the generation of brittle intermetallic compounds could be suppressed. Gerd et al. [6, 7] found that the brittle intermetallic compounds generated at the interface could be reduced by adding an interlayer consisting of silver (Ag) or nickel (Ni) foil between the aluminum and copper substrate. This method also increased the strength and toughness of the joint. The formation of brittle binary-phase compounds at the interface was inhibited because Ag and Ni can interact with Al and Cu to produce ternary-phase compounds. Furthermore, the addition of Ni foil imposed no significant effects on the strength of welded joint, while the addition of Ag foil remarkably enhanced their tensile strength and fatigue strength, and that the location of the light spot could also affect the strength of welded joint. Xiao et al. [8] developed new laser deep penetration-braze welding technique base on the traditional laser brazing technique. With this new technique, the focused laser beam acted directly on the low-melting-point base metal, and because the power density of the beam exceeded the laser deep-penetration threshold of base metal, the lower melting-point base metal can be melted by deep-penetration welding mode. And then, the liquid low-melting-point base metal infiltrated the high-melting-point base metal interface to form the brazing joint [9–11]. During the laser deep penetration-braze welding process, the low-melting-point base metal was melted using deep-penetration melting method. As a result, the energy utilization



ratio of laser power, as well as the welding efficiency, could be greatly improved compared with conventional laser braze welding. The connections of the butt joints of thick dissimilar materials could also be achieved. Accordingly, the problem that the uncontrollable intermetallic compounds induced by excessive melting of two kinds of base metals could be successfully overcome. Laser deep penetration-braze welding therefore provides new ideas for the welding of aluminum and copper alloys.

In this study, aluminum alloy (1060) and pure copper (T2) were welded using laser deep penetration-braze welding. By optimizing several technological parameters, such as laser power, welding speed and the focus deviation from the interface of Al/Cu, the welded joints with three characteristics, namely laser fusion welding, laser deep penetration braze-fusion welding and laser deep penetration braze welding were achieved. Furthermore, the microstructures, micro-hardness and mechanical properties of these joints were also investigated.

## 2 Experiments

The metals used in the experiment were 1060 aluminium alloy with a 99.6% minimum aluminium content, and rolled commercially pure copper with a 99.9% minimum copper content. The dimensions of the rectangular plates were 100 mm × 50 mm, and 3 mm thick. The nominal compositions of the base materials are listed in Table 1. The surfaces of the plates were ground with grade 800 SiC abrasive papers and cleaned using acetone to remove the oil and dust before welding.

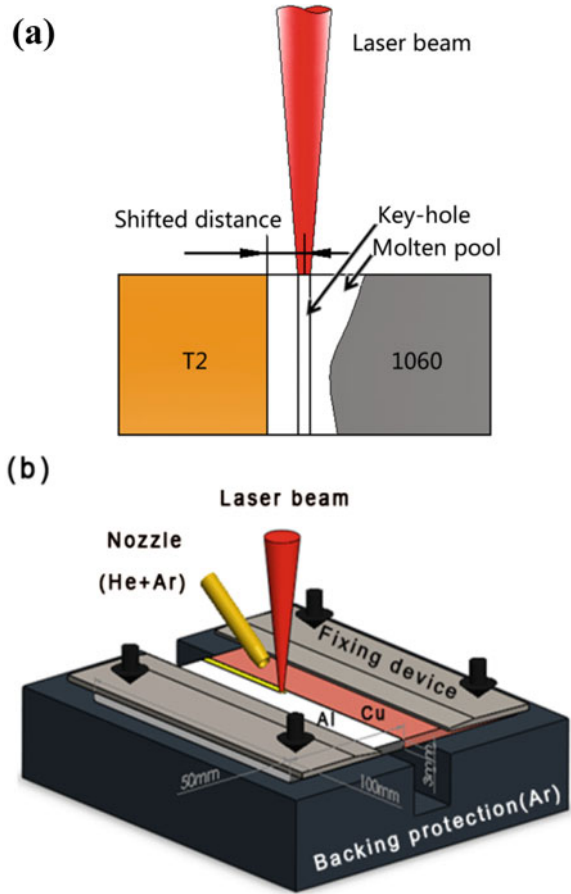
A 4 kW Yb:YAG disk laser (DS040HQ, Rofin, Germany) was used in experiment. The beam quality BPP (beam parameter product) was less than 10 mm mrad. The laser beam was delivered using a 200 μm diameter fibre. The beam was collimated using a 200 mm length collimation and a 300 mm focal length lens that resulted in a focal diameter of approximately 310 μm.

Figure 1a shows the schematic illustration for the laser deep penetration-braze welding experiment. The laser beam is focused on the aluminium side and the aluminium was melted by the key-hole effect. The liquid aluminium infiltrated the copper interface to form the joint. Based on preliminary welding experiments [12], a laser fusion joint (denoted as LF joints, as follow), a laser deep penetration-brazing/fusion joint (denoted as LPB-F joints, as follow) and a laser deep penetration-brazing joint (denoted as LPB joints, as follow) can be obtained depending on the amount of melted copper in the interface of aluminum-copper joint. The welding

**Table 1** Chemical composition of AA1060 and T2 (wt%)

1060	Si	Fe	Cu	Mn	Mg	Zn	Ti	Others	Al
	0.25	0.4	0.05	0.05	0.05	0.05	0.03	0.03	> 99.5
T2	Zn	Sn	Ni	S	Pb	Fe	O	As	Cu
	0.005	0.002	0.005	0.005	0.005	0.005	0.006	0.002	≥ 99.9

**Fig. 1** Schematic illustration for laser deep penetration-braze welding of aluminum-copper joints



parameters in detail are listed in Table 2. Because copper and aluminium are oxidized readily, the samples for welding were protected by a double layer nozzle with helium inside and argon outside for the front, and a holding device with argon for the back, as shown in Fig. 1b.

The samples were cut perpendicularly to the welding direction to conduct metallographic analysis. After grinding and polishing, the aluminium and the welded metal were etched with Keller’s reagent (1 ml HF, 1.5 ml HCl, 2.5 ml HNO<sub>3</sub> and 95 ml

**Table 2** Experimental parameters

Welding parameters	LF joint	LPB-F joint	LPB joint
Laser power (W)	3500	3500	3000
Welding speed (m/min)	1	2	2
Beam shifted distance to the interface of Al/Cu	0.4	0.4	0.4

H<sub>2</sub>O solution), and the copper was etched with 5 g FeCl<sub>3</sub>, 25 ml HNO<sub>3</sub>, 70 ml H<sub>2</sub>O solution. The weld cross-section was examined using an Olympus GX51 optical microscope (OM) and an Olympus CLS3100 confocal laser-scanning microscope (CLSM). The mechanical properties of the joint were measured using a Micromet 5103 microhardness meter and MTS810.22 material testing system. The fractured morphology of the specimens was analysed by an FEI Quanta 200 scanning electron microscope (SEM).

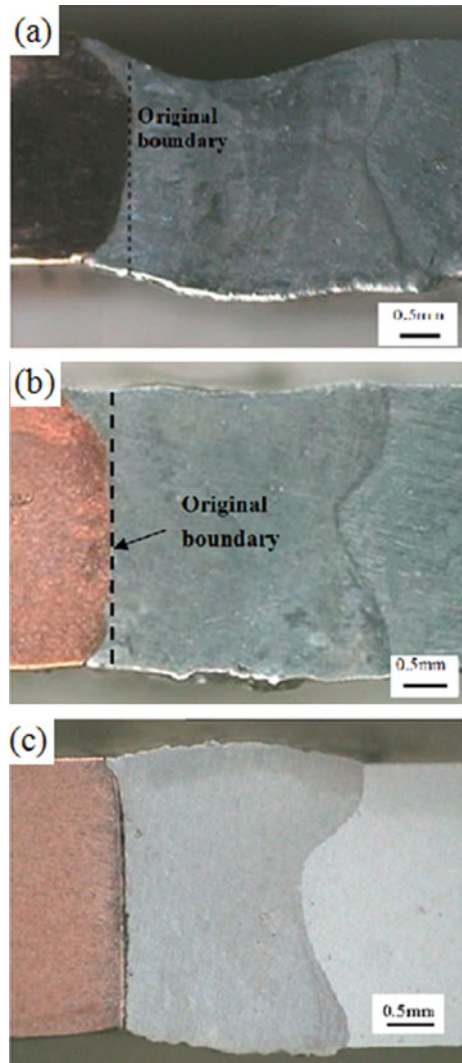
### 3 Results and Discussion

#### 3.1 Forming Characteristics of the Joints

Depending on the amount of melted copper in the interface of aluminum-copper joint, three welded joints with different characteristics were obtained. Figure 2 displays the typical cross-sections of the LF joint, LPB-F joint and LPB joint, respectively. In the LF joint, the Cu substrate melted completely, and the original interface tended to be inconspicuous, as shown in Fig. 2a. Most of Cu in upper part of interface is melted due to the high energy of the laser, while the Cu in the lower part of interface only partly melted under the stirring of molten pool. For the LPB-F joint, the Cu is melted in the upper and lower part of the interface which is similar with LF joints. However, the original interface was retained in the middle of the joint, as shown in Fig. 2b. During this welding process, the liquid-state Al alloy interacted with the solid-state Cu to form the fusion brazing joints. In the LPB joint, the original interface showed no distinct melting, as shown in Fig. 2c. This is likely due to the relatively low energy acted on the Al–Cu interface due to higher welding speed or a greater offset between the beam and the interface. Except for the parts which directed contact with the liquid-state Al alloy, little of the Cu melted by heat conduction, and accordingly, the original interface was retained mostly in LPB joints.

The three welded joints exhibited the similar morphologies on the Al side of the joint, i.e., the weld widths in the upper and lower regions were comparatively wide and the weld width in the center region was narrow. It is a typical laser deep-penetration welding characteristics. The reason is that the laser energy was relatively low at the center region, and rapidly dissipated from Al substrate. Therefore, this region quickly cools down and solidified the earliest. Comparatively, in the upper and lower regions of the joints, the heat was dissipated primarily by air conduction, and thus the heat dissipation and cooling were relatively slow in these regions.

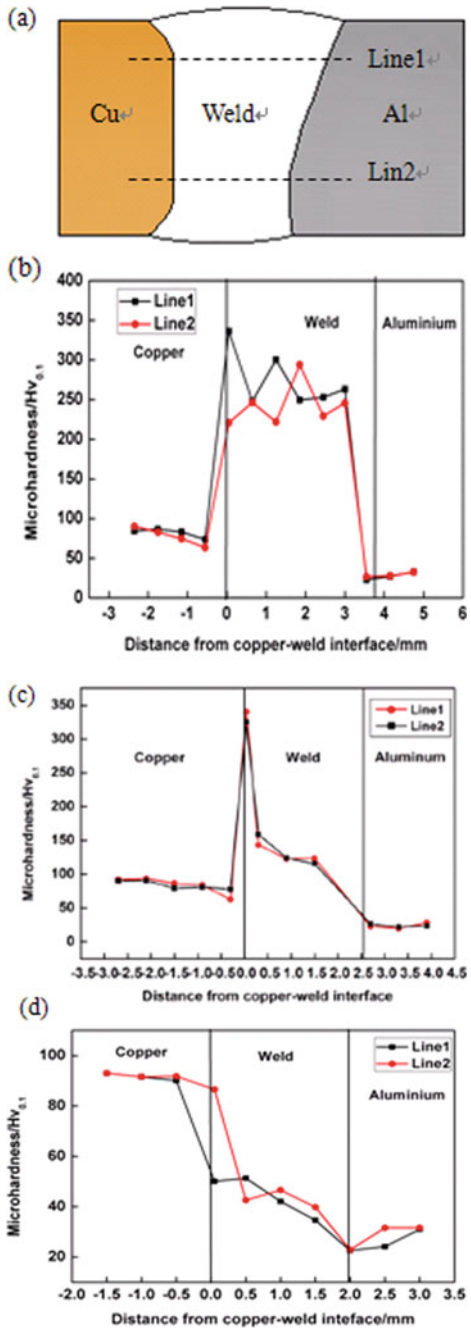
**Fig. 2** The typical Cross sections of copper–aluminum joint. **a** LF joint, **b** LPB-F joint, **c** LPB joint



### 3.2 Micro-hardness Distributions of the Joints

The results of Vickers microhardness of the LF joints, LPB-F joints and LPB joints are shown in Fig. 3. Line1 and Line2 are the upper part and lower part of the joint, respectively. From the Fig. 3, we can find that the microhardness of the LF joint is remarkably higher than that of the LPB-F and LPB joints. Furthermore, in LF joints, the microhardness of weld metal is higher than that in the both base metals, because of the very fine grains and high-hardness intermetallic compounds. With regard to the LPB-F joint, although the micro-hardness of the joint was higher than the base

**Fig. 3** Micro-hardness of joints with different amount melting of copper. **b** LF joint, **c** LPB-F joint, **d** LPB joint



metals Al and Cu, the mean micro-hardness was below that of the LF joint because the fine crystalline grains in the LPB-F joint and little intermetallic compounds exist in the transition layer of the interface resulting the hard regions exist near the interface. But for the LPB joints, there is little Cu melted in interface, Comparatively, the microstructures of the LPB joint are mainly composed of  $\alpha$  (Al), this is the main reason for the relatively low micro-hardness in the LPB joint. Additionally, due to the rapid heating and cooling processes that occurring during laser welding, the crystal grains in the joint are fine, while the micro-hardness of the fusion zone was higher than Al base, and lower than the Cu base.

### 3.3 Mechanical Properties of the Joints

The amount of melted copper greatly affects the mechanical properties of the Al–Cu joints produced using laser deep penetration-braze welding. Figure 4 shows the tensile strength and the fractography of the LF, LPB-F and LPB joints. For the LF joint, the tensile strength was approximately 79 MPa. The facture surface of the LF joint is uneven and randomly distributed, which is a distinctly brittle fracture. With regard to the LPB-F joint, the maximum tensile strength was up to 94.5 MPa, this is close to that of the 1060 aluminium alloy. The facture occurred in the Al base side

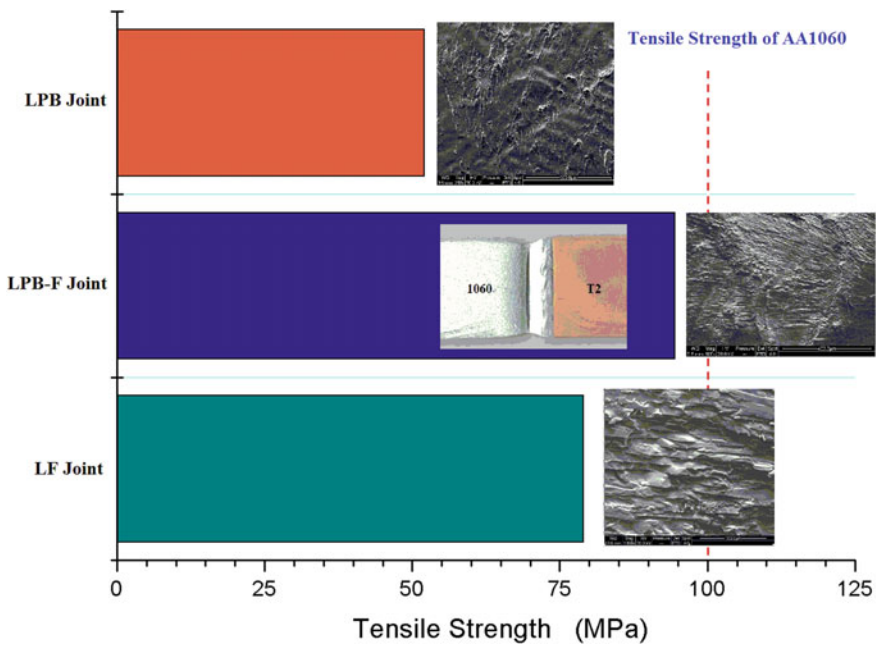


Fig. 4 Tensile strength and fractography of the LF, LPB-F and LPB joint

or the transition layer, and the fracture morphology shows a multiple characteristics of cleavage and intergranular fractures. In the fracture surface of LPB-F joint, the cleavage steps can be observed in the parallel cleavage plane at various heights. At the same time, some comparatively smooth platforms existed between the intergranular fractures and the cleavage plane, exhibiting an obvious characteristic of brittle fracture. The concentration of stress generated by the hardness gradient between the transition layer and the other positions of the fusion zone, and the fact that the brittle intermetallic compound  $Al_2Cu$  occurred in interface, led to the cracks produced and the fractures formed during the tensile tests [13, 14]. However, for the LPB joint, the tensile strength was lowest at approximately 52 MPa. The fracture occurred at the combined position between the intermetallic compound layer and the eutectic layer. The fracture morphology shows that there are no obvious concave or convex morphologies and the cleavage steps existed in the parallel cleavage planes with different heights, and the fractures were also characterized by brittle fractures. Actually, the mechanical properties of the joints are related to the microstructures, and the microstructures of the three joints are discussed in another paper.

## 4 Conclusion

Using laser welding, aluminum alloy (1060) and pure copper (T2) were welded with three characteristics denoted as laser fusion welding (LF joints), laser deep penetration braze-fusion welding (LPB-F joints) and laser deep penetration braze welding (LPB joints) according of the amount of melted copper in the interface of aluminum-copper joint. The amount of melted Cu substrate greatly influenced the mechanical performance of the joints. The tensile strength of LF joints, LPB-F joints and LPB joints are 79 MPa, 94.5 MPa and 52 MPa, respectively. A maximum tensile strength is obtained in LPB-F joints, which is close to that of the 1060 aluminium alloy. The fractures in LPB-F joints occurred in the Al substrate or the transition layer with an obvious characteristic of brittle fracture.

**Acknowledgments** This work is financially supported by the National Natural Science Foundation of China (NSFC) under the Grant No. 50875005 and the Beijing Natural Science Foundation under the Grant No. 3102005.

## References

1. Schbert E, Klassen M, Zerner et al (2001) Light-weight structures produced by laser beam joining for future applications in automobile and aerospace industry. *J Mater Proc Tech* 115(1):2-8
2. Sun Z, Ion JC (1995) Review laser welding of dissimilar metal combinations. *J Mater Sci* 30(17):4205-4214

3. Yu G, Zhao S, Zhang Y et al (2009) Research on key issues of laser welding of dissimilar metal. *Chin J Lasers* 36(2):261–268
4. Yan S, Hong Z, Watanabe T et al (2010) CW/PW dual-beam YAG laser welding of steel/aluminum alloy sheets. *Chin J Lasers* 37(4):1132–1137
5. Mai TA, Spowage AC (2004) Characterization of dissimilar joints in laser welding of steel-kovar, copper-steel and copper-aluminum. *Mater Sci Eng A* 374(1–2):224–233
6. Gerd E, Ihor M, Michael S (2004) Laser micro welding of copper and aluminum using filler materials. *Proc SPIE* 5662:337–342
7. Ihor M, Michael S (2006) Laser micro welding of copper and aluminum. *SPIE* 6107:610703
8. Xiao R, Dong P, Chen K (2009) Laser beam welding of dissimilar materials. *Proc ICALEO* 660–665
9. Pi Y, Dong P, Yang W, Xiong R et al (2007) Laser penetration brazing of brass and low carbon steel. *Chin J Lasers* 34(11):1562–1566
10. Chen K, Xiao R, Pei Y et al (2009) Laser penetration brazing of brass and low carbon steel. *Proc ICALEO* 577–581
11. Lan T, Peng D, Rongshi X (2010) Analysis of laser deep penetration brazing of aluminium and titanium alloys. *Trans China Welding Inst* 31(8):109–112
12. Dong P, Chen K, Xiao R (2009) Laser welding of dissimilar metals between aluminum and copper. In: *Proceedings of 13th Nationwide Nontraditional Machining Academic Meeting*, pp 459–462
13. Baker H (1992) *ASM handbook*. ASM, USA, pp 291–292
14. Xu Y (2010) *Principles of metallography*. Metallurgy Industry Press, Beijing, pp 220–272